

Contents

• Welcome Address	3
• Committees	4
• Guideline for Speakers	8
• Floor Plan	10
• Exhibition	11
• Program	13
Program (Nov. 12)	16
Program (Nov. 13)	18
Program (Nov. 14)	20
• Tutorials	22
• Plenary Speakers	23
• Invited Speakers	28
• Special Sessions	31
• Oral sessions (Day 1 – Nov. 12)	41
• Oral Sessions (Day 2 – Nov. 13)	43
• Oral Sessions (Day 3 – Nov. 14)	49
• Poster Sessions (Day 1 – Nov. 12)	55
• Poster Sessions (Day 2 – Nov. 13)	65
 [Papers]	
• Author Index	75
• Plenary & Invited Lectures	93
• Special Sessions	141
• Oral Sessions	211
• Poster Sessions	285

Welcome Address

The IBEC2015 is second meeting jointly organized by the Korean Society of Medical and Biological Engineering and Korean Society of Biomechanics. About 800 expected researchers, clinicians, and other professionals in the biomedical, we hope the conference will serve as an invaluable venue where all members of Korean biomedical research communities come together to share their research, and enhance mutual interchange between international experts. In addition, since the conference is organized by many biomedical engineering societies, it is our hope that this will create a synergistic effect that will foster future collaborations. Under the theme of "Road to Better Life through Biomedical Engineering", a wide range of scientific programs will be organized, and also there will be a session on the Korean government policy of convergence technology. Under this year's theme, we hope that the gap between basic and clinical research, among countries, and various biomedical fields will be bridged through the IBEC2015.

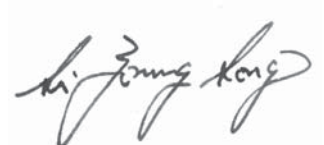
We are certain this conference will be a highly rewarding educational and networking experience for all. We cordially invite you to take this opportunity to explore the field of biomedical engineering and also unique Korean culture.

We look forward to seeing you at the IBEC2015 in Gyeongju, Korea this coming November.



Si Young Song

Chair, Organizing Committee of IBEC2015



Committees

Organizing Committee

Chair: Si Young Song (Yonsei University, Korea)

Co-Chair: Sung-Jae Lee (Inje University, Korea)

Eun Jong Cha (Chungbuk National University, Korea)

Member: Kwangsuk Park (Seoul National University, Korea)

Kuiwon Choi (Korea Institute of Science and Technology, Korea)

Eung Je Woo (Kyung Hee University, Korea)

Chang-Hwan Im (Hanyang University, Korea)

Gye Rae Tack (Konkuk University, Korea)

Dong-Hyun Kim (Yonsei University, Korea)

Won-Jin Yi (Seoul National University, Korea)

Dohyung Lim (Sejong University, Korea)

Inchan Youn (Korea Institute of Science and Technology, Korea)

International Advisory Committee

Chair: Kwangsuk Park (Seoul National University, Korea)

Co-Chair: Kuiwon Choi (Korea Institute of Science and Technology, Korea)

Member: Arthur Mak (The Chinese University of Hong Kong, Hong Kong)

Constantinos S. Pattichis (University of Cyprus, Cyprus)

Danilo De Rossi (University of Pisa, Italy)

Fong-Chin Su (Cheng-Kung University, Taiwan)

Hee Chan Kim (Seoul National University, Korea)

James Cho Hong Goh (National University of Singapore, Singapore)

Ki H. Chon (University of Connecticut, USA)

Luvsan Ajnai (Mongolian National University of Medical Sciences, Mongolia)

Masaki Makikawa (Ritsumeikan University, Japan)

Masaki Yoshida (Osaka Electro-communication University, Japan)

Nigel H. Lovell (University of South Wales, Australia)
Niilo Saranummi (VTT Technical Research Centre, Finland)
Paolo Bonato (Harvard Medical School, USA)
Sergio Cerutti (Politecnico di Milano, Italy)
Takeo Matsumoto (Nagoya Institute of Technology, Japan)
V.R.Singh (National Physical Laboratory, India)
Vicente Traver (University Politecnica de Valencia, Spain)
Wan-Young Chung (Pukyong National University, Korea)

Scientific Program Committee

Chair: Eung Je Woo (Kyung Hee University, Korea)
Co-Chair: Chang-Hwan Im (Hanyang University, Korea)
Gye Rae Tack (Konkuk University, Korea)
Member: Dong-Hyun Kim (Yonsei University, Korea)
Gi-Ja Lee (Kyung Hee University, Korea)
Hongki Yoo (Hanyang University, Korea)
Inchan Youn (Korea Institute of Science and Technology, Korea)
Jennifer H. Shin (Korea Advanced Institute of Science and Technology (KAIST), Korea)
Kyeihan Rhee (Myongji University, Korea)
Seungbum Koo (Chung-Ang University, Korea)
Yong Jeong (Korea Advanced Institute of Science and Technology (KAIST), Korea)
Euiheon Chung (Gwangju Institute of Science and Technology, Korea)
Yongnam Song (Korea University, Korea)
Yoonkey Nam (Korea Advanced Institute of Science and Technology, Korea)
Young Bin Choy (Seoul National University College of Medicine, Korea)

Finance Committee

Co-Chair: Won-Jin Yi (Seoul National University, Korea)
Inchan Youn (Korea Institute of Science and Technology, Korea)

Secretary General

Chair: Inchan Youn (Korea Institute of Science and Technology, Korea)

Local Organizing Committee

Chair: Dong-Woo Cho (Pohang University of Science and Technology, Korea)

Member: Chulhong Kim (POSTECH, Creative IT Engineering, Korea)

Dong Jun Yang (Mega'gen Implant CO. LTD, Korea)

Hui-Suk Yun (Korea Institute of Materials Science, Korea)

Jeonghun Ku (Keimyung University, Korea)

Jinho Suh (Korea Institute of Robot and Convergence, Korea)

Jong In Youn (Catholic University of Daegu, Korea)

Jung Hoon Ro (Pusan National University, Korea)

Junsang Doh (POSTECH, Korea)

Jun-Uk Chu (Korea Institute of Machinery and Materials, Korea)

Ok Chan Jeong (Inje University, Korea)

Sang Hee Nam (Inje University, Osong Medical Innovation Foundation, Korea)

Sebyung Kang (Ulsan National Institute of Science and Technology, Korea)

Seo Suk Tae (Daegu-Gyeongbuk Medical Innovation Foundation Medical Device Development Center, Korea)

Soocheol Lee (Daegu University, Korea)

Sukyong Kim (Yeungnam University, Korea)

Tae Kwan Um (Austem, Korea)

Young Joon Chee (University of Ulsan, Korea)

Program Track Chair

T1. Biomedical Imaging and Optics

Byungjo Jung (Yonsei University, Korea)

Dong-Hyun Kim (Yonsei University, Korea)

T2. Biosignal Processing and Neural Engineering

Yoon Key Nam (Korea Advanced Institute of Science and Technology, Korea)

Jong-Ha Lee (Keimyung University, Korea)

T3. Nanobiosensor and Instrumentation

Young Bin Choy (Seoul National University College of Medicine, Korea)

Gi-Ja Lee (Kyung Hee University, Korea)

T4. Therapeutic and Diagnostic Devices and Systems

Sung Min Kim (Dongguk University, Korea)

Euiheon Chung (Gwangju Institute of Science and Technology, Korea)

T5. Biomechanics

Gye Rae Tack (Konkuk University, Korea)

Yongnam Song (Korea University, Korea)

T6. Biomedical Robotics and Rehabilitation Engineering

Seung-Jong Kim (Korea Institute of Science and Technology, Korea)

Seungbum Koo (Chung-Ang University, Korea)

T7. Molecular and Cellular Biomechanics, Tissue Engineering and Biomaterials

Jeong Woog Shin (Inje University, Korea)

Jennifer H. Shin (Korea Advanced Institute of Science and Technology, Korea)

T8. Cardiovascular and Respiratory System Engineering

Kyehan Rhee (Myongji University, Korea)

Sang-Wook Lee (Ulsan University, Korea)

Guideline for Speakers

Oral Presentation

In order to ensure that the program runs smoothly, speakers are requested to submit and stand by presentation file with operator in each session starts.

Presentation time

Presentation	Time
Plenary Lecture	45 min
Invited Lecture	30 min
Oral	15 min

The beam projector with notebook computer will be prepared in each presentation room. You could bring your own computer.

Poster Presentation

※ Punctuality is imperative for the author to be reviewed for the student paper competition.

1. Poster Presentation Schedule

(1) For authors to have poster presentations on Day 1 (November 12_Thu)

- Posters should be placed before 13:30 on Nov. 12 (Thu)
- Poster display time: 13:30 on Nov. 12 (Thu) – 18:30 on Nov. 12 (Thu)
- Poster presentation time: 14:45 – 15:45 on Nov. 12 (Thu)
- Posters should be removed: 08:00 – 09:00 on Nov. 13 (Fri)

(2) For authors to have poster presentations on Day 2 (November 13_Fri)

- Posters should be placed before 10:00 on Nov. 13 (Fri)
- Poster display time: 10:00 on Nov. 13 (Fri) – 11:45 on Nov. 14 (Sat)
- Poster presentation time: 11:30 – 12:30 on Nov. 13 (Fri)
- Posters should be removed: 11:45 – 12:45 on Nov. 14 (Sat)

2. Presentation venue: Exhibition Hall (Convention C, B1)

[Notice]

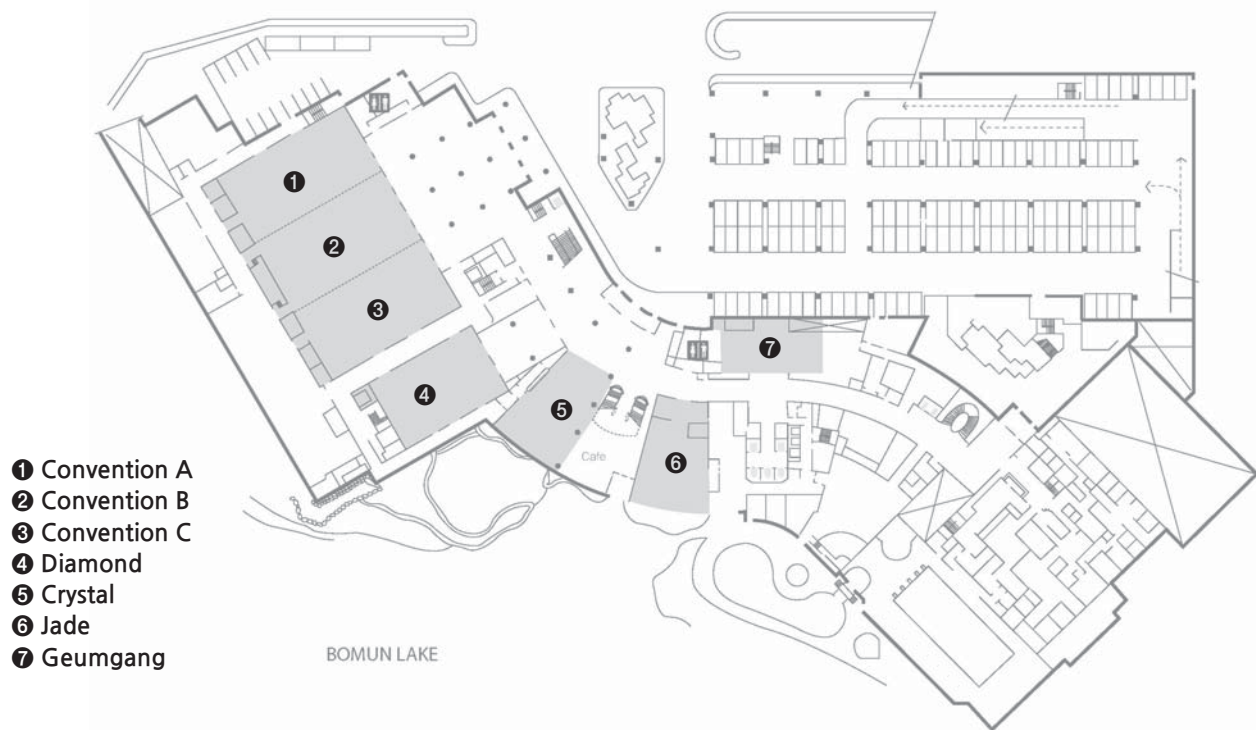
- The presentation number will be posted at the top of each panel.
Please use a correct board labeled with your presentation number.
- Presenters are expected to be available near their poster during the presentation time and stand by near the poster area for discussion with the participants.
- Presenters are required to keep the presentation schedule to be reviewed for the student paper competition.
- Please use a scotch tape only for attaching your poster. Using pins is strictly prohibited on the board.

Information for Session Chair

Chairs of each session should arrive at the session room 10 minutes earlier the session and check the attendance of speakers in the session.

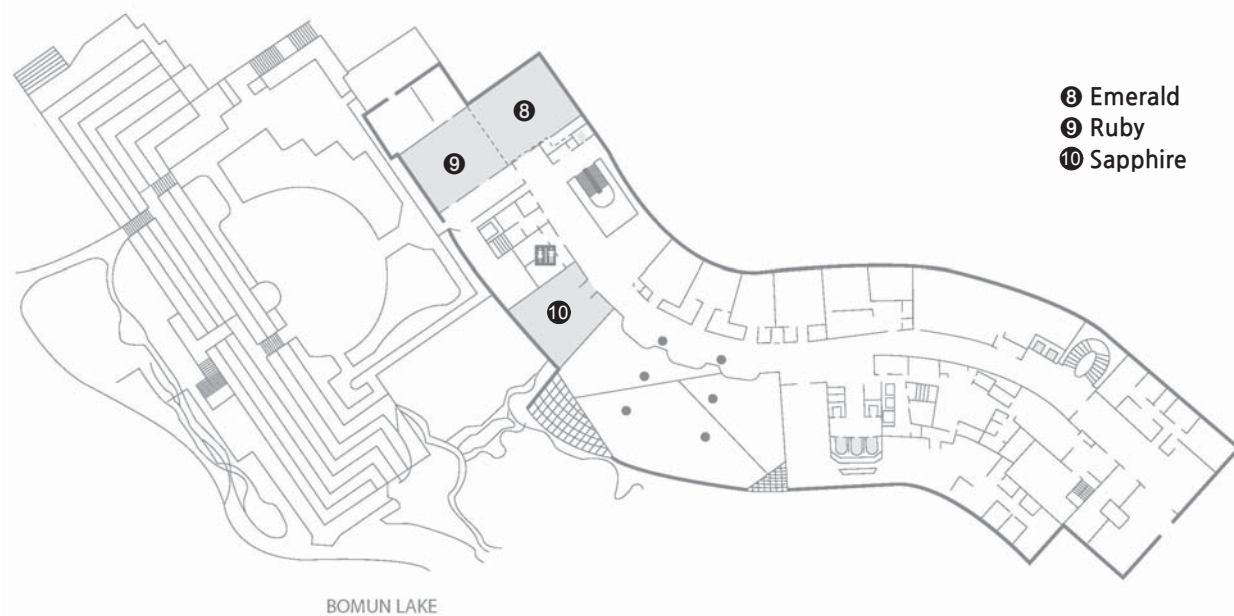
Floor Plan

B1F



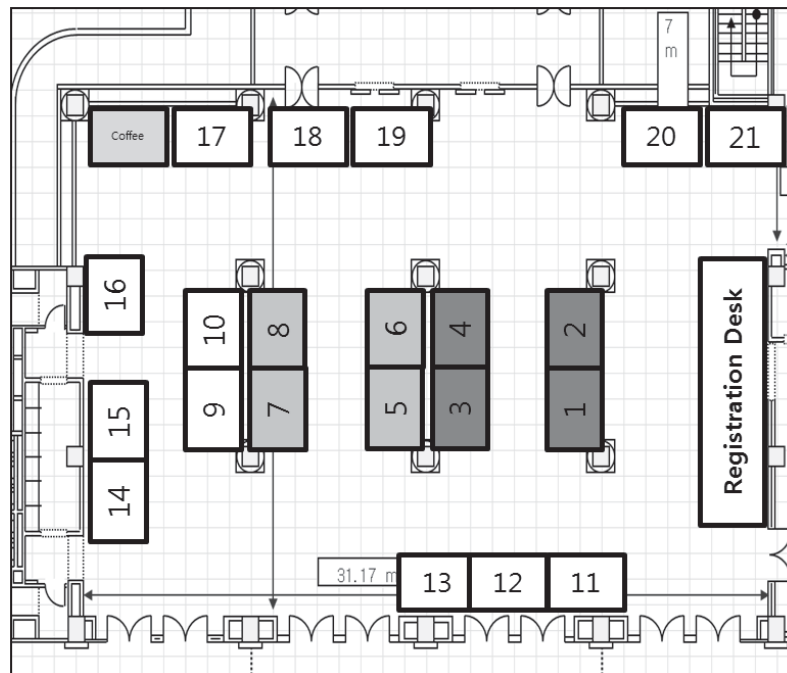
- ❶ Convention A
- ❷ Convention B
- ❸ Convention C
- ❹ Diamond
- ❺ Crystal
- ❻ Jade
- ❼ Geumgang

2F



- ❸ Emerald
- ❹ Ruby
- ❺ Sapphire

Exhibition



No.	Exhibitors	Booth
1,2	U&I	Platinum
3,4	OLYMPUS KOREA	Platinum
5	GS Medical	Gold
6	Corentec	Gold
7	Department of Medical Device Management and Research, SKKU	Gold
8	Korea Institute of Science and Technology (KIST)	Gold
9	Mediana	Silver
10	SEEDTECH	Silver
11	DGMIF : Daegu-Gyeongbuk Medical Innovation Foundation	Silver
12	"Hospital - company connective medical device R&D platform" construction project	Silver
13	Medyssey	Silver
14	Tobii Technology Korea	Silver
15	DooRee System Technology	Silver
16	Meta-biomed	Silver
17	Life Science Technology	Silver
18	Targeted Precision Treatment Research Center	Silver
19	Impedance Imaging Research Center	Silver
20	The Advanced Research Team For Nurturing Special Personnel In Human-Oriented Core Technical Components Of Smart Vehicles, created and supported by National Research Foundation of Korea(NRF)	Silver
21	Biopac	Silver

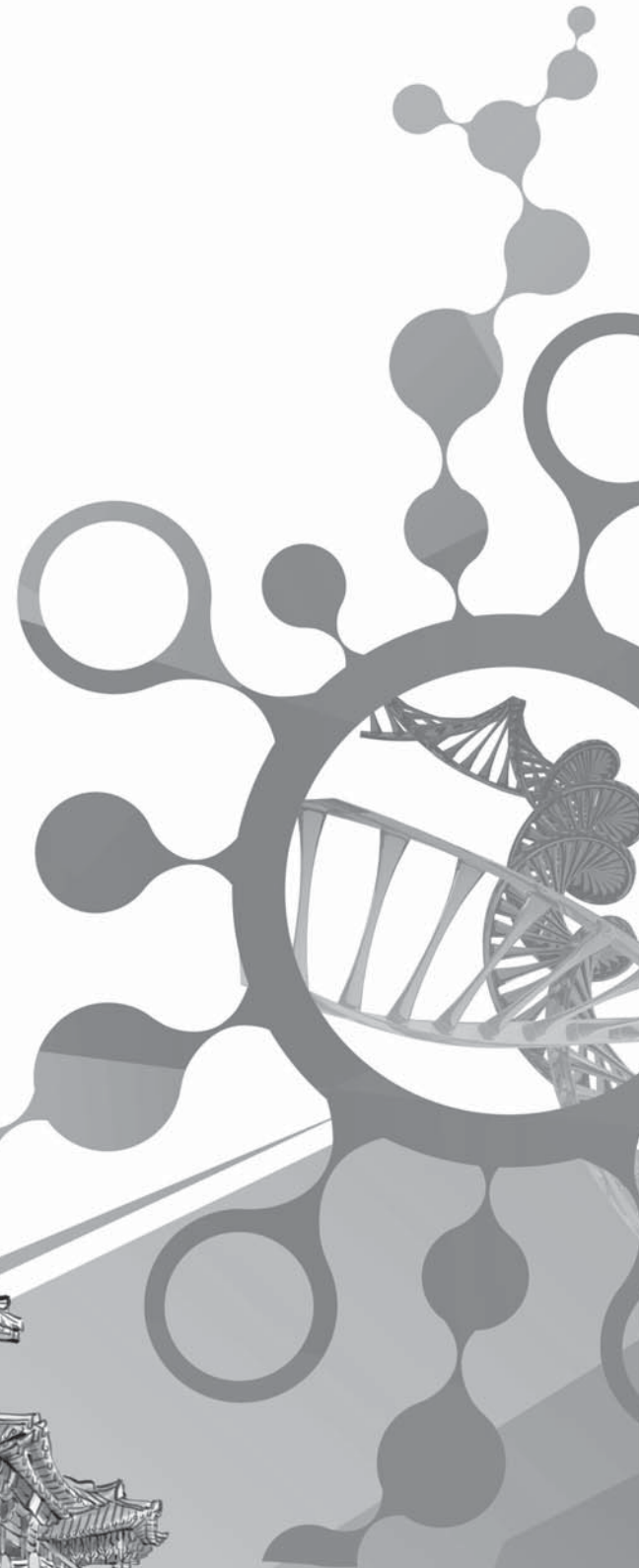
IBEC

International Biomedical
Engineering Conference 2015

2015

Road to Better Life through Biomedical Engineering

PROGRAM



Program at a Glance

Time/Date	November 12 (Thu)		November 13 (Fri)	November 14 (Sat)		
08:30-09:00			Registration	Registration		
09:00-09:15			Oral Session	Oral Session		
09:15-09:30						
09:30-09:45						
09:45-10:00						
10:00-10:15						
10:15-10:30						
10:30-10:45			Break (15 min)	Plenary Lecture 4		
10:45-11:00						
11:00-11:15	Tutorial		Plenary Lecture 2	Closing Ceremony		
11:15-11:30						
11:30-11:45						
11:45-12:00			Poster Session 2			
12:00-12:15	Registration		Lunch			
12:15-12:30						
12:30-12:45						
12:45-13:00						
13:00-13:15						
13:15-13:30			Plenary Lecture 3			
13:30-13:45	Opening Ceremony					
13:45-14:00			Oral Session			
14:00-14:15	Plenary Lecture 1					
14:15-14:30			Oral Session			
14:30-14:45	Poster Session 1					
14:45-15:00						
15:00-15:15						
15:15-15:30						
15:30-15:45						
15:45-16:00	Oral Session		Break (15 min)			
16:00-16:15						
16:15-16:30						
16:30-16:45						
16:45-17:00						
17:00-17:15			Break (15 min)			
17:15-17:30	Break (15 min)					
17:30-17:45	KOSOMBE General Meeting	KSB General Meeting				
17:45-18:00			Break (15 min)			
18:00-20:00			Banquet			

Program (Nov. 12)

from	to	Lobby (B1)	Convention C	Convention A	Convention B	Diamond	Crystal			
9:30	11:00	Registration	<div style="border: 1px solid black; padding: 10px; width: fit-content; margin: auto;"> <p>Tutorial 1: Bio-photonics</p> </div>							
11:00	11:15									
11:15	11:30									
11:30	11:45									
11:45	12:00									
12:00	13:30									
13:30	13:45									
13:45	14:00									
14:00	14:15									
14:15	14:30									
14:30	14:45		<div style="border: 1px solid black; padding: 10px; width: fit-content; margin: auto;"> <p>Opening Ceremony</p> </div>							
14:45	15:00									
15:00	15:15		<div style="border: 1px solid black; padding: 10px; width: fit-content; margin: auto;"> <p>Plenary Lecture 1 Andrew F. Laine Chair: Kwang Suk Park (Seoul National University, Korea)</p> </div>							
15:15	15:30									
15:30	15:45		<div style="border: 1px solid black; padding: 10px; width: fit-content; margin: auto;"> <p>Poster Presentation 1</p> </div>							
15:45	16:00									
16:00	16:15									
16:15	16:30									
16:30	16:45									
16:45	17:00									
17:00	17:15									
17:15	17:30									
17:30	17:45									
17:45	18:00									
18:00	18:15	<table border="1" style="width: 100%; text-align: center;"> <tr> <td style="width: 25%;"> T1.S1: Biomedical Imaging and Optics (1) Chair: Dong-Hyun Kim (Yonsei University, Korea) </td> <td style="width: 25%;"> SS1: Role and Work of Biomedical Engineers in Research-driven Hospitals Chair: Si Young Song (Yonsei University, Korea) </td> <td style="width: 25%;"> T5.S1: Biomechanics Chair: Wenming Chen (Inje University, Korea) </td> <td style="width: 25%;"> SS2: Artificial Nerve Networking Pioneer Project Chair: In Chan Youn (KIST, Korea) </td> </tr> </table>					T1.S1: Biomedical Imaging and Optics (1) Chair: Dong-Hyun Kim (Yonsei University, Korea)	SS1: Role and Work of Biomedical Engineers in Research-driven Hospitals Chair: Si Young Song (Yonsei University, Korea)	T5.S1: Biomechanics Chair: Wenming Chen (Inje University, Korea)	SS2: Artificial Nerve Networking Pioneer Project Chair: In Chan Youn (KIST, Korea)
T1.S1: Biomedical Imaging and Optics (1) Chair: Dong-Hyun Kim (Yonsei University, Korea)	SS1: Role and Work of Biomedical Engineers in Research-driven Hospitals Chair: Si Young Song (Yonsei University, Korea)						T5.S1: Biomechanics Chair: Wenming Chen (Inje University, Korea)	SS2: Artificial Nerve Networking Pioneer Project Chair: In Chan Youn (KIST, Korea)		
18:15	18:30									

Jade	Geumgang	Emerald(2F)	Ruby(2F)	Sapphire(2F)	from	to
Tutorial 2: Electro-chemistry	KOSOMBE Council Meeting	KSB Council Meeting			9:30	11:00
					11:00	11:15
					11:15	11:30
					11:30	11:45
					11:45	12:00
					12:00	13:30
					13:30	13:45
					13:45	14:00
					14:00	14:15
					14:15	14:30
					14:30	14:45
					14:45	15:00
					15:00	15:15
					15:15	15:30
SS3: Targeted POP Cancer Treatment Techniques Chair: Hun K. Park (Kyung Hee University, Korea)	T3.S1: Nanobiosensor and Instrumentation (1) Chair: Young Bin Choy (Seoul National University, Korea)	T7.S1: Cell & Tissues I Chair: Jeong Woog Shin (Inje University, Korea)			15:30	15:45
					15:45	16:00
					16:00	16:15
					16:15	16:30
					16:30	16:45
Break					16:45	17:00
					17:00	17:15
					17:15	17:30
	KOSOMBE General Meeting	KSB General Meeting			17:30	17:45
					17:45	18:00
					18:00	18:15
					18:15	18:30

Program (Nov. 13)

from	to	Lobby (B1)	Convention C	Convention A	Convention B	Diamond	Crystal								
8:00	9:00	Registration		<p>T1.S2: Biomedical Imaging and Optics (2) Chair: TBA</p>	<p>SS4: Endoscopic Imaging for POP Cancer Treatment Chair: Kyung Min Byun (Kyung Hee University, Korea)</p>	<p>T5.S2: General Biomechanics Chair: Yongnam Song (Korea University, Korea)</p>	<p>SS5: Medical Robot Chair: Sungwan Kim (Seoul National University, Korea) Dong-Soo Kwon (KAIST, Korea) Chiwon Lee (Seoul National University, Korea)</p>								
9:00	9:15														
9:15	9:30														
9:30	9:45														
9:45	10:00														
10:00	10:15														
10:15	10:30														
10:30	10:45														
10:45	11:00														
11:00	11:15							<p>Plenary Lecture 2 Hak Hyun Nam Chair: Eung Je Woo (Kyung Hee University, Korea)</p>							
11:15	11:30														
11:30	11:45														
11:45	12:00							<p>Poster Presentation 2</p>							
12:00	12:15														
12:15	12:30														
12:30	12:45							<p>Luncheon Seminar 1 [DS Maref] [U&I]</p>		<p>Luncheon Seminar2 [Lutronic]</p>		<p>Luncheon Seminar 3 [MEK-ICS] [Healcerion]</p>		<p>Luncheon Seminar 4 [KBIO] [DGMIF]</p>	
12:45	13:00														
13:00	13:15														
13:15	13:30														
13:30	13:45														
13:45	14:00							<p>Plenary Lecture 3 Kevin John Otto Chair: In Chan Youn (KIST, Korea)</p>							
14:00	14:15														
14:15	14:30														
14:30	14:45							<p>SS7: Recent Progresses in Sleep Monitoring Chair: Kwang Suk Park (Seoul National University, Korea)</p>		<p>SS8: Brain-on-a-Chip Technology Chair: SangHoon Lee (Korea University, Korea)</p>		<p>T5.S3: Sports Biomechanics Chair: Seyong Lee (Yonsei University, Korea)</p>		<p>SS9: Medical Devices in Traditional Medicine - Pulse Diagnostic System and Pulse Simulator Chair: Jaeuk Kim (Korea Institute of Oriental Medicine, Korea)</p>	
14:45	15:00														
15:00	15:15														
15:15	15:30														
15:30	15:45														
15:45	16:00														
16:00	16:15														
16:15	16:30	<p>T2.S1: Biosignal Processing Chair: Yoon Key Nam (Korea Advanced Institute of Science and Technology, Korea) Jong-Ha Lee (Keimyung University, Korea)</p>		<p>T6.S1: Biomedical Robotics Chair: Seungbum Koo (Chung-Ang University, Korea)</p>		<p>T1.S3: Biomedical Imaging and Optics (3) Chair: Hyungsoek Yoo (University of Ulsan, Korea)</p>									
16:30	16:45														
16:45	17:00														
17:00	17:15														
17:15	17:30														
17:30	17:45														
17:45	18:00														
18:00	20:00	<p>Banquet</p>													

Jade	Geumgang	Emerald(2F)	Ruby(2F)	Sapphire(2F)	from	to
					8:00	9:00
T8.S1: Cardiovascular and Respiratory System Engineering Chair: Kyeihan Rhee (Myongji University, Korea)	SS6: KHIDI Forum for Sharing of Domestic Medical Device Industry R&D Chair: JinSu Lee (KDIDI, Korea)	T7.S2: Biochips & Cellular Analysis Chair: Jennifer H. Shin (Korea Advanced Institute of Science and Technology, Korea)	T4.S1: Bio-signal Measurement Chair: Byeong Cheol Choi (Choonhae College of Health Sciences, Korea) Honggu Chun (Korea University, Korea)		9:00	9:15
					9:15	9:30
					9:30	9:45
					9:45	10:00
					10:00	10:15
Break					10:15	10:30
					10:30	10:45
					10:45	11:00
					11:00	11:15
					11:15	11:30
					11:30	11:45
					11:45	12:00
					12:00	12:15
					12:15	12:30
Luncheon Seminar 5 [KOHEA] Chair: Sung Min Kim (Dongguk University, Korea)					12:30	12:45
					12:45	13:00
					13:00	13:15
					13:15	13:30
					13:30	13:45
					13:45	14:00
					14:00	14:15
					14:15	14:30
SS10: Current Studies at Biomedical Engineering, Yonsei University Chair: Byungjo Jung (Yonsei University, Korea)	SS11: Laser Tactile Sensation Chair: Jae-Hoon Jun (Konkuk University, Korea)	T7.S3: Biomaterials Chair: Kwideok Park (KIST, Korea)	T4.S2: Medical Imaging Chair: Sun Kook Yoo (Yonsei University, Korea) Eui Heon Chung (Gwangju Institute of Science and Technology, Korea)	T3.S2: Nanobiosensor and Instrumentation (2) Chair: Gi-Ja Lee (Kyung Hee University, Korea)	14:30	14:45
					14:45	15:00
					15:00	15:15
					15:15	15:30
					15:30	15:45
					15:45	16:00
Break					16:00	16:15
SS12: Frontiers in Translational Neurotechnology Chair: Chang-Hwan Im (Hanyang University, Korea) Dong-Pyo Jang (Hanyang University, Korea)	SS13: Recent Progress in the Artificial Retina Research Chair: Jong-Mo Seo (Seoul National University, Korea)	T7.S4: Cell & Tissues II Chair: In-Kyu Park (Cheonnam University, Korea)	T4.S3: Medical Diagnostic System Chair: Sang Joon Lee (Sun Moon University, Korea) Sung Min Kim (Dongguk University, Korea)		16:15	16:30
					16:30	16:45
					16:45	17:00
					17:00	17:15
					17:15	17:30
					17:30	17:45
					17:45	18:00
					18:00	20:00

Program (Nov. 14)

from	to	Lobby (B1)	Convention C	Convention A	Convention B	Diamond	Crystal		
8:00	9:00	Registration		T1.S4: Biomedical Imaging and Optics (4) Chair: TBA	T2.S2: Neural Engineering Chair: Chang-Hwan Im (Hanyang University, Korea) Sang Beom Jun (Ewha Womans University, Korea)	T6.S2: Biomedical Robotics Chair: Sung Chan Jun (Gwangju Institute of Science and Technology)	SS14: Measurement, Uncertainty, and Reference Standards for Biomedical Engineers Chair: Jung Hoon Ro (Pusan National University, Korea)		
9:00	9:15								
9:15	9:30								
9:30	9:45								
9:45	10:00								
10:00	10:15								
10:15	10:30								
10:30	10:45								
10:45	11:00							Plenary Lecture 4 Jin Woo Chang Dong-Hyun Kim (Yonsei University, Korea)	
11:00	11:15								
11:15	11:30	Closing Ceremony							
11:30	11:45								

Jade	Geumgang	Emerald(2F)	Ruby(2F)	Sapphire(2F)	from	to
					8:00	9:00
SS15: Recent Developments in Electrical Impedance Imaging Chair: Tong In Oh (Kyung Hee University, Korea)		T7.S5: 3D Printing & Tissue Engineering Chair: Seheang Oh (Dankook University, Korea)			9:00	9:15
					9:15	9:30
					9:30	9:45
					9:45	10:00
					10:00	10:15
					10:15	10:30
					10:30	10:45
					10:45	11:00
					11:00	11:15
					11:15	11:30
					11:30	11:45

Tutorials

Tutorial 1: Nov. 12, 2015 (Thu) 11:00-11:50 / Room: Crystal

Bio-photonics

Euiheon Chung (Gwangju Institute of Science and Technology, Korea)

Biophotonics, integrating biology and photonics, enables early detection of diseases and new light-guided treatment modalities based on the interactions between light and biological matter. This tutorial covers core knowledge for biomedical engineers or clinical scientists to utilize modern biophotonic technology.

Tutorial 2: Nov. 12, 2015 (Thu) 11:00-11:50 / Room: Jade

Electro-chemistry

Gi-Ja Lee (Kyung Hee University, Korea)

Electrochemistry is an important branch of chemistry that deals with the chemical action of electricity and/or the production of electricity by chemical reactions. It plays a significant role in biological reactions. This course will address the basics of electrochemistry including electrode potentials & Nernst equation, electrode reaction. And the most common techniques used in electrochemistry such as linear and cyclic voltammetry, chronoamperometry, potentiometry and others will be presented. The course will deal also with practical topics and applications in electrochemistry including amperometric biosensors, immunoassays, electrochemistry of DNA, biofuel cells, whole cell biosensors, in vivo applications and bioelectrosynthesis.

Plenary Speakers

Nov. 12, 2015 (Thu) 14:00-14:45 / Room: Convention A, B

Quantitative imaging informatics in cost effective pet imaging and classification of lung disease

Andrew F. Laine

Percy K. and Vida L. W. Hudson Professor, Chair, Department of Biomedical Engineering, Professor of Radiology (Physics), Department of Radiology, Director, Heffner Biomedical Imaging Laboratory, Columbia University, New York, NY



This talk presents a novel method for emphysema quantification, based on parametric modeling of intensity distributions in the lung and a hidden Markov measure field model to segment emphysematous regions. The framework adapts to the characteristics of an image to ensure a robust quantification of emphysema under varying CT imaging protocols and differences in parenchymal intensity distributions due to factors such as inspiration level.

Compared to standard approaches, the present model involves a larger number of parameters, most of which can be estimated from data, to handle the variability encountered in lung CT scans. The method was used to quantify emphysema on a cohort of 87 subjects, with repeated CT scans acquired over a time period of 8 years using different imaging protocols. The scans were acquired approximately annually, and the data set included a total of 365 scans. The results show that the emphysema estimates produced by the proposed method have very high intra-subject correlation values. By reducing sensitivity to changes in imaging protocol, the method provides a more robust estimate than standard approaches. In addition, the generated emphysema delineations promise great advantages for regional analysis of emphysema extent and progression, possibly advancing disease subtyping, including COPD.

An important tool for studying brain disorders is positron emission tomography (PET), a nuclear imaging technology that allows for the in vivo functional characterization and quantification of blood flow, metabolism, protein distribution, and drug occupancy using radioactively tagged probes (tracers). Full quantification of PET images requires invasive arterial input function (AIF) measurement through online arterial blood sampling for the duration of the scan (1-2 hours). The AIF is used to correct images by accounting for the tracer bioavailability, which depends on an individual's physiological capacity for clearance, distribution and metabolism of

the tracer. However, AIF measurement is invasive, risky, time consuming, uncomfortable for patients, and costly. Perhaps most importantly, it is impractical at the point-of-care and therefore limits clinical utility of PET. We believe an integrative multi-modal approach is possible via the amount of personalized information about the physiological and biochemical makeup of individuals available in their electronic health record (EHR). This talk will outline a novel approach to combine EHR and dynamic PET imaging data in an optimization framework based on simulated annealing to non-invasively estimate the AIF. Techniques that will be outlined are applicable across imaging modalities, organs and diseases, such as functional imaging of prostate cancer images where increasingly more complex tracers are utilized for assessment and require AIF measurement.

Nov. 13, 2015 (Fri) 10:45-11:30 / Room: Convention A, B

Development and business of biosensor-based medical devices

Hakhyun Nam

*Department of Chemistry, Kwangwoon University, Seoul Korea,
i-SENS, Inc., Seocho-gu, Seoul, Korea*



Scientists and Engineers are often asked to include a lengthy justification of their R&D in terms of current or assumed economic values and also requested to provide useful products to the society they belong as the output of their funded researches. The success of the funded R&D's, especially in the biomedical science and engineering area, are often measured by the demonstration with engineered mock-ups. On the other hand, most R&D results are archived in the database after demonstrations and lengthy reports, and never be delivered to intended markets. Some researchers who believe the innovation and the economic potential of their own R&D results venture out of their laboratories to make business.

I and my colleague, Prof. Geun Sig Cha have been worked together to develop bio- and chemical sensors for academic interests and/or industrial applications since 1992.

They include ion sensors, immunoassay sensors, lab-on-a-chip type devices for environmental and biomedical applications and point-of-care testing devices with the governmental and/or industrial R&D funds. After the economic crisis of Korea in 1997, researchers in universities and various institutes are encouraged and legally allowed to make business with their R&D products. Prof. Cha and I, and several graduate students in my lab took the opportunity in year 2000 and started the laboratory-based company i-SENS.

While there were several possible R&D products we could develop for the market of that time, we chose to start in a highly competitive glucose sensor business. As the business grows, we also tried to develop several other products, such as the electrolyte analyzer, lab-on-a-chip type immunosensors, HbA1c analyzer, and so on. In this presentation, I will summarize why and how we made R&D and business decisions and how they had resulted in failure or actual business. Although my talk will mostly focus on our own limited experiences in Korea, it may give some guide for those who wish to venture out of their laboratory.

Nov. 13, 2015 (Fri) 13:45-14:30 / Room: Convention A, B

Neuroengineering the interface of micro-devices with the brain

Kevin John Otto

J. Crayton Pruitt Family Department of Biomedical Engineering, University of Florida



Direct interfacing of micro-devices with the brain has the potential to revolutionize the medical treatment of many neurological diseases or injuries. Unfortunately, chronic implantation and utilization of neural micro-devices results in a reactive tissue response that both functionally isolates the device from the tissue as well as triggers neuronal apoptosis or migration. The tissue response presents a fundamental obstacle to the design of neuroprostheses. Previous research has shown that the tissue responds to: 1) the initial device insertion, 2) the device indwelling, and 3) the application of the electrical stimulation. The goal of our ongoing research is to understand and mitigate this tissue response, thus enabling the development of multi-channel neural interfaces for clinical therapy.

In particular, our primary research objective is to determine the interdependent effects of device design, electrophysiological recording, electrical stimulation, optical stimulation, and the reactive tissue response on the efficacy of neural interfaces. To this end, we conduct psychophysical experiments using multi-channel cortical implants in the cortex. Furthermore, we collect longitudinal electrochemical and electrophysiological data via the implanted devices. We investigate several chemically- and electrically-based tissue-response mitigation strategies. Finally, we use advanced histological approaches to evaluate the device-tissue interface. I will discuss the results of these various approaches and their implications for reliable chronic neural interfacing via micro-devices. We expect that these data will enable further neuroprosthetic development for many potential applications of neural interfaces.

Nov. 14, 2015 (Sat) 10:30-11:15 / Room: Convention A, B

Stereotactic & functional neurosurgery: A unique interface of research environment

Jin Woo Chang

Department of Neurosurgery, Yonsei Univ. College of Medicine, Seoul, Korea



Our knowledge of the nervous system in health and disease has, however, increased considerably during the last fifty years and today, neurosurgery reveals promising new stereotactic strategies such as neuromodulation by the thermal lesioning, deep brain stimulation, radiosurgery, or etc to deal with diseases of the nervous system. These stereotactic procedures have been one of the unique surgical techniques mainly used for the treatment of functional brain disorders. As well, the functional neurosurgery has progressed markedly in its technical and theoretical aspects due to the rapid development of the basic neuroscience, computerized imaging techniques and advanced medical instruments. Some of these results have been implemented with success in the treatment of Parkinson's disease by deep brain stimulation, a common neurodegenerative disease affecting approximately 1% of the population aged seventy or more. And, the renaissance of functional neurosurgery in the treatment of neurodegenerative diseases has sparked also the interest in other diseases of the nervous system, which are refractory to medical treatment. Future developments in this rapidly advancing area will no doubt include widening indications for this relatively safe surgical procedure, elucidation of the mechanisms of action of electrical stimulation, and technological advancements improving effectiveness and convenience. It is therefore possible that deep brain stimulation in motor circuit in the basal ganglia as well as in other targets could become a potent therapeutic tool in the near future for diseases of the nervous system.

As well, at the interface between the old and new surgical paradigms such as MR guided focused ultrasound surgery (MRgFUS) to reduce the damage in normal brain tissue and further improvements in the precision of surgery will be try out.

Although there are some points to be clarified and estimated in the future, these new tendencies will stand to the next century, and further progress will definitely be achieved because it contains some truth in the light of the modern neuroscience.

In this presentation, I would like to summarize the available past and present data and the future perspectives in the field of the stereotactic & functional functional neurosurgery.

Invited Speakers

Date	Time	Room	T1. Biomedical Imaging and Optics
Nov. 13 (Fri)	09:00–9:30	Convention A	[TI-001] MHz speed wavelength swept laser for biomedical imaging <i>Chang Suk Kim (Pusan University, Korea)</i>
Nov. 13 (Fri)	09:30–10:00	Convention A	[TI-002] Intergration of laser with high intensity focused ultrasound for bladder tumor treatment: In vitro study <i>Seung Yoon Nam (Pukyong University, Korea)</i>
Nov. 13 (Fri)	16:15–16:45	Crystal	[TI-003] Ultra-fast functional magnetic resonance imaging using highly parallel detection <i>Fa-Hsuan Lin (National Taiwan University, Taiwan)</i>
Nov. 13 (Fri)	16:45–17:15	Crystal	[TI-004] High resolution diffusion tensor imaging and its preliminary application in cervical spondylotic myelopathy <i>Hua Guo (Tsinghua University, China)</i>
Nov. 13 (Fri)	17:15–17:45	Crystal	[TI-005] Imaging deep brain structures using magnetic susceptibility imaging <i>Jongho Lee (Seoul National University, Korea)</i>
Date	Time	Room	T2. Biosignal Processing and Neural Engineering
Nov. 13 (Fri)	16:15–16:45	Convention B	[TI-006] Arrhythmia detection in the real world <i>Gali Clifford (Univ of Oxford, UK)</i>
Nov. 13 (Fri)	16:45–17:15	Convention B	[TI-007] Tactile Sensation Processing for Artificial Palpation <i>Jong-Ha Lee (Keimyung University, Korea)</i>
Date	Time	Room	T3. Nanobiosensor and Instrumentation
Nov. 12 (Thu)	15:45–16:15	Geumgang	[TI-008] Iron oxide based multifunctional nanomaterials prepared by novel thermal treatment processes for bioimaging and drug delivery <i>Yuanzhe Piao (Seoul National University, Korea)</i>
Nov. 12 (Thu)	16:15–16:45	Geumgang	[TI-009] Better bioaffinity sensing platforms with gold nanoparticles for biomedical applications <i>Hye Jin Lee (Kyungpook National University, Korea)</i>
Nov. 13 (Fri)	14:30–15:00	Sapphire	[TI-010] Biomimetic self-assembled structures for sensor applications <i>Byung Yang Lee (Korea University, Korea)</i>
Nov. 13 (Fri)	15:00–15:30	Sapphire	[TI-011] Functional microfluidics and nanoparticles for cancer and stem cell fate <i>Bong Geun Chung (Sogang University, Korea)</i>
Date	Time	Room	T4. Therapeutic and Diagnostic Devices and Systems
Nov. 13 (Fri)	09:00–9:30	Ruby	[TI-012] Translational medicine using fully automated circulating tumor cell systems <i>J. -M. Park¹, and M. S. Kim² (¹Samsung Electronics, Ltd., Korea, ²Konyang University, Korea)</i>

Nov. 13 (Fri)	09:30-10:00	Ruby	[TI-013] Bi-modal neuromodulatory effect of low-intensity focused ultrasound (LIFU): A parameter optimization study <i>H.C.Baek, H. Kim (Center for Bionics, Korea Institute of Science and Technology, Seoul, Korea)</i>
Nov. 13 (Fri)	14:30-14:50	Ruby	[TI-014] Applications of near-infrared optical sensor to meet the medical needs <i>Jae Gwan Kim (Gwangju Institute of Science & Technology, Korea)</i>
Nov. 13 (Fri)	14:50-15:10	Ruby	[TI-015] High-frequency ultrasound microbeam techniques for measurement of cell mechanics <i>J. M. Park, J. H. Kim, and J. Y. Hwang (DGIST, Daegu, Korea)</i>
Nov. 13 (Fri)	15:10-15:30	Ruby	[TI-016] Automatic segmentation of lumen and media-adventitial borders in sequential IVUS images <i>J. H. Lee¹, Y. N. Hwang¹, G. Y. Kim², and S. M. Kim^{1,2} (¹Dongguk University-Seoul, Korea, ²Dongguk University-Bio Medi Campus, Korea)</i>
Nov. 13 (Fri)	16:15-16:45	Ruby	[TI-017] Three-dimensional visualization of plaque distribution in a curved artery using intravascular ultrasound imaging <i>Hyunggun Kim (University of Texas Health Science Center at Houston, USA)</i>
Nov. 13 (Fri)	16:45-17:00	Ruby	[TI-018] Dissolving microneedles for transdermal drug delivery: Fabrication and in vivo evaluation <i>Seong-O Choi (Kansas State University, USA)</i>
Nov. 13 (Fri)	17:00-17:15	Ruby	[TI-019] Development of pediatric artificial heart valve: Investigating time-profile of geometric orifice area <i>Kwon Soo Chun (Baylor College of Medicine, USA)</i>
Date	Time	Room	T5. Biomechanics
Nov. 13 (Fri)	09:00-09:20	Diamond	[TI-020] Modeling cochlear micro-structures: From mechanics to sensory-neural response <i>Yong Jin Yoon (Nanyang Technological University, Singapore)</i>
Nov. 13 (Fri)	09:20-09:40	Diamond	[TI-021] Biomechanical approach to parkinson's disease -quantification of bradykinesia, rigidity, and freezing of gait- <i>Gwang-Moon Eom¹, Ji-Won Kim¹, Seong-Beom Koh² (¹Konkuk University, Korea, ²Korea University College of Medicine, Korea)</i>
Nov. 13 (Fri)	09:40-10:00	Diamond	[TI-022] Bone-conduction pathways of hearing: Computational approaches <i>Nam Keun Kim (Incheon National University, Korea)</i>
Nov. 13 (Fri)	14:30-14:50	Diamond	[TI-023] TBA <i>Seyong Lee (Yonsei University, Korea)</i>
Nov. 13 (Fri)	14:50-15:10	Diamond	[TI-024] Biomechanics of downhill running <i>Sang-Kyoon Park¹, Hyun-Min Jeon², Sukhoon Yoon¹, and Jiseon Ryu¹ (¹Motion Innovation Centre, Korea National Sport University, Korea, ²Korea Armed Forces Athletic Corps, Korea)</i>
Nov. 13 (Fri)	15:10-15:30	Diamond	[TI-025] The effects of overloaded warm-ups on the athletic performance <i>Young-Kwan Kim (Chonnam National University, Korea)</i>
Date	Time	Room	T6. Biomedical Robotics and Rehabilitation Engineering
Nov. 13 (Fri)	16:15-16:45	Diamond	[TI-026] Critical gaps in rehabilitation and assistive robotics research <i>Ang Wei Tech (Nanyang Technological University, Singapore)</i>

Nov. 13 (Fri)	16:45-17:15	Diamond	[TI-027] Rehabilitation robots and translational research in NRC, Korea <i>Won-Kyung Song (Translational Research Program for Rehabilitation Robots, National Rehabilitation Center, Korea)</i>
Nov. 14 (Sat)	09:00-09:30	Diamond	[TI-028] Assistive robotics based on biomechanical signals <i>Jung Kim (Korea Advanced Institute of Science and Technology, Korea)</i>
Date	Time	Room	T7. Molecular, Cellular, and Tissue Engineering and Biomaterials
Nov. 12 (Thu)	15:45-16:15	Emerald	[TI-029] Bio-inspired materials for promoting direct reprogramming <i>Seung-Woo Cho (Yonsei University, Seoul, Korea)</i>
Nov. 12 (Thu)	16:15-16:45	Emerald	[TI-030] Origami-based tissue engineering <i>Nathaniel S. Hwang (Seoul National University, Korea)</i>
Nov. 13 (Fri)	09:00-09:30	Emerald	[TI-031] A microfluidic platform for programmable cell culture environments <i>Minseok Kim, Ji Won Lim and Taesung Kim (Ulsan National Institute of Science and Technology, Korea)</i>
Nov. 13 (Fri)	09:30-10:00	Emerald	[TI-032] Dynamic micropatterning of cells on complex nanostructured surfaces using a cell-friendly photoresist <i>Junsang Doh (POSTECH, Korea)</i>
Nov. 13 (Fri)	14:30-15:00	Emerald	[TI-033] An external shape memory support to prevent vein failure <i>Timothy C. Boire, Christy Guth, Colleen Brophy, Hak-Joon Sung (Vanderbilt University, USA)</i>
Nov. 13 (Fri)	15:00-15:30	Emerald	[TI-034] Biocompatible polymeric nanoparticle for efficient delivery of therapeutic materials <i>In-Kyu Park (Chonnam National University, Korea)</i>
Nov. 13 (Fri)	16:15-16:40	Emerald	[TI-035] Quantitative imaging of cellular mechanotransduction at the subcellular level <i>Sungsoo Na (Indiana University, USA)</i>
Nov. 13 (Fri)	16:40-17:05	Emerald	[TI-036] Cell-derived matrix engineering for tissue regeneration <i>In Gul Kim, Ping Du, Muhammad Suhaeri and Kwideok Park (KIST, Korea)</i>
Nov. 13 (Fri)	17:05-17:30	Emerald	[TI-037] Oxygen producing 3D matrices for prolonged cell survival under hypoxic environment <i>H. Y. Lee¹, J. H. Lee², and S. H. Oh¹ (¹Dankook University, Korea, ²Hannam University, Korea)</i>
Nov. 14 (Sat)	09:00-09:30	Emerald	[TI-038] The role of bioimaging in 3D bioprinting and tissue engineering <i>Hak Soo Choi (Harvard University, USA)</i>
Nov. 14 (Sat)	09:30-10:00	Emerald	[TI-039] 3D integrated organ printing technology and its tissue engineering applications <i>Hyun-Wook Kang (Ulsan National Institute of Science and Technology, Korea)</i>
Date	Time	Room	T8. Cardiovascular and Respiratory System Engineering
Nov. 13 (Fri)	09:00-09:30	Jade	[TI-040] Electromechanical dyssynchrony in heart failure under various mechanical afterload conditions: A computational study <i>Ki Moo Lim (Kumoh National Institute of Technology, Korea)</i>

Special Sessions

Special Sessions 1: Nov. 12, 2015 (Thu) 15:45-17:15 / Room: Convention B

• Chair: Si Young Song (Yonsei University, Korea)

Time	SS1. Role and Work of Biomedical Engineers in Research-Driven Hospitals
15:45-16:00	The Korea research-driven hospital project : Hospital viewpoint <i>Si Young Song (Yonsei University, Korea)</i>
16:00-16:15	Progress of the research-driven hospital project in Korea University Anam Hospital <i>Sang-Heon Lee (Korea University, Korea)</i>
16:15-16:30	Progress of the research-driven hospital project in Seoul National University Hospital <i>Hee Chan Kim (Seoul National University, Korea)</i>
16:30-16:45	Progress of the research-driven hospital project in Asan Medical Center <i>Jaesoon Choi (Ulsan University, Korea)</i>
16:45-17:00	The Korea research-driven hospital project : Industry viewpoint <i>Felix K. Yie (CTO of Intromedic, Korea)</i>
17:00-17:15	Panel Discussion

Special Sessions 2: Nov. 12, 2015 (Thu) 15:45-17:15 / Room: Crystal

• Chair: In Chan Youn (KIST, Korea)

Time	SS2. Artificial Nerve Networking Pioneer Project
15:45-16:00	[SS001] Development of agarose scaffolds via enhancement of a mechanical properties to promote an axons regeneration <i>Sang Jin Lee¹, Min Heo¹, Eun Young Heo¹, Dong Nyoun Heo¹, Kuiwon Cho² and Il Keun Kwon¹ (¹Kyung Hee University, Seoul, Korea, ²Korea Institute of Science and Technology, Korea)</i>
16:00-16:15	[SS002] Flexible neural electrodes with hydrogel scaffolds for artificial neural networking of injured spinal cord <i>Jinwoo Jeong, Wonsuk Choi, Sunyoung Jung, Woohyun Jung, Hyungdal Park, Sungmin Han, Inchan Youn, Jun-Kyo Francis Suh, and Jinseok Kim (Korea Institute of Science and Technology, Seoul, Korea)</i>
16:15-16:30	[SS003] A novel unsorted spike feature based real-time sensory event detection for closed-loop control <i>S. Han^{1,2}, J. U. Chu³, K. Choi¹, J. W. Park², and I. Youn^{1,4} (¹Korea Institute of Science and Technology, Korea, ²Korea University, Korea, ³Korea Institute of Machinery and Materials, Korea, ⁴Korea University of Science and Technology, Korea)</i>
16:30-16:45	[SS004] Study on evaluation techniques for injured spinal cord regeneration after transplantation of porous polymeric nerve electrodes <i>Jee Y. Lee¹, Hae Y. Choi¹, Eun Y. Huh¹, Jin W. Jung², Sugmin Han², Il K. Kwon¹, Jin S. Kim², Inchan Youn² and Tae Y. Yune¹ (¹Kyung Hee University, Korea, ²Korea Institute of Science and Technology, Korea)</i>

16:45–17:00	[SS005] Development of efficient transplantation method of artificial nerve networking system <i>Joongkee Min, Sang Ryong Jeon (University of Ulsan, Korea)</i>
-------------	--

Special Sessions 3: Nov. 12, 2015 (Thu) 15:45-17:15 / Room: Jade

• **Chair: Hun K. Park (Kyung Hee University, Korea)**

Time	SS3. Targeted POP Cancer Treatment Techniques
15:45–16:02	[SS006] Cancer-selective drug delivery and imaging <i>C. Kang (Kyung Hee University, Korea)</i>
16:02–16:24	[SS007] Synthesis and characterization of multifunctional nanophosphor materials for bioimaging and drug delivery applications <i>Jae Su Yu (Kyung Hee University, Korea)</i>
16:24–16:48	[SS008] Employment of near-infrared irradiation and targeted gold nanoheaters for photothermal cancer treatment <i>Kyung Min Byun (Kyung Hee University, Korea)</i>
16:48–17:10	[SS009] Tunable microenvironments regulating expansion and differentiation of stem cells and cellular reprogramming <i>Bogyu Choi, Kwang-Sook Park, Soo-Hong Lee (CHA University, Korea)</i>

Special Sessions 4: Nov. 13, 2015 (Fri) 09:00-10:30 / Room: Convention B

• **Chair: Kyung Min Byun (Kyung Hee University, Korea)**

Time	SS4. Endoscopic Imaging for POP Cancer Treatment
09:00–09:30	[SS010] The past, present and future of image-enhanced endoscopy focusing on narrow-band imaging: A clinical perspective <i>Jung-Wook Kim, Jae-Young Jang (Kyung Hee University, Korea)</i>
09:30–10:00	[SS011] Listening to light and seeing through: In vivo multiscale photoacoustic imaging <i>Chulhong Kim (POSTECH, Korea)</i>
10:00–10:30	[SS012] Multimodal endoscopic imaging system for detection of gastric lesions <i>S. Yun and J. Y. Hwang (DGIST, Korea)</i>

Special Sessions 5: Nov. 13, 2015 (Fri) 09:00-10:30 / Room: Crystal

- Chair: **Sungwan Kim (Seoul National University, Korea)**
Dong-Soo Kwon (Korea Advanced Institute of Science and Technology, Korea)
Chiwon Lee (Medical Research Center, Seoul National University, Korea)

Time	SS5. Medical Robot
09:00-09:10	[SS013] A development of enabling technology for next generation laparoscopic surgical robot using novel end-effector, novel master interface, and da Vinci Research Kit (dVRK) <i>C. Lee, M. Kim, H. J. Kim, and S. Kim (Seoul National University, Korea)</i>
09:10-09:20	[SS014] Multi/Single Port Surgical Robot System with Elbow Equipped Instruments <i>Un-Je Yang, Min-Ho Hwang, Hyun-Young Lee, Deok-Gyun Jeong, Deok-You Gong, Dong-Ho Lee, and Dong-Soo Kwon (KAIST, Korea)</i>
09:20-09:30	[SS015] Control of multi-DOF robotic arm based on 3D hand trajectories predicted from neural signals <i>Y. J. Kim, H. S. Nam, M. S. Bang, C. K. Chung, and S. Kim^{2,3} (Seoul National University, Korea)</i>
09:30-09:40	[SS016] A Flexible endoscopic surgery robot for NOTES with its in-vivo animal trials <i>M. Hwang¹, J. Lee¹, Y. Park¹, J. Suh¹, S. Kim¹, Y. Na¹, Y. Kim², S. Jeong², D. S. Kwon¹ (¹KAIST, Korea, ²Choongnam University, Korea)</i>
09:40-09:50	[SS017] A study on the development of a robot-assisted automatic laser hair removal system and its clinical trial results <i>H. W. Lim¹, D. H. Lee¹, M. Cho¹, S. Park¹, W. Koh², Y. Kim¹, J. H. Chung¹, and S. Kim¹ (¹Seoul National University, Korea, ²JMO Dermatology, Korea)</i>
09:50-10:00	[SS018] A novel surgical pen-type master device using vibrotactile feedback <i>H. Lee, U. Yang, and D.S Kwon (KAIST, Korea)</i>

Special Sessions 6: Nov. 13, 2015 (Fri) 09:00-10:30 / Room: Geumgang

- Chair: **JinSu Lee (KDIDI, Korea)**

Time	SS6. KHIDI Forum for Sharing of Domestic Medical Device Industry R&D
09:00-09:20	[SS019] Support by the government for development and commercialization of domestic medical device <i>Huiseok Chae (KDIDI, Korea)</i>
09:20-09:40	[SS020] Dongguk medical device innovation center <i>Sung Jae Kim (Dongguk Medical Device Innovation Center, Korea)</i>
09:40-10:00	[SS021] Commercialization of new biomaterial through multi-collaborations <i>SungYoun Cho¹*, KyeongJin Har², HyungKwang Seok³ (¹U&i Corporation, ²Ajou University, Korea, ³Institute of Science & Technology, Korea)</i>
10:00-10:20	[SS022] Renal denervation system development and korean-singapore R&D joint call: An example case <i>Eul-Joon Park (HANKOK Inc., Korea)</i>

Special Sessions 7: Nov. 13, 2015 (Fri) 14:30-16:00 / Room: Convention A

• Chair: Kwang Suk Park (Seoul National University, Korea)

Time	SS7. Recent Progresses in Sleep Monitoring
14:30-15:00	[SS023] On sleep and sleep monitoring: Clinical implications <i>Do-Un Jeong</i> (Seoul National University, Korea)
15:00-15:30	[SS024] Recent developments in automated low cost mHealth sleep analysis: From accelerometry to video <i>Gari, D. Clifford</i> (University of Oxford, U.K.)
15:30-16:00	[SS025] Nonintrusive approaches for sleep monitoring and analysis <i>Kwang Suk Park, Hwan Hwang, Da Woon Jung, and Hee Nam Yoon</i> (Seoul National University, Korea)

Special Sessions 8: Nov. 13, 2015 (Fri) 14:30-16:00 / Room: Convention B

• Chair: SangHoon Lee (Korea University, Korea)

Time	SS8. Brain-on-a-Chip Technology
14:30-15:00	[SS026] Central nervous system (CNS) on a chip ¹ – present & future <i>SangHoon Lee</i> (Korea University, Korea)
15:00-15:30	[SS027] Building biological neural networks on a chip: From axon guidance to modular networks <i>Yoonkey Nam</i> (KAIST, Korea)
15:30-16:30	[SS028] High-density microelectrode array recordings to reveal the origin of the extracellular action potential <i>U. Frey, M. E. Obien</i> (RIKEN, Japan)

Special Sessions 9: Nov. 13, 2015 (Fri) 14:30-16:00 / Room: Crystal

• Chair: Jaeuk Kim (Korea Institute of Oriental Medicine, Korea)

Time	SS9. Medical Devices in Traditional Medicine - Pulse Diagnostic System and Pulse Simulator
14:30-14:50	[SS029] Pulse diagnosis system and pulse simulator <i>Jaeuk U. Kim, Young-Min Kim, Young Ju Jeon, and Jong Yeol Kim</i> (Korea Institute of Oriental Medicine, Korea)
14:50-15:10	[SS030] Hemodynamic study of pulse wave with cardiovascular simulator <i>J. Y. Lee, M. Jang, S.Y. Seo, M.W. Lee, and S. H. Shin</i> (Sangji University, Korea)
15:10-15:30	[SS031] Modeling of the anatomically accurate arterial tree in the human upper extremity from MRI data for the numerical hemodynamic study <i>Keewon Kim¹, Young Sun Jeon¹, Jaeuk. U. Kim², Sung Kyun Kim¹</i> (¹ Konkuk Univ, Korea, ² Korea Institute of Oriental Medicine, Korea)
15:30-16:00	[SS032] Performance evaluation of a new radial pulsation simulator <i>Tae-Heon Yang¹, Young-Min Kim², and Sam-Yong Woo¹</i> (¹ KRISS, Korea, ² KIOM, Korea)

Special Sessions 10: Nov. 13, 2015 (Fri) 14:30-16:00 / Room: Jade

• Chair: Byungjo Jung (Yonsei University, Korea)

Time	SS10. Current Studies at Biomedical Engineering, Yonsei University
14:30-14:45	[SS033] Institute of yonsei biomedical engineering and biomedical industry in Korea <i>Young Ro Yoon (Yonsei University, Korea)</i>
14:45-15:00	[SS034] Dielectrophoretic tweezers and its' biological application <i>Sang Woo Lee (Yonsei University, Wonju, Korea)</i>
15:00-15:15	[SS035] Development of nanoparticles for cancer theranostics <i>Jaehong Key (Yonsei University, Korea)</i>
15:15-15:30	[SS036] Ultrasound mediated drug delivery: Sonoporation <i>G. Song, O. Cha, and J. Seo (Yonsei University, Wonju, Korea)</i>
15:30-15:45	[SS037] Decoding and connectivity analysis of neural signal – application to clinical/cognitive neuroscience <i>Kyung Hwan Kim (Yonsei University, Korea)</i>
15:45-16:00	[SS038] Introduction to biomedical optics lab at Yonsei University <i>Byungjo Jung (Yonsei University, Korea)</i>

Special Sessions 11: Nov. 13, 2015 (Fri) 14:30-16:00 / Room: Geumgang

• Chair: Jae-Hoon Jun (Konkuk University, Korea)

Time	SS11. Laser Tactile Sensation
14:30-14:50	[SS039] Investigation of mechanical effects induced by pulsed laser absorption in human skin <i>J.-R. Park¹, H.-S. Kim², J.-H. Jun², and S.-C. Chung² (¹Chosun University, Korea, ²Konkuk University, Korea)</i>
14:50-15:10	[SS040] Human responses to tactile sense induced by pulsed laser stimulation <i>Hyung-Sik Kim¹, Ji-Sun Kim¹, Jae-Hoon Jun¹, Jong-Rak Park², Sung-Phil Kim³, Seungmoon Choi⁴, Sung-Jun Park¹, Mi-Hyun Choi¹ and Soon-Cheol Chung¹ (¹Konkuk University, Korea, ²Chosun University, Korea, ³Ulsan National Institute of Science and Technology, Korea, ⁴Pohang University of Science and Technology (POSTECH), Korea)</i>
15:10-15:30	[SS041] Cortical activity patterns in response to non-nociceptive laser stimuli <i>S. P. Kim (Ulsan National Institute of Science and Technology, Ulsan, Korea)</i>
15:30-15:50	[SS042] Physical analysis of indirect laser radiation for Mid-air tactile stimulation <i>Hojin Lee, Seungmoon Choi (Pohang University of Science and Technology, Korea)</i>

Special Sessions 12: Nov. 13, 2015 (Fri) 16:15-17:45 / Room: Jade

- Chair: **Chang-Hwan Im (Hanyang University, Korea)**
Dong-Pyo Jang (Hanyang University, Korea)

Time	SS12. Frontiers in Translational Neurotechnology
16:15-16:33	[SS043] New techniques for optogenetic neural interface <i>Sang Beom Jun, and Chang Hyun Ji (Ewha Womans University, Korea)</i>
16:33-16:51	[SS044] Tactile information processing in the human brain and its implications in the haptic technology <i>Junsuk Kim¹ and Sung-Phil Kim² (¹Korea University, Korea, ²Ulsan National Institute of Science and Technology, Korea)</i>
16:51-17:09	[SS045] Prediction of speech intelligibility in cochlear implant users using a computational model <i>Jihwan Woo (University of Ulsan, Korea)</i>
17:09-17:27	[SS046] Towards personalized transcranial current stimulation (tCS) <i>Chang-Hwan Im (Hanyang University, Korea)</i>
17:27-17:45	[SS047] Closed-loop smart deep brain stimulation technology <i>D. P. Jang¹, K. E. Bennet², and K. H. Lee² (¹Hanyang University, Korea, ²Mayo Clinic, USA)</i>

Special Sessions 13: Nov. 13, 2015 (Fri) 16:15-17:45 / Room: Geumgang

- Chair: **Jong-Mo Seo (Seoul National University, Korea)**

Time	SS13. Recent Progress in the Artificial Retina Research
16:15-16:45	[SS048] Bionic vision australia <i>Gregg Suaning (University of New South Wales, Australia.)</i>
16:45-17:15	[SS049] Seoul artificial retina <i>Joonsoo Jeong (Seoul National University, Korea)</i>
17:15-17:45	[SS050] Updates of the artificial retina research <i>Jong-Mo Seo (Seoul National University Biomedical Research Institute, Korea)</i>

Special Sessions 14: Nov. 14, 2015 (Sat) 09:00-10:30 / Room: Crystal

- Chair: **Jung Hoon Ro (Pusan National University, Korea)**

Time	SS14. Measurement, Uncertainty, and Reference Standards for Biomedical Engineers
09:00-09:45	[SS051] Metrology in medicine – traceability and uncertainty <i>Jong Oh Choi (KRISS Daejeon, Korea)</i>
09:45-10:30	[SS052] Measurement issues for biomedical developers <i>Wonsik Ahn (Kyung Hee University Hospital, Korea)</i>


Special Sessions 15: Nov. 14, 2015 (Sat) 09:00-10:30 / Room: Jade

• Chair: Tong In Oh (Kyung Hee University, Korea)

Time	SS15. Recent Developments in Electrical Impedance Imaging
09:00-09:20	[SS053] Clinical electrical impedance tomography: Monitoring lung ventilation <i>K. Lee, L. Zhou, and J. K. Seo (Yonsei University, Korea)</i>
09:20-09:40	[SS054] Application of electrical impedance measurement and electrical impedance tomography in Japan <i>S. Nebuya (Kitasato University, Japan)</i>
09:40-10:00	[SS055] Microscopic electrical impedance based monitoring of engineered cartilage during <i>in vitro</i> tissue construction <i>E. A. Lee, T. I. Oh, Y. Son, and E. J. Woo (Kyung Hee University, Korea)</i>
10:00-10:20	[SS056] Medical applications of electrical impedance imaging and impedance spectroscopy <i>T. I. Oh and E. J. Woo (Kyung Hee University, Seoul, Korea)</i>

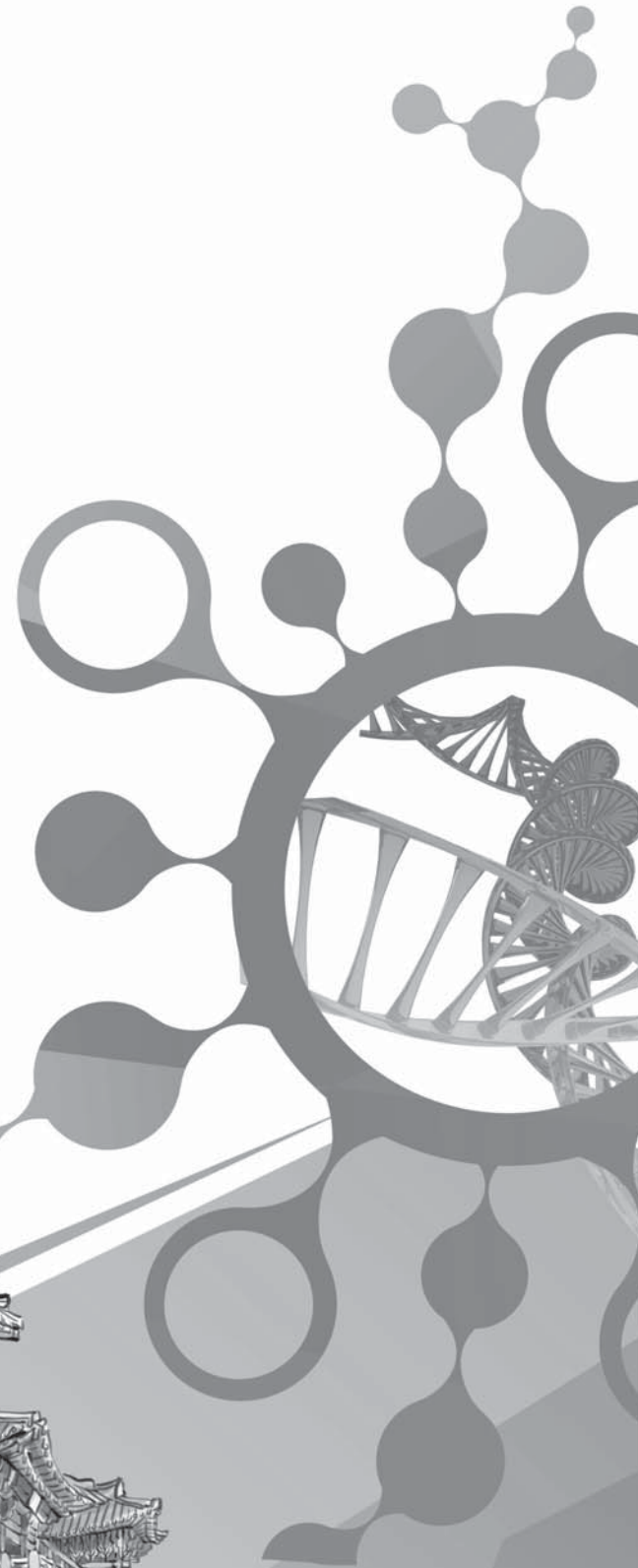
IBEC

International Biomedical
Engineering Conference 2015

2015

Road to Better Life through Biomedical Engineering

ORAL SESSIONS



Oral Sessions (Nov. 12)

T1. Biomedical Imaging and Optics

- Chair: Dong-Hyun Kim (Yonsei University, Korea)
- 15:45-17:15 / Room: Convention A

Time	S1: Biomedical Imaging and Optics (1)
15:45-16:00	[TO001] Designing one Board VLC Receiver for various medical data transmission with multichannel WDM <i>J.Y. An, K. H. Lim, and W. Y. Chung (Pukyong National University, Korea)</i>
16:00-16:15	[TO002] A new motion tracking system for medical imaging using an inertial sensor and an optical sensor <i>J. S. Kim¹, Y. H. Cho², Y. K. Yoon¹, and Y. D. Son¹ (1Gachon University, Korea, 2Samsung Medical Center, Korea)</i>
16:15-16:30	[TO003] Relation between anxiety, depression, and obesity in terms of dysfunctions in default mode network <i>B. Park¹ and H. Park^{1,2} (1Sungkyunkwan University, Korea, 2CNIR, Institute for Basic Science, Korea)</i>
16:30-16:45	[TO004] Implementation of anisotropic conductivity in canine brain using a combination of DTI and MREIT <i>N. Katoch¹, B.K. Cho¹, W.C. Jeong¹, S.Z.K. Sajib¹, H.J. Kim¹, O.I. Kwon¹ and E.J. Woo¹ (1Kyung Hee University, Korea, 2Konkuk University, Korea)</i>
16:45-17:00	[TO005] Experimental mapping of electric field distribution in ex vivo anisotropic muscle tissue using DT-MREIT <i>W.C. Jeong¹, S.Z.K. Sajib¹, N. Katoch¹, B.K. Cho¹, H.J. Kim¹, O.I. Kwon² and E.J. Woo¹ (1Kyung Hee University, Korea, 2Konkuk University, Korea)</i>
17:00-17:15	[TO006] The changes of cerebral hemodynamics during dexmedetomidine induced sedation in a rat model <i>SH Kim¹, JY Bae¹, DH Cho¹, D. Cho¹, JS. Ham¹, JY. Park¹, BR. Lee¹, HI. Kim¹, TJ Shin³ and JG. Kim^{1,2} (1Gwangju Institute of Science and Technology (GIST), Korea, 3Seoul National University, Korea)</i>

T3. Nanobiosensor and Instrumentation

- Chair: Young Bin Choy (Seoul National University, Korea)
- 15:45-17:15 / Room: Geumgang

Time	S1: Nanobiosensor and Instrumentation (1)
15:45-16:15	[TI-008] Iron oxide based multifunctional nanomaterials prepared by novel thermal treatment processes for bioimaging and drug delivery <i>Yuanzhe Piao (Seoul National University, Korea)</i>
16:15-16:45	[TI-009] Better bioaffinity sensing platforms with gold nanoparticles for biomedical applications <i>Hye Jin Lee (Kyungpook National University, Korea)</i>
16:45-17:00	[TO015] Bioengineering System for Prediction and Early Prenosological Diagnostics of Stomach Diseases Based on Energy Characteristics of bioactive Points with Fuzzy Logic <i>Riad Al-Kasasbeh¹, Nikolay Korenevskiy², Mahdi Alshamasin¹ (1Faculty of Engineering Technology, Al-Balqa Applied University, 2Faculty of Biomedical Engineering, Kursk State Technical University)</i>

17:00-17:15	[TO016] Effect of Substrates on Surface Enhanced Raman Scattering Platform using AgNPs-based Successive Ion Layer Absorption and Reaction Method <u>W. Kim, H. K. Park, and S. Choi*</u> (Kyung Hee University, Korea)
-------------	---

T5. Biomechanics

- Chair: Wenming Chen (Inje University, Korea)
- 15:45-17:15 / Room: Diamond

Time	S1: Biomechanics
15:45-16:00	[TO031] Reliability of a smartphone pedometer with low frequency accelerometry <u>Jaehyun Park, Namkeun Kim</u> (Incheon National University (INU), Korea)
16:00-16:15	[TO032] Biomedical assessment of plantar soft tissue changes due to advanced tissue glycation in diabetic patients <u>J. C. Teoh¹, D. Y. Lee², and T. Lee³</u> (¹ National University of Singapore, Singapore, ² Seoul National University Hospital, Korea, ³ Dongguk University, Korea)
16:15-16:30	[TO033] Gait characteristics in patients with Parkinson's disease during the timed up and go test <u>M. J. Son and C. H. Youm</u> (¹ Dong-A University, Korea)
16:30-16:45	[TO034] Finite element simulations in foot ulcer prevention: New strategies towards subject-specific anatomical model generation <u>W. M. Chen¹, P. V. Lee², and S. J. Lee¹</u> (¹ Inje University, Korea, ² University of Melbourne, Australia)
16:45-17:00	[TO035] The feedback/forward controller of joint could achieve the center of mass motion during running with gains determined by natural frequency <u>H. R. Lim and S. K. Park</u> (KAIST, Korea)
17:00-17:15	[TO036] Evaluation of feasibility of two depth sensor-based Microsoft Kinect cameras for abduction-adduction motion analysis <u>C. Y. Kim, J. S. Hong, and K. J. Chun</u> (Korea Institute of Industrial Technology, Korea)

T7. Molecular, Cellular, and Tissue Engineering and Biomaterials

- Chair: Jeong Woog Shin (Inje University, Korea)
- 15:45-17:15 / Room: Emerald

Time	S1: Cell & Tissues I
15:45-16:15	[TI-029] Bio-inspired materials for promoting direct reprogramming <u>Seung-Woo Cho</u> (Yonsei University, Korea)
16:15-16:45	[TI-030] Origami-based tissue engineering <u>Nathaniel S. Hwang</u> (Seoul National University, Korea)
16:45-17:00	[TO048] Cell contractility established by RhoA/Rock and TGF β /BMP signaling mediates load induced chromatin condensation in MSCs <u>Su-jin Heo¹, Spencer E. Szczesny¹, Randall L. Duncan² and Robert L. Mauck¹</u> (¹ University of Pennsylvania, USA, ² University of Delaware, USA)
17:00-17:15	[TO049] Photothermal poly (N-isopropylacrylamide)/ melanin nanoparticle hydrogel for anticancer drug delivery <u>A. GhavamiNejad, M. Samarikhalaj, L.E. Aguilar, J.I. Kim, T. Batgerel, C. H. Park, and C.S. Kim</u> (Chonbuk National University, Korea)

Oral Sessions (Nov. 13)

T1. Biomedical Imaging and Optics

- Chair: TBA
- 09:00-10:30 / Room: Convention A

Time	S2: Biomedical Imaging and Optics (2)
09:00-09:30	[TI-001] MHz speed wavelength swept laser for biomedical imaging <i>Chang Suk Kim (Pusan University, Korea)</i>
09:30-10:00	[TI-002] Intergration of laser with high intensity focused ultrasound for bladder tumor treatment: In vitro study <i>Seung Yoon Nam (Pukyong University, Korea)</i>
10:00-10:15	[TO007] Integration of laser with high intensity focused ultrasound for bladder tumor treatment: In vitro study <i>Van Phuc Nguyen, Junghwan Oh, and Hyun Wook Kang (Pukyong National University, Busan, Korea)</i>
10:15-10:30	[TO008] Near-infrared autofluorescence imaging of parathyroid glands for surgical guidance <i>Seo Hyun Song^{1,2}, Sung Won Kim¹, Hyoung Shin Lee¹, Chulho Oak¹, Kang Dae Lee¹, Yeh-Chan Ahn^{1,2} (¹Kosin University, Korea, ²Pukyong National University, Korea)</i>

- Chair: Hyungsoek Yoo (University of Ulsan, Korea)
- 16:15-17:45 / Room: Crystal

Time	S3: Biomedical Imaging and Optics (3)
16:15-16:45	[TI-003] Ultra-fast functional magnetic resonance imaging using highly parallel detection <i>Fa-Hsuan Lin (National Taiwan University, Taiwan)</i>
16:45-17:15	[TI-004] High resolution diffusion tensor imaging and its preliminary application in cervical spondylotic myelopathy <i>Hua Guo (Tsinghua University, China)</i>
17:15-17:45	[TI-005] Imaging deep brain structures using magnetic susceptibility imaging <i>Jongho Lee (Seoul National University, Korea)</i>

T2. Biosignal Processing and Neural Engineering

- Chair: Yoon Key Nam (Korea Advanced Institute of Science and Technology, Korea)
Jong-Ha Lee (Keimyung University, Korea)
- 16:15-17:45 / Room: Convention B

Time	S1: Biosignal Processing
16:15-16:45	[TI-006] Arrhythmia detection in the real world <i>Gali Clifford (Univ of Oxford, UK)</i>
16:45-17:15	[TI-007] Tactile Sensation Processing for Artificial Palpation <i>Jong-Ha Lee (Keimyung University, Korea)</i>

17:15-17:30	[TO015] A brain connectivity analysis under anesthesia using transfer entropy <i>J.Ham, D.Cho, D.H.Choi, S.H.Kim, Jae G.Kim, H.I.Kim and B.Lee (Gwangju Institute of Science and Technology (GIST), Korea)</i>
17:30-17:45	[TO016] Preclinical functional MRI for drug development <i>Taekwan Lee¹, Alan Jasanoff², and Choong-Yong Kim¹ (¹Daegu Gyeongbuk Medical Innovation Foundation, Korea, ²MIT, USA)</i>

T3. Nanobiosensor and Instrumentation

- Chair: Gi-Ja Lee (Kyung Hee University, Korea)
- 14:30-16:00 / Room: Sapphire

Time	S2: Nanobiosensor and Instrumentation (2)
14:30-15:00	[TI-010] Biomimetic self-assembled structures for sensor applications <i>Byung Yang Lee (Korea University, Korea)</i>
15:00-15:30	[TI-011] Functional microfluidics and nanoparticles for cancer and stem cell fate <i>Chung Bong Geun (Sogang University, Korea)</i>
15:30-15:45	[TO025] Synthesis of close-packed gold nanostructures on anodic aluminum oxide using self-assembled APTMS monolayer <i>Hyung Joon Park¹, Sang Won Lee¹, Wonseok Lee², Yoonhye Kim¹, Dae Sung Yoon¹ * and Kyu Back Lee¹ * (¹Korea University, Korea, ²Yonsei University, Wonju, Korea)</i>
15:45-16:00	[TO026] Sensitivity enhancement of silver-TiO ₂ double layered surface plasmon resonance biosensor based on dispersion relation engineering <i>Sherif H. El-Gohary, Munsik Choi, Seyoung Eom, Tae-Seong Kim, and Kyung Min Byun * (Kyung Hee University, Korea)</i>

T4. Therapeutic and Diagnostic Devices and Systems

- Chair: Byeong Cheol Choi (Choonhae College of Health Sciences, Korea)
Honggu Chun (Korea University, Korea)
- 09:00-10:30 / Room: Ruby

Time	S1: Bio-signal Measurement
9:00-9:30	[TI-012] Translational medicine using fully automated circulating tumor cell systems <i>J. -M. Park¹, and M. S. Kim² (¹Samsung Electronics, Ltd., Korea, ²Konyang University, Korea)</i>
9:30-10:00	[TI-013] Bi-modal neuromodulatory effect of low-intensity focused ultrasound (LIFU): A parameter optimization study <i>H.C.Baek, H. Kim (Korea Institute of Science and Technology, Korea)</i>
10:00-10:15	[TO027] The development of auto-pressure-control system for hyperbaric oxygen chamber based on pid <i>H. S. Kim, Y. R. Jang, S. Y. Shin, W. H. Choi, T. M. Shin (Yonsei University, Korea)</i>
10:15-10:30	[TO028] Development of a smart all-in-one cardiopulmonary support system: Preliminary performance of pump driver and control unit on a mock circulation loop <i>J. H. Park¹, D. A. Shin¹, J. S. Lee¹, M. C. Shin², J. C. Lee¹, H. C. Kim¹ * (¹Seoul National University, Korea, ²Jain Technology Co., Ltd, Korea)</i>

- Chair: Sun Kook Yoo (Yonsei University, Korea)
Eui Heon Chung (Gwangju Institute of Science and Technology, Korea)
- 14:30-16:00 / Room: Ruby

Time	S2: Medical Imaging
14:30-14:50	[TI-014] Applications of near-infrared optical sensor to meet the medical needs <i>Jae Gwan Kim</i> (Gwangju Institute of Science & Technology, Korea)
14:50-15:10	[TI-015] High-frequency ultrasound microbeam techniques for measurement of cell mechanics <i>J. M. Park, J. H. Kim, and J. Y. Hwang</i> (DGIST, Daegu, Korea)
15:10-15:30	[TI-016] Automatic segmentation of lumen and media-adventitial borders in sequential IVUS images <i>J. H. Lee¹, Y. N. Hwang¹, G. Y. Kim², and S. M. Kim^{1,2}</i> (¹ Dongguk University-Seoul, Korea, ² Dongguk University-Bio Medi Campus, Korea)
15:30-15:45	[TO029] Automated quantification of human skin wrinkles using optical coherence tomography <i>Juyoung Oh¹, Andrey Vavilin², Yujin Ahn², Songye Baek², Sungbea Bar² and Woonggyu Jung^{1,2,†}</i> (¹ Ulsan National Institute of Science and Technology, Korea, ² Institute of Basic Science, Korea)
15:45-16:00	[TO030] A phantom study on MR compatible RF hyperthermia system <i>Han-Joong Kim¹, Jong-Min Kim¹, Seong-Dae Hong¹, Suchit Kumar¹, Seung-Koo Lee², Chulhyun Lee³, and Chang-Hyun Oh^{1,*}</i> (¹ Korea University, Korea, ² Unionmedical Corporation, Korea, ³ The MRI Team, Korea Basic Science Institute, Korea)

- Chair: Sang Joon Lee (Sun Moon University, Korea)
Sung Min Kim (Dongguk University, Korea)
- 16:15-17:45 / Room: Ruby

Time	S3: Medical Diagnostic System
16:15-16:45	[TI-017] Three-dimensional visualization of plaque distribution in a curved artery using intravascular ultrasound imaging <i>Hyunggun Kim</i> (University of Texas Health Science Center at Houston, USA)
16:45-17:15	[TI-018] Dissolving microneedles for transdermal drug delivery: Fabrication and in vivo evaluation <i>Seong-O Choi</i> (Kansas State University, USA)
17:15-17:45	[TI-019] Development of pediatric artificial heart valve: Investigating time-profile of geometric orifice area <i>Kwon Soo Chun</i> (Baylor College of Medicine, USA)

T5. Biomechanics

- Chair: Yongnam Song (Korea University, Korea)
- 09:00-10:30 / Room: Diamond

Time	S2: General Biomechanics
09:00-09:20	[TI-020] Modeling cochlear micro-structures: From mechanics to sensory-neural response <i>Yong Jin Yoon</i> (Nanyang Technological University, Singapore)
09:20-09:40	[TI-021] Biomechanical approach to parkinson's disease -quantification of bradykinesia, rigidity, and freezing of gait- <i>Gwang-Moon Eom¹, Ji-Won Kim¹, Seong-Beom Koh²</i> (¹ Konkuk University, Korea, ² Korea University College of Medicine, Korea)
09:40-10:00	[TI-022] Bone-conduction pathways of hearing: Computational approaches <i>Nam Keun Kim</i> (Incheon National University, Korea)

10:00–10:15	[TO037] Incorporation of center of pressure excursion in a compliant running model may improve re-production of human running dynamics <i>C. Jung¹ and S. Park² (¹The Robotics Program, Korea, ²Department of Mechanical Engineering, Korea)</i>
10:15–10:30	[TO038] Body weight support with pelvic motion facilitation significantly reduces muscle activation durations of lower limbs <i>K. R. Mun, and H. Yu (National University of Singapore, Singapore)</i>

• **Chair: Seyong Lee (Yonsei University, Korea)**

• **14:30-16:00 / Room: Diamond**

Time	S3: Sports Biomechanics
14:30–14:50	[TI-023] TBA <i>Seyong Lee (Yonsei University, Korea)</i>
14:50–15:10	[TI-024] Biomechanics of downhill running <i>Sang-Kyoon Park¹, Hyun-Min Jeon², Sukhoon Yoon¹, and Jiseon Ryu¹ (¹Motion Innovation Centre, Korea National Sport University, Korea, ²Korea Armed Forces Athletic Corps, Korea)</i>
15:10–15:30	[TI-025] The effects of overloaded warm-ups on the athletic performance <i>Young-Kwan Kim (Chonnam National University, Korea)</i>
15:30–15:45	[TO039] Restriction of pelvic motions during over-ground walking changes gait kinematic and descriptive parameters <i>K. R. Mun, and H. Yu (National University of Singapore, Singapore)</i>
15:45–16:00	[TO040] An Experimental Method on Mechanical Behavior of Soft Tissue subjected to an External Impact <i>Y. Bahn, Deok-Kee Choi (¹Dankook University, Korea)</i>

T6. Biomedical Robotics and Rehabilitation Engineering

• **Chair: Seungbum Koo (Chung-Ang University, Korea)**

• **16:15-18:00 / Room: Diamond**

Time	S1: Biomedical Robotics (1)
16:15–16:45	[TI-026] Critical gaps in rehabilitation and assistive robotics research <i>Ang Wei Tech (Nanyang Technological University, Singapore)</i>
16:45–17:15	[TI-027] Rehabilitation robots and translational research in NRC, Korea <i>Won-Kyung Song (Translational Research Program for Rehabilitation Robots, National Rehabilitation Center, Korea)</i>
17:15–17:30	[TO041] Virtual Surgery planning and surgical guide design using automatic active contour segmentation for maxillofacial reconstruction surgery <i>Youngjun Kim¹, Sunhee Kim¹, Hannah Kim¹, Hyunchul Cho¹, Deukhee Lee¹, Laehyun Kim¹, Sehyung Park¹, and Jung-Woo Lee² (¹Korea Institute of Science and Technology, Korea, ²Kyung Hee University, Korea)</i>
17:30–17:45	[TO042] Design of a 7 DOF force-torque sensor for a master device with a pinching action <i>Suyong Kim, Cheongjun Kim, and Doo Yong Lee (Korea Advanced Institute of Science and Technology, Korea)</i>
17:45–18:00	[TO043] Design issues of tangible tabletop system as a cognitive rehabilitation for stroke patients <i>Kyuve Song^{1,2}, Gyu Hyun Kwon³, Sung-Bom Pyun⁴, Laehyun Kim^{1,2} (¹Center for Bionics Korea Institute of Science and Technology, Korea, ²Department of HCI&Robotics University of Science and Technology, Korea, ³Hanyang University, Korea, ⁴Korea University College of Medicine, Korea)</i>

T7. Molecular, Cellular, and Tissue Engineering and Biomaterials

- Chair: Jennifer H. Shin (Korea Advanced Institute of Science and Technology, Korea)
- 09:00-10:30 / Room: Emerald

Time	S2: Biochips & Cellular Analysis
09:00-09:30	[TI-031] A microfluidic platform for programmable cell culture environments <i>Minseok Kim, Ji Won Lim and Taesung Kim (Ulsan National Institute of Science and Technology, Korea)</i>
09:30-10:00	[TI-032] Dynamic micropatterning of cells on complex nanostructured surfaces using a cell-friendly photoresist <i>Junsang Doh (POSTECH, Korea)</i>
10:00-10:15	[TO050] Microdroplet-based 3D gastric cancer model for evaluation of drug resistance <i>Minjeong Jang¹, Seungwon Jung¹, Jae-Ho Cheong², Pilnam Kim¹ (¹KAIST, Korea, ²Yonsei University, Korea)</i>
10:15-10:30	[TO051] Label-free imaging of subendothelial migration of T cells by interference reflection microscopy (IRM) <i>Jaehyun Lee¹, Kwang Hoon Song², Taeyeob Kim², Junsang Doh^{1,2,*} (¹School of Interdisciplinary Bioscience and Bioengineering (I-Bio), ²POSTECH, Korea)</i>

- Chair: Kwideok Park (KIST, Korea)
- 14:30-16:00 / Room: Emerald

Time	S3: Biomaterials
14:30-15:00	[TI-033] An external shape memory support to prevent vein failure <i>Timothy C. Boire, Christy Guth, Colleen Brophy, Hak-Joon Sung (Vanderbilt University, USA)</i>
15:00-15:30	[TI-034] Biocompatible polymeric nanoparticle for efficient delivery of therapeutic materials <i>In-Kyu Park (Chonnam National University, Korea)</i>
15:30-15:45	[TO052] Injectable hydrogel for long-term chemical drug/gene combination therapy <i>C.-H Kim^{1,2}, Y.-M Kim¹, and S.-C. Song^{1,2} (¹Korea Institute of Science and Technology, Korea, ²Korea University of Science and Technology, Korea)</i>
15:45-16:00	[TO053] In vitro therapeutic efficacy of drug-loaded CoFe ₂ O ₄ nanoparticles combining magnetic hyperthermia and drug delivery for breast cancer <i>Yunok Oh¹, Hansu Seo¹, Won Ho Cho², and Junghwan Oh¹ (¹Pukyong National University, Korea, ²Pusan National University Hospital, Korea)</i>

- Chair: In-Kyu Park (Chonnam National University, Korea)
- 16:15-17:45 / Room: Emerald

Time	S4: Cell & Tissues II
16:15-16:40	[TI-035] Quantitative imaging of cellular mechanotransduction at the subcellular level <i>Sungsoo Na (Indiana University, USA)</i>
16:40-17:05	[TI-036] Cell-derived matrix engineering for tissue regeneration <i>In Gul Kim, Ping Du, Muhammad Suhaeri and Kwideok Park (KIST, Korea)</i>
17:05-17:30	[TI-037] Oxygen producing 3D matrices for prolonged cell survival under hypoxic environment <i>H. Y. Lee¹, J. H. Lee², and S. H. Oh¹ (¹Dankook University, Korea, ²Hannam University, Korea)</i>
17:30-17:45	[TO054] Quantification of mitochondrial morphologies during endothelial differentiation induced by shear stress <i>J. W. Shin, Y. G. Kang, S. H. Park, Y. Wu, S. R. Gu, H. Y. Ban, Y. M. Kim, M. J. Kim, J-W. Shin* (Inje University, Gimhae, Korea)</i>

T8. Cardiovascular and Respiratory System Engineering

- Chair: Kyehan Rhee (Myongji University, Korea)
- 09:00-10:15 / Room: Jade

Time	S1: Cardiovascular and Respiratory System Engineering
09:00-09:30	[TI-040] Electromechanical dyssynchrony in heart failure under various mechanical afterload conditions: A computational study <i>Ki Moo Lim (Kumoh National Institute of Technology, Korea)</i>
09:30-09:45	[TO057] Autonomous sensor node for monitoring HRV using RFID technology <i>Thang Viet Tran, Nam Trung Dang, Wan-Young Chung (Pukyong National University, Korea)</i>
09:45-10:00	[TO058] Computational simulation of passive leg raising effects on hemodynamics during cardiopulmonary resuscitation <i>D.A. Shin, J.H. Park, J.C. Lee, H.C. Kim (Seoul National University, Korea)</i>
10:00-10:15	[TO059] Multi-scale computational fluid dynamics for patient-specific coronary flow simulations <i>Minh Tuan Nguyen¹, Hyoung G. Choi², Sang-Wook Lee¹ (¹University of Ulsan, Korea, ²Seoul National University of Science and Technology, Korea)</i>

Oral Sessions (Nov. 14)

T1. Biomedical Imaging and Optics

• Chair: TBA

• 09:00-10:30 / Room: Convention A

Time	S4: Biomedical Imaging and Optics (4)
09:00-09:15	[TO009] Efficiency of indocyanine green in in-vivo photoacoustic imaging with animal tumor models <i>Jung-Eun Park^{1,2}, Nguyen Van Phuc¹, Yu-Gyeong Chae^{1,2}, Yeh-Chan Ahn^{1,2}*, Junghwan Oh¹, Hyun Wook Kang¹, Sung Won Kim^{2,3}, Chulho Oak^{2,3}, Je-Hun Kim^{2,3} and Eun-Kee Park^{2,3}</i> (¹ Pukyong National University, Korea, ² Innovative Biomedical Technology Research Center, Korea, ³ Kosin University, Busan, Korea)
09:15-09:30	[TO010] Quantification of tissue clearing techniques with optical coherence tomography <i>Eunji Cho¹, Sunwoo Jung^{1,2}, Junwon Lee¹, Eunjung Min¹ and Woonggyu Jung^{1,2}*</i> (¹ Ulsan National Institute of Science and Technology, Korea, ² Institute for Basic Science (IBS), Korea)
09:30-09:45	[TO011] Three-dimensional visualization hair follicle and quantification using optical coherence tomography <i>Myeongseo Yoon¹, Songye Baek¹, Youjin Ahn¹, Junwon Lee¹, Juyoung Oh¹, Andrey Vavilin¹ and Woonggyu Jung^{1,2}</i> (¹ Ulsan National Institute of Science and Technology, Korea, ² Institute for Basic Science (IBS), Korea)
09:45-10:00	[TO012] Intravascular ultrasonic-photoacoustic (IVUP) endoscope with 2.2-mm-diameter catheter for atherosclerotic plaque detection in pig artery <i>Q. N. Bui, K. K. Hlaing, Yun-Ok Oh, Xiao Feng Fan and Junghwan Oh</i> (Pukyong National University, Korea)
10:00-10:15	[TO013] Comparison between interstitial LLLT and vibration therapy on tibial defect <i>S. Lee, S. Jang, D. Hwang, S. You, M. Ha, J. Park, H. Kim and B. Jung*</i> (Yonsei Univ., Wonju, Korea)
10:15-10:30	[TO014] Feasibility of simulating vessel phantom using laser speckle imaging system <i>S. K. Yu, M. J. Ha, J. H. Park, S. Y. Lee, S. G. Jang and B. J. Jung*</i> (Yonsei University, Wonju, Korea)

T2. Biosignal Processing and Neural Engineering

• Chair: Chang-Hwan Im (Hanyang University, Korea)

Sang Beom Jun (Ewha Womans University, Korea)

• 09:00-10:30 / Room: Convention B

Time	S2: Neural Engineering
09:00-09:15	[TO017] Extracellular recordings of local field potentials and spikes from clustered neuronal networks using planar-type microelectrode arrays <i>S. Joo and Y. Nam</i> (Korea Advanced Institute of Science and Technology, Korea)
09:15-09:30	[TO018] Early detection of Driver's drowsiness by utilization of hybrid EEG/fNIRS <i>Thien Nguyen, Sangtae Ahn, Hyojung Jang, Sung Chan Jun, Jae Gwan Kim</i> (Gwangju Institute of Science and Technology (GIST), Korea)

09:30-09:45	[TO019] Improved electrooculogram-based eye-writing recognition using a new feature extraction method <i>Won-Du Chang, Ho-Seung Cha, Chang-Hwan Im (Hanyang University, Korea)</i>
09:45-10:00	[TO020] Enhancement of motor imagery training efficiency using a real-time feedback system <i>Yubing Jiang, Hyeon-seok Lee, Gang Li and Wan-Young Chung (Pukyong National University, Korea)</i>
10:00-10:15	[TO021] Temporal and spatial mapping of neuronal signals in brain slice with optical coherence tomography <i>Geonho Choi¹, Jeonghyeon Lee¹, Jaemyung Jang², Nam Hyun Cho³, Songye Baek¹, Noo Li Jeon⁴ and Woonggyu Jung^{1,3,*} (¹Ulsan National Institute of Science and Technology (UNIST), Korea, ²Korea Brain Research Institute, Korea, ³Institute for Basic Science (IBS), Korea, ⁴Seoul National University, Korea)</i>
10:15-10:30	[TO022] Carbon-fiber based neural probe for chronic neural recording <i>Yena Lee¹, Yoonseob Lim², Seoyoung Hwang¹, Jaewoo Shin³, Jin Woo Chang³, Sang Beom Jun^{1,4,*} (¹Ewha Womans University, Korea, ²Korea Institute of Science and Technology, Korea, ³Yonsei University, Korea, ⁴Ewha Womans University, Korea)</i>

T6. Biomedical Robotics and Rehabilitation Engineering

- Chair: Sung Chan Jun (Gwangju Institute of Science and Technology, Korea)
- 09:00-10:30 / Room: Diamond

Time	S2: Biomedical Robotics (2)
09:00-09:30	[TI-028] Assistive robotics based on biomechanical signals <i>Jung Kim (KAIST, Korea)</i>
09:30-09:45	[TO044] Automatic bernard quadrant method for knee ACL localization using a polygonal model <i>Cong-Bo Phan¹, Kang-Min Sohn², Joon-Ho Wang², Seungbum Koo^{1,*} (¹Chung-Ang University, Korea, ²Samsung Medical Center, Korea)</i>
09:45-10:00	[TO045] A robotic mechanism for multiple needle manipulation in biopsy <i>Y. Moon, J. Won, and J. Choi (Asan Medical Center, Korea)</i>
10:00-10:15	[TO046] Tissue-electrode interface may be important in the subdural cortical stimulation - computational study <i>Jun-Kil Been, Donghyeon Kim, Hyeon Seo, Sung Chan Jun* (Gwangju Institute of Science and Technology, Korea)</i>
10:15-10:30	[TO047] Effectiveness of new balance rehabilitation training considering resistance exercise function: Evaluation of kinematic ability <i>L. Alizadeh Saravi, H. H. Jung, D. H. Lim* (Sejong University, Korea)</i>

T7. Molecular, Cellular, and Tissue Engineering and Biomaterials

- Chair: Seheang Oh (Dankook University, Korea)
- 09:00-10:30 / Room: Emerald

Time	S5: 3D Printing & Tissue Engineering
09:00-09:30	[TI-038] The role of bioimaging in 3D bioprinting and tissue engineering <i>Hak Soo Choi (Harvard University, USA)</i>
09:30-10:00	[TI-039] 3D integrated organ printing technology and its tissue engineering applications <i>Hyun-Wook Kang (Ulsan National Institute of Science and Technology, Korea)</i>
10:00-10:15	[TO055] 3D cell printing of tissue mimetic microenvironment <i>Jinah Jang¹, Hun-Jun Park², Seok-Won Kim¹, Heejin Kim², Ju Young Park¹, Soo Jin Na², Hyeon Ji Kim¹, Moon Nyeo Park¹, Seung Hyun Cho³, Sun Hwa Park², Sung Won Kim², Sang-Mo Kwon³, Pum-Joon Kim², Dong-Woo Cho^{1*} (¹Pohang University of Science and Technology (POSTECH), Korea, ²The Catholic University of Korea, Korea, ³Pusan National University, Korea)</i>
10:15-10:30	[TO056] A rational strategy based on 3D printing for long-segment circumferential tracheal reconstruction <i>Jeong Hun Park¹, Ju Young Park¹, Inn-Chun Nam², Jae Yeon Lee³, Seok Hwa Cho³, Sung Won Kim² and Dong-Woo Cho¹ (¹Pohang University of Science and Technology (POSTECH), Korea, ²The Catholic University of Korea, Korea, ³Chungbuk National University, Korea)</i>

IBEC

International Biomedical
Engineering Conference 2015

2015

Road to Better Life through Biomedical Engineering

POSTER SESSIONS



Poster Sessions (Nov. 12)

Presentation No.	T1. Biomedical Imaging and Optics
TP001	Material decomposition framework using the spectral attenuation coefficient ratios by multiple discriminant analysis <i>W. J. Lee, S. R. Kang, S. Y. Woo, S. J. Lee and W. J. Yi (Seoul National University, Korea)</i>
TP002	Semi-automatic polyp segmentation in colonoscopy videos <i>J. H. Won¹, N. Lee¹, B. Park¹, and H. Park^{1,2}, (¹Sungkyunkwan University, ²Center for Neuroscience Imaging Research (CNIR), Institute for Basic Science, Korea)</i>
TP003	Age-Related difference of superior medial frontal gyrus between ADHD and normal subjects using connectivity resting-state functional MRI <i>J. Hong¹, H. Park^{1,2} (¹Sungkyunkwan University, ²Center for Neuroscience Imaging Research (CNIR), Institute for Basic Science, Korea)</i>
TP004	Imaging genetics of parkinson's disease at putamen <i>Mansu Kim and Hyunjin Park* (Sungkyunkwan University, Korea)</i>
TP005	Development of a device for light guided vocal fold injection <i>Wonjae Cha¹, Soo-Geun Wang¹, Gye-Rok Jeon² and Jung Hoon Ro² (¹Pusan National University Hospital, Korea, ²Pusan National University, Korea)</i>
TP006	Photoacoustic computed tomography based on inverse-reconstruction of circularly arranged transducers <i>Jae-Ho Han, Seung-beom Yu, Seungbae Ji, and Ji-hyun Kim (Korea University, Korea)</i>
TP007	Fabrication of multilayered port wine stain phantom for laser treatment <i>Hye Jin Kim, Han-na Kim, Van Phuc Nguyen, and Hyun Wook Kang (Pukyong National University)</i>
TP008	Correction of motion artifacts in MR images using ESPIRiT combined with compressed sensing <i>Y. Seo^{1,2} (¹Korea Research Institute of Standards and Science, ²University of Science and Technology, Korea)</i>
TP009	A study on the gender differences of node betweenness centrality in obstructive sleep apnea <i>Min-Hee Lee¹, Yoon Ho Hwang¹, Areum Min¹, Bong Soo Han¹, Seung Ku Lee², Chol Shin², Chang-Ho Yun³ and Dong Youn Kim¹ (¹Yonsei University, ²College of Medicine Korea University Ansan Hospital, ³Seoul National University Bundang Hospital, Korea)</i>
TP010	The relationship between dental implant stability and trabecular bone microstructure <i>Se-Ryong Kang, Woo-Jin Lee, Sang-Yoon Woo, Sang-Jeong Lee and Won-Jin Yi (Seoul National University, Korea)</i>
TP011	Fabrication of multilayered optical tissue phantoms with 3D deposition for phototherapeutics <i>H. N. Kim¹, T. H. Nguyen¹, Y. G. Chae¹, B. Lee², and H. W. Kang^{1,*} (¹Pukyong National University, ²Korea Photonics Technology Institute (KOPTI), Korea)</i>
TP012	Osteotomy line guidance system for orthognathic surgery using a tablet PC based augmented reality <i>Sang-Jeong Lee, Sang-Yoon Woo, Woo-Jin Lee, Se-Ryong Kang and Won-Jin Yi (Seoul National University, Korea)</i>
TP013	A new device for angle measurement using infrared sensors <i>Bong-Jun Goh, Ji-Sun Kim, Han-Byeol Oh, A-Hee Kim, Jun-Sik Kim, Eun-Suk Lee, Jin-Young Baek, Ye-Ji Shin, and Jae-Hoon Jun* (Konkuk University, Korea)</i>

TP014	A study of angular measuring system using optical fibers <i>Jun-Sik Kim, Ji-Sun Kim, Han-Byeol Oh, A-Hee Kim, Bong-Jun Goh, Eun-Suk Lee, Jin-Young Baek, Ye-Ji Shin, and Jae-Hoon Jun*</i> (Konkuk University, Korea)
TP015	Quantitative measurement of the color change of bracket <i>Eun-Suk Lee, Ji-Sun Kim, Han-Byeol Oh, A-Hee Kim, Bong-Jun Goh, Jun-Sik Kim, Jin-Young Baek, Ye-Ji Shin, and Jae-Hoon Jun*</i> (Konkuk University, Korea)
TP016	Feasibility of 1H-MRS for characterizing non-alcoholic fatty liver rat disease using 3T <i>J. Y. Kim^{1,2}, H. M. Baek² and T. S. Lee¹</i> (¹ Chungbuk National University, ² Korea Basic Science Institute, Korea)
TP017	Additive Manufacturing of clavicle fracture model for orthopedic surgery planning <i>J. P. Lee¹, S. Y. Moon¹, H. W. Jang¹, K. J. Park², and T. S. Lee¹</i> (¹ Chungbuk National University, ² Chungbuk National University Hospital, Korea)
TP018	Intravascular ultrasonic-photoacoustic (IVUP) endoscope with 2.2-mm-diameter catheter for atherosclerotic plaque detection in pig artery <i>Q. N. Bui, K. K. Hlaing, Y. O. Oh, X. F. Fan and J. Oh</i> (Pukyong National University, Korea)
TP019	Measurement of mechanical property of tibialis anterior muscle using optical coherence elastography <i>Yu-Gyeong Chae^{1,2*}, Young-Sik Kim^{2,3*}, Eun-Kee Park^{2,3}, Min Yong Jeon⁴, Byeong-Hwan Jeon^{5**} and Yeh-Chan Ahn^{1,2***}</i> (¹ Pukyong National University, ² Innovative Biomedical Technology Research Center, ³ Kosin University, ⁴ Chung Nam National University, ⁵ Kyungsoo University, Korea)
TP020	A fabricated PMN-PZT needle hydrophone for photoacoustic imaging <i>Xiaofeng Fan, Kanglyeol Ha, Hyun Wook Kang, Junghwan Oh</i> (Pukyong National University, Korean)
TP021	Corpus callosum segmentation using hybrid method of sparse approximation and probability map <i>Gilsoon Park¹, Kichang Kwak¹, Bohyun Kim¹, Sang Won Seo², Duk L. Na², Jong-Min Lee^{1*}</i> (¹ Hanyang University, ² Sungkyunkwan University School of Medicine, Korea)
TP022	The relationships between morphological asymmetry and functional connectivity in the default mode network <i>Dong-Kyun Lee¹, Jun-Sung Park², Jung-ho Cha¹, Sang Won Seo³, Duk L. Na³, and Jong-Min Lee¹</i> (¹ Hanyang University, ² Medical System Lab., DMC R&D Center SAMSUNG Electronics, ³ Sungkyunkwan University School of Medicine, Korea)
TP023	Analysis of default mode network in resting state brain using batch self-organizing map <i>J. M. Hwang, J. H. Cha, J. S. Lee, Y. H. Park and J.M. Lee</i> (Han-Yang University, Korea)
TP024	Sparse representation method for Alzheimer's disease diagnosis <i>Kichang Kwak, Hyuk Jin Yun, Gilsoon Park, Eun Kyoung Kim, Jong-Min Lee</i> (Hanyang University, South Korea)
TP025	Relationship between white matter myelination and gray matter morphology in deep sulcal landmarks <i>Hyuk Jin Yun, Jong-Min Lee*</i> (Hanyang University, Korea)
TP026	Complementary Characteristics of Structural Correlation Networks <i>J. J. Yang, H. K. Kwon, J. M. Lee*</i> (Hanyang University, Korea)
TP027	Single-subject metabolic network analysis in Alzheimer's disease <i>Oh-Hun Kwon, Yong-Ho Choi, Sun-Il Kim, Jong-Min Lee</i> (Hanyang University, Korea)
TP028	3D image acquisition of ultrasound using schlieren method <i>O. Cha, J. Won, J. Kim, G. Song and J. Seo</i> (Yonsei University, Korea)
TP029	Brain network analysis of Parkinson's disease patients based on SPECT images <i>Seong-Jin Son¹ and Hyunjin Park^{1,2*}</i> (¹ Sungkyunkwan University, ² Center for Neuroscience Imaging Research (CNIR), Institute for Basic Science, Korea)

TP030	Automatic hyoid bone tracking from videofluoroscopic swallowing images <i>J.C. Lee¹, H.J. Ahn¹, J.Y. Kim¹, H.P. Kim¹, K.W. Nam¹, J.S. Ryu², I. Y. Kim¹ (¹Hanyang University, ²Seoul National University college of Medicine, Korea)</i>
TP033	Fabrication and performance evaluation of high-frequency ultrasonic needle transducer for intra-vascular ultrasound (IVUS) image <i>J. H. Sung, S. M. Ji, S. M. Kim, and J. S. Jeong* (Dongguk University, Korea)</i>
TP034	Reconstructing structural brain network using Cross Diffusion <i>Yong-Ho Choi, Collins Kwadwo Boahen, Jong-Min Lee (Hanyang University, Korea)</i>
TP035	Scale-Independent network hub of the diffusion weighted structural network <i>Hunki Kwon¹, Oh-Hun Kwon¹, Yong-Ho Choi¹, Sang Won Seo², Jong-Min Lee¹ (¹Hanyang University, ²Sungkyunkwan University School of Medicine, Korea)</i>
TP036	Preliminary survival analysis based on PRM method for HCC patients treated by TACE <i>Jonghoon Kim¹, Hyunjin Park^{1,2,*} (¹Sungkyunkwan Univ, ²Center for Neuroscience Imaging Research (CNIR), Institute for Basic Science, Korea)</i>
TP037	Differences among normal subjects and ADHD subtypes based on three connectivity parameters <i>Seunghak Lee¹, Hyunjin Park^{1,2,*} (¹Sungkyunkwan Univ, ²Center for Neuroscience Imaging Research (CNIR), Institute for Basic Science, Korea)</i>
TP038	Temporal domain analysis for dynamic PET diagnosis <i>JeongHee Shin¹, JungSoo Kim², YoungJin Jung¹ (¹Dongseo University, ²Dongnam Health University, Korea)</i>
TP039	Gender differences on cortical alteration in adolescent with internet addiction <i>A. Min¹, M. H. Lee¹, Y. H. Hwang¹, D. Y. Kim¹, B. S. Han¹ and H. S. Seo¹ (¹Yonsei University, Wonju, ²Korea University Ansan Hospital, Korea)</i>
TP041	MR-based electrical conductivity imaging of brain metabolites <i>W.C. Jeong, S.Z.K. Sajib, N. Katoch, B.K. Choi, H.J. Kim and E.J. Woo (Kyung Hee University, Korea)</i>
TP042	Submillimeter resolution MREIT conductivity images of rat brain <i>B. K. Choi, N. Katoch, S. Z. K. Sajib, W. C. Jeong, H. J. Kim and E. J. Woo (Kyung Hee University, Korea)</i>
TP043	Image processing about cell-detection using DWT on electrode surface <i>H. W. Kim, J. H. Heo, J. H. Lee, E. I. Cho, J. J. Lee, J. H. Im and Y. R. Yoon (Yonsei Univ., Wonju, Korea)</i>
TP044	The study of breast cancer classification for FNA using k-NN algorithm based on machine learning <i>J. H. Heo, H. R. Heo, H. W. Kim, J. J. Lee and Y.R. Yoon (Yonsei University, Korea)</i>
TP045	Liver metabolites in animal model of high-fat diet induced abnormal intrahepatic triglyceride storage using ¹ H-MRS with external standard method <i>K.H. Song, C.H. Yoo, S.I. Lim, and B.Y. Choe (The Catholic University of Korea College of Medicine, Korea)</i>
TP046	A preliminary study on centrum modeling for diagnosing scoliosis: Estimation of spine using kinect <i>S. Y. Shin, H. R. Heo, M. Song, and T. M. Shin (Yonsei University, Wonju, Korea)</i>
TP047	Effect of Binge Ethanol Intoxication and Abstinence on Neurometabolite Changes in Rats Detected by Ex Vivo ¹ H MR Spectroscopy <i>S.I. Lim, D. W. Lee, K.H. Song, C.H. Yoo and B.Y. Choe (The Catholic University of Korea College of Medicine, Korea)</i>
TP048	Cerebral metabolite differences and correlations in short-term binge ethanol-exposed rats: A study of ex vivo proton nuclear magnetic resonance spectroscopy at 11.7-T <i>C.H. Yoo, D.W. Lee, K.H. Song, S.I. Lim, and B.Y. Choe (The Catholic University of Korea College of Medicine, Korea)</i>

TP049	A new method for fabricating pigmented skin disease in solid optical phantoms: Ink injection <i>Jeonghwan Son, Jihoon Park, Sangyeob Lee, and Byungjo Jung* (Yonsei University, Wonju, Korea)</i>
TP050	Development of phantom with varying agarose and CuSO ₄ concentrations for mimicking human tissues in 3T MRI <i>K.H. Ryu, Y.J. Shin, J.M. Kim, D Han and D.H. Kim (Yonsei University, Korea)</i>
TP051	<i>In vitro</i> calcium imaging of spontaneous neuronal activity <i>Jungmin Hong, Hee jin Park, Chanmi Yeon, Jihee Ryu, Sohee Kim, Euiheon Chung* (Gwangju Institute of Science and Technology, Korea)</i>
TP052	Simulation study of abdominal fat imaging with electrical impedance tomography <i>G. Y. Jang¹, S. Z. K. Sajib¹, H. Wi², T. I. Oh¹, and E. J. Woo¹ (¹Kyung Hee University, ²Yonsei University, Korea)</i>
TP053	Pseudo-color optical biopsy using multichannel confocal microscopy <i>Juehyung Kang¹, Hyeong Soo Nam¹, ByungSeon Chun², Incheon Song², Dae Kyung Sohn³, Kwang Gi Kim³, Hyunjin Kim³ and Hongki Yoo¹ (¹Hanyang University, ²Nanoscope Systems, Inc., ³Research Institute and Hospital, National Cancer Center, Korea)</i>
TP054	System development and motion compensation of full-field swept-source optical coherence tomography integrated with surgical microscope <i>Chang-Soo Kim¹, Hyeong Soo Nam¹, Hyunki Lee², Hongki Kim², Hongki Yoo^{1,*} (¹Hanyang University, ²Koh Young Technology, Inc., Korea)</i>
TP055	Segmentation of subcortical area based on graph cuts algorithm <i>J. W. Hong¹, S. B. Park², K. C. Kwak³, J. M. Lee³, U. C. Yoon¹ (¹Catholic University of Daegu, ²Samsung Medical Center, ³Hanyang University, Korea)</i>
TP056	Atlas-based diffusion tensor analysis with partial volume effect <i>W. H. Choi¹, K. H. Kang², and U. C. Yoon¹ (¹Catholic University of Daegu, ²Kyungpook National University, Korea)</i>
TP057	The effect of Micro-current therapy on Adjuvant Induced Rheumatoid Arthritis <i>H. A. Lee¹, S. H. Kim¹, D.H. Hwang¹, S. K. Cho², Y.J. Park¹, D.H. Seo¹, J. H. Park¹ and H. S. Kim^{1,2} (¹Yonsei University, ²Yonsei-Fraunhofer IZFP Medical Device Lab, Korea)</i>
TP058	Assessment of temperature difference between tumor and normal region using infrared thermography <i>Soonjoo Hwang¹, Yeon-Mi Ryu², Gyungseok Oh³, Su Woong Yoo¹, Jiyoung Shin², Sang-Yeob Kim², Seung-Jae Myung², and Euiheon Chung^{1,3,*} (¹Gwangju Institute of Science and Technology (GIST), ²Asan Medical Center, University of Ulsan College of Medicine, ³Gwangju Institute of Science and Technology (GIST), Korea)</i>
TP059	The effect of hypoxia on the cerebral blood oxygenation of gerbil measured by functional near-infrared spectroscopy <i>S. Hong¹, Yeon Hee Yu², Duk-Soo Kim², and K. S. Park¹ (¹Seoul National University, ²Soonchunhyang University, Korea)</i>
TP060	Frequency domain analysis of laser speckle in mouse cerebral cortex <i>Abdul M. Safi, Ahra Cho, Chanmi Yeon, Euiheon Chung* (Gwangju Institute of Science and Technology (GIST), Korea)</i>
TP061	Development of dental 3D scanner system for direct impression scanning <i>Sang-Hyub Kim, Jun-Min Kim, Woo-Ram Lee (Seoul National University, Korea)</i>
TP062	Blood flow analysis by correlation analysis of the laser speckle images <i>Sang-Hyub Kim, Jong-Mo Seo (Seoul National University, Korea)</i>
TP063	A quantitative evaluation of normal appearing white matter in multiple sclerosis using new myelin water imaging, ViSTa <i>J. Y. Choi¹, I. H. Jeong², S. H. Kim², J. Y. Hyun², A. Joung², H. J. Kim^{2*}, J. Lee^{1*} (¹Seoul National University, ²Research Institute and Hospital of National Cancer Center, Korea)</i>

TP064	In-vivo measurement of aggregated myelin thickness map (g-ratio) using MRI <i>J. W. Jung, J. Lee* (Seoul National University, Korea)</i>
TP065	Comparison of laryngeal stroboscopic images using both strobing flash and continuous light <i>J. H. Ro¹, G. R. Jeon¹, G. H. Kim², H. J. Park³, D. H. Kang¹, S. G. Wang² (¹Pusan National University, ²Pusan National Hospital, ³Choonhae College, Korea)</i>
TP306	Study of technical conditions for improvement of angiographic image quality. <i>Myagmarnaran.Ts¹, Enkhbaatar.A² (¹Mongolian National University of Medical Sciences, ²Nuclear Energy Agency, Mongolia)</i>
TP309	Study on the optical density measurements for grasp cell density of the clinical specimen in the liquid-based cytology <i>M. G. Mun¹, D. W. Kim¹, and C. H. Kim² (¹Chonbuk National University, Korea, ²PATHtech Co.,Ltd)</i>
Presentation No.	T3. Nanobiosensor and Instrumentation
TP076	Density-dependent changes of dielectric properties in live human breast cancer cell <i>Kwan Hwi Ko, Min Hyung Kim, Seungyeop Choi, Myeonggu Son and Sang Woo Lee* (Yonsei University, Wonju, Korea)</i>
TP074	Pressure sensors using conductive fabric and PU/PVDF nanoweb <i>Y. J. Jeong¹, T.I. Oh¹, K. J. Kim², and E. J. Woo¹ (¹Kyung Hee University, ²Kyung Hee University, Yongin, Korea)</i>
TP067	An instant electrical power generating air cathode paper battery <i>Y. J. Ahn, J. C. Lee, H. K. Park, and S. Choi* (Kyung Hee University, Korea)</i>
TP073	Analysis of trap stiffness concerning the 3-dimensional position variations of the particles in dielectrophoretic tweezers <i>Myeonggu Son, Kwan Hwi Ko, Min Hyung Kim, Seungyeop Choi, Sang Woo Lee* (Yonsei University, Wonju, Korea)</i>
TP072	Enzymatic fiber biofuel cell for implantable applications <i>Cheong Hoon Kwon, Young Bin Park, and Seon Jeong Kim* (Hanyang University, Korea)</i>
TP071	Electrochemical immunosensors for pepsin detection in saliva utilizing 3D network nanostructured polypyrrole <i>Doyeon Lee, Yong Jin Ahn, Young Ju Lee, Hun-Kuk Park, and Gi-Ja Lee* (Kyung Hee University, Korea)</i>
TP070	Colorimetric detection of hydrogen sulfide utilizing silver in gas permeable membrane <i>Yong Jin Ahn, Doyeon Lee, Young Ju Lee, Hun-Kuk Park, and Gi-Ja Lee* (Kyung Hee University, Korea)</i>
TP305	Bacteria screening system using aptamer probed electrical impedance spectroscopy gap capacitance biosensor <i>H. W. Lee¹, H. G. Kwon¹, J. H. Lee¹, D. S. Kim¹, S. W. Lee², and O.C. Jeoung¹ (¹Inje University, Korea, ²The University of Tokyo, Japan)</i>
TP069	Surface potential mapping of DNA capped nanoparticles for point mutation detection <i>H. Lee¹, W. Lee¹, S. W. Lee², S. W. Lee¹ and D. S. Yoon² (¹Yonsei University, Wonju, ²Korea University, Korea)</i>
TP068	Direct measurement of the interaction force between hemicytosinium duplexes using dielectrophoretic force spectroscopy <i>Seungyeop Choi¹, Min Hyung Kim¹, Kwan Hwi Ko¹, Gyudo Lee¹, Myeonggu Son¹, Sei-Young Lee¹, Dae Sung Yoon², Sang Woo Lee^{1*} (¹Yonsei University, Wonju, ²Korea University, Korea)</i>
TP066	Fabrication of paper-based air-breathing microbial fuel cells via pencil <i>S. H. Lee, H. K. Park, and S. Choi* (Kyung Hee University, Korea)</i>

Presentation No.	T5. Biomechanics
TP077	Characteristics of muscle fatigue during pedaling <i>J. W. Seo, D. W. Kang, D. H. Kim, S. T. Yang, J. S. Choi and G. R. Tack (Konkuk University, Korea)</i>
TP078	Quantification of plantar soft tissues stiffness according to the change of the BMI <i>Yuri Kim¹, Haein Lee¹, Young-Seong Kim¹, Jung Hyun Park¹, Eunji Lee¹, Yisuk Kim², Taeyong Lee^{1,*} (¹Dongguk University, ²Korea Advanced Institute of Science and Technology, Korea)</i>
TP079	Characterizing the dynamical structure of postural sway in the faller using entropy <i>D. W. Kang, J. W. Seo, D. H. Kim, S. T. Yang, J. S. Choi, and G. R. Tack (Konkuk University, Korea)</i>
TP080	Effects of functional treatment on gastrocnemius spasticity using the ultrasound in patients with stroke <i>Y. H. Jeon, H. J. Lee, and K. S. Tae (Konyang University, Korea)</i>
TP081	Development of humanoid dummy for optimizing driving posture <i>D.H Kim, Y.E Song, S.G Kim and H.S Kim (Yonsei University, Won-ju, Korea)</i>
TP082	Comparison in the on-off timing of lower limbs muscle between the young and the elderly during pedaling <i>Y. H. Shin¹, J. H. Hong¹, J. S. Kong¹, E. S. Jung¹, J. H. Roh¹, J. W. Seo², J. S. Cho² and G. R. Tack² (¹Daegu Gyeongbuk Medical Innovation Foundation, Daegu, ²Konkuk University, Chungju, Korea)</i>
TP083	Emotional response to thermal stimuli applied to the back for the elderly <i>C. Y. Ko, S. Y. Jung, G. S. Kim, J. Ryu, M. Mun (Korea Orthopedics Rehabilitation Engineering Center, Korea)</i>
TP084	A study of EMG signal processing for gait intention detection <i>Taekyeong Lee, Heesuk Roh, Hunhee Kim and Junghwa Hong[#] (Korea University, Korea)</i>
TP085	The study of active muscle property by contraction experiment of animals gastro-intestine <i>Youngho Lee, Soonmoon Jung, Jaemin Kim, Dongwook Yang and[#]Junghwa Hong (Korea University, Korea)</i>
TP086	Characteristics of stent expansion according to plaque composition and structural design <i>D. H. Hwang¹, S. H. Kim¹, B. S. Namgung², S. H. Kim², H. S. Kim^{1,3} and S. K. Cho^{3*} (¹Yonsei University, Korea, ²National University of Singapore, Singapore, ³Yonsei-Fraunhofer IZFP Medical Device Lab, Korea)</i>
TP087	Evaluation of preferred driving posture on car seat <i>S. G. Kim, D. H. Kim, Y. E. Song, Y. K. Cho, H. S. Kim (Yonsei University, Wonju, Korea)</i>
TP088	Differences in kinematic characteristics by pedal types <i>I. G. Han, D. W. Kang, J. W. Seo, D. H. Kim, J. S. Choi and G. R. Tack (Konkuk University, Chungju, Korea)</i>
TP089	Comparison of pedicle screw designs upon pull-out test using FEM <i>Gihyun Lee¹, Dong-Ah Shin², and Sohee Kim^{1*} (¹Gwangju Institute of Science and Technology, ²Yonsei University College of Medicine, Korea)</i>
TP090	A study on the effect of vibratory stimulation with perception threshold on muscle functions <i>H. G. Kim, K. Y. Kwak, and D. W. Kim (Chonbuk National University, Korea)</i>
TP091	Cognitive ability evaluation and analysis according to LED illumination for light-care contents <i>S. J. Lee¹, W. B. Park², H. C. Kim³ and D. W. Kim¹ (¹Chonbuk National Univ, ²USys co.,Ltd, ³AinA co.,Ltd, Korea)</i>
TP092	Biomechanical change of ankle according to perception threshold of applied vibration during gait <i>K. Y. Kwak, H. G. Kim, and[*]D. W. Kim (Chonbuk National University, Korea)</i>
TP093	Which threshold define best for muscle onset time in MMG and EMG? <i>S. J. Kim, H. S. Lee, M. Jo, I. S. Shin and Y. H. Kim (Yonsei University, Wonju, Korea)</i>

TP094	Coupling of upper body parts in patients with Parkinson's disease during level walking <i>J. W. Kim, Y. R. Kwon, and G. M. Eom (Konkuk University, Choonju, Korea)</i>
TP095	Effect of sensory stimulation for suppression of action tremor <i>J.H. Heo¹, J.W. Kim¹, Y.R. Kwon¹, G.M. Eom¹, D.Y. Kwon², and C.N. Lee³, K.W. Park³ (¹Konkuk University, ²Korea University, Ansan, ³Korea University, Korea)</i>
TP096	Study on the effect of spine deformities on the intervertebral disc <i>Bokku Kang, Han Sung Kim (Yonsei University, Wonju, Korea)</i>
TP097	Use of Microsoft Kinect for detecting gait event while three kinds of walking speeds on a treadmill <i>S. T. Yang, J. S. Choi, D. W. Kang, J. W. Seo, D. H. Kim, and G. R. Tack[#] (Konkuk University, Korea)</i>
TP098	The effect of brake force on human response during low speed rear-end collision <i>JiHye Han¹, LeeYong Song¹, JaeYeong Lee¹, HyungJoo Kim², Inju Lee², Dohyung Lim¹ (¹Sejong University, ²Hyundai Motor Group, Korea)</i>
TP099	Identification of potential injury risk via analysis of human responses during low speed front-head collision <i>JaeYeong Lee¹, LeeYong Song¹, JiHye Han¹, HyungJoo Kim², Inju Lee², Dohyung Lim^{1*} (¹Sejong University, ²Hyundai Motor Group, Korea)</i>
TP100	Biomechanical assessment of the proximal interphalangeal implants following collateral ligament re-release using a finite element analysis <i>W. H. Kim¹, J. H. Park², J. W. Park², J. W. Jang³, J. W. Lee¹, W. M. Chen¹, S. J. Lee¹ (¹Inje University, Gimhae, ²Korea University College of Medicine, ³R&D center, Medyssey Co., Ltd, Korea)</i>
TP101	Effects of dual-task difficulty and priority option during gait <i>J.M. Kim, E.K. Choi, I.S. Shin, S.J. Ahn, S.J. Kim, J.S. Ryu and Y.H. Kim* (Yonsei University, Wonju, Korea)</i>
TP102	Biomechanical efficacies of a new surgical procedure using metatarsal sliding osteotomy for the treatment of the metatarsalgia <i>J. D. Eom¹, W. M. Chen¹, H. C. Gwak², J. H. Lee³ and S.J. Lee¹ (¹Inje University, Kimhae, ²Inje University Baik Hospital, ³Korea Orthopaedic Hospital, Korea)</i>
TP103	Comparative biomechanical analysis of postoperative lumbar spine implanted with 3D printed porous cage in terms of various porosity levels <i>S. H. KIM¹, S. J. Yoo¹, J. W. Lee¹, S. H. Woo², J. W. Jang², K. M. Lim², D. S. Huh³, S. S. Chung⁴, H. Yong⁵, W. M. Chen¹ and S. J. Lee¹ (¹Inje University, ²R&D Center, Medyssey Co., Ltd, ³CM Chungmu General Hospital, ⁴Samsung Hospital, Korea, ⁵Chaoyang Hospital, Capital Medical University, China)</i>
TP104	Alterations in cervical spine kinematics and implant stresses following uni- and bi- lateral laminoplasty procedures for the surgical treatment of cervical spondylotic myelopathy <i>S. J. Yoo¹, J. W. Lee¹, S. H. Woo², J. W. Jang², K. M. Lim², K. D. Riew³, G. R. Tark⁴, W. M. Chen¹ and S. J. Lee¹ (¹Inje University, ²R&D center, Medyssey Co., Ltd, Korea, ³Columbia University Medical Center, New York, U.S.A, ⁴Konkuk University, Korea)</i>
TP105	Possibility of potential bone resorption occurrence in revision total knee arthroplasty used with metal block augmentation: Mechanical experiment <i>Kwan-Soo Kang¹, Trinh Ngoc Tien¹, Young-Woong Jang², Oui Sik Yoo², Myung Chul Lee³, [#]Dohyung Lim¹ (¹Sejong University, ²Central R&D Center, Corentec Co. Ltd., ³Seoul National University, Korea)</i>
TP106	Study on the features of 3-axis accelerometer signal for activity monitoring and step-count detection <i>H. S. Park^{1,2}, I. W. Jung¹, Y. J. Lee¹, and I. Youn¹ (¹Korea Institute of Science and Technology, ²Korea University of Science and Technology, Korea)</i>
TP107	A Predictable development infant head-cervical spine model for measureable cranial deformation <i>Youngho Lee, Hoechan Kim and Junghwa Hong[#] (Korea University, Korea)</i>
TP108	Gait phase detection using FSRs during level-ground walking <i>J. Y. Cha, J. U. Chu, Y. H. Choi and J. U. Jung (Korea Institute of Machinery & Materials, Korea)</i>

TP109	A study of artificial disc nucleus replacement for human lumbar spine discs restoration <i>Taekyeong Lee, Junghwa Hong[#] (Korea University, Korea)</i>
TP110	Characteristics of cycle pedaling cadence by index of effectiveness <i>J. W. Seo, D. W. Kang, D. H. Kim, S. T. Yang, J. S. Choi and G. R. Tack (Konkuk University, Korea)</i>
TP111	Regularity of the upper body accelerations during walking in patients with Parkinson's disease <i>J. W. Kim, Y. R. Kwon, and G. M. Eom (Konkuk University, Choonju, Korea)</i>
TP112	Basic gait analysis of knee brace for leisure sports gear <i>S.J. Kang, Y.H. Chang C.Y. Ko, J.C. Ryu, M.S.Mun (Korea Orthopedics & Rehabilitation Engineering Center Research Team, Korea)</i>
TP113	Biomechanical assessment of novel bone lengthening plate by changing material properties of supporting axis <i>T. G. Jung¹, S. W. Suh², J. H. Yang², and D. W. Han³ (¹Osong Medical Innovation Foundation, ²Korea University Guro Hospital, ³Pusan National University, Korea)</i>
TP114	A novel jig system of expulsion test for intervertebral fusion device <i>J. W. Yang, J. H. Park, D. G. Kim, J. Y. Jeong, Y. H. Jeong, and T. G. Jung (Osong Medical Innovation Foundation, Korea)</i>
TP115	Evaluation of contact pressure at articular surface of knee in neutral, varus and valgus alignment <i>Jeongwoo Seo¹, Oui Sik Yoo¹, Yong In², Byoung Min Kang², Doo Hoon Sun^{1,3}, Yong-Sik Kim² (¹R&D Center, Corentec Co., Ltd., Cheonan, ²Seoul ST. Mary's Hospital, ³Sun General Hospital, Korea)</i>
TP116	The quantitative assessment of the tibia bony surface for proper screw insertion angle by re-aligning CT coordinate in high tibial osteotomy <i>Yong Seuk Lee¹, Myung Chul Lee², Deok Gill Choi³, Doo Hoon Sun³ and Oui Sik Yoo³ (¹Seoul National University College of Medicine, Bundang Hospital, ²Seoul National University Hospital, ³Central R&D Center, Corentec Co. Ltd., Korea)</i>
TP117	Mechanical evaluation of the novel laser-aided direct metal tooling for porous coating on arthroplasty <i>Tae-Jin Shin¹, Kwan-Soo Kang², Sung-Jae Park¹, Soon-Yong Kwon³, Young-Wook Lim³, and Dohyung Lim² (¹Central R&D Center, Corentec Co. Ltd., ²Sejong University, ³St. Mary's Hospital, Catholic University, Korea)</i>
TP118	Comparative analysis between asymmetric and symmetric tibial stem position using the virtual surgical planning of TKA <i>Y. K. Lee¹, J. W. Kim², O. S. Yoo², D. S. Sun^{2,3}, Y. S. Kim⁴, and J. S. Kim^{1*} (¹Konyang University, ²R&D Center, Corentec Co., Ltd., ³Sun General Hospital, ⁴Seoul St. Mary's Hospital, Korea)</i>
TP119	Measuring shooting-postural stability using an accelerometer <i>Tanmoy Chowdhury, Hyo Sung Joo, Minjung Woo, Hyejin Yang, Jihwan Woo (University of Ulsan, Korea)</i>
TP120	Stiffness sensing ability of bovine aortic endothelial cells (BAECs) on collagen type I coated surface <i>Yujin Shin¹, Jinwon Kim², Hongki Yoo¹, and Bomi Gweon¹ (¹Hanyang University, ²Korea University Guro Hospital, Korea)</i>
TP121	Kinematics of the Lower Extremities during V-shaped Slope Walking <i>Jiyoung Jeong, and Choongsoo S. Shin (Sogang University, Korea)</i>
TP122	The relationship between crush extent and injury severity in occupant motor vehicle accident <i>J. H. Lee¹, H. Y. Lee¹, J. I. Lee¹, I. H. Kang¹, K. K. Wijenayake^{1,2}, B. V. A. Mendis^{1,3} and K. H. Lee¹ (¹Wonju College of Medicine, Yonsei University, Korea, ²Base Hospital Avissawella, Sri Lanka, ³Base Hospital Tangalle, Sri Lanka)</i>
TP123	Ankle kinematics during triangle-shaped slope walking <i>Yoon No G. Hong, Pankwon Kim, and Choongsoo S. Shin (Sogang University, Korea)</i>

Presentation No.	T7. Molecular, Cellular, and Tissue Engineering and Biomaterials
TP124	Enhanced apoptotic cell death by magnetic hyperthermia with chitosan-coated MnFe ₂ O ₄ nanoparticles <i>Yunok Oh, and Junghwan Oh (Pukyong National University, Korea)</i>
TP125	Chitosan-polypyrrole nanocomposites for anticancer drug delivery <i>Bian Jang¹, Panchanathan Manivasagan¹, Seungjae Lee², Junghwan Oh^{1,*} (¹Pukyong National University, ²Hankuk Academy of Foreign Studies, Korea)</i>
TP126	Development of three-dimensional fibrous cellulose scaffold via post electrospinning treatment for tissue engineering applications <i>Mahesh Kumar Joshi, Arjun Prasad Tiwari, Bikendra Maharjan, Han Joo kim, Chan Hee Park*, Cheol Sang Kim* (Chonbuk National University, Korea)</i>
TP127	Heterogeneous Tissue Engineered Constructs (hetTECs) Recapitulate the Micromechanical and Mechanobiologic Complexity of Native Dense Connective Tissues <i>Su-jin Heo¹, Woojin M. Han¹, Claire M. McLeod¹, Dawn M. Elliott² and Robert L. Mauck¹ (¹University of Pennsylvania, USA, ²University of Delaware, USA)</i>
TP128	The study on MG-63 cells proliferation with various mechanical stimulation on auxetic hybrid scaffold <i>Hongjin Choi, JinHo Kang, JunJae Lee, JeongKoo Kim* (Inje University, Korea)</i>
TP129	A comprehensive electric field analysis of cylinder-type multi-nozzle electrospinning system for mass production of nanofibers <i>In Gi Kim, Jung-Ho Lee, Afeesh Rajan Unnithan, Do Hee Lee, Sung Won Ko, Chan-Hee Park*, Cheol Sang Kim* (Chonbuk National University, Korea)</i>
TP131	High sensitive detection of apple scar skin viroid (ASSVd) by using loop-mediated isothermal amplification (LAMP) <i>Se Hee Lee, Ga-Young Park, Gna Ahn, Eunji Lee, and Ji-Young Ahn* (Chungbuk National University, Korea)</i>
TP133	Improvement of multifunctional loading rate system on dielectrophoretic tweezers <i>M. H. Kim, K. H. Ko, S. Choi and S. W. Lee (Yonsei University, Wonju, Korea)</i>
TP134	Fabrication, maturation, and implantation of a tissue-engineered composite intervertebral disc <i>D.H. Kim^{1,2}, J.T. Martin^{1,2}, S.E. Gullbrand^{1,2}, and R.L. Mauck^{1,2,*} (¹University of Pennsylvania, USA, ²Philadelphia VA Medical Center, USA)</i>
TP135	Dielectrophoresis force spectroscopy for defining the directional effect of intermolecular bonds <i>I. S. Park, K. H. Ko, M. H. Kim, S. W. Lee (Yonsei University, Won-Ju, Korea)</i>
TP136	Mucoadhesive polymer loaded nanostructured microparticles for their enhanced retention in gastrointestinal tract <i>C. G. Park, B. K. Huh, S. N. Kim, S. H. Lee, M. Park, H. R. Hong, K. R. Kim, H. Won, and Y. B. Choy* (Seoul National University, Korea)</i>
TP137	Absorbable fibrin glue formulated with plga microparticles for sustained delivery of bupivacaine <i>S. N. Kim¹, B. H. Choi², B. K. Huh¹, S. H. Lee¹, H. K. Kim^{2,*} and Y. B. Choy^{1,*} (¹Seoul National University, ²Korea University Guro Hospital, Korea)</i>
TP138	In vitro evaluation of doxorubicin loaded fucoidan reduced gold nanoparticles for anticancer drug delivery <i>Panchanathan Manivasagan¹, Seo Jaehoon², Junghwan Oh^{1,*} (¹Pukyong National University, ²Baejung High School, Korea)</i>
TP139	Biomimetic of bone like apatite nanostructure via anodization / hydrothermal processes on magnesium alloy for bone implant <i>Hamouda M. Mousa, Jinwoo kim, Madhav Prasad Neupane, Woo Jin Lee, Chan Hee Park*, Cheol Sang Kim* (Chonbuk National University, Korea)</i>

TP140	An osteogenic composite scaffold for bone tissue engineering: A unique combination of growth factor and nanotopography induced osteogenesis <i>Afeesh Rajan Unnithan*</i> , Sunny Lee, Jin Woo Kim, Sung Won Ko, Joshua Lee, Min Hyuk Kim, Francis.O.Obiweluozor, Chan Hee Park, Cheol Sang Kim (Chonbuk National University, Korea)
TP141	g-C ₃ N ₄ sheet decorated ZnO flowers with improved photocatalytic activity <i>Surya Prasad Adhikari, Jun Hee Kim, Min Hyeok Kim, Jeong In Kim, Bishnu Kumar Shrestha, Arjun Tiwari, Ganesh Awasthi, Bikendra Maharjan, Chan Hee Park, Cheol Sang Kim</i> (Chonbuk National University, Korea)
TP142	Micro-tube cell organization for artificial micro-blood vessel <i>J. Choi, S. Lee, S. Lee, K. Koo</i> (University of Ulsan, Korea)
TP143	Effect of tourmanium on muscle atrophy following sciatic nerve injury <i>D. H. Hwang¹, S. H. Kim¹, D. H. Seo¹, S. K. Cho² and H. S. Kim^{1,2}</i> (¹ Yonsei University, ² Yonsei-Fraunhofer IZFP Medical Device Lab, Korea)
TP144	Protective effect of nitric oxide releasing nanofiber in hypoxia/reoxygenation-induced cardiomyocytes injury <i>Young Ju Lee¹, Ki Bum Kim², Jae Ho Shir², Hun-Kuk Park¹ and Gi-Ja Lee¹</i> (¹ Kyung Hee University, ² Kwangwoon University, Korea)
TP145	Developing the uniaxial 3D scaffold for highly matured skeletal muscle <i>Suk-Hee Park¹, Ung Hyun Ko², Jinseung Choung², and Jennifer H. Shin²</i> (¹ Micro/Nano Scale Manufacturing R&BD Group, Korea Institute of Industrial, ² KAIST, Korea)
TP146	Characterization of cellular transition within the expanding cell monolayer <i>Youngbin Cho¹, Bomi Gweon², Jacob Notbohm³, Ung Hyun Ko¹, Hwanseok Jang⁴, Yongdoo Park⁴, and Jennifer H. Shin¹</i> (¹ KAIST, ² Hanyang University, Korea, ³ Harvard University, MA, USA, ⁴ Korea University, Korea)
TP147	Mesenchymal stem cells labeled with indocyanine green for noninvasive tracking using ultrasonic and photoacoustic imaging, in vitro study <i>Kyu Kyu Hlaing, Nhat Quang Bui, Jin Myoung Yoo, Yun-Ok Oh, Seung Yun Nam and Junghwan Oh*</i> (Pukyong National University, Korea)
TP148	The effect of three-dimension(3D) scaffolds using Poly-L-Lactic Acid(PLLA) and Tricalcium Phosphate(TCP) on bone regeneration in rat calvarial defect model. <i>JiYun Nam¹, SeungHoon Kang¹, Hong-Hee Jung², JoonHo Wang*</i> (¹ Sungkyunkwan University, ² Samsung Medical Center, Korea)
TP149	Silicon-doped hydroxyapatite coating on low elastic titanium alloy for dental implant application <i>Y. H. Jeong¹, T. G. Jung¹, J. W. Yang¹, J. Y. Jeong¹, H. C. Cho²</i> (¹ Osong Medical Innovation Foundation, ² Chosun University, Korea)
TP152	Applying biomechanical stresses to cells on a stretchable substrate using bioreactor <i>GeonHui Lee¹, Sung Ho Ko¹, Soo Hyun Kim², Sang-Hoon Lee^{*1}</i> (¹ Korea University, ² Biomaterials Research Center, Korea Institute of Science and Technology, Korea)
TP153	Cytotoxic distending toxin of Escherichia coli's and their virulence <i>Tuyatsatsral .L¹ and Sarantuya. J²</i> (¹ Midwifery, Mongolia, ² School of Pharmacy and Bio-Medicine, Mongolia)
TP154	Different therapeutic potential of non-responder and responder MSCs in SOD1 mice <i>H. Kim^{1,2}, H.Y. Kim², H. Jang¹, W. Jo¹, K.S. KIM³, C.Y. KIM¹ and S.H. KIM²</i> (¹ Daegu-Gyeongbuk Medical Innovation Foundation, ² Hanyang University, ³ Bioengineering Institute, Corestem Inc., Korea)
TP155	To explain results of hepatocellular modeling in Mongolians by non linear theory <i>B.Odmaa, B.Tserennadmid, M.Tuul</i> (School of Pharmacy and Bio-Medicine MNUMS)
TP156	The study of location and structure of blue spots in Mongolian children aged from 0 to 3 in Ulaanbaatar city <i>Baigalmaa.B, Avirmed.A, Amgalanbaatar.D</i> (School of Pharmacy and Bio-Medicine, MNUMS, Mongolia)

Poster Sessions (Nov. 13)

Presentation No.	T7. Molecular, Cellular, and Tissue Engineering and Biomaterials
TP151	Decellularization with pulsatile perfusion <i>S. M. Park, S. R. Yang, S. W. Choi, J. R. Park, J. W. Yang, H. Lee, E. C. Kim (Kangwon National University, Korea)</i>
Presentation No.	T2. Biosignal Processing and Neural Engineering
TP157	Estimation of core body temperature from heart rate monitoring based on multiple regression analysis <i>Soo Young Sim, Kwang Min Joo, Han Byul Kim, and Kwang Suk Park* (Seoul National University, Korea)</i>
Presentation No.	T1. Biomedical Imaging and Optics
TP158	A method for reducing artifact of MR image due to the implantable hearing aid <i>H. J. Ahn, H. G. Lim, S. T. Woo, J. H. Lee, K. W. Seong, M. N. Kim and J. H. Cho* (Kyungpook National University, Korea)</i>
Presentation No.	T2. Biosignal Processing and Neural Engineering
TP159	Post-load glucose levels as indicators of glycemic control in vivo <i>Min Hyuk Lim, Tae Jung Oh, Karam Choi, Jung Chan Lee, Young Min Cho* and Sungwan Kim* (Seoul National University, Korea)</i>
TP160	Novel estimation method for signal source position inside human heart using switching voltage divider electrodes <i>Y. Sakaue and M. Makikawa (Ritsumeikan University, Kusatsu, Japan)</i>
TP161	Comparison of unipolar and bipolar methods for 2ch EEG based BCI system <i>Hyeon-Seok Lee, Yubing Jiang, and Wan-Young Chung (Pukyong National University, Korea)</i>
TP162	Performance stabilization and evaluation for brain diagnostic monitoring system based on near infra-red spectroscopic imaging <i>Jae-Ho Han and Seungbae Ji (Korea University, Korea)</i>
TP163	The ptosis auto diagnosis system and algorithm using surface electromyogram <i>Mi Sung Kwon, Jong-Ha Lee*, Hee-Jun Park, and Dae Gu Son (Keimyung University, Korea)</i>
TP164	Non-contact medical imaging control system using a 3D motion controller <i>Su-Yang, Jeong-Hun Ku, and Jong-Ha Lee* (Keimyung University, Korea)</i>
TP165	Obstructive sleep apnea-hypopnea syndrome diagnosis using quantitative analysis of sleep macro-structure <i>D. W. Jung, H. N. Yoon, Y. J. Lee, D. U. Jeong, and K. S. Park (Seoul National University, Korea)</i>
TP166	An effect of the sampling frequency to the pulse rate variability analysis <i>Hangsik Shin and Yoon La Yang (Chonnam National University, Korea)</i>
TP167	Relation between the maximum systolic location of photoplethysmography waveform and sampling frequency <i>Hangsik Shin and Sooji Park (Chonnam National University, Korea)</i>

TP168	Compare the accuracy of estimated blood pressure value at the finger with that of ear <i>J. H. Lee, J. H. Heo, J. J. Lee, H. W. Kin and Y. R. Yoon (Yonsei University, Wonju, Korea)</i>
TP169	Blink detection using ambient light sensor <i>J. H. LEE, J. H. HAN, J. H. IM, H. W. KIM and Y. R. YOON (Yonsei University, Wonju, Korea)</i>
TP170	Implementation of a Wireless Hearing Aid System with Ezairo 7100 Development Kit <i>Yuyong Jeon, Yongdeok Park, Han-sok Suh, Hyeon-min Shim, Gyutae Kim, Chenghao Quan, Sangmin Lee (Inha University, Korea)</i>
TP171	Estimation for individual binaural beat characteristics by an android application <i>Woo-Hyeong Cho, Kang Lee, Hyeon-min Shim, Jangwoo Kwon, Kyu-Sung Kim and Sangmin Lee (Inha University, Korea)</i>
TP172	Split and merge algorithm for deep learning <i>Hongsub An, Sang-Ick Kang, Sang-pyo Hong, Gyuseok Park and Sangmin Lee (Inha University, Korea)</i>
TP173	Pulse wave extraction from cellphone camera image using small region of interest(ROI) <i>J. J. Lee, J. H. Lee, J. H. HEO, H. W. KIM and Y. R. Yoon (Yonsei University, Wonju, Korea)</i>
TP174	Effective Electrode placement for Monitoring of Respiration with AED <i>J.H. HAN, J.H. HEO, H.W. KIM, J.J. LEE and Y.R. YOON (Yonsei University, Wonju, Korea)</i>
TP175	A posture classification algorithm based on SVM with RBF kernel <i>S.Y. Ma, S.K. Kim, H.M. Shim, S.S. Kim and S. Lee (Inha University, Korea)</i>
TP176	Smart pad e-book application for quadriplegic using portable sEMG device <i>E. I. Cho, H. W. Kim, J. H. Im and Y. R. Yoon (Yonsei University, Wonju, Korea)</i>
TP177	Detection of characteristic points of pulse wave using persistent homology <i>J. H. Im, J. D. Piao, E. I. Cho, and Y. R. Yoon (Yonsei University, Wonju, Korea)</i>
TP178	Optimal pulse-wave foot point detection algorithm verification for calculating pulse-wave velocity <i>J. Y. Park, J. H. Im, and Y. R. Yoon (Yonsei University, Wonju, Korea)</i>
TP179	Auditory steady-state response test using hearing loss simulator for brain-computer interface <i>J. H. Hwang, J. M. Ahn, K. W. Nam and I. Y. Kim (Hanyang University, Korea)</i>
TP180	Eye-blink detection using electrodes attached around the ears <i>J. Yoon, J. M. Ahn, J. H. Hwang, K. W. Nam, and I. Y. Kim (Hanyang University, Korea)</i>
TP181	Speech-induced EEG classification using the minimum distance to riemannian mean <i>Woosoo Choi, and Boreom Lee (Gwangju Institute of Science and Technology, Korea)</i>
TP182	Individualization strategy for EEG-based passive brain-computer interfaces considering test-retest reliability of EEG features <i>C.-H. Han, J.-H. Lim, J.-H. Lee, and C.-H. Im (Hanyang University, Korea)</i>
TP183	Speech enhancement algorithm using 2-D binary mask in wavelet domain <i>G. H. Lee, S. D. Na, J. N. Lee, Y. J. Lee, J. H. Cho, and M. N. Kim (Kyungpook National University, Korea)</i>
TP184	Feasibility study of 808nm near-infrared stimulation on cultured cells <i>Seongwon Min¹, Minsu Yoo², Youngmin Moon¹ and Sohee Kim¹ (¹GIST, Korea, ²University of Chicago, USA)</i>
TP185	A study on the effect of the vibration stimulus for blood flow on wrist <i>L. Y. Hwang, H. W. Jin, S. H. Jeon, W. H. Choi, and T. M. Shin (Yonsei University, Wonju, Korea)</i>
TP186	EEG-based drowsiness detection using SVM algorithm <i>S. H. Choi, S. H. Hong, H. B. Kwon, and K. S. Park (Seoul National University, Korea)</i>

TP187	The development of physical activity analysis system attached to shoes based on ergonomic design <i>Y. R. Jang, S. Y. Shin, H. S. Kim, W. H. Choi, and T. M. Shin (Yonsei University, Wonju, Korea)</i>
TP188	A study on the optimal frequency of vibration stimulus for activation of the biceps brachii muscle <i>S. H. Jeon, H. S. Kim, Y. R. Jang, S. Moon, W. H. Choi and T. M. Shin (Yonsei University, Wonju, Korea)</i>
TP189	Biometric authentication based on ECG signal <i>E. H. Lee, D.H. Kim, S.H. Song, S.J. Hong, J. S. Lee, and I. Y. Kim[†] (Hanyang University, Korea)</i>
TP190	May reduction of blue light-induced oxidative stress be influenced on performance of p300 speller? – preliminary study <i>Kyungjin Lee¹, Hohyun Cho², Hee-Gu Kim³, and Sung Chan Jun^{2*} (¹Gachon University, Korea, ²Gwangju Institute of Science and Technology, Korea, ³BM Biotechnology Co., Ltd, Korea)</i>
TP191	A smart health monitoring wheelchair for nonintrusive measurement of biological signals <i>J. Heo, S. Y. Sim, S. H. Hong, S. H. Choi, Y. J. Kim, S. K. Ko, I. J. Hong, S. Kim and K. S. Park (Seoul National University, Korea)</i>
TP192	Sensory neuro-modulation by low-intensity pulsed ultrasound stimulation <i>H. Jung^{1,2}, S. Han^{1,3}, M. Kim^{1,2}, H. Kim^{1,2}, J. Park^{1,3}, H. Shin^{1,2}, I. Youn^{1,2,#} (¹Korea Institute of Science and Technology, Korea, ²University of Science and Technology, Korea, ³Korea University, Korea)</i>
TP193	Long-time intra-cortical signal analysis for stroke rehabilitation analysis <i>Kyungsoo Kim, Seung Jun Yoo, Jae-Eun Jang, Minkyu Je, Cheil Moon, Ji-Woong Choi (DGIST, Korea)</i>
TP194	Changes in movement-related cortical activities during self-paced gait initiation and externally-cued gait initiation <i>K. S. Cha, J. W. Choi, J. H. Park, H. S. Jeon, and K. H. Kim (Yonsei University, Wonju, Korea)</i>
TP195	Dynamic stopping for P300 classification with SWLDA and BLDA <i>M. H. Chang and K. S. Park (Seoul National University, Korea)</i>
TP196	Classification method for detecting the deep sleep in human sleep based on machine learning <i>K. M. Joo, H. N. Yoon, D. W. Jung, S. H. Choi, H. B. Kwon, D. S. Lee and K. S. Park (Seoul National University)</i>
TP197	Relative power distribution for tremor detection in Parkinson's disease <i>Hyoseon Jeon, Hong Ji Lee, Hyeyoung Park, Woongwoo Lee, Sang Kyong Kim, Hanbyul Kim, Beom Seok Jeon, Kwang Suk Park (Seoul National University, Korea)</i>
TP198	The estimation of blood pressure groups using self-pressure of finger on PPG <i>H. J. Lee, J. S. Lee, and K. S. Park (Seoul National University, Korea)</i>
TP200	EEG based human identification using eye blinking signals <i>Jeehoon Kim¹, Changho Choi², Sunho Lee², Chungmin Ha³, and Kwangsuk Park¹ (¹Seoul National University, Korea, ²Gyeonggi Science High School, Korea, ³University of Texas at Austin, U.S.A.)</i>
TP201	Possibility of thermal comfort estimation with wrist skin temperature <i>M.J. Koh, S.Y. Shim, K.M. Joo, H.B. Kim, K.S. Park (Seoul National University, Korea)</i>
TP202	Detection of unilateral tremor using directionality analysis <i>S.K. Kim, H.J. Lee, H.S. Jeon, H.B. Kim, B.S. Jeon, K.S. Park (Seoul National University, Seoul, Korea)</i>
TP203	Novel alignment algorithm of synchronized burst based on Gaussian filter convolution <i>Hyungsup Lee and Yoonkey Nam (KAIST, Korea)</i>
TP204	The measurement of Ear-EEG signals using dry electrodes <i>H. B. Kwon, S. H. Hong, S. H. Choi, and K. S. Park (Seoul National University, Korea)</i>
TP205	Novel noise reduction algorithm for electrocardiography for wearable devices <i>D. S. Lee, S. J. Kwon, J. H. Kim, and K. S. Park (Seoul National University, Korea)</i>

TP206	Possibility of thermal comfort estimation with wrist skin temperature <i>M.J. Koh, S.Y. Shim, K.M. Joo, H.B. Kim, K.S. Park (Seoul National University, Korea)</i>
TP207	Temporal encoding of chemical stimulation by nociceptive neurons in mouse hairy skin <i>K. W. Cho¹, J. B. Cho¹, S. P. Kim², S. J. Jung¹, D. P. Jang^{1*} and I. Y. Kim¹ (¹Hanyang University, Korea, ²Ulsan National Institute of Science and Technology, Korea)</i>
TP208	Decoding the bimanual arm movement from the brain signal: Using epidural ECoG in non-human primate <i>K. R. Min¹, H.S. Choi¹, J. Y. Lee¹, K. H. Ahn², K. M. Lee², I. Y. Kim¹, and D. P. Jang¹ (¹Hanyang University, Korea, ²Seoul National University Hospital, Korea)</i>
TP209	System performance improvement in the olfactory event related potential by odorants changing <i>J. H. Kim[*], Y. M. Park, J. S. Park, D. P. Jang, I. Y. Kim, S. H. Cho (Hanyang University, Seoul, Korea)</i>
TP210	Evaluation of smartphone feature combination to detect freezing of gait <i>Hanbyul Kim¹, Hong Ji Lee¹, Woongwoo Lee², Sungjun Kwon¹, Sang Kyong Kim¹, Hyo Seon Jeon¹, Hyeyoung Park¹, Chae Won Shin¹, Won Jin Yi¹, Beom S. Jeon¹, and Kwang S. Park¹ (¹Seoul National University, Korea, ²Eulji General Hospital, Seoul, Korea)</i>
TP211	Alterations in field potentials after anodal transcranial direct current stimulation on the motor cortex of anesthetized rats <i>Ho Koo¹, Yong-Il Shin², Yu Fan¹, Sang Hu Han¹ and Min Sun Kim¹ (¹Wonkwang University, Korea, ²Pusan National University Yangsan Hospital, Korea, ³Wonkwang University, Iksan, Korea)</i>
TP212	The effects of clinical test time on the auditory late response and the spontaneous EEG in the gap-in-tense sound paradigm <i>J.Y. Kim, Y.S. Ku, J.W. Ahn, D.Y. Kim, C.H. Kwon, M.W. Suh, J.H. Lee, S.H. Oh, and H.C. Kim[*] (Seoul National University, Korea)</i>
TP213	Implementation of a low power consumption and small area processor for fully implantable middle ear hearing device <i>D. W. Kim¹, J. H. Kim², Y. S. Park², J. H. Lee³, H. G. Lim², M. N. Kim² and J. H. Cho^{2*} (¹Kyungpook Regional Headquarters, Korea Testing Certification, ²Kyungpook National University, Korea, ³Kyungpook National University Hospital)</i>
TP214	Implementation of analysis tool of electromyograph(EMG) signals for biosemi's activetwo system <i>J. Park, C. Kwon, and H. Kang (Soonchunhyang University, Korea)</i>
TP215	Obstructive sleep apnea detection using a single channel signal for healthcare applications <i>U. Erdenebayar, J. U. Park, P. S. Jeong and K. J. Lee (Yonsei University, Wonju, Korea)</i>
TP216	Assessment of sleep efficiency based on cardiopulmonary coupling analysis <i>J. U. Park, P. S. Jeong, and K. Y. Lee (Yonsei University, Wonju, Korea)</i>
Presentation No.	T4. Therapeutic and Diagnostic Devices and Systems
TP217	Cytokinetic inter nuclei distance stimulates apoptosis of the cancer cell <i>Pawan K. Tiwari (Catholic University of Daegu, Korea)</i>
TP218	Thermal damage control in kidney tumor model during diffuser-assisted photocoagulation <i>Trung-Hau Nguyen, Kyu Kyu Hlaing, Yu Gyeong Chae, and Hyun Wook Kang (Pukyong National University, Korea)</i>
TP220	Cancer detection and treatment with ultrasound technique <i>V.R.Singh Fellow-IEEE (National Physical Laboratory, India)</i>
TP221	Hypoxic gas inhalation to predict the outcome of chemotherapy <i>Hyeryun Jeong, Songhyun Lee, Jae Gwan Kim[*] (Gwangju Institute of Science and Technology (GIST), Korea)</i>

TP222	Objective skin pigmentation assessment: Analysis of skin photo type III <i>Ahmad Fadzil M. Hani¹ and Hermawan Nugroho² (¹CISIR, Universiti Teknologi PETRONAS, Malaysia, ²SEGi University, Malaysia)</i>
TP223	pH controlled release of paclitaxel via electrospun Polyurethane/Eudragit® L100-55 composite mat for duodenal stent cover application <i>L.E. Aguilar, J.P. Soriano, S.W. Ko, S.N. Lee, J.W. Kim, T. Batgerel, A. Ghavaminejad, M. Samarikhajaj, J.I. Kim, C.H. Park*, C.S. Kim* (Chonbuk National University, Korea)</i>
TP224	Magnetic nanovector for the down regulating CD44 and imaging of microRNA <i>Hwunjae Lee¹, C. Hyunkyung Park¹, Seungjoo Haam¹, Jin-Suck Suh¹, Eun-Kyung Lim²* and Yong-Min Huh¹* (¹Yonsei University, Korea, ²Korea Research Institute of Bioscience and Biotechnology, Korea)</i>
TP225	Application of circumferential irradiation for low-temperature laser lipolysis <i>Jieun Hwang¹, Nguyen Trung Hau¹, Minwoo Ahn¹, Sung Yeon Park², and Hyun Wook Kang¹* (¹Pukyong National University, Busan, Korea, ²University of California, CA, USA)</i>
TP226	Experiment for comparing the performances of heterogeneous devices for measuring heart rate and respiratory rate using the IR-UWB <i>Young-Jin Park, Hong-Kun Lyu, and Hui-Sup Cho (DGIST, Korea)</i>
TP227	Application of non-compliant balloon catheters for photothermal treatment <i>Jinoh Park, Trung Hau Nguyen, Jieun Hwang, and Hyun Wook Kang* (Pukyong National University, Busan, Korea)</i>
TP228	The study on design of metal plate for improvement of optical property <i>K.T. Kim¹, J.S. Kim¹, Y.H. Shin¹, M.J. Han¹, Y.J. Heo¹, J.K. Park², S.H. Nam¹ (¹Inje University, ²International University of Korea, Jinju, Korea)</i>
TP229	Inhibition Effect of Ascorbic acid against Formation of Amyloid-like Fibrils <i>W. Lee¹, H. Lee¹, I. Kim², S. W. Lee², S. W. Lee¹ and D. S. Yoon² (¹Yonsei University, Wonju, ²Korea University, Korea)</i>
TP230	Correlation between trabecular bone score(TBS) and age, body size, and bone mineral density(BMD) : The Korean population <i>Junghyun Park, Young-Seong Kim, Eunji Lee, and Taeyong Lee* (Dongguk University, Ilsan, Korea)</i>
TP231	The effect of sonic vibration massage system to prevent low back pain caused by driving postures <i>I. J. Jang, and J. I. Youn* (Catholic University of Daegu, Korea)</i>
TP232	The study on electrical property according to the change of bottom electrode for bendable sensor <i>G.Y. Choi, R.Y Yun, Y.H. Shin, M.J. Han, K.T. Kim, Y.J. Heo, K.M. Oh, S.H. Nam (Inje University, Korea)</i>
TP233	The study on electrical properties of radiation sensor according to the change of mixing ratio of metal oxide <i>R.Y. Yun¹, G.Y. Choi¹, M.J. Han¹, K.T. Kim¹, Y.J. Heo¹, K.M. Oh¹, S.K. Park², S.H. Nam¹ (¹Inje University, ²Busan paik hospital, Korea)</i>
TP234	The development of radiation detector improved reproducibility study using oxide materials in radio-therapy <i>M.J. Han¹, G.Y. Choi¹, R.Y. Yun¹, Y.H. Shin¹, K.T. Kim¹, J.S. Kim¹, S.K. Park², S.H. Nam¹ (¹Inje University, ²Busan paik hospital, Korea)</i>
TP235	Development of belt type falling and heart rate detection system with remote monitoring smartphone application <i>Y.H. Cho, E.I. Cho, J.H. Heo, J.H. Cho, Y.R. Yoon (Yonsei Univ., Wonju, Korea)</i>
TP236	A new way for cancer surgery: Fluorescence imaging guided surgery with augmented reality <i>Jungsuk Heo¹, Minji Kim¹, Yu Hua Quar², Youngwoon Choi¹, Hyun Koo Kim² and Beop-Min Kim¹ (¹Korea University, ²Korea University Guro Hospital, Korea)</i>

TP237	Development of a control device automatically determining the angle difference between the X-ray source and detector on portable digital radiography system <i>D. W. Heo¹, J. H. Ryu¹, C. W. Jeong¹, T. H. Kim¹, H. Y. Jun¹, S. C. Kang¹, and K. H. Yoon¹ (Wonkwang University, Korea)</i>
TP238	A computational parameter study of noninvasive electrical stimulation to the epiphyseal plate <i>H. J. Park¹, J. H. Ku² and S. Kim¹ (¹Gwangju Institute of Science and Technology, ²Keimyung University, Korea)</i>
TP239	Trainable Hearing Aid Algorithm for Hearing-Impaired Persons <i>S. H. Yoon, H. P. Kim, J. Y. Kim, H. J. Ahn, K. W. Nam, and I. Y. Kim (Hanyang University, Korea)</i>
TP240	CNT/PDMS ECG electrode for long-term recording <i>H.C Jung¹, S.K. Yoo¹, S.A. Lee¹, Jin-Hee Moon¹ and S.H-Lee² (¹Osong Medical Innovation Foundation, ²Korea University, Korea)</i>
TP241	Objective severity assessment system for the unilateral facial palsy based on 3-dimensional depth information <i>S. M. You, E. H. Lee, K. H. Lee, J.S. Cho, J. S. Lee, and I. Y. Kim[†] (Hanyang University, Korea)</i>
TP242	A study on development of safety and performance test for ultrasonic dental scaling system <i>Eun-Jeong Cho, Hong-Won Yeon, In-Hye Kim, Chang-Hyeong Lee, Hyeok Ju Kim (Medical Device Research Division, Ministry of Food and Drug Safety, Cheongju-Si, Korea)</i>
TP243	Passive ultrasonic images constructed with acoustic emission from cavitation activities in water produced by a clinical extracorporeal shock wave source <i>Gwansuk Kang, Sung Chan Cho, and Min Joo Choi (Jeju National University, Korea)</i>
TP244	Development of multi-channel bio-admittance imaging probe to detect tissue property change due to the stimulation <i>Y. E. Kim¹, G. Y. Jang¹, H. Wi², T. I. Oh¹, and E. J. Woo¹ (¹Kyung Hee University, ²Yonsei University, Korea)</i>
TP245	Preliminary study on the development of automatic measuring instrument for range of motion in patients with spondyloarthritis <i>M. Kim^{1,*}, C. Lee¹, H. M. Kwon², D. J. Go², J. Y. Moon², E. B. Lee², and S. Kim^{1,2,+} (¹Seoul National University, ²Seoul National University College of Medicine Korea)</i>
TP246	Twinkling artifact significantly enhanced by a mechanical impact <i>Jeonghwa Yang¹, Gwansuk Kang², and Min Joo Choi² (¹Cheju Halla Univ., ²Jeju Nat'l Univ., Korea)</i>
TP247	The 1st high intensity line focused ultrasonic surgical device <i>Sung Chan Cho¹, Gwansuk Kang², and Min Joo Choi² (¹KORUST Ltd., Anyang, ²Jeju National University, Korea)</i>
TP248	Passive ultrasonic images constructed with acoustic emission from cavitation activities in water produced by a clinical extracorporeal shock wave source <i>Gwansuk Kang¹, Sung Chan Cho², and Min Joo Choi¹ (¹Jeju National University, ²KORUST Ltd., Anyang, Korea)</i>
TP249	A Study for Visible Adipose Tissue Mimic Phantom to Estimate the Thermal Denaturation in Ultrasonic Lipolysis Therapy <i>J. Y. Kim¹, J. Y. Kim¹, S. C. Noh², and H. H. Choi¹ (¹Inje University, ²International University of Korea, Jinju, Korea)</i>
TP250	Electrochemical Impedance Spectroscopy for Aptamer-based Biosensors <i>H. J. Yoo, W. K. Sun, S. J. Yang, J. H. Park, C. H. Ji, S. B. Jun* (Ewha Womans University, Korea)</i>
TP251	Polyimide-pdms electrodes for human body communication between binaural hearing aids <i>J. H. Moon¹, H. C. Jung¹, S. A. Lee¹, S. K. Yoo¹, I. H. Song¹, D. J. Moon¹ and S. H. Lee^{2,3} (¹Osong Medical Innovation Foundation, ²Korea University, ³Korea University, Korea)</i>

TP252	Development of biopsy gun for aspiration and drug injection <i>J.M.Cho, K.G.Kim, H.G.Kang (National Cancer Center, Goyang-si, Korea)</i>
TP253	Development of Strabismometry Software <i>H.-W. Moon¹, Y.-J. Kim¹, H.-K. Yang², J.-M. Hwang², and K.-G. Kim¹ (¹National Cancer Center, Goyang-si, ²Seoul National University Bundang Hospital, Korea)</i>
TP254	Investigation of venous blood flow during intermittent pneumatic compression <i>W. Lee, J. H. Seo, H. B. Kim, S. H. Chung, K. G. Kim, and H. G. Kang (National Cancer Center, Goyang-si, Korea)</i>
TP256	Development of an alarm system for a concerned high cervical cord injury patient <i>J. H. Ro, G. R. Jeon, S. H. Kim, J. S. Lee, Y. B. Shin (Pusan National University, Korea)</i>
TP257	Development of flexible and stretchable dry electrode using metal electroplating on a porous elastomer <i>Jeong hun Kim, Joonghoon Lee, Hanseop Kim and Sang-Hoon Lee (Korea University, Korea)</i>
TP258	A highly conductive and soft CNT/AgNW/PDMS-based electrodes for continuous and insensible EEG recording <i>Joonghoon Lee, Hanseop Kim, Jeonghun Kim, Ji-Young Hwang, Sang-Hoon Lee (Korea University, Korea)</i>
TP259	Development of GUI program for objective assessment of facial nerve palsy <i>H. S. Kim¹, S. Y. Kim², Y. H. Kim¹, and K. S. Park¹ (¹Seoul National University, ²Seoul National University Hospital, Korea)</i>
TP260	Anthropometric study on Mongolians with metabolic syndrome <i>Dashdulam.Ts, Otgonbat.J, Tuul.B, Enebish.S, Amgalanbaatar.D, (School of Pharmacy and Bio-Medicine, MNUMS, Mongolia.)</i>
Presentation No.	T6. Biomedical Robotics and Rehabilitation Engineering
TP261	Development of the EDAMS using algometer and bio-potential measurement <i>S. S. Kim¹, J. H. Ro¹, J. H. Kim² and G. R. Jeon¹ (¹Pusan National University, ²Inje University, Korea)</i>
TP262	Implementation of bellows type electromagnetic transducer for round window drive-type middle-ear implants <i>D. H. Shin¹, H. G. Lim¹, Y. J. Jo¹, E. S. Jung², K. W. Seong³, M. N. Kim³ and J. H. Cho^{1*} (¹Kyungpook National University, ²Daegu-Gyeongbuk Medical Innovation Foundation, ³Kyungpook National University Hospital, Korea)</i>
TP263	Development of wireless charging low-frequency stimulator for wearable <i>Hojong Chang[*], Hyeon Dock Kim (KAIST, Korea)</i>
TP264	Closed-loop control of functional neuromuscular stimulation using cuff electrode for sit-to-stand maneuver in spinal cord injury animal model <i>Kang-Il Song^{1,2}, Joongkee Min³, Sunghee E. Park^{1,3}, Kuiwon Choi¹, Dosik Hwang², and Inchan Youn^{1,*} (¹Korea Institute of Science and Technology, ²Yonsei University, ³ASAN Medical Center, University of Ulsan College of Medicine, Korea)</i>
TP265	Study on verifying detection of the gait intention by IMU sensors using rollator during walking <i>H. J. Lee¹, S. R. Kang¹, G. T. Yang¹, Y. S. Kim², H. S. Shim², C.U. Hong¹ and T. K. Kwon¹ (¹Chonbuk National University, ²EasyMove Co., Ltd., Korea)</i>
TP266	Development of a mobile game and wearable device for upper limb rehabilitation. <i>H. J. Lim, J. H. Ku (Keimyung University, Korea)</i>
TP267	Neurofeedback guided upper extremity rehabilitation using smartphone <i>Hyunmi Lim, Jeonghun Ku (Keimyung University, Korea)</i>

TP268	Gait characteristics of flexed knee type of RGO for paraplegia: A preliminary study <i>Y. H. Chang, H. J. Choi, B. R. Jeong, J. C. Ryu, and M. S. Mun (Korea Orthopedic & Rehabilitation Engineering Center, Korea)</i>
TP269	Rollover detection of indoor mobile devices using an inertia sensor unit <i>S.J. Ahn, E.K. Choi, M. Jo, J.M. Kim and Y.H. Kim (Yonsei University, Wonju, Korea)</i>
TP270	Development of emotion & gesture recognition system using eMotion glove <i>K. H. Lee, J. S. Cho, S. I. Kang, S. J. Lee, J. S. Lee, and I. Y. Kim* (Hanyang University, Korea)</i>
TP271	Stimulation frequency compensation of a vibration system based on the open-loop circuit for the body stimulation <i>H. W. Jin, S. H. Jeon, L. Y. Hwang, W. H. Choi, and T. M. Shin (Yonsei University, Wonju, Korea)</i>
TP272	Personalized toe spreaders with three-dimensional scanning and printing for Hallux Valgus <i>Sung Jae Kim, BS¹, Yong Ho Cha, MS², Geun ho Lee, MS², Jae Lim Kim, MD², Dong Kyu Kim, BS², Sang Jun Kim, MD, PhD² (¹SAHIST, Sungkyunkwan University, ²Samsung Medical Center, Sungkyunkwan University School of Medicine, Korea)</i>
TP273	A study on human gait analysis in accordance with change of body-weight support percentage <i>S. M. Song¹, C. H. Yu¹, K. Kim², J. J. Kim², W. K. Song³, C. U. Hong¹ and T. K. Kwon¹ (¹Chonbuk National University, ²Chonbuk National University Automobile-parts & mold Technology Innovation Center, ³National Rehabilitation Center, Korea)</i>
TP274	Real-time, simultaneous and propositional myoelectric control for robotic rehabilitation therapy of stroke survivors <i>Hae Yean Park¹, JunYong Hong², Harold Martin³, Leonard Elbaum³, Hye-Min EJ Kang³, Mangai Prabakar³, Nagarajan Prabakar³, Kyuwon Park⁴, Jong-Hoon Kim³, YoungJin Jung^{2,3} (¹Yonsei University, Wonju, ²Radiological Science, Dongseo, Busan, Korea, ³Florida International University, ⁴University of Miami, Miami, FL, USA)</i>
TP275	Proportional Myoelectric Control based on Frequency Features for Robotic Rehabilitation Therapy <i>Hae Yean Park¹, Hye-Min EJ Kang², JunYong Hong³, Jong-Hoon Kim⁴, YoungJin Jung^{3,4} (¹Yonsei University, Wonju, Korea, ²University of Minnesota, MN, USA, ³Radiological Science, Dongseo, Busan, Korea, ⁴Florida International University, Miami, USA)</i>
TP278	A new similarity metric and its application for 2D image registration <i>Duc-Manh Ta, Seungbum Koo* (Chung-Ang University, Korea)</i>
TP279	Full-bridge ultrasound pulser circuit for muscle rehabilitation system using low intensity focused ultrasound stimulation <i>S. Oh¹, K. Song^{1,2}, H. Kim¹, and I. Youn^{1,*} (¹Korea Institute of Science and Technology (KIST), ²Yonsei University, Korea)</i>
TP280	Quantification of mechanical properties of multi-layer elastic specimen using an indentation method <i>Yoon Kwak, Seungbum Koo (Chung-Ang University, Korea)</i>
TP282	A preliminary study on robot-guided orthognathic surgery system <i>Sang-Yoon Woo, Sang-Jeong Lee, and Won-Jin Yi (Seoul National University, Korea)</i>
TP284	Quantitative analysis on gait-training effect of stroke rats <i>J. K. Ko, C.B. Yeo, and C. Song* (Daegu Gyeongbuk Institute of Science and Technology (DGIST), Korea)</i>
TP285	Optimization of TMS coil position using magnetic vector potential <i>Donghyeon Kim, Sung Chan Jun* (Gwangju Institute of Science and Technology, Korea)</i>
TP286	Analyze human skin injury types caused by collision <i>Moony Young Park¹, Ki Hong Kim², Min Kyung Shin¹, Sung Soo Rhim², Kyung Sook Kim^{1,*} (¹Kyung Hee University, ²Kyung Hee University, Gyeonggi-do, Korea)</i>

Presentation No.	T8. Cardiovascular and Respiratory System Engineering
TP287	STEMYNA: A smartphone application for cardiorespiratory endurance evaluation in daily environment <i>S. J. Kwon and K. S. Park (Seoul National University, Korea)</i>
TP288	Hazardless environment monitoring system by multichannel VLC using CMOS camera <i>ZhenYang Ong and Wan-Young Chung (Pukyong National University, Korea)</i>
TP289	Two steps association rule mining for medical clinical data <i>Sang Hun Han, Ho Sun Shon, Kyung Ah Kim, Eun Jong Cha, and Keun Ho Ryu (Chungbuk National University, Korea)</i>
TP290	A preliminary study on simulation of electrocardiogram using neural oscillators and networks <i>Min Hyuk Lim, and Sungwan Kim* (Seoul National University College of Medicine, Korea)</i>
TP291	Method of ballistocardiogram measurement for infants <i>W. K. Lee, H. Yoon, and K. S. Park (Seoul National University, Korea)</i>
TP292	The effect of electrical conduction velocity on cardiac electromechanical delay and pumping efficacy: Computational study <i>A. R. Yuniarti, A. K. Heikhmakhtiar, and K. M. Lim* (Kumoh National Institute of Technology, Korea)</i>
TP294	Increased variation in blood pressure during REM sleep detected from ballistocardiogram <i>H. Yoon¹, S. H. Hwang¹, J. W. Cho², Y. J. Lee², D. U. Jeong², and K. S. Park¹ (¹Seoul National University, ²Seoul National University Hospital, Korea)</i>
TP295	Simulation study of bio-impedance measurements to estimate the cardiovascular disease <i>H. Wi¹, G. Y. Jang², T. I. Oh², and E. J. Woo² (¹Yonsei University, ²Kyung Hee University, Korea)</i>
TP296	NT-ProBNP as a predictor of cardiovascular events in patients with non ST-segment elevation myocardial infarction <i>Ho Sun Shon, Keun Ho Ryu, Eun Jong Cha, Kyung Ah Kim (Chungbuk National University, Korea)</i>
TP304	Application of pig model in development of a simple mechanical anastomosis device <i>J. S. Kim, S. H. An, K. S. Jeon, S. D. Kim, D. B. Kim, C. Y. Kim* (Daegu-Gyeongbuk Medical Innovation Foundation (DGMIF), Korea)</i>
TP297	Establishment of evaluation method for wearable cardiac defibrillators in a pig model with induction of cardiac arrhythmia <i>K. S. JEON, S. D. KIM, D. B. KIM, S. H. AN, J. S. KIM, S. T. SEO, J. H. HONG, C. Y. KIM* (Daegu-Gyeongbuk Medical Innovation Foundation (DGMIF), Korea)</i>
TP298	Motion noise reduction from wrist-type photoplethysmography (PPG) based on empirical mode decomposition <i>S.J. Hong, S.H. Song, D.H. Kim, S.I. Kang, J.S. Lee and I.Y. Kim (Hanyang University, Korea)</i>
TP299	The development of convergence diagnostic mobile device and platform <i>J. Y. Lee¹, W. S. Kim², J. E. Lee¹, H. Kim^{1,2} (¹Sungkyunkwan University, ²Samsung Medical Center, Korea)</i>
TP300	Prediction of the effect of IABP pumping phase on ventricular mechanics by using 3D cardiac electro-mechanical model <i>K. M. Lim¹, and E. B. Shim² (¹Department of Medical IT Convergence Engineering, Gumi, ²Department of Mechanical & Biomedical Engineering, Chuncheon, Korea)</i>
TP301	Combined effect of LVAD and CRT on cardiac electromechanical delay: A simulation study <i>A. K. Heikhmakhtiar¹, A. J. Ryu², Y. S. Kim¹, E. B. Shim², and K. M. Lim^{1*} (¹Kumoh National Institute of Technology, ²Kangwon National University, Korea)</i>

TP302	Effects of the mechanical properties of the atherosclerotic coronary wall on fibrous cap stress <i>J.H. Park, M. Kang, and K. Rhee (Myongji University, Yongin, Korea)</i>
Presentation No.	T3. Nanobiosensor and Instrumentation
TP072	Enzymatic fiber biofuel cell for implantable applications <i>Cheong Hoon Kwon, Young Bin Park, and Seon Jeong Kim* (Hanyang University, Korea)</i>
Presentation No.	T7. Molecular, Cellular, and Tissue Engineering and Biomaterials
TP150	Cell-based scaffolds for bioartificial muscle by PEDOT/MWCNT <i>Tae Hyeob Kim*, Cheong Hoon Kwon*, and Seon Jeong Kim (Hanyang University, Korea)</i>
Presentation No.	T1. Biomedical Imaging and Optics
TP040	Current density of in vivo canine brain during transcranial direct current stimulation (tDCS) <i>S.Z.K. Sajib¹, W.C. Jeong¹, N. Katoch¹, B.K. Choi¹, H.J. Kim¹, O.I. Kwon² and E.J. Woo¹ (¹Kyung Hee University, ²Konkuk University, Korea)</i>
TP303	Development of multi-fusion MR image-based 3D advanced radiation treatment planning techniques <i>B.Y. Choe, K.H. Song, C.H. Yoo, S.I. Lim (The Catholic University of Korea College of Medicine, Korea)</i>
Presentation No.	T4. Therapeutic and Diagnostic Devices and Systems
TP307	Meshed silver nanowires with flexible substrate for mechanical-stable and transparent electrodes. <i>Hyejin Jang, Tae Hyung Kim, Jooseung Lee, Tae-il Kim* (Sungkyunkwan University, Korea)</i>
TP308	Ultrasensitive mechanosensor based geometrically modulated nanoscale cracks <i>Byeonghak Park, Jisun Kim, Chanhoo Jeong, Tae-il Kim† (Sungkyunkwan University, Korea)</i>

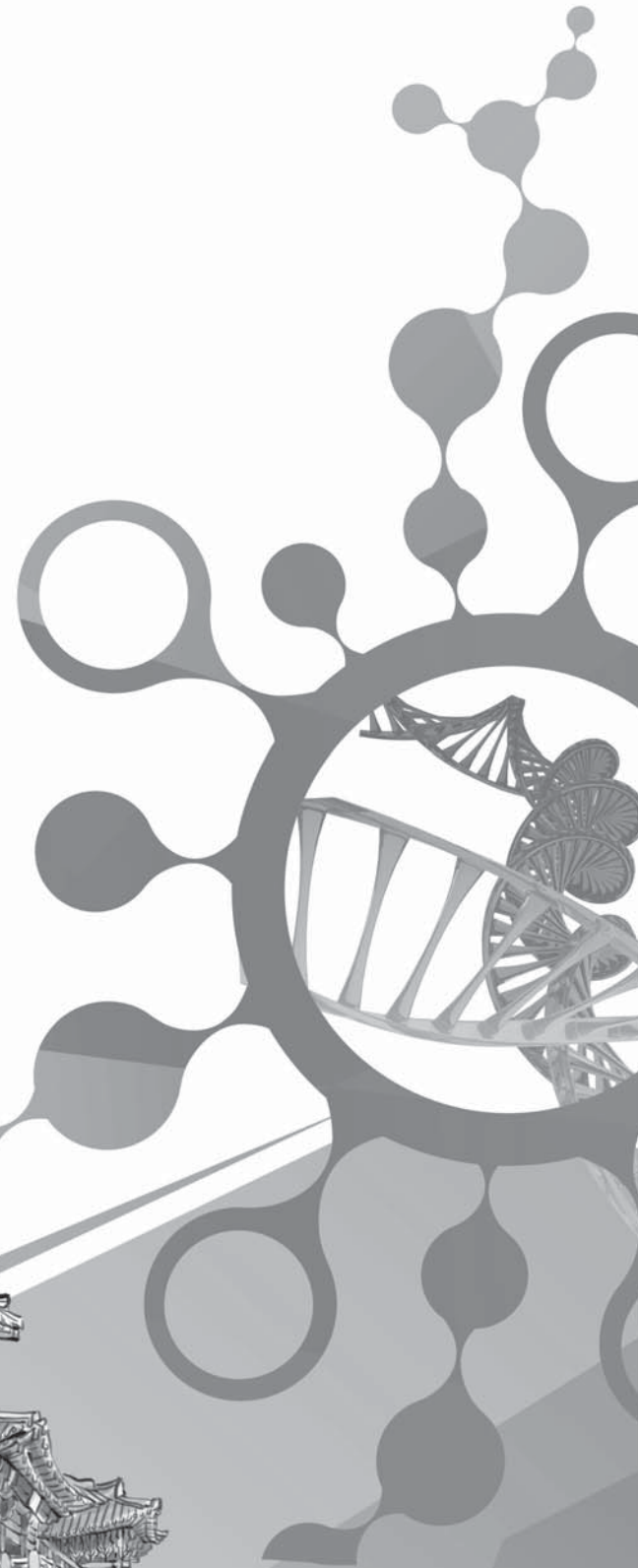
IBEC

International Biomedical
Engineering Conference 2015

2015

Road to Better Life through Biomedical Engineering

AUTHOR INDEX



A

Adhikari, Surya Prasad	TP141
Aguilar, L.E.	TO049
Aguilar, L.E.	TP223
Ahn, Gna	TP131
Ahn, H. J.	TP158
Ahn, H. J.	TP239
Ahn, H.J.	TP030
Ahn, J. M.	TP179
Ahn, J. M.	TP180
Ahn, J.W.	TP212
Ahn, Ji-Young	TP131
Ahn, K. H.	TP208
Ahn, Minwoo	TP225
Ahn, S.J.	TP101
Ahn, S.J.	TP269
Ahn, Sangtae	TO018
Ahn, Wonsik	SS052
Ahn, Y. J.	TP067
Ahn, Yeh-Chan	TO008
Ahn, Yeh-Chan	TO009
Ahn, Yeh-Chan	TP019
Ahn, Yong Jin	TP070
Ahn, Yong Jin	TP071
Ahn, Youjin	TO011
Ahn, Yujin	TO029
Amgalanbaatar., D	TP156
Amgalanbaatar., D	TP260
An, Hongsub	TP172
An, J.Y.	TO001
AN, S. H.	TP297
An, S. H.	TP304
Avirmed., A	TP156
Awasthi, Ganesh	TP141

B

Bae, JY	TO006
Baek, H. M.	TP016
Baek, H.C.	TI-013
Baek, Jin-Young	TP013
Baek, Jin-Young	TP014
Baek, Jin-Young	TP015
Baek, Songyee	TO011
Baek, Songyee	TO021
Baek, Songyee	TO029
Bahn, Y.	TO040
Baigalmaa., B	TP156

Ban, H. Y.	TO054
Ban, Sungbea	TO029
Bang, M. S.	SS015
Batgerel, T.	TO049
Batgerel, T.	TP223
Been, Jun-Kil	TO046
Bennet, K. E.	SS047
Boahen, Collins Kwadwo	TP034
Boire, Timothy C.	TI-033
Brophy, Colleen	TI-033
Bui, Nhat Quang	TP147
Bui, Q. N.	TO012
Bui, Q. N.	TP018
Byun, Kyung Min	SS008
Byun, Kyung Min	TO026

C

Cha, Eun Jong	TP289
Cha, Eun Jong	TP296
Cha, Ho-Seung	TO019
Cha, J. H.	TP023
Cha, J. Y.	TP108
Cha, Jung-ho	TP022
Cha, K. S.	TP194
Cha, O.	SS036
Cha, O.	TP028
Cha, Wonjae	TP005
Cha, Yong Ho	TP272
Chae, Huiseok	SS019
Chae, Y. G.	TP011
Chae, Yu Gyeong	TP218
Chae, Yu-Gyeong	TO009
Chae, Yu-Gyeong	TP019
Chang, Hojong	TP263
Chang, Jin Woo	PL4
Chang, Jin Woo	TO022
Chang, M. H.	TP195
Chang, Won-Du	TO019
Chang, Y. H.	TP268
Chang, Y.H.	TP112
Chen, W. M.	TO034
Chen, W. M.	TP100
Chen, W. M.	TP102
Chen, W. M.	TP103
Chen, W. M.	TP104
Cheong, Jae-Ho	TO050
Cho, Ahra	TP060
Cho, D.	TO006
Cho, D.	TO015

Cho, D.	TO015
Cho, Dong-Woo	TO055
Cho, Dong-Woo	TO056
Cho, E. I.	TP043
Cho, E. I.	TP176
Cho, E. I.	TP177
Cho, E.I.	TP235
Cho, Eun-Jeong	TP242
Cho, Eunji	TO010
Cho, Hohyun	TP190
Cho, Hui-Sup	TP226
Cho, Hyunchul	TO041
Cho, J. H.	TP158
Cho, J. H.	TP183
Cho, J. H.	TP213
Cho, J. H.	TP262
Cho, J. S.	TP270
Cho, J.H.	TP235
Cho, J.M.	TP252
Cho, J.S.	TP241
Cho, K. W.	TP207
Cho, M.	SS017
Cho, Nam Hyun	TO021
Cho, S. H.	TP209
Cho, S. K.	TP057
Cho, S. K.	TP086
Cho, S. K.	TP143
Cho, Seung-Woo	TI-029
Cho, Sung Chan	TP243
Cho, Sung Chan	TP247
Cho, Sung Chan	TP248
Cho, SungYoun	SS021
Cho, Won Ho	TO053
Cho, Woo-Hyeong	TP171
Cho, Y. K.	TP087
Cho, Y.H.	TP235
Cho, Young Min	TP159
Cho, Youngbin	TP146
Choe, B.Y.	TP045
Choe, B.Y.	TP047
Choe, B.Y.	TP048
Choe, B.Y.	TP303
Choe, H. C.	TP149
Choi, B. H.	TP137
Choi, B. K.	TP042
Choi, B.K.	TO004
Choi, B.K.	TO005
Choi, B.K.	TP040
Choi, B.K.	TP041
Choi, Bogyu	SS009

Choi, Changho	TP200	Choi, S.W.	TP151		
Choi, D.H.	TO015	Choi, Seok Hwa	TO056	D	
Choi, D.H.	TO015	Choi, Seong-O	TI-018		
Choi, Deok Gill	TP116	Choi, Seung Hyun	TO055	Dang, Nam Trung	TO057
Choi, Deok-Kee	TO040	Choi, Seungmoon	SS040	Dashdulam., Ts	TP260
Choi, DH	TO006	Choi, Seungmoon	SS042	Doh, Junsang	TI-032
Choi, E.K.	TP101	Choi, Seungyeop	TP068	Doh, Junsang	TO051
Choi, E.K.	TP269	Choi, Seungyeop	TP073	Du, Ping	TI-036
Choi, G.Y.	TP232	Choi, Seungyeop	TP076	Duncan, Randall L.	TO048
Choi, G.Y.	TP233	Choi, W. H.	TO027		
Choi, G.Y.	TP234	Choi, W. H.	TP056	E	
Choi, Geonho	TO021	Choi, W. H.	TP185		
Choi, H. H.	TP249	Choi, W. H.	TP187	Elbaum, Leonard	TP274
Choi, H. J.	TP268	Choi, W. H.	TP188	El-Gohary, Sherif H.	TO026
Choi, H.S.	TP208	Choi, W. H.	TP271	Elliott, Dawn M.	TP127
Choi, Hae Y.	SS004	Choi, Wonsuk	SS002	Enebish., S	TP260
Choi, Hak Soo	TI-038	Choi, Woosu	TP181	Enkhbaatar., A	TP306
Choi, Hongjin	TP128	Choi, Y. H.	TO002]	Eom, G. M.	TP094
Choi, Hyoung G.	TO059	Choi, Y. H.	TP108	Eom, G. M.	TP111
Choi, J. B.	TP207	Choi, Yong-Ho	TP027	Eom, G.M.	TP095
Choi, J. S.	TP077	Choi, Yong-Ho	TP034	Eom, Gwang-Moon	TI-021
Choi, J. S.	TP079	Choi, Yong-Ho	TP035	Eom, J. D.	TP102
Choi, J. S.	TP088	Choi, Youngwoon	TP236	Eom, Seyoung	TO026
Choi, J. S.	TP097	Choung, Jinseung	TP145	Erdenebayar, U.	TP215
Choi, J. S.	TP110	Chowdhury, Tanmoy	TP119		
Choi, J. W.	TP194	Choy, Y. B.	TP136	F	
Choi, J. W.	TP294	Choy, Y. B.	TP137		
Choi, J. Y.	TP063	Chu, J. U.	SS003	Fan, X. F.	TP018
Choi, J.S.	TP082	Chu, J. U.	TP108	Fan, Xiao Feng	TO012
Choi, J.	TO045	Chun, ByungSeon	TP053	Fan, Xiaofeng	TP020
Choi, J.	TP142	Chun, K. J.	TO036	Fan, Yu	TP211
Choi, Ji-Woong	TP193	Chun, Kwon Soo	TI-019	Fellow-IEEE, V.R.Singh	TP220
Choi, Jong Oh	SS051	Chung, Bong Geun	TI-011	Frey, U.	SS028
Choi, K.	SS003	Chung, C. K.	SS015		
Choi, Karam	TP159	Chung, Euiheon	TP051	G	
Choi, Kuiwon	SS001	Chung, Euiheon	TP058		
Choi, Kuiwon	TP264	Chung, Euiheon	TP060	GhavamiNejad, A.	TO049
Choi, Mi-Hyun	SS040	Chung, J. H.	SS017	Ghavaminejad, A.	TP223
Choi, Min Joo	TP243	Chung, S. H.	TP254	Go, D. J.	TP245
Choi, Min Joo	TP246	Chung, S. S.	TP103	Goh, Bong-Jun	TP013
Choi, Min Joo	TP247	Chung, S.-C.	SS039	Goh, Bong-Jun	TP014
Choi, Min Joo	TP248	Chung, Soon-Cheol	SS040	Goh, Bong-Jun	TP015
Choi, Munsik	TO026	Chung, W. Y.	TO001	Gong, Deok-You	SS014
Choi, S. H.	TP186	Chung, Wan-Young	TO020	Gu, S. R.	TO054
Choi, S. H.	TP191	Chung, Wan-Young	TO057	Gullbrand, S.E.	TP134
Choi, S. H.	TP196	Chung, Wan-Young	TP161	Guo, Hua	TI-004
Choi, S. H.	TP204	Chung, Wan-Young	TP288	Guth, Christy	TI-033
Choi, S.	TP066	Clifford, Gali	TI-006	Gwak, H. C.	TP102
Choi, S.	TP067	Clifford, Gari. D.	SS024	Gweon, Bomi	TP120
Choi, S.	TP133			Gweon, Bomi	TP146

H

Ha, Kanglyeol	TP020	Heo, J.H.	TP235	Hwang, J. H.	TP180
Ha, M. J.	TO014	Heo, J.	TP191	Hwang, J. M.	TP023
Ha, M.	TO013	Heo, Jungsuk	TP236	Hwang, J. Y.	SS012
Haam, Seungjoo	TP224	Heo, Min	SS001	Hwang, J. Y.	TI-015
Ham, J.	TO015	Heo, Su-Jin	TO048	Hwang, J.-M.	TP253
Ham, J.	TO015	Heo, Su-Jin	TP127	Hwang, Jieun	TP225
Ham, JS.	TO006	Heo, Y.J.	TP228	Hwang, Jieun	TP227
Han, B. S.	TP039	Heo, Y.J.	TP232	Hwang, Ji-Young	TP258
Han, Bong Soo	TP009	Heo, Y.J.	TP233	Hwang, L. Y.	TP185
Han, C.-H.	TP182	Hlaing, K. K.	TO012	Hwang, L. Y.	TP271
Han, Chungmin	TP200	Hlaing, K. K.	TP018	Hwang, M.	SS016
Han, D. W.	TP113	Hlaing, Kyu Kyu	TP147	Hwang, Min-Ho	SS014
Han, D	TP050	Hlaing, Kyu Kyu	TP218	Hwang, Nathaniel S.	TI-030
Han, I. G.	TP088	Hong, C. U.	TP273	Hwang, S. H.	TP294
HAN, J. H.	TP169	Hong, C.U.	TP265	Hwang, Seoyoung	TO022
HAN, J.H.	TP174	Hong, H. R.	TP136	Hwang, Soonjoo	TP058
Han, Jae-Ho	TP006	Hong, I. J.	TP191	Hwang, Y. H.	TP039
Han, Jae-Ho	TP162	Hong, J. H.	TP082	Hwang, Y. N.	TI-016
Han, JiHye	TP098	HONG, J. H.	TP297	Hwang, Yoon Ho	TP009
Han, JiHye	TP099	Hong, J. S.	TO036	Hyeryun, Jeong,	TP221
Han, KyeongJin	SS021	Hong, J. W.	TP055	Hyun, J. Y.	TP063
Han, M.J.	TP228	Hong, J.	TP003		
Han, M.J.	TP232	Hong, Junghwa	TP084		
Han, M.J.	TP233	Hong, Junghwa	TP085		
Han, M.J.	TP234	Hong, Junghwa	TP107	Im, C.-H.	TP182
Han, S.	SS003	Hong, Junghwa	TP109	Im, Chang-Hwan	SS046
Han, S.	TP192	Hong, Jungmin	TP051	Im, Chang-Hwan	TO019
Han, Sang Hun	TP289	Hong, JunYong	TP274	Im, J. H.	TP043
Han, Sang Hu	TP211	Hong, JunYong	TP275	IM, J. H.	TP169
Han, Sugnmin	SS004	Hong, S. H.	TP186	Im, J. H.	TP176
Han, Sungmin	SS002	Hong, S. H.	TP191	Im, J. H.	TP177
Han, Woojin M.	TP127	Hong, S. H.	TP204	Im, J. H.	TP178
Hani, Ahmad Fadzil M.	TP222	Hong, S.J.	TP189	In, Yong	TP115
Hau, Nguyen Trung	TP225	Hong, S.J.	TP298		
Heikhmakhtiar, A. K.	TP292	Hong, S.	TP059		
Heikhmakhtiar, A. K.	TP301	Hong, Sang-pyo	TP172		
Heo, D. W.	TP237	Hong, Seong-Dae	TO030	Jaehoon, Seo	TP138
Heo, Dong Nyoung	SS001	Hong, Yoon No G.	TP123	Jang, Jae-Young	SS010
Heo, Eun Young	SS001	Huh, B. K.	TP136	Jang, Bian	TP125
Heo, H. R.	TP044	Huh, B. K.	TP137	Jang, D. P.	SS047
Heo, H. R.	TP046	Huh, D. S.	TP103	Jang, D. P.	TP207
Heo, J. H.	TP043	Huh, Eun Y.	SS004	Jang, D. P.	TP208
Heo, J. H.	TP044	Huh, Yong-Min	TP224	Jang, D. P.	TP209
Heo, J. H.	TP168	Hwang, D. H.	TP086	Jang, G. Y.	TP052
HEO, J. H.	TP173	Hwang, D. H.	TP143	Jang, G. Y.	TP244
Heo, J.H.	TP095	Hwang, D.H.	TP057	Jang, G. Y.	TP295
HEO, J.H.	TP174	Hwang, D.	TO013	Jang, H. W.	TP017
		Hwang, Dosik	TP264	Jang, H.	TP154
		Hwang, Hwan	SS025	Jang, Hwanseok	TP146
		Hwang, J. H.	TP179	Jang, Hyejin	TP307

I

J

Jang, Hyojung	TO018	Jeong, Deok-Gyun	SS014	Jun, Sang Beom	TO022
Jang, I. J.	TP231	Jeong, Do-Un	SS023	Jun, Sung Chan	TO018
Jang, J. W.	TP100	Jeong, I. H.	TP063	Jun, Sung Chan	TO046
Jang, J. W.	TP103	Jeong, J. S.	TP033	Jun, Sung Chan	TP190
Jang, J. W.	TP104	Jeong, J. Y.	TP114	Jun, Sung Chan	TP285
Jang, Jae-Eun	TP193	Jeong, J. Y.	TP149	Jung, B. J.	TO014
Jang, Jaemyung	TO021	Jeong, Jinwoo	SS002	Jung, B.	TO013
Jang, Jae-Young	SS009	Jeong, Jiyoung	TP121	Jung, Byungjo	SS038
Jang, Jinah	TO055	Jeong, Joonsoo	SS049	Jung, Byungjo	TP049
Jang, M.	SS030	Jeong, P. S.	TP215	Jung, C.	TO037
Jang, Minjeong	TO050	Jeong, P. S.	TP216	Jung, D. W.	TP165
Jang, S. G.	TO014	Jeong, S.	SS016	Jung, D. W.	TP196
Jang, S.	TO013	Jeong, W. C.	TP042	Jung, Da Woon	SS025
Jang, Y. R.	TO027	Jeong, W.C.	TO004	Jung, E. S.	TP082
Jang, Y. R.	TP187	Jeong, W.C.	TO005	Jung, E. S.	TP262
Jang, Y. R.	TP188	Jeong, W.C.	TP040	Jung, H. C.	TP251
Jang, Young-Woong	TP105	Jeong, W.C.	TP041	Jung, H. H.	TO047
Jasanoff, Alan	TO016	Jeong, Y. H.	TP114	Jung, H.C	TP240
Jasanoff, Alan	TO016	Jeong, Y. H.	TP149	Jung, H.	TP192
Je, Minkyu	TP193	Jeong, Y. J.	TP074	Jung, Hong-Hee	TP148
Jeon, B.S.	TP202	Jeoung, O.C.	TP305	Jung, I. W.	TP106
Jeon, Beom S.	TP210	Ji, C. H.	TP250	Jung, J. U.	TP108
Jeon, Beom Seok	TP197	Ji, Chang Hyun	SS043	Jung, J. W.	TP064
Jeon, Byeong-Hwan	TP019	Ji, S. M.	TP033	Jung, Jin W.	SS004
Jeon, G. R.	TP065	Ji, Seungbae	TP006	Jung, S. J.	TP207
Jeon, G. R.	TP256	Ji, Seungbae	TP162	Jung, S.Y.	TP083
Jeon, G. R.	TP261	Jiang, Yubing	TO020	Jung, Seungwon	TO050
Jeon, Gye-Rok	TP005	Jiang, Yubing	TP161	Jung, Soonmoon	TP085
Jeon, H. S.	TP194	Jin, H. W.	TP185	Jung, Sunwoo	TO010
Jeon, H.S.	TP202	Jin, H. W.	TP271	Jung, Sunyoung	SS002
Jeon, Hyo Seon	TP210	Jo, M.	TP093	Jung, T. G.	TP113
Jeon, Hyoseon	TP197	Jo, M.	TP269	Jung, T. G.	TP114
Jeon, Hyun-Min	TI-024	Jo, W.	TP154	Jung, T. G.	TP149
JEON, K. S.	TP297	Jo, Y. J.	TP262	Jung, Woohyun	SS002
Jeon, K. S.	TP304	Joo, Hyo Sung	TP119	Jung, Woonggyu	TO010
Jeon, Min Yong	TP019	Joo, K. M.	TP196	Jung, Woonggyu	TO011
Jeon, Noo Li	TO021	Joo, K.M.	TP201	Jung, Woonggyu	TO021
Jeon, S. H.	TP185	Joo, K.M.	TP206	Jung, Woonggyu	TO029
Jeon, S. H.	TP188	Joo, Kwang Min	TP157	Jung, YoungJin	TP038
Jeon, S. H.	TP271	Joo, S.	TO017	Jung, YoungJin	TP274
Jeon, Sang Ryong	SS005	Joshi, Mahesh Kumar	TP126	Jung, YoungJin	TP275
Jeon, Y. H.	TP080	Joung, A.	TP063		
Jeon, Young Ju	SS029	Jun, H. Y.	TP237		
Jeon, Young Sun	SS031	Jun, J.-H.	SS039		
Jeon, Yuyong	TP170	Jun, Jae-Hoon	SS040	Kang, Hyun Wook	TP225
Jeong, B. R.	TP268	Jun, Jae-Hoon	TP013	Kang, Bokku	TP096
Jeong, C. W.	TP237	Jun, Jae-Hoon	TP014	Kang, Byoung Min	TP115
Jeong, Chanho	TP308	Jun, Jae-Hoon	TP015	Kang, C.	SS006
Jeong, D. U.	TP165	Jun, S. B.	TP250	Kang, D. H.	TP065
Jeong, D. U.	TP294	Jun, Sang Beom	SS043	Kang, D. W.	TP077

K

Kang, D. W.	TP079	Kim, C. H.	TP309	Kim, G.S.	TP083
Kang, D. W.	TP088	Kim, C. Y.	TO036	Kim, Gyutae	TP170
Kang, D. W.	TP097	KIM, C. Y.	TP297	Kim, H. B.	TP254
Kang, D. W.	TP110	Kim, C. Y.	TP304	Kim, H. C.	TO028
Kang, Gwansuk	TP243	Kim, C.-H	TO052	Kim, H. C.	TP091
Kang, Gwansuk	TP246	Kim, C.S.	TO049	Kim, H. G.	TP090
Kang, Gwansuk	TP247	Kim, C.S.	TP223	Kim, H. J.	SS013
Kang, Gwansuk	TP248	KIM, C.Y.	TP154	Kim, H. J.	TP042
Kang, H. G.	TP254	Kim, Chang Suk	TI-001	Kim, H. J.	TP063
Kang, H. W.	TP011	Kim, Chang-Soo	TP054	Kim, H. K.	TP137
Kang, H.G.	TP252	Kim, Cheol Sang	TP126	Kim, H. N.	TP011
Kang, H.	TP214	Kim, Cheol Sang	TP129	Kim, H. P.	TP239
Kang, Hye-Min EJ	TP274	Kim, Cheol Sang	TP139	Kim, H. S.	TO027
Kang, Hye-Min EJ	TP275	Kim, Cheol Sang	TP140	Kim, H. S.	TP057
Kang, Hyun Wook	TO007	Kim, Cheol Sang	TP141	Kim, H. S.	TP086
Kang, Hyun Wook	TO009	Kim, Cheongjun	TO042	Kim, H. S.	TP087
Kang, Hyun Wook	TP007	Kim, Choong-Yong	TO016	Kim, H. S.	TP143
Kang, Hyun Wook	TP020	Kim, Choong-Yong	TO016	Kim, H. S.	TP187
Kang, Hyun Wook	TP218	Kim, Chulhong	SS011	Kim, H. S.	TP188
Kang, Hyun Wook	TP227	KIM, D. B.	TP297	Kim, H. S.	TP259
Kang, Hyun-Wook	TI-039	Kim, D. B.	TP304	Kim, H. W.	TP043
Kang, I. H.	TP122	Kim, D. G.	TP114	Kim, H. W.	TP044
Kang, JinHo	TP128	Kim, D. H.	TP077	KIM, H. W.	TP169
Kang, Juehyung	TP053	Kim, D. H.	TP079	KIM, H. W.	TP173
Kang, K. H.	TP056	Kim, D. H.	TP087	Kim, H. W.	TP176
Kang, Kwan-Soo	TP105	Kim, D. H.	TP088	Kim, H.B.	TP201
Kang, Kwan-Soo	TP117	Kim, D. H.	TP097	Kim, H.B.	TP202
Kang, M.	TP302	Kim, D. H.	TP110	Kim, H.B.	TP206
Kang, S. C.	TP237	Kim, D. S.	TP305	Kim, H.C.	TO058
Kang, S. I.	TP270	Kim, D. W.	TP090	Kim, H.C.	TP212
Kang, S. R.	TP001	Kim, D. W.	TP091	Kim, H.G.	TP092
Kang, S. R.	TP265	Kim, D. W.	TP092	Kim, H.I.	TO015
Kang, S.I.	TP298	Kim, D. W.	TP213	Kim, H.I.	TO015
Kang, S.J.	TP112	Kim, D. W.	TP309	Kim, H.J.	TO004
Kang, Sang-Ick	TP172	Kim, D. Y.	TP039	Kim, H.J.	TO005
Kang, Se-Ryong	TP010	Kim, D.H.	TP050	Kim, H.J.	TP040
Kang, Se-Ryong	TP012	Kim, D.H.	TP134	Kim, H.J.	TP041
Kang, SeungHoon	TP148	Kim, D.H.	TP189	Kim, H.P.	TP030
Kang, Y. G.	TO054	Kim, D.H.	TP298	Kim, H.-S.	SS039
Katoch, N.	TO004	Kim, D.H	TP081	Kim, H.S	TP081
Katoch, N.	TO005	Kim, D.Y.	TP212	Kim, H.	TI-013
Katoch, N.	TP040	Kim, Dong Kyu	TP272	Kim, H.	TO013
Katoch, N.	TP041	Kim, Dong Youn	TP009	Kim, H.	TP154
Katoch, N.	TP042	Kim, Donghyeon	TO046	Kim, H.	TP192
Key, Jaehong	SS035	Kim, Donghyeon	TP285	Kim, H.	TP279
Kim, A-Hee	TP013	Kim, Duk-Soo	TP059	Kim, H.	TP299
Kim, A-Hee	TP014	Kim, E. C.	TP151	KIM, H.W.	TP174
Kim, A-Hee	TP015	Kim, Eun Kyoung	TP024	Kim, H.Y.	TP154
Kim, Beop-Min	TP236	Kim, G. H.	TP065	Kim, Han Byul	TP157
Kim, Bohyun	TP021	Kim, G. Y.	TI-016	Kim, Han Joo	TP126

Kim, Han Sung	TP096	Kim, J. W.	TP111	Kim, Jong-Min	TO030
Kim, Hanbyul	TP197	Kim, J. W.	TP118	Kim, Jun Hee	TP141
Kim, Hanbyul	TP210	Kim, J. Y.	TP016	Kim, JungSoo	TP038
Kim, Han-Joong	TO030	Kim, J. Y.	TP239	Kim, Jung	TI-028
Kim, Hannah	TO041	Kim, J. Y.	TP249	Kim, Jung-Wook	SS010
Kim, Han-na	TP007	Kim, J. Y.	TP249	Kim, Jun-Min	TP061
Kim, Hanseop	TP257	Kim, J.I.	TO049	Kim, Jun-Sik	TP013
Kim, Hanseop	TP258	Kim, J.I.	TP223	Kim, Jun-Sik	TP014
Kim, Hee-Gu	TP190	Kim, J.M.	TP050	Kim, Jun-Sik	TP015
Kim, Heejin	TO055	Kim, J.M.	TP101	Kim, Junsuk	SS044
Kim, HI.	TO006	Kim, J.M.	TP269	Kim, K. G.	TP254
Kim, Hoechan	TP107	Kim, J.S.	TP228	Kim, K. H.	TP194
Kim, Hongki	TP054	Kim, J.S.	TP234	Kim, K. J.	TP074
Kim, Hunhee	TP084	Kim, J.	TP028	Kim, K. R.	TP136
Kim, Hye Jin	TP007	Kim, J.W.	TP095	Kim, K.G.	TP252
Kim, Hyeon Dock	TP263	Kim, J.W.	TP223	Kim, K.-G.	TP253
Kim, Hyeok Ju	TP242	Kim, J.Y.	TP030	KIM, K.S.	TP154
Kim, Hyeon Ji	TO055	Kim, J.Y.	TP212	Kim, K.T.	TP228
Kim, Hyun Koo	TP236	Kim, Jae G.	TO015	Kim, K.T.	TP232
Kim, Hyunggun	TI-017	Kim, Jae G.	TO015	Kim, K.T.	TP233
Kim, HyungJoo	TP098	Kim, Jae Gwan	TI-014	Kim, K.T.	TP234
Kim, HyungJoo	TP099	Kim, Jae Gwan	TO018	Kim, K.	TP273
Kim, Hyung-Sik	SS040	Kim, Jae Gwan	TP221	Kim, Keewon	SS031
Kim, Hyunjin	TP053	Kim, Jae Lim	TP272	Kim, Ki Bum	TP144
Kim, I. Y.	TP030	Kim, Jaemin	TP085	Kim, Ki Hong	TP286
Kim, I. Y.	TP179	Kim, Jaeuk U.	SS029	Kim, Kwang Gi	TP053
Kim, I. Y.	TP180	Kim, Jaeuk. U.	SS031	Kim, Kyung Ah	TP289
Kim, I. Y.	TP189	Kim, Jeehoon	TP200	Kim, Kyung Ah	TP296
Kim, I. Y.	TP207	Kim, Je-Hun	TO009	Kim, Kyung Hwan	SS037
Kim, I. Y.	TP208	Kim, Jeong hun	TP257	Kim, Kyung Sook	TP286
Kim, I. Y.	TP209	Kim, Jeong In	TP141	Kim, Kyungsoo	TP193
Kim, I. Y.	TP239	Kim, Jeonghun	TP258	Kim, Kyu-Sung	TP171
Kim, I. Y.	TP241	Kim, JeongKoo	TP128	Kim, Laehyun	TO041
Kim, I. Y.	TP270	Kim, JG.	TO006	Kim, Laehyun	TO043
Kim, I.	TP229	Kim, Ji-hyun	TP006	Kim, M. H.	TP133
Kim, I.Y.	TP298	Kim, Jin S.	SS004	Kim, M. H.	TP135
Kim, In Gi	TP129	Kim, Jin Woo	TP140	Kim, M. J.	TO054
Kim, In Gul	TI-036	Kim, Jinseok	SS002	Kim, M. N.	TP158
Kim, In-Hye	TP242	Kim, Jinwon	TP120	Kim, M. N.	TP183
Kim, J. H.	TI-015	Kim, Jinwoo	TP139	Kim, M. N.	TP213
Kim, J. H.	TP205	Kim, Ji-Sun	SS040	Kim, M. N.	TP262
Kim, J. H.	TP209	Kim, Ji-Sun	TP013	Kim, M. S.	TI-012
Kim, J. H.	TP213	Kim, Ji-Sun	TP014	Kim, M.	SS013
Kim, J. H.	TP261	Kim, Ji-Sun	TP015	Kim, M.	TP192
Kim, J. J.	TP273	Kim, Jisun	TP308	Kim, M.	TP245
Kim, J. S.	TO002	Kim, Ji-Won	TI-021	Kim, Mansu	TP004
Kim, J. S.	TP118	Kim, Jong Yeol	SS029	Kim, Min Hyeok	TP141
KIM, J. S.	TP297	Kim, Jonghoon	TP036	Kim, Min Hyuk	TP140
Kim, J. S.	TP304	Kim, Jong-Hoon	TP274	Kim, Min Hyung	TP068
Kim, J. W.	TP094	Kim, Jong-Hoon	TP275	Kim, Min Hyung	TP073

Kim, Min Hyung	TP076	Kim, Seon Jeong	TP072	Kim, Youngjun	TO041
Kim, Min Sun	TP211	Kim, Seon Jeong	TP072	Kim, Young-Kwan	TI-025
Kim, MinJi	TP236	Kim, Seon Jeong	TP150	Kim, Young-Min	SS029
Kim, Minseok	TI-031	Kim, SH	TO006	Kim, Young-Min	SS032
Kim, Nam Keun	TI-022	Kim, Sohee	TP051	Kim, Young-Seong	TP078
Kim, Namkeun	TO031	Kim, Sohee	TP089	Kim, Young-Seong	TP230
Kim, Pankwon	TP123	Kim, Sohee	TP184	Kim, Young-Sik	TP019
Kim, Pilnam	TO050	Kim, Soo Hyun	TP152	Kim, Yuri	TP078
Kim, Pum-Joon	TO055	Kim, Sung Jae	SS020	Kin, H. W.	TP168
KIM, S. D.	TP297	Kim, Sung Jae	TP272	Ko, C.Y.	TP083
Kim, S. D.	TP304	Kim, Sung Kyun	SS031	Ko, C.Y.	TP112
Kim, S. G.	TP087	Kim, Sung Won	TO008	Ko, J. K.	TP284
Kim, S. H.	TP057	Kim, Sung Won	TO009	Ko, K. H.	TP133
Kim, S. H.	TP063	Kim, Sung Won	TO055	Ko, K. H.	TP135
Kim, S. H.	TP086	Kim, Sung Won	TO056	Ko, Kwan Hwi	TP068
Kim, S. H.	TP086	Kim, Sung-Phil	SS040	Ko, Kwan Hwi	TP073
KIM, S. H.	TP103	Kim, Sung-Phil	SS044	Ko, Kwan Hwi	TP076
Kim, S. H.	TP143	Kim, Sungwan	TP159	Ko, S. K.	TP191
Kim, S. H.	TP256	Kim, Sungwan	TP290	Ko, S.W.	TP223
Kim, S. J.	TP093	Kim, Sunhee	TO041	Ko, Sung Ho	TP152
Kim, S. M.	TI-016	Kim, Sun-Il	TP027	Ko, Sung Won	TP129
Kim, S. M.	TP033	Kim, Suyong	TO042	Ko, Sung Won	TP140
Kim, S. N.	TP136	Kim, T. H.	TP237	Ko, Ung Hyun	TP145
Kim, S. N.	TP137	Kim, Tae Hyeob	TP150	Ko, Ung Hyun	TP146
Kim, S. P.	SS041	Kim, Tae Hyung	TP307	Koh, M.J.	TP201
Kim, S. P.	TP207	Kim, Tae-il	TP307	Koh, M.J.	TP206
Kim, S. S.	TP261	Kim, Tae-il	TP308	Koh, Seong-Beom	TI-021
Kim, S.	TP191	Kim, Tae-Seong	TO026	Koh, W.	SS017
Kim, S. Y.	TP259	Kim, Taesung	TI-031	Kong, J. S.	TP082
Kim, S.G	TP081	Kim, Taeyeob	TO051	Koo, Ho	TP211
Kim, S.H.	TO015	Kim, W. H.	TP100	Koo, K.	TP142
Kim, S.H.	TO015	Kim, W. S.	TP299	Koo, Seungbum	TO044
KIM, S.H.	TP154	Kim, Y. E.	TP244	Koo, Seungbum	TP278
Kim, S.J.	TP101	Kim, Y. H.	TP093	Koo, Seungbum	TP280
Kim, S.K.	TP175	Kim, Y. H.	TP259	Ku, J. H.	TP238
Kim, S.K.	TP202	Kim, Y. J.	SS015	Ku, J. H.	TP266
Kim, S.S.	TP175	Kim, Y. J.	TP191	Ku, Jeong-Hun	TP164
Kim, S.	SS013	Kim, Y. M.	TO054	Ku, Jeonghun	TP267
Kim, S.	SS015	Kim, Y. S.	TP118	Ku, Y.S.	TP212
Kim, S.	SS016	Kim, Y. S.	TP265	Kumar, Suchit	TO030
Kim, S.	SS017	Kim, Y. S.	TP301	Kwak, K. C.	TP055
Kim, S.	TP238	Kim, Y.H.	TP101	Kwak, K. Y.	TP090
Kim, S.	TP245	Kim, Y.H.	TP269	Kwak, K.Y.	TP092
Kim, Sang Jun	TP272	Kim, Y.-J.	TP253	Kwak, Kichang	TP021
Kim, Sang Kyong	TP197	Kim, Y.-M	TO052	Kwak, Kichang	TP024
Kim, Sang Kyong	TP210	Kim, Y.	SS016	Kwak, Yoon	TP280
Kim, Sang-Hyub	TP061	Kim, Y.	SS017	Kwon, Cheong Hoon	TP150
Kim, Sang-Hyub	TP062	Kim, Yisuk	TP078	Kwon, C.H.	TP212
Kim, Sang-Yeob	TP058	Kim, Yong-Sik	TP115	Kwon, C.	TP214
Kim, Seok-Won	TO055	Kim, Yoonhye	TO025	Kwon, Cheong Hoon	TP072

Kwon, Cheong Hoon	TP072	Lee, D. Y.	TO032	Lee, Hyungsup	TP203
Kwon, D. S.	SS016	Lee, D.W.	TP047	Lee, Hyunki	TP054
Kwon, D.S	SS018	Lee, D.W.	TP048	Lee, Hyun-Young	SS014
Kwon, D.Y.	TP095	Lee, Deukhee	TO041	Lee, Inju	TP098
Kwon, Dong-Soo	SS014	Lee, Do Hee	TP129	Lee, InJu	TP099
Kwon, Gyu Hyun	TO043	Lee, Dong-Ho	SS014	Lee, J. C.	TO028
Kwon, H. B.	TP186	Lee, Dong-Kyun	TP022	Lee, J. C.	TP067
Kwon, H. B.	TP196	Lee, Doo Yong	TO042	Lee, J. E.	TP299
Kwon, H. B.	TP204	Lee, Doyeon	TP070	Lee, J. H.	TI-016
Kwon, H. G.	TP305	Lee, Doyeon	TP071	Lee, J. H.	TI-037
Kwon, H. K.	TP026	Lee, E. A.	SS055	Lee, J. H.	TP043
Kwon, H. M.	TP245	Lee, E. B.	TP245	Lee, J. H.	TP102
Kwon, Hunki	TP035	Lee, E. H.	TP189	Lee, J. H.	TP122
Kwon, Il K.	SS004	Lee, E. H.	TP241	Lee, J. H.	TP158
Kwon, Il Keun	SS001	Lee, Eunji	TP078	Lee, J. H.	TP168
Kwon, Jangwoo	TP171	Lee, Eunji	TP131	LEE, J. H.	TP169
Kwon, Mi Sung	TP163	Lee, Eunji	TP230	Lee, J. H.	TP173
Kwon, O.I.	TO004	Lee, Eun-Suk	TP013	Lee, J. H.	TP213
Kwon, O.I.	TO005	Lee, Eun-Suk	TP014	Lee, J. H.	TP305
Kwon, O.I.	TP040	Lee, Eun-Suk	TP015	Lee, J. I.	TP122
Kwon, Oh-Hun	TP027	Lee, G. H.	TP183	Lee, J. J.	TP043
Kwon, Oh-Hun	TP035	Lee, GeonHui	TP152	Lee, J. J.	TP044
Kwon, S. J.	TP205	Lee, Geun ho	TP272	Lee, J. J.	TP168
Kwon, S. J.	TP287	Lee, Gihyun	TP089	Lee, J. J.	TP173
Kwon, Sang-Mo	TO055	Lee, Gi-Ja	TP070	Lee, J. M.	TP026
Kwon, Soon-Yong	TP117	Lee, Gi-Ja	TP071	Lee, J. M.	TP055
Kwon, Sungjun	TP210	Lee, Gi-Ja	TP144	Lee, J. N.	TP183
Kwon, T. K.	TP265	Lee, Gyudo	TP068	Lee, J. P.	TP017
Kwon, T. K.	TP273	Lee, H. A.	TP057	Lee, J. S.	TO028
Kwon, Y. R.	TP094	Lee, H. J.	TP080	Lee, J. S.	TP023
Kwon, Y. R.	TP111	Lee, H. J.	TP198	Lee, J. S.	TP189
Kwon, Y.R.	TP095	Lee, H. J.	TP265	Lee, J. S.	TP198
		Lee, H. S.	TP093	Lee, J. S.	TP241
		Lee, H. W.	TP305	Lee, J. S.	TP256
		Lee, H. Y.	TI-037	Lee, J. S.	TP270
		Lee, H. Y.	TP122	Lee, J. W.	TP100
Laine, Andrew F.	PL1	Lee, H.J.	TP202	Lee, J. W.	TP103
Lee, B.	TO015	Lee, H.	SS018	Lee, J. W.	TP104
Lee, B.	TO015	Lee, H.	TP069	Lee, J. Y.	SS030
Lee, B.	TP011	Lee, H.	TP151	Lee, J. Y.	TP208
Lee, Boreom	TP181	Lee, H.	TP229	Lee, J. Y.	TP299
Lee, BR.	TO006	Lee, H.	TP078	Lee, J.C.	TO058
Lee, Byung Yang	TI-010	Lee, Haein	SS042	Lee, J.C.	TP030
Lee, C.N.	TP095	Lee, Hojin	TP197	Lee, J.-H.	TP182
Lee, C.	SS013	Lee, Hong Ji	TP210	Lee, J.H.	TP212
Lee, C.	TP245	Lee, Hong Ji	TP224	LEE, J.J.	TP174
Lee, Chang-Hyeong	TP242	Lee, Hwunjae	TI-009	Lee, J.M.	TP023
Lee, Chulhyun	TO030	Lee, Hye Jin	TO020	Lee, J.S.	TP298
Lee, D. H.	SS017	Lee, Hyeon-seok	TP161	Lee, J.	SS016
Lee, D. S.	TP196	Lee, Hyeon-Seok	TO008	Lee, J.	TP063
Lee, D. S.	TP205	Lee, Hyoung Shin			

Lee, J.	TP064	Lee, S. H.	TP137	Lee, Songhyun	TP221
Lee, Jae Yeon	TO056	Lee, S. H.	TP251	Lee, Soo-Hong	SS009
Lee, Jaehyun	TO051	Lee, S. J.	TO034	Lee, Sunho	TP200
Lee, JaeYeong	TP098	Lee, S. J.	TP001	Lee, Sunny	TP140
Lee, JaeYeong	TP099	Lee, S. J.	TP091	Lee, T. S.	TP016
Lee, Jee Y.	SS004	Lee, S. J.	TP100	Lee, T. S.	TP017
Lee, Jeonghyeon	TO021	Lee, S. J.	TP103	Lee, T.	TO032
Lee, Jong-Ha	TI-007	Lee, S. J.	TP104	Lee, Taekwan	TO016
Lee, Jong-Ha	TP163	Lee, S. J.	TP270	Lee, Taekwan	TO016
Lee, Jong-Ha	TP164	Lee, S. W.	TP069	Lee, Taekyeong	TP084
Lee, Jongho	TI-005	Lee, S. W.	TP069	Lee, Taekyeong	TP109
Lee, Jong-Min	TP021	Lee, S. W.	TP133	Lee, Taeyong	TP078
Lee, Jong-Min	TP022	Lee, S. W.	TP135	Lee, Taeyong	TP230
Lee, Jong-Min	TP024	Lee, S. W.	TP229	Lee, W. J.	TP001
Lee, Jong-Min	TP025	Lee, S. W.	TP229	Lee, W. K.	TP291
Lee, Jong-Min	TP027	Lee, S. W.	TP305	Lee, W.	TP069
Lee, Jong-Min	TP034	Lee, S. Y.	TO014	Lee, W.	TP229
Lee, Jong-Min	TP035	Lee, S.A.	TP240	Lee, W.	TP254
Lee, Joonghoon	TP257	Lee, S.H	TP240	Lee, Wonseok	TO025
Lee, Joonghoon	TP258	Lee, S.J.	TP102	Lee, Woo Jin	TP139
Lee, Jooseung	TP307	Lee, S.N.	TP223	Lee, Woo-Jin	TP010
Lee, Joshua	TP140	Lee, S.	TO013	Lee, Woo-Jin	TP012
Lee, Jung Chan	TP159	Lee, S.	TP142	Lee, Woongwoo	TP197
Lee, Jung-Ho	TP129	Lee, S.	TP142	Lee, Woongwoo	TP210
Lee, Jung-Woo	TO041	Lee, S.	TP175	Lee, Woo-Ram	TP061
Lee, JunJae	TP128	Lee, Sang Jin	SS001	Lee, Y. J.	TP106
Lee, Junwon	TO010	Lee, Sang Won	TO025	Lee, Y. J.	TP165
Lee, Junwon	TO011	Lee, Sang Woo	SS034	Lee, Y. J.	TP183
Lee, K. H.	SS047	Lee, Sang Woo	TP068	Lee, Y. J.	TP294
Lee, K. H.	TP122	Lee, Sang Woo	TP073	Lee, Y. K.	TP118
Lee, K. H.	TP241	Lee, Sang Woo	TP076	Lee, Yena	TO022
Lee, K. H.	TP270	Lee, SangHoon	SS026	Lee, Yong Seuk	TP116
Lee, K. J.	TP215	Lee, Sang-Hoon	TP152	Lee, Young Ju	TP070
Lee, K. M.	TP208	Lee, Sang-Hoon	TP257	Lee, Young Ju	TP071
Lee, K. Y.	TP216	Lee, Sang-Hoon	TP258	Lee, Young Ju	TP144
Lee, K.	SS053	Lee, Sang-Jeong	TP010	Lee, Youngho	TP085
Lee, Kang Dae	TO008	Lee, Sang-Jeong	TP012	Lee, Youngho	TP107
Lee, Kang	TP171	Lee, Sang-Jeong	TP282	Li, Gang	TO020
Lee, Kyu Back	TO025	Lee, Sangmin	TP170	Lim, D. H.	TO047
Lee, Kyungjin	TP190	Lee, Sangmin	TP171	Lim, Dohyung	TP098
Lee, M. H.	TP039	Lee, Sangmin	TP172	Lim, Dohyung	TP099
Lee, M.W.	SS030	Lee, Sang-Wook	TO059	Lim, Dohyung	TP105
Lee, Min-Hee	TP009	Lee, Sangyeob	TP049	Lim, Dohyung	TP117
Lee, Myung Chul	TP105	Lee, Se Hee	TP131	Lim, Eun-Kyung	TP224
Lee, Myung Chul	TP116	Lee, Sei-Young	TP068	Lim, H. G.	TP158
Lee, N.	TP002	Lee, Seung Ku	TP009	Lim, H. G.	TP213
Lee, P. V.	TO034	Lee, Seunghak	TP037	Lim, H. G.	TP262
Lee, S. A.	TP251	Lee, Seungjae	TP125	Lim, H. J.	TP266
Lee, S. H.	TP066	Lee, Seung-Koo	TO030	Lim, H. R.	TO035
Lee, S. H.	TP136	Lee, Seyong	TI-023	Lim, H. W.	SS017

Lim, Hyunmi	TP267	Moon, S.	TP188	Noh, S. C.	TP249
Lim, J.-H.	TP182	Moon, Y.	TO045	Notbohm, Jacob	TP146
Lim, Ji Won	TI-031	Moon, Youngmin	TP184	Nugroho, Hermawan	TP222
Lim, K. H.	TO001	Mousa, Hamouda M.	TP139		
Lim, K. M.	TP103	Mun, K. R.	TO038	O	
Lim, K. M.	TP104	Mun, K. R.	TO039		
Lim, K. M.	TP292	Mun, M. G.	TP309	Oak, Chulho	TO008
Lim, K. M.	TP300	Mun, M. S.	TP268	Oak, Chulho	TO009
Lim, K. M.	TP301	Mun, M.S.	TP112	Obien, M. E.	SS028
Lim, Ki Moo	TI-040	Mun, M.	TP083	Obiweluozor, Francis.O.	TP140
Lim, Min Hyuk	TP159	Myagmarnaran., Ts	TP306	Odmaa, B.	TP155
Lim, Min Hyuk	TP290	Myung, Seung-Jae	TP058	Oh, Chang-Hyun	TO030
Lim, S.I.	TP045			Oh, Gyungseok	TP058
Lim, S.I.	TP047	N		Oh, Han-Byeol	TP013
Lim, S.I.	TP048			Oh, Han-Byeol	TP014
Lim, S.I.	TP303	Na, Duk L.	TP021	Oh, Han-Byeol	TP015
Lim, Yoonseob	TO022	Na, Duk L.	TP022	Oh, J.	TP018
Lim, Young-Wook	TP117	Na, S. D.	TP183	Oh, Junghwan	TO007
Lin, Fa-Hsuan	TI-003	Na, Soo Jin	TO055	Oh, Junghwan	TO009
Lyu, Hong-Kun	TP226	Na, Sungsoo	TI-035	Oh, Junghwan	TO012
		Na, Y.	SS016	Oh, Junghwan	TO053
		Nam, H. S.	SS015	Oh, Junghwan	TP020
		Nam, Hakhyun	PL2	Oh, Junghwan	TP124
Ma, S.Y.	TP175	Nam, Hyeong Soo	TP053	Oh, Junghwan	TP125
Maharjan, Bikendra	TP126	Nam, Hyeong Soo	TP054	Oh, Junghwan	TP138
Maharjan, Bikendra	TP141	Nam, Inn-Chun	TO056	Oh, Junghwan	TP147
Makikawa, M.	TP160	Nam, JiYun	TP148	Oh, Juyoung	TO011
Manivasagan, Panchanathan	TP125	Nam, K. W.	TP179	Oh, Juyoung	TO029
Manivasagan, Panchanathan	TP138	Nam, K. W.	TP180	Oh, K.M.	TP232
Martin, Harold	TP274	Nam, K. W.	TP239	Oh, K.M.	TP233
Martin, J.T.	TP134	Nam, K.W.	TP030	Oh, S. H.	TI-037
Mauck, R.L.	TP134	Nam, S.H.	TP228	Oh, S.H.	TP212
Mauck, Robert L.	TO048	Nam, S.H.	TP232	Oh, S.	TP279
Mauck, Robert L.	TP127	Nam, S.H.	TP233	Oh, T. I.	SS055
McLeod, Claire M.	TP127	Nam, S.H.	TP234	Oh, T. I.	SS056
Mendis, B. V. A.	TP122	Nam, Seung Yoon	TI-002	Oh, T. I.	TP052
Min, A.	TP039	Nam, Seung Yun	TP147	Oh, T. I.	TP244
Min, Areum	TP009	Nam, Y.	TO017	Oh, T. I.	TP295
Min, Eunjung	TO010	Nam, Yoonkey	SS027	Oh, T.I.	TP074
Min, Joongkee	SS005	Nam, Yoonkey	TP203	Oh, Tae Jung	TP159
Min, Joongkee	TP264	Namgung, B. S.	TP086	Oh, Y. O.	TP018
Min, K. R.	TP208	Nebuya, S.	SS054	Oh, Yun-Ok	TO012
Min, Seongwon	TP184	Neupane, Madhav Prasad	TP139	Oh, Yunok	TO053
Moon, Cheil	TP193	Nguyen, Minh Tuan	TO059	Oh, Yunok	TP124
Moon, D. J.	TP251	Nguyen, T. H.	TP011	Oh, Yun-Ok	TP147
Moon, H.-W.	TP253	Nguyen, Thien	TO018	Ong, ZhenYang	TP288
Moon, J. H.	TP251	Nguyen, Trung Hau	TP227	Otgonbat., J	TP260
Moon, J. Y.	TP245	Nguyen, Trung-Hau	TP218	Otto, Kevin John	PL3
Moon, Jin-Hee	TP240	Nguyen, Van Phuc	TO007		
Moon, S. Y.	TP017	Nguyen, Van Phuc	TP007		

P

Park, B.	TO003	Park, J. H.	TO014	Park, K.S.	TP202
Park, B.	TP002	Park, J. H.	TO028	Park, K.S.	TP206
Park, Byeonghak	TP308	Park, J. H.	TP057	Park, K.W.	TP095
Park, C. G.	TP136	Park, J. H.	TP100	Park, Kwang S.	TP210
Park, C. H.	TO049	Park, J. H.	TP114	Park, Kwang Suk	SS025
Park, C. Hyunkyung	TP224	Park, J. H.	TP194	Park, Kwang Suk	TP157
Park, C.H.	TP223	Park, J. H.	TP250	Park, Kwang Suk	TP197
Park, Chan Hee	TP126	Park, J. M.	TI-015	Park, Kwang-Sook	SS009
Park, Chan Hee	TP139	Park, J. R.	TP151	Park, Kwangsuk	TP200
Park, Chan Hee	TP140	Park, J. S.	TP209	Park, Kwideok	TI-036
Park, Chan Hee	TP141	Park, J. U.	TP215	Park, Kyuwon	TP274
Park, Chan-Hee	TP129	Park, J. U.	TP216	Park, M.	TP136
Park, Eul-Joon	SS022	Park, J. W.	SS003	Park, Moon Nyeo	TO055
Park, Eun-Kee	TO009	Park, J. W.	TP100	Park, Moony Young	TP286
Park, Eun-Kee	TP019	Park, J. Y.	TP178	Park, S. B.	TP055
Park, Ga-Young	TP131	Park, J.H.	TO058	Park, S. H.	TO054
Park, Gilsoon	TP021	Park, J.H.	TP302	Park, S. K.	TO035
Park, Gilsoon	TP024	Park, J.K.	TP228	Park, S. M.	TP151
Park, Gyuseok	TP172	Park, J.-R.	SS039	Park, S.K.	TP233
Park, H. J.	TP065	Park, J.	TO013	Park, S.K.	TP234
Park, H. J.	TP238	Park, J.	TP192	Park, S.	SS017
Park, H. K.	TP066	Park, J.	TP214	Park, S.	TO037
Park, H. K.	TP067	Park, Jaehyun	TO031	Park, Sang-Kyoon	TI-024
Park, H. S.	TP106	Park, Jeong Hun	TO056	Park, Sehyung	TO041
Park, H.	TO003	Park, Jihoon	TP049	Park, Sooji	TP167
Park, H.	TP002	Park, Jinoh	TP227	Park, Suk-Hee	TP145
Park, H.	TP003	Park, Jong-Rak	SS040	Park, Sun Hwa	TO055
Park, Hae Yean	TP274	Park, Ju Young	TO055	Park, Sung Yeon	TP225
Park, Hae Yean	TP275	Park, Ju Young	TO056	Park, Sunghhee E.	TP264
Park, Hee jin	TP051	Park, Jung-Eun	TO009	Park, Sung-Jae	TP117
Park, Hee-Jun	TP163	Park, Junghyun	TP078	Park, Sung-Jun	SS040
Park, Hun-Jun	TO055	Park, Junghyun	TP230	Park, W. B.	TP091
Park, Hun-Kuk	TP070	Park, Jun-Sung	TP022	Park, Y. H.	TP023
Park, Hun-Kuk	TP071	Park, JY.	TO006	Park, Y. M.	TP209
Park, Hun-Kuk	TP144	Park, K. J.	TP017	Park, Y. S.	TP213
Park, Hyeyoung	TP197	Park, K. S.	TP059	Park, Y.J.	TP057
Park, Hyeyoung	TP210	Park, K. S.	TP165	Park, Y.	SS016
Park, Hyung Joon	TO025	Park, K. S.	TP186	Park, Yongdeok	TP170
Park, Hyungdal	SS002	Park, K. S.	TP191	Park, Yongdoo	TP146
Park, Hyunjin	TP004	Park, K. S.	TP195	Park, Young Bin	TP072
Park, Hyunjin	TP029	Park, K. S.	TP196	Park, Young Bin	TP072
Park, Hyunjin	TP036	Park, K. S.	TP198	Park, Young-Jin	TP226
Park, Hyunjin	TP037	Park, K. S.	TP204	Phan, Cong-Bo	TO044
Park, I. S.	TP135	Park, K. S.	TP205	Phuc, Nguyen Van	TO009
Park, In-Kyu	TI-034	Park, K. S.	TP259	Piao, J. D.	TP177
Park, J. -M.	TI-012	Park, K. S.	TP287	Piao, Yuanzhe	TI-008
		Park, K. S.	TP291	Prabakar, Mangai	TP274
		Park, K.S.	TP294	Prabakar, Nagarajan	TP274
			TP201	Pyun, Sung-Bom	TO043

Q

Quan, Chenghao TP170
Quan, Yu Hua TP236

R

Rhee, K. TP302
Rhim, Sung Soo TP286
Riew, K. D. TP104
Ro, Jung Hoon TP005
Ro, J. H. TP065
Ro, J. H. TP256
Ro, J. H. TP261
Roh, Heesuk TP084
Roh, J. H. TP082
Ryu, A. J. TP301
Ryu, J. C. TP268
Ryu, J. H. TP237
Ryu, J.C. TP112
Ryu, J.S. TP030
Ryu, J.S. TP101
Ryu, J. TP083
Ryu, Jihee TP051
Ryu, Jiseon TI-024
Ryu, K.H. TP050
Ryu, Keun Ho TP289
Ryu, Keun Ho TP296
Ryu, Yeon-Mi TP058

S

Safi, Abdul M. TP060
Sajib, S. Z. K. TP042
Sajib, S. Z. K. TP052
Sajib, S.Z.K. TO004
Sajib, S.Z.K. TO005
Sajib, S.Z.K. TP040
Sajib, S.Z.K. TP041
Sakaue, Y. TP160
Samarikhalaj, M. TO049
Samarikhalaj, M. TP223
Sarantuya., J TP153
Saravi, L. Alizadeh TO047
Seo, D. H. TP143
Seo, D.H. TP057
Seo, H. S. TP039
Seo, Hansu TO053
Seo, Hyeon TO046

Seo, J. H. TP254
Seo, J. K. SS053
Seo, J. W. TP077
Seo, J. W. TP079
Seo, J. W. TP088
Seo, J. W. TP097
Seo, J. W. TP110
Seo, J. SS036
Seo, J. TP028
Seo, J.W. TP082
Seo, Jeongwoo TP115
Seo, Jong-Mo SS050
Seo, Jong-Mo TP062
SEO, S. T. TP297
Seo, S.Y. SS030
Seo, Sang Won TP021
Seo, Sang Won TP022
Seo, Sang Won TP035
Seo, Y. TP008
Seok, HyungKwang SS021
Seong, K. W. TP158
Seong, K. W. TP262
Shim, E. B. TP300
Shim, E. B. TP301
Shim, H. S. TP265
Shim, H.M. TP175
Shim, Hyeon-min TP170
Shim, Hyeon-min TP171
Shim, S.Y. TP201
Shim, S.Y. TP206
Shin, Chae Won TP210
Shin, Chol TP009
Shin, Choongsoo S. TP121
Shin, Choongsoo S. TP123
Shin, D. A. TO028
Shin, D. H. TP262
Shin, D.A. TO058
Shin, Dong-Ah TP089
Shin, H. TP192
Shin, Hangsik TP166
Shin, Hangsik TP167
Shin, I. S. TP093
Shin, I.S. TP101
Shin, J. W. TO054
Shin, Jae Ho TP144
Shin, Jaewoo TO022
Shin, Jennifer H. TP145
Shin, Jennifer H. TP146
Shin, JeongHee TP038
Shin, Jiyoung TP058

Shin, J-W. TO054
Shin, M. C. TO028
Shin, Min Kyung TP286
Shin, S. H. SS030
Shin, S. Y. TO027
Shin, S. Y. TP046
Shin, S. Y. TP187
Shin, T. M. TO027
Shin, T. M. TP046
Shin, T. M. TP185
Shin, T. M. TP187
Shin, T. M. TP188
Shin, T. M. TP271
Shin, Tae-Jin TP117
Shin, TJ TO006
Shin, Y. B. TP256
Shin, Y. H. TP082
Shin, Y.H. TP228
Shin, Y.H. TP232
Shin, Y.H. TP234
Shin, Y.J. TP050
Shin, Ye-Ji TP013
Shin, Ye-Ji TP014
Shin, Ye-Ji TP015
Shin, Yong-Il TP211
Shin, Yujin TP120
Shon, Ho Sun TP289
Shon, Ho Sun TP296
Shrestha, Bishnu Kumar TP141
Sim, S. Y. TP191
Sim, Soo Young TP157
Sohn, Dae Kyung TP053
Sohn, Kang-Min TO044
Son, Dae Gu TP163
Son, Jeonghwan TP049
Son, M. J. TO033
Son, Myeonggu TP068
Son, Myeonggu TP073
Son, Myeonggu TP076
Son, Seong-Jin TP029
Son, Y. D. TO002
Son, Y. SS055
Song, C. TP284
Song, G. SS036
Song, G. TP028
Song, I. H. TP251
Song, Incheon TP053
Song, K.H. TP045
Song, K.H. TP047
Song, K.H. TP048

Song, K.H.	TP303	Tiwari, Arjun	TP141	Woo, Sam-Yong	SS032
Song, K.	TP279	Tiwari, Pawan K.	TP217	Woo, Sang-Yoon	TP010
Song, Kang-Il	TP264	Tran, Thang Viet	TO057	Woo, Sang-Yoon	TP012
Song, Kwang Hoon	TO051	Tserennadmid, B.	TP155	Woo, Sang-Yoon	TP282
Song, Kyuye	TO043	Tuul, M.	TP155	Wu, Y.	TO054
Song, LeeYong	TP098	Tuul., B	TP260		
Song, LeeYong	TP099	Tuyatsatsral., L	TP153		
Song, M.	TP046			Y	
Song, S. M.	TP273	U		Yang, Dongwook	TP085
Song, S.-C.	TO052			Yang, G. T.	TP265
Song, S.H.	TP189	Unnithan, Afeesh Rajan	TP129	Yang, H.-K.	TP253
Song, S.H.	TP298	Unnithan, Afeesh Rajan	TP140	Yang, Hyejin	TP119
Song, Seo Hyun	TO008			Yang, J. H.	TP113
Song, W. K.	TP273	V		Yang, J. J.	TP026
Song, Won-Kyung	TI-027			Yang, J. W.	TP114
Song, Y. E.	TP087	Vavilin, Andrey	TO011	Yang, J. W.	TP149
Song, Y.E	TP081	Vavilin, Andrey	TO029	Yang, J. W.	TP151
Soriano, J.P.	TP223			Yang, Jeonghwa	TP246
Suaning, Gregg	SS048	W		Yang, Multi/Single Un-Je	SS014
Suh, Han-sok	TP170			Yang, S. J.	TP250
Suh, J.	SS016	Wang, Joon-Ho	TO044	Yang, S. R.	TP151
Suh, Jin-Suck	TP224	Wang, JoonHo	TP148	Yang, S. T.	TP077
Suh, Jun-Kyo Francis	SS002	Wang, S. G.	TP065	Yang, S. T.	TP079
Suh, M.W	TP212	Wang, Soo-Geun	TP005	Yang, S. T.	TP097
Suh, S. W.	TP113	Wi, H.	TP052	Yang, S. T.	TP110
Suhaeri, Muhammad	TI-036	Wi, H.	TP244	Yang, Tae-Heon	SS032
Sun, D. S.	TP118	Wi, H.	TP295	Yang, U.	SS018
Sun, Doo Hoon	TP115	Wijenayake, K. K.	TP122	Yang, Yoon La	TP166
Sun, Doo Hoon	TP116	Won, H.	TP136	Yeo, C.B.	TP284
Sun, W. K.	TP250	Won, J. H.	TP002	Yeon, Chanmi	TP051
Sung, Hak-Joon	TI-033	Won, J.	TO045	Yeon, Chanmi	TP060
Sung, J. H.	TP033	Won, J.	TP028	Yeon, Hong-Won	TP242
Su-Yang	TP164	Woo, E. J.	SS055	Yi, W. J.	TP001
Szczesny, Spencer E.	TO048	Woo, E. J.	SS056	Yi, Won Jin	TP210
		Woo, E. J.	TP042	Yi, Won-Jin	TP010
T		Woo, E. J.	TP052	Yi, Won-Jin	TP012
		Woo, E. J.	TP074	Yi, Won-Jin	TP282
Ta, Duc-Manh	TP278	Woo, E. J.	TP244	Yong, H.	TP103
Tack, G. R.	TP077	Woo, E. J.	TP295	Yoo, C.H.	TP045
Tack, G. R.	TP079	Woo, E.J.	TO004	Yoo, C.H.	TP047
Tack, G. R.	TP082	Woo, E.J.	TO005	Yoo, C.H.	TP048
Tack, G. R.	TP088	Woo, E.J.	TP040	Yoo, C.H.	TP303
Tack, G. R.	TP097	Woo, E.J.	TP041	Yoo, H. J.	TP250
Tack, G. R.	TP110	Woo, Jihwan	SS045	Yoo, Hongki	TP053
Tae, K. S.	TP080	Woo, Jihwan	TP119	Yoo, Hongki	TP054
Tark, G. R.	TP104	Woo, Minjung	TP119	Yoo, Hongki	TP120
Tech, Ang Wei	TI-026	Woo, S. H.	TP103	Yoo, Jin Myoung	TP147
Teoh, J. C.	TO032	Woo, S. H.	TP104	Yoo, Minsu	TP184
Tien, Trinh Ngoc	TP105	Woo, S. T.	TP158	Yoo, O. S.	TP118
Tiwari, Arjun Prasad	TP126	Woo, S. Y.	TP001	Yoo, Oui Sik	TP105

Yoo, Oui Sik	TP115	Yoon, U. C.	TP056	Youn, Inchan	TP264
Yoo, Oui Sik	TP116	Yoon, Y. K.	TO002	Youn, J. I.	TP231
Yoo, S. J.	TP103	Yoon, Y. R.	TP043	Yu, C. H.	TP273
Yoo, S. J.	TP104	Yoon, Y. R.	TP168	Yu, H.	TO038
Yoo, S. K.	TP251	YOON, Y. R.	TP169	Yu, H.	TO039
Yoo, S.K.	TP240	Yoon, Y. R.	TP173	Yu, Jae Su	SS007
Yoo, Seung Jun	TP193	Yoon, Y. R.	TP176	Yu, S. K.	TO014
Yoo, Su Woong	TP058	Yoon, Y. R.	TP177	Yu, Seung-beom	TP006
Yoon, Hee Nam	SS025	Yoon, Y. R.	TP178	Yu, Yeon Hee	TP059
Yoon, D. S.	TP069	Yoon, Y.R.	TP044	Yun, Chang-Ho	TP009
Yoon, D. S.	TP229	YOON, Y.R.	TP174	Yun, Hyuk Jin	TP024
Yoon, Dae Sung	TO025	Yoon, Y.R.	TP235	Yun, Hyuk Jin	TP025
Yoon, Dae Sung	TP068	Yoon, Yong Jin	TI-020	Yun, R.Y.	TP233
Yoon, H. N.	TP165	Yoon, Young Ro	SS033	Yun, R.Y.	TP234
Yoon, H. N.	TP196	You, S. M.	TP241	Yun, R.Y	TP232
Yoon, H.	TP291	You, S.	TO013	Yun, S.	SS012
Yoon, H.	TP294	Youm, C. H.	TO033	Yune, Tae Y.	SS004
Yoon, J.	TP180	Youn, I.	SS003	Yuniarti, A. R.	TP292
Yoon, K. H.	TP237	Youn, I.	TP106		
Yoon, Myeongseo	TO011	Youn, I.	TP192		
Yoon, S. H.	TP239	Youn, I.	TP279		
Yoon, Sukhoon	TI-024	Youn, Inchan	SS002	Zhou, L.	SS053
Yoon, U. C.	TP055	Youn, Inchan	SS004		

Z



PUBLISHED BY

The Korean Society of Medical & Biological Engineering

1407, Seocho World Office Build., 19, Seoun-ro, Seocho-gu,
Seoul 06732, Korea

Tel: 02-921-8551, 8552, Fax: 02-921-8502

Email: kosombe@kosombe.or.kr

PRINTED BY

MEDrang Inc.

8-17 Worldcupbuk-ro 5ga-gil, Mapo-gu, Seoul 04001, Korea

Tel: 02-325-2093, Fax: 02-325-2095

E-mail: info@medrang.co.kr

Homepage: www.medrang.co.kr

IBEC International Biomedical Engineering Conference 2015 2015

Road to Better Life through Biomedical Engineering

PLENARY & INVITED LECTURES



“QUANTITATIVE IMAGING INFORMATICS IN COST EFFECTIVE PET IMAGING AND CLASSIFICATION OF LUNG DISEASE”

Andrew F. Laine, D.Sc.

Percy K. and Vida L.W. Hudson Professor of Biomedical Engineering
Professor, Department of Radiology (Phycis)
Chair, Department of Biomedical Engineering
Columbia University, New York, NY
USA

This talk presents a novel method for emphysema quantification, based on parametric modeling of intensity distributions in the lung and a hidden Markov measure field model to segment emphysematous regions. The framework adapts to the characteristics of an image to ensure a robust quantification of emphysema under varying CT imaging protocols and differences in parenchymal intensity distributions due to factors such as inspiration level. Compared to standard approaches, the present model involves a larger number of parameters, most of which can be estimated from data, to handle the variability encountered in lung CT scans. The method was used to quantify emphysema on a cohort of 87 subjects, with repeated CT scans acquired over a time period of 8 years using different imaging protocols. The scans were acquired approximately annually, and the data set included a total of 365 scans. The results show that the emphysema estimates produced by the proposed method have very high intra-subject correlation values. By reducing sensitivity to changes in imaging protocol, the method provides a more robust estimate than standard approaches. In addition, the generated emphysema delineations promise great advantages for regional analysis of emphysema extent and progression, possibly advancing disease subtyping, including COPD.

An important tool for studying brain disorders is positron emission tomography (PET), a nuclear imaging technology that allows for the *in vivo* functional characterization and quantification of blood flow, metabolism, protein distribution, and drug occupancy using radioactively tagged probes (tracers). Full quantification of PET images requires invasive arterial input function (AIF) measurement through online arterial blood sampling for the duration of the scan (1-2 hours). The AIF is used to correct images by accounting for the tracer bioavailability, which depends on an individual's physiological capacity for clearance, distribution and metabolism of the tracer. However, AIF measurement is invasive, risky, time consuming, uncomfortable for patients, and costly. Perhaps most importantly, it is impractical at the point-of-care and therefore limits clinical utility of PET. We believe an integrative multi-modal approach is possible via the amount of personalized information about the physiological and biochemical makeup of individuals available in their electronic health record (EHR). This talk will outline a novel approach to combine EHR and dynamic PET imaging data in an optimization framework based on simulated annealing to non-invasively estimate the AIF. Techniques that will be outlined are applicable across imaging modalities, organs and diseases, such as functional imaging of prostate cancer images where increasingly more complex tracers are utilized for assessment and require AIF measurement.

Development and Business of Biosensor-based Medical Devices

Hakhyun Nam

Department of Chemistry, Kwangwoon University, Seoul Korea

i-SENS, Inc., Seocho-gu, Seoul, Korea

Scientists and Engineers are often asked to include a lengthy justification of their R&D in terms of current or assumed economic values and also requested to provide useful products to the society they belong as the output of their funded researches. The success of the funded R&D's, especially in the biomedical science and engineering area, are often measured by the demonstration with engineered mock-ups. On the other hand, most R&D results are archived in the database after demonstrations and lengthy reports, and never be delivered to intended markets. Some researchers who believe the innovation and the economic potential of their own R&D results venture out of their laboratories to make business.

I and my colleague, Prof. Geun Sig Cha have been worked together to develop bio- and chemical sensors for academic interests and/or industrial applications since 1992. They include ion sensors, immunoassay sensors, lab-on-a-chip type devices for environmental and biomedical applications and point-of-care testing devices with the governmental and/or industrial R&D funds. After the economic crisis of Korea in 1997, researchers in universities and various institutes are encouraged and legally allowed to make business with their R&D products. Prof. Cha and I, and several graduate students in my lab took the opportunity in year 2000 and started the laboratory-based company i-SENS.

While there were several possible R&D products we could develop for the market of that time, we chose to start in a highly competitive glucose sensor business. As the business grows, we also tried to develop several other products, such as the electrolyte analyzer, lab-on-a-chip type immunosensors, HbA1c analyzer, and so on. In this presentation, I will summarize why and how we made R&D and business decisions and how they had resulted in failure or actual business. Although my talk will mostly focus on our own limited experiences in Korea, it may give some guide for those who wish to venture out of their laboratory.

Neuroengineering the interface of micro-devices with the brain

Kevin Otto, Ph.D.

Biomedical Engineering, University of Florida, USA

Direct interfacing of micro-devices with the brain has the potential to revolutionize the medical treatment of many neurological diseases or injuries. Unfortunately, chronic implantation and utilization of neural micro-devices results in a reactive tissue response that both functionally isolates the device from the tissue as well as triggers neuronal apoptosis or migration. The tissue response presents a fundamental obstacle to the design of neuroprostheses. Previous research has shown that the tissue responds to: 1) the initial device insertion, 2) the device indwelling, and 3) the application of the electrical stimulation. The goal of our ongoing research is to understand and mitigate this tissue response, thus enabling the development of multi-channel neural interfaces for clinical therapy. In particular, our primary research objective is to determine the interdependent effects of device design, electrophysiological recording, electrical stimulation, optical stimulation, and the reactive tissue response on the efficacy of neural interfaces. To this end, we conduct psychophysical experiments using multi-channel cortical implants in the cortex. Furthermore, we collect longitudinal electrochemical and electrophysiological data via the implanted devices. We investigate several chemically- and electrically-based tissue-response mitigation strategies. Finally, we use advanced histological approaches to evaluate the device-tissue interface. I will discuss the results of these various approaches and their implications for reliable chronic neural interfacing via micro-devices. We expect that these data will enable further neuroprosthetic development for many potential applications of neural interfaces.

Stereotactic & functional neurosurgery: A unique interface of research environment

Jin Woo Chang, M.D.

Department of Neurosurgery,

Yonsei Univ. College of Medicine, Seoul, Korea

e-mail: jchang@yuhs.ac

Our knowledge of the nervous system in health and disease has, however, increased considerably during the last fifty years and today, neurosurgery reveals promising new stereotactic strategies such as neuromodulation by the thermal lesioning, deep brain stimulation, radiosurgery, or etc to deal with diseases of the nervous system. These stereotactic procedures have been one of the unique surgical techniques mainly used for the treatment of functional brain disorders. As well, the functional neurosurgery has progressed markedly in its technical and theoretical aspects due to the rapid development of the basic neuroscience, computerized imaging techniques and advanced medical instruments. Some of these results have been implemented with success in the treatment of Parkinson's disease by deep brain stimulation, a common neurodegenerative disease affecting approximately 1% of the population aged seventy or more. And, the renaissance of functional neurosurgery in the treatment of neurodegenerative diseases has sparked also the interest in other diseases of the nervous system, which are refractory to medical treatment. Future developments in this rapidly advancing area will no doubt include widening indications for this relatively safe surgical procedure, elucidation of the mechanisms of action of electrical stimulation, and technological advancements improving effectiveness and convenience. It is therefore possible that deep brain stimulation in motor circuit in the basal ganglia as well as in other targets could become a potent therapeutic tool in the near future for diseases of the nervous system.

As well, at the interface between the old and new surgical paradigms such as MR guided focused ultrasound surgery (MRgFUS) to reduce the damage in normal brain tissue and further improvements in the precision of surgery will be try out.

Although there are some points to be clarified and estimated in the future, these new tendencies will stand to the next century, and further progress will definitely be achieved because it contains some truth in the light of the modern neuroscience.

In this presentation, I would like to summarize the available past and present data and the future perspectives in the field of the stereotactic & functional functional neurosurgery.

MHz speed wavelength swept laser for biomedical imaging

Abstract

Wavelength swept laser with active mode locking fiber cavity were demonstrated for various biomedical imaging applications. Due to the filter-less wavelength tuning mechanism, flexible wavelength tuning and switching are possible with a high swept rate of up to MHz in the various wavelength bands such as 800, 1000, 1310 and 1550nm.

Chang-Seok KIM, Ph.D., Professor

Department of Optics and Mechatronics Engineering, Pusan National University

Educations:

- Ph.D. Johns Hopkins University, Baltimore, USA, 2004..
- M.S. Johns Hopkins University, Baltimore, USA, 2002.
- M.S. Gwangju Institute of Science and Technology (GIST), Korea, 1999.
- B.S. Korea Advanced Institute of Science and Technology (KAIST), Korea, 1996.

Employments:

- Pusan National University, Busan, Korea, Professor, March 2005 ~ Current .
- Beckman Laser Institute and Medical Clinic, Irvine, CA, Postdoctoral Researcher, March 2004 - February 2005.
- Korea Telecom, WDM Research Division, Optical Communication Team, Access Network Research Laboratory, Korea, March 1999 - June 2000.

Noninvasive monitoring of stem cells and tissue regeneration using combined ultrasound and photoacoustic imaging

Seung Yun Nam, PhD, Assistant Professor

Department of Biomedical Engineering
Pukyong National University, Busan 608-737, Korea

E-mail : synam@pknu.ac.kr

Abstract

Skin burn is a prevalent injury which can easily occur via various mechanisms, such as electrical, chemical, and thermal sources. In addition, full-thickness and large surface area burn injury can result in serious infection, severe pain, and high mortality risk. Stem cell-based therapies, in combination with 3D hydrogel systems, have a great potential to improve skin tissue regeneration due to differentiation and paracrine effects. Furthermore, sophisticated imaging techniques are needed for advanced therapeutic approaches such as noninvasive monitoring of stem cells seeded and applied in a biomedical 3D scaffold to enhance wound repair. However, current biomedical imaging tools have limitations in accurately diagnosing the burn injury and subsequent tissue regeneration. This presentation will introduce a novel application of combined ultrasound (US) and photoacoustic (PA) imaging to assess burn severity and skin tissue regeneration after stem cell therapy of burns. Tissue structural damage and bleeding up to the subcutaneous skin layer is noninvasively visualized using US/PA imaging. Gold nanoparticle-labeled adipose-derived stem cells (ASCs) in a PEGylated fibrin 3D gel are implanted in the rat skin wound. ASCs are successfully tracked up to two weeks and were distinguished from host tissue components through spectroscopic PA imaging. The structure and function of blood vessels (vessel density and perfusion) in the wound bed undergoing skin tissue regeneration are monitored qualitatively and semi-quantitatively by the developed imaging approach. Imaging-based analysis demonstrates ASC localization in the top layer of skins and a higher density of regenerating blood vessels in the treated groups. The results are corroborated with histological analysis showing localization of fluorescently-labeled ASCs and smooth muscle alpha actin-positive blood vessels.

Ultra-fast functional magnetic resonance imaging using highly parallel detection

Fa-Hsuan Lin
National Taiwan University, Taiwan

Functional magnetic resonance imaging (fMRI) using BOLD contrast has become a major tool in non-invasive study of human brain function and dysfunction. However, most studies focus on localizing functional areas or characterizing spatial patterns, while temporal features are mostly neglected. This can be attributed to the common belief that the BOLD fMRI signal is temporally smooth and the technical challenge in data acquisition.

Based on the hypothesis that neurophysiologically important information can be monitored in the dynamics of BOLD fMRI signal, we developed the inverse imaging (InI) method, which has demonstrated to achieve 10 Hz sampling (about 20 times faster than conventional approach) with 5 mm spatial resolution at cortex and whole-brain coverage. InI has demonstrated its application in monitoring physiological noise in high field fMRI experiments. Hemodynamic responses measured by InI with sub-second precision were found to be correlated with behaviors and electrophysiological recordings. The InI method also led to the finding that inter-regional modulations between functional brain areas were significant at frequencies higher than 1 Hz.

We will briefly summarize both the technical development and applications of inverse imaging. Recent methodological advancement and applications will also be introduced. We believe that ultra-fast fMRI using highly parallel detection is the method holding the promise of sensitive fMRI and multimodal imaging of the human brain.

High Resolution Diffusion Tensor Imaging and its Preliminary Application in Cervical Spondylotic Myelopathy

Hua Guo, PhD

Center for Biomedical Imaging Research, Department of Biomedical Engineering, Tsinghua University, Beijing, China

Cervical spondylotic myelopathy (CSM) is a progressively degenerative disease, which is caused by compression of the spinal cord by surrounding bony or ligamentous structures. Traditional diagnosis of CSM is based on clinical symptoms and neurologic function. MRI can provide anatomical information using T1 and T2 weighted images and has been used commonly in the clinical. Various studies have shown that diagnosis based on signal intensity from T1 or T2 weighted images has low sensitivity (1-3) and low predictive value (1,4-6). Compared with T1 and T2 imaging, diffusion weighted imaging (DWI) is a more promising technique for CSM diagnosis because it can provide microstructural tissue information and thus potentially functional or viable change of spinal cords (7). For the widely adopted diffusion imaging, it uses a single-shot echo planar imaging (EPI) method as it is fast and motion insensitive. However, it has low image resolution and distortion artifacts. Particularly, for spinal cord DWI, it is much more challenging than for other organs. The underlying reasons include small cross-sectional area of spinal cord, image distortions by field inhomogeneities, severe motion artifacts (8,9), low signal noise ratio and long scan time. In this study, we applied our recently developed high-resolution DWI method, SYnergistic iMAGE reconstruction using PHase variatiOns and seNsitivity (SYMPHONY), in patients with CSM. The key idea of this new theory is that phase variations are not treated as a source of imaging artifacts, but as a kind of image encoding. The k-space correlation of different shots and channels can be used for data interpolation of each shot. Then the fully recovered k-space data can be transformed and summed to form final DWI images. Using this method, we investigated the change of diffusion metrics, including FA, axial diffusivity (AD) and radial diffusivity (RD), before and after surgery therapy in 7 CSM patients. In addition, we studied the relationship between DTI and traditional examinations. Preliminary results show SYMPHONY DWI has better performance than image domain based methods when there exists image mismatch between image echoes and navigators, because the calculation is conducted in k-space (10). Diffusion metrics showed significant changes after the surgery. Therefore, high resolution DTI may be a promising tool to evaluate neurologic severity of compressed spinal cord, select CSM patients for surgery, and monitor the therapy response.

Reference:

1. Demir A, Ries M, Moonen CT, et al. Diffusion-weighted MR imaging with apparent diffusion coefficient and apparent diffusion tensor maps in cervical spondylotic myelopathy. *Radiology*

- 2003;229(1):37-43.
2. Takahashi M, Yamashita Y, Sakamoto Y, Kojima R. Chronic cervical cord compression: clinical significance of increased signal intensity on MR images. *Radiology* 1989;173(1):219-224.
 3. Matsumoto M, Toyama Y, Ishikawa M, Chiba K, Suzuki N, Fujimura Y. Increased signal intensity of the spinal cord on magnetic resonance images in cervical compressive myelopathy. Does it predict the outcome of conservative treatment? *Spine* 2000;25(6):677-682.
 4. Uchida K, Nakajima H, Takeura N, et al. Prognostic value of changes in spinal cord signal intensity on magnetic resonance imaging in patients with cervical compressive myelopathy. *Spine J* 2014;14(8):1601-1610.
 5. Nakamura M, Fujimura Y. Magnetic resonance imaging of the spinal cord in cervical ossification of the posterior longitudinal ligament. Can it predict surgical outcome? *Spine* 1998;23(1):38-40.
 6. Sato T, Horikoshi T, Watanabe A, et al. Evaluation of cervical myelopathy using apparent diffusion coefficient measured by diffusion-weighted imaging. *AJNR American journal of neuroradiology* 2012;33(2):388-392.
 7. Wheeler-Kingshott CA, Stroman PW, Schwab JM, et al. The current state-of-the-art of spinal cord imaging: applications. *NeuroImage* 2014;84:1082-1093.
 8. Kharbanda HS, Alsop DC, Anderson AW, Filardo G, Hackney DB. Effects of cord motion on diffusion imaging of the spinal cord. *Magnetic resonance in medicine* 2006;56(2):334-339.
 9. Spuentrup E, Buecker A, Koelker C, Guenther RW, Stuber M. Respiratory motion artifact suppression in diffusion-weighted MR imaging of the spine. *European radiology* 2003;13(2):330-336.
 10. Ma X, Zhang Z, Wang Y, Dai E, Guo H. High Resolution Spine Diffusion Imaging using 2D-navigated Interleaved EPI with Shot Encoded Parallel-imaging Technique (SEPARATE). *Proceedings of the 23th Annual Meeting of ISMRM; 2015. p. 2799.*

Imaging deep brain structures using magnetic susceptibility imaging

Jongho Lee, Ph.D.

Assistant Professor, Department of Electrical and Computer Engineering, School of Engineering
Seoul National University, Seoul, KOREA
Email: jonghoyi@snu.ac.kr

Magnetic susceptibility imaging is a clinically important imaging methodology that helps to visualize tissue iron and calcium in the brain. Recently, new methods have been developed to measure tissue magnetic susceptibility more accurately and quantitatively. In this presentation, I will review recent progresses in magnetic susceptibility imaging and present a new type of magnetic susceptibility imaging methods that takes advantages of both magnetic susceptibility weighted magnitude images and magnetic susceptibility weighted phase images in order to create substantially improved susceptibility contrast. The new method reveals previously invisible small structures (e.g. nigrosome 1 in substantial nigra) helping to diagnose Parkinson's disease.

Jongho Lee received B.S. degree in Electrical Engineering at Seoul National University (1998) and completed M.S. (2004) and Ph.D. (2007) degrees in Electrical Engineering at Stanford University with a Ph.D minor in Psychology. From 2007 to 2010, he worked at the National Institute of Neurological Disorders and Stroke, National Institutes of Health, USA as a research fellow. From 2010 to 2014, he continued his academic career as an Assistant Professor at the Department of Radiology, University of Pennsylvania. In 2014, he moved back to Korea to join a faculty position at the Department of Electrical and Computer Engineering, Seoul National University.

Dr. Lee is a recipient of International Rotary Foundation Ambassadorial scholarship for his M.S. and Samsung Scholarship Foundation scholarship for his Ph.D. He awarded Young Investigator Grant Award from Korean-American Scientists and Engineers Association (2012) and Young Investigator Award at White Matter Study Group workshop, International Society for Magnetic Resonance in Medicine (2013).

Arrhythmia detection in the real world

Gari. D. Clifford,
Associate Prof. of Biomedical Engineering and Informatics
Depts of Biomedical Informatics and Biomedical Engineering
Emory University & Georgia Institute of Technology
Deputy Editor, Physiological Measurement, Institute of Physics and Engineering
Honorary Professor, The Sleep & Circadian Neuroscience Institute, University of Oxford
Founding Director, Centre for Affordable Healthcare Technology, Kellogg College

Atrial fibrillation (AF) is the most common cardiac arrhythmia, but is currently under-diagnosed since it can be asymptomatic. AF is associated with a five-fold risk of stroke and so early detection and treatment of AF is extremely important. mHealth applications have been recently proposed for early screening of paroxysmal AF and several accurate automatic AF detection algorithms have been described in the literature. These algorithms are mainly based on features extracted from the beat-to-beat (RR) interval time-series derived from the electrocardiogram (ECG), since this is more robust to ambulatory noise than p-wave based algorithms or pulsatile signals such as the photoplethysmogram. (The RR interval features highlight the irregularity and unpredictability of the rhythm due to the chaotic electrical conduction through the heart's AV node.) Such approaches have proved to be accurate on openly available databases, which are generally subject to manual annotations. When automated annotations are used, they are accepted as the gold standard. However, our research has shown that even small errors in R-peak detection can lead to large errors in AF detection. The recent rise of mHealth and other quantified self approaches to sourcing physiological data, particularly through subclinical quality wrist worn devices is likely to lead to an enormous amount of noisy data that cannot be manually annotated, even with extensive crowd sourcing approaches.

We present an in depth analysis of the performance of the most accurate noise-resistant AF detection algorithms as a function of noise and R-peak detection performance. We show a linear decrease of AF detection accuracy with respect to the signal to noise ratio. Finally, we will demonstrate how the use of an automatic signal quality index (SQI) can ensure a given level of performance in AF detection, and in particular, a 95% AF detection accuracy for ECG segments with a median SQI greater than 80%. The calibration and reporting of SQIs into screening algorithms is shown to provide confidence limits for diagnoses and allow user to estimate the expected false alarm rate in order to apportion resources appropriately, avoiding Big Data Overload.

Tactile Sensation Processing for Artificial Palpation

Jong-Ha Lee

Assistant Professor in Department of Biomedical Engineering, Keimyung University

Elasticity is an important indicator of tissue health, with increased stiffness pointing to an increased risk of cancer. We investigated a tissue inclusion characterization method for the application of early breast tumor identification. A tactile sensation imaging system (TSIS) is developed to capture images of the embedded lesions using total internal reflection principle. From tactile images, we developed a novel method to estimate that size, depth, and elasticity of the embedded lesion using 3-D finite-element-model based forward algorithm, and neural-network-based inversion algorithm are employed. The proposed characterization method was validated by the realistic tissue phantom with inclusions to emulate the tumors.

Iron oxide based multifunctional nanomaterials prepared by novel thermal treatment processes for bioimaging and drug delivery

Yuanzhe Piao

Graduate School of Convergence Science and Technology, Seoul National University,

Seoul 151-742, South Korea

parkat9@snu.ac.kr

ABSTRACT

Iron oxide nanoparticles have attracted increased attention in biomedical applications due to their low cost, low cytotoxicity, and interesting magnetic properties. In this talk, I will review our recent progress in the preparation of various iron oxide based multifunctional nanomaterials for biomedical applications. (I) A general “wrap/bake/peel process” is developed for nanostructural and chemical transformation. The overall process is composed of the wrapping of nanoparticles with a silica coating, heat treatment and the etching of the silica layer. Depending on the thermal treatment conditions, hollow iron oxide nanocapsules of either hematite or magnetite were able to be produced. The as-prepared iron oxide nanocapsules exhibited a high surface area and formed stable dispersions in aqueous solution. The nanocapsules were successfully used as a drug-delivery vehicle and a T₂ magnetic resonance imaging contrast agent. (II) A simple and versatile strategy to transform hydrophobic iron oxide nanoparticles to hydrophilic and biocompatible maghemite nanocrystals by thermal treatment followed by dextran coating is reported. Iron oxide nanoparticles dispersed in non-polar organic solvent were mixed with salt fine powder. The powder was thoroughly mixed and the organic solvent was evaporated. The resulting mixture was calcined in air. Dextran derivative was dissolved in water and the annealed mixture of iron oxide nanoparticles and salt was added slowly to the dextran derivative solution under stirring. Dextran coated iron oxide nanoparticles were collected by centrifugation. Removal of salt and the dextran coating using a dextran derivative solution were repeated three times. The resulting nanoparticles were dispersed in distilled water. Through the process, highly crystalline bare maghemite nanoparticles with high magnetization were produced. Polyanionic CM-dextran coated iron oxide nanoparticles are stable under various conditions. In vivo MR imaging using these nanoparticles successfully showed significant signal enhancement. (III) Water well-dispersible ultra small iron oxide nanoparticles were synthesized in PEG solution. 1, 2-ethylenediamine was introduced to the surface of the nanoparticles via DCC coupling. The resulting amine functionalized ultra small iron oxide nanoparticles were conjugated with FITC (FITC@USPIO). These iron oxide nanoparticles show high stability even at high salt concentration and broad range of pH. The cytotoxicity, relaxivity and biodistribution study of FITC@USPIO were also conducted. The cytotoxicity of the FITC@USPIO was measured using SKOV3 cell by MTT analysis at different concentrations.

KEYWORDS

Iron oxide nanoparticles, drug delivery, multifunctional nanoparticles, multimodal imaging, core/shell.

Better Bioaffinity Sensing Platforms with Gold Nanoparticles for Biomedical Applications

Hye Jin Lee

*Department of Chemistry, Kyungpook National University, Daegu 702-701, Korea.
E-mail: hyejinlee@knu.ac.kr*

During the past two decades, tremendous research efforts have been made to enhance biosensors performance for a wide spectrum of biomedical research applications. In this talk, we will highlight our recent developments made on the combined use of biofunctionalized gold nanoparticles, surface sandwich formation and enzyme reactions to improve the sensitivity and selectivity of bioaffinity sensors for the potential applications to medical diagnostics. The first example includes the development of a novel surface-based sandwich assay combined with biofunctionalized Au nanoparticles (NPs) for the attomolar detection of disease related biomarker proteins [1] using surface plasmon resonance (SPR) technique. In addition, SPR bioaffinity sensors in a sandwich assay was developed for the detection of Alzheimer's disease biomarker proteins [2]. Another examples include the creation of new electrochemical surface sandwich assay platforms in tandem with biofunctionalized Au nanoparticles and surface enzyme reactions for the femtomolar sensing of β -amyroid and H5N1 proteins in biological fluids [3]. Finally, some challenging issues and future prospects of our surface sandwich bioaffinity sensing technologies for bio and environmental applications will be discussed.

References

- [1] S. H. Baek, A. W. Wark, **H. J. Lee***, *Anal. Chem.*, **2014**, 86, 9824–9829
- [2] S. Kim, **H. J. Lee***, *Anal. Chem.*, **2015**, 87, 7235–7240
- [3] D. F. Sharmin, S. Kim, **H. J. Lee***, *Biosens. Bioelectron.*, **2015**, 72, 355-361

Biomimetic self-assembled structures for sensor applications

Byung Yang Lee
Korea University, Korea

Functional microfluidics and nanoparticles for cancer and stem cell fate

Bong Geun Chung
Sogang University, Korea

Translational Medicine Using Fully Automated Circulating Tumor Cell Systems

J. -M. Park¹, and M. S. Kim²

¹Samsung Electronics, Ltd., Suwon, Korea

²Department of Biomedical Engineering, Konyang University, Daejeon, Korea
E-mail: dodakdl@konyang.ac.kr

Abstract— We demonstrate a novel rare cell isolation system which satisfies not only high recovery rate but purity. To achieve full automation for circulating tumor cell isolation from blood, we adopted a centrifugal microfluidic technology. The disc-based device could process 10 mL of blood sample at a time and the purity of the finally isolated fraction was enough to work direct sequencing for mutation analysis.

Keywords— Cell isolation, Circulating tumor cell (CTC), Centrifugal microfluidics, Cancer diagnosis

I. INTRODUCTION

Metastasis, the spread of cancer from a primary tumor to a distant site, is largely responsible for cancer's lethality. Research into circulating tumor cells (CTCs) has suggested an important role for these cells in metastatic spread, inspiring hope of new and more effective ways to diagnose and treat aggressive disease. Detection of the exceedingly rare cells within the circulation may provide important clues regarding cancer prognosis and progression, potentially advancing the assessment of anticancer drug treatment and optimization of individualized therapy. In developing CTC technology, the critical criteria are high recovery rates and high purity. Current isolation methods suffer from an inherent trade-off between these two goals. Moreover, ensuring minimal cell stress and robust reproducibility is also important for the clinical application of CTCs. In this talk, I will introduce several kinds of approaches to efficiently isolate the rare cells and share the progress that CTC isolation systems are developed. The systems represent a potentially significant advance toward ensuring highly efficient isolation of these sparsely populated target cells in μ TAS study contributing, therefore, to the sensitive and robust clinical validation of studies with CTCs and their applications.

II. METHODS

A. Ethic statement

Human blood samples were obtained from Yonsei University (Seoul, Korea). Informed written consent was obtained from all participants in all cases, and this

study was approved by the Institutional Review Board (IRB) at the Yonsei University, Seoul, Korea.

B. Fabrication of a disc-based device

The plastic disposable disc is composed of a top and a bottom plate. The top and bottom plates are made of polycarbonates, and the microfluidic channels and chambers were fabricated using a computer-numerical-controlled process. The detailed procedure of the fabrication and the protocols are described elsewhere. [1]

C. Molecular analysis

CTCs isolated by the disc were subjected to whole genome amplification (GenomePlex WGA4, Sigma Aldrich). The amplified DNA product was purified with GenElute PCR Cleanup kit (Sigma Aldrich) and quantified by UV absorbance using ND-1000 instrument (NanoDrop Technologies, Rockland, DE). In each sample, EGFR mutation was identified by allele-specific real-time PCR using PNAclamp kit (PNAclamp, Panagene, Korea) and DNA sequencing.

III. RESULTS

A. Operation of the centrifugal microfluidic separation

When Five milliliters of blood plus microbeads (100 μ L) and DGM were injected into the blood and DGM chambers (Figure 1a), the device was begun to rotate. During centrifugation, a plasma layer (yellow color) begins to form (Figure 1b). The plasma could be easily removed to the waste chamber by opening a valve (Figure 1c). After mixing process, the blood sample was transferred onto the density gradient medium and heavier particles including CTC conjugated with microbeads and pure microbeads were moved to the collection chamber (Figure 1d).

B. Analysis of point mutation for tailored therapy

To detect the EGFR mutation, the CTC fraction was subjected to cell lysis and whole-genome amplification. Direct sequencing of the amplified PCR products from the CTC fractions clearly displayed the deletion mutation in EGFR exon 19 of HCC827 [2], indicating that the HCC827 cells accounted for the majority of the CTC fraction. Minute leukocyte contamination was

indicated by the low amplitude of the wild-type sequence tracing in the chromatogram from the CTC fraction (Figure 2).

IV. CONCLUSION

From the centrifugal microfluidic platform, we could successfully isolate the rare cancer cells automatically. In addition, we identified EGFR mutation as a model of molecular analyses using CTCs that can potentially be used in clinical practice.

Platform with Large-Volume Capacity Based on Lab-on-a-Disc,” *Anal. Chem.*, vol. 86, pp. 3735-3742, 2014.

2. B. A. Helfrich, D. Raben, M. Varella-Garcia, D. Gustafson, D. C. Chan, L. Bemis, C. Coldren, A. Baron, C. Zeng, W. Franklin, F. R. Hirsch, A. Gazdar, J. Minna and P. A. Bunn, *Clin. Cancer Res.*, vol. 12, pp. 7117–7125, 2006.

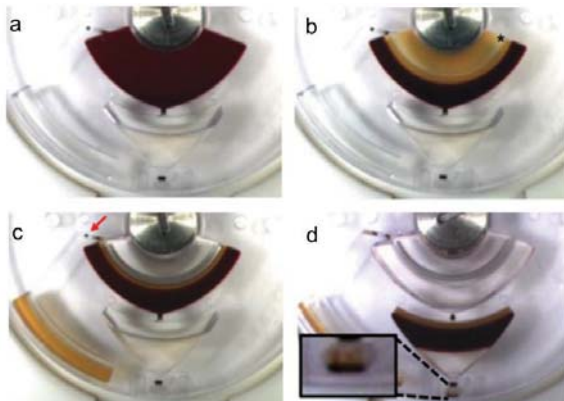


Fig. 1. Automated CTC isolation using a centrifugal microfluidic system.

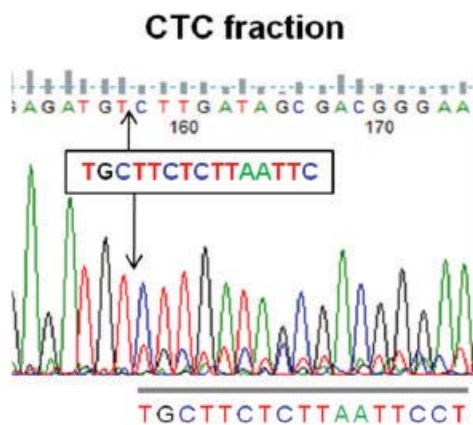


Fig. 2. Tracings of the EGFR nucleotide sequencing from the reverse direction.

ACKNOWLEDGEMENT

This work was supported by the Bio Research Center at the Samsung Advanced Institute of Technology.

REFERENCES

1. J.-M. Park, M. S. Kim, H.-S. Moon, C. E. Yoo, D. Park, Y. J. Kim, K.-Y. Han, J.-Y. Lee, J. H. Oh, S. S. Kim, W.-Y. Park, W.-Y. Lee and N. Huh, “Fully Automated Circulating Tumor Cell Isolation

Bi-modal neuromodulatory effect of low-intensity focused ultrasound (LIFU): A parameter optimization study

H.C.Baek^a, H. Kim^{a,*}

^aCenter for Bionics, Korea Institute of Science and Technology, Seoul, Republic of Korea
E-mail: hk@kist.re.kr

Abstract— We adopted the low-intensity focused ultrasound (LIFU) to verify its intervening role to stimulate and suppress neural activity. We derived successful pulsed sonication parameters of 1-5 ms tone-burst duration, 50% duty cycle, 300 ms sonication duration, and 350 kHz fundamental frequency to stimulate the motor responses at the lowest possible acoustic intensity (I_{sppa} : 4.9-5.6 W/cm², I_{spta} : 2.5-2.8 W/cm²). We were also able to suppress the magnitude of visual-evoked potentials during the sonication using a 5% duty cycle (pulse-repetition frequency of 100 Hz) at 3 W/cm² I_{sppa} .

Keywords—Neuromodulation, Focused Ultrasound, Low-intensity, Non-invasive

I. INTRODUCTION

Low-intensity focused ultrasound (LIFU) has been researched as a novel non-invasive neuromodulation method for its excellence in spatial resolution and depth penetration. The application of bi-modal feature in LIFU-mediated neuromodulation allows both stimulate and suppress the excitability of neural substrates; this suggests that with the development of optimal sonication parameters, LIFU promises exceptional potentials in neurotherapeutics.

II. METHODS

A. Experimental protocol for the stimulation

We compared the threshold acoustic intensities (AIs) among the three duty cycles (DCs: 30, 50, and 70%); three sonication durations (SDs: 200, 300, and 400 ms); and two fundamental frequencies (FFs: 350 and 650 kHz) to detect synchronized tail motions induced by LIFU stimulation on rat's motor cortex. Once the tail movement was successfully elicited, the sonication parameters were then adjusted; AI was subsequently reduced down to 4 W/cm² spatial-peak pulse-average intensity (I_{sppa}) and incrementally increased about 10% of the preceding I_{sppa} for each step until the criterion for the presence of tail movement was achieved.

B. Experimental protocol for the suppression

Visual-evoked potentials (VEPs) were used to estimate the degree of impact of LIFU parameters among three DCs (1, 5, and 8.3%); and AIs (1, 3, and 5 W/cm² I_{sppa}) on the activity of rat visual cortex. After

the dark adaptation of at least 5 min, rats were exposed to the 20-ms-long stroboscopic light stimulation 100 times to both eyes in 1s intervals. We used the magnitude of between the first positive and negative peaks of the VEP (i.e. P1-N1), which is the most universally established in amplitudes and latencies, as the indication of the modulatory response from the sonication. The VEPs were obtained nine times in every 150s, representing the pre-sonication (3 times, baseline), sonication (or control, 1 time), post sonication (5 times, resting after sonication).

III. RESULTS

A. Optimal parameter for stimulatory LIFU sonication

As a result of comparing of threshold AIs, data suggest that the use of 50% DC and 300 ms SD elicited motor responses at lower AIs, favoring its use at lower I_{sppa} (compared to 30% DC) as well as a lower spatial-peak temporal-average intensity (I_{spta} ; compared to 70% DC).

B. Optimal parameter for suppressive LIFU sonication

The pulsing parameters that successfully suppress the VEP in this study were 3 W/cm² I_{sppa} and a 5% DC, which is comparable to that of rabbits (3.3 W/cm² I_{sppa}) (Yoo et al., 2011). When FUS was administered at 3 W/cm² I_{sppa} at 5% DC significantly reduced the VEP peak (i.e. $-13.2 \pm 9.6\%$, mean \pm SD) was observed during the sonication period ($p = 0.02$).

IV. CONCLUSION

We examined a range of sonication parameters that stimulates and suppresses the rat's neural activity. The differential neuromodulatory capacity of LIFU would urge a new beginning of therapy in various neuropsychiatric disorders. Future study is warranted to include more systematic method for the combination of sonication parameters and to normalize the level of anesthesia in LIFU-mediated neuromodulation.

REFERENCES

- King RL, Brown JR, Newsome WT, Pauly KB (2013) Effective Parameters for Ultrasound-Induced In Vivo Neurostimulation. *Ultrasound in Medicine & Biology* 39:312-331.
Yoo SS, Bystritsky A, Lee JH, Zhang Y, Fischer K, Min BK, McDannold NJ, Pascual-Leone A, Jolesz FA (2011) Focused ultrasound modulates region-specific brain activity. *NeuroImage* 56:1267-1275.

Applications of Near-infrared Optical Sensor to Meet the Medical Needs

Jae Gwan Kim^{1,2}

¹Department of Medical System Engineering, ²School of Information and communications,
Gwangju Institute of Science and Technology (GIST), Gwangju, The Republic of Korea
E-mail: jaekim@gist.ac.kr

Abstract—Near-infrared spectroscopy has been adapted to various medical applications in our lab including breast cancer therapy monitoring, diagnosis of erectile dysfunction, personalization of cupping therapy, early detection of driver's drowsiness, anesthesia depth monitoring and so on.

Keywords— Near-infrared spectroscopy, Optical sensor, biomedical application

I. INTRODUCTION

Near-infrared spectroscopy (NIRS) has been popular in the field of biophotonics research due to its relatively deep penetration in tissue and its capability of providing functional information such as blood oxygenation and its volume. A few application of NIRS are briefly described in the following section.

II. APPLICATIONS

A. Breast Cancer Chemotherapy Monitoring

Early prediction of chemotherapy efficacy can save the unnecessary treatment, and therefore, it can guide the direction of treatment in addition to the side effect reduction. NIRS was applied to monitor the vascular reactivity during respiratory challenges and the preliminary results showed the potential of early detection of chemotherapy efficacy prior to the change of tumor volume.

B. Diagnosis of Erectile Dysfunction

Erectile dysfunction is currently diagnosed by a commercial system, Rigi-Scan, but there is a need to develop a more comfortable system. We applied a semiconductor based NIRS sensor onto both brain and genital organ to monitor the hemodynamic change during visual sexual stimulation. The results showed the difference of penile hemodynamics depending on the position of sensor and the discrepancy between brain and genital organ during visual sexual stimulation.

C. Personalization of Cupping Therapy

Cupping therapy has been popular from ancient not only in Asia but also in Western society. It applies a negative pressure inside of a cup which may stimulate blood circulation of tissue to enhance the wound

healing and to reduce pain. However, each person has different tissue mechanical properties which implies the same application of negative pressure during cupping therapy may not work for everyone. For the personalized cupping therapy, we added a NIRS sensor into a cup to monitor the tissue oxygenation and blood volume during cupping therapy.

D. Early Detection of Driver's Drowsiness

Drowsiness during a driving can cause a deadly accident, and therefore, there have been studies to monitor the state of driver to give an alarm. We applied a combined EEG/NIRS system to monitor both neuronal electrical activity and cerebral hemodynamics. The results showed that EEG signal can classify the state of driver between sleepy and awake. With the combination of EEG and NIRS, the classification accuracy is improved. The onset of sleeping could be found a few seconds earlier by monitoring EEG and NIRS before the driver fell asleep.

E. Anesthesia Depth Monitoring

Bispectral index (BIS) is currently used in a surgical room to monitor the depth of anesthesia. However, it has been known that BIS may provide incorrect values of anesthesia depth from patients who have brain diseases. Meanwhile, it has been known that cerebral metabolism gets lower during anesthesia which can be a potential parameter to monitor its depth. In our study, simultaneous monitoring of EEG and NIRS signals were obtained with the variation of isoflurane concentration.

IV. CONCLUSION

Tissue hemodynamics can provide a key information of how tissue is functioning. The applications shown here are the examples of how NIRS can be used in medical demands and it implies the need of developing a portable, wearable, wireless sensor system to monitor the physiological signals.

ACKNOWLEDGEMENT

This work was supported by a grant from NRF (2012K1A2B1A03000757, 2013R1A1A2013625) and institute of Medical System Engineering at GIST.

High-frequency Ultrasound Microbeam Techniques for Measurement of Cell Mechanics

J. M. Park¹, J. H. Kim¹, and J. Y. Hwang¹

¹Department of Information and Communication Engineering, DGIST, Daegu, S. KOREA
E-mail: jyhwang@dgist.ac.kr

Abstract—We demonstrate non-contact high-frequency ultrasound microbeam techniques based on acoustic radiation force impulse microscopy and acoustic trapping, capable of probing cell mechanics. For evaluation of our developed techniques, they were here employed to quantify the mechanical properties of breast cancer cells including highly- and weakly-invasive breast cancer cells. The results showed that they enabled to quantify the cell mechanics, allowing us to discriminate between highly- and weakly-invasive breast cancer cells.

Keywords— High-frequency ultrasound, acoustic tweezers, acoustic radiation force, photoacoustic, cell mechanics.

I. INTRODUCTION

Cell mechanics may play a key role in the differentiation, migration, and gene expression of cells [1]. The cell mechanics can be altered by various external and internal factors including disease and variations in cell nature. Therefore, the measurement of cell mechanics is highly important to identify cellular phenotypes, alternation, and etc.

We thus developed novel non-contact high-frequency ultrasound microbeam techniques which are capable of measuring mechanical properties of cells. In particular, an acoustic radiation force impulse microscopic and an acoustic trapping technique were developed with a 30 MHz lithium niobate (LiNbO₃) ultrasound transducer for measurement of cell mechanics. Using the developed technique, the mechanics of breast cancer cells including highly- and weakly-invasive breast cancer cells were measured, followed by quantitative analysis of the outcomes.

II. METHODS

A. Press-focused Ultrasound Transducer

A press-focused LiNbO₃ ultrasound transducer was fabricated to generate highly focused ultrasound microbeams with conventional procedures. The center frequency and f-number of the transducer were ~ 30 MHz and ~ 0.75, respectively.

B. High-frequency Ultrasound Microbeam System

A high-frequency ultrasound microbeam system, allowing acoustic radiation force impulse microscopy and acoustic trapping, was developed. The transducer incorporated into the system was utilized not only to

generate ultrasound microbeams and acoustic radiation force impulses but also detect photoacoustic signals from excitation of targets by 532 nm Q-switch laser light. The system was utilized to measure mechanics of breast cancer cells with different invasiveness.

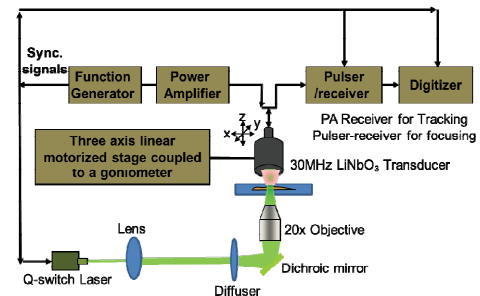


Fig. 1. High-frequency ultrasound microbeam system

III. RESULTS

A. Measurement of mechanics of highly- and weakly-invasive breast cancer cells

The mechanical properties of breast cancer cells were measured by using our developed system. It was here found that the deformation of highly-invasive breast cancer cells was larger than that of weakly-invasive breast cancer cells due to acoustic trapping. On the other hands, the highly-invasive breast cancer cells exhibited larger displacement than the weakly invasive breast cancer cells due to acoustic radiation force impulse application. Therefore, these results indicated that highly-invasive breast cancer cells are softer than weakly-invasive breast cancer cells.

IV. CONCLUSION

In this study, we developed high-frequency ultrasound microbeam techniques to measure cell mechanics in a non-contact manner. They allowed to measure mechanical properties of highly- and weakly-invasive breast cells, enabling to discriminate between them, quantitatively. Altogether, the results suggest that the high-frequency ultrasound microbeam techniques have potentials to probe the mechanics of breast cancer cells with different invasiveness.

ACKNOWLEDGEMENT

This work was supported by the National Research Foundation of Korea (NRF) and DGIST grant (NRF-2014R1A1A2054934, NRF-2014M3A9D7070668, and 15-HRLA-01).

REFERENCES

1. Y. L. Wang, and D. E. Discher, Cell Mechanics, San Diego: Academic Press, 2007.

Automatic Segmentation of Lumen and Media-Adventitial Borders in Sequential IVUS Images

J. H. Lee¹, Y. N. Hwang¹, G. Y. Kim², and S. M. Kim^{1,2}

¹Department of Medical Devices Industry, Dongguk University-Seoul, Republic of Korea

²Department of Medical Biotechnology, Dongguk University-Bio Medi Campus, Republic of Korea

E-mail: smkim@dongguk.edu

Abstract—The purpose of this study was to automatically segment the inner and outer borders of arterial wall in sequential IVUS images. To remove the speckle noises, the pre-processing was employed in the original IVUS image. Each boundary was detected automatically by using non-parametric deformable model. The experimental results indicates superior performance of the proposed method for segmenting intima and media-adventitial borders from the IVUS scans. These results indicated that the proposed approach has high clinical applicability for IVUS-based diagnostics.

Keywords— Enter up to five keywords and separate them by commas.

I. INTRODUCTION

Intravascular ultrasound (IVUS) is a relatively new invasive imaging modality for diagnosing cardiovascular diseases. Unlike conventional angiography, IVUS allows for detection of plaque rupture and intraluminal thrombus presence [1].

Major types of plaques are located between the intima and media-adventitial borders. Thus, the plaque characterization of this region helps to select the proper treatment. The first step towards this goal is to detect the contours of arterial wall by segmenting the lumen and media-adventitial regions.

Although manual segmentation is usually performed by experts, the manual processing may be a tedious and time-consuming procedure. In addition, the manual segmentation is susceptible to inter- and intra-observer variability. This study presents an automatic segmentation approach based on geometric deformable model for segmentation of inner and outer borders in IVUS images.

II. METHODS

Considering the similarity of sequential image frames obtained from the same arterial segment, the initial estimation of the lumen and media-adventitial borders was given by manually only for the first frame of the sequence. After the initialization, appropriate pre-processing was applied to remove speckle noises and improve the weak or missing boundaries. Each boundary of regions of interest was automatically detected by using non-parametric deformable model

from sequential IVUS images [2]. Border segmentation was performed twice for each frame and the final border information was utilized as the initial estimation for the next frame.

III. RESULTS

From the Bland-Altman analysis, it was found that the proposed method perform with a low mean bias and less dispersion with the manual segmentation. Moreover, the Bland-Altman plot indicated a good agreement between the manual and automated segmentation methods, irrespective of image types. Linear regression analysis resulted in high correlation coefficients for all evaluation parameters at the same significant level ($p < 0.001$). The results indicate that the proposed method can reliably extract the inner and outer borders in IVUS images.

IV. CONCLUSION

The experimental results found superior performance of the proposed method for segmenting intima and media-adventitial borders from the IVUS 2D scans. Moreover, the proposed method significantly corresponded to the manual segmentation in terms of all evaluation parameters. These results indicate that the proposed approach has high clinical applicability for IVUS-based diagnostics.

ACKNOWLEDGEMENT

This work was supported by International Collaborative R&D Program funded by the Ministry of Knowledge Economy (MKE), Korea. (N01150049, Developing high frequency bandwidth [40-60MHz] high resolution image system and probe technology for diagnosing cardiovascular lesion)

REFERENCES

1. G. Unal, S. Bucher, S. Carlier, G. Slabaugh, T. Fang, and K. Tanaka, "Shape-driven segmentation of the arterial wall in intravascular ultrasound images", *IEEE T. Inf. Technol. Biomed.*, vol. 12, no. 3, pp. 335-347, 2008.
2. C. Li, C. Xu, C. Gui, and M. D. Fox, "Distance regularized level set evolution and its application to image segmentation", *IEEE Trans. Image Process.*, vol. 19, no. 12, pp. 3243-3254, 2010.

Three-dimensional visualization of plaque distribution in a curved artery using intravascular ultrasound imaging

Hyunggun Kim

University of Texas Health Science Center at Houston, USA

Intravascular ultrasound (IVUS) imaging provides an excellent tool for evaluation of the type, morphology, extent, and severity of atheroma. Three-dimensional (3D) IVUS can offer additive information pertaining to morphology of the arterial structures and volumetric plaque distributions. A novel 3D IVUS technique was developed for volumetric demonstration of a curved artery. A virtual 3D curved arterial phantom consisting of varying degrees of cross-sectional shape, wall thickness and brightness was utilized to validate the nonlinear interpolation technique to create in-between IVUS images. IVUS imaging was performed for the iliofemoral arterial segment of an atherosclerotic Yucatan miniswine model. These in-vivo IVUS data were utilized for in-between IVUS image generation and volumetric 3D IVUS visualization. Smooth transitional changes of cross-sectional shape, wall thickness and brightness were found between the in-between images and the original slices. Volumetric demonstration of the unfolded curved iliofemoral artery provided realistic luminal surface images of the arterial segment with physiologic grayscale intensity information. This 3D IVUS demonstration technique offers a tool to help with assessment of 3D plaque distribution across the curved arterial structure, and improve 3D molecular imaging of atheroma components.

Dissolving microneedles for transdermal drug delivery: Fabrication and in vivo evaluation

Seong-O Choi, Ph.D.

Assistant Professor

Department of Anatomy and Physiology

Nanotechnology Innovation Center of Kansas State (NICKS)

Kansas State University, Manhattan, KS 66506, USA

Recently microneedle technology has received great attention as a promising method for transdermal and intracellular drug delivery, which offers a number of advantages over the conventional drug delivery methods. Microneedles are microstructures originally designed to create micron-scale pathways across the stratum corneum, the outermost barrier layer of the skin, thereby delivering pharmaceutical compounds in the epidermal and/or dermal layers. These microstructures can also be applied to deliver biomolecules such as proteins and DNA into cells by overcoming the cell's plasma membrane.

Among various types of microneedles, this talk will present dissolving microneedles for transdermal drug delivery. Dissolving microneedle is made of water-soluble materials such as carboxymethyl cellulose (CMC) and polyvinyl alcohol (PVA) so that it dissolves away by interacting with body fluid once it is inserted into the skin. Therefore, there is no sharp waste remained after use that could minimize the risk of transmission of blood borne disease caused by needle reuse. Also, compared to drug-coated microneedles, dissolving microneedle can encapsulate more drugs so that it could be used for high-dose applications. Dissolving microneedles are fabricated by a successive micromolding process, which requires a robust microneedle master. This talk will introduce various microfabrication techniques to form a master structure and discuss in vivo experimental results, including vaccination and human growth hormone delivery. The results suggest that dissolving microneedle can deliver various molecules across the skin and could be an alternative way to conventional hypodermic injection.

Development of pediatric artificial heart valve: Investigating time-profile of geometric orifice area

Kwon Soo Chun
Baylor College of Medicine, USA

MODELING COCHLEAR MICRO-STRUCTURES: FROM MECHANICS TO SENSORY-NEURAL RESPONSE

Prof. Yong Jin YOON

School of Mechanical & Aerospace Engineering,
Nanyang Technological University, Singapore

Abstract

Cochlear physiologies for four species; gerbil, chinchilla, cat, and human, are studied using two separate refinements to the three-dimensional hydrodynamic cochlear models presented in Yoon *et al.*, 2007. One refinement is the application of the time-averaged Lagrangian density. The other refinement is the incorporation of a “push-pull” mechanism to examine the active case of hair cell motility. The objective of this work is to create a computational model of cochlear dynamics that could more accurately reflect existing cochlear physiological measurements for the following parameters: (i) basilar membrane (BM) velocity (V_{BM}); (ii) intracochlear pressure in the scala tympani (P_{ST}); (iii) cochlear input impedance (Z_C); and (iv) BM vibration and its effect on neural threshold regulation. Good agreement in both magnitude and phase is found between simulation results and physiological measurements for V_{BM} and P_{ST} for the gerbil and chinchilla. The large phase excursion observed in the previous models (Lim and Steele, 2002; Yoon *et al.*, 2007) is rectified. Similarly, good agreement is found between the calculated and measured results for Z_C in gerbil, chinchilla, cat and human. Interspecies BM vibration thresholds are estimated by matching the simulation results to the neural threshold measurements. The V_{BM} threshold curve shows a better fit to the neural threshold curves than the BM displacement threshold curve suggesting that inner hair cells respond more strongly to the BM velocity. This gives support to our suggestion that the present model is close to the actual behavior of mammalian cochleae including gerbil, chinchilla, cat, and human cochlea.

**BIOMECHANICAL APPROACH TO
PARKINSON'S DISEASE
-QUANTIFICATION OF BRADYKINESIA,
RIGIDITY, AND FREEZING OF GAIT-**

Gwang-Moon Eom¹, Ph.D., Ji-Won Kim¹, Ph.D., Seong-Beom Koh², M.D.&Ph.D.

¹School of Biomedical Engineering, Konkuk University, Chungju, Korea

¹Department of Neurology, Korea University College of Medicine, Seoul, Korea

Major movement disorders of Parkinson's disease (PD) include slowing of body motion (bradykinesia), increased resistance of a joint to passive movement (rigidity), and freezing at the initiation and turning of a gait (freezing of gait: FOG). The severity of these symptoms is rated by medical staff based on a coarse-graded scale (discontinuous grades of 0, 1, 2, 3, and 4) based on the clinically agreed rating scale called as UPDRS. The rating is used for diagnosis, monitoring, and prescription, so the reliability and precision of the rating are important. However, UPDRS is fundamentally a qualitative measure and suffer from low reliability (intra and inter-rater) and low precision.

Therefore, we tried to make new quantitative mechanical measures of major three symptoms of PD, i.e., bradykinesia, rigidity, and FOG, which would be more reliable and precise than UPDRS.

Bradykinesia was quantified by mechanical measures derived from angular velocity signal measured by gyro sensors attached on corresponding body parts. Included were the bradykinesia of finger tapping, wrist rotation (forearm pronation and supination), and toe tapping. Suggested measures included mean amplitude (root mean square: RMS) of velocity, mean amplitude of angle, peak and total power, variation of peak velocity and peak angle, etc. Mechanical measures showed good validity (correlation with clinical score) and could discriminate different clinical scores well. Furthermore, multiple regression models of mechanical variables showed better performance than a single variable. The suggested new measures are expected to be a great help in objective rating of bradykinesia.

Rigidity was quantified by viscoelasticity (damping and spring) and other mechanical quantities such as work and impulse. Damping constants were the best in terms of correlation with the clinical score and discrimination of different clinical scores. Because the rigidity is used as the index of optimality of stimulation setting (electrode position and stimulation parameters) in Deep Brain Stimulation (DBS) surgery, the viscoelasticity was tested for multiple settings during DBS. Damping constant could discriminate the optimal setting from baseline and showed good correlation with clinical scores. As an approach to find the source of rigidity, antagonistic co-contractions were investigated. Co-contraction of antagonistic muscle pair was significantly enhanced in patients than in normal subjects, suggesting that the enhanced co-contraction is associated with the rigidity.

FOG was detected by a time-domain method and the performance was compared to that of conventional frequency method, both utilizing acceleration signal in the outsole of a shoe. The time-domain method showed FOG detection performance comparable to the frequency-domain method and calculation load 1,154 times less than the frequency-domain method, suggesting that the time domain method is much more practical.

Title: Bone-conduction pathways of hearing: Computational approaches

Nam Keun Kim

Incheon National University, Korea

Abstract:

We developed 3D finite-element models to simulate the response of the cochlea to the bone conduction (BC) and air conduction hearing pathways based on μ CT imaging.

The box cochlear model indicates that the BM responses are determined by the anti-symmetric pressure component between the scala vestibuli and scala tympani, regardless of the direction of inertial stimulation to the box cochlea. The coiled cochlear model revealed the following points: 1) The BM response was shown to be a function of the direction of acceleration, but with the travelling wave instead being initiated by the hook region of the cochlea. 2) With a superior-semicircular-canal dehiscence (SSCD), BC hearing thresholds are clinically observed to improve for frequencies below about 1 kHz, and in the model this was shown to be due to a new fluid path between the RW and SSCD.

A number of observations in normal and diseased configurations of finite-element ear models are paving the way towards new theories and improved understanding of the BC pathways of hearing.

TBA

Seyong Lee
Yonsei University, Korea

BIOMECHANICS OF DOWNHILL RUNNING

Sang-Kyoon Park¹, Hyun-Min Jeon², Sukhoon Yoon¹, and Jiseon Ryu¹

¹Motion Innovation Centre, Korea National Sport University, Seoul, Korea

²Korea Armed Forces Athletic Corps, Mungyeong, Korea

Background: Downhill running has been found to provide higher impact on the body which may cause soreness of the muscles and future injuries of the lower extremity. However, the understanding of biomechanical characteristics during downhill running in terms of the adaptation of locomotion from the level to slope is still limited(Hreljac, Marshall & Hume, 2000). Therefore, the purpose of this investigation was to find how joint kinematics and kinetics during downhill running change compared to the level running.

Methods: Fifteen recreational runners (mean age: 25.6±4.27yrs; mean mass: 75.38±5.02kg; mean height: 177.0±5.0cm) ran at a controlled speed of 3.2 m/s on a force plated imbedded treadmill at the level, -6°, and -9°. Ten steps of each slope were selected to analyze the changes in joint angle, moment, and power in the sagittal plane.

Findings: Increased knee flexion with decreased ankle plantar-flexion and hip flexion was found during downhill running compared to the level running ($p < 0.05$). Decreased peak propulsive ground reaction force and posterior impulse were found during downhill running compared to the level running ($p < 0.05$). Additionally, increased extension moment at the knee with increased negative joint power at knee and hip joints were found while decreased plantar-flexion moment with negative joint power at the ankle were found during downhill running compared to the level running ($p < 0.001$).

Interpretation: Downhill running change kinematics and kinetic strategy as it decreases the range of motion at the ankle but increases the range of motion with increased negative joint power at knee and hip joints during downhill running compared to the level running.

Reference:

Hreljac, A., Marshall, R.N. & Hume, P.A. (2000). Evaluation of lower extremity overuse injury potential in runners. *Medicine and Science in Sports and Exercise*, 32: 1635-1641.

The Effects of Overloaded Warm-ups on the Athletic Performance

Young-Kwan Kim

Chonnam National University, Korea

The purpose of this study was to investigate the effects of overloaded warm-up in both open kinetic chain motion and closed kinetic chain motion on the athletic performance. In order to obtain general conclusion, we performed two separate studies for an open kinetic chain motion (golf swing) and a closed kinetic chain motion (vertical jump). Regarding golf swing experiment, nine high school golfers (age: 18 ± 1 yrs, height: 173.33 ± 7.2 cm, mass: 74.1 ± 17.0 kg, experience: 3.7 ± 2.4 yrs) were recruited. Electromagnetic motion data collecting system and shaft weight of 300g (Power Sleeve®) were applied to overloaded condition. There was significant club speed improvement in golf swing immediately after overloaded warm-up swings. This was mainly attributed to increased temporal delay between arm swing and club swing and increased peak angular velocities between these two motions. For the vertical jump study, twelve college students (age: 20.9 ± 0.3 yrs, height: 173.7 ± 5.4 cm, mass: 67.5 ± 5.8 kg) participated in vertical jump study and performed two different overloaded vertical jumps such as 5% and 10% extra mass with weighted vest. There was no main effect of overloaded warm-up jumps on the vertical jump heights. However, the significant mean differences on jump heights between pre- and post-warm ups at 5% overloaded warm-up condition. This improvement was well explained by the increased peak angular velocity of hip joint during propulsive phase and increased muscle activation of biceps femoris and tibialis anterior. In addition, there was no significant transient effect of post-activation potentiation after overloaded warm-up jumps. However, there was a tendency of a drop of jumping height in successive jumps immediately after overloaded warm-up indicating the plausible effect of post-activation potentiation. Conclusively, the overloaded warm-ups gave an effect on the performance in both open and closed kinetic chain motions. Especially the location of extra mass affected the neighbored joint motions and overall athletic performance. Further studies associated with finding an optimal extra mass of warm-ups for individual physical status and the optimal location of an extra mass are needed to enhance athletic performance further.

Critical Gaps in Rehabilitation and Assistive Robotics Research

Ang Wei Tech

Nanyang Technological University, Singapore

After years of development, notwithstanding the well-documented benefits of using robots to assist patients in rehabilitation, there is still no large scale deployment of rehabilitation robots in clinical rehabilitation. The evidences from various studies were insufficient to prove that the benefits outweigh the hefty cost of rehabilitation robots in most countries. The development of Assistive Robotics is on a different trajectory compared to Rehabilitation Robotics, but suffers the same fate in large scale adoption. The talk discusses the critical gaps in current rehabilitation and assistive robotics research which hinder these technologies from going mainstream in the near future.

Rehabilitation Robots and Translational Research in NRC, Korea

Won-Kyung Song, Ph.D.^{1,2}

¹Department of Rehabilitative and Assistive Technology,

²Translational Research Program for Rehabilitation Robots,
National Rehabilitation Center, Korea

Email: wksong@nrc.go.kr

The number of registered people with disabilities due to illnesses, injuries, and the natural aging process has already exceeded 2.5 million, i.e., 4.9 % of the population, in Korea. More than one-third of these disabled people are the elderly. The older people with disability increase due to longer life spans and a decline in birthrate. The healthcare cost of the senior citizen increases. Effective handling this issue with restricted resources is crucial.

We review rehabilitation and rehabilitation robots. According to the World Health Organization, *rehabilitation of people with disabilities is a process aimed at enabling them to reach and maintain their optimal physical, sensory, intellectual, psychological and social functional levels. Rehabilitation provides disabled people with the tools they need to attain independence and self-determination.* Rehabilitation robots include robotic devices for rehabilitation. We present commercialized or developing rehabilitation robots for upper extremity, lower extremity, and truck.

As brand new research in National Rehabilitation Center, Korea, we are constructing the infrastructure of translational research for rehabilitation robots in order to help rehabilitation robots enter the market and improve quality of life for people with disabilities and the elderly. We would like to grow industry of rehabilitation robots via translational research that promotes the connection between existing technology-driven R&D findings and clinical researches. The program consists of (1) an intramural translational research for rehabilitation robots, (2) an extramural translational research for rehabilitation robots, and (3) a testbed “Robot Gym” of rehabilitation robots. Robot Gym is a sharing space between engineers and clinicians to progress translational research for rehabilitation robots. We mention a future pathway of translational research for rehabilitation robots such as (1) simultaneous developing cost-effective/premium devices, (2) supporting early phase of clinical research, (3) acceleration of clinical research including other research programs, and (4) multi-purpose application to people with disabilities and the elderly.

In addition, we show some results of NRC, i.e., an Immersive Upper Extremity Exercise Environments with 2D and 3D visual feedback, and a NRC Robotic Exoskeleton (NREX).

Keyword: rehabilitation robot, translational research

Assistive robotics based on biomechanical signals

Jung Kim (jungkim@kaist.ac.kr)

Professor, Department of Mechanical Engineering, KAIST, Rep. of Korea

Inspired by imminent an aging society and the success of physical training robots, assistive robotics or wearable robotics has been an important research area for everyday life environments including hospital, senior care center and even home. These **assistive robots** perform a physical task for the well-being of a person with a disability or weakened muscle forces due to accidents or aging. The person with the disability controls the robotic devices based on interpreted motion intentions from the central nervous or peripheral nervous systems. In this talk, we are going to discuss for assistive robotics technologies for disabled or elderly people. As examples, we will present about upper limb assistant devices based on hybrid motion intention extraction algorithms and ankle foot orthosis designs, which are designed to provide a dditional muscle forces/torques to the user, based on motion intention extraction technologies from biosignals such as electromyography and ground reaction forces. Finally, we discuss important key technologies of assistive robotics based on their difficulty of access.

Bio-inspired Materials for Promoting Direct Reprogramming

Seung-Woo Cho, Ph.D.

Department of Biotechnology, College of Life Science and Biotechnology
Yonsei University, Seoul, Korea
Email: seungwoocho@yonsei.ac.kr

Cellular reprogramming has been highlighted for control of cell fate to induce pluripotency and transdifferentiation. Direct reprogramming can contribute to generation of tissue-specific cell types for therapeutic applications, but low efficiency of conversion still remains a major challenge. The use of viral vectors for transcriptional factor gene delivery also causes serious safety issues. In this presentation, bio-inspired devices and materials will be introduced to promote direct conversion of primary fibroblasts to functional neuronal lineage cells. The micro-devices and biomimetic substrates generating external stimulation and allowing for microenvironmental control are applied for enhancing the efficiency of polymer nanoparticle-mediated nonviral direct conversion of skin fibroblasts to induced neuronal (iN) cells and shortening the time scale required for the conversion process. These platforms also generate highly functional iN cells exhibiting electrophysiological activities and channel activation specific to mature neuron. The devices and substrates reported herein can provide biomedical platforms to improve cellular reprogramming for the treatment of neurodegenerative diseases.

Origami-based Tissue Engineering

Nathaniel S. Hwang ^{*,1,2}

¹ *School of Chemical and Biological Engineering, Seoul National University, Republic of Korea*

² *Interdisciplinary Program in Bioengineering, Seoul National University, Republic of Korea*

*nshwang@snu.ac.kr

In this talk, I present a novel method for assembling biofunctionalized paper into a 3-dimensionally (3D) structured complex scaffold system for reliable tissue regeneration using an origami-based approach. The surface of a paper was conformally modified with a poly(styrene-co-maleic anhydride) (PSMa) layer via initiated chemical vapor deposition (iCVD) followed by the immobilization of poly-L-lysine (PLL) and deposition of Ca^{2+} . This procedure ensures the formation of alginate hydrogel on the paper due to Ca^{2+} diffusion. Furthermore, strong adhesion of the alginate hydrogel on the paper onto the paper substrate was achieved due to an electrostatic interaction between the alginate and PLL. The developed scaffold system was highly versatile and allowing area-selective cell seeding. Also, the hydrogel-laden paper could be folded freely into 3D tissue-like structures using the simple origami-based method. The cylindrical hydrogel-laden paper with chondrocyte was transplanted into a three-ring defect trachea in rabbits for the purpose of tracheal reconstruction. The transplanted engineered tissues replaced the native trachea without stenosis after 4 weeks. As for the custom-built scaffold system, the hydrogel-laden paper system will provide a robust and versatile method for the formation of complex tissues mimicking native tissue constructs.

A Microfluidic Platform for Programmable Cell Culture Environments

Minseok Kim¹, Ji Won Lim² and Taesung Kim^{1,2}

¹Department of Mechanical Engineering, Ulsan National Institute of Science and Technology, Ulsan, Korea

²Department of Biomedical Engineering, Ulsan National Institute of Science and Technology, Ulsan, Korea

E-mail: tskim@unist.ac.kr

Abstract—We describe a simple, robust mass-transport-control mechanism by using a nanoscale hydrodynamic film formed between two sandwiched elastomer surfaces. The thin fluid film enables to actively control the transport of small molecules from a surrounding outside channel to a compartmentalized microchamber array at the center. Thus, a variety of chemical environments can be temporally applied to cells in a high-throughput manner, showing remarkable potential for sequential bioprocesses on a chip.

Keywords—Microfluidic platform, microchamber array, cell culture environments, and bioprocesses.

I. INTRODUCTION

A multilayered microfluidic device made of Polydimethylsiloxane (PDMS) provides precisely controlled micro-environments for various applications such as cell culture, protein crystallization, enzyme activity test, single-cell genomics, high-throughput screening, and so on [1]. The device usually consists of a flow channel, a control channel, and a thin PDMS membrane between the two channel networks and utilizes elastic deformation of the membrane to control the flows in the device. However, for the high throughput analysis or screening, the device requires many and complex microfluidic channel networks to commend on-chip valves and pumps which are connected with external pressure regulating systems. In this work, we report a novel and simple microfluidic platform for versatile bioprocesses on a chip.

II. METHODS

Fabrication and Experiment

The standard photolithography technology in conjunction with soft-lithography was used to fabricate two-layered PDMS devices. The top-layer was used for controlling pneumatic pressures while the bottom-layer was done for a two-level microfluidic channel network. A microscopic image-based feedback loop was used for controlling the pneumatic valves during the entire period of cell culture.

III. RESULTS

A. Manipulation of mass transport through nanoscale hydrodynamic film

The pneumatic pressure was adjusted to control the mass transport through the nanoscale hydrodynamic film that chemically connected the microchamber array at the center and the surrounding outside channel. In case of continuous flow along the surrounding channel, the culture condition of the microchamber array remained constant while a batch-culture mode was obtained by filling the surrounding channel with oil because the diffusion was almost prevented at the water-oil interface.

B. Programming chemical environments of a microchamber array

A microchamber array was used to concentrate target cells and then nutrients were provided with the cells through the nanoscale hydrodynamic film that completely suppressed pressure-driven flows but allowed the diffusion based mass transport of small molecules in the solution. This working principle made it possible to actively manipulate the chemical cell culture environments of the microchamber array.

IV. CONCLUSION

We characterized mass transport of small soluble molecules through the nanoscale fluid films and utilized the mechanism to develop a microchemostat array that can actively control cell-culture conditions such as cell populations in a chamber and nutrient feed-modes. We demonstrated that the microfluidic platform could facilitate bioprocessing optimization, cell-based screening, drug test at cellular levels, and even tissue engineering studies.

ACKNOWLEDGEMENT

This work was supported by the National Research Foundation of Korea (NRF) grant funded by the Korea government (MSIP) (NRF-2014R1A2A1A10050431) and by the grant from the Next-Generation BioGreen 21 program (SSAC, PJ01118601), Rural Development Administration, Republic of Korea.

REFERENCES

1. D. B. Weibel, W.R. DiLuzio, and G.M. Whitesides, "Microfabrication meets microbiology", *Nature Reviews Microbiology*, vol. 5(3), pp. 209-218, 2007.
2. M. Kim and T. Kim, "Crack-Photolithography for Membrane-Free Diffusion-Based Micro/Nano fluidic Devices", *Anal. chem.*, 2015.

Dynamic micropatterning of cells on complex nanostructured surfaces using a cell-friendly photoresist

Junsang Doh

Department of Mechanical Engineering/I-Bio,
Pohang University of Science and Technology (POSTECH), South Korea

Cellular dynamics under complex topographical microenvironments is important for many biological processes in development and diseases, but systematic investigation has been limited due to lack of technology. To address this problem, we developed a new dynamic cell patterning method based on a cell-friendly photoresist polymer poly(2,2-dimethoxy nitro-benzyl methacrylate-r-methyl methacrylate-r-poly(ethylene glycol) methacrylate) (PDMP). PDMP thin films were casted on nanostructured surfaces by spincoating. Upon UV exposure, PDMP thin films become soluble in near-neutral aqueous buffers such as PBS and tissue culture media with minimal cytotoxicity. To create micro-patterns on PDMP thin film, microscope projection photolithography (MPP) technique was used. By performing series of MPP on PDMP thin films and sequentially depositing cells on nanostructured surfaces exposed by UV-irradiation, we could successfully create single cell arrays of adhering cells on nanostructured surfaces. Then, various dynamic cellular processes such as cell spreading, adherens junction formation, and collective cell migration were triggered by removing PDMP thin films surrounding cells in single cell arrays by UV illumination. Using this new method, we quantitatively compared spreading dynamics of cells on nanostructured surfaces and flat surfaces. Furthermore, we investigated how cells behaved when they simultaneously encountered two topographically distinct surfaces during spreading. This method will allow many exciting opportunities in the study of fundamental questions in cellular dynamics.

An external shape memory support to prevent vein failure

Timothy C. Boire¹, Christy Guth², Colleen Brophy², Hak-Joon Sung¹

¹Department of Biomedical Engineering, ²Division of Vascular Surgery, Vanderbilt University, Nashville, TN, USA
E-mail: hak-joon.sung@vanderbilt.edu

Abstract— We are developing an external stent that can minimize neointimal formation by providing mechanical support, and promoting outward instead of inward vein remodeling in the arterial circulation. Existing external mesh supports applied in other settings, such as to saphenous vein grafts in heart bypass grafting surgeries, have demonstrated some promise but cannot be applied in hemodialysis vascular access surgeries because they cannot be applied to the foci of neointimal formation at the venous anastomosis. Our novel shape memory polymers (SMPs) enable facile wrapping of the external support around the venous anastomosis that is most critical to maintaining vein patency.

Keywords—External vascular stent; shape memory polymers; AV grafting; anti-intimal hyperplasia

I. INTRODUCTION

HSV is the most commonly used conduit for vascular bypass grafting. However, approximately 40% of grafts fail within 12-18 months because of intimal hyperplasia (IH). External mesh supports applied to saphenous vein grafts have demonstrated promise to inhibit IH by promoting adventitial microvessel growth (i.e. neo-vasa vasorum formation). The materials used to date, however, are highly rigid and inflexible, in contrast to the compliant nature of the artery. This increases restenotic risks and precludes application to curvaceous arterial regions, including the anastomoses most responsible for vein graft failure. To address this issue, a mechanically compliant, biocompatible, bioresorbable, macroporous shape memory stent was fabricated that can be custom fit around the anastomoses.

II. METHODS

For stent fabrication, 88%poly(ϵ -caprolactone)-co-12%(α -allyl carboxylate ϵ -caprolactone) (88%PCL-12%ACPCL) was chosen because it is biocompatible/biodegradable and highly malleable at CABG operating temperatures ($T_m = 33.1$ °C)¹. Glass rods were dipped into a 10 wt/vol% polymer solution containing DMPA and UV crosslinked to obtain a thickness of 1 mm. Pores were generated with an Epilog Laser Engraver. HSVs were obtained from patients at VUMC according to IRB protocols. HSV samples were treated with external supports by wrapping the HSV with the SMP support scaffold. IH was then tested in a well-established *ex vivo* model.

III. RESULTS

Shape memory external stents were fabricated with 332 μ m pores (**Figure 1D**). In HSV samples treated

with the external support, there was a reduction in intimal area after 14 days of *ex vivo* culture compared to untreated controls (**Figure 1B – C**, yellow bars). Intimal, medial and adventitial areas in the stent-treated group were similar to baseline (day 0). Staining with α -SMA reveals fewer proliferating and migrating SMCs in the stent-treated samples (**Figure 1E**) compared to the untreated control (**Figure 1F**). Staining with vWF revealed an intact endothelial layer in both treated and untreated groups, with more abundant staining in the adventitia indicating neo-vasa vasorum growth induced by the external support (**Figure 1G**).

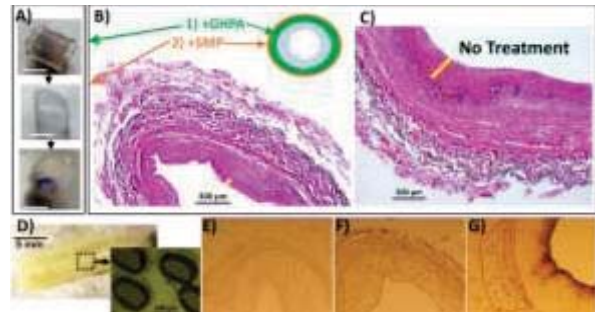


Figure 1: A) HSVs wrapped with the SMP support. HSV samples treated with B) external supports exhibited a marked reduction in intimal thickening (yellow bar) compared to C) untreated controls. D) Fabricated stent with macropores (332 μ m). E) α -SMA staining of stent-treated and F) untreated samples. G) vWF staining of treated groups, with neo-vasa vasorum encircled.

IV. CONCLUSION

A mechanically-compliant, porous shape memory external support capable of wrapping around the anastomoses was fabricated. Our data in an *ex vivo* AVG model with human saphenous veins (HSV) indicates an ability of these external supports to reduce neointimal formation and, in turn, obviate the subsequent adverse clinical repercussions. An *in vivo* porcine model of saphenous vein to carotid interposition grafting is being conducted to validate these findings.

ACKNOWLEDGEMENT

This work was supported by NSF CAREER CBET 1056046, NIH R01 HL070715, and NSF Icorp 1450684.

REFERENCES

- Boire TC *et al*, "Pendant Allyl Crosslinking as a Tunable Shape Memory Actuator for Vascular Applications" *Acta Biomaterialia* [Invited Special Issue]. 2015;24:53-63.

BIOCOMPATIBLE POLYMERIC NANOPARTICLE FOR EFFICIENT DELIVERY OF THERAPEUTIC MATERIALS

In-Kyu Park

Department of Biomedical Sciences, Chonnam National University Medical School,
Gwangju 501-746, South Korea

Gene therapy to treat the genetic disease like cancer, restenosis has lot of importance in the field of biomedical science. Successful delivery of gene to the target site without side effects has been the aim to many researchers for more than a decade. Delivered gene has to be expressed efficiently in the target site, which is another area of concern. In order to overcome the drawbacks, cationic polymers have been employed to aid in the delivery of genes. But the cationic polymers were not degradable and its toxicity was an issue. In order to solve the issue, we employed the cationic polymer with modifications to deliver the genes. Modifications include polyethylene glycol attachment, introduction of disulfide bond and sorbitol group to the cationic polymer along with the degradable esters. Once these modifications were done the gene delivery was efficient without compromising the bio-compatibility. Imaging the delivery of the gene will help in visualizing the target place accumulation and distribution, so we have loaded the imaging agents like quantum dots, superparamagnetic ironoxides, indocyanin green etc to the modified polymeric carriers. Replacement of the missing genes or suppression of the overexpressed gene can be done through plasmid DNA, siRNA and microRNA delivery. Initial study we have loaded the quantum dots in to the polysuccinimide, Polyethylenimine (PEI) and polyethylene glycol polymersome to deliver the killer red plasmid DNA. In the next study disulfide modified PEI was employed to deliver the anti-proliferative siRNA. Finally the sorbitol modified PEI was used to deliver the microRNA which can suppress the cancer cell proliferation.

Quantitative imaging of cellular mechanotransduction at the subcellular level

Sungsoo Na, PhD

Department of Biomedical Engineering, Indiana University-Purdue University,
Indianapolis, IN 46032, USA

Weldon School of Biomedical Engineering, Purdue University,
West Lafayette, IN 47907, USA

Mechanotransduction is the process by which cells sense and respond to their physical microenvironments and convert them into biochemical signaling that affects their various functions including growth, survival, differentiation, and migration. Changes in physical microenvironments, such as magnitude and frequency of mechanical forces or stiffness and geometry of extracellular matrices, result in altered mechanotransduction signaling, and consequently lead to, or at least contribute to, physiological or pathophysiological outcomes of tissue and organ development and functions. Thus, understanding the molecular mechanism of mechanotransduction has important implications in human health and disease.

The measurement and visualization of such activities at the sub-cellular or molecular level require tools of high spatial and temporal resolution and sensitivity. Recent advancements in live cell imaging and genetically-encoded biosensors based on fluorescence resonance energy transfer (FRET) offer greater understanding of the dynamic molecular activities in living cells at the high spatial and temporal resolutions. In this talk, I will present our group's approach to monitor and manipulate target proteins in living cells using such tools. Current research efforts on elucidating mechanotransduction mechanisms, particularly in skeletal, cancer, and vascular systems, will also be discussed.

Cell-derived matrix engineering for tissue regeneration

In Gul Kim¹, Ping Du¹, Muhammad Suhaeri^{1,2} and Kwideok Park^{1,2*}

¹Center for Biomaterials, Korea Institute of Science and Technology, Seoul 02792, Republic of Korea

²Department of Biomedical Engineering, University of Science and Technology, Daejeon, Republic of Korea

E-mail: kpark@kist.re.kr

Abstract—Extracellular matrix (ECM) environment is a very critical aspect for cells, as ECM provides adhesive support for cell proliferation, migration, morphogenesis and differentiation. In this study, 3D mesh scaffold and collagen hydrogel was functionalized via hFDM, respectively and their potential for mesenchymal stem cell (MSC) differentiation and vasculogenesis is evaluated.

Keywords—ECM, MSC differentiation, vasculogenesis, mesh scaffold, collagen hydrogel.

I. INTRODUCTION

Construction of 3D functional tissues using bioactive materials and stem cells has shown a great advance toward tissue regeneration [1]. In this study, 3D mesh scaffold and collagen hydrogel was functionalized using hFDM, respectively and their potential for MSC differentiation and vasculogenesis is evaluated.

II. METHODS

A. Cell culture

Human lung fibroblast (WI-38, ATCC[®] CCL-75) and MSCs were cultured in DMEM, supplemented with 10% fetal bovine serum (FBS), 100 IU/ml penicillin, and 100 µg/ml streptomycin (Invitrogen), respectively. HUVECs (2517A; Lonza) were cultured in endothelial growth medium (EGM)-2 (CC-3162). All the cells are maintained at 37 °C under a 5% CO₂ humidified atmosphere.

B. Collagen hydrogel for HUVECs vasculogenesis

Different doses of hFDM were incorporated into Col I hydrogel with HUVECs (2x10⁶ cell/ml) to evaluate its effect on HUVECs morphogenesis at day 3 and 7. After then, the synergistic effect of hFDM and growth factors (GFs) was investigated by Q-PCR and confocal microscopy.

C. Combination of mesh scaffold and hFDM

Decellularized ECM from human lung fibroblasts (hFDM) was coated onto the surface of the PLGA/PLA based mesh scaffold, upon which heparin was conjugated onto hFDM via EDC chemistry. TGF-β1 was subsequently immobilized onto the mesh scaffolds.

D. Induction of chondrogenesis of MSCs

Human umbilical cord blood-derived mesenchymal stem cells (UCB-MSCs) were cultured in four different groups of mesh scaffolds to examine the potential as a mesenchymal condensation-inducible scaffold during *in vitro* chondrogenesis and to evaluate efficacy of cartilage repair through a rabbit cartilage defect model.

III. RESULTS

A. Effect of hFDM and GFs on vasculogenesis

The co-incorporation of hFDM and GFs exhibited a synergistic effect for HUVECs vasculogenesis, compared to collagen alone or collagen/hFDM (Fig. 1).

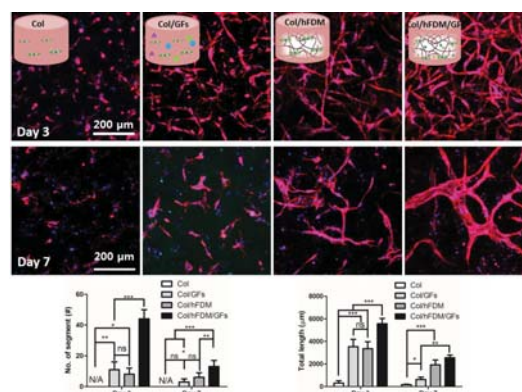


Fig. 1. Synergistic effect of GFs and hFDM on HUVECs vasculogenesis in 3D environment.

B. Chondrogenic induction via mesh scaffold/hFDM

Chondrogenic differentiation of UCB-MSCs cultured in the hFDM/TGF-β1 microfiber scaffolds is verified by the chondrogenic nodules formation as examined via collagen type II immunofluorescent staining.

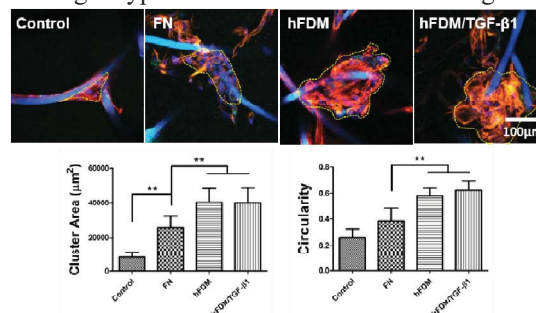


Fig. 2. *In vitro* chondrogenic differentiation of UCB-MSCs via mesenchymal condensation.

IV. CONCLUSION

Current studies have strongly indicated that hFDM has a great potential in advancing not only vasculogenesis of HUVECs but chondrogenesis of MSCs.

ACKNOWLEDGEMENT

This work was supported by an intramural grant 2E25260 (KIST) and a National Research Foundation of Korea (NRF) grant (No. 2015R1A2A2A04004469) from the Ministry of Science, ICT and Future Planning, Republic of Korea.

REFERENCES

- Kim IG et al. "Bioactive cell-derived matrices combined with polymer mesh scaffold for osteogenesis and bone healing," *Biomaterials*. vol. 50, pp. 75-86, 2015.

Oxygen Producing 3D Matrices for Prolonged Cell Survival under Hypoxic Environment

H. Y. Lee¹, J. H. Lee², and S. H. Oh¹

¹Department of Nanobiomedical Science, Dankook University, Cheonan, Republic of Korea

²Department of Advanced Materials, Hannam University, Daejeon, Republic of Korea

E-mail: seheangoh@dankook.ac.kr

Abstract—Perfluorooctane emulsion (oxygen carrier)-loaded hollow microparticles (PFO-HPs) were prepared as a scaffolding system which can allow timely release of oxygen to cells adhered on the HPs to prevent cell necrosis in a hypoxic environment until new blood vessels are formed in the 3D cell construct, and thus may produce appropriate tissues/organs with a clinically relevant volume. From the *in vitro* and *in vivo* experiment, we could suggest that the cell-based PFO-HPs can be a promising system to produce a clinically applicable large tissue mass.

Keywords—Hollow microparticle, oxygen release, perfluorocarbon, scaffold, tissue engineering

I. INTRODUCTION

The survival and functional maintenance of cells in the 3D matrix until the ingrowth and maturation of blood vessels is the most important challenge in tissue engineering. Although innovative tissue engineered tissues/organs such as the skin, trachea, and bladder have been reported, their limited dimensions caused by slow vascularization in the scaffold and limited oxygen diffusion into the non-vascularized scaffold before blood vessel formation, which lead to insufficient oxygen supply to cells, are significant hurdles for clinical application. To overcome the inherent limitation of tissue engineering, several strategies including the use of oxygen carriers and angiogenic factors have been incorporated into the scaffolds. Although promising results from the strategies, producing a clinically applicable large tissue mass continues as a significant challenge.

II. METHODS

A. Preparation of PFO emulsion-loaded PCL HPs

PCL HPs were fabricated using a modified W/O/W emulsion solvent evaporation method. The PFO emulsion was infiltrated into the PCL HPs through the shell membrane with a micropore under positive pressure when the syringe piston was pushed in.

B. *In vitro* cell culture

To investigate cell survival in a hypoxic environment using the PBS-HPs and PFO-HPs, the murine calvaria

pre-osteoblast (MC3T3-E1) was used as the cell model. The cell-adhered HPs were incubator in hypoxic incubator for 14 days.

C. Animal study

BALB/c athymic nude mice (8 weeks old) were selected as the animal model to evaluate viable cell distribution and blood vessel ingrowth in the implanted cell (MC3T3-E1)/HP groups.

III. RESULTS

A. Characterization of PFO emulsion-loaded PCL HPs

The prepared PCL HPs exhibited a spherical structure (like a micro balloon) with micron-sized pores. The PFO emulsion was easily infiltrate into the HPs through the porous shell membrane and stably maintained in the HPs.

B. *In vitro* cell culture

The number of cells on the PFO-HPs was increased to ~200 % at 5 days compared to the initial value, indicating an appropriate oxygen environment for cell proliferation. In the initial number of cells on the PFO-HPs remained constant for up to for ~10 days in hypoxic environment.

C. Animal study

At 14 days after injection, the cells (red color) the adhered on the PFO-HPs were evenly distributed in the implanted matrix, and the blood vessels had infiltrated into the matrix at the central region (depth ~2 mm) through the space between the HPs.

IV. CONCLUSION

Our findings in the *in vitro* cell culture and the *in vivo* animal study demonstrated that the PFO-HPs can be a promising scaffold that helps to fulfill our aim, in terms of controlled oxygen release from the PFO-HPs for a sufficient time period, and prolonged cell survival until the ingrowth of new blood vessels.

REFERENCES

1. H.Y. Lee et al., "Controlling oxygen release from hollow microparticles for prolonged cell survival under hypoxic environment," *Biomaterials*, vol. 53, pp. 583-591, 2015.

Category: Tissue Engineering and 3D bio-printing

Keywords: Optical imaging, biodegradable scaffold, molecular and cellular trafficking

The Role of Bioimaging in 3D Bioprinting and Tissue Engineering

Hak Soo Choi*

Department of Medicine, Beth Israel Deaconess Medical Center, Harvard Medical School, Boston, MA 02215

Center for Molecular Imaging, Beth Israel Deaconess Medical Center, Boston, MA 02215

Noninvasive imaging of transplanted cells, host tissue infiltrates, and scaffold degradation is of significant importance in the field of tissue engineering and 3D bioprinting. Ideally, the transplanted stem cells with tissue-engineered or bioprinted scaffolds for tissue regeneration need to be monitored longitudinally without sacrificing animals. Currently, however, a large number of samples and animals are required to track biodegradation of implanted scaffolds, and such nonconsecutive single-time-point information from various batches result in inaccurate conclusions. To overcome this limitation, we developed functional biodegradable scaffolds by employing invisible near-infrared (NIR) fluorescence and followed their degradation behaviors longitudinally *in vitro* and *in vivo*. Using optical fluorescence imaging, the scaffold degradation could be quantified in real-time, while tissue ingrowth was tracked by measuring vascularization using magnetic resonance imaging in the same animal over a month. Since light scattering and absorption in human tissue are the major obstacles in optical fluorescence imaging, NIR wavelength can efficiently minimize tissue autofluorescence, resulting in less background interference and enhanced signal-to-background ratio. Moreover, we optimized the *in vitro* process of enzyme-based biodegradation to predict implanted scaffold behaviors *in vivo*, which was closely related to the site of inoculation. This combined multimodal imaging will benefit tissue engineers by saving time, reducing animal numbers, and offering more accurate conclusions.

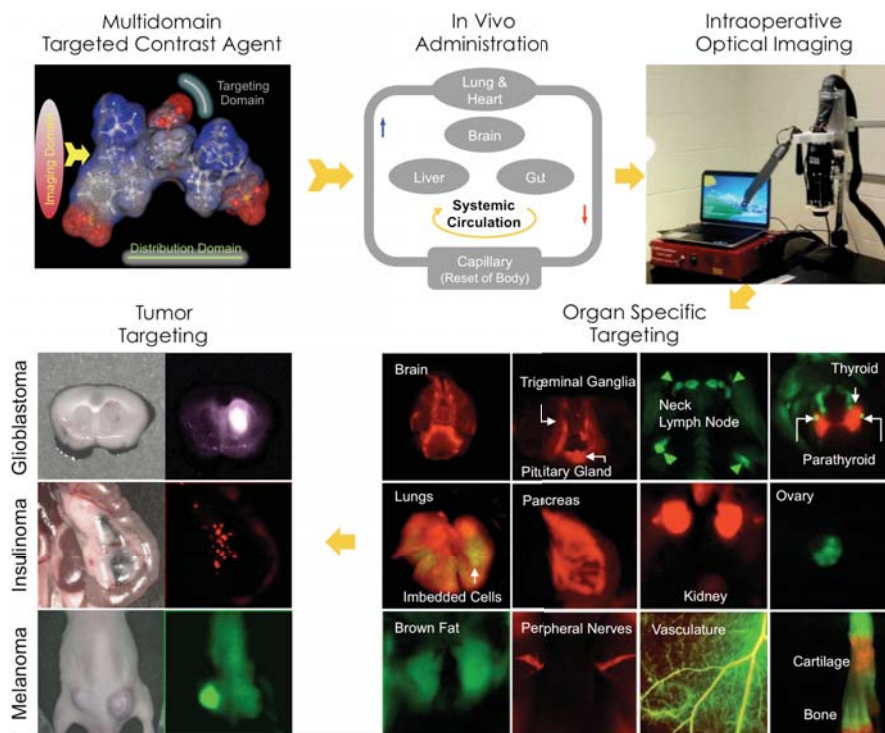


Figure 1. Tissue- and organ-specific nanoprobes for bioimaging and tissue engineering.

3D Integrated Organ Printing Technology and Its Tissue Engineering Applications

Hyun-Wook Kang

Biomedical Engineering, Ulsan National Institute of Science and Technology
hkang@unist.ac.kr

Key Words: organ printing, tissue engineering, bio-ink

Organ printing technology makes it possible to not only fabricate 3-D freeform shape, but also precisely place various cell in a single structure. Many researchers have been giving an attention to the technology because the technology can produce tissue engineered constructs imitating complex organ or tissue structure. However, the introduced printing technologies cannot produce a construct with substantial size and enough physical properties required for clinical application because the technology only permits the process of cell mixed hydrogels which has weak mechanical property. In addition, channel incorporation for nutrient and oxygen supply is not easy with the soft material, which is one of crucial points for tissue regeneration. As such, new technology was developed, which names as integrated organ printing. It concurrently delivers high strength polymer and cell mixed hydrogels to overcome the current limitations. The printing system was constructed by combining multi-cartridge module, 3-axis stages and chamber equipped with temperature and humidity controller. And new bio-ink was developed for co-printing process of thermoplastic and bio-ink. Then the system was applied into artificial ear reconstruction and bone and muscle tissue engineering. The results successfully demonstrated the new technology could produce clinical relevant, cellular constructs in terms of size and shape.

Electromechanical Dyssynchrony in Heart Failure under Various Mechanical Afterload Conditions: A Computational Study

Ki Moo Lim, Ph.D.

Department of Medical IT Convergence Engineering, Kumoh National Institute of Technology

One of the subset of the heart failure (HF) is dyssynchrony of the heart depolarization and the myofiber shortening. Time interval between the heart depolarization (electrical activation) and onset of myofiber shortening (mechanical activation) in one cycle of heart rhythm is known as electromechanical delay (EMD). Experimental study of Russell et al. (1) in dog and human heart also showed that mechanical load prolonged the EMD. These studies leads to a presumable solution that if the mechanical load of the ventricle is decreased, the EMD will also be decreased. However, no one ever proved that. To measure the mechanical load effect on three-dimensional (3D) EMD distribution cannot be obtained experimentally so far due to the limitation of measurement devices. The purpose of the study is to quantify the effect of mechanical afterload on EMD by using 3D cardiac physiome model.

To construct an integrated model of a cardiovascular system, we combined the 3D image-based electromechanical model of failing human ventricles with a lumped model of the circulatory system. In order to apply various mechanical afterload condition, we changed the resistance of systemic arteries with scale factors of 0.5, 1.0, 2.0, 3.0, 4.0, and 5.0. The local electrical activation times, which is obtained from Durrer et al., were mapped to the ventricular computational mesh. The local mechanical activation time was defined as the 10% of the lowest strain value of the ventricle models following Constantino et al. (2). Therefore, EMD can be derived by subtracting EAT from MAT in space. Finally, EAT, MAT and EMD were compared among in silico experimental groups.

We obtained cardiac responses such as cardiac tension, strain, ATP consumption, mechanical activation time (MAT), and EMD, etc. The MAT and EMD increased in the degradation of Ca^{2+} concentration level, which means that the MAT and EMD are emphasized under more severe HF condition induced by Ca^{2+} remodeling. And we found that the MAT and EMD increased depending on mechanical afterload. Ventricles with five times higher flow resistance of systemic arteries induced almost 20% more prolonged EMD than normal case. Although this study have proved that mechanical afterload increases EMD with computational method, it can be used for treatment of patients who suffer from prolonged EMD in novel way.

1. K. Russell, O. A. Smiseth, O. Gjesdal, E. Qvigstad, P. A. Norseng, I. Sjaastad, A. Opdahl, H. Skulstad, T. Edvardsen, and E. W. Remme, "Mechanism of prolonged electromechanical delay in late activated myocardium during left bundle branch block," *American Journal of Physiology-Heart and Circulatory Physiology*, vol. 301, no. 6, pp. H2334–H2343, 2011.
2. J. Constantino, Y. Hu, A. C. Lardo, and N. A. Trayanova, "Mechanistic insight into prolonged electromechanical delay in dyssynchronous heart failure: a computational study," *American Journal of Physiology-Heart and Circulatory Physiology*, vol. 305, no. 8, pp. H1265–H1273, 2013.

IBEC

International Biomedical
Engineering Conference 2015

2015

Road to Better Life through Biomedical Engineering

SPECIAL SESSIONS



Development of Agarose Scaffolds via Enhancement of a Mechanical Properties to Promote an Axons Regeneration

Sang Jin Lee¹, Min Heo¹, Eun Young Heo¹, Dong Nyoung Heo¹, Kuiwon Choi² and Il Keun Kwon^{1*}

¹Department of Maxillofacial Biomedical Engineering and Institute of Oral Biology, School of Dentistry, Kyung Hee University, 26, Kyunghedae-ro, Dongdaemun-gu, Seoul 130-701, Republic of Korea.

²Biomedical Research Institute, Korea Institute of Science and Technology, 39-1 Hawolgok-dong, Seongbuk-gu, Seoul 136-791, Republic of Korea

*E-mail: kwoni@khu.ac.kr

Abstract— This study of major aim is to enhance the mechanical property of agarose scaffolds to promote an axons regeneration by introducing nanorods and nanotube. The mechanical properties of developed scaffolds were characterized by rheology test. The results showed that our outcomes may provide a better environment for axons regeneration.

Keywords— Aminolysis, Nanotube, Nanorods, Agarose, Electrospinning

I. INTRODUCTION

A strong mechanical properties of the scaffold is one of important factor for axons regeneration. Thus, development of scaffolds is essential for use as means of axons regenerative scaffolds. In this case, poly-L-lactide (PLLA) nanorods and multi-walled carbon nanotube (CNT) can enhance the physical properties. In this study, we designed the agarose scaffolds embedded with a reinforcing agent which may promote a mechanical property of scaffolds for effective axons regeneration.

II. METHODS

A. Preparation of PLLA nanorods and CNT

For aminolysis, electrospun PLLA nanofibers were immersed in a solution of aqueous 1,6-hexanmethylenediamine (HMDA) at concentration of 10 % in 37 °C of iso-propanol incubator under shaking for 2h. Aminolyzed PLLA nanofibers were stored in 50 % ethanol. Aminolyzed PLLA nanofibers were treated by ultra-sonication system to fabricate the nanorods for 40 min. the outcomes were centrifuged at 3000 rpm for 5min and then lyophilized¹. The CNTs were purchased from TCI with 20-40 nm.

III. RESULTS

A. Characterization of scaffolds

In the Scanning electron microscope (SEM) images, developed morphology were observed as porous nanocylinder type. Further study of rheological analysis, mechanical modulus were considerably enhanced compared with control.

IV. CONCLUSION

The scaffold containing the nanorods and nanotube showed that the enhanced mechanical property compared with agarose alone. The results suggested that developed scaffold will provide a better environment for axons regeneration.

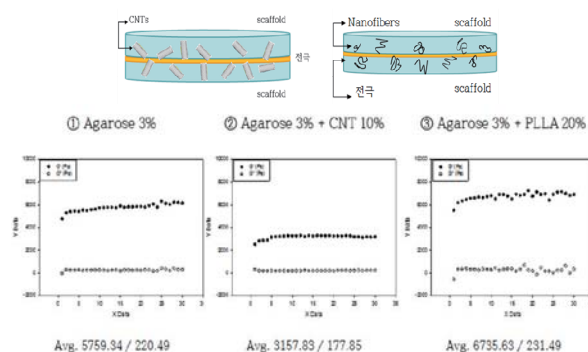


Fig. 1. Characterization of mechanical properties against developed agarose scaffolds.

ACKNOWLEDGEMENT

This research was supported by the National Research Foundation of Korea (NRF) funded by the Ministry of Education, Science and Technology (NRF-2010-0019346).

REFERENCES

1. Lee, Jung Bok, et al. "Highly porous electrospun nanofibers enhanced by ultrasonication for improved cellular infiltration." *Tissue Engineering Part A* 17.21-22 (2011): 2695-2702.

Flexible Neural Electrodes with Hydrogel Scaffolds for Artificial Neural Networking of Injured Spinal Cord

Jinwoo Jeong, Wonsuk Choi, Sunyoung Jung, Woohyun Jung, Hyungdal Park,
Sungmin Han, Inchan Youn, Jun-Kyo Francis Suh, and Jinseok Kim

Center for Bionics, Korea Institute of Science and Technology, Seoul, South Korea

E-mail: jinwoo@kist.re.kr, jinseok@kist.re.kr

Abstract— In order to restore functionality of injured spinal cord, a flexible neural electrode with hydrogel scaffold for linear axon regeneration was designed. By repeating surgical trials using small animal models, the many issues for *in-vivo* applications were found in the point of mechanical stability. Optimization of the polymer's material properties and connector shapes, and surgical methods will be discussed.

Keywords— Neural electrode, hydrogel scaffold, spinal cord injury, neural engineering.

I. INTRODUCTION

Many literatures about neural connection of injured nerves have been published in neural engineering field. Especially many types of flexible neural electrodes are hot topics for practical applications such as bionic prosthesis and neural disease treatments [1]. Also biocompatible scaffold with drugs or cell therapies are drawing more and more attention of doctors and neuroscientists [2]. Nevertheless, spinal cord injury is still tough due to its limited regeneration capability and plasticity [2].

In this special topic presentation, the experimental results about the design optimization issues of the neural electrode will be shown.

II. METHODS

A. Sieve-type Electrode Fabrication

The components of the suggested neural device, flexible electrode and hydrogel scaffolds are separately fabricated. The flexible electrode with the thickness of about 36~38 μ m is fabricated using micro fabrication process. Each of the polyimide layers are formed by high temperature thermal curing after spin coating of liquid polyimide (VTEC-1388, RBI Inc., PA). Electrode metal layers are patterned by standard semiconductor process such as metal evaporation, photolithography, and so on. Final shaping is done by reactive ion etching with CF₄ and O₂ chemistry.

Hydrogel scaffolds are fabricated using injection molding technique. First, hot molten agarose liquid are poured into the specially designed jig. Then, the jig is removed after enough cooldown for the gel formation.

B. Evaluation of Material Properties

The material properties of the neural devices are measured by a tabletop electromechanical universal

tester (EZ-S series, Simadzu, Japan). The experimental groups are classified by the connector width, polymer materials of the devices, and time length of *in-vivo* implantation in small animal model, Sprague Dawley female rat with the weight of 270g to 300g.

C. Evaluation of Surgical Implantation Methods

A variety of surgical methods was considered for the optimized long-term *in-vivo* implantation. To protect the device from the mechanical abrasion by the tissues and muscle, encapsulation method based on polymer materials was tried. After a month, the rat subjects are sacrificed and the mechanical stabilities of the implanted devices are examined.

III. RESULTS

The evaluation results of the material properties shows the consistent fact that polyimide is not altered by the width and 1 month *in-vivo* implantation. Also, parylene-C has weaker yield strength, but higher durability under longer elongation condition.

Although many surgical methods were applied to the implantation of the devices, the mechanical rupture of them was unavoidable. The suspicious reasons are the low position stability of the device encapsulations and relatively large shear forces by the tissue in the direction of craniocaudal axis.

IV. CONCLUSION

The experimental results indicate that the device connection should endure under transient stretching condition in rat body. Also, flexibility only is not enough for implantable device. Stretchability of the device encapsulation is absolutely necessary.

ACKNOWLEDGEMENT

This research was supported by the Pioneer Research Center Program through the National Research Foundation of Korea funded by the Ministry of Science, ICT & Future Planning (NRF-2010-0019347).

REFERENCES

1. Akhil Srinivasan, *et. al.*, "Microchannel-based regenerative scaffold for chronic peripheral nerve interfacing in amputees", *Biomaterials*, vol. 41, pp. 151-165, 2015.
2. Mingyong Gao, *et. al.*, "Templated agarose scaffolds for the support of motor axon regeneration into sites of complete spinal cord transection", *Biomaterials*, vol. 34, pp. 1529-1536, 2013.

A novel unsorted spike feature based real-time sensory event detection for closed-loop control

S. Han^{1,2}, J. U. Chu³, K. Choi¹, J. W. Park², and I. Youn^{1,4}

¹ Biomedical Research Institute, Korea Institute of Science and Technology, Seoul, Korea

² Department of Biomedical Science, Korea University, Seoul, Korea

³ Daegu Research Center for Medical Devices and Rehabilitation Engineering, Korea Institute of Machinery and Materials, Daegu, Korea

⁴ Department of Biomedical Engineering, Korea University of Science and Technology, Daejeon, Korea

E-mail: iyoun@kist.re.kr

Abstract— The goal of the current study was to investigate the possibility of sensory event detection from the afferent signal recorded by using a multi-channel micro-electrode on the dorsal root ganglion without spike sorting. We particularly considered to extract the most informative feature vector from recorded neural signals using feature combination of previous studies such as electroneurography signals, electromyography signals and neural spikes. Principal component analysis was used to reduce dimensionality of feature vector, and multilayer perceptron classifier was used to detect sensory events. In this study, a novel unsorted spike-based feature extraction methods was proposed to enhance the detection accuracy of sensory events.

Keywords— Sensory event detection, Sensory feedback, Unsorted spike

I. INTRODUCTION

In functional neuromuscular stimulations, sensory feedback based closed-loop control can be useful for restoring lost function in patients with paralysis. A closed-loop control system should respond continuously to sensory feedback (events) in real-time, so that it mimics the natural control of motor task without time delay. Thus, a robust and computationally efficient sensory event detection algorithm is necessary to classify and control motor functions. In this study, we propose a novel unsorted spike-based feature extraction method. To evaluate detection accuracy, the tactile afferent signals were recorded from a multi-channel micro-electrode on the dorsal root ganglion, and multilayer perceptron (MLP) classifier was used to detect sensory event.

II. METHODS

A. Data Acquisition

Neural signals were recorded from the dorsal root ganglion of five adult male Sprague-Dawley rats. The 16-channel microelectrode was inserted longitudinally into the left fourth lumbar ganglion, and sensory events were generated by mechanical stimulation of three different areas of the left hindpaw using von Frey monofilament.

B. Feature Extraction

The combination of unsorted spike-based time series of the firing rate, waveform length, mean absolute value, and wavelet packet transform was used to construct feature vector.

III. RESULTS

A. Classification Performance

Sensory event detection performance was investigated using the proposed feature vector, principal component analysis, and MLP classifier. Total mean detection accuracy for the five rats was $99.26 \pm 0.33\%$ and total processing time was 36 ms.

IV. CONCLUSION

We proposed to detect sensory event using unsorted spike-based feature vector. The proposed method showed high detection accuracy, and processing time was less than 200 ms which is enough to meet the real-time feedback.

ACKNOWLEDGEMENT

This research was partially supported by the Pioneer Research Center Program through the National Research Foundation of Korea funded by the Ministry of Science, ICT & Future Planning (20100019348), a grant of the Korea Health Technology R&D Project through the Korea Health Industry Development Institute (KHIDI), funded by the Ministry of Health & Welfare, Republic of Korea (HI14C3477), and KIST Institutional Program.

REFERENCES

1. J. U. Chu, K. I. Song, S. Han, S. H. Lee, J. Y. Kang, D. Hwang, J. K. F. Suh, K. Choi, and I. Youn, "Gait phase detection from sciatic nerve recordings in functional electrical stimulation systems for foot drop correction," *Physiol. Meas.*, vol. 34, no. 5, pp. 541-65, May, 2013.
2. S. Raspopovic, J. Carpaneto, E. Udina, X. Navarro, and S. Micera, "On the identification of sensory information from mixed nerves by using single-channel cuff electrodes," *J Neuroeng Rehabil*, vol. 7, Apr 27, 2010.

Study on evaluation techniques for injured spinal cord regeneration after transplantation of porous polymeric nerve electrodes

Jee Y. Lee¹, Hae Y. Choi¹, Eun Y. Huh², Jin W. Jung³, Sugmin Han⁴, Il K. Kwon², Jin S. Kim⁴, Inchan Youn⁴ and Tae Y. Yune¹

¹Age-Related and Brain Diseases Research Center, School of Medicine, Kyung Hee University, Seoul, Korea

²Department of Maxillofacial Biomedical Engineering, School of Dentistry, Kyung Hee University, Seoul, Korea

³Center for Bionics, Korea Institute of Science and Technology, Seoul, Korea

⁴Biomedical Research Center, Korea Institute of Science and Technology, Seoul, Korea

E-mail: tyune@khu.ac.kr

Abstract—In this study, we estimate the effects of the porous polymer including the transplanted-neural electrode device on spinal cord regeneration. For this purpose, we established optimal spinal cord injury (SCI) model from a variety of animal models such as complete transaction, hemisection, dorsal cutting. To increase regeneration ability, we have tried a variety of channels arranged in agarose scaffold. In addition, we have performed an operation to determine the electrode type that can be present stably in a living body. As a result, we observed axon regeneration within the scaffold channels. To detect the nerve signal of regenerative axon, we transplanted electrode into the injured spinal cord. Alternatively, we inserted the electrode into the transplanted scaffold channels. Until now, it did not measure the electrical signals within the damaged spinal cord. Currently we are experimenting to solve various problems using *in vivo* system. If this application may promote the recovery of motor and physiological function, this study will support and enhance the possibility of the clinical application of the new therapeutic device for SCI.

Keywords—Spinal cord injury, transplantation, axon, agarose scaffold, regeneration

I. INTRODUCTION

While several strategies can stimulate axonal regeneration with in injured spinal cord, the growth of axons is generally disorganized and random [1]. Therefore multilumen nerve guidance scaffolds offer a means of simulating the native organization of projection axonal tracts through sites of SCI, a feature that could be combined with other growth-promoting strategies to stimulate axonal regeneration.

II. METHODS

A. Spinal cord injury

Adult Sprague-Dawley rats were anesthetized and a laminectomy was performed at the T9-T10 level [1]. Complete transaction was performed using a surgical blade (no. 11). For lateral hemisection and dorsal hemisection, aspiration was done.

B. Agarose scaffold and electrode transplantation

Immediately after SCI, we transplanted the 3% agarose scaffold filled with matrigel or electrode into the injured spinal cord and set topped with agarose film and collagen film.

C. Immunohistochemistry

Immunohistochemistry was performed as described previously [2].

III. RESULTS

A. Dorsal hemisection and 3% agarose scaffolds is suitable *in vivo*.

Among various injury types and scaffold materials, dorsal hemisection was the most suitable for transplant and 3% agarose scaffold is the most biocompatible material.

B. Scaffolds are stable in spinal cord and support linear growth of axons

One month after *in vivo* implantation, agarose scaffolds were stable and biocompatible supporting vascularization and promoting linear axonal growth.

IV. CONCLUSION

Porous agarose (3%) filled with matrigel might be a suitable scaffold for axonal regeneration. For the success of the measurement signal it seems to require a longer development time and technique.

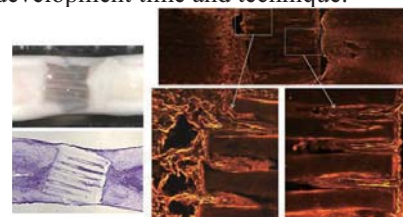


Fig. 1. Axon regeneration with in scaffold channels

ACKNOWLEDGEMENT

This research was supported by National Research Foundation of Korea funded by the Ministry of Science, Information and Communications Technology & Future Planning (grant number: 2010-0019349).

REFERENCES

1. J Neurosci. Vol. 27, pp. 7751-7761. 2007.
2. Endocrinology. Vol.151, pp.3815-3826. 2010.

Development of efficient transplantation method of artificial nerve networking system

Joongkee Min, Ph.D.¹, Sang Ryong Jeon, M.D., Ph.D.¹

¹Department of Neurological Surgery, Asan Medical Center, University of Ulsan College of Medicine, Seoul, Republic of Korea
E-mail: srjeon@amc.seoul.kr

Abstract- This study was performed transplantation of artificial nerve networking system (ANNS) in spinal cord injured rat. After transplantation, we were performed to solve the problems and develop an efficient surgery method.

Keywords- Spinal cord injury, artificial nerve networking system (ANNS), electrode.

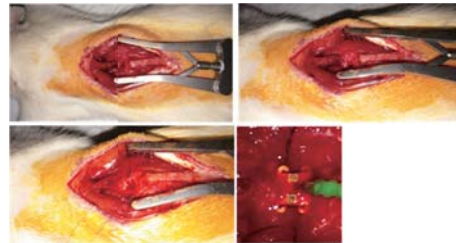


Fig. 1. Transplantation procedure

I. INTRODUCTION

Spinal cord injury (SCI) in adults often leads to permanent functional deficits because the regeneration of the injured axon and the reorganization of the remaining circuitry are insufficient in the human central nervous system. Therefore, promoting axonal regeneration is one of essential goals to be achieved for effective repair from SCI. However, we still have many problems. Thus, in one way, we were transplanted of Artificial Nerve Networking System (ANNS) to address these problems. First of all, we consider that system can be maintained in spine for long term. Second, we consider that transplantation can be performed by efficient surgical method.

II. METHODS

A. Spinal cord injury

A total of 10 female SD rats were injured at the T7–8 level with an IH impactor (200 kdyn). One week after injury, all rats were transection in lesion site spinal cord (3mm).

B. ANNS transplantation

After transection, we were performed made two holes of each lateral side in vertebrate by micro drill. Then, system was fixed by 7-0 silk in medial of vertebrate. And we were covered the cap for electrode protection.

III. RESULTS

A. Development of an efficient surgery method

After transection, we were performed made two holes of each lateral side in vertebrate by micro drill. Then, system was fixed by 7-0 silk in medial of vertebrate. Finally, we were closed skin (Fig. 1).

And we were covered the cap for electrode protection. This cap is upper side of eppi tube. The reason for covering the cap, prevent damage and long term preservation of electrode. However, MRI could not take because the transplanted cap (Fig 2).



Fig. 2. Covering the cap for electrode protection

Also, mortality was high because the cap was to be exposed to the outside of skin. However, we were found a stable sustain electrode during the four weeks after transplantation.

IV. CONCLUSION

Our studies suggest that the efficient transplantation of ANNS. Also, we were confirmed that system can be maintained in spine for long term.

ACKNOWLEDGEMENT

This work was supported by the Pioneer Research Center Program through the National Research Foundation of Korea funded by the Ministry of Science, ICT, & Future Planning (NRF-2010-0019351).

REFERENCES

1. Suh HI, Min J, et al. Axonal regeneration effects of Wnt3a-secreting fibroblast transplantation in spinal cord-injured rats. *Acta neurochirurgica*. 2011;153:1003-10.
2. Park JH, Min J, et al. Enhanced neuroregenerative effects by scaffold for the treatment of a rat spinal cord injury with Wnt3a-secreting fibroblasts. *Acta Neurochir (Wien)*. 2013;155:809-16.

Cancer-selective drug delivery and imaging

C. Kang

East-West Medical Science, Kyung Hee University, Yongin 446-701, Korea.
E-mail: kangch@khu.ac.kr

Abstract— The anticancer drug delivery systems (DDSs) composed of fluorescent part, anticancer and linker parts are developed and its drug releasing location and drug efficacy are verified. Using these technologies, cancer-selective fluorescent sensor compatible with endoscopic diagnosis will be developed in our laboratory. They will contribute to safer and much efficient diagnosis of early stage of cancer in the gastrointestinal track

Keywords— Enter up to five keywords and separate them by commas.

I. INTRODUCTION

The targeted drug delivery systems (DDSs) have a strong advantage over a simple drug administration, minimizing side effects due to undesired drug delivery to normal tissues. They are composed of a prodrug and a targeting unit, which are connected each other through a linker, cleavable in the biological environment by intracellular thiols, enzymes, or changes in pH. The targeting unit can selectively deliver the system to a specific type of cells, for example, cancer cells. Recently, our laboratory has attempted adding monitoring capability to the targeted DDSs for an accurate and quantitative measurement of the drug release process.[1-4] The recent progresses in the lab regarding this theranostic DDS are introduced in the presentation.

II. METHODS

A. Organic synthesis

Folate-, biotin- and RGD-derivatives of some anticancer drugs with fluorogenic delivery capability were synthesized and the details are described in the literatures.¹⁻⁴

B. The other experiments

The drug release from the DDSs and its delivery to the target cells were characterized and visualized with confocal microscopy, respectively. The anticancer efficacy of the DDS systems is demonstrated using cell viability assay.

III. RESULTS

A. Folate-based gemcitabine delivery system [1]

A heptamethine cyanine derivative bearing a carbamate ethyl disulfide group and gemcitabine is synthesized. The prodrug is preferentially up-taken by folate-positive cells over folate-negative cells via receptor-mediated endocytosis to release gemcitabine causing cell death and to emit fluorescence in endoplasmic reticulum. And, its pharmaceutical efficacy was demonstrated by dorsal subcutaneous injection to mice.

B. Biotin-based anticancer drug delivery [2-3]

The design, synthesis, optical properties and in vitro biological assessments of the theranostic prodrugs in which a near IR fluorophore or coumain is conjugated with a cancer cell-directing biotin unit; further it is linked with an anti-cancer drug gemcitabine via a disulfide bond. Upon the presence of glutathione, disulfide bond cleavage occurs as well as the active drug release and concomitantly fluorescence intensity increases. The present drug delivery system is a new theranostic agent, wherein both a therapeutic effect and drug uptake can be readily monitored at the subcellular level by two photon fluorescence imaging.

C. RGD-based drug delivery system [4]

Design, synthesis, spectroscopic characterization, and preliminary in vitro biological evaluation of a RGD peptide-appended naphthalimide pro-camptothecin (CPT) are introduced. The DDS is composed of a disulfide bond as a cleavable linker, a naphthalimide moiety as a fluorescent reporter, an RGD cyclic peptide as a cancer-targeting unit, and CPT. Confocal microscopic experiments reveal that it is preferentially taken up by U87 cells over C6 cells through an endocytic pathway. In U87 cells, the active CPT payload is released within the endoplasmic reticulum.

IV. CONCLUSION

The present drug delivery systems (DDSs) could represent a new approach to so-called theranostic agent development, wherein both a therapeutic effect and drug uptake-related imaging information are produced

and can be readily monitored at the subcellular level. In due course, the strategy embodied in conjugate 1 could allow for more precise monitoring of dosage levels, as well as an improved understanding of cellular uptake and release mechanisms.

Using these technologies, cancer-selective fluorescent sensor compatible with endoscopic diagnosis will be developed in our laboratory. They will contribute to safer and much efficient diagnosis of early stage of cancer in the gastrointestinal track.

ACKNOWLEDGEMENT

This work was supported by the NRF grant (2015037656).

REFERENCES

1. Z. Yang, J. H. Lee, H. M. Jeon, J. H. Han, N. Park, Y. He, H. Lee, K. S. Hong, C. Kang, J. S. Kim, "Folate-based near-infrared fluorescent theranostic gemcitabine delivery," *J. Am. Chem. Soc.*, vol. 135, pp. 11657-62. 2013.
2. S. Bhuniya, M. H. Lee, H. M. Jeon, J. H. Han, J. H. Lee, N. Park, S. Maiti, C. Kang, J. S. Kim. "A fluorescence off-on reporter for real time monitoring of gemcitabine delivery to the cancer cells", *Chem Commun (Camb)*. vol. 49, pp. 7141-3, 2013.
3. S. Maiti, N. Park, J. H. Han, H. M. Jeon, J. H. Lee, S. Bhuniya, C. Kang, J. S. Kim. "Gemcitabine-coumarin-biotin conjugates: a target specific theranostic anticancer prodrug", *J Am Chem Soc*. vol. 135, pp. 4567-72, 2013.
4. M. H. Lee, J. Y. Kim, J. H. Han, S. Bhuniya, J. L. Sessler, C. Kang, J. S. Kim. "Direct fluorescence monitoring of the delivery and cellular uptake of a cancer-targeted RGD peptide-appended naphthalimide theragnostic prodrug", *J Am Chem Soc*. vol. 134, pp12668-74. 2012

Synthesis and Characterization of Multifunctional Nanophosphor Materials for Bioimaging and Drug Delivery Applications

Jae Su Yu

Department of Electronics and Radio Engineering, Kyung Hee University, Korea

There are increasing efforts on the development of nontoxic multifunctional mesoporous and nano materials for bioimaging, selective targeting, drug delivery, therapy applications. Recently, various biocompatible materials with different shapes and compositions, including metals (gold, silver, etc.), metal oxides, polymeric materials, and carbon particles, have been used as multifunctional biomaterials for cancer cell targeting and imaging. For this, many research groups have focused on the conjugating of polyethylene glycol (PEGylation) with metal or metal oxide nano or mesoparticles for improving the penetration capability with cell nucleus and the development of core and silica mesoporous shell structured morphologies.

Meanwhile, fluorescence bioimaging which is an important technique for monitoring behavior and activity in vivo has become one of the increasingly demanded areas in biophotonic fields. Rare-earth (RE) ions provide up- and down-conversion luminescent properties. The emission properties of different RE ions doped various micro/nano particles based host materials have widely studied for solid-state lighting and biomedical applications. These luminescent materials can be synthesized via different synthesis routes such as solid-state reaction, sol-gel method, hydrothermal method, etc. The luminescent properties of phosphor materials strongly depend on the kind of dopants and the synthesis method.

In this presentation, the synthesis and luminescent properties of RE ions activated nano/mesoporous phosphors through a facile synthesis route will be explored. Based on the unique and important structural and luminescent properties of the RE³⁺ ions activated PEGylated mesoporous particles and silica coated core-shell nanoparticles, their suitability for bioimaging and drug delivery applications will be presented.

Employment of Near-Infrared Irradiation and Targeted Gold Nanoheaters for Photothermal Cancer Treatment

Kyung Min Byun*

Department of Biomedical Engineering, Kyung Hee University, Korea

*kmbyun@khu.ac.kr

Metallic or magnetic nanoparticles interacting with electromagnetic waves have been successful in modulating cellular functions through a conversion of external optical or magnetic energy into a thermal heat. Interestingly, illuminating gold nanorods (GNRs) at their resonant wavelengths leads to efficient light absorption and local field enhancement, called localized surface plasmon resonance. Since such plasmonic nanoheaters can generate a local temperature elevation more efficiently, near-infrared irradiation incorporating GNRs has a potential for destroying cancer cells through photothermal effect in a nano- or microscale dimension.

Cell specific targeting of nanoparticles has been applied in a variety of research fields such as phototherapy of cancer cells and tumors, targeted delivery of drugs, and optical bioimaging. For example, surface-modified superparamagnetic nanoparticles bound to the target cell could remotely modulate cellular functions by converting a radio-frequency magnetic signal into a local heat. Recently, we presented that near-infrared irradiation combined with plasmonic nanoheaters injected in a proximity of neuron cells could significantly enhance the neural responses of a rat sciatic nerve *in vivo*. However, unconjugated nanoparticles can be washed out of nerve tissues if they are exposed to an internal fluidic environment. Strongly bound nanoparticles to the target site are critical because body fluid such as cerebrospinal fluid in the central nervous system flows continuously through living cells to dump out the metabolic wastes.

Based on our previous experience of photothermal neural stimulation, we intend to suggest an advanced point-of-procedure technique of endoscope based on surface-modified nanoheaters of GNRs that are targeted to cancer cells. Once GNRs are attached to a cell membrane, local heat elevation occurs by pulsed near-infrared illumination, heating and killing cancer cells without harming the surrounding healthy tissue. It is expected that our study could provide new possibilities of non-invasive photothermal treatment of cancer cells and tumors.

Tunable Microenvironments Regulating Expansion and Differentiation of Stem Cells and Cellular Reprogramming

*Bogyu Choi, Kwang-Sook Park, **Soo-Hong Lee****

Department of Biomedical Science, CHA University, 335 Pangyo-ro, Bundang-gu, Seongnam-si, Gyeonggi-do, 463-400 Rep. of KOREA

* Corresponding author: * soohong@cha.ac.kr

ABSTRACT

It is essential to regulate stem cell behaviors such as adhesion, proliferation and differentiation for medical applications. Because most of stem cells bind to the surface of substrate called anchorage effect, stem cells during in vitro culture continuously interact with the surface of substrate and subsequently their fate is determined depending on signals from the interactions. Recently, substrate modification for stem cell niche with physical, chemical and biological factors has extensively employed to increase the expansion and differentiation of stem cells. For expansion and differentiation of stem cells, however, substrate condition has neither optimized nor elucidated the underlying mechanism. This work employed cell culture substrates with physical topology such as lotus and nano-featured structure or poly-L-lysine (PLL), a positively charged synthetic amino acid chain. We investigated indeed whether the substrates would be able to regulate adipose-derived stem cells and hematopoietic stem cells and also tried to suggest the mechanism between stem cells and substrate. Furthermore, we also hypothesize that the surface stiffness may induce the abnormal phenotype which is able to increase the cell reprogramming. To control the surface stiffness, this work employed polyacrylamide hydrogels with various concentrations of acrylamide and bis-acrylamide. And then we observed the effect of surface stiffness on cell morphology and gene expression related to generation of induced pluripotent stem cells (iPSCs). Compared to stiff hydrogels, it was found that soft hydrogels induced the round shape while stiff hydrogels did the widely spread shape. In addition, soft hydrogels induce the higher gene expression of epithelial markers such as E-cadherin followed by increase in the generation of Oct4-GFP colonies

KEYWORDS

Tunable Microenvironment, Stem Cells, Expansion, Differentiation, Reprogramming

The past, present and future of image-enhanced endoscopy focusing on narrow-band imaging: a clinical perspective

Jung-Wook Kim, MD, PhD & Jae-Young Jang, MD, PhD

Division of Gastroenterology, Department of Internal Medicine, College of Medicine, Kyung Hee University, Seoul, Korea

Abstract

In the field of gastrointestinal endoscopy, the desire to better recognize entities such as malignancies, which may be difficult to distinguish from inflammation or trauma, has accelerated the development of endoscopic techniques. Image-enhanced endoscopy (IEE) refers to endoscopic imaging technologies that provide detailed contrast enhancement of the mucosal surface and blood vessels, which, in turn, facilitates selection of the optimal treatment. IEE encompasses various means of enhancing contrast during endoscopy using dye-based, optical, and/or electronic methods. Several IEEs using optical and/or electronic methods are now available and include narrow-band imaging (NBI), autofluorescence imaging, i-scans, and flexible spectral imaging color enhancement. Of these, NBI is the most frequently used and a relatively well studied modality because of its convenience and clear visualization. The NBI is based on the modification of optical filter spectral characteristics in the light source, which improves the visibility of mucosal structures. Several recent studies have described correlations between NBI appearance and pathology of the neoplastic lesions. However, there are some disadvantages, such as its darkness, a need of magnifying function, and a lack of standardized classification of the NBI findings. To date, IEE is advancing due to the development of endoscopic technology. If the advantages and disadvantages of the various techniques are taken into consideration, IEE can assist the diagnosis and treatment of gastrointestinal abnormalities. In the near future, IEE is expected to become a standard endoscopic technique that enables rapid, safe and accurate diagnosis of minute and/or ambiguous lesions.

Listening to Light and Seeing Through: In Vivo Multiscale Photoacoustic Imaging

Chulhong Kim, Ph.D.

Department of Creative IT Engineering, POSTECH

Email: chulhong@postech.edu

High-resolution volumetric optical imaging modalities, such as confocal microscopy, two-photon microscopy, and optical coherence tomography, have become increasingly important in biomedical imaging fields. However, due to strong light scattering, the penetration depths of these imaging modalities are limited to the optical transport mean free path (~ 1 mm) in biological tissues. Photoacoustic imaging, an emerging hybrid modality that can provide strong endogenous and exogenous optical absorption contrasts with high ultrasonic spatial resolution, has overcome the fundamental depth limitation while keeping the spatial resolution. The image resolution, as well as the maximum imaging depth, is scalable with ultrasonic frequency within the reach of diffuse photons. In biological tissues the imaging depth can be up to a few centimeters deep.

In this presentation, the following topics of photoacoustic imaging will be discussed; (1) multi-scale photoacoustic imaging systems (i.e., Photoacoustic Nanoscopy, Optical-Resolution Photoacoustic Microscopy, Fast 2-Axis MEMS based Optical-Resolution Photoacoustic Microscopy and Endoscopic Probe, Intravascular Photoacoustic/Ultrasound Catheter, Virtual Intraoperative Surgical Photoacoustic Microscopy, Acoustic-Resolution Photoacoustic Microscopy, Clinical Photoacoustic/Ultrasound Scanner), (2) morphological, functional, and molecular photoacoustic imaging, (3) potential clinical applications, and (4) contrast agents for photoacoustic imaging.

Multimodal Endoscopic Imaging System for Detection of Gastric Lesions

S. Yun¹ and J. Y. Hwang¹

¹Department of Information and Communication Engineering, DGIST, Daegu, S. Korea
E-mail: jyhwang@dgist.ac.kr

Abstract— We built a multimodal endoscopic imaging system capable of fluorescence intensity, reflectance/fluorescence multi-spectral, and real-time 3-dimensional (3D) stereoscopic imaging. The capability of each imaging modality was evaluated with tissue phantoms and then it was applied to image tumors *ex vivo*. Our developed system here allowed to obtain different but complementary information on gastric lesions such as auto-fluorescence intensity, spectral signatures, and 3D surface curvatures, thus may enhance the contrast in the early detection of gastric lesions.

Keywords— Multimodal imaging, auto-fluorescence, multispectral, 3D imaging.

I. INTRODUCTION

To date, various types of endoscopic imaging systems have been developed for diagnosis of gastric lesions. However, the detection and localization of early gastric tumors *in vivo* with high specificity and sensitivity still remain very challenging by using conventional white-light reflectance endoscopes. Therefore, many researchers have so far developed a variety of advanced endoscopic imaging systems with combination of different imaging modalities.

In this paper, we built a novel multimodal endoscopic imaging system capable of fluorescence intensity, reflectance/fluorescence multispectral, and real-time 3D imaging via General Purpose Graphics Processing Units (GPU) processing. Each imaging modality was here evaluated with tissue-mimicking phantoms and then applied to detect gastric lesions.

II. METHODS and RESULTS

A. Fluorescence intensity, Reflectance/Fluorescence Multispectral Imaging

For fluorescence imaging, the light emitted from gastric lesions excited by light at 480 nm was selected with a bandpass filter at 530 nm and recorded in a charge-coupled device (CCD). The strong fluorescent regions in the image (Fig 1) indicate fluorescent dyes.

For reflectance spectral imaging, the light from a mercury lamp was delivered to a specimen after passing through a furcated multimode fiber. The reflected light from the specimen was collected by GRIN lenses attached to two optical fiber bundles. Sequential wavelength selection from 500 nm to 680 nm was then realized by bandpass filters installed in a motorized

filter wheel and then recorded in CCD to create a 3-D image cube. In contrast, for fluorescence multispectral imaging, light at 480 nm was applied to gastric lesions of interest for excitation. The wavelength of the emitted light was sequentially selected with the aforementioned manner, followed by spectral classification. In the spectral classified image (Fig 1), the green-color represents fluorescence regions while the brown-color represents auto-fluorescence regions.

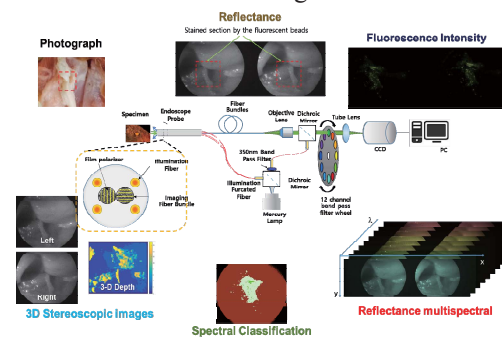


Fig. 1. A multimodal 3D endoscope and the images obtained using each imaging modality

B. Real-time 3-D stereoscopic imaging

Two optical fiber bundles are utilized for real-time 3-D stereoscopic imaging. A sum of absolute difference method based on GPU programming was employed to construct a 3-D image (1). The 3-D image here provided 3-D surface curvatures of the gastric lesions (Fig.1).

IV. CONCLUSION

Our developed system provides multiple information on the gastric lesions of interest and therefore may allow more reliable outcomes in the early detection of gastric lesions with high sensitivity and specificity. Furthermore, the developed system will be integrated with a high-frequency ultrasound system to obtain anatomical information below the surface of gastric lesions.

ACKNOWLEDGEMENT

This work was supported by the NRF grant (NRF-2014M3A9D7070668 and 2014R1A1A2054934).

REFERENCES

1. F. Islam, A. Amir-Khalili, et al., "Real-time GPU implementation of correlation based dense matching of stereo endoscopic images for surface reconstruction," *Qatar Foundation Annual Research Conference*, 2013.

A development of enabling technology for next generation laparoscopic surgical robot using novel end-effector, novel master interface, and da Vinci Research Kit (dVRK)

C. Lee¹, M. Kim², H. J. Kim³, and S. Kim^{1,4}

¹Institute of Medical and Biological Engineering, Medical Research Center, Seoul National University, Seoul, Korea

²The Interdisciplinary Program for Bioengineering, Graduate School, Seoul National University, Seoul, Korea

³Department of Mechanical & Aerospace Engineering, Seoul National University College of Engineering, Seoul, Korea

⁴Department of Biomedical Engineering, Seoul National University College of Medicine, Seoul, Korea

E-mail: lcwkf16@snu.ac.kr, kimmj08@snu.ac.kr, hjinkim@snu.ac.kr, sungwan@snu.ac.kr

Abstract—Robot-assisted laparoscopic surgery offers several advantages compared with open surgery and conventional minimally invasive surgery. However, several issues, such as non-uniform gripping force and inconvenience of master interface, still have to be resolved. For this purpose, mathematical modeling for uniform gripping force in end-effector, novel end-effector driven by pneumatic force, and novel master interface have been developed and integrated with da Vinci Research Kit for developing enabling technology for next generation laparoscopic surgical robot.

Keywords— Surgical Robot, Laparoscopic Surgery, End-effector, Novel Master Interface, da Vinci Research Kit (dVRK)

I. INTRODUCTION

Laparoscopic surgery has emerged as a new paradigm for surgical operation because it offers many advantages such as short-term hospitalization period, faster recovery, smaller incision, and reduced hemorrhaging compared to open surgery [1]. To maximize the benefit of laparoscopic surgery, laparoscopic surgical robot has been rapidly developed in many research groups [2]. However, it suffers from some disadvantages: absence of haptic feedback, longer time for surgery, non-uniform gripping force and inconvenience of master interface. To resolve these limitations, mathematical modeling for uniform gripping force in end-effector, novel end-effector driven by pneumatic force, and novel master interface have been developed in this research. Using da Vinci Research Kit (dVRK), the development of additional enabling technology for next generation laparoscopic surgical robot will be proceeded.

II. METHODS

A. Mathematical Modeling for Surgical Robot End-effector

Mathematical Model of an EndoWrist (MME) is developed and validated with a real gripping force measurements. Using the posture angles and the gripping forces, the MME is constructed. Then, expected gripping force values obtained from MME are compared with actual measurements of da Vinci EndoWrist to validate the proposed model.

B. Novel End-effectors

A novel end-effector using micro motors and pneumatic system was developed. End-effector's outer diameter was 8 mm. To enhance the DOF, 6-axis external arm is integrated.

C. Novel Master Interface

A novel master interface is a wireless communication interface consists of a multidirectional switch, an encoder, a bluetooth module, and a button cell battery. The multidirectional switch has eight ways with a center push as shown in Fig. 1, and each of them was encoded as a four-digit number by the ten to four-line encoder. The four-digit number enters to the bluetooth module for sending the data to the controller wirelessly. The designed circuit of the novel master interface was printed on a 35 mm × 33 mm printed circuit board. After assembling with several parts, two novel master interfaces were developed.

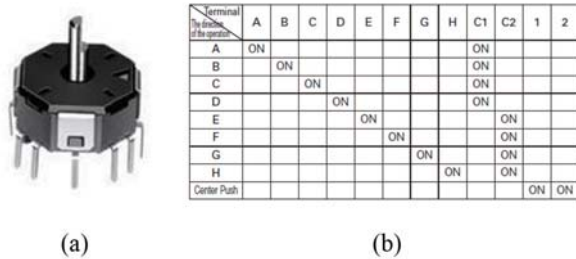


Fig. 1. (a) Multi-way switch used in the NMI. (b) Truth table for the multi-way switch [3].

D. da Vinci Research Kit (dVRK)

The dVRK system comprises one foot pedal, two master tool manipulators (MTMs), two patient side manipulators (PSMs), and one stereo viewer to provide a three-dimensional stereo view for the user. Two webcams are installed to provide images. Each MTM is able to manipulate its respective PSM during laparoscopic surgery. The developed two novel master interfaces were then attached on both of the master tool manipulators (MTMs) of the dVRK system to control the developed novel end-effector.



Fig. 2. da Vinci Research Kit (dVRK).

III. RESULTS

The MME's prediction errors were observed by 10.69 – 16.25% for three different EndoWrists.

The novel end-effector's mean gripping force (after 1,000 repetitions) at a pressure of 0.3 MPa was measured to be 5.8 N. The reaction time was found to be 0.2 s. To evaluate the system's clinical applicability, the simple peg task experiment and workspace simulation are performed with five novice volunteers using a Fundamentals of Laparoscopic Surgery (FLS) board kit.

The proposed novel master interface successfully sent bluetooth signal to the controller in real time and integrated with dVRK system.

IV. CONCLUSION

From MME, surgeons will be beneficial with the understandings of actual gripping force being

applied to tissue. This is important to prevent serious injury by maintaining a proper force to tissue.

In FLS test, all novice volunteers could complete the simple peg task within a mean time of 176 s (cut-off time: 300 s). The system's workspace was calculated to be 11,157.0 cm³. The proposed novel end-effector will be expected to be widely used.

Using the integrated system of novel end-effector, novel master interface, and dVRK system, a preliminary surgical evaluation is currently underway and it is expected that surgeons are satisfied with the continuously operable capability of the surgical robot.

ACKNOWLEDGEMENT

This work was supported by a National Research Foundation of Korea grant funded by the Korean Government (Grant Number: 2011-0012389), the Interdisciplinary Research Initiatives Program from College of Engineering and College of Medicine, Seoul National University, BK21 Plus Program through the National Research Foundation of Korea (NRF) funded by the Ministry of Education (Grant Number: 22A20130011025), and Global Ph. D. Fellowship Program through the National Research Foundation of Korea funded by the Ministry of Education (Grant 2014H1A2A1020384). The da Vinci Research Kit was donated by Intuitive Surgical, Inc. (Sunnyvale, CA, USA) in 2014.

REFERENCES

1. C. Lee, W. Park, M. Kim, S. Noh, C. Yoon, C. Lee, Y. Kim, H. Kim, H. Kim, and S. Kim, "Pneumatic Type of Laparoscopic Surgical Robot's End-effector for Surgical-Operation-By-Wire," *BioMedical Engineering OnLine*, vol. 13, pp. 1-19, 2014.
2. P. Abolmaesumi, G. Fichtinger, T. M. Peters, I. Sakuma, G. Z. Yang, "Introduction to Special Section on Surgical Robotics," *IEEE Trans. Biomed. Eng.*, vol. 60, pp. 887-891, 2013.
3. "8-directional Stick Switch (with Center-push Function) RKJXL Series", available at: <http://www.alps.com/prod/info/E/HTML/MultiControl/Switch/RKJXL/RKJXL100401V.html>

Multi/Single Port Surgical Robot System with Elbow Equipped Instruments

Un-Je Yang¹, Min-Ho Hwang¹, Hyun-Young Lee¹, Deok-Gyun Jeong¹,
Deok-You Gong¹, Dong-Ho Lee¹, and Dong-Soo Kwon¹

¹Mechanical engineering, KAIST, Daejeon, Korea

E-mail: yanguj@robot.kaist.ac.kr, leehy@robot.kaist.ac.kr, kwonds@kaist.ac.kr

Abstract— Instead of multiple incisions associated with traditional laparoscopic surgery, the SPS technique makes only one incision through the umbilicus. A compact surgical robot system for the SPS is being developed at KAIST. A surgical instrument with six degrees of freedom (D.O.F.) enables the external arm to be simpler and more compact, while satisfying the workspace constraints for SPS. Its novel elbow joint and the improved wrist joint structure also overcome technical limitations during SPS.

Keywords— Minimally invasive surgery, Robotic surgery, Laparoscopic surgery

I. INTRODUCTION

In single-port surgery (SPS), the surgical tools and laparoscope are inserted into a single incision to perform the surgery. Therefore, SPS can minimize the cosmetic procedure of surgery because it leaves few scars. SPS implementations include appendectomy, colon resection, hysterectomy, surgery on adrenal glands, and spleen resection. The SPS robot system makes a single incision into the abdominal cavity. In this paper, we propose a SPS robot system with elbowed surgical instrument.

II. MECHANICAL DESIGN

Our single-port surgical robot platform uses a direct-drive mechanism to reduce its production cost, and has a modularized robot arm that can be easily attached to the H-shaped base console. Reducing the overall size of the robot allows small hospitals to use our surgical robot platform. The design is shown in Fig. 1.

The KAIST surgical robot platform comprises of an H-shaped base console, a master system, a passive positioning arm, an active robot arm, and surgical tools appropriate for performed functions.

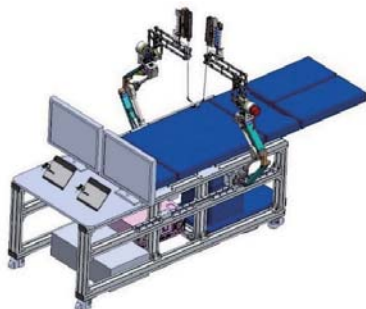


Fig. 1. 3D model of the KAIST single-port surgical robot

A. H-shaped Base Console

The H-shaped base console is an elongated cart. A surgical bed can be fixed inside of the base console. The console has long rails on either side that can set the passive positioning arm to the desired position. A computer and motor control box are located in the free space in the middle of the console. The master console and the slave console do not need to be separated, since our robotic platform integrates both the master and the slave in the base console. This greatly simplifies electrical wiring between the two consoles and reduces the space occupied by the consoles in the surgery room considerably.

B. Master System

The master system is located in the H console at the patient's head. A doctor who performs the surgery can observe patient and robot system simultaneously. The master system consists of the master device, a 3D monitor, and a foot pedal. When doctor needs to correct his posture, the foot pedal functions as a clutch system. The desirable characteristics of the master device in such an MIS system are minimal back-drive friction, low inertia, reduced backlash, and ergonomic features for the human operator [1].

An example of a specialized MIS system is the master device of the da Vinci system. The master of the da Vinci system employs ergonomic features but is comparatively bulky due to the greater length of links securing a workspace [2].

In general, haptic devices that have six D.O.F. (degrees of freedom), such as Geomagic Touch (Sensable Technologies Inc.), are used as master device to develop MIS systems. However, these devices have several problems such as small workspace (especially when scaling is considered), low intuitiveness in kinematic structures when compared with slave systems, and the absence of an ergonomic grip over motion.

We propose two types of master devices that have low inertia and a large workspace (Fig. 2).



Fig. 2. 3D model of link-type master system (left) and pen-type master system (right)



Fig 3. Commercial ball joint links (Left) [3] and 3D design of the passive positioning arm (Right)

The proposed link-type master device that was developed is based on an existing slave system that includes a 2-D.O.F. active robot arm and a 4-D.O.F. surgical tool. The master device has the same joint alignment with the movement of the surgical tool in an abdominal cavity. The wrist joints resemble those of the surgical tool. The overall mass and inertia were minimized, leading to reduced muscle fatigue for surgeons.

The proposed pen-type master device provides 6 D.O.F. commands. The 3 D.O.F. positioning of the surgical instrument's end effector is obtained by using a tablet and a vision system. The 3 D.O.F. orientation of the surgical instrument's wrist is obtained by an IMU Sensor and a vision system. The pen-type master device may provide force feedback with vibrotactile feedback.

C. Passive Positioning Arm

The passive positioning arm adjusts the position and angle of approach between the surgical instrument and the H-shaped base console. Using ball joint links, the positioning arm can be locked up at once, making this design more effective compared with other positioning arms, which generally require brakes for each joint. It was confirmed that using a counterbalance mechanism, the positioning arm can be positioned with less force. The design consists of an articulated robot arm with a parallelogram link structure and has 4 D.O.F. We used commercial ball joint links fabricated by NOGA Engineering [3]. The parallelogram structure is constructed using ball joints links. This structure causes the positioning arm to move in parallel, and as a result, the orientation of the arm is kept parallel (Fig. 3).

D. Active Robot Arm

The active robot arm provides external movement through RCM (remote center of motion) at the incision point. The active robot arm has 2 D.O.F in RCM movement (pitch: 120 degrees; roll: 180 degrees), and one translation movement like other surgical robot



Fig. 4. 3D model of the active robot arm

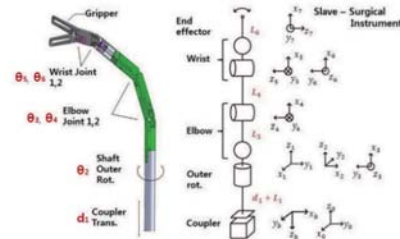


Fig. 5. Design of elbow equipped instrument

systems such as da Vinci. Motors to drive the surgical instrument tip are located on the robot arm, which removes complicated cable-driven systems. A spring is used for gravity compensation and to reduce the motor power for movements. The surgical instruments are provided with two degrees of freedom of the elbow joint. Since there is no need for a high-speed external motor, a direct coupling motor system is possible. The drive range of the robot arm is also reduced for the same reason. A 3D model of the active robot arm is shown in Fig. 4.

E. Surgical Tool

To perform SPS, triangulating with surgical instruments inside the abdominal is important. To perform triangulation, we attach the elbow joint to the instrument. With the elbow joint, not only can system makes a triangulation inside of the body, but it is also able to have larger workspace without frequently operating the active arm on which the instrument is attached.

The proposed surgical instrument has six D.O.F., grippers, a wrist, an elbow, and inner and outer rotations for humanlike surgery performance. The elbow joint on the instrument must hold its position for operating the wrist and gripper joint freely. There are two possible combinations of elbow joint: pitch, roll and pitch, yaw/yaw, pitch. The pitch, roll combination is referred to as A-type the pitch and yaw combination as B-type. An A-type prototype has already been developed and analyzed [4]. Our proposed elbowed instrument is shown in Fig. 5.

III. RESULT

Fig. 6 shows the single-port surgical robot platform that was developed.

We implemented a block transfer test. The formal block transfer test involves transferring a rubber block onto a peg that was located under the robot arm. Our system successfully carried out this test. Block transfers took 20 seconds on average.

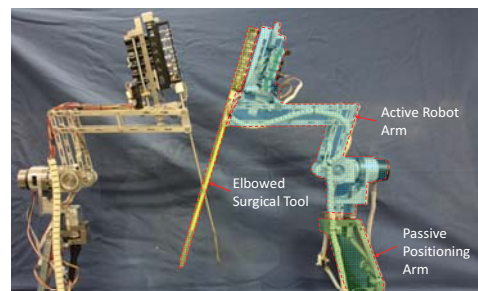


Fig. 6. Photograph of the KAIST single-port surgery robot platform



Fig. 7. Dry-Lab test of SPS robot platform: Block transfer (left), Galvanocautery test (right)

We also performed a galvanocautery test to verify the feasibility of the SPS robot platform. This test involves cutting raw meat located on the tip of the instrument with high-voltage electricity, similar to how tissues are cut during robot surgery. Electricity was charged only to the tip of the instrument, while other parts were completely insulated. Fig. 7 shows the dry-lab tests of the SPS robot platform.

IV. CONCLUSION

Advancing along recent trends in surgery, we developed SPS robot, and experimentally verified its performance. The feasibility of the SPS robot system was demonstrated in dry-lab tests. In future work, we will enhance the precision and reliability of the modules of the SPS robot system. In all, we expect a minimally invasive surgical robot with a reasonable price can be developed through continued research.

REFERENCES

1. M. Tavakoli, R. V. Patel and M. Moallem, "Design Issues in a Haptics-Based Master-Slave System for Minimally Invasive Surgery," International Conference on Robotics & Automation, Vol. 1, pp.371-376, 2004.
2. J. H. Kaouk et al., "Robotic Single-port Transumbilical Surgery in Humans: Initial Report," British Journal of Urology International, Vol. 3, pp. 366-369, 200.
3. Noga Engineering: <http://www.noga.com/>
4. Won-Ho Shin and Dong-Soo Kwon, "Surgical Robot System for Single-Port Surgery with Novel Joint Mechanism," Biomedical Engineering, Vol. 60, No4, April 2013.

Control of multi-DOF robotic arm based on 3D hand trajectories predicted from neural signals

Y. J. Kim¹, H. S. Nam², M. S. Bang^{2,3}, C. K. Chung^{2,3}, and S. Kim^{2,3,*}

¹Interdisciplinary program for bioengineering, Seoul National University, Seoul, Korea

²Seoul National University College of Medicine, Seoul, Korea

³Seoul National University Hospital, Seoul, Korea

E-mail: sungwan@snu.ac.kr

Abstract—A brain-machine interface (BMI) is expected to help people with disabilities by replacing their lost motor functions. To replace a lost arm function, development of a robot arm based on neural signal has been tried and achieved using invasive methods. In this study, 3D hand trajectories were predicted from non-invasive and less-invasive neural signals, and the 6-DOF robotic arm was controlled by using non-invasive ones. For feature extraction, electroencephalography (EEG) and magnetoencephalography (MEG) were used respectively for non-invasive neural signals. As a less-invasive neural signal, electrocorticography (ECoG) was used.

Keywords— Brain-machine interface, Robot arm, MEG, EEG, ECoG, 3D trajectory

I. INTRODUCTION

Since the BMI concept was first proposed in the 1970s, scientists and engineers have improved the technology to develop human controlled external effectors without physical movement. Recently, humans have controlled a seven-degree of freedom (DOF) robot arm based on invasive neural signal as if it were their own arm [1, 2]. Although the invasive neural signal provides high spatial resolution, it is still burdensome for patients and possibility of infection and brain tissue damage is difficult to deny. Therefore in this study, 3D hand trajectories are predicted from non-invasive and less-invasive neural signals and the trajectories from non-invasive ones are used to control multi-DOF robotic arm.

II. METHODS

A. Multi-DOF Robotic Arm

Denso robotic arm (VS-6556G, DENSO, Japan) was used for off-line control. For on-line control, it was replaced to Jaco robotic arm (JACO-3fingers, Kinova Robotics, Canada) which is widely known in rehabilitation field. Jaco robotic arm has reduced weight and size compared to Denso robotic arm.

B. Signal Processing

Band-pass filtering and multiple linear regression method are used to predict 3D hand trajectories.

C. Verification

To verify the predicted 3D hand trajectories, they were used to control Denso robotic arm in off-line, and the quantitative performances were measured.

III. RESULTS

A. EEG and MEG

First of all, 3D hand trajectories were predicted from EEG and MEG respectively (Fig. 1). The performances of predicted trajectories were measured as Terminal Point Error (TPE), Root Mean Squared Error (RMSE), and Correlation Coefficient (CC). It is demonstrated in Table 1.

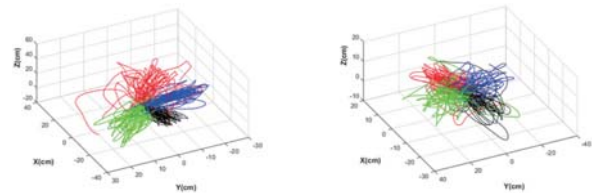


Fig. 1. Predicted trajectories (L) MEG (R) EEG [3]

Denso robotic arm was controlled by EEG and MEG respectively for off-line verification. (Fig. 2). To measure the performance, success rate for touching (Touching), and grasping (Grasping) motions are calculated as Table 1.

Table 1. Accuracy of MEG and EEG [3]

Performance	MEG	EEG
TPE	9.71 cm	11.43 cm
RMSE	11.15 cm	13.72 cm
CC	0.705	0.684
Touching	52.50%	58.75%
Grasping	18.75%	7.50%

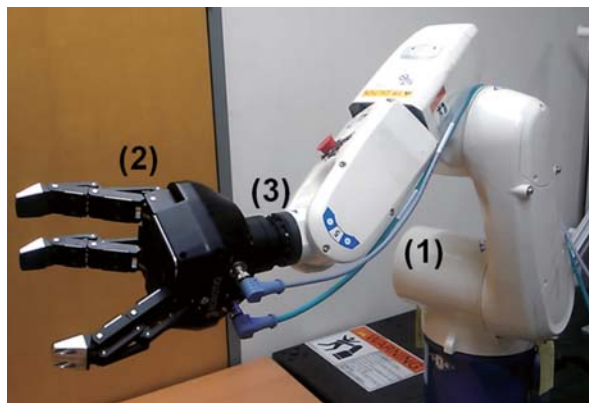


Fig. 2. (1) Denso robotic arm for off-line verification (2) Robot gripper (3) Coupling [3]

Even though Denso robotic arm has advantage that it is sufficiently fast to move as human arm, it is too bulky to be used for on-line system. Therefore, the robotic arm was replaced by Jaco robotic arm and on-line system was implemented as Fig. 3 The on-line system is not sufficiently accurate and it will be improved with additional sensors such as vision camera.

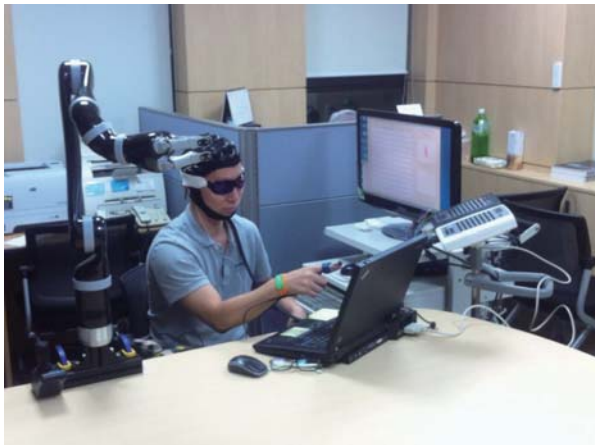


Fig. 3. Jaco robotic arm integrated with EEG system

B. ECoG

By replacing non-invasive neural signal with less-invasive neural signal such as ECoG, the performance can be highly improved. Algorithm for predicting 3D hand trajectory from ECoG is developed and applied to signal which is acquired from ECoG electrodes implanted in brain of epilepsy patients. Furthermore, Jaco robotic arm was integrated with ECoG system to implement on-line BMI system.

IV. CONCLUSION

In this study, 3D hand trajectories were predicted from EEG and MEG with a linear regression method. Furthermore, the multi-DOF robotic arm was controlled by the predicted trajectories in off-line. For most cases, the robot approached the target very closely, whereas the success rate was not quite high because the non-invasive neural signal is less accurate.

Even though the performance of implemented non-invasive BMI system is not practically applicable currently, it has potential to be better with assist of additional sensors such as vision camera.

ECoG was also used to predict 3D hand trajectory, and the BMI system to control multi-DOF robotic arm was implemented. The implemented system is not yet sufficiently verified. With additional optimization for the stability, safety, and performance, it will be applied to clinical trial.

ACKNOWLEDGEMENT

This study was supported by the following: (1) a grant (NRCTR-EX13006, NRCTR-EX15002) of the Translational Research Center for Rehabilitation Robots, Korea National Rehabilitation Center, Ministry of Health & Welfare, Korea (2) the 2012 Seoul National University Brain Fusion Program Research Grant and (3) the BK21 Plus Program through the National Research Foundation (NRF) funded by the Ministry of Education (grant numbers 22A20130011025).

REFERENCES

1. L. R. Hochberg, D. Bacher, B. Jarosiewicz, N. Y. Masse, J. D. Simeral, J. Vogel, S. Haddadin, J. Liu, S. S. Cash, P. van der Smagt *et al*, "Reach and grasp by people with tetraplegia using neutrally controlled robotic arm", *Nature*, vol. 485, pp. 372-375, 2012.
2. J. L. Collinger, B. Wodlinger, J. E. Downey, W. Wang, E. C. Tyler-Kabara, D. J. Weber, A. J. McMorland, M. Velliste, M. L. Boninger, and A. B. Schwartz, "High-performance neuroprosthetic control by an individual with tetraplegia" *The Lancet*, vol. 381, pp. 557-564, 2013.
3. Y. J. Kim, S. W. Park, H. G. Yeom, M. S. Bang, J. S. Kim, C. K. Chung, and S. Kim, "A study on a robot arm driven by three-dimensional trajectories predicted from non-invasive neural signals", *BioMedical Engineering OnLine*, vol. 14, No. 81, 2015.

A Flexible Endoscopic Surgery Robot for NOTES with its In-vivo Animal Trials

M. Hwang¹, J. Lee¹, Y. Park¹, J. Suh¹, S. Kim¹, Y. Na¹,
Y. Kim², S. Jeong², D. S. Kwon^{1*}

¹Department of Mechanical Engineering, KAIST, Daejeon, South Korea

²Department of Veterinary Medicine, Choongnam University, Daejeon, South Korea

E-mail: gkgk1215@gmail.com

Abstract—Natural Orifice Transluminal Endoscopic Surgery (NOTES) is a recently developed surgical technique through natural orifice, and thus makes no external incisions. However conventional flexible endoscope has limitations to perform NOTES – mainly not enough force and dexterity of end-effector, in-line viewing problem, non-intuitive controlling. A flexible endoscopic surgery robot has been developed to overcome these limitations. It consists of an overtube, an articulated camera, two dexterous surgical arm, navigation system, and ergonomic master console. Through preliminary tests and three times in-vivo trials, the clinical possibility of robotic NOTES has been showed.

Keywords— NOTES, Flexible Endoscopic Surgery, Snake robot, Articulated robot, Surgical Joint.

I. INTRODUCTION

Efforts to minimize invasiveness in surgery have resulted in various benefits for patient. In the context, no-scar surgery, which is called NOTES (Natural Orifice Transluminal Endoscopic Surgery), has been developed. It is performed with an endoscope passed through a natural orifice. NOTES using conventional endoscope, however, has some critical limitations including not enough force and dexterity to manipulate organ, in-line viewing, hard to access to the target organ, and lack of intuitiveness and ergonomics for controlling endoscope and instruments. [1]

Based on these requirements, we designed a multi-tasking robotic platform for NOTES. It consists of an overtube, two surgical arm, an articulated camera, navigation system, and master console. (Fig. 1)

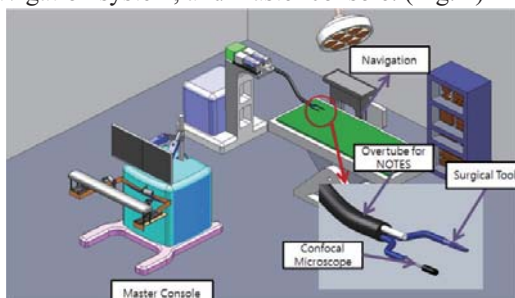


Fig. 1. Conceptual Design of Robotic NOTES Platform

Most of flexible endoscopic platforms have chosen the similar concept. They commonly have tried to put more DOFs at the tip of instrument to make dexterous manipulation. Detailed design specifications cannot be found in the literature, but it is assured that lack of force and improper orientation of camera still remain problems. (EndoSAMURAI, Anubis, MASTER)

II. METHODS

Flexible endoscopic robot platform have been prototyped. Overtube has 2 (DOF) for positioning camera and instruments. Locking mechanism enables overtube to endure up to 15(N) weight so that stable manipulation of the end effector is possible. Camera has 2 pitch joint to make off-line view. Experiments were conducted to show that task performance is remarkably reduced with in-line viewing. Surgical arm has 2 (DOF) for each, and it was measured to lift over 4(N) weight. To validate the proposed system, preliminary test was performed with tissue. Kinematic analysis, motor control and grasping and cauterizing function were successfully tested.



Fig. 2. K-NOTES: Flexible Endoscopic Robot Platform

III. RESULTS & CONCLUSION

With help of laparoscopic instruments, trans-anus NOTES cholecystectomy was successfully performed. Multi-directional traction, camera orientation, and tip functioning were also tested. Even though the robotic platform has overcome some limitations, there are still several technical difficulties to be solved. It was discovered that surgical arm could not make enough force to lift and push the organ. The trade-off relationship between force and size of instrument is still remained problems.

REFERENCES

1. D. Ratter, A. Kalloo, "ASGE/SAGES Working Group on Natural Orifice Transluminal Endoscopic Surgery", *Surgical Endoscopy*, vol. 20, pp. 329-333, 2006.

A Study on the Development of a Robot-assisted Automatic Laser Hair Removal System and its Clinical Trial Results

H. W. Lim¹, D. H. Lee², M. Cho¹, S. Park¹, W. Koh³, Y. Kim⁴, J. H. Chung²,
and *S. Kim⁵

¹Interdisciplinary Program for Bioengineering, Seoul National University College of Engineering, Seoul, Republic of Korea

²Dept. of Dermatology, Seoul National University College of Medicine, Seoul, Republic of Korea

³JMO Dermatology, Seoul, Republic of Korea

⁴Dept. of Mechanical and Aerospace Engineering, Seoul National University College of Engineering, Seoul, Republic of Korea

⁵Dept. of Biomedical Engineering, Seoul National University College of Medicine, Seoul, Republic of Korea

⁶Institute of Medical and Biological Engineering, Seoul National University, Seoul, Republic of Korea

E-mail: krnboss@snu.ac.kr

Abstract—The robot-assisted automatic laser hair removal (LHR) system is developed to automatically detect any arbitrary shape of the desired LHR treatment area and to provide uniform laser irradiation to the designated skin area. The proposed system's performance and efficacy is evaluated .

Keywords— Medical Robot, Laser Hair Removal, Selective Photothermolysis.

I. INTRODUCTION

The principle of Selective Photothermolysis involves damaging hair follicles without causing collateral damage to the surrounding tissues [1,2]. It has been more than two decades since the emergence of the medical laser device and laser hair removal has ranked top 3rd on nonsurgical procedure category and nearly 0.8 million cases were practiced in the US during 2014 [3,4]. LHR is economical, less painful to the patients, and time efficient compared with other hair removal practices such as electrolysis/thermolysis, shaving, and tweezing. However, LHR has its own drawback; the exact location of the laser is difficult to be traced. It does not leave any traces on the skin. Also the practitioner often loses focus during wide coverage treatment area such as hip, back, thighs and legs. The practitioner may mistakenly not treat of a site or overexpose one of the patient's treatment sites. Hairs on the omitted laser irradiation will continue to have normal hair growth which leads to suboptimal outcome and overexposed area may lead to unwanted results such as light erythema and overdose of laser irradiation [5]. Therefore, an adequate amount of fluence and a uniform distribution of laser treatment are crucial for safe and effective laser treatment. This study is focused on achieving a safe and effective LHR system using uniform laser irradiation and its performance has been evaluated by the following clinical trials.

II. METHODS

This study protocol was approved by the IRB of the MFDS of Korea (approval no.:474) and SNUH (IRB No. C-1303-017-470). The study was conducted in accordance with the 2008 revision of the Declaration of Helsinki.

A. Devices and Work Planning

The proposed system has a LHR device, a laser distance sensor and a web came fixed at the 6-axis robot's end-effector. The camera automatically detects any arbitrary shaped and sized target in red. After it detects the target, the robot executes the "pick and place" motion on the target's entire area. The laser is irradiated only when its laser output window (LOW) is in contact with the skin, for maximal efficacy and safety. The system's hardware is shown in Fig.1 [6]

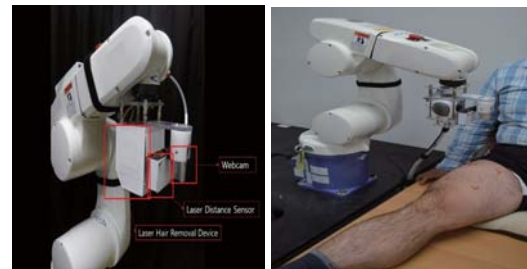


Fig.1 The system's hardware and the subject's pose

B. Subjects and Treatment

Six healthy male subjects on the age of 20 to 40 with Fitzpatrick skin types III-IV and black hair were registered in this study. Each patient made total 5 visits; 4 clinical and 1 photograph sessions. The inclusion criteria were a minimum of 35 hairs within an area of 90 x 120mm² on each thigh and an equivalent amount of hairs on both thighs. The treatment schedule and conditions used in both the automatic and physician-directed procedures were equivalent. One thigh is treated by the LHR system while the other is treated by the practitioner. The area's edge was marked in red non-toxic marker [7].

C. Result measures

The results were presented by the number of irradiations, treatment duration and hair removal rate. The photographs were taken on every subject’s visits. Each hair were counted through photograph that is within the 4 edges marked on the thighs.

$$\text{Hair Removal Rate} = \frac{\text{baseline} - 5\text{th visit}}{\text{baseline}} \times 100 \text{ (eq.1)}$$

Hair removal rate is the primary effective assessment and eq.1 shows how it was calculated.

III. RESULTS

A. Practice Time Duration and Number of Irradiation

Average from 1st to 4th visit

	LHR System		Physician	
	Duration (mm:ss)	Shots irradiated	Duration	Shots irradiated
Subj.1	18:58	266.2	3:00	66
Subj.2	18:58	248.5	3:00	70.2
Subj.3	17:24	254.2	2:54	67.7
Subj.4	19:01	269.5	3:27	81.2
Subj.5	18:50	257	3:09	65.5
Subj.6	17:53	262.5	3:37	87
Avg.	18:30	260	3:11	73
SEM	0:33	5.7	0:15	5.9

* The robot’s movement velocity was purposely slowed down to meet subject’s comfort level.

B. Hair Removal Rate

	LHR System	Physician
Subj.1	58.0	45.9
Subj.2	35.6	17.9
Subj.3	35.7	17.4
Subj.4	52.6	34.3
Subj.5	60.5	31.7
Subj.6	51.5	29.6
Avg.	49.0	29.5
SEM	9.9	9.8

All six subjects safely and successfully completed the clinical trials. No signs of long-term side effects were shown.

IV. CONCLUSION

The clinical results has shown and confirmed the effectiveness of the uniform distribution of the LHR system. The automatic LHR system nearly achieved the uniform distribution of the laser irradiation. Simple and routine tasks can be better achieve by the assistance of the robot and many medical techniques will be focused on the complementing the human vulnerabilities in near future.

ACKNOWLEDGEMENT

This work was supported in part by the BK21 Plus Program through the NRF grant (22A20130011025) and the Seoul Ocean Aquarium (No. 0411-20130059).

REFERENCES

1. R.R.Anderson, J.A. Parrish., “Selective photothermolysis: precise microsurgery by selective absorption of pulsed radiation.” *Science*. 220(4596):524-527, 1983;.
2. G. B. Altshuler, R.R. Anderson, D. Manstein, H.H Zenzie, M.Z. Smirnov. “Extended theory of selective photothermolysis.” *Lasers in surgery and medicine*. 29(5):416-432, 2001.
3. ASAPS 2014 Cosmetic Surgery National Data Bank Statistics. 2014
<http://www.surgery.org/sites/default/files/ASAPS-2014-Stats.pdf>
4. S. Noh, W. Koh, H. W. Lim, C. Yoon, Y. Kim, J.H. Chung, H.C. Kim and S. Kim, “Tool to visualize and evaluate operator proficiency in laser hair-removal treatments” *BME Online*, 13:40, 2014
5. O.A. Ibrahim, M.M Avram, C.W. Hanke , S. L. Kilmer, R.R. Anderson. “Laser hair removal.” *Dermatologic therapy*. Jan-Feb 2011;24(1):94-107
6. H. W. Lim, S. Park, S. Noh, D. H. Lee, C. Yoon, W. Koh, Y. Kim, J.H. Chung, H.C. Kim and S. Kim, “A Study on the Development of a Robot-Assisted Automatic Laser Hair Removal System”, *Photomedicine and Laser Surgery*, vol. 32, pp.633-641, 2014.
7. H. W. Lim, D. H. Lee, M. Cho, S. Park, W. Koh, Y. Kim, J.H. Chung, H.C. Kim and S. Kim, “Comparison of Efficacy Between Novel Robot-Assisted Laser Hair Removal and Physician-Directed Hair Removal”, *Photomedicine and Laser Surgery*, vol. 33, 2015

A Novel Surgical Pen-type Master Device using Vibrotactile Feedback

H. Lee¹, U. Yang¹, and D.S Kwon^{1*}

¹Department of mechanical engineering, KAIST, Daejeon, South Korea
E-mail: leehy@robot.kaist.ac.kr

Abstract—A novel pen-type master device with vibrotactile feedback for robotic minimally invasive surgery system was. To verify the feasibility of the vibrotactile feedback, a simple knot-tying task was performed. The result shows that the vibrotactile feedback helps users to maintain adequate tension limits.

Keywords— Minimally invasive surgery, Master device, Vibrotactile feedback, Suturing.

I. INTRODUCTION

Master-slave systems have been considered standardized platforms for developing a robotic assisted surgery system. Surgeons control the slave systems by manipulating the master devices. However, heavy-weight of the device, complex mechanism and lack of force-feedback have been considered as major drawbacks in designing a master device for a robotic system [1]. For the convenience of surgeons, a light-weight and user-friendly master device should be developed. In this paper, we have proposed a novel pen-type master device having vibrotactile feedback for robotic surgery systems

II. METHODS

A. Pen-type master design

The proposed pen-type master device provides 6-DoF commands. The 3-DoF end effector position of the surgical instrument is obtained by using a tablet and a vision system. The remaining 3-DoF orientation of the surgical instrument's wrist is obtained by an IMU sensor and a vision system. The proposed master device has a commercialized haptuator that provides vibrotactile feedback as shown in Fig. 1.

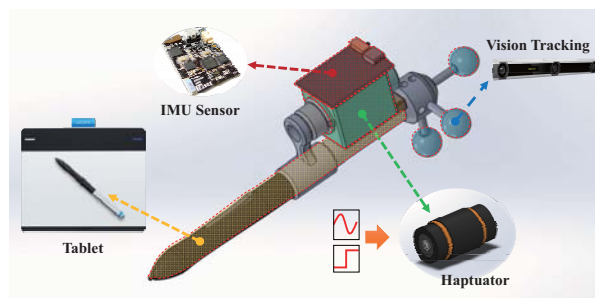


Fig. 1. Proposed pen-type master device

B. Knot-tying experiment

To verify the feasibility of the vibrotactile feedback for in suturing, we simulated the process of knot-tying. Fig. 2 shows the knot-tying simulator consists of the developed pen-type master device, and 1-DoF tension-measurement experimental equipment. 4 subjects all consist of engineering students were selected and they performed the task for 3 times. Subjects were required to maintain the suture tension near 5N for several seconds. The vibrotactile feedback was proportional to the tension of a suture, and it was transmitted to the subjects.

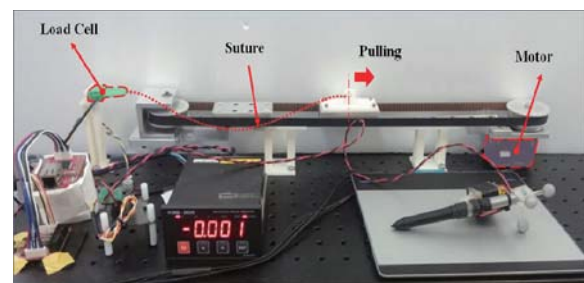


Fig. 2. Knot-tying simulator set up

III. RESULTS

Fig. 3 shows the experimental results of the suture tension with (left), and without (right) vibrotactile feedback.

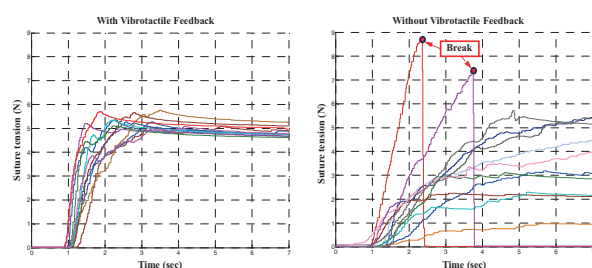


Fig. 3. Suture tension experimental results

The result shows that within 3 seconds, the suture tension attains a value close to 5N, which is considered to be adequate for suturing with vibrotactile feedback. However, in case of suturing without vibrotactile feedback, the suture tensions were not converged to adequate force ranges, and even several instances of breaking occurred.

IV. CONCLUSION

In this paper, we proposed a light-weight intuitive pen-type master device with vibrotactile feedback. The experimental result clearly shows that the vibrotactile feedback improves the performance of the suturing task while maintaining an adequate amount of tension. In our future work, a gripper module will be implemented for performing grasping motion, and a miniature disposable force sensor will be adapted on the surgical tool for force-sensing.

REFERENCES

1. O. A. J. Van der Meijden, and M. P. Schijven, "The value of haptic feedback in conventional and robot-assisted minimal invasive surgery and virtual reality training: a current review," *Surgical endoscopy*, vol. 23, no.6, pp. 1180-1190, 2009.

Support by the government for development and commercialization of domestic medical device

Huiseok Chae
KDIDI, Korea

Dongguk medical device innovation center

Sung Jae Kim
Dongguk Medical Device Innovation Center, Korea



Commercialization of new biomaterial through multi-collaborations

SungYoun Cho^{1,*}, KyeongJin Han², HyungKwang Seok³

¹ Division of L'DISQ & Biodegradable Metal, U&i Corporation, ² Department of Orthopaedic Surgery, Ajou University School of Medicine, ³Center for Biomaterials, Korea, Institute of Science & Technology

BACKGROUND: Medical device industry is very promising because it can provide the endless dream to human – longer and better life. Ten years ago, one idea called biodegradable magnesium was introduced to the company and was incubated through collaboration of academy, research institute, industry, venture capital and government supported projects. Initially the alloy was designed and evaluated for feasibility to human use. Then preliminary tests were performed based on government supported projects. Finally, preclinical and clinical study of small bone screw made of alloy was performed according to global standard to evaluate the safety and efficacy for human use in hand fracture. Preclinical study showed excellent biocompatibility of this bone screw. After confirming toxicological safety of alloy in the preclinical study, more than 50 patients showed perfect fracture healing and restoration of hand function without any device related complication in 1-year follow up.

METHODOLOGY: Alloy design and manufacturing process of biodegradable magnesium were developed by KIST (Korea Institute of Science and Technology). Intellectual properties were applied and reinforced internationally by industry, U&I corporation. Device were designed and reviewed by industry and Ajou University Hospital. Finally the small bone screw of the alloy was fabricated and determined to be commercialized first. Preclinical study including, cytotoxicity, sensitization, systemic toxicity, genotoxicity, and irritation tests were performed according to ISO 10993 standards. Then clinical protocol for human clinical study was developed to evaluate the effectiveness and safety of the biodegradable screw made of the alloy. Primary endpoint was bone union in fracture site at 6 months after surgery. PROM (Passive Range of Motion), TAM (Total Active Motion), Power, DASH (Disability of the Arm, Shoulder and Hand) scale and pain were also included in the protocol as secondary endpoint. Following this protocol, the small bone screws made of the alloy were implanted to the patient with hand fracture. All patients with 1 year follow-up were evaluated with radiography and hand function.

Result: Small bone screw made of biodegradable magnesium showed good biocompatibility according to ISO standard. All fracture in all patients has good bone union without complication such as hydrogen gas pocket, re-fracture, re-operation, malfunction, inflammation sign including fever, swelling, redness, and pain. This small screw showed normal healing process like as titanium screw. Finally this medical device was approved by Korean regulatory agency, MFDS (Ministry of Food and Drug Safety).

CONCLUSION: Small bone screw made of only human constituents were developed and commercialized through multi-collaboration. Although mechanical strength of the alloy is lower than titanium, stainless steel, and chrome cobalt alloy, small bone screw made of Mg alloy showed normal healing process. Eventually it was replaced with new bone in the long term. Therefore, this alloy is considered biocompatible and effective enough to use in human. So this device will be very attractive in the surgical industry. For this kind of success, good multi-collaboration and sustainable support like government supported project are essential to commercialization.

ACKNOWLEDGEMENTS: Seoul R&BD program, Seoul Development Institute, Republic of Korea; contract grant number: SS100008
The Korea Healthcare Technology R&D Project, Ministry of Health and Welfare, Republic of Korea; contract grant, number: A101942

의료기기 개발 및 국제공동연구 협력 사례 - (주) 한독칼로스메디칼 박을준 대표

Hypertension, or high blood pressure, is one of the most common chronic diseases today. It is a major risk factor for heart disease, stroke, congestive heart failure, and renal disease. Despite the wide spread use of antihypertensive medication, many patients are still unable to control their blood pressure—referred to as resistant hypertension. Resistant hypertension is a very serious disease with no medical treatment option.

Generalized sympathectomy in the anatomical region of the kidneys pioneered as a treatment for hypertension in the mid-20th century by a handful of physicians. The concept of renal denervation, a catheter-based minimum-invasive partial sympathectom, has been proven to be an effective medical treatment option for resistant hypertension by global medical device players like Medtronic, St. Jude Medical, Boston Scientific, and the other players.

Handok Kalos Medical, a spin-off company from Handok, has been developing her own first generation renal denervation system. By utilizing the Korea-Singapore R&D Joint Call, Handok Kalos Medical initiated the development for the 2nd and 3rd generation renal denervation system.

The speaker will introduce the Handok Kalos Medical's renal denervation system development efforts, as an example, to cover a typical medical device development cycle.

On sleep and sleep monitoring: Clinical implications

Do-Un Jeong
Seoul National University, Korea

Recent developments in automated low cost mHealth sleep analysis: from accelerometry to video

Gari. D. Clifford,
Associate Prof. of Biomedical Engineering and Informatics
Depts of Biomedical Informatics and Biomedical Engineering
Emory University & Georgia Institute of Technology
Deputy Editor, Physiological Measurement, Institute of Physics and Engineering
Honorary Professor, The Sleep & Circadian Neuroscience Institute, University of Oxford
Founding Director, Centre for Affordable Healthcare Technology, Kellogg College

As the fervor surrounding the quantified self increases, there is the danger that we are deriving meaningless metrics in a huge variety of scientifically unreproducible and (publicly) undocumented ways. Never-the-less, the IoT integration of temperature control, lighting, surveillance cameras and other household sensors, together with modern machine learning and cloud computing capacity, holds great promise for diagnostic and preventative medicine in a subject's natural environment. In this talk I will focus on sleep and address some of the potential benefits, and the dangers, together with examples of solutions which incorporate device-independent and patient-specific methods for extracting health data.

Nonintrusive approaches for sleep monitoring and analysis

Kwang Suk Park, Hwan Hwang, Da Woon Jung, and Hee Nam Yoon

Abstract—Based on the progress of information and sensor technologies, there is wide range of studies and application extending the sleep study out of hospital. Here we reviewed the nonintrusive sleep monitoring methods for estimation of sleep structure and sleep-related disorders. These methods are based on several type of sensors. First, load-cell-installed bed was applied for sleep-wake and slow-wave sleep monitoring with information extracted from movements and ballistocardiogram. Second, capacitively coupled electrodes were used for estimating sleep postures based on the morphology of QRS complex. Lastly, film type sensors were used for sleep/wake, sleep apnea, and rapid eye movement sleep monitoring based on the ballistocardiogram and respiration signal. Analytic methods estimated the 3 stages or 4 stages of sleep with high performance.

I. INTRODUCTION

The golden standard for sleep monitoring in clinics is polysomnography (PSG). PSG evaluates the sleep structure as well as sleep-related disorder. However, numerous sensors are attached to the subject's face and body for PSG recording which can interrupt comfortable sleep. Thus non-intrusive monitoring, which refers to without attaching any sensors directly on the body, is required to extend the sleep monitoring system into home environment.

II. METHODS AND RESULTS

Among the physiological signals, signals reflecting the autonomic activation are the most probable signals for nonintrusive sleep monitoring. Since cardiac activity contains the autonomic activity, sensors which can measure cardiac activity in nonintrusive way can be considered as the first candidate for this goal. Several type of sensors measure heart beats and pattern with reasonable SNR in nonintrusive setting in addition to the movement of the body and respiration.

First, body movement and ballistocardiogram (BCG) signals of the subjects were measured by a load-cell-installed bed. From the measured movement, an automatic algorithm scored each 30s epoch of the recordings for either 'wake' or 'sleep' and the mean epoch-by-epoch accuracy between the system and PSG was 95.2% [1]. From the BCG signal, heart rate variability (HRV) parameters were extracted and sleep was classified into two stages: slow-wave/non slow-wave sleep [2]. The mean epoch-by-epoch accuracy between the

proposed method and PSG was 92.5% and Cohen's kappa was 0.62. Second, electrocardiogram (ECG) signals were measured. using twelve capacitively coupled (CC) electrodes and a conductive textile sheet [3]. The features were extracted from the morphology of the QRS complex and sleep posture estimation process was conducted with support vector machine (SVM) classifier. SVM with RBF kernel had the highest performance with an accuracy of 98.4% for four sleep postures (supine, prone, left-, right- lateral) classifications.

Lastly, BCG and respiration signals were measured using the polyvinylidene fluoride (PVDF)-based sensors on a bed mattress. With BCG, heart rate and movement information were extracted to develop an algorithm for classifying sleep and wake epochs [4]. Wake epochs were detected with an average accuracy of 97.4% for normal subjects. As with respiration signals, apnea monitoring method was proposed based on the standard deviation of the PVDF signals. The apnea-hypopnea index extracted from the proposed method and PSG were highly correlated (0.94, $p < 0.001$) [5]. In addition, rapid-eye-movement (REM) sleep was estimated with the average rate and variability of respiration from PVDF signals. REM sleep were classified with an average accuracy of 88.9% [6].

III. CONCLUSION

Nonintrusive methods for sleep monitoring is very promising. Recent studies verified that these methods can be applied in home environment in sensing point of view. The subject's sleep can be monitored without interrupting their ordinal way of sleep at home for a long term period. These methods should be integrated with health information platform to develop clinically useful applications.

REFERENCES

- [1] B. H. Choi, et. al., "Non-constraining sleep/wake monitoring system using bed actigraphy," *Med. Bio. Eng. Comput.*, vol. 45, no. 1, pp. 107–114, 2007.
- [2] B. H. Choi, et. al., "Slow-wave sleep estimation on a load-cell-installed bed: a non-constrained method," *Physiol. Meas.*, vol. 30, no. 11, pp. 1163–1170, 2009.
- [3] H. J. Lee, et. al., "Estimation of Body Postures on Bed Using Unconstrained ECG Measurements," *IEEE J. Biomed. Health Inform.*, vol. 17, no. 6, pp. 985–993, 2013.
- [4] D. W. Jung, et. al., "Nocturnal Awakening and Sleep Efficiency Estimation Using Unobtrusively Measured Ballistocardiogram," *IEEE Trans. Biomed. Eng.*, vol. 61, no. 1, pp. 131–138, 2014.
- [5] S. H. Hwang, et. al., "Unconstrained Sleep Apnea Monitoring Using Polyvinylidene Fluoride Film-Based Sensor," *IEEE Trans. Biomed. Eng.*, vol. 61, no. 7, pp. 2125–2134, 2014.
- [6] S. H. Hwang, et. al., "Unconstrained REM Sleep Monitoring Using Polyvinylidene Fluoride Film-Based Sensor in the Normal and the Obstructive Sleep Apnea Patients," *J. Biomed. Eng. Res.*, vol. 35, no. 3, pp. 55–61, 2014.

K. S. Park is with the Department of Biomedical Engineering, Seoul National University, Seoul 110-799, Korea (corresponding author, phone: +82-2-2072-3135; fax: +82-26-1175; e-mail: pks@bmsil.snu.ac.kr).

S. H. Hwang, D. W. Jung, and H. N. Yoon are with the Interdisciplinary Program of Bioengineering, Graduate School, Seoul National University, Seoul 110-799, Korea (e-mail: lostzoo@bmsil.snu.ac.kr, dwjung@bmsil.snu.ac.kr, hnyoon@bmsil.snu.ac.kr)

Central Nervous System (CNS) on a Chip' – Present & Future

Department of Biomedical Engineering, Korea University, Korea
SangHoon Lee

Understanding the mechanisms of CNS functions and causes of diseases requires well defined CNS model. Animal-based CNS disease models have been popularly used as CNS model, however, these in vivo approaches have various limitations, such as high costs, low-throughput, time-consuming processes and experimental variations. Recent progress in microfluidics and microelectromechanical systems (MEMS) enables to develop in vitro CNS models mimicking the in vivo environment as similar as possible. In this presentation, diverse in vitro CNS models established on a chip will be introduced including our recently developed 2D and 3D 'Brain on a Chip' model. These models can realize various in vitro CNS disease models such as AD, PD, MS, migraine, diffuse axonal injury (DAI), neuronal migration disorders and epilepsy and BBB environment. Especially, the effect of amyloid protein to the Alzheimer's disease will be discussed using 2D and 3D brain model. Finally, the future applications and progress of 'CNS on a Chip' will be discussed.

((Reference))

1. Y.Y. Yi et al., "Central Nervous System and its Disease Models on a Chip", Trends in Biotechnology , in press
2. Y.J. Choi, et al., "Neurotoxic amyloid beta oligomeric gradient assemblies recreated in microfluidic platform with interstitial level of slow flow", Sci Rep., 3:1921, 2013..

Building Biological Neural Networks on a Chip: From axon guidance to modular networks

Yoonkey Nam

Department of Bio and Brain Engineering, KAIST, Korea

Well-defined neuronal networks in vitro can be a useful model for the investigation of neural information processing in the brain. Constructing a defined neuronal network requires the manipulation of live neurons in multi-scales ranging from submicron to millimeter. In this talk, I will present recent studies on the application of microtechnology to for the design of neuronal networks in a dish. Primary neurons from rat hippocampus or cortex were used as building blocks of 'biological' neural networks and electrical or optical recording methods were used to characterize physiological functions of designed neuronal networks. Three different studies were performed. First, micro-contact printing was used to investigate a single cell control based on sub-cellular micropatterns of cell-adhesive biomolecules (e.g. poly-D-lysine, laminin). Second, the neuronal adhesion of the substrate was controlled by micro-patterning 'cell-repulsive' agarose hydrogel to develop a simple and reliable method for the fabrication of micro-sized clustered neural networks composed of tens of neurons. To design various patterns of clustered neural networks composed of circular nodes of 100 μm diameter and bridges of 10 μm width, agarose hydrogel structures were molded using MIMIC (Micromolding in capillaries) on a planar-type microelectrode array (MEA). Third, modular neuronal networks composed of hundreds of neurons were designed by micro-channel devices to study the interaction between multi-compartmental neuronal networks. Cross-correlations and axonal signaling were analyzed using optical imaging or multi-channel microelectrode array recordings.

Session: Brain-on-a-Chip technology

High-density Microelectrode Array Recordings to Reveal the Origin of the Extracellular Action Potential

U. Frey, M. E. Obien

RIKEN Quantitative Biology Center, RIKEN, Kobe, Japan

Microelectrode arrays (MEAs) and microprobes have been widely utilized to measure neuronal activity, both *in vitro* and *in vivo*. The key advantage is the capability to record and stimulate neurons at multiple sites simultaneously. We introduce the ongoing advancements in MEA technology, with focus on achieving higher resolution and quality of recordings by means of monolithic integration with on-chip circuitry using complementary-metal-oxide semiconductor (CMOS) technology. Such high-density microelectrode arrays (HDMEAs) with more than 3000 electrodes per mm^2 and sensing areas of 3 mm^2 or more are a suitable tool to capture neuronal activity at various scales, such as axons, somas, dendrites, entire neurons, and networks.

Action potentials of single neurons are recorded by MEAs or neuronal probes as extracellular action potentials (EAPs). The exact origin and the biophysics behind such EAPs have been the focus of many previous studies and modeling efforts. HDMEAs are an ideal tool to significantly increase the spatial measurement resolution of EAPs and to refine our understanding of the origin of EAPs. Moving to the network scale, the signal of an assembly of neurons is recorded as local field potentials (LFPs) with HDMEAs. HDMEAs can capture LFPs both at high resolution and over a large area, simultaneously recording EAPs too. Combining our refined understanding of single neuron EAPs together with LFP recordings, we are striving to contribute to a better understanding of the underlying mechanisms contributing to LFP signals.

Here we show a set of recording and analysis targeting these goals. We start by studying the potentials recorded by an HDMEA from a point current source. We measure the potentials from a glass pipette stimulated with a current sine/square wave in a homogenous medium and in an acute brain slice. Next, we record the EAP of a single Purkinje cell in cerebellar slice. And finally, we record LFPs of an acute cortical slice with the HDMEA.

From these experiments, we find that the spatial distribution and amplitude of HDMEA-recorded potentials are affected by the details and boundaries of the volume conductor (e.g. HDMEA surface, thickness of the brain slice, saline, etc.). For single neuron recordings, we are able to identify the origin of highest EAP amplitudes at subcellular resolution. For network recordings, we are able to map local connectivity between Layers 2/3 and 5. Together, these results show that HDMEAs can capture neuronal and network dynamics needed to study brain function.

Pulse Diagnosis System and Pulse Simulator

Jaek U. Kim, Young-Min Kim, Young Ju Jeon, and Jong Yeol Kim

KM Fundamental Research Division, Korea Institute of Oriental Medicine, Daejeon, Korea
E-mail: jaeukkim@kiom.re.kr

Abstract—Pulse diagnosis is an important diagnostic modality in traditional medicine and it attracts attention for the possibility of applications for smart healthcare system especially in connection with smart band or smart watch. At the Korea Institute of Oriental Medicine and its collaboration institutes, we initiated a project to modernize the pulse diagnosis and to transform the pulse diagnostic techniques towards futuristic medicine. In this special session, we introduce our effort to modernize the pulse diagnosis, with focus on the development of the pulse diagnosis system, pulse simulator and hemodynamic study.

Keywords— Pulse diagnosis, Pulse simulator, Hemodynamics.

I. Introduction

Pulse diagnosis has long been an important diagnostic modality in traditional east Asian medicine including traditional Korean medicine and traditional Chinese medicine. With the advance of medical engineering technology, there have been ceaseless efforts to develop pulse diagnostic devices in Korea, China, Taiwan, Singapore, and Russia [1,2]. In Korea, the first modern pulse diagnostic device was developed by B. K. Lee in 1960s, based on a piezoelectric sensor and a strap for fixing the sensor on palpation location [2]. With some improvements on sensor and robot technology, currently, a new generation pulse diagnostic device named 3-D MAC (Daeyomedi Co., Korea) is on the market; an array-type sensor in which 5 unit sensors are arrayed in cross within a fingertip size is controlled with three degrees of freedom by an automated sensing algorithm [2].

Despite the technical advancements of modern pulse diagnostic devices including 3-D MAC, the pulse diagnostic devices are not popularly used in clinics. The primary reason is that they are lack of reliability and reproducibility of the pulse measurement. Secondly, the diagnostic contents are not attractive enough or cost-effective for clinical use [3-4]. To challenge these obstacles for the modernization of pulse diagnosis and to find novel clinical applicability of traditional pulse diagnostics, the Korea Institute of Oriental Medicine (KIOM) initiated a new development project.

II. Project Schema

The KIOM project to modernize the pulse diagnosis is initiated in 2014 with the title “Development of pulse analysis system for personalized medicine by converging hemodynamics and pulse diagnostics”. The project is composed of four parts; (a) Part I : fundamental research based on hemodynamics and physiopathology, (b) Part II : the development of pulse diagnostic system based on sensor and engineering technology, (c) Part III : the development of pulse diagnostic contents based on clinical study, and (d) Part IV : the development of pulse simulator.

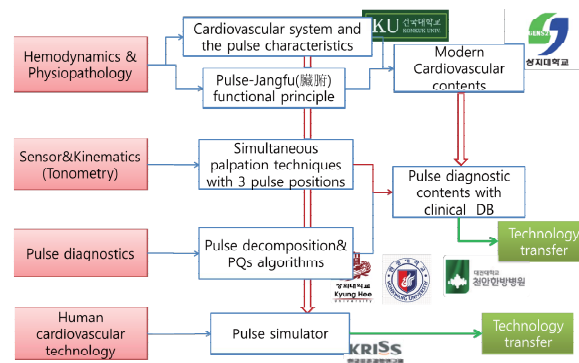


Fig. 1. Development strategy for a next generation pulse diagnostic device and pulse simulator

The development of pulse simulator (Part IV) is in collaboration with the Korea Research Institute of Standards and Science (KRISS). Konkuk University and Sanji University are in collaboration for the hemodynamic study. To design and conduct clinical studies, Hospitals of Korean Medicine such as Kyung Hee University Hospital, Wonkwang University Hospital, and Daejeon University Hospital joined as our partners.

III. Conclusion

Modernization of pulse diagnosis is a key aspect for successfully transforming the traditional Korean medicine into contemporary and futuristic healthcare system. In this special session, we introduce the project of the development of pulse diagnostic system and pulse simulator conducted by the KIOM and its collaboration institutes.

ACKNOWLEDGEMENT

This work was supported by the "Development of pulse analysis system for personalized medicine by converging hemodynamics and pulse diagnostics" (K15020) funded by Korea Institute of Oriental Medicine.

REFERENCES

1. Z. F. Fei, *Contemporary Sphygmology in Traditional Chinese Medicine*, Beijing, China, People's Medical Publishing House, 2003.
2. K. C. Kim and H. J. Kang, *Study Methodology of Pulse Engineering*, Ansan, Korea, Pulse Engineering Study Group, 2008.
3. Y. J. Lee, J. Lee, and J. Y. Kim, "Suggestion on an innovative pulse diagnosis system based on technical trend analysis," *Korean Journal of Oriental Physiology & Pathology*, vol. 23, pp. 174-179, 2009.
4. J. Y. Kim, K. Y. Kim, and K. D. Ko, "A study on the problems and the method for improvement of pulse analyzers," *The Journal of the Korea Institute of Oriental Medical Diagnostics*, vol. 3, pp. 28-36, 1999.

Hemodynamic study of pulse wave with cardiovascular simulator

J. Y. Lee¹, M. Jang¹, S.Y. Seo², M.W. Lee³, and S. H. Shin³

¹ Department of East-West Medical Engineering, Sangji University, Wonju 220-702, Korea

² College of Oriental Medicine, Sangji University, Wonju 220-702, Korea

³ Department of Oriental Biomedical Engineering, Sangji University, Wonju 220-702, Korea

E-mail: shshin@sangji.ac.kr

Abstract—The purpose of this study was to develop a cardiovascular simulator for pulse diagnosis. The vessel part was made of bifurcating silicon model with similar human stiffness and arterial tree structure. The pressure generation part consisted of piston-cylinder system. To assess the performance of the simulator, clinical data was compared with measured pressure waves and input impedance of the ascending aorta. The result showed a good agreement with the physiological characteristics of the arterial system.

Keywords — Cardiovascular simulator, arterial tree, elastic tube

I. INTRODUCTION

Most cardiovascular studies have been conducted through clinical trials. However, gathering subjects of interest and studying *in vivo* can be extremely challenging for its cost and physiological reasons. A simulator replicating the physical phenomenon of actual arterial system allows us to study cardiovascular mechanisms in a fast and accurate manner at a reasonable cost. The purpose of this study was to develop a simulator that recreates hemodynamic properties matching those of clinical data: blood pressure and blood flow characteristics.

II. MATERIALS AND METHODS

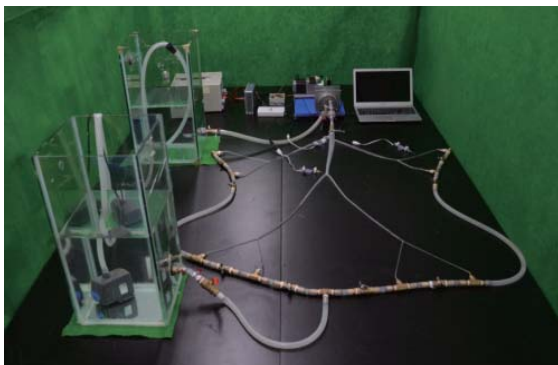


Figure 1. Cardiovascular simulator

A. Experimental set-up

The simulator has three parts; the heart, the vessel and the working fluid. The heart produces a pulsatile flow, and is composed of a reservoir, two check valves, and pressure-generating part. The vessel part was consisted of a well-defined large conduit arteries in systematic circulation, and the dimensions identical to Avolio (1). The working fluid, 63%-37% water-glycerin mixture, was used to represent the viscosity of the blood (2).

B. Input data selection

In this study, heart rate was set as 60 bpm, systole-diastole ratio as 1:2, and stroke volume as 40 ml/s. Peripheral resistance was controlled by the flow control valves at each end of the vessel tube.

III. RESULTS

A. Blood pressure waveform according to position

Figure 2 shows the measured pressure waves in the three points.

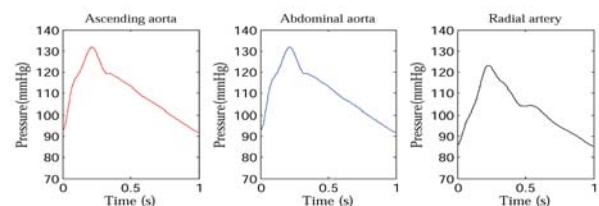


Figure 2. Pressure waveform according to the position of the mock arterial branch. (a) Pressure waveform in the ascending aorta, (b) abdominal aorta, and (c) radial artery.

B. Aortic input impedance

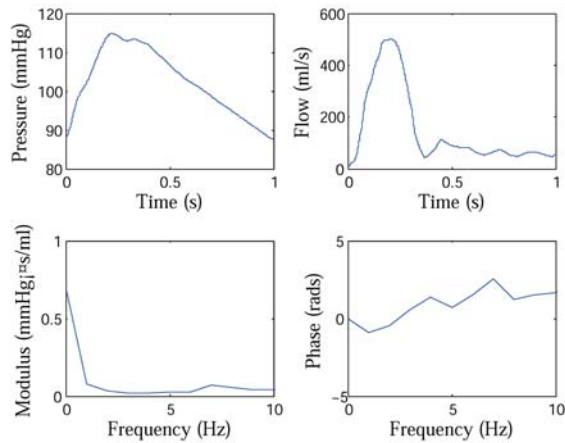


Figure 3. Input impedance. (a) Pressure waveform at the ascending aorta and (b) flow waveform. (c and d) Input impedance modulus (above) and phase (below).

Figure 3 shows the input impedance of the ascending aorta. Input impedance was rapidly decreased until 1 Hz, and was 0.69 mmHg × s/ml at 0 Hz. The first minimum frequency of input impedance was 3 Hz. The characteristic impedance was 0.036 mmHg × s/ml, which is the average of input impedance values larger than 2 Hz(3).

IV. CONCLUSION

A cardiovascular simulator with the elastic arterial branch configuration was developed in this study. The pressure and flow generated with simulator were measured and the analyzed against the clinical data. The results showed the ability of the simulator to produce physiological characteristics of human arterial system.

REFERENCES

1. A. P. Avolio, "Multi-branched model of the human arterial system," *Med Bio Eng Comput.*, vol. 18, pp.709-718, 1980.
2. D. Legendre, J. Fonseca, A. Andrade et al, "Mock circulatory system for the evaluation of left ventricular assist devices, endoluminal prostheses, and vascular diseases," *Artif Organs.*, vol. 32, pp.461-467, 2008.
3. W. W. Nichols, C. R. Conti, W. E. Walker and W. R. Milnor, "Input impedance of the systemic circulation in man," *Circ Res.*, vol. 40, pp.451-458, 1977.

Modeling of the anatomically accurate arterial tree in the human upper extremity from MRI data for the numerical hemodynamic study

Keewon Kim¹, Young Sun Jeon¹, Jaek. U. Kim², Sung Kyun Kim^{1†}

¹ Dept. of Mechanical Engineering, Konkuk Univ.

² Korea Institute of Oriental Medicine

E-mail: sungkim@konkuk.ac.kr

Abstract—To investigate blood flows in the arterial tree of human upper extremity, a three dimensional computer model (from brachial to digital arteries) was created from MRI data. A computational fluid dynamic method was employed to investigate blood flow velocity, pressure and wall shear stress (WSS) on this complicated arterial system.

Keywords— Upper Extremity, Arterial Tree Model, MRI, Hemodynamics, CFD

I. INTRODUCTION

Investigations on the blood flow in the upper extremity arterial tree had been rare performed. We created a three dimensional model of arterial tree in a Korean adult's left hand (from brachial to digital arteries) from magnetic resonance imaging (MRI) data, for the first time. By using commercial CFD software, the blood flows in the model were investigated. Special attention was paid to the flow near branches (radial and deep-palmar-arch arteries, ulnar and superficial-palmar-arch artery).

II. METHODS

A. Creation of arterial tree model

The building of anatomically accurate 3D computer model is indispensable in successful numerical simulation of flow in complicated arterial system. With our long experiences in creating human upper airway

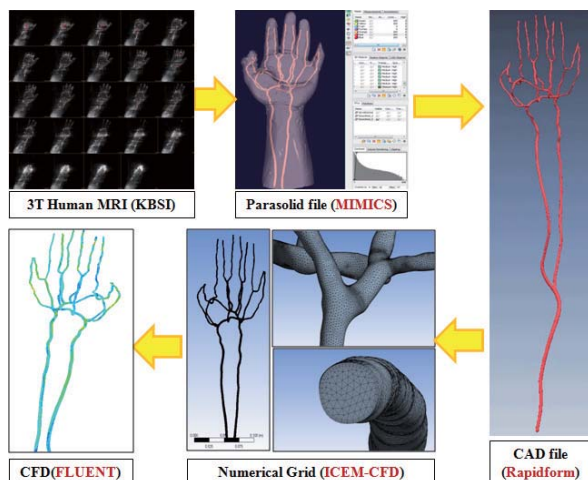


Fig. 1. Creation of 3D upper-extremity arterial tree model and numerical grid system from MRA images

models[1-2], a 3D model of arterial tree, larger than about 1 mm, was created from 3T MRI data (Fig.1.)

B. Numerical simulation

Continuity and Navier–Stokes equations for laminar incompressible flow with a density of plasma were solved numerically. Physiological blood pressure data³ at brachial artery was used as inlet boundary condition, as shown in Fig.2. Approximately 2 million (periodic flow) and 4 million (steady flow case) unstructured tetrahedral elements with five-layer prismatic-elements were created in the models

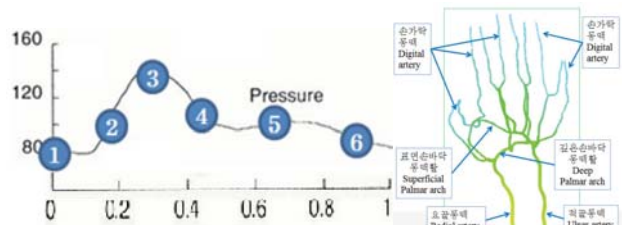


Fig. 2. Physiological Blood Pressure at Brachial artery during a cycle and main branches at hand

III. RESULTS

First, CFD results of steady systole flow (Newtonian Fluid) were given in Fig. 3. Flow allocation from radial and ulnar artery to each digital artery was different. Characteristics of blood flow in 2 major branches were considered as depicted in Fig.4.

For the periodic flow cases, Velocity distributions in arterial tree (Fig.4) and digital arteries (Fig.5) during a cycle were obtained. Since compliance of arterial wall was not considered, there existed no phase changes for brachial to digital arteries.

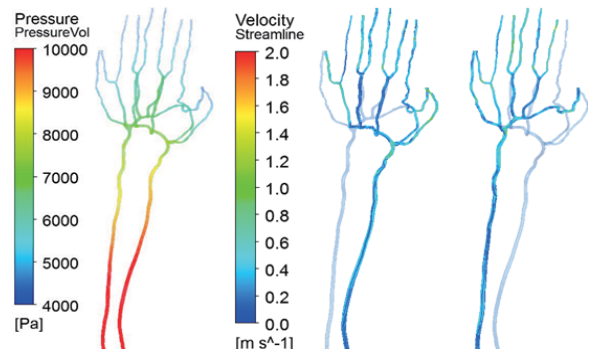


Fig. 3. Pressure Variation and Streamlines from Radial artery

and Ulnar artery: Steady flow

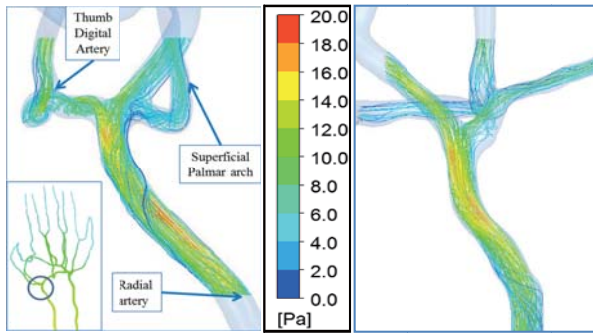


Fig. 4. Streamline and velocity profile at branch of palmar arches and radial (left), ulnar (right) artery

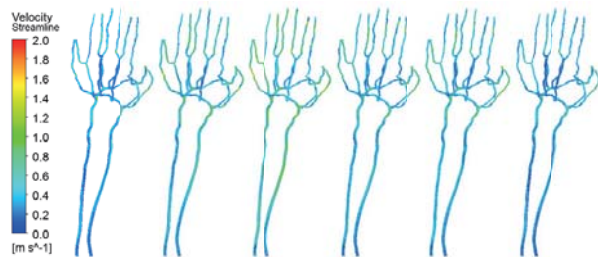


Fig. 5. Streamlines and velocity distributions during a period: time interval = 0.2 second

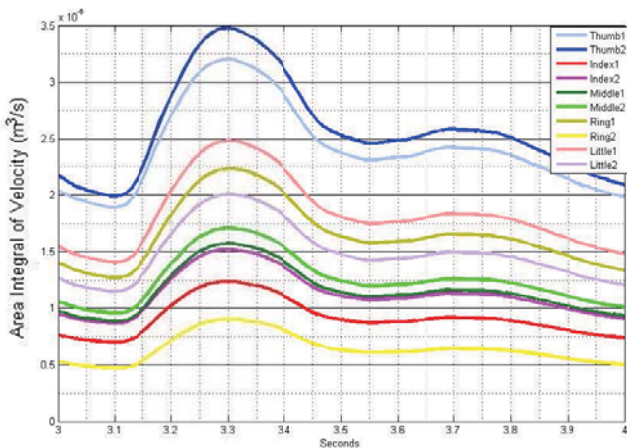
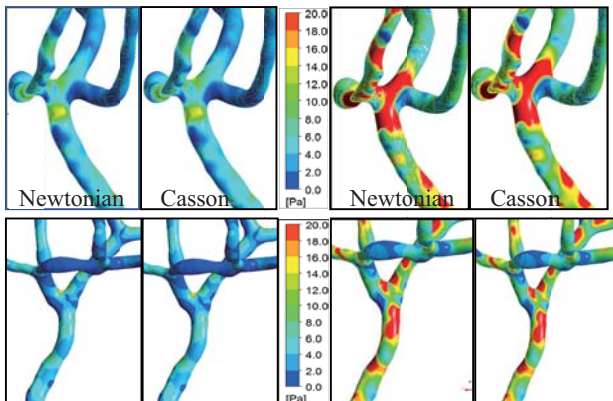


Fig. 6. Velocity profile at finger tips during 1 period



(a) Diastole ($P_1 = 80$ mmHg) (b) Systole ($P_1 = 120$ mmHg)

Fig. 7. Wall shear stress distributions at branches near radial (up), ulnar (down) artery: Newtonian and Casson models

Special cares on vessel wall shear distributions were paid. Low WSS (<0.4 Pa) regions, where there existed the potential occurrence of **Atherosclerosis** [4], were shown for the cases of steady flows with systole and diastole pressures at inlet (Fig.5). Low WSS regions were expanded in the diastole phase. There existed no big difference (less than 5%) in the low WSS region between results with Newtonian and non-Newtonian (Casson model) fluid models, except for the case of systole phase in ulnar artery branch (12%).

IV. CONCLUSION

Numerical simulation of blood flow in the arterial tree of Korean adult's upper extremity was conducted, for the first time. For this study, an anatomically realistic arterial tree model was created from MRA data. Steady and periodic flows in the model with Newtonian and non-Newtonian fluid were explored.

This work will be the first step on the hemodynamic research on the haptic diagnosis of the oriental medicine.

ACKNOWLEDGEMENT

This work was supported by the Korean Institute of oriental medicine (Grand No. K15021).

REFERENCES

1. S.K. chung, Y. on, S. Shin, S.K. Kim, "Nasal airflow during respiratory cycle," Am. J. Rhinol. 20, 379-384, 2006.
2. S.K. Kim, N. Yang, J. Kim b, S. Chung, "Patient specific CFD models of nasal airflow: Overview of methods and challenges," Journal of Biomechanics 46 (2013) 299-306, 2013.
3. Y. C. Fung, "Biomechanics : Circulation," Springer, New York, pp. 108-205, 1997
4. K.R. Kensey, Y.I. Cho, "The origin of atherosclerosis," EPP Medica, pp. 43-55, 2001.

Performance Evaluation of a New Radial Pulsation Simulator

Tae-Heon Yang¹, Young-Min Kim², and Sam-Yong Woo¹

¹Center for Mass and Related Quantities, KRISS, Daejeon, Republic of Korea

²KM Fundamental Research Division, KIOM, Daejeon, Republic of Korea

E-mail: sywoo@kriss.re.kr

Abstract—The importance of measuring and simulating a radial pulsation is steadily increased in medical science area, because the radial pulsation is a surrogate maker to estimate a central aortic pressure waveform which is clinically imperative for predicting cardiovascular diseases. Due to technical limits, mathematical relationship between the central and radial pressures has not been reliably demonstrated. Hence, we developed a new radial pulsation simulator prototype similar to a human cardiovascular system. The proposed radial pulsation simulator consists of a ventricular part, an atrial part, an aorta part and a radial arterial part. The central and radial pressure waveforms measured by built-in pressure sensors show similar waveforms with a human's pressure. The developed radial pulsation simulator could replicate pressure waves similar to those of the human body. The results show that the developed simulator has potentials to create both the central and radial pressure waveform, simultaneously in further works. It implies the simulator can be applied to validate the generalized transfer function between the central and radial pressures.

Keywords—Radial pulsation, Pulsatile blood pressure, Cardiovascular simulation, Mock circulatory system

I. INTRODUCTION

There have been researches to develop cardiovascular simulators used for in-vitro tests of artificial organs [1-3]. The mock circulatory simulator is useful to evaluate the performances of heart assist devices [4-5]. Recently, the significance of investigating a radial pulsation waveform is steadily increased in the medical fields, because the radial pulsation is an important indicator for estimating a central aortic pressure waveform [6]. To presume the central aortic pressure waveform by using measured radial pulsation waveform, mathematical relationship between the central and radial pressures should be clinically evaluated. However, the clinical test to define generalized function requires huge efforts. Hence, the human-like cardiovascular simulator which generates both aortic and radial pressure waveforms is required. The purpose of this study is to demonstrate potentials for replicating both central and radial pressure waveforms in the simulator prototype. The radial pulsation simulator prototype was developed consisting of a ventricular part, an atrial part, an aorta part and a radial arterial part. The developed simulator was

evaluated using built-in precision pressure sensors. The measured results show that the developed simulator has potentials to replicate human pressure waveforms representing cardiovascular diseases.

II. MATERIALS AND METHODS

In order to validate relationship between radial pulsatile wave and central aortic wave in the system, we construct a new circulatory system including a ventricular part, an atrial part, an aorta part and a radial artery part as described in Fig. 1. Fig. 1(a) shows an acrylic piston and cylinder with inflow/outflow check valves of the ventricle. Fig. 1(b) illustrates a high-speed stepping motor with a linear ball screw to linearly actuate the piston. Fig. 1(c) is a compliant silicone aorta with a vascular resistance valve. The silicone aorta is connected to the outflow check valve of the ventricular cylinder. Fig. 1(d) shows a silicone radial artery bifurcated from the aorta. The fluid flows into the radial artery and the reservoir from the aorta (Fig. 1(e)). A precision pressure transducer connected to the silicone vessel for monitoring radial pressure waveform. Fig. 1(f) is a pressure control unit including an air cylinder and a linear actuating module for pressurizing the fluid in the reservoir. The pressurization causes to regulate the reference level of aortic and radial pressure wave in the system. When the stepping motor pushes the piston forward, the ventricle infuses the fluid to the silicone aorta. The resulting forward propagated wave encountered the inherent fluid in the bifurcation of the arteries. The reflected wave in the bifurcation propagated backward, and it created pressure augmentation. The generated central pressure waveform with an augmented shoulder is transmitted to the radial artery.

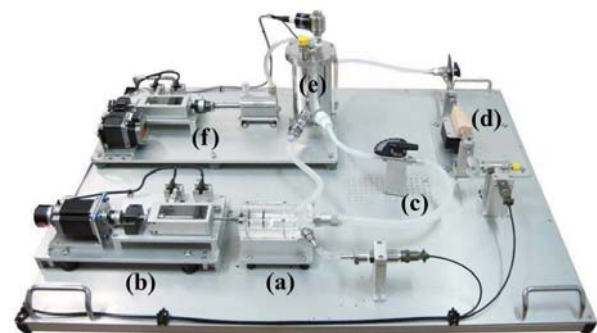


Fig. 1. A new circulatory system consisting of (a) ventricular cylinder and piston, (b) a ventricular linear actuating element, (c) a silicone aorta, (d) a silicone radial artery with a pressure

transducer, (e) an atrial reservoir, and (f) an atrial pressure control element.

III. RESULTS AND DISCUSSIONS

Radial pressure waveform was measured using the radial pressure transducer. Fig. 2 shows the measured pressure waveform. As the control signal is applied to the stepping motor of the ventricular system, the stepping motor pushes the piston forward, and the cylinder infuses the fluid to the silicone aorta through the outflow check valve. The forward transmitted wave (Fig. 2(a)) is reflected at the bifurcation of the arteries. The reflected wave transmitted backward, and it is reflected again at the backside of the outflow check valve. The second reflected wave creates a dicrotic notch in pressure wave (Fig. 2(b)). The third reflection is occurred by the peripheral resistance (Fig. 2(c)). The difference between the maximum and the lowest radial pressure is around 40mmHg similar human's radial blood pressure range. From the measurement results, we conclude that the developed simulator can demonstrate the reflecting phenomenon of the human vessel in human's blood pressure range. However, there is still limitation. Since human's radial pressure ranges from 80 mmHg to 120 mmHg, the reference pressure of the generated radial waveform needs to be shifted to replicate human's radial pressure waveform for further studies.

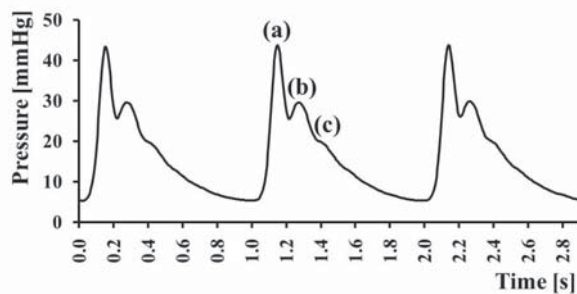


Fig. 2. Measured radial pulsation pressure waveform: (a) forward transmitted pressure wave, (b) pressure wave reflected by an outflow check valve and (b) pressure wave reflected by the peripheral resistance

IV. CONCLUSION

The radial pulsation is an alternate indicator to evaluate a central aortic pressure waveform which is clinically important for foreseeing cardiovascular diseases. We are developing the radial pulsation simulator which the central and radial pressure waveforms are able to simultaneously demonstrate. We constructed a new radial pulsation prototype consisting of a ventricular part, an atrial part, an aorta part and a radial artery part. The central and radial pressure waveforms measured by built-in pressure sensors to demonstrate similar waveforms with a real human's pressure wave. The developed radial pulsation simulator currently shows a potential to generate radial

pressure waveforms similar to those of human. The result shows that the developed simulator has possibilities to create both central and radial pressure waveforms representing cardiovascular diseases, and it further implies the simulator can be applied to validate the generalized transfer function between the central and radial pressures.

ACKNOWLEDGEMENT

This work was supported by the "Development of pulse analysis system for personalized medicine by converging hemodynamics and pulse diagnostics" (K15020) funded by Korea Institute of Oriental Medicine.

REFERENCES

1. J.-Y. Lee, M. Jang and S.-H. Shin, "Mock circulatory system with a silicon tube for the study of pulse waves in an arterial system", *J. Korean Physical Society* 65(7) (2014) pp. 1134~1141
2. D. Legendre, J. Fonseca, A. Andrade, J. F. Biscegli, R. Manrique, D. Guerrino, A. K. Prakasan, J. P. Ortiz, and J. C. Lucchi, "Mock circulatory system for the evaluation of left ventricular assist devices, endoluminal prostheses, and vascular diseases", *Artificial Organs* 32(6) (2008) pp. 461-467
3. R. Zannoli, I. Corazza, and A. Branzi, "Mechanical simulator of the cardiovascular system", *Physica Medica*. 25 (2009) pp. 94-100
4. Y. Yokoyama, O. Kawaguchi, T. Shinshi, U. Steinseifer and S. Takatani, "A new pulse duplicator with a passive fill ventricle for analysis of cardiac dynamics", *J. Artificial Organs* 13(4) (2010) pp.189-196
5. J. Brum, D. Bia, N. Benech, G. Balay, R. Armentano and C. Negreira, "Set up of a cardiovascular simulator: application to the evaluation of the dynamical behavior of atheroma plaques in human arteries", *Phys. Procedia*. 3(1) (2010) pp. 1095-1101
6. M. R. Nelson, J. Stepanek, M. Cevette, M. Covalciuc, R. T. Hurst, and A. J. Tajik, "Noninvasive measurement of central vascular pressures with arterial tonometry: clinical revival of the pulse pressure waveform?", *Mayo Clin. Proc.* 85(5) (2010) pp.460-472

Institute of yonsei biomedical engineering and biomedical industry in Korea

Young Ro Yoon
Yonsei University, Korea

Dielectrophoretic Tweezers and Its' biological Application

Sang Woo Lee*

Department of Biomedical Engineering, Yonsei University, Wonju, Korea

*E-mail: yusuklee@yonsei.ac.kr

Dielectrophoretic (DEP) tweezers¹⁻⁴ that has been originally developed by my research group enables the simultaneous manipulation of lots probes as applying a wide range of loading rate in a given environment. This tool can also measure rupture events consisted by different intermolecular interactions. This advantage allows DEP tweezers to implement a novel force spectroscopy or a new type of cell property analyzer. In this talk, I present the operating mechanism of DEP tweezers for the implementation of both methods. Moreover, I also introduce biological applications that my lab have been doing using DEP tweezers

References

- [1] S. W. Lee et. al., Applied Physics Letters, **90**, 22391, (2007)
- [2] S. W. Lee et. al., Analytical Chemistry, **81**, 7737-7742, (2009)
- [3] S. W. Lee et. al., ACS Nano, **6**, 8665-8573, (2012)
- [4] S. W. Lee et. al., Analytical Chemistry, **87**, 5914-5920, (2015).

Keywords: dielectrophoresis tweezers, force spectroscopy, intermolecular weak binding interactions, energy landscape, cellular response

Development of nanoparticles for cancer theranostics

Jaehong Key
Yonsei University, Korea

Ultrasound mediated drug delivery: Sonoporation

G. Song, O. Cha, and J. Seo

Department of Biomedical Engineering, College of Health Sciences, Yonsei University, Wonju, Republic of Korea

ABSTRACT

Sonoporation indicates ultrasound mediated drug delivery into cell membrane. Considering precise focus control with ultrasound transducer, spatially targeted drug delivery can be implemented by adapting 2D phased array transducer in sonoporation. The main mechanism of sonoporation is cavitation of microbubbles near by biological barrier such as cell membrane, endothelial barrier, and blood brain barrier (BBB). In this introductory presentation, we will discuss stable and inertia cavitation of microbubbles located closely to biological barriers and their effects on barrier function. Engineered microbubbles, which are cavitation seed and can also be carrier of various pharmaceutical molecules including cancer medicine, gene, and radio-nucleotide for imaging, will be covered in depth. As an example of sonoporation applications, Adenine nucleotide translocase-2 (ANT2) shRNA-based RNA interference (RNAi), which has been researched as a potential pharmaceuticals to hormone dependent cancer such as breast cancer and ovarian cancer, was delivered to xenocraft mouse model using sonoporation. The results indicates that significant tumor regression (* $p < 0.05$) as well as an increased survival rate by sonoporation with ANT2 shRNA. In addition, we confirmed that there was no toxicity on aspartate aminotransferase (ALT) and alanine aminotransferase (AST) levels at liver and albumin (ALB), blood urea nitrogen (BUN), or creatine kinase (CRE) levels at kidney following the gene delivery. Accordingly, we expect sonoporation could be a powerful and safe means for drug delivery in various diseases including cancer.

Key words: Sonoporation, Ultrasound mediated drug delivery, Microbubbles, Cavitation, Gene Delievery, ANT2 shRNA

Decoding and connectivity analysis of neural signal - application to clinical/cognitive neuroscience

Kyung Hwan Kim
Yonsei University, Korea

Introduction to biomedical optics lab at Yonsei University

Byungjo Jung
Yonsei University, Korea

Investigation of Mechanical Effects Induced by Pulsed Laser Absorption in Human Skin

J.-R. Park^{1*}, H.-S. Kim², J.-H. Jun², and S.-C. Chung²

¹Department of Photonic Engineering, Chosun University, Gwangju, Republic of Korea

²Department of Biomedical Engineering, Research Institute of Biomedical Engineering, College of Biomedical & Health Science, Konkuk University, Chungju, Republic of Korea

*E-mail: ejrpark@chosun.ac.kr

Abstract—Recent reports on evoking tactile sensations by laser-induced thermoelastic effects are reviewed. Mechanical effects induced by pulsed laser absorption in human skin are discussed from a theoretical point of view.

Keywords—Laser–tissue interactions, thermoelastic effects, photomechanical effects, pulsed laser absorption, human skin

I. INTRODUCTION

Recently, it has been reported that tactile sensations can be evoked by pulsed laser absorption in human skin via laser-induced thermoelastic effects [1,2]. With the help of physical, perceptual, and simulation investigations, haptic stimulation using pulsed laser absorption in human skin was demonstrated [1]. Moreover, the response characteristics of laser-induced tactile sensation were evaluated in detail [2]. In this study, the recent reports on laser-induced tactile sensation are reviewed briefly. Then, mechanical effects that can be induced by pulsed laser absorption in human skin are discussed in detail with emphasis on theoretical aspects.

II. METHODS

Numerical simulations, including Monte Carlo simulation of light transport and absorption in human skin, simulation of the heat-transfer equation, and simulation of the thermoelastic wave equation, are performed extensively in order to investigate the mechanical effects induced by pulsed laser absorption in human skin theoretically.

III. RESULTS

For effective generation of the laser-induced thermoelastic effects in human skin, very short and localized irradiation and absorption of a laser pulse is essential. Wavelength-dependent optical properties give rise to strongly wavelength-dependent thermal and mechanical response characteristics. The characteristic time scale of the thermal diffusion in human skin is by far larger than the stress confinement

time for laser pulses with pulse durations in the nanosecond regime. Time-scale-dependent response characteristics of human skin are presented. One-dimensional solution to the thermoelastic wave equation provides profound insight concerning the mechanical effects induced by pulsed laser absorption in human skin. Three-dimensional solution, however, is inevitable to fully understand the underlying physics. Peculiar features of the three-dimensional solution are given.

IV. CONCLUSION

In this study, thermal and mechanical responses of human skin induced by laser-induced thermoelastic effects are theoretically investigated and analyzed in detail.

ACKNOWLEDGEMENT

This research was supported by the Pioneer Research Center Program through the National Research Foundation of Korea funded by the Ministry of Science, ICT & Future Planning (Grant No. 2011-0027920).

REFERENCES

1. J.-H. Jun, J.-R. Park, S.-P. Kim, Y. M. Bae, J.-Y. Park, H.-S. Kim, S. Choi, S. J. Jung, S. H. Park, D.-I. Yeom, G.-I. Jung, J.-S. Kim, and S.-C. Chung, "Laser-induced thermoelastic effects can evoke tactile sensations," *Sci. Rep.*, vol. 5, 11016, 2015.
2. H.-S. Kim, J.-S. Kim, G.-I. Jung, J.-H. Jun, J.-R. Park, S.-P. Kim, S. Choi, S.-J. Park, M.-H. Choi, and S.-C. Chung, "Evaluation of the possibility and response characteristics of laser-induced tactile sensation," *Neurosci. Lett.*, vol. 602, pp. 68-72, 2015.

Human Responses to Tactile Sense Induced by Pulsed Laser Stimulation

Hyung-Sik Kim¹, Ji-Sun Kim¹, Jae-Hoon Jun¹, Jong-Rak Park², Sung-Phil Kim³,
Seungmoon Choi⁴, Sung-Jun Park¹, Mi-Hyun Choi¹ and Soon-Cheol Chung¹

¹Department of Biomedical Engineering, BK21+ Research Institute of Biomedical Engineering, College of Biomedical & Health Science, Konkuk University, Chungju, Republic of Korea

²Department of Photonic Engineering, Chosun University, Gwangju, Republic of Korea

³Department of Human and Systems Engineering, Ulsan National Institute of Science and Technology, Ulsan, Republic of Korea

⁴Department of Computer Science and Engineering, Pohang University of Science and Technology (POSTECH), Pohang, Gyung-sangbuk-do, Republic of Korea

E-mail: scchung@kku.ac.kr

Abstract—In this study, we investigate perceptual responses of tactile sense induced by pulsed laser stimulation. Three different energy was irradiated on the distal phalanx of the fingertip. The results of shows that laser energy could cause and control the tactility of the laser stimulation

Keywords— Tactile sense, Pulse laser, Perceptual responses.

I. INTRODUCTION

Laser is widely used in medical, military, industrial, and entertainment area because it can adjust transfer the energy to focused spots at long distances with light speed. One of the effects from the pulsed laser when it irradiated to the materials, the photomechanical effect is caused mainly in the spot area and lead a damage to the target object [1]. However, if the magnitude of the pulse energy are used below the material ablation threshold, a stress wave generated by the photomechanical effect without causing damage to the object [2]. Recently, a research is carried to induce the tactile sensation using this phenomenon [3].

To prove the fidelity of the tactile sensation technology using the laser, we examined the tactility from different three type of energies of pulsed laser with other laser parameters were fixed such as spot diameter, pulse duration and repetitive rate.

II. METHODS

Fifteen males and four female college students participated in this study. They were also confirmed to be right handed and. None of the participants were reported to have a neurological disorders. The setup used for the laser-induced tactile perception experiment is shown in Fig. 1. The laser system used was a frequency-doubled Q-switched laser with wavelength of 532 nm and 5 ns pulse width. Laser energies of 1.3 mJ, 1.6 mJ, and 1.9 mJ, were pulsed and sham stimulation also used. Every responses after laser stimulation were recorded using PC keyboard by pressing a predefined number. A contingency table was configured to categorize the responses.

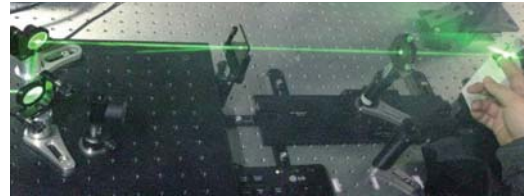


Fig. 1. Experimental setup of laser stimulation

III. RESULTS

Table 1 shows the results of the responses from the different three types of energies.

Table 1. Contingency table of laser-induced tactile sensation

	Laser irradiation	
	Yes	No
Response	349	3
	No	155
		171

From the table, accuracy, precision and sensitivity were 0.767, 0.991, and 0.692 respectively. An accuracy and sensitivity were not high, but precision were high.

IV. CONCLUSION

In the present study, we examined the human responses of laser-induced tactile sensation with three types of laser energy and confirmed that with only energy parameters could induce the tactile sensation. However, in order to enhance the response rate to be a robust tactile technology, an additional parameters such as spot diameter, pulse duration and others should be considered for further work.

ACKNOWLEDGEMENT

This work was supported by the Pioneer Research Center Program through NRF of Korea funded by the MEST (2011-0027920).

REFERENCES

1. G. Paltauf and P.E. Dyer, "Photomechanical processes and effects in ablation," *Chem Rev.*, Vol. 103, pp. 487-518, 2003.
2. J. Jiao and Z. Guo, "Thermal interaction of short-pulsed laser focused beams with skin tissues," *Phys. Med. Biol.*, Vol. 54, pp. 4225-4241, 2009.
3. J.H. Jun, J.R. Park, S.P. Kim, Y.M. Bae, J.Y. Park, S. Choi, S.H. Park, D.I. Yeom, H.S. Kim, G.I. Jung, J.S. Kim, and S.C. Chung, "Laser-induced thermoelastic effects can evoke tactile sensations," *Sci. Rep.*, Vol. 5, p. 11016, 2015.

Cortical activity patterns in response to non-nociceptive laser stimuli

S. P. Kim¹

¹Department of Human and Systems Engineering, Ulsan National Institute of Science and Technology, Ulsan, Republic of Korea
E-mail: spkim@unist.ac.kr

Abstract—Previous studies have revealed a possibility of providing a non-contact laser stimulation to evoke innocuous tactile feeling in humans. To investigate cortical responses to this stimulation, we explored human cortical activity when subjects received both nociceptive and non-nociceptive laser stimuli as well as mechanical and thermal stimuli. The analysis of the cortical activity patterns for these four stimuli showed that cortical responses to the mechanical stimulus generated the most similar pattern to that generated by the non-nociceptive laser stimulus.

Keywords— Laser, Tactile, EEG, Cortical activity

I. INTRODUCTION

Laser has been used to investigate pain mechanisms in human somatosensory system [1]. Recently, Jun *et al.* have reported a feasibility of non-painful tactile sensation by laser [2]. Subjective evaluations of tactile feelings induced by laser stimulation also indicated that laser induced non-painful tactile feelings [2-3]. However, more objective data are required to justify the existence of non-nociceptive tactile perception in humans by laser. Therefore, this study aimed to obtain objective measurements using human electroencephalographic (EEG) signals during the perception of laser stimuli as well as other tactile stimuli. A neural computational analysis method was employed to assess similarities between EEG patterns elicited by various stimuli.

II. METHODS

A. Participants

Twenty one healthy people (seven female) participated in the study. All participants provided a written consent after the study procedure was informed.

B. Stimuli

Participants received mechanical, laser, and heat stimuli in their right index fingertip while their EEG signals were recorded by a 16-channel EEG equipment. A frequency-doubled Q-switched laser was used to irradiate a single-shot pulsed laser with parameters of 532-nm wavelength, 5-ns pulse width, 0.48 mm spot diameter, and 1.90 mJ, being kept under the maximum permissible exposure level [3]. The mechanical

stimulus was provided using a stick to press the fingertip lightly for 0.1 s. Heat was delivered to the fingertip skin based on cylindrical coils with electric currents. We divided the laser experimental data into nociceptive and non-nociceptive epochs based on the subjects' responses [2].

Spatio-temporal patterns of EEG spectral power over sensorimotor cortex were analyzed. Similarity between two EEG patterns was measured by examining how difficult it was to discriminate between them.

III. RESULTS

The EEG patterns generated by non-nociceptive laser stimulation was the most similar to those generated by mechanical stimulation. The EEG patterns between non-nociceptive laser and nociceptive laser or between non-nociceptive laser and thermal stimuli showed less similarities.

IV. CONCLUSION

Computational analysis of the cortical activity patterns based on EEG in response to laser stimulation showed that EEG patterns elicited by non-nociceptive laser was more similar to those by mechanical stimulation than those by nociceptive laser. It suggests that non-nociceptive laser stimulation might evoke tactile senses close to mechanical tactile perception. Further investigation on neurophysiological responses in the somatosensory afferents to laser may be required to justify our findings.

ACKNOWLEDGEMENT

This work was supported by the Pioneer Research Center Program through NRF of Korea funded by the MEST (2011-0027920).

REFERENCES

1. T.T. Raij, N. Forss, A. Stancak and R. Hari "Modulation of motor-cortex oscillatory activity by painful Delta-and C-fiber stimuli," *Neuroimage*, vol. 23, pp. 569-573, 2004.
2. J.H. Jun *et al.*, "Laser-induced thermoelastic effects can evoke tactile sensation," *Scientific Report.*, 5, p. 11016, 2015.
3. H.S. Kim *et al.*, "Evaluation of the possibility and response characteristics of laser-induced tactile sensation," *Neuroscience Letters*, Vol.602, pp.68-72, 2015.

Physical Analysis of Indirect Laser Radiation for Mid-air Tactile Stimulation

Hojin Lee, Seungmoon Choi

Department of Computer Science and Engineering, Affiliation, City, Country

E-mail: {hojini33, choism}@postech.ac.kr

Abstract—This paper reports the physical property of a laser-induced sensation on the skin after a laser is radiated on a thin light-absorbing elastic medium. In our early finding, laser radiation to the medium creates elastic waves on the basis of thermoelastic effects and the waves can convey a sensation of short mechanical tap. We attached a light-weight accelerometer and obtained an acceleration profile to justify our approach.

Keywords— Laser, Haptics, Midair tactile rendering, Signal measurement, Acceleration

I. INTRODUCTION

Various haptic interfaces are using solid actuators which allow effective energy transmission to the skin. Recently, however, *mid-air haptic displays* such as air jets or ultrasound haptic displays [1] enabled transmitting tactile stimulus without a solid transmission. Nevertheless, these devices share an important problem that their transmission space is limited because of relatively large attenuation.

As an alternative, we have found that a laser directly radiated on the skin can provide a tactile sensation which is attributable to the thermoelastic effect [2]. However, this method faced large individual differences in the induced sensation. To solve this problem, we have developed an approach named *indirect radiation*, which can evoke sensations by irradiating lasers on a light-absorbing elastic medium on the skin [3]. The main topic of this paper is about analyzing the physical characteristics of indirect radiation using an accelerometer.

II. METHODS

We used a frequency-doubled Q-witched laser device (Centurion+, Quantel) with wavelength 532 nm and pulse width 7.76 ns. The radiation of the laser was set to 27.3 mJ, which cannot damage the elastic medium for 100 repetitive radiations at 1 Hz. The medium was made by two 1-mm thick acrylic tapes (See [3] for more details).

Because the weight of the medium was very light (about 0.8-0.9 g), we used a light-weight accelerometer (352C23, PCB Piezotronics) which has a lighter weight (0.18 g). We recorded acceleration data of a laser pulse shot to the elastic medium, using a typical oscilloscope in 250 kHz.

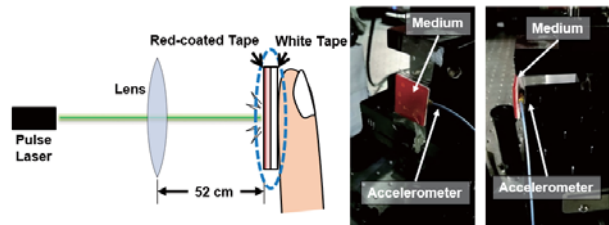


Fig. 1. (Left) Illustration of Indirect Radiation, (Right) The laser setup for measurement

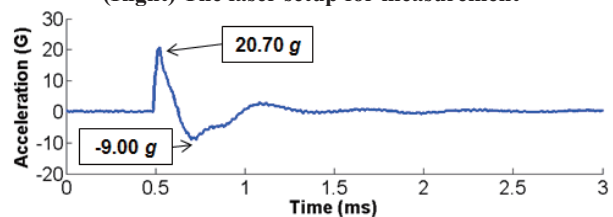


Fig. 2. The acceleration profile measured during indirect laser radiation. Laser was irradiated at $t = 0.5$ ms. A positive force presses the medium in the normal direction to its frontal face, while a negative force pulls the tape.

III. RESULTS AND CONCLUSION

Fig. 2 shows an acceleration profile of our measurement. The duration of fluctuating samples was about 1-2 ms, and the peak amplitude in the positive direction (pressing the tape) was 20.70 g (gravitational acceleration unit). Therefore, we could verify that the laser-induced sensation is large enough to elicit a short mechanical tap, in agreement with the results in [3].

ACKNOWLEDGEMENT

This work was supported by a Pioneer Research Center Program 2011-0027994 from the National Research Foundation of Korea.

REFERENCES

1. T. Hoshi, M. Takahashi, T. Iwamoto, and H. Shinoda, "Noncontact tactile display based on radiation pressure of airborne ultrasound," *IEEE Transactions on Haptics*, vol. 3, no. 3, pp. 155-165, 2010.
2. J.-H. Jun, J.-R. Park, S.-P. Kim, Y. M. Bae, J.-Y. Park, S. Choi, S. H. Park, D.-I. Yeom, H.-S. Kim, G.-I. Jung, J.-S. Kim, and S.-C. Chung, "Laser-induced thermoelastic effects can evoke tactile sensations," *Scientific Reports*, vol. 5, no. 11016, pp.1-16, 2015.
3. H. Lee, J.-S. Kim, S. Choi, J.-H. Jun, J.-R. Park, A.-H. Kim, H.-B. Oh, H.-S. Kim, and S.-C. Chung, "Mid-air tactile stimulation using laser-induced thermoelastic effects: the first study for indirect radiation," In *Proceedings of the IEEE World Haptics Conference (WHC)*, pp. 374-380, 2015.

New Techniques for Optogenetic Neural Interface

Sang Beom Jun^{1,2}, and Chang Hyun Ji¹

¹Department of Electronics Engineering, ²Department of Brain & Cognitive Sciences, Ewha Womans University, Seoul 120-750, Korea

E-mail: juns@ewha.ac.kr

Abstract—Recent advances in optogenetics have enabled various neuroscience researches due to the precise genetic selection of cells for expression of opsins and fluorescence sensors such as channelrhodopsin2, halorhodopsin, GCaMP calcium indicators, and so forth. As the optogenetic technique becomes popular, the implantable optical systems are becoming more sophisticated and optimized. In the present study, we introduce the current status of implantable optical neural interfaces for optogenetic applications and present our implantable multichannel optical neural interfaces.

Keywords— optigenetics, neuroscience, optical neural interface

I. INTRODUCTION

For the last ten years, the optogenetic technique has become one of the most popular tools in neuroscience research since the specific neurons can be exclusively modulated. Initially, the main idea of optogenetics is to stimulate or inhibit neurons by shedding light to the light-sensitive ion channels expressed in the specific types of neurons. Later, instead of modulating neuronal activity, it has become also possible to monitor neural activity by genetically modifying specific neurons to express activity-correlated fluorescence signals. Therefore, the optogenetic neural recording enables the detection of activity from specific types of neurons. Nowadays, these optogenetic methods to control or monitor neural activity are being widely applied to the research in neuroscience and neural engineering.

II. METHODS

A. single channel optical interface

The optogenetic neural recording system is implemented using optic fibers implanted into the brain of mice. When combined with Cre-dependent selective expression of genetically-encoded Ca^{2+} indicators (GECIs), this system enables the measurement of the neural activity from a specific population of cells in mice performing behavioral tasks. As an example, we used viral expression of GCaMPs in striatal projection neurons (SPNs) and recorded the fluorescence changes associated with calcium transients from animals performing a lever-pressing operant task. The simultaneously recorded fluorescence signals and behavior events can be used to explore the relationship between the neural activity of specific brain circuits and the behavior.

B. Multichannel implantable optical interface

In order to control or monitor neuronal activity from wider brain region, we proposed MEMS-based implantable multichannel optical neural interface system. The optical probe is designed to be assembled with etched optical fibers, MEMS guide holes, and integration of glass microlens as shown in Figure 1.

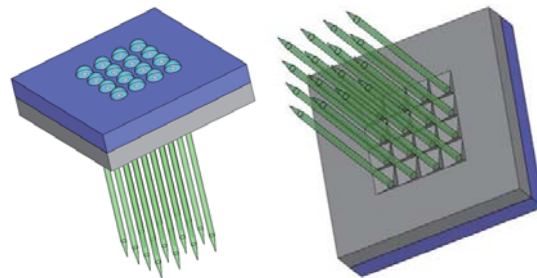


Fig. 1. Design of multichannel optical neural interface

III. RESULTS

The described technique is applied to investigate a neural circuit in basal ganglia, subcortical nuclei that control voluntary actions. They are known to be affected by a number of debilitating neurological disorders. We specifically measured the direct- and indirect-pathway SPN activity. We observed transient increases in neural activity in both direct and indirect-pathway SPNs when animals initiated actions, but not when they were inactive.

IV. CONCLUSION

The proposed system is expected to contribute to the verification of the various neural pathways which have been impossible to be clarified with the conventional electrophysiological techniques.

ACKNOWLEDGEMENT

This work was supported by CISS by MEST as GFP (CISS-2012M3A6A6054204) and NRF-2014R1A1A1A05003770.

REFERENCES

1. Cui G, Jun SB, Jin X, Pham MD, Vogel SS, Lovinger DM, Costa RM, "Concurrent activation of striatal direct and indirect pathways during action initiation," *Nature*, Vol. 494, No. 7436, pp238-242, 2013

Tactile information processing in the human brain and its implications in the haptic technology

Junsuk Kim¹ and Sung-Phil Kim²

¹Department of Brain and Cognitive Engineering, Korea University, Seoul, Korea

²School of Design and Human Engineering, Ulsan National Institute of Science and Technology, Ulsan, Korea

E-mail: spkim@unist.aks.kr

Abstract—We present our recent work on human neural processing of tactile information based on functional magnetic resonance imaging technology. We will introduce the findings about neural bases for discrimination of tactile stimuli, individual variations of tactile sensitivity and adaptive characteristics of somatosensory cortical activity. In addition, we will discuss how these fundamental results may be translated into haptic applications.

Keywords— fMRI, tactile, brain, somatosensory, cortex.

I. INTRODUCTION

Recent advances in haptic technology have driven many neuroscientists to investigate how the human brain perceives and processes tactile stimuli. However, compared to other senses, neural mechanisms for tactile information processing are rarely uncovered. Hence, we explore the human brain activity regarding tactile sensations using neuroimaging technology as well as particular data analysis techniques. Several preliminary findings about human neural processing of tactile information are presented here.

II. METHODS

A. fMRI recordings

A 3T fMRI scanner was commonly used to acquire the human brain activity data for several studies presented here.

B. Data analysis

For many studies, we employed the multi-voxel pattern analysis (MVPA) technique to enhance the sensitivity to changes in the BOLD signal [1]. Also, we used a regular univariate analysis method such as a generalized linear model to mark out differences between multi-voxel versus single-voxel approaches.

C. Behavioral tasks

Participants performed behavioral tasks designed to examine the perception of given tactile stimuli. Often, response time data as well as verbal reports were collected from the tasks.

III. RESULTS

A. Neural processing of tactile information

Our studies revealed that tactile information might be processed in not only somatosensory cortical areas but also other connected areas such as motor cortex and insula [2]. Also, the MVPA often allowed us to find neural patterns in the areas related to tactile processing, which would have been unseen by the univariate method only [3]. As a result, we observed a hierarchical processing of the tactile information over the human somatosensory cortical system. Individual differences in perceiving tactile stimuli were partially elucidated by the examination of brain activity [4]. Adaptation to a sustained tactile stimulus, which is presumably one of the key characteristics of human tactile perception, was evident in one of our studies in the view of cortical activity [5].

IV. CONCLUSION

Here, we present several findings regarding human brain mechanisms underlying tactile information processing. These findings may widen possibilities of developing better haptic technologies by virtue of the understanding of how humans perceive tactile stimuli.

REFERENCES

1. J. V. Haxby "Multivariate pattern analysis of fMRI: the early beginnings," *Neuroimage*, vol. 62, pp. 852-855, 2012.
2. Y.G. Chung, S.W. Han, H.-S. Kim, S.-C. Chung, J.-Y. Park, C. Wallraven and S.-P. Kim, "Intra- and inter-hemispheric effective connectivity in the human somatosensory cortex during pressure stimulation," *BMC Neuroscience*, 15, p. 43, 2014.
3. J. Kim, K.-R. Muller, Y.G. Chung, S.-C. Chung, J.-Y. Park, H.H. Buelthoff, and S.-P. Kim, "Distributed functions of detection and discrimination of vibrotactile stimuli in the hierarchical human somatosensory system," *Front. Human Neurosci.*, vol. 8, p. 1070, 2014.
4. J. Kim, Y.G. Chung, J.-Y. Park, S.-C. Chung, C. Wallraven, H.H. Buelthoff and S.-P. Kim, "Decoding accuracy in supplementary motor cortex correlates with perceptual sensitivity to tactile roughness," *PLoS ONE*, vol. 10, p. e0129777, 2015.
5. Y.G. Chung, S.W. Han, H.-S. Kim, S.-C. Chung, J.-Y. Park, C. Wallraven, S.-P. Kim, "Adaptation of cortical activity to sustained pressure stimulation on the fingertip," *BMC Neuroscience*, in press, 2015.

Prediction of speech intelligibility in cochlear implant users using a computational model

Jihwan Woo

School of Electrical Engineering, Department of Biomedical Engineering, University of Ulsan,
Republic of Korea

A cochlear implant (CI) is an auditory prosthesis that provides hearing function by electrically stimulating the auditory nerves. Although the progress in CI signal processing strategies has resulted in a significant improvement in speech perception, the CI users still have limitations in hearing sounds in noise and listening to music. Behavioral testing is conducted in clinics to evaluate new devices and CI speech processing strategies. However, it may not be feasible to test various types of stimulus strategies with such subjective trials.

In this presentation, an objective method to predict the speech intelligibility of a CI user by using a computational model is introduced. The biophysical auditory nerve fiber model was used to simulate the electrically stimulated neural response. Speech intelligibility was predicted using a neurogram similarity index. The effects of stimulation rate and background noise on speech intelligibility were evaluated. The result obtained using the computational model was consistent with the data from CI subjects. The proposed model can be used to effectively evaluate various types of CI speech processing strategies. This research was supported by Basic Science Research Program through the National Research Foundation of Korea (NRF) funded by the Ministry of Education (2015R1D1A3A01016128).

Towards Personalized Transcranial Current Stimulation (tCS)

Chang-Hwan Im

Department of Biomedical Engineering, Hanyang University, Seoul, Republic of Korea
E-mail: ich@hanyang.ac.kr

Abstract—In this talk, recent efforts to implement personalized transcranial current stimulation are introduced, particularly focusing on the results from the Computational Neuroengineering Lab. at Hanyang University, Korea.

Keywords—transcranial current stimulation (tCS), image-guided stimulation, multi-channel tCS

I. SUMMARY

Transcranial current stimulation (tCS), represented by transcranial direct current stimulation (tDCS), transcranial random noise stimulation (tRNS), and transcranial alternating current stimulation (tACS), is a new type of noninvasive neuromodulation techniques, which can facilitate or inhibit cortical excitability by transmitting a small amount of current between a pair of scalp electrodes [1]. Although the underlying mechanisms are not well understood, tCS has been studied in a variety of clinical fields as a potential treatment tool for neuropsychiatric diseases and neurological disorders including stroke, depression, epilepsy, Alzheimer's disease, chronic pain, and Parkinson's disease. Recent studies have shown that computer-based numerical field simulations can provide cortical current distributions for a given electrode configuration, and thus help practitioners to determine electrode locations that can deliver increased current to a target brain area [2, 3]. Indeed, a series of recent studies have demonstrated that enhanced field concentrations in target brain areas can be achieved with the aid of three-dimensional electric field analyses, actualizing the customized and individualized noninvasive brain stimulation [4]. However, since only a few research groups could utilize this technology, most researchers have relied on their intuition, experience, and previous literature for determining the electrode configurations and/or locations. Therefore, it is of great necessity to develop effective methods that allow practitioners to readily determine optimal electrode locations. In this talk, recent advances in personalized tCS will be introduced. The topics will include necessity of personalized tCS, numerical methods for field-analysis-based tCS, and the image-guided tCS technique.

ACKNOWLEDGEMENT

This research was supported by the Brain Research Program through the National Research Foundation of Korea (NRF) funded by the Ministry of Science, ICT & Future Planning (NRF-2015M3C7A1031969).

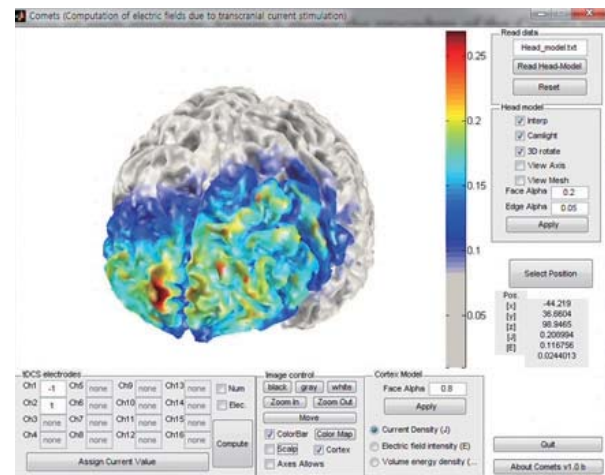


Fig. 1. COMETS – A Matlab toolbox for 3D simulation of tDCS induced current (www.cometstool.com)

REFERENCES

1. C.-H. Han, H. Song, Y.-G. Kang, B.-M. Kim, and C.-H. Im, "Hemodynamic responses in rat brain during transcranial direct current stimulation: a functional near-infrared spectroscopy study," *Biomedical Optics Express.*, vol. 5, no. 6, pp. 1812-1821, 2014.
2. J.-H. Kim, D.-W. Kim, W. H. Chang, Y.-H. Kim, K. Kim, and C.-H. Im, "Inconsistent outcomes of transcranial direct current stimulation may originate from anatomical differences among individuals: Electric field simulation using individual MRI data," *Neuroscience Letters.*, vol. 564, pp. 6-10, 2014.
3. C.-H. Im, J.-H. Park, M. Shim, W. H. Chang, and Y.-H. Kim, "Evaluation of local electric fields generated by transcranial direct current stimulation (tDCS) with an extracephalic reference electrode based on realistic 3D body modeling," *Physics in Medicine and Biology.*, vol. 57, pp. 2137-2150, 2012.
4. J.-H. Park, S. B. Hong, D.-W. Kim, M. Suh, and C.-H. Im, "A Novel Array-type Transcranial Direct Current Stimulation (tDCS) System for Accurate Focusing on Targeted Brain Areas," *IEEE Transactions on Magnetics.*, vol. 47, no. 5, pp. 882-885, 2011.

Closed-Loop Smart Deep Brain Stimulation Technology

D. P. Jang¹, K. E. Bennet², and K. H. Lee³

¹Department of Biomedical Engineering, Hanyang University, Seoul, Korea

²Division of Engineering, Mayo Clinic, Rochester, MN, USA

³Department of Neurosurgery, Mayo Clinic, Rochester, MN, USA

E-mail: dongpjang@hanyang.ac.kr

Abstract—Conventional deep brain stimulation (DBS) relies on an open-loop system in which stimulation parameters are adjusted until desired therapeutic effects are achieved without neural feed-back. In this research, we propose closed-loop smart DBS system based on neurochemical monitoring.

Keywords— deep brain stimulation (DBS), closed-loop smart DBS system, fast-scan cyclic voltammetry (FSCV), dopamine (DA).

I. INTRODUCTION

Current strategy for DBS therapy is postoperative adjustment of stimulation parameter until adverse effects are minimized. This procedure has to be repeated every few months because the efficacy of therapeutic effects decline. Therefore, development of closed-loop smart DBS system that can change personalized stimulation parameter automatically is paramount for improving the therapeutic efficacy of DBS. Electrophysiology and imaging techniques have been proved as DBS affects neural network activity and development of closed-loop DBS devices has largely focused on using electrophysiological activity as feedback signal. Neurochemical-based feedback to control DBS has been demonstrated to offer finer and intuitive control of DBS parameters. Herein, we propose the initial steps toward individualized closed-loop smart DBS system including neurochemical information.

II. METHODS

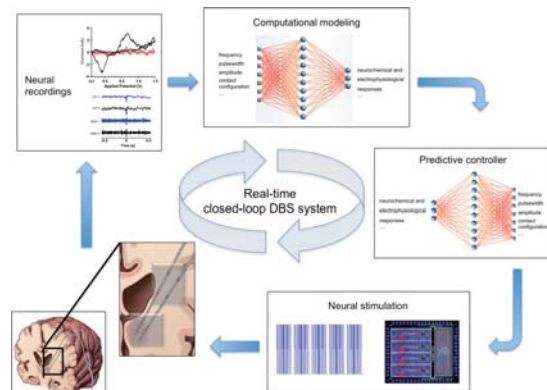


Figure 1 Real-time closed-loop deep brain stimulation system [1]

A. Wireless Instantaneous Neurochemical Concentration Sensing System (WINCS) Harmoni

To integrate neurochemical recording with neurostimulation, the authors developed the WINCS Harmoni, a novel, wirelessly controlled stimulation device designed to interface with FSCV in multi-channel [2].

B. Development of Conductive Boron-Doped Diamond Electrode

Building on diamond characteristics such as hardness, chemical inertness and low electron emission threshold voltage, the current microscopic, spectroscopic and voltammetric investigations are directed towards improving the properties of electrode coating materials for their future use in clinical studies of deep brain stimulation via FSCV [3].

C. Absolute concentration of dopamine measurement using FSCV

Estimation of specific concentration of DA using an optimized FSCV technique based on adsorption and desorption reaction.

III. RESULTS and CONCLUSION

By combining electrochemical monitoring, we can potentially replace the trial-and-error process commonly used in clinical treatment. Also the chronic implantation problem could be solved by using diamond electrodes. Overall, the integration of chemical monitoring technic and electrophysiological signal in WINCS Harmoni with the signal interpretation technic into proper stimulation parameters can be the alternative to the conventional open-loop DBS system.

ACKNOWLEDGEMENT

This research was supported by the NIH 1U01NS090455-01 award.

REFERENCES

1. Grahn, P.J., et al., *A neurochemical closed-loop controller for deep brain stimulation: toward individualized smart neuromodulation therapies*. *Frontiers in Neuroscience*, 2014. **8**.
2. Chang, S.Y., et al., *Development of the Mayo Investigational Neuromodulation Control System: toward a closed-loop electrochemical feedback system for deep brain stimulation*. *J Neurosurg*, 2013. **119**(6): p. 1556-65.
3. Bennet, K.E., et al., *Development of conductive boron-doped diamond electrode: a microscopic, spectroscopic, and voltammetric study*. *Materials*, 2013. **6**(12): p. 5726-5741.

The Phoenix⁹⁹ Retina Implant – passive chronic implantation performance

Gregg Suaning^{1,2}, Nigel Lovell¹, Natalie James¹, Adrian Fung^{2,3}

1. Graduate School of Biomedical Engineering, UNSW Australia
2. Save Sight Institute, Discipline of Ophthalmology and Eye Health, University of Sydney
3. Faculty of Medicine and Health Sciences, Macquarie University, Sydney

Abstract.

The chronic performance of a visual prosthesis comprising 98 stimulation electrodes on an array placed within the suprachoroidal space, a small hermetic capsule containing a single microchip and monopolar return electrode fixed to the globe, and a flexible wire leading to a hermetically-sealed telemetry implant for the transmission of data and power was assessed in passive form, *in vivo* in the *Ovis aries* (sheep).

Sheep (N=4) were implanted for a period of not less than 90 days with fully-implantable, passive systems. Performance in terms of device stability, macroscopic tissue response, and material robustness was assessed through means including X-ray, indirect ophthalmoscopy, infra-red imaging, micro-CT, optical coherence tomography and visual inspection of the surgical sites during microscopic explant dissection.

Other than one event where the flexible lead-wire became dislodged from the orbital margin, all devices remained stable in their intended position, showed no significant adverse tissue responses, and maintained their material integrity through implantation, testing, and explant phases.

Pending histological analysis outcomes will determine if the devices should now proceed to fully active systems for the assessment of the effects of stimulation on the retina.

Acknowledgment. This work was supported by UNSW Australia and the Australian Research Council's Special Research Initiative in Bionic Vision Research and Technology granted to Bionic Vision Australia.

Seoul Artificial Retina

Seoul Artificial Retina aimed for the restoration of vision in the visually impaired patients. For this purpose, a novel retinal prosthesis was fabricated using a new biomaterial of liquid crystal polymer (LCP). Monolithically fabrication process was established to realize an all-polymer device which is miniaturized, eye-conformable and long-term reliable. The developed device was evaluated in vitro to test its long-term reliability in implanted condition through accelerated soak test. In vivo rabbit experiment was performed to assess the long-term biocompatibility and implantation stability. Further investigation including clinical trial will be performed.

Updates of the artificial retina research

Vision rehabilitation in the blind seems to be the ultimate goal of ophthalmologic treatments. Among the several different approaches, electrical retinal stimulation showed the most promising results for restoring vision. Microelectrode arrays based on a flexible polymer developed and used for pattern electrical retinal stimulation, and epiretinal, subretinal and suprachoroidal approaches are adopted for the surgical implantation of electrodes. Stimulation patterns can be provided from an external stimulator through wireless signal transfer or can be given by implanted photodiode arrays with an external power supply. In vitro and in vivo studies revealed that the retinal implant can be used for clinical purposes, and clinical trials showed that blind volunteers who were subjected to retinal implant surgery could recognize various shapes and their surroundings.

Metrology in Medicine – Traceability and Uncertainty

Jong Oh Choi

KRISS Daejeon, Korea

E-mail: choijongoh@kriss.re.kr

Abstract— Because of critical importance in medicine and especially in critical care, confusion in terms and definitions should be avoided either in the inter-physician communications or in the understanding of manufacturers' and engineers' instructions and limitations when using devices. Metrology, the science of measurement, provides physician, medical laboratory and manufacturer with worldwide accepted guidance to the development of medical device and terminology of measurement. In order to step into metrology, the concepts and definitions of measurement, traceability, uncertainty and error are introduced, based on 'Vocabulary in metrology' and 'Guide to the uncertainty in measurement'.

Keywords—Measurement. Uncertainty. Traceability.

I. Measurement

Process of experimentally obtaining one or more quantity values that can reasonably be attributed to a quantity

The objective of a measurement is to determine the value of the measurand, that is, the value of the particular quantity to be measured. A measurement therefore begins with an appropriate specification of the measurand, the method of measurement and the measurement procedure. In general, the result of a measurement is only an approximation or estimate of the value of the measurand and thus is complete only when accompanied by a statement of the uncertainty of that estimate. In practice, the required specification or definition of the measurand is dictated by the required accuracy of measurement. The measurand should be defined with sufficient completeness with respect to the required accuracy so that for all practical purposes associated with the measurement its value is unique.

2. Traceability

Property of a measurement result where by the result can be related to a reference through a documented unbroken chain of calibrations, each contributing to the measurement uncertainty

Establishing metrological traceability of measurement results is a prerequisite to obtaining metrological comparability of measurement results. In recent years, the concept "traceability" in measurement has received an extraordinary amount of attention. Still, the interpretation of "metrological traceability" is in the confusion.

3. Uncertainty

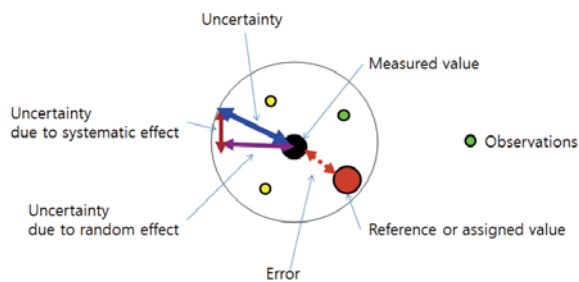
Parameter that characterizes the dispersion of the quantity values that are being attributed to a measurand, based on the information used.

The word "uncertainty" means doubt, and thus in its broadest sense "uncertainty of measurement" means doubt about the validity of the result of a measurement. Moreover, uncertainty has nothing to do with error.

4. Error

Measured quantity value minus a reference quantity value

In general, a measurement has imperfections that give rise to an **error** in the measurement result. Traditionally, an error is viewed as having two components, namely, a **random** component and a **systematic** component. Error is an idealized concept and errors cannot be known exactly.



The metrological terms in this abstract will be explained. Audience is expected to understand the uncertainty approach against the error approach in measurement and the difference between uncertainty and error. The following will be understood.

“Measurement starts with traceability and ends with uncertainty.”

REFERENCES

1. BIPM, IEC, IFCC, ISO, IUPAC, IUPAP, OIML (1995) Guide to the expression of uncertainty in measurement (GUM), 2nd edn. International Organization for Standardization (ISO), Geneva. JCGM 100:2008, BIPM, Sevres
2. BIPM et al (2008) International vocabulary of metrology—basic and general concepts and associated terms (VIM), 3rd edn. International organization for standardization (ISO), Geneva. JCGM 200:2012. <http://www.bipm.org/vim>

Measurement Issues for Biomedical Developers

Wonsik Ahn

Blood Flow Data Center, Kyung Hee University Hospital, Seoul, Korea
E-mail: aws@snu.ac.kr

Abstract—Medical devices use measurement. Clinical measurements are related to measurand, traceability, uncertainty, and reference standards. So, medical devices should be developed under the concept of measurement. I would like to introduce measurement issues with blood pressure measurement, hemoglobin measurement, pulse oximetry, and electrocardiogram.

Keywords— Measurement, measurand, traceability, uncertainty, reference standards.

I. INTRODUCTION

New invention of medical device is usually evaluated by its effectiveness and safety. The evaluation of effectiveness and safety are based on some measurements. Diagnostic and therapeutic medical devices are also related to clinical measurements. Measurement needs some targets called “measurand”. “Measurement starts with traceability and ends with uncertainty.” So, medical devices for clinical measurements should be related to measurand, traceability and uncertainty for the evaluation of effectiveness and safety and adequate clinical application.

Many medical devices include internal decision criteria. The collection of decision criteria is called reference standards, which include measurement traceability and uncertainty. Therefore, if we develop new medical devices or improve quality of some medical devices, we should recognize the concept of reference standards, too.

I would like to introduce some medical devices to biomedical engineers, which are related to measurand, measurement traceability, uncertainty, and reference standards.

II. Measurement Issues in Bioengineering

A. Measurand in blood pressure measurement

Human body needs oxygen and glucose for energy production. If blood contains adequate amount of oxygen and glucose, the key point is the delivery called “blood flow”. Blood flow is hard to measure. Therefore blood pressure is substituted for the blood flow due to easy measurement. Bioengineers should

differentiate the blood flow and blood pressure to develop new device for circulation of blood [1-2].

B. Traceability in hemoglobin level measurement

There are several devices for hemoglobin measurement. Hemoglobin level 10 mg/dL is transfusion criteria. Sometimes there are debates for adequate transfusion between surgeons and anesthesiologists based on their own measurement devices. Though the traceability of devices should be considered, clinicians usually do not have the concept. Bioengineers should ensure the traceability of their devices and should set up the maintenance schedule for the adequacy of their devices.

C. Uncertainty in pulse oximetry

Pulse oximeters have some degree of uncertainty. However, almost all pulse oximeters do not display uncertainty of their measurement. Clinicians should decide clinical action based on not by the measurement results but by their own experience [3].

D. Reference standards in electrocardiogram

An electrocardiogram device has an internal diagnostic system. The diagnostic system should include some database for decision criteria. Until now, the databases are based on foreign volunteers. “National Center for Standard Reference Data” and “Blood Flow Data Center” are developing database for Korean electrocardiogram [4].

III. CONCLUSION

Medical devices should be developed based on the concept of measurand, traceability, uncertainty, and reference standards.

REFERENCES

1. J. Sim, H. Park, W. Ahn, “Three blood pressure measurements and comparison of results,” *Kor. J. Anesthesiol.*, Vol. 52, pp. 495-497, 2007.
2. W. Ahn, “Problems in cardiac output measurement and clinical understanding,” *Kor. J. Anesthesiol.*, Vol. 54, pp. 241-255, 2008.
3. J. Sim, W. Ahn, “Assumption in algorithm of photoplethysmogram for pulse oximetry and clinical interpretation,” *Kor. J. Anesthesiol.*, Vol. 52, pp. 376-379, 2007.
4. <http://www.srd.re.kr>

Clinical Electrical Impedance Tomography: Monitoring Lung Ventilation

K. Lee, L. Zhou, and J. K. Seo

Department of Computational Science & Engineering,
Yonsei University, Korea
E-mail: seoj@yonsei.ac.kr

Abstract— **Electrical impedance tomography (EIT) has the great potential clinical advantages for regional lung function monitoring at the bedside [1], owing to the indispensable capability to provide long-term, continuous monitoring and portability. This paper focuses on robust image reconstruction to deal with technical difficulties of the forward modeling errors and the inherent ill-posed nature in the reconstruction.**

Keywords— **Electrical impedance tomography, Relative impedance changes, Lung ventilation.**

I. INTRODUCTION

EIT uses multiple surface electrodes to provide tomographic imaging of tissue’s electrical properties, where electrodes are used to measure the boundary current-voltage relations. EIT has fundamental drawbacks because EIT data depends strongly on the boundary geometry and electrode positions, whereas it is much less sensitive to a local perturbation of away from the measuring electrodes. Even in difference EIT, which is less affected by the forward modeling errors, the quality of the reconstructed image depend on the accuracies of the geometry of the body and electrode positions. This paper combines the standard EIT method with a physiological process-based regularization technique to reduce ill-posedness and a recent 3D scanning technique to reduce the reconstruction errors due to the forward modeling errors.

II. METHODS

We uses 3D handheld scanner to extract the boundary geometry and electrode positions, as shown in shown in Fig. 1.

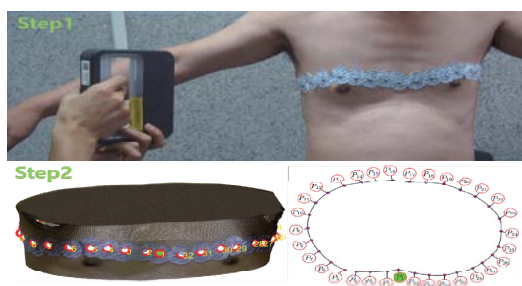


Fig. 1. 3D-scan procedure, and the obtained boundary geometry and electrode positions

We apply a low-pass filtering to the EIT data to extract ventilation related data. This filtered data enables us to use the lung function-based regularization [2]. The conductivity in the lung region can be regarded as monotonically changing with respect to time during inhalation and exhalation. The proposed method improves time-difference EIT image quality significantly, owing to reduction of forward modelling errors and the use of the forward modeling errors.

III. RESULTS

Human experiment is conducted with Swisstom BB2 EIT system. Results are shown in Fig. 2.

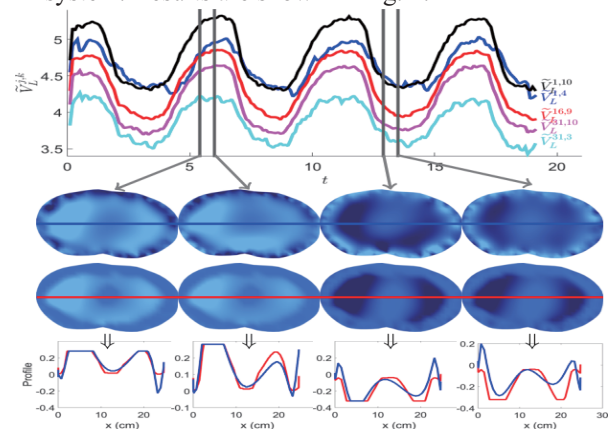


Fig. 2. (1st row) monotonic period; (2nd row) SLM; (3rd row) SLM with monotonicity constraints; (4th row) the profiles.

IV. CONCLUSION

The proposed reconstruction methods allow lung EIT to visualize the monotonically varying conductivity distribution during inhalation and exhalation.

ACKNOWLEDGEMENT

This work was supported by the NRF grant (2011-0028868,2012R1A2A1A03670512).

REFERENCES

1. E. Teschner and M. Imhoff, "Electrical impedance tomography: the realization of regional ventilation monitoring, *Drager. Technology for Life*, 2011.
2. L. Zhou, B. von Harrach, and J. K. Seo, "Monotonicity-based Electrical Impedance Tomography for Lung Imaging", *submitted to IEEE Trans. Medical. Imaging*, 2015.

Application of Electrical Impedance Measurement and Electrical Impedance Tomography in Japan

S. Nebuya

Graduate School of Medical Sciences, Kitasato University, 1-15-1 Kitasato, Minato, Sagami-hara, Kanagawa, Japan
E-mail: nebuya@kitasato-u.ac.jp

Abstract— Technology of electrical impedance measurement and electrical impedance tomography has been studied for several decades in Japan. In this paper, some applications of our group were introduced in research fields as healthcare, psychology, dialysis, and intensive care.

Keywords— electrical impedance measurement, electrical impedance tomography, tidal volume, subcutaneous & visceral fat, lung density, wearable impedance tomography

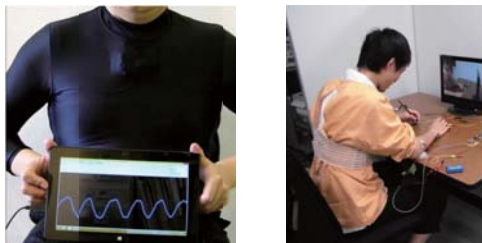
I. INTRODUCTION

Electrical impedance measurement and tomography have been studied and applied for many research fields for several decades in Japan. However, only few applications had only been used with commercially successful as a body fat analyser for the last decade. However, many applications have been occurring as improvement of wearable electronics technology. In this paper, some of novel technologies and applications were introduced based on our research group in Japan.

II. TECHNOLOGIES AND APPLICATIONS

A. Monitoring shirts for respiration.

Fig. 1 shows an example of a monitoring shirt that can measure tidal volume using electrical impedance measurement. Textile and electrodes were set into the shirt and tidal volume was possible to measure without electrode contact with body surface. The function is considered to be useful for detecting sleep apnea. In addition, heart rate was also possible to measure with or without electrode contact. Both parameters have been used for evaluating physiological variation during stress tasks in psychological research field.



(a) respiratory monitoring (b) stress experiment

Fig. 1. Respiratory monitoring using a wearable shirt

B. Subcutaneous & visceral fat measurement

A body fat analyser has been considered as the most successful commercial device using bio-impedance measurement in Japan. However, the rate of body fat is

indirect index. Subcutaneous fat sickness is considered as ‘direct and intuitive index’ for healthy people who want to keep healthy body shape. Furthermore, it has been considered that there was a relationship between visceral fat accumulation and arteriosclerotic disease. The visceral fat area has been measured using X-ray CT method that was not easy to use for healthy people.

Fig. 2 shows examples of a measuring device for subcutaneous fat sickness and a belt for visceral fat area that we have been developed.



(a) subcutaneous fat meas. (b) visceral fat area meas.

Fig. 2. Wearable measuring devices for subcutaneous fat sickness and visceral fat area measurement

C. A bandage with a bleeding sensor

We developed a bandage with a bleeding sensor using conductive thread to prevent from a needle removal accident during a dialysis. The sensor system had been designed for identify both saline & blood using impedance spectroscopy.

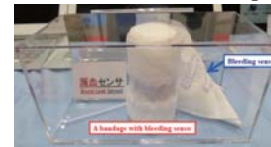


Fig. 3. A bandage with a bleeding sensor

D. Wearable electrical impedance tomography

A wearable electrical impedance tomography (EIT) had been developed for intensive care unit (ICU) use. Fig. 4 shows one of the developed wearable EIT systems and its application in ICU. Eight or sixteen textile electrodes could be used to measure EIT and the system was driven via USB cable connected with a notebook PC. Total length and weight included EIT was 1,005 mm and approximately 200g respectively.



Fig. 4. A wearable EIT and application in ICU

III. CONCLUSION

Some of technologies and applications were introduced in this paper. Further applications and information will be presented at the conference.

Microscopic electrical impedance based monitoring of engineered cartilage during *in vitro* tissue construction

E. A. Lee¹, T. I. Oh², Y. Son¹, and E. J. Woo²

¹College of Life Science & Graduate School of Biotechnology, Kyung Hee University, Geonggi-do, Republic of Korea

²Department of Biomedical Engineering, Graduate School of Medicine, Kyung Hee University, Seoul, Republic of Korea

E-mail: eunahlee@khu.ac.kr

Abstract—Tissue engineering field showed enormous progress in engineering transplantable tissue by *in vitro* tissue construction and cultivation. However, current methodologies of monitoring tissue formation still involves destructive and invasive trait making continuous monitoring infeasible. In this study, changes in electrical tissue property during *in vitro* chondrogenesis was measured and their significance in interpreting tissue complexity was investigated.

Keywords— Tissue Engineering, Articular Cartilage, Electrical Impedance, Extra-Cellular Matrix, Chondrogenesis.

I. INTRODUCTION

Literatures show that various kinds of tissues can be constructed *in vitro*, even in its provisional form, for transplantation. However, few tissues can be engineered *in vitro* to the point of being analogous to its normal counterpart. Being one of these tissue, cartilage might be engineered *in vitro* to the point of showing similarity to natural tissue by realizing tissue complexity [1]. To evaluate and control the tissue formation, non-destructive monitoring of tissue reconstruction is essentially required.

II. METHODS

A. Bio-Impedance Spectroscopy (BIS)

17-electrode BIS probe and a conductivity estimation algorithm [2] was used to collect current-voltage data and examine electrical tissue property.

B. *In vitro* Chondrogenic Differentiation

Chondrocyte isolated from costal cartilage were expanded *in vitro* and subjected to chondrogenic differentiation to form disc-type cartilage.

III. RESULTS

A. Electrical Property of *In vitro* Cultivated Cartilage

Chondrocytes were subjected to disc-type *in vitro* chondrogenesis for 6 weeks. Along the time point, conductivity and anisotropy were measured both on top and bottom surface of disc-type cartilage, which

showed consistent difference throughout the culture period as shown in Fig. 2.

B. Correlation between Stroma Maturation and Electrical Tissue Property

While thickness of tissue showed no correlation with BIS measured value, different maturation state of stroma in disc-type cartilages induced by ascorbic acid showed difference in BIS measurement.

IV. CONCLUSION

Microscopic bioimpedance tensor probing method can measure ECM maturation state without harmful effect on *in vitro*-cultivated cartilage tissue.

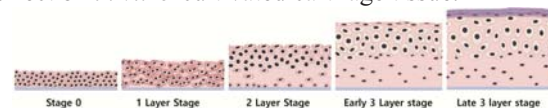


Fig. 1. Schematic drawing of *in vitro* chondrogenesis

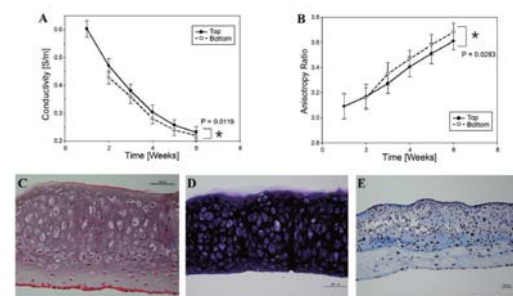


Fig. 2. Changes in electrical property of *in vitro* cultivated cartilage tissue.

ACKNOWLEDGEMENT

This work was supported by Mid-career Research Program (NRF-2015R1A2A2A04006172) through NRF grant funded by the MEST.

REFERENCES

1. L. Kock, C. C. van Donkelaar, and K. Ito, "Tissue engineering of functional articular cartilage: The current status", *Cell Tissue Res.*, vol. 347, pp. 613-627, 2012
2. H. Kwon, H. Wi, B. Karki, E. J. Lee, A. McEwan, E. J. Woo, B. Harrach, J. K. Seo, T. I. Oh, "Bioimpedance spectroscopy tensor probe for anisotropic measurements" *Electron. Lett.*, vol. 48, pp.1253-1255, 2012

Medical applications of electrical impedance imaging and impedance spectroscopy

T. I. Oh and E. J. Woo

Department of Biomedical Engineering, Kyung Hee University, Seoul, Republic of Korea

E-mail: tioh@khu.ac.kr

Abstract— Electrical properties of living tissues/organs present the physiological and pathological state of a subject. In this paper, we introduce potential applications of impedance imaging and impedance spectrum based our research works. Real-time functional lung monitoring and blood perfusion imaging are the leading candidates. Cancer detection is a good application using multi-frequency impedance spectrum. Recently, it can be used for estimating the treatment of ablation.

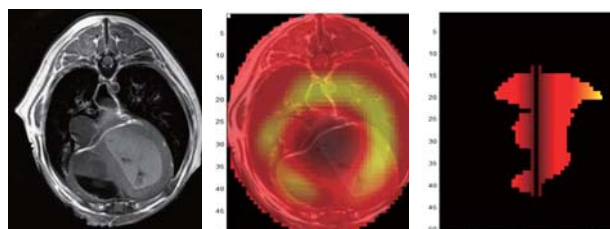
Keywords— Electrical impedance tomography, monitoring, medical application, impedance spectrum.

I. INTRODUCTION

Electrical impedance tomography can produce functional images of conductivity variations associated with physiological events such as cardiac and respiratory cycles [1]. After it was introduced by Brown and Seagar, EIT has developed and clinical studies have been performed, however it still needs the breakthrough to apply EIT in clinic [2]. EIT has advantages of high temporal resolution and portable, however, it must overcome the intrinsic properties of low sensitivity and low spatial resolution. In this paper, we introduced several potential applications in medical area based on our research works.

II. METHODS & RESULTS

EIT system is required high performance and high stability in order to be used in clinical application. In order to be used for several potential applications, we developed the high performance impedance measurement module (IMM) and assembled the imaging system with multiple IMMs [3]. When 16 electrodes are attached around the chest, we could get regional lung volume changes overlapped with MR cine images.



(a) MR image

(b) EIT image

(c) Normalized ΔZ in Lungs

Fig. 1. Functional lung monitoring on an animal

We placed small array electrodes on the head to monitor and estimate of bleeding in the ventricles. Since the brain is covered with highly resistive skull, the impedance change is attenuated. However, we could detect the small bleeding in the brain. Also, we could estimate the volume of bleeding from the impedance changes.

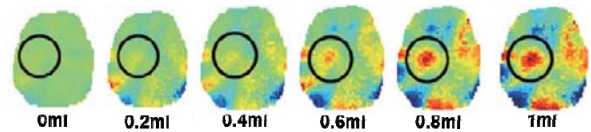


Fig. 2. Intra-Ventricle Hemorrhage model and continuous monitoring with impedance images.

Recently, early detection method of disease and minimally invasive treatment method are helpful to alleviate patient's sufferings. Ablation method is the problem for high recurrence rate even if it is a good minimally invasive treatment method. EIT can help to monitor the treatment in real-time, also it can provide the estimation result of ablation treatment.

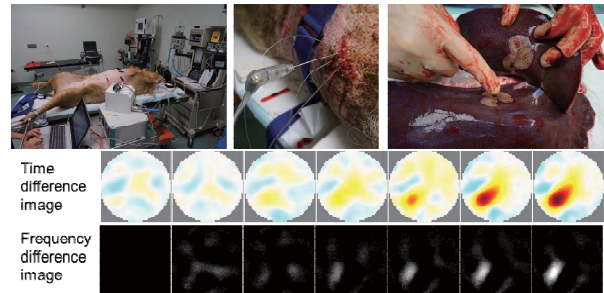


Fig. 3. EIT based ablation monitoring.

III. CONCLUSION

We have developed the high accurate measurement system and imaging algorithms for using EIT in several medical applications. From the pilot results, EIT has a potential for functional imaging and real-time monitoring method.

ACKNOWLEDGEMENT

This work was supported by Mid-career Research Program (NRF-2015R1A2A2A04006172) through NRF grant funded by the MEST.

REFERENCES

1. D. S. Holder, "Electrical Impedance Tomography: Methods, History and Applications," IOP, Bristol, UK, 2005.
2. B. H. Brown and A. D. Seagar, "The Sheffield data collection system," *Clin. Phys. Physiol. Meas.* Vol. 8 91-97, 1987.
3. H. Wi, H. Sohal, A. L. McEwan, E. J. Woo, and T. I. Oh, "Multi-frequency electrical impedance tomography system with automatic self-calibration for long-term monitoring," *IEEE Trans. Biomed. Circ. Sys.* 8 (1) 119-28, 2014

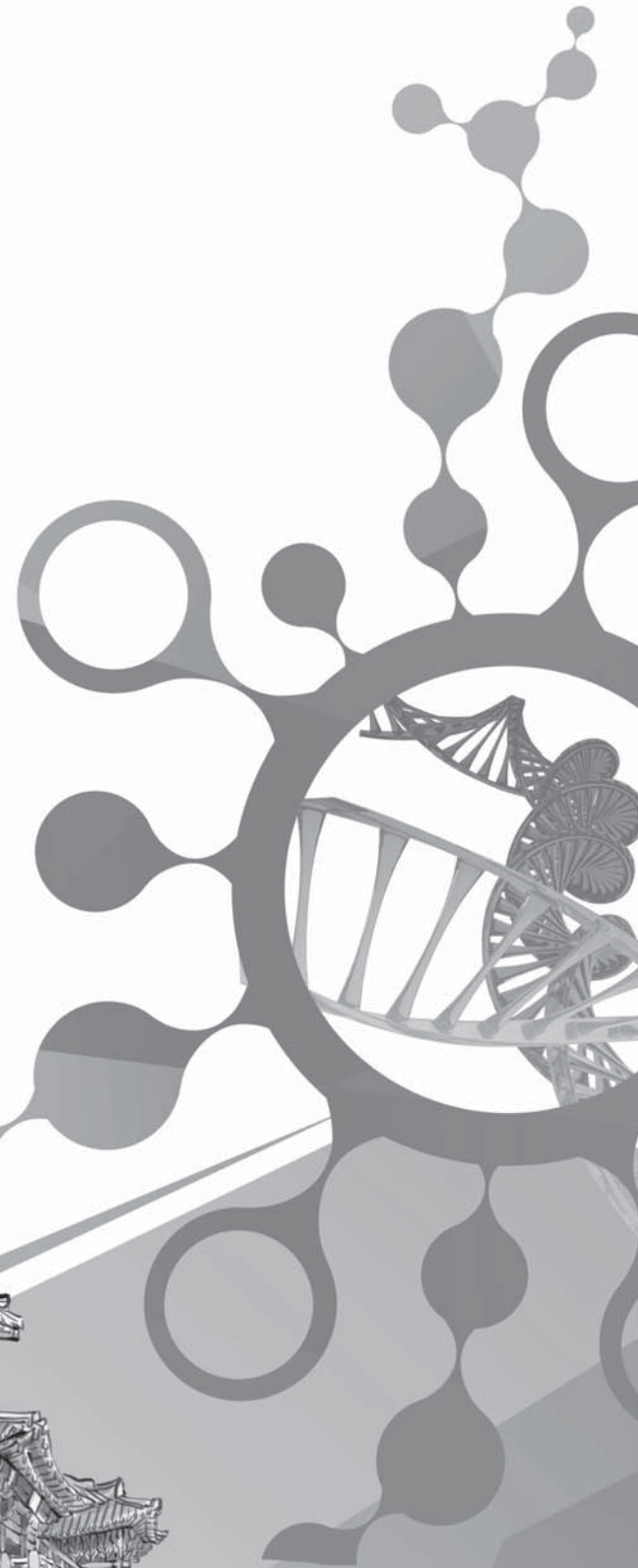
IBEC

International Biomedical
Engineering Conference 2015

2015

Road to Better Life through Biomedical Engineering

ORAL SESSIONS



Designing One Board VLC Receiver for various Medical Data Transmission with Multichannel WDM

J. Y. An¹, K. H. Lim¹, and W. Y. Chung¹

¹Department of Electronics Engineering, Pukyong National University, Busan, South Korea
E-mail: wychung@pknu.ac.kr

Abstract—This paper proposes a modified VLC (Visible Light Communication) receiver, which is simply designed by one PCB board based on Arduino to detect healthcare information. Optical signals transmitted by 3 different color LEDs are detected by the proposed VLC receiver and observed by the self-design monitoring system.

Keywords—Visible light communication, Multi-channel, Healthcare information

I. INTRODUCTION

Visible light communication (VLC) has emerged as an alternative wireless communication system due to its ubiquity and energy efficiency [1]. Visible light is a part of electromagnetic spectrum which covers wavelengths between 400 to 700 nm. When VLC acts as a data communication tool and illumination device at the same time, a white color LED is chosen, where it can be produced by Red, Green and Blue (RGB) light combination. The each RGB intensity in the white light RGB LED can be manipulated to represent 3 different data for multi-channel transmission [2].

II. SYSTEM OVERVIEW

In order to transmit various medical data in a wireless channel, 3 different colors of LEDs are used, where adopted colors of Red, Green and Blue, carry the Electrocardiograph (ECG) data, Photoplethysmograph (PPG) data, and the temperature of the patient, respectively [2]. Each packet data consists of 5 frames (Sync. byte, Header, ID, Data, and end byte) and the data transfer rate of each channel is around 60kbps, which ensures that the light source does not exhibit a flickering effect. An optical signal transmitted through the different color channel is detected by a newly designed VLC receiver, which is composed of a photo detector and a microcontroller (mega2560) on a small PCB board, such as Fig. 1. A color sensor in the photo detector is employed to differentiate each RGB light by using internal three photodiodes including each color filter and pass it through the respective output. The differentiated analog signals are then converted to the digital signal by microcontroller on the same board.

Our system with low complexity is implemented by using only three LED sources and a single color sensor as photo detector. Furthermore, a multichannel VLC

using different colors and one board VLC receiver including single color photodetector and micro-controller is yet to exploit in the VLC area.

III. RESULTS

The transmitted medical signal is observed by the developed PC monitoring system. Heart rate is calculated by the use of R-R interval in the collected ECG data. Systolic blood pressure (SBP) and diastolic blood pressure (DBP) are calculated using the collected PPG data. Pulse Transit Time (PTT) is measured using the time difference between successive systolic peak and diastolic valley.

IV. CONCLUSION

Wavelength division multiplexing with the suggested receiver in VLC was successfully demonstrated by transmitting different data simultaneously using different color LEDs. No interference was shown in between the test by the use of this band pass color filter technique.

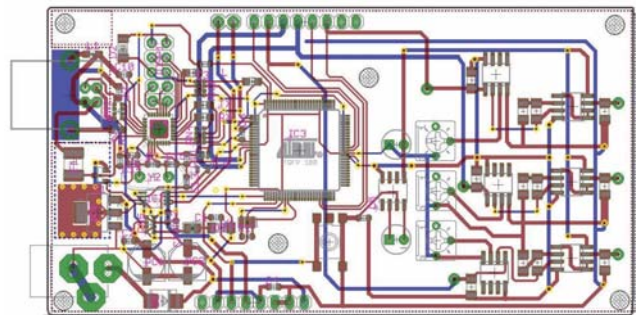


Fig. 1. Circuit design of one board VLC Receiver

REFERENCES

1. T. Komine, M. Nakagawa, Fundamental analysis for visible-light communication system using LED lights, *Consumer Electronics, IEEE Transactions on* 50.1 (2004): 100-107.
2. L. K. hui, H. S. Lee and W. Y. Chung, "Multichannel visible light communication with Wavelength Division for Medical Date Transmission," *Proc. of ICBEB 2015*, pp. 1-2, Aug. 2015

A New Motion Tracking System for Medical Imaging Using an Inertial Sensor and an Optical Sensor

J. S. Kim¹, Y. H. Choi², Y. K. Yoon¹, and Y. D. Son¹

¹Department of Biomedical Engineering, Gachon University, Incheon, Korea

²Department of Radiology, Samsung Medical Center, Seoul, Korea

E-mail: ydson@gachon.ac.kr

Abstract— A patient's unintended movement gives rise to crucial artifacts in medical imaging. We proposed a new motion tracking system by combining an inertial sensor and a CCD camera, which detect 3-DOF rotations and 3-DOF translations, respectively, with high precision. Based on obtained motion data from the proposed system, motion artifact can be effectively removed.

Keywords—motion tracking, medical imaging, inertial sensor, optical sensor

I. INTRODUCTION

General commercial motion tracking systems usually incorporated two CCD cameras in parallel positions to measure 6 DOF motion parameters[1]. However, in many medical imaging environments, such as MRI and PET, the measurements by two CCD cameras is not easily implemented due to the limited access of the system bore. Also, owing to the fact that the CCD camera shows poor accuracy for the rotation in some directions, an application of an inertial sensor is potent replacement for the rotational measurements. In this way, we proposed a simple and compact design to measure the 6DOF motion parameters with improved accuracy.

II. METHODS

Design of the system

Conventional motion capture systems are bulky, since they are usually comprised of two or more optical sensors. The novel design of the proposed system is composed of a single wearable device, which includes an inertial sensor (STT-IBS, STT systems, Spain), an optical marker, and an optical sensor (Fig. 1.), which is a CCD camera (XC-ES30, Sony, Japan). This design makes the system more compact and easily operable inside of a narrow bore.

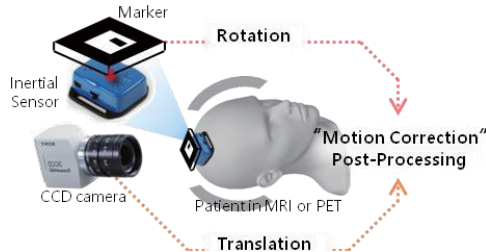


Fig. 1. Overall process of motion tracking system

Data calibration and evaluating precision

Estimation of 6 DOF parameters of the 3D translation and rotation from the CCD camera was implemented by the ARToolkit library[2]. Camera distortion was considerably calibrated by the iterative methods before measuring. Estimation of 3 DOF

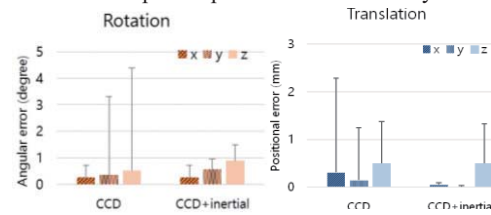
parameters of 3D rotation from the inertial sensor was implemented by the SDK provided by the vendor. In order to improve the performance, the poor rotational parameters of the CCD camera were replaced by the accurate values obtained by the inertial sensor.

The translational and rotational accuracy of each axes was measured repeatedly with the known distance by the precision linear positioning XY-axis stage (Kwonsys, Incheon, Republic of Korea) and by the house-made angular stage. The average errors and standard deviations were measured in each axis.

III. RESULTS

This new system data is compared to conventional CCD camera-only motion tracking system. A measured mean data is drawn with error bar and it showed dramatic improvement in accuracy for both rotation and translation. In two rotation axes, 8.8 and 6.4 times of more precise data was provided and there were greater improvements also in translation axes.

Table 1. Expected precision of the new system



IV. CONCLUSION

Unlike earlier motion tracking system, the newly proposed system provided both compact design and the improved accuracy with a CCD camera and an inertial sensor. With this wearable motion tracking system, lots of patient who could not stand as a medical imaging instrument's beneficent are free from unintended tremor and motion.

ACKNOWLEDGEMENT

This research was supported by Basic Science Research Program through the National Research Foundation of Korea (NRF) funded by the Ministry of Science, ICT & Future Planning (NRF-2015R1C1A1A 02037686) and the Creative Korea II (CK-II) Program through the National Research Foundation of Korea (NRF) funded by the Ministry of Education..

REFERENCES

1. B. J. Lopresti, A. Russo and D. W. Townsend, "Implementation and Performance of an Optical Motion Tracking System for High Resolution Brain PET Imaging", *IEEE Trans. Nuclear Sci.*, vol. 46, pp.2059-2067, 1999.
2. H. Kato and M. Billingham "Marker Tracking and HMD calibration for a video-based augmented reality conferencing system", 2nd Int'l Workshop on Augmented Reality, pp.85-94, 1999

Relation between anxiety, depression, and obesity in terms of dysfunctions in default mode network

B. Park¹ and H. Park^{2,3*}

¹Department of Electronic, Electrical and Computer Engineering, Sungkyunkwan University, Suwon, Korea

²School of Electronic Electrical Engineering, Sungkyunkwan University, Suwon, Korea

³Center for Neuroscience Imaging Research (CNIR), Institute for Basic Science, Suwon, Korea

E-mail: by6860@skku.edu, hyunjinp@skku.edu*

Abstract— Obesity is a medical condition that causes mental diseases. In this study, we found resting-state functional connectivity alterations in default mode network in people with obesity. Network features of default mode network showed significant correlation with anxiety and depression scores. In conclusion, people with obesity have brain alterations in default mode network and the alterations are associated with anxiety and depression.

Keywords— Obesity, resting-state functional connectivity, default mode network, anxiety, depression

I. INTRODUCTION

People with obesity frequently suffer from anxiety and depression than health weight (HW) subjects [1,2]. A previous neuroimaging study using resting-state functional magnetic resonance imaging (rs-fMRI) found default mode network (DMN) alterations in people with obesity [3].

In this study, we aimed to find dysfunctions in DMN using resting-state functional connectivity. Regions of interest (ROIs) were defined using group independent component analysis (ICA) [4]. Network features of DMN were correlated with clinical variables including anxiety and depression scores.

II. METHODS

A. Subjects and imaging data

We obtained rs-fMRI data from Nathan Kline Institute - Rockland Sample (NKI-RS) database. Total 30 subjects were divided into 15 HW and 15 people with obesity (Table 1). The groups were classified using waist-hip ratio (WHR). WHR equal or greater than 0.9 for male and 0.85 for female was considered as obese and WHR less than 0.85 for male and 0.8 for female was considered as health weight. Sex ratio and age did not showed significant differences ($p > 0.05$) between HW and people with obesity.

Table 1. Demographic data of HW and people with obesity

HW	People with obesity	p -value
----	---------------------	------------

Sex (M:F)	7:8	8:7	0.7263
Age	36.7 (10.0)	37.0 (10.7)	0.9443
WHR (M)	0.79 (0.05)	0.98 (0.12)	0.0015
WHR (F)	0.73 (0.04)	0.88 (0.02)	< 0.001

HW, Health weight; M, Male; F, Female

B. Image pre-processing

Rs-fMRI data were pre-processed using FSL software [5]. Non-brain tissue was removed and magnetic field bias was corrected. Head motion and slice timing correction was performed. Spatial smoothing with full width at half maximum (FWHM) of 6mm was applied. Intensity normalization with value of 10,000 and high-pass filter with cutoff of 100 second was applied. Functional images were registered onto the high resolution structural image, and then registered onto the Montreal Neurological Institute (MNI) standard space. All data were resampled to 3mm isotropic resolution.

C. Group ICA

Group ICA was performed using FSL's MELODIC package to generate spatial maps, called independent components (ICs). Subject-wise time series were estimated by regressing each IC to each subject's 4D data. The obtained ICs were correlated with reference resting state networks (RSNs), and functionally interpretable ICs were selected with threshold of 0.35 [6].

D. Network construction and connectivity analysis

Only functionally interpretable ICs were considered as ROIs (nodes). Correlation of the time series between two different nodes were computed and the values were entered into the matrix, called correlation matrix. Weighted network measure was constructed on the correlation matrices using soft thresholding [7], and then Fisher's r -to- z transformation was performed. Betweenness centrality (BC), the number of shortest paths between any two nodes that pass through that node was calculated on each node [8]. BC is a local network parameter indicating the importance of a node.

E. Correlation with clinical variables

The anxiety and depression scores were measured using Adult Self Report (ASR) and Trauma Symptom Checklist for Adults (TSC-40). The correlation between BC values and each score was performed.

F. Statistical analysis

Differences of BC values between HW and people with obesity were assessed using permutation tests 5,000 times randomly assigning HW and people with obesity. Differences in BC values were deemed significant if they did not belong to the 95% of the null distribution derived from the permutation tests ($p < 0.05$, corrected).

III. RESULTS

A. Spatial maps from Group ICA

Seventy ICs were automatically generated from FSL’s MELODIC package. Cross correlation between obtained ICs and reference RSNs was performed and only functionally interpretable fifteen ICs were remained (Fig. 1). We grouped remained ICs according to the reference ICs [6]. IC 1, 2, and 3 cover visual network. IC 4 covers DMN. IC 5 covers sensorimotor network. IC 6 covers auditory network. IC 7 covers executive control network. IC 8 and 9 cover frontoparietal network.

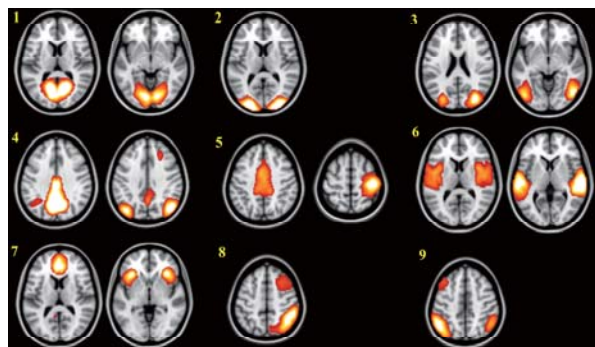


Fig. 1. Fifteen functionally interpretable ICs

B. Differences in connectivity

Group-wise differences between HW and people with obesity were assessed using weighted BC values. Two of fifteen ICs involved in DMN (IC 4) showed significant group-wise differences ($p = 0.0332$; $p = 0.0032$, corrected, respectively). IC 4 covers dorsolateral bilateral prefrontal cortex, posterior cingulate cortex, precuneus, and angular gyrus.

C. Correlation with clinical variables

Correlation between BC values of IC 4 and anxiety and depression scores were assessed (Table 2). One of two IC 4 showed significant ($p < 0.05$) correlation with anxiety and depression scores.

Table 2. Correlation between BC values of IC 4 and anxiety and depression scores

ASR anxiety and depression		TSC-40 anxiety		TSC-40 depression	
<i>r</i>	<i>p</i>	<i>r</i>	<i>p</i>	<i>r</i>	<i>p</i>
-0.4219	0.0202	-0.4836	0.0068	-0.5270	0.0028

IV. CONCLUSION

In this study, we found group-wise resting-state functional connectivity differences in DMN between HW and people with obesity. The BC values of DMN were significantly correlated with anxiety and depression scores. Our study demonstrated brain dysfunctions in DMN are related to anxiety and depression in people with obesity. Our results might provide brain functional information in finding connections between obesity and mental diseases.

ACKNOWLEDGEMENT

This study was supported by the Institute for Basic Science (grant number IBS-R015-D1).

REFERENCES

1. Eremis S, Cetin N, Tamar M, et al., “Is obesity a risk factor for psychopathology among adolescents?”, *Pediatrics International.*, vol. 46, pp. 296-301, 2004.
2. Strine TW, Mokdad AH, Dube SR, et al., “The association of depression and anxiety with obesity and unhealthy behaviors among community-dwelling US adults”, *General Hospital Psychiatry.*, vol. 30, pp. 127-137, 2008.
3. Tregellas JR, Wylie KP, Rojas DC, et al., “Altered Default Network Activity in Obesity”, *Obesity*, vol. 19, pp. 2316-2321, 2011.
4. Smith SM, Hyvärinen A, Varoquaux G, et al., “Group-PCA for very large fMRI datasets”, *Neuroimage.*, vol. 101, pp. 738-749, 2014.
5. Jenkinson M, Beckmann CF, Behrens TEJ, et al., “FSL”, *Neuroimage.*, vol. 62, pp. 782-790, 2012.
6. Smith SM, Fox PT, Miller KL, et al., “Correspondence of the brain’s functional architecture during activation and rest”, *Proceedings of the National Academy of Sciences of the United States of America.*, vol. 31, pp. 13040-13045, 2009.
7. Mumford JA, Horvath S, Oldham MC, et al., “Detecting network modules in fMRI time series: A weighted network analysis approach”, *Neuroimage*, vol. 52, pp. 1465-1476, 2010.
8. Rubinov M and Sporns O, “Complex network measures of brain connectivity: Uses and interpretations”, *Neuroimage*, vol. 52, pp. 1059-1069, 2010.

Implementation of anisotropic conductivity in canine brain using a combination of DTI and MREIT

N. Katoch¹, B.K. Choi¹, W.C. Jeong¹, S.Z.K. Sajib¹, H.J. Kim¹, O.I. Kwon¹ and E.J. Woo¹

¹Department of Biomedical Engineering, Kyung Hee University, Seoul, Korea

²Department of Mathematics, Konkuk University, Seoul, Korea

E-mail: ejwoo@khu.ac.kr

Abstract—Diffusion tensor magnetic resonance electrical impedance tomography (DT-MREIT) is one of useful method to visualize the anisotropic conductivity of biological tissues. We report anisotropic conductivity image of a canine brain reconstructed by combining the diffusion tensor with the position-dependent scalar factor from the MREIT scan.

Keywords— MRI, diffusion tensor, animal imaging, MREIT, anisotropy, conductivity.

1. INTRODUCTION

A new anisotropic conductivity imaging method called DT-MREIT developed by Kwon *et al* [1]. This method is based on the assumption that the conductivity tensor ($\mathbf{C} = \eta\mathbf{D}$) [3] is a scalar multiple of the water diffusion tensor (\mathbf{D}). After acquiring a diffusion tensor image, we used the measured MREIT data to determine the position-dependent scale factor η . In this paper, we present the experimental result of the canine brain anisotropy conductivity tensor map.

II. METHODS

A. MREIT Imaging setup

We attached four carbon hydrogel electrodes on the canine head and injected 10mA of electric current synchronized with MRI pulse sequence.

B. Diffusion tensor imaging

Single-shot spin-echo EPI (SS-SE-EPI) sequence was used to collect diffusion tensor image data.

C. Anisotropic conductivity estimation

Using the spoiled multi-gradient echo sequence, we measured magnetic flux densities. We determine the scale factor η based on the linear relation between diffusion tensor and conductivity tensor.

III. RESULT

We determine scale factor η by DT-MREIT algorithm [2]. Fig. 1(a) is the MR magnitude image of the canine head in the chosen imaging slice. Fig. 1(b) and (c) are the images of the induced magnetic flux densities $B_{z,1}$ and $B_{z,2}$. Fig. 1(d) is the color-coded fractional

anisotropic map from the diffusion tensor images. Fig. 2(a) shows the reconstructed scale factor. The scale factor clearly shows the position dependence. Fig. 2(b-d) plots the diagonal terms of the anisotropic conductivity tensor.

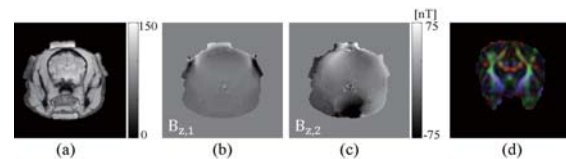


Fig. 1. (a) MR magnitude image. (b, c) $B_{z,1}$ and $B_{z,2}$ images subject to the horizontal and vertical current injections. (d) Color-coded fractional anisotropy map from the diffusion tensor images.

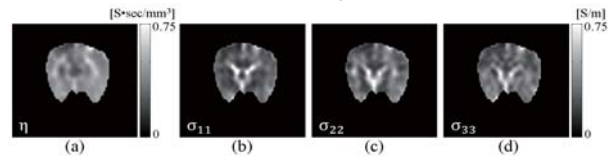


Fig. 2. (a) Reconstructed image of the scale factor. (b-d) Images of the diagonal terms of the anisotropic conductivity tensor.

IV. CONCLUSION

Combining both diffusion tensor and conductivity tensor information from DT-MREIT, we are able to reconstruct anisotropic conductivity image of the canine brain.

ACKNOWLEDGEMENT

This work was supported by the National Research Foundation (NRF) of Korea grant funded by the Korean government (MSIP) (No. 2013R1A2A2A04016066, 2014R1A2A1A09006320).

REFERENCES

1. J. K. Seo and E. J. Woo, "Electrical tissue property imaging at low frequency using MREIT," *IEEE Trans. Biomed. Eng.*, 61, 1390-9, 2014
2. Kwon, W. C. Jeong, S. Z. K. Sajib, H. J. Kim, and E. J. Woo, "Anisotropic conductivity tensor imaging in MREIT using directional diffusion rate of water molecules," *Phys. Med. Biol.*, 59, 2955-74, 2014.
3. D. S. Tuch, V. J. Wedeen, A. M. Dale, J. S. George, and J. W. Belliveau, "Conductivity tensor mapping of the human brain using diffusion tensor MRI," *Proc. Natl. Acad. Sci.*, 98, 11697-701, 2001.

Experimental mapping of electric field distribution in *ex vivo* anisotropic muscle tissue using DT-MREIT

W.C. Jeong¹, S.Z.K. Sajib¹, N. Katoch¹, B.K. Choi¹, H.J. Kim¹, O.I. Kwon² and E.J. Woo¹

¹Department of Biomedical Engineering, Kyung Hee University, Seoul, Korea

²Department of Mathematics, Konkuk University, Seoul, Korea

E-mail: ejwoo@khu.ac.kr

Abstract—We propose a novel MREIT technique to map the electric field in anisotropic as well as isotropic regions. We utilize the anisotropic conductivity estimation method where diffusion tensor imaging is combined with MREIT. This method show the electric field maps with a wider coverage than the previous method.

Keywords— Electric field, anisotropic conductivity, DTI, MREIT, electroporation.

I. INTRODUCTION

Estimation of electric field distribution from the knowledge of current density and conductivity, Kranjc et al. reported the feasibility of the MREIT technique [1]. However this method is based on the direct application of Ampere's law and Ohm's law without considering the effects of tissue anisotropy.

In this study, we performed DT-MREIT [2] imaging experiments using *ex vivo* muscle tissues to present the estimated electric field map in the anisotropic muscle tissue.

II. METHODS

A. imaging experiment setup

We inserted two silver-wire electrodes into the muscle tissue as shown in Fig. 1. Electric pulses were applied through the electrode pair with 100 V for 3T MREIT data collection. Single-shot spin-echo EPI (SS-SE-EPI) sequence was used to collect diffusion tensor image data. The multi-gradient echo pulse sequence was used to acquire MREIT data.

B. Current density estimation

Since we could acquire only one component B_z of the magnetic flux density $\mathbf{B} = (B_x, B_y, B_z)$, we adopted the projected current density method.

C. Anisotropic conductivity tensor estimation

We adopted the assumption about the linear relationship between the conductivity tensor and the water diffusion tensor. Therefore, we set the conductivity tensor as a scalar multiple of the water diffusion tensor.



Fig. 1. Experimental setup

III. RESULTS

Fig. 2(a) is the recovered electric field map using the anisotropic conductivity tensor. Fig. 2(b) shows the electric field map obtained by using the equivalent isotropic conductivity distribution.

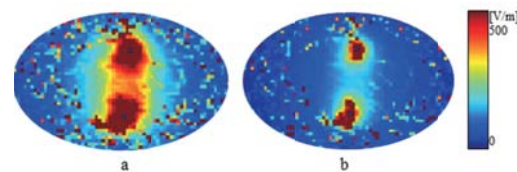


Fig. 2. Electric field maps determined by using (a) the anisotropic conductivity tensor and (b) the equivalent isotropic conductivity distribution.

IV. CONCLUSION

We found that the electric field map obtained by using the anisotropic conductivity tensor from the DT-MREIT method is different from the one obtained by using the equivalent isotropic conductivity from the conventional MREIT method.

ACKNOWLEDGEMENT

This work was supported by the National Research Foundation (NRF) of Korea grant funded by the Korean government (MSIP) (No. 2013R1A2A2A04016066, 2014R1A2A1A09006320).

REFERENCES

1. M. Kranjc et al., "In Situ Monitoring of Electric Field Distribution in Mouse Tumor during Electroporation," *Radiology.*, vol. 274, pp.115-123, 2015.
2. O.I. Kwon et al., "Anisotropic conductivity tensor imaging in MREIT using directional diffusion rate of water molecules," *Phys. Med. Biol.*, vol. 59, pp.2955-2974, 2014.

The Changes of Cerebral Hemodynamics during Dexmedetomidine Induced Sedation in a Rat Model

SH Kim¹, JY Bae¹, DH Choi¹, D.Cho¹, JS. Ham¹, JY. Park¹, BR. Lee¹, HI. Kim¹, TJ Shin³ and JG. Kim^{1,2*}

¹Department of Medical System Engineering, School of Information and Communications, Gwangju Institute of Science and Technology (GIST), Gwangju, South Korea

³Department of Dental Anesthesiology, School of Dentistry, Seoul National University, Seoul, Republic of Korea
E-mail: jaekim@gist.ac.kr

Abstract—Due to its function to provide sedation without causing a respiratory depression, the use of dexmedetomidine is increasing in clinics. In this study, we employed a near-infrared spectroscopy (NIRS) to observe cerebral hemodynamic changes induced by dexmedetomidine in rats to see if NIRS can be used to monitor the depth of sedation non-invasively in a real-time.

Keywords— Anesthesia, NIRS, Dexmedetomidine, hemodynamic change

I. INTRODUCTION

Dexmedetomidine is a highly selective and specific agonist at the alpha-2 adrenoceptor. [1] In this study, the cerebral hemodynamics from near infrared spectroscopy and the neuronal electrical activities from EEG were monitored from rats during a bolus injection of dexmedetomidine to see if NIRS provides a comparable information to that from EEG.

II. METHODS

A. NIRS system setup

Our NIRS system consists of a tungsten-halogen lamp (20W), a NIR range spectrometer, a computer and a pair of fiber-optic patch cables. A spectrum in the range of 730-850 nm were acquired at 3 Hz.

B. Animal model

In order to measure the NIR signals and EEG signals from the brain, we implanted optodes that we have developed into two positions (Right/Left frontal cortex) on the skull of the rat (Long-Evans, male, 400~500g).

C. Experimental Procedure

We acquired EEG and NIRS signals 20 minutes from freely moving rats as a baseline. Afterwards rats were administered dexmedetomidine (0.01 mg/kg) by intraperitoneal route, and the acquisition of EEG and NIRS signals were continued during the sedation and until the rat awakes.

D. Data Processing

The acquired intensity values at 5 wavelengths (730, 750, 800, 830, 850 nm) were used to estimate the concentration of deoxy- (RHb), oxy- (OHb) and total- (THb) hemoglobin changes in rat brain by using the modified Beer-Lambert's law. These hemodynamic changes were compared with the EEG signals.

III. RESULTS

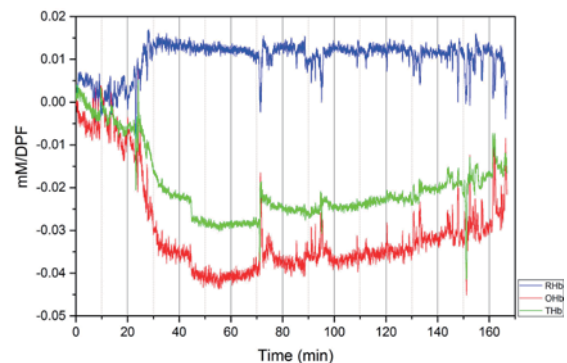


Fig. 1. The changes of NIR signals after dexmedetomidine i.p. administration.

Figure 1 shows the changes of oxy- (OHb), deoxy- (RHb), and total (THb) hemoglobin concentration after dexmedetomidine i. p. injection (0 min). The [OHb] decrease could be caused by either the suppression of cardiovascular function or the drop of cerebral metabolism.

IV. CONCLUSION

From this study, cerebral hemodynamic changes in rats were shown during the dexmedetomidine injection. Overall hemodynamic response is very different from isoflurane inhalation. Further investigations are needed to characterize the factors that affect hemodynamics.

ACKNOWLEDGEMENT

This work was supported by a grant from institute of Medical System Engineering at GIST.

REFERENCES

1. Doze, V. A., B. X. Chen, and M. Maze. "Dexmedetomidine produces a hypnotic-anesthetic action in rats via activation of central alpha-2 adrenoceptors." *Anesthesiology*, 71(1), (1989): 75-79.

Integration of laser with high intensity focused ultrasound for bladder tumor treatment: in vitro study

Van Phuc Nguyen,¹ Junghwan Oh,² and Hyun Wook Kang²

¹Interdisciplinary Program of Marine-Bio, Electrical & Mechanical Engineering, Pukyong National University, Busan, Korea

²Department of Biomedical Engineering and Center for Marine-Integrated Biomedical Technology (BK 21 Plus), Pukyong National University, Busan 608-737, Korea

E-mail: wkang@pknu.ac.kr

Abstract—The purpose of the current study was to investigate the potential treatment of bladder tumor by integrating laser system with high intensity focused ultrasound (HIFU). To identify the position of bladder tumor pre-and post-treatments, photoacoustic imaging was utilized. The results showed that the temperature rise improved by 1.6 and 3 folds, compared with laser or HIFU treatments. In vitro PA imaging vividly visualized the position of the bladder tumor as well as the thermally treated regions.

Keywords— Laser, photoacoustic imaging, bladder tumor, high intensity focused ultrasound, and thermal therapy

I. INTRODUCTION

Recently, laser ablation therapy and high intensity focused ultrasound (HIFU) have been investigated as noninvasive or minimally invasive thermal therapeutic methods to treat various types of bladder tumors [1]. However, the limitations of these techniques include unpredictable coagulation volume, low ablation rate, shallow optical penetration depth of 1-2 mm, which can lead to difficult treatments for larger size of lesions and essentially damage the adjacent tissue. Therefore, the aim of the current study was to demonstrate the feasible integration of laser with HIFU for bladder tumor treatment as a dual-therapeutic approach. Particularly, the dual-thermal treatments at lower power levels were tested to enhance the treatment temperature as well as to expand the degree of tissue denaturation for bladder tumor.

II. METHODS

An 80-W 532-nm clinical laser system (GreenLight™ PV, AMS, San Jose, CA, USA) and high intensity focused ultrasound were utilized for dual-thermal treatment on fresh bladder tumors. During the experiments, the HIFU transducer was operated in a burst mode with a pulse duration of 190 ms at 5 Hz and the applied intensity (I_H) ranged from 250 to 1100 W/cm². The applied laser power (P_L) varied from 0.17 to 0.90 W. Photoacoustic imaging (PAI) has been utilized as a guidance tool to locate the position of tumor before and after treatment with the dual heat sources.

III. RESULTS

Regardless of treatment method, the peak temperature linearly increased with I_H and P_L . According to Fig. 1(a), HIFU treatment increased the tissue temperature from 41 ± 4.1 °C at 250 W/cm² up to 56.8 ± 4.2 °C at 1100 W/cm². In the case of laser-combined HIFU treatment ($P_L = 0.9$ W), the peak temperature changed from 56.1 ± 6.2 °C at 250 W/cm² up to 68.9 ± 2.6 °C at 1100 W/cm², indicating that the overall temperature rise was approximately 15°C, compared to the HIFU sonication (Fig. 1(a)). Similarly, the laser-integrated HIFU treatment induced the temperature elevation from 51.6 ± 3.0 °C at 0.17 W to 63.6 ± 3.9 °C at 0.90 W whereas the laser treatment increased the temperature from 33.8 ± 0.5 °C at 0.17 W to 45.2 ± 0.7 °C at 0.90 W (Fig. 1(b)). Thus, the additional temperature increase from the dual-thermal treatment was around 18 °C. Figure 1(c) demonstrates PA images of bladder samples before and after the dual-thermal treatment. The PA image contrast from the coagulated tissue was 34 and 8 times high as those from background and untreated tissue, respectively.

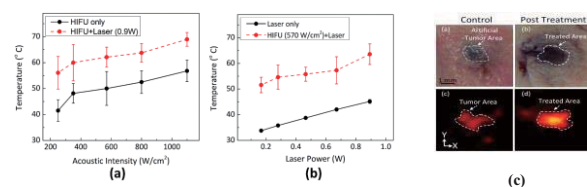


Fig. 1. Temperature changes as function of: (a) acoustic intensity of HIFU, (b) laser power, and (c) Photoacoustic imaging of tissue acquired before and after treatment.

IV. CONCLUSION

The proposed PAI-guided dual-treatment can be a feasible therapeutic modality to thermally treat bladder tumor in a safe and effective manner

ACKNOWLEDGEMENT

This work was supported by a grant from Marine Biotechnology Program (20150220) funded by Ministry of Oceans and Fisheries, Korea.

REFERENCES

1. T.R.W. Herrmann, E.N. Liatsikos, U. Nagele, O. Traxer and A.S. Merseburger, "EAU Guidelines on Laser Technologies," Eur. Urol., vol. 6, pp. 783-795, 2012.

Near-infrared autofluorescence imaging of parathyroid glands for surgical guidance

Seo Hyun Song^{1,4}, Sung Won Kim^{1,2}, Hyoung Shin Lee^{1,2}, Chulho Oak^{1,3}
Kang Dae Lee^{1,2}, Yeh-Chan Ahn^{1,4}

¹Innovative Biomedical Technology Research Center, College of Medicine, Kosin University, Busan, Korea

²Department of Otolaryngology-Head and Neck Surgery, College of Medicine, Kosin University, Busan, Korea

³Department of Internal Medicine, College of Medicine, Kosin University, Busan, Korea

⁴Department of Biomedical Engineering and Center for Marine-Integrated Biomedical Technology, Pukyong National University, Busan, Korea

E-mail: ahny@pknu.ac.kr

Abstract—In this study, we present intraoperative near-infrared autofluorescence imaging system in order to identify the precise location of parathyroid and distinguish the parathyroid from thyroid and surrounding tissues such as fat or connective tissues.

Keywords—Autofluorescence, Parathyroidectomy, Near-infrared, Parathyroid, Intraoperative.

I. INTRODUCTION

Patients having thyroid cancer have thyroidectomy and central compartment neck dissection, CCND. During the operations, surgeons should preserve the parathyroid gland to maintain calcium homeostasis. However, it is difficult to distinguish the parathyroid gland from thyroid and surrounding tissues with the naked eye. [1] So, we present near-infrared autofluorescence imaging system using that the parathyroid has intrinsic NIR fluorophore. [2]

II. METHODS

Nine patients having thyroid cancer were included in this study. The patients had thyroidectomy and central compartment neck dissection, CCND. Seventeen parathyroid glands were measured. Near-infrared autofluorescence imaging system was composed of 780nm collimated led light source with excitation filter, DSLR camera with emission filter and IR illuminator. IR illuminator was used for checking the anatomical positions of the parathyroid from surrounding tissues.

III. RESULTS



Figure 1.

Figure 1. (a) Visible image of right parathyroid and thyroid using DSLR camera without IR filter.

(b) autofluorescence and NIR image of right parathyroid and thyroid. (c) autofluorescence image of right parathyroid and thyroid.

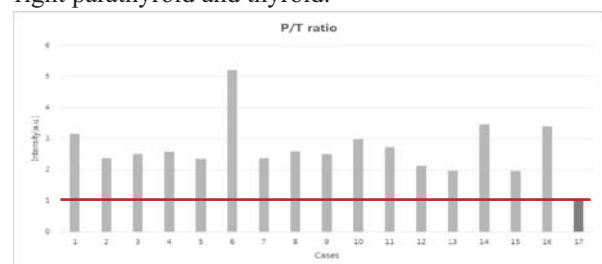


Figure 2.

Figure 2. The ratio as ratio of area averaged autofluorescence intensity of parathyroid to area averaged fluorescence intensity of the thyroid. Case 17 was the case of parathyroid adenoma.

The minimum of P/T ratio was 1.95 and maximum of P/T ratio was 5.20 except for the case 17 of parathyroid adenoma. The P/T ratio of case 17 was 1.02. Moreover, we obtained 100% sensitivity.

IV. CONCLUSION

We could obtain the NIR autofluorescence images of the parathyroid even it was covered by fat or connective tissues and even it was located at unusual locations. It offers good method to determine unambiguous locations of the parathyroid for surgeons in the operating room.

ACKNOWLEDGEMENT

This research was supported by a grant from Marine Biotechnology Program (20150220) Founded by Ministry of Oceans and Fisheries, Korea

REFERENCES

1. Mariani G, Gulec SA, Rubello Det al. Preoperative localization and radioguided parathyroid surgery. *Journal of Nuclear Medicine* 2003;44:1443-1458.
2. Paras C, Keller M, White L, Phay J, Mahadevan-Jansen A. Near-infrared autofluorescence for the detection of parathyroid glands. *Journal of Biomedical Optics* 2011;16:067012.

Efficiency of indocyanine green in in-vivo photoacoustic imaging with animal tumor models

Jung-Eun Park^{1,2,3}, Nguyen Van Phuc^{1,2}, Yu-Gyeong Chae^{1,2,3}, Yeh-Chan Ahn^{1,2,3*}, Junghwan Oh^{1,2}, Hyun Wook Kang^{1,2}, Sung Won Kim^{3,4}, Chulho Oak^{3,5}, Je-Hun Kim^{3,4} and Eun-Kee Park^{3,6}

¹Department of Biomedical Engineering, Pukyong National University, Busan, Republic of Korea

²Center for Marine-Integrated Biomedical Technology, Pukyong National University, Busan, Republic of Korea

³Innovative Biomedical Technology Research Center, Busan, Republic of Korea

⁴Department of Otolaryngology, College of Medicine, Kosin University, Busan, Republic of Korea

⁵Department of Internal Medicine, College of Medicine, Kosin University, Busan, Republic of Korea

⁶Department of Medical Humanities and Social Medicine, College of Medicine, Kosin University, Busan, Republic of Korea

*E-mail: ahnyc@pukyong.ac.kr

Abstract— Photoacoustic (PA) imaging is known as a useful way to image microvasculature with optical contrast and ultrasonic penetration depth. In this study, we developed animal models with anaplastic thyroid (AT), conjunctival, tunica vaginalis (TV) tumors that were important due to its high aggressiveness, a relationship with HIV infection, and fatal mesothelioma caused by exposure to asbestos, respectively. Then, we used PA imaging as a feasible diagnostic tool for the diseases. PA imaging was able to show tumor-angiogenesis at an early state with/without Indocyanine green (ICG). PA images were compared to ultrasonic (US) and histologic images.

Keywords— In-vivo photoacoustic imaging, Anaplastic thyroid tumor, Conjunctival carcinoma, Tunica vaginalis tumor

I. INTRODUCTION

Importance of early diagnosis of cancers has been steadily posed with various imaging modalities. We chose PA imaging, which has enough imaging depth and image contrast to microvasculature. One of tumor models we made before was AT carcinoma, which had aggressiveness to make diagnosis difficult [1], another was conjunctival carcinoma that was known as a tumor related with HIV infection and UV radiation [2], and the other was TV tumor known as one of mesotheliomas, which is fatal and hard to study due to long latent period [3]. With these cases, we wanted to confirm the usefulness of PA imaging/ICG for diagnosis.

II. METHODS

For these experiments we chose a lab-made dark-field reflection-mode PA imaging system. It was composed of a Q-switched Nd:YAG laser (5ns pulse duration at 10Hz), a tunable OPO laser, and a single-element ultrasound transducer (5MHz). The irradiated beam had a wavelength of 780nm and a power within ANSI safety limit. Then, we used a Matlab code to reconstruct images. The depth and transverse resolutions were 144 and 590 μ m, respectively. We also used a commercial

US system and got histology to know structure in each case.

III. RESULTS

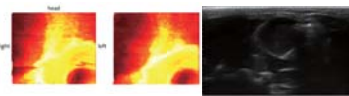


Figure 1. PA images with AT carcinoma at 3mm down from the surface and US image in 2D

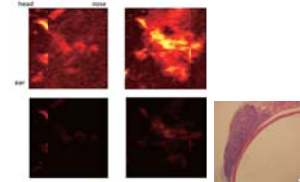


Figure 2. PA images with conjunctival carcinoma at 2mm down from the surface and histology

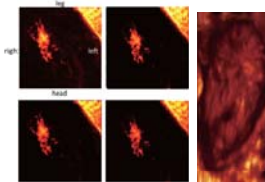


Figure 3. PA images with TV tumor at 3mm down from the surface and US image in 3D

Figure 1, 2 and 3 are in-vivo PA images at 780nm (the left images are without ICG/the right are with ICG, and the upper images are before normalized/the lower are normalized images), ex-vivo US images or histology, which show usefulness of PA imaging to distinguish the tumor from the normal tissue. Especially, in case of conjunctival carcinoma ICG makes a dramatic change. In the future study we should develop our system to fit in in-vivo real time imaging and co-locate PA images with structure images. Our next work is to get PA images at different wave lengths.

ACKNOWLEDGEMENT

This research was supported by grants from National Research Foundation of Korea (2013R1A1A4A01011-631) and Marine Biotechnology Program (20150220) funded by Ministry of Oceans and Fisheries, Korea.

REFERENCES

1. D. Giuffrida and H. Gharib, "Anaplastic thyroid carcinoma: Current diagnosis and treatment," *Annals of Oncology* 11:1083-1089, 2000.
2. KM Waddell, S Lewallen, et al. "Carcinoma of the conjunctiva and HIV infection in Uganda and Malawi," *British Journal of Ophthalmology*, 1996;80:503-508.

3. Eugen Plas, Claus R. Ried and Heinz Pflüger,
“Malignant mesothelioma of the tunica vaginalis
testis”, *Cancer*, vol. 83, Issue 12, pages 2437-2446,
1998

Quantification of Tissue Clearing Techniques with Optical Coherence Tomography

Eunji Cho¹, Sunwoo Jung^{2,3}, Junwon Lee², Eunjung Min² and Woonggyu Jung^{2,3*}

¹ Department of Biomedical Science, Ulsan National Institute of Science and Technology, Ulsan, Republic of Korea

² Department of Biomedical Engineering, Ulsan National Institute of Science and Technology, Ulsan, Republic of Korea

³ Center for Soft and Living Matter, Institute for Basic Science (IBS), Ulsan, Republic of Korea

E-mail: wgjung@unist.ac.kr

Abstract— Tissue clearing is an emerging technique to resolve light penetration issue in optical deep brain imaging, because the limited penetration is significantly extended by reducing light scattering. However, there has been no research to quantify the enhancement of light transmission. Hence, we take advantage of optical coherence tomography (OCT) to analyze the several tissue clearing techniques quantitatively. In this study, it is expected that this analysis would facilitate quantitative use of optical clearing technique.

Keywords—Tissue Clearing, Optical Coherence Tomography, Quantification, Deep Brain Imaging

I. INTRODUCTION

Optical imaging modalities have been essentially used to identify neural function in the past decade. However, they have inherent limitation of penetration depth because of light scattering. To overcome this limitation, optical clearing has been presented as a key solution since it results in deeper penetration by reducing scattering. Up to now, a number of tissue clearing techniques have been developed. Unfortunately, there has been no specific study on assessment of different techniques. Hereby, we propose a method to quantitatively evaluate the existing techniques based on optical coherence tomography (OCT). OCT is a novel imaging technique which can perform volumetric imaging in high resolutions. In this study, we monitor the diverse tissue clearing effect to find out optimal clearing method.

II. METHODS

A. Sample Preparation

8-week-old C57BL/6 mice were anesthetized and then transcardially perfused with PBS followed by 4% PFA. For post-fixation, dissected brain were incubated in the 4% PFA for 1 day. Fixed brains were embedded in 2-3% agarose gel and then sliced with thickness of 3 mm. For tissue clearing, brain slices were immersed in the clearing solution for 2 days.

B. OCT System

Spectral-Domain OCT (SD-OCT) operating at the center wavelength of 1310 nm and bandwidth of 70 nm was utilized. It results in axial resolution and lateral resolution of 10 μm , respectively.

III. RESULTS

OCT demonstrates that light intensity varies depending on the clearing technique and brain region. Figure 1A illustrates that Clear^T allows the deeper light penetration. In figure 1B, we measured depth profile to analyze penetration depth quantitatively. The profiles indicate light intensity is maintained better than controlled one, and the tissue clearing was more prominent in Corpus Callosum.

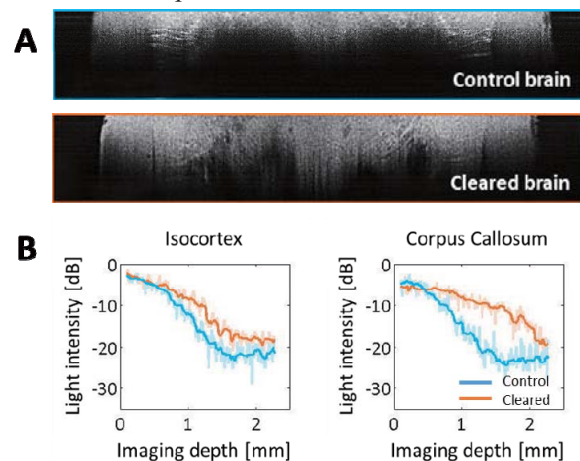


Figure 1. (A) OCT cross-sectional image of control and cleared brain, (B) OCT depth profile in different region

IV. CONCLUSION

In a result, we confirmed that optical clearing improves the imaging depth, and tissue clearing effect differs depending on brain region. This study demonstrates that tissue clearing enables us to achieve deep brain imaging and OCT is capable of quantifying the enhancement of light transmission. Furthermore, it is expected that this study will be general approach of tissue clearing evaluation for deep brain imaging.

ACKNOWLEDGEMENT

This work was supported by the ICT R&D program of MSIP/IITP. (R0190152072)

REFERENCES

1. Chung, K, et al. "Structural and molecular interrogation of intact biological systems." Nature 497, 332-337, 2013

Three-Dimensional Visualization Hair Follicle and Quantification using Optical Coherence Tomography

Myeongseo Yoon¹, Songye Baek¹, Youjin Ahn¹, Junwon Lee¹, Juyoung Oh²,
Andrey Vavilin¹ and Woonggyu Jung^{1,3}

¹Department of Biomedical Engineering, Ulsan National Institute of Science and Technology, Republic of Korea

²Department of Computer Engineering, Ulsan National Institute of Science and Technology, Ulsan, Republic of Korea

³Center for Soft and Living Matter, Institute for Basic Science (IBS), Ulsan, Republic of Korea

E-mail: wgjung@unist.ac.kr

Abstract—At the dermis of the skin structure, hair follicles are located and provide several essential functions in our body. Unfortunately, existing diagnostic tools are hard to examine the diseases and observe the structure at the hair follicles. Optical coherence tomography (OCT) has been widely used in various fields due to its non-invasive imaging method. In here, we used swept-source optical coherence tomography (SS-OCT) to acquire the volumetric image of hair follicle structures and analyze the pore size through quantification of the OCT data. Through this research we anticipate that our result would be used in various fields in dermatology.

Keywords—Optical coherence tomography, Skin structure, Dermatology, High-resolution imaging.

I. INTRODUCTION

Hair follicle is the cutaneous tissues which makes a hair to situate in an epidermal tube. It helps to regulate the heat of the body, and secretes sebum by joining with sebaceous gland. Recently, several studies have found the correlation between aging and follicle structures [1]. However, diseases related to morphological changes such as folliculoma and folliculitis are hard to diagnose with existing diagnostic tools non-invasively. From the decades, OCT has been introduced to dermatology to image the structure of dermis in non-invasive method. Therefore, in this study, we utilized high-resolution SS-OCT system to obtain three-dimensional(3D) image of normal skin and hair removed skin of mouse models in a time basis, and quantified the images.

II. METHODS

8 weeks old male C57BL/6 mice were used. Mice were removed their hair on the back side. After 0, 3, 7, and 14 days hair removal, we took the *in vivo* and *ex vivo* skin samples from the mice.

Swept-source laser centered at 1310nm with bandwidth of 100nm was used in SS-OCT system. The system enables 50kHz line scanning and generates 3D image that comprises $1024 \times 500 \times 768$ pixels over field of view of $5 \times 5 \times 1.5$ mm³. The optics in the system was specially designed for follicle imaging.

III. RESULTS

We visualized the *in vivo* and *ex vivo* volumetric skin structure from various mice, and quantified the size and the number of hair follicles from crosses sectional images of mouse skin.

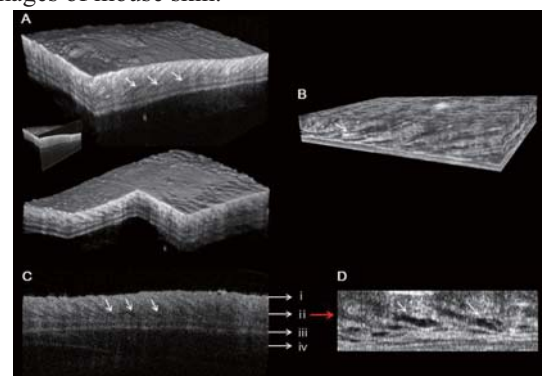


Fig. 1. (A) *In-vivo* 3D skin OCT image. The white arrows indicate hair follicles. (B) *Ex-vivo* 3D high-resolution OCT image (10 \times). (C) *In-vivo* 2D skin OCT image. (i) Epidermis, (ii) dermis, (iii) muscle, and (iv) subcutaneous tissue. (D) *Ex-vivo* 2D high-resolution OCT image (10 \times).

IV. CONCLUSION

In this research, we achieved volumetric images and quantification using SS-OCT system. The result in here provides the information to understand the physical, quantitative, and qualitative change of the follicle structures over time. Furthermore, 3D visualization and quantification show the potential of application to the dermatology researches related to the skin diseases and can be utilized to verify the effects of cosmetics products on hair follicle.

ACKNOWLEDGEMENT

This work was supported by a grant of the Korean Health Technology R&D Project (HN13C0078) through Ministry of Health & Welfare.

REFERENCES

1. Giangreco, Adam, et al. "Epidermal stem cells are retained *in vivo* throughout skin aging." *Aging cell* 7.2 (2008): 250-259.

Intravascular Ultrasonic-Photoacoustic (IVUP) Endoscope with 2.2-mm-diameter Catheter for Atherosclerotic Plaque Detection in Pig Artery

Q. N. Bui¹, K. K. Hlaing¹, Yun-Ok Oh¹, Xiao Feng Fan¹ and Junghwan Oh^{2,3}

¹Interdisciplinary Program of Biomedical Mechanical & Electrical Engineering, Pukyong National University, Busan, South Korea

²Department of Biomedical Engineering, Pukyong National University, Busan, South Korea

³Center of Marine-Integrated Biomedical Technology (BK21 Plus), Pukyong National University, Busan, South Korea

E-mail: jungoh@pknu.ac.kr

Abstract—In this study, by integrating a single-element, high-frequency intravascular ultrasound (IVUS) imaging catheter with a multi-mode optical fiber, we developed a 2.2-mm diameter integrated intravascular ultrasonic-photoacoustic (IVUP) imaging catheter to provide the spatial and functional information of light distribution in a turbid sample. Simultaneously, IVUS imaging was co-registered to intravascular photoacoustic (IVPA) imaging to reconstruct 3D volumetric sample images. In a phantom study, a polyvinyl alcohol tissue-mimicking arterial vessel phantom with macrophages loaded with indocyanine green (ICG) was used to demonstrate the feasibility of mapping the biological dye, which is used in cardiovascular diagnostics. For *ex vivo* studies, excised sample of a pig artery with ICG-labeled macrophages was utilized to target the biomarkers present in the atherosclerotic plaques with the proposed hybrid technique. The IVUP imaging clearly reveals both the structure and composition of the samples. The results indicated that the IVUP endoscope with the 2.2-mm diameter catheter could be a useful tool for medical imaging.

Keywords— Three-dimensional image processing, imaging systems, endoscopic imaging, photoacoustic imaging, ultrasound imaging

I. INTRODUCTION

Intravascular ultrasound (IVUS) imaging of atherosclerosis is extremely important for detection and characterization of vulnerable plaques. Recently, intravascular photoacoustic (IVPA) imaging has been used to differentiate the composition of biological tissues with high optical contrast and ultrasonic resolution [1, 2]. The combination of these imaging techniques could provide morphological information and molecular screening to characterize of vulnerable plaques, which helps physicians to ensure vital therapeutic and prognostic significance for patients with early diagnosed atherosclerosis before commencing therapy [2].

II. METHODS

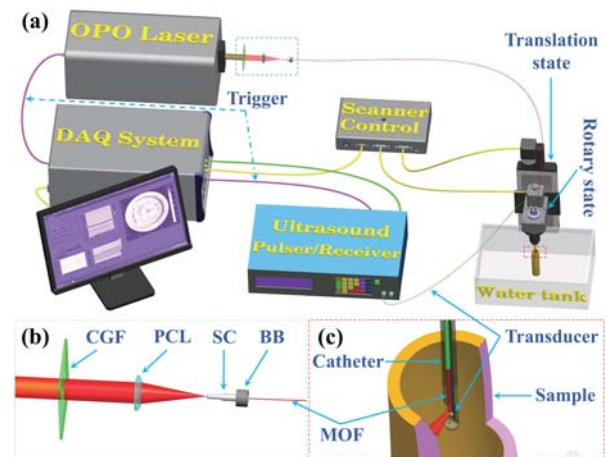


Fig. 1. Illustration of IVUP imaging system. (a) Overall structure of the experimental setup for IVUP imaging in *ex vivo*. (b) Enlarged view of the green dashed rectangle in (a). (c) Enlarged view of the red dashed rectangle in (a). DAQ: data acquisition; OPO: optical parametric oscillator; CGF: colored glass filter; PCL: plano-convex lens; SC: SMA connector; BB: ball bearing; MOF: multi-mode optical fiber.

III. RESULTS

A. IVUP imaging of a vessel phantom

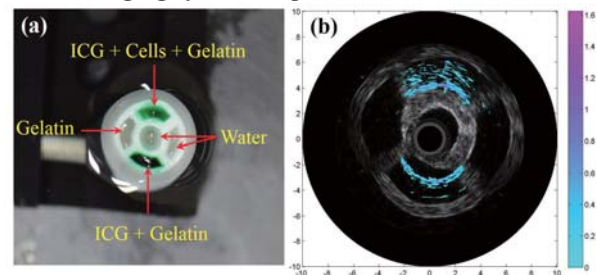


Fig. 2. (a) Top view of PVA phantom with four compartments. (b) IVUP image at 800-nm wavelength. Color-map: standard cool. Measurement unit: mm

B. IVUP imaging of a tissue sample in ex vivo

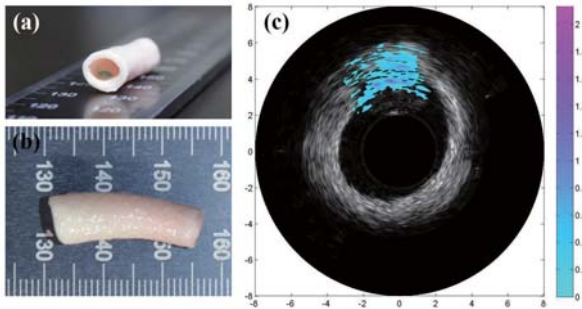


Fig. 3. IVUP imaging of 8-mm pig artery with ICG-loaded macrophages injected at 800-nm wavelength. (a) Side views. (b) Top views. (c) IVUP images. Color-map: standard cool. Measurement unit: mm

C. 3D IVUP volumetric image of the pig artery

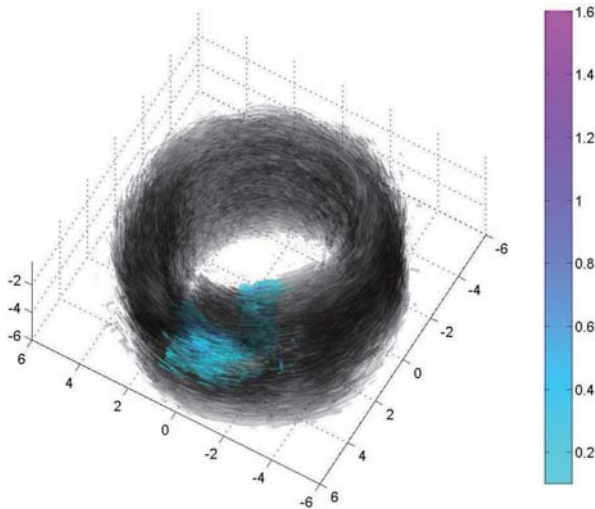


Fig. 4. 3D volumetric IVUP image of 8-mm pig artery injected with ICG-loaded macrophages. Color-map: standard cool. Measurement unit: mm

IV. CONCLUSION

IVUP imaging provides a way of visualizing the spatial and functional information on light distribution in atherosclerotic lesions. We successfully developed custom designed IVUP endoscope, and demonstrated its potential application for mapping biological dye in *ex vivo*. The results of this study indicated that the IVUP endoscope could produce IVUP images of internal organ, detect and localize certain biomarkers in the atherosclerotic plaques based on both their structure and functional composition. According to the ability adjust the catheter, the IVUP endoscope system could be performed on samples of up to 20 mm in diameter. Further studies will be conducted on rats to demonstrate its *in vivo* imaging capability for certain clinical applications.

ACKNOWLEDGEMENT

This research was supported by a grant from Marine Biotechnology Program (20150220) funded by Ministry of Oceans and Fisheries, Republic of Korea.

REFERENCES

1. E. De Montigny, "Photoacoustic Tomography: Principles and applications," (OCIS, 2011).
2. N. Q. Bui, K. K. Hlaing, V. P. Nguyen, T. H. Nguyen, Y.-O. Oh, X. F. Fan, Y. W. Lee, S. Y. Nam, H. W. Kang, and J. Oh, "Intravascular ultrasonic-photoacoustic (IVUP) endoscope with 2.2-mm diameter catheter for medical imaging," *Computerized Medical Imaging and Graphics* **45**, 57-62 (2015).

Comparison between interstitial LLLT and vibration therapy on tibial defect

S. Lee¹, S. Jang¹, D. Hwang¹, S. You¹, M. Ha¹, J. Park¹, H. Kim¹ and B. Jung^{1*}

¹Department of biomedical engineering, Yonsei Univ., Wonju, Republic of Korea

E-mail: bjung@yonsei.ac.kr

Abstract—Tibial defect is fatal musculoskeletal disorder which make patient passive and painful. Low level laser therapy (LLLT) and vibration therapy are already known as very convenient and good method for treatment. In this study, we compared between interstitial LLLT and vibration therapy on tibial defect. We suggest that interstitial LLLT may affect early phase of bone regeneration and can be used in various musculoskeletal disease.

Keywords— Bone, Bone fracture, Bone defect, musculoskeletal disorder, Vibration, Vibration therapy, Laser, Light therapy, LLLT.

I. INTRODUCTION

In case of injury during exercise, tibial fractures are easy to occur suddenly. If tibial defect do not recover in early phase, nonunion may occur which needs costly treatment. So, many studies including light and vibration therapy for bone regeneration are going to figure out fast bone healing in early phase. This study shows that the interstitial low level therapy is effective way to cure bone defect.

II. METHODS

A. Interstitial Low Level Laser Therapy

Scattering and absorption obstruct musculoskeletal therapy which need accurate light delivery. In this study, we use Interstitial Low Level Laser Therapy (ILLLT) which can overcome limit of light penetration depth.

B. Vibration Therapy

Vibration therapy was performed by using vibration therapy device (SONIX, SONICWORLD Co., Ltd.).

C. Animal Experimental design

Twelve experimental animals (mouse, C57BL/6) were divided into three groups: animals that applied ILLLT (660nm; power 20mW; total energy 10J), animals that applied VT (45Hz; intensity 40; 10min) and animals not treated. All animals were performed surgical treatment to make tibial defect on right crest of tibia. Defect size was 1mm diameter circle. ILLLT group and VT group were treated once per 48 hours. Bone volume and X-ray attenuation coefficient were measured on 14th day by u-CT.

III. RESULTS

A. Bone volume and X-ray attenuation coefficient

Results show that bone volume of ILLLT group after 2 weeks was more improved than VT group and control. Bone volume of ILLLT group was about 2 times bigger than control. After 2 weeks, X-ray attenuation coefficient of control group was 0.023345mm^{-1} . VT's was 0.024503mm^{-1} and ILLLT's is 0.025085mm^{-1} . They had very slight differences among them, but ILLLT group had more improvement than other groups. Also, u-CT images show that ILLLT group have more structural improvement than control.

IV. CONCLUSION

These results suggest that interstitial LLLT through laser needle system may more positively affect early healing phase of bone than vibration therapy. And interstitial LLLT can be used in various musculoskeletal disease.

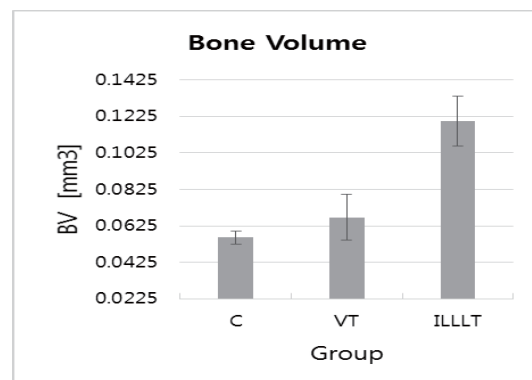


Fig. 1. Bone volume of each group measured by u-CT

ACKNOWLEDGEMENT

This research was supported by the Leading Foreign Research Institute Recruitment Program through the National Research Foundation of Korea (NRF) funded by the Ministry of Science, ICT & Future Planning (2010-00757).

REFERENCES

1. A. P. Lirani-galvao, et al, "Comparative study of how low-level laser therapy and low-intensity pulsed ultrasound affect bone repair in rats," *Photomedicine and Laser Surgery*, vol. 24, pp. 735-740, 2006.

Feasibility of simulating vessel phantom using laser speckle imaging system

S. K. Yu¹, M. J. Ha¹, J. H. Park¹, S. Y. Lee¹, S. G. Jang¹ and B. J. Jung^{1*}

¹Department of biomedical engineering, Yonsei university wonju campus, Wonju, Korea, Republic of
E-mail:bjung@yonsei.ac.kr

Abstract—Double layer optical tissue phantom (DLOTP) was designed with silicone tube array to simulate epidermis-dermis structure including blood vessel. In order to determine the functional feasibility of the DLOTP, a laser speckle imaging system was used to visualize the flow in the tube.

Keywords— Optical tissue phantom, Vascular modeling, Laser speckle

I. INTRODUCTION

Optical tissue phantoms (OTPs) mimicking human skin tissue have been widely used and studied in Biomedical optics. However, many of them just focused on mimicking optical properties of human tissue. This study suggests OTP model simulating both optical property and structure of epidermis-dermis skin structure including blood vessel. Finally, a laser speckle contrast index (LSCI) images were analyzed to assess the feasibility of the DLOTP

II. METHODS

A. Optical tissue phantom

Epidermis-dermis OTPs including 1mm and 2mm-inner-diameter silicone tubes were fabricated with the fabrication method introduced in previous study¹.

B. Simulating blood circulation

Milk was used as the substitute of blood, then circulated through a peristaltic pump which was connected to the tube array.

C. LSCI system

An 830nm diode laser was used to the light source and Sequential 30 laser speckle images were captured at 20ms exposure time, and then LSCI as a function of the velocity of flow (at every 10rpm) was calculated.

$$K = \frac{\sigma_s}{\langle I \rangle} \quad (1)$$

III. RESULTS AND CONCLUSION

LSCI images were reconstructed with calculated LSCI values as shown in Fig. 1.

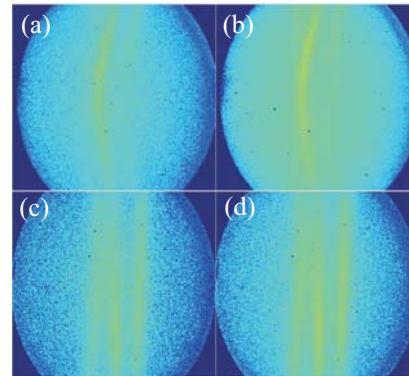


Fig. 1. LSCI images indicating the differences in flow velocity and the diameter of tube. (a) 40rpm and 1mm, (b) 80rpm and 1mm, (c) 40rpm and 2mm, (d) 80rpm and 2mm

Fig. 1 shows LSCI images of OTPs with different thickness tubes at 40 and 80rpm. The thinner tube OTP shows more diffused speckle signal around the tube than the thicker. However, speckle signal showed more clear array shadow with higher speed.

In this study, we assessed the feasibility of DLOTP including tube array for simulation of blood circulation. We expect that OTP mimicking blood vessel can be practically utilized with quantified technique as a further study.

ACKNOWLEDGEMENT

This research was financially supported by the Ministry of Trade, Industry & Energy(MOTIE), Korea Institute for Advancement of Technology(KIAT) and Gyeongbuk Institute for Regional Program Evaluation(DGIRPE) through the Regional Specialized Industry Development

REFERENCES

1. Jihoon Park *et al.*, "Fabrication of double layer optical tissue phantom by spin coating method", Proc. Of SPIE 8583, 85830G, 2013.
2. David A. Boas and Andrew K. Dunn, "Laser speckle contrast imaging in biomedical optics", *Journal of Biomedical Optics* (2010).

A brain connectivity analysis under anesthesia using transfer entropy

J.Ham¹, D.Cho¹, D.H.Choi¹, S.H.Kim¹, Jae G.Kim^{1,3}, H.I.Kim^{1,2} and B.Lee^{1,2}

¹Department of Medical System Engineering, ²School of Mechatronics, ³School of Information and Communication
Gwangju Institute of Science and Technology (GIST), Gwangju, South Korea

E-mail: trueham@gist.ac.kr

Abstract—Currently, the mechanism of loss of consciousness remains unclear despite of its importance. To investigate this mechanism, we applied transfer entropy: a kind of brain connectivity analysis. In this study, we observed the change of brain connectivity depending on the depth of anesthesia using transfer entropy.

Keywords—Electroencephalogram (EEG), Effective connectivity, Transfer Entropy (TE), Depth of anesthesia (DOA), Loss of consciousness (LOC)

I. INTRODUCTION

In anesthesiology, it is an important issue to investigate the mechanism of loss of consciousness (LOC) caused by anesthesia. For this reason, a lot of research about this field is still in progress; however, the mechanism of LOC remains unclear [1]. In order to identify this mechanism, various brain connectivity analyses using electroencephalogram (EEG) are generally used. Therefore, we implanted electrodes on rat brain for EEG recording and analyzed EEG data using transfer entropy (TE): a model-free measure based on information theory [2]. In this study, this method is utilized to determine the change of brain connectivity depending on the concentration of anesthetic agent.

II. METHODS

A. Animal model

Four adult male Long-Evans rats (12 to 16 weeks; 400 to 500g) were used in this experiment. 4 micro-electrodes and 2 depth-electrodes were implanted on the right/left frontal area, parietal area and thalamus for EEG recording.

B. Experimental procedure

In order to record EEG, we applied self-developed hardware (Sampling Frequency: 300Hz, Gain: 5000). Before the EEG recording, rats were anesthetized with isoflurane (3% induction and 2.5% maintenance). Then, during anesthetic state, the EEG was recorded three times at the concentration of 2.5%, 1% and 2.5% again, with 5 minutes in each concentration. In addition, before and after anesthesia, EEG was recorded for 30 minutes in order to obtain reference signal.

C. Data processing

To investigate the change of brain connectivity, we calculated TE from the raw signal, and filtered signals including beta and gamma frequency bands. When TE was obtained, we set 4 parameters: trials = 7, time delay = 20, embedding dimension = 10, number of neighbors = 4 [2].

III. RESULTS

Fig.1 shows the TE values of beta, gamma and raw signal. We found that the alteration of TE along with varied concentration was noticeable in the gamma frequency band. Especially, the direction of connectivity between thalamus and frontal area in awoken state was reversed in the anesthetic state in the gamma frequency band. However, this reversed pattern was not observed in the relation between thalamus and parietal area.

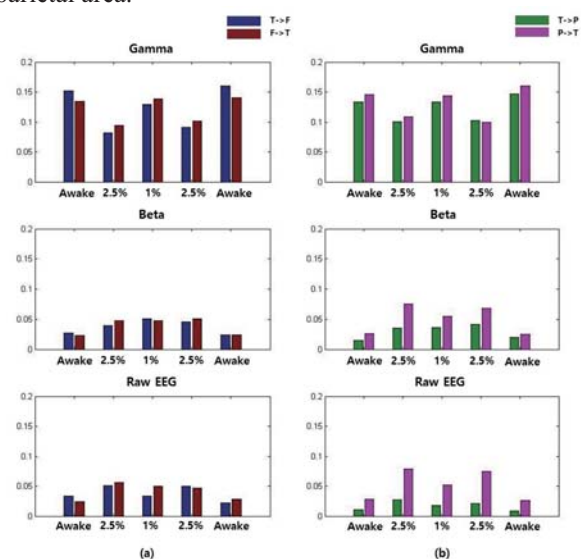


Fig. 1. TE values depending on anesthesia concentration
(a) Thalamus-Frontal area connection
(b) Thalamus-Parietal area connection

IV. CONCLUSION

In summary, TE is useful to investigate the change of brain connectivity [1-2]. In particular, TE of gamma band is a best indicator for reflecting the brain connectivity depending on the depth of anesthesia.

ACKNOWLEDGEMENT

The research was supported by a grant from the Institute of Medical System Engineering (iMSE) in the GIST, Korea.

REFERENCES

- Xu, Xinyu, Guolin Wang, and Xin Tian, "Effects of Anesthesia on Effective Connectivity in the Brain," *World Journal of Neuroscience.*, vol. 5, pp.99-107, 2015.
- Vicente, Raul et al., "Transfer entropy—a model-free measure of effective connectivity for the neurosciences," *Journal of computational neuroscience.*, vol. 30, pp.45-67, 2011.

Preclinical functional MRI for drug development

Taekwan Lee¹, Alan Jasanoff², and Choong-Yong Kim¹

¹Laboratory Animal Center, Daegu Gyeongbuk Medical Innovation Foundation, Daegu, Korea

²Biological Engineering, MIT, Cambridge, MA, USA

E-mail: tklee@dgmif.re.kr

Abstract— We present preclinical imaging technique for drug development. Recently, we developed dopamine specific MRI contrast agent and measured volumetric dopamine release evoked by reward-related lateral hypothalamic brain stimulation of rat [1]. In addition, we demonstrate in vivo zinc labeling of the hippocampus using porphyrin based contrast agent [2]. Combinations of molecular imaging techniques and animal brain disease models can be utilized for screening drug efficacy.

Keywords— neuroimaging, drug development, MRI, dopamine, brain disorder

I. INTRODUCTION

Functional magnetic resonance imaging (MRI) based on blood oxygen level dependent (BOLD) signals has been widely applied to study brain functions in both humans and animals. Although BOLD fMRI became essential tool in human research, it is fundamentally limited by indirect measurement of neural activity. In this talk, I will show recent progress in MRI contrast agents and applications to measure molecular signals in the brain.

II. METHODS

Rats were implanted with electrodes targeted to the medial forebrain bundle (MFB), and operant responses to MFB stimulation were verified behaviorally. Animals were then anesthetized, tracheostomized, artificially ventilated, and injected with 80 mg/kg L-DOPA in preparation for dopamine imaging. During imaging with gradient echo T1-weighted contrast, the dopamine sensor was infused into brain (0.1 $\mu\text{L}/\text{min}$.) to fill large regions of the ventral striatum. Following initial infusion, MFB stimuli (2 ms pulses, 60 Hz, 250 μA) were delivered in blocks of 16 s, alternating with 300 s epochs of rest

III. RESULTS

Statistical analysis revealed significant stimulation-associated MRI signal changes across the ventral striatum, with the strongest responses observed in the medial part of nucleus accumbens shell. Average time series data indicated signal changes of up to 2%, consistent with peak dopamine concentrations of approximately 10 μM binding to the sensor. These responses varied in a manner dependent on the stimulus parameters, and were not observed using an inactive

form of the MRI sensor. Parallel measurements using electrochemical detection verified that dopamine concentrations determined by MRI were realistic, and confirmed that sensor binds dopamine in vivo.

IV. CONCLUSION

These experiments offer a novel and qualitatively unique spatiotemporal view of phasic dopamine signaling, and provide direct evidence for the spatial heterogeneity of dopamine release in the ventral striatum. This technique can be further used for drug development.

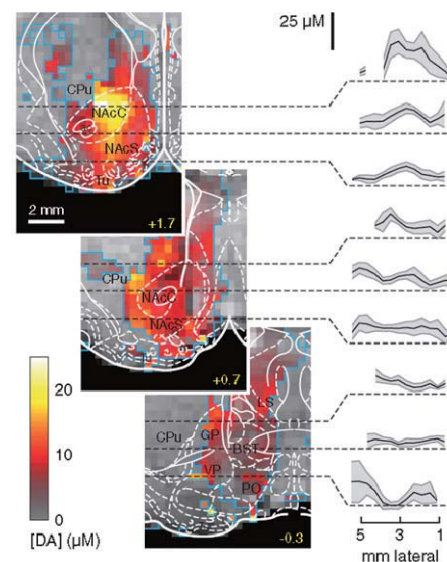


Fig. 1. Quantitative functional imaging of dopamine concentrations in the ventral striatum.

REFERENCES

1. Lee, T., Cai, L. X., Lelyveld, V. S., Hai, A., & Jasanoff, A., "Molecular-Level Functional Magnetic Resonance Imaging of Dopaminergic Signaling", *Science*, 344, 533-535, 2014
2. Lee, T., Zhang, X., Dhar, S., Faas, H., Lippard, S. J., & Jasanoff, A., "In vivo imaging with a cell-permeable porphyrin-based MRI contrast agent.", *Chemistry & Biology*, 17 (6), 665-673, 2010

Extracellular recordings of local field potentials and spikes from clustered neuronal networks using planar-type microelectrode arrays

S. Joo and Y. Nam

¹Department of Bio and Brain Engineering, Korea Advanced Institute of Science and Technology, Daejeon, Republic of Korea
E-mail: ynam@kaist.ac.kr

Abstract— The recording of Local field potential (LFP) by extracellular recording methods enable us to infer the physiological activity of a population of neurons. In this work, we could get both LFP signal and spike from the patterned neural network and analyzed correlation between LFP and spikes. we showed that LFP and spike from clustered neural network was successfully measured by microelectrode array (MEA) system.

Keywords— Microelectrode array, MEA, Primary neuron, Spike, LFP.

I. INTRODUCTION

Local field potential (LFP) is the electrical potential that reflects the summed electric current flowing from multiple neurons in a local neuronal assembly. The recording of LFP by extracellular recording methods enable us to infer the physiological activity of a population of neurons. Even if the analysis of LFP was important to understand the information transfer principles of the brain, no previous studies have examined the LFP in cultured neural networks. Here, we report the recordings of LFPs and spikes from in vitro neuronal circuits cultured on the microelectrode array (MEA). In this work, we could get both LFP signal and spike from the patterned neural network and analyzed correlation between LFP and spikes.

II. METHODS

We cultured clustered neural network on 60-channel ITO MEA (MCS, MultiChannel Systems, Germany) by agarose hydrogel structures which were molded using MIMIC (Micromolding in capillaries) [1]. Spontaneous electrical activity recordings from MEA were performed using an MEA1060-inv-BC amplifier (Gain: 50, bandwidth: 0.02 Hz ~ 8 kHz, MCS). Signals were sampled at 25 kHz and 16-bit resolution and acquired through the data acquisition card (USB-ME64, MCS) and MC_Rack software (MCS). To gain LFP signal from raw signal, raw signal were filtered by a 2nd order butterworth low pass filter with a cut off frequency of 10 Hz. And, to gain spike from raw signal, the signal were filtered by a 2nd order butterworth high pass filter with a cut off frequency of 200 Hz.

III. RESULTS

Figure 1a shows the Schematic illustration of the procedures to gain LFP traces and spikes from microelectrode recordings. We successfully cultured clustered neural network on an MEA by agarose MIMIC method. From the networks, electrical signals which were measured by amplifier with wideband filter (Gain: 50, bandwidth: 0.02 Hz ~ 8 kHz) contained both spiking activity with high frequency component and LFP with low frequency component. Spike data and LFP traces were successfully separated by individual digital filtering (LFP: low pass filter, Spike: high pass filter). Most of the LFPs were observed with the spikes. We analyzed correlation between number of spikes and amplitude of following LFP trace based on measured signals. According to linear regression analysis ($R^2=0.42$), between number of spikes and amplitude of following LFP trace did not have linearity.

IV. CONCLUSION

In this study, we showed that LFP and spike from clustered neural network was successfully measured by MEA system. Also, we tried to analyze correlation between number of spikes and amplitude of LFP trace. Our method can provide diversity about LFP parameter for studying of neural network dynamics with in vitro cultured neural network.

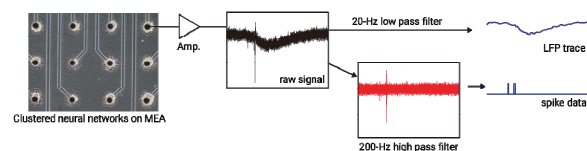


Fig. 1. Figure caption

ACKNOWLEDGEMENT

This work was supported by Mid-career Researcher Program through National Research Foundation grant (NRF-2015R1A2A1A09003605), and the Brain Research Program through National Research Foundation grant (NRF-2011-0019213) funded by the Ministry of Science, ICT and Future Planning.

REFERENCES

1. G. Kang, J. H. Lee, C. S. Lee, and Y. Nam, "Agarose microwell based neuronal micro-circuit arrays on microelectrode arrays for high throughput drug testing," *Lab. Chip.*, vol. 9, pp. 3236-42, 2009.

Early Detection of Driver's Drowsiness by Utilization of Hybrid EEG/fNIRS

Thien Nguyen¹, Sangtae Ahn², Hyojung Jang², Sung Chan Jun², Jae Gwan Kim^{1,2}

¹Department of Medical System Engineering, ²School of Information and communications,

Gwangju Institute of Science and Technology (GIST), Gwangju, The Republic of Korea

E-mail: jaekim@gist.ac.kr

Abstract—This study combines EEG with fNIRS to investigate electrical activity and hemodynamic change of brain when driver undergoes drowsiness. The result showed that the depletion of beta relative band power from EEG and increment of oxy-hemoglobin from fNIRS occur earlier than drowsiness onset shown in camera.

Keywords— Hybrid EEG/fNIRS, drowsiness detection.

I. INTRODUCTION

Driver's drowsiness is one of many causes in annually increasing number of traffic accidents. Therefore, early detection of drowsiness during driving will help to reduce the number of car accidents.

II. METHODS

A. Hybrid fNIRS/EEG

A homemade 10Hz sampling rate functional near-infrared spectroscopy (fNIRS) system was combined with a commercial 512Hz sampling rate EEG (Bioactive two) system. EEG system has 64 channels, covering whole brain and fNIRS system has 8 channels, covering prefrontal lobe. fNIRS light source emits 735nm and 850nm wavelengths and it is placed 3cm apart from detector.

B. Experimental design

Experiments were performed under a driving simulation task with 11 healthy subjects, 10 male, and 1 female. Subject mean age was 26.7 with a variation of 2.3. Before experiment, subject was asked to have enough sleep in previous night, and not to use any caffeine containing substances. During experiment, subject sat in a comfortable chair and drove around an oval shape track until he/she showed an expression of drowsiness. A sleepiness level estimation survey was conducted before and after experiment. A high definition webcam was used to record and monitor the subject's behavior in real time.

C. Data analysis

EEG signal was filtered using a band pass filter (1Hz to 50Hz) and then decomposed into five basic bands. Relative power level (RPL) of each band was computed with a 120s moving window. Oxy- (HbO), deoxy-

(HbR), and total (THb) hemoglobin change was calculated from detected light intensity based on modified Beer-Lamberts' Law.

III. RESULTS

Fig.1 shows Beta band RPL and HbO change in 80 seconds, 24 minutes after the experiment started. Subject's drowsiness was observed by a camera at 24 minute 52 seconds after driving. Corresponding to subject's state change, there was a decrease in Beta band RPL and an increase followed by a gradual decrease of HbO change. In drowsy state, subjects were highly sleepy, but they had to focus on driving, so from time to time, they unconsciously felt asleep in several seconds (micro-sleep). Micro-sleep dramatically reduces subject's cognitive function, resulting in alteration of Beta band RPL and HbO change. Compare to drowsiness onset observed by the camera, Beta RPL and HbO changes occurred earlier.

IV. CONCLUSION

Former change of brain signals, Beta band RPL decrease and HbO change increase, provide a reliable approach to detect driver's drowsiness in advance, which will help to reduce the chance of traffic accidents.

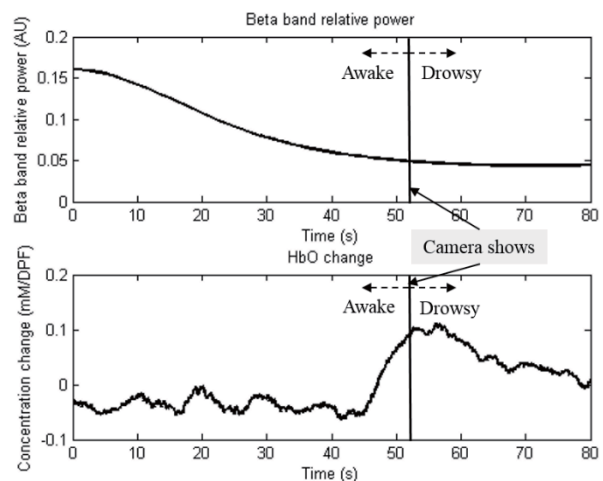


Fig. 1. Beta band RPL and HbO change during awake to drowsiness transition

ACKNOWLEDGEMENT

This work was supported by institute of Medical System Engineering at GIST and Hyundai Motor Company.

Improved Electrooculogram-based Eye-writing Recognition Using a New Feature Extraction Method

Won-Du Chang, Ho-Seung Cha, Chang-Hwan Im

Department of Biomedical Engineering, Hanyang University, Seoul, Republic of Korea

E-mail: ich@hanyang.ac.kr

Abstract—This paper introduces a new method to improve the accuracy of electrooculogram-based eye-written digit recognition. The proposed method combined global and local features, and was compared with conventional methods having been used for handwritten character recognition.

Keywords— EOG, Eye-writing, DTW, DPW, SVM.

I. INTRODUCTION

In last decades, electrooculogram (EOG) has been widely studied as a useful tool for human-computer interface applications, where most studies utilized only the information of eye movement directions. Recently, a new concept was introduced to allow users to write digits directly by moving gazes, so that the gaze traces on a monitor draws the shapes of the digits [1] (This process is referred to as *eye-writing*). In this paper, a new method to improve the accuracy of EOG-based eye-writing recognition is proposed.

II. METHODS

A. Data and Preprocessing

An EOG dataset in [2] was utilized in this paper, which includes 10 participants' EOG data acquired while they were eye-writing Arabic numbers three times. In the preprocessing phase, source signals were resampled, median-filtered, and baseline-corrected. Eye blink artifacts were automatically detected [3], and linearly interpolated.

B. Saccade detection and data resampling

Continuous Wavelet Transform—Saccade Detection [4] was utilized to extract eye movement data. After the saccade detection, the signals were resampled to have the same Euclidean distance between adjust points, and the sizes of the signals were normalized.

C. Global Features (GFs)

Eight GFs representing the characteristics of written digits are as follows: 1) width to height ratio, 2-5) number of local minima/maxima in horizontal/vertical EOG, 6-7) trace length of horizontal/vertical movement, and 8) trace length in 2 dimension (2D).

D. Local Features

Dynamic time warping (DTW) is a dissimilarity measure between two signals having different lengths; and dynamic positional warping (DPW) is a sort of DTW for 2D signals [5]. To combine these measures

with GFs, a distance-set of a test pattern to the templates of all digits was used as features. Please note that the templates were created manually.

E. Feature space reduction and pattern classification

Linear discriminant analysis (LDA) was used to reduce feature dimensions, and support vector machine (SVM) was used to classify the patterns.

III. RESULTS

The methods were tested using 10-fold validation, and the results are shown in Table 1. The best accuracy was achieved by combining GFs, DPW, LDA, and SVM.

Table 1. Recognition accuracies according to methodologies.

Methods*	a	b	c	d	e	f	g	h	i
Mean	77.3	93.7	92.0	97.3	98.3	93.0	97.7	93.3	98.7
Std.	20.7	10.2	11.9	6.3	4.2	6.2	1.6	5.9	1.7

* a: GFs, b: DTW, c: DPW, d: DTW+SVM, e: DPW + SVM, f: GFs + DTW + SVM, g: GFs + DPW + SVM, h: GFs + DTW + LDA + SVM, i: GFs + DPW + LDA + SVM.

IV. CONCLUSION

This study showed that high accuracy can be achieved by combining global and local features in EOG digit recognition.

ACKNOWLEDGEMENT

This work was supported in part by the Basic Science Research Program through the National Research Foundation of Korea (NRF) funded by the Ministry of Education (NRF-2014R1A1A2A16052334).

REFERENCES

1. J.-Z. Tsai, C.-K. Lee, C.-M. Wu, J.-J. Wu, and K.-P. Kao, "A feasibility study of an eye-writing system based on electro-oculography," *J. Med. Biol. Eng.*, 28(1), 39–46, 2008.
2. H.-S. Cha, J.-Y. Lim, D.-S. Jeon, W.-D. Chang, and C.-H. Im, "Implementation of a real time EOG-based digits input device," in *Proc: 50th conf. Korean Soc. Med. Bio. Eng.*, 2015.
3. W.-D. Chang, H.-S. Cha, and C.-H. Im, "A new method for detecting eye-blink artifacts from a single-channel electroencephalogram," in *Proc: 36th annual int. conf. IEEE Eng. Med. Biol. Soc.*, 2014.
4. A. Bulling, J. A. Ward, H. Gellersen, and G. Tröster, "Eye movement analysis for activity recognition using electrooculography," *IEEE Trans. Pattern Anal. Mach. Intell.*, 33(4), 741–753, 2011.
5. W.-D. Chang and J. Shin, "Dynamic positional warping: dynamic time warping for online handwriting," *Int. J. Pattern Recognit. Artif. Intell.*, 23(5), 967–986, 2009.

Enhancement of Motor Imagery Training Efficiency using a Real-time Feedback System

Yubing Jiang, Hyeon-seok Lee, Gang Li and Wan-Young Chung

Department of Electronic Engineering, Pukyong National University, Busan, Korea

E-mail: wychung@pknu.ac.kr

Abstract—Motor imagery (MI)-related mu/beta rhythms, which can be voluntarily modulated by subjects, has been widely used in electroencephalogram (EEG)-based brain computer interface (BCI) system. A crucial approach to improve the performance of a BCI is real-time feedback. The aim of this study is to develop an efficient real-time feedback system to enhance the reliability of MI-based BCI.

Keywords— motor imagery, brain-computer interface, electroencephalogram, feedback.

I. INTRODUCTION

The feedback performance of brain computer interface (BCI) depends largely on the initial classifier model. However, the training data contains insufficient discriminability at the beginning of training, particularly when subjects are unfamiliar with the system. So, we proposed a real-time feedback system which is able to collect reliable training data for initial classifier and can enhance the MI training efficiency.

II. METHODS

A. Data Acquisition and Subjects

EEG signals were recorded from a 2-channel wireless EEG device produced by Cognionics, Inc. Electrodes were placed over central (C3, C4) locations according to the 10-20 international system.

Two normal subjects (two males, both right-handed) participated in our experiment. Due to the long time of repeated training, the fewer number of subjects is not uncommon in the research field of MI, such as [1].

B. Experiments

The experiment consists of two main stages:

- (1) Model training stage: the execution of motor imagery task with delayed feedback (stage 1).
- (2) Model testing stage: the execution of motor imagery task with real-time feedback (stage 2).

Fig.1 (A) is the model training stage with delayed feedback which was used to build the classifier model. After this stage, we could collect the data from the trials which have successful feedbacks for the classifier, where the feedback is triggered by event-related desynchronization (ERD) value. Fig.1 (B) shows the testing stage with real-time feedback which is triggered by classifier. The feedback was updated every 500ms.

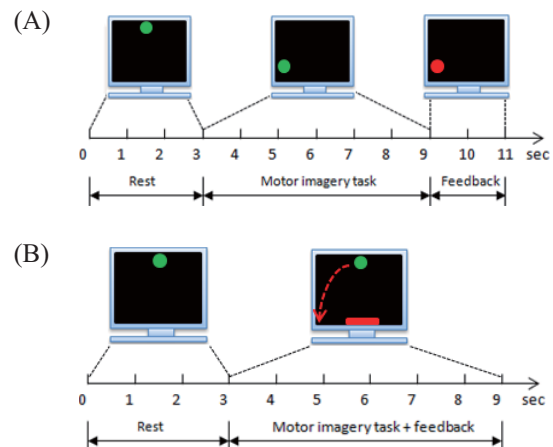


Fig. 1. Example of one trial of experiment with feedback. Depending on the direction of the green falling ball, the subjects were instructed to imagine open-close of the left or right hand (A) and imagine open-close of the left or right hand to control the red bar to catch the green falling ball (B).

III. RESULTS

By using the stage 1 to train SVM classifier model, the final accuracy of the classifier is 96% for subject 1 and 98.5% for subject 2. Then after another 2 weeks of training using stage 2, the real-time control accuracy can reach 72.5 % for subject 2 which is higher than the accuracy 60%~70% in previous study [2].

IV. CONCLUSION

A real-time feedback BCI system is designed which can collect efficient data to train classifier and can enhance the MI training efficiency.

ACKNOWLEDGEMENT

This work was supported by the BK21 Plus Program funded by the Ministry of Education(MOE, Korea) and National Research Foundation of Korea(NRF).

REFERENCES

1. Ramoser, Herbert, Johannes Muller-Gerking, and Gert Pfurtscheller. "Optimal spatial filtering of single trial EEG during imagined hand movement." *Rehabilitation Engineering, IEEE Transactions on* 8.4 (2000): 441-446.
2. Bi, Luzheng, Xin-An Fan, and Yili Liu. "EEG-based brain-controlled mobile robots: a survey." *Human-Machine Systems, IEEE Transactions on* 43.2 (2013): 161-176.

Temporal and Spatial Mapping of Neuronal Signals in Brain Slice with Optical Coherence Tomography

Geonho Choi¹, Jeonghyeon Lee¹, Jaemyung Jang², Nam Hyun Cho³, Songye Baek¹,
Noo Li Jeon⁴ and Woonggyu Jung^{1,3,*}

¹Department of Biomedical Engineering, School of Life Sciences, Ulsan National Institute of Science and Technology (UNIST), Ulsan, Republic of Korea

²Korea Brain Research Institute, Daegu, Republic of Korea

³Center for Soft and Living Matter, Institute for Basic Science (IBS), Ulsan, Republic of Korea

⁴School of Mechanical and Aerospace Engineering, Seoul National University, Seoul, Republic of Korea
E-mail: wjung@unist.ac.kr

Abstract—Micro-electrode array (MEA) is useful device for studying neuronal network to record extracellular field potentials and single action potential in the multiple sites. However, MEA has restriction to use upright microscopy configuration, because it is hard to observe position of electrodes located beneath brain tissue. Here, we present new method, optical mapping system which enables to monitor the location of electrodes and brain tissue structure using optical coherence tomography (OCT). Also, it can offer the temporal and spatial mapping on OCT image. Through our research, we expect that our system could be very useful tool to study connectivity of neuronal network.

Keywords— Micro-electrode array, Brain slice, Optical coherence tomography.

I. INTRODUCTION

Electrophysiology is the study of the electrical characteristics of cells and tissues through the measurements of electric current or voltage change. Therefore, in this field, micro-electrode array (MEA) has been used to study neuronal circuits [1]. However, MEA has limitation for observing electrode because of the thickness of tissue. In order to overcome this limitation, we used OCT which is label-free, non-invasive and 3D cross-sectional imaging tool [2]. Therefore, in this research, we suggest the novel system that consists of 60-channel extracellular recording MEA and OCT technique.

II. METHODS

A. Brain slice

Brain slice was dissected from ICR mouse. The brain was sliced to a thickness of 400 μm using a vibratome (Leica VT1000 S).

B. OCT system

A fiber based swept-source optical coherence tomography (SS-OCT) system was constructed with a broadband swept laser source.

C. Neuronal recording MEA electrophysiology

All recordings were performed on 60 channel extracellular recording system (USB-ME64, Multichannel systems) at a sampling rate of 10 kHz.

III. RESULTS

Optical imaging technique acquires 3D structural images of brain tissue and features of individual electrodes. Also, 60 electrode channels of MEA under brain slice recode neuronal signals. The dynamics of temporal-sequential neuronal activities was mapped spatially on the volumetric OCT image.

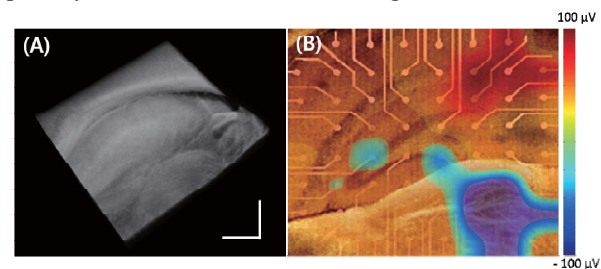


Fig. 1. (A) 3D OCT image of brain slice (scale bar: 500 μm), (B) Temporal and spatial mapping on OCT image

IV. CONCLUSION

In this research, we made temporal and spatial mapping system that enables monitoring state of brain slice using acquisition of 3D optical images with high resolution as well as recording neural activities on the MEA. Therefore, we believe that our system could be very helpful to study connectivity of neuronal network.

ACKNOWLEDGEMENT

This work was supported by the ICT R&D program of MSIP/IITP (R0190-15-2072).

REFERENCES

1. Ferrea, E. et al, "Large-scale, high-resolution electrophysiological imaging of field potentials in brain slices with microelectronic multielectrode arrays", *Frontiers in neural circuits*, vol. 6, pp. 80, 2012.
2. Huang, D. et al, "Optical coherence tomography", *Science*, vol. 254(5035), pp. 1178-1181, 1991.

Carbon-fiber based neural probe for chronic neural recording

Yena Lee¹, Yoonseob Lim², Seoyoung Hwang¹, Jaewoo Shin³,
Jin Woo Chang³, Sang Beom Jun^{1,4,*}

¹Department of Electronics Engineering, Ewha Womans University, Seoul, South Korea

³Center for Robotics Research, Robotics and Media Institute, Korea Institute of Science and Technology

³Department of neurosurgery, College of Medicine, Yonsei University, Seoul, South Korea

⁴Department of Brain & Cognitive Sciences, Ewha Womans University, Seoul, South Korea

*E-mail: juns@ewha.ac.kr

Abstract—In order to reduce the reactive tissue response around implanted neural electrodes for neural recording, carbon fiber-based microelectrode arrays are developed. Since the diameter of the carbon fiber (7 μm in diameter) is much smaller than the conventional micro-wires or the microfabricated silicon-based electrodes, it is expected that the carbon fiber neural probe is appropriate for the long-term neural recording. We introduce the multi-channel microelectrode array, each channel of which is composed of multiple carbon fiber bundles and show the preliminary neural responses recorded in motor cortex of anesthetized rat. While each carbon fiber is too flexible to be inserted in the rat brain, the bundle of carbon fibers can sustain each other to insert the electrode into the brain.

Keywords— microelectrode arrays, carbon fiber, tissue reaction

I. INTRODUCTION

Microelectrode arrays are commonly used for electrophysiological recording from individual neurons to study neural pathways in the brain or to develop brain-computer interface. However, the long-term recording is still limited due to the tissue reaction around the implanted microelectrodes even though the chronic neural recording is becoming more and more essential for long-term applications. It is believed that the geometry of the electrode such as the size is the most critical component which can determine the degree of the chronic tissue damage. In this study, in order to reduce the reactive tissue response, carbon fiber-based microelectrode arrays are fabricated and examined.

II. METHODS

A. Carbon fiber electrode fabrication

An acrylic structure has four paths 9 mm long, 100 μm width, 200 μm deep designed to increase the stiffness of probe. Combine the acrylic structure and printed circuit board (PCB). About 16 pieces of carbon fiber coated with parylene for insulation become a single bundle and insert in a path of the acrylic structure. An electrode is composed of four bundles of the carbon fiber.

B. Evaluation for long-term neural recording

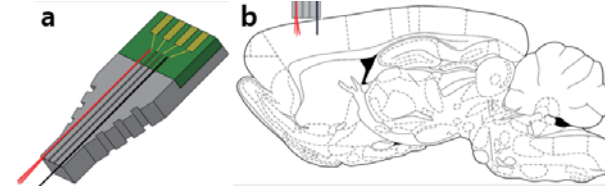


Fig. 1. A single bundle of carbon-fiber microelectrode array and a tungsten electrode are assembled and implanted.

Carbon-fiber based microelectrode and traditional tungsten-based electrode (diameter: 100 μm) are implanted in primary motor cortex of rat. Distance between electrodes is 1.4mm. The probe was inserted 1.5mm deep into the brain (primary motor cortex) from the surface by penetrating dura mater (Carbon fiber AP : 2.5mm, ML : 2.5mm, tungsten AP : 1.1mm, ML : 2.5mm).

III. RESULTS

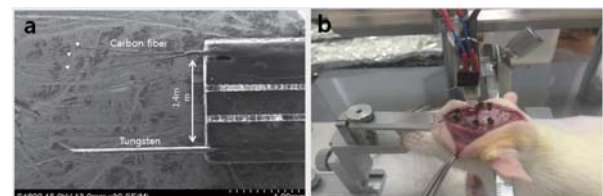


Fig. 2. (a) Two different types of electrode are assembled on the same PCB (Carbon fiber and Tungsten). (b) the electrodes implanted in primary motor cortex of a rat

The microelectrode bundled with thin carbon fibers (diameter: 7 μm) were successfully developed. The impedance and neural signals are recorded while electrodes are chronically implanted. Neural signals were reliably recorded with carbon-based microelectrode over 1 month long whereas we were unable to identify the neural spikes from the tungsten electrode.

IV. CONCLUSION

Based on the results of neural recording and impedance measurements, it is expected that the carbon fiber creates lower immune response than

tungsten electrode. Immunohistochemistry of tissue around electrode is required in the future. Further assessment of chronically recorded neural signal and impedance of electrode during implantation period are also required to confirm the usability of carbon fiber-based microelectrode arrays for long-term neural recording experiment.

ACKNOWLEDGEMENT

This work was supported by NRF grant funded by Korea government (MEST) (2014R1A2A2A09052449, NRF-2014R1A1A1A05003770), the smart IT convergence system research center as global frontier project (CISS-2012M3A6A6054204) and also supported by The Ministry of Trade, Industry and Energy (Grant number: 10041629)

REFERENCES

- [1] Grigori Guitchounts, Jeffrey E Markowitz, William A Liberti and Timothy J Gardner, J. Neural Eng. 10 (2013) 046016 (13pp)
- [2] Timothy J Gardner, William Liberty, Jeffrey Markowitz, Grigori Guitchounts, Minimally invasive splaying microfiber electrode array and methods of fabricating and implanting the same, US Patent (Patent number: WO 2015003185 A2)

Bioengineering System for Prediction and Early Prenosological Diagnostics of Stomach Diseases Based on Energy Characteristics of bioactive Points with Fuzzy Logic

Riad Al-Kasasbeh

Faculty of Engineering Technology, Al-Balqa Applied University
Jordan

Email: rjordanjo@mail.ru

Nikolay Korenevskiy

Faculty of Biomedical Engineering, Kursk State Technical University
Russia

Email: kstu-bmi@yandex.ru

Mahdi Alshamasin

Faculty of Engineering Technology, Al-Balqa Applied University
Jordan

Email: mahdism@hotmail.com

Abstract— We apply mathematical models for the interaction of the internal and biologically active points of meridian structures. Amongst the diseases for which reflex diagnostics are effective are those of the stomach disease. It is shown that use of fuzzy logic decision-making yields good results for the prediction and early diagnosis of gastrointestinal tract diseases, depending on the reaction energy of biologically active points (acupuncture points). It is shown that good results for the prediction and early diagnosis of diseases from the reaction energy of biologically active points (acupuncture points) are obtained by using fuzzy logic decision-making.

Keywords—Acupuncture points, fuzzy logic, diagnostically important points (DIP), confidence factors, membership functions, stomach diseases.

Effect of Substrates on Surface Enhanced Raman Scattering Platform using AgNPs-based Successive Ion Layer Absorption and Reaction Method

W. Kim^{1,2}, H. K. Park^{1,2}, and S. Choi^{1,2*}

¹Department of Medical Engineering, Kyung Hee University, Seoul 130-701, Korea

²Department of Biomedical Engineering, College of Medicine, Kyung Hee University, Seoul 130-701, Korea

*E-mail: medchoi@khu.ac.kr

Abstract—We introduce to fabricate the surface enhanced Raman scattering (SERS) platform using AgNPs by successive ion layer absorption and reaction (SILAR) method according to substrates. Among substrates including aluminum foil, glass, paper, and Si wafer, the paper showed the best SERS effect.

Keywords— AgNPs, SILAR, substrate, SERS.

I. INTRODUCTION

Noble metals such as gold (Au) and silver (Ag) leading the surface enhanced Raman scattering (SERS) effect can be easily fabricated with nanoparticles (NPs). We performed that AgNPs were produced on various substrates, aluminum foil, glass, paper, and Si wafer, that could easily get around by successive ion layer absorption and reaction (SILAR) method [1]. In this study, we introduce the preliminary finding regarding the investigation of the coffee ring effect by the substrate and the SERS effect of the AgNPs according to the substrate.

II. METHODS

For deposition of AgNPs, the various substrates were fabricated through SILAR method which the substrates were dipped in aqueous 20 mM AgNO₃, rinsed with distilled water and dipped in 20 mM NaBH₄ solution to reduce the silver and then rinsed with distilled water again. All aqueous dipping time was 30 sec. The optimized effect was realized by five cycles. In order to confirm the coffee ring effect by the droplet and the SERS effect by AgNPs on various substrates, a 2- μ L 1-mM Rhodamine B (RhB) used probe molecule of Raman signal was dropped. The Raman spectra were obtained a 10 mW, 785 nm diode laser source with 5 cm⁻¹ resolution for twice 30 sec acquisitions.

III. RESULTS

A. Substrate-based Coffee Ring Effect

Figure 1 shows the drop distribution of RhB on the various substrates. The substrates such as aluminum foil (Fig. 1A), glass (Fig. 1B) and Si wafer (Fig. 1C) were not absorbed the droplet of sample and a coffee ring effect occurred; however the paper with porous structure was uniformly absorbed the droplet of sample

from the center to the ring without coffee ring effect (Fig. 1D).

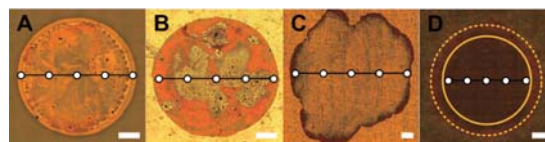


Fig. 1. Coffee ring effect according to substrates

B. AgNP-active SERS Effect

Since the sample distribution by coffee ring effect was different on rigid substrate, the deviation of the Raman intensities to measuring position was very great (Fig. 2A-C). However, Figure 2D shows that uniformly AgNP-coated paper was constant Raman signals and the SERS effect compared to other substrates.

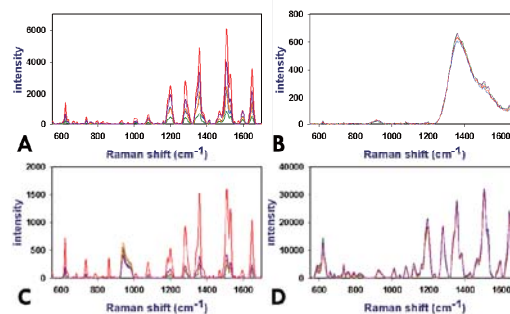


Fig. 2. Substrate-based SERS effects.

IV. CONCLUSION

The AgNPs were uniformly deposited on the paper with the porous property via SILAR method and also showed an increased SERS effect. This paper platform is likely to be suitable to rapid analysis in point-of-care (POC) applications.

ACKNOWLEDGEMENT

This work was supported by the NRF grant (2014R1A1A2054452) and the Korean Health Technology Research & Development Project grant by the Ministry of Health & Welfare (HI14C2241).

REFERENCES

1. K. G. Stamplecoskie and J. S. Manser, "Facile SILAR approach to air-stable naked silver and gold nanoparticles supported by alumina," *ACS Appl. Mater. Interfaces*, vol. 6, pp. 17489-17495, 2014.

Synthesis of close-packed gold nanostructures on anodic aluminum oxide using self-assembled APTMS monolayer

Hyung Joon Park¹, Sang Won Lee², Wonseok Lee³, Yoonhye Kim⁴,
Dae Sung Yoon^{2*} and Kyu Back Lee^{1,2,4*}

¹School of Biomedical Engineering, Department of Biomicrosystem Technology, Korea University, Seoul 136-701, Republic of Korea.

²School of Biomedical Engineering, Department of Bio-convergence engineering, Korea University, Seoul 136-701, Republic of Korea.

³Department of Biomedical Engineering, Yonsei University, Wonju 220-710, Republic of Korea

⁴Department of Biomedical Engineering, Korea University, Seoul 136-701, Republic of Korea

*E-mail: kblee@korea.ac.kr

Abstract— Densely close-packed two dimensional or three dimensional nanostructure have been received considerable interest in scientific communities, because they are important for revealing new or enhanced properties. In this study, we made closely packed gold nanoparticle monolayer through the application of anodic aluminum oxide (AAO).

Keywords— Anodic Aluminum Oxide (AAO), Gold nanoparticle, self-assembled monolayer, AFM, SEM

I. INTRODUCTION

Various methods to form nanostructures using nanoparticles are developed to enhanced properties and to apply in bio-medical application field [1]. However, those methods exhibit some defects because it is difficult to control the interfaces between nanoparticles uniformly. Moreover some methods show low reproducibility, others become complex to form nanoparticle structures [2]. Herein, we used anodic aluminum oxide membrane as template to form two dimensional (2D) gold nanoparticle structure conveniently and uniformly through self-assembly method with large area of gold nanostructure.

II. METHODS

Ultrapure aluminum plates (99.999%, Goodfellow, UK) are electro-polished in perchloric acid. Then two-step electrolytic anodizing is performed. Electropolished aluminum plates are anodized in 0.3M oxalic acid and etched out with chromic acid solution. More well-ordered AAO is formed during second anodizing in the same conditions. Pore widening is performed to make the pores to be 70 nm in diameter in phosphoric acid solution. To make electrical bonds between AAO and gold nanoparticles (AuNPs), aminopropyltriethoxysilane (APTMS) is induced on AAO membrane. Stabilized gold nanoparticle solution (100 nm in size) is purchased from Sigma Aldrich. The high concentrated gold nanoparticle solution is prepared to form close-packed nanostructure on AAO membrane. The gold nanostructure is observed by SEM (Jeol 6701F, Tokyo, Japan) and its height is measured by AFM (Innova, Veeco, CA, USA).

III. RESULTS

Hole-size 70nm of AAO membrane is observed by SEM. APTMS self assembled monolayer is verified by ATR-FTIR spectroscopy and fluorescence spectroscopy using FITC bound to amine groups. Well ordered gold nanostructures is formed successfully on AAO membrane (Fig.1).

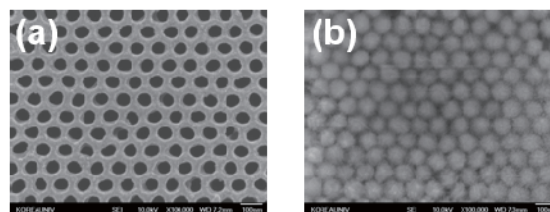


Fig.1. SEM images of gold nanoparticle on AAO. (a) Anodic Aluminum Oxide membrane. (b) Self-assembled gold nanoparticle on AAO membrane.

IV. CONCLUSION

Metal nanoparticles have attracted attention because of their unique properties in electronic, optical, and catalytic field [3]. Aligning nanoparticles is of great importance for these metal nanoparticles to be applied in practical areas. We have demonstrated well-ordered arrays of nanoparticles using regular structure of AAO membrane. The dense packing of gold nanoparticles can be used in biological sensors and optoelectronic devices.

ACKNOWLEDGEMENT

This study was supported in part by Basic Science Research Program (NRF-2014R1A2A2A) and Mid-career Researcher Program (03007861) through the National Research Foundation of Korea (NRF) funded by the Ministry of Science, ICT & Future Planning and by the Industrial Strategic Technology Development Program, (No. R1416612) funded by the Ministry of Trade, Industry & Energy, Republic of Korea.

REFERENCES

1. Guo, S and Dong, S, *J. Mater. Chem.*, Vol. 21, pp. 16704 - 16716, 2011.
2. Qing, Y, Hongwen, H, Xinsheng, P and Zhizhen, Y, *Nanoscale*, Vol. 3, pp. 3686 - 3875, 2011.
3. Yu, A., Liang, Z., Cho, J., & Caruso, F. *Nano letters*, 3(9), 1203-1207. 2003.

Sensitivity Enhancement of Silver–TiO₂ Double Layered Surface Plasmon Resonance Biosensor based on Dispersion Relation Engineering

Sherif H. El-Gohary, Munsik Choi, Seyoung Eom, Tae-Seong Kim, and Kyung Min Byun*

Department of Biomedical Engineering, Kyung Hee University, Yongin 446-701, Korea

*E-mail: kmyun@khu.ac.kr

Abstract— Sensitivity characteristics of surface plasmon resonance (SPR) biosensor have been extensively investigated to detect target samples with a low molecular weight. In order to increase the sensitivity of molecules detection, we utilize a highly correlation between dispersion relation and sensor sensitivity. We propose SPR structure based on silver film with an optimum thickness of titanium oxide that could produce an enhanced sensitivity with respect to a conventional structure.

Keywords— Biosensor, Surface Plasmon Resonance, Dispersion Relation, Rigorous Coupled-Wave Analysis, Titanium Oxide.

I. INTRODUCTION

Investigation of molecular binding using biosensing procedures is a key aspect to numerous fields of research and can lead to higher performance materials, drug synthesis, virus and bacteria detection and substantially more applications. Surface Plasmon Resonance (SPR) biosensor is classified as one of most effective category of sensor as label free method and real time analysis [1]. The physical process which occurred at metal layer (silver for example) interface with dielectric by plane-polarized light under total internal reflection conditions is called SPR. Most of biosensing methods are based on changing the refractive index at the sensor surface, so sensitivity of detection consider as substantial parameters in both design and measurement.

II. MODEL and METHODS

A. Proposed Model

Titanium oxide (TiO₂) evaporated onto a silver film is proposed as SPR biosensor as shown in Fig.1.

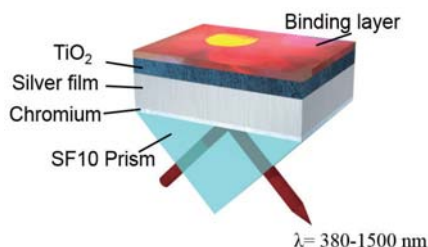


Fig. 1. Silver-TiO₂ double layered SPR biosensor structure. A 50-nm thick silver film was evaporated on an SF10 glass substrate via 2-nm thick chromium adhesion layer.

B. Numerical Methods & Performance Analysis

We utilized transfer-matrix method and the rigorous coupled-wave analysis methods to verify the experimental results. SPR sensor performance could be reliably analyzed and optimized based on a strong correlation between the slope of dispersion curve characteristics and the SPR angle shift.

III. RESULTS

Introduction of TiO₂ layer can overcome the limitations associated with instability of silver films when used in biosensing applications due to oxidation. Moreover, based on dispersion relation analysis, use of 20-nm and 30-nm thick TiO₂ layer can lead to enhanced sensitivity by more than 6 folds for water and air ambient, respectively.

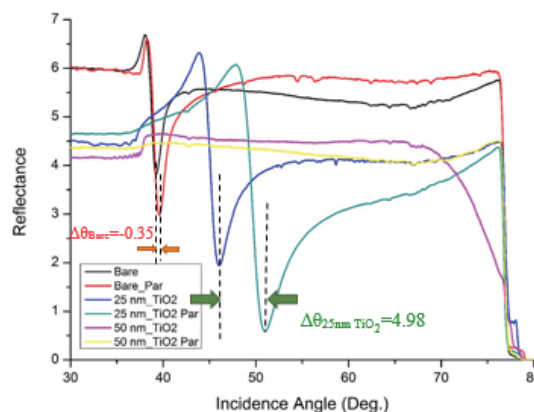


Fig. 2. Experimental results of SPR curve characteristic for bare silver, 25 and 50 nm TiO₂ with/without binding layer.

IV. CONCLUSION

Analysis of SPR sensors based on correlation between sensor sensitivity and dispersion relation can lead to enhance the performance by optimizing geometric parameters. Optimum selection of TiO₂ thickness on surface of silver can not only prevent oxidation of silver but lead to improve performance by increasing the sensitivity by more than 5 times.

ACKNOWLEDGEMENT

This work was supported by the NRF grants (2014R1A2A2A09052449 & 2015037656).

REFERENCES

1. J. Homola. "Present and future of surface plasmon resonance biosensors," *Anal. Bioanal. Chem.*, vol. 377(3), pp. 528–539, 2003.

The Development of Auto-pressure-control System for Hyperbaric Oxygen Chamber Based on PID

H. S. Kim, Y. R. Jang, S. Y. Shin, W. H. Choi, T. M. Shin

Department of Biomedical Engineering, Yonsei University, Wonju, Korea

E-mail: hyunsung17@naver.com

Abstract— The problems occur when operators control hyperbaric oxygen chambers manually. In this study, we have developed an auto-pressure-control system based on PID to solve the problems.

Keywords— Hyperbaric oxygen therapy, Auto-pressure control, PID control.

I. INTRODUCTION

Hyperbaric oxygen chambers operate with controlling a pressurization valve and a ventilation valve while checking the pressure of the chambers via a pressure gauge manually by operators. Therefore, Operators should pay attention to the chambers from the beginning to the end of treatment with checking the pressure of the chambers accurately and judging. The controlling the chambers by inexperienced operators or mistakes could cause safety accidents.

In this study, therefore, an auto-pressure-control system that controls the pressure of the chambers according to a profile using PID(Proportional Integral Derivative) algorithms was developed.

II. METHODS

A. System Configuration

The system for Auto-Pressure-Control is composed of three parts as Fig 1. The first part is an input part based on a pressure sensor. The second part is a processing part for determining the diameter of proportional valves. The third part is an output part including proportional valves.

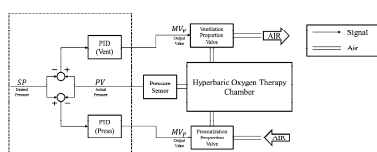
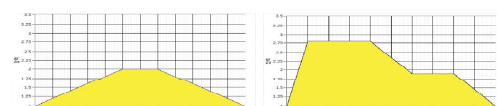


Fig. 1. Block Diagram

B. Control method

The pressure of the chambers is adjusted to the given profile by treatment purposes as Fig 2. The pressure by the profile is set as a SP(Set Point), and the actual pressure received from a pressure sensor is set as a PV(Process Variable). Error value is the difference between SP and PV, and the error value is input to the PID algorithm which applied proper coefficients. Two

PID algorithms were applied for controlling each valve[1], a pressurization proportional valve and a ventilation proportional valve. Each valve operates oppositely. Calculated MV via PID algorithms for controlling each valve is out.



a) Normal treatment profile b) DCS treatment profile

Fig. 2. Treatment Profile

III. RESULTS

As a result, the pressure of the chambers applied auto-pressure-control system was adjusted well according to each profile. Also, the average errors versus maximum values of pressure by each profile were as Table 1. Average error is the average of the difference between SP and PV through each profile. The average errors were 0.005.

Table 1. Result

No.	Average Error of a(bar)	Average Error of b(bar)
1	0.005	0.005
2	0.004	0.005
3	0.004	0.006
4	0.005	0.004
5	0.004	0.005

IV. CONCLUSION

In this study, the algorithm and the system of an auto-pressure-control based on PID algorithms for controlling hyperbaric oxygen chambers are developed. As a result, the average errors were 0.005. It is considered to complement the disadvantages of controlling hyperbaric oxygen chambers manually.

ACKNOWLEDGEMENT

This work was supported by the Korea industrial complex corporation grant funded by the Korea government (MOTIE). (1415135942)

REFERENCES

1. J. Bao, J. F. Forbes, and P. J. McLellan, "Robust Multiloop PID Controller Design: A Successive Semidefinite Programming Approach," *Ind. Eng. Chem. Res.*, Vol. 38, No. 9, pp. 3407-3419, 1999.

Development of a smart all-in-one cardiopulmonary support system: preliminary performance of pump driver and control unit on a mock circulation loop

J. H. Park¹, D. A. Shin¹, J. S. Lee¹, M. C. Shin², J. C. Lee³, H. C. Kim^{3,*}

¹ Interdisciplinary Program for Bioengineering, Graduate School, Seoul National University, Seoul, Korea

² Jain Technology Co., Ltd, Seoul, Korea

³Department of Biomedical Engineering, College of Medicine and Institute of Medical and Biological Engineering, Medical Research Center, Seoul National University, Seoul, Korea

E-mail: jp592@melab.snu.ac.kr

Abstract— Most cardiopulmonary support systems currently available in market are bulky and uncomfortable to use in the intensive care unit (ICU) environment. Accordingly, we aimed to develop a portable and cost-effective smart all-in-one cardiopulmonary support system (SACSS) that is capable of interactively and autonomously operating in accord with various indications of patients. In this study, we present a prototype of SACSS with preliminary performance result of pump driver and control unit on a mock circulation loop.

Keywords— cardiopulmonary support system, smart, all-in-one, performance evaluation

I. INTRODUCTION

Since H1N1 Influenza virus swept the whole world in 2009, extracorporeal membrane oxygenation (ECMO) care has received great attention by discovering high survival benefits with ECMO use for patients suffering from severe respiratory failure.

ECMO system is one of the representative model of cardiopulmonary support system (CSS), which requires a number of sensors and control systems in order to monitor physiological conditions that could vary by patients [1].

Therefore, portability and versatility of the system is very important to appropriately use in the intensive care unit (ICU) environment by achieving compactness of the system and to accommodate different clinical situations. However, most CSSs currently available in market are highly expensive, bulky, and complicated to use. Accordingly, we aimed to develop a portable and cost-effective smart all-in-one cardiopulmonary support system (SACSS) that is capable of interactively and autonomously operating in accord with various indications of patients (e.g. heart failure and lung failure). In this study, we present a preliminary performance of developed sensors and control units on a mock circulation loop and a prototype of SACSS that is portable.

II. METHODS

We first constructed a control unit that includes a centrifugal pump driver, user interface, emergency driving unit, and core sensor modules composed of clamp-on type ultrasonic flow meter (Jain Technology Co., Ltd, Korea), bubble sensor, and pressure sensors (Fig.1).

We built a mock circulation loop that comprises a mechanical valve for resistance control, turbine flowmeter for performance evaluation of the developed clamp-on type ultrasonic flowmeter, and two acrylic chambers; one for filling and drawing the fluid and the

other for compliance control with air pump (configuration not shown).

After the performance evaluation of the control unit using the mock circulation loop, we focused on the product design considering the most appropriate positioning of each component and portability.

III. RESULTS

With our pump driver, we could create a pump performance curve of Terumo pump head similar to its real specification (Fig. 1A). We also demonstrated the performance of the developed ultrasonic flowmeter by comparing with that of Transonic's (Fig. 1B). Responses of other sensors were successfully implemented into our user interface for real-time monitoring (Fig. 1C) and finally we were able to develop the first prototype of SACSS (Fig. 1E) by integrating all the sensors and the control unit.

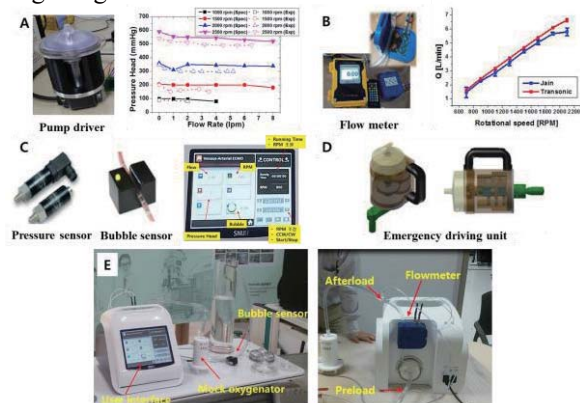


Fig. 1 (A-D) Control unit development and their performance test results; (E) prototype of SACSS equipped within a mock circulation loop

IV. CONCLUSION

With further improvements by focusing more on the clinician-oriented usability, our effort to develop SACSS is believed to make a success in the medical market shortly.

ACKNOWLEDGEMENT

This work was supported by BK21 Plus Program through the National Research Foundation of Korea(NRF) funded by the Ministry of Education (grant numbers 22A20130011025) and The Korean Health Technology R&D Project of the Ministry of Health & Welfare, Republic of Korea (grant number:HI14C0746).

REFERENCES

1. G. Ailawadi, and R. K. Zacour, "Cardiopulmonary Bypass/Extracorporeal Membrane Oxygenation/Left Heart Bypass: Indications, Techniques, and Complications," *Surgical Clinics of North America*, vol. 89, pp. 781, 2009.

Automated Quantification of Human Skin Wrinkles using Optical Coherence Tomography

Juyoung Oh¹, Andrey Vavilin², Yujin Ahn², Songye Baek², Sungbea Ban²
and Woonggyu Jung^{2,3,†}

¹Department of Computer Engineering, Ulsan National Institute of Science and Technology, Ulsan, Republic of Korea

²Department of Biomedical Engineering, Ulsan National Institute of Science and Technology, Ulsan, Republic of Korea

³Center for Soft and Living Matter, Institute of Basic Science, Ulsan, Republic of Korea

E-mail: wjung@unist.ac.kr

Abstract— With the development of cosmetics and dermatologic treatment, anti-aging process such as reducing wrinkles have attracted worldwide attention. Thus, skin care industry has dramatically boomed, and various anti-wrinkle products are available in the market. However, there has been no automatic tool for detecting and visualizing wrinkles quantitatively, and there are only a few image-based algorithms applied to 2D skin image. Hereby, as an emerging tool for wrinkle quantification, we used OCT providing high-resolution 3D images of skins in non-invasive manner. In this study, it is expected to enable making fine assessment of skin wrinkles in automatic way.

Keywords— Optical Coherence Tomography (OCT), Quantitative wrinkles analysis, Image processing

I. INTRODUCTION

As people seek for their beauty in appearance, cosmetic companies are more demanded to produce anti-aging products having the function of reducing wrinkles. Thus, a unique tool is required for accurate evaluation of effect of anti-aging product. Prior work to approach skin study has been processed mainly by microscope which is impossible to acquire 3D skin geometry though wrinkles are 3D structure. Thus, we developed specific measuring tool and a novel algorithm for automated quantification of skin wrinkles. We utilize optical sectioning technique by OCT, which is capable of visualizing the 3D internal structure in a non-invasive manner and giving high-resolution. We deliver quantitative information of skin wrinkles in terms of depth, volume, and direction

II. METHODS

A. OCT system

A fiber based swept-source optical coherence tomography (SS-OCT) system constructed with a broadband swept laser source and a Mach-Zender interferometer with balanced photo-detector. 1310nm center wavelength with 100nm bandwidth laser provides $\sim 8\mu\text{m}$ in axial direction. The B-scan acquired at $>40\text{frames/s}$ with $\sim 17\mu\text{m}$ lateral resolution. The

OCT images were acquired $10\text{mm} \times 10\text{mm} \times 3.4\text{mm}$ in size consisted of $1000\text{pixels} \times 500\text{pixels} \times 400\text{pixels}$.

B. Image processing

The image processing based on B-mode tomographic images. We processed an image which spaces between local maxima of wrinkles are filled. By overlapping the original image with preprocessed image, the depth and area information of wrinkles was extracted out. By summing all the area of wrinkles over the C-mode direction, the total volume of wrinkles was computed as well. The directional information of wrinkles is analyzed using the *en-face* of volumetric skin image.

III. RESULTS

We extracted volumetric segmentation of targeted skin wrinkles. Quantified wrinkle distribution were represented by color variation in depth.

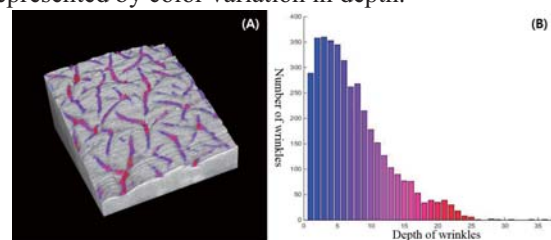


Fig 1. (A) Visualized quantification information of wrinkles
(B) The histogram of depth distribution of wrinkles

IV. CONCLUSION

The OCT is powerful tool to be used in skin assessment capable of detecting and visualizing skin wrinkles. Also, newly developed algorithm enabled to make specific quantification of targeted skin wrinkles in automatic way. It is expected that our study will play important role in measuring the capability of anti-wrinkle products and dermatology-related study.

ACKNOWLEDGEMENT

This work was supported by a grant of the Korean Health Technology R&D Project (HN13C0078) through Ministry of Health & Welfare.

REFERENCES

1. Carina Trojahn, et al, "Measuring skin aging using optical coherence tomography in vivo :a validation study," *Journal of Biomedical Optics*, vol. 20, 2015

A Phantom Study on MR Compatible RF Hyperthermia System

Han-Joong Kim¹, Jong-Min Kim¹, Seong-Dae Hong¹, Suchit Kumar², Seung-Koo Lee³,
Chulhyun Lee⁴, and Chang-Hyun Oh^{1,*}

¹Department of Electronics and Information Engineering, Korea University, Seoul, Korea

²Department of Biomicrosystem Technology, Korea University, Seoul, Korea

³Unionmedical Corporation, Uijeongbu, Korea

⁴The MRI Team, Korea Basic Science Institute, Cheongju, Korea

*Corresponding author, E-mail: ohch@korea.ac.kr

Abstract—The radio frequency (RF) hyperthermia treatment with capacitive driving can be a clinically effective and suitable tool for various tumor therapy. This process can be carried out more safely with MR temperature imaging with the body temperature monitoring. Simulation was performed on the effect of RF electric field application and resulting heat generation in the tissue mimic phantom. The MR compatible RF hyperthermia system is working properly without degrading the MR images and the experimental MR thermometry results are compared with the thermal simulation results.

Keywords— RF hyperthermia, MR thermometry, EM simulation, Thermal Simulation, Cancer treatment.

I. INTRODUCTION

The radio frequency (RF) hyperthermia treatment with capacitive driving seems to be a clinically effective and suitable tool for various tumor therapy. Many reports suggest that hyperthermia is every effective treatment and also suggests that it increases the efficiency when combined with other tumor treatment methods in late stage patient. The tumorous tissue have higher ionic concentration having higher electric conductivity than the normal tissue. When the RF electric field is applied, the more electric current is drawn by the tumor cell resulting in the increased temperature around the tumor. At low-temperature between 37 and 41.5 °C, heat enhances the tumor tissue growth and at high-temperature above 47 °C, heat damages both normal and tumor tissue [1]. This process can be carried out more safely with accuracy if we can monitor the treatment process including the body temperature simultaneously. In this paper, we proposed MR compatible RF hyperthermia system with simultaneous therapy and temperature monitoring.

II. METHODS

A. Tissue Mimic Phantom

A tissue-mimic phantom has been constructed with a simplified structure with liver and tumor part. The tumor region (agar, 15 g/L; NaCl, 16 g/L) is sealed with a thin plastic wrap and placed inside the liver-mimic region (agar, 15 g/L; NaCl, 2 g/L; CuSO₄, 1 g/L). Electric conductivity and relative permittivity

were measured using dielectric assessment kit, DAK (DAK, SPEAG, Zurich, Switzerland) and thermal conductivity and specific heat capacity are calculated [2,3]. The electric and thermal properties of tissue mimic phantom are listed in Table 1.

Table 1. The electric and thermal properties of tissue mimic agar-water gel phantom

		Liver	Tumor
Electric conductivity	[S/m]	0.35	2.5
Relative permittivity		85	260
Thermal conductivity	[W/m/K]	0.6057	0.6057
Specific heat capacity	[J/kg/K]	4181.4	4181.4

B. Simulation

We simulated the effect of radio frequency electric field and resulting heat generation in the tissue mimic agar-water gel phantom. The structure is shown in Fig. 1.

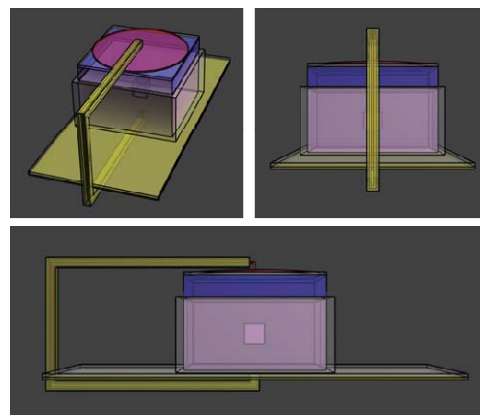


Fig. 1. Simulation modeling of RF hyperthermia system

Using the finite difference time domain (FDTD) method, the SAR map of in the phantom is calculated. This SAR information is used as a map of thermal energy source for our simulation. The radio wave frequency is 13.56 MHz and the power is normalized to 100 W. Total simulation time was 2 hour. Electromagnetic (EM) and thermal simulation analysis were performed using Sim4Life (Sim4Life V2.0, SPEAG, Zurich, Switzerland).

C. Experiment

We have designed, constructed, and tested experimentally the MR compatible RF hyperthermia

system working at 13.56 MHz without affecting the MR image acquisition at 128 MHz. The installed MR compatible RF hyperthermia system is shown in Fig. 2.



Fig. 2. The RF hyperthermia system installed in the MRI system

The phantom in the MRI bore is properly heated as expected (13.56 MHz, 100 W) for 2 hours. And MR temperature images of the phantom were obtained every 20 minutes using a 3.0 T MRI (Achieva, Philips, Best, Netherlands) in KBSI in Cheongju, Korea. PRFs methods (FFE sequence, TE = 15 msec, TR = 300 msec) was used for MR thermometry [4].

III. RESULTS

Figures 3 and 4 show the simulation results of temperature change as a function of power delivered by the electrode we made. In the tumor region, temperature rise was about 5 °C/hour and the difference in temperature between tumor and liver region goes up to about 2 °C as the thermal simulation continues.

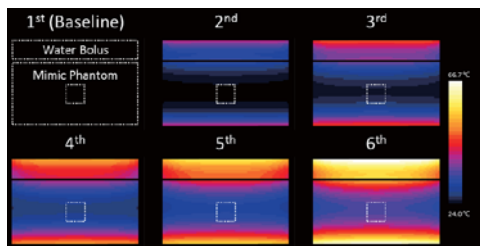


Fig. 3. Thermal simulation results: temperature distribution

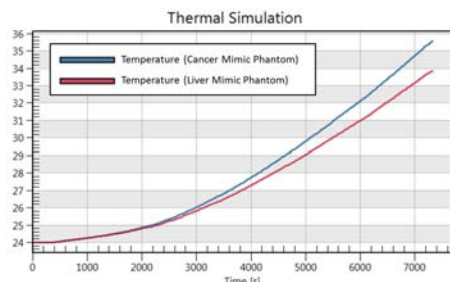


Fig. 4. Thermal simulation results: Temperature change in the tumor and liver phantom

The experimental results based on MR thermometry measurements are shown in Figs. 5 and 6. It can be seen that the temperature rise in experimental setup is almost similar to those in the thermal simulation results. Also the temperature rise and the temperature difference in MRI are in high correlation with the simulation result.

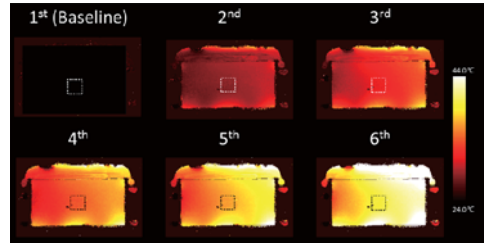


Fig. 5. Experimental results: Series of MR temperature images

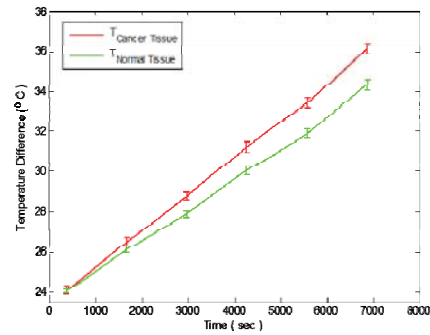


Fig. 6. Experimental results: Temperature change in the tumor and liver phantom

IV. CONCLUSION

In conclusion, experimental MR temperature imaging were conducted and simulations were performed to predict the thermal response in tumor and tissue model. They are in very good relation with each other. This study confirms the utility and feasibility of the MR compatible RF hyperthermia system with capacitive driving.

ACKNOWLEDGEMENTS

This work was supported by KEIT and MOTIE (project # 10047904) of Korea and Brain Korea 21 Plus Program through the National Research Foundation of Korea (NRF) funded by the Ministry of Science, ICT and Future Planning. Authors thank ZMT for providing free license of Sim4Life used in this study.

REFERENCES

1. A. Y. Cheung and A. Neyzari, "Deep local hyperthermia for cancer therapy: external electromagnetic and ultrasound techniques," *Cancer Research*, vol. 44, 4736-4744, 1984.
2. F. J. González, "Thermal simulation of breast tumors," *Revista Mexicana de Fisica*, vol. 53, 323-326, 2007.
3. S. Denys, J. G. Pieters, and K. Dewettinck, "Combined CFD and experimental approach for determination of the surface heat transfer coefficient during thermal processing of eggs," *Journal of Food Science*, vol. 63, 46-48, 1993.
4. V. Rieke and K. B. Pauly, "MR thermometry," *Journal of Magnetic Resonance Imaging*, vol. 27, 376-390, 2008.

Reliability of a smartphone pedometer with low frequency accelerometry

Jaehyun Park¹, Namkeun Kim²

¹Dept. of Industrial & Management Eng., Incheon National University (INU), Incheon, South Korea

²Dept. of Mechanical Eng. & Robotics., Incheon National University (INU), Incheon, South Korea

E-mail: jaehpark@inu.ac.kr

Abstract— This study aims to examine smartphone-based pedometer with low frequency, considering that low performance wearable devices have been widely used nowadays. As results, frequencies less than 20 Hz were difficult to be used to predict steps.

Keywords—Pedometer, Accelerometer, Low frequency, Smartphone

I. INTRODUCTION

With technology advancing at a fast-growing rate, mobile devices such as smartphones can provide sophisticated physiological information which was gathered by expensive equipment in past. Nowadays, smartphones load various sensors, including an inertial measurement unit (IMU). Typical IMU equipment of mobile devices contains accelerometer, gyroscope and magnetometer.

Many studies have used smartphones to analyze human body postures or movements, consisting of sitting, lying, standing, walking, running, jumping, stair ascent/descent, and falling [1, 2]. In many cases, assessed data has been analyzed by machine learning algorithms such as support vector machine, artificial neural networks, and K nearest neighbors [3, 4].

This study aims to examine reliability of a smartphone-based pedometer within the wide frequency range of 1-50 Hz. Considering that low performance wearable devices has increased and most of them has equipped with IMU, the reliability of low frequency pedometer seems to be investigated.

II. METHODS

The accelerometer of a smartphone provides three components (x, y, z). Note that Samsung Galaxy S4 was used as an experimental device. This study uses direction tracking method for detecting steps (Eq. 1).

$$(\cos \alpha)_i = \frac{x_i x_{i-1} + y_i y_{i-1} + z_i z_{i-1}}{\sqrt{x_i^2 + y_i^2 + z_i^2} \sqrt{x_{i-1}^2 + y_{i-1}^2 + z_{i-1}^2}} \quad (\text{Eq.1})$$

where x_i , y_i , and z_i are i th accelerometer components respectively, α indicates the changes in the direction of the vector of accelerometer.

In laboratory, a controlled experiment was carried out to assess physiology data in walking. Using android application program interface (API), accelerometer measurements were gathered in various frequency

setting (i.e., 1, 5, 10, 20, 30, 40, and 50 Hz). A participant was required to repeat walking activities twice for each frequency.

III. RESULTS AND CONCLUSION

As results, an average accuracy rate of the experimental prototype was 73%, while the average accuracy rate was 104% when the frequencies were equal to or higher than 20 Hz. Detailed accuracy rates were 9%, 25%, 63%, 100%, 98%, 112%, and 104% for 1, 5, 10, 20, 30, 40, and 50 Hz. An example was shown at Fig. 1.

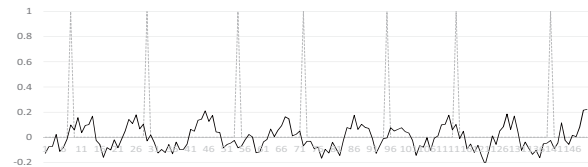


Fig. 1. Moving average of $\cos \alpha$ in 50 Hz (Dotted line indicates actual steps)

Although there were several limitations of this study (e.g., algorithm used in analysis and sample size of subjects), results reveal that low frequency, less than 20, may be difficult to assess the physical activity via smartphones. In the future, efficient algorithms and noise canceling methods for smartphone sensor data handling would be investigated.

REFERENCES

1. He, Y., and Li, Y., "Physical activity recognition utilizing the built-in kinematic sensors of a smartphone," *Int. J. Distrib. Sens. Netw.*, 2013.
2. Anguita, D., Ghio, A., Oneto, L., Parra, X., and Reyes-Ortiz, J.L., "Human activity recognition on smartphones using a multiclass hardware-friendly support vector machine," *Ambient Assist. Living Home Care*, vol. 7657, pp. 216-223, 2012.
3. Khan, A.M., Tufail, A., Khattak, A.M., and Laine, T.H., "Activity recognition on smartphones via sensor-fusion and KDA-based SVMs," *International Int. J. Distrib. Sens. Netw.*, 2014.
4. Thiemjarus, S., Henpraserttae, A., and Marukatat, S., "A study on instance-based learning with reduced training prototypes for device-context-independent activity recognition on a mobile phone," *In Proceedings of the IEEE International Conference on Body Sensor Networks (BSN)*, pp. 1-6, 2013.

Biomedical Assessment of Plantar Soft Tissue Changes due to Advanced Tissue Glycation in Diabetic Patients

J. C. Teoh¹, D. Y. Lee², and T. Lee³

¹Department of Biomedical Engineering, Faculty of Engineering, National University of Singapore, Singapore

²Department of Orthopaedic Surgery, Seoul National University Hospital, Seoul, South Korea

³Department of Medical Biotechnology, Dongguk University, Seoul, South Korea

E-mail: tlee@dongguk.edu

Abstract—This study explores the relationship plantar tissue stiffness and several parameters, e.g. age, diabetes mellitus (DM) duration, body mass index (BMI) and HbA_{1c} level. Understanding of these associations is certainly helpful in understanding the levels of diabetic foot risk.

Keywords— plantar soft tissues, stiffness, diabetes

I. INTRODUCTION

The exposure to high blood glucose level due to DM leads to several fatal complications. Diabetic foot is one of them. Diabetic foot risk is usually graded based on neurological assessment such as monofilaments and vibration perception which are predictive of peripheral neuropathy. However, loss of sensation is not the direct reason. In fact, abnormally stiffened tissue that fails to withstand the impact force is a more straightforward explanation to foot ulceration.

The objective of this study is to evaluate the relationship of plantar tissue stiffness and parameters, e.g. age, DM duration, BMI and HbA_{1c} level.

II. METHODS

100 DM patients were recruited. The localized response of plantar soft tissue at selected regions, i.e. hallux, 2nd sub-metatarsal head (MTH) pad, and heel pad, were measured using the indentation system which consisted of a stylus driven by a stepper motor.

III. RESULTS

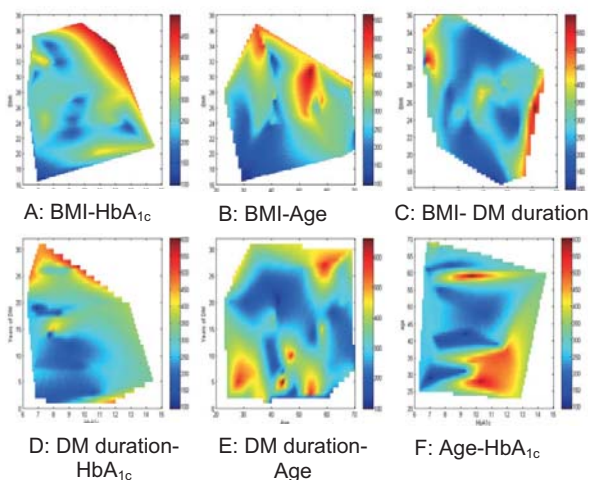


Fig.1. Triadic relationship at 2nd sub-MTH pad

As shown in Fig.1A,1D,1F, it can be deduced that HbA_{1c} level that denote the blood glucose level have a more influential role in altering the tissue stiffness in plantar soft tissues. HbA_{1c} level measures the average level of blood sugar over a period of weeks or months. Prolonged exposure to high blood glucose causes pathological changes by enhancing reactions between reducing glucose and cellular protein that increases the formation of advanced glycation end products (AGEs). Accumulation of these compounds decreases the elasticity of tissue by the increased intermolecular cross linking and adversely modified side-chains [1]. Studies have shown the stiffer plantar tissue in DM patients as compared to their age-matched control.

Based on the results, BMI (Fig. 1A-1C) also plays a key role in increasing the plantar soft tissue stiffness. This may be explained by the strong relationship between high BMI and DM has been previously reported [2]. It is also postulated that the loss in weight and BMI effectively improve glycemic control [3]. In other words, high BMI may cause increase in HbA_{1c} which may undesirably stiffen the tissue. On the hand, age and DM duration did not affect the tissue response much. Even in young patients with short duration of diabetes, the tissue stiffness may still be adversely increased as long as the HbA_{1c} level is high.

IV. CONCLUSION

The results recommended that in the effort to design the foot care plan, patient's HbA_{1c} score and BMI should be paid more attention. Special consideration should be given to the high risk group of high HbA_{1c} score above 9% or BMI >25 kgm⁻².

REFERENCES

1. A.J. Bailey,. "Molecular mechanisms of ageing in connective tissues." *Mechanismsof AgeingandDevelopment* 122(7):735-755,2001.
2. H. C. Looker, W. C. Knowler and R. L. Hanson, "Changes in BMI and weight before and after thedevelopment of type 2 diabetes." *Diabetes Care*24(11): 1917-1922, 2001.
3. L. K. Heilbronn, M. Noakes and P. M. Clifton "Effect ofenergyrestriction, weight loss, anddiet composition on plasma lipids and glucose in patients with type 2 diabetes." *Diabetes Care*22(6): 889-895, 1999.

Gait Characteristics in Patients with Parkinson's Disease during the Timed Up and Go Test

M. J. Son¹ and C. H. Youm²

¹Department of Medicine, Graduate School, Dong-A University, Busan, Korea

²Department of Health Care and Science, Dong-A University, Busan, Korea

E-mail: chyoun@dau.ac.kr

Abstract—The purpose of this study was to investigate the gait characteristics of patients with Parkinson's disease (PD) during the Timed Up and Go (TUG) test using 3-dimensional analysis. The results of this study showed significant differences between patients with PD at stage 2.5 and 3 of the Hoehn and Yahr scale (Group I) and those at stage 2.0 of the Hoehn and Yahr scale (Group II). Group I and II had poor gait ability during the turning phase of the TUG compared to the control group. The TUG test might be a useful tool to identify the gait characteristics of Parkinson's disease.

Keywords—Parkinson's disease, Timed Up & Go, Kinematics, Hoehn & Yahr stage.

I. INTRODUCTION

Patients with Parkinson's disease (PD) experience a considerable amount of difficulty when walking, turning, and performing complex motor tasks and cognitive tasks [1]. Many researchers have attempted to investigate the gait characteristics of patients with PD by using various tasks. The Timed Up and Go (TUG) test involves rising from a chair, walking, turning, and returning to the chair, and has been used as a measure of balance and mobility in the elderly. However, most studies obtained measurements using a watch and an accelerometer during the TUG test [2,3]. Therefore, the purpose of this study was to investigate the gait characteristics of patients with PD during TUG using 3-dimensional analysis in order to classify the severity of PD.

II. METHODS

This study included a total of 30 subjects, 10 patients with PD at stage 2.5 and 3 of the Hoehn and Yahr scale (H&Y; Group I), 10 patients with PD at stage 2.0 of the H&Y scale (Group II), and 10 controls (Table 1). The performance of the TUG test was captured on an 8-meter walkway using six infrared cameras (Vicon, MX-T10, UK).

PD patients also performed the TUG tasks after a minimum 12-h withdrawal from antiparkinsonian medications. Herein, TUG was analyzed in two steps after the turn started.

The average values for the spatiotemporal and kinematic variables after 3 repetitions of the tasks were analyzed. All statistical analyses were performed using SPSS 21.0 (Chicago, IL). A mixed-model ANOVA with one between factor (3 groups) and one within factor (dominant and non-dominant step) was used to compare interaction and main effects. The significance level was set at .05.

Table 1. Subject Characteristics

	Group I (n=10)	Group II (n=10)	Controls (n=10)
Age (years)	71.2±5.4	69.9±5.4	63.6±6.1
Height (m)	1.56±0.10	1.60±0.07	1.60±0.1
Body mass (kg)	55.8±6.7	59.8±6.1	62.3±6.7
BMI (kg/m ²)	22.9±1.9	23.5±2.3	24.5±2.5
MMSE (score)	27.4±1.6	28.1±1.7	28.6±1.0
UPDRS total (score)	52.1±11.7	41.9±10.2	-
UPDRS III (score)	36.4±6.6	29.2±7.9	-
Hoehn and Yahr stage	2.8±0.3	2.0±0.0	-
Disease duration (years)	8.2±6.4	5.1±2.4	-

UPDRS, unified Parkinson's disease rating scale

III. RESULTS

Walking speed, step length, asymmetry of step length, range of motion (ROM) for the knee and shoulder, and foot clearance height significantly differed between groups. Furthermore, the ROM of the knee significantly differed within steps. The ROM of the hip and shoulder showed a significant interaction.

IV. CONCLUSION

This results of the study indicated significant differences between Group I and Group II. Group I and II had inferior gait ability during the turning phase of the TUG test compared to the control group. The TUG test might be a useful tool to identify the gait characteristics of patients with PD.

REFERENCES

1. D.J. Gelb, E. Oliver, and S. Gilman. "Diagnostic criteria for Parkinson disease." *Archives of neurology*, vol. 56, pp. 33-39, 1999.
2. S. Morris, M. Morris, and R. Iansak. "Reliability of measurements obtained with the Timed "Up & Go" test in people with Parkinson disease." *Physical therapy*, vol. 81, pp. 810-818, 2001.

3. Weiss et al. "Can an accelerometer enhance the utility of the Timed Up & Go Test when evaluating patients with Parkinson's disease?" *Medical engineering & physics*, vol. 32, pp. 119-125, 2010.

Finite Element Simulations in Foot Ulcer Prevention: New Strategies towards Subject-Specific Anatomical Model Generation

W. M. Chen¹, P. V. Lee², and S. J. Lee¹

¹Department of Biomedical Engineering, Inje University, Gimhae, South Korea

²Department of Mechanical Engineering, University of Melbourne, VIC, Australia

E-mail: wmchen@bme.inje.ac.kr

Abstract— Foot ulcers are among the most devastating complications of diabetes. Previous studies have suggested that peak plantar pressure, peak plantar shear, and internal tissue deformation are highly associated with tissue breakdown in the diabetic foot. Finite element (FE) modeling of foot and footwear offers a unique computational tool, as it allows a complete stress/strain analysis to be conducted. However, the complex foot structure makes the construction of an anatomically accurate FE foot model costly and time consuming. In this work, a new approach has been developed, which automates the construction of a 3D FE model of the human foot. The segmentation scheme used a clustering-based algorithm to identify different tissues from coronal CT images of the foot, followed by sequential summation of image masks. From the preliminary results, it was shown that a normal plantar pressure pattern could be replicated. Furthermore, soft tissue compressive deformations under individual metatarsal heads could be efficiently identified. Although only a normal foot model was considered in this study, using the developed methodology, a diseased patient-specific foot model can similarly be built and analyzed within a reasonable time frame.

Keywords—Foot model; Subject-specific analysis; Soft tissue injury; Plantar pressure; Mesh refinement;

I. INTRODUCTION

Foot ulceration is a common type of chronic wound, and a leading cause of limb amputation, mortality and morbidity in people with diabetes [1]. It has been shown that neuropathic diabetic people had abnormally high stresses under the foot, increasing the risks of tissue breakdown [2]. For early diagnosis of ulceration, efforts have been made to develop capacities to compute stress, strain and strain energy density within foot's soft tissues. Use of anatomically accurate and subject-specific finite element (FE) models of the foot overcome the limitations associated with models of simplified geometries, improving the specificity and accuracy of injury predictions [3]. Unfortunately, the complex anatomy of the foot makes the construction of a structurally accurate foot FE model extremely

difficult [4]. The present study aims (1) to develop an automated method for rapid construction of FE model of the human foot directly from medical image data, and (2)) to evaluate the quality of the mesh, in terms of shape of the element and volume distortion.

II. METHODS

High-resolution computer tomography (CT) images of the foot were obtained, and the data was processed using a multi-parametric clustering method to extract the regions of soft tissues, bones, and cartilages. A total of 125 CT images of the forefoot (five metatarsal bones, the fourteen phalanges and associated soft tissue structures) were imported into the MATLAB custom algorithm. Surface meshes were extracted for each tissue component using a Delaunay Tetrahedralization in CGAL (www.cgal.org/). Volumetric mesh was created to fill the closed surfaces using TetGen (wias-berlin.de/software/tetgen/). Individual element sets were generated to facilitate subsequent assignment of the material properties to each tissue components [2]. The FE mesh was finally written into ABAQUS input file format to execute FE analysis.

The volumetric tetrahedral meshes used to fill the enclosed iso-surfaces were at certain mesh resolution. Often, it is desirable to produce meshes with different resolution that can be used in convergence tests (where progressive mesh refinements are necessary). This can be achieved by changing meshes of iso-surfaces, because interior volumetric meshes generated by TetGen preserves the input surface meshes (i.e. using existing nodes at iso-surfaces). In addition, it is practically important to increase mesh resolution at plantar surface to ensure accuracy during foot-ground/insole contact interactions. Furthermore, as the area around the bone-tissue interface has the greatest stress intensity, increasing mesh resolution there should also improve the accuracy of the model's prediction. It is thus desirable to adjust the surface mesh resolution at the plantar surface and bones to control the volumetric mesh of the entire model. In this study, the forefoot model was created with five different densities by controlling the average element edge length of 6.0 mm, 4.5 mm, 3.5 mm, 2.5 mm and 1.5 mm.

The entire procedure uses MATLAB as the main platform to call freely-availably external command or executable file, and enables a highly-automated method for directly converting CT images into FE models (Fig. 1). FE analysis are strongly influenced by mesh quality in particular to the shape distortion, such as element collapse. The generated mesh quality was evaluated by assessing elements' aspect ratio. The aspect ratio for a tetrahedron (Tet) element is computed by taking the ratio of the height (h_i) of a vertex to the square root of the area (A_i) of the opposing face. A "perfect" element in the shape of an equilateral Tet will equal one.

III. RESULTS

The generated forefoot mesh with an element edge length of 6.0 mm consisted of 11,128 tetrahedral elements. For mesh at this resolution, the entire modelling process (including the image segmentation part) took 45 seconds to run in a desktop computer. By refining triangulation (i.e. to adjust surface element edge length) at iso-surfaces, a series of FE models with different mesh refinement i.e. coarse to fine, can be generated with little effort. As mesh refines, the total number of elements increased by more than 1.8-fold (from 11,128 to 31,213), and the processing time increased from 45 to 102 sec. The mesh generated were generally free from poorly-shaped elements with extreme large AR. The average AR for different resolution models were in the range of 1.45 to 2.43, with a maximum of 8.75 found in the model with element edge length 2.5. The above results were summarized in Table 1.

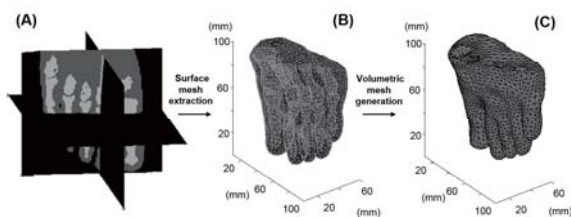


Fig. 1. Automated FE Mesh generation for the forefoot

IV. CONCLUSION

This study describes a new automated approach to the segmentation and meshing of a human forefoot for FE modelling. This approach is fast and robust in dealing with soft tissue-bone interface, and fast remeshing capabilities for mesh convergence tests, which provides a highly efficient tool for creating patient-specific foot models for clinical applications.

Table 1. Mesh quality for the produced FE models at different element edge length

Edge length (mm)	No. of elms, Total	Computational time (Sec)	AR (Avg)	AR (Max)
6.0	11,128	45	1.51	7.97
4.5	14,584	60	2.11	6.82
3.5	20,974	91	1.47	7.64
2.5	25,779	95	2.43	8.75
1.5	31,213	102	1.53	5.10

REFERENCES

1. R. Pecoraro, G. Reiber EB. Pathways to DiabeticPathways to diabetic limb amputation. Basis for prevention.; *Diabetes Care*. 13:513–21. 1990.
2. Chen W-M, Lee T, Lee PV-S, Lee JW, Lee S-J. Effects of internal stress concentrations in plantar soft-tissue--A preliminary three-dimensional finite element analysis. *Med Eng Phys*;32:324–31. 2010.
3. Chen W-M, Park J, Park S-B, Shim VP-W, Lee T. Role of gastrocnemius-soleus muscle in forefoot force transmission at heel rise - A 3D finite element analysis. *J Biomech*;45:1783–9. 2012.
4. Telfer S, Erdemir A, Woodburn J, Cavanagh PR. What Has Finite Element Analysis Taught Us about Diabetic Foot Disease and Its Management? A Systematic Review. *PLoS One*;9:e109994. 2014.

The feedback/forward controller of joint could achieve the center of mass motion during running with gains determined by natural frequency

H. R. Lim¹ and S. K. Park¹

¹Mechanical Engineering, KAIST, Daejeon, Korea
E-mail: sukyungp@kaist.ac.kr

Abstract—Mass-spring running model demonstrates the motion of center of mass (CoM) of human and corresponding ground reaction force. To examine the joint torque generation which could achieve the CoM motion of the model, we combined the passive model and the segments of lower limb. By formulating the joint torque equation as feedback controller, we found that the feedback gain could be formulated as a function of natural frequency related to the CoM motion.

Keywords— Running, Mass-spring model, Joint torque, Feedback gain

I. INTRODUCTION

Mass-spring running model demonstrates the motion of center of mass (CoM) of human and corresponding ground reaction force during running [1]. The passive running model can explain the dynamics of CoM, but the CoM motion is achieved by each joint motion. Thus, in this study, we examined the joint torque generation to achieve the CoM motion by combining the passive model and the segments of lower limb.

II. METHODS

We obtained the relationship between joint motions which could reconstruct CoM motion of the passive model and corresponding joint torques. The joint dynamics were obtained under the conditions of negligible trunk dynamics and the coincident motion of hip joint and the CoM of model as shown in Fig. 1.

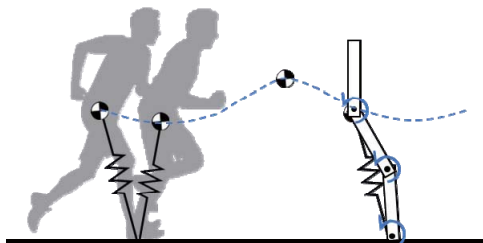


Fig. 1. Mass-spring running model and the schematic of three segmental pendulum running model.

The obtained joint torque equations were formulated as a feedback controller form by representing the kinematics of each segment as the kinematics of CoM and approximating the formulation of CoM motion as a harmonic equation.

III. RESULTS

The joint torque equations could be formulated as the feedback and feedforward controller with feedback gains determined by mass, length and the natural frequency of mass-spring model.

$$\begin{bmatrix} T_{ank} & T_{knee} & T_{hip} \end{bmatrix}^T = K(m, l, \omega_n) \begin{bmatrix} \theta_{sh} & \theta_{th} \end{bmatrix}^T + T_{feedforward} \quad (1)$$

The feedback gain matrix and the feedforward control input show time-varying nonlinearity, but they can be determined by desired running speed, related to the natural frequency as shown in Fig. 2.

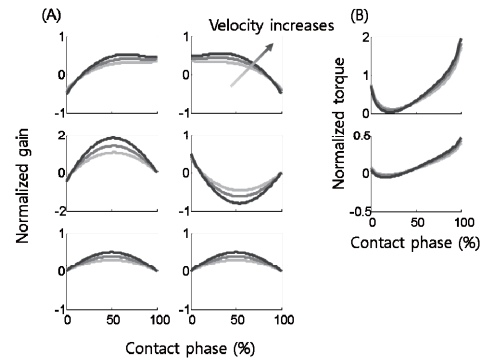


Fig. 2. Normalized trajectories of (A) feedback gain and (B) feedforward input during contact phase with running speed.

IV. CONCLUSION

The results imply that the feedback/forward controller of joint could achieve the center of mass motion during running with gains determined by natural frequency.

ACKNOWLEDGEMENT

This research was supported by the project of Korea Hydro & Nuclear Power Co., LTD and Basic Science Research Program through the National Research Foundation of Korea(NRF) funded by the Ministry of Education (No. 2013R1A1A2A10012604).

REFERENCES

1. R. Blickhan, "The spring-mass model for running and hopping", *J Biomech.*, vol. 22, pp. 1217-27, 1989.

Evaluation of feasibility of two depth sensor-based Microsoft Kinect cameras for abduction-adduction motion analysis

C. Y. Kim, J. S. Hong, and K. J. Chun

Advanced Biomedical Engineering Lab., Korea Institute of Industrial Technology, Cheonan, Korea
E-mail: cnddus911@kitech.re.kr

Keywords— Phase difference, Pearson's coefficient, Limit of Agreement, abduction-adduction, motion analysis

I. INTRODUCTION

Motion analysis now involves infrared camera-based three-dimensional (3D) systems and inertia sensor-based motion capture systems^{1,2}. The infrared camera-based approach is the most accurate, but is limited by the space required for test equipment installation. In contrast, the inertial sensor approach can measure any human motion without space limitation because it uses a suit with attached sensors. However, this system is expensive as the infrared camera-based system.

To address this problem, Kinect camera motion capture system based on depth data was developed³. However, no quantitative motion analysis using Kinect camera system has been done. This study investigated the extent to a depth sensor-based Kinect camera can accurately evaluate motion.

II. METHODS

The abduction-adduction motions of the dummy and human participants were measured simultaneously using 10 infrared camera-based 3D motion capture systems, two depth sensor-based Kinect cameras and an IMU sensor. To evaluate the accuracy of the motion capture systems, the VICON camera was the reference used to calculate correlation coefficients and phase differences of Kinect camera and IMU sensor. Kinematic movement of the dummy and the humans was induced by abduction-adduction motions to a maximum angle of 60°. Each test was performed at angles of 0°, 30°, 45°, 60°, and 90° assigned as the standing position angle (Fig. 1).

III. RESULTS

Phase difference occurred at $3.87 \pm 0.54^\circ$ (6.5%), $4.05 \pm 0.93^\circ$ (6.8%), $6.46 \pm 0.96^\circ$ (10.8%), $3.68 \pm 0.29^\circ$ (6.1%), and $3.29 \pm 0.43^\circ$ (5.5%) at a standing position angle of 0°, 30°, 45°, 60°, and 90°, respectively. At the standing position angle of 45°, the phase difference was significantly higher than other angles because of the arm motion and viewpoint of one Kinect camera totally matched in the same line, which made it difficult to clearly record the depth images from the

one camera. Statistical analysis of the phase difference of the IMU sensor and Kinect camera compared with the VICON camera using the general linear model was revealed that the phase difference of Kinect camera was significantly lower than the IMU sensor ($p=0.027$). Kinect camera is judged to be more effective in motion analysis than the IMU sensor, at about 1/7 of the cost. Statistical analysis of the correlation between the VICON camera and Kinect camera revealed a Pearson's correlation coefficient 0.96, 0.96, 0.84, 0.96, and 0.94, and LoA score of 95.0%, 96.4%, 94.7%, 96.0%, and 95.8% at a standing position angle of 0°, 30°, 45°, 60°, and 90°, respectively.

IV. CONCLUSION

The two Kinect cameras had similar motion tracking data as the VICON cameras at about minimum 1/100 of the cost. Kinect camera should prove useful for analysis of overall motion because of the high correlation coefficient and LoA score.

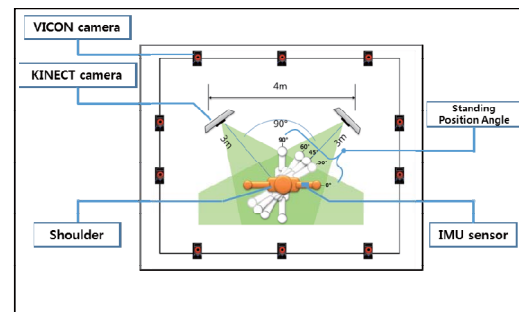


Fig. 1. Schematic diagram of experimental setup

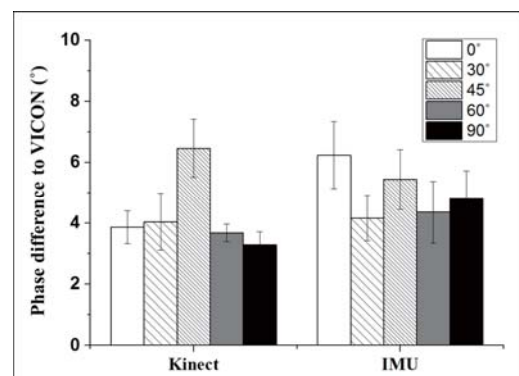


Fig. 2. Phase difference of Kinect camera and IMU sensor compared with the VICON camera for each standing position angle of human test results

Table 1. Stastical analysis of Kinect and VICON cameras at each standing position angle

Standing Position angle (°)	Mean difference	Standard deviation	95% LoA Score	Pearson's Correlation coefficient (γ)
0	0.59	5.77	95.0 % (950 / 1000)	0.96
30	-0.22	5.89	96.4 % (964 / 1000)	0.96
45	1.63	12.25	94.7 % (947 / 1000)	0.84
60	-0.91	6.23	96.0 % (960 / 1000)	0.96
90	-0.63	7.47	95.8 % (958 / 1000)	0.94

ACKNOWLEDGEMENT

This research was supported by the Korea Institute of Industrial Technology (KITECH), Republic of Korea.

REFERENCES

1. T. D. Albright and G. R. Stoner, “Visual motion perception”, Proc. Natl. Acad. Sci. USA, Vol. 92, No. 7, 2433-2440, 1995.
2. T. Krosshaug et al., “Estimating 3D joint kinematics from video sequences of running and cutting maneuvers—assessing the accuracy of simple visual inspection”, Gait & Posture, Vol. 26, No. 3, 378-385, 2007.
3. J. Shotton et al., “Real-time human pose recognition in parts from single depth images”, Communications of the ACM, Vol. 56, No. 1, 116-124, 2013

Incorporation of center of pressure excursion in a compliant running model may improve reproduction of human running dynamics

C. Jung¹ and S. Park²

¹The Robotics Program, Daejeon, Korea

²Department of Mechanical Engineering, Daejeon, Korea

E-mail: sukyungp@kaist.ac.kr

Abstract— In this study, we propose a running model that incorporates the CoP excursion and evaluated whether this can improve reproduction of human running dynamics. The result indicates that this model may solve overestimation issues in previous SLIP.

Keywords— Running model, running dynamics, CoP excursion, ground reaction forces,

I. INTRODUCTION

In attempts to reproduce human running dynamics using mathematical models, a spring-loaded inverted pendulum is widely used as a simulation template. The model successfully captures characteristic dynamics of running, such as ground reaction forces (GRF) and oscillatory center of mass (CoM) propagation in the space [1]. However, the model has few limitations in reproducing human running dynamics, especially in force directions. This is mainly due to point foot of the model, because the foot restricts the forward movement of center of pressure (CoP), which in human is approximately 18% of the lower limb [2]. In this study, we aim to propose a running model which incorporates the CoP excursion and continuous running dynamics.

II. METHODS

A. CoP excursion Model

The CoP excursion was represented as a pivot translation in a continuous path, the CoP excursion function. It was modelled as a sinusoidal function to be differentiable and take model parameters, foot length and leg stiffness, to decide amplitudes of the function. The leg stiffness is considered to decide contact time similarly in previous research [3].

B. Incorporation of CoP excursion in running model

Since the acceleration profile of CoP excursion is non-zero and continuous, its effect on the running model is introduced as an inertial force.

III. RESULTS

As a result, for the same horizontal CoM movement, overestimations in Horizontal GRF reduced as spring

angle reduced. It also achieved continuous running dynamics with CoP excursion: CoM trajectories, Forward velocity, and GRF.

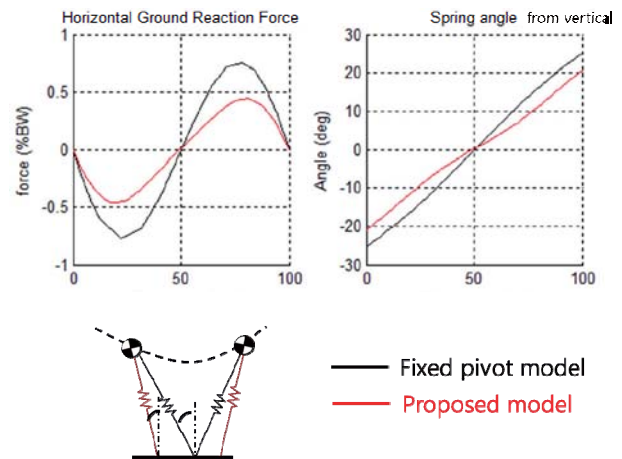


Fig. 1. Figure caption

IV. CONCLUSION

The proposed model was able to reproduce continuous running dynamics in running, as well as to solve overestimation issues in previous SLIP.

ACKNOWLEDGEMENT

This research was supported by the Basic Science Research Program (NRF-2013R1A1A2A10012604) funded by the Ministry of Education, Science and Technology.

REFERENCES

1. H. Geyer, A. Seyfarth, and R. Blickhan, "Compliant leg behavior explains basic dynamics of walking and running", *Proc. R. Soc. B.*, vol. 272, pp. 2861, 2006
2. S.R. Bullimore, and J.F. Burn, "Consequences of forward translation of the point of force application for the mechanics of running". *J. Theo. Bio.*, vol. 238, pp. 211-219, 2005
3. C. Jung and S. Park, "Compliant bipedal model with the center of pressure excursion associated with oscillatory behavior of the center of mass reproduces the human gait dynamics", *J. Biomech.*, vol. 47, pp 223-229, 2014

Body Weight Support with Pelvic Motion Facilitation Significantly Reduces Muscle Activation Durations of Lower Limbs

K. R. Mun¹, and H. Yu¹

¹Biomedical Engineering, National University of Singapore, Singapore
E-mail: a0082798@u.nus.edu

Abstract— The aim of this study is to investigate the effects of body weight support on muscle activation patterns during over-ground walking. Using a newly developed robotic walker which can facilitate pelvic motions, we examined the muscle activations of lower limb for ten healthy subjects with incremental levels of body weight, ranging from 0% to 40% at 10% intervals. Linear and significant reductions in the duration of muscle activation were observed with increasing BWS levels, without altering normative EMG patterns. The results of this study show an important indication of reduced burden for neurologically challenged patients and increased efficiency for the gait rehabilitation.

Keywords— Body Weight Support (BWS), Over-ground Walking, Gait Rehabilitation, Muscle Activation Patterns.

I. INTRODUCTION

Body weight support (BWS), which is routinely used in gait rehabilitation, promotes better functional outcomes for neurologically challenged patients. Despite the established effectiveness of BWS in gait rehabilitation, the findings on biomechanical effects of BWS training still remain contradictory [1]. A possible reason for the controversy observed among different researchers may be the use of an overhead harness in treadmill-based devices which causes a different gait pattern by restricting pelvic motions from an actual over-ground gait. Therefore, the aim of this study is to investigate the effects of BWS on muscle activation patterns during over-ground walking with a newly developed robotic walker.

II. METHODS

A. Provision of BWS with a Robotic Walker

A novel robotic walker which can provide 6 degree of freedoms (DoFs) to ensure a natural gait pattern was developed. The use of a BWS system which provides active unloading of the body mass of the subject to the desired percentage with unrestricted pelvic motion was proposed for effective BWS training [2].

B. Subjects and Experimental Protocols

We compared muscle activation of ten healthy subjects during walking on 10m distance walkway with incremental amount of BWS unloading forces from 0% to 40% at 10% intervals. Muscle activation patterns and

duration were calculated from nine muscles attached to the tibialis anterior (TA), gastrocnemius (GA), soleus (SOL), vastus medialis (VM), rectus femoris (RF), biceps femoris (BF), gluteus maximus (GMax), gluteus medius (GMed) and adductor longus (AL).

III. RESULTS

The muscle activation patterns were significantly and linearly decreased in accordance with the BWS level. During the stance phase, for ankle joint plantarflexor and dorsiflexor, duration of TA at 30% and 40% of BWS, and GA at 20%, 30%, and 40% of BWS were significantly shortened as compared to 0% BWS. For knee extensor and hip flexor, the duration of VM at 40%, and RF at 20% was significantly shortened as compared to 0% of BWS. Likewise, hip joint flexor/extensor and ad/abductor, GMax in all conditions, GMed in 30% and 40%, and AL in all conditions were significantly reduced compared with 0% of BWS.

IV. CONCLUSION

It is important to note that the linearly declined muscle activation without observing abnormal patterns is a clear indication that the BWS training with pelvic motion support can extract the proportionately scaled motor responses required for normative gait. The findings of this study demonstrate the linearly decreased muscle activation, and high muscle efficiency for weight bearing and propulsion.

ACKNOWLEDGEMENT

This work was supported by the Academic Research Fund Tier 1 (FRC) of the Ministry of Education, Singapore under WBS no. R-397-000-218-112.

REFERENCES

1. M.K. Aaslund, and R. Moe-Nilssen, "Treadmill walking with body weight support: Effect of treadmill, harness and body weight support systems," *Gait Posture*, 28(2), 303-308.
2. K.R. Mun, Z. Guo, and H. Yu, "Development and Evaluation of a Novel Over-ground Robotic Walker for Pelvic Motion Support", 14th IEEE/RAS-EMBS International Conference on Rehabilitation Robotics (ICORR), Singapore, 2015

Restriction of Pelvic Motions during Over-ground Walking Changes Gait Kinematic and Descriptive Parameters

K. R. Mun¹, and H. Yu¹

¹Biomedical Engineering, National University of Singapore, Singapore, Singapore
E-mail: a0082798@u.nus.edu

Abstract— The influences of pelvic lateral and rotational motions during over-ground walking were investigated in this study. The pelvic motions were restricted through a newly developed robotic walker. Variations in gait descriptive parameters as well as joint kinematics were measured to indicate gait difference caused by pelvic restrictions. The results showed that pelvic restriction significantly shortened gait spatial parameters. It was also observed that the restriction caused a significant reduction in the range of motion (RoM) of the ankle, knee, and hip joints with altered kinematic profiles. We concluded that the pelvic restriction significantly altered normal gait dynamics, thus inhibiting the efficacy of gait rehabilitation.

Keywords— Pelvic restriction, over-ground walking, robotic gait rehabilitation, gait training.

I. INTRODUCTION

Pelvis plays a central role in human locomotion and controls whole body balance, force transmission between lower and upper limbs, and increases energy efficiency of the gait. Recently, the importance of facilitating pelvic lateral displacement (LD) and rotational (RT) motions has been emphasized in the area of gait rehabilitation in order to give a natural and aesthetic gait pattern. With prevalent use of robotic devices for gait rehabilitation, however, these movements are often limited by such devices. Therefore, it is imperative to investigate contributions and influences of pelvic LD and RT motions on human gait for a better clinical application. Therefore, this study aimed to evaluate the effects of pelvic restriction on lower limb dynamics including gait kinematic and descriptive parameters during over-ground walking.

II. METHODS

The gait experiments with the robotic walker with and without the pelvic lateral and rotational movements have been conducted (Fig. 1). The experiment was performed under 3 different scenarios; 1) walking without the walker, 2) walking with walker, while pelvic lateral and rotational motions are allowed (no restriction, NR); 3) walking with walker, while both pelvic lateral and rotation motion were restricted (both restriction, BR). 12 healthy young subjects participated in this study. All subjects were instructed to walk naturally with their preferred speed on the 10m distance

walk way in the gait lab. Kinematic profiles and gait descriptive parameters such as normalized stride length, step length, step width, and gait velocity were calculated.

III. RESULTS

There were significant reductions in ankle plantarflexion at terminal stance, knee flexion at mid-swing, and hip extension at mid-stance in BR conditions. The RoMs of ankle, knee, and hip joints were reduced in BR. In addition, the pelvic restriction significantly reduced the stride and step length as well as gait velocity, and increased ratio of stance phase.

IV. CONCLUSION

In agreement with a previous study on pelvic fixation during gait [1], pelvic restriction severely affected gait dynamics. Thus, the results of this study complemented other studies and proved the importance of facilitating pelvic lateral and rotational movements to elicit correct afferent input to restore defective gait patterns of stroke survivors after gait training.



Fig. 1. The design concept and actual prototype of the novel robotic walker for pelvic motion support.

ACKNOWLEDGEMENT

This work was supported by the Academic Research Fund Tier 1 (FRC) of the Ministry of Education, Singapore under WBS no. R-397-000-218-112.

REFERENCES

1. J.F. Veneman, J. Menger, E.H. van Asseldonk, F.C. van der Helm, and H. van der Kooij, "Fixating the pelvis in the horizontal plane affects gait characteristics", *Gait Posture* 28:157-63.

An Experimental Method on Mechanical Behavior of Soft Tissue subjected to an External Impact.

Y. Bahn¹, Deok-Kee Choi²

¹Dankook University, Yongin-si, Gyeonggi-do, Korea

²Department of Mechanical Engineering, Dankook University, Yongin-si, Gyeonggi-do, Korea

E-mail: dkchoi@dku.edu

Abstract— An experimental method to grasp the motion of a soft tissue subjected an external stimuli where sensors or devices are not mountable, is presented. The method consists of a series of procedures: cell elements, image processing, finite deformation theory, and domain mappings.

Keywords— brain, soft tissue, cell element, finite deformation, material modelling, hyperelasticity.

I. INTRODUCTION

Damage estimation of a human brain under sudden loadings or impacts, which are commonly brought by car accidents, is an important issue in everyday life. Human brain has significant degree of complexity that it is difficult to assess damage occurring inside a brain with conventional methods which come with various types of sensors that are not installable. The present method contains a series of experimental and numerical procedures, in which there are development of a specimen, construction of cell elements, image processing and deformation calculation, to come up with complex biomechanical topics such as the motion or deformation of a soft tissue subjected to various external stimuli including car accidents.

II. METHODS

In order to simulate the behavior of a soft tissue, good specimens need to be developed in such a way that it obeys constitutive laws of soft tissues. For example, gelatin may be chosen as a specimen for brain tissue simulation [1]. A cell element is a term to denote a physical element constructed by colored markers building up triangular or quadrilateral shapes shown in Fig. 1, which are placed on the surface of a soft tissue. Once the cell elements are completed, snapshots are taken with a high-speed camera during the motion; thereby they undergo an image-processing program to generate the coordinates of the elements. The deformation of a soft tissue can be obtained with the mapping between configurations: the parent, the initial, and the current configurations. With the isoparametric concept, the coordinates of the element at the initial configuration \mathbf{X}_i and those at the current configuration

\mathbf{x}_i are expressed with the shape functions $N_\alpha(\xi, \eta)$, respectively:

$$\mathbf{X}_i = \sum_{\alpha=1}^n N_\alpha(\xi, \eta) \mathbf{X}_{\alpha,i}, \quad \mathbf{x}_i = \sum_{\alpha=1}^n N_\alpha(\xi, \eta) \mathbf{x}_{\alpha,i} \quad (1)$$

where α is the number of nodes of a cell element. Since the deformation of a soft tissue is usually large, the deformation is derived from the finite deformation theory [2].

III. RESULTS

In the present study, it is shown that the cell element method can play an important role to grasp the motion of a soft tissue subjected to an external impact. With a high-speed camera, instantaneous motions in responding to external stimuli can be captured to be used to measure the deformation. An in-house image processing program written in the Python script language correctly reads the coordinates of the elements from the images taken with the camera as shown in Fig. 1.

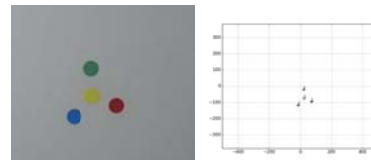


Fig. 1. Colored markers constructing cell elements placed on the surface of the specimen. A snapshot of the current configuration (left), taken with a high-speed camera, and the processed configuration with the image processing software (right).

IV. CONCLUSION

In the present study, a novel experimental method based on the cell element is introduced, which may be extended to be applicable to more complex systems such as three-dimensional motion analysis of brain tissues, liver tissues, or blood vessels where conventional experimental methods are hardly feasible.

REFERENCES

1. Y. Bahn and D. K. Choi, "Numerical and Experimental Study on Mechanical Properties of Gelatin as Substitute for Brain Tissue" *Trans.*

Korean Soc. Mech. Eng. B., vol. 39, no. 2, pp.169-176, 2015.

2. G. A. Holzapfel, *Nonlinear Solid Mechanics*, New York: Wiley, 2001.

Virtual Surgery Planning and Surgical Guide Design using Automatic Active Contour Segmentation for Maxillofacial Reconstruction Surgery

Youngjun Kim¹, Sunhee Kim¹, Hannah Kim¹, Hyunchul Cho¹, Deukhee Lee¹,
Laehyun Kim¹, Sehyung Park¹, and Jung-Woo Lee²

¹Center for Bionics, Korea Institute of Science and Technology, Seoul, Republic of Korea

²Department of Oral & Maxillofacial Surgery, School of Dentistry, Kyung Hee University, Seoul, Republic of Korea

E-mail: junekim@kist.re.kr

Abstract— We have developed a software for virtual surgery planning (VSP) and surgical guide design for maxillofacial reconstruction surgery (MRS). This software can reduce preparation time through automatic segmentation and easy user interface.

Keywords— Virtual Surgery Planning, Maxillofacial Reconstruction, Surgical Guide Design, Automatic Segmentation

I. INTRODUCTION

VSP and surgical guide design for MRS have advantages that can reduce the surgical time and enhance the surgical outcome. Compared to commercial software such as Mimics/Proplan/3-Matic (Materialise, Belgium) and VSP reconstruction (Medical Modeling, USA), our research aims at reducing the preparation time by providing automated algorithms such as active contour model (ACM) and more user-friendly software functions for MRS.

II. METHODS

Based on the patient's computer tomography (CT) images, the mandible and fibula are automatically segmented using an ACM algorithm [1] that captures both strong and weak boundaries. The initial contour is obtained using a histogram-based multi-phase segmentation on a representative axial image, and it sequentially extracts contours for all of the axial images. After obtaining a 3D mesh model from the extracted contours, we perform VSP. The developed software provides tools to help a surgeon to preoperatively plan the MRS in a virtual space. The surgeon defines the cutting positions of the mandible and fibula using virtual simulation of the MRS. Then surgical guide templates are designed according to the VSP. Finally, a tactile model of the patient and surgical guide templates are fabricated by 3D printing and prepared for the MRS.

III. RESULTS

The results of the automatic segmentation by the ACM algorithm are shown in Fig. 1. The automated results were evaluated by an expert. It took 5 s for skin and 130 s for mandible segmentation (i7 CPU/8GB RAM), which reduced the VSP preparation time for

MRS. Conventional manual segmentation for MRS requires more time and labor.

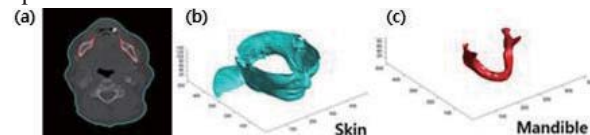


Fig. 1. (a) Automatic segmentation results by the ACM. 3D mesh models: (b) skin and (c) mandible.

Fig. 2 shows the VSP results (Fig. 2(a)) and 3D-printed tactile mandible model with the surgical guides based on the simulation (Fig. 2(b)). As shown in Fig. 2(a), a part of the mandible was replaced with fibula free flap.

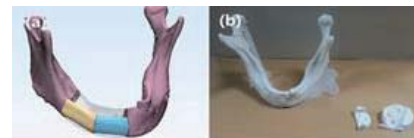


Fig. 2. (a) Virtual simulation of MRS. (b) 3D printed mandible and surgical guide.

The 3D-printed tactile patient model is used to help to understand the patient's anatomy and verify the surgical outcome. The fabricated surgical guides can be used to accurately cut the bones according to the virtually planned positions.

IV. CONCLUSION

The developed software for VSP and surgical guide design is expected to be useful because it can reduce the preparation time and enhance the success rate of MRS. Although further development and accuracy analysis are required, we confirmed the feasibility of the proposed method and its clinical application to MRS.

ACKNOWLEDGEMENT

This work was supported by the KIST Institutional Program (Project No. 2E25250).

REFERENCES

1. S. Kim and et al., "Automatic Segmentation of Leg Bones by Using Active Contours", EMBC, pp. 4695-8, 2014.

Design of a 7 DOF force-torque sensor for a master device with a pinching action

Suyong Kim¹, Cheongjun Kim¹, and Doo Yong Lee¹

¹Department of Mechanical Engineering, Korea Advanced Institute of Science and Technology, Daejeon, Korea
E-mail: leedy@kaist.ac.kr

Abstract—This paper proposes a 7 DOF force-torque (F/T) sensor with 16 strain gauges for the master device with a pinching capability. It is necessary to measure the force and torque at the master device to render high-fidelity haptic feedback. The sensor is designed to measure 7 DOF force and torque and guarantee its durability. Aluminum alloy 6061 is used to form a beam with thickness of 3mm. Performance and durability of the sensor system are verified through SolidWorks simulation.

Keywords—force sensor, torque sensor, master device, strain gauge

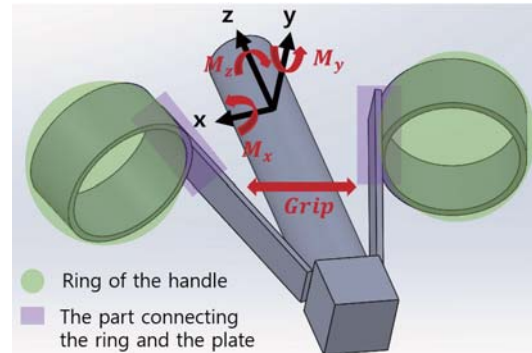


Fig 1. Two parts of measuring force and torque at a handle of a master device

I. INTRODUCTION

It is necessary to measure 3 DOF force, 3 DOF torque and 1 DOF gripping force exerted by the handle of a finger-type master device to render high-fidelity haptic feedback [1]. However, there are structural and economic problems to install 6 DOF force-torque sensor in the master device of the surgical robot. It is necessary to develop a light and small sensor system to reduce the inertial effect and user fatigue, which is not available commercially.

II. METHODS

Fig. 1 shows two parts to measure forces and torques at the handle of the master device. The first one is the ring of the handle, because a doctor use thumb and index fingers to control the master device. The second one is the part connecting the ring and the plate. The sensor that can measure forces and torques of these two parts is designed to maximize the device's strain and guarantee its durability.

Strain gauge will be used on the sensor is N11-FA-1-120-11-P4-VSE3-A. The length of strain gauge base is 3.4mm, and width of the base is 1.3mm. Aluminum alloy, common steel and stainless steel are applicable material for beam that strain gauge will be attached on. Aluminum alloy 6061 is lightweight and cost effective material. Therefore aluminum alloy 6061 is used to form a beam with thickness of 3mm. Thickness of the beam is designed to endure up to 8N.

Generated strain and durability of system are verified by static simulation using SolidWorks software. The position of attaching the strain gauge is selected based on the result of the simulation.

III. RESULTS

A. Force measurement

Fig. 2 and Table.1 show the results of simulation when 1N force is applied on the sensor in x, y and z direction, respectively. The red-colored part of the Fig. 3 demonstrates the place where the biggest strain is generated, and it can measure up to 8N. Strain gauges will be attached on that place.

Table. 1 shows the results of generated strain when 1N force is applied. Generated strain on part A, B and C is coupled. When the x-axis force is applied, strain is occurred at the strain gauges for measuring y and z-axis force. Therefore, the sensor is coupled between each physical DOF.

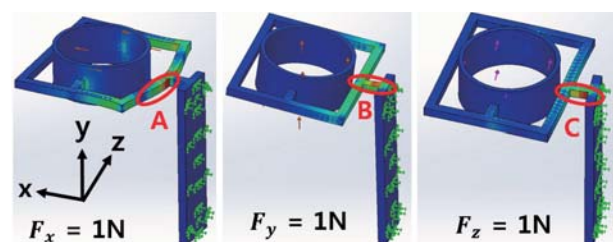


Fig 2. Result of force measurement

Table 1. Result of generated strain

Part	F_x	F_y	F_z
A	3.15×10^{-5}	8.84×10^{-5}	3.72×10^{-5}
B	2.63×10^{-6}	1.52×10^{-4}	7.43×10^{-5}
C	2.63×10^{-6}	6.32×10^{-5}	1.49×10^{-4}

B. Torque and grip force measurement

When the torque in y-direction is applied as Fig.3, forces in z-direction occurs at the both of rings. Therefore, the torque in y-direction can be estimated by measuring the forces in z-direction.

$$M_y = 2(l_1 \sin\theta + l_2 \cos\theta)F_z$$

Where, l_1 is the length of the gripper link, l_2 is the length between the ring and the gripper link, and θ means the angle between the ring and center axis. It is possible to measure torques in other direction (x and y direction) and force that occurs at the gripping motion by the same method.

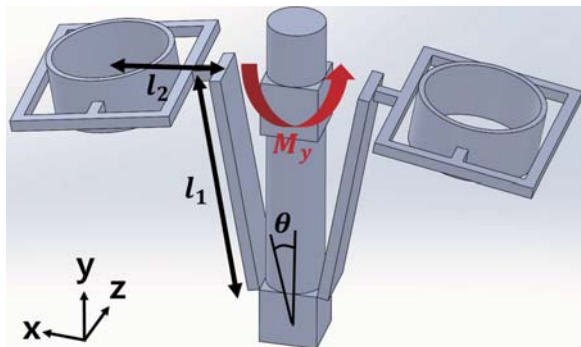


Fig 3. Result of torque measurement

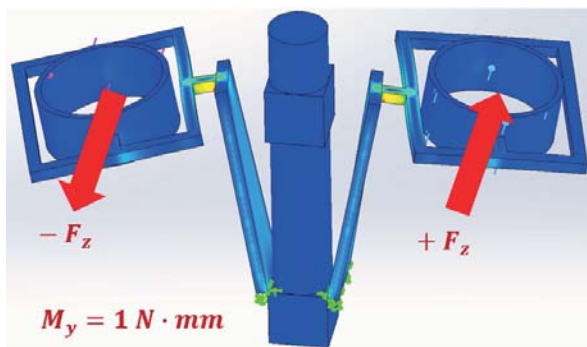


Fig 4. Result of y-axis torque measurement

IV. CONCLUSION

The designed sensor with 16 strain gauges can measure 7 DOF force-torque (3 DOF force, 3 DOF torque, and 1 DOF gripping force) for the handle of a master device with a pinching action. The result of sensing 7 DOF F/T is verified using the SolidWorks simulation.

The maximum interaction force in robot-assisted surgery for suturing is 6N [3]. Desired sensor can measure up to 8N. Therefore desired sensor can be applicable at the master device for measuring forces and torques.

The sensor is coupled between each physical DOF as shown in Table 1. Calibration test is needed to get a decoupling matrix is needed [4].

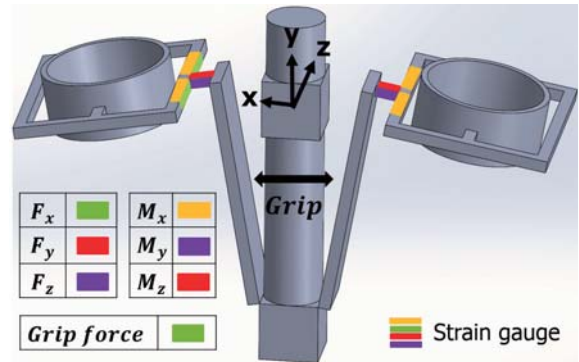


Fig 5. 7-DOF force-torque sensor for the master device

ACKNOWLEDGEMENT

This work was supported by the Industrial Strategic Technology Development Program (No. 10035145, Development of Multi-arm Surgical Robot for Minimally Invasive Laparoscopic Surgery) funded by the Ministry of Trade, Industry & Energy (MOTIE, Korea).

REFERENCES

1. C. R. Wagner, R. D. Howe, and N. Stylopoulos, "The Role of Force Feedback in Surgery : Analysis of Blunt Dissection," presented at the Proceedings of the 10th Symposium on Haptic Interfaces for Virtual Environment and Teleoperator Systems, 2002.
2. Fingertip controls. Available online : http://www.intuitivesurgical.com/products/davinci_surgical_system/davinci_surgical_system_si/surg_eon-control.html (Access on 18 September 2015)
3. A.M. Okamura, "Methods for Haptic feedback in teleoperated robot-assisted surgery", *Industrial Robot*, vol. 31, pp 499-508, 2004.
4. Bo Wu, Ping Cai, "Decoupling Analysis of a Sliding Structure Six-axis Force/Torque Sensor", *MEASUREMENT SCIENCE REVIEW*, vol. 13, 10.2478, No 4. 2013

Design issues of Tangible Tabletop System as a Cognitive Rehabilitation for Stroke Patients

Kyuye Song^{1,2}, Gyu Hyun Kwon³, Sung-Bom Pyun⁴, Laehyun Kim^{1,2}

¹Center for Bionics Korea Institute of Science and Technology, Seoul, Republic of Korea

²Department of HCI&Robotics University of Science and Technology, Daejeon, Republic of Korea

³Graduate School of Technology & Innovation Management, Hanyang University, Seoul, Korea

⁴Department of Physical Medicine and Rehabilitation Korea University College of Medicine, Seoul, Republic of Korea

E-mail: kysong@ust.ac.kr

Abstract— Stroke is one of the leading causes of cognitive and physical impairments since it damages the brain directly. Cognitive rehabilitation is a treatment to help stroke patients to restore normal cognitive functions. We developed a cognitive rehabilitation system based on a tangible tabletop interface named E-CORE (Embodied Cognitive Rehabilitation). To evaluate suitability of the system as a cognitive rehabilitation intervention, we conducted qualitative study such as an observation and focus group interview. In this study, we find that E-CORE system is required to redesign considering the characteristics of stroke patients.

Keywords— Stroke; Cognitive rehabilitation; Tangible objects; System design

I. INTRODUCTION

Stroke is a major public health problem in globally. A stroke damages the brain and makes cognition problems such as attention, memory, language, and visuospatial function. Stroke survivors also have physical impairment caused by a stroke. To improve neurological and physical treatment effect, the rehabilitation is necessary to stroke patients [1].

In this paper, we propose design issues of tangible tabletop interface as a cognitive rehabilitation system based on qualitative study.

II. METHODS

A. Tangible tabletop system 'E-CORE'

In cognitive rehabilitation, the body movement is important to improve rehabilitation efficacy. We developed cognitive rehabilitation system using tangible tabletop named 'E-CORE (Embodied Cognitive Rehabilitation). E-CORE focuses on the coupling between body movement and cognition to reinforce the cognitive training effects [2]. The system is composed of two components: the tabletop interface and tangible objects. They are shown in figure 1. The system consists of tangible objects such as cookie cutters, brush, stamps, and topping containers. The content of E-CORE is a cookie making game as an activity daily of living (ADL) task training. There are

five steps in cookie making game: creating the shape of the cookies using cookie cutter, calculating a proper temperature of oven, moving the cookies, serving the syrup using brush, and sprinkling the topping using topping containers.



Figure 1. Tangible objects of cookie making game.
(a) Brush (b) Topping container (c) Cookie cutter (d) Stamp

With regard to cognitive training, each step requires attention and concentration, calculations, memory, spatial recognition, and visuomotor coordination. The examples of stages are shown in figure 2.



Figure 2. The image of topping and baking stage

The requirements of body movements for each stage are reaching, grasping, stamping, painting, and sprinkling. The gestures are shown in figure 3.

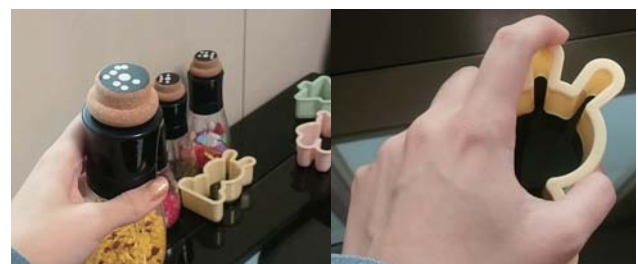


Figure 3. The requirements of gesture in cookie making game

B. Observation and focus group interview

We observed stroke patients with cognitive impairment at Korea University Medical Center. Our criteria of observation was focused on their behavior especially aspects of cognitive disability and movements of the upper limbs. We also conducted a focus group interview about E-CORE system’s usability design for stroke patients. We interviewed two experts (two medical doctors specialized in physical medicine and rehabilitation) at Korea University Medical Center.

C. ISO 9241: criteria of interface usability in terms of ergonomics

To assess E-CORE system, we referred ISO 9241 standard. ISO 9241 presents criteria of evaluation for aspects of ergonomics of human-computer interaction. It provides ergonomic principles of hardware, software and environment [3]. Some standards of ISO 9241 are shown in table 1.

Table 1. Standards of ISO 9241

ISO 9241 Hardware interface	Workstation layout and postural requirements
	Guidance on the work environment
	Requirements for display with reflections
	Requirements for displayed colours
	Requirements for non-keyboard input devices
ISO 9241 Software interface	Presentation of information
	User guidance
	Menu dialogues
	Command dialogue

III. RESULTS

A. Observation

Most of the stroke patients had physical impairments such as loss of range of motion, and muscle weakness. They had difficulty in reaching and grasping along with the perception. In addition, the damaged cognitive abilities made stroke patients to have trouble with expressing and understanding. According to a series of symptoms of stroke, patients have experienced emotional change such as a depression.

B. Implications for system design

Main topic of focus group interview was evaluation of E-CORE system design as a cognitive rehabilitation intervention for stroke patients based on standards of ISO 9241. Aspects of hardware usability design, display screens should be read safely, comfortably, and efficiently to perform tasks. Since glare and reflections of display can disturb patient’s view, we installed tilting equipment. It is possible to adjust the angle of display screen. Based on criteria of displayed colours,

we used a high chroma color to distinguish easily types of syrup and topping. Workstation layout and postural requirements are the most important aspects of system design, since it is related with safety of patients. The system needs proper space under the screen because almost stroke patients use wheelchair. Aspects of software usability design, various contents are required because of learning effect. The criteria of user guidance, it is necessary to give appropriate feedback for patients to improve concentration of cognitive training. To increase effects of training, menu and command dialogues should be matched patient’s mental model, which explains user’s thought process.

IV. CONCLUSION

In this study, we conducted qualitative study to suggest critical aspects of system design as a cognitive rehabilitation intervention based on ISO 9241. According to the observation and the focus group interview, the current system was not intensive enough for efficient cognitive rehabilitation. To solve the problem, we consider stroke patient’s behavior and symptoms such as the movements and the level of cognition of stroke patients. Based on the results of our qualitative study, we will redesign the hardware and software of E-CORE to improve effectiveness of the system as a cognitive rehabilitation intervention for stroke patients.

REFERENCES

1. Warlow, C., Sandercock, P., Hankey, G., et al. Stroke: Practical Management. Blackwell Publishing, 2008.
2. Jung, J., Kim, L., Park, S., & Kwon, G. H. (2013). E-CORE (Embodied COgnitive REhabilitation): A Cognitive Rehabilitation System Using Tangible Tabletop Interface. In *Converging Clinical and Engineering Research on Neurorehabilitation* (pp. 893-897). Springer Berlin Heidelberg.
3. Bevan, Nigel. "International standards for HCI and usability." *International journal of human-computer studies* 55.4 (2001): 533-552.

Automatic Bernard quadrant method for knee ACL localization using a polygonal model

Cong-Bo Phan¹, Kang-Min Sohn², Joon-Ho Wang², Seungbum Koo^{1*}

¹Chung-Ang University, Seoul, Republic of Korea

²Samsung Medical Center, Seoul, Republic of Korea

*E-mail: skoo@cau.ac.kr

Abstract — An accurate localization of anterior cruciate ligament (ACL) insertion point play an important role to understand ACL injury and treatments. In this study, we proposed an automatic computational method of quantifying the ACL insertion site on three-dimensional (3D) knee model based on the Bernard quadrant method. Forty knee CT images were used to quantify average ACL insertion site.

Keywords— bundle, Bernard quadrant, knee surgery, tunnel localization, ACL reconstruction.

I. INTRODUCTION

The tunnel localization during anterior cruciate ligament (ACL) surgery could significantly affect the joint function after reconstruction [1]. It is necessary to locate the ACL insertion site with high accuracy. Previously, Bernard et al. suggested a radiographic method for determining the insertion site of ACL using a quadrant [2]. Forsythe et al. also applied original quadrant method to quantify the positions of ACL bundles using 3D knee models [3]. However, accuracy of these methods vary according to observer's experience. In this study, we proposed an automatic quadrant method of quantifying the ACL insertion site on 3D knee model. Forty knee CT images were used to quantify average ACL insertion site.

II. METHODS

Forty knees CT images were obtained from the image database in Radiology department with approval of IRB of Chung-Ang University Hospital. Distal femur were reconstructed into 3D polygonal models from the CT images using Seg3D software. A clinician manually localized ACL insertional sites from the 3D models.

An automatic quadrant method was implemented using MATLAB. The 3D femoral model was imported and its initial position was calculated by aligning with a template model which were pre-determined [4]. Bone contours of the central sections in each of the medial and lateral condyles in sagittal plane were extracted [5]. Internal-external and abduction-adduction rotation angles were determined by aligning the medial and lateral bone contours to obtain anatomical sagittal view. Points of the polygonal model in the intercondylar region were extracted and projected onto sagittal plane to find the intercondylar curve. Points in the lateral half of the model were projected onto sagittal plane to obtain a bone contour. Blumensaat's line was identified by applying a linear regression to the intercondylar curve. A line parallel to the Blumensaat's line and

tangent to bone contour were calculated to obtain the Bernard quadrant. Percent distance along the Blumensaat's line, %t, and percent distance perpendicular to the Blumensaat's line, %h, of the ACL insertion site were calculated.

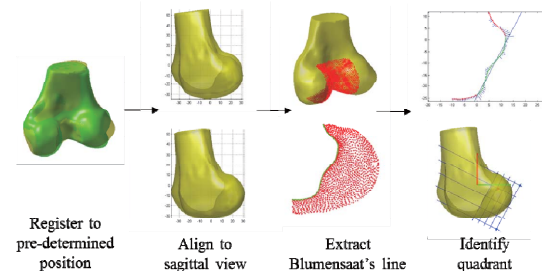


Fig. 1. The flow of automatic quadrant identification based on 3D model.

III. RESULTS

The measurement of the %t and %h were reported in Table 1. In which, the mean (standard deviations) of %t and %h are 22.8 (± 2.5) and 29.3 (± 3.8). Bernard et al. previously reported the mean of %t and %h as 24.8% and 28.5%, respectively, which are similar to our automatic method results [2].

Table 1. The mean (std) and range of %t and %h using automatic method

	Auto Method (40 subjects)		Bernard et al. (10 subjects)	
	%t	%h	%t	%h
Mean (std)	22.8 (2.5)	29.3 (3.8)	24.8 (2.2)	28.5 (2.5)
Range	18.3-27.5	19.9-37.0	23-27	26-31

IV. CONCLUSION

An automatic computational method was developed for drawing the quadrant grid based on 3D surface of distal femur. This method could also be used for the computer assisted surgery system to locate the ACL insertion point in single bundle ACL reconstruction or AM and PL insertion points in double bundle ACL reconstruction.

ACKNOWLEDGEMENT

This study was supported by the NRF of Korea 2013R1A2A2A03015668 and 2012R1A1A2043793.

REFERENCES

1. Johnson D.L., et al., *Clin Orthop Relat Res.*, vol. 325, pp. 100-109, 1996.
2. Bernard, M., et al., *Am J Knee Surg.*, vol. 10, pp. 14-21, 1996.
3. Forsythe, B., et al., *J Bone Joint Surg Am.*, vol. 92, pp. 1418-1426, 2010.
4. Phan, C.B., Koo, S., *Int J Comput Assist Radiol Surg.*, 2015.
5. Li, Kang, et al., *Ann Biomed Eng.*, vol. 38, pp. 2928-2936, 2010.

A Robotic Mechanism for Multiple Needle Manipulation in Biopsy

Y. Moon¹, J. Won¹, and J. Choi¹

¹Asan Institute for Life Sciences, Asan Medical Center, Seoul, Korea

E-mail: fides@amc.seoul.kr

Abstract—Image-guided robotic assist system for biopsy or intervention procedure has been long researched and some early commercial systems have been introduced recently. While most are focusing on image guided instrument manipulation, a novel robotic mechanism toward whole procedure automation is proposed by the authors. A 5-DOF robotic mechanism for multiple biopsy needle manipulation has successfully shown the feasibility by prototype test.

Keywords— Biopsy, automation, robot, intervention, sampling.

I. INTRODUCTION

Biopsy is a typical needle type intervention procedure performed under radiographic image equipment such as computed tomography (CT) and cone-beam CT [1]. In order to reduce the radiation exposure and improve accuracy in targeting of the needle, there have been various attempts using robot technology. Mainly the devices developed so far are for accurate positioning of the needle, not to perform full procedure of biopsy including actual tissue sampling. A robotic end-effector of a master-slave tele-operated needle type intervention robot system has been proposed to perform entire biopsy procedure [2]. A novel design of robotic mechanism and protocol for automatic biopsy based on spring-loaded biopsy gun concept has been developed. The mechanism and sequential process of operation have been implemented to meet the requirements for multiple tissue sampling as well as insertion of the guide needle for lung biopsy.

II. METHODS

The processes required to perform full biopsy procedure include insertion of a guide needle and biopsy needles, tissue sampling by a spring-loaded mechanism, reloading of the spring for repetitive sampling, return of guide needle, and axial rotation of the needles, if needed. The prototype of the robotic mechanism to meet the tasks is shown in Fig. 1. The mechanism is attached to the end link of an articulated robot arm which is used to adjust the pose of the mechanism including the needle. Total five actuators, DC motors (Maxon Motor AG, Switzerland) are used to 1) rotate a cartridge storing the needles, 2) axially rotate the needles, 3) horizontally translate a holding block that

holds the head of the needles, 4) vertically translate the holding block, and 5) rotate a lever for triggering the spring in the holding block and reloading the spring.

III. RESULTS

The developed robotic mechanism successfully performed the functions required for the biopsy procedure automation.

IV. CONCLUSION

For better practical application, tissue cutting speed and overall procedure time need more optimization.

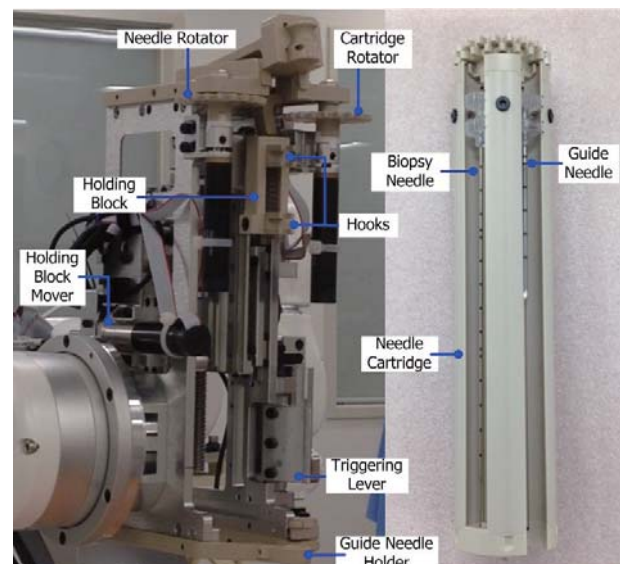


Fig. 1. Robotic mechanism for automatic biopsy

ACKNOWLEDGEMENT

This work was supported by the Industrial Strategic Technology Development Program (10041618) of the Ministry of Trade, Industry and Energy, Korea.

REFERENCES

1. J. Y. Choo, C. M. Park, N. K. Lee, S. M. Lee, H. J. Lee, and J. M. Goo, "Percutaneous transthoracic needle biopsy of small (1cm) lung nodules under C-arm cone-beam CT virtual navigation guidance," *European Radiology*, vol. 23, pp. 712-719, 2013.
2. Y. Moon and J. Choi, "Development of a robotic mechanism for teleoperation-based needle interventions," 44th International Symposium on Robotics (ISR). doi: 10.1109/ISR.2013.6695725, 2013

Tissue-Electrode Interface may be Important in the Subdural Cortical Stimulation – Computational Study

Jun-Kil Been, Donghyeon Kim, Hyeon Seo, Sung Chan Jun*

School of Information and Communication, Gwangju Institute of Science and Technology, Gwangju, South Korea

E-mail: {jkbeen, danielkim, hseo, scjun}@gist.ac.kr

Abstract— Subdural cortical stimulation (SuCS) is an effective intervention therapy to rehabilitate brain diseases or disorders. Since electrodes are contacted directly above the cortex, it is important to understand the electric field distribution depending on the degree of contact between an electrode and gray matter. Thus, we analyzed efficiency of SuCS in a various contact degree using finite element method. We found that tissue-electrode interface in SuCS is quite important in doing accurate targeting of stimulation and estimating reasonable stimulation effect.

Keywords— Subdural cortical stimulation, tissue-electrode interface, finite element analysis.

I. INTRODUCTION

Subdural cortical stimulation is one of the electrical brain stimulation (EBS) method to modulate neuronal activation and treat various brain disorders. Since electrodes are contacted directly on the gyrus, it may have different effects of stimulation depending on a degree of contact between an electrode and the cortex. In this study, we developed 3D finite element models and compared the distributions and intensities of electric field (EF) on gray matter, white matter and cerebrospinal fluid (CSF) on each degree of tissue-electrode contact.

II. METHODS.

A. Calculating the tissue-electrode contact degree

For quantifying the degree of contact, we define tissue-electrode contact degree D as a ratio between an interfaced (contacted with gray matter) area ($A_{\text{contacted}}$) in an electrode and an electrode area ($A_{\text{electrode}}$). D is represented as follows:

$$D = \frac{A_{\text{contacted}}}{A_{\text{electrode}}} \times 100(\%)$$

Lower D means that an electrode is more exposed to CSF and less contacted to gray matter.

B. 3D finite element models of SuCS

We developed 3D finite element models representing the precentral gyrus [1]. For comparison, we modified gray matter shape interfaced with a fixed electrode (Fig. 1). A disc-type electrode with 4mm radius 0.1mm height was used and surrounded by substrate. We used monopolar stimulation (1mA) and overall electric field

distributions were computed by finite element method (FEM)

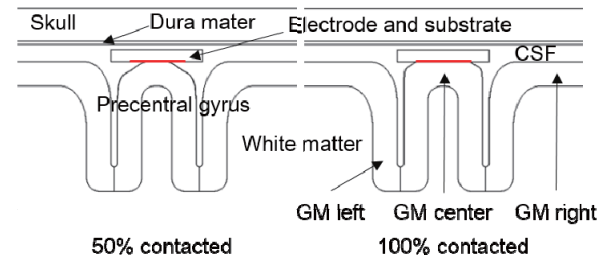


Figure 1. 3D extruded slab model for D of 50% (left) and D of 100% (right).

III. RESULTS

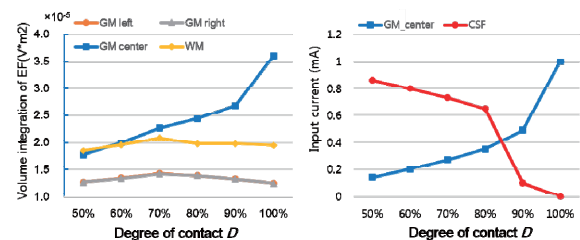


Figure 2. (a) The volume integration of electric field on each tissue and (b) input current of gray matter and CSF.

As expected, D and EF volume right beneath electrode were mainly linearly related, but EF volumes in other areas looked less related. As well, the wider interfaced area of electrode yielded the higher injected input current to gray matter.

IV. CONCLUSION

The relationship of degree of contact D and the electric field magnitude of gray matter was investigated. The stimulation efficiency was the biggest when an electrode is completely contacted on the cortex. For an effective and safe stimulation, the degree of contact may be one of critical factors to be considered.

ACKNOWLEDGEMENT

This work was supported by a grant from the Integrative Aging Research Center of GIST

REFERENCES

1. Seo H *et al.*, Conf. Proc. IEEE Eng. Med. Biol. Soc. 1892–5, 2012.

Effectiveness of New Balance Rehabilitation Training considering Resistance Exercise Function: Evaluation of Kinematic Ability

L. Alizadeh Saravi¹, H. H. Jung¹, D. H. Lim^{1*}

¹Mechanical Department, Sejong University, Seoul, South Korea

E-mail: dli349@sejong.ac.kr

Abstract— Balance is a crucial factor for the functional performance during daily life. The methodological purpose of this study is to evaluate equilibrium kinematic characteristics in human after training using new balance training system considering resistance exercise function. The experiment is done on 3 elderly volunteers using a three-dimensional motion-capture system employing infrared cameras to characterize center of body mass (COM), in order to investigate the effects of meaningful, stimulating as well as intensively training on balance behavior. The results show improvements in balance kinematic ability where the experiments were accompanied by entertaining resistance interface.

Keywords— Balance Rehabilitation Training, Optimized Strategy, Resistance Interface

I. INTRODUCTION

Several studies underline the importance of balance to decrease the falling risk in elderly daily lives. Diverse balance training strategies have been recently suggested to recover effectively the balance ability of the elderly [1]. However, little researches have been developed into optimized strategies for balance rehabilitation training. In this study the effects of entertaining resistance interface on center of mass and consequently on balance kinematic ability is investigated.

II. METHODS

Three elderly men with no musculoskeletal or nervous system-related diseases (age: 61 ± 1 years, height: 172 ± 4.1 cm, body mass: 69.2 ± 2.9 kg), were selected to investigate the balance rehabilitation training using customized rehabilitation equipment accompanied entertaining soccer game interface for 9 weeks.

Rotation of the base plate of the balance rehabilitation system was controlled by participants intention in medial-lateral (ML) direction considering a soccer game as an interface to induce this intention. These experiments were done three times per week, three ten-minute trials with 5 minutes rest between each. After every 3 weeks of training, the COM trajectories were measured in 8 directions. A three-dimensional motion-capture system employing infrared cameras has been used to determine the COM.

Changes in the COM are used as balance index to analyze balance characteristics, whereas augmentation in COM trajectory leads to superior balance ability.

III. RESULTS

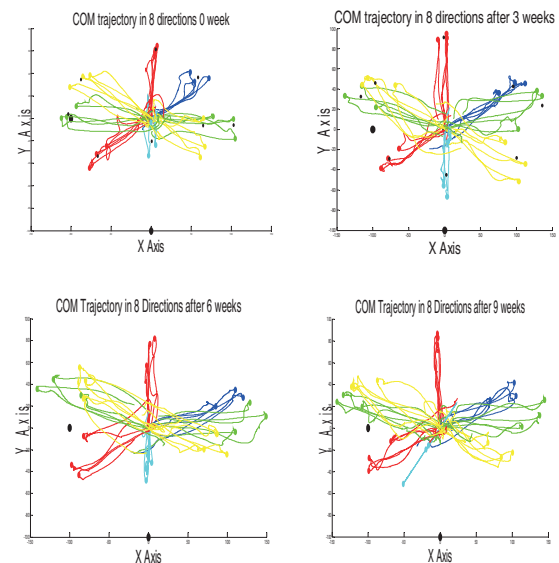


Fig. 1: COM trajectory of one elderly during 9 weeks training

These results indicate significant modifications in COM trajectory in 8 directions after 3 weeks training specifically in anterior-posterior (AP) and medial-lateral (ML) directions. Following 6 weeks were ‘stability augmentation period’ since there were not significant augmentation in COM trajectories.

IV. CONCLUSION

The results show kinematic features of balance ability might be dependent on the consequential and intensive training method. Accordingly, balance rehabilitation combined with entertaining resistance interface, may lead to effective balance training as well as balance kinematic ability.

REFERENCES

1. Lange B, Flynn S, Proffitt R, Chang CY, Rizzo A, “Development of an interactive Game-based rehabilitation tool for dynamic balance training.” *Top Stroke Rehabil* 17(5):345-352, 2010.

Cell contractility established by RhoA/Rock and TGF β /BMP signaling mediates load induced chromatin condensation in MSCs

Su-Jin Heo¹, Spencer E. Szczesny¹, Randall L. Duncan² and Robert L. Mauck¹

¹Dept. Bioengineering, University of Pennsylvania, Philadelphia, PA, USA

²Dept. Biological Science, University of Delaware, Newark, DE, USA

E-mail: lemauck@mail.med.upenn.edu

Abstract— Dynamic loading (DL) plays important roles in modulating mesenchymal stem cell (MSC) lineage-specification. However, the mechanism by which mechanical perturbation influences fate decisions in MSCs and the consequence of changing nuclear structure are not fully understood. Here, we show that DL rapidly alters chromatin condensation in MSCs, and that cellular contractility established by RhoA/ROCK and TGF β /BMP signaling is essential for this process.

Keywords— MSC, Dynamic loading, Chromatin, Cell contractility, TGF β /BMP signaling

I. INTRODUCTION

Mechanical forces play important roles in MSC lineage specification. However, little is known regarding the mechanism by which these cues guide MSC fate. We have previously shown that DL elicits a rapid release of ATP from cells, which is essential for subsequent chromatin remodeling [1] and that cellular contractility is required for cytoskeletal strain transfer to the nucleus [2]. Nevertheless, it is still unclear how this basal contractility impacts chromatin remodeling in response to DL. Here, we investigated how different loading conditions (i.e. frequency/duration) regulate chromatin condensation, and identified a central role for cellular contractility in this process. Also, given that exogenous ligand activation of the TGF β /BMP signaling can instigate changes in chromatin remodeling, we queried its role in the response to mechanical perturbation.

II. METHODS

DL was applied to MSC seeded nanofibrous scaffolds using a custom bioreactor [1] at varying frequencies and durations. An image-based edge detection algorithm was used to determine a chromatin condensation parameter (CCP) [1]. ATP in the load-conditioned media was measured using an ATP Assay Kit (Abnova). To investigate the role of cell contractility, constructs were pre-treated with the Rho kinase (ROCK) inhibitor Y27632 (Y27). Similarly, the ROCK agonist lysophosphatidic acid (LPA) was used to transiently increase contractility. To determine whether TGF β /BMP signaling participated in DL-induced chromatin condensation, constructs were pre-treated with either SB431542 (SB) or LDN193189 (LDN) to inhibit TGF β /BMP signaling. MSC traction forces were measured on polyacrylamide gels [2].

III. RESULTS

DL led to chromatin condensation in MSC nuclei, increasing the number of visible edges (Fig. 1A). When cells were pre-treated with Y27 (Y27/DL, Fig. 1A, B), no changes were observed. In terms of DL conditions, no change in CCP was observed after 30s of DL, except in the case of DL applied at 2 Hz. After 150s of DL, CCP increased with 1 and 2 Hz, but not with 0.2 or 0.5 Hz (Fig. 1B). With 600s of DL, CCP increased in all conditions, independent of loading frequency (Fig. 1B). Baseline CCP values increased with the addition of LPA, and superposition of DL in the presence of LPA (LPA/DL) resulted in increases in CCP within 30 s, independent of loading frequency (Fig. 1B). Conversely, pretreatment with Y27 (Y27/DL) abolished the DL-induced chromatin condensation (Fig. 1B) and ATP release (not shown). Interestingly, when TGF β /BMP signaling was blocked, DL-induced ATP release and chromatin condensation was also abolished (not shown). Traction force generation in MSCs was significantly decreased with SB and LDN, reaching levels similar to Y27 treatment (not shown).

IV. CONCLUSION

These new data suggest that DL triggers ATP release, leading to chromatin condensation and this release is mediated by acto-myosin based cellular contractility that is in part established by TGF β /BMP signaling.

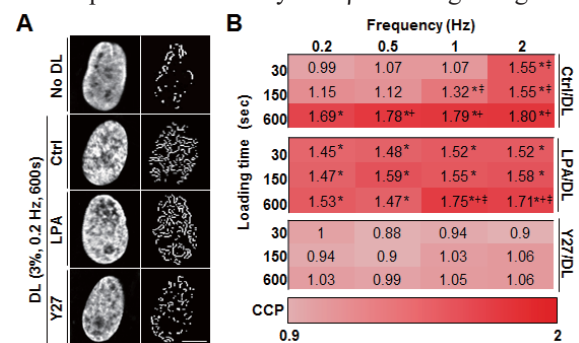


Fig. 1: A) DAPI stained nuclei (left) and corresponding edge detection (right), bar = 3 μ m. B) Heat maps of CCP values (normalized to unloaded conditions) ($n = -20$, *: $p < 0.05$ vs. Ctrl, +: $p < 0.05$ vs. 0.2 Hz, ‡: $p < 0.05$ vs. 0.5 Hz).

ACKNOWLEDGEMENT

This work was supported by the NIH (AR056624 and EB02425).

REFERENCES

1. SJ Heo et al., "Mechanically induced purinergic and calcium signaling directs chromatin condensation in mesenchymal stem cells," *ORS* 2015.
2. TP Driscoll et al., "Cytoskeletal to nuclear strain transfer regulates YAP signaling in mesenchymal stem cells.," *Biophys J* 16;108(12):2783-93, 2015

Photothermal Poly(N-isopropylacrylamide)/ Melanin nanoparticle Hydrogel for anticancer drug delivery

A. GhavamiNejad, M. Samarikhalaj, L.E. Aguilar, J.I. Kim, T. Batgerel, C. H. Park, and C.S. Kim*

Bionano Systems Engineering Department, Chonbuk National University, Jeonju 561-756, Republic of Korea
E-mail: chskim@jbnu.ac.kr

Abstract— Cancer has been one of the major threats to the lives of human beings for centuries. Current cancer therapies mainly include surgery, chemotherapies, and radiotherapies. While surgery in many occasions is not able to completely remove all cancer cells in the human body, chemotherapy and radiotherapy all suffer from their severe toxic side effects to normal tissues and limited specificities to cancer cells. Phototherapies induced by light, preferably near-infrared (NIR) light with superior tissue penetration ability, usually involve phototherapeutic agents with little toxicity in dark, and are able to selectively kill cancer cells under light irradiation, without causing much damage to normal tissues in dark. In this work, we report a simple and environmentally friendly route for the preparation of PNIPAM/Dopamine nanocomposite hydrogels by incorporating dopamine nanoparticle into a monomer solution prior to the gelation step. The composite hydrogel can be self-heating on exposure to an NIR laser and, consequently, can display shape transitions. Similar to the shape transition of the pure PNIPAM hydrogel, the swelling and deswelling transitions of composite hydrogels are also completely reversible. Moreover, the NIR-induced temperature can be adjusted by varying the dopamine nanoparticle loading and the irradiation time. The drug delivery properties were also studied by encapsulating the DOX drug into the hydrogels. The results indicated that our composite hydrogels shows good ability to release DOX in a sustained manner under physiological conditions.

Keywords— PNIPAM, Dopamine nanocomposite, NIR, Hydrogel

I. INTRODUCTION

Surgery is a common clinical treatment of tumors.

However, the incomplete excision and easy recurrence are still difficult problems for cancer therapy. One of the most essential strategies in dealing with malignancy is chemotherapy to either inhibit the rapid recurrence and proliferation of primary tumors after surgery or treat those with unresectable tumors. Doxorubicin (DOX) is one of the most frequently used chemotherapeutic drugs for clinical management of solid tumors. However, the therapy efficacy of DOX

applied to a cancer patient is restricted by the rapid clearance during circulation, rapidly metabolized by the liver, non-specific distribution in the target tumor and dose-dependent toxicity effects. Therefore, localized delivery of DOX is thought to be a simple and effective strategy to improve both safety and efficacy.

II. METHODS

Chemicals : N-isopropylacrylamide (NIPAM) was obtained from the Shanghai Chemical technology Co. N ,methylenebisacrylamide (MBA) , potassium permanganate (KMnO₄), sodium nitrate, hydrogen peroxide, and sulfuric acid (98%) were purchased from sigma Aldrich. All of the reagents were used as received.

III. RESULTS

We report a simple and environmentally friendly route for the preparation of PNIPAM/Dopamine nanocomposite hydrogels by incorporating dopamine nanoparticle into a monomer solution prior to the gelation step. The composite hydrogel can be self-heating on exposure to an NIR laser and, consequently, can display shape transitions. Similar to the shape transition of the pure PNIPAM hydrogel, the swelling and deswelling transitions of composite hydrogels are also completely reversible. Moreover, the NIR-induced temperature can be adjusted by varying the dopamine nanoparticle loading and the irradiation time. The drug delivery properties were also studied by encapsulating the DOX drug into the hydrogels. The results indicated that our composite hydrogels shows good ability to release DOX in a sustained manner under physiological conditions.

ACKNOWLEDGEMENT

This research was supported by grants from the Basic Science Research Program through the National Research Foundation of Korea (NRF), funded by the Ministry of Education, Science and Technology (Project no.2015-020449 and 2013R1A2A2A04015484).

Microdroplet-based 3D gastric cancer model for evaluation of drug resistance

Minjeong Jang¹, Seungwon Jung¹, Jae-Ho Cheong², Pilnam Kim¹

¹Department of Bio and Brain Engineering, KAIST, Daejeon, Korea

²Department of Surgery, Yonsei University College of Medicine, Seoul, Korea

E-mail: pkim@kaist.ac.kr

Abstract— Gastric cancer is common malignant tumor with high incidence and mortality in worldwide. Gastric cancer distinguishes two types of gastric cancer, intestinal and diffuse types, by Lauren's classification. Since these types show distinctly different clinic-pathological features, new strategy for the cancer therapy depending on the two pathological variants of gastric cancer is necessary in *in vitro* preclinical models. Herein, we performed droplet-based microfluidics to construct and characterize *in vitro* 3D gastric cancer model depending on two different types. To evaluate proposed 3D gastric cancer models, we confirmed cell morphology and viability in ECM bead, EMT, and changes in expression of drug resistance-related protein, as well as drug resistance against anticancer drug, 5-fluorouracil (5-FU).

Keywords— Gastric cancer, microfluidics, *in vitro* 3D cell culture, EMT, chemoresistance

I. INTRODUCTION

Gastric cancer is aggressive malignant tumor with high incidence and mortality in worldwide despite the recent advances in anti-cancer drugs. According to the morphological features, Lauren's classification distinguishes two types of gastric cancer, intestinal and diffuse types.¹ Since diffuse- and intestinal-type gastric cancers show distinctly different clinic-pathological features, new strategy for the cancer therapy depending on the two pathological variants of gastric cancer is necessary in *in vitro* preclinical models.¹ For advanced *in vitro* preclinical model, we performed droplet-based microfluidics to construct and characterize *in vitro* 3D gastric cancer model depending on two different types. To mimic gastric intestinal and diffuse type cancer, we used two types of gastric cancer cell lines, and demonstrated growth characteristics in 2D monolayer cultures.

II. METHODS

A. Microdroplet-based gastric cancer model

The generation of 3D microtumor, consisting of cells embedded in an extracellular matrix (ECM) was carried out in flow-focusing device. To prevent ECM gelation during droplet formation, the flow-focusing device was maintained below 10 °C. After droplet

generation, microtumors are collected and maintained at 37 °C for ECM gelation.

B. Analysis of cell morphology in collagen bead

The cell morphology observed through F-actin and nucleus staining and viability is examined by Live/Dead cell staining.

III. RESULTS

A. Microfluidic droplet based ECM bead

To construct 3D gastric cancer model, we fabricated ECM microbead by flow-focusing technique (Figure A, B) to make size-controllable microbeads.

B. Cell viability and morphology in collagen bead

We identified high cell viability after 7 days through Live/Dead cell staining (Figure C). The two different gastric cancer cell lines displayed different phenotypes in collagen bead. AGS represents spheroid formation with expansive growth. On the other hand, HS746T shows a single cell migration with infiltrative growth pattern, and consists of scattered cells (Figure D).^{2,3}

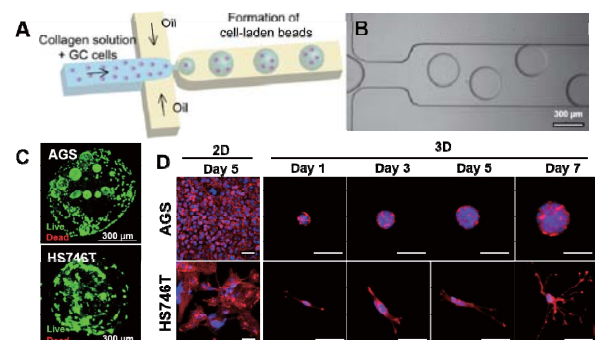


Figure 1. (A) Scheme of microfluidic gastric microtumor formation, (B) Microfluidic channel, (C) Viability test after 7days, (D) Morphology of gastric cancer cell within ECM microbead (F-actin (red), Nucleus (blue)).

IV. CONCLUSION

Conclusively, we developed *in vitro* 3D gastric cancer model system for analysis and confirmation of morphology, and drug resistance in ECM beads. Our results suggest that *in vitro* 3D models of gastric cancer represent a biologically relevant platform for

studying gastric cancer cell biology, tumorigenesis, and for accelerating the development of novel therapeutic targets. We believe that the microdroplet-cancer model is highly suitable to prove useful in high-throughput drug testing and screening for preclinical 3D cell culture platform.

ACKNOWLEDGEMENT

This research was supported by the National Research Foundation of Korea (NRF) (NRF-2014R1A1A104985 and NRF-2015M3A9B3028685) and by a grant of the Korea Health Technology R&D Project through the Korea Health Industry Development Institute (KHIDI), funded by the Ministry of Health & Welfare, Republic of Korea (HI14C0042).

REFERENCES

1. M. Katoh, 2005, "Epithelial-mesenchymal transition in gastric cancer (Review)," *International of oncology*, vol. 27, pp. 1677~1683
2. P. Friedl, J. Locker, E. Sahai, and J. E. Segall, 2012, "Classifying collective cancer cell invasion," *Nature cell biology*, vol. 14, pp. 777-783
3. I. Y. Wong, S. Javaid, E. A. Wong, S. Perk, D. A. Haber, M. Toner, D. Irimia, 2014, "Collective and individual migration following the epithelial - mesenchymal transition," *Nature materials*, vol. 13, pp. 1063~1071

Label-free imaging of subendothelial migration of T cells by interference reflection microscopy (IRM)

Jaehyun Lee¹, Kwang Hoon Song², Taeyeob Kim², Junsang Doh^{1,2,*}

¹School of Interdisciplinary Bioscience and Bioengineering (I-Bio), ²Department of Mechanical Engineering, Pohang University of Science and Technology (POSTECH), 77, Cheongam-ro, Nam-gu, Gyeongsangbuk-do, Korea
E-mail: jsdoh@postech.ac.kr

Abstract— Leukocytes interact with activated endothelial cells (ECs) in order to infiltrate into damaged/inflamed tissue or cancer from blood stream. Subendothelial migration of leukocytes, which occurs abluminal spaces formed between ECs and underlying substrates, have been frequently observed in recent intravital imaging, but mechanisms for subendothelial migration have not been fully understood. Here, using interference reflection microscopy (IRM), we simultaneously visualized T cells under EC layers and focal adhesions (FAs) formed in ECs in a label-free fashion. By quantitatively analyzing interactions between FAs of ECs and T cells underneath EC layers, we attempted to identify rules determining directionality of T cells undergoing subendothelial migration.

Keywords— T cell, Subendothelial migration, Interference reflection microscopy, Focal adhesion, Inflammation

I. INTRODUCTION

Leukocyte extravasation plays a key role in host defense against tissue injury, infection, and cancer. The process includes sequential steps – rolling, firm adhesion, luminal crawling, transendothelial migration (TEM), subendothelial crawling and penetration of basement membrane. While mechanisms of each step have been topics of extensive study, how subendothelial migration is regulated hasn't been clear.

Interference reflection microscopy (IRM) has been widely used in cell adhesion and migration study. It provides information about a degree of proximity of cells to the substrate surface in a label-free manner. In this study, we utilized IRM to visualize how T cells undergoing subendothelial migration interacts with adhesion formed between ECs and substrates.

II. METHODS

The TNF α -activated monolayer of bEnd.3 cells were mounted on a shear chamber. DO11.10 T cells were perfused over the bEnd.3 cell monolayer at 0.25 dyne/cm² for 10 min to accumulate T cells, and then at 2 dyne/cm² for 30 min with culture medium. The dynamics of T cells were observed using a 40 \times objective lens by time-lapse imaging of DIC and IRM with 15 s of interval as described previously [1].

III. RESULTS

A. Classification of FAs of ECs

As shown in Fig. 1A, two different types of FAs were observed: 'side-by-side' FAs were located near junctions, and typically more than 3 adjacent FAs were located within 2 μ m of distances. In contrast, 'free-standing' FAs were relatively isolated ones.

B. Migration of T cells with respect to FA of ECs

Depending on the type of the FAs, distinct behaviors of T cells were observed (Fig. 1B). When T cell encountered 'side-by-side' FAs, they either crawled along them or changed their direction as if they encountered a rigid wall. In contrast, when T cells encounter 'free-standing' FAs, they stretched lamellipodia and migrated around the FAs.

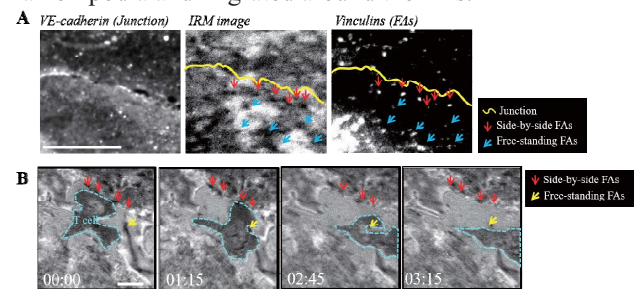


Fig. 1 (A) Two distinct types of FAs observed in IRM images, (B) Migration trajectories of T cells with respect to different types of FAs.

IV. CONCLUSION

In summary, we observed interactions between FAs of ECs and T cells undergoing subendothelial migration by label-free imaging based on IRM. Quantitative image analysis revealed that FAs of ECs provided a guiding cue for subendothelial migration of T cells.

ACKNOWLEDGEMENT

This research was supported by National Research Foundation of Korea (NRF) grants funded by the Korea government (MSIP) (Grant No. 2011-0030075 to JD and Global Ph.D. Fellowship to JL).

REFERENCES

1. K.H. Song, et al, "T cells sense biophysical cues using lamellipodia and filopodia to optimize intraluminal path finding" *Integr Biol.* 6, 450, 2014.

Injectable hydrogel for long-term chemical drug/gene combination therapy

C.-H Kim^{1,2}, Y.-M Kim¹, and S.-C. Song^{1,2}

¹Center for Biomaterials, Korea Institute of Science and Technology, Seoul, Korea

²Department of Medical Engineering, Korea University of Science and Technology, Daejeon, Korea

E-mail: mongtan07@gmail.com

Abstract—We developed a chemical drug/gene dual delivery platform system for long-term combination therapy. Nano-sized thermo-sensitive polymer/chemical drug/gene complexes showing sol-gel transition were prepared by simple mixing of three components, the complexes. The hydrogel showed sustained release of chemical drug and genes and showed anti-cancer effects *in vitro* and in an *in vivo* xenograft model upto 1 month.

Keywords—Gene delivery, combination therapy, phosphazenes, siRNA, injectable micelleplex hydrogel, long-term therapy

I. INTRODUCTION

Drug delivery carriers for therapies combining chemotherapy with gene therapy have been used to overcome limitations of chemical therapy. However, multiple administrations of the carriers are necessary to achieve an anti-cancer effect¹. Thermosensitive hydrogels have been applied for sustained and long-term therapy without repeated administration, however it requires an additional material to deliver genes². We propose a dual delivery platform system with only one material for sustained release of anti-cancer drugs (docetaxel, DTXs) and genes (siRNAs for Bcl-2) within the tumor site for long-term combination therapy using injectable hydrogel. DTXs/siRNAs were released for more than 1 month and the combinational therapeutic effects were demonstrated by anti-cancer effects in *in vivo* xenograft model.

II. METHODS

A. In vitro siRNAs and DTX release assay from the hydrogel

The gel was placed in a tube and DEPC water was added. At a predetermined time, 500 μ l of sample were obtained and replaced with 500 μ l of fresh DEPC water. The released siRNAs and DTXs were estimated by Ribogreen assay and UV spectrometry at 230 nm.

B. In vivo anti-tumor activity test

After formation of tumors, the hydrogel was administered through intra-tumoral injection to the mice, and body weights and tumor volumes were monitored for 1 month at predetermined time intervals.

III. RESULTS

A. In vitro siRNAs and DTX release assay from the hydrogel

Concentrations of DTXs changed the release patterns of DTXs and siRNAs from the hydrogels. Increased hydrophobicity of the hydrogel by high concentrations of DTX results in the sustained dissociation of the complexes from the hydrogel and siRNAs.

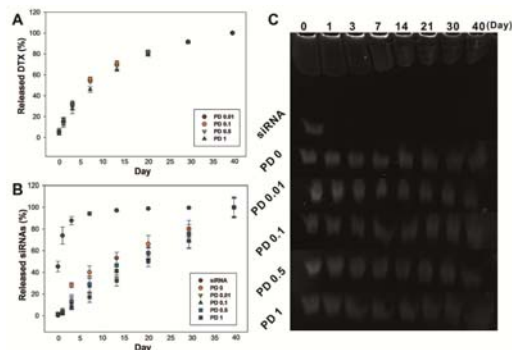


Fig. 1. *In vitro* release and stability tests of the complexes from the hydrogel

B. In vivo anti-tumor activity test

The anti-tumor effects were assessed by measuring the tumor size after intra-tumoral injections. DTX concentration-dependent tumor inhibitory effects were observed. The increased efficiency of PD 1 group than DTX only could be explained by the hydrogel-mediated localization effect and the gene silencing effect. No significant decreases of the hydrogels mean that the anti-tumoral activity was not affected by the toxicity.

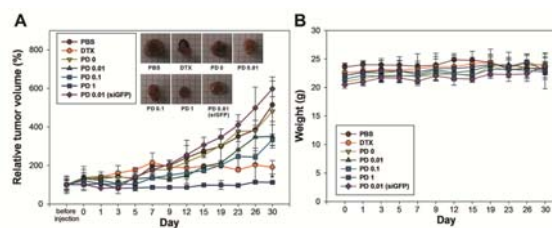


Fig. 2. *In vivo* anti-tumor and weight loss tests of the hydrogels until day 30

IV. CONCLUSION

We firstly developed a long-term chemical drug/gene dual delivery system that can adjust the release profile with chemical drug doses. We expect that this system can have many applications, such as cancer stem cell therapy, which requires combinatorial therapy.

ACKNOWLEDGEMENT

This research is financially supported by Korea Institute of Science and Technology and the Ministry of Education, Science and Technology of Korea.

REFERENCES

1. Y. Zhao, D. Y. Alakhova, and A. V. Kabanov, "Can nanomedicines kill cancer stem cells?" *Adv. Drug Deliv. Rev.*, vol. 65, pp. 1763-1783, 2013.
2. Y. H. Bae and K. Park, "Targeted drug delivery to tumors?: Myths, reality and possibility" *Adv. Drug Deliv. Rev.*, vol. 153, pp. 198-205, 2011.

***In vitro* therapeutic efficacy of drug-loaded CoFe₂O₄ nanoparticles combining magnetic hyperthermia and drug delivery for breast cancer**

Yunok Oh¹, Hansu Seo², Won Ho Cho³, and Junghwan Oh^{1,2,4}

¹Center for Marine-integrated Biotechnology (BK21 Plus), Pukyong National University, Busan, Korea

²Interdisciplinary Program of Marine-Bio, Electrical & Mechanical Engineering, Pukyong National University, Busan, Korea

³Department of neurosurgery, Pusan National University Hospital, Busan, Korea

⁴Department of Biomedical Engineering, Pukyong National University, Busan, Korea

E-mail: jungoh@pknu.ac.kr

Abstract—Magnetic nanoparticles (MNPs) with single units, of which are sized 1~100 nm have attracted significant attention for theranostic application and offer excellent possibility for the diagnosis and treatment of cancer. Main cancer treatments are presently limited to surgery, radiotherapy, and cancer drugs. But, these methods have a risk of most typical side effect to normal tissues or imperfect elimination of the cancer. Thus, to achieve high performance of cancer treatment, drug-loaded magnetic hyperthermia was demonstrated as a dual modality of hyperthermia and anticancer treatments.

Keywords— Magnetic nanoparticles, magnetic hyperthermia, doxorubicin.

I. INTRODUCTION

Cancer is the general term describing a cluster of cells undergoing uncontrolled growth in the body. One method of destroying cancer cells is magnetic hyperthermia. Magnetic hyperthermia using magnetic nanoparticles is a minimal invasive cancer therapy. Cancer cells die at elevated temperatures in the range of 42~46 °C and since local hyperthermia does not require surgery to administer, the therapy is a very efficient and non-invasive approach for treating cancer. Magnetic hyperthermia is a way to advance the efficiency of chemotherapy or radiotherapy by raising the temperature of a cancer to 41~45 °C. Thus, magnetic hyperthermia for cancer treatment can reduce side effects in comparison to the therapies of cancer like radiotherapy and chemical drugs. In this study, we focused on developing and evaluating drug-loaded MNPs that can be utilized as a multimodal theranostic agent for high performance in cancer treatment.

II. METHODS

Preparation of drug-loaded MNPs

Figure 1 illustrates a synthesis process for doxorubicin-loaded CoFe₂O₄ (DOX-CoFe₂O₄) nanoparticles. CoFe₂O₄ magnetic nanoparticles were synthesized by thermal decomposition procedure reported by sun et al [1]. CoFe₂O₄ nanoparticles were transferred to be hydrophilic by a ligand exchange reaction using DMSA [2]. For the electrostatic

interaction with doxorubicin, the DMSA-coated CoFe₂O₄ aqueous solution was incubated with doxorubicin solution for 6 hr at room temperature [3]. The mixture was purified by ultrafiltration and characterized by FT-IR, XRD, TEM, MPMS, TGA, UV-vis spectroscopy and DLS.

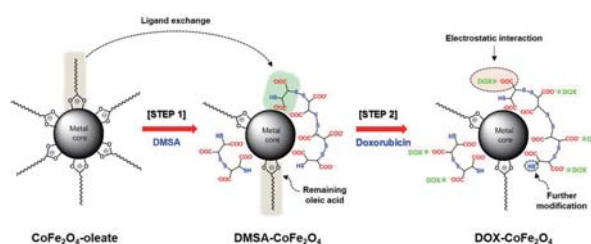


Figure 1. Schematic diagram of synthesis of DOX-CoFe₂O₄ nanoparticles

In vitro cell death induced by dual modality

MDA-MB-231 breast cancer cells were used for *in vitro* MHT of the DOX-CoFe₂O₄ nanoparticles. MDA-MB-231 cancer cells were seeded at a density of 2×10^5 cells/mL in a 35 mm culture dish of 2 mL medium. To investigate MHT effects of DOX-CoFe₂O₄ nanoparticles on MDA-MB-231 cancer cells *in vitro*, breast cancer cells were further incubated with 0.5 mg (magnetic atoms)/mL of DOX-CoFe₂O₄ nanoparticles for 24 hr. The cell dish was subjected to A/C magnetic field of 0.6 Tesla, of which the field generator contained 3-turn and 65 mm of inner radius of copper coil equipped with an optical thermocouple for 30 min.

III. RESULTS

The size and morphology of the synthesized DOX-CoFe₂O₄ nanoparticles were characterized by HR-TEM (Figure 2). Highly ordered ~16 nm circle-like doxorubicin-coated CoFe₂O₄ nanoparticles were successfully synthesized by thermal decomposition and electrostatic interaction. DOX-CoFe₂O₄ nanoparticles showed a high cytotoxicity effect on cell viability and colloidal stability in aqueous solution.

Figure 3 demonstrates fluorescence microscopic images of MDA-MB-231 cells with 0.2 mg of doxorubicin and 0.5 mg (magnetic atoms)/ml of DOX-

CoFe₂O₄ nanoparticles after 24-hr incubation to evaluate the efficiency of MTH. Hoechst 33342 assay and Annexin V-FITC Apoptosis Detection Kit were used to qualitatively distinguish the progression of apoptosis and necrosis under various testing conditions. Control showed no green and red fluorescence induced by Annexin V-FITC and PI double staining in Figures 3(a), indicating no apoptotic and necrotic cell death. Blue fluorescence from Hoechst 33342 and overlay images also represented approximately 100% live cells, which mirrors no effect of MNPs on the cellular death (i.e., no green or red fluorescence). On the other hand, CD-42 presented the low degree of early apoptosis (green fluorescence from Annexin V FITC) and late apoptosis/necrosis (red fluorescence from PI) in Figure 3(b). Once the cells were magnetically treated with MNPs at 42 °C (CD-42), both intense green and red fluorescence lights were considerably generated in Figure 3(c). Due to the intensity of green and red fluorescence, CD-42 was more efficient cancer treatment than CD in light of early apoptosis (green) and late apoptosis/necrosis (red). As the overlay image for MHT-42 confirmed that all the fluorescence lights (blue, green, and red) were almost overlapped at the same position, the number of viable cells quickly decreased and the apoptosis proceeded from the early stage to the late stage within 24 h after MHT at 42 °C.

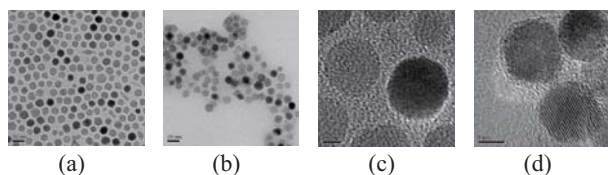


Figure 2. TEM and HR-TEM images of CoFe₂O₄ (a, c) and Dox-CoFe₂O₄ (b, d) nanoparticles.

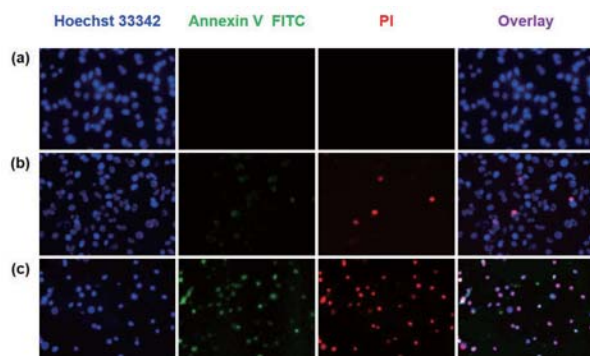


Figure 3 Fluorescence microscopic images of MDA-MB-231 cells with 0.2 mg of doxorubicin and 0.5 mg (magnetic atoms)/mL of DOX-CoFe₂O₄ nanoparticles after 24 h incubation: (a) control (untreated cells without MNPs and MHT), (b) CD (cells treated with doxorubicin without MHT), (c) CD-42 (cells treated with MNPs and MHT for 30 min at 42 °C). The cells were stained with Hoechst 33342 and Annexin V FITC/PI conjugate staining agents.

IV. CONCLUSION

The therapeutic effects of cancer hyperthermia were greatly improved by the combining magnetic hyperthermia and doxorubicin delivery. The induced-heat during magnetic hyperthermia can trigger the doxorubicin release from DOX-CoFe₂O₄ nanoparticles increase cell sensitivity to medication. As a result, multimodal DOX-CoFe₂O₄ nanoparticles yielded multiple synergistic effects on the cell viability. Ultimately, multifunctional drug-loaded nanoparticles integrated with magnetic hyperthermia and drug delivery system can be an effective theranostic approach for early-detection and treatment of small-sized cancer.

ACKNOWLEDGEMENT

This research was supported by a grant from Marine Biotechnology Program (20150220) funded by the Ministry of Oceans and Fisheries, Republic of Korea.

REFERENCES

1. Shouheng S, Hao Z, David B R, Simone R, Philip M R et al, "Monodisperse MFe₂O₄ (M =Fe, Co, Mn) nanoparticles," *J. Am. Chem. Soc.*, vol. 126, pp. 273-279, 2003.
2. Lee J H, Jang J T, Choi J S, Moon S H, Noh S H, Kim J W, Kim J G, Kim I S, Park K I and Cheon J, "Exchange-coupled magnetic nanoparticles for efficient heat induction," *Nat Nanotechnol*, vol.6, pp. 418-22, 2011.
3. Susanne K, Julia G, Piere.C, Alfonso L, Anotnio A et al, "Efficient treatment of breast cancer xenografts with multifunctionalized iron oxide nanoparticles combining magnetic hyperthermia and anti-cancer drug delivery," *Breast Cancer Research*, vol. 17, pp. 1-17, 2015.
- 4.

Quantification of mitochondrial morphologies during endothelial differentiation induced by shear stress

J. W. Shin¹, Y. G. Kang¹, S. H. Park¹, Y. Wu², S. R. Gu²,
H. Y. Ban¹, Y. M. Kim¹, M. J. Kim¹, J-W. Shin^{1,2,3*}

¹Department of Biomedical Engineering, Inje University, Gimhae, Korea

²Department of Health Science and Technology, Inje University, Gimhae, Korea

³Cardiovascular and Metabolic Disease Center/Institute of Aged Life Redesign/UHARC, Inje University, Gimhae, Korea

E-mail: biomechshin@gmail.com

Abstract— Recent studies suggested the importance of mitochondrial morphology in relation to physiological functions. In this study mitochondrial morphologies were classified according to endothelial differentiation and it was found that the mitochondrial morphology became simpler with progression of differentiation.

Keywords— Mitochondria, Mitochondrial morphology, Mesenchymal stem cells, Shear stress, Endothelial differentiation.

I. INTRODUCTION

Recent studies revealed that mitochondria morphology changes continuously accompanying various specific cellular functions. However, most previous reports mentioned only fragmentation or elongation of mitochondria in relation to mitochondria fusion/fission proteins. This study analyzed mitochondrial morphology quantitatively based on the image processing techniques along the differentiation.

II. METHODS

A. Induction of endothelial differentiation

Human mesenchymal stem cells were seeded on the miniature fluid-chip (1×10^4 cells/cm²) and were induced in Dulbecco's modified Eagle's medium with low glucose containing vascular endothelial growth factor, 5% fetal bovine serum, 100 U/ml penicillin and 100 mg/ml streptomycin. Shear stress was applied for 24h hours after stabilization.

B. Flow-induced shear stress

To apply flow-induced shear stress, a gear pump was used to provide a steady flow. A miniature fluid chip was fabricated utilizing polydimethylsiloxane. By adjusting the flow rate two magnitudes of shear stress (2.5 or 10.0 dyne/cm²) were applied for 24h after stabilization.

C. Immunostaining and quantification of mitochondrial morphology

Mitochondria were stained with 200 nM MitoTracker Deep Red FM at 37°C for 30 min. And then, cells were

fixed 4% paraformaldehyde and stained with Willebrand factor to confirm the endothelial differentiation. To quantify the networking of a mitochondrion, MATLAB 2012a was used to analyze images of single cells acquired within the region of interest.

III. RESULTS

A. Shear stress with VEGF induces differentiation of hMSCs into endothelial-like cells

hMSCs were effectively differentiated into endothelial cells when simultaneously subjected to shear stress and VEGF. Specifically, the cells began to express vWF 24 hours after induction with higher shear stress (10.0 dyne/cm²) than lower shear stress (2.5 dyne/cm²).

B. hMSCs were experienced dramatic mitochondrial morphological changes during differentiation

The total mass and average length of mitochondria in the cell tended to be decreased with progression of differentiation along the endothelial lineage. And the mitochondrial network in the cells became simpler with differentiation along with the endothelial lineage.

IV. CONCLUSION

This study was performed to investigate various changes in mitochondria using image analysis techniques. This study would contribute to mitochondrial morphology studies in relation to various cellular activities, especially in differentiation, along with physiological and biological relevances.

ACKNOWLEDGEMENT

This work was supported by the Human Resource Training Program for Regional Innovation and Creativity through the Ministry of Education and National Research Foundation of Korea (NRF-2014H1C1A1066694)

3D Cell Printing of Tissue Mimetic Microenvironment

Jinah Jang¹, Hun-Jun Park², Seok-Won Kim¹, Heejin Kim², Ju Young Park³, Soo Jin Na², Hyeon Ji Kim¹, Moon Nyeo Park¹, Seung Hyun Choi^{4,5,6}, Sun Hwa Park^{7,8}, Sung Won Kim^{7,8}, Sang-Mo Kwon^{4,5,6}, Pum-Joon Kim², Dong-Woo Cho^{1*}

¹Department of Mechanical Engineering, Pohang University of Science and Technology (POSTECH), Korea.

²Division of Cardiovascular Medicine, The Catholic University of Korea, College of Medicine, Cardiovascular Center, Korea.

³Division of Integrative Biosciences and Biotechnology, Pohang University of Science and Technology (POSTECH), Korea.

⁴Medical Research Institute, School of Medicine, ⁵Laboratory for Vascular Medicine and Stem Cell Biology, Department of Physiology, School of Medicine, ⁶Convergence Stem Cell Research Center, Immunoregulatory Therapeutics Group in Brain Busan 21 Project, Pusan National University, Korea.

⁷Department of Otolaryngology-Head and Neck Surgery, College of Medicine, The Catholic University of Korea, Korea.

⁸Department of Biomedical Science, College of Medicine, The Catholic University of Korea, Korea

* E-mail: dwcho@postech.ac.kr

Abstract— Stem cell therapy emerges as a new therapeutic method for the treatment of advanced ischemic heart diseases. However, a major challenge of the therapeutic use of stem cells for cardiac repair, such as poor cell retention, prohibits the therapeutic efficacy of stem cells *in vivo* after transplantation. 3D cell printing technology is considered as a promising approach to regenerate the tissue architecture similar to cardiac niche by depositing various cells with a printable hydrogel called ‘bioink’. In this study, we developed a 3D functionalized cardiac patch using bioink composed of heart-derived decellularized extracellular matrix (hdECM), embedded by cardiac progenitor cells for cardiac muscle tissue and mesenchymal stem cells with vascular endothelial growth factor for vascular tissue.

Keywords— 3D cell printing, bioink, cardiac tissue engineering, stem cells, myocardial infarction

I. INTRODUCTION

Towards the enhancement of therapeutic efficiency, a functionalized patch type cell delivery platform can be a potential alternative to achieve high retention, survival, engraftment, and differentiation of cells. Although there have been many successful results, fabricating an organized vascular plexus within the 3D structure remains a key barrier to enhancement of cell survival and function.

II. METHODS

To print the patch for stem cell delivery, we used three different bioinks’ formulation as follow: 1) CPCs-laden hdECM bioink (Bioink I), 2) MSCs-laden hdECM bioink with 10 $\mu\text{g}/\text{ml}$ VEGF (Bioink II) for vessel formation and 3) the mixture of CPCs and MSCs-laden hdECM bioink with 10 $\mu\text{g}/\text{ml}$ VEGF (Bioink III). We printed the cell deliverable patch

spatially alternating Bioink I and Bioink II (patterned patch) using multi-head bioprinter. The mixed patch was fabricated using Bioink III. The printed patches were implanted either in the mice subcutaneous site to investigate the vascularization capability or transplanted the printed patch into rat MI model to verify the therapeutic effect of the patch.

III. RESULTS

hdECM bioink enhanced angiogenesis and promoted fetal reprogramming through the endogenous paracrine signaling of epicardium compared to fibrin bioink. In addition, the patterned patch shortened the time for inosculation with the host circulatory system and promoted strong vasculogenesis which is distinct from the capillary formation made by the mixed patch. After 8 weeks of transplantation of the patch, the major cardiac functions were significantly enhanced in the group of patterned patch (ejection fraction $8.12 \pm 1.1\%$, fractional shortening $6.24 \pm 2.46\%$ compared to baseline). Moreover, cardiomyogenesis was progressed in both the implanted patch and the infarct region. The larger number of cells were migrated from the patterned patch to the infarct and differentiated into the endothelium compared to the mixed patch.

IV. CONCLUSION

A major advantage of the developed platform technology is the spatial patterning of each cell to promote rapid vascularization in the 3D structure and prolonged survival of delivered cells *in vivo*. This 3D pre-vascularized stem cell delivery platform may open new avenues for delivering cells with high retention capability and regenerating ischemic tissue area

ACKNOWLEDGEMENT

This work was supported by the National Research Foundation of Korea (NRF) grant funded by the Korea government (MSIP) (No. 2010-0018294).

A rational strategy based on 3D printing for long-segment circumferential tracheal reconstruction

Jeong Hun Park¹, Ju Young Park², Inn-Chun Nam³, Jae Yeon Lee⁴, Seok Hwa Choi⁴,
Sung Won Kim³ and Dong-Woo Cho¹

¹Department of Mechanical Engineering, Pohang University of Science and Technology (POSTECH), Pohang, Korea

²Division of Mechanical Engineering, Pohang University of Science and Technology (POSTECH), Pohang, Korea

³Department of Otolaryngology and HNS, College of Medicine, The Catholic University of Korea, Korea

⁴ Veterinary Medical Center, Chungbuk National University, Cheongju, Korea

E-mail: dwcho@postech.ac.kr

Abstract—In this research, a 3D printing based tissue engineered tracheal graft was developed as a rational strategy for long-segment tracheal reconstruction with accelerated tracheal epithelial regeneration. The mature tracheal epithelium with predominant ciliated cells was regenerated on the entire luminal surface of the tissue engineered tracheal graft within 2 months after anastomosis in a rabbit model.

Keywords— Long-segment circumferential tracheal reconstruction, Bellows architecture, Indirect 3D printing, tedECM, hTMSC sheets,

I. INTRODUCTION

It is well known that long-segment circumferential defects still represent a major reconstructive problem that needs much time for epithelial regeneration on the luminal surface. In this regard, a rational strategy for long-segment circumferential tracheal reconstruction needs to be developed.

II. METHODS

Native trachea-mimetic framework of the tissue-engineered tracheal graft was designed with bellows architecture and its mechanical behavior under three-point bending and radial compression was analyzed using FEM analysis. Bellows scaffold was then 3D printed indirectly using poly (ϵ -caprolactone) (PCL). Tracheal epithelial decellularized extracellular matrix (tedECM) bio-ink was stratified on the luminal surface of the bellows scaffold reinforced with silicon rings and human inferior turbinate mesenchymal stem cell (hTMSC) sheets were transplanted to the tedECM layer. Tissue-engineered tracheal grafts with tedECM and hTMSC sheets were stabilized in vitro for 3 days and anastomosed end to end to the cervical trachea in a rabbit model. Tracheal epithelial regeneration was then assessed by bronchoscopy, macroscopic, x-ray, histological and immune-histochemical examinations at 2 months after implantation.

III. RESULTS

The mature tracheal epithelium with predominant ciliated cells was completely regenerated on the entire luminal surface of the tissue-engineered tracheal graft within 2 months after implantation (Fig. 1).

IV. CONCLUSION

The reconstruction of long-segment circumferential tracheal defect using a tissue-engineered tracheal graft was successfully performed. A 3D printing based tissue-engineered tracheal graft with tedECM and hTMSC sheets might be a novel concept of tracheal substitute for tracheal reconstruction.

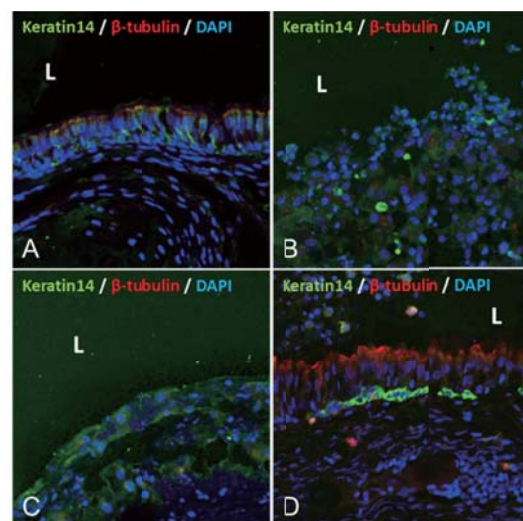


Fig. 1. Immunofluorescent staining ($\times 600$) of (A) the native tracheal epithelium and regenerated tissue in the middle luminal surface of the grafts in (B) group I, (C) group II, and (C) group III. L indicates airway lumen. Red and green represent a positive reaction against the abovementioned antibodies. Blue represents nuclei stained with DAPI.

ACKNOWLEDGEMENT

This work was supported by the National Research Foundation of Korea (NRF) grant funded by the Korea government (MSIP) (Nos. 2010-0018294) and by the Korea Health Industry Development Institute (KHIDI) funded by the Ministry of Health and Welfare (HI14C3228).

Autonomous Sensor Node for Monitoring HRV using RFID technology

Thang Viet Tran¹, Nam Trung Dang¹, Wan-Young Chung¹

¹Department of Electronic Engineering, Pukyong National University, Busan 608-737, South Korea

E-mail: tvthang@pknu.ac.kr; dangtrungnam2809@gmail.com; wychung@pknu.ac.kr

Abstract—This paper proposes a batteryless sensor node to collect electrocardiography (ECG) signals for monitoring heart rate variability (HRV). The proposed node can supply power independently by using the RFID technology for wirelessly transmitting data and the 915 Mhz-RF energy harvester for supplying power to the sensor module. The proposed node can collect raw ECG signals and detect R-peaks by using a robust peak detection algorithm. The R-peaks are then transmitted to the host over RFID link for monitoring HRV.

Keywords— Autonomous node, RFID, energy harvester, ECG, heart rate variability.

I. INTRODUCTION

Wearable wireless devices are widely deployed in health and athlete performance monitoring system nowadays. However, most of the distributed body sensor nodes consume more power due to wireless data transmission power [1]. To overcome the serious drawback, a UHF RFID technology that do not require power is used to transmit collected data to base station instead of conventional wireless methods such as the ZigBee, BlueTooth, and wifi standards. In addition, a 915 MHz-RF energy harvester is used to gather RF power for supplying power to the ECG sensor module. Therefore, the proposed node completely becomes an autonomous sensor node.

II. METHODS

Fig. 1 shows the block diagram of the proposed sensor node, including a semi-active UHF RFID tag (SL900A, AMS Co., Australia), a XLP microcontroller unit, an ECG module, and a 915 MHz-RF energy harvester. Both tag and RF harvester can operate at the same frequency band of 915 Mhz, therefore the reader

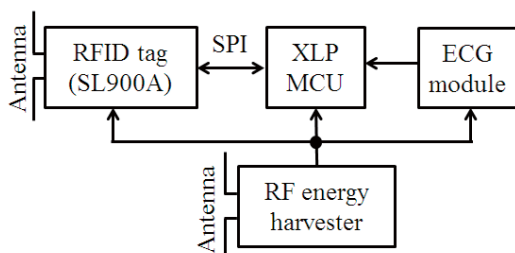


Fig. 1. Block diagram of the ECG sensor tag.

can simultaneously communicate and supply power for the proposed node. The MCU can process raw ECG signals collected by the ECG module, and then detect R-peak by using a modified real-time peak detection algorithm before transmitting to the host via the SL900A [2].

III. RESULTS

The proposed RF energy harvester can gather RF power of the 2W-RFID reader within maximum range of ~1 m for significantly supplying power to the proposed node. The proposed node can easily gather the raw ECG signals, and then the R-peaks detected by the MCU module are transmitted to the host over RFID link for monitoring HRV as shown in Fig. 2.

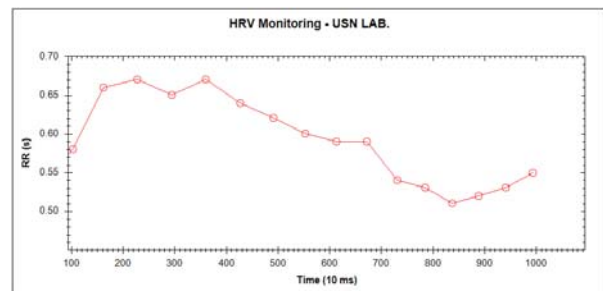


Fig. 2. HRV waveforms of the collected ECG signals.

IV. CONCLUSION

The autonomous sensor node using RFID technology is designed and implemented to collect the ECG signal for monitoring HRV. The propose sensor can supply power itself; therefore the proposed method can overcome the serious drawback of the wearable sensor devices due to assisted battery. This study can provide a useful solution for wearable bio-signal sensor devices.

ACKNOWLEDGEMENT

This research was supported by the Research Grant of BB (Brain Busan) 21 project of 2014.

REFERENCES

1. M. Magno and L. Benini, "An Ultra-Low Power High Sensitivity Wake-up Radio Receiver with Addressing Capability," 2nd Int. works. Green Opt. Wirel. Networks, pp. 92-99, 2014 .
2. T. V. Tran and W.-Y. Chung, "A Robust Algorithm for Real-time Peak Detection of PPG Using a Personal Computer Mouse," *IEEE Sen. J.*, vol. 15, pp. 4651-4659, 2015.

Computational simulation of passive leg raising effects on hemodynamics during cardiopulmonary resuscitation

D.A. Shin¹, J.H. Park¹, J.C. Lee², H.C. Kim²

¹Interdisciplinary Program for Bioengineering, Graduate School, Seoul National University, Seoul, Korea

²Department of Biomedical Engineering, Seoul National University College of Medicine, Seoul, Korea

E-mail: 1012sda@gmail.com

Abstract—Effects of passive leg raising (PLR) maneuver during cardiopulmonary resuscitation (CPR) is not yet fully understood due to lack of clinical evidence. In this paper, we developed a computational model that couples hemodynamic behavior during standard CPR and the PLR maneuver. The simulation results show that PLR maneuver during CPR significantly improves cardiac output (CO) as well, compared to the standard CPR only.

Keywords— cardiopulmonary resuscitation (CPR), passive leg raising (PLR), mathematical model

I. INTRODUCTION

Passive leg raising (PLR) maneuver has been used for patients with circulatory failure to improve cardiac output by transferring venous blood from the lower limbs toward the heart with leg elevation. Considering that increasing cardiac output is also a major interest during cardiopulmonary resuscitation (CPR), PLR may play a critical role during CPR by creating synergy effects. However, validation of such efficacy has been limited to animal experiments which are highly expensive and labor intensive. Accordingly, we developed a computational model that couples standard CPR and PLR maneuver (CPR-PLR model) in order to simulate hemodynamic effects with quantitative changes of angles of the leg raise. With CPR-PLR model, we were able to find out significance of PLR maneuver during CPR by comparative analysis with the standard CPR model.

II. METHODS

The standard CPR model was built based on the mathematical model proposed by Babbs [1]. For CPR-PLR model, PLR maneuver was complemented to the standard CPR model based on orthostatic stress model proposed by Heldt et al.[2]. Simulations of human circulatory system during standard CPR and during CPR-PLR were carried out using Matlab software (The MathWorks, Inc., Natick, MA, USA).

The standard CPR model that couples human circulatory system and mechanical chest compression is composed of 14 vascular compartments as lumped models for vascular compliance and resistance, which accord with the following differential equation:

$$\begin{aligned} \Delta P &= \frac{1}{C} (i_{out} - i_{in}) \Delta t \\ &= \frac{\Delta t}{C} \left[\frac{P_{out1} - P_{in1}}{R_1} - \frac{P_{out2} - P_{in2}}{R_2} \right] \end{aligned} \quad (1)$$

The PLR maneuver is represented by hydrostatic pressure acting on lower limbs including femoral veins (FV) and arteries (FA). When the lower limbs were lifted, the hydrostatic pressure directly influence on blood flow and pressure. The hydrostatic pressure in the lower limbs is defined as follows.

$$\begin{aligned} P_{hydro} &= \rho g h \cdot \sin(\theta(t)) \\ \Delta P &= \frac{1}{C} (i_{out} - i_{in}) \Delta t \pm \Delta P_{hydro} \end{aligned} \quad (2)$$

III. RESULTS

Both the CPR-PLR and the standard CPR models were simulated under the same conditions of chest compression cycle with 80cycles/min, initial pressure with 5mmHg, and maximum chest compression force with 400N. The simulation results clearly show that the PLR maneuver improves the cardiac output (CO), compared to the result from the standard CPR model.

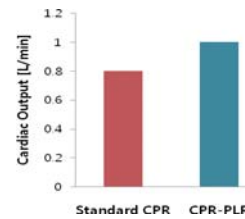


Fig. 1. Cardiac output during standard CPR and CPR-PLR

IV. CONCLUSION

Our computational model was able to prove the hemodynamic effects of PLR maneuver. We believe this model would become an essential means for studying PLR effects during CPR.

ACKNOWLEDGEMENT

This work was supported by The Korean Health Technology R&D Project of the Ministry of Health & Welfare, Republic of Korea (HI14C0746).

REFERENCES

1. C. F. Babbs, "Effects of an impedance threshold valve upon hemodynamics in Standard CPR: Studies in a refined computational model", *Resuscitation*, vol. 66, pp. 335–345, 2005.
2. T. Heldt, E. B. Shim, R. D. Kamm, and R. G. Mark, "Computational modeling of cardiovascular response to orthostatic stress", *J Appl Physiol*, vol. 92, pp. 1239–1254, 2002.

Multi-Scale Computational Fluid Dynamics for Patient-Specific Coronary Flow Simulations

Minh Tuan Nguyen¹, Hyoung G. Choi², Sang-Wook Lee¹

¹ School of Mechanical Engineering, University of Ulsan, Ulsan, Korea

²Dept. of Mechanical & Automotive Engineering, Seoul National University of Science and Technology, Seoul, Korea

E-mail: leesw@ulsan.ac.kr

Abstract—We introduce the development of clinically practical CFD tool for complex coronary blood flow dynamics simulations with aims of accelerating clinical outcomes, basically by bench to bedside approach. Fully implicit P2-P1 finite element code was developed using four-step fractional scheme with stabilization technique of SUPG and parallel computing by domain decomposition method. The techniques enable computational solutions of patient-specific coronary hemodynamics to be available within a half hour’s computing time.

Keywords— Computational fluid dynamics, Parallel computing, multi-scale modeling, patient-specific model, coronary hemodynamic

I. INTRODUCTION

In this paper, we introduce the development of multi-scale CFD tool for coronary flow dynamics simulations with aims of accelerating clinical outcomes, basically by bench to bedside approach.

II. NUMERICAL METHODS

2.1 Numerical Algorithm

Fully implicit P2-P1 finite element code was developed using four-step fractional scheme introduced by Choi and Moin [1].

$$\alpha^2 \frac{u_i^n - u_i^{n-1}}{\Delta t} + Re \frac{1}{2} (\partial_j u_{i,j} + u_j^n \partial_j u_i^n) = -Re p_j^n + \frac{1}{2} (\partial_j u_{i,j} + u_j^{n-1} \partial_j u_i^{n-1}) \quad (1)$$

$$\alpha^2 \frac{u_i^n - u_i^{n-1}}{\Delta t} = Re p_j^n \quad (2)$$

$$p_j^{n-1} = \frac{\alpha^2}{Re \Delta t} u_{i,j}^n \quad (3)$$

$$\alpha^2 \frac{u_i^{n+1} - u_i^n}{\Delta t} = -Re p_j^{n+1} \quad (4)$$

2.2 MPI Parallel Algorithm

The computational domain is decomposed into multiple subdomains. The computing work for each subdomain is distributed to the corresponding processor by MPI parallelization technique and runs simultaneously.

2.3 Integrated Multiscale Modeling (3D+0D)

The accuracy of 3D CFD solutions based on patient-specific data highly depends on the boundary conditions. However, in vivo data from each patient are not always available. To estimate physiologically adequate boundary conditions, lumped parameter models (LPM, 0D models) were adapted. Then, 3D CFD modeling and 0D modeling for the rest of distal vascular system were implicitly coupled. Fig. 1 shows the typical LPM for coronary vascular systems. The procedure to determine the value of resistance and capacitance in coronary vascular system can be found in detail in the study of Sankaran [2].

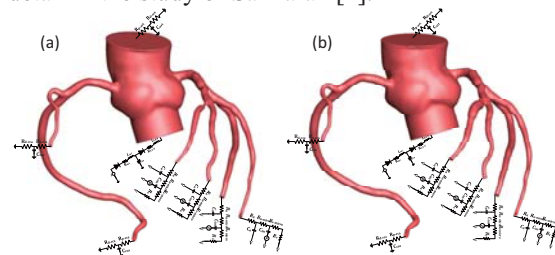


Fig. 1 Lumped parameter model of coronary vascular systems. (a) Pre-stent, (b) Post-stent

IV. CONCLUSION

We developed a fast, robust and physiologically reasonable multiscale CFD tool for coronary blood flow dynamics simulations, which may be useful in routine clinical practices. In order to improve the accuracy, LPM modeling techniques for each outlet branch based on patient-specific data need to be studied further.

ACKNOWLEDGEMENT

This work was supported by IITP grant (No. R0101-15-0171) funded by the Korea government (MSIP)

REFERENCES

1. Choi, H. et al., “Effects of the computational time step on numerical solutions of turbulent flow,” *Journal of Computational Physics*. Vol. 113, pp. 1-4, 1994.
2. Sankaran et al., “Patient-specific multi-scale modeling of blood flow for coronary artery bypass graft surgery,” *Annals of Biomedical Engineering*, Vol. 40, pp. 2228-2242, 2012.

IBEC

International Biomedical
Engineering Conference 2015

2015

Road to Better Life through Biomedical Engineering

POSTER SESSIONS



Material Decomposition Framework using the Spectral Attenuation Coefficient Ratios by Multiple Discriminant Analysis

W. J. Lee¹, S. R. Kang², S. Y. Woo², S. J. Lee² and W. J. Yi³

¹Interdisciplinary Program in Radiation Applied Life Science Major, Seoul National University, Seoul, South Korea

²Department of Biomedical Radiation Sciences, Graduate School of Convergence Science and Technology, Seoul National University, Seoul, South Korea

³Department of Oral and Maxillofacial Radiology, School of Dentistry, Seoul National University, Seoul, South Korea

E-mail: lwj0616@snu.ac.kr

Abstract— Spectral CT imaging using photon-counting detector plays an important role in advanced imaging applications due to its capability of material decomposition. The aim of this research was to develop a spectral CT system using a photon counting detector, and to decompose materials by applying multiple discriminant analysis (MDA) to the energy-dependent attenuation coefficient ratios. The attenuation coefficients were measured via reconstructed spectral images, and the linear attenuation ratio was used for material identification. The MDA projection matrix, determined from training phantoms, was used to identify the four materials in testing phantoms. For quantification purposes, relationships between attenuation coefficients at multiple energy bins and concentrations were characterized by the least square method for each material. The results of experiments showed that a spectral CT system based on the photon-counting detector with MDA can precisely decompose the four materials.

Keywords— Photon counting detector, Multi-energy CT, Multiple discriminant analysis (MDA), Material decomposition, Concentration quantification.

I. INTRODUCTION

Spectral CT provides not only anatomical information but also composition information of scanned objects [1]. Recently, a photon-counting detector has been developed to acquire spectral information. We have used multiple discriminant analysis to decompose material.

II. METHODS

A. Multi-energy CT acquisition

We used a photon-counting detector (Timepix, X-Ray Imatek, Barcelona, Spain). Multi-energy images were acquired using energy thresholds of 32, 36, 40, 44, 48, 52, 56, 60. Conventional X-ray source (SB-120-350, Source-Ray Inc, Ronkonkoma, USA) was used.

B. Material decomposition

In Spectral CT imaging, the linear attenuation coefficient is represented as Eq. (1).

If we assume that each voxel is consisted of one material, each voxel can be treated as consisting of a

single material. The attenuation coefficient ratio Eq. (2) is independent of material concentration. The vector \mathbf{x} is composed of attenuation coefficient ratio Eq. (3).

$$\mu_L(E_n, \vec{x}) = \sum_{i=1}^K \rho_i(\vec{x}) \mu_{M,i}(E_n) \quad \text{----- (1)}$$

$$\mu_R(E_n) = \frac{\mu_L(E_n)}{\mu_L(E_{n+1})} \quad \text{----- (2)}$$

$$\mathbf{x} = (\mu_R(E_1), \mu_R(E_2), \dots, \mu_R(E_{n-1})) \quad \text{----- (3)}$$

Then we used MDA algorithm to classify the feature vectors of materials.

III. RESULTS

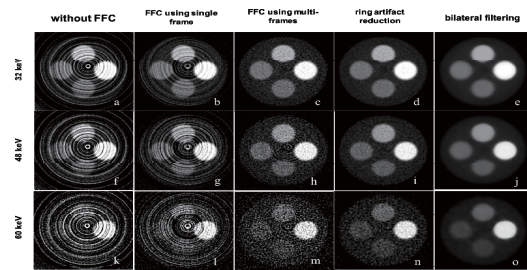


Fig. 1. Reconstructed multi-energy images.

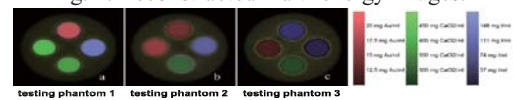


Fig. 2. Decomposed and quantified images

The reconstructed images were enhanced by applying preprocessing (Fig. 1). The multi-dimensional ratio vector of the materials at all voxels was classified into four materials by MDA. (Fig. 2).

IV. CONCLUSION

We studied the problem of linear dimensionality reduction of the linear attenuation coefficient for the task of material classification. The results of the experimental study showed that a CT system based on CdTe detector with MDA can be used to decompose materials.

ACKNOWLEDGEMENT

This work was supported by the National Research Foundation of Korea (NRF) grant funded by the Korea government (MEST) (No. 2013R1A2A2A03067942).

REFERENCES

1. T.J. Vrtiska, N. Takahashi, J.G. Fletcher, R.P. Hartman, L. Yu, and A. Kawashima, "Genitourinary Applications of Dual-Energy CT," *AJR.*, vol. 194, pp. 1434-1442, 2010.

Semi-Automatic Polyp Segmentation in Colonoscopy Videos

J. H. Won¹, N. Lee¹, B. Park², and H. Park^{1,3},

¹School of Electronic Electrical Engineering, Sungkyunkwan University, Suwon, Korea

²Department of Electronic, Electrical and Computer Engineering, Sungkyunkwan University, Suwon, Korea

³Center for Neuroscience Imaging Research (CNIR), Institute for Basic Science, Suwon, Korea

E-mail: jihyelo@skku.edu, qptnm@skku.edu, by6860@skku.edu, hyunjinp@skku.edu*

Abstract— Colonoscopy is a primary measurement for detecting colorectal polyps that might progress to cancer. Accurate detection of pre-cancerous colon polyps might decrease risks of colon cancer. Our goal is to detect and segment polyps using colonoscopy videos in a semi-automatic fashion. We used watershed and color intensity based algorithms to segment colon polyps. Our study yielded a miss rate of 11 percent obtaining improved result compared to the existing research.

Keywords— Colonoscopy; Colon polyps; segmentation

I. INTRODUCTION

According to the World Cancer Research Fund International, 1.4 million people were diagnosed to colorectal cancer in 2012, and it was recorded as the third most common disease in the world. Many studies are in progress to detect colorectal cancer [1].

Colon polyp is a small lesion located on the colon. Some colon polyps might turn into colorectal cancer. [2,3] Colon polyps usually do not cause pain, and thus it is important to detect them using colonoscopy videos [3].

Many studies adopted imaging techniques to detect and segment colon polyps, but the false positive rate was almost 13 percent [4]. We segmented colon polyps by using color, shape, and texture as imaging features, and reduced the false positive rate.

II. METHODS

A. Imaging data

Colonoscopy videos were obtained from CVC-Clinic database [5]. The video was consisted of 29 sequences and each sequence contained 5 to 25 frames. We applied our algorithms after extracting the particular frame from the frame source of video.

B. Image pre-processing

Image pre-processing was performed using MATLAB. The light effect of colonoscopy and small bubbles were considered as noise and removed. The edges of the polyps were sharpened to identify edge boundaries and increase the contrast around the edges.

C. Colon polyp segmentation

The approximate coordinate of the center of the colon polyp in the image was selected manually. Fuzzy c-means (FCM) algorithm was applied to make clusters for distinguishing polyps from the background. Two different algorithms based on watershed and color were applied to the image. Watershed algorithm that segment images based on a height was applied to find local minimum and maximum of the intensity. The image was divided into three sub-images based on red, green, and blue (RGB) colors. Green based image was converted to the binary mask image. The images obtained from watershed algorithm and color segmentation algorithm were multiplied, and produced candidate colon polyps. Region growing algorithm was performed with seed of manually predefined coordinate, and produced a mask of the colon polyp. The mask was warped to each candidate colon polyp and finally real colon polyp was generated

III. RESULTS

A. Colon polyp segmentation

We performed segmentation on an arbitrarily selected colon polyp. Edge information were extracted using the gradient (Fig. 1). We then applied watershed (Fig. 2) and RGB algorithm (Fig. 3). We only considered overlapped regions between the results derived from watershed and RGB algorithms (i.e., AND approach) as colon polyp.

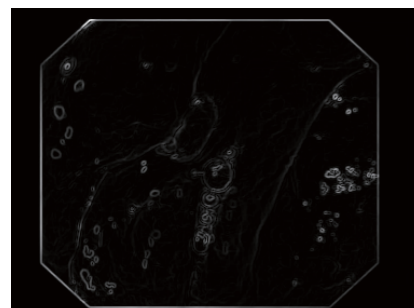


Fig. 1. Edge of the image

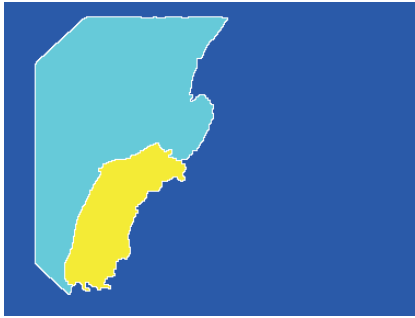


Fig. 2. Watershed ridge lines

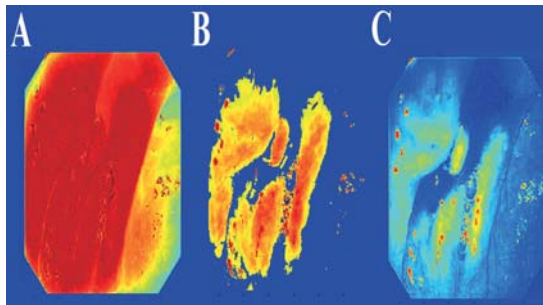


Fig. 3. Three sub-images divided into (A) red, (B) green, and (C) blue color

B. Assessing accuracy of the segmentation

The accuracy of the colon polyp segmentation was assessed by comparing with the ground truth image (Fig. 4). The overlapped ratio between the segmented and ground truth image was 89%.

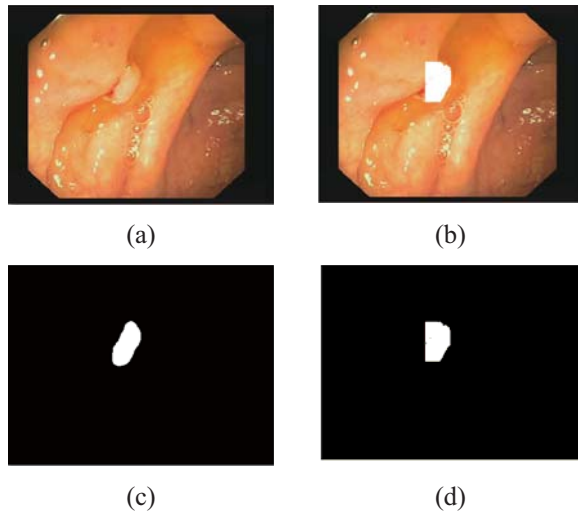


Fig. 4. (a) The original image, (b) the segmented image of polyps, (c) the mask of the ground truth image, and (d) the mask of the segmented image

IV. CONCLUSION

We performed semi-automatic polyp segmentation algorithms to reduce the false positive rates using colonoscopy videos. Watershed and color based algorithms were applied to detect polyps. Our study yielded the miss rate of 11 percent, and it is better than

the existing research [4]. Our algorithm could not identify polyps if the intensity of the image was too dark. Adjusting the light effect is remained for future works.

ACKNOWLEDGEMENT

This study was supported by the Institute for Basic Science (grant number IBS-R015-D1).

REFERENCES

1. World Cancer Research Fund International, Colorectal cancer statistics, 2015. Online at <http://www.wcrf.org/int/cancer-facts-figures/data-specific-cancers/colorectal-cancer-statistics>
2. B. Morson, "The Polyp-cancer Sequence in the Large Bowel," *Journal of the Royal Society of Medicine*, vol. 67, pp. 451-457, 1974.
3. S. M. Krishnan, X. Yang, K. L. Chan, S. Kumar, and P. M. Y. Goh, "Intestinal abnormality detection from endoscopic images," *IEEE*, vol. 20, pp. 895-898, 1998.
4. S. Hwang, J. H. Oh, W. Tavanapong, J. Wong, and P. C. de Groen, "Polyp detection in colonoscopy video using elliptical shape feature," *IEEE*, vol. 2, pp. 465-468, 2007.
5. J. Bernal, F. J. Sánchez, G. Fernández-Esparrach, D. Gill, C. Rodríguez de Miguel, and F. Vilariño, "WM-DOVA Maps for Accurate Polyp Highlighting in Colonoscopy: Validation vs. Saliency Maps from Physicians," *Computerized Medical Imaging and Graphics (in press)*, 2015.

Age-Related difference of superior medial frontal gyrus between ADHD and normal subjects using connectivity resting-state functional MRI

J. Hong¹, H. Park^{2,3}

¹Department of Electronics Electrical and Computer Engineering, Sungkyunkwan University, Suwon, Korea

²School of Electronic and Electrical Engineering, Sungkyunkwan University, Suwon, Korea

³Center for Neuroscience Imaging Research (CNIR), Institute for Basic Science, Suwon, Korea

E-mail: ¹bal25ne@skku.edu, ²hyunjinp@skku.edu

Abstract—Attention-Deficit/Hyperactivity disorder (ADHD) is one of the most common behavioral disorders showing abnormalities in attention, cognition and motor control. Previous studies found that these symptoms are related to superior medial frontal gyrus. In this study, we assessed group-wise differences using a network parameter obtained from connectivity analysis of resting-state functional magnetic resonance imaging (fMRI) between ADHD and normal subjects. Our results showed that differences of connectivity decreased in the superior medial frontal gyrus between two groups as people get older.

Keywords—Attention-Deficit/Hyperactivity disorder, ADHD, fMRI, betweenness centrality, connectivity analysis

I. INTRODUCTION

Attention-Deficit/Hyperactivity disorder is a one of the most commonly found behavioral disorders which can be described by abnormality in attention, cognition, executive function, motor control, response inhibition and motor control [1].

ADHD patients usually showing less impulsivity as they get old and this symptom is related to superior medial frontal gyrus (Figure 1) [2].



Fig. 1. Location of superior medial frontal gyrus

In this study, we assessed functional connectivity between ADHD and normal group to find differences in the superior medial frontal gyrus with age.

II. METHODS

A. Participants

We used resting-state functional magnetic resonance imaging (fMRI) data of 15 ADHD subjects and 15 normal subjects. The entire subjects were male. Each group was divided into 3 groups: child, adolescent, and adult. We used the definition of World Health Organization (WHO) to classification.

B. Image preprocessing

Resting state fMRI images were reconstructed using Athena pipeline (<http://www.nitrc.org/plugins/mwiki/index.php/neurobureau:AthenaPipeline>). This pipeline uses FSL and AFNI to preprocess both structural and functional magnetic resonance images. First, slice timing correction was performed. The 4D images were registered onto T1 weighted structural images, and then registered onto Montreal Neurological Institute (MNI) space. Non-brain tissues were removed. Band-pass filtering (0.009Hz-0.08Hz) was applied.

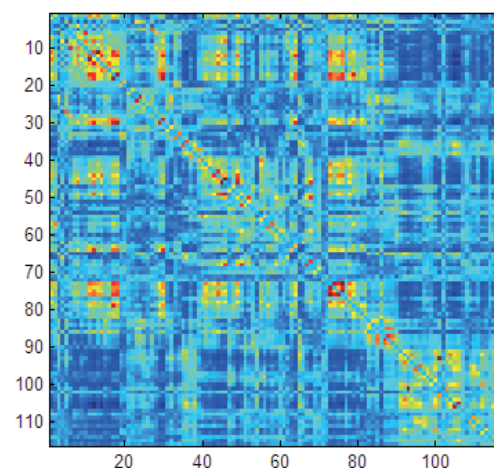


Fig. 2. Whole brain correlation map from one of the normal child subjects

The whole brain correlation maps were produced by computing correlation of timecourses between two different brain regions (Figure 2). In this step, the registered fMRI data were segmented into 116 regions using the AAL template.

C. Network parameter

Betweenness centrality (BC) was calculated by using Brain Connectivity Toolbox. BC is defined as the fraction of all shortest paths in the network that pass through a given node. For this reason, BC is a local parameter representing the importance of a given node [3].

D. Difference between groups

The mean BC values of superior medial frontal gyrus were calculated on each group. Then, these mean values were used to compute the differences between normal groups and ADHD groups.

III. RESULTS

A. The differences of mean BC values across subjects between ADHD and normal groups

The differences of mean BC values across subjects between ADHD and normal groups were computed for all age groups (Table 1, Figure 3). The differences of BC values showed linearly decreasing pattern as age increased.

Table 2. Age-related Differences of mean BC values across subjects between ADHD and normal group

	Mean BC (ADHD)	Mean BC (Normal)	ΔBC (ADHD-Normal)
Child	65.918	180.282	-114.965
Adolescent	66.191	143.902	-77.712
Adult	92.213	91.516	0.697

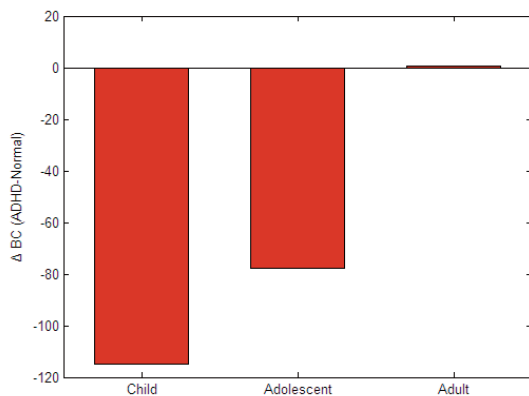


Fig. 3. Age-related Differences of mean BC values across subjects between ADHD and normal group. The negative difference means that betweenness centrality in superior medial frontal gyrus of the ADHD groups is lower than that of the normal groups.

IV. CONCLUSION

As we hypothesized, the differences between normal group and ADHD group was linearly decreased as age increased in superior medial frontal region. It may represent that the impulsivity of ADHD patients would decrease but, this cannot state the general development. More subjects will be required in future study.

ACKNOWLEDGEMENT

This study was supported by the Institute for Basic Science (grant number IBS-R015-D1).

REFERENCES

1. American Psychiatric Association, *Title of a Boo Diagnostic and Statistical Manual of Mental Disorders*, American Psychiatric Association, 2000.
2. Sang Soo Cho, "Morphometric Correlation of Impulsivity in Medial Prefrontal Cortex," *Brain Topography*, vol. 26, pp. 419-487, 2013.
3. Ed Bullmore, "Complex brain networks: graph theoretical analysis of structural and functional systems," *Neuroscience*, vol. 10, pp. 186-198, 2009.

Imaging genetics of Parkinson's disease at Putamen

Mansu Kim¹ and Hyunjin Park^{2,3*}

¹Department of Human ICT convergence, Sungkyunkwan University, Suwon, Korea

²School of Electronic and Electrical Engineering, Sungkyunkwan, Suwon, Korea

³Center for Neuroscience Imaging Research (CNIR), Institute for Basic Science, Suwon, Korea

E-mail: mansooru@skku.edu, hyunjinp@skku.edu

Abstract—Parkinson's disease (PD) is the second most common neurodegenerative disorder characterized by loss of dopaminergic neurons in the substantia nigra (SN) and those project to the striatum. Specifically, degeneration of dopaminergic striatal neurons are known to cause PD. In this study, we adopted the imaging genetic model for genetic variants using degree centrality of putamen as an intermediate phenotype. A total of 34 SNPs showed significant difference between PD and normal control. Of these, 4 SNPs corresponded to findings of previous studies and 31 SNPs were new findings of this study.

Keywords— Imaging genetics, Diffusion tensor imaging, Parkinson's disease, Network analysis.

I. INTRODUCTION

Parkinson's disease (PD) is a second most common neurodegenerative disorder characterized by loss of dopaminergic neurons in the substantia nigra (SN) and those project to the striatum. Specifically, putamen, part of striatum, known for critical terminal of dopaminergic neurons and degeneration of dendrite in striatal neurons cause PD [1].

Recent researchers were attempting to use magnetic resonance imaging techniques as intermediate phenotype (i.e., endo-phenotype) between genetic variants and disease diagnosis, known as imaging genetics. This technique has been used to differentiate between neuropsychiatric disease, such as Alzheimer, anxiety disorder and Attention deficit hyperactivity disorder. However, there is less attention to Parkinson's disease. . Thus, the focus of this study was to identify genetic influence using image feature as intermediate phenotype.

In this paper, we propose the imaging genetic model for genetic variants that associated with PD using image feature based on network analysis as intermediate phenotype. The imaging genetics model consist of two steps: (1) image feature were selected based on network analysis which associated with disease phenotype; (2) common genetic variants are identified to explain the selected feature using genetic analysis.

II. METHODS

A. Subject and MRI acquisition

We applied our method on the Parkinson's disease Progressive Marker Institute (PPMI) dataset that includes T1-, T2- and diffusion weighted MR images and 196,524 genetic variants [2]. We obtained a total of 80 participants and classified them into NC (n = 40) and PD (n = 40) categories. The age and sex ratio of each group were matched as shown in the Table 1. Details about the subjects, including MDS-UPDRS scores, are also given in the Table 1.

Table 1. Participants' information

	NC	PD	p-value
Number of subject	40	40	-
Sex (M:F)	32 : 8	28 : 12	0.30
Age	62.7	60.5	0.59

B. Genetic data quality control.

We used the ENIGMA protocol to population stratification and quality control [3]. Shortly, we remove SNP based on the basis of standard quality control criteria, e.g. low minor allele frequency (< 0.01), poor genotype call (call rate $< 95\%$) and Hardy-Weinberg equilibrium ($P < 0.000001$).

C. Image processing and Construct Network

Overall processing steps were required to extract fiber information from DTI data and construct structural connectivity network. Image pre-processing was performed using the Connectome Mapping Toolkit (CMTK). The image processing consisted of the following steps: for each subject, (1) the T1-, T2- and diffusion weighted images were aligned to the Montreal Neurological Institute space (MNI) by a non-linear registration using FSL [4]; (2) segmentation of cortical and subcortical region of interest (ROI) based on the registered T1-weighted image using Freesurfer [5]; (3) tractography was performed using Diffusion Toolkit and construct connectivity matrix based on fiber density.

Structural connectivity was assessed using 88 regions, pre-defined in Desikan Kiliany atlas, considered as nodes and fiber density of these connections were considered as edges of a graph. Fiber density considers

the number of fibers connecting the regions and normalizes for the area of the brain regions.

D. Network analysis and Extract Image feature

Weighted network measure was constructed on the structural connectivity measure using soft threshold [6]. Degree centrality, the total sum of weight between any two nodes that pass through that node was calculated on each node. Degree centrality is a sensitive measure of centrality in anatomical networks.

For each subject, we extract degree centrality as image feature from specific region, Putamen, which significantly different within PD and NC and associated with PD. Each elements of participants among the two groups (i.e., PD and NC) were stacked into column matrix and were tested using two-sample t-test to separate PD and NC. We reported corrected p-value using permutation test. Correlation analysis was performed to detect possible link between image feature and clinical scores (i.e., MDS-UPDRS scores).

C. Genetic analysis

Genotype data were analyzed using an additive model, with regression coefficients and image feature as intermediate phenotype using PLINK [7]. We use linear regression to analysis relationship between the image feature, degree centrality, and genetic variants. Permutation test was performed 10,000 times to obtain empirical P-value.

III. RESULTS

A. Genetic data quality control

A total of 523 individuals had genotype data available. Of these, 377 were excluded by no MR image data. Therefore, 146 individuals (NC: 40, PD: 106) were available with genotype and MR image data. Finally, 80 individual of European population (NC: 40, PD: 40) with age and sex matched were selected. Using ENIGMA protocol, 136,350 SNPs were selected.

B. Extract image feature based on Network Analysis

The degree centrality of PD patients in putamen was significantly different compared with NC (corrected P = 0.005). Correlation analysis was performed to identify possible links between degree centrality of putamen and clinical score (i.e. MDS-UPDRS). The result show that degree centrality of putamen was correlated with MDS-UPDRS scores(R = -0.3137).

C. Genetic variants for image feature

We investigate the influence of genetic variants on image feature, degree centrality of putamen. Table 2. show that four SNPs at PARK2 gene, rs645575,

rs1071892, rs10945764 and rs9347662, were significantly difference within PD and NC. We found that 31 additional SNPs which were significantly different between PD and NC. The details were shown in Table3.

Table 2. Results for analyzed SNPs at PARK2

Gene	SNP	Allele	Empirical P-value
PARK2	rs6455745	A	0.006
	rs1071892	T	0.040
	rs10945764	A	0.044
	rs9347662	C	0.020

Table 3. Results for analyzed additional SNPs

Gene	SNP	Allele	Empirical P-value
TRRAP	rs2056659	G	0.007
	rs6952161	G	
	rs4729516	G	< 0.001
	rs10953281	G	
ARHGEF38	rs2726453	G	< 0.001
	rs2726471	A	0.005
ATP8A1	rs2881215	A	< 0.001
	rs10012449	A	
PCDH17	rs2026516	C	< 0.001
	rs12430075	G	0.006
RASD2	rs5756562	C	
	rs762921	A	
	rs5756565	G	
	rs5756566	A	
	rs35435644	C	
	rs13053175	T	
	rs56153764	G	
	rs56141786	T	
	rs6000613	A	
	rs5750398	T	
	rs9607427	A	
	rs2187750	A	
	rs9607428	G	
	rs4820272	A	< 0.001
	rs4820273	T	
	rs4821605	G	
	rs4821608	A	
	rs4820275	T	
	rs4821609	A	
	rs4821610	T	
	rs933221	T	
rs933222	T		
rs933223	G		
rs9607429	T		
rs5756568	C		
rs9610671	A		
s9610677	T		
rs6000617	A		

rs6000618	A
rs2899284	A
rs5756569	T

IV. CONCLUSION

We proposed and demonstrated the imaging genetics model for identifying genetic variants and image feature associated with PD. We identify the significant difference between image feature and disease statuses based on network analysis. After that we investigate genetic variants to explain the selected image feature.

Our result is preliminary finding using traditional imaging genetic model. We expected to use advanced probabilistic model to get confidence results.

ACKNOWLEDGEMENT

This study was supported by the Institute for Basic Science (grant number IBS-R015-D1).

REFERENCES

1. Zaja-Milatovic S, Milatovic D, Schantz A, Zhang J, Montine K, Samii A, et al. Dendritic degeneration in neostriatal medium spiny neurons in Parkinson disease. *Neurology*. 2005;64:545-7.
2. Marek K, Jennings D, Lasch S, Siderowf A, Tanner C, Simuni T, et al. The parkinson progression marker initiative (PPMI). *Progress in neurobiology*. 2011;95:629-35.
3. Team EGS. ENIGMA2 1KGP Cookbook (v3) [Online]. The Enhancing Neuroimaging Genetics through MetaAnalysis (ENIGMA) Consortium. http://enigma.ini.usc.edu/wpcontent/uploads/2012/07/ENIGMA2_1KGP_cookbook_v3.pdf. 13 November 2013.
4. Smith SM, Jenkinson M, Woolrich MW, Beckmann CF, Behrens TE, Johansen-Berg H, et al. Advances in functional and structural MR image analysis and implementation as FSL. *Neuroimage*. 2004;23 Suppl 1:S208-19.
5. Fischl B. FreeSurfer. *Neuroimage*. 2012;62:774-81.
6. Mumford JA, Horvath S, Oldham MC, Langfelder P, Geschwind DH, Poldrack RA. Detecting network modules in fMRI time series: a weighted network analysis approach. *Neuroimage*. 2010;52:1465-76.
7. Purcell S, Neale B, Todd-Brown K, Thomas L, Ferreira MA, Bender D, et al. PLINK: a tool set for whole-genome association and population-based linkage analyses. *The American Journal of Human Genetics*. 2007;81:559-75.

Development of a Device for Light Guided Vocal Fold Injection

Wonjae Cha¹, Soo-Geun Wang¹, Gye-Rok Jeon² and Jung Hoon Ro²

¹Department of Otorhinolaryngology, Pusan National University Hospital, Busan, Korea

²Department of Biomedical Engineering, School of Medicine, Pusan National University, Busan, Korea

E-mail: jhro@pnu.edu

Abstract—A device for real-time light-guided vocal fold injection was developed and evaluated using an excised canine larynx.

Keywords—Vocal fold injection, transcutaneous, injection laryngoplasty, laser, optic fiber, light guided.

I. INTRODUCTION

Vocal fold injection is a minimally invasive technique for various vocal fold pathologies [1]. The shortcomings of the cricothyroid (CT) membrane approach are mainly related to invisibility of the injection needle [2]. If localization of the needle tip can be improved during vocal fold injection with the CT approach, the current problems of the technique can be overcome.

We have conceptualized real-time light-guided vocal fold injection that enables simultaneous injection under precise localization.

II. METHODS

A. Device Design

A single optic fiber is inserted in an unmodified 25-gauge needle, and a designated connector is attached to the needle, the optic fiber, and the syringe. The diameter of a single optic fiber is 200 μ m, and a laser diode module (635 nm, 5 mW) is used as the light source as shown in Fig.1.

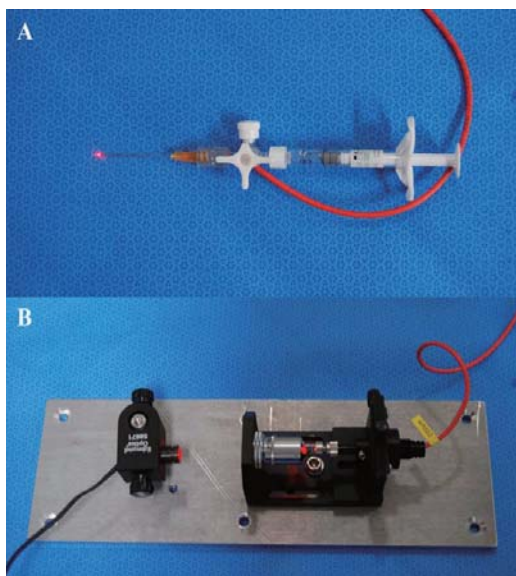


Fig. 1. The device for real-time light-guided vocal fold injection.

B. Excised Canine Larynx Model

Male dogs weighing about 30 kg were used in this study. The larynges were excised from the fourth tracheal ring to the hyoid bone. An apparatus was designed to hold the prepared excised larynx in place so that the endoscope could be moved back and forth at an appropriate distance from the mode. Hyaluronic acid (Restylane; Galderma, Lausanne, Switzerland) was used as the injection material for the vocal fold injections.

III. RESULTS

The lighted needle was introduced into canine vocal folds via a submucosal pathway using the CT approach. The red light at the needle tip could be seen in the vocal folds without difficulty. The needle tip was accurately localized, and the depth from the mucosa could be estimated by the brightness and size of the red light spot as shown in Fig. 2.

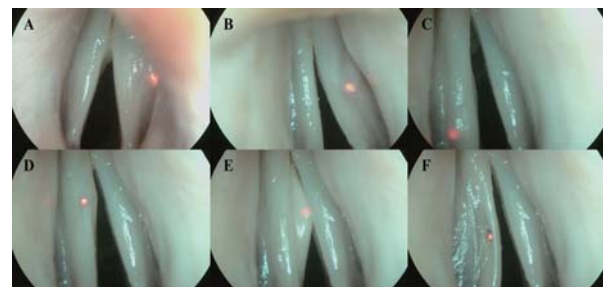


Fig. 2. Localization of the needle tip using the device for real-time light-guided vocal fold injection.

IV. CONCLUSION

Real-time light-guided vocal fold injection might be a feasible and promising technique for treatment of vocal fold pathology. It is expected that this technique could improve the precision of vocal fold injection and expand its indication in laryngology.

REFERENCES

1. C. A. Rosen, M. R. Amin, L. Sulica, et al, "Advances in office-based diagnosis and treatment in laryngology," *Laryngoscope*, vol. 119, pp. 185-212, 2009.
2. P. S. Mallur, C. A. Rosen, "Vocal fold injection: review of indications, techniques, and materials for argumentation," *Clin. Exp. Otorhinolaryngol*, vol. 3, pp. 177-182, 2010.
3. D. K. Chhetri, N. Jamai, "Percutaneous injection laryngoplasty," *Laryngoscope*, vol. 124, pp. 742-745, 2014.

Photoacoustic Computed Tomography Based on Inverse-Reconstruction of Circularly Arranged Transducers

Jae-Ho Han, Seung-beom Yu, Seungbae Ji, and Ji-hyun Kim

Department of Brain and Cognitive Engineering, Korea University, Seoul, South Korea

E-mail: hanjaeho@korea.ac.kr

Abstract— In order to achieve a photoacoustic tomographic imaging in vivo, wide-area illumination of laser source which covers all the region of interest for the specimen under test can provide more efficient and simpler system than that of using narrower point source scanning. In this study, we focused on the effect of the irregularity of the beam shape on the computed tomography based on inverse-reconstruction from a receiver with circularly arranged transducers.

Keywords—Imaging, Photoacoustic, Reconstruction, Tomography, Transducers.

I. Introduction

As an emerging technology, photoacoustic (PA) imaging has been of great interest in biomedical imaging by overcoming the optical diffusion limit. The PA imaging system is based on the phenomenon of a converted energy of light absorption of short-pulsed laser beams in the target object that induces to acoustic emission in ultrasonic waves as pressure arisen in the matters from the thermoelastic expansion. PA imaging system can also provide advanced spatial and temporal resolution as compared with the other techniques of non-invasive modalities. However, scattering effect of light source can cause contrast reduction in the PA imaging. In addition, in deep tissue imaging, attenuation of light intensity brings less image contrast. Therefore, image signal processing has been widely used to compensate the poor image quality and image reconstruction.

II. Methods and Results

In order to achieve a practical photoacoustic tomographic imaging in vivo, wide-area illumination of laser source which covers all the region of interest for the specimen under test can provide more efficient and simpler system than that of using narrower point source scanning. However, due to the non-uniform beam profile of the source output itself, the corresponding detected signals create irregular results by the different strength of response signals while reconstructing the tomographic image. In our recent study, we focused on the effect of this irregularity of the beam shape on the computed tomography based on inverse-reconstruction. The overall system comprises of circularly displaced

transducers or in the form of arrays which detect the ultrasonic signals for image recovery with a non-uniform beam of 10 ns pulsed Nd- YAG laser with 15 Hz repetition rate at 532 nm. As a result, we observed the effect of the non-uniform distribution of the beam spot on the results of the tomographic images.

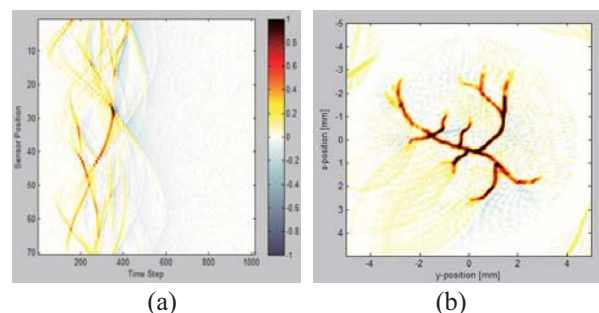


Fig. 1. Signal reconstruction based on circularly arrayed transducers in PA imaging system: (a) collected signals. (b) reconstructed image result.

ACKNOWLEDGEMENT

This work was supported by Samsung Research Funding Center of Samsung Electronics under Project Number SRFC-IT1301-02.

REFERENCES

1. L. V. Wang and S. Hu, "Photoacoustic tomography: in vivo imaging from organelles to organs," *Science*, vol. 335, pp. 1458–1462, March 2012.
2. J.-M. Yang, C. Favazza, R. Chen, J. Yao, X. Cai, K. Maslov, Q. Zhou, K. K. Shung, and L. V. Wang, "Simultaneous functional photoacoustic and ultrasonic endoscopy of internal organs in vivo," *Nat. Med.*, vol. 18, pp. 1297–1302, 2012.
3. N. C. Burton, M. Patel, S. Morscher, W. H. P. Driessen, J. Claussen, N. Beziere, T. Jetzfellner, A. Taruttis, D. Razansky, B. Bednar, and V. Ntziachristos, "Multispectral opto-acoustic tomography (MSOT) of the brain and glioblastoma characterization," *NeuroImage*, vol. 65, pp. 522–528, January 2013.
4. S. Wang, C. Tao, X. Wang, and X. Liu, "Quantitative detection of stochastic microstructure in turbid media by photoacoustic spectral matching," *Appl. Phys. Lett.*, vol. 102, pp. 114102, 2013.

Fabrication of multilayered Port Wine Stain phantom for laser treatment

Hye Jin Kim,¹ Han-na Kim,² Van Phuc Nguyen,^{2,1} and Hyun Wook Kang^{1,3,*}

¹Department of Biomedical Engineering, Pukyong National University, Busan, Korea

²Interdisciplinary Program of Marine-Bio, Electrical & Mechanical Engineering, Pukyong National University, Busan, Korea

³Center for Marine-Integrated Biomedical Technology, Pukyong National University, Busan, Korea

*E-mail: wkang@pknu.ac.kr

Abstract—Multilayered skin phantoms were fabricated to emulate a vascular disease, port wine stain. Polydimethylsiloxane-based phantoms represented skin color as well as optical properties of epidermis and dermis. Artificial blood vessels were embedded in the phantom and selectively removed by 532-nm laser light. The port wine stain phantoms can provide a feasible tool to evaluate efficacy and safety of laser treatment for human skin disease.

Keywords—multilayered skin phantom, port wine stain, laser treatment, PDMS

I. INTRODUCTION

Port Wine Stain (PWS) (i.e., nevus flammeus) is a common birthmark that occurs to three out of every 1,000 kids. Although laser therapy has been one of successful non-invasive treatments for PWS, long-term and complete removal of PWSs is still poorly understood. The aim of the current study was to develop artificial PWS phantoms to mimic vascular diseases and to optimize laser parameters to improve clinical outcomes.

II. METHODS

Hydrophobic PDMS (polydimethylsiloxane, Sylgard 184, Dow corning) was selected as a base material for PWS phantoms. Due to low viscosity [1], PDMS can thermally be cured to construct multilayered structures. As absorbing agents, coffee and nigrosine were used for epidermis and dermis layers, respectively. For scattering agents, TiO₂ was used for all the layers [2]. After sonication and degassing, the final PDMS solution was poured into a customized mold and cured [3]. Artificial blood vessels were also embedded at the interface between the epidermis and the dermis layers by using an oil-based red ink. Optical properties of the PWS phantoms were estimated by using an inverse adding-doubling (IAD) method. A Q-switched 532-nm laser was implemented to selectively remove the blood vessels in the PWS phantom.

III. RESULTS

A 3D printed mold was able to control the thickness of each phantom layer. An optical coherence tomography (OCT) confirmed that the fabricated epidermis and

dermis layers were approximately 100~150 μm and 1~1.5 mm thick, respectively. IAD with double-integrating spheres demonstrated that absorption and reduced scattering coefficients were estimated to be around 21 and 530 cm^{-1} for epidermis and 2.2 and 156 cm^{-1} for dermis. Photoacoustic imaging vividly exhibited the patterns and position of the blood vessels embedded at the interface between the epidermis and the dermis layers. Due to high absorption by red color, a Q-switched 532-nm laser system was able to selectively eliminate the artificial blood vessels from the PWS phantoms.

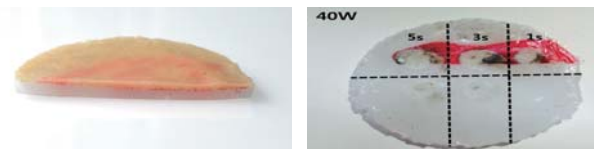


Fig. 1. Images of fabricated phantom with artificial blood vessel embedded (left) and irradiated phantom (40W, right)

IV. CONCLUSION

Application of multilayered PWS phantoms can be a cost-/time-efficient approach to optimize therapeutic parameters of laser treatment for various vascular disorders in a safe manner.

ACKNOWLEDGEMENT

This work was supported by a grant from Marine Biotechnology Program (20150220) funded by Ministry of Oceans and Fisheries, Korea.

REFERENCES

1. K. L. Lurie, G. T. Smith, S. A. Khan, J. C. Liao, A. K. Ellerbee, "Three-dimensional, distendable bladder phantom for optical coherence tomography and white light cystoscopy", *Journal of Biomedical Optics*, vol 19, 036009-1-036009-9, 2014
2. R. B. Saager, C. Kondru, K. Au, K. Sry, F. Ayers, A. J. Durkin, "Multi-layer silicone phantoms for the evaluation of quantitative optical techniques in skin imaging", *SPIE*, vol. 7567, 756706-1-756706-8, 2010
3. B. Samel, M. K. Chowdhury, G. Stemme, "The fabrication of microfluidic structures by means of full-wafer adhesive bonding using a poly(dimethylsiloxane) catalyst", *Journal of Micromechanics and Microengineering*, vol.17, 1710-1714, 2007

Correction of motion artifacts in MR images using ESPIRiT combined with compressed sensing

Y. Seo^{1,2}

¹Center for Medical Metrology, Korea Research Institute of Standards and Science, Daejeon, Korea

²Department of Medical Physics, University of Science and Technology, Daejeon, Korea

E-mail: yseo@kriss.re.kr

Abstract—This study corrects motion artifacts in phantom experiments mimicking human liver motion using ESPIRiT combined with compressed sensing.

Keywords—MR image, motion artifacts, correction, ESPIRiT, compressed sensing.

I. INTRODUCTION

Patient motion or motion of an object causes blurring or ghosting artifacts in MR images because the acquisition is time-dependent and thus k-space is inconsistently sampled. It is necessary to reduce the acquisition time combined with motion correction techniques in order to acquire motion artifact-free MR images

II. METHODS

A Philips 3 T Achieva TX whole-body MRI system was employed to acquire experimental data with FLASH sequence (TR/TE=9.8/4.6 ms, 12 slice, 20x20 cm² FoV, 200x200 matrix size, and flip angle=10°). During MRI scans, an organic hydrophilic polymer gel phantom (10 cm diameter by 12 cm high) was made and moved in a controlled fashion to simulate a respiratory-like motion with amplitude of 1.5 cm and frequency of 0.25 Hz using a MD-2 dual stepper motion system. MRI datasets were post-processed using a workstation running custom software written in MATLAB. Detection and correction of the motion artifacts of the mobile phantom performed using ESPIRiT [1] combined with compressed sensing [2].

III. RESULTS

Figure 1 represents motion corrupted and corrected images. MR magnitude images of the phantom without motion (Fig. 1, top), motion corrupted (Fig. 1, left) and motion corrected MR images (Fig. 1, right) are shown. The signal-to-noise ratio (SNR) values before and after the phantom motion were 54.5 ± 3.5 and 33.6 ± 2.9 , respectively. The SNR dropped by 38% due to the motion.

IV. CONCLUSION

Liver motion modeling was investigated using MR imaging with prospective gating, but it is found that the gating created impractically long acquisition times. Liver motion artifacts induced by respiratory movement have been reduced by using fast MR imaging techniques: EPI combined with respiratory gating. This technique, however, does not provide co-registration among all time points, sacrifices SNR, spatial resolution, or temporal resolution, and has not always proven practical in human imaging. In this work, the motion artifacts of the phantom mimicking the human liver motion were effectively reduced by ESPIRiT combined with compressed sensing even though there is a tradeoff between short acquisition time and SNR loss.

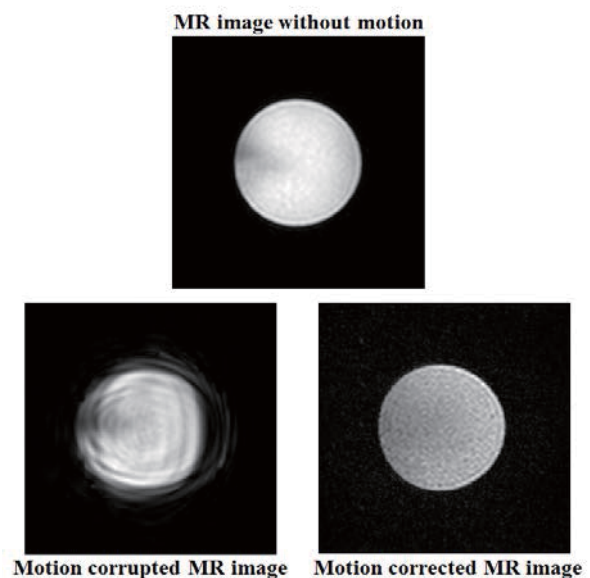


Fig. 1. MR magnitude images of the phantom without motion (top), motion corrupted (left) and corrected (right).

ACKNOWLEDGEMENT

This work was supported by the NRF grant (2014R1A1A2054037).

REFERENCES

1. M. Uecker, P. Lai, M. Murphy et al., *Magn. Reson. Med.* vol. 71, pp. 990-1001, 2014.
2. M. Lustig, D. Donoho, and J.M. Pauly, *Magn. Reson. Med.* vol. 58, pp.1182-95, 2007.

A study on the gender differences of node betweenness centrality in obstructive sleep apnea

Min-Hee Lee¹, Yoon Ho Hwang¹, Areum Min¹, Bong Soo Han², Seung Ku Lee³,
Chol Shin³, Chang-Ho Yun⁴ and Dong Youn Kim¹

¹Department of Biomedical Engineering, Yonsei University, Wonju, Republic of Korea

²Department of Radiological Science, Yonsei University, Wonju, Republic of Korea

³Institute of Human Genomic Study, College of Medicine Korea University Ansan Hospital, Ansan, Republic of Korea

⁴Department of Neurology, Seoul National University Bundang Hospital, Seongnam, Republic of Korea

E-mail: MinHLee@yonsei.ac.kr

Abstract— We investigated the differences of altered brain regions between OSA and healthy for male (OHM), and OSA and healthy for female (OHF). For this, we compared the node betweenness centrality which measures the importance of nodes. In this paper, we found that altered brain regions were different between OHM and OHF at the statistical significance level of 0.05.

Keywords— Brain network, Obstructive sleep apnea, Node betweenness centrality

I. INTRODUCTION

Obstructive sleep apnea (OSA) is the most common among sleep related breathing disorders. Male and female with OSA have shown differences in accompanying disease and damaged brain regions [1]. Using node betweenness centrality, we examined the altered brain regions in male and female with OSA.

II. METHODS

A. Data acquisition

We acquired diffusion tensor imaging data using 1.5 Tesla MR scanner (General Electric, Milwaukee, WI) from 7 healthy male and 7 female, 7 male and 7 female with OSA. Ages of subjects range from 51 to 61.

B. Brain network construction

We used automated anatomical labeling template which includes 90 brain regions to determine the nodes. Two nodes were connected by an edge if any endpoints of fiber exist in both regions.

C. Node betweenness centrality (NBC)

NBC measures the importance of nodes for information transfers with other nodes in the network. NBC of any node is defined as the fraction of all paths with shortest path length that pass through a node [2].

III. RESULTS

Male with OSA have shown decreased NBC in left orbitofrontal cortex and increased in right middle cingulate gyrus ($p < 0.05$, Fig. 1(a)). NBC of female with OSA is decreased in right superior frontal and postcentral gyrus. Also, female with OSA have higher NBC in right orbitofrontal, middle and inferior frontal gyrus, thalamus and left temporal pole ($p < 0.05$, Fig. 1(b)).

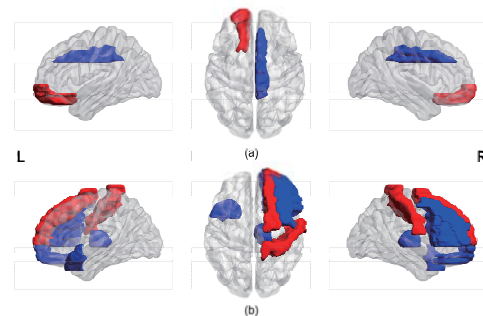


Fig. 1. The results of NBC comparison. (a) male group. (b) female group. Red: healthy > OSA; Blue: OSA > healthy

IV. CONCLUSION

We found gender differences for altered brain regions. It is likely that the differences of clinical symptom between male and female with OSA may result from alteration of different brain regions.

ACKNOWLEDGEMENT

This research was supported by the Leading Foreign Research Institute Recruitment Program through the National Research Foundation of Korea (NRF) funded by the Ministry of Science, ICT & Future Planning (2010-00757).

REFERENCES

1. P. M. Macey, R. Kumar, F. L. Yan-Go, M. A. Woo, and R. M. Harper, "Sex differences in white matter alterations accompanying obstructive sleep apnea," *Sleep*, vol. 35, pp. 1603-1613, 2012.
2. L. C. Freeman, "A set of measures of centrality based on betweenness," *Sociometry*, vol. 40, pp. 35-41, 1977.

The relationship between dental implant stability and trabecular bone microstructure

Se-Ryong Kang¹, Woo-Jin Lee², Sang-Yoon Woo¹, Sang-Jeong Lee¹ and Won-Jin Yi^{1,2,3}

¹Department of Biomedical Radiation Sciences, Graduate School of Convergence Science and Technology, Seoul National University, Seoul, Korea

²Interdisciplinary Program in Radiation Applied Life Science, College of Medicine, Seoul National University, Seoul, Korea

³Department of Oral and Maxillofacial Radiology, School of Dentistry, Seoul National University, Seoul, Korea

E-mail: seryongkang@snu.ac.kr

Abstract— The objective of this study was to investigate the relationship between the primary implant stability by impact response frequency and the microstructural parameters of trabecular bone with excluding the effect of cortical bone thickness. The peak frequency of the impact response spectrum was used as a criterion for the implant stability (SPF). The SPF had significant correlation with the microstructural parameters ($P < 0.01$).

Keywords— Dental implant stability, Spectrum peak frequency, Trabecular bone microstructure, Micro-CT, Bone strength

I. INTRODUCTION

Primary implant stability is one of the most important factors in the assessment of dental implantation success. Quantitative methods for implant stability can yield valuable information for the success of dental implants [1]. Previously, we developed a method for measuring implant stability using an inductive sensor [2]. The purpose of this study was to investigate the relationship between the primary implant stability by impact response frequency and the microstructural parameters of trabecular bone.

II. METHODS

The inductive sensor measured the impact response of dental implant placed into pig rib bone specimens consisting of only trabecular bones without the cortical bone layer. The peak frequency of the impact response spectrum was used as a criterion for the implant stability (SPF). The 3D microstructural parameters were also calculated from images obtained using a micro-CT scanner for the bone specimens. The relationships between SPF and bone microstructural parameters were evaluated using Pearson's correlation analysis using SPSS 21 (SPSS Inc., IL, USA).

III. RESULTS

While the SPF had significantly positive correlations with the BV/TV, BV, BS, IS, BSD, Tb.Th, Tb.N and FD, the BS/BV, Tb.Sp, Tb.Pf and SMI showed significantly negative correlations ($P < 0.01$). In the stepwise forward regression analysis, there is an increase in implant stability prediction by combining BV/TV and SMI.

IV. CONCLUSION

The 3D microstructural parameters related with bone strength are significantly correlated with the implant stability. The combination of bone density parameters and architectural parameters can improve the prediction of the implant stability.

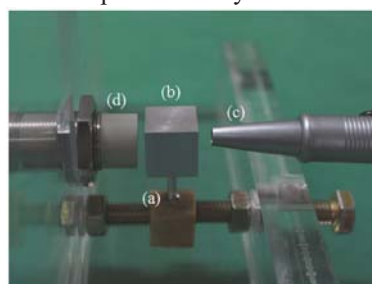


Fig. 1. Measurement of implant stability with an inductive sensor at different bone samples. The implant (a) with an adaptor (b) was placed into the pig bone, and was tapped using the tapping rod of the Periotest (c). An inductive sensor (d) measured the vibration of the adapter-implant assembly.

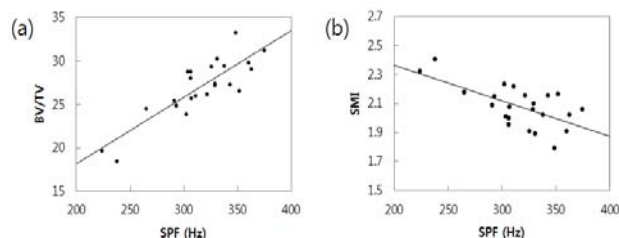


Fig. 2. Relationships between the SPF and 3D bone parameters ((a) BV/TV and (b) SMI) ($P < 0.01$).

ACKNOWLEDGEMENT

This work was supported by the National Research Foundation of Korea (NRF) grant funded by the Korea government (MEST) (No. 2013R1A2A2A03067942), South Korea.

REFERENCES

1. Meredith N. Assessment of Implant Stability as a Prognostic Determinant. *Int J Prosthodont* 1998;11:491–501.
2. Kim DS, Lee WJ, Choi SC, Lee SS, Heo MS, Huh KH, Kim TI, Yi WJ. Comparison of dental implant stabilities by impact response and resonance frequencies using artificial bone. *Med Eng Phys* 2014;36: 715-20.

Fabrication of multilayered optical tissue phantoms with 3D deposition for phototherapeutics

H. N. Kim,¹ T. H. Nguyen,¹ Y. G. Chae,¹ B. Lee,² and H. W. Kang^{1,3*}

¹Interdisciplinary Program of Marine-Bio, Electrical & Mechanical Engineering, Pukyong National University, Busan, Korea

²Korea Photonics Technology Institute (KOPTI), Korea

³Department of Biomedical Engineering and Center for Marine-Integrated Biomedical Technology (BK21 Plus), Pukyong National University, Busan, Korea

*E-mail: wkang@pknu.ac.kr

Abstract— To mimic human skin tissue, we demonstrate a new fabrication method of a multilayer optical tissue phantom with 3D printing technique. An inverse adding-doubling method demonstrated that both absorption and reduced scattering coefficients were 0.07 and 2.23 mm^{-1} (epidermal and dermal layers). The phantom thickness was estimated to be $100.0 \pm 3.3 \text{ }\mu\text{m}$ for epidermal and $1.8 \pm 0.1 \text{ mm}$ for dermal layer. The proposed optical tissue phantoms can be a feasible model to predict tissue responses during laser-skin interactions.

Keywords— Tissue phantom, 3D printing, optical properties, compression modulus

I. INTRODUCTION

Various optical techniques have been studied for skin tissue measurements in the fields of dermatology and cosmetology. Human skin tissue mainly consists of three layers (epidermis, dermis, and subcutaneous) that have different optical properties and physical dimensions. In this study, we proposed the fabrication of optical tissue phantoms with 3D printing technique by reflecting not only optical properties but also tissue thickness.

II. METHODS

Both gelatin and agar components were mixed with distilled water at the weight ratio of 10%. Color ink was added to the solution at the weight of 1:5 to mimic skin color. To reflect optical properties of various skin types (I~VI), coffee and TiO_2 powder were lastly added to the gelatin-agar solution. A customized 3D printing system was used to fabricate 3-D phantom structures in an area of $2 \times 2 \text{ cm}^2$. Double integrating spheres with inverse adding-doubling (IAD) were used to measure optical properties (absorption and reduced scattering coefficients) of each layer for the fabricated optical tissue phantoms at $600\text{--}900 \text{ nm}$ (Fig.1 (a)). Optical coherence tomography (OCT) was implemented to estimate the thickness of the phantoms. Finally,¹ compression modulus of the phantom was measured to validate mechanical similarity to human skin (Fig 1(b)).

III. RESULTS

According skin color evaluations, the color difference ΔE between skin types and phantom was found to be 2.54, 7.22, and 7.51 for skin type I, III, and IV. The optical property measurements showed that the absorption and reduced scattering coefficients decreased with wavelength. IAD found that absorption and reduce scattering coefficients at 755 nm were 0.58 and 2.6 mm^{-1} for epidermis and 0.08 and 2.65 mm^{-1} for dermis, which were slightly higher ($\sim 10\%$) than those of the human skin (Type III). OCT measurements confirmed that the thicknesses of the epidermal and dermal layers were measured to be $100 \pm 3.3 \text{ }\mu\text{m}$ and $1.8 \pm 0.1 \text{ mm}$ ($N = 5$), respectively. Compression modulus of the phantoms increased with the amount of the mixed agar powder. The estimated modulus was approximately 133 kPa , which was 40% higher than that of the human skin ($\sim 95 \text{ kPa}$).

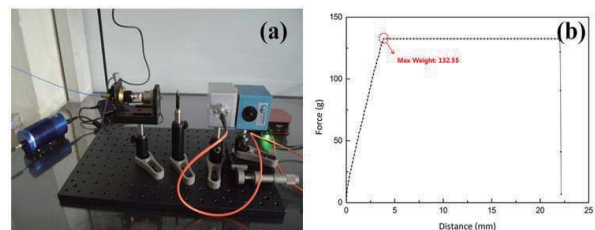


Figure 1. (a) Set-up of optical measurements and (b) result of compression modulus for phantom

IV. CONCLUSION

The proposed optical tissue phantoms can be a feasible model to indirectly evaluate tissue responses for laser treatment on skin pigmented lesions.

ACKNOWLEDGEMENT

This work was supported by a grant from Marine Biotechnology Program (20150220) funded by Ministry of Oceans and Fisheries, Korea.

REFERENCES

1. S. H. Tseng, P. Bargo, A. Durkin, N. Kollias, "Chromophore concentrations, absorption and scattering preoperties of human skin in-vivo", *Opt Express*, 17(17):14599-14617, 2009

Osteotomy Line Guidance System for Orthognathic Surgery using a Tablet PC based Augmented Reality

Sang-Jeong Lee¹, Sang-Yoon Woo¹, Woo-Jin Lee², Se-Ryong Kang¹ and Won-Jin Yi³

¹Department of Biomedical Radiation Sciences, Graduate School of Convergence Science and Technology, Seoul National University, Seoul, Korea

²Interdisciplinary Program in Radiation Applied Life Science, College of Medicine, Seoul National University, Seoul, Korea

³Department of Oral and Maxillofacial Radiology, School of Dentistry, Seoul National University, Seoul, Korea

E-mail: sjlee89@snu.ac.kr

Abstract— Orthognathic surgery is aimed at appropriate correction of acquired and inherited dento-facial defects. Several former studies have been developed image-guided surgery system for orthognathic surgery using medical imaging modalities, such as computed tomography (CT) or magnetic resonance (MR) imaging to do surgical planning and intraoperative navigation. In this study, we added an augmented reality (AR) technology to the existing image-guided orthognathic surgery system (IGOSS). Furthermore, we provided the osteotomy line guidance for surgeon to enhance accuracy and safety.

Keywords— Orthognathic Surgery, Osteotomy Line Guidance, Tablet PC, Augmented Reality, Image-guided surgery, Computer vision

I. INTRODUCTION

An orthognathic surgery is aimed at correction of dento-facial defects. Several IGOSS using virtual reality have been developed and applied to the patients. Their systems used optical tracking system (OTS) to navigate jaw segment and visualized virtual reality images during operation. [1, 2] However, the systems have a several limitations. First, the systems didn't provide a genuine camera image to the surgeon. It caused misunderstanding of surgical processes. Second,

To address this issue, we developed an IGOSS adding a tablet PC based augmented reality. The system could provide a real-time camera image. Also, our system augmented the osteotomy line on the video image for accurate guidance.

II. METHODS

A. System overview

The system was consisted of a workstation, tablet-PC (Sony, Seoul, Korea), and the optical tracking system (NDI Spectra, Waterloo, Canada) (Fig. 1). Serial communication and TCP/IP communication were used to deliver tracking information between each device.

B. CT scanning and model

The CT image was obtained using a MDCT (Siemens Medical Solutions, Munich, Germany) under 120 kVp, 80 mAs with slice thickness of 0.75 mm [1, 2].

The 3D model structures were produced and saved as STL objects by the software, then loaded into a Visualization Toolkit actors.

C. Image registration

The process was divided into two independent steps. Matching the patient's physical space with the CT image space was the first step. Another is to match the CT image space with the AR image space. A Point-to-point registration method was used in both processes [1, 2].

D. Augmented reality (AR) guidance

For AR based guidance, the present system provide two separated modes. The first one was a default mode that a whole skull model image was overlapped on the patient's face and tracked. The other mode was an osteotomy line guide mode. This mode augmented the cutting line on the surface of the patient's face.

For tracking, a reference tracking tool was attached on a forehead of the patient and a tablet tracking tool and maxillary tracking tool were attached on the tablet and a splint of the patient respectively. During the operation, movement of the patient and the tracking tools were continuously tracked by the system. The movement of the augmented model was as follows Eq. 1

$$T_{Model} = M_{CT_NDI} M_{CT_AR} (T_{Init_Tab}^{-1} T_{Curr_Tab})^{-1} T_{Init_Max}^{-1} T_{Curr_Max} \quad \text{--- (1)}$$

T_{Model} : current position model, M_{CT_NDI} : registration matrix between CT and OTS, M_{CT_AR} : registration matrix between CT and AR, T_{Init_Tab} and T_{Init_Max} : initial positions of the tablet and maxillary tracking tool, and T_{Curr_Tab} and T_{Curr_Max} : current positions of the tablet and maxillary tracking tool.

III. RESULTS

In order to overcome the limitations of the conventional IGOSS, we added the tablet PC based AR technology to our system. We augmented AR images on the patient's face by overlapping the 3D model segment and the osteotomy line.

IV. CONCLUSION

The new tablet based AR image-guided surgery system provided real-time video image and an intuitive guidance to the surgeon. For the future work, the system have to be applied in the operating room.

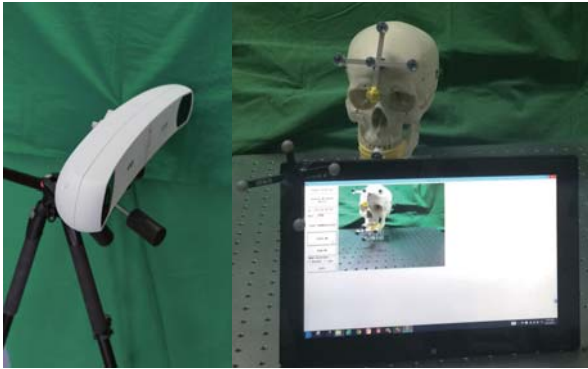


Fig. 1. System Overview. OTS tracked each tracking tool continuously during repositioning.

ACKNOWLEDGEMENT

This study was supported by a grant of the Korean Health Technology R&D Project, Ministry of Health & Welfare, Republic of Korea (HI13C1491).

REFERENCES

1. S. H. Kim, D. S. Kim et al, "Direct and continuous localization of anatomical landmarks for image-guided orthognathic surgery" *Oral Surg Oral Med Oral Pathol Oral Radiol*, vol. 116, pp. 402-410, 2013
2. D. S. Kim et al., "An integrated orthognathic surgery system for virtual planning and image-guided transfer without intermediate splint" *Journal of Cranio-Maxillo-Facial Surgery*, vol. 42, pp.2010-2017, 2014

A new device for angle measurement using infrared sensors

Bong-Jun Goh, Ji-Sun Kim, Han-Byeol Oh, A-Hee Kim, Jun-Sik Kim,
Eun-Suk Lee, Jin-Young Baek, Ye-Ji Shin, and Jae-Hoon Jun*

Department of Biomedical Engineering, BK21 Plus Research Institute of Biomedical Engineering, College of Biomedical & Health Science, Konkuk University, Chungju, Republic of Korea
E-mail: jjun81@kku.ac.kr

Abstract—In this study, we developed a new measurement device to evaluate the joint angle using infrared sensors with low cost and high durability. The results of this study can be expected to be used in rehabilitation and sports science.

Keywords—Measurement device, Joint angle, Infrared sensor, Rehabilitation, PSD (position sensing detector)

I. INTRODUCTION

Due to the development of medical techniques, there are a growing interest in sport medicine and rehabilitation. Especially, from a medical standpoint, the joint angle is an important measure of patient's recovery process. The current angle measuring techniques have shortcomings such as high cost and low durability [1-2]. The purpose of this study is to develop an optical device for easier detecting the joint angle using PSD sensor.

II. METHODS

Fig. 1 shows the experimental setup for joint measurements using optical sensors. These optical sensors can measure a position of a light spot around sensors and convert the values to angular information with high resolution. The digital goniometer was used to be compared with optical sensor values. We have conducted experiments using two sensors. The sensor 1 was attached on a moving arm and the sensor 2 was fixed on reflector parts. As a result, angular displacement can be measured by detecting outputs from reflected signals.

III. RESULTS

Fig. 2 shows the sensor outputs by angular displacement. The sensor 1 was effective for low angular changes and the sensor 2 can be used for angle measurements in a range of 60 – 180 degree. Mathematical models were applied for proper curve fittings.

IV. CONCLUSION

In this study, the position sensing detectors were used for joint angle measurements. The results indicate that the proposed method can be used inexpensively to evaluate joint angle.

The proposed method will be easily, inexpensive for evaluate joint angle[3].

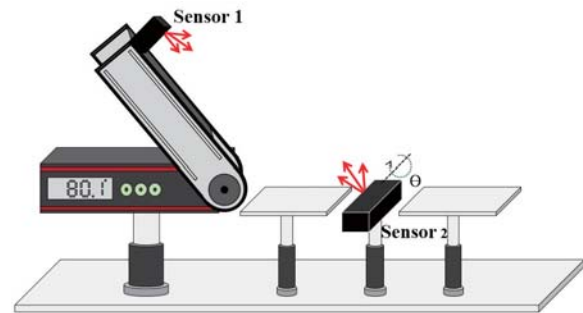


Fig. 1. Experimental setup used in this study

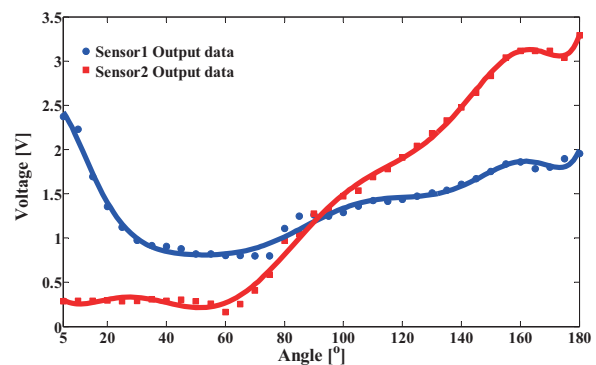


Fig 2. Sensor outputs by angular displacement

ACKNOWLEDGEMENT

This research was supported by the Pioneer Research Center Program through the National Research Foundation of Korea funded by the Ministry of Science. ICT & Future planning (No.2011-0027920)

REFERENCES

1. H. Saito, T. Watanabe and A. Arifin, "Ankle and Knee Joint Angle Measurements during Gait with Wearable Sensor System for Rehabilitation" *IFMBE*, Vol 25/9, pp 506-509, 2009
2. J. M. Soucie, C. Wang, A. Forsyth, S. Funk, M. Denny, K. E. Roach, D. Boone "Range of motion measurements: reference values and a database for comparison studies" *HAEMOPHILIA*, Vol 17, Issue 3, pp 500–507, May 2011
3. R. A. Malinzak, S. M. Colby, D. T. Kirkendall, B. Yu, W. E. Garrett, "A comparison of knee joint motion patterns between men and women in selected athletic tasks" *CLIN BIOMECH*, Vol 16, Issue 5, Pages 438–445, June 2001

A Study of Angular Measuring System using Optical Fibers

Jun-Sik Kim, Ji-Sun Kim, Han-Byeol Oh, A-Hee Kim, Bong-Jun Goh, Eun-Suk Lee,
Jin-Young Baek, Ye-Ji Shin, and Jae-Hoon Jun*

Department of Biomedical Engineering, BK21 Plus Research Institute of Biomedical Engineering,
College of Biomedical & Health Science, Konkuk University, Chungju, Republic of Korea
E-mail: jjun81@kku.ac.kr

Abstract— The purpose of this study was to design angular measuring system using optical fibers. Angle was measured by the variable light intensity according to shift position of light source and optical fiber. Optical elements were connected to the optical fiber effectively in passing light signals. In this study, the suggested method can measure the angle without being restricted by surrounding environment and can be applied to various industrial fields.

Keywords— Optical fiber, Angular Measurement, Optical method

I. INTRODUCTION

Angle measurement has been used for various industry fields. Also, it is an important technique on the research. For more elaborate products and high reliability research, accurate measuring techniques are needed [1,2]. For user friendliness, easy method without being restricted by surrounding environment must be supplied. For this reasons, the use of optical methods and LED which enables it to mount small-size phototransistors and optical fibers reduced the spatial constraints. Optical fibers were used for effectively transmit the optical signal of LED light.

This study is intended to lay the foundation for building a system to measure the angle using the differences in the light signal which varies depending on the locational change of the optical fibers and emitting parts

II. METHODS

In this study, two optical fibers were used in light emitting part and light collecting part to be connected with each part. The distance between two optical fibers (light emitting part and light collecting part) is varied in 10, 12, and 14 mm. The light emitting part was rotated on light collecting part from 0° to 180° and the optical signals were gathered at an interval of 5°. The detected light signals were transmitted to computer through DAQ and saved in LabVIEW for angle measurements.

III. RESULTS

Figure 1 shows the change of light signal according to distance of two optical fibers. The light signal

increased depending on nearing distance of two optical fibers. Mathematical models were applied to calculate angular changes with detected light signals and LabVIEW program was used to display angular information.

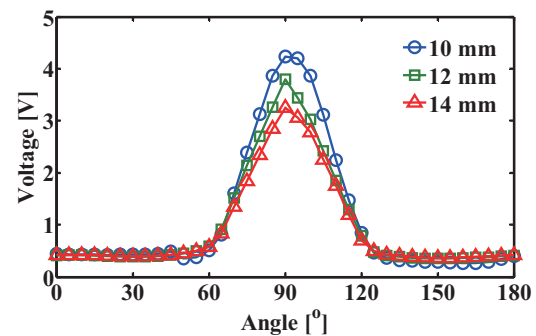


Fig. 1. Change of light signal according to distance

IV. CONCLUSION

In this study, the basic experiment for angular measurement system using optical fiber was performed. As a result, measured light outputs according to distance between light emitting part and light collecting part, showed the different shape and intensity of light signal depending on distance. A better condition was identified for angular measurement for high accuracy and resolution. The result can be implemented for an advanced angular measurement system with various parameters.

ACKNOWLEDGEMENT

This research was supported by the Pioneer Research Center Program through the National Research Foundation of Korea funded by the Ministry of Science. ICT & Future planning (No.2011-0027920)

REFERENCES

1. D. Massimiliano, P. Elia, N. Di, "Wearable low-cost system for human joint movements monitoring based on fiber-optic curvature sensor", *IEEE*, vol. 57, pp. 1614-1620, 2008.
2. H. Di, "Sensing principle of fiber-optic curvature sensor", *Opt Laser technol*, Vol.62, pp.44-48, 2014.

Quantitative Measurement of the Color Change of Bracket

Eun-Suk Lee, Ji-Sun Kim, Han-Byeol Oh, A-Hee Kim, Bong-Jun Goh, Jun-Sik Kim, Jin-Young Baek, Ye-Ji Shin, and Jae-Hoon Jun*

Department of Biomedical Engineering, BK21 Plus Research Institute of Biomedical Engineering, College of Biomedical & Health Science, Konkuk University
E-mail: jjun81@kku.ac.kr

Abstract— Recently, the demand for orthodontics bracket is increasing. In this paper, the degree of color change according to the coloring time of the bracket exposed to various foods was measured quantitatively with color sensors. The detected red, green, and blue values of the bracket appeared differently for each substance. The results can be useful in dental orthodontics.

Keywords— color sensor, bracket, RGB value, color measurement of bracket, color change of bracket

I. INTRODUCTION

The patients with orthodontic brace wish to fulfill an aesthetic trend that is increasing in dental application. Even though the resin bracket is widely used for aesthetic purpose, it has the disadvantage of discoloration of resin part by long exposure with foods[1].

This study investigated the degree of coloration of the resin bracket exposed to foods. The detected signals were analyzed with R, G, and B values through color sensors[2].

II. METHODS

As substances for coloring the resin bracket in the experiment, ssam-jang, ketchup, and chocolate milk were selected. The brackets were soaked in each substance for 3 -12 hours. After each exposure, the color change of the bracket was measured with color sensor.

At this time, the R, G, and B values of the bracket were collected and analyzed with TCS3200 color sensor. Each experiment was repeated three times and the average of the result value compared and analyzed.

III. RESULTS

Figure 1 shows the RGB values of each colored bracket of ssam-jang, ketchup, and chocolate milk for different soaking times. As a result, the most color change of the bracket was detected for ssam-jang especially for long soaking time. The B value showed the most decrease among R, G, and B values.

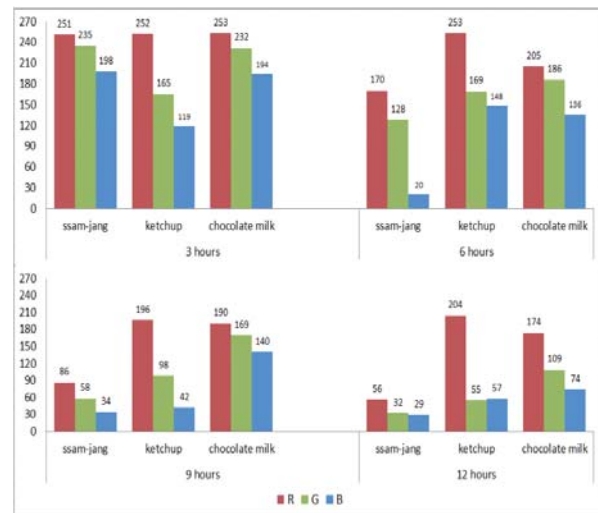


Fig. 1. The RGB values of measurement by the color sensor

IV. CONCLUSION

The suggested method can represent the color information to get quantitative R, G, and B values in detecting the degree of coloration of the resin bracket. This is considered to help the color change evaluation according to the duration of exposure to foods in orthodontic brace applications.

ACKNOWLEDGEMENT

This research was supported by the Pioneer Research Center Program through the National Research Foundation of Korea funded by the Ministry of Science, ICT & Future planning (No. 2011-0027920).

REFERENCES

1. Eliades, Theodore, et al, "Color stability of orthodontic adhesive resins.", *The angle orthodontist*74.3, vol. 74, pp.391-393, 2004.
2. Raja, A. Sivanantha, K. Sankaranarayanan, "Use of RGB color sensor in colorimeter for deter clinical measurement of blood glucose.", *BIME Journal*6.1, vol. 06, pp.23-28, 2006.

Feasibility of ^1H -MRS for Characterizing Non-alcoholic Fatty Liver Rat Disease Using 3T

J. Y. Kim^{1,2}, H. M. Baek² and T. S. Lee¹

¹Department of Biomedical Engineering, Chungbuk National University, Cheongju, Chungbuk, South Korea

²Department of Bioimaging Research Team, Korea Basic Science Institute, Cheongju, Chungbuk, South Korea

E-mail: jooyun8992@kbsi.re.kr

Abstract—Non-alcoholic fatty liver disease is the most common cause of chronic liver diseases. This study was to characterize early hepatic lipid changes in fatty liver rat model by *in vivo* short-echo time (TE) ^1H -MRS. Each the examinations were measured from liver parenchyma in rats at 0, 2, 4, 6, 8 weeks followed by high fat diet, respectively. Significant increase in lipid signals. 0.9, 1.3, 2.3, 2.8, and 5.3 ppm was found in animals with 2 weeks ($p < 0.001$). Therefore, ^1H -MRS is useful in detecting and characterizing various hepatic lipid alterations as early as 2 weeks for the start high fat diet.

Keywords— MRI, ^1H -MRS, Short TE, Fatty liver model, Liver lipid content

I. INTRODUCTION

Non-alcoholic fatty liver disease is the most common cause of chronic liver diseases [1]. Liver lipid content has been suggested to play an important pathogenic role in the development of liver fibrosis and cirrhosis [2]. In addition, hepatic fat plays a major role in metabolic diseases including obesity, diabetes, and non-alcoholic fatty liver disease [3]. Proton magnetic resonance spectroscopy (^1H -MRS) allows the study of cellular biochemistry and metabolism, and provides a non-invasive mean to determine disease abnormalities and progression *in vivo* and longitudinally. ^1H -MRS permits longitudinal assessment of fat fraction, saturated and unsaturated [4]. The aim of this study was to characterize early hepatic lipid changes in fatty liver rat model by *in vivo* short-echo time (TE) ^1H -MRS.

II. METHODS

Twelve male Sprague-Dawley rats with 60% high fat diet were included in this study. MR imaging an single-voxel ^1H -MRS was performed using a PRESS sequence at 3T. The examinations (voxel size, $8 \times 8 \times 8 \text{ mm}^3$) were measured from liver parenchyma in rats at 0 week and 2 weeks followed by high fat diet, respectively. Total lipid and choline-containing compounds (Cho) were quantified by dividing peak area of H_2O . In addition, total saturated fatty acid (TSFA), total unsaturated fatty acid (TUFA), total unsaturated

bond (TUB), and polyunsaturated bond (PB) were estimated. For multivariate statistical analysis, SIMCA-P 13.0 software (Umetrics Inc.) was used to process the numeric data. Principal component analysis (PCA) and partial least squares regression discriminant analysis (PLS-DA) were performed to distinguish between the two groups. To identify which variables were responsible for the separation, the variable influence on the projection (VIP) parameter was used.

III. RESULTS

The typical liver MR image and ^1H -MRS spectra from a rat animal assessed at 0 week and 2 weeks after the start of high fat diet (Fig. 1). Significant increase in lipid signals, 0.9, 1.3, 2.1, 2.3, 2.8, and 5.3 ppm was found in animals with 2 weeks ($p < 0.01$). However, no significant differences were observed in Cho, TSFA, TUFA, TUB, PB, and UI between baseline and 2 weeks ($p > 0.05$) (Fig. 2). In a PLS-DA model, the relative discriminatory potential of the ^1H -MRS measured in the differentiation of the two groups are shown in Fig. 3 (bottom) in terms of VIP. ^1H -MRS measures (e.g., Lip 0.9, 1.3, 2.1, 2.3, and 5.3 ppm) with $\text{VIP} > 1$ are those detectable in ^1H -MRS spectra. Using these 5 ^1H -MRS measures an optimal model was constructed, and it did allow a significant separation between the two groups (Fig. 3(top)).

IV. CONCLUSION&DISCUSSION

The present study demonstrated that *in vivo* ^1H -MRS can be used to detect the hepatic lipid abnormalities in fatty liver disease [5]. The optimal PLS-DA model allowed a good separation of the two groups (e.g., at 0 week and 2 weeks).

In this study, the total saturated fatty acid (TSFA) was higher in the fatty liver rats, but not significant between 0 week and 2 weeks ($p > 0.05$). The TSFA increase in liver may reflect the lipid-induced cell toxicity, which has been suggested to be related with activated apoptosis induced by saturated fatty acids. Therefore, ^1H -MRS is useful in detecting and characterizing various hepatic lipid alterations as early as 2 weeks for the start high fat diet.

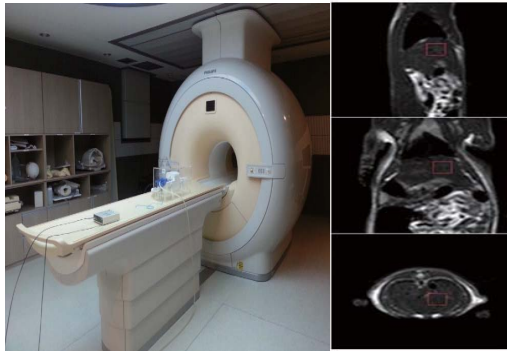


Fig. 1. 3T Human MRI (Philips Achieva TX System) and MR imaging showing volume of interest.

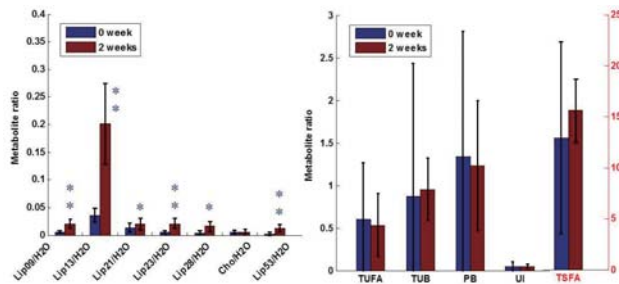


Fig. 2. Lipid signals, choline-containing compound (Left) and fat fraction (Right) quantified in 0 week and 2 weeks after high fat diet. Data shows mean± SD for each group using a two tailed *t*-test with significance threshold of **p* < 0.01 and ***p* < 0.001.

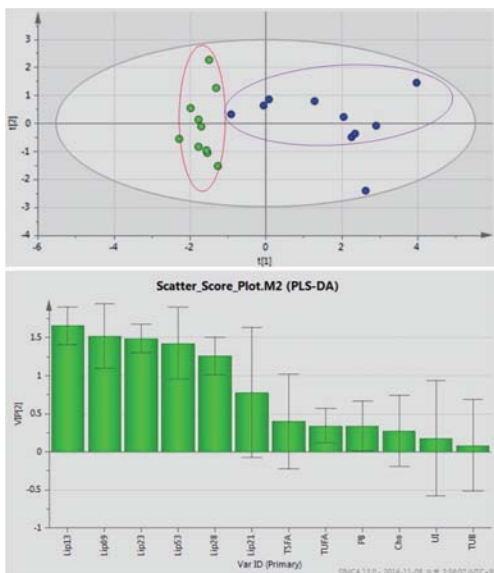


Fig. 3. The variables with VIP values in PLS-DA model (bottom) and PLS-DA scores plot (top). The model did allow a good separation of the two groups (e.g., at 0 week and 2 weeks).

ACKNOWLEDGEMENT

This work was supported in part by KBSI- #E34600.

REFERENCES

1. C.L. Gentile, M.J. Pagliassotti "The role of fatty acids in the development and progression of nonalcoholic fatty liver disease" *J Nutr Biochem*, September 2008.
2. L.F. Hourigan, G.A. Macdonald, V.H. Whitehall, C. Shorthouses, A. Clouston, E.E. Powell "Fibrosis in chronic hepatitis C correlates significantly with body mass index and steatosis" *Hepatology*, April 1999.
3. C. Zancanaro, R. Nano, C. Marchioro, A. Sbarbati, A. Boicelli, F. Osculati "Magnetic resonance spectroscopy investigations of brown adipose tissue and isolated brown adipocytes" *J Lipid Res*, December 1994.
4. K. Zhong, T. Emst "Localized in vivo human 1H MRS at very short echo times" *Magn Reson Med*, Oct 2004.
5. G. Hamilton, M.S. Middleton, M. Bydder, T. Yokoo, J.B. Schwimmer, Y. Kono, H.M. Patton, J.E. Lavine, C.B. Sirlin "Effect of PRESS and STEAM sequences on magnetic resonance spectroscopic liver fat quantification" *J Magn Reson Imaging*, Jul 2009.

Additive Manufacturing of clavicle fracture model for orthopedic surgery planning

J. P. Lee¹, S. Y. Moon¹, H. W. Jang¹, K. J. Park², and T. S. Lee¹

¹Department of Biomedical Engineering, Chungbuk National University, Cheongju, Chungbuk, Korea

²Department of Orthopaedic Surgery, Chungbuk National University Hospital, Cheongju, Chungbuk, Korea

E-mail: jplee87@chungbuk.ac.kr

Abstract—This study explores the application examples of 3D printing technology in clinical environment, specifically in bone fracture surgery. CT images stored in clinical PACS were processed to produce the fracture model by 3D printer, and simulate for surgery planning, through which more rapid and accurate operation was targeted. Volume rendering technique was used to visualize the fracture and remove the surrounding tissues. 3D computer graphics fracture model was made and stored as STL file and transformed to G-code file at SD card, and used to make the fracture model by 3D printer. 3D printed fracture model enabled the clinical simulation and surgery planning, through which the size and fixation angle and location of metal plate could be decided. As the additively manufactured fracture model has the same size and shape with the patients' fracture, surgeons will be able to carry it into operating room to shorten the operation time and prevent secondary damage.

Keywords— 3D printer, Fracture surgery, Volume Rendering, Computed tomography, Surgery planning

I. INTRODUCTION

Clavicle fracture shows its occurrence frequency of 5-10% of all the human fractures [1]. Cause of clavicle fracture is a strong impact and it is taken place while experiencing accident or doing exercise in most cases and just one side of bone that is vulnerable to fracture is fractured or both sides are fractured.

Fractured site of clavicle is divided into medial (2~3%), medium (69~82%), lateral (21~28%) depending on fracture location and medium fracture shows the highest occurrence frequency. Most of clavicle fracture hardly shows symptom after fusion [2] and overall nonunion rate is below 1% and its occurrence frequency is generally low [1].

In case that clavicle is fractured, diversified treatment methods are available but the most common method is to fix fractured site with metal plate of screw after putting dislocated bone together by exposing fractured site. Use of locking compression metal plate in fracture has more solid pinning force owing to angular and rotational stability biomechanically and so, it could be used in treatment of diversified fractures effectively [3].

Clavicle fixation operation using metal plate has an advantage that immediate strong fixation is enabled, pain is relieved promptly, rehabilitation is fast and serious reduction could be overcome and also, it has other advantage of simple anatomical structure.

Minimally Invasive Plate Osteosynthesis(MIPO) make incision 2-3 cm on end of each side of clavicle fracture, and then through clavicle fracture CT (Computed tomography) image metal plate were fit the angle formed by fracture to a method of fixation by the screw[4].

At present, operation method and using tool of clavicle fracture conditions are determined by acquiring information of cross section and 3D image through radiation screening and CT [5].

However, this method has a limitation that it is hard to confirm correct central part by each clavicle site and it has to be confirmed just based on visible form.

In this study, operation time was intended to be shortened in a way that clavicle model of patient was directly confirmed after manufacturing it in actual size through 3D printer by using CT image of clavicle-fractured patient pre-operatively, size, angle, fixation location of metal plate were determined through pre-operative plan to make a minimize incision using MIPO and secondary damage to be taken place inter-operatively was prevented.

II. MATERIAL AND METHOD

A. Study Subject

By targeting clavicle-fractured patients due to traffic accident, sports, 20 clavicle-fractured patients who hospitalized in Chungbuk National University hospital during the period from January, 2014 to May, 2015 were selected.

B. 3D Printer

Using CT images stored in PACS, DICOM image with CT space of 1mm of 20 clavicle-fractured patients was acquired. Joint part in addition to clavicle was removed by using VR (Volume Rendering) skill as shown on Fig. 1 and 3D image reconstitution method is based on acquired CT DICOM image. By separating each LT/RT clavicle, it was converted to 3D image and in case of normal clavicle, it was converted by using mirror technique additionally [6]. Mirror technique is inversion scheme being performed for manufacturing

normal clavicle as a product of anatomical shape like fractured clavicle.

In order to manufacture each separated clavicle by VR technique, reconstituted image was converted to STL (Stereo Lithography) file. Clavicle fracture model file and normal clavicle model file using mirror technique were set to be made as imagery of optimal resolution by changing setting values so that its size and image would be coincided with that of actual human bone by using G-code file generation program. Time required for saving generated G-code file in SD card and manufacturing saved file as 3D printing was total 6 hours. Used 3D printer is EDISON 3D PRINTER manufactured by Rocket Co., based on FDM (Fused Deposition Modeling) method by using PLA (Poly Lactic Acid).

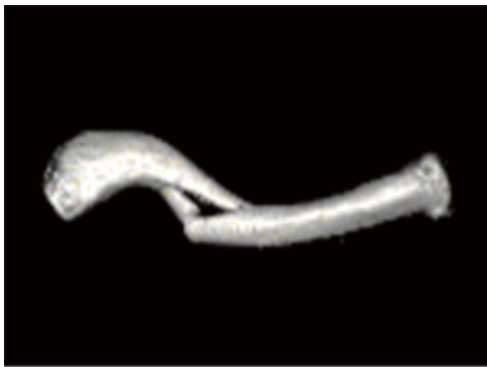


Fig. 1. 3D reconstructed VR image of fractured clavicle.

C. Operation Plan

In case of existing metal plate fixation, as metal plate is available in the market as ready-made one, at the time of fixation, size and angle are matched inter-operatively in operation room by carrying several metal plates. In case of using 3D printer, normal clavicle manufactured by using mirror technique was compared with image of fractured clavicle through pre-operative simulation and after confirming fracture degree, angle of metal plate is set. At this time, operation plan could be established while confirming whether any error is evident by using metal plate being used in actual MIPO operation. Through this operation plan, secondary damage could be prevented, incision will be minimized and metal plate could be fixed at correct position.

III. RESULTS

The time required to convert the STL file with OsiriX is about 30 minutes, and the time needed to convert a STL file into a G-code file took about 15 minutes. By using the G-code file to manufacture on 3D printer took approximately 6 hours.

The angle of metal plate to be used for MIPO operation could be modified to be fit for anatomical structure after measuring pre-operative length by using

clavicle model manufactured with 3D printer. Preoperative metal plate-fixating simulation and surgery planning using the clavicle model were shown on Fig 2.



Fig. 2. Preoperative metal plate-fixating simulation and surgery planning using the clavicle model.

Before clavicle fracture operation using product to simulation could reduce 5 minutes to 10 minutes and during operation time secondary damage was prevented.

IV. DISCUSSION AND CONCLUSION

By rapid prototyping the fracture model by using patient's CT images pre-operatively, the degree, location, and size of fracture could be accurately confirmed. As the additively manufactured fracture model has the same size and shape with the patients' fracture, orthopedic surgeons will be able to carry it into operating room to shorten the MIPO operation time and prevent secondary damage.

ACKNOWLEDGEMENT

This work was supported by the research grant of Chungbuk National University in 2012

REFERENCES

1. C. S. Neer, "Nonunion of the clavicle," *JAMA*, vol. 172, pp. 1006-1011, 1960.
2. D. Stanley and S. H. Norris, "Recovery following fractures of the clavicle treated conservatively," *Injury*, vol. 19, pp. 162-164, 1988.
3. J. W. Kim, H. J. Kang and S. H. No, "Operative Treatment of the Displaced Midshaft Clavicle Fracture Using Precontoured Locking Compression Plate," *J Korean Shoulder Elbow Soc*, vol. 15, pp.117-122, 2012.
4. J. Y. Yang, K.J. Rhee, J.K. Lee, D.S. Hwang, H. D. Shin and H. H. Lee, "Minimally Invasive Percutaneous Plate Osteosynthesis for Distal Tibial Shaft Fracture," *KISS*, vol. 15, pp. 286-291, 2002.
5. W. K. Oh, K. S. Lim and T. S. Lee "Additive manufacturing of pelvic fracture model using 3D printing," *48th Annual Conference of The Korean Society of Medical & Biological Engineering*, 2013.

6. J. R. Honiball, "The Application of 3D Printing in reconstructive surgery," *Dissertation presented in fulfillment of the requirements for the degree MscIng in Industrial Engineering at the University of Stellenbosch*, 2010.

Intravascular Ultrasonic-Photoacoustic (IVUP) Endoscope with 2.2-mm-diameter Catheter for Atherosclerotic Plaque Detection in Pig Artery

Q. N. Bui¹, K. K. Hlaing¹, Y. O. Oh¹, X. F. Fan¹ and J. Oh^{2,3}

¹Interdisciplinary Program of Biomedical Mechanical & Electrical Engineering, Pukyong National University, Busan, South Korea

²Department of Biomedical Engineering, Pukyong National University, Busan, South Korea

³Center of Marine-Integrated Biomedical Technology (BK21 Plus), Pukyong National University, Busan, South Korea

E-mail: jungoh@pknu.ac.kr

Abstract—In this study, by integrating a single-element, high-frequency intravascular ultrasound (IVUS) imaging catheter with a multi-mode optical fiber, we developed a 2.2-mm diameter integrated intravascular ultrasonic-photoacoustic (IVUP) imaging catheter to provide the spatial and functional information of light distribution in a turbid sample. Simultaneously, IVUS imaging was co-registered to intravascular photoacoustic (IVPA) imaging to reconstruct 3D volumetric sample images. In a phantom study, a polyvinyl alcohol tissue-mimicking arterial vessel phantom with macrophages loaded with indocyanine green (ICG) was used to demonstrate the feasibility of mapping the biological dye, which is used in cardiovascular diagnostics. For *ex vivo* study, excised sample of a pig artery with ICG-labeled macrophages was utilized to target the biomarkers present in the atherosclerotic plaques with the proposed hybrid technique. The IVUP imaging clearly reveals both the structure and composition of the samples. The results indicated that the IVUP endoscope with the 2.2-mm diameter catheter could be a useful tool for medical imaging.

Keywords— Three-dimensional image processing, imaging systems, endoscopic imaging, photoacoustic imaging, ultrasound imaging

I. INTRODUCTION

Intravascular ultrasound (IVUS) imaging of atherosclerosis is extremely important for detection and characterization of vulnerable plaques. Recently, intravascular photoacoustic (IVPA) imaging has been used to differentiate the composition of biological tissues with high optical contrast and ultrasonic resolution [1, 2]. The combination of these imaging techniques could provide morphological information and molecular screening to characterize of vulnerable plaques, which helps physicians to ensure vital therapeutic and prognostic significance for patients with early diagnosed atherosclerosis before commencing therapy [2].

II. METHODS

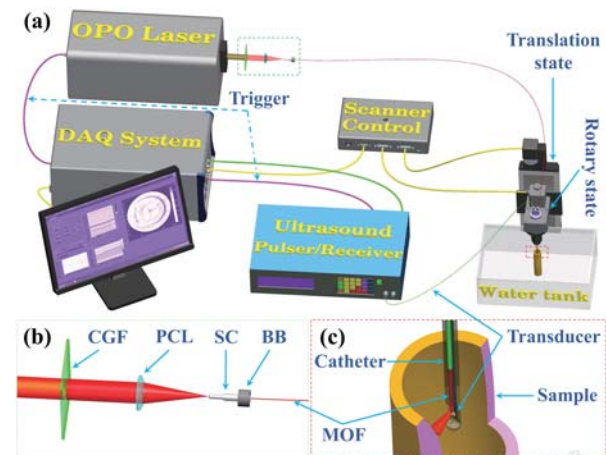


Fig. 1. Illustration of IVUP imaging system. (a) Overall structure of the experimental setup for IVUP imaging in *ex vivo*. (b) Enlarged view of the green dashed rectangle in (a). (c) Enlarged view of the red dashed rectangle in (a). DAQ: data acquisition; OPO: optical parametric oscillator; CGF: colored glass filter; PCL: plano-convex lens; SC: SMA connector; BB: ball bearing; MOF: multi-mode optical fiber.

III. RESULTS

A. IVUP imaging of a vessel phantom

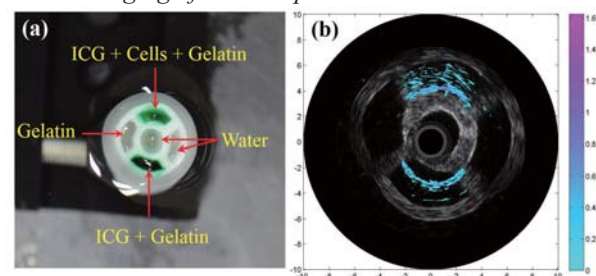


Fig. 2. (a) Top view of PVA phantom with four compartments. (b) IVUP image at 800-nm wavelength. Color-map: standard cool. Measurement unit: mm

B. IVUP imaging of a tissue sample in *ex vivo*

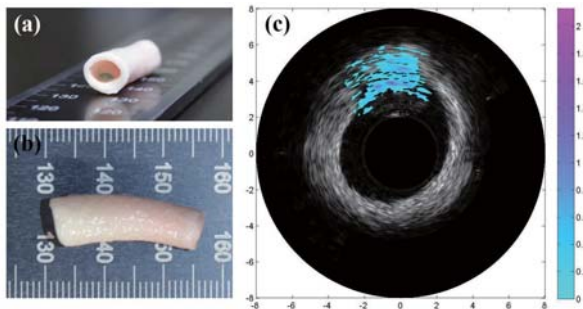


Fig. 3. IVUP imaging of 8-mm pig artery with ICG-loaded macrophages injected at 800-nm wavelength. (a) Side views. (b) Top views. (c) IVUP images. Color-map: standard cool. Measurement unit: mm

C. 3D IVUP volumetric image of the pig artery

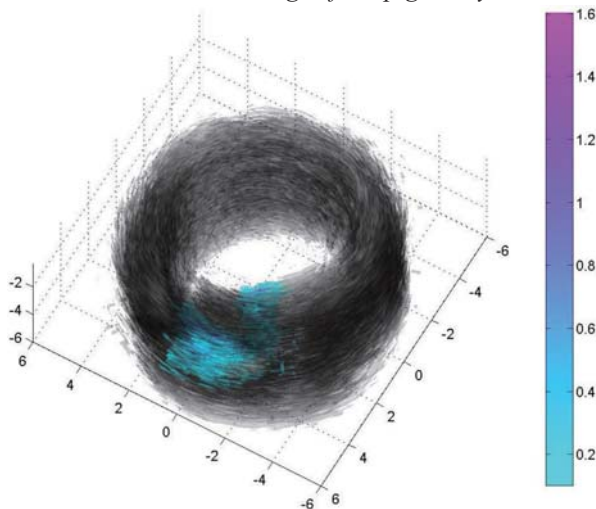


Fig. 4. 3D volumetric IVUP image of 8-mm pig artery injected with ICG-loaded macrophages. Color-map: standard cool. Measurement unit: mm

IV. CONCLUSION

IVUP imaging provides a way of visualizing the spatial and functional information on light distribution in atherosclerotic lesions. We successfully developed custom designed IVUP endoscope, and demonstrated its potential application for mapping biological dye in *ex vivo*. The results of this study indicated that the IVUP endoscope could produce IVUP images of internal organ, detect and localize certain biomarkers in the atherosclerotic plaques based on both their structure and functional composition. According to the ability adjust the catheter, the IVUP endoscope system could be performed on samples of up to 20 mm in diameter. Further studies will be conducted on rats to demonstrate its *in vivo* imaging capability for certain clinical applications.

ACKNOWLEDGEMENT

This research was supported by a grant from Marine Biotechnology Program (20150220) funded by Ministry of Oceans and Fisheries, Republic of Korea.

REFERENCES

1. E. De Montigny, "Photoacoustic Tomography: Principles and applications," (OCIS, 2011).
2. N. Q. Bui, K. K. Hlaing, V. P. Nguyen, T. H. Nguyen, Y.-O. Oh, X. F. Fan, Y. W. Lee, S. Y. Nam, H. W. Kang, and J. Oh, "Intravascular ultrasonic-photoacoustic (IVUP) endoscope with 2.2-mm diameter catheter for medical imaging," *Computerized Medical Imaging and Graphics* **45**, 57-62 (2015).

Measurement of Mechanical Property of Tibialis Anterior Muscle Using Optical Coherence Elastography

Yu-Gyeong Chae^{1, 2*}, Young-Sik Kim^{2, 3*}, Eun-Kee Park^{2, 4}, Min Yong Jeon⁵,
Byeong-Hwan Jeon^{6**} and Yeh-Chan Ahn^{1, 2***}

¹Department of Biomedical Engineering and Center for Marine-Integrated Biomedical Technology, Pukyong National University, Busan, 608-737, Korea

²Innovative Biomedical Technology Research Center, Busan, 608-737, Korea

³Department of Physical Medicine and Rehabilitation, College of Medicine, Kosin University, Busan, 602-702, Korea

⁴Department of Medical Humanities and Social Medicine, Kosin University College of Medicine, Busan, 602-702, Korea

⁵Department of Physics, Chung Nam National University, Daejeon, 305-764, Korea

⁶School of Sports and health, Kyung Sung University, Busan, 608-736, Korea

* The authors equally contributed to this work.

E-mail: ** mooaworld@ks.ac.kr and ***ahny@pknu.ac.kr

Abstract—In this study, we made a diabetes rat model to induce atrophy. Mechanical properties of tibialis anterior muscles under active and passive condition were measured by optical coherence elastography (OCE). Uniaxial strain rates of tissue were acquired by cross-correlation of speckles.

Keywords— Mechanical property, Muscle, Optical coherence elastography, Electrical muscle stimulator

I. INTRODUCTION

Mechanical property of muscle changes as atrophy is induced by diabetes or other diseases. Since OCE has a higher spatial resolution ($\sim\mu\text{m}$) than ultrasound or magnetic resonance elastography, it could be a great help for early diagnosis and confirmation of treatment efficacy. We measured the strains of normal and atrophic muscles with/without electrical muscle stimulator (EMS).

II. METHODS

We made a diabetes rat model using streptozotocin and this model was compared to normal group. Two structural optical coherence tomography (OCT) images (load and unload) were acquired at the same position for three different condition: without EMS *in vivo*, with EMS *in vivo*, *ex vivo*. External loading was applied on the upper surface of tissue using a stack of piezoelectric rings that located under focusing lens of OCT sample arm. To keep the same preload, we added a silicon phantom with known mechanical property between the piezoelectric ring and tissue. Uniaxial strains were obtained using cross-correlation speckle tracking.

III. RESULTS

Figure 1 represents of typical OCT and local strain images of control group. We measured and compared overall strains in two groups for the three different conditions with a constant applied force (Fig. 2)

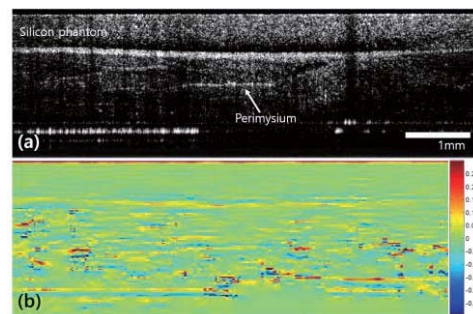


Fig. 1 (a) OCT image of control group, (b) Axial local strain image of (a)

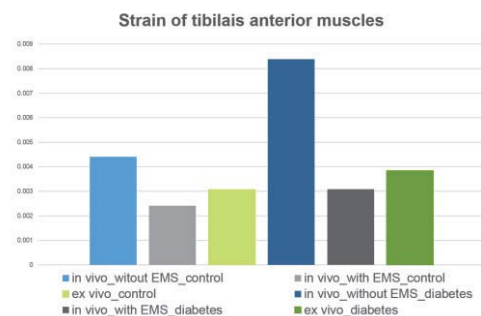


Fig. 2 Strain of TA muscle in each conditions and groups.

IV. CONCLUSION

All of strain of control group was smaller than diabetes and we confirm the trend that *in vivo* EMS group has lowest strain and then *in vivo* without EMS group and *ex vivo* group in sequence.

ACKNOWLEDGEMENT

This research was supported by grants from National Research Foundation of Korea (2013S1A5A2A03045562, 2013R1A1A4A01011631) and Marine Biotechnology Program (20150220) funded by Ministry of Oceans and Fisheries, Korea.

REFERENCES

1. J. M. Schmitt, "OCT elastography: imaging microscopic deformation and strain of tissue", *Opt. Express.*, vol. 3, pp.199-211, 1998.
2. X. Liang, A. L. Oldenburg, V. Crecea, E. J. Chaney, and S. A. Boppart, "Optical micro-scale mapping of dynamic biomechanical tissue properties", *Opt. Express.*, vol. 16, pp.11052-11064, 2008.

A Fabricated PMN-PZT Needle Hydrophone for Photoacoustic Imaging

Xiaofeng Fan¹, Kanglyeol Ha¹, Hyun Wook Kang¹, Junghwan Oh¹

¹Biomedical mechanical and electrical department, Pukyong National University, Busan, Korean
E-mail: fanxen2011@gmail.com

Abstract— In this study we have fabricated a new type needle hydrophone made of lead magnesium niobate-lead titanate (PMN-PZT) piezoelectric single crystal. It was consisted by a small size ($0.5 \times 0.5 \text{ mm}^2$) PMN-PZT with two matching layers on the tip of the needle. It was characterized with high sensitivity and wide bandwidth in the range of 1~10 MHz. Also, we applied the hydrophone to a PA imaging system and the obtained PA signals by the hydrophone are compared with those by a conventional PVDF needle hydrophone [1]. It is noted that the photoacoustic images obtained by the fabricated hydrophone have high resolution and high contrast.

Keywords—Phoacoustic, Ultrasound transducer, PMN-PZT, Needle hydrophone, Imaging

I. INTRODUCTION

In this study we have fabricated a new type needle hydrophone made of lead magnesium niobate-lead titanate (PMN-PZT) piezoelectric single crystal [2] with high sensitivity and wide bandwidth in the range of 1~10 MHz. The sensing part of the hydrophone is small ($0.5 \times 0.5 \text{ mm}^2$) and has two matching layers on the tip of the needle. Construction and performance are compared with other types of needle hydrophones. It was characterized to be more sensitive than PVDF needle hydrophones of the similar structure, and it was confirmed by experiment. The photoacoustic image with high resolution and high contrast of the ICG specimen was obtained by the fabricated needle hydrophone.

II. METHODS



Fig. 1. Structure of the needle hydrophone

Fig.1 shows the structure of the PMN-PZT needle hydrophone. The single crystal PMN-PZT with an active area of $0.5 \times 0.5 \text{ mm}^2$ and a thickness of 0.31 mm was used as the active element of the needle hydrophone. In the design, we considered the structure of Cu (41.6 Mrayl) backing and two matching layers (Comico_11 and Comico_10, KoMiCo company) for the PMN-PZT needle hydrophone.

III. RESULTS

Fig.2 shows the comparison of the amplitude of measured signals. Fig.3 shows the PA image of the ICG.

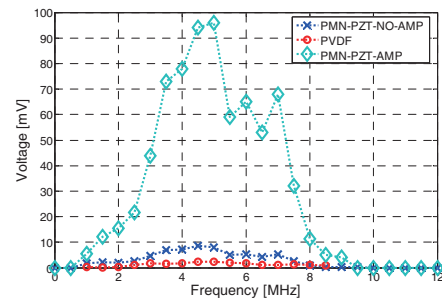


Fig. 2. Comparison of the PMN-PZT and PVDF needle hydrophones

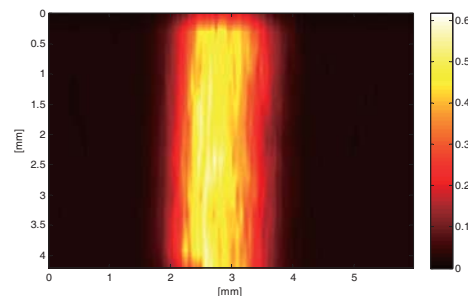


Fig. 3. PA image of ICG specimen

IV. CONCLUSION

In this study, we have designed and fabricated a needle hydrophone by using the piezoelectric single crystal PMN-PZT. The fabricated needle hydrophone has high sensitivity in the frequency range of 1~10 MHz and be used for photoacoustic imaging with high resolution and high contrast.

ACKNOWLEDGEMENT

This research was supported by a grant from Marine Biotechnology Program (20150220) funded by Ministry of Oceans and Fisheries, Republic of Korea.

REFERENCES

1. H. Takeuchi , H. Masuzawa , C. Nakaya, Y. Ito, Proc. 1990 IEEE Ultrason. Symp., pp.697-705 1990.
2. C. S. DeSilets, J. D. Fraser, G. S. Kino, IEEE Trans. Sonics and Ultrasonics, Vol. 25(3), pp. 115-125, 1978

Corpus callosum segmentation using hybrid method of sparse approximation and probability map

Gilsoon Park¹, Kichang Kwak¹, Bohyun Kim¹, Sang Won Seo², Duk L. Na², Jong-Min Lee^{1*}

¹Department of Biomedical Engineering, Hanyang University, Seoul, South Korea

²Department of Neurology, Samsung Medical Center, Sungkyunkwan University School of Medicine, Seoul, South Korea
E-mail: pks1207@bme.hanyang.ac.kr

Abstract— Corpus Callosum (CC) is the largest white matter structure of the human brain, which connects the two cerebral hemispheres. Its features such as size and shape have been contribute to analyze neurological disease progression. Accuracy and stabile extraction of the features rely on segmentation performance. In this paper, we introduced novel CC segmentation method that is hybrid of sparse approximation and probability map using Bayesian inference.

Keywords— Corpus callosum, Segmentation, Sparse approximation, Multi-atlas, Bayesian inference

I. INTRODUCTION

Corpus callosum (CC) is the largest white matter structure in human brain, which is communication passage between two cerebral hemispheres. Variation in CC structure features such as size and shape is associated with many neurological diseases progression (e.g. epilepsy [1] and Alzheimer's disease [2]). CC segmentation technique is directly linked to accuracy and stable neurological study using CC features. In this paper, we designed novel CC segmentation method combination of sparse approximation and probability map.

II. METHODS

A. Pre-processing

Pre-processing is equally applied to atlas images we know CC and unseen target image. In the beginning, the skull is removed from all brain images. The skull-stripped images were aligned with MNI152 space, and done intensity normalization in predetermined range.

B. Multi-atlas based segmentation

The atlas images are aligned a target image using nonlinear registration, which is generating probability map included prior information of CC shape and location.

C. Sparse approximation based segmentation

First the atlas images similar to target image selected among all atlas images. The selected images generate foreground and background dictionary thorough CC labels we know. Sparse approximation is carried out in two dictionary matrices. We can calculate percentage

error value with respect to each sparse approximated patch. The error value is used to decide CC or background in corresponded voxel in target image.

D. Bayesian inference based segmentation

In multi-atlas step and sparse approximation, we got CC probability map and error value. One voxel in target image is assigned label whether CC or the other using posterior probability resulting from Bayesian inference. Prior probability and likelihood value can be substituted CC probability map and error value each.

III. RESULTS

Method	Dice index	
	Mean	Standard deviation
Multi-atlas	88.56	4.46
Sparse approximation	89.40	3.09
Bayesian inference	91.89	3.34

Table. 1. Dice index for segmentation results

The Dice index over all segmentation methods are presented in Table. 1. The index between Bayesian inference and the other methods show significant different.

IV. CONCLUSION

We can show that Bayesian segmentation performance is the best compared to the other. In the future, we plan to improve the segmentation performance by configuring more accurately each construction of Bayesian method.

ACKNOWLEDGEMENT

This work was supported by the National Research Foundation of Korea (NRF) grant funded by the Korea government (MEST) (2011-0028333).

REFERENCES

1. O'Dwyer, R., et al., Differences in corpus callosum volume and diffusivity between temporal and frontal lobe epilepsy. *Epilepsy Behav*, 2010. 19(3): p. 376-82.
2. Zhu, M., et al., Corpus callosum atrophy and cognitive decline in early Alzheimer's disease: longitudinal MRI study. *Dement Geriatr Cogn Disord*, 2014. 37(3-4): p. 214-22.

The relationships between morphological asymmetry and functional connectivity in the default mode network

Dong-Kyun Lee¹, Jun-Sung Park², Jung-ho Cha¹, Sang Won Seo³, Duk L. Na³,
and Jong-Min Lee¹

¹Department of Biomedical Engineering, Hanyang University, Seoul, South Korea

²Medical System Lab., DMC R&D Center SAMSUNG Electronics, Suwon, South Korea

³Department of Neurology, Samsung Medical Center, Sungkyunkwan University School of Medicine, Seoul, South Korea

E-mail: dongkyun@bme.hanyang.ac.kr

Abstract—The functional and structural hemispheric asymmetry is expected to be related by inter-hemispheric connectivity. We investigated the relationships between functional, structural inter-hemispheric connectivity and cortical thickness asymmetry in default mode network region. Then, we showed that brain morphological asymmetry was affected by functional and structural inter-hemispheric connectivity within posterior cingulate and precuneus.

Keywords— Brain asymmetry; Inter-hemispheric connectivity; Default mode network; resting state fMRI; cortical thickness.

I. INTRODUCTION

The functional and structural hemispheric asymmetry was reported by several neuro imaging studies. This hemispheric asymmetry is expected to be related by inter-hemispheric connectivity. In order to investigate the source of brain morphological asymmetry, we used different measurements of brain asymmetry and inter-hemispheric connectivity from the multi-modality images.

II. METHODS

To test this relationships, we defined ROIs as default mode network component using group spatial ICA in resting state fMRI on a group of 47 subjects. The BOLD signals in the pre-defined DMN ROIs were averaged. Subsequently, the inter-hemispheric synchronization was estimated through the correlation statistics between bilateral pairs of the pre-defined DMN ROIs. Structural aspect of inter-hemispheric connectivity was frequently reported by callosal extent and microstructural property such as fractional anisotropy (FA) value. We estimated inter-hemispheric connectivity as the multiplication of FA value and callosal thickness which reveal micro- and macro structural properties. Simultaneously, morphological asymmetry was estimated using cortical thickness measurement on T1 weighted MRI. Finally, we investigated the relationships between functional and structural inter-hemispheric connectivity and cortical thickness asymmetry in default mode network regions.

III. RESULTS

The results revealed that the asymmetry of cortical thickness in posterior cingulate and precuneus regions have significantly relationship with functional inter-hemispheric connectivity of fMRI signal. And, The callosal posterior body and the isthmus of DTI was observed inverse relationship with structural hemispheric connectivity and asymmetry of cortical thickness.

IV. CONCLUSION

These finding showed that brain morphological asymmetry was affected by functional and structural inter-hemispheric connectivity within posterior cingulate and precuneus.

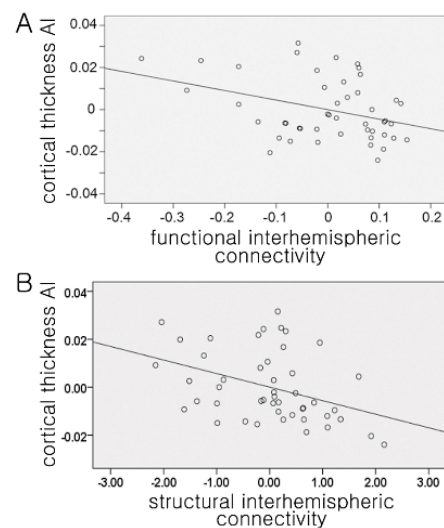


Fig. 1. Partial regression plots

ACKNOWLEDGEMENT

"This research was supported by the Brain Research Program through the National Research Foundation of Korea funded by the Ministry of Science, ICT & Future Planning (NRF-2014M3C7A1046050)."

REFERENCES

1. Park JS, Lee JM, "The relations between extent and microstructural properties of the midsagittal corpus callosum in human brain", *NeuroImage*, 56:174-184, 2011.

Analysis of Default Mode Network in Resting State Brain using Batch Self-Organizing Map

J. M. Hwang¹, J. H. Cha¹, J. S. Lee¹, Y. H. Park¹ and J.M. Lee¹

¹Department of Biomedical Engineering, Han-Yang University, Seoul, South Korea
E-mail: luckyjm7364@bme.hanyang.ac.kr

Abstract— There are several networks in functional connectivity in the brain. One of well-known networks is default mode network (DMN) that increases in the absence of a driving task. Since reference signals from seed-based analysis in each subject are different due to individual biases, this may not be proper to detect DMN individually. Alternative is to use a batch SOM (self-organizing map) derived from the SOM, which is appropriate to large scales data. The analysis revealed that DMN was observed well. These findings indicate that the batch SOM is a suitable method to analyze DMN.

Keywords— default mode network, self-organizing map, batch self-organizing map

I. INTRODUCTION

The default mode network (DMN) is that activation is ongoing at rest in the brain [1]. To observe the DMN, there is a general method called as seed-based analysis. The use of seed, however, is not an ideal way to detect DMN since location or size of posterior cingulate cortex (PCC) is different according to the subjects [2]. The self-organizing map (SOM) is dimension reduction and data visualization by training input data. The batch SOM is speedier and less dependent to noises comparing to traditional method while the properties are sustained. The present demonstrate that using batch SOM offers alternative method for exploring DMN without user-biased.

II. METHODS

A. Pre-processing

All steps were performed with Analysis of Functional NeuroImage (AFNI). For steady magnetic field, first to five volumes were removed. Following step performed time and motion correction for time courses. After the T1 image was registered to EPI space, registered image is normalized to MNI 152 template. Band-pass filter ($0.009 < f < 0.08$) and spatial smoothing with 6 mm were implemented.

B. Post-processing

The 10x10 map was initialized randomly and updated iteratively with input until exemplar time courses were not changed. Unlike SOM, this batch SOM is not recursive when updating weight. Hence, this had advantage that is faster in computation and less affected to noises without loss of conventional properties [3]. After applying to hierarchical clustering, the signals sharing same label are averaged. Correlation coefficient (CC) was calculated to whole voxel using the mean signals and converted to fisher z value. Finally, the one

of results similar with DMN was chosen by visual inspection.

III. RESULTS

The PCC, medial prefrontal cortex (MPFC) and inferior parietal lobule (IPL) known as anatomical location in DMN are showed clearly to all of subjects in Fig 1. Also, the PCC and MPFC, which have high activation within DMN in previous studies are showed high correlation coefficient as shown color distribution in Fig 1.

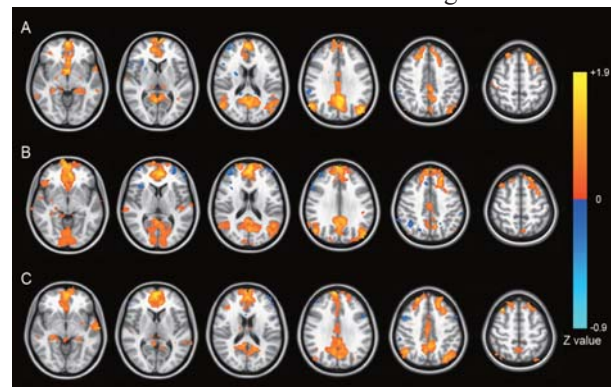


Fig. 1. The result of batch SOM. Each row (A,B and C) indicates control subjects.

IV. CONCLUSION

The research manifests that the batch SOM is useful method to analyze DMN. This approach does not need location or size of seed according to individual state.

ACKNOWLEDGEMENT

This research was supported by the Brain Research Program through the National Research Foundation of Korea funded by the Ministry of Science, ICT & Future Planning (NRF-2014M3C7A1046050).

REFERENCES

1. Greicius MD, Krasnow B, Reiss AL, Menon V, "Functional connectivity in the resting brain : a network analysis of the default mode hypothesis," *Proc Natl Acad Sci USA* 2003; 100:253-8.
2. Cordes D, Haughton VM, Arfanakis K, Wendt GJ, Turski PA, Moritz CH, Quigley MA, Meyerand ME, "Mapping functionally related regions of brain with functional connectivity MR imaging," *AJNR Am J Neuroradiol* 2000;21:1636.
3. Kohonen, T. Self-organizing maps. Vol. 30. Springer; Heidelberg: 1997.

Sparse representation method for Alzheimer's disease diagnosis

Kichang Kwak, Hyuk Jin Yun, Gilsoon Park, Eun Kyoung Kim, Jong-Min Lee

Department of Biomedical Engineering, Hanyang University, Seoul, South Korea
E-mail: kichang1001@bme.hanyang.ac.kr

Abstract— We used the complementary features by incorporating the gray matter (GM) density map and uptake of 18-fluorodeoxyglucose-positron emission tomography (FDG-PET) as the brain structural-functional relationship.

Keywords— MRI, FDG-PET, sparse representation, Alzheimer's disease, diagnosis

I. INTRODUCTION

In recent years, many studies have been proposed to automatically discriminate between Alzheimer's disease (AD)/mild cognitive impairment (MCI) and healthy controls. Its discriminative approach is necessary to use feature thus playing an important role in the classification performance.

II. METHODS

Pre-Processing

Data used in the preparation of this article were obtained from the Alzheimer's disease Neuroimaging Initiative (ADNI) database. At first, the native MRI data of all subjects were registered into the template using linear transform and corrected for intensity non-uniformity artifacts[1]. And then, an artificial neural network classifier was applied to identify gray matter, white matter and cerebrospinal fluid. Finally, partial volume levels, MRI intensity-mixing at the tissue interfaces due to the finite resolution of the imaging device, were estimated and corrected using a trimmed minimum covariance determinant method[2]. Subsequently, the FDG-PET images were rigidly registered to its corresponding structural MRI, segmented the cerebellum, where glucose utilization is relatively preserved. The hippocampus segmentation was performed using an automated method using graph cuts combined with atlas-based segmentation and morphological opening.

Sparse representation

In the sparse representation[3], patches of target voxel are considered as a dictionary, and then the sparse coefficients can be obtained by solving the l_0 -norm equation. And the group label value for the target patch is assigned as the group with the minimum residual over all groups.

III. RESULTS

Fig. 1 shows illustration of our proposed method. Also, Fig. 2 shows the best results of different group classification. The results clearly show that the sparse representation-based method for AD classification.

IV. CONCLUSION

In this paper, we proposed a sparse patch-based approach using combination of structural MRI and FDG-PET to separate different groups of subjects. The patch has been extracted using the voxels of hippocampus ROI instead of whole voxels, it is more discriminative and low dimensional.

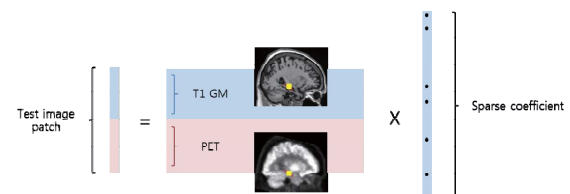


Fig. 1. Figure caption

Table 1. The classification accuracy using a sparse representation

	AD vs NL	AD vs MCI	MCI vs NL
Sen. (%)	89.33	85.33	86.67
Spec. (%)	93.33	88	85.33
Prec. (%)	93.06	87.67	85.53
Acc. (%)	91.33	86.67	86

ACKNOWLEDGEMENT

This work was supported by the National Research Foundation of Korea (NRF) grant funded by the Korea government (MEST) (2011-0028333).

REFERENCES

1. Sled, J.G., A.P. Zijdenbos, and A.C. Evans, *A nonparametric method for automatic correction of intensity nonuniformity in MRI data*. IEEE Trans Med Imaging, 1998. **17**(1): p. 87-97.
2. Tohka, J., A. Zijdenbos, and A. Evans, *Fast and robust parameter estimation for statistical partial volume models in brain MRI*. Neuroimage, 2004. **23**(1): p. 84-97.
3. Wright, J., et al., *Robust face recognition via sparse representation*. IEEE Trans Pattern Anal Mach Intell, 2009. **31**(2): p. 210-27.

Relationship between White matter Myelination and Gray matter morphology in Deep Sulcal Landmarks

Hyuk Jin Yun, Jong-Min Lee*

Department of Biomedical Engineering, Hanyang University, Seoul, Korea, Republic of,
E-mail: yunhj@bme.hanyang.ac.kr

Abstract— We investigate that brain morphological features are affected by diffusion parameters in deep sulcal landmarks.

Keywords— Sulcal pits, mean diffusivity, brain morphology, myelination, brain folding

I. INTRODUCTION

The deep sulcal regions in major sulci, called sulcal pits, are thought to be landmark of cortical growth and first folded area under genetic control [1]. In GM development, cortical folding is dependent on tension of connected tracks in WM [2].

In the present study, we investigate that deep sulcal morphometry are associated with integrity of WM in deep sulcal landmarks.

II. METHODS

A. Extracting morphological features

Cortical thickness, absolute mean curvature, surface area and sulcal depth were extracted using previous algorithms [3,4]. The sulcal pits (Fig.1) were identified by watershed algorithm [1] on WM depth map [4] with brain size normalization.

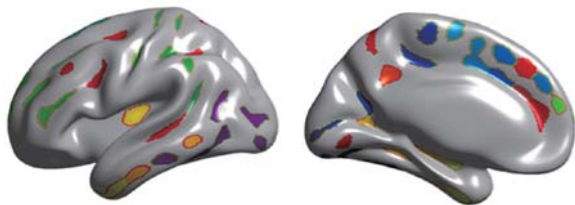


Figure 1. Map of sulcal pits in adults group

B. Calculating diffusion parameter

The mean diffusivity (MD) and fractional anisotropy (FA) were measured in diffusion images co-registered to their structural MRIs, and calculated in WM regions around sulcal pits with 5mm distance threshold (Fig.2).

C. Statistical analysis

General linear models were employed to investigate linear effect among measures and age.

III. RESULTS

The linear models with age are significant for MD ($t = -5.16$; $p < 0.001$) and absolute mean curvature ($t = -2.62$; $p = 0.011$). Cortical thickness ($t = 2.10$; $p = 0.039$) and sulcal depth ($t = 2.12$; $p = 0.038$) correlate

positively with MD, although the linear effects of age on them are not significant. FA shows only significant correlation with age ($t = 2.47$; $p = 0.016$).

IV. CONCLUSION

The results of the relationship between diffusion parameter and morphological features further demonstrate possibility that cortical growth in the first folded area could be associated with WM integrity.

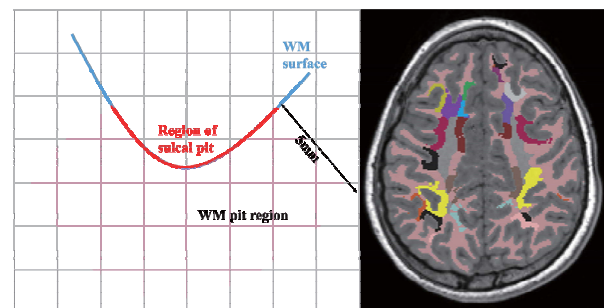


Figure 2. Illustration of the algorithm for detecting WM regions around sulcal pits (left) and an example data (right).

ACKNOWLEDGEMENT

This work was supported by the National Research Foundation of Korea(NRF) grant funded by the Korea government(MEST) (2011-0028333).

REFERENCES

1. Im K, Jo HJ, Mangin JF, Evans AC, Kim SI, et al. (2010) Spatial distribution of deep sulcal landmarks and hemispherical asymmetry on the cortical surface. *Cereb Cortex* 20: 602-611.
2. Kochunov P, Glahn DC, Lancaster J, Thompson PM, Kochunov V, et al. (2011) Fractional anisotropy of cerebral white matter and thickness of cortical gray matter across the lifespan. *Neuroimage* 58: 41-49.
3. Im K, Lee JM, Lyttelton O, Kim SH, Evans AC, et al. (2008) Brain size and cortical structure in the adult human brain. *Cereb Cortex* 18: 2181-2191.
4. Yun HJ, Im K, Jin-Ju Y, Yoon U, Lee JM (2013) Automated sulcal depth measurement on cortical surface reflecting geometrical properties of sulci. *PLoS One* 8: e55977.

Complementary Characteristics of Structural Correlation Networks

J. J. Yang, H. K. Kwon, J. M. Lee*

Department of Biomedical Engineering, Hanyang University, Seoul, South Korea

E-mail: jinju@bme.hanyang.ac.kr

Abstract—In this study, we examined the characteristics of connection patterns to determine the difference in structural topology between the three structural correlation networks of cortical thickness, surface area, and gray matter (GM) volume. This may allow complementary accounting for spatial and topological information when combined with network parameters.

Keywords—Structural correlation network, Graph theory, cortical thickness, surface area, gray matter volume

I. INTRODUCTION

Structural correlation networks of cortical thickness, surface area, and gray matter volume have statistically different structural topology [1, 2]. However, there is no report directly describing their connection patterns in view of interregional covariance. Here, we examined the characteristics of the connection patterns in three structural correlation networks of cortical thickness, surface area, and gray matter volume using a Venn diagram concept across 314 normal subjects.

II. METHODS

A. Data acquisition

We used the set of cross-sectional data from the Open Access Series of Imaging Studies (OASIS) database (<http://www.oasis-brains.org>). We selected 314 healthy normal subjects (age range, 18–94 years) from the present study. The healthy normal subjects were 44.9 ± 23.79 years old (mean \pm standard deviation (SD)) with a sex ratio of 195/119 (women/men). All the magnetic resonance imaging (MRI) data were sagittal T1-weighted images with typical dimensions of 256×256 and resolutions of $1 \text{ mm} \times 1 \text{ mm} \times 1.25 \text{ mm}$.

B. Image processing

CIVET software was used to extract cortical surfaces. A surface model for each hemisphere consisted of 81924 vertices with polygonal meshes. Cortical thickness was calculated as the Euclidean distance between the corresponding vertices of inner and outer surfaces using a t-link method. Surface area was measured by calculating the Voronoi area assigned to

any vertices. GM volume was obtained from the segmented GM images in native space.

C. Construction of networks

The automated anatomical labeling (AAL) template was used to parcellate the entire cerebral cortex into 78 cortical regions excluding the cerebellum and subcortical regions, which represented nodes of the network. The interregional symmetric correlation matrix was constructed by calculating the Pearson correlation coefficients across the 314 individuals between the morphological measures of every regional pair. Finally, three 78×78 symmetric correlation matrices were obtained for cortical thickness, cortical surface area, and GM volume.

D. Characteristics of connection patterns

We partitioned the spatially distributed edges into seven parts and classified them into four different connection types to characterize the various connection patterns of cortical volume, thickness, and surface area networks. The number of edges belonging to each connection type in seven partitions respectively yields quantitative information of overlap ratio (OR) about the connection patterns of networks. We also calculated network hubs to explore whether the characteristics of connection pattern have an effect on the network properties.

E. Statistical analysis

We generated 1000 random networks with the same degree of distribution in the same sparsity. We also obtained 1000 bootstrap samples of the connection matrices by selecting random samples; that is, the 80% from 314 subjects. The OR was estimated in random networks and validated the differences between the observed samples and random networks using a two-sample t test.

III. RESULTS

A. Characteristics of structural correlation networks

Our findings showed that over 60% of all nonoverlapping connection patterns emerged from distinct structural phenotypes, that is, thickness, surface area, and GM volume-based networks. The findings support the hypothesis that the different structural

phenotypes of cerebral cortex have different network properties [1, 2]. While the global network parameters gave us an abstraction of the complex human brain topology as a single value, we provided the complementary characteristics of network topology such as the percentage of similarities between these networks and the connection types of edges. We can better understand and explain quantitatively the differences of brain network topology in terms of how they are similar or dissimilar between these networks and which types of connections they have.

B. Connection patterns and network properties

We examined which hub regions of the networks were similar to those of each partition. The similarity between hub regions of the networks and subnetworks of each partition showed that the hubs were strongly associated with their intrinsic connection patterns. We also examined the network parameters such as the clustering coefficient, characteristic path length, and global efficiency; these were significantly different between these networks, which was consistent with previous studies [1, 2].

IV. CONCLUSION

Our results demonstrated that structural correlation networks of distinct structural phenotypes have different connection patterns and different network properties.

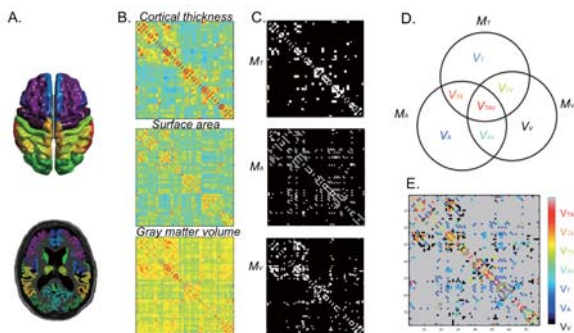


Fig. 1. Schematic showing processing for constructing structural correlation networks and the Venn diagram concept.

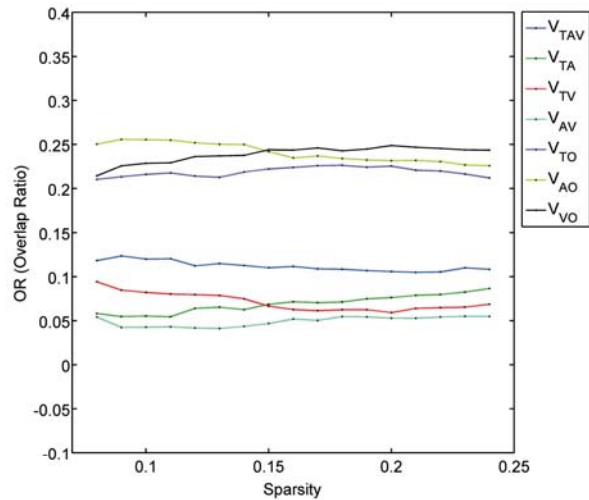


Fig. 2. The overlap ratio (OR) in seven partitions.

ACKNOWLEDGEMENT

This research was supported by the Brain Research Program through the National Research Foundation of Korea funded by the Ministry of Science, ICT & Future Planning (NRF-2014M3C7A1046050).

REFERENCES

1. Joshi AA, et al. "Evaluation of connectivity measures and anatomical features for statistical brain networks." Biomedical Imaging: From Nano to Macro, 2011 IEEE International Symposium on IEEE.
2. Sanabria-Diaz G, Melie-Garcia L, Iturria-Medina Y, Aleman-Gomez Y, Hernandez-Gonzalez G, Valdes-Urrutia L, Galan L, Valdes-Sosa P "Surface area and cortical thickness descriptors reveal different attributes of the structural human brain networks." Neuroimage 50:1497-1510, 2010

Single-subject metabolic network analysis in Alzheimer's disease

Oh-Hun Kwon¹, Yong-Ho Choi¹, Sun-Il Kim¹, Jong-Min Lee¹
Alzheimer's Disease Neuroimaging Initiative

¹Department of Biomedical Engineering, Hanyang University, Seoul, South Korea.
E-mail: ohkwon@bme.hanyang.ac.kr

Keywords— Graph Theory, Magnetic Resonance Image

I. INTRODUCTION

We investigated the graph theoretic properties of the metabolic brain network and compared metabolic and structural network in AD, MCI and healthy elder control. The methodology of previous studies limited the investigation of graph properties to group-level analyses. In present study, we extracted individual brain networks in single subject.

II. METHODS

A. Data & Preprocessing

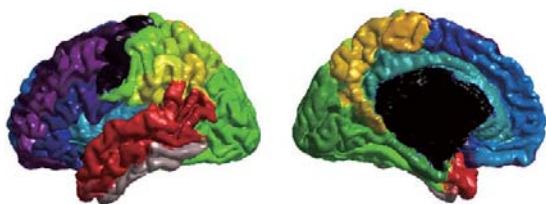
The cortical surfaces were extracted using CLASP, and measured the cortical thickness using the t-link method¹. The FDG-PET image was co-registered with the corresponding pre-processed T1-weighted image using rigid body transformation. The intensity of FDG-PET image was normalized with respect to the signal in cerebellum of each subject.

B. Connectivity Matrix

Nodes were represented by 78 regions of interest (ROI) defined using automated anatomical labeling (AAL) template. Edges was defined using correlative information between pair of ROIs².

$$s(i, j) = \exp\left(\frac{d(i, j)}{2\sigma^2}\right), \quad d(i, j) = [t(i) - t(j)]^2$$

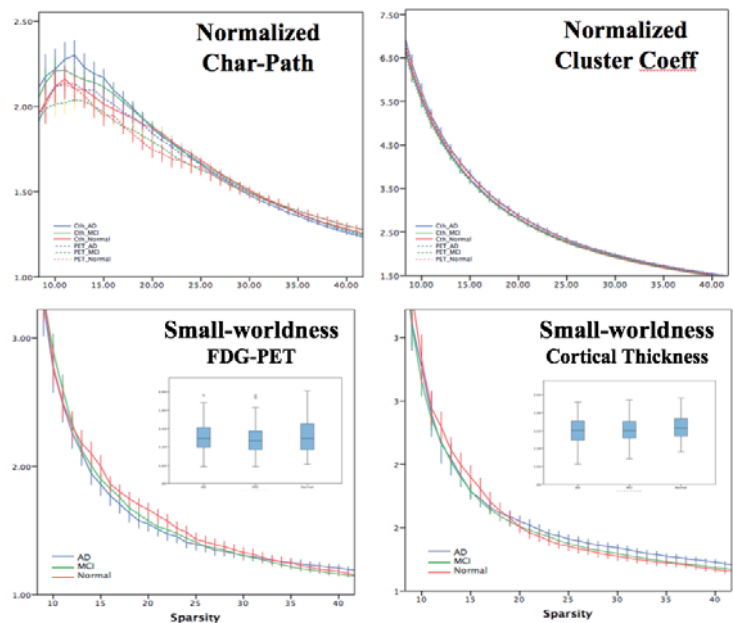
- $t(i)$ and $t(j)$: the regional mean cortical thickness and FDG uptake of regions i th and j th, respectively.
- σ : the standard deviation of regional cortical thickness and FDG uptake of regions i th and j th.



Node Definition on cortical surface

ADNI data set	Control (n=85)	MCI (n=163)	AD (n=71)	P
Age, years	75.7±4.5	74.7±7.2	75.1±7.0	0.52
Sex, M/F	54/31	110/53	41/30	0.35
MMSE	28.9±1.1	27.1±1.7	23.3±2.1	<0.0001

III. RESULTS



IV. CONCLUSION

Metabolic graph give better characterization of graph topological changes in AD and MCI than structural graph. AD metabolic and structural graphs would be characterized by a more random properties than those from control subjects.

This research was supported by the Brain Research Program through the National Research Foundation of Korea funded by the Ministry of Science, ICT & Future Planning (NRF-2014M3C7A1046050).

REFERENCES

1. Kim, J. S. et al. Automated 3-D extraction and evaluation of the inner and outer cortical surfaces using a Laplacian map and partial volume effect classification. *Neuroimage* 27, 210-221.
2. Chong-Yaw Wee. et al. Prediction of Alzheimer's Disease and Mild Cognitive Impairment Using Cortical Morphological Patterns. *Human Brain Mapping* 34, 3411-3425.

3D image acquisition of ultrasound using schlieren method

O. Cha¹, J. Won¹, J. Kim¹, G. Song¹ and J. Seo¹

¹Department of Biomedical Engineering, College of Health Sciences, Yonsei University, Wonju, Republic of Korea
E-mail: cha037@naver.com

Abstract—This study is to visualize 3D ultrasound field in transparent liquids based on Schlieren image method. The 3D Schlieren system was designed and utilized to visualize the fields of pressure generated from an 1.1Mhz transducer. In order to increase the contrast image subtraction was also applied. . 3D Schlieren technology might be useful for fast measure of relatively strong ultrasound used in therapeutic ultrasound.

Keywords— ultrasound, 3D image, schlieren

I. INTRODUCTION

Schlieren system technology has been applied in ultrasound visualization for decades. The principle of Schlieren imaging is based on the changes of the refraction index in water according to pressure field. As ultrasound field formed, local pressure fluctuation leads to local water density fluctuation and local refraction index also changes accordingly. Therefore, the projection image to light of ultrasonic field will present diffraction pattern induced by ultrasound field, which is visible to human eyes [1].

In this study, 2D Schlieren imaging was further exploited to visualize 3D ultrasonic field adopting CT imaging reconstruction technique. The collimated light was radiated to the region of ultrasound sonication to photograph the changes in refraction index of water. All told, 180 two dimensional Schlieren images were taken as the transducer rotates 180 degrees at every degree, then 3D ultrasonic field was reconstructed

II. METHODS

A. Schlieren system components.

Schlieren system consists of LED Light(White, 80W,KOMI, KR), Rotation system, Concave mirror(Uniotech, KR), Water tank, Knife edge, Transducer(1.1Mhz, precision acoustic, UK), CCD Camera(D800, Nikon, JP).

All of the system configurations, from the light source to a mirror, are fixed on the optical bench horizontally. The transducer is attached to the rotation system which is placed above the water tank, so that the ultrasound can radiate inside the water. Ultrasound absorber (F48, precision acoustic, UK) is installed under the tank to block any reflected ultrasound wave from interfering.

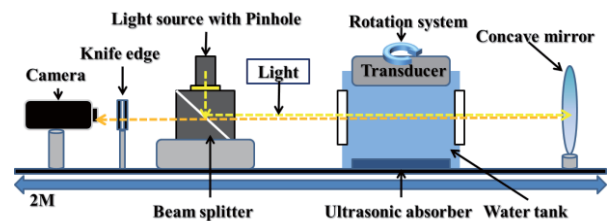


Fig. 1. Location of the field planes in the Schlieren system

B. Acquire Schlieren image

In this system, knife-edge is placed where the reflected light from the light source is focused. The rays of reflected light that has passed the sonication region cannot reach the focal point of reflected light, and makes the portion darker than the other. [2],[3] 2D images were sampled at every 1° of rotation, as the system rotates the transducer 180°

c. Schlieren 3D image process

3D schlieren image is acquired by transforming all 2D images to gray scale and reconstructing them by using sinogram and back projection method.

To proceed Reconstruction process in order to obtain a 3D schlieren image. The 2D image that has been acquired is converted into gray scale image. Then by the Radon transform, to complete the 3D image by die placement death.

Radon transform in two dimensions is the integral transform consisting of the integral of a function over straight line. (Eq.1)

$$R_{\theta}(x') = \int_{-\infty}^{\infty} f(x' \cos\theta - y' \sin\theta, x' \sin\theta + y' \cos\theta) dy' \quad (1)$$

III. RESULTS

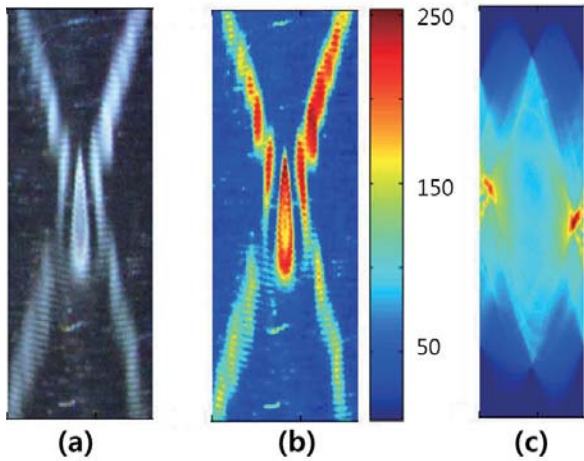


Fig. 2. (a) Original image (b) gray scale image (c) Radon Transform image

Fig.2 (a) shows the area that ultrasound to 2D schlieren image has been progress when 1.1Mhz transducer generated ultrasonic. To make a sinogram, gray scale image was prepared from RGB image.(Fig.2 (b)) Fig.2 (c) was a photograph that was radon transform from gray scale image

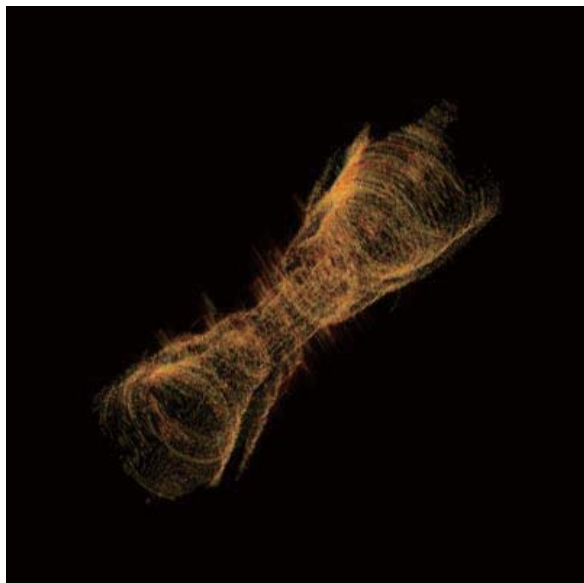


Fig. 3. 3D schlieren image

Fig.3. The 2D schlieren image by utilizing Rotation system, and rotated 180 ° and rotated by 1 ° Then it is possible to confirm that we have created a 3D schlieren image 180 sheets 2D image through a process of reconstruction.

IV. CONCLUSION

Ultrasound schlieren image can be constructed as 3D and express acoustic field easily visible. The concave

mirror which has 180 cm focal length was used to make schlieren image so the total system composed total 2m. To minimize the system, collimate of focused lens to reduce focal length less than 1 m. Laser source could enhance the image resolution instead of LED.

ACKNOWLEDGEMENT

This work was supported by the NRF grant (NRF-2014M3A6A3063636), and (2013R1A2A2A04016262)

REFERENCES

1. T Neumann, H Ermert, "Schlieren visualization of ultrasonic wave fields with high spatial resolution" Ultrasonics., vol.44, pp.1561-1566, 2006
2. A Hanafy, CI Zanelli "Quantitative real-time pulsed Schlieren imaging of ultrasonic waves" Ultrasonics Symposium., vol.2, pp.1223-1227, 1991
3. PA Chinnery, VF Humphrey, "The schlieren image of two-dimensional ultrasonic fields and cavity resonances" Acoustical Society of America vol.101 , 1997

Brain network analysis of Parkinson's disease patients based on SPECT images

Seong-Jin Son¹ and Hyunjin Park^{2,3*}

¹Department of Electronic, Electrical and Computer Engineering, Sungkyunkwan University, Suwon, Korea

²School of Electronic Electrical Engineering, Sungkyunkwan University, Suwon, Korea

³Center for Neuroscience Imaging Research (CNIR), Institute for Basic Science, Suwon, Korea

E-mail: sjinson@skku.edu, hyunjinp@skku.edu*

Abstract— Parkinson's disease (PD) is a degenerative disorder of the central nervous system. In this study, we found functional network alterations in brain regions of AAL atlas between normal control and Parkinson's disease patients. Network measure (i.e., betweenness centrality) of whole brain network showed significant differences in regions related PD. This study might be the first study to perform network analysis of PD based on SPECT imaging.

Keywords— SPECT, Parkinson's disease, Network analysis, Graph-theoretical approach

I. INTRODUCTION

Parkinson's disease is a common neurodegenerative disorder characterized by the motor features of akinesia, tremors, rigidity which are associated with the loss of dopaminergic neurons in dopamine pathways[1].

Single photon emission tomography (SPECT) imaging provides contrast information derived from local radiotracer activity. SPECT imaging using ¹²³I-FP-CIT is specific binding to dopamine transporter[2].

In this study, we aimed to find dysfunctions in regions of dopamine pathways using SPECT functional network. Betweenness centrality is used network measure for finding importance of a given node in terms of network organization. This study is the first study to perform graph-theoretical approach for SPECT imaging.

II. METHODS

A. Subjects and imaging data

We obtained SPECT imaging data from Parkinson's Progression Markers Initiative (PPMI) database. Total 60 subjects were divided into 30 normal control (NC) and 30 Parkinson's disease (PD) patients (Table 1). NC and PD were classified as MDS-UPDRS score by PPMI database.

	NC	PD	<i>p</i> -value
Sex (M:F)	22:8	19:11	-
Age	61.6 (10.5)	59.7 (9.2)	0.459
UPDRS score	1.17 (3.23)	20.8 (8.14)	< 0.001

NC, Normal control; PD, Parkinson's disease; M, Male; F, Female; UPDRS, Unified Parkinson's disease rating scale

B. Image pre-processing

The SPECT images in the PPMI database were standardized from different systems using a system of pre-processing steps. We used an automatic method to propagate ROIs from a pre-defined atlas onto the standard space. A well-known atlas with 90 labeled ROIs is available as a result of previous research. We applied an image registration software based on C/C++ to register the atlas with the standard space of PET using mutual information cost function and affine geometric transform. Once the atlas was registered onto the standard space, we transferred the atlas ROI information onto the PET volume.

C. Network construction and network analysis

Each edge value of correlation matrix was assumed to be the correlation value between two ROIs[3], [4]. Correlation values were computed as a partial correlation, regressing out the effects of age and sex. We adopted a simple network model where un-directed and weighted edges were considered. Weighted network measure was constructed on the correlation matrices using soft thresholding, and then Fisher's *r*-to-*z* transformation was performed for removing the noise signal and comparing between networks. Betweenness centrality (BC), the number of shortest paths between any two nodes that pass through that node was calculated on each node. BC is a local network parameter indicating the importance of a node.

D. Statistical analysis

Group-wise differences based on the network measure were assessed using non-parametric permutation test. Total 60 participants were randomly assigned to the NC

Table 1. Demographic data of NC and PD groups

group, and the remaining participants were assigned to the PD group. For the newly-assigned groups, the correlation matrices were computed for each group, and the three network parameters were subsequently computed. The process was repeated 10,000 times, yielding a null distribution that would be used for group-wise differences. Differences in BC values were deemed significant if they did not belong to the 95% of the null distribution derived from the permutation tests ($p < 0.01$, corrected).

III. RESULTS

A. Significant differences in regions related to PD

We found significant different connection related to PD as follows. The caudate, putamen, thalamus, globus pallidus, associative cortex, limbic cortex and sensorimotor cortex were connected each other ($p < 0.05$). The connections reported in study, used DTI images[5].

B. Alteration of functional hubs

A hub node is a node whose betweenness centrality is higher than the betweenness centrality of nodes in the rest of the brain network. Thus a hub node is considered to be an important region in the brain. We assessed changes in the betweenness centrality of hub nodes in the NC and PD groups. Three regions were identified, as follows. The Left amygdala, left supramarginal gyrus and left angular were found to have group-wise differences in betweenness centrality. The regions reported that reduced in patients with PD[6], [7].

Table 2. Betweenness centrality in altered regions

Region	NC	PD	p-value
Amygdala_L	982	44	< 0.01
Supramarginal_L	714	0	< 0.01
Angular_L	332	0	< 0.01

IV. CONCLUSION

In this study, we found group-wise network differences between NC and PD using SPECT. Furthermore, we first report altered hub regions based on betweenness centrality. Our results contribute to provide brain functional information using SPECT imaging analysis.

ACKNOWLEDGEMENT

This study was supported by the Institute for Basic Science (grant number IBS-R015-D1).

REFERENCES

1. J. M. Shulman, P. L. De Jager, and M. B. Feany, "Parkinson's disease: genetics and pathogenesis.," *Annu. Rev. Pathol.*, vol. 6, pp. 193–222, 2011.
2. L. Wang, Q. Zhang, H. Li, and H. Zhang, "SPECT molecular imaging in Parkinson's disease," *J. Biomed. Biotechnol.*, vol. 2012, 2012.
3. D. Watts and S. Strogatz, "Collective dynamics of 'small-world' networks," *Nature*, vol. 393, pp. 440–442, 1998.
4. E. Bullmore and O. Sporns, "Complex brain networks: graph theoretical analysis of structural and functional systems.," *Nat. Rev. Neurosci.*, vol. 10, no. 3, pp. 186–98, Mar. 2009.
5. M. Sharman, R. Valabregue, V. Perlbarg, L. Marrakchi-Kacem, M. Vidailhet, H. Benali, A. Brice, and S. Lehericy, "Parkinson's disease patients show reduced cortical-subcortical sensorimotor connectivity," *Mov. Disord.*, vol. 28, no. 4, pp. 447–454, 2013.
6. A. Antonini and R. DeNotaris, "PET and SPECT functional imaging in Parkinson's disease," *Sleep Med.*, vol. 5, no. 2, pp. 201–206, 2004.
7. A. J. Harding, E. Stimson, J. M. Henderson, and G. M. Halliday, "Clinical correlates of selective pathology in the amygdala of patients with Parkinson's disease.," *Brain*, vol. 125, no. Pt 11, pp. 2431–2445, 2002.

Automatic hyoid bone tracking from videofluoroscopic swallowing images

J.C. Lee¹, H.J. Ahn¹, J.Y. Kim¹, H.P. Kim¹, K.W. Nam¹, J.S. Ryu², I. Y. Kim¹

¹Department of Biomedical Engineering, Hanyang University

²Department of Rehabilitation Medicine, Seoul National University college of Medicine, Seongnam, Korea

E-mail: jchlee@bme.hanyang.ac.kr

Abstract— In this study, we propose automatic hyoid bone tracking algorithm for dysphagia diagnosis using Local Binary Pattern (LBP) and Multi-scale Local Binary Pattern (MLBP). This algorithm can visualize the movement of the hyoid bone during swallowing into a 2D graph even when the hyoid bone overlaps with the mandible during swallowing.

Keywords— videofluoroscopic, dysphagia, Local Binary Pattern, multi-scale Local Binary Pattern, hyoid bone.

I. INTRODUCTION

Dysphagia is the most prevalent clinical symptom among the patients with neurologic disorders, such as dysphagia [1], and the most popular technique for dysphagia diagnosis is the videofluoroscopic swallowing study (VFSS). In conventional VFSS, 2D moving trajectory of a hyoid bone during swallowing is extracted by manual-analysis of the images [2]. In this study, we propose a semi-automatic hyoid bone tracking algorithm using by Local Binary Pattern(LBP) and Multi-scale Local Binary Pattern (MLBP).

II. METHODS

Automatic hyoid bone tracking was implemented on the basis of both the local binary pattern (LBP) and the multi-scale local binary pattern (MLBP) algorithms [32]. In the first frame, LBP and MLBP models of reference window were calculated, and histograms of reference window calculated. From the next frame on, LBP and MLBP models and histograms of the search window were calculated. Then, position of the hyoid bone was determined by comparing Euclidean distances between values of LBP/MLBP in reference window and values of LBP/MLBP in search window.

III. RESULTS

Percent errors of hyoid bone tracking (missed frame / total frame * 100%) were in the range of 0 – 5.4% ($1.6 \pm 2.0\%$) at 20 non-mandible-overlapped images and 0 – 17.9% ($3.9 \pm 5.7\%$) at 20 mandible-overlapped images (among the 40 images, 22 images showed no errors in overall frames).

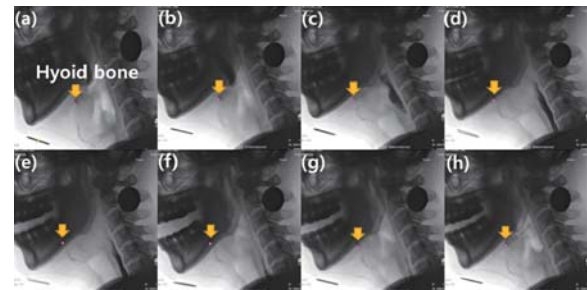


Fig. 1. Step-by-step hyoid bone tracking (fully-automatic) for a mandible-overlapped VF image.

IV. CONCLUSION

We conclude that the proposed algorithm can successfully determine the position of hyoid bone from the VFSS images.

ACKNOWLEDGEMENT

This work was supported by the Basic Science Research Program through the National Research Foundation of Korea (NRF) funded by the Ministry of Science, ICT and Future Planning (NRF-2013R1A1A1004622).

REFERENCES

1. Ertekin, C, Aydogdu, I, Yüceyar, N, Kiylioglu, N, Tarlaci, S, and Uludag, B, "Pathophysiological mechanisms of oropharyngeal dysphagia in amyotrophic lateral sclerosis," *Brain*, vol. 123, pp. 125-140, 2000.
2. Paik N.J., Kim S.J., Lee H.J., Jeon J.Y., Lim J.Y., and Han T.R., "Movement of the hyoid bone and the epiglottis during swallowing in patients with dysphagia form different etiologies," *J Electromyogr Kinesiol*, vol. 18, pp.329-335, 2008.
3. T. Ojala, M. Pietikäinen, and D. Harwood, "A comparative study of texture measures with classification based on featured distributions," *Pattern Recogn.*, vol. 29, pp.51-59, 1996.

Fabrication and Performance Evaluation of High-Frequency Ultrasonic Needle Transducer for Intravascular Ultrasound (IVUS) Image

J. H. Sung, S. M. Ji, S. M. Kim, and J. S. Jeong*

Department of Medical Biotechnology, Dongguk University, Goyang, Republic of Korea
E-mail: jjsspace@dongguk.edu*

Abstract—In diagnosis or monitoring a procedure of therapy, intravascular ultrasound (IVUS) technique is widely used, and therefore a resolution of IVUS image is very important. Consequently, the center frequency of IVUS transducer should be increased to get better image quality. In this paper, high-frequency needle type side-looking IVUS transducer was fabricated and its performance was evaluated by calculating center frequency and -6 dB fractional bandwidth. The results were measured at center frequency of 63 MHz and -6 dB fractional bandwidth of 43 %. Further demonstrate of its feasibility was performed by acquiring IVUS B-mode image with the designed IVUS transducer, which presents that the quality of IVUS B-mode image using the fabricated IVUS transducer can be effectively improved.

Keywords— Ultrasound, IVUS, High-Frequency, ultrasonic needle transducer.

I. INTRODUCTION

Intravascular ultrasound (IVUS) technique is widely used for diagnosing cardiovascular disease or monitoring its therapy [1-2]. Since IVUS transducer is injected to vessel directly and acquires data of inner vessel wall, an IVUS image gives useful information, such as lumen boundary, lumen diameter, or an area of cross sectional vessel wall to a clinician. For precise diagnosis or monitoring therapy, a performance of IVUS transducer plays an important role. A typical way to improve performance of IVUS transducer for a good image quality is increasing center frequency of the IVUS transducer. In this paper, we fabricated high-frequency needle type side-looking IVUS transducer and evaluated its performance by measuring center frequency and -6 dB fractional bandwidth. Finally the result of an IVUS B-mode image with the designed IVUS transducer was shown herein.

II. METHODS

A. Materials and Methods

PMN-PT was used as piezoelectric material and a single matching and a backing layers were used. Silver particle loaded epoxy was used for the matching layer and its acoustic impedance was 7.3 MRayl [1]. The

backing layer was conductive epoxy with acoustic impedance of 5.9 MRayl. To produce IVUS stack, bulk PMN-PT layer was lapped for 60 MHz center frequency and silver particle loaded epoxy was casted on the anterior surface of piezoelectric layer as a matching layer. After that the backing layer was in the rear surface of piezoelectric layer with thickness of 0.4 mm. Later on, the bulk IVUS stack was diced producing several IVUS stacks having aperture size of 0.5 x 0.5 mm and one of those IVUS stack was placed on an IVUS housing with diameter of 1.5 mm. Finally, a signal wire and ground were attached to the conductive matching and backing layers respectively, and a SMA connector was connected to rear part of IVUS housing. Fig. 1 shows fabricated high-frequency needle type side-looking IVUS transducer.

B. Performance Evaluation

To evaluate the performance of the designed transducer, pulse-echo test was conducted. A quartz was used for target and center frequency and -6 dB bandwidth were measured using received signal. Subsequently, its feasibility was further demonstrated by acquiring IVUS B-mode image using the fabricated IVUS transducer. Four cylindrical targets with diameter of 0.72 mm were used. Each target was situated at a distance of 2 mm, 2.5 mm, 3 mm and 3.5 mm from the transducer, and with 90° interval from each other. The scanlines were achieved with 1° interval to acquire 360° rotated image data.

III. RESULTS

A. Pulse-Echo response

Fig. 2 shows the results of single pulse-echo response with the quartz target. The center frequency was measured at 63 MHz and the -6 dB fractional bandwidth was 43 %. Therefore, improved IVUS image can be acquired by using the fabricated transducer because of its high center frequency.

B. IVUS imaging

Fig. 3 shows acquired IVUS B-mode image and the dynamic range was 20 dB. Since the center frequency of the designed transducer was high, the targets were

shown very clearly. Although it seems that there were two targets located at 3 mm instead of two targets located at 3 mm and at 3.5 mm each, it is because of experimental error, and it could be corrected by increasing precision of alignment.

IV. CONCLUSION

In this paper, high-frequency needle type side-looking IVUS transducer was fabricated and its performance was evaluated by measuring center frequency and -6 dB fractional bandwidth at single pulse-echo response, and by producing IVUS B-mode image using the designed IVUS transducer. The results show that the fabricated IVUS transducer can effectively improve the quality of IVUS image.

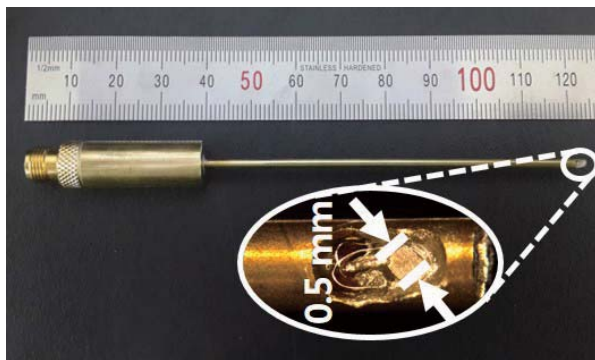


Fig. 1. Fabricated 63 MHz needle type side-looking IVUS transducer

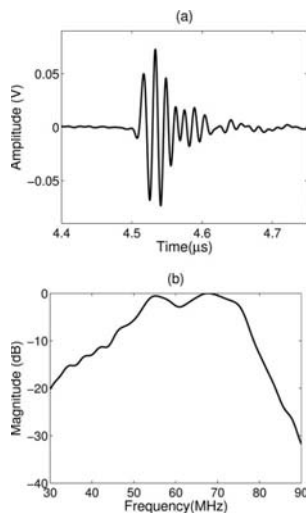


Fig 2. Pulse-echo response of the fabricated 63 MHz needle type side-looking IVUS transducer



Fig. 3. IVUS B-mode image using the fabricated IVUS transducer.

ACKNOWLEDGEMENT

This work was supported by International Collaborative R&D Program funded by the Ministry of Trade, Industry & Energy (MOTIE), Korea (N01150049, Developing high frequency bandwidth [40~60MHz] high resolution image system and probe technology for diagnosing cardiovascular lesion), the MSIP (Ministry of Science, ICT and Future Planning), Korea, under the C-ITRC (Convergence Information Technology Research Center) (IITP-2015-H8601-15-1004) supervised by the IITP (Institute for Information & communications Technology Promotion), and R&D Program of ministry of Trade, industry and Energy/Korea Evaluation institute of industrial Technology (Grant No, MOTIE/KEIT 10048528, Development of ICT based Wireless Ultrasound Solution for Point-of-Care Applications).

REFERENCES

1. X. Li, W. Wu, Y. Chung, Y. Shih, W. Shih, Q. Zhou, K. K. Shung, "80-MHz intravascular ultrasound transducer using PMN-PT free-standing film," *IEEE Trans. Ultrason., Ferroelectr. Freq. Control*, vol. 58, pp. 2281-2288, 2011.
2. Q. Zhou, X. Xu, J. Gottlieb, L Sun, J. M. Cannata, H. Ameri, M. S. Humayun, P. Han, K. K. Shung, "PMN-PT single crystal, high-frequency ultrasonic needle transducer for pulse-wave Doppler application," *IEEE Trans. Ultrason. Ferroelectr. Freq. Control*, vol.54, pp. 668-675, 2007

Reconstructing structural brain network using Cross Diffusion

Yong-Ho Choi¹, Collins Kwadwo Boahen¹, Jong-Min Lee¹

¹Department of Biomedical Engineering, Hanyang University, Seoul, South Korea

E-mail: chldydgh0128@bme.hanyang.ac.kr

Abstract—We propose a method of reconstructing structural brain network by combining morphological information from gray and white matter.

Keywords— Structural correlation network, connectivity network, combined network.

I. INTRODUCTION

Recently, graph representations of brain connectivity have attracted a lot of interest and used to analysis brain network property. We propose a method of reconstructing structural brain network by combining morphological information from gray and white matter. And combined network is analyzed to compare characteristics [1,2].

II. METHODS

A. Subjects

The present study adopted 80 participants of Human Connectome Project S500 data released in June 2014.

B. Structural correlation network (SCN)

Structural images were processed using CIVET pipeline to calculate cortical thickness. And we use automated anatomical labeling template to separate cerebral cortex into 78 regions. For each subject, mean thickness of vertices belonging to that region is calculated. To remove the effect of multiple variables as age, gender and mean thickness, linear regression was performed. The residual of regression was used to construct a correlation matrix by calculating Pearson correlation coefficient between all pairs of regions.

C. Group connectivity network (GCN)

Diffusion images were preprocessed using the HCP Diffusion pipeline and DSI studio. A deterministic fiber tracking algorithm was used [3]. The angular threshold was 45 degrees. The step size was 0.625 mm. Estimated fiber trajectories in white matter were smoothed by averaging the propagation direction with 20% of the previous direction. The fiber tracking results were used to calculate quantities between any two regions. These quantities were used for constructing the structural connectivity network. Since structural correlation network is derived from the population, we averaged individual connectivity network

D. Combine network using Cross Diffusion (DN)

A nonlinear method that iteratively updates two networks used to making similar to the others [2].

III. RESULTS

A. Network properties

Table 1. Network Properties

Property	SCN	GCN	DN
Density	0.44	0.4	0.4
Global Efficiency	0.85	0.82	0.92
Characteristic Path Length	1.24	1.37	1.15
Clustering Coefficient	1.5	1.54	1.65
Smallworldness	1.21	1.12	1.44

IV. CONCLUSION

We proposed combined network, which has information from gray and white matter. It is analyzed and confirmed a result, it presents human brain properties.

ACKNOWLEDGEMENT

This work was supported by the NRF grant funded by the Korea government (MEST) (2011-0028333).

Data were provided by the Human Connectome Project, WU-Minn Consortium (Principal Investigators: David Van Essen and Kamil Ugurbil) funded by 16 NIH Institutes and Centers that support the NIH Blueprint for Neuroscience Research; and by the McDonnell Center for Systems Neuroscience at Washington University.

REFERENCES

1. Rubinov, M., Sporns, O., "Complex network measures of brain connectivity: uses and interpretations," *Neuroimage.*, vol. 52 pp. 1059-69, 2010.
2. Wang, B., Jiang, J., Wang, W., Zhou, Z.-H. & Tu, Z., "Unsupervised metric fusion by cross diffusion," *IEEE Comput. Vis. Pattern Recognit.*, pp. 2997-3004, 2012.
3. F. C. Yeh, V. J. Wedeen and W. Y. Tseng, "Generalized q-sampling imaging," *IEEE Trans Med Imaging.*, vol. 29, pp. 1626-1635, 2010.

Scale-Independent Network Hub of the Diffusion Weighted Structural Network

Hunki Kwon¹, Oh-Hun Kwon¹, Yong-Ho Choi¹, Sang Won Seo², Jong-Min Lee¹

¹Department of Biomedical Engineering, Hanyang University, Seoul, South Korea

²Department of Neurology, Samsung Medical Center, Sungkyunkwan University School of Medicine, Seoul, South Korea

E-mail: khk11103@bme.hanyang.ac.kr

Abstract—Network hub plays a key role in network for efficient communication, to interpret network as a complex system. In this work, we hypothesized that network hub should be consistent while nodal scale is varied in certain range. We proposed the methodological framework to test our hypothesis. Some network hub regions derived from our method can be used for group comparison in terms of various effects such as age, gender and disease.

Keywords— diffusion tensor imaging; connectome; network hub; neuroimaging; spatial resolution

I. INTRODUCTION

Network hub has been considered as one of the most important topological properties, which plays a key role in network for efficient communication, to interpret network as a complex system [1]. Previous structural connectome studies have reported the network hub regions based on various nodal resolutions [2]. Interestingly, these studies reported the different hub regions, which suggested that network hub regions have strong dependence on network nodal scale. We proposed the methodological framework to define optimal network hub map considering various nodal scale.

II. METHODS

A. Subjects

The present study included data set from 54 normal subjects by the Samsung Medical Center, Seoul, Korea.

B. Image preprocessing

An automated processing-pipeline (CIVET) is used to extract surfaces of the inner and outer cortex. DTI data was processed using the FMRIB Software Library (<http://www.fmrib.ox.ac.uk/fsl>). The DTI tractography was performed using FACT algorithm implemented in Diffusion Toolkit in the diffusion MR space and about 100,000 fibers were extracted in each subject.

C. Parcellating the cortex with different resolution scales

Each neocortical hemisphere was then parcelled twenty times into 100, 200, 300, 400, 500, 600 ROIs using the k-means algorithm informed with the

Euclidean distances between coordinates on sphere model. The parcelled ROIs transformed to white matter surface matched with sphere model. Finally, weighted structural networks represented by symmetric ROIs * ROIs matrices were constructed for each individual using FA value in connected fibers.

D. Mapping network parameters to average surface

All individual network hub maps were smoothed with a 10 mm full width at half maximum kernel, to decrease spatial variability between subjects of assumed hub areas.

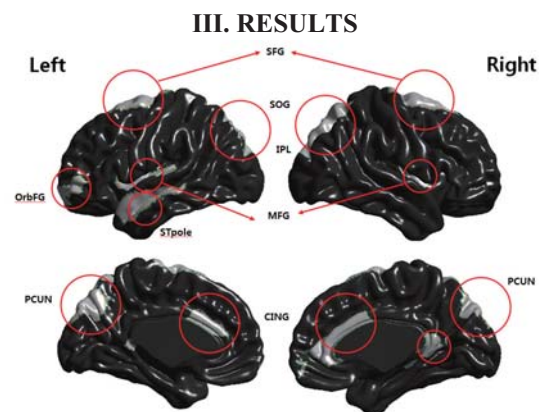


Fig. 1. Group network hub area

III. RESULTS

IV. CONCLUSION

We proposed the methodological framework for defining scale-independent structural network hub. Clusters divided from this method can be used for group comparison in terms of various effects such as age, gender and disease.

ACKNOWLEDGEMENT

This work was supported by the National Research Foundation of Korea(NRF) grant funded by the Korea government(MEST) (2011-0028333).

REFERENCES

1. Sporns, O., G. Tononi, and R. Kötter, The human connectome: A structural description of the human brain. *PLoS Comput Biol*, 2005. 1(4): p. e42.
2. Zalesky, A., et al., Whole-brain anatomical networks: does the choice of nodes matter? *Neuroimage*, 2010. 50(3): p. 970-83.

Preliminary survival analysis based on PRM method for HCC patients treated by TACE

Jonghoon Kim¹, Hyunjin Park^{2,3}

¹Department of Electronic Electrical and Computer Engineering, Sungkyunkwan Univ, Suwon, Korea

²School of Electronic and Electrical Engineering, Sungkyunkwan Univ, Suwon, Korea

³Center for Neuroscience Imaging Research (CNIR), Institute for Basic Science, Suwon, Korea

E-mail: jhkim4915@skku.edu, hyunjinp@skku.edu

Abstract— It is important to predict patient's survival after a given treatment for so that therapy planning could be improved. A novel image analysis method called parametric response mapping (PRM) was applied hepatocellular carcinoma (HCC) patients treated with transcatheter arterial chemoembolization (TACE) in this study. Here, we applied to PRM to distinguish between response and non-response groups and analyzed overall survival among groups stratified by manual and automatic methods using Kaplan-Meier approach. We found better survival predictors based on advance image processing algorithm, PRM.

Keywords— HCC, Parametric response mapping, Survival analysis, Longitudinal study, Dynamic CT.

I. INTRODUCTION

HCC is the third leading cause of cancer deaths worldwide, with over 500,000 people affected [1]. TACE is being widely used and has become the standard treatment modality for patients with unresectable, specifically those with inter-mediate-stage HCC [2]. In previous researches, cross-sectional imaging with computed tomography (CT) scanning and magnetic resonance imaging (MRI) is most commonly used to detect HCC. An image analysis method, parametric response mapping has been shown to be more sensitive at detecting changes of treatment response than conventional approaches [3]. In brief, the PRM approach spatially aligns longitudinal images before and after treatment and then classifies voxels within a given ROI into three types of unchanged, increased, and decreased in intensity. In this study, we examined to identify whether survival analysis based on PRM method is better predictor than based on manual approach.

II. METHODS

A. Subjects and CT Imaging

Twenty subjects with HCC are recruited and underwent longitudinal multiphase liver CT scan before and after TACE. Among a triple phase CT (i.e., arterial, portal, and equilibrium phases), arterial phase is used for this study. All patients were required more

than three follow-up CT images for PRM analysis longitudinally. All patients were stratified by modified Response Evaluation Criteria in Solid Tumor (RECIST) for assessing tumor response after treatment manually [4].

B. PRM analysis and Longitudinal study

We considered the longitudinal arterial phase of dynamic CT for a given patient. Two consecutive scans, arterial phase image of early time point and arterial phase image of late time point, considered for the PRM analysis. A non-rigid registration was applied to model the complex deformation between longitudinal scans. Then, two ROIs of the tumors were drawn on the early time image and the mapped late time image. Individual voxels within the ROI were classified based on the extent of change observed in voxel intensity measure in Hounsfield Unit (HU). The PRM approach yields scatter plot including three regions which experienced gain in value greater than a pre-determined threshold were designated red, decreased by more than the threshold were designated blue, and otherwise designated green indicating no significant change and obtains more sensitive changes than conventional analysis. Also, we computed slope between PRM+ values in follow-up CT.

C. Survival and Statistical Analysis

Overall survival was defined as the time from TACE to death or final follow-up visit. The Kaplan-Meier model was used to estimate survival. Differences in the survival rate were assessed by log-rank testing. Comparisons were performed using Student's *t*-test, and $P < 0.05$ indicated statistical significance.

III. RESULTS

A. Group Difference using PRM analysis

We applied the PRM analysis twenty patients, obtained the PRM values and computed slope values between PRM values in longitudinal datasets. Two groups are stratified by auto-threshold calculated by slope values, Response-Auto (mean[std], 0.01[0.09]) and Non-response-Auto (mean[std], -0.13[0.02]). There is significant difference, p-value of 0.0019, between two groups, (Fig 1).

B. Survival analysis using Kaplan-Meier Approach

Median overall survival after TACE was 18.8 and 7.2 months for the each group, Response and Non-response, while, in automatic approach, median overall survival was 21 and 7.2 months. In manual approach, the survival curves yielded, [hazard ratio (HR), 0.12; p-value 0.049], (Fig 2). In PRM approach, the result was, [hazard ratio (HR), 0.03; p-value 0.02], (Fig 3).

IV. CONCLUSION

We confirmed significant difference of p-values between slope of PRM+ values. Our proposed approach suggested the improved classifier as distinguishing between Response and non-response as imaging biomarker. Then, we observed overall survival curves in manual and PRM approach. Two approaches represented slightly difference of the values, hazard ratio (HR) and median overall survival. In our approach, response group showed more survival rate than manual approach. In this study, we confirmed that manual assessment of imaging features did not lead to good prediction of survival for HCC patients after TACE. Therefore, we expect to better survival predictor based on advance image processing algorithm, PRM.

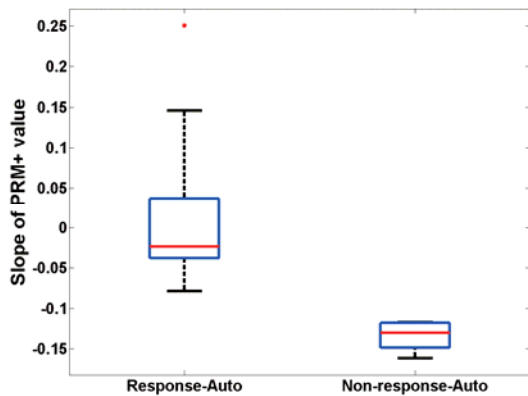


Fig. 1. Slope of PRM+ value

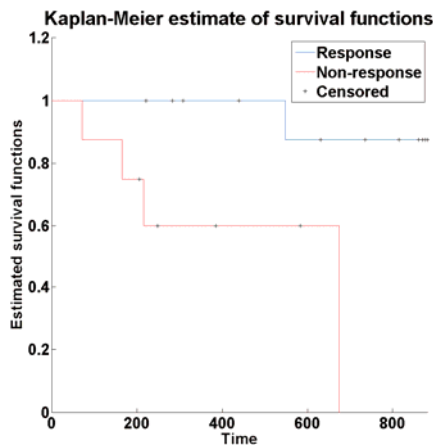


Fig. 2. Overall Survival Curve in manual Approach

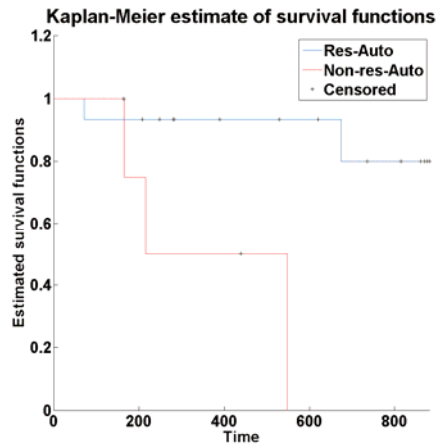


Fig. 3. Overall Survival Curve in PRM Approach

ACKNOWLEDGEMENT

This study was supported by the Institute for Basic Science (grant number IBS-R015-D1).

REFERENCES

1. El-Serg HB. "Hepatocellular carcinoma: an epidemiology view," *J Clin Gastroenterol* 2002., 35(Suppl. 2): S72-8.
2. Llovet JM, Bruix J. "Systematic review of randomized trials for unresectable hepatocellular carcinoma: chemoembolization improves survival," *Hepatology* 2003; 37: 429-42
3. C.J. Galbán, T.L. Chenevert, C.R. Meyer, C. Tsien, T.S. Lawrence, D. Hamstra, L. Junck, P.C. Sundgren, T.D. Johnson, D.J. Ross, A. Rehemtulla, and B.D. Ross, "The parametric response map is an imaging biomarker for early cancer treatment outcome.," *Nature medicine*, vol. 15, no. 5, pp. 572-6, 2009 .
4. Lencioni R, Llovet JM. "Modified RECIST (mRECIST) assessment for hepatocellular carcinoma," *Semin Liver Dis.*, 30(1):52-60.
5. Therneau T, Grambsch P. "Modeling Survival Data: Extending the Cox Model," *New York: Springer-Verlag, 2000.*

Differences among normal subjects and ADHD subtypes based on three connectivity parameters

Seunghak Lee¹, Hyunjin Park^{2, 3,*}

¹Department of Electronic Electrical and Computer Engineering, Sungkyunkwan Univ, Suwon, Korea

²School of Electronic and Electrical Engineering, Sungkyunkwan Univ, Suwon, Korea

³Center for Neuroscience Imaging Research (CNIR), Institute for Basic Science, Suwon, Korea

E-mail: sunghark87@skku.edu¹, hyunjinp@skku.edu^{*}

Abstract— Attention-deficit/hyperactivity disorder (ADHD) is a wide-spread psychiatric disorder. ADHD is further sub-divided into inattention (IA), Hyperactivity/impulsive (HI), and combined (C) subtypes. In this study, we considered normal, inattention subtype and combined subtypes subjects. We hypothesized that functional MRI connectivity analysis can be used to differentiate between normal and two sub types of ADHD. As a result, we found brain regions ($p < 0.05$) with significant connective differences among normal and three ADHD sub groups.

Keywords— ADHD, fMRI, Functional connectivity, ADHD subtypes

I. INTRODUCTION

Attention-deficit/hyperactivity disorder (ADHD) is a one of most famous in psychiatric disorder. ADHD divided into three sub type; inattention (IA), hyperactive/impulsive (HI) and combined (C) type referenced by Diagnostic and Statistical Manual of Mental Disorders (DSM) [1, 2]. Functional connectivity is the connectivity between separated brain regions using fMRI. The connectivity had many parameters including betweenness centrality (BC), degree (DEG) and Eigen vector centrality (EVC).

Here we compare brain network parameter between normal group and ADHD sub type groups using task fMRI.

II. METHODS

A. Subject and Imaging data

fMRI data were acquired from Human connectom Project database [3]. Image data of each subjects received as follows; using Siemens Skyra 3T scanner. Image matrix = 104x90; number of slices = 1200; pixel resolution = 2 mm isotropic; slice thickness = 2 mm; TR = 720 ms; TE = 33 ms.

We chose thirty subjects for four groups. First group is normal group (male: 4, female: 6 and mean age:

29.5). Second group is IA group (male: 7, female: 3 and mean age: 27.9) and third group belonged to Combined (male: 4, female: 6 and mean age: 27.2). Fourth group was selected randomly subjects in ADHD sub group (IA: 5 subjects, C: 5subjects). Each group had ten subjects and was classified according to Diagnostic and Statistical Manual of Mental Disorders (DSM) score. (See the Table 1.)

Table 1 Subject information (C: combined; IA: inattention)

	C	IA	NORMAL
SEX (M:F)	4:6	7:3	4:6
AGE	27.2	27.9	29.5
DSM INATTENTION	8.6	8.3	2.3
DSM COMBINED	14.7	11.4	4.5

B. Image processing

All imaging data pre-processed using FreeSurfer [4] and FSL [5]. First we corrected gradient field non-linearity using FreeSurfer. Head motion was corrected by rigid body transformation using FSL' FLIRT and Time series images were registered onto T1 structural image. Using FSL, we resliced onto the T1 to standard Montreal Neurological Institute (MNI) space. Intensity normalization was applied the time series dataset and nuisance variables were regressed out. Finally we applied band-pass filter ranging 0.009 and 0.08Hz to dataset.

C. Connectivity analysis

The Automated Anatomical Labeling (AAL) with 116 ROIs was co-registered fMRI data. The node of a correlation matrix represents ROI and edge represents the correlation value between two different regions. We adopted a simple network model considering undirected and unweighted edges. The raw correlation matrices were z-transformed using Fisher's r-to-z transformation (See the figure.1). We adopted various network parameters including BC, DEG and EVC that represent the degree of importance of a given node.

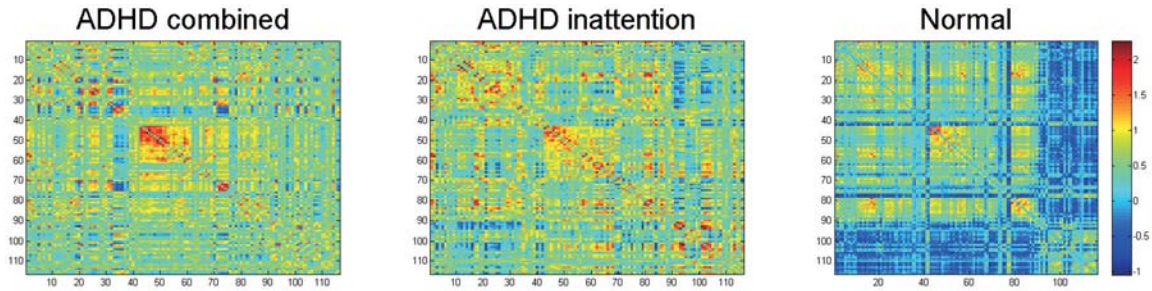


Figure 1 Whole brain connectivity matrix. The axis value varies between 1 and 116. Each axis value corresponds to one row in the correlation matrix.

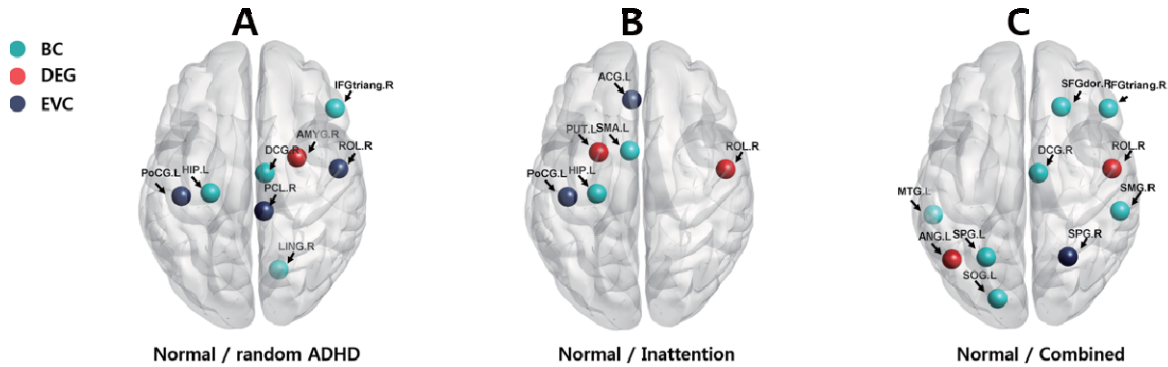


Figure 2 Visualization of difference regions between Normal / random ADHD, Normal / Inattention and Normal / Combined. (IFGtriang.R = Inferior gyrus triangular part, DCG.R = Median cingulate and paracingulate gyri, HIP.L = left hippocampus, LING.R = Right lingual gyrus, PoCG.L = Left postcentral gyrus, AMYG.R= Right amygdala, ROL.R = Rolandic operculum, PoCG.L = Left postcentral gyrus, PCL.R = Right paracentral lobule, SFGdor.R = Right superior frontal gyrus, SOG.L = Left superior occipital gyrus, Left superior parietal lobule, SMG.R = Right supramarginal gyrus, MTG.L = Left middle temporal gyrus, ANG.L = Left angular gyrus, SPG.R = Right superior parietal lobule, SMA.L = Left supplementary motor area, PUT.L = Left putamen, ACG.L = Left anterior cingulate gyrus, PoCG.L = Left postcentral gyrus)

III. RESULTS

A. Normal vs. random ADHD group

We found significant region BC, DEG and EVC between normal group and randomly ADHD group. (See the Figure.2A) BC value had five significant difference regions ($p < 0.05$; Inferior gyrus triangular part ($p = 0.044$), Median cingulate and paracingulate gyri ($p = 0.008$), left hippocampus ($p = 0.023$), Right lingual gyrus ($p = 0.031$), Left postcentral gyrus ($p = 0.021$)). DEG value had only one significant difference region ($p < 0.05$; Right amygdala ($p = 0.037$)). Finally EVC value had three regions ($p < 0.05$; Right Rolandic operculum ($p = 0.037$), Left postcentral gyrus ($p = 0.005$), Right paracentral lobule ($p = 0.023$)).

B. Normal vs. sub group

We also tested between sub group (IA, combined) and found significant regions. In IA case, BC value had seven significant difference regions ($p < 0.05$; Right superior frontal gyrus ($p = 0.012$), Right inferior frontal gyrus ($p = 0.033$), Right midcingulate area ($p = 0.014$), Left superior occipital gyrus ($p = 0.039$), Left superior

parietal lobule ($p = 0.049$), Right supramarginal gyrus ($p = 0.029$), Left middle temporal gyrus ($p = 0.011$)). DEG had two difference region ($p < 0.05$; Right Rolandic operculum ($p = 0.043$), Left angular gyrus ($p = 0.027$)). EVC had two difference regions ($p < 0.05$; Right superior parietal lobule ($p = 0.044$), Left angular gyrus ($p = 0.012$); See the Figure.2B).

In combined case, BC value had two difference region ($p < 0.05$; Left supplementary motor area ($p = 0.032$), Left hippocampus ($p = 0.021$)). DEG value had two difference regions ($p < 0.05$; Left putamen ($p = 0.021$), Right Rolandic operculum ($p = 0.032$)). EVC had four difference regions ($p < 0.05$; Right Rolandic operculum ($p = 0.021$), Left anterior cingulate gyrus ($p = 0.02$), Left postcentral gyrus ($p = 0.032$), Left putamen ($p = 0.001$); See the Figure.2C).

IV. CONCLUSION

As a result, we found some difference regions between normal group and ADHD sub group using BC, DEG and EVC. But, we tested limited subject, so our result had not powerful statistical power. Therefore we will collect more ADHD sample, medical parameter and gene parameter for increasing statistical power.

ACKNOWLEDGEMENT

This study was supported by the Institute for Basic Science (grant number IBS-R015-D1).

REFERENCES

1. American Psychiatric Association (1994), 'Diagnostic and Statistical Manual of Mental Disorders, 4th ed.', Washington, DC, American Psychiatric Press.
2. Bush G, Valera EM, Seidman LJ (2005), 'Functional neuroimaging of attention-deficit/hyperactivity disorder: a review and suggested future directions', *Biol Psychiatry* vol. 57, pp. 1273–1284.
3. David C. Van Essen, Stephen M. Smith, Deanna M. Barch, Timothy E.J. Behrens, Essa Yacoub, Kamil Ugurbil, for the WU-Minn HCP Consortium. (2013). The WU-Minn Human Connectome Project: An overview. *NeuroImage* 80(2013):62-79.
4. Fischl B (2012), 'FreeSurfer', *Neuroimage* vol. 62, pp. 774–781.
5. Jenkinson M, Beckmann CF, Behrens TE, Woolrich MW, Smith SM (2012) FSL. *Neuroimage* 62:782-790.

Temporal Domain Analysis for Dynamic PET Diagnosis

JeongHee Shin¹, JungSoo Kim², YoungJin Jung¹

¹Radiological Science, Dongseo University, Busan, 47011 South Korea

²Radiological Science, Dongnam Health University, Suwon, 16328 South Korea

E-mail: microbme@dongseo.ac.kr

Abstract— In this study, A novel approach for dynamic PET data analysis was demonstrated. In order to extract significant PET imaging from original dynamic PET data, spatio-temporal domain information was employed over singular value decomposition. Results from this study show the potential of clinical translation.

Keywords—PET, temporal analysis, singular value decomposition.

I. INTRODUCTION

Positron emission tomography (PET) is often utilized using single-time-point image of tracer uptake or static imaging that can provide a functional map of regional tracer concentration. Although static PET image can provide significant evidence for diagnosis, there is no temporal information that can provide more information about in vivo biology by delineating both the temporal and spatial pattern of tracer uptake.

In order to overcome this issue, Dynamic PET imaging can be golden solution for various clinical purposes. However, in-sufficient measuring time do not allow to provide good image quality thereby limiting to apply clinical applications.

We proposed a novel approach that can enhance the image quality of dynamic PET by employing a spatio-temporal analyzing technology.

II. METHODS

For reduction of noise component from dynamic PET image, the singular value decomposition (SVD) was employed to linearly decompose a measured dynamic PET images [1]. Fig. 1 show the total procedure of proposed approach for spatio-temporal analysis.

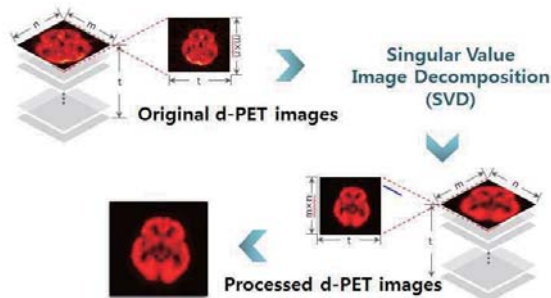


Fig. 1 Procedure of proposed approach for improving image quality of dynamic PET. The measured dynamic PET images subjected to SVD for image processing

III. RESULTS

A. Spatio-temporal analysis for dynamic PET images.

Fig. 2 show a significant difference between original PET image and processed PET image according to time. Especially, Fig. 3 demonstrated how to decompose the original dynamic PET image in order to reduce noise component.

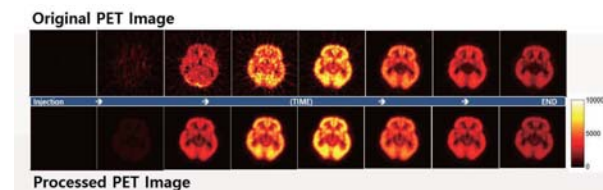


Fig. 2 a comparison between original PET image and processed PET image. First row is original image, second row image is SVD processed image.

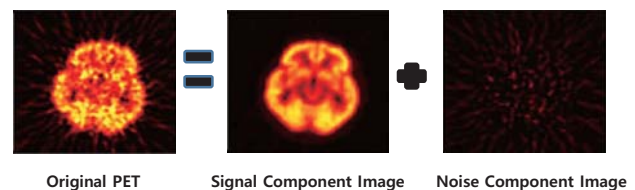


Fig. 3 Difference between original and signal component PET image at the same time position.

IV. CONCLUSION

In this study, the spatio-temporal analysis technique was developed to analyze 2D PET image in order to utilize temporal information for extension of clinical application of dynamic PET test. The proposed approach show a significant enhancement of image quality, can be promise tool for clinical translation.

ACKNOWLEDGEMENT

This research was supported by the Brain Research Program through the National Research Foundation of Korea(NRF) funded by the Ministry of Science, ICT & Future Planning (NRF-2015M3C7A1031969).

REFERENCES

- [1] Y.-J. Jung, J. Gonzalez, and A. Godavarty, "Functional near-infrared imaging reconstruction based on spatiotemporal features: venous occlusion studies," *Appl. Opt.*, vol. 54, no. 13, pp. D82–D90, 2015.

Gender differences on cortical alteration in adolescent with internet addiction

A. Min¹, M. H. Lee¹, Y. H. Hwang¹, D. Y. Kim¹, B. S. Han² and H. S. Seo³

¹Department of Biomedical Engineering, Yonsei University, Wonju, Korea

²Department of Radiological Science, Yonsei University, Wonju, Korea

³Department of Radiology, Korea University Ansan Hospital, Ansan, Korea

E-mail: areummin@yonsei.ac.kr

Abstract— Internet addiction(IA) is recently becoming one of serious mental health issues. We investigated differences in the cortical surface area and volume between IA and control groups in male and female. Male with IA showed more reduction of cortical surface area and volume in occipital, parietal and frontal regions than control. Female with IA showed more reduction of cortical surface area and volume in frontal regions than control ($p < 0.05$).

Keywords— Internet addiction, Cortical surface area, Cortical volume

I. INTRODUCTION

Compulsive internet use might lead to negative effects on daily life and emotional stability. This phenomenon is called internet addiction(IA). Male and female with IA showed differences in the clinical symptom and internet use [1]. These differences may be associated with those of the brain changes between genders with IA. Therefore, we compared the differences in male group and female group by measuring the cortical surface areas and volumes.

II. METHODS

A. Subjects and data acquisition

We analyzed T1-weighted data acquired from 3T MR scanner(Siemens, Germany) for 15 subjects(7 female) IA and 15control subjects(7 female). Age range of all subjects is 11-18 years old. Each subject was matched for age and handedness. In this study, we employed Internet Addiction Test to classify the subjects into IA or control group.

B. Cortical analysis

The Freesurfer 5.3.0 package was used to make a cortical surface of 3D model for measuring cortical surface area and continuity information from the MR volume to construct representation of white matter surface and pial surface [2]. We investigated differences in cortical surface area and volume between IA and control group in male and female. For the statistical analysis, we used one-way ANOVA.

III. RESULTS

Male with IA showed more reduction of cortical surface area and volume in frontal, occipital and

parietal regions than control male. Female with IA showed more reduction of cortical surface area and volume in frontal regions than control female.

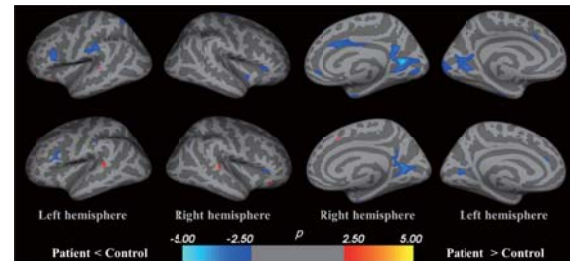


Fig. 1. Significant differences between IA and control group in male upper: cortical area, bottom: cortical volume.

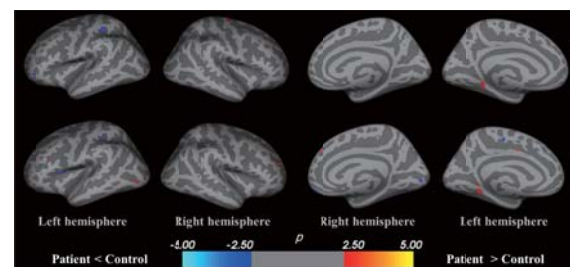


Fig. 2. Significant differences between IA and control group in female upper: cortical area, bottom: cortical volume.

IV. CONCLUSION

In this study, we found differences between male and female groups with IA in some regions which showed alteration of the cortical areas or volumes. Our findings are considered to result from difference in internet use between the two groups [1].

ACKNOWLEDGEMENT

This research was supported by the Leading Foreign Research Institute Recruitment Program through the National Research Foundation of Korea (NRF) funded by the Ministry of Science, ICT & Future Planning (2010-00757).

REFERENCES

1. Z. Oktuğ, "Gender differences in Internet addiction and tendency to express emotions," *The Online Journal of Counselling and Education*, vol. 39, 2013.
2. A. M. Dale, B. Fischl, and M. I. Sereno, "Cortical surface-based analysis: I. Segmentation and surface reconstruction," *Neuroimage*, vol. 9.2, pp. 179-194, 1999.

Current density of *in vivo* canine brain during transcranial direct current stimulation (tDCS)

S.Z.K. Sajib¹, W.C. Jeong¹, N. Katoch¹, B.K. Choi¹, H.J. Kim¹, O.I. Kwon² and E.J. Woo¹

¹Department of Biomedical Engineering, Kyung Hee University, Seoul, Korea

²Department of Mathematics, Konkuk University, Seoul, Korea

E-mail: ejwoo@khu.ac.kr

Abstract—MR-based current density imaging technique is developed to monitor the current flow inside the brain tissue during tDCS. Though tDCS has proved its effectiveness for treating certain neuropsychiatric diseases but the underlying mechanism still challenging and important research issue. However, quantitative visualization of the induced current density could help to understand the neuro-modulatory effect of tDCS treatment.

Keywords— tDCS, current density, conductivity, diffusion tensor, MREIT.

I. INTRODUCTION

Transcranial direct current stimulation (tDCS) is a neuro-modulatory technique for treating neuropsychiatric diseases. During tDCS, DC current is injected into the head through a pair of electrodes attached on the scalp. Therefore, imaging of the current density play an important role to understand the therapeutic effects. Lately, Kwon *et al.* [1] proposed a method to visualize the current density distribution by combing directional information obtained from DT-MRI scan with the measured magnetic flux density data [2]. In this paper, we report the results of our first animal experiment of current density imaging during tDCS.

II. METHODS

A. Animal imaging experiment

In this study, we use a beagle as an animal subject. For imaging experiment, we anesthetized the dog and clipped hair on the head to attach the electrodes and positioned inside the 3 T MRI scanner. Using custom design of current source we inject 3 mA current inside the head. We collect the B_z data of three slice position using T1-mFFE sequence. We also perform the DTI experiment using the SS-SE-EPI sequence with the b -value 1000 sec/mm². The experimental protocol was approved by IACUC (Kyung Hee University).

B. Reconstruction of current density image

At the beginning, we numerically solve the Laplace equation and determine the model predicted current density and magnetic flux density. Here we assume that, the conductivity tensor is a scalar multiple of the water diffusion tensor. By comparing the error

differences between the measured and computed magnetic flux density data, we then iteratively update the internal distribution of current density [1],

$$\mathbf{J}^{n+1} = \mathbf{J}^n + \frac{1}{\mu_0} \left(\frac{\partial(B_z - B_z^n)}{\partial y}, -\frac{\partial(B_z - B_z^n)}{\partial x} \right) \quad (1)$$

III. RESULTS

Figure 1(a) shows the acquired MR magnitude images of the first two slices. The magnitude of the reconstructed current density at different iteration steps of the same slices were displayed in figure 1(b).

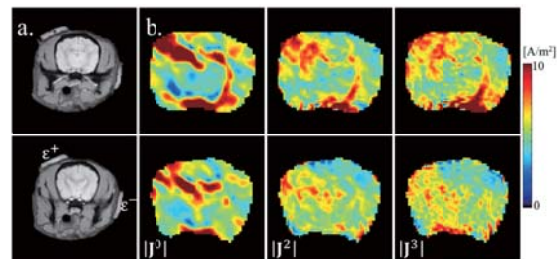


Fig.1. MR magnitude and reconstructed current density map inside the brain region at two slice position.

IV. CONCLUSION

Success of the tDCS treatment depends on the induced current density distribution within different anatomical structures of the brain. We hope, quantitative visualization of the current density distribution in the brain will play an important role in monitoring the tDCS treatment.

ACKNOWLEDGEMENT

This work was supported by the National Research Foundation (NRF) of Korea grant funded by the Korean government (MSIP) (No. 2014R1A2A1A09006320).

REFERENCES

1. O.I. Kwon et al., "Current Density Imaging during Transcranial Direct Current Stimulation (tDCS) using DT-MRI and MREIT: Algorithm Development and Numerical Simulations," *IEEE Trans. Biomed. Eng.*, article in press.

IBEC2015, Road to Better Life through Biomedical Engineering

2. J.K. Seo, and E.J. Woo “Electrical Tissue Property Imaging at Low Frequency Using MREIT”, *IEEE Trans. Biomed. Eng.*, vol. 61, pp. 1390-1399, 2014.

MR-based electrical conductivity imaging of brain metabolites

W.C. Jeong, S.Z.K. Sajib, N. Katoch, B.K. Choi, H.J. Kim and E.J. Woo

Department of Biomedical Engineering, Kyung Hee University, Seoul, Korea

E-mail: cjwoo@khu.ac.kr

Abstract—The purpose of this study is to show new approach of brain metabolites mapping. We propose electrical conductivity-based metabolite mapping with highly sensitive to its concentration changes. Together with *in vitro* measurement of metabolites by concentration changes, we performed phantom imaging to evaluate the proposed method showing a significant relationship between concentration and electrical conductivity of brain metabolites.

Keywords— Electrical conductivity, ion concentration, brain metabolites, MRI, MREIT.

I. INTRODUCTION

Electrical tissue conductivity is primarily determined by concentration and mobility of ions. If electrical current is carried by dissolved ions, the more ions generate more currents. In addition, the mobility of ions is restricted by heterogeneous membrane, current density of tissue dependent on the physical environment even though it has uniform ion concentration. Using MREIT technique [1], we provide electrical conductivity-based metabolite mapping with highly sensitive to its concentration changes.

II. METHODS

A. Conductivity measurement

To investigate the relationship between concentration and electrical conductivity of brain metabolites, we measured the actual conductivities of each brain metabolites by changing their concentration using an impedance analyzer (SI1260A, AMETEK Inc., UK) as shown in Fig. 1(a).

B. Imaging experiment

Using a current source, the imaging currents were injected between one opposing pair of electrodes as shown in Fig. 1(b). We obtained two different sets of data from *in vitro* phantom imaging. One is data from agarose anomalies of single metabolite without any other metabolites (marked “metabolite only”). The other is data from agarose anomalies of single metabolite with other metabolites having a fixed concentration of their natural condition in living tissue

(marked “metabolite dominant”). After the imaging, absolute conductivity image was reconstructed [2].

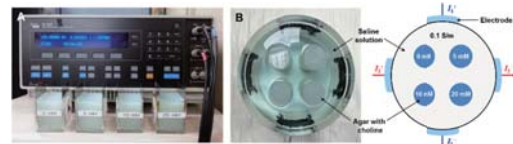


Fig. 1. *In vitro* measurements of electrical conductivity (a) and setup for phantom imaging (b).

III. RESULTS

Fig. 2(a) shows the results of direct measurement of actual conductivities from each brain metabolites with the changes of their concentration. Electrical conductivity images at two different conditions show “metabolite only” (b) and “metabolite dominant” (c).

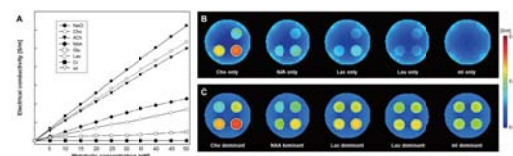


Fig. 2. Graph for relationship between concentration and measured electrical conductivity (a) and electrical conductivity image (b and c).

IV. CONCLUSION

In this study, the conductivity images of choline showed highly sensitive with the changes of its concentration among the brain metabolites. Since the choline is regarded as a tumor marker and/or cell wall marker in brain diseases, the conductivity-based choline mapping is promising for the detection of brain tissue abnormalities.

ACKNOWLEDGEMENT

This work was supported by the National Research Foundation (NRF) of Korea grant funded by the Korean government (MSIP) (No. 2013R1A2A2A04016066, 2014R1A2A1A09006320).

REFERENCES

1. J.K. Seo and E.J. Woo., “Magnetic resonance electrical impedance tomography (MREIT),” *SIAM REVIEW.*, vol. 53, pp.40-68, 2011.
2. S.Z.K. Sajib et al., “Regional absolute conductivity reconstruction using projected current density in

IBEC2015, Road to Better Life through Biomedical Engineering

MREIT," *Phys. Med. Biol.*, vol. 57, pp.5841-5859,
2012.

Submillimeter resolution MREIT conductivity images of rat brain

B. K. Choi, N. Katoch, S. Z. K. Sajib, W. C. Jeong, H. J. Kim and E. J. Woo

Department of Biomedical Engineering, Kyung Hee University, Seoul, Korea

E-mail: cjwoo@khu.ac.kr

Abstract—In order to visualize a conductivity distribution with a pixel size of submillimeter-scale, we performed rat brain conductivity imaging experiment using a 3 Tesla MREIT system with using advanced MR techniques.

Keywords— Rat, brain, conductivity, MRI, MREIT

I. INTRODUCTION

Current MREIT technique provides a conductivity image with a resolution of millimeter-scale. Since the precise measurement of electrical conductivity under the tissue levels can provide alternative information in a wide range of biomedical applications, it is necessary to develop high-resolution MREIT technique to enhance its availability. In this study, we performed submillimeter resolution conductivity imaging experiment in rat brain using advanced MR techniques, such as multi-echo pulse sequence, multi-channel RF coil, and phase optimization methods [1]. We evaluate the performance of high-resolution MREIT technique.

II. METHODS

A. Animal preparations

We used Sprague-Dawley rat which were 8 weeks of age and weighing 250–300 g. After administered euthanasia with carbon dioxide, we attached four carbon-hydrogel electrodes of $10 \times 10 \text{ mm}^2$ on the head as shown in Fig. 1(a).

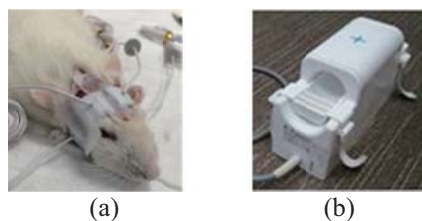


Fig. 1. (a) Imaging experiment setup and (b) 8channel RF receiver coil

B. MREIT imaging experiment

The imaging objects were located inside the bore of a 3 T MR scanner. We used 8-channel small volume RF coil with 72mm diameter for sub-millimeter resolution in Fig. 1(b). The multi-spin-echo injected current nonlinear encoding (ICNE) pulse sequence was used for minimizing phase drift effect [2].

C. Conductivity image reconstruction

We calculated MR magnitude and phase images from acquired complex data. The magnitude image was used

for segmentation and phase image was used for creating magnetic flux density image. Finally, conductivity image was reconstructed by using CoReHA program which is implemented harmonic B_z algorithm [3].

III. RESULTS

MR magnitude image in Fig. 2(a) show the anatomical structure of rat head such as white matter, gray matter and muscle. Fig. 2(b) is the optimized magnetic flux density image using multiple data acquired from the multi-echo pulse sequence and multi-channel RF receiver coil. And Fig. 2(c) is the reconstructed conductivity image with $400 \mu\text{m}$ pixel size which can distinguish different tissues inside the brain as well as it shows that white matter has higher conductivity than gray matter.

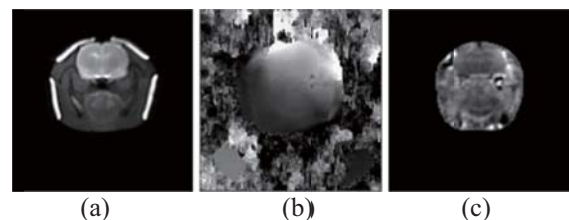


Fig. 2. (a) MR magnitude image, (b) magnetic flux density image and (c) conductivity image.

IV. CONCLUSION

We provided non-invasive, cross-sectional electrical conductivity distribution of biological tissues using a MREIT technique with sub-millimeter resolution.

ACKNOWLEDGEMENT

This work was supported by the National Research Foundation (NRF) of Korea grant funded by the Korean government (MSIP) (No. 2013R1A2A2A04016066, 2014R1A2A1A09006320).

REFERENCES

1. W.C. Jeong et al., "Optimization of magnetic flux density measurement using multiple RF receiver coils and multi-echo in MREIT," *Phys. Med. Biol.*, vol.59, pp.4827-4844, 2014.
2. C. Park et al., "Measurement of induced magnetic flux density using injection current nonlinear encoding in MREIT," *Physiol. Meas.*, vol.28, pp.117-127, 2007.

IBEC2015, Road to Better Life through Biomedical Engineering

3. K.W. Jeon et al., "MREIT conductivity imaging of the postmortem canine abdomen using CoReHA," *Physiol. Meas.*, vol.30, pp.957-966, 2009.

Image processing about cell-detection using DWT on electrode surface

H. W. Kim¹, J. H. Heo¹, J. H. Lee¹, E. I. Cho¹, J. J. Lee¹, J. H. Im¹ and Y. R. Yoon¹

¹Department of Biomedical Engineering, Yonsei Univ., Wonju, Korea, Republic of.

E-mail: yoony@yonsei.ac.kr

Abstract—This study is about image processing technique of cell-detection on the specially manufactured electrode. We did discrete wavelet transform(DWT), histogram analysis and binarization to obtain clear cell image.

Keywords— cell detection, edge removal, discrete wavelet transform, histogram analysis, binarization

I. INTRODUCTION

Handling cell image is critical area in molecular biology. We can obtain important information concerned of variety of bio research and application. Traditional cell image analysis and comparison work have been done manually by expert of this field. But this kind of work has disadvantage of wasting time and effort[1]. There has been research about cell detection by detecting edge of cell. DWT was done to make it[2]. In this study, we suggest cell-detecting technique by discrete wavelet transform and histogram analysis which is applied on electrode surface.

II. METHODS

A. Image acquisition

In this study, we acquired cell-included image by using microscope. To acquire cell-excepted image and cell-included image both, we replace target plate once. Raw image is gray-scaled.

B. Gap elimination

We conducted DWT to eliminate the horizontal wall called “gap”. We decomposed image to level 2 experimentally not to lose local information of cell.

C. Cell detection

Histogram analysis and binarization was conducted to distinguish cell and windows. Because the index of the inside of cell lies between that of window and gap, proper threshold was adapted to binarize the image. Threshold is 200 in this study.

III. RESULTS

A. Gap elimination

The result of gap elimination is shown in <Fig. 1.>. Low frequency component(diagonal coefficient of lv1) represents gap-eliminated image.

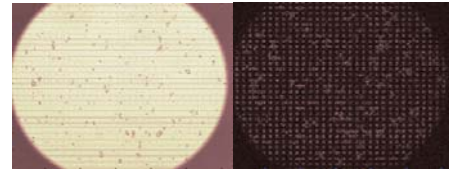


Fig. 1. Original image(left) and gap-eliminated image(right)

B. Binarization

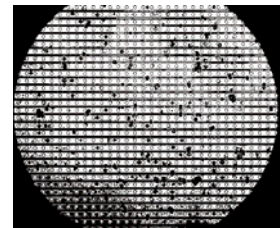


Fig. 2. Binarized image

Histogram analysis and binarization is applied as shown in Fig. 2. Most cells are emphasized as dark spot.

IV. CONCLUSION

Cell detection should be conducted prior to cell tracking and special situation like electricity-applied environment should be considered. To obtain cell image clearly, other structure must be eliminated. We erased structure like electrode by DWT and obtained cell-emphasized image by histogram analysis. Before tracking cell, preprocess like morphological method such as dilation and erosion should be applied to obtain distinguishable cell shape.

ACKNOWLEDGEMENT

This research was supported by the corporate associated research development manpower training Program of the Ministry of Trade, Industry and Energy (N0001130).

REFERENCES

1. C. H. Han, I. H. Song, and S. W. Lee, “Efficient Cell Tracking Method for Automatic Analysis of Cellular Sequences,” *The Korea Contents Association, vol.5, Issue 11, pp. 32-40, 2011.*
2. T. Y. Lee, and H. W. Shen, “Efficient Local Statistical Analysis via Integral Histograms with Discrete Wavelet Transform,” *IEEE Trans. Visualization and Computer graphics, vol. 19, Issue 12, pp. 2693-2702, 2013.*

The study of breast cancer classification for FNA using k-NN algorithm based on machine learning

J. H. Heo¹, H. R. Heo¹, H. W. Kim¹, J. J. Lee¹ and Y.R. Yoon¹

¹ Department of Biomedical Engineering, Yonsei University*
E-mail: yoon@yonsei.ac.kr

Abstract— The accuracy of breast cancer diagnosis is conditional on some factors. For efficient and coherent diagnosis, we evaluated existing data according to logistic regression. Then data applied to k-Nearest Neighbor algorithm. A result of k-NN algorithm has the accuracy of 95%. It can be improved by additional step so this process can be used to automatic diagnosis.

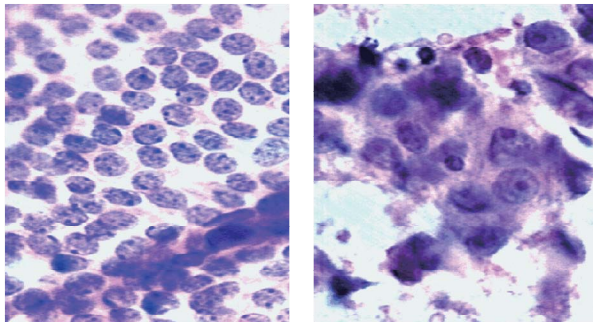
Keywords— Machine Learning, k-NN algorithm, Automatic diagnosis

I. INTRODUCTION

Fine Needle Aspiration(FNA) is a helpful/valuable and trustworthy method to diagnosis for breast cancer[1]. However, the accuracy of diagnosis using FNA is conditional on some factors like the diagnostic skills of the cytopathologist[2]. To reduce effects of these factors, we can diagnosis through machine learning, especially k-Nearest Neighbor algorithm (k-NN algorithm).

II. METHODS

A. Breast Cancer Data



(a) Image of benign (b) Image of malignant
Fig. 1. Images were taken from FNA of breast masses.

Fig. 1 is a part of FNA images that the breast cancer data was extracted. Data features are consisted of patient's ID, diagnosis and 30 real-valued input features.

B. k-Nearest Neighbor algorithm

k-NN algorithm, one of machine learning, classifies the object assigned to the most common entries among the k-nearest neighbor objects. For training and testing, we eliminated patient's ID feature and divided the entire data(569) into training data(469) and testing data(100).

C. Analysis

R is programming language that widely used for statistical software and data analysis. Also it provides a variety of statistical techniques. By using this, prepared data was applied on k-NN algorithm and analyzed. To compare effect of each features on diagnosis result, logistic regression was performed.

III. RESULTS

Table 1. The results of k-NN algorithm

	True negative	True positive	False negative	False positive	Accuracy
All features	77	21	2	0	98%
15-features	74	21	2	3	95%

Depending on the results of logistic regression analysis, the features that has estimate value in top 15 are selected. Table 1 shows the results that applied entire features and only 15-features. When applied 15-features, the accuracy was slightly decreased. Despite all that, it was confirmed to have a relatively high accuracy.

IV. CONCLUSION

After selecting 15-features by evaluating existing data, selected data was applied in k-NN algorithm. This process has advantage of diagnosis speed improvement. Additionally accuracy can be increased by giving weight and adjusting k value. So, we can do efficient automatic diagnosis using existing data.

ACKNOWLEDGEMENT

This research was supported by the corporate associated research development manpower training Program of the Ministry of Trade, Industry and Energy (N0001130).

REFERENCES

1. Q. He, X. Fan, T. Yuan, L. Kong, X. Du, D. Zhuang and Z. Fan, "Eleven years of experience reveals that fine-needle aspiration cytology is still a useful method for preoperative diagnosis of breast carcinoma." *The Breast*, 16.3 , 303-306, 2007.
2. G. Kocjan, "Fine needle aspiration cytology: diagnostic principles and dilemmas", *Springer Science & Business Media*, 2006.

Liver Metabolites in Animal Model of High-Fat Diet induced Abnormal Intrahepatic Triglyceride Storage Using ^1H -MRS with External Standard Method

K.H. Song¹, C.H. Yoo¹, S.I. Lim¹, and B.Y. Choe¹

¹ Department of Biomedical Engineering, and Research Institute of Biomedical Engineering, The Catholic University of Korea College of Medicine, Seoul, Korea
E-mail: bychoe@catholic.ac.kr

Abstract— The objective of this research is to characterize the metabolic changes in a fatty liver rat model induced by a high-fat diet. In this study, we show the feasibility of accurately measuring hepatic lipids, with a correction of relaxation time, and a practical external standard method.

Keywords— Magnetic resonance spectroscopy, Fatty liver, High-fat diet, Normal-chow diet, Choline-containing compounds

I. INTRODUCTION

Disease progression can be prevented by early diagnosis, treatment, and characterization of fatty liver disease using computed tomography, ultrasonography, and magnetic resonance imaging techniques. Proton magnetic resonance spectroscopy (^1H MRS) has also been used to monitor and characterize liver disease, including fatty liver [1]. Typically, the spectra obtained from in vivo ^1H MRS of liver tissues show various lipids peaks, as well as choline-containing compounds (CCC) [2]. Changes of lipid content, namely saturated- and unsaturated-fatty acid, have also been associated with the pathogenesis of fatty liver [2]. Therefore, accurate measurement of lipid fraction composition is preferred over measurement of total lipids. The objective of this research is to characterize the metabolic changes in a fatty liver rat model induced by a high-fat (HF) diet.

II. METHODS

Phantoms were used for testing T1 and T2 estimation and coil performance for quantification of metabolites. To test coil performance, a lipid standard phantom containing canola oil, and a choline (Cho) standard phantom containing 6mM phosphocholine chloride, copper sulfate (CuSO_4 , 3mM) and trimethylsilyl-propionic acid (TSP, 1mM) in sodium chloride (NaCl , 34mM) were prepared in a cylindrical bottle. These phantoms were used for measurement of T1-, T2-relaxation time. The calibration phantom contained an identical 6mM phosphocholine chloride, CuSO_4 , NaCl ,

and TSP solution, prepared in a conical tube. Male Sprague-Dawley rats ($n=12$) fed the HF diet, with weight-matched normal-chow (NC) diet rats were housed with ad libitum access to water. The HF diet comprised pellets composed of 60% fat. Examinations were performed on a 3.0T scanner (Achieva Tx 3.0T; Philips Medical Systems, Netherlands) by using 4-channel animal coil. Localized point-resolved spectroscopy sequence was used for periodically acquiring liver spectrum at fortnightly intervals with the following parameters: repetition time (TR)/echo time (TE) = 1500/35ms; the number of signal averages (NSA) = 64; the iterative volume of interest (VOI) shim and total scan was ≤ 10 minutes. The water signal of each VOI was suppressed by variable pulse power and optimized relaxation delays applied before the scan. Cho T1 measurements (VOI, $0.8 \times 0.8 \times 0.8 \text{ cm}^3$; TE, 40ms; TR, 600-1400ms; 64 acquisitions) and Cho T2 measurements (TR, 6000ms; TE, 40-220) were obtained. For relative quantification, total lipid ($(-\text{CH}_2)_n / \text{noise}$), saturated fatty acid ($3(-\text{CH}_2-) / 2(-\text{CH}_3)$), total unsaturated fatty acid ($3(-\text{CH}_2-\text{C}=\text{C}-\text{CH}_2-) / 4(-\text{CH}_3)$), total unsaturated bond ($3(-\text{CH}=\text{CH}-) / 2(-\text{CH}_3)$), and polyunsaturated bond ($3(=\text{C}-\text{CH}_2-\text{C}=\text{C}-) / 2(-\text{CH}_3)$) were quantified [2]. Raw spectral data were analyzed by using a commercially available linear combination of model spectra (LCModel, version 6.3-1H, Stephen W. Provencher) software.

III. RESULTS

Fig. 1a shows the lipid standard phantom and a typical spectrum from the canola oil sample. Fig. 1b shows the linear relationship between signal intensity and volume, with respect to the VOI (Cho, $R^2 = 0.9040$; lipid, $R^2 = 0.8897$) located from the center of the coil. Fig. 1c and 1d show the signal intensity of the isocenter for the sensitivity distribution of the coil (Cho, x-axis: 7-8%, y-axis: 17-18%). Fig. 2b and 2c show the spectrum with voxel position (Fig. 2a) selected in anatomical image. The Cho concentration in HF diet rats was to be $6.0 \pm 2.7\text{mM}$; the Cho concentration in NC rats was $5.4 \pm 1.3\text{mM}$. The total lipid of HF diet rats at 4 weeks ($8.3 \pm 2.2 \times 10^3$) and 8

weeks ($8.2 \pm 2.1 \times 10^3$) was similar values. These values were higher than those of NC rats ($1.7 \pm 0.6 \times 10^3$). The total saturated fatty acid of HF diet rats at 4 weeks (14.7 ± 4.5) and 8 weeks (17.2 ± 4.7) were similar. The 8 weeks value of HF rats was higher than that of NC diet rats. HF diet rats had a higher total unsaturated bond and polyunsaturated bond at 4 weeks and 9 weeks, compared with NC diet rats.

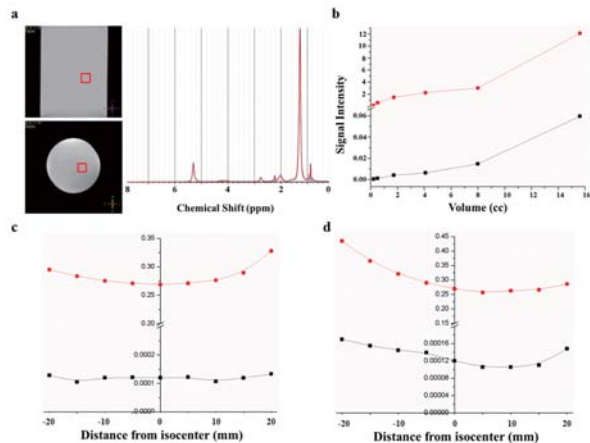


Fig. 1. (a) Sagittal image and axial image with a voxel position (red box) in lipid phantom and typical MRS spectrum from canola oil. (b) Linear relationship between voxel size and signal intensity from 0.6 cm^3 to 2.5 cm^3 . Spatial variation in relative intensity measured within voxel size of $0.8 \times 0.8 \times 0.8 \text{ cm}^3$ right-to-left (c), anterior-posterior (d) with lipid (red line), Cho (black line).

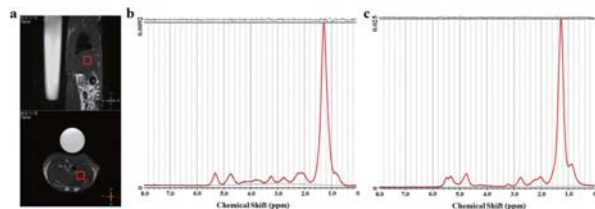


Fig. 2. (a) Sagittal image (top) and axial image (bottom) with the chosen VOI (red box) and corresponding in vivo liver spectrum with Cho and lipid region. Typical liver ^1H MRS spectrum showing various lipid and CCC peaks, with effectively suppressed water signals from NC diet rat (b), and HF diet rat (8 weeks) (c).

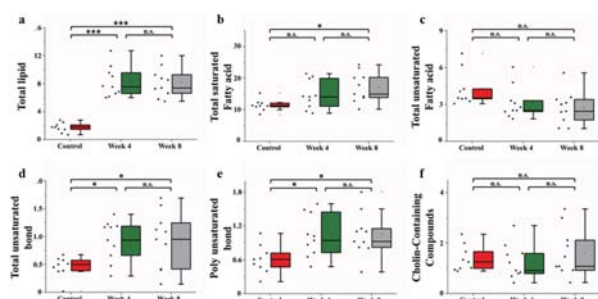


Fig. 3. Comparison of NC and HF diet rats by using one-way analysis of variance with the Turkey multiple comparison test; (a) Total lipid, (b) total saturated fatty acid, (c) total unsaturated fatty acid, (d) total unsaturated bond, (e) poly unsaturated bond, and (f) choline-containing compounds in

NC and HF diet rats. (***, $p < 0.001$; **, $p < 0.01$; *, $p < 0.05$; n.s, not significant)

IV. CONCLUSION

For metabolite quantification, the external method with high spectral resolution was conducted sufficient signal-to-noise and T1 and T2 relaxation times of major metabolite in fatty liver. In this study, we show the feasibility of accurately measuring hepatic lipids, with a correction of relaxation time, and a practical external standard method. The results are applicable to the study of liver disease in both human and animal models.

ACKNOWLEDGEMENT

This study was supported by grants (2012-007883) from the Mid-career Researcher Program through the National Research Foundation (NRF) funded by the Ministry of Science, ICT & Future Planning (MSIP) of Korea. And, this research was supported by a grant of the Korea Health Technology R&D Project through the Korea Health Industry Development Institute (KHIDI), funded by the Ministry of Health & Welfare, Republic of Korea (grant number: HI14C1135). And, this research was supported by a grant of The Catholic University of Korea – Sogang University Joint Research Project [B0001-00015, Development of MR-Ultrasound guided High Intensity Focused Ultrasound treatment system].

REFERENCES

1. S Traussnigg, E Halilbasic, C Kienbacher, et al. "High-field MR-spectroscopy in patients with NAFLD allows novel insights in altered hepatic lipid and energy metabolism with potential distinction of NASH and advanced fibrosis" *J Hepatol.* vol. 58, pp. S551, 2013.
2. J.S. Cheung, S. J. Fan, D. S. Gao, et al, "In vivo lipid profiling using proton magnetic resonance spectroscopy in an experimental liver fibrosis model" *Acad Radiol.* vol. 18, no. 3, pp. 377-383, 2011.

A Preliminary Study on Centrum Modeling for Diagnosing Scoliosis : Estimation of Spine Using Kinect

S. Y. Shin¹, H. R. Heo², M. Song³, and T. M. Shin⁴
Department of Biomedical Engineering, Yonsei University, Wonju, Korea
E-mail: shinsy_93@naver.com

Abstract—In this paper, the algorithm of estimating spine using depth image and color image acquired from Microsoft Kinect V2 was developed. The results show that RMS error was 1.573mm and the developed algorithm has high accuracy compared with Rasterstereography.

Keywords— Scoliosis, Depth Image, Back Surface, Spine, Kinect V2

I. INTRODUCTION

Scoliosis is a medical condition in which a person's spinal axis has a three-dimensional deviation[1]. In severe case, internal organs can be functionally disordered.

Rasterstereography is typical non-radioactive method for diagnosing a scoliosis. Rasterstereography reconstruct vertebral body by analyzing a back surface from back's depth data, using the character that the back surface curves transformed by vertebral body's transform mainly appear at spine[2]. But because of its expensive price, it is necessary to develop the cheap and precise diagnosis algorithm.

In this paper, therefore, the algorithm of estimating spine using depth image and color image acquired from Microsoft Kinect V2 was developed[3].

II. METHODS

Eight subjects in their 20s were participated in the experiment for scanning the depth image of the back surface.

Microsoft Kinect V2 was used for scanning the depth image of the back surface. First, the real spine of subject was marked by a pen to compare the spine estimated from the depth image with the real spine of the subject described in Fig. 1. Second, Kinect was placed to meet that distance between Kinect and the subject was more than 50cm and Kinect is adjusted to be parallel with the wall. Finally, the color image and depth image of the back of subject at the same time.

The estimated spine was based on lowest point between the two highest points of both sides divided by stapes on the transverse plane of the depth image of the back surface. Next, the estimated spine was displayed on the image derived by contour and compared with real spine described in Fig. 1.



Fig. 1. Real image, Depth image, and contour image of spine

III. RESULTS

Table 1 shows that RMS error between the position of real spine and estimated spine based on depth image and color image scanned by Kinect.

Table 1. RMS error between measured and estimated spine

	n	RMS(mm)
Female	3	2.038
Male	5	1.295
Total	8	1.573

IV. CONCLUSION

In this paper, the algorithm of estimating spine using depth image and color image acquired from Microsoft Kinect V2 was developed. The performance of the developed algorithm was tested by using RMS error between the position of real spine and estimated spine based on depth image and color imaged scanned by Kinect. The results show that RMS error is 1.573mm. However, the certainty should be compared through later research because the results have not been compared to Rasterstereography yet.

V. Reference

1. Per Trobisch, Olaf Suess, Frank Schwab, "Idiopathic Scoliosis", *Disch Arztebi Int.*, Vol. 107, No. 49, pp. 875-884, 2010.
2. B Drerup, E Hierholzer, "Back shape measurement using video rasterstereography and three-dimensional reconstruction of spinal shape", *IEEE Trans. Biomed. Eng.*, Vol. 26, pp. 111-119, 1994.
3. E. Lachat, H. Macher, M. -A. Mittet, T. Landes, P. Grussenmeyer, "First experience with kinect v2 sensor for close range 3d modelling", *ISPRS*, Vol. XL-5/W4, pp. 93-100, 2015.

Effect of Binge Ethanol Intoxication and Abstinence on Neurometabolite Changes in Rats Detected by *Ex Vivo* ^1H MR Spectroscopy

S.I. Lim¹, D.W. Lee¹, K.H. Song¹, C.H. Yoo¹ and B.Y. Choe¹

¹ Department of Biomedical Engineering, and Research Institute of Biomedical Engineering, The Catholic University of Korea College of Medicine, Seoul, Korea
E-mail: bychoe@catholic.ac.kr

Abstract—The aim of the study is to determine the influence of the time-dependent effects of short-term intermittent ethanol exposure and abstinence on cerebral neurochemical changes in rats with *ex vivo* ^1H nuclear magnetic resonance spectroscopy (NMRS). The study results indicate several potential metabolic markers for the time-dependent influence of short-term intermittent ethanol exposure on the frontal cortex.

Keywords—Magnetic resonance spectroscopy, Magic angle spinning, Ethanol, Frontal cortex, Metabolism

I. INTRODUCTION

Alcohol is the most commonly abused intoxicating substance among young and middle-aged adults, and is a major cause of disability and mortality[1]. A quantitative assessment of the neurochemical effects of binge ethanol intoxication on specific regions of the brain is necessary for a better understanding of the neurological effects of ethanol abuse. However, the influence of abstinence periods must be taken into account. We studied the effects of short-term intermittent ethanol (SIE) exposure and abstinence on cerebral neurochemical changes with *ex vivo* ^1H nuclear magnetic resonance spectroscopy (NMRS), it has not been experimentally investigated. This study aimed to determine the influence of the time-dependent effects of SIE exposure on cerebral neurochemical differences using *ex vivo* high-resolution spectra.

II. METHODS

A. Animal

8-week-old male Wistar rats ($n=40$; mean body weights, 304.4 ± 5.7 g; range, 291.0–314.5 g) were divided into 4 groups: control rats (CNTL, distilled water administration, $n = 10$); six-hour-recovery rats (SIE-06H, ethanol dose of 2.0 g/kg, $n = 9$); three-day-recovery rats (SIE-03D, ethanol dose of 2.0 g/kg, $n = 11$); and seven-day-recovery rats (SIE-07D, ethanol dose of 2.0 g/kg, $n = 10$).

B. Binge Ethanol Intoxication

The 30 rats in the SIE-06H, -03D, and -07D groups received an initial dose of 5.0 g/kg through oral gavage,

and then received an additional dose of 2.0 g/kg every 8 h (at 03:00, 11:00, and 19:00 h) for 4 days. The 10 rats in the sham CNTL group received an equivalent volume of distilled water at comparable times (at 04:00, 12:00, and 20:00 h). Oral-gavage ethanol was administered according to body weight, using the Majchrowicz binge-alcohol protocol[2].

C. *Ex vivo* ^1H HR-MAS NMR Spectroscopy

Six hours (CNTL, and SIE-06H), 3 days (SIE-03D), and 7 days (SIE-07D) after the last gavage, all animals were euthanized by carbon dioxide inhalation and immediately decapitated. Forty frontal cortex tissue samples were carefully harvested using a brain slicer matrix. *Ex vivo* ^1H high-resolution magic angle spinning (HR-MAS) NMRS was performed on an Agilent Technologies Korea VNMRS-500 instrument (11.7-T). All HR-MAS spectra were acquired with a Carr-Purcell-Meiboom-Gill pulse sequence (complex data number, 16,384; spectral width, 8 kHz; acquisition time, 2.05 s; relaxation delay time, 5.0 s; presaturation time, 2.0 s; interpulse delay, 0.4 ms; number of acquisitions, 128; total scan time, 15 min, 24 s). The acquired raw data were analyzed and quantified with MestReNova.

III. RESULTS

Cerebral Metabolite Changes

Fig. 1A–D shows representative 11.7-T NMR spectra obtained from the frontal cortex regions of the 40 samples from the four groups (A, CNTL, $n = 10$; B, SIE-06H, $n = 9$; C, SIE-03D, $n = 11$; and D, SIE-07D, $n = 10$). Fig. 2A–D illustrates the normalized cerebral metabolite levels quantified from the 40 acquired *ex vivo* spectra from the frontal cortex region. Our results showed significantly higher Lac ($p = 0.010$) and significantly lower mIns ($p = 0.022$) signals in the SIE-06H rats compared to the CNTLs. The GSH ($p = 0.036$) and GABA ($p = 0.036$) signals were significantly higher in the SIE-07D rats than in CNTLs. In addition, the GSH ($p = 0.042$) signals were also significantly higher in the SIE-03D rats than in the CNTLs. The vertical lines on each of the bars in Fig. 2. indicate the (+) standard deviation of the mean values. Significance levels (independent t-test): *, $p < 0.05$; **, $p < 0.01$.

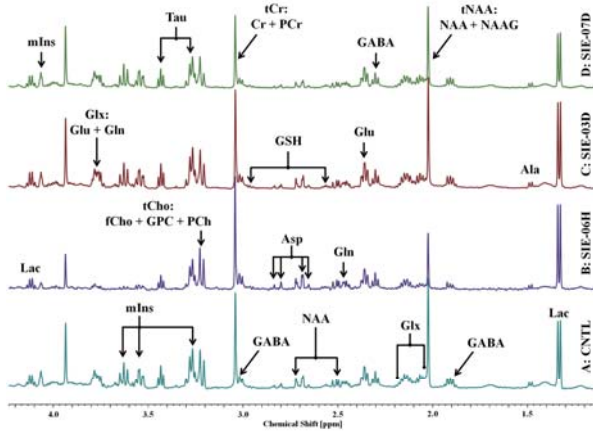


Fig. 1. Representative *ex vivo* ¹H NMR spectra acquired in the frontal cortex at 11.7 T from 4 groups

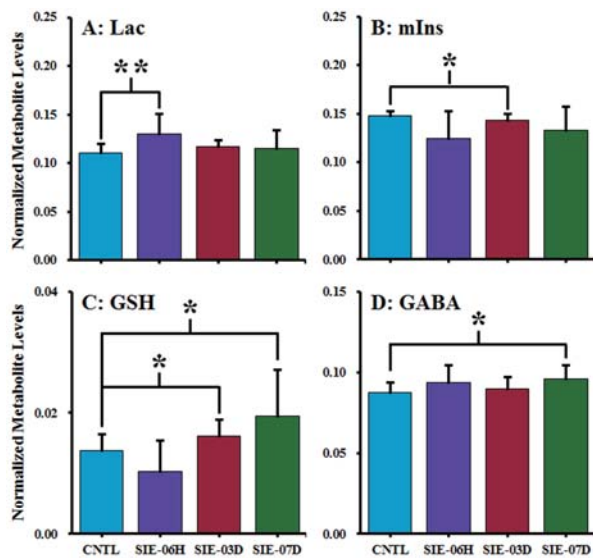


Fig. 2. Mean normalized metabolite levels in the frontal cortex for 4 groups

IV. CONCLUSION

In summary, the present study conducted *ex vivo* ¹H HR-MAS NMR spectroscopy in a rat model to determine the effect of SIE exposure on metabolite concentrations in the rat frontal cortex. Significantly higher the Lac signals in rat frontal cortex 6 h after the SIE exposure may reflect alteration of the anaerobic respiration system or abnormal hypoxia. Significantly lower mIns signals in rat frontal cortex 6 h after the SIE exposure might indicate acute hypo-osmolality and hyponatremia in astrocytes[3]. Moreover, significantly higher GSH signals possibly indicate that increasing abstinence time after SIE exposure (3 days or more) may lead to oxidative stress, possibly due to stimulation of lipid peroxidation through the formation of free radicals and/or abnormalities of the antioxidant defense activities in the frontal cortex of the SIE-exposed rats[4]. Significantly higher GABA signals in

the frontal cortex 7 days after the last SIE exposure may reflect alterations in GABA synthesis and GABAA receptor densities[5]. Our *ex vivo* ¹H NMR spectroscopy results indicate several potential metabolic markers for the time-dependent influence of short-term intermittent ethanol exposure on the frontal cortex.

ACKNOWLEDGEMENT

This study was supported by grants (2012-007883) from the Mid-career Researcher Program through the National Research Foundation (NRF) funded by the Ministry of Science, ICT & Future Planning (MSIP) of Korea. And, this research was supported by a grant of the Korea Health Technology R&D Project through the Korea Health Industry Development Institute (KHIDI), funded by the Ministry of Health & Welfare, Republic of Korea (grant number: HI14C1135). And, this research was supported by a grant of The Catholic University of Korea – Sogang University Joint Research Project [B0001-00015, Development of MR-Ultrasound guided High Intensity Focused Ultrasound treatment system].

REFERENCES

1. M. Teesson, W. Hall, T. Slade, K. Mills, R. Grove, L. Mewton, A. Baillie, and P. Haber, "Prevalence and correlates of DSM-IV alcohol abuse and dependence in Australia: findings of the 2007 National Survey of Mental Health and Wellbeing.," *Addiction*, vol. 105, no. 12, pp. 2085–94, 2010.
2. E. Majchrowicz, "Induction of physical dependence upon ethanol and the associated behavioral changes in rats.," *Psychopharmacologia*, vol. 43, no. 3, pp. 245–54, 1975.
3. Z. Braunová, S. Kasparová, V. Mlynárik, S. Mierisová, T. Liptaj, I. Tkác, and A. Gvozdjaková, "Metabolic changes in rat brain after prolonged ethanol consumption measured by 1H and 31P MRS experiments.," *Cell. Mol. Neurobiol.*, vol. 20, no. 6, pp. 703–15, 2000.
4. E. Agar, M. Boşnak, R. Amanvermez, S. Demir, M. Ayyildiz, and C. Celik, "The effect of ethanol on lipid peroxidation and glutathione level in the brain stem of rat.," *Neuroreport*, vol. 10, no. 8, pp. 1799–801, 1999.
5. S. S. Smith and Q. H. Gong, "Ethanol effects on GABA-gated current in a model of increased $\alpha 4\beta\delta$ GABAA receptor expression depend on time course and preexposure to low concentrations of the drug," *Alcohol*, vol. 41, no. 3, pp. 223–231, 2007.

Cerebral Metabolite Differences and Correlations in Short-Term Binge Ethanol-Exposed Rats: A Study of Ex Vivo Proton Nuclear Magnetic Resonance Spectroscopy at 11.7-T

C.H. Yoo¹, D.W. Lee¹, K.H. Song¹, S.I. Lim¹, and B.Y. Choe¹

¹ Department of Biomedical Engineering, and Research Institute of Biomedical Engineering, The Catholic University of Korea College of Medicine, Seoul, Korea
E-mail: bychoe@catholic.ac.kr

Abstract— The goal of this study was to determine the influence of dose-dependent short-term binge ethanol (SBE) exposure on cerebral neurochemical differences and correlations between the metabolite-metabolite levels using ex vivo 1H high-resolution magic angle spinning (HR-MAS) NMR spectroscopy. The results of this study suggest novel metabolic markers for assessing the dose-dependent effects of SBE exposure in the hippocampal region.

Keywords— Alcohol, Brain disorders, Magnetic Resonance Spectroscopy

I. INTRODUCTION

Numerous studies have shown that binge ethanol-exposed rats exhibit metabolic abnormalities, functional impairments, neuronal changes. These include cerebral metabolite changes, cognitive deficits, neuronal dysfunction, degeneration/recovery in the hippocampus, temporal cortex, olfactory bulb. However, the short-term dose effects of binge ethanol exposure on cerebral neurochemical differences in the hippocampal region have not been experimentally assessed with ex vivo 1H NMR spectroscopy. Therefore, the first goal of this study was to determine the influence of dose-dependent short-term binge ethanol (SBE) exposure on cerebral neurochemical differences among sham controls (CNTL), low- (SBE-1.5) and high-dose (SBE-2.5) ethanol-exposed rats, by ex vivo 1H high-resolution magic angle spinning (HR-MAS) NMR spectroscopy. The second goal was to determine the correlations between the metabolite-metabolite levels (pairs of metabolite levels).

II. METHODS

A. Animal

Eight-week-old male Wistar rats ($n = 28$) were divided into 3 groups: a control group (CNTL, ethanol dose of 0.0 g/kg; distilled water, $n = 10$), two short-term binge ethanol (SBE) groups: a low-dose (SBE-1.5, ethanol dose of 1.5 g/kg, 25% w/v ethanol solution, $n = 10$) and high-dose group (SBE-2.5, ethanol dose of 2.5 g/kg, 25% w/v ethanol solution, $n = 8$). For the initial exposure (day 1; at 17:00 h), the 18 rats in the SBE-1.5 and -2.5 groups received an initial dose of 5.0 g/kg

ethanol (30% w/v solution) through oral gavage, and subsequent doses of 1.5 g/kg and 2.5 g/kg (25% w/v solution), respectively, every 8 h (at 01:00, 09:00, and 17:00 h) for 4 days. The 10 rats in the sham CNTL group received an equivalent volume (about 2.85 mL) of distilled water at comparable times (at 02:00, 10:00, and 18:00 h). Oral gavage ethanol was administered according to body weight, as described by the Majchrowicz binge alcohol protocol.

B. Ex vivo ¹H HR-MAS NMR Spectroscopy

After 4 days of oral gavage, all animals were sacrificed, brain tissues were harvested from the hippocampus. Ex vivo 1H HR-MAS NMR spectroscopy was performed at Agilent VNMR5-500 (11.7 T). Ex vivo HR-MAS spectra were acquired from all 28 tissue samples using Carr-Purcell-Meiboom-Gill sequence (complex data number = 16384, spectral width = 8 kHz, acquisition time = 2.05 sec, relaxation delay time = 5.0 sec, presaturation time = 2.0 sec, inter-pulse delay (τ) = 0.4 msec, number of acquisitions = 128, total scan time = 15 min 24 sec).

III. RESULTS

Figure 1 shows the representative 11.7 T NMR spectra obtained from the hippocampus of CNTL rats. One-way ANOVA revealed a significant ethanol effect on the normalized metabolite levels. 4 days of intermittent ethanol intoxication resulted in altered normalized metabolite levels among the three groups for Asp [F(2,21) = 2.768, $p = 0.046$], GABA [F(2,22) = 5.913, $p = 0.009$], GSH [F(2,22) = 6.586, $p = 0.006$], Lac [F(2,22) = 3.500, $p = 0.048$], Tau [F(2,22) = 5.668, $p = 0.010$], and tCr [F(2,27) = 3.488, $p = 0.048$], significantly lower Asp ($p = 0.029$), GABA ($p = 0.004$), GSH ($p = 0.005$), and Tau ($p = 0.003$) signals in SBE-2.5 rats compared to CNTL rats. Also significantly higher GABA ($p = 0.006$), GSH ($p = 0.002$), and Tau ($p = 0.030$) signals in SBE-1.5 rats compared to SBE-2.5 rats. The Lac ($p = 0.016$) and tCr ($p = 0.015$) of SBE-2.5 rats were significantly higher than the CNTL and SBE-1.5 rats, respectively. To visualize the normalized metabolite levels, the pairs of normalized metabolite levels that changed the most were selected

for linear scatter plots (Figure 2A–P). The clusters of individual data from the 28 rats were significantly correlated in sixteen scatter plots. The illustrations in A–P show the relationships between the pairs of normalized metabolite levels as follows: GABA vs. Glu (A), GABA vs. Lac (B), GABA vs. Tau (C), GABA vs. tCr (D), Glu vs. mIn (E), Glu vs. tCho (F), Glu vs. Glx (G), GSH vs. Lac (H), GSH vs. Tau (I), mIns vs. Tau (J), mIns vs. Glx (K), mIns vs. Lac (L), mIns vs. tCh (M), Lac vs. Tau (N), tCho vs. tNAA (O), and tCho vs. Glx (P). The selected correlated scatter plots exhibited significant levels and reliable correlation coefficients.

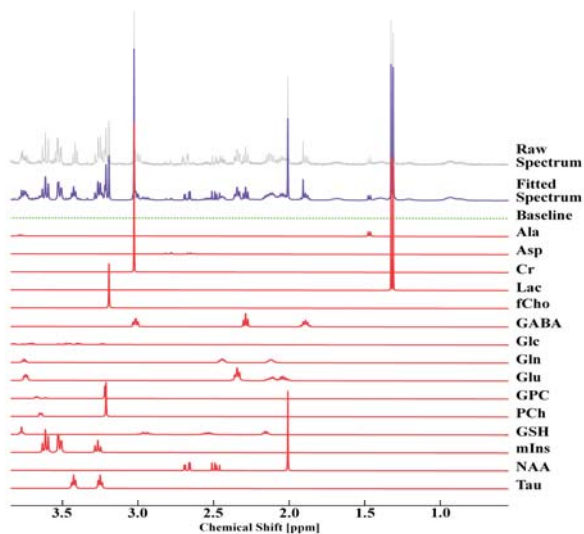


Fig. 1. Representative ex vivo 1H NMR spectra acquired at 11.7 T from short-term binge ethanol-exposed rats in the hippocampal region.

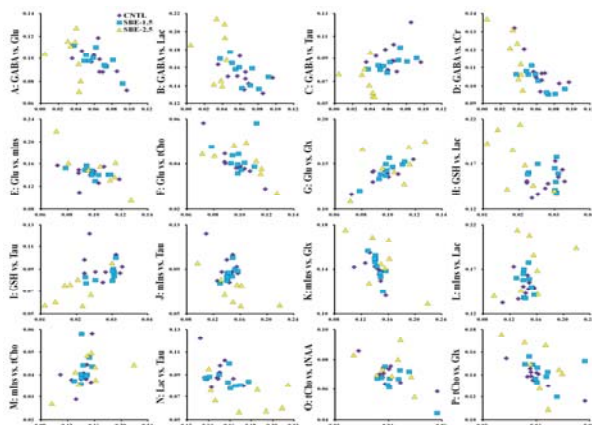


Fig. 2. Scatter plots of the metabolite-metabolite level correlations of CNTL (purple rhombus), SBE-1.5 (blue square), and SBE-2.5 (yellow triangle) rats.

IV. CONCLUSION

In the present study, we conducted ex vivo NMR spectroscopy in a rat model to quantitatively assess the dose-dependent effects of SBE exposure on cerebral

neurochemical changes in the rat hippocampus. Consistent with previous studies, we report altered Asp, GABA, GSH, Lac, Tau, and tCr signals in SBE-exposure rats which indicate that SBE exposure leads to biological changes, such as altered synthesis rate of GABA, glucose, impairment of an antioxidant system, abnormal ATP function, dysfunctions of anaerobic respiration. Overall, our ex vivo 1H NMR spectroscopy results suggest novel metabolic markers for assessing the dose-dependent effects of SBE exposure in the hippocampal region.

ACKNOWLEDGEMENT

This study was supported by grants (2012-007883) from the Mid-career Researcher Program through the National Research Foundation (NRF) funded by the Ministry of Science, ICT & Future Planning (MSIP) of Korea. And, this research was supported by a grant of the Korea Health Technology R&D Project through the Korea Health Industry Development Institute (KHIDI), funded by the Ministry of Health & Welfare, Republic of Korea (grant number: HI14C1135). And, this research was supported by a grant of The Catholic University of Korea – Sogang University Joint Research Project [B0001-00015, Development of MR-Ultrasound guided High Intensity Focused Ultrasound treatment system].

REFERENCES

1. NM. Zahr , D. Mayer , T. Rohlfling , MP. Hasak , O. Hsu , S. Vinco , J. Orduna , R. Luong, EV. Sullivan , A. Pfefferbaum , “Brain injury and recovery following binge ethanol: evidence from in vivo magnetic resonance spectroscopy.” *Biol Psychiatry.* ;67(9):846-54, 2010.
2. E. Majchrowicz, “Induction of physical dependence upon ethanol and the associated behavioral changes in rats,,” *Psychopharmacologia*, ;vol. 43, no. 3, pp. 245–54, 1975.
3. D.-W. Lee, Y.-K. Nam, T.-K. Kim, J.-H. Kim, S.-Y. Kim, J.-W. Min, J.-H. Lee, H.-Y. Kim, D.-J. Kim, and B.-Y. Choe, “Dose-dependent influence of short-term intermittent ethanol intoxication on cerebral neurochemical changes in rats detected by ex vivo proton nuclear magnetic resonance spectroscopy,” *Neuroscience.* ;vol. 262, pp. 107–117, 2014.

A new method for fabricating pigmented skin disease in solid optical phantoms: ink injection

Jeonghwan Son¹, Jihoon Park¹, Sangyeob Lee¹, and Byungjo Jung*

¹Department of Biomedical Engineering, Yonsei University, Wonju, South Korea

E-mail: sonjhing@gmail.com

Abstract— As a new method for fabricating pigmented skin disease, we suggest ink injection method and assume its possibilities. Certain spread formation of Indian ink in Si based and Epoxy based optical phantom could be used for pigmented skin model.

Keywords— Optical phantom, solid optical phantom, skin disease, pigmented skin disease, pigmented skin lesion.

I. INTRODUCTION

In Biomedical optics industry optical tissue phantom which is tissue-simulating object for mimicking optical and biological property of human tissue have been used [1]. With endeavor to idealize optical property, structure analogy with human tissue is also required. In this paper, we suggest a new possible method for fabricating pigmented skin lesion.

II. METHODS

A. Prepare solid optical phantom base

In this work, in order to make solid optical phantom base, we used two type materials: Silicone (KE-1606, Shin-Etsu Chemical Co., Tokyo, Japan), Epoxy (KE-300NS, KPS Inc., Korea). Mixed materials with hardening agents: Silicone agents (CAT-RG, Shin-Etsu Chemical Co., Tokyo, Japan), Epoxy agents (KH-700NS, KPS Inc., Korea), into ratio 9:1, 3:1 respectively, thus total amounts of both material are 50ml in internal dimension 85.60mm petri dish.

B. Inject Indian ink

Indian ink (WINSOR&NETWON INK Ltd., England) is used for imitating pigmented skin characters. First, injected 1ml ink in a 3ml syringe into one of each silicone base and epoxy base vertically as Fig. 1. This process have to do at first as soon as base formula is prepared. Secondly repeat the first process with mixture of 1ml ink and base concentration mixture; thus total ink concentration is 1.96%. Before pouring silicone, 1ml ink was mixed, and pulverized homogeneously using a sonicator (Sonic505, Hwashin Co., Korea), which have 60 amplitude and 5 minutes processing time. After injecting, the results were cooled down at room temperature.

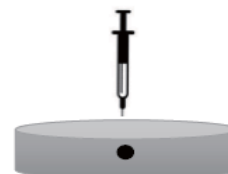


Fig. 1. Scheme of injecting ink method

III. RESULTS

A. Inject pure ink

Since Silicone have higher viscosity than Epoxy, injected pure ink spread slightly and formed circular, to the contrast in Epoxy where ink drop was flowing and solidified with peripheral white line as Fig. 2. However, formation is constant with injection pattern.

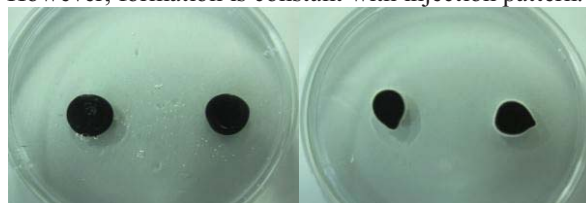


Fig. 2. Ink spread formation in Silicone base (left) and Epoxy base (right)

B. Inject mixture of ink and equal concentration with base

Homogeneously mixed ink mixture was quite widely spread in Epoxy base compared with Silicone as Fig. 3. Also, ink mixture was relatively flattened in Epoxy base.

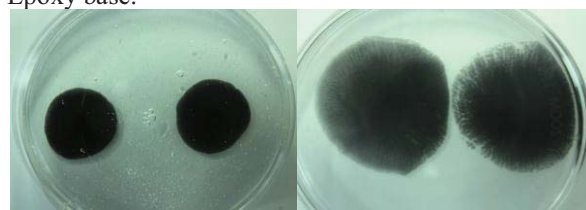


Fig. 3. Ink mixture spread formation in Silicon base (left) and Epoxy base (right)

IV. CONCLUSION

The four different spread pattern noticed these result could be possible for mimicking morphologically variated pigmented skin structure. More advanced research is required on the value of analogy with target.

REFERENCES

1. Brian W. Pogue and Michael S. Patterson, "Review of tissue simulating phantoms for optical", *Journal of Biomedical Optics.*, pp. 114, 041102, 2003.

A Method for Reducing Artifact of MR Image due to the Implantable Hearing Aid

H. J. Ahn¹, H. G. Lim¹, S. T. Woo¹, J. H. Lee², K. W. Seong², M. N. Kim⁴ and J. H. Cho^{1,3*}

¹Graduate School of Electronics Engineering, Kyungpook National University, Daegu, Korea

²Department of Biomedical Engineering, Kyungpook National University Hospital, Daegu, Korea

³Institute of Biomedical Engineering Research, Kyungpook National University, Daegu, Korea

⁴Department of Medical and Biological Engineering, Kyungpook National University, Daegu, Korea

*E-mail: jhcho@ee.knu.ac.kr

Abstract—When a Magnetic resonance imaging (MRI) scan goes, implantable hearing aids containing a magnet should not be possessed in the body because it makes dangerous extrusion of magnet and generate severe image artifacts. Thus, a method for reducing the artifact using an external compensation coil is proposed.

Keywords— Implantable hearing aid, MRI, Image artifact, Homogeneity.

I. INTRODUCTION

Recently, implantable hearing aids, which have a power receiving module from outside the body, are frequently used to treat the hearing impaired patients. Most of implantable hearing aid systems are adopted magnet pairs to couple between internal and external devices for the enhancement of power transmission. Usually, the internal device which containing a magnet in the center of receiving coil is implanted under the skin of the temporal bone.

In case of MRI scanning to a patient who has such implant, the static magnetic fields of the MRI might be interfered by the fields of the implanted magnet in the skin. From the reasons above, the image from MRI is degraded by large area of artifact, so that diagnostics are almost impossible in deteriorated region [1].

In this paper, we propose an external coil that can compensate the magnetic fields due to the internal coupling magnet. By applying the optimum current in the external coil, it can produce optimum cancellation magnetic field for these interferences. And finally, the effectiveness of the proposed coil by using finite element analysis is verified.

II. METHODS

A. Simulation Environments

As shown in Fig. 1(a), the simulation environment was implemented using finite element analysis (COMSOL Multi-physics, COMSOL Inc.). We made a uniform 1.5T magnetic field such as a real MRI bore (Whole body, Siemens). According to homogeneity guarantee of the MRI, threshold of magnetic flux density due to the image artifact could be determined by 0.0075mT. Head size used a standard of the men of

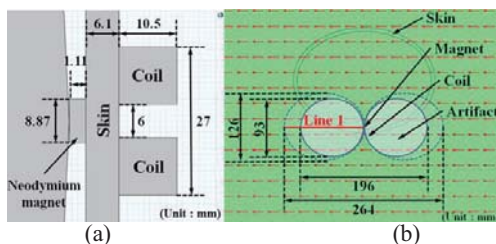


Fig. 1 (a) The simulation environment and (b) the analyzed artifact area.

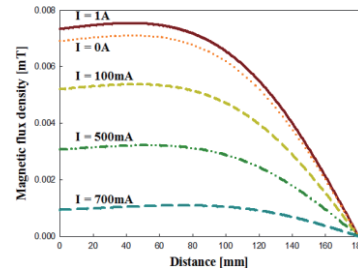


Fig. 2. Simulated artifact area vs current in the external coil at horizontal region (Line 1).

the Size Korea (Korea human dimensions research, Korea). And the thickness of the skin was selected as 6.1mm. The external coil for the artifact reduction was designed. In the external coil, wire thickness, turns, height, and diameter were represented as 0.7mm, 225, 10.5mm, and 27mm, respectively. Magnetic flux density of permanent magnet used 130mT.

B. Analysis of Artifact Area

To analyze artifact area, the magnetic flux density in MRI was simulated according to varying electric current (0-1A) applied to the external coil. If calculated value at a specific point is higher than the threshold of magnetic flux density, it assumed that the point will be make artifact. Using the method, the artifact area was extracted.

III. RESULTS

Using the analysis, plotted artifact area due to the permanent magnet is shown in Fig. 1(b). When there is no current in the external coil, it appeared to horizontal axis of 264mm and vertical axis of 126mm (dashed ellipse). As shown in Fig. 2, the artifact area was minimized in case of 700mA supply. Then, it appeared to horizontal axis of 196mm and vertical axis 93mm (solid ellipse).

IV. CONCLUSIONS

In this study, because the permanent magnet of implantable hearing aid makes the severe artifact, a method using the external coil's current was proposed to reduce artifacts of MRI image. In the simulated results, the artifact area can effectively be reduced as compared with the results due to the internal permanent magnet. Hereafter, optimal design of the external coil corresponding to a magnet will be needed.

ACKNOWLEDGEMENT

This work was supported by the National Research Foundation of Korea (NRF) grants funded by the Korea government (No. 2013R1A2A1A09015677).

REFERENCES

1. P. A. Wackym *et al.*, "Effect of magnetic resonance imaging on internal magnet strength in MED-EL combi 40+ Cochlear Implants," *Laryngoscope*, vol. 114, no. 8, pp. 1355-1361, 2004.

Development of phantom with varying agarose and CuSO₄ concentrations for mimicking human tissues in 3T MRI

K.H. Ryu¹, Y.J. Shin¹, J.M. Kim¹, D Han¹ and D.H. Kim¹

¹Department of Electrical and Electronic Engineering, Yonsei University, Seoul, KOREA
E-mail: nelson666@naver.com

Abstract—3T MRI phantom experiments were performed by combination of various concentration of agarose and CuSO₄. Based on the phantom results, specific concentrations of agarose and CuSO₄ were proposed to construct phantom equivalent to T₁, T₂ values of human tissues.

Keywords— phantom, T₁, T₂, agarose, CuSO₄

I. INTRODUCTION

MRI phantoms are widely used for various purposes: development and validation of new systems and pulse sequences. However, only a few researches were proposed to develop dedicated human tissue mimicking phantoms [1, 2]. Thus we developed dedicated 3T MRI phantom with various concentration combination of agarose and CuSO₄ which can successfully mimic human tissues.

II. METHODS

A. Phantom Design



Fig 1. An example of the phantom (left), magnitude image of the phantom (right).

At each experiment, 25 vials were set to be same agarose concentration. The 5 vials situated in the same row have the same CuSO₄ concentration but varies along the different set of row. The CuSO₄ concentrations were set to be 0.005, 0.01, 0.023, 0.033, 0.05 % for each different set of row. The 25 vials were constructed in this fashion for four times with different agarose concentration by 1.0, 1.2, 1.4, 1.8 %.

B. T₁, T₂ mapping methods

For T₁ mapping, inversion recovery spin echo data with varying inversion recovery time were collected. Specific scan parameters were TI=50 100 150 200 250 300 350 400 450 500 750 1000 1500 2000ms, TR=5s TE=8.5ms, FOV=256x256mm², matrix size : 128x256. For T₂ mapping, single spin echo data with different echo times were collected. TE=10 20 30 40 50 60 70 80 90 100 120 140 160ms, TR=5s, FOV=256x256mm²,

matrix size : 128x256. Non-linear least square fitting was used to measure T₁, T₂ values from the collected data. Signals from each vials were averaged to increase the accuracy of the fitting.

III. RESULTS

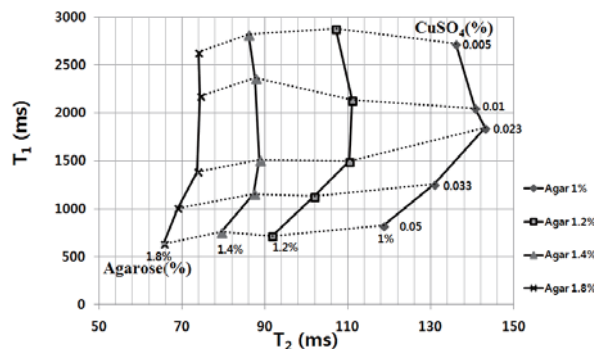


Fig. 2. T₁ and T₂ mapping results for each agarose and CuSO₄ concentrations.

Fig 2 shows the measured T₁, T₂ values from the proposed phantom experiments. From the result, T₁ values of the phantom decreased as CuSO₄ concentration increases. T₂ values mainly decreased as agarose concentration increases and less affected by CuSO₄ concentration changes.

Table 1. Agar & CuSO₄ concentration for mimicking tissue

Tissue	T ₂ (ms)	T ₁ (ms)	Agar	CuSO ₄
GM	99	1820	1.3%	0.016%
WM	80	832	1.46%	0.045%

Using interpolation method, agarose and CuSO₄ concentrations were proposed in order to mimic T₁, T₂ values of gray matter and white matter in human brain (Table 1).

IV. CONCLUSION

We successfully acquired the relationship between agarose, CuSO₄ concentrations and T₁, T₂ values. From this observation, recipes which mimic human tissue relaxation times were proposed. This can be useful to validate new techniques in MRI before doing in vivo experiment.

REFERENCES

1. K. Hattori, et al, "Development of MRI phantom equivalent to human tissues for 3.0-T MRI," *Medical Physics.*, vol. 40, No.3, March 2013.
2. M. D. Mitchell et al, "Agarose as a tissue equivalent phantom material for NMR imaging," *Magnetic Resonance Imaging.*, vol. 4, pp. 263~266,1986.

In vitro Calcium Imaging of Spontaneous Neuronal Activity

Jungmin Hong¹, Hee jin Park², Chanmi Yeon¹, Jihee Ryu¹, Sohee Kim^{1,2}, Euiheon Chung^{1,2,*}

¹Department of Medical System, Gwangju Institute of Science and Technology, Gwangju, South Korea

²School of Mechatronics, Gwangju Institute of Science and Technology, Gwangju, South Korea

*E-mail: ogong50@gist.ac.kr

Abstract—Calcium imaging has been used widely to monitor neuronal activity. With cultured primary neurons, we obtained fluorescence imaging of calcium spiking and analyzed the temporal activities toward connectivity of networked neurons.

Keywords — primary neurons, calcium imaging, fluorescence imaging, spontaneous neuronal activity

I. INTRODUCTION

Calcium imaging is often used to study functional connectivity, brain mapping, and analyze patterns of spike signals. With fluorescence microscopy, spontaneous neuronal activity can be examined at individual cellular level. This approach allows to study functional connectivity in in vitro or in vivo setting for further investigation of understanding the response of neuronal networks with respect to neuronal stimulation that could shed light on the neuromodulation that is already in use in clinic without detailed mechanistic understanding.

II. METHODS

Primary hippocampal neurons were cultured, incubated with calcium dye, and imaged for analysis.

A. Preparation of Primary Neuron

Embryos were taken out from a rat on the 18th day of pregnancy. After decapacitation, hippocampi were extracted and dissociated using papain solution (papain + HBSS) and DNase1. Dissociated neurons were plated on cover slips in Petri dishes.

B. Loading of OGB-1AM Calcium Dye

Artificial cerebral spinal fluid (ACSF) containing the following concentration (in mM) was made: 125 NaCl, 2.5 KCl, 1.25 NaH₂PO₄, 26 NaHCO₃, 1 MgCl₂, 25 glucose, 2 CaCl₂·2H₂O. Calcium dying solution was prepared with the following method: Dissolve 50 µg of Oregon Green 488 BAPTA-1-AM (OGB-1AM) in 48 µl of DMSO and 2 µl Pluronic acid F-127. Dilute 2.5 µl of OGB solution into 1 ml of bACSF (ACSF mixed with HEPES (10 mM)). Prior to calcium imaging, the solution was spread on the cell for an hour.

C. Calcium Imaging

Imaging was performed with an upright Microscope (Olympus BX51) and an EM-CCD camera (Andor iXon3 897). The neurons were kept on a heating plate at 37 °C.

D. Analysis of Calcium Fluorescence from Neurons

We used Fluorescence Single Neuron and Network Analysis Package (FluoroSNNAP) [2]

<http://www.ncbi.nlm.nih.gov/pubmed/25629800>.

Fluorescence signals were computed as the ratio of change in fluorescence.

III. RESULTS

Spontaneous calcium activity of neurons were obtained with green fluorescence (Fig. 1A) Total 76 neurons are identified, and 7 % of them showed recognizable spontaneous calcium activity. A representative time trace of neuron No. 70 was analyzed with the brightness of fluorescence (Fig. 1B) and its relative change (Fig. 1C) are shown..

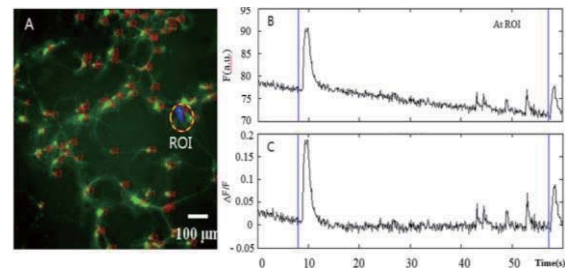


Fig. 1. Primary neuron imaging and calcium spike signal (A) Loaded neuron cells, (B) Calcium fluorescence, (C) Ratio of change in fluorescence

ACKNOWLEDGEMENT

This research was supported by a grant from Institute of Medical System Engineering (iMSE) and a GIST-Caltech Research Collaboration grant in GIST. We thank Min Jee Jang from Prof. Yoon-Key Nam's Lab at KAIST; Prof. Myung-Han Yoon's Lab at GIST; Minsu Yoo, SeongWon Min, Natasha Powell, and members of Bioscopy Lab for technical assistance and discussion.

REFERENCES

1. M. Tada, et al. "A highly sensitive fluorescent indicator dye for calcium imaging of neural activity *in vitro* and *in vivo*," *European journal of Neuroscience.*, vol. 39, iss. 11, pp. 1720-1728, 2014.
2. Patel, Tapan P., et al. "Automated quantification of neuronal networks and single-cell calcium dynamics using calcium imaging," *Journal of neuroscience methods*, vol. 243, pp. 26-38, 2015.

Simulation study of abdominal fat imaging with electrical impedance tomography

G. Y. Jang¹, S. Z. K. Sajib¹, H. Wi², T. I. Oh¹, and E. J. Woo¹

¹Department of Biomedical Engineering, Kyung Hee University, Seoul, Republic of Korea

²Department of Computational Science and Engineering, Yonsei University, Seoul, Republic of Korea

E-mail: tioh@khu.ac.kr

Abstract—A fundamental cause of metabolic syndrome is abdominal obesity. Specially, accumulation of visceral fat is highly related with health problems. In this study, we numerically simulated the possibility of electrical impedance tomography method for distinguishing between visceral fat obesity and abdominal subcutaneous fat from the reconstructed conductivity images with different measurement protocols.

Keywords— Electrical impedance tomography, visceral fat, subcutaneous fat, metabolic syndrome, measurement protocol.

I. INTRODUCTION

Metabolic syndrome is highly related with lifestyles and health problems. Specially, abdominal obesity and accumulation of visceral fat are main reasons for it [1]. Dual energy x-ray absorptiometry (DXA), X-ray CT, or MRI is primarily used to measure the body composition and fat content with a high degree of accuracy in the hospital. However, it's too expensive and bulky to screen all people. We require a smaller, more inexpensive, safer device for visceral fat quantitation in order to screen the patients with a high risk for metabolic syndrome. Tissue characterization method or imaging method using electrical impedance may be a candidate for body fat estimation with the safer method [2].

In this study, we developed the numerical model based on anatomical structure of abdomen with tissue conductivities and simulated with different measurement protocols to evaluate the EIT method for fat mass estimation.

II. METHODS & RESULTS

A. Cross-sectional abdomen model

We segmented the body shape, fat, muscle, kidney and bone from MR image based on anatomical sense and generated the cross-sectional abdomen model (Fig.1) using Comsol 3.5a.

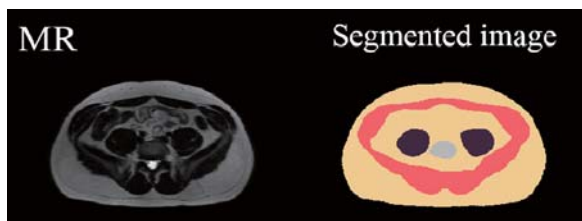


Fig. 1. MR image (left) and segmented model (right)

B. Mesh generation and conductivity setting

For forward and inverse numerical computation, we generated the 2D FEM models (forward and inverse mesh, respectively) and attached 16 electrodes for current injection and voltage measurements. After meshing, we set the conductivity of the fat, muscle, kidney, and bone, respectively (Fig. 2).

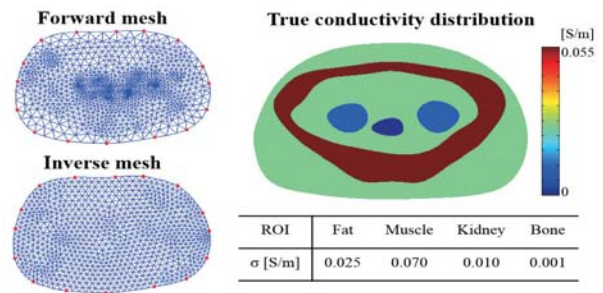


Fig. 2. FEM model (left) and conductivity setting (right)

C. Numerical Simulation with measurement protocols

We injected the current with adjacent or diagonal methods and measured induced voltage with adjacent pairs of electrodes. Two data sets (adjacent and diagonal) were used to reconstruct absolute conductivity images and we solved using the following regularized inverse method (7 times iteration).

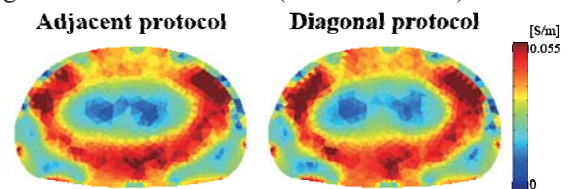


Fig. 3. Reconstructed absolute conductivity images using adjacent and diagonal protocols

III. CONCLUSION

From the reconstructed absolute conductivity images (Fig.3) can distinguish each region for fat (green), muscle (red), and kidney (blue). Depending on the measurement protocols, the sensitivity of center area was slightly different. Diagonal protocol was more sensitive inside than adjacent protocol.

ACKNOWLEDGEMENT

This work was supported by a grant of the Korean Health Technology R&D Project, Ministry of Health and Welfare, Republic of Korea (HI14C0743).

REFERENCES

1. J. P. Després, and I. Lemieux, "Abdominal obesity and metabolic syndrome," *Nature*, vol. 444, pp. 881-887, 2006.
2. M. Ryo *et al.*, "A new simple method for the measurement of visceral fat accumulation by bioelectrical impedance," *Diabetes Care*, vol. 28, pp. 451-453, 2005.

Pseudo-color optical biopsy using multichannel confocal microscopy

Juehyung Kang¹, Hyeong Soo Nam¹, ByungSeon Chun², Incheon Song²,
Dae Kyung Sohn³, Kwang Gi Kim³, Hyunjin Kim³ and Hongki Yoo¹

¹Dept. of Biomedical Engineering, Hanyang University, Seoul, South Korea

²Nanoscope Systems, Inc., Daejeon, South Korea

³Research Institute and Hospital, National Cancer Center, Gyeonggi-do, South Korea

E-mail: hyoo@hanyang.ac.kr

Abstract— Grayscale confocal images are converted to resemble hematoxylin and eosin staining for frozen sections. The pseudo-color confocal images allow pathologists to identify cancer cells without additional training.

Keywords— Optical biopsy, Fluorescence Confocal Microscopy, H&E staining, Pseudo-color

I. INTRODUCTION

Confocal microscopes are able to create optical biopsy from a tissue. Its main strength is its ability to optically section thick tissues which allows pathologists to evaluate tissue samples with a cellular level resolution without physically slicing the sample. The limited field of view of the confocal microscopes can be effectively expanded with strip mosaicking[1].

The result images of a multichannel confocal microscope are either in grayscale or simple pseudo-color such as green and blue given by the microscope's default program. We have devised a method to convert the grayscale image into pseudo-color H&E (Hematoxylin and Eosin) image to resemble frozen histology.

This technique would be especially useful during Mohs surgery. The surgical process requires patients to wait in the surgery room with their surgery spot open for up to 2 to 3 hours. Most of the waiting time is spent during the process of freezing, slicing and staining the sample to be viewed with a microscope. Due to the ability of confocal microscopes to optically section thick tissues, this time can be saved significantly, cutting the surgery time to around 20 to 30 minutes.

II. METHODS

A. Confocal image acquisition & tissue preparation

Confocal images were obtained using a multichannel confocal microscope (Carl Zeiss LSM-510, Plan-Neofluar 10x, 20x/0.5). Eosin Y (Ex. 488 nm/ Em. 499-633 nm) and Hoechst 33342 (Ex. 405 nm/ Em. 410-513 nm) were used in staining actin and nuclear, respectively. Tissue slices of Calu-3 lung cancer cell xenograft carried in Balb-c/nu mouse were used.

B. Creating H&E colormap & pseudo-color image

H&E histology was selected to create a colormap for the pseudo-color image. The colormap was created by comparing the grayscale intensity of the histology to the red, green and blue intensity of the digitally scanned H&E histology. Interpolation was done to select the best fit for each grayscale intensity. Single RGB values were assigned to each grayscale value to create a colormap. By using the colormap, grayscale images from the confocal microscope were converted into pseudo-color H&E image

III. RESULTS

The results suggest that H&E pseudo-color image can be made to resemble actual frozen histology as shown in Fig1..

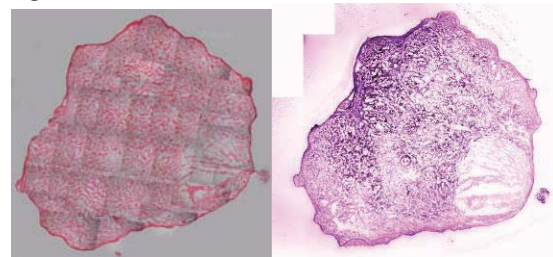


Fig. 1. Frozen histology (left), pseudo-color image(right)

IV. CONCLUSION

With the help of H&E pseudo-color images, the multichannel confocal microscope can be more pathologist-friendly, without the hassle of freezing and slicing the tissue or go through training to examine grayscale confocal images. Same method can be used to create a new type of colormap to emphasize specific cellular components which would allow pathologists to identify lesion.

ACKNOWLEDGEMENT

This work was supported by the MOTIE grant (10049773).

REFERENCES

1. Sanjee Abeytunge, Yongbiao Li, Bjorg Larson, Gary Peterson, Emily Seltzer, Ricardo Toledo-Crow and Millind Rajadhyaksha, "Confocal microscopy with strip mosaicing for rapid imaging over large areas of excised tissue", *Journal of Biomedical Optics*, vol. 18, pp 061227, 2013
2. Rafael C. Gonzalez and Richard E. Woods, *Digital image processing*, New Jersey, Prentice-Hall, 2002

System development and motion compensation of full-field swept-source optical coherence tomography integrated with surgical microscope

Chang-Soo Kim¹, Hyeong Soo Nam¹, Hyunki Lee², Hongki Kim², Hongki Yoo^{1,*}

¹Department of Biomedical Engineering, Hanyang University, Seoul, Korea, Republic of

²Koh Young Technology, Inc., Seoul, Korea, Republic of

*E-mail: hyoo@hanyang.ac.kr

Abstract— We present a full-field swept-source optical coherence tomography (FF-SS-OCT) integrated with a surgical microscope to observe the tomographic structures and the macroscopic image of the sample simultaneously. Also, we present an algorithm to compensate the motion artifact of the sample, which is severe in FF-SS-OCT. The OCT image blur by the motion-induced phase shift in the interference fringe pattern can be estimated and compensated by using the short-time Fourier transform.

Keywords— Full-field swept-source optical coherence tomography (FF-SS-OCT), Motion compensation, Surgical microscope, Short-time Fourier transform (STFT)

I. INTRODUCTION

In the operating room, surgeons observe the surgical site in detail using surgical microscopes. Full-field swept-source optical coherence tomography (FF-SS-OCT) achieves high-speed 3D volumetric imaging due to parallel acquisition without a need of beam scanning [1]. Combination of FF-SS-OCT and surgical microscope would enable to observe the macroscopic image and the tomographic structures of surgical site simultaneously.

The sample motion during the acquisition distorts the interference fringe pattern [2], and affects the image quality significantly in FF-SS-OCT. The motion-induced phase shift in the interference fringe pattern can be corrected by the short-time Fourier transform (STFT).

II. METHODS

A. FF-SS-OCT system integrated with surgical microscope

We employed a swept wavelength tunable laser (Broadsweeper 785HP, Superlum Ltd., Ireland) which has a center wavelength of 795nm with a bandwidth of 50nm. 1000 images of 2048×2000 pixels were acquired during the laser sweeping for 8.33 seconds synchronized with 4M pixel CMOS camera (CMB4MCL, Sentech Co., Ltd, Japan) which has a frame rate of 120fps, corresponding to an A-line rate of 480kHz. The volumetric image was acquired with a field of $8.45 \times 8.25 \times 3.2\text{mm}^3$ ($2048 \times 2000 \times 512$ pixels). The dispersion induced from the surgical

microscope was measured and compensated by placing the 2mm SF11 rod in the reference path.

B. Estimation and correction of the sample motion

STFT was applied to estimate the motion during the acquisition. We calculated the compensation function from the estimated motion, and by using its phase information, the motion-induced blurring can be minimized after the motion compensation.

III. RESULTS

Figure 1 shows 3D image of a phantom sample made of two-layered semi-transparent tape (Scotch 3M magic tape) which has an air-gap acquired by the FF-SS-OCT system integrated with surgical microscope.

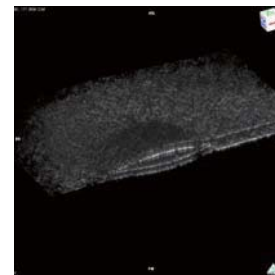


Fig. 1. Three-dimensional image of two-layered phantom.

IV. CONCLUSION

We integrated the FF-SS-OCT with the surgical microscope which enables high-speed 3D tomographic imaging while surgeons observe the macroscopic image, simultaneously. Also, we developed the motion compensation algorithm to improve image quality by correcting the phase information of acquired OCT information.

ACKNOWLEDGEMENT

This work was supported by Koh Young Technology, Inc.

REFERENCES

1. Považay, B., Unterhuber, A., Hermann, B., Sattmann, H., Arthaber, H., and Drexler, W., "Full-field time-encoded frequency-domain optical coherence tomography," *Opt. Express* 14(17), 7661–7669 (2006).
2. S. H. Yun., G. J. Tearney, J. F. de Boer, and B. E. Bouma, "Motion artifacts in optical coherence tomography with frequency-domain ranging," *Opt. Express* 12(13), 2977–2998 (2004).

Segmentation of subcortical area based on graph cuts algorithm

J. W. Hong¹, S. B. Park², K. C. Kwak³, J. M. Lee³, U. C. Yoon¹

¹Department of Biomedical Engineering, Catholic University of Daegu, Gyeongsan, South Korea

²Department of Neurology, Samsung medical center, Seoul, South Korea

³Department of biomedical engineering, Hanyang University, Seoul, South Korea

E-mail: yoouuc@cu.ac.kr

Abstract— Segmentation of subcortical area was very difficult since it was small and covered by white matter. The proposed method was validated with well-known program using dice similarity index (SI), recall, precision values. It was significantly better than the other (SI (left, right): 0.875 ± 0.016 , 0.870 ± 0.016 vs. 0.868 ± 0.018 , 0.870 ± 0.012 ; Recall : 0.867 ± 0.020 , 0.881 ± 0.021 vs. 0.864 ± 0.029 , 0.880 ± 0.022 ; Precision : 0.884 ± 0.025 , 0.860 ± 0.035 vs. 0.872 ± 0.019 , 0.862 ± 0.027).

Keywords— MRI, Segmentation, Putamen, Graph cuts

I. INTRODUCTION

Graph cuts algorithm with one or more prior information is efficient segmentation method [1]. And basal ganglia had low contrast-to-noise ratio so that it was very difficult to segment this structure, especially putamen using automated method. In this paper, we proposed graph cuts algorithm for segmentation of putamen and compared with well-known program, FSL-FIRST.

II. METHODS

Subjects and gold standard data were drawn from the Imperial College of Science Technology & Medicine [2]. Preprocessing for graph cuts algorithm was consisted of three steps which were nonuniformity correction of MRI, spatial normalization to the standard space and tissue classification. The final step subdivided brain to white matter (WM), gray matter (GM) and cerebrospinal fluid (CSF) and estimated partial volume of each tissue class. After then, a prior information of graph cuts algorithm was taken from atlas-based segmentation. Putamen is essentially GM but surrounded by WM. Consequently, foreground of prior information was modified by GM partial volume map but background was corrected by WM one. Finally, graph cuts algorithm was used to find a global minimum of energy function with minimum cut / maximum flow approach.

III. RESULTS



Fig. 1. Segmentation results (yellow : even, red : overestimation, blue : underestimation)

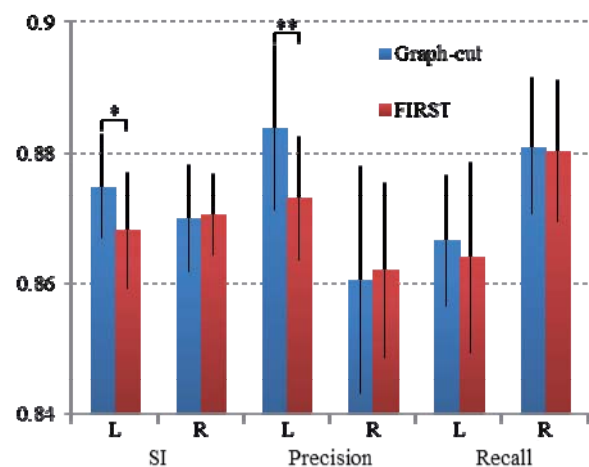


Fig. 2. Plot of statistical values for each segmentation method. (* $p < 0.05$, ** $p < 0.01$ where p indicates the statistical significance)

IV. CONCLUSION

We proposed an automated framework of segmentation method for putamen which was significantly better than FSL-FIRST.

ACKNOWLEDGEMENT

This work was supported by Basic Science Research Program through the National Research Foundation of Korea (NRF) funded by the Ministry of Science, ICT & Future Planning (2014R1A1A1005536).

REFERENCES

1. B. Peng et al., "Iterated graph cuts for image segmentation," *Computer Vision-ACCV 2009. Springer Berlin Heidelberg*, pp. 677-686, 2010
2. A. Hammers et al., "Three-dimensional maximum probability atlas of the human brain, with particular reference to the temporal lobe," *Human brain mapping*, vol. 19, pp.224-227, 2003

Atlas-based diffusion tensor analysis with partial volume effect

W. H. Choi ¹, K. H. Kang ², and U. C. Yoon ¹

¹Department of Biomedical Engineering, Catholic University of Daegu, Gyeongsan South Korea

²Department of Neurology, School of Medicine, Kyungpook National University, Daegu South Korea

E-mail: yoonu@cu.ac.kr

Abstract—In this study, we proposed region of interest (ROI) study of diffusion tensor image (DTI) and improved its accuracy using partial volume effect (PVE). PVE is used to reduce an amount of gray matter (GM) and cerebral spinal fluid (CSF) within ROI of WM. The result showed that the averages of fractional anisotropy (FA) and mean diffusivity (MD) within ROI were increased and decreased, but standard deviation was decreased when PVE was incorporated with ROI study. Therefore, it suggested that the proposed method was suitable to improve an accuracy of ROI study for DTI.

Keywords—Diffusion tensor imaging, Partial volume effect, Fractional anisotropy, Mean diffusivity.

I. INTRODUCTION

ROI study needs to improve its accuracy using automated segmentation method. However, most study disregarded a portion of CSF or GM within ROI of WM [1]. PVE could be used to reduce an amount of GM and CSF within ROI of WM. In this study, we assessed averages of FA and MD within ROI of DTI after applying PVE. In addition, we identified the effects of PVE on group analysis.

II. METHODS

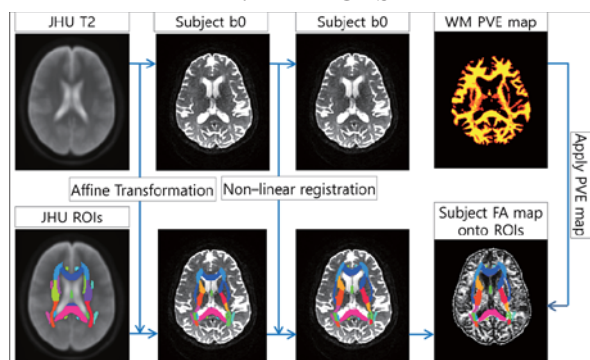


Fig. 1. Processing Diagram

T2 weighted reference brain from the Johns Hopkins University (JHU) labels atlas was spatially normalized to individual subject b0 image using affine transform and non-linear registration. These transform matrices were applied to each ROI in the JHU atlas essentially resulting in ROIs within each subject b0 space.

Individual PVE map was spatially aligned to each subject native image using affine transform.

III. RESULTS

The comparison of statistical results with and without PVE is shown at Fig. 2. It showed averages of FA and MD within ROI were increased and decreased, respectively, but standard deviation was decreased.

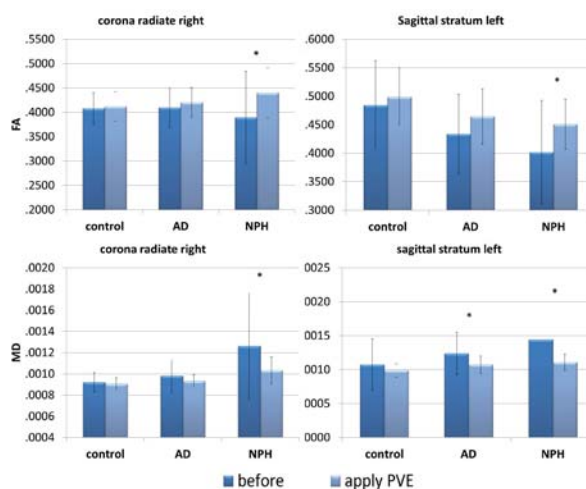


Fig. 2. Bar graphs showing the means and standard deviations of FA and MD with and without PVE.

IV. CONCLUSION

We proposed an ROI study method which improved its accuracy using PVE. The result showed that it could be used for a more accurate group analysis.

ACKNOWLEDGEMENT

This work was supported by Basic Science Research Program through the National Research Foundation of Korea (NRF) funded by the Ministry of Science, ICT & Future Planning (2014R1A1A1005536).

REFERENCES

1. K. Oishi, et al. "Atlas-based whole brain white matter analysis using large deformation diffeomorphic metric mapping," *Neuroimage*, vol. 46, pp. 486-499, 2009.

The effect of Micro-current therapy on Adjuvant Induced Rheumatoid Arthritis

H. A. Lee¹, S. H. Kim¹, D.H. Hwang¹, S. K. Cho², Y.J. Park¹, D.H. Seo¹, J. H. Park¹
and H. S. Kim^{1,2}

¹Department of Biomedical Engineering, Yonsei University, Korea

²Yonsei-Fraunhofer IZFP Medical Device Lab, Korea

E-mail: hanskim@yonsei.ac.kr

Abstract— This study evaluated whether micro-current therapy (MET) may be effective on the reduction of inflammation according to rheumatoid arthritis. Micro CT images were used to analyze the bone qualities. 15 male mice (8-week-old C57BL/6) were allocated into three groups; normal (N), induction of rheumatoid arthritis without (RA) and with (M) treatment. From the comparative result between without and with treatment, bone volume and bone mineral density in the M group had relatively higher values than that of RA group after 2 weeks. In this study, we can estimate that MET may be applicable to treat rheumatoid arthritis.

Keyword— Micro-current therapy, Rheumatoid arthritis, In-vivo micro CT

I. INTRODUCTION

Micro-current therapy is able to stimulate cellular physiology through increasing ATP generation and protein synthesis. The properties of MET eventually accelerate healing for various clinical conditions including musculoskeletal disorders. This study analyzed the effect of MET on rheumatoid arthritis.

II. METHODS

A. Animals and induced rheumatoid arthritis

The protocols for all the procedures were approved by the Yonsei University Animal Care Committee. 15 male 8-week-old C57BL/6 mice were randomized into 3 groups (5 mice each); normal (N) group, induced rheumatoid arthritis (RA) group and rheumatoid arthritis with 22 μ m of micro-current therapy (M) group. Injecting CFA into both sole of mice in (N) and (M) groups in order to cause rheumatoid arthritis. All mice were freely accessed to food and water. The mice were kept under a 12:12-hour light-dark cycle (25 \pm 1 $^{\circ}$ C, 50 \pm 5% humidity).

B. Micro-current therapy

The treatment group was stimulated by micro-current with the intensity of 22 μ m for 2 weeks. (5 days per week, temperature 37 $^{\circ}$ C, 1hr).

C. Micro-CT

Third metatarsal for both feet of each mouse were scanned by using in-vivo micro-CT (Skyscan 1076,

Bruker, Germany) at 0week (before stimulation), 1 week and 2weeks (after stimulation).

III. RESULTS

A. Bone volume and bone mineral density

To refer Fig. 1, bone volume and bone mineral density in the M group had relatively higher values than that of RA group after 2 weeks.

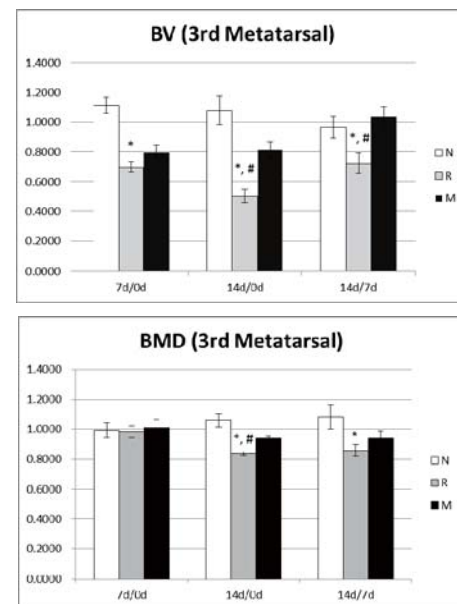


Fig. 1 Bone volume and bone mineral density of 3rd Metatarsal

IV. CONCLUSION

Rheumatoid arthritis is a major cause of synovial inflammation and joint destruction. We evaluated the effects of micro-current therapy on Rheumatoid arthritis since it alleviates the symptoms by increasing amino acid transport. The results represented that MET therapy with the intensity of 22 μ m increases bone volume ratio and bone mineral density. Therefore, MET can be an effective treatment or inhibition of rheumatoid arthritis.

ACKNOWLEDGEMENT

This research was supported by the Leading Foreign Research Institute Recruitment Program through the National Research Foundation of Korea (NRF) funded by the Ministry of Science, ICT & Future Planning (2010-00757).

Assessment of temperature difference between tumor and normal region using infrared thermography

Soonjoo Hwang¹, Yeon-Mi Ryu², Gyungseok Oh³, Su Woong Yoo¹, Jiyoung Shin²,
Sang-Yeob Kim², Seung-Jae Myung^{2,4}, and Euiheon Chung^{1,3,*}

¹Department of Medical System Engineering, Gwangju Institute of Science and Technology (GIST), Gwangju, South Korea

²Asan Institute for Life science, Asan Medical Center, University of Ulsan College of Medicine, Seoul, South Korea

³School of Mechatronics, Gwangju Institute of Science and Technology (GIST), Gwangju, South Korea

⁴Department of Gastroenterology, Asan Medical Center, University of Ulsan College of Medicine, Seoul, South Korea

*E-mail: ogong50@gist.ac.kr

Abstract—Infrared thermography is an emerging technology with a potential to differentiate tumor from normal tissue based on temperature difference. With xenograft tumor model, the thermographic temperature distribution and tumor growth is compared. Infrared thermography may provide a novel screening tool for tumor detection.

Keywords—Infrared thermography, tumor detection.

I. INTRODUCTION

Nowadays, the incidence rate of colorectal cancer has been accelerating. As a molecular imaging approach to diagnose cancer within gastrointestinal tract, fluorescence endoscopy with molecular probe has proven to be a potential tool [1]. However there are only few fluorescent probes that are compatible with human use. Here we suggest a novel label-free approach to differentiate tumor from normal tissue based on infrared thermography that has a potential to be endoscopic modality in the future..

II. MATERIALS & METHODS

Xenograft model of nude mouse (BALB/c nu/nu) was made with a human colon cancer cell line (HCT-116 and SW-620).

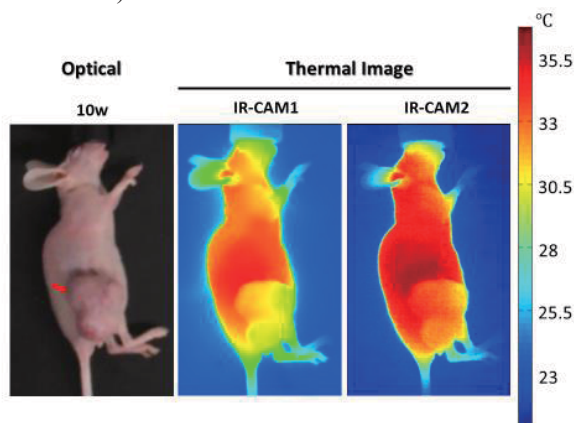


Fig. 1. Infrared Thermography on xenograft model. Two thermal camera was used. Arrow indicates tumor. Tumor volume: $\sim 3500 \text{ mm}^3$. Temperature difference is -2.6°C and -1.6°C by IR-CAM1, IR-CAM2, respectively.

Thermal images were acquired with two separate IR cameras (IR-CAM1: FLIR T600 (FLIR Systems Inc.), IR-CAM2: Therm-App(Opgal Optronic Industries Ltd., Karmiel, Israel).

III. RESULTS & CONCLUSIONS

The longitudinal measurements of tumor volume and temperature differences with two thermal cameras are conducted (Fig. 2). Surprisingly, the tumor temperature drops while the tumor gets bigger. This results might be due to the compression and collapse of intratumour vessels [2]. Our results indicate that tumor has detectable temperature difference compared with neighboring normal tissue, and thus this thermographic approach may provide a potentially new way of early cancer detection without any exogenous labeling.

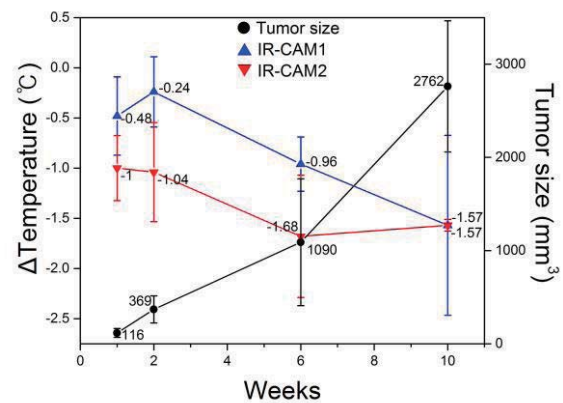


Fig. 2. Thermographic temperature changes during tumor growth (n=3-5)

ACKNOWLEDGEMENT

This research was supported by the Bio & Medical Technology Development Program of the National Research Foundation (NRF) funded by the Korean Government (MEST) (2011-0019633) and by a grant (2015-7402) from the Asan Institute for Life Sciences, Asan Medical Center, Seoul, Korea and also a grant from institute of Medical System Engineering (iMSE) in GIST.

REFERENCES

1. Goetz, Martin, and Thomas D. Wang. "Molecular imaging in gastrointestinal endoscopy." *Gastroenterology* vol. 138, iss. 3, pp. 828-833, 2010
2. Padera, Timothy P., et al. "Pathology: cancer cells compress intratumour vessels." *Nature* vol. 427, Iss.6976 pp. 695-695, 2004.

The Effect of Hypoxia on the Cerebral Blood Oxygenation of Gerbil Measured by Functional Near-infrared Spectroscopy

S. Hong¹, Yeon Hee Yu², Duk-Soo Kim², and K. S. Park³

¹Interdisciplinary Program of Bioengineering, Graduate School, Seoul National University, Seoul, Republic of Korea

²Departments of Anatomy, College of Medicine, Soonchunhyang University, Cheonan, Republic of Korea

³Department of Biomedical Engineering, College of Medicine, Seoul National University, Seoul, Republic of Korea

E-mail: hongsh@bmsil.snu.ac.kr

Abstract—In this study, the effect of hypoxia on the cerebral blood oxygenation was observed by fNIRS for the comparison between two gerbils simultaneously. The result showed the different amplitude levels and did not show distinguishable difference between two subjects.

Keywords— functional Near-infrared Spectroscopy, fNIRS, hypoxia

I. INTRODUCTION

The graded hypoxia is one of method to derive the hemodynamics [1]. We applied the methodology to measure the blood oxygenation in the brain of two mongolian gerbils simultaneously using functional near-infrared spectroscopy(fNIRS) in a chamber.

II. METHODS

A. fNIRS measurement

We measured the cerebral blood oxygenation of the gerbils the using an in-house fNIRS system. The fNIRS system handled two-wavelength LED (770nm and 850nm) using continuous-wave modulation [2]. The two LED- photodetector pairs were positioned on a seizure-resistant (SR) gerbil and a seizure-sensitive (SS) gerbil respectively. We adjusted 8th butterworth Low pass filter (cutoff frequency=0.2Hz) to the digitized data (10Hz).

B. Experimental protocol

The mongolian gerbils (9weeks, 50g) were anesthetized by after a single intraperitoneal dose of urethane (1.4 g/kg body wt). We positioned the animals in an airtight chamber which has airway to control the oxygen-nitrogen mixture. We changed the fraction of inspired oxygen (FiO₂) for hypoxia using 10, 8, 6, and 4% mixtures of oxygen balanced with nitrogen. We conducted 5 minutes hypoxia periods followed by the 5 minutes recovery period with the mixture of FiO₂ 30%.

III. RESULTS AND CONCLUSION

Fig 1 showed the normalized relative quantity of deoxy-hemoglobin(HbR) and oxy-hemoglobin(HbO) of two gerbils. The hypoxia period began from the dash-double dotted line to the solid line.

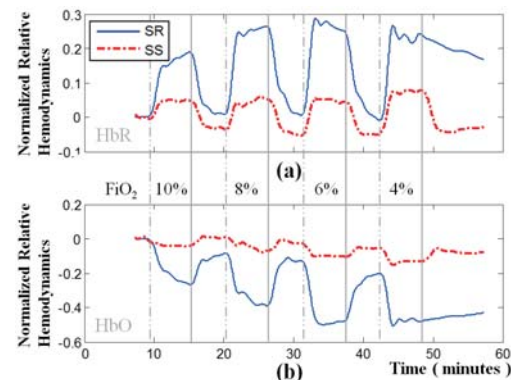


Fig. 1. The estimated values of the hemoglobin from gerbils

We derived the maximum HbR and minimum HbO observing cerebral blood oxygenation of the gerbils(Table 1). The results showed that the increase of HbR and the decrease of HbO during hypoxia periods by the reduction of FiO₂ from 10% to 4% as shown in the previous study[1] with the exceptions of maximum HbR of SR in FiO₂ 4% because of the death and of SS in FiO₂ 6%. The main finding was the different amplitude levels of two channels for SR and SS. It is because that the different formation of channels with the innate fur density and tissues in different subjects. However, the tendencies of the hemodynamics of SR and SS are not distinct.

Table 1. Extreme Values of Hemodynamics

HB	SR/SS	FiO ₂	FiO ₂	FiO ₂	FiO ₂
		10%	8%	6%	4%
Max HbR	SR	0.189	0.265	0.289	0.243
	SS	0.040	0.048	0.043	0.069
Min HbO	SR	-0.275	-0.398	-0.508	-0.515
	SS	-0.052	-0.086	-0.113	-0.162

REFERENCES

1. A. E. El-Desoky, A. M. Seifalian and B. R. Davidson, "Effect of graded hypoxia on hepatic tissue oxygenation measured by near infrared spectroscopy," *Journal of Hepatology*, vol. 31, pp. 71-76, 1999.
2. S. Hong, J. Heo, H. J. Baek, and K. S. Park, "The estimation of activated prefrontal brain area due to the execution of mental tasks using fNIRS," in *Proc. 50th KOSOMBE*, Seoul, Korea, May, 2015.

Frequency Domain Analysis of Laser speckle in Mouse Cerebral Cortex

Abdul M. Safi¹, Ahra Cho¹, Chanmi Yeon², Euiheon Chung^{1,2*}

¹School of Mechatronics, Gwangju Institute of Science and technology (GIST), Gwangju, South Korea

²Department of Medical System Engineering, Gwangju Institute of science and Technology (GIST), Gwangju, South Korea

*E-mail: ogong50@gist.ac.kr

Abstract—We introduce a novel frequency domain laser speckle imaging (FDLSI) for more quantitative analysis and obtained correlation function using animal stroke model based on photothrombosis.

Keywords— Laser speckle, frequency domain laser speckle imaging, stroke model, correlation function

I. INTRODUCTION

Laser speckle contrast imaging (LSCI) is an efficient and simple approach to obtain functional wide field imaging of blood flow as it provides spatial and temporal resolution. However, LSCI only provide semi-quantitative information due to the presence of static scatters in tissue. Recently, frequency domain laser speckle imaging (FDLSI) has shown the capability of quantitative flow information by analyzing speckle in frequency domain rather than time domain [2].

Here we show FDLSI for in vivo imaging of animal stroke model.

II. METHODS

A. Theory

Theory of temporal laser speckle contrast imaging has been discussed in detail [1]. We have calculated temporal domain contrast with single pixel over 25 temporal sequences of raw images. For FDLSI, we converted intensity $I(t)$ of each pixel from temporal domain to frequency domain and obtained the correlation curve using the eq.(1) [2].

$$C_t(t) = \int |\bar{I}(\omega)|^2 e^{i\omega t} d\omega - \langle I \rangle^2 \quad (1)$$

B. Animal preparation

C57BL/6 mouse with cranial window were used for the experiments. Mouse were anesthetized with Zoletil (10 μ L/BW g) and kept warm at 37°C on a heating plate during experiments. Rose Bengal dye solution (0.03 mg/g BW, diluted to 10 mg/ml of PBS100 ; dye: pBS = 0.1 g: 10 ml) was injected into mouse tail vein for photothrombosis model [3].

C. Laser speckle contrast imaging and photoactivation system

Light source for LSCI imaging: 633 nm He-Ne laser (633 nm) was coupled with single mode fiber and for LSCI for illuminated illumination at an incidence angle

of 30-45°. For photothrombosis, 532 nm laser was focused onto a single blood vessel reaction after i.v. injection of Rose Bengal dye [3]. Images were acquired using Andor Neo sCMOS camera at 40 Hz at an exposure time of 5 ms.

III. RESULTS

Our results shows LSI using temporal scheme (Fig. 1) which provide better spatial resolution. From Fig. 2 we see that frequency domain imaging provides sufficient result for each ROI: one on the vessel and the other outside of vessel.

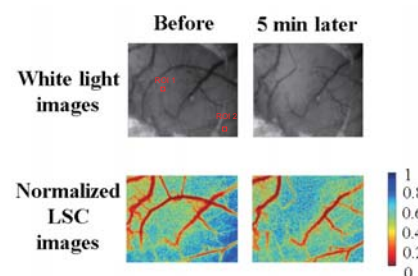


Fig. 1. White light and temporal domain LSC images before and after photothrombosis

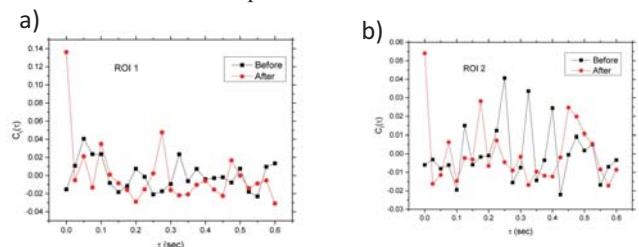


Fig. 2. Changes in correlation function before and after photothrombosis for ROI 1 (a) and ROI 2 (b)

ACKNOWLEDGEMENT

This work was supported by a grant from the Institute of Medical System Engineering of GIST and the “Gist-Caltech Research Collaboration” Project through a grant provided by GIST in 2015.

REFERENCES

- Cheng, Haiying, et al. “Modified laser speckle imaging method with improved spatial resolution.” *Journal of Biomedical Optics*, vol. 8, iss. 3 pp. 559-564, 2003.
- Li, Hao, et al. “..” *Optics express*, vol. 22, iss. 17, pp. 21079-21087, 2014.
- Sigler, A, A. Goroshkov, et al. “Hardware and methodology for targeting single brain arterioles for photothrombotic stroke on an upright microscope.” *Journal of neuroscience methods*, vol 170, iss. 1, pp-35-44, 2008.

Development of Dental 3D Scanner System for Direct Impression Scanning

Sang-Hyub Kim, Jun-Min Kim, Woo-Ram Lee

Abstract— This paper presents development of dental 3D scanner system for direct impression scanning. The proposed system has capability of scanning deeply incisive inner structures, which appear frequently in dental impressions. Direct impression scanning allows reducing manufacturing steps of plaster model of tooth structure.

I. PURPOSE

3D scanning technology combined with 3D printers is making huge impacts on manufacturing process in various fields such as dental industry. One promising application is fabricating a plaster model of tooth structure from 3D printing.

A traditional process of manufacturing a model includes 1) obtaining an impression, 2) fabricating a plaster model of the counterpart of the impression, 3) making a model of impression out of the counterpart model, 4) finally manufacturing a plaster model of tooth structure out of the impression model made in step 3). As 3D printing technology enters into the dental industry, step 3) and 4) can be replaced with the current 3D scanning/printing system. The 3D scanning system scans the outward dimensions of a plaster model which is generated from step 2), and then manufactures a final model through the 3D printer.

A question may arise why one doesn't scan images directly from the impression of a patient in step 1), and then print the plaster model. An impression of human tooth structure has complicated incisive inner structures due to sharp intraoral objects such as front tooth. Most 3D scanners available in dental industry use video imaging method with triangular measurement which basically projects laser or light on the object to scan and register based on the captured images [1] [2][3]. A part of impression imprinted by front teeth has deep and sharp incisive structure, so the light reflected can't return to the image sensor correctly or there would be multiple reflections on the incisive surface. This incurs data corruption in captured images, so leads to poor 3D registration performance.

In this paper, we present a new method to alleviate or remove obscurity due to deep and sharp incisive structures by

applying flexible stage architecture to change the position of the impression to scan.

II. METHODS

In order to prevent loss of light reflection or multiple reflections from the objects, we propose a flexible stage with 3 degrees of freedom and adaptive recognition algorithm. The flexible stage adjusts the position of the impression to be aligned with the light source and camera to avoid the light path to be blocked by the incisive structure. The stage moves on z-axis, rotates on z-axis and rolls over y-axis (Fig. (1)).

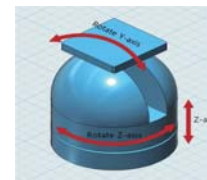


Fig. 1 A flexible stage system

The movement of the stages is controlled by the adaptive recognition algorithm. The algorithm first detects if the shadow zone is acquired from the current capturing. It recognizes the zone while calculating the point clouds. If the shadow zone is detected, then it estimates relationship of the current positions of the light source, camera, and object (the impression). Based on the estimate, it adjusts the position of the stage so that the light reflected from the surface returns to the camera without interference. As the captured images accumulate, the estimate becomes refined so to be able to achieve the best alignment position for the stage within least iterations of adjusting. Reducing the number of iterations, hence the total scan time, is an important matter, since the number of model manufactured in a given time is critical in a business point of view.

ACKNOWLEDGMENT

This research was supported by Entrepreneurship & Technology Support Program through the Korea Technology & Information Promotion Agency for SMEs.

REFERENCES

- [1] Douglas Lanman, Gabriel Taubin, "Build Your Own 3D Scanner: SD Photography for Beginners" in *SIGGRAPH 2009 Course Notes*.
- [2] Laura Ekstrand, Nikolaus Karpinsky, et al., "High-resolution, High-speed, Three-dimensional Video Imaging with Digital Fringe Project Techniques", in *Journal of Visualized Experiments Optics December 2013*.
- [3] Furqan Ullah, Gunn Soo Lee, Kang, "Development of a Real-time 3D Intraoral Scanner Based on Fringe-Projection Technique", in *Transactions of the Society of CAD/CAM Engineers, 2012*.

*Research supported by Korea Technology & Information Promotion Agency for SMEs.

Sang-Hyub Kim is with the Dept. of Electrical and Computer Engineering, Seoul National University, Seoul Korea (1 Gwanak-ro, Gwanak-gu, Seoul 151-744 (e-mail: icebug@snu.ac.kr).

Jun-Min Kim is with the Dept. of Electrical and Computer Engineering, Seoul National University, Seoul Korea (e-mail: ssipjul1@snu.ac.kr).

Woo-Ram Lee is with the Dept. of Electrical and Computer Engineering, Seoul National University, Seoul Korea (e-mail: wool001@snu.ac.kr).

Blood Flow Analysis by Correlation Analysis of the Laser Speckle Images

Sang-Hyub Kim, Jong-Mo Seo

Abstract— This paper analyzes characteristics of blood flow velocity using the correlation of consecutive laser speckle images. The major idea proposed here is the computation of similarity map between pairs of two consecutive laser speckle images under the controlled image capture period. The phantom liquid with the polystyrene particles is used instead of real blood for the analysis.

I. PURPOSE

Since the laser speckle photography/imaging was introduced for visualization of analyzing retinal blood flow in 1980s, the speckle imaging has been widely used for blood velocity analysis in many applications [1]. Basically the concept of the laser speckle imaging is to display relative flow velocity map with the contrast value of the speckle patterns shown as intensity. This gives a good understanding of overall velocity information in the entire image area.

Based on the concept of the laser speckle imaging, the temporal and spatial statistical processing methods have been developed in order to obtain the motion of scattering particles by enhancing intensity variations due to the speckle patterns [2]. The spatial speckle contrast that eventually provides 2-D maps of blood velocimetry is calculated by quantifying the blurring of the speckles over the camera exposure time. On the other hand, one obtains the temporal speckle contrast from the temporal standard deviation and the mean intensity of serial captured images to suppress high frequency temporal intensity fluctuations [3]. Both of statistical processing methods use contrast to draw relative velocity of the flow.

The new idea suggests a different method of measuring the flow velocity by applying Normalized Cross Correlation (NCC). The NCC processing outcomes the similarity of source and target images ranging between 0 and 1 [4]. The NCC is used to determine the spatial displacement of the objects in the two adjacent speckle images. With a given capture time and quantity of the displacement, the quantitative amount of particle moving speed can be obtained.

II. METHODS

In this paper, we performed the characteristic analysis of blood flow velocity with consecutive laser speckle images grabbed at the constant capture period. A 660nm laser diode is used for coherent illuminating. The capture speed of the full HD camera (KP-HD20A, HITACHI) which is attached to a

microscope (NIKON, C-DS) is controlled by setting shutter speed to 1/100s. Instead of real blood, three kinds of phantom liquid are used. The phantoms are composed of distilled water with three different sizes of polystyrene particles (SPHERO™, Spherotech, Inc.) of 0.53um, 5.98um and 8.49um, respectively. A syringe pump is used to inject the phantom fluid at a constant flow speed. The flow speed is set to satisfy the condition of laminar flow. With considering the viscosity of water and particle size, the injection speed by the pump is determined to have Reynolds number of the fluid flow less than 1.

The similarity map was calculated between two adjacent speckle images using the NCC. With the constant capture period and distance information extracted from the similarity map, the speed of particle flowing is calculated and compared with the known speed of phantom flow. The similarity map is computed from Eq (1),

$$S(i, j) = \text{NCC}(I_{n+1}(i, j), I_n(i, j)) \quad (1)$$

where $I_n(i, j)$ is the image with the window centered at (i, j) , and n is the index of the consecutive capture images. Based on the experiment, a window size of 20x20 is used.

ACKNOWLEDGMENT

This research was supported by Future-based Technology Development Program (Nano Fields) through the National Research Foundation of Korea (NRF) funded by the Ministry of Education, Science and Technology.

REFERENCES

- [1] J.D. Briers, A.F. Fercher, "Retinal blood-flow visualization by means of laser speckle photography" in *Invest. Ophthalmol. Vis. Sci., Assoc. for Res. In Vis. And Ophthal., Inc.*, February 1982.
- [2] David A. Boas, Andrew K. Dunn, "Laser speckle contrast imaging in biomedical optics", in *Journal of Biomedical Optics 15(1)*, January/February 2010.
- [3] Pengcheng Li, Songlin Ni et al., "Imaging cerebral blood flow through the intact rat skull with temporal laser speckle imaging", in *Optics Letters Vol. 31, No. 12, June 15, 2006*.
- [4] YiChang Shih, Abe Davis, Samuel W. Hasinoff, Fredo Durand, William T. Freeman, MIT CSAIL, "Laser Speckle Photography for Surface Tampering Detection"

Sang-Hyub Kim is with the Dept. of Electrical and Computer Engineering, Seoul National University, Seoul Korea (1 Gwanak-ro, Gwanak-gu, Seoul 151-744 (e-mail: icebug@snu.ac.kr).

Jong-Mo Seo is with the Dept. of Electrical and Computer Engineering, Seoul National University, Seoul Korea (e-mail: callme@snu.ac.kr).

A Quantitative Evaluation of Normal Appearing White Matter in Multiple Sclerosis Using New Myelin Water Imaging, ViSta

J. Y. Choi¹, I. H. Jeong², S. H. Kim², J. Y. Hyun², A. Joung², H. J. Kim^{2*}, J. Lee^{1*}

¹Department of Electrical and Computer Engineering, Seoul National University, Seoul, Korea

²Department of Neurology, Research Institute and Hospital of National Cancer Center, Goyang, Korea

E-mail: jychoi717@snu.ac.kr

Abstract— ViSta MWI is more sensitive to detection of myelin damage in NAWM in MS than the conventional MWI.

Keywords— Multiple sclerosis, myelin water imaging, ViSta, brain.

I. INTRODUCTION

This study aimed to investigate myelin damage in normal appearing white matter (NAWM) in multiple sclerosis (MS) using a new myelin water imaging (MWI) method, direct visualization of short transverse relaxation time component (ViSta) [1].

II. METHODS

Twenty seven MS patients and 14 healthy controls (HC) who provided the written consent were participated. Data were acquired using a 32 channel head coil at 3T MRI (Trio, Siemens, Germany).

For the ViSta MWI, 3D segmented EPI based ViSta sequence was performed using parameters used in the previous paper. For comparison, a conventional MWI was acquired using a 3D conventional spin echo MWI with a gradient echo and spin echo (GRASE) sequence and the acquired data were processed using a nonnegative least-square fitting method to calculate MWF values. To detect lesions in the brain, T₂ weighted image was acquired.

All MWIs were coregistered with T₂ weighted images using FSL (Oxford, UK) and brain NAWM masks were generated after excluding lesions in the T₂ weighted images. Student T-test was used to compare MWF values between MS and HC for both the conventional and ViSta MWIs. Additional statistical analysis was performed for comparison between MS in the early stage and HC. A *p*-value < 0.05 was considered to indicate statistical significance.

III. RESULTS

Representative T₂ weighted image, conventional and ViSta MWI in a MS are shown in Figure 1. As shown in Figure 1, ViSta MWI provided improved image quality compared to the conventional MWI.

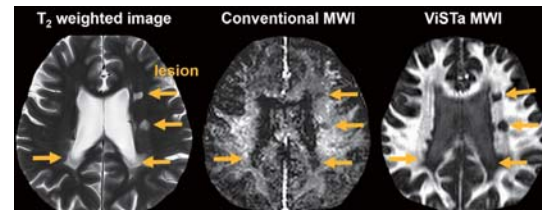


Fig. 1. T₂-weighted image, conventional, and ViSta MWI in a MS patient

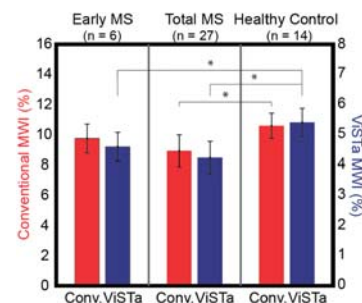


Fig. 2. Myelin water fraction in MS and healthy controls (**p* < 0.05)

Figure 2 shows MWFs of the conventional and ViSta MWI for MS and HC. When comparing MWF between total MS and HC, both the conventional and ViSta MWI show significance difference. However, only significant difference was found in ViSta MWI when comparing early MS and HC.

IV. CONCLUSION

This study shows the applicability of ViSta MWI to detect myelin damage in NAWM in MS. ViSta MWI may be sensitive to myelin damage in NAWM than conventional MWI

ACKNOWLEDGEMENT

This research was supported by the Brain Research Program through the National Foundation of Korea (NRF) funded by the Ministry of Science, ICT & Future Planning (NRF-2015M3C7A1031969).

This work was funded by UCB Pharma, Seoul, Korea.

REFERENCES

1. S. H. Oh, et al., "Direct visualization of short transverse relaxation time component (ViSta)," *Neuroimage*, vol. 83, pp. 485-492, 2013.

***In-vivo* measurement of aggregated myelin thickness map (g-ratio) using MRI**

J. W. Jung¹, J. Lee^{1*}

¹Department of Electrical and Computer Engineering, Seoul National University, Seoul, Korea
E-mail: wjjung93@snu.ac.kr

Abstract— Combined with NODDI and MWI using GRE is a new method of calculating g-ratio of *in vivo* human brain.

Keywords— Myelin water imaging, Diffusion tensor imaging, Magnetic resonance imaging, Brian.

I. INTRODUCTION

This study aimed to calculate g-ratio of *in vivo* human brain, defined as the ratio of the inner (axon) to the outer (axon + myelin) diameters, using advanced MRI neuroimaging methods.

To compute g-ratio, we measured axon volume fraction (AVF) and myelin volume fraction (MVF) instead of their diameter due to limitation of MRI resolution.

II. METHODS

Two sequences were performed *in vivo* in one healthy man using a 32 channel phased array head coil at 3T MRI (Trio, Siemens, Erlangen, Germany).

For computing MVF, multi-gradient echo (GRE) sequence was used and the acquired data were processed Levenberg-Marquardt method which can solve a nonlinear least squares problem. A 16-echo GRE sequence was used with following parameters: TR=67 ms, TE=1.5-32 ms, and voxel size=2.0×2.0×2.0 mm³.

AVF was calculated by using previous data acquired from GRE, diffusion tensor images (DTI), and post processing known as neurite orientation dispersion and density imaging (NODDI). To use NODDI processing, DTI were performed with 4 different b-values: 0, 300, 700, 2000 s/mm², same resolution with GRE sequence and TE=95 ms.

After acquiring MVF and AVF, whole-brain g-ratio map was approximated by the equation, $g = \sqrt{1/(1 + MVF/AVF)}$.

III. RESULTS

Optic radiation is well known for having higher myelin volume fraction than white matter. As shown in Figure 1, the final map of MVF accord closely with this statement. Furthermore, AVF of optic radiation were computed lower than an adjacent white matter due to high value of MVF.

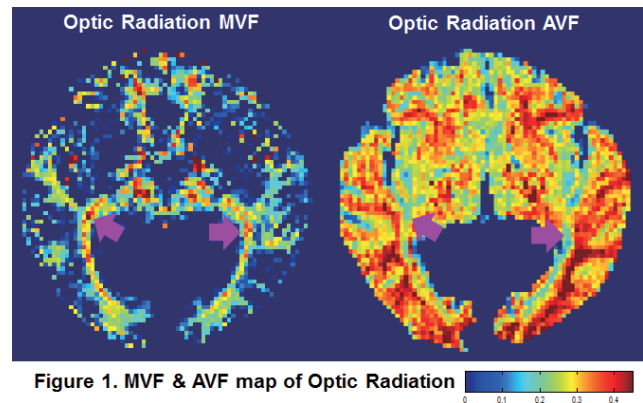


Figure 1. MVF & AVF map of Optic Radiation

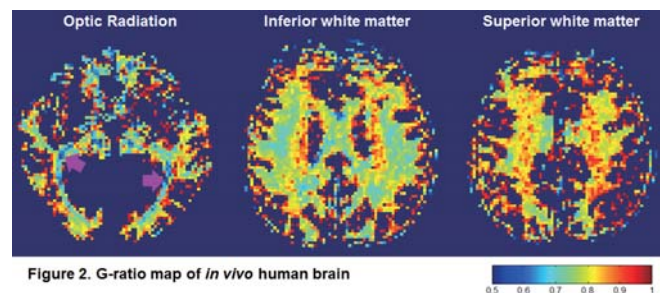


Figure 2. G-ratio map of *in vivo* human brain

According to the equation has shown in section II, the thicker the myelin sheath is, the lower g-ratio is computed. Following this statement, we succeeded to observe g-ratio of optic radiation was lower than the adjacent white matter as shown in Figure 2. In addition, g-ratio of white matter increased as we go superior slice of brain.

IV. CONCLUSION

There is a significant difference between g-ratio of optic radiation and the adjacent white matter.

G-ratio changes 0.76 to 0.82 in white matter. This range is in accordance with electromicroscopic results [1].

ACKNOWLEDGEMENT

This research was supported by the Brain Research Program through the National Foundation of Korea (NRF) funded by the Ministry of Science, ICT & Future Planning (NRF-2015M3C7A1031969).

REFERENCES

1. Nikola Stikov, et al., "In vivo histology of the myelin g-ratio with magnetic resonance imaging," *Neuroimage*, vol. 118, pp. 397-405, 2015.

Comparison of Laryngeal Stroboscopic Images using both Strobing Flash and Continuous Light

J. H. Ro¹, G. R. Jeon¹, G. H. Kim², H. J. Park³, D. H. Kang⁴, S. G. Wang²

¹Department of Biomedical Engineering, School of medicine, Pusan National University, Busan, Korea

²Department of otorhinolaryngology, Pusan National Hospital, Busan, Korea

³Department of Health Sciences, Choonhae College, Ulsan, Korea

⁴Pusan National University, Busan, Korea

E-mail: jhro@pnu.edu

Abstract— The image quality between strobing flash light and continuous light is compared. If the camera has a function of external trigger, it would be advantageous to use in combination of continuous light source.

Keywords— Strobing Flash light, Continuous light

I. INTRODUCTION

Stroboscopy is a special method used to visualize vocal fold vibration [1]. The image quality between strobing flash light and continuous light in laryngeal videostroboscopy is compared.

II. METHODS

Strobing flash light system : synchronization of strobing flash using vibration pick-up connected with external trigger and shutter speed is 1/100 s.

Continuous light system : sampling of image using vibration pick-up connected with external trigger, shutter speed is 1/2,000 s

III. RESULTS

In the strobing flash light, the shutter speed of 1/100 s was captured the best image quality of fan motor. In the continuous light, the shutter speed of 1/4,000 s was captured the best image quality.



Fig. 1. Images of laryngeal stroboscopy

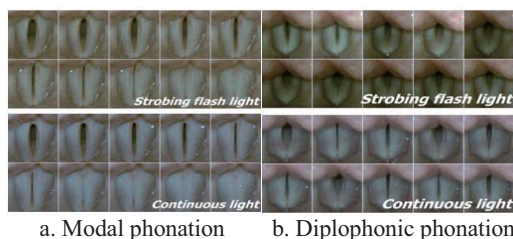


Fig. 2. Clarity: (a) Modal phonation, (b) Nonperiodic diplophonic phonation

In modal phonation, flicker was often perceived in laryngeal stroboscopy using strobing flash light, while flicker was not perceived using continuous light (Fig. 2a). In nonperiodic diplophonic phonation, it was difficult to observe the vocal folds vibration in strobing flash light due to flickering (Fig. 2b).

Table 1. Compare Strobing flash light with Continuous light

Strobing flash light(led)	Continuous light (Xenon)
Flickering	Flickerless (flicker free)
Inconvenient to convert videolaryngoscopy	Easy to convert videolaryngoscopy
LED(inexpensive)	Xenon (expensive)
Noiseless	Noisy
Color & resolution : natural but less clear	Color & resolution : clear but less natural
Cannot examine the vocal cords in nonperiodical vibration	Can examine the vocal cords even in nonperiodical vibration
External trigger : synchronize the strobing flash	External trigger : Control the sampling rate of image
popular	Less popular

IV. CONCLUSION

Each light source has its own advantages and disadvantages. If the camera has the function of external triggering, it would be advantageous to use in combination of continuous light source.

REFERENCES

1. M. Hirano, "Morphological structure of the vocal cord as a vibrator and its variations", *Folia Phoniatr (Basel)* vol. 26, pp 89-94, 1974.
2. T. Andrews, D. Purves, "The wagon-wheel illusion in continuous light," *Trends Cogn Sci.*, vol. 9, pp. 261-263, 2005.
3. S. G. Wang, H. J. Park, "Laryngealstroboscopy," *Sclerotherapy*, vol. 26, pp. 1-7, 2015.

Study of technical conditions for improvement of angiographic image quality.

Myagmarnaran.Ts¹, Enkhbaatar.A²

¹School of Nursing, Mongolian National University of Medical Sciences, Ulaanbaatar, Mongolia

²Nuclear Energy Agency, Ulaanbaatar, Mongolia

E-mail:myagmarnaran@mnums.edu.mn

Abstract

Introduction: The purpose of this study was to explore the quality of angiography equipment in diagnosis and treatment used in Mongolia, compare the use of angiography in Mongolia to international standards, type and number of angiography examinations, radiologist and patient's health safety from the effects of X-rays, and the study the benefits of the quality control tests of X-rays and how they affect image quality and other factors.

Methods: By experimental method, used an ionization chamber and test object for x-ray image quality to assess angiographic image quality based on The Mongolian National Standard MNS 5391:2004. A total of 5 angiographies were studied. Measurement acceptance of kV (kilo voltage) assurance, linearity, repetition of kV, mA (mill Amper), mAs (mill Amper second), image resolution were not higher 5% from reference values.

Results: Standard derivation of kV assurance was moderate (St.derivation< 1.2%). The repetitions of kV,mA,mAs were in normal range (derivation coefficient<0.01). Image resolution was acceptable (1.4-3.1 lp/mm)

Conclusions: Review of this study I observed following problems such as we use and installed the oldest equipments from other countries, those were worked over than 10 years; spare parts were not manufactured; not installed software for measurement and process of patients and angiographic staff x-ray doses; not having optional units for evaluating and fixing image quality; quality control performance is made by Nuclear Energy Agency of Mongolia just one time a year; not acceptance of image processing, delivering and printing system. Therefore, more important things are in this field are development and renovation of equipments.

Key words: Kilo voltage, image resolution, linearity

Study on the optical density measurements for grasp cell density of the clinical specimen in the Liquid-based Cytology

M. G. Mun¹, D. W. Kim^{2,3}, and C. H. Kim⁴

¹Department of Healthcare Engineering, Chonbuk National Univ

²Division of Biomedical Engineering, Chonbuk National Univ

³Research Center of Healthcare & Welfare Instrument for the Aged, Chonbuk National Univ, Jeonju, Korea

⁴PATHtech Co.,Ltd

E-mail: biomed@jbnu.ac.kr

Abstract— since it can be difficult to perform inspection depending on the cell density of the clinical specimen in the Liquid-based Cytology, it is important to grasp the cell density of the clinical specimen. The existing turbidimetry method is used for grasping the cell density, but this method has the disadvantage of errors occurring due to increase in scattering light amount caused by floating matters. To overcome this disadvantage, this research proposes optimal LED brightness to obtain the brightness value of images, and aims to grasp the cell density of the clinical specimen as the brightness value of clinical specimen images. Clinical specimen images were filmed through the device developed with Arduino UNO and CCD camera module (ArduCam) and by the use of Matlab, it was converted the RGB values of the image to the lightness value. The lightness value is the mean value of the lightness values in the certain section on the light source part of clinical specimen images, and to raise the reliability, the mean value was calculated through 10 times repetition per clinical specimen. As a result, the reliability was higher, and the values were evenly distributed, in 1.6LUX than in 2.2LUX. The reliability of the brightness value of images filmed in 1.6LUX is considered highest.

Keywords—Liquid-Based Cytology, turbidimetry, cell concentration, optics base

I. INTRODUCTION

It is important to grasp the density of the clinical specimen because, if the density of the specimen is too high or too low in the Liquid-based Cytology, the number of cells smeared on the slide glass is not optimal, so it is difficult to perform the inspection [1,2].

Among the methods to grasp the density, there is the turbidimetry method that measures scattering light but in the case of turbidimetry method, the scattering light amount increases due to floating matters such as blood clot, which causes errors [3].

Accordingly, this research aims to obtain the lightness value through the images of the clinical specimen to overcome the disadvantages of the existing turbidimetry method that uses the scattering light and to find the clinical specimen that has the

density suitable to Liquid-based Cytology with the optical method by proposing the LED brightness that is most suitable to obtaining the brightness value through changing LED brightness.

II. METHODS

A. Realization of the specimen image acquisition device

To film the images to measure the lightness value, the equipment to obtain the clinical specimen images using Arduino UNO and CCD camera module (ArduCam) was developed. Arduino UNO and CCD camera module (ArduCam) exchange data through SPI communications and CCD camera is developed as shown in Fig. 1.

As shown in Fig.2, to maintain the form of the light source in a circle in the images of the clinical specimen, the distance between the light source and the clinical specimen container was maintained closely, and to maintain the constant size of the light source, the distance between CCD camera module (ArduCam) and the clinical specimen container was maintained to be constant 45mm. To prevent from adjusting the amount of light automatically in the image filming process, the automatic exposure control function and the automatic white balance function were removed so that CCD camera module (ArduCam) could not adjust the amount of light automatically and then the images of the clinical specimen were obtained.

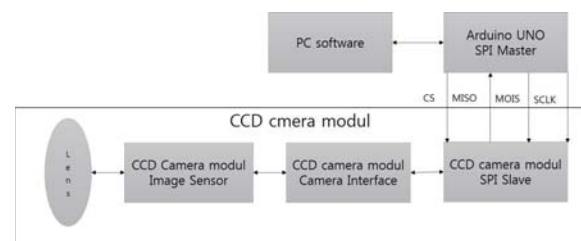


Fig. 1. Hardware Block diagram

B. Captured images of the clinical specimens

A total of 20 clinical specimens were chosen at a regular intervals according to the turbidity values, and by changing the LED brightness at 0.1LUX intervals

from (b)1.6LUX in which brightness changes of the light source part begin to be seen in the images of the clinical specimen with the highest turbidity value to (h)2.2LUX in which there were almost no brightness changes of the light source part in the images of the clinical specimen with the lowest turbidity value, the images of the clinical specimens were obtained as shown in Fig. 2.

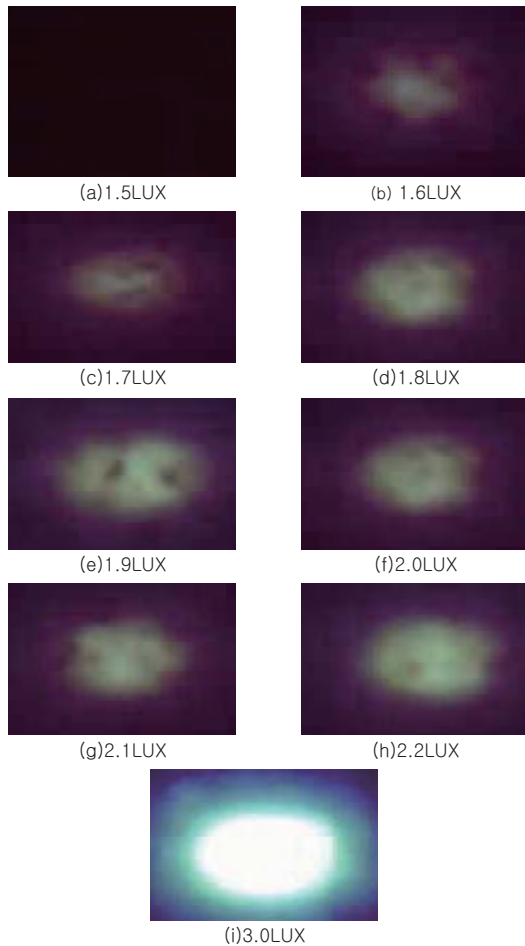


Fig. 2. 342NTU turbidity value of clinical specimen images

C. measuring turbidity value of the clinical specimen

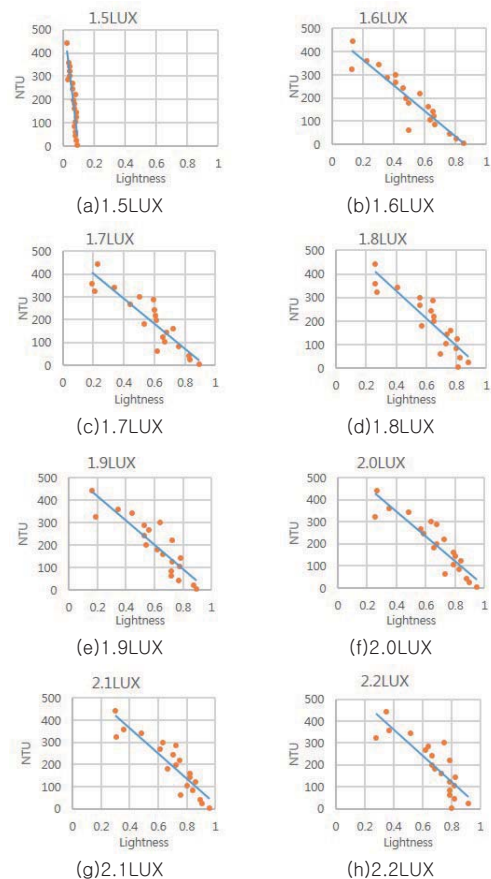
To examine the correlation between the existing turbidity meter that uses the scattering light method and the method that uses the image lightness value proposed by this research, the turbidity value of the clinical specimen was measured. To find the accurate turbidity value of the clinical specimen, calibration was conducted after measuring 3 times, and the container was cleansed after measuring turbidity of the clinical specimen. The turbidity value of each clinical specimen was measured 3 times and the mean value of the measured turbidity values was calculated.

D. lightness value of analysis

Since the obtained images were RGB images, to find the lightness value, each pixel RGB value of the image was converted by Matlab to the lightness value of the image. Changes of brightness can be shown best in the range of the section that is considered the light source in the clinical specimen images, so only the lightness values of the light source sections were extracted. The algorithm to find the mean value of the lightness values was developed, and by use the algorithm, the lightness values of the clinical specimen images were found.

III. RESULTS

To find the clinical specimen with suitable cell density, the method of finding the lightness value of clinical specimen images proposed in this research and the turbidity values were compared. As a result, in the clear clinical specimens whose turbidity value is low, the lightness value becomes higher, and in the turbid clinical specimens with high turbidity value, the lightness value becomes lower, resulting in the inverse graph as shown in Fig. 2.



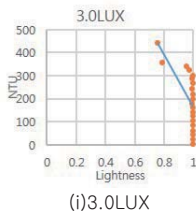


Fig. 3. The Lightness distribution graph to the turbidity value

IV. CONCLUSION

In this research, to find the clinical specimen with cell density suitable to the Liquid-based Cytology, the lightness value was found in the images of the clinical specimens, and the changes of lightness value were found by adjusting the LED brightness from 1.5LUX to 3.0LUX. In 3.0LUX, it was so bright, as shown in (i) of Fig. 2, that there were few changes of the images of the clinical specimens with low degree of turbidity. In the brightness range from 1.5LUX to 2.2LUX where the changes of brightness of any clinical specimen can be observed, the brightness values were measured, and it was considered that according to the distribution of the distribution values of Table 1, the most optimal clinical specimen image can be filmed in 1.6LUX.

Table 1. Brightness according to a clinical specimen of dispersion value

Brightness	dispersion value
1.5LUX	0.836
1.6 LUX	0.866
1.7 LUX	0.825
1.8 LUX	0.809
1.9 LUX	0.8
2 LUX	0.824
2.1 LUX	0.810
2.2 LUX	0.713
3 LUX	0.412

It is considered that if the results are used in the processing stage before liquefied cell inspection through follow-up researches, it will be easy to find the cell density that is suitable to the inspection.

ACKNOWLEDGEMENT

This work (Grants No. C0220554) was supported by Business for Academic-industrial Cooperative establishments funded Korea Small and Medium Business Administration in 20.

REFERENCES

1. Pisani, P, Bray, F, Parkin .D.M, “Esti mation of the worldwide prevalence of cancer for 25 sites in the

adult population,” *Int J Cancer.*, vol.97, pp72-81,2002

2. G.M. Mun, D.W. Kim, H.C. Kim, ” Study based on optical density measurements for liquid cytology specimen for proper implementation of the concentration,” *the Korea Society of Medical & Biological Engineering*, 2015 May 050
3. J.H. Park, S.H. Park, and M.S. Ryu, ”The Turbidity Measured by Division Image Analysis in Flow Type Sample,” *Journal of the Korean Industrial and Engineering Chemistry*, Vol.20, No.6, 681-684, 2009

Development of multi-fusion MR image-based 3D advanced radiation treatment planning techniques

B.Y. Choe¹, K.H. Song¹, C.H. Yoo¹, S.I. Lim¹

¹ Department of Biomedical Engineering, and Research Institute of Biomedical Engineering, The Catholic University of Korea College of Medicine, Seoul, Korea
E-mail: bychoe@catholic.ac.kr

Abstract— The purpose of this project is to develop the multi-fusion magnetic resonance (MR) image-based 3D advanced radiation treatment planning (RTP) techniques. In this study we developed and evaluated the high-precision RTP technique of early diagnosis and basic technology for clinical application.

Keywords— Brain tumor, perfusion MR imaging, diffusion MR imaging, multi-fusion MR image, pseudo-CT image

I. INTRODUCTION

The purpose of this project is to develop the multi-fusion magnetic resonance (MR) image-based 3D advanced radiation treatment planning (RTP) techniques included in anatomical and functional information of tumor and to apply biological diagnosis. Ultimately, it is to develop and to evaluate the high-precision RTP technique of early diagnosis and basic technology for clinical application.

II. METHODS

A. Optimization of metabolic image mapping & high-precision radiotherapy application

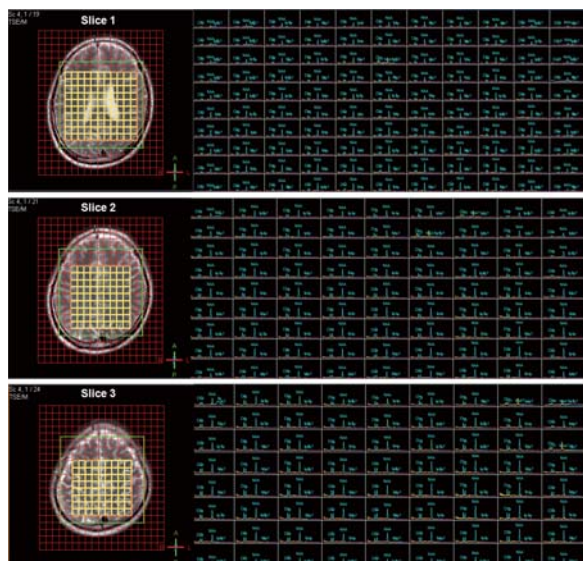


Fig. 1. The Spectrum of 3D MRSI.

For the optimization of radiation dose map, we assessed the R2 values of MR imaging using BANG3 polymer gel. Moreover, to optimize 3D MR spectroscopic (MRS) imaging, we developed a novel concept of fused MRI-MRS phantom. Also we developed MR image based pseudo-CT images for non-invasive diagnosis in perspective of RTP.

B. Optimization of diffusion MR imaging and high-resolution fiber tractography for high-precision radiotherapy application

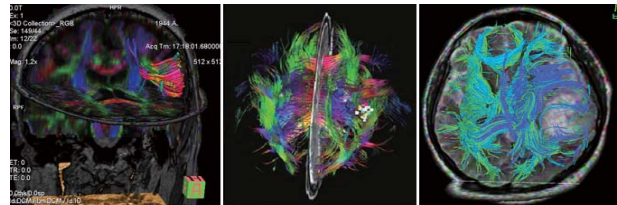


Fig. 2. Diffusion tensor image (DTI) from the brain tumor patients and applied 3D volume rendering method for visualization of tumor volume

To optimize the diffusion MR imaging parameters and image correction, we developed a novel image technique for correction of distortion. For the more accurate diagnosis for brain tumor, we optimized the algorithm of 3D streamline/probabilistic fiber tractography. For the application to the high-precision radiotherapy, optimization of diffusion MR imaging and high-resolution fiber tractography was verified

C. Optimization of perfusion MR imaging and high-resolution fiber tractography for high-precision radiotherapy application

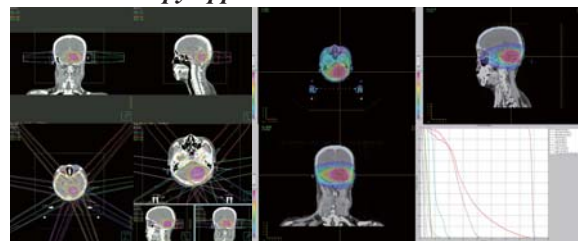


Fig. 3. Perfusion image based radiation treatment planning (RTP) system and dose volume histogram (DVH) for radiation therapy for brain tumor

We optimized the perfusion MR imaging parameters in dynamic contrast enhanced (DCE), dynamic susceptibility contrast (DSC) technique. Moreover, advanced perfusion MR imaging parameters, such as rCBV, rCVF, MTT, Ktrans, PS map were determined and optimized. For the application to the 3D high-precision radiation therapy planning (RTP) optimization of DWI/PWI/MRSI multi-fusion MR images was conducted.

III. Expected RESULTS

In the first stage of research, we optimized various 3D multi-fusion MR images for biological/pathological acquisition in brain tumor, and 3D multimodal image registration framework was established for high-precision radiotherapy and a future diagnosis/treatment integrated system. Our system in this study expected to be helpful for increasing rate of treatment efficiency in radiotherapy if the multi-modal image based optimal model properly used for 3D high-precision RTP technique. Diagnosis and therapy integrated system for radiation therapy based on multimodal image is capable of providing physical/biological functional information of tumor tissues. Our results are considered to optimizing the radiation therapy for brain tumor patients.

ACKNOWLEDGEMENT

This study was supported by grants (2012-007883) from the Mid-career Researcher Program through the National Research Foundation (NRF) funded by the Ministry of Science, ICT & Future Planning (MSIP) of Korea.

Estimation of Core Body Temperature from Heart Rate Monitoring based on Multiple Regression Analysis

Soo Young Sim¹, Kwang Min Joo¹, Han Byul Kim¹, and Kwang Suk Park^{2,*}

¹ Interdisciplinary Program for Bioengineering, College of Engineering, Seoul National University, Seoul 03080, Republic of Korea

² Department of Biomedical Engineering, College of Medicine, Seoul National University, Seoul 03080, Republic of Korea

*E-mail: pks@bmsil.snu.ac.kr

Abstract— Although core body temperature has been well-documented as a reliable marker for circadian rhythm, current thermometers are impractical in daily life. Therefore, we proposed the technique of core body temperature estimation from heart rate monitoring based on multiple regression analysis.

Keywords— Core body temperature, Circadian rhythm, Heart rate, Multiple regression analysis

I. INTRODUCTION

Core body temperature is one of the vital signs that should be measured when assessing one's health status. In addition, core body temperature monitoring in daily life can provide circadian rhythm. As the characteristics of the rhythm are changed in various health diseases such as insomnia and depression, daily body temperature monitoring is important [1]. However, none of the current thermometers are not suitable in daily routine due to invasiveness or restriction. Therefore, in this study, we proposed the body temperature estimation technique based on multiple regression analysis combined with heart rate parameters. We expect that this technique would reduce subject's burden during body temperature monitoring and facilitate chronobiology studies based on circadian body temperature rhythm.

II. METHODS

A. Experimental protocol

Seventeen young, healthy subjects were participated in the experiment. Core body temperature was monitored by ingestible Jonah temperature capsule (Philips Respironics, USA). And Electrocardiogram was measured by T-REX monitor (Taewoong medical, Korea). Participants were instructed to follow their routine daily schedule and both of physiological signals were simultaneously monitored.

B. Physiological signal monitoring

After adjusting ectopic R-peaks, 20 heart rate variability (HRV) parameters - RRI, MHR, nMHR, SDHR, SDNN, CVRR, RMSSD, pNN20, and pNN50, VLF, LF, HF, TF, nVLF, nLF, nHF, dLFHF, SMI, VMI, and SVI - were calculated from

Electrocardiogram. HRV parameters were calculated based on 5 min analysis. And we averaged the core temperature measurement every 5 min.

C. Estimation of body temperature

Seventeen dataset were divided into 2 groups - model development group (12 dataset) and model validation group (5 dataset). Then, multiple regression analysis was implemented to investigate the relationship between body temperature and heart rate variability parameters. Regression analysis was executed based on stepwise method. Then, root mean square error (RMSE) and bias were calculated to evaluate the estimation performance.

III. RESULTS

As a result of stepwise method, 7 heart rate parameters - MHR, nLF, VMI, pNN20, pNN50, SVI, and dLFHF - were included in the regression model. In model validation, mean RMSE was 0.38 ± 0.12 °C. Mean bias was -0.06 ± 0.26 °C.

IV. CONCLUSION

We investigated the feasibility of applying multiple regression analysis combined with heart rate parameters to body temperature estimation. And the model provided a mean RMSE less than 0.40 °C. We expect that this noninvasive and convenient method for estimating the body temperature could contribute to reducing the discomfort associated with monitoring body temperature in daily life. And this could facilitate more clinical studies based on circadian body temperature rhythm.

ACKNOWLEDGMENT

This research was supported by the Bio & Medical Technology Development Program of the NRF funded by the Korean government, MSIP (NRF - 2014M3A9E3064623).

REFERENCES

1. Lack, Leon C., *et al.*, "The relationship between insomnia and body temperatures." *Sleep. Med. Rev.*, vol.12, no.4, pp. 307-317, 2008.

Post-load glucose levels as indicators of glycemic control in vivo

Min Hyuk Lim¹, Tae Jung Oh², Karam Choi³, Jung Chan Lee¹, Young Min Cho^{2*}
and Sungwan Kim^{1*}

¹Department of Biomedical Engineering, Seoul National University College of Medicine

²Department of Internal Medicine, Seoul National University College of Medicine

³Interdisciplinary Program of Bioengineering, College of Engineering, Seoul National University

E-mail: dizzyday@gmail.com, *: co-corresponding authors

Abstract— Rapid measurements of insulin sensitivity and beta-cell response are important in harsh environments such as space. Post-load glucose levels are highly correlated with the indices of the oral minimal model. Thus post-load glucose levels would be helpful to prevent and treat diabetes in simple and effective manners.

Keywords— Diabetes, Space medicine, Post-load glucose, Insulin sensitivity, Beta-cell response

I. INTRODUCTION

Insulin sensitivity and beta-cell response should be rapidly and simply measured in space environments to prevent and treat diabetes. Post-glucose level can be indicators as insulin sensitivity and beta-cell function and be easily obtained during oral glucose tolerance test (OGTT). The oral minimal model, which can describe the dynamics of glycemic control in vivo, provides indices for insulin sensitivity and beta-cell function.

II. METHODS

A. Subjects in this study

Subjects consisted of normal glucose tolerance group (n=10), impaired glucose tolerance group (n=4) and type 2 diabetes group (n=14). A 180 min 75 g oral glucose tolerance test was performed. Plasma glucose levels were measured every 5 min for 120 min and thereafter every 20 min for 180 min. Venous blood was taken at 0, 15, 30, 60, 90, 120, and 180 min for measurement of plasma insulin and C-peptide concentration.

B. The model structure

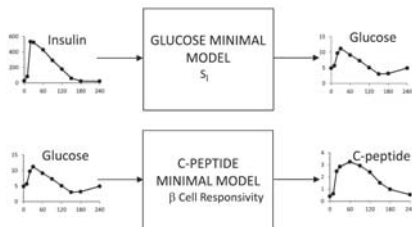


Fig. 1. The structure of the oral minimal model[1]

C. Correlation analyses

Spearman correlation analyses between indices of the oral minimal model and post-load glucose level.

III. RESULTS

A. fasting glucose level and indices of the oral minimal model

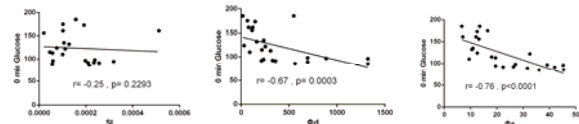


Fig. 2. Correlations between the indices of the oral minimal model and fasting glucose level

Insulin sensitivity was significantly correlated with the fasting glucose level.

B. 120 min post-load glucose level and indices of the oral minimal model

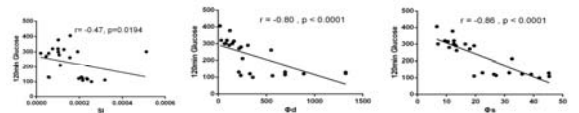


Fig. 3. Correlations between the indices of the oral minimal model and 120 min post-load glucose level

Insulin sensitivity, dynamic beta-cell responsivity, and static beta-cell responsivity were significantly correlated with the 120 min post-load glucose level. Moreover, 90 min post-load glucose level showed only the negative correlation with the dynamic responsivity.

IV. CONCLUSION

Post-load glucose levels are important to predict the characteristics of glycemic control in vivo. This diagnostic approach would be helpful to estimate the indices of the oral minimal model in certain environments which has some limitations of fully measuring dynamics of physiological phenomena such as space.

ACKNOWLEDGEMENT

This work was supported by National Research Foundation of Korea (NRF) grants funded by the Korean Government (2015M1A3A3A02012636)

REFERENCES

1. Cobelli C, Dalla Man C, Toffolo G, Basu R, Vella A, Rizza R. "The oral minimal model method." *Diabetes*, vol.63, pp.1203-13, 2014.
2. G. Casella, S. Fienberg, I. Olkin. *An Introduction to Statistical Learning: with Applications in R*. 1th ed. New York: Springer; 2013.

Novel Estimation Method for Signal Source Position inside Human Heart using Switching Voltage Divider Electrodes

Y. Sakaue¹ and M. Makikawa²

¹Graduate School of Science and Engineering, Ritsumeikan University, Kusatsu, Japan

²College of Science and Engineering, Ritsumeikan University, Kusatsu, Japan

E-mail: rr003035@ed.ritsumei.ac.jp

Abstract—This paper presents a novel method of estimating signal source position inside the human heart. This method can simultaneously obtain body surface potential and internal resistance between a signal source and measurement electrodes. An experiment conducted using the method estimated the R wave signal source position to be in the vicinity of the ventricle.

Keywords—human heart, internal resistance, signal source estimation, switching voltage divider

I. INTRODUCTION

Estimation of signal source position inside the human heart was studied because of its usefulness in the diagnosis and treatment of cardiac diseases. Previous methods have only obtained the body surface potential. We proposed a novel estimation method that can simultaneously obtain body surface potential and internal resistance R_b between a signal source and measurement electrodes [1]. The signal source is estimated at the intersection of some curved surfaces, on which the signal source would exist, calculated from R_b . The method was validated using a water tank imitating the human body. This study evaluated the method's effectiveness for the human heart.

II. METHODS

The signal source was assumed as two point potential sources of positive and negative poles with the same magnitude, and the positions of the poles were estimated. One healthy male subject (30 years old) participated in the experiment. Body surface electrocardiograph (ECG) was measured using switching voltage divider electrodes [1]. Nine signal electrodes were attached at the positions V1–V6 for 12-lead ECG; electrodes at the second and third intercostal #1 and #2 had the same position as V2, and those at the second intercostal #3 had the same position as V4 (Fig. 1). The ground electrode was placed 3 cm from the sternum lower end. The positions of these electrodes were obtained by a 3D digitizing system. The subject was asked to sit on a chair in an electrically shielded room during ECG measurement for 240 s.

Initially, data in which the polarization potential was small were extracted from the original data, and the

effect of polarization potential was removed using linear regression. The data were separated for each heartbeat and then averaged over 10 beats to remove white noise. The R_b of R wave at each signal electrode was calculated, and the R wave signal source position was estimated.

III. RESULTS AND DISCUSSION

Fig. 1 shows an example of the estimated R wave signal source position in the frontal plane; the green dots form the outline of subject's thoracic part. The R wave originates from the electrical activity of the heart ventricle, and the estimated position would be in the vicinity of the ventricle. Therefore, the estimation result can be considered to be reasonable.

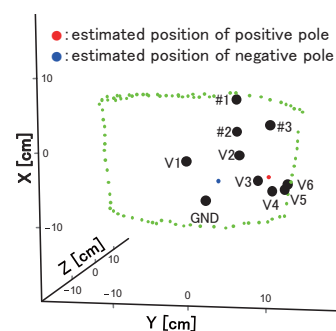


Fig. 1. Example of estimated signal source position in the frontal plane.

IV. CONCLUSION

The presented method can estimate the R wave signal source position inside the human heart.

ACKNOWLEDGEMENT

This study was supported by Grants-in-Aid for Scientific Research (Grant Number 25282137). The authors would like to thank Mr. Junichi Matsumura, Mr. Tatsuya Okada, Ms. Chisa Inaka, and the staff at R&D Division, Toray Engineering Co. Ltd., Shiga, Japan, for providing technical advice.

REFERENCES

1. Y. Sakaue and M. Makikawa, "Novel estimation method of signal source position inside a human body using switching voltage divider: A preliminary study," *Biomed. Eng. Lett.*, in press, 2015.

Comparison of Unipolar and Bipolar methods for 2ch EEG based BCI system

Hyeon-Seok Lee¹, Yubing Jiang¹, and Wan-Young Chung¹

Department of Electronic Engineering, Pukyong National University, Busan 608-737, South Korea.

E-mail: wychung@pknu.ac.kr

Abstract—This paper presents about comparison of Unipolar and Bipolar method for Brain-Computer Interface (BCI) system. Most of researches perform analysis of Motor Imagery (MI) and Brain map using Unipolar EEG device. But there is 2 method for measuring EEG, Unipolar and Bipolar. In this study, we compare ERD/ERS result measured by using both methods for which method is more effective.

Keywords— EEG, Unipolar, Bipolar, BCI system, Motor Imagery, ERD/ERS.

I. INTRODUCTION

BCI system is a system that can bypass conventional channels of communication and provide direct communication and control between the brain and physical devices by translating different patterns of brain activity into commands in real time [1]. Signal recordings of brain activity in BCI can be either invasive or noninvasive. Noninvasive BCI can use various brain signals as inputs, such as electroencephalograms (EEG) [2]. Due to the low cost and convenient in practical uses, EEG has been the most popular signal that is used to develop BCI systems. For measuring EEG, there are 2 types of methods which are Unipolar and Bipolar. In this paper, comparison is carrying out for efficiency and robustness of Unipolar method and Bipolar method.

II. METHODS

A. Experiment Environment

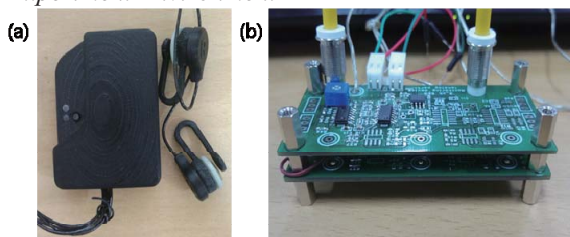


Fig. 1. 2ch EEG device for experiment. (a) Unipolar 2ch EEG device. (b) Bipolar 2ch EEG device.

Fig.1 shows the devices that used in experiment. Experiments are carried out by using 2ch Bipolar EEG wearable device developed by our lab and 2ch EEG Unipolar wearable device by Cognionics, Inc. Wet electrodes are placed on central (C3, C4) locations in the 10-20 international system.

B. Data Analysis

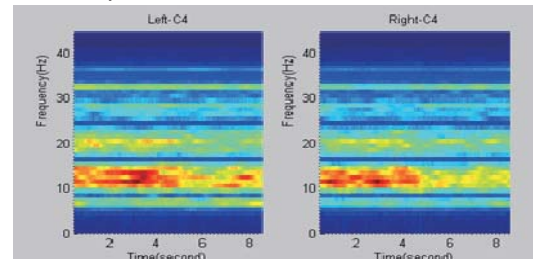


Fig. 2. ERD/ERS change by time zone

EEG data measured by each device is analyzed using Matlab. After EEG raw data passed through the FFT, ERD/ERS is analyzed through the power change by time zone as shown in Fig. 2. Graph of mu rhythm is drawn for further analysis.

III. RESULTS

The ERD/ERS of EEG data using a bipolar device is clearly observed in Power maps and graphs. While EEG data measured by using a unipolar device, the ERD/ERS is also observable but it is not clear and very sensitive to noise.

IV. CONCLUSION

The bipolar method in 2ch wearable EEG device is stronger to environmental noises and takes better ERD/ERS analysis result than unipolar method when we measure EEG for MI.

ACKNOWLEDGEMENT

This work was supported by the BK21 Plus Program funded by the Ministry of Education(MOE, Korea) and National Research Foundation of Korea(NRF).

REFERENCES

1. J. d. R. Millan, R. Rupp, G. R. Muller-Putz, R. Murray-Smith, C. Giugliemma, M. Tangermann, C. Vidaurre, F. Cincotti, A. Kubler, R. Leeb, C. Neuper, K.-R. Muller, and D. Mattia, "Combining brain-computer interfaces and assistive technologies state-of-the-art and challenges," *Frontiers Neurosci.*, vol. 4, pp. 1-15, 2010.
2. A. Nijholt, D. Tan, G. Pfurtscheller, C. Brunner, J. del R. Millan, B. Allison, B. Graimann, F. Popescu, B. Blankertz, and K.-R. Muller, "Brain-computer interfacing for intelligent systems," *IEEE Intell. Syst.*, vol. 23, no. 3, pp. 72-79, 2008.

Performance Stabilization and Evaluation for Brain Diagnostic Monitoring System Based on Near Infrared Spectroscopic Imaging

Jae-Ho Han and Seungbae Ji

Department of Brain and Cognitive Engineering, Korea University, Seoul, South Korea

E-mail: hanjaeho@korea.ac.kr

Abstract— Near infrared spectroscopic imaging is an emerging modality for research and clinical practice diagnosing various diseases in brain. This system measures the changes of hemodynamics so that physiological information can be noninvasively obtained in a compact and low-cost method. In this work, we will present various methods for stabilizing the system and guidelines to evaluate the systems it in terms of safety and performance which is commercialized and widely used these days.

Keywords— Imaging; Near Infrared; Monitoring; Spectroscopy; Performance; Stabilization.

I. Introduction

For non-invasive brain imaging and monitoring, optical method could be more efficient than other non-optical methods considering both the spatial and temporal resolutions as well as the equipment sizes. In particular, near infrared (NIR) spectroscopic system could be an optimized candidate for achieving the imaging resolutions with less space. In this system, the change of optical properties of the brain activity which is expressed in forms of regional hemodynamic responses is detected. In other words, near infrared tissue absorption locally varies with metabolic variations by neural activity changes which lead to changes in blood flow and oxygenation of hemoglobin. In this work, we report and introduce effective methods for stabilized performance of the NIR spectroscopic system in order to overcome signal artifacts such as high frequency electrical noise, cardiac cycle, instrument drift, low frequency physiology, and probe effects (sliding contacts) during measurement. In addition, we will discuss how to evaluate the performance and safety of the equipment for human testing as well.

II. Methods and Results

Artifacts are prone to occur due to the relatively unstrained environment of NIRS measurement system. Particularly, NIRS signal is very sensitive to spontaneous physiological fluctuations arising from cardiac pulse, respiration, heart rate variability, blood pressure spontaneous oscillations, both of systemic and cerebral origins. Therefore, identifying the artifacts and removing or correcting for them is essential

without removing the activation signal but the physiological noise. Still, noises occur in the same frequency ranges as the hemodynamic responses. For simple artifact identification, visual identification could be either laborious or not objective. Thus, methods such as threshold, principal component analysis (PCA), and wavelet decomposition are applied to identify outliers in the intensity-based activation signals. Recently, in addition to PCA and wavelet decomposition, various methods have been introduced in order to correct the artifact such as Kalman filtering, spine interpolation, correlation-based signal improvement.

ACKNOWLEDGEMENT

This research was supported by a grant (15172MFDS430) from Ministry of Food and Drug Safety in 2015. The authors would like to thank J. Jeong and J. Shin for the help in this work.

REFERENCES

1. M. Ferrari and V. Quaresima, "A brief review on the history of human functional near-infrared spectroscopy (fNIRS) development and fields of application," *Neuroimage*, vol. 63, no. 2, pp. 921–935, 2012.
2. F. Scholkmann, S. Kleiser, A. J. Metz, R. Zimmermann, J. M. Pavia, U. Wolf, and M. Wolf, "A review on continuous wave functional nearinfrared spectroscopy and imaging instrumentation and methodology," *Neuroimage*, vol. 85, no. 1, pp. 6–27, 2014.
3. S. Lloyd-Fox, A. Blasi, and C. E. Elwell, "Illuminating the developing brain: The past, present and future of functional near infrared spectroscopy," *Neurosci. Biobehav. Rev.*, vol. 34, no. 3, pp. 269–284, 2010.
4. F. C. Robertson, T. S. Douglas, and E. M. Meintjes, "Motion artifact removal for functional near infrared spectroscopy: A comparison of methods," *IEEE Trans. Biomed. Eng.*, vol. 57, no. 6, pp. 1377–1387, 2010.
5. L. Kocsis, P. Herman, and A. Eke, "The modified Beer-Lambert law revisited," *Phys. Med. Biol.*, vol. 51, no. 5, pp. N91–N98, 2006.
6. D. G. Nair, "About being BOLD," *Brain Res. Rev.*, vol. 50, no. 2, pp. 229–243, 2005.

The Ptosis Auto Diagnosis System and Algorithm Using Surface Electromyogram

Mi Sung Kwon¹, Jong-Ha Lee*¹, Hee-Jun Park¹, and Dae Gu Son²

¹Department of Biomedical Engineering, Keimyung University, School of Medicine, Daegu, South Korea

²Department of Plastic Surgery, Keimyung University Dongsan Medical Center, Daegu, South Korea

E-mail: lesile4781@naver.com *segeberg@kmu.ac.kr

Abstract—The phenomenon is called the ‘Ptosis’ that eyelids droop and edge of eyelids can’t lift on normal level. If the people have the ptosis, they use the frontalis muscle when the eyes open. In this study, the frontalis muscle’s EMG was measured for stare angle. People who have the ptosis were confirmed for use the frontalis muscle more than normal people. Therefore, this study verified that the ptosis is concerned in movement of muscle around the eyes and designed a system to quantify levels of frontalis muscle EMG

Keywords— Ptosis, Electromyography, Computer diagnosis, Auto detection, Signal processing

I. INTRODUCTION

Today, standardized way to diagnose the ptosis is Margin Reflex Distance_1 (MRD_1) and Levator function (LF). These index are convenient to measure in a hospital but these are subjective ways. Therefore, this study propose a system to quantify the ptosis with Electromyography (EMG) levels of frontalis muscle. Through experiment proved the valid relation between the ptosis index (MRD_1 and LF) and EMG signal level [1], [2].

II. METHODS

A. Subjects

This experiment was conducted with Korean men and women aged 20 to 24 years (n=17; mean age, 21.4 years). Muscle activity was recorded with a QEMG-4 system (LXM 3204, Laxtha, Korea). People were attached to 4 electrodes (2 lead) on the left and right frontalis muscle using QEMG-4. Ground was attached on the collarbone.

B. Methods

People who attached electrode began experiment without movement while they sat in a comfortable position. Experiment step was as follows: to had 7 seconds take each step. 1) Closing eyes in a comfortable position. 2) Staring forward. 3) Staring 40~50° upwards from the front. 4) Staring 70~80° upwards from the front.

C. Surface Electromyography Analysis

Each EMG signals that only recorded for 5 seconds excluded first 1 second and last 1 second of each segment were analyzed through the Band Pass Filter (BPF) and the Root Mean Square (RMS). After EMG signals analysis, compared analyzed signals with the ptosis index (MRD_1 and LF).

III. RESULTS

Fig. 1 compared left frontalis muscle’s EMG during staring 70~80° upwards from the front and the MRD_1 index. The normal level of MRD_1 is 4-5mm. All people except 3 people are normal level in MRD_1. The 2 people of excepted 3 people did not included in the normal range of the LF index. The normal level of LF is 6-12mm or more than. The results can be determined the ptosis more than 19.05mV of frontalis muscle EMG levels [1], [2].

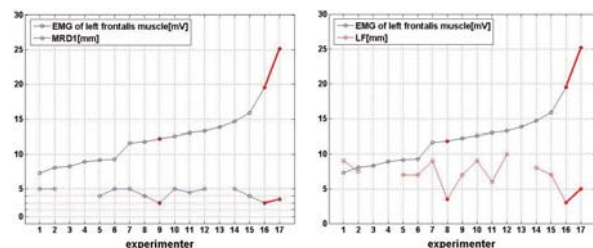


Fig. 1. Graph that compare left frontalis muscle’s EMG and the ptosis index (MRD_1 and LF)

IV. CONCLUSION

This study composed a system to quantify the ptosis by using EMG signals of frontalis muscle.

ACKNOWLEDGEMENT

This research was supported by Basic Science Research Program through the National Research Foundation of Korea (NRF) funded by the Ministry of Education (2014R1A1A2056420).

REFERENCES

1. Omofolasade Kosoko-Lasaki and Millicent Palmer, “Upper Eyelid Ptosis Revisited” *American Journal of Clinical Medicine*, vol 6, no. 3, 2009.

Non-contact medical imaging control system using a 3D motion controller

Su-Yang¹, Jeong-Hun Ku¹, and Jong-Ha Lee^{1*}

¹Dept. of Biomedical Engineering,
School of Medicine Keimyung University, Daegu, South Korea
E-mail: segeberg@gmail.com

Abstract

In this paper, load a 3D anatomical model extracted from the DICOM file and the DICOM file in Unity3D, utilizing Leapmotion of non-contact 3D motion controllers, we have developed a non-contact type medical image control system that can be interaction with the medical image in a sterile environment through the movement of the hands of the doctor himself

Keywords— non-contact, Leapmotion, DICOM, 3D anatomical model, medical imaging

I. INTRODUCTION

Because the doctor in the operating room must be ensured freedom of action for the prevention of cross-contamination and surgery, it is difficult to directly control the medical imaging such as CT images. Therefore, surgical assistants under the direction of the doctor is to control the medical imaging. However, these indirect medical imaging control method often make the mistake caused by incorrect communication or cause the inconvenience caused by the delay in controlling the medical image. If the surgeon is a risk of cross-contamination when using a mouse or a keyboard directly to the medical image control. Therefore, it is necessary noncontact medical imaging control system for resolving this inconvenience.

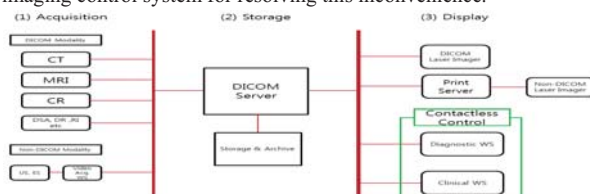


Fig. 1. The purpose of non-contact medical imaging control system

II. METHODS

Through the following five action, we zoom in or out or stop, or rotate to a 3D anatomical models should be able to see from various angles.

A. Utilizing gesture

(1) Straightening one finger gesture: an arrow pointer appears. And the role of the arrow pointer, another 3D anatomical models and select a DICOM file, and brings up. The arrows point in the scene gets the DICOM file performs a function passing the DICOM file in the left-right sequence.

(2) Vertical and horizontal position of the hand movement changes: the 3D model is implemented to be rotatable when received by the motion sensor recognizes the vertical and horizontal position of the hand changes.

(3) The fist gesture: If the stream is interrupted recognize vertical and horizontal position of the hand changes to a fist action is taken to stop the rotation of the 3D model.

(4) Swipe gesture: Taking a Swipe gesture in the DICOM scene goes back to the 3D anatomical model scene.

(5) Back and forth change of the position of the hand: change in position of the hand back and forth causes expansion and reduce the size of the 3D anatomical model

III. RESULTS

A. Implementation



Fig. 2 UI description of the implemented application

GUI screen configuration of the implemented application model, model selection, DICOM file selection(exclamation point icon), Help button, and a cursor.

B. Demonstration picture



Fig. 3. The heart and head image

Moving the slide in accordance with hand movement. And you can return to the previous screen through Swipe gesture



Fig. 4. The heart and head 3D model image

It can rotate and zoom in and out in accordance with the model of the hand movements.

IV. CONCLUSION

The purpose of this study is to develop a non-contact type medical imaging control system by using a non-contact motion sensor. Currently we have researched and developed a system for the non-contact controllable 3D anatomical models extracted from DICOM files and DICOM files by using the motion sensor. By updating the system interface to enable the service to the hospital in the future, the system will have to help reduce the risk of cross-contamination and errors in communication between doctors and surgical assistants.

ACKNOWLEDGEMENT

This research was supported by Basic Science Research Program through the National Research Foundation of Korea (NRF) funded by the Ministry of Education (2014R1A1A2056420).

REFERENCES

1. Will. Goldstone, *Unity3.x Game Development Essentials*, 에이콘 출판, 2012.
2. Packt Publishing, *Game Terrain Modeling with Ogre3, Udk, and Unity3d*, Packt Publishing, 2015.
3. Creighton, *Unity 3D Game Development by Example Beginner's Guide*, Packt Publishing, 2010.
4. J. W. Lee, J. Y. Ahn, J. H. Kim, H. S. Kang, "K. S. Park, Image Processing Model on PACS Environment Based DICOM", *대한 PACS 학회지*, Kor., pp. 49-52, 2001.

Obstructive Sleep Apnea-Hypopnea Syndrome Diagnosis using Quantitative Analysis of Sleep Macrostructure

D. W. Jung¹, H. N. Yoon¹, Y. J. Lee², D. U. Jeong², and K. S. Park³

¹Interdisciplinary Program for Biomedical Engineering, Seoul National University Graduate School, Seoul, Republic of Korea

²Department of Psychiatry and Behavioral Science, Seoul National University College of Medicine and Center for Sleep and Chronobiology, Seoul National University Hospital, Seoul, Republic of Korea

³Department of Biomedical Engineering, Seoul National University College of Medicine, Seoul, Republic of Korea

E-mail: dwjung@bmsil.snu.ac.kr

Abstract— The purpose of our study was to suggest an innovative approach that utilizes quantitative analysis of sleep macrostructure as a useful measure for diagnosing obstructive sleep apnea-hypopnea syndrome (OSAHS). The percentage transition probability from non-rapid eye movement sleep stage 2 to stage 1, denoted by $TP_{N2 \rightarrow N1}$, showed significant association with the apnea-hypopnea index (AHI). The relationship between the AHI and $TP_{N2 \rightarrow N1}$ could be interpreted as the result of interruption of the sleep stages forward progression due to the apneic or hypopneic attacks. The nonlinear regression model employing $TP_{N2 \rightarrow N1}$ to estimate the AHI provided a noteworthy performance. Consequently, the OSAHS diagnostic performance, determined by the developed AHI estimation model, suggested the potential of our method as a reliable measure for diagnosing OSAHS without acquiring overnight respiratory signals.

Keywords— Apnea-hypopnea index, obstructive sleep apnea-hypopnea syndrome, sleep macrostructure, sleep stage transition probability.

I. INTRODUCTION

Obstructive sleep apnea-hypopnea syndrome (OSAHS), characterized by recurrent cessation or substantial reduction in breathing during sleep, is a serious medical concern. Although a significant relationship between OSAHS and sleep macrostructure has been revealed in several studies, useful application of this relationship has been limited. The aim of this study was to suggest a novel approach using quantitative analysis of sleep macrostructure as a helpful measure for estimating the apnea-hypopnea index (AHI), which is commonly used to diagnose OSAHS.

II. METHODS

A. Subject and Polysomnography

We collected polysomnographic recordings from a total of 132 subjects who had undergone nocturnal polysomnography (PSG) because of suspected OSAHS

at the Center for Sleep and Chronobiology of Seoul National University Hospital. Patients with insomnia, parasomnia, or sleep-related movement disorders were excluded from the study. PSG recordings were scored by certified sleep technologists and verified by sleep physicians in accordance with the 2007 American Academy of Sleep Medicine (AASM) manual [1]. Study subjects were divided into training and test sets. The training set was used to develop a regression model, and the test set was used to validate the model's performance. Each set included 66 subjects consisting of 18 and 48 subjects belonging to the OSAHS-negative (AHI < 5 events/h) and OSAHS-positive (AHI ≥ 5 events/h) groups, respectively.

B. Sleep Macrostructure Parameters

The quantification of sleep macrostructure was dependent on sleep stage scored as wakefulness stage (Stage W), rapid eye movement (REM) stage (Stage R), and non-REM (NREM) stages 1, 2, and 3 (Stage N1, N2, and N3, respectively) for consecutive 30-sec epochs [1]. Without being bound by conventional sleep macrostructure parameters, percentage transition probability from Stage X to Y ($TP_{X \rightarrow Y}$; X and Y denote W, R, N1, N2, or N3, respectively) were extracted as new parameters.

C. Statistical Analysis

Sleep macrostructure parameters were used as explanatory variables in the regression analysis for estimating the AHI. Between the estimated AHI and the reference AHI determined by PSG, a root mean square error (RMSE) and a Pearson's correlation coefficient were computed. The OSAHS diagnostic performance of our method at AHI cut-offs of ≥ 5, 15, and 30 events/h was evaluated.

III. RESULTS

The nonlinear regression model employing $TP_{N2 \rightarrow N1}$ to estimate the AHI exhibited a determination coefficient (R^2) of 0.86. Fig. 1 shows a scatter plot of the AHI determined by PSG against $TP_{N2 \rightarrow N1}$. The best-fitting curve (Fig. 1, solid line) to the experimental data

(Fig. 1, solid circles) was derived from the Morgan-Mercer-Flodin (MMF) function. Between the estimates and the reference values of the AHI, a RMSE of 7.11 events/h and a Pearson’s correlation coefficient of 0.93 ($P < 0.01$) were obtained for the training set. For the test set, a RMSE of 7.46 events/h and a Pearson’s correlation coefficient of 0.93 ($P < 0.01$) were achieved.

Table 1 summarizes the OSAHS diagnostic performance of our method at AHI cut-offs of ≥ 5 , 15, and 30 events/h for the test set.

IV. CONCLUSION

This study validates the applicability of sleep macrostructure quantitative analysis for diagnosing OSAHS. We extended the notion of sleep macrostructure and extracted new sleep macrostructure parameters without being bound by conventional parameters.

Sleep is known to proceed in cycles of REM and NREM, usually four or five cycles per night. Each sleep cycle consists of a sequential progression of stages, in the order of Stage N1, N2, N3, N2, and R. During sleep apnea or hypopnea, respiratory muscles produce mechanical inspiratory effort in order to overcome occlusion. However, insufficient or ineffective effort to inhale causes hypoxia. The response to this hypoxia is an arousal event that occurs to reactivate the physiological systems and restore normal respiration [2]. The transient but frequent arousals caused by apneic or hypopneic attacks usually shift the subject’s sleep from deep (Stage N3) to light (Stage N1 and N2) [2]. The interruption of the forward progression at Stage N3 might cause backward progression to Stage N2 and N1.

Nowadays, several commercial home-based sleep structure monitoring systems are readily available and relatively affordable. Application of our method to these sleep structure monitoring systems would allow the provision of additional information about OSAHS without acquiring overnight respiratory signals.

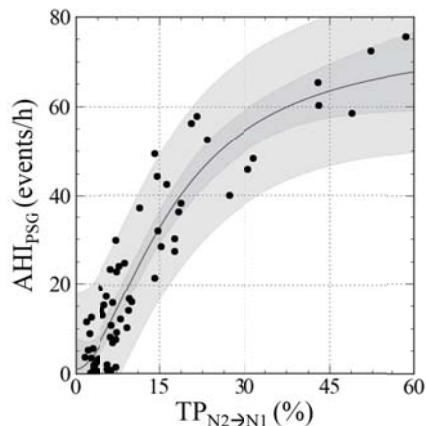


Fig. 1. Scatter plot showing the relationship between the percentage transition probability from non-rapid eye movement sleep stage 2 to stage 1 ($TP_{N2 \to N1}$) and the apnea-hypopnea index determined by polysomnography (AHI_{PSG}). The inner and outer gray areas represent 95% confidence and prediction bands, respectively.

Table 1. Obstructive sleep apnea-hypopnea syndrome diagnostic performance

	AHI cut-off value (events/h)		
	≥ 5	≥ 15	≥ 30
Sensitivity (%)	91.7	87.9	90.0
Specificity (%)	77.8	90.9	93.5
PPV (%)	91.7	90.6	85.7
NPV (%)	77.8	88.2	95.6
Accuracy (%)	87.9	89.4	92.4
Cohen’s kappa coefficient	0.69	0.79	0.82

AHI, apnea-hypopnea index; PPV, positive predictive value; NPV, negative predictive value.

Cohen’s kappa coefficient ranging from 0.61 to 0.80 and from 0.81 to 1.00 indicate substantial and almost perfect agreement, respectively.

ACKNOWLEDGEMENT

This work was financially supported by the Samsung Electronics, Inc.

REFERENCES

1. C. Iber, S. Ancoli-Israel, A. Chesson, and S. F. Quan, *The AASM manual for the scoring of sleep and associated events: rules, terminology and technical specifications*, 1 ed., Westchester IL, USA: American Academy of Sleep Medicine, 2007.
2. American Sleep Disorders Association, “EEG arousals: scoring rules and examples,” *Sleep*, vol. 15, no. 2, pp. 174-184, 1992.

An Effect of the Sampling Frequency to the Pulse Rate Variability Analysis

Hangsik Shin and Yoon La Yang

Department of Biomedical Engineering, Chonnam National University, Yeosu, Republic of Korea
E-mail: hangsik.shin@jnu.ac.kr, diddbsfk@gmail.com

Abstract—The purpose of this research is to investigate the effect of sampling frequency to the pulse rate variability analysis. We analyzed PRV with 1,000, 500, 250, 100, 50, 25 Hz-sampled PPG signal, and compared with result of HRV analysis. As a result, meaningful differences were not found in every case except on SDS, RMSSD, NN20, pNN20 and nLF at 25 Hz-sampled signal.

Keywords— Heart Rate Variability, Pulse Rate Variability, Sampling Frequency

I. INTRODUCTION

Although it has been controversial, pulse rate variability (PRV), a variability derived from pulse-to-pulse interval of plethysmography waveform, has regarded as a promising surrogate of heart rate variability (HRV) in resting condition [1]. However, in contrast to the HRV, guideline for deriving PRV is seldom found. The purpose of this research is to find the effect of sampling frequency to the result of PRV analysis. In this research, we investigate the proper sampling frequency for each analytic variable.

II. METHODS

We use 59 datasets which includes ECG and photoplethysmography (PPG) recorded simultaneously with 1 kHz during 5-minute. To generate down-sampled PPG, we decimated the signal by 2, 4, 10, 20 and 40 based on 1 kHz signal. QRS complex and systolic peaks of PPG were confirmed manually after finding by [2] and [3], respectively.

In comparison of HRV and PRV, we calculate AVNN, SDNN, SDS, RMSSD, NN50, pNN50, NN20, pNN20, VLF, LF, HF, LF/HF, nLF and nHF [4] of time- and frequency-domain analysis in every signal including down-sampled signal. Derived results are statistically validated by one-way ANOVA. As a *post-hoc* test, when the variances can be assumed to be equal, we used *Bonferroni's* test. Otherwise, we used *Tamhane's T2* test for the *post-hoc* test.

III. RESULTS

Table 1 shows the statistical significance of difference of variables between HRV and PRV analysis. Result has meaningful difference in SDS, RMSSD, NN20, pNN20 and nLF analysis of 25 Hz sampling frequency. Over 50 Hz sampling, every

variable shows the equivalent result statistically. Significance is gradually decreased by decreasing sampling frequency. However, over 250 Hz, the significance was not declined in every variable.

Table 1. Statistical significance of difference (P-value) of variables between HRV and PRV

Variable	Sampling Frequency of PPG [Hz]					
	1,000	500	250	100	50	25
AVNN	1.000 [†]	1.000 [†]	1.000 [†]	1.000 [†]	1.000 [†]	1.000 [†]
SDNN	1.000 [†]	1.000 [†]	1.000 [†]	1.000 [†]	1.000 [†]	1.000 [†]
SDS	1.000 [†]	1.000 [†]	1.000 [†]	1.000 [†]	1.000 [†]	**
RMSSD	1.000 [†]	1.000 [†]	1.000 [†]	1.000 [†]	1.000 [†]	**
NN50	1.000 [†]	1.000 [†]	1.000 [†]	1.000 [†]	1.000 [†]	1.000 [†]
pNN50	1.000 [†]	1.000 [†]	1.000 [†]	1.000 [†]	1.000 [†]	1.000 [†]
NN20	1.000 [†]	1.000 [†]	1.000 [†]	0.947 [†]	0.094 [†]	***
pNN20	1.000 [†]	1.000 [†]	1.000 [†]	0.985 [†]	0.183 [†]	**
VLF	1.000 [†]	1.000 [†]	1.000 [†]	1.000 [†]	1.000 [†]	1.000 [†]
LF	1.000 [†]	1.000 [†]	1.000 [†]	1.000 [†]	1.000 [†]	1.000 [†]
HF	1.000 [†]	1.000 [†]	1.000 [†]	1.000 [†]	1.000 [†]	1.000 [†]
LF/HF	1.000 [†]	1.000 [†]	1.000 [†]	1.000 [†]	1.000 [†]	0.109 [†]
nLF	1.000 [†]	1.000 [†]	1.000 [†]	1.000 [†]	0.237 [†]	***
nHF	1.000 [†]	1.000 [†]	1.000 [†]	1.000 [†]	1.000 [†]	0.240 [†]

***P<0.001, **P<0.01, †not significant

IV. CONCLUSION

Result suggests that minimum sampling frequency for PRV analysis is around 50 Hz. However, it also shows that 250 Hz or higher sampling frequencies are recommended for more reliable analysis.

ACKNOWLEDGEMENT

This research was supported by the MSIP, Korea, under the CITRC (IITP-2015-IITP-2015-H8601-15-1009) supervised by the IITP.

REFERENCES

- Schäfer and J. Vagedes, "How accurate is pulse rate variability as an estimate of heart rate variability?: A review on studies comparing photoplethysmographic technology with an electrocardiogram," *Int. J. Cardiol.*, vol. 166, pp. 15-29, 2013
- J. Pan and W.J.Tompkins, "A real-time QRS detection algorithm," *IEEE Trans. Biomed. Eng.* pp. 230-236, 1985.
- H. Shin, C. Lee and M. Lee, "Adaptive threshold method for the peak detection of photoplethysmographic waveform," *Comput. Biol. Med.*, vol. 39, pp. 1145-1152, 2009.
- Task Force of the European Society of Cardiology, "Heart rate variability standards of measurement, physiological interpretation, and clinical use," *Eur Heart J*, vol. 17, pp. 354-381, 1996.

Relation between the Maximum Systolic Location of Photoplethysmography Waveform and Sampling Frequency

Hangsik Shin and Sooji Park

Department of Biomedical Engineering, Chonnam National University, Yeosu, Republic of Korea
 E-mail: hangsik.shin@jnu.ac.kr, susie.soo718@gmail.com

Abstract—To investigate the effect of sampling frequency to the features of Photoplethysmography waveform, we calculated mean absolute errors of maximum systolic point location and heart rate between down-sampled PPG and reference (1 kHz sampled). As a result, temporal errors of maximum systolic peak location were 0.99, 1.35, 2.74, 5.18 and 10.13 ms, and errors of heart rate were 0.055, 0.107, 0.259, 0.518 and 1.030 bpm in 500 Hz, 250 Hz, 100 Hz, 50 Hz and 25 Hz, respectively.

Keywords—Biomedical Measurement, Heart Rate, Photoplethysmography, Sampling Rate

I. INTRODUCTION

Latest personalized wearable devices usually have the Photoplethysmography (PPG) system. Most usage of PPG is beat-based application. For example, beat information from PPG is used in calculating heart rate as well as heart rate variability [1]. In these applications, detecting exact location of beats is quite important. The sampling frequency have to be decided carefully in PPG recording because it could change not only the temporal resolution of signal but also the overall cost of hardware. In this research, we investigate the temporal location of systolic feature of PPG waveform according to the sampling frequency.

II. METHODS

We use the dataset from twenty-eight subjects who has no cardiovascular disease such as arrhythmia. Data was recorded with 3 times repetitions per subject with 1 kHz during 5-minute. Finally, 59 data are used for analysis excluding noisy data. Based on 1 kHz sampled signal, we decimated the signal by 2, 4, 10, 20 and 40 to obtain 500 Hz, 250 Hz, 100 Hz, 50 Hz and 25 Hz sampled signal. To find the systolic peaks, we use [2]. To investigate the effect of the sampling frequency to the peak location, we calculated the mean absolute error of peak locations (MAE_P) of down-sampled PPG to the reference (1 kHz sampled) as well as the difference of heart rate of each down-sampled PPG.

III. RESULTS

Fig. 1 shows the MAE_P to the reference. Temporal differences of systolic peaks are 0.99, 1.35, 2.74, 5.18 and 10.13 milli-seconds in 500 Hz, 250 Hz, 100 Hz, 50

Hz and 25 Hz-sampled signal, respectively. Table 1 shows the MAE_P and mean absolute error of heart rate (MAE_{HR}) according caused by the down-sampling. Here, heart rate is derived from peak-to-peak interval.

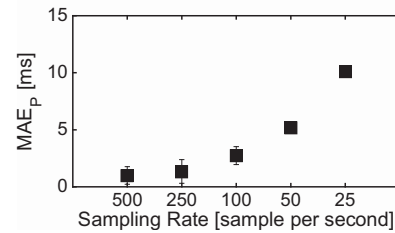


Fig. 1. Mean and standard error of mean absolute temporal differences of down-sampled signals.

Table 1. Mean absolute errors of down-sampled signal compared with reference (bpm: beats per minute)

Error	Sampling Frequency (Hz)				
	500	250	100	50	25
MAE_P (ms)	0.99	1.35	2.74	5.18	10.13
MAE_{HR} (bpm)	0.055	0.107	0.259	0.518	1.030

IV. CONCLUSION

From the result, we confirmed quantitatively that the temporal error of the maximum systolic point of PPG waveform is increased by decreasing sampling frequency. This result could suggest the guideline for development of PPG system. For example, developers have to choose 100 Hz or more sampling frequency if they want to develop PPG system which has less than 1 bpm error of heart rate detection.

ACKNOWLEDGEMENT

This research was supported by the Ministry of Science, ICT and Future Planning, Korea, under the Convergence Information Technology Research Center (IITP-2015-IITP-2015-H8601-15-1009) supervised by the Institute for Information & communications Technology Promotion

REFERENCES

1. J. Allen, "Photoplethysmography and its application in clinical physiological measurement," *Physiol. Meas.*, vol. 28, pp. R1, 2007.
2. H. Shin, C. Lee and M. Lee, "Adaptive threshold method for the peak detection of photoplethysmographic waveform," *Comput. Biol. Med.*, vol. 39, pp. 1145-1152, 2009.

Compare the Accuracy of estimated Blood Pressure Value at the finger with that of Ear

J. H. Lee¹, J. H. Heo¹, J. J. Lee¹, H. W. Kin¹ and Y. R. Yoon¹
¹Department of Biomedical Engineering, Yonsei University, Wonju, Korea
 E-mail: yoony@yonsei.ac.kr

Abstract— The purpose of this study is estimation of blood pressure using various features of Photoplethysmography(PPG) measured at the ear. The estimated Coefficients of Determination(R^2) of systolic and diastolic by various feature points are 0.372 and 0.909 respectively. The average accuracy of them are 98.07% and 97.04 % respectively.

Keywords— Photoplethysmography, Blood pressure.

I. INTRODUCTION

Various features can be extracted by PPG in systole and diastole[1]. The blood pressure can be estimated indirectly by using the PPG measured at the finger[2]. In this paper, we compare the accuracy of estimated blood pressure value at the finger with that of ear.

II. METHODS

A. Subject and Equipment

We selected five men and three women subjects at age twenty. MP 150, PPG100C data Acquisition equipment (Biopac Systems, Inc) and Automatic Blood Pressure Monitor(Omron, Inc) were used.

B. Procedure

While the experiment, subjects were seated, we measured blood pressure 3 times each subjects at the left brachial. At the same time we measured PPG at the right ear and the right index finger. Sampling rate was 200Hz, gain was 100 and frequency band was 0.5Hz ~ 3Hz.

C. Analyzing

We extracted 9 parameters described in Fig. 1. We derived equation by multiple linear regression analysis using IBM SPSS Statistics 21.

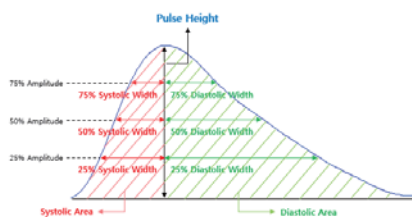
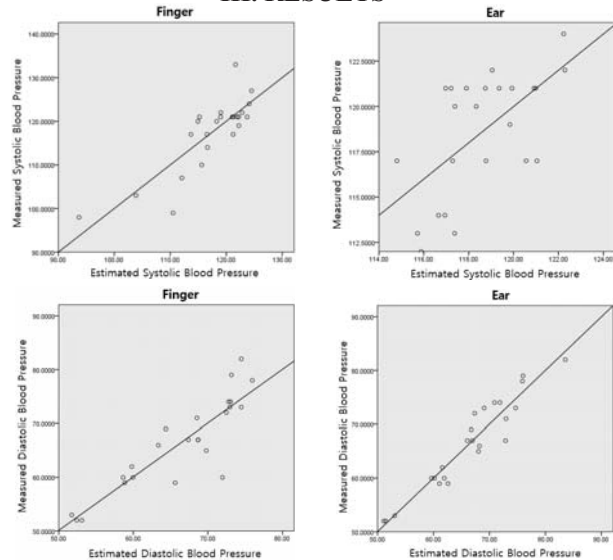


Fig. 1. PPG parameters

III. RESULTS



	Finger		Ear	
	Systolic	Diastolic	Systolic	Diastolic
R^2	0.707	0.782	0.372	0.909
Accuracy(%)	97.14	96.06	98.07	97.04

Fig. 2. The results of blood pressure estimation

IV. CONCLUSION

As a result, it seems that the diastolic blood pressure can be estimated by using PPG measured at the ear. However, the R^2 of the systolic blood pressure is lower than that of diastolic blood pressure. If we improve the estimation method of systolic blood pressure, it seems to be able to develop a module for estimating the blood pressure using PPG at the ear indirectly.

ACKNOWLEDGEMENT

This research was supported by the corporate associated research development manpower training Program of the Ministry of Trade, Industry and Energy (N0001130).

REFERENCES

1. Mohamed Elgendi, "On the Analysis of Fingertip Photoplethysmogram Signals," *Current Cardiology Reviews*, vol.8, No.1, pp.14-25, 2012.
2. Logan Porter, Gleb V.Tcheslavski, "Using Photoplethysmography for Blood Pressure Estimation with Telemedicine Application," *International Journal of Engineering Research & Technology*, vol.2, Issue 11, pp.2202-2205, 2013.

Blink Detection using Ambient Light Sensor

J. H. LEE¹, J. H. HAN¹, J. H. IM¹, H. W. KIM¹ and Y. R. YOON¹

¹Department of Biomedical Engineering, Yonsei University, Wonju, Korea
E-mail: yoon@yonsei.ac.kr

Abstract—The purpose of this study is detection of blink using Cadmium Sulfide(CdS) ambient light sensor. Two CdS sensors are used to detecting blink. One is toward to eye, the other is toward to face. We compared estimated blink counts using CdS sensors with number of blink counts. The average of the accuracy of blink detection is 96.5%, the standard deviation is 1.2.

Keywords— Blink detection, Ambient Light Sensor.

I. INTRODUCTION

There is the method of infrared-based blink detection[1]. However the method has a potential hazard to eyes. In this paper, we use the ambient light sensor to overcome for this weakness of the method using infrared.

II. METHODS

A. Subject and Equipment

We selected 6 men and 4 women subjects at age twenty. We used 9P5-C CdS sensors(ADD ELECTRONIC, Co. Ltd) and voltage distribution system to measure reflected light of eye and face. We used the method described in Fig. 1. to acquire output signal. CdS1 was toward to eyes, CdS2 was toward to face.

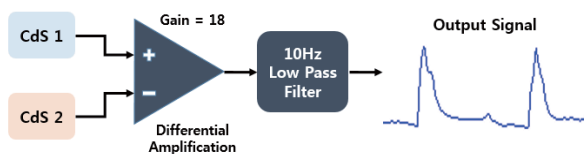


Fig. 1. Method of acquiring output signal

B. Procedure

Blink was estimated 5 times for each subjects in seating condition. Subjects blinked every 3 seconds for 1 minute wearing glasses equipped with the CdS sensors. Sampling rate was 20Hz.

C. Analyzing

Output signal was converted to digital signal by analog to digital converter. Differential waveform of output signal is described in Fig. 2. We set Up-Threshold Value(UT) and Down-Threshold Value(DT) experimentally. We considered the eye was closed when differential value was larger than UT. Likewise,

we considered the eye was opened when differential value was smaller than DT.

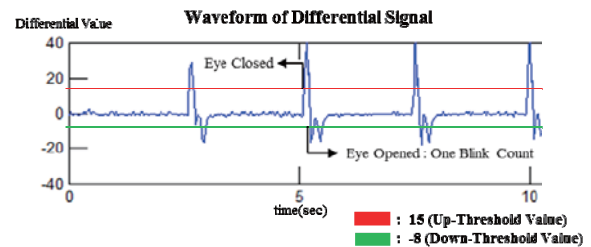


Fig. 2. Differential waveform of output signal and method of detecting blink

III. RESULTS

Table 1. The results of blink detection

	Subjects									
	1	2	3	4	5	6	7	8	9	10
Test1	21	20	20	21	20	22	21	21	21	21
Test2	20	19	19	22	22	20	20	20	20	22
Test3	20	19	18	20	21	20	22	20	22	20
Test4	21	20	20	21	21	20	20	21	22	20
Test5	20	20	21	20	21	19	22	20	20	20
Accuracy(%)	98	98	96	96	95	97	95	98	95	97

The results are estimated blink counts described in Table 1. The average of the accuracy is 96.5%, the standard deviation is 1.2.

IV. CONCLUSION

As a result, it seems that the blink can be detected by using the CdS sensor. Also there will be no potential hazard to the eyes using the CdS sensors. Furthermore we will be able to develop the system for detect blink counts by using this method.

ACKNOWLEDGEMENT

This research was supported by the corporate associated research development manpower training Program of the Ministry of Trade, Industry and Energy (N0001130).

REFERENCES

1. Alice Frigerio, Tessa A Hadlock, Elizabeth H Murray, and James T Heaton, "INFRARED-BASED BLINK DETECTING GLASSES FOR FACIAL PACING:TOWARDS A BIONIC BLINK," *JAMA Facial Plast Surg.*, vol. 16(3), pp. 211-218, 2014.

Implementation of a Wireless Hearing Aid System with Ezairo 7100 Development Kit

Yuyong Jeon¹, Yongdeok Park¹, Han-sok Suh¹, Hyeon-min Shim², Gyutae Kim²,
Chenghao Quan², Sangmin Lee^{1,2}

¹Department of Electronic Engineering, Inha University, Incheon, Korea

²Institute for Information and Electronics Research, Inha University, Incheon, Korea

E-mail: nicejyy@gmail.com

Abstract— In this study, we implement a wireless hearing aid system with On Semiconductor Ezairo 7100 development kit. Algorithms we implemented are WDRC and FBC. And an Android application that can connect to the Bluetooth module was implemented and Bluetooth module is connected to the development kit with UART. To evaluate system, we simulated a hearing loss and feedback path. As a result, hearing aid algorithm was acceptable.

Keywords— Hearing aid System, Wireless System, Bluetooth Control, Hearing Aid Algorithm, Android Application

I. INTRODUCTION

Recently Ezairo series chip and development board have been used for development of hearing aid [1-2]. However very up to date, hearing aid have been developed more and more with wireless system. Wireless control in the hearing aid system can help user to control easily without the audiologist.

We implemented a wireless hearing aid system with Ezairo 7100 development kit and Bluetooth module as shown in Fig.1. And to control this system through wireless, we implemented the Android application to connect with hearing aid system and control the system.

II. METHODS

A. Hearing Aid Algorithm System

In the hearing aid system, wide dynamic range compression (WDRC) and feedback cancellation(FBC) are implemented. Input signal was sampled as 16kHz by ADC with stereo and every frame consisted of 8 sample respectively. The samples of one frame was analyzed by WOLA filterbank in HEAR core of Ezairo 7100. As a result, 16-band of power was extracted and gains of 8-channel were calculated based on this power.

Coefficients for FBC was calculated based on peak to average power ratio and it control the notch filter in FENG core.

B. Bluetooth and UART Control

In this hearing aid system, there is an additive Bluetooth module to communicate with smartphone application. Bluetooth module is connected to Ezairo with UART and connected to Android smartphone with Bluetooth. AT commands for Bluetooth control and data transition were stored in EEPROM of Ezairo.

To control the hearing aid, we made an Android application. The application is connected to Bluetooth module with serial port profile (SPP) and can sent commands or receive states.

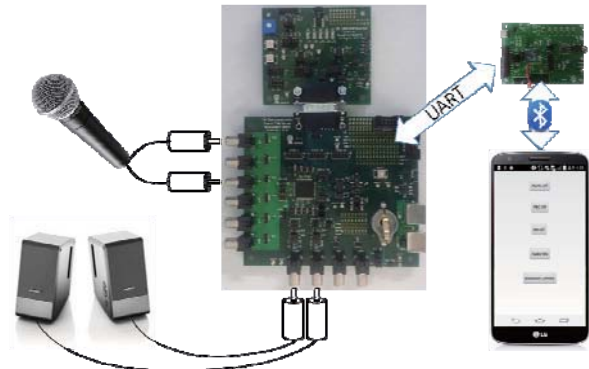


Fig. 1. Wireless hearing aid system with Ezairo 7100 development kit

III. RESULTS

A. Evaluation of Algorithm

To evaluate WDRC algorithm, we provide a sine tone as an input signal and extract gain table in every frame. An average difference between calculated and expected was under 1%.

And we made a feedback path between microphone and speaker for evaluation of FBC. When FBC was enabled, additive WDRC gain without feedback was 15dB.

B. Evaluation of Wireless System

Fail rate of wireless system using Bluetooth was about under 1%, 7%, 2%, 10% when WDRC and FBC is disabled, only WDRC is enabled, only FBC is enabled and all algorithm is enabled.

IV. CONCLUSION

In this study, we implemented a wireless hearing system and Android application to control the hearing

aid system. The hearing aid algorithm was acceptable but fail rate of wireless communication is not. It because CPU clock of hearing aid system was low (2.56MHz) and apportionment of algorithm was not efficient. Next study, we will use CM3 core for algorithm although it is for peripheral control.

ACKNOWLEDGEMENT

This research was supported by Basic Science Research Program through the National Research Foundation of Korea(NRF) funded by the Ministry of Education(2010-0020163)

This research was supported by Basic Science Research Program through the National Research Foundation of Korea(NRF) funded by the Ministry of Science, ICT & Future Planning(NRF-2013R1A2A2A04014796)

REFERENCES

1. Jarng, Soon-Suck. "An Experimental Study on the Fitting of 64 Channel Digital Hearing Aid by In-situ Method." *The Journal of the Acoustical Society of Korea* vol.31, Issue 5, pp.273-279, 2012
2. Gibson, P. L., Hedin, D. S., Davies-Venn, E. E., Nelson, P., & Kramer, K. "Multi-microphone adaptive array augmented with visual cueing." *Engineering in Medicine and Biology Society (EMBC), 2012 Annual International Conference of the IEEE. IEEE*, pp. 1000-1003, 2012.

Estimation for individual binaural beat characteristics by an Android Application

Woo-Hyeong Cho¹, Kang Lee¹, Hyeon-min Shim², Jangwoo Kwon³, Kyu-Sung Kim⁴ and Sangmin Lee^{1,2}

¹Department of Electrical Engineering Inha University, Incheon, Korea

²Institute for Information and Electronics Research Inha University, Incheon, Korea

³Department of Computer Information Engineering Inha University, Incheon, Korea

⁴Department of Otolaryngology-Head & Neck Surgery Inha University Hospital, Incheon, Korea

Abstract— In this paper, individual binaural beat characteristics were implemented an Android application for estimation. The application applies various sounds with various frequency for measurement of the phenomenon of binaural beat. The estimation of the individual binaural beat characteristics is performed by open and blind tests. In *t*-test result, there was no difference between open and blind tests.

Keywords— binaural beat, *t*-test, android application

I. INTRODUCTION

The binaural beat seems to be closely related to the ability of the auditory system to process phase differences at the two ears [1]. These may be heard when a tone of one frequency is presented to one ear, via headphones, and a tone of slightly differing frequency is presented to the other ear [2].

In this paper, the Android application was implemented for an efficient measurement of this phenomenon of binaural beat.

II. METHODS

JAVA language and Eclipse, Android SDK (Software Development Kit) are used for materializing the application for the measurement of the binaural beat. This application contains help frame and input frame which has seek bar for adjusting sound frequency band and keypad.

III. RESULTS

In this study, ten healthy male having no problem in their hearing organs participated in the experiment. Table 1 shows the test results of open and blind tests, and the frequency bands for the experiment were 200Hz, 400Hz, 600Hz, 800Hz and 1000 Hz, etc. In the open test, the frequency information was provided to the subjects to find out the phenomenon of binaural beat. In the case of the blind test, a priori information was not given to the subjects and then they were listened by the randomly selected sound frequency. To clarify the difference of the two tests, the *t*-test was

carried out. Especially, in the sound frequency range of 400Hz, the subjects were able to sense the difference of the two test. Through the two kinds of tests, it confirmed that there was no difference between open and blind tests.

Table 1. Comparison of Test result

Subject	Open test					Blind test				
	Frequency (Hz)					Frequency (Hz)				
	200	400	600	800	1000	200	400	600	800	1000
S1		√	√				√	√		
S2	√	√	√			√	√			
S3	√	√	√			√	√			
S4	√	√	√		√	√	√	√		√
S5	√	√				√	√			
S6		√	√			√	√	√	√	
S7	√	√	√		√	√	√	√		√
S8	√	√				√	√			
S9		√	√			√	√	√	√	
S10		√	√	√			√	√	√	

IV. CONCLUSION

We implemented an Android application to estimate the individual binaural beat characteristics. It was confirmed through the two kinds of tests that there was no difference between open and blind tests. Binaural beat can be differentiated regardless of a priori information. There is no personal distinction of the phenomenon of binaural beat because it is not speech but tone.

ACKNOWLEDGEMENT

This work was supported by Basic Research Program through the National Research Foundation of Korea (NRF) funded by the Ministry of Education (2010-0020163) and the MSIP Korea, under the C-ITRC (IITP-2015-H8601-15-1003)

REFERENCES

- Gerken G.M., Moushegian G., Stillman R.D. and Rupert A.L., "Human frequency-following responses to monaural and binaural stimuli," *Electroencephalography and Clinical Neuro Physiology* 38(4)379 – 386, 1975.
- Brian C. J. Moore, *An Introduction to the Psychology of Hearing*, Seoul, KOREA: HAKJISA, 2011., pp.233-267

Split and Merge Algorithm for Deep Learning

Hongsub An¹, Sang-Ick Kang¹, Sang-pyo Hong¹, Gyuseok Park¹ and Sangmin Lee^{1,2}

¹Department of Electronic Engineering Inha University, Incheon, Korea

²Institute for Information and Electronics Research, Inha University, Incheon, Korea

E-mail: lunatic0831@gmail.com

Abstract—In this paper, we propose a novel split training and merge algorithm for deep learning. The algorithm is motivated by the genetic algorithm (GA) and is composed of two procedures. The first procedure initializes two individual networks using restricted Boltzmann machines (RBMs), and the second procedure merges the two networks using the GA. The results show that the proposed algorithm has a lower error rate than the DBNs,

Keywords— genetic algorithm, deep belief network, deep neural network

I. INTRODUCTION

RBMs are trained using an unsupervised learning method for pre-training DBNs. A joint probability between the visible layer and the hidden layer is defined using an energy function in RBMs [1]. This probability distribution is used to obtain weights and biases between the visible layer and the hidden layer via the steepest descent method. To obtain the expected model values, this process starts from any random state of the visible units and takes a long time to perform the alternating Gibbs sampling [2]. However, Hinton assigned the states of the visible units to a training vector and performed alternating Gibbs sampling only once to achieve a faster learning procedure. This one-step contrastive divergence algorithm (CD-1) [3] generated satisfactory training results.

II. PROPOSED ALGORITHM

Fig. 1 shows the flow diagram of the proposed algorithm. First, $S_{training}$ is divided into two subsets. Subsequently, the two subsets are trained using their corresponding RBMs. The trained weights and biases of each subset as for RBMs input data are used as chromosomes in the merge phase. Moreover, crossover and mutation occur in this phase. The weight and bias used as the chromosome in the crossover process are composed of one matrix between each layer. The first matrix column corresponds to biases, and the other columns are weights. Thus, biases and weights between

the lower layer neurons and the upper layer neurons are one matrix row.

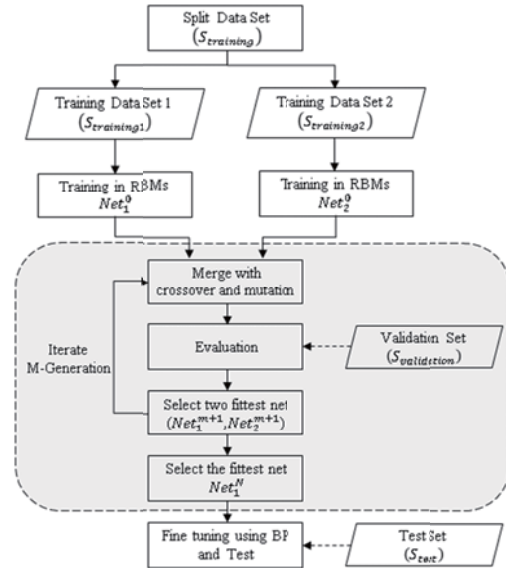


Fig. 1. Flow diagram of the split and merge algorithm

The performance of each offspring created after the merge phase is evaluated by counting the number of errors (zero-one loss) using a validation set.

After evaluating for offspring, the fittest two offsprings, Net_1^{m+1} and Net_2^{m+1} are selected, where, the subscript is the ranking in the validation test, and both networks are used to compose the next generation in the merge phase.

After iterating for M generations, the fittest offspring Net_1^N ($N \leq M$) is finally selected. This offspring network is composed of the biases and weights matrix that is used as the dominant feature extractor. However, these values are not optimized. Therefore, fine-tuning based on the BP is required, and the $S_{training}$ dataset is used for fine-tuning.

III. EXPERIMENT AND RESULT

The GA parameters used in the proposed algorithm are presented in Table 1. These parameters were obtained to

Table 1. Parameters setting of the GA

Number of Offspring	100
Crossover Rate	0.7

Mutation Probability	0.002	Fraction Ratio	0.5
Generation Number	500		

Table 2. Performance comparison of deep belief networks (DBNs) and the proposed algorithm in four networks. The error rates are measured from 100 BP epochs. Subscript denotes networks types and parentheses indicate the decreasing percentage of the error rate.

	DBN ₁	Proposed ₁	DBN ₂	Proposed ₂	DBN ₃	Proposed ₃	DBN ₄	Proposed ₄
Network Structure	784-100-100-10		784-200-200-10		784-100-100-100-10		784-200-200-200-10	
RBM Learning Rate	1		1		0.1		0.2	
RBM Epochs	50		100		100		100	
RBM Mini-batch	100		100		50		50	
BP Learning Rate	2		0.5		0.5		0.1	
BP Epochs	100		100		100		100	
BP Mini-batch	100		100		50		50	
Fittest Generation		500		483		493		340
Error Rate	2.46	2.30(6.5%)	2.13	1.78(16.43%)	2.12	2.01(5.19%)	2.01	1.85(7.96%)

be optimized for the proposed algorithm through repeated experiments. All experiments used a Mixed National Institute of Standards and Technology (MNIST) database for handwritten digits of zero to nine that contained 60,000 training images and 10,000 test images [4].

The networks meta-parameters and all experimental results are presented in Table 2. In this table, the values in parentheses indicate the decreasing percentage of the error rate. As it can be seen, the proposed algorithm reduces the error rate more than the original DBNs. In all experiments, the most suitable generation may or may not be optimized to a smaller generation from a predetermined generation.

IV. CONCLUSION

In this paper, we have presented an improved pre-training algorithm for improving the classification accuracy. The devised approach uses a GA-based feature extractor selection algorithm for detecting optimized initial parameters of DNNs. The trained networks with different training sets have different feature extractors. In order to find a more suitable combination of feature extractors for the entire training dataset the proposed algorithm merged these different networks using the GA. As a result of the combination of feature extractor using GA, the network initialization was optimized, making it possible to extract the dominant features during the learning procedure for DNNs.

ACKNOWLEDGEMENT

This research was supported by the KERI Primary Research Program through the Korea Research Council for Industrial Science & Technology funded by the Ministry of Science, ICT and Future Planning (No. 15-12-N0101-46) and Basic Science Research

Program through the National Research Foundation of Korea(NRF) funded by the Ministry of Science, ICT and Future Planning(NRF-2013R1A2A2A04014796)

REFERENCES

1. Hopfield, J.J., 1982. Neural networks and physical systems with emergent collective computational abilities. *Proceedings of the national academy of sciences* 79, 2554–2558.
2. Hinton, G., 2010. A practical guide to training restricted boltzmann machines. *Momentum* 9, 926.
3. Hinton, G.E., 2002. Training products of experts by minimizing contrastive divergence. *Neural computation* 14, 1771–1800.
4. LeCun, Y., Cortes, C., 1998. The mnist database of handwritten digits.

Pulse Wave Extraction from Cellphone Camera Image using Small Region of Interest(ROI)

J. J. Lee¹, J. H. Lee¹, J. H. HEO¹, H. W. KIM¹ and Y. R. Yoon¹

¹Department of Biomedical Engineering, Yonsei University, Wonju, Korea

E-mail: yoona@yonsei.ac.kr

Abstract— The purpose of this study is extraction of pulse wave from cellphone camera image using small region of interest(ROI). The ROI was separated into the three RGB channels. Then, We extracted pulse wave using independence component analysis(ICA). The result of comparing the heart rate of photoplethysmography(PPG) measured at the finger with pulse wave extracted from the face is 99.05%.

Keywords— Photoplethysmography, ROI, ICA, Camera Image

I. INTRODUCTION

Now a days, studies that measuring the heart rate using a extracted pulse wave from face image taken by the camera have been conducted actively[1-2]. But, most studies have problem such as computational complexity and slow operating speed. Because they set an entire face as the ROI. In this paper, we extract pulse wave from face image using small ROI.

II. METHODS

A. Experimental Procedure

We selected five male subjects at 20 age. All of face images were taken for 1 minute by using cellphone camera(Galaxy S6 Edge, SAMSUNG Inc.) at 30frame/s. At the same time, we measured a pulse wave using a PPG sensor(MP150 PPG Module, BIOPAC Inc.) on the finger at 200Hz/s.

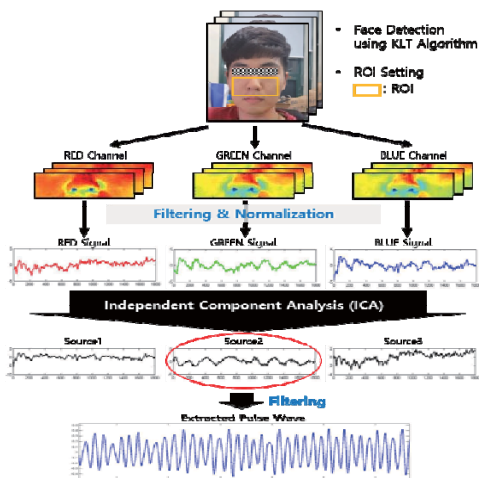


Fig. 1. PPG Extraction Process

B. Analysis

ROI was detected by face detection algorithm from Computer Vision library. We modified ROI as 65% width, 30% height. The ROI was separated into the red, green and blue channels. Next we extracted the signal from each channel by averaging all pixels in each ROI. Finally, These signals were normalized. After that, pulse wave is extracted using ICA based on the joint approximate diagonalization of eigenmatrices (JADE) algorithm. Finally, we yielded the heart rate using peak detection algorithm based on threshold method and compared the heart rate from PPG on finger with from face image.

III. RESULTS

Fig 2 shows the result of comparing the PPG signal from finger with from face image. The mean accuracy of the extracted PPG from face image is 99.05%.

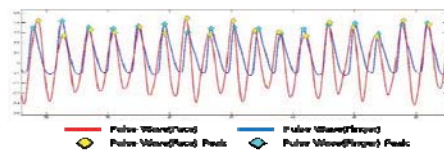


Fig. 2. The results of PPG extraction

IV. CONCLUSION

This study shows the high accuracy of heart rate from extracted PPG. Compared with previous studies, the above method reduce computational complexity and increase operating speed by using small ROI.

ACKNOWLEDGEMENT

This research was supported by the corporate associated research development manpower training Program of the Ministry of Trade, Industry and Energy (N0001130).

REFERENCES

1. Daniel McDuff, Sarah Gontarek, Rosalind W. Picard, "Remote Detection of Photoplethysmographic Systolic and Diastolic Peaks Using a Digital Camera", *IEEE Transactions on biomedical engineering*, vol.61, No.12, pp.2948-2954, 2014
2. Mayank Kumar, Ashok Veeraghavan, Ashutosh Sabharwal, "DistancePPG: Robust non-contact vital signs monitoring using a camera", *Biomedical optics express*, vol.6, No.5, pp.1565-1588, 2015.

Effective Electrode placement for Monitoring of Respiration with AED

J.H. HAN¹, J.H. HEO¹, H.W. KIM¹, J.J. LEE¹ and Y.R. YOON¹

¹Department of Biomedical Engineering, Yonsei University, Wonju, South Korea
E-mail: yoon@yonsei.ac.kr

Abstract— AED(Automated External Defibrillator) utilize impedance measurements for ventilation monitoring. The purpose of this study is to find the optimal electrode placement for monitoring of respiration with two extra electrodes in addition to the two AED electrodes. By analyzing impedance baseline and impedance change(ΔZ), we show that the effective electrodes for four electrode configurations with AED electrodes.

Keywords —electrodes placement, AED, respiration, Thoracic impedance.

I. INTRODUCTION

Some AED measure Thoracic Impedance(TI) in order to monitor respiration. It is more beneficial to add two extra electrodes than use only two AED electrodes. [1] But there is no research to find the proper electrode placement in this four electrode setup with AED electrodes. It is believed that ventilation detection can be improved if the impedance measurement system was more advanced for this task.

II. METHODS

A. Subject and Equipment

Five healthy male volunteers participated in this study. Average age was 27years (24-33). All impedance measurement was used two-channel with four electrodes electrical impedance circuit. AC amplitude was 1Vpp at 30kHz.

B. Electrode placement

Fig. 1 show the position of measurement electrodes for the pair of current electrodes and the voltage electrodes. [2] The AED electrodes are CU1007S and the small ECG electrodes are 100 Foam Electrodes.

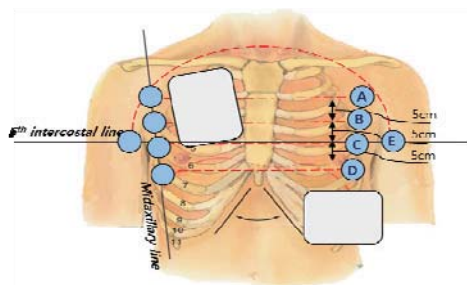


Fig. 1. The four electrode configuration

C. Procedure

We measured thoracic impedance for 60s of spontaneous breathing. Subsequently impedance was measured when subject inhaled maximally and exhaled maximally. Lastly the same procedure was repeated including change of electrode placement.

III. RESULTS

Table 1. Resistance result with position A

Test Person	Num Vents analyzed	Mean baseline [ohm]	Mean Vents [ohm]	Normalized vent amp	TI Increase [%]
1	13	87.9	1.26	1.4%	7.3%
2	12	75.4	1.12	1.5%	8.8%
3	11	71.6	1.20	1.7%	8.0%
4	11	65.2	1.22	1.9%	9.5%
5	10	84.5	1.34	1.6%	7.7%

By analyzing resistance data of each placement, A is the lowest mean baseline placement and the highest impedance increase percent placement. Table1 shows the resistance result with position A on each subjects.

IV. CONCLUSION

We conclude that the effective placement of two extra electrodes were placed near underarm. Position A and Position B shows similar results. This new configuration combined with AED electrodes can help AED Algorithm.

ACKNOWLEDGEMENT

This research was supported by the corporate associated research development manpower training Program of the Ministry of Trade, Industry and Energy (N0001130)

REFERENCES

- OG. Martinsen, et al. "Bioimpedance-Based Respiration Monitoring With a Defibrillator" *IEEE Trans. Biomed. Eng.*, vol. 61, pp. 1858-1862, 2014.
- Seppä, Ville-Pekka, et al. "Novel electrode configuration for highly linear impedance pneumography." *Biomedizinische Technik/Biomedical Engineering*, vol. 58, pp 35-38, 2013

A posture classification algorithm based on SVM with RBF kernel

S.Y. Ma¹, S.K. Kim¹, H.M. Shim², S.S. Kim³ and S. Lee^{1,2}

¹Department of Electronic Engineering, Inha University, Incheon, Korea

²Institute for Information and Electronics Research, Inha University, Incheon, Korea

³PPYPLE INC, Incheon, Korea

Abstract—In this paper, a posture classification algorithm based on support vector machine(SVM) is proposed. The optimized parameters of SVM were found by the grid-search method. As a result, it was verified that the classification performance of SVM with the optimum parameters was improved.

Keywords— posture, SVM, RBF kernel, upper bound of Lagrange multiplier, grid-search

I. INTRODUCTION

Most of modern people spend their time sitting at a desk. However, they are disturbed their posture immediately after sitting on a chair. Postures of incorrectly sitting cause physical disorders such as lumbar disc, scoliosis or other spinal problems[1].

In this study, an algorithm to sitting posture classification is proposed. To measure posture, the device has developed an inertial measurement unit(IMU) built-in neckband, and three types of data were measured. The posture was classified by the support vector machine(SVM).

II. METHODS

SVM is the group of hyperplane to classify the class of the data group. However, kernel is used when the data is impossible to utilize linear classification. Radial basis function(RBF) is generally much used. SVM which used kernel function as RBF is affected by the change of σ . Input vector is impossible to be classified with linear classification, the SVM which used RBF kernel is the equation (1).

$$f(x) = \text{sign}\left(\sum_{i=1}^N \alpha_{o,i} d_i k(X_i, X) + b_0\right) \quad (1)$$

$\alpha_{o,i}$ means the C of upper bound of Lagrange multiplier which takes the object function as a maximum. Also, when it comes to using the RBF kernel, $k(X_i, X)$ means the equation (2) and σ should be designated by the users[2].

$$\text{RBF} = \exp\left(-\frac{\|X - X_i\|^2}{2\sigma^2}\right) \quad (2)$$

Grid-search is one of the parameter optimization methods[3]. The range of the computed parameter values were $C = [2^{-15}, 2^{-14}, \dots, 2^5]$, $\sigma = [2^{-15}, 2^{-14}, \dots, 2^3]$

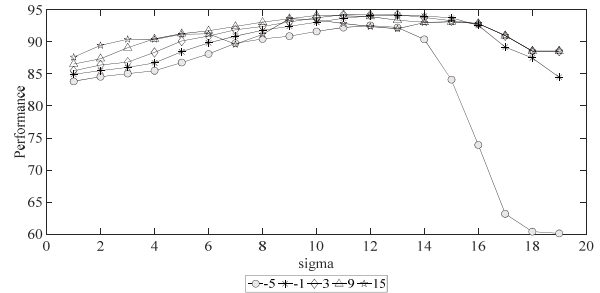


Fig. 1. Classification results with RBF kernel depending on σ

III. RESULTS

Five healthy males participated in the experiment. They put on the IMU built-in neckband, and maintained three types of sitting positions: Neutral, smart-phoning and writing in the ten minutes, respectively. From the extracted feature vectors, 20,000 vector elements were selected randomly to be used as the input of SVM. Figure 1 showed the accuracy of classification by the kernel parameter. The x-axis meant the data of $\sigma = 2^i$ and the legend meant the data of $C = 2^j$. The data showed the performance with 94.25% in the following condition: $\sigma = 2^{11}$ and $C = 2^9$.

IV. CONCLUSION

We proposed a novel approach for posture classification based on the SVM with adjustable parameter of the RBF kernel. It is verified that the proposed algorithm could effectively find the target parameters. The proposed scheme of posture classification shows better performance.

ACKNOWLEDGEMENT

This research was supported by the SW Convergence R&D supporting business of MISP, Incheon and IIS (R17-71-013) and the MSIP, Korea under the C-ITRC (IITP-2015-H8601-15-1003).

REFERENCES

1. D. Falla and P. Hodges, "Effect of Neck Exercise on Sitting Posture in Patients with Chronic Neck Pain," *Physical Therapy*, vol. 87, no. 4, 2007
2. C.C. Chang and C.J. Lin, "LIBSVM: A Library for Support Vector Machines," <https://www.csie.ntu.edu.tw/~cjlin/libsvm/>, 2004
3. C.W. Hsu, C.C. Chang and C.J. Lin, "A practical Guide to Support Vector Classification," Technical report, 2005

Smart pad e-book application for quadriplegic using portable sEMG device

E. I. Cho¹, H. W. Kim¹, J. H. Im¹ and Y. R. Yoon¹

¹Department of Biomedical Engineering, Yonsei Univ., Wonju, Korea, Republic of.

E-mail: yoony@yonsei.ac.kr

Abstract— This study is about portable e-book system for quadriplegic using surface electromyography. We aim general paralysis person who can only act 2 muscle, procerus muscle and levator anguli oris muscle. We made android tablet e-book application which work with portable sEMG system. Its accuracy is 98.5 % and malfunction ratio is just 0 %.

Keywords— Quadriplegic, Human Computer Interface, E-Book, Electromyography, Portable system

I. INTRODUCTION

Most of quadriplegic people have two kinds of desire. One is express their feeling and opinion. The other is get and increase their knowledge. Recently many researches related to expression are undergoing and media reports about them. But there is very few researches related to get information. So we try to develop portable e-book system for quadriplegic who can only use procerus muscle and levator anguli oris.

II. METHODS

A. Signal Acquisition System

We developed portable signal acquisition system. It has 2 sEMG circuit, recharging circuit and Bluetooth module. It displayed in Fig. 1. A is sEMG sensor connector. B is micro 5pin USB cable connector to recharge and C is battery connector. We get sEMG data using 1000Hz sampling rate, 8Bit resolution ADC. It can work more than 20 hours with 500mAh battery.

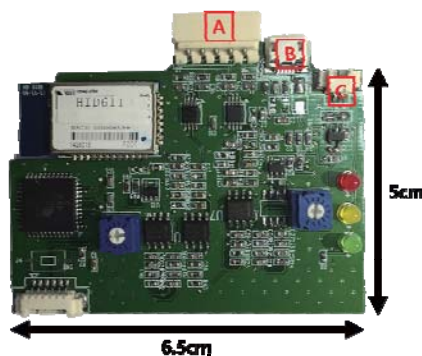


Fig. 1. Signal Acquisition System

B. Algorithm

We want to measure only muscle active. So we use root mean square (RMS). First to get baseline level, we measure sEMG for 1 second and calculate average.

After that, measure 1 more second to calculate RMS. RMS window size is 50 samples (50ms). And automatically set RMS threshold as 1.4 times of maximum RMS value in idle state. During e-book application running, if RMS value is bigger than threshold, set flag. And when RMS value is lower than threshold for more than 0.2 seconds, clear flag.

C. Android Tablet E-book Application

Android tablet e-book application has connect device menu, and open pdf file menu. When reading pdf file, it can go to next page via act procerus muscle, and go to previous page via act levator anguli oris muscle. If act muscle longer than 2.5 seconds, move 5 page/sec.

III. RESULTS

10 subjects act each muscle for 10 times to get accuracy of algorithm. As the result, accuracy of procerus muscle act is 98 % and levator anguli oris muscle is 99 %.

10 subjects stay in resting state for 1 minute to get malfunction ratio. They did this test for 10 times. As the result, no malfunction occurred. So malfunction ratio is 0 %.

IV. CONCLUSION

The module which is developed in this study can help quadriplegic to read pdf file at outside. It means, quadriplegic can study and get knowledge during move with vehicle. But it use wet type electrodes. So as a further study, we have to improve electrodes.

ACKNOWLEDGEMENT

This research was supported by the corporate associated research development manpower training Program of the Ministry of Trade, Industry and Energy (N0001130).

REFERENCES

1. A. Phinyomark, P. Phukpattaranout and C. Limsakul, "Feature reduction and selection for EMG signal classification" *Expert Systems with Applications*, vol.39, pp. 7420-7431, 2012.
2. I.H. Moon, M.J. Lee, J.U. Chu and M.S. Mun, "Wearable EMG-based HCI for Electric-Powered Wheelchair Users with Motor Disabilities" *IEEE International Conference on Robotics and Automation*, April 2005.

Detection of Characteristic Points of Pulse Wave using Persistent Homology

J. H. Im¹, J. D. Piao¹, E. I. Cho¹, and Y. R. Yoon¹

¹Department of Biomedical Engineering, Yonsei University, Wonju, Korea
E-mail: yoon@yonsei.ac.kr

Abstract—The Pulse wave tends to overlap with moving artifact arising from a patient's movement. This study is a pilot experiment for removing motion artifacts of the pulse wave. We use the pulse wave be measured using oscillometric method and Persistent Homology to detect characteristic points of the pulse wave.

Keywords— Pulse Wave, Oscillometric method, Persistent Homology

I. INTRODUCTION

The pulse wave have several characteristic points. The second derivative of the pulse wave is used to diagnose the stiffness of blood vessels by detecting the significant points. These points are inclined to overlap with moving artifact. It is important to reduce the effect of noise in order to get pulse wave signal.

This study used Persistent Homology to remove the effect of noise on the pulse wave.

II. METHODS

A. Persistent homology

Persistent homology is a method for measuring topological features of function. Small size features are seen as a noise in persistent homology. The method is used to de-noise or smooth signal [1].

B. Data acquisition

The pulse wave is measured using the cuff (W.A.BAUM Corp, 18to26cm arm circumference, single tube). It is because the sensor position in oscillometric method is not a crucial factor compared with tonometric method. The pulse wave is measured during 1minute, sampled 200Hz with an 8bit resolution analog to digital conversion, and then passed through a 15Hz cutoff frequency FIR low-pass filter for smoothing the sampled pulse wave.

Differentiation is used to get accelerated plethysmography (APG). APG has five characteristic points. To detect these points, persistent homology is used. And an artificial noise signal that replaces moving artifact is added to the filtered pulse wave.

The frequency of each type of moving artifacts ranges from 0.01-10Hz, the sinusoidal signals with specific frequency (0.01-10Hz) are added to the filtered pulse wave. The persistent homology method is used to confirm persistence of each critical points [1, 2]. The characteristic points appear relatively far from the diagonal line($y=x$) in persistent diagram. All process is conducted by MATLAB R2014.

III. RESULTS

Typical Results are show in Fig.1. A 2Hz sinusoidal wave is added to filtered signal as a noise in Fig.1 (b). The second derivative of noise data is as Fig.1 (C). All extrema are expressed in green dots in Fig.1 (d). The specific characteristic points are expressed in blue and red dots in Fig.1 (e). (Persistence of extrema > 0.01 , red dot is global minimum value)

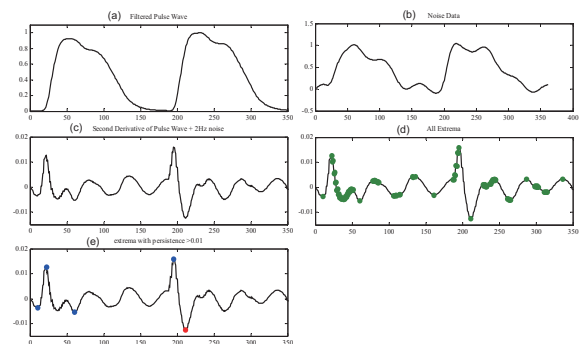


Fig. 1. Pulse Wave signal Processing Process

IV. CONCLUSION

In this study, the persistent homology method is used to remove the noise of pulse wave. It is verified that the persistent homology is effective to reduce the impact of noise on original signal. It seem that this noise reduction method can be used in wearable device to measure patient's pulse wave, heartrate and so on. To remove the noise effect on signals which have moving artifact occurred from specific movements is a further study.

ACKNOWLEDGEMENT

This research was supported by the corporate associated research development manpower training Program of the Ministry of Trade, Industry and Energy (N0001130).

REFERENCES

1. S. Emrani, T. S. Saponas, D. Morris, and H.Krim, "A novel framework for pulse pressure wave analysis using persistent Homology", *IEEE SIGNAL PROCESSING LETTER*, vol. 22, pp. 1879-1883, 2015.
2. J. W. Lee & J. H. Nam, "Design of filter to reject motion artifacts of PPG signal by Using Two Photosensors", *Journal of information and communication convergence engineering*, vol. 10(1), pp. 91-95, 2012.

Optimal Pulse-wave Foot Point Detection Algorithm Verification For Calculating Pulse-wave velocity

J. Y. Park¹, J. H. Im¹, and Y. R. Yoon¹

¹Department of Biomedical Engineering, Yonsei University, Wonju, Korea
E-mail: yoon@yonsei.ac.kr

Abstract— In order to develop the continuous blood pressure measurement devices, pulse-wave velocity (PWV) calculation method are used. So it is important to detect the pulse wave characteristic point (Peak or Foot point) to calculate the PWV. So we compared foot point and peak for verifying which more appropriate characteristic point is by calculating PWV and comparing their standard deviation. After that we compare 3 algorithms for verifying which algorithm is appropriate to detect foot point by comparing their detection rate and standard deviation. In conclusion, the second derivate maximum method is the most appropriate algorithm for measuring continuous blood pressure.

Keywords— Continuous blood pressure measurement, Pulse-wave velocity, Foot point

I. INTRODUCTION

PWV is a velocity of blood flow. It is an indicator of cardiovascular stiffness. It is important to notice correct characteristic point in order to calculate precise PWV. The algorithms that detect the characteristic point of pulse wave are compared in this study.

II. METHODS

A. Measuring Equipment and Analytical program

BIOPAC MP150 (PPG100C and ECG100C) is used to measure PPG and ECG. Acqknowledge 3.9.1 software program is used to analyze the signals. And MATLAB 2014a is used to detect the foot points of each PPG signals. PPG sensor and wet type electrode ECG sensor is used to measure the parameter.

B. Data acquisition

The subject group consisted of 7 subjects (4male and 3 female) between the ages of 23 and 27 years. Signals are acquired by 200Hz sampling rate and then analyzed to calculate PWV.

The characteristic point (foot points or peak point) were detected by using 4 methods. These methods are as in the following.

- 1) Tangent Intersection Method(TI Method)
Foot point is located at the intersection of the straight-lines drawn through the rear and the forefronts of the pulse wave.
- 2) APW foot approximation method(AFA Method)
Foot point is located at in 10% point from minimum point of relaxation period to systolic peak point.

- 3) The second derivate maximum method(SDM Method)
Foot point is located at the peak point of second derivative of pulse wave.
- 4) Peak detection algorithm(PDA)
Characteristic point is located at the peak point of pulse wave.

III. RESULTS

The result of algorithm comparison of efficiency is as followed Table 1. Error means that the ratio of the number of correct point to all extracted points.

Algorithm subject	PWV Standard deviation				Error (%)			
	TI Method	AFA Method	SDM Method	PEAK Algorithm	TI Method	AFA Method	SDM Method	PEAK Algorithm
Subject1	14.5006	117.2576	9.7447	44.4454	100	94.55	100	100
Subject2	5.5418	4.0309	5.3461	15.4315	100	100	100	100
Subject3	3.4920	8.4975	3.4894	9.2102	100	100	100	100
Subject4	4.4836	5.8568	4.0207	13.7852	100	100	100	100
Subject5	3.4549	3.5267	3.4805	45.1561	100	100	100	99.03
Subject6	12.6881	13.9027	11.9753	471.5311	100	100	100	99.07
subject7	4.7999	4.8632	4.7983	23.8751	100	100	100	100
Average	6.9944	22.5622	6.1221	89.0621	100	99.22	100	99.73

Table 1. PWV calculation result of each algorithm

IV. CONCLUSION

Foot point detection is suitable for PWV calculation comparison with peak point detection. Peak point detection algorithm's average PWV standard deviation was higher than foot point's one. The second derivate maximum method is the most suitable for detecting the characteristic points seeing that the average PWV standard deviation is smallest in Table1.

ACKNOWLEDGEMENT

This research was supported by the corporate associated research development manpower training Program of the Ministry of Trade, Industry and Energy (N0001130).

REFERENCES

1. E. Kazanavicius, R. Gircys, A. Vrubliauskas, and S. Lugin, "Mathematical methods for determining the foot point of the arterial pulse wave and evaluation of proposed methods", *Information Technology and control*, vol. 34(1), 2015.

Auditory steady-state response test using hearing loss simulator for brain-computer interface

J. H. Hwang¹, J. M. Ahn¹, K. W. Nam¹ and I. Y. Kim¹

¹Department of Biomedical Engineering, Hanyang University, Seoul, Korea

E-mail: jongho2000@bme.hanyang.ac.kr

Abstract— In this study, auditory steady-state response (ASSR)-based brain computer interface (BCI) test using hearing loss-reflected auditory stimuli was performed using hearing loss simulator (HLS). The stimulus was sinusoidal amplitude modulation (SAM) sound passed the HLS.

Keywords— Auditory steady state response, Electroencephalography, Brain computer interface, Hearing loss simulator.

I. INTRODUCTION

There have been many auditory BCI (aBCI) studies, but most of them did not consider the degree of sensorineural hearing impairment of the motor-disabled patients. In this study, hearing loss-reflected auditory stimuli were utilized for ASSR-based binary aBCI.

II. METHODS

A. HLS verification

Main symptoms of the hearing loss patients are deteriorated hearing threshold and widen auditory filter bandwidth. To simulate these symptoms, a HLS (Cochlear Implant and Hearing Loss Simulator; TigerSpeech Technology, China) was utilized. To verify the performance of the utilized HLS, the two experiments were conducted. First, a white noise was entered to the HLS to verify the similarity of the HLS output with the audiogram pattern. Second, a 1000 Hz sine wave was entered to the HLS to verify the similarity of the HLS output with the auditory filter bandwidth measured by Glasberg et al..

B. Auditory stimuli

Left ear stimulus: SAM with carrier frequency(CF) = 500 Hz and modulation frequency (MF) = 37 Hz. Right ear stimulus: CF = 2,000 Hz and MF = 43 Hz. Two SAM sounds were passed through the HLS with moderate, moderately severe, and severe hearing loss setup.

C. Electrode

Three dry EEG electrodes were attached on Cz, C3 and C4 in 10-20 system, and ground/reference electrodes were attached on right/left mastoid.

D. Signal process

15 sec EEG signal were recorded for each testing condition. After 256-point FFT (1 sec window with 50% overlap), 60 ratio features were calculated, and among them, three representative ratios were selected for aBCI. At last, 10-fold cross validation was performed.

III. RESULTS

A. HLS

HLS could successfully simulate the audiograms and auditory bandwidth entered by the user.

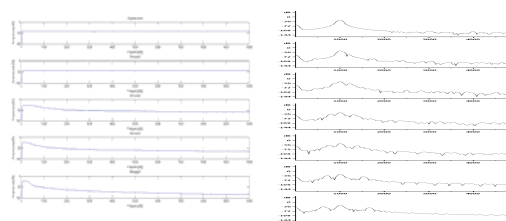


Fig. 1. Output of HLS (audiogram and auditory bandwidth)

B. aBCI

The aBCI result showed the following accuracy.

HL type	ML	MSL	SL
Accuracy	66.6	83.3	50.0
Total accuracy			66.6

IV. CONCLUSION

This results demonstrate the possibility that the degree of hearing impairment may affect the performance of ASSR-based aBCI.

ACKNOWLEDGEMENT

This work was supported by the Research fund of Defense Development of Korea (ADD-14-01-08-13).

REFERENCES

1. D. W. Kim, H. J. Hwang, J. H. Lim, Y. H. Lee, K. Y. Jung and C. H. Im, "Classification of selective attention to auditory stimuli: Toward vision-free brain-computer interfacing.", *Journal of Neuroscience Methods*, vol. 197, pp. 180–185, 2011
2. R. Glasberg and B. C. Moore, "Auditory filter shapes in subjects with unilateral and bilateral cochlear impairments.", *J. Acoust. Soc. Am.*, vol 79, pp. 1020-33, 1986

Eye-blink detection using electrodes attached around the ears

J. Yoon¹, J. M. Ahn¹, J. H. Hwang¹, K. W. Nam¹, and I. Y. Kim¹
¹Department of Biomedical Engineering, Hanyang University, Seoul, Korea
 E-mail: yjm@bme.hanyang.ac.kr

Abstract— Eye-blink signal is commonly measured from the electroencephalography (EEG) electrode on forehead. However, recent trend of bio-signal acquisition system is miniaturization and compactness. The aim of this paper is to find where we could detect eye-blink signal from, excepting forehead.

Keywords— Eye blink, Ear-EEG, Kurtosis, Neural Network.

I. INTRODUCTION

The eye-related signals can be measured in the frontal and prefrontal regions of the brain [1]. So, in most conventional studies, the eye-blink signal is measured from the forehead. However, when we want to apply eye blink-control functionality to the headset-type hearing-support devices, it is necessary to get eye blink signals not from forehead but from around-ear position.

II. METHODS

A. Electrodes arrangement

We tried several arrangements of three disc-type electrodes to find the best for detecting eye-blink signal. The optimal arrangement of electrodes around the ear we found: a signal electrode is attached above the right ear, a reference electrode is attached behind and below the right ear, and a ground electrode is attached behind the left ear.

B. Eye-blink detection protocol

To extract eye-blink patterns, three subjects were required to blink once every two seconds. Recorded data was processed sequentially: pre-processing, feature extraction (maximum, minimum amplitude, and Kurtosis), and classification [1]. Three-layer ANN was utilized as a binary classifier (blink or no blink). Fig. 1. shows the eye-blink detection protocol implemented.

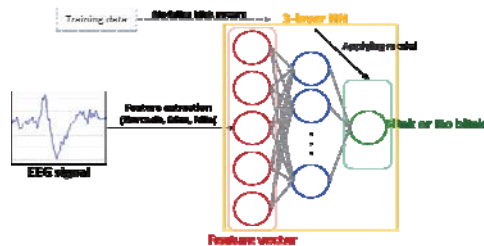


Fig. 1. ANN-based eye-blink detection protocol

III. RESULTS

A. Recorded eye-blink signal

Fig. 2. shows the eye-blink signal recorded from the electrodes attached around the ears.

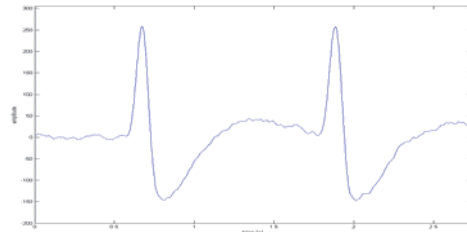


Fig. 2 Eye-blink signal from the electrodes arrangement

B. Performance of eye-blink detection

Fig. 3. shows the performance of the proposed eye-blink detection protocol as a confusion matrix and ROC curves.

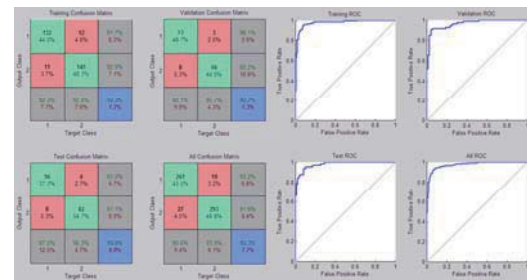


Fig. 3. Confusion matrix (left) and ROC curves (right)

IV. CONCLUSION

We could successfully detect eye blink signals from electrodes attached around the ears.

ACKNOWLEDGEMENT

This work was supported by the Research fund of Defense Development of Korea (ADD-14-01-08-13).

REFERENCES

1. B. Chambayil, R. Singla, and R. Jha, "EEG eye blink classification using neural network," *Proc WCE'10*, vol. 26, Vol. 1. 2010. p. 2-5.

Speech-induced EEG Classification using the Minimum Distance to Riemannian Mean

Woosu Choi, and Boreom Lee

Department of Medical System Engineering, Gwangju Institute of Science and Technology, Gwangju, Republic of Korea
E-mail: leebr@gist.ac.kr

Abstract—The objective of this study is to classify speech perception EEG data into appropriate classes using the calculation of minimum distance to Riemannian mean. By using this method, we estimated not only binary classification but also multiclass classification rate. Mean accuracy of classification for whole stimulus is 61.3% for binary class and 45.0% for 3-class in one subject.

Keywords— EEG, Minimum Distance to Riemannian Mean, Vowel speech perception.

I. INTRODUCTION

Common spatial pattern (CSP) has been widely used to analyze EEG dataset which is composed of two different conditions because of its performance. Barachant et al. suggested novel method to classify motor imagery EEG dataset in terms of Riemannian geometry and their results showed reasonable performance compared to CSP algorithm [1]. In this study, we applied this concept to classify auditory EEG signals produced by speech stimuli.

II. METHODS

A. Experiment and Subject

In this study, three vowels were chosen for stimulus: /a/, /i/, and /u/. Each stimulus has the same duration and their amplitudes were normalized. Stimulus was provided to the subjects through earphone for one second for each trial. Three healthy Korean subjects participated in this study,

B. Data Acquisition and Preprocessing

All EEG dataset was recorded using 64-channel EEG device by Electrical Geodesics, Inc. Sampling rate of this recording was set at 250Hz. EEG was recorded for 40 trials in each stimulus. After acquiring EEG dataset, we applied Butterworth (order: 5) IIR bandpass filter to get EEG data which contains theta (4-7Hz), alpha (8-12Hz) and beta band (13-25Hz).

C. Minimum Distance to Riemannian Mean

Riemannian means of covariance matrices for each class are calculated for training dataset. Then we calculate Riemannian distance from mean covariance matrix of each class to covariance matrix of test dataset. Finally,

test dataset are classified into appropriate class which has minimum distance to Riemannian mean (MDRM).

III. RESULTS

A. Binary Class

First of all, 10 fold cross validation was used to divide training and test dataset. After that, we performed binary classification using MDRM. Table 1 shows subject 1's means and standard deviations of each classification rate. Although we only processed bandpass filtering before calculating each covariance matrix, results are reasonable compared to previous research using CSP. [2]

Table 1. Classification rate

	/a/	/i/	/u/
/a/		64.2±19.7	60.0±16.6
/i/	64.2±19.7		63.3±11.3
/u/	60.0±16.6	63.3±11.3	

B. Multiclass

Furthermore, we performed multiclass classification for 3 classes. Mean of total classification rate for 3 classes is 35.4%. Especially, subject 1 showed the rate of 48.9%.

IV. CONCLUSION

MDRM method shows comparable performance in vowel speech perception EEG data. But, it is much faster than CSP and it can be easily extended to multiclass classification, which showed a possibility of applying it to real-time EEG analysis.

ACKNOWLEDGEMENT

This research was supported by the Pioneer Research Center Program through the National Research Foundation of Korea funded by the Ministry of Science, ICT & Future Planning (grant no. 2012-0009462).

REFERENCES

1. Barachant, Alexandre et al. "Multiclass brain-computer interface classification by Riemannian geometry." *IEEE Trans. Biomed. Eng.*, vol. 59(4), pp.920-928, 2012.
2. Kim, Jongin, Suh-Kyung Lee, and Boreom Lee. "EEG classification in a single-trial basis for vowel speech perception using multivariate empirical mode decomposition." *J. Neural Eng.* vol. 11(3), pp.920-928, 2014.

Individualization Strategy for EEG-based Passive Brain-Computer Interfaces Considering Test-retest Reliability of EEG Features

C.-H. Han, J.-H. Lim, J.-H. Lee, and C.-H. Im

Department of Biomedical Engineering, Hanyang University, Seoul, Republic of Korea

E-mail: ich@hanyang.ac.kr

Abstract—The objective of this study was to develop an individualization process for EEG-based passive brain-computer interfaces considering test-retest reliability of EEG features. Our preliminary results showed that selecting individual best feature with high test-retest reliability could effectively improve the overall performance of the system.

Keywords—electroencephalography, vigilance, test-retest reliability, individualization, d2-test

I. INTRODUCTION

Passive brain-computer interface (pBCI) is a branch of BCI technology that estimates the mental status of a user. Vigilance, the ability to sustain attention over prolonged time periods, is one of the important indices that have a variety of potential applications in pBCI. For past decades, various electroencephalography (EEG) features have developed to monitor vigilance state; however, it is still difficult to develop practical applications adopting these features due to large individual variability and low test-retest reliability [1]. In this study, to overcome these limitations, we developed a new individualization strategy considering test-retest reliability of EEG features.

II. METHODS

Five participants took part in our experiments. In this study, the ‘d2-test of attention’ paradigm was used to test vigilance of individuals, and 32 EEG electrodes were placed on the participants’ scalp according to the international 10-20 system.

The proposed individualization process was as follows: First, each individual feature database was constructed using spectral band power, asymmetry measure, and cross frequency coupling features. Second, we calculated a correlation coefficient between each feature and a behavioral measure called concentration performance (CONC), with which we constructed a correlation matrix. Finally, test-retest reliability of all features was evaluated, and the features with high average rank as well as small deviation between trials were selected.

To validate the performance of our individualization process, we compared average correlation coefficients of individual best features and the universally best feature. In addition, average ranks of individual best

features selected by conventional method and those by the proposed individual process were compared to confirm whether the proposed method could select features with high test-retest reliability.

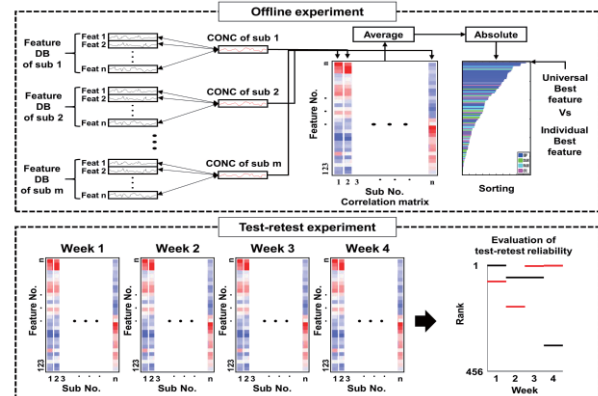


Fig. 1. The proposed individualization process

III. RESULTS AND CONCLUSION

Average correlation coefficient of individual best features selected by the proposed individualization process was 280% higher than that of the universal best feature. Moreover, the average ranks of individual best features were higher when the proposed method was used than when the conventional method was used. From these experimental results, we could confirm that the test-retest reliability needs to be considered in the individualization process of pBCI applications.

Table 1. Average rank of features selected by conventional (CV) and proposed (PR) method

	Sub 1	Sub 2	Sub 3	Sub 4	Sub 5	Avg
CV (%)	25	46	28	10	16	25
PR (%)	14	18	4	10	11	11

ACKNOWLEDGEMENT

This work was supported by the ICT R&D program of MSIP/IITP. [10045452, Development of Multimodal Brain-Machine Interface System Based on User Intent Recognition]

REFERENCES

1. R. E. Dustman, D. E. Shearer, and R. Y. Emmerson, “Life-span changes in EEG spectral amplitude, amplitude variability and mean frequency,” *Clinical Neurophysiology.*, vol. 26, pp. 110, 1399-1409, 1999.

Speech Enhancement Algorithm using 2-D Binary Mask in Wavelet Domain

G. H. Lee¹, S. D. Na¹, J. N. Lee¹, Y. J. Lee², J. H. Cho², and M. N. Kim²

¹Department of Medical & Biological Engineering, Graduate School, Kyungpook National University, Daegu, Korea

²Department of Biomedical Engineering, School of Medicine, Kyungpook National University, Daegu, Korea

E-mail: kimmn@knu.ac.kr

Abstract—In this paper, we proposed a new speech enhancement algorithm based on 2-D binary mask in wavelet domain. We performed experiments in variety SNR environments, and show that the proposed algorithm achieves significantly better performances compared with logMMSE SPU.

Keywords— Speech enhancement, Binary mask, Wavelet transform.

I. INTRODUCTION

Many of the numerous approaches to single-channel speech enhancement process the signal in a transform domain in which both speech and noise signals are sparse[1]. However these approaches very complicated and have poor performance in low SNR environments. In this paper, we proposed a new speech enhancement algorithm which is simple and has good performance in low SNR environment.

II. METHODS

A. Modified Wavelet Packet Decomposition

To create 2-D structure of a speech signal, we used modified wavelet packet decomposition. The speech signal is decomposed to 18 sub-bands of the wavelet coefficient $w_m(k)$. It is optimized for proposed 2-D binary mask. Where m is m th sub-band and k is number of a window. The window is used 25ms Hamming window.

B. Mask Feature Extraction and 2-D Mask

The mask feature (μ_m) is extracted using standard deviation, average, and number of samples of first 25ms. 2-D binary mask is made using Eq.1.

$$M_m(k) = \begin{cases} 1 & \text{if } w_m(k) > \mu_m \\ 0 & \text{otherwise} \end{cases} \quad (1)$$

C. Speech Enhancement using 2-D Binary Mask

The decomposed speech signal which has 2-D structure is applied to the 2-D binary mask (M_m). And then, output signal is reconstructed by inverse wavelet transform. Finally, the enhanced speech signal is obtained.

III. EXPERIMENTS AND RESULTS

To test the performance of the proposed algorithm, speech signal sample from the TIMIT database and a noise signal sample from NOISEX-92 are used in variety SNR environments (0 dB, 5 dB, 10 dB, and 15 dB). The graphical results of speech enhancement are shown in Fig. 1 and the average SNRs of enhancement that compare with logMMSE SPU are shown in Table 1 about more over 100 samples. Fig. 1 shows that the proposed algorithm has good performance of noise reduction and speech enhancement. The objective results of the performance can be confirmed in Table 1.

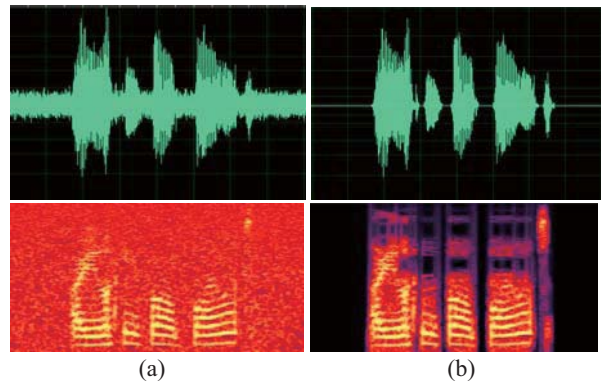


Fig. 1. Results of enhancement in white noise of 5dB SNRs (a) noisy speech signal and (b) enhanced speech signal

Table 1. Results of enhancement in white noise environments

	logMMSE SPU	Proposed
0 dB	8.10 dB	9.00 dB
5 dB	11.38 dB	12.33 dB
10 dB	14.37 dB	15.92 dB
15 dB	17.05 dB	19.80 dB

ACKNOWLEDGEMENT

This work was supported by a grant from the National Research Foundation of Korea (NRF), which was funded by the Korean government (MSIP) (No. 2013R1A2A1A09015677) and the National Research Foundation of Korea(NRF) grant funded by the Korea government(MSIP) (No. 2015R1A2A2A03006113).

REFERENCES

1. S. Gonzalez and M. Brookes, "Mask-based enhancement for very low quality speech", Acoustics, Speech and Signal Processing (ICASSP 2014), pp. 7029-7033, 2014.

Feasibility Study of 808nm Near-Infrared Stimulation on Cultured Cells

Seongwon Min¹, Minsu Yoo³, Youngmin Moon² and Sohee Kim^{1,2}

¹Department of Medical System Engineering, GIST, Gwangju, Korea

²School of Mechatronics, GIST, Gwangju, Korea

³Department of Neurobiology, University of Chicago, Chicago, USA

E-mail: soheekim@gist.ac.kr

Abstract—Optical stimulation has been studied as an alternative that can replace the conventional electrical stimulation method to modify neural activities. In a previous study, we demonstrated that 808nm near-infrared (NIR) laser caused neural modulation in globus pallidus and subthalamus in vivo. In the present study, we stimulated cultured hippocampal cells using the same laser and recorded electrical signals by multi-electrode array (MEA), resulting in no obvious neural modulation effects. We speculate that the temperature increase to cause changes in neural activities was insufficient.

Keywords—Optical stimulation, Hippocampus, Cell culture, 808nm, Electrical signals, Multi-electrode array, MEA

I. INTRODUCTION

Previously, we demonstrated that laser at 808nm wavelength could make neural modulation in in vivo rats [1]. In the present study, we investigate the feasibility of optical stimulation by 808nm laser on cultured cells to take the advantage of in vitro setup in parametric studies using MEA measurement system.

II. METHODS

A. Cell Culture

Embryos (18 days) were removed from pregnant Sprague-Dawley rats and the hippocampi were dissected. The hippocampi were dissociated to neurons and these were cultured on MEA for 2 weeks in a humidified incubator with 5% CO₂ and 37°C (MCO-5AC, Sanyo, Japan).

B. Laser source

All experiments employed a custom-made low-power laser system that has a continuous laser source at 808nm wavelength and controllable power (0 to 40.7mW). We used an optical fiber with 62.5um core diameter, and the power output measured at the fiber end was from 0 to 35mW.

C. Extracellular recording

We used in vitro multi-electrode recording system manufactured by ETRI. The amplification gain was 1000 times, input impedance was 100GΩ and sampling rate was 10000Hz.

III. RESULTS

We recorded first 30s without stimulation to know the initial neural activity and stimulated for 30s. After stimulation, we rested for 30s and repeated 12 times,

resulting in the total recording session of 750s. Commercial analysis software was used for spike detection and signal processing (Spike2, CED, England). In our 12 trials, 6 times of decrease and 6 times of increase of spikes were observed. Thus, we concluded that 808nm NIR laser with 35mW maximum power could not make modulation effect in cultured cells.

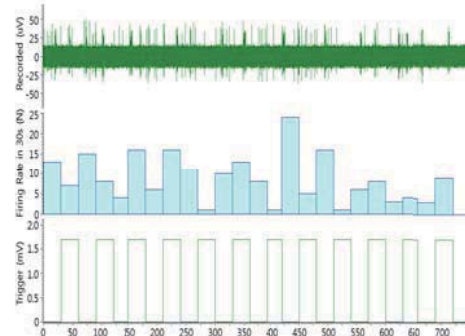


Fig. 1. Spike detected, histogram per 30s and laser on/off control signals

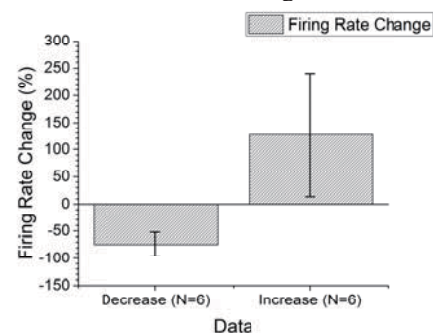


Fig. 2. Firing change of stimulation

IV. CONCLUSION

In this study, we studied the feasibility of 808nm NIR (max 35mW) laser for neural modulations of cultured cells. It did not make modulation effects and we speculate that the used laser source was insufficient to generate sufficient temperature increases for neural modulations.

ACKNOWLEDGEMENT

The authors would like to thank Prof. Myeonghan Yoon for culturing cells. This work was supported by the Institute of Medical System Engineering (IMSE) at GIST, Korea.

REFERENCES

1. M. Yoo, H. Koo, M. Kim, H.-I. Kim, and S. Kim, "Near-infrared stimulation on globus pallidus and

IBEC2015, Road to Better Life through Biomedical Engineering

subthalamus.” *J. Biomed. Opt.*, vol. 18, no. 12, p. 128005, Dec. 2013.

A study on the effect of the vibration stimulus for blood flow on wrist

L. Y. Hwang, H. W. Jin, S. H. Jeon, W. H. Choi, and T. M. Shin

Department of Biomedical Engineering, Yonsei University, Wonju, Korea

E-mail: layoung.hwang@hotmail.com

Abstract—There are less study about the effect of the vibration stimulus on local site while many study about the effect of whole body vibration were carried out. In this study, the research about the effect of the vibration stimulus for blood flow on wrist was proposed. For this purpose, Electrocardiogram (ECG) and Photoplethysmogram(PPG) were measured before and after vibration stimulus for calculating Pulse Transit Time(PTT), and the difference of PTTs was calculated to 5.95ms. Hence, there is no positive effect of the vibration stimulus for blood flow on wrist.

Keywords— Wrist, Vibration, Blood flow, Pulse Transit Time

I. INTRODUCTION

There are less study about the effect of the vibration stimulus on local site while many study about the effect of whole body vibration on human body were carried out[1]. There may be positive effect of the vibration stimulus on local site because whole body vibration also has positive effect for human body.

In this study, therefore, PTTs[2] were calculated before and after vibration stimulus for blood flow on wrist for researching the effect of the vibration stimulus on wrist.

II. METHODS

A. Subjects

Eight subjects in their 20s were participated in the experiment for measuring ECG and PPG before and after vibration stimulus for calculating PTTs.

B. Methods

BIOPAC MP150(BIOPAC Systems Inc, USA) was used for measuring ECG and PPG. First, ECG and PPG were measured during 3 minutes at the same time. Second, subjects' wrist was stimulated by vibration of 30Hz frequency during 3 minutes. Finally, ECG and PPG were measured during 3 minutes again. Fig. 1 shows ECG and PPG measured at the same time.

PTTs were calculated by using ECG and PPG measured before and after vibration stimulus, and the values were compared as average.

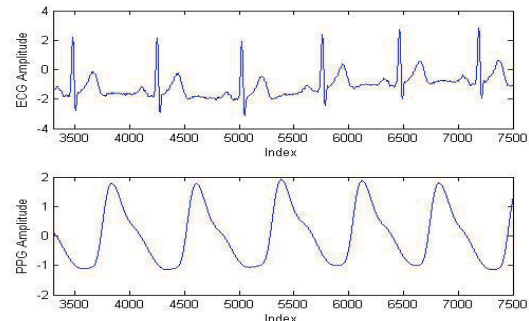


Fig. 1. ECG and PPG measured at the same time

III. RESULTS

Table 1 shows average PTTs calculated before and after vibration stimulus.

Table 2. Average PTTs before and after vibration stimulus

	Before	After	Difference
PTT(ms)	396.01	401.96	5.95

IV. CONCLUSION

In this study, the research about the effect of the vibration stimulus for blood flow on wrist was proposed. For this purpose, PTTs were calculated before and after vibration stimulus, and the difference of PTTs was calculated to 5.95ms. Hence, there is no positive effect of the vibration stimulus on wrist.

But complementation for variation of stimulus frequency according to subjects' physical condition is needed because the vibration system based on the open-loop circuit was used.

REFERENCES

1. M Cardinale, MH Pope, "The effects of whole body vibration on humans: Dangerous or advantageous?", *Acta Physiologica Hungarica*, Vol. 90, No. 3, pp. 195-206, 2003.
2. Heiko Gesche, Detlef Grosskurth, Gert Kuchler, Andreas Patzak, "Continuous blood pressure measurement by using the pulse transit time: comparison to a cuff-based method", *Eur J Appl Physiol*, Vol. 112, No. 1, pp. 309-315, 2011.

EEG-based drowsiness detection using SVM algorithm

S. H. Choi¹, S. H. Hong¹, H. B. Kwon¹, and K. S. Park²

¹Interdisciplinary Program of Bioengineering in Seoul National University, Seoul, Korea

²Department of Biomedical Engineering, College of Medicine, Seoul National University, Seoul, Korea

E-mail: csh412@bmsil.snu.ac.kr

Abstract—Drowsiness while driving is one of the main reasons of car accident. In this study, we confirmed the possibility of SVM algorithm to identify drowsiness using EEG-derived parameters. We extracted 16 parameters from the each EEG channel. The maximum accuracy for detecting drowsiness was 80.3%.

Keywords— Drowsiness, Electroencephalogram, Support vector machine.

I. INTRODUCTION

Drowsiness is one of the main causes of car accident. Thus, it needs to develop the algorithm which monitoring the drivers' cognitive status and detecting drowsiness. Previous studies observed that electroencephalogram fluctuates from alertness to drowsiness. In this paper, we detected drowsiness using SVM which represents a classification tool based on pattern recognition.

II. METHODS

A. Driving simulation

To replace actual driving situation, we used the driving simulator. In the simulation, car driving speed was fixed at 100 km/h and made the car randomly drift out of the lane toward left or right side.

B. Reaction time

Local reaction time (RT) is defined as the time difference between the deviation onset and response onset. Global RT is defined as the average of the local RT to evaluate the long-term transition of the vigilance state. Fig.1 shows the distribution of local RT and global RT. Alertness is classified when both local RT and global RT are less than 1 seconds and drowsiness is classified when both local RT and global RT are more than 1.8 seconds.

C. Participant and EEG acquisition

6 healthy people participated the experiment and average experiment time was 67 minute. We recorded 16-channel EEG signals at a sampling rate of 500 Hz by g.USBAMP device.

D. SVM algorithm

We extracted 16 parameters from each channel. From the total 256 parameters, we selected significantly different parameters between alertness and drowsiness data using T-test ($p < 0.05$). We conducted 10 fold cross validation and calculated the accuracy of SVM classification.

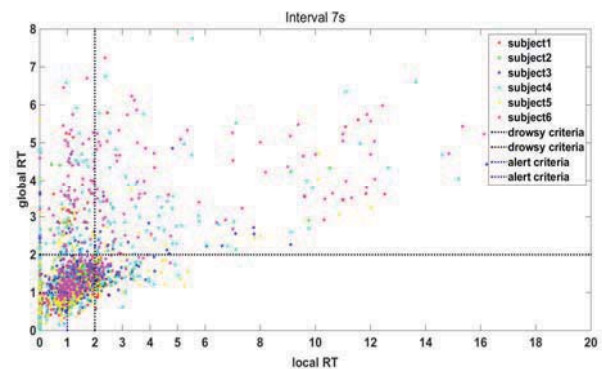


Fig. 1. The distribution of all trials with the local RT and global RT.

Table 1. Accuracy of the classification results

Data extraction length		Accuracy (%)
Before deviation onset (s)	After deviation onset (s)	
1	0	67.9
2	0	73.1
3	0	72.6
1	1	72.8
2	2	76.9
3	3	80.3

III. RESULTS & CONCLUSION

We calculated the accuracy as changing the extraction data length on the basis of deviation onset time. Table 1 shows the results. The maximum accuracy was 80.3 % when using 3s data length which extracted from before deviation onset and after deviation onset, respectively.

In this study, we detected drowsiness using SVM algorithm based on EEG features. This study shows that detection of drowsiness is possible by SVM.

ACKNOWLEDGEMENT

This research was funded by Samsung Electronics Co. Ltd.

The Development of Physical Activity Analysis System Attached to Shoes Based on Ergonomic Design

Y. R. Jang, S. Y. Shin, H. S. Kim, W. H. Choi, and T. M. Shin

Department of Biomedical Engineering, Yonsei University, Wonju, Korea

E-mail: y19286@gmail.com

Abstract— In this study, physical activity analysis system attached to shoes based on Ergonomic Design was developed to minimize energy loss caused by artifacts. The results are that loss of energy was minimized by wearing the system on foot and the reliability of the system has improved.

Keywords— Physical Activity, Ergonomic Design

I. INTRODUCTION

As interest in the daily health management is growing recently, a study on physical activity analysis has been proceeding actively. The existing system of physical activity analysis is relying on acceleration signal data from the device placed on the body. There are basically types of this device: wristband, armband and chest-band. However, measuring in the position of wrist, arm and chest brings energy loss of acceleration signal because of extraneous body motion and device movement. Therefore, purpose of this study is to develop physical activity analysis system to minimize these energy losses. The system attempts to measure acceleration signal on foot tracking body motion effectively by attaching the device to shoes. Also, the system intends to be designed ergonomically to reduce the effect of artifacts caused by the space between the device and the body and by obstacles like a sweat.

II. METHODS

Hardware module of physical activity analysis system is devised. Structure of the system is described in Fig.1. This system analyzes physical activity using 9-axis Inertial Sensor consisting of 3 acceleration channels, 3 angular rate channels and 3 magnetic field channels. The MCU controls the sensor through SPI communication and transmits data using Bluetooth.

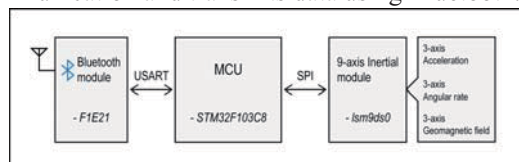


Fig. 1. System hardware block diagram

A case is designed to fix hardware module of the system. Fig.2 shows design of the case. The case has a shape being tight on shoes. Also the case ensures usability and mobility by being compact.

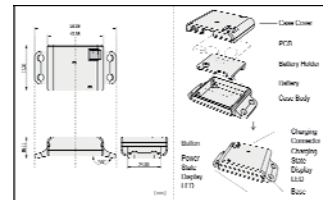


Fig. 2. Projection and assembling drawing of the case

III. RESULTS

The system developed for physical activity analysis measured the signal on foot as shown in Fig.3.

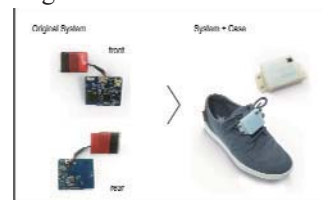


Fig. 3. The system combining with the case

There was an experiment to confirm accuracy of the system. A subject with the system performed physical activity involving climbing stairs and walking straight at typical paces. The 3-D graph in Fig.4 shows the result that the system tracked physical activities of the subject accurately.

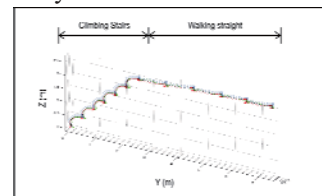


Fig. 4. Experimental data

IV. CONCLUSION

The system using 9-axis Inertial Sensor and measuring the signal in position of foot having minimal energy loss was developed to minimize artifacts caused by the space between the system and foot on physical activity analysis. It was considered on ergonomic side by getting rid of feeling of constriction in the body and obstacles like a sweat. This system is expected to improve the reliability of physical activity analysis by measuring the signal accurately.

REFERENCES

1. D. K. Kang, "A study on form factor of Heart rate measurement wearable fitness tracker in human factor perspective", *Kookmin Univ., Korea*, 2014.

A study on the optimal frequency of vibration stimulus for activation of the biceps brachii muscle

S. H. Jeon, H. S. Kim, Y. R. Jang, S. Moon, W. H. Choi and T. M. Shin

E-mail: jeon311251@gmail.com

Abstract— this study investigated the effect of the optimal frequency of the vibration stimulation to activate the biceps muscle. For this purpose, Electromyogram (EMG) signal of the biceps muscle was measured during the Dumbbell Curls exercise, before and after stimulating it in 30~60Hz frequency vibration. The result shows that the biceps muscle was activated most at 35, 40, 50, 55Hz. Most optimal frequency of vibration to activate the biceps muscle is near 40Hz.

Keywords— optimal frequency, vibration stimulus, biceps brachii muscle, EMG

I. INTRODUCTION

Muscle strength refers to the amount of force a muscle can produce with a single maximal effort. Size of muscle cells and the ability of nerves to activate them are related to muscle strength. As the muscle strength reduce, some disease, such as bone density decrease, depression, might be caused. Once of the methods to raise the muscle activation to prevent such diseases is the vibration stimulation [1]. This study evaluated the level of the muscle activation to find the most optimal frequency of the vibration stimulation by measuring EMG signal of the biceps muscle during the Dumbbell Curls exercise, before and after giving the vibration stimulation.

II. METHODS

A. Subjects

To evaluate the muscle activation level followed by the vibration stimulation, we studied with 6 subjects in twenties.

B. Methods

Firstly, we measured the EMG signal during the exercise by training the group for 6 secs Dumbbell Curls exercise with 2kg dumbbell and let them take a rest for 30 secs. Secondly, we stimulate the biceps muscle with eccentric motor at 30-60 Hz frequency vibration for 30 secs. Lastly, we measured the EMG signal during the exercise at the same level of the first training.

III. RESULTS

We evaluated the level of the muscle activation by calculating the 1 sec window RMS data to EMG signal measuring data. Table 1 shows the optimal frequency data by the each frequency.

Table 1 activated frequency

Subject number	activated frequency(Hz)
1	50
2	55
3	35
4	40
5	40
6	40

IV. CONCLUSION

This study investigated the effect of the optimal frequency of the vibration stimulation to activate the biceps muscle. We measured EMG signal of the biceps muscle during the Dumbbell Curls exercise, before and after stimulating it in 30~60Hz frequency vibration. As a result, the biceps muscle is activated most at near 40Hz.

In the next study, we expect to investigate the optimal vibration stimulation by increase the number of subjects and using close-loop vibration system to apply the same vibration stimulus.

REFERENCES

1. Seung Rok Kang, Gu Young Jeong, et al. "Effect of Muscle Function and Muscular Reaction of Knee Joint in the Twenties on the Whole Body Vibration Exercise," *J. Korean Soc. Precis. Eng.*, Vol. 30, No. 7, pp. 762-768

Biometric authentication based on ECG signal

E. H. Lee¹, D.H. Kim¹, S.H. Song¹, S.J. Hong¹, J. S. Lee¹, and I. Y. Kim^{1†}

¹Department of Biomedical Engineering, Hanyang University, Seoul, Korea

E-mail: eunhye@bme.hanyang.ac.kr

Abstract— This paper presents a new method for human authentication using ECG signal. First, preprocessing technique is used to perform the denoising. Then, QRS detection, modified PT(Pan and Tompkins), and DOM method are utilized to detect features from preprocessed data. Finally, Artificial Neural Network is used to classify the extracted features. The experimental result based on the proposed method shows the good performance in human authentication.

Keywords— biometrics, ECG, authentication, DOM method.

I. INTRODUCTION

Biometrics is the science of recognizing the identity of a person based on the physical, chemical or behavioral attributes of the individual such as face, fingerprints, and iris. Recently, the Electrocardiogram(ECG) has been proposed as a biometric for human identification. The ECG-based human identification has an advantage in security because it must be acquired from a living body. This paper proposes a new method for human authentication using single-lead ECG signal. In this work, we present a feasibility study which carries on quantifying the potential of the ECG for biometric human identification with low error rate.

II. METHODS

A. Acquiring Data

The ECG signals were obtained from a single-lead, with the electrodes placed both wrists. Signals were recorded with a Biopac system. We acquired the ECG signal from 5 subjects. Each of the 5 subjects had 20 seconds of ECG signals and recorded on 10 different days.

B. Preprocessing

The collected ECG records contain noise which has to be removed. Generally, an ECG record embraces low frequency noise components such as power-line interferences. To eliminate the effects of noise, in this paper, we apply a Butterworth band-pass filter of order 4. The cutoff frequencies of the filter are 1Hz-40Hz based on empirical results.

C. Feature Detection

This paper modified the “Difference Operation Method(DOM)” to detect the QRS complex. The DOM includes two stages, The first stage is to find the point R by applying the difference equation operation to the ECG signal. The second stage looks for the points Q and S according to the point R.

D. Classification

Classification was performed using Artificial Neural Network with different weights.

III. RESULTS

A. Experimental Performance

As with any verification system, there are two errors that can take place, either false acceptance (FAR) or false rejection (FRR). The obtained equal error rate (EER) is 15.0%.

IV. CONCLUSION

Biometric authentication system have potential applications in various areas where the identity of a person needs to be verified or higher security levels are desired. The biometric performance of the proposed authentication technique was shown to be superior compared to the traditional techniques.

ACKNOWLEDGEMENT

This research was supported by a grant of the Korea Health Technology R&D Project through the Korea Health Industry Development Institute (KHIDI), funded by the Ministry of Health & Welfare, Republic of Korea (grant number : HI14C0771).

REFERENCES

1. J.A.Unar, Woo Chaw Seng, and Almas Abbasi, “A review of biometric technology along with trends and prospects” *Elsevier. Pattern Recognition.*, vol. 47, pp. 2673-2688, 2014.
2. Yun-Chi Yeh and Wen-June Wang, “QRS complexes detection for ECG signal:The Difference Operation Method”, *Elsevier. Computer methods and programs in biomedicine*, vol. 9, pp. 245-254, 2008.

May Reduction of Blue Light-induced Oxidative Stress be influenced on performance of P300 Speller? – Preliminary Study

Kyungjin Lee¹, Hohyun Cho², Hee-Gu Kim³, and Sung Chan Jun^{2*}

¹Department of Biomedical Engineering, Gachon University, Incheon, South Korea

²School of information and Communications, Gwangju institute of Science and Technology, Gwangju, South Korea

³BM Biotechnology Co., Ltd, Suncheon, South Korea

E-mail: scjun@gist.ac.kr

Abstract—Purpose of this study is to investigate effects of reducing blue light-induced oxidative stress on brain computer interfacing using p300-speller. It was found that amplitudes of P300 signal on experimental group wearing glasses containing ethanol extracts of mixed medicinal plants got increased, however, P300 speller performance was not that significantly influenced.

Keywords—Blue light, Oxidative stress, BCI, EEG, P300

I. INTRODUCTION

P300-speller is a brain computer interface (BCI) application [1]. It decodes P300 (result of cognitive brain process around 300ms after flashing stimulus) from the user and helps to spell characters without any limb movements. However, the frequent flashing (containing blue light) stimulus can cause eye discomfort and fatigue [2]. Glasses containing ethanol extracts of mixed medicinal plants is known to yield reduction of blue light-induced oxidative stress [2]. In this study, we investigated whether or not reduction of blue light-induced oxidative stress by wearing such glasses may improve the performance of P300-speller.

II. METHODS

Subjects (ages: 23 ~ 28, 8 males) participated in this study. Experimental group are four subjects wearing glasses containing ethanol extracts of mixed medicinal plants, and others are control group with glasses without ethanol extracts. All subjects were healthy and signed written consent letter, got questionnaire before experiment. Emotiv Epoc consisting of 16 channels with sampling rate of 128 Hz was used for measuring brain waves. P300-speller was designed in BCI2000.

10 letters were typed for 1 run and all subjects conducted 6 runs. After each run was finished, subjects wrote questionnaire. Collected data was bandpass filtered with 0.1 Hz ~ 40 Hz in MATLAB. To check behavior of P300 brain waves, r-square values were computed between control and experimental groups [1].

III. RESULTS

Fig. 1(A) shows that r-square values of experimental group appeared more strongly than those of control group over most channels around 300ms after flashing stimulus.

IV. CONCLUSION

Experimental group showed bigger P300 response in averaged r-square value. However, it was found that performance of P300 speller was not that significantly different between experimental and control groups as Fig. 1(B). A future study is under way in collecting more data, thus more statistically sound conclusion may be drawn.

ACKNOWLEDGEMENT

This work was supported by Ministry of Culture, Sports and Tourism (MCST) and Korea Creative Content Agency (KOCCA) in the Culture Technology (CT) Research & Development Program 2015.

REFERENCES

1. G. Schalk, D. J. McFarland, T. Hinterberger, N. Birbaumer, and J. R. Wolpaw, "BCI2000: a general-purpose brain-computer interface (BCI) system." *Biomed. Eng., IEEE Trans.*, 51(6), 1034-1043, 2004.
2. J. B. Lee, S. H. Kim, S. C. Lee, H. G. Kim, H. G. Ahn, Z. Li., and K. C. Yoon, "Blue light-induced oxidative stress in human corneal epithelial cells: protective effects of ethanol extracts of various medicinal plant mixtures," *Investigative ophthalmology & visual science*, 55(7), 4119-4127, 2014.

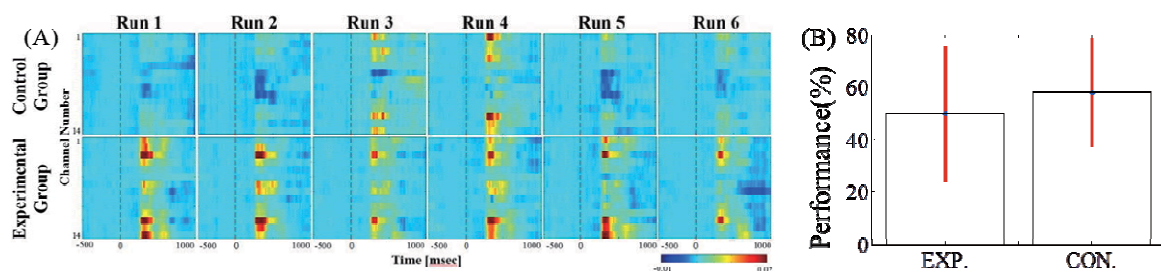


Fig. 1 (A) Averaged r-square value for each group. Dotted line is stimulus onset. R-square means discriminability between target and non-target signal. (B) P300 performance (%) comparison between experimental(EXP.) and control(CON.) group.

A Smart Health Monitoring Wheelchair for Nonintrusive Measurement of Biological Signals

J. Heo¹, S. Y. Sim¹, S. H. Hong¹, S. H. Choi¹, Y. J. Kim¹, S. K. Ko¹, I. J. Hong¹,
S. Kim² and K. S. Park²

¹Interdisciplinary Program of Bioengineering in Seoul National University, Seoul, Korea

²Department of Biomedical Engineering, College of Medicine, Seoul National University, Seoul, Korea

E-mail: hjeong20@bmsil.snu.ac.kr

Abstract—In this study, we developed a smart health monitoring wheelchair for nonintrusive measurement of physiological signal. Electrocardiogram, Photoplethysmogram, Ballistocardiogram were measured unobtrusively when user seat on the wheelchair.

Keywords— Elderly, Wheelchair, Physiological signal, Biological signals, ECG, PPG, BCG.

I. INTRODUCTION

South Korea is projected to become a super-aged society in 2030 in the world's fastest pace [1]. Elderly people with poor mobility spent most of the time in wheelchair. Nowadays nonintrusive health monitoring technologies on the wheelchair became important challenge.

II. METHODS

A. Electrocardiogram (ECG)

ECG sensors were placed at the back of seat, safety belt and controller which can be contacted with user's back, chest and both hands respectively. ECG signals were measured through clothes by capacitive coupling method [2].

B. Photoplethysmogram (PPG)

Three PPG sensors were placed located at the seat where is contacted with user's right thigh. To measure PPG through pants, sensors were composed with high intensity LEDs and high sensitive photo detector (PD) [3].

C. Ballistocardiogram (BCG)

BCG sensor was placed under the seat. EMFIT (Electro-Mechanical Film) were used to measure ballistic forces of the heart.

III. RESULTS

Peak-to-peak intervals extracted from measured signals on the developed wheelchair was highly correlated with extracted from conventional physiological signal monitoring systems (>0.95).

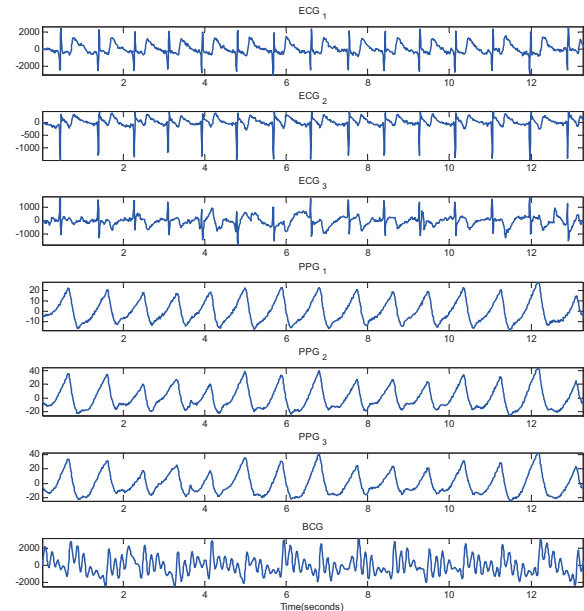


Fig. 1. Physiological signals which were measured on the smart health monitoring wheelchair

ACKNOWLEDGEMENT

This research was funded by Samsung Electronics Co. Ltd.

REFERENCES

1. C. M. Rim, "Korea's Age Boom: How South Korea is Addressing the Reality of Low Fertility and a Rapidly Aging Society", *AARP The Journal*, 2013.
2. Y. G. Lim, K. H. Hong, K. K. Kim, J. H. Shin, S. M. Lee, G. S. Chung, H. J. Baek, D. U. Jeong, K. S. Park, "Monitoring Physiological Signals using Nonintrusive Sensors Installed in Daily Life Equipment" *Biomedical Engineering Letters*, Vol.1, No.1, pp.11-20, 2011
3. H. J. Baek, G. S. Chung, K. K. Kim, J. S. Kim, K. S. Park, "Photoplethysmogram Measurement Without Direct Skin-to-Sensor Contact Using an Adaptive Light Source Intensity Control", *IEEE Transactions on Information Technology in Biomedicine*, Vol.13, No.6, pp.1085-1188, 2009

Sensory Neuro-Modulation by Low-Intensity Pulsed Ultrasound Stimulation

H. Jung^{1,2}, S. Han^{1,3}, M. Kim^{1,2}, H. Kim^{1,2}, J. Park^{1,3}, H. Shin^{1,2}, I. Youn^{1,2,#}

¹ Biomedical Research Institute, Korea Institute of Science and Technology, Seoul, Korea

² Department of Biomedical Engineering, University of Science and Technology, Daejeon, Korea

³ Department of Biomedical Science, Korea University College of Medicine, Seoul, Korea

E-mail: iyoun@kist.re.kr

Abstract—This research is a pilot study for investigating utility of low-intensity ultrasound as a neuro-modulation technic. We observe calcium influx caused by low-intensity pulsed ultrasound (LIPU) in single layer cultured dorsal root ganglion (DRG). Through this result, this study can be a basic research for investigating clinical feasibility of low-intensity focused ultrasound (LIFU) as non-invasive neuro-modulation technic.

Keywords— Low-Intensity Pulsed Ultrasound Stimulation, Sensory Neuron, Calcium Imaging, Dorsal Root Ganglion.

I. INTRODUCTION

Currently, LIFU has been remarked as non-invasive technic that stimulate internal tissue of the body [1]. The goal of present study was to investigate possibility of sensory neuron activation by LIFU stimulation. By calcium imaging technic, we observed low-intensity pulsed ultrasound (LIPU) stimulation enhance calcium influx in single layer cultured DRGs. According to our result, low intensity ultrasound stimulation has possibility which could be used to non-invasive sensory neuro-modulation.

II. METHODS

A. Single layer DRG culture

2day old ICR mice DRG were plated by dissociation culture and cell intensity was 500cells/mm². Neurobasal medium, supplemented with B-27 supplement, penicillin/streptomycin & L-glutamine was used for culture medium. And half of medium is changed by 2days.

B. Calcium imaging

After 6day culture, DRG culture medium is changed to HBSS based artificial cerebrospinal fluid (aCSF) which supplemented with 10mM HEPES, 2mM CaCl₂, 0.1mM MgCl₂, 5μM glycine [2]. OGB-1 is used as calcium indicator, calcium imaging is operated with Nikon TU-U-inverted microscope and imageJ – microimage program.

C. Measurement of ultrasound intensity

Ultrasound intensity measurement is operated by Hydrophone (Onda) with degassed water.

D. LIPU stimulation

With aCSF circulation system, calcium imaging is operated by 6min. 300ms LIPU stimulation is operated by non-focused ultrasound transducer, and after 1min pre-stimulation, calcium imaging is continued by 5min after LIPU stimulation.

Table 1. LIPU stimulation parameter

Stimulation Parameter	
Resonance Frequency	350kHz
PRF	500Hz
Tone Burst Duration	1ms
Ispta	9.1mW/cm ²
Isppa	18.2mW/cm ²

III. RESULTS

A. Calcium influx in DRGs by LIPU

Calcium influx in DRGs caused by LIPU stimulation is observed through OGB-1 and fluorescence microscope. We found that LIPU stimulation activated Ca²⁺ influx in DRG neurons ($\Delta F/F_0 = 1.61$, maximum 61%; Fig. 1).

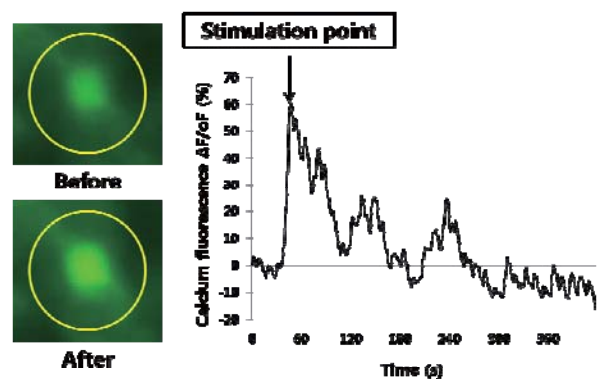


Fig. 1. Ca²⁺ Influx in DRG sensory neuron induced by LIPU.

B. Viability measure after LIPU stimulation

Measured LIPU stimulation intensity ($I_{spta} = 9.1\text{mW/cm}^2$ $I_{sppa} = 18.2\text{mW/cm}^2$) is harmless in standard of FDA [3]. In addition, Live&Dead assay show LIPU stimulation in stronger intensity than DRG

neuron activation ($I_{spta} = 10.15\text{mW/cm}^2$ $I_{sppa} = 20.3\text{mW/cm}^2$, 5times per 10s stimulation) is harmless. Green light shows live cells, and red light shows dead cells. Through image analysis, dead cells caused by LIPU stimulation is not found. (Fig. 2).

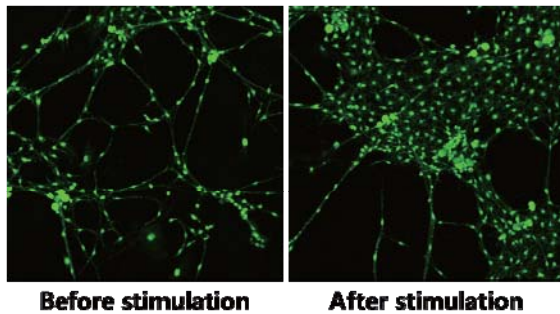


Fig. 2. LIPU stimulation is harmless to DRG sensory cells.

IV. CONCLUSION

In this study, LIPU stimulation has significant enhancement of calcium influx in DRG. From now on, we investigate differences in activation degree with different parameters, and mechanism of LIPU stimulation in various neurons. This study can be a basic research for investigating clinical feasibility of LIFU as non-invasive neuro-modulation technic.

ACKNOWLEDGEMENT

This Research was supported by a grant of the Korea Health Technology R&D Project through the Korea Health Industry Development Institute (KHIDI), funded by the Ministry of Health & Welfare, Republic of Korea (HI14C3477) and the KIST Institutional Program (Project No. 2E25505).

REFERENCES

1. Y. Tufail, A. Matyushov, N. Baldwin, M. L. Tauchmann, J. Georges, A. Yoshihiro, S. I. H. Tillery, W. J. Tyler, "Transcranial pulsed ultrasound stimulates intact brain circuits," *Neuron.*, vol. 66, pp. 681-694, 2010.
2. H. Ohshiro, S. Ogawa, K. Shinjo, "Visualizing sensory transmission between dorsal root ganglion and dorsal horn neurons in co-culture with calcium imaging," *J. Neuroscience Methods*, vol. 165, pp. 49-54, 2007.
3. R. Phillips, G. Harris, "Information for manufacturers seeking marketing clearance of diagnostic ultrasound systems and transducers," *U.S. Food and Drug Administration*, 2008.

Long-time Intra-cortical Signal Analysis for Stroke Rehabilitation Analysis

Kyungsoo Kim¹, Seung Jun Yoo², Jae-Eun Jang¹, Minkyu Je¹, Cheil Moon², Ji-Woong Choi¹

¹ Department of Information and Communication Engineering, DGIST, Republic of Korea

² Department of Brain and Cognitive Science, DGIST, Republic of Korea

E-mail: ssi09@dgist.ac.kr, yoosj@dgist.ac.kr, jang1@dgist.ac.kr, minkyu.je@dgist.ac.kr, cmoon@dgist.ac.kr, jwchoi@dgist.ac.kr

Abstract— We introduce two methods that can analyze brain plasticity for stroke rehabilitation analysis. Intra-cortical recording is utilized by a 16 channel electrode within gray matter at primary motor cortex (M1) which is damaged indirectly by middle cerebral artery (MCA) stroke. Spike and local field potential (LFP) are analyzed and the result shows brain plasticity can be observed.

Keywords— Intra-cortical recording, Extracellular, local field potential, spike, sorting.

I. INTRODUCTION

Stroke is a dangerous brain disease caused by abnormal blood flow. Since 1990s, the study of electrical stimulation (ES) for stroke rehabilitation was studied [1]. However, there has been no proper method that can monitor the brain potential change and spike firing containing brain plasticity information for long-time i.e., more than 2 weeks, to understand ES effect for brain rehabilitation. This study introduces long-time local field potential (LFP) analysis and global spike sorting (GSS) which can track spike firing along each neuron.

II. METHODS

A. Stroke and rehabilitation condition

In order to obtain different brain signals influenced by ES, four Sprague Dawley rats are separated into two groups, ES treated group (Stim) and no stimulation (N. Stim) group. The rats experienced by middle cerebral artery (MCA), and only Stim group is treated by ES on primary motor cortex (M1). The signal is measured from M1. The recording protocol follows resting for 30sec, running for 40sec, resting for 20sec.

B. Long-time local field potential analysis

High gamma band power is calculated at every second in a daily recording data. In order to represent the result in depth and time domain, color representation is applied marking high power in red and low power in yellow.

C. Global spike sorting

GSS searches Principal Components (PCs) in long-time daily signal to find the global PCs which do not

change daily. Therefore, it provides long-time spike firing from the same spike waveform.

III. RESULTS

Fig. 1 shows that LFP band power in both group decrease after stroke. LFP band power in Stim group increases more after D+9 than the power before stroke i.e., D-1, but LFP power in the control group stays lower for more days than Stim group.

Fig. 2 is obtained by GSS and shows that after stroke, spike firing pattern in Stim group is changed as showing more correlation to the task, but control group is not.

IV. CONCLUSION

In this study, we applied long-time intra-cortical electrical signal analysis. The analysis method can show how the brain electrical signal changes for long-time presenting that Stim group recovers the electrical potential earlier than control group.

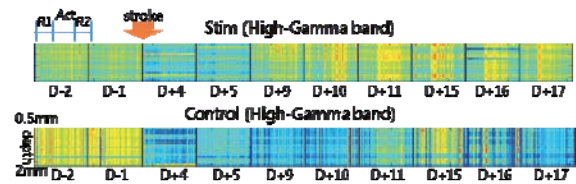


Fig. 1. LFP analysis for Stim group (first row) and control group (second group).

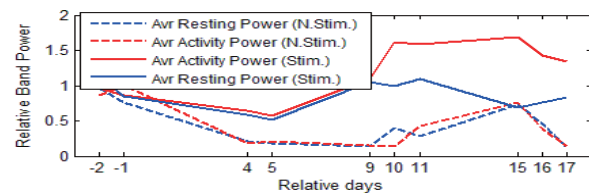


Fig. 2. Spike firing analysis for Stim group (blue solid line) and control group (red dot line).

ACKNOWLEDGEMENT

This work was supported by the DGIST R&D Program of the Ministry of Science, ICT and Future Planning (15-BD-0404).

REFERENCES

1. Q. Zhou et al., "Cortical electrical stimulation alone enhances functional recovery and dendritic structures after focal cerebral ischemia in rats," *Brain Research*, vol.1311, pp. 148-157, 2010.

Changes in movement-related cortical activities during self-paced gait initiation and externally-cued gait initiation

K. S. Cha¹, J. W. Choi¹, J. H. Park², H. S. Jeon², and K. H. Kim¹

¹Department of Biomedical Engineering, Yonsei University, Wonju, Korea

²Department of Physical Therapy, Yonsei University, Wonju, Korea

E-mail: khkim0604@yonsei.ac.kr

Abstract— Self-paced gait initiation (GI) and externally-cued gait initiation are performed by different control strategies in the nervous system. Two different GI were modulated by different level in neural systems by observing changes in neural activities during two different GI types.

Keywords— Electroencephalogram (EEG), Gait initiation, Motor control, Motor-related potential

I. INTRODUCTION

Self-paced and externally-cued movement initiations are controlled by strategies in the central nervous system, but the mechanisms remain unknown [1]. In order to compare control mechanisms between the two different movement initiations, we analyzed the movement-related electroencephalograms (EEGs) during self-paced and externally-cued gait initiations (GIs).

II. METHODS

A. Subject

17 volunteers with no record of neuromuscular disorders were enrolled in this study.

B. Experimental paradigm

Subjects were requested to perform an immediate forward gait in response to a visual cue sign, or a self-paced forward gait after the visual cue.

C. EEG recording

During the task performance, 32-channel EEGs and force platform signals were recorded.

D. Movement-related potential (MRP)

The EEG waveforms were segmented in $-5000\sim 6000$ ms interval based on the gait onset determined by the force platform signal for each trial. In addition to the averaged movement-related (MP) waveform analysis, event-related spectral perturbation (ERSP) analysis was performed to observe Mu rhythm.

III. RESULTS

A. Bereitschaftspotential (BP)

At $-100\sim 0$ ms period, BP was observed at central areas for both initiation conditions. The BP amplitude

was significantly higher for the self-paced GI than for the externally-cued GI (Fig. 1).

B. Mu rhythm

The greatest increases of Mu rhythm was observed from that -200 ms for both initiation conditions. However, at $-200\sim 0$ ms period, Mu rhythm was significantly stronger for the self-paced GI than for the externally-cued GI.

IV. CONCLUSION

Considering that pre-movement MRP and Mu rhythm in motor area are devoted to the preparation and planning of movement, the increased BP amplitude, Mu rhythm in self-paced GI may reflect the higher cognitive load required for determining the type and timing of movement [2].

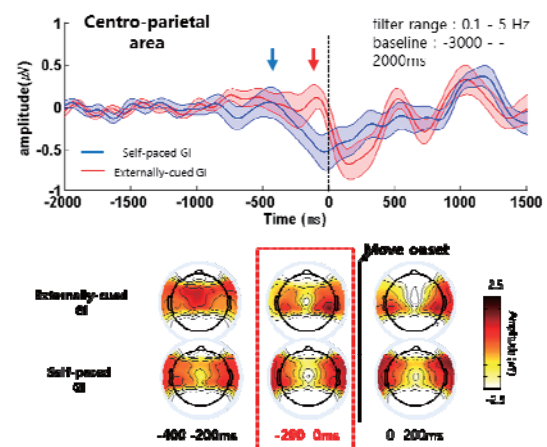


Fig. 1. MRP waveform at centro-parietal area and topographical distribution during two different GI types

ACKNOWLEDGEMENT

This study was supported by the National Research Foundation of Korea (NRF) grant funded by the Korea government (MSIP) (No. 2014R1A2A2A04003858).

REFERENCES

1. S. Jankelowitz and J. Colebatch, "Movement-related potentials associated with self-paced, cued and imagined arm movements" *Exp Brain Res*, vol. 147.1, pp. 98-107, 2012.

IBEC2015, Road to Better Life through Biomedical Engineering

2. M. P. Deiber, E. Sallard, C. Ludwig, C. Ghezzi, J. Barral, and V. Ibanez, "EEG alpha activity reflects motor preparation rather than the mode of action selection" *Front Integr Neurosci*, vol. 6, 2012.

Dynamic stopping for P300 classification with SWLDA and BLDA

M. H. Chang¹ and K. S. Park²

¹Interdisciplinary program for Bioengineering, Seoul National University, Seoul, Republic of Korea

²Department of Biomedical Engineering, Seoul National University, Seoul, Republic of Korea

E-mail: pks@bmsil.snu.ac.kr

Abstract—In this paper, a dynamic stopping method for P300-based BCIs was compared between step-wise linear discriminant analysis (SWLDA) and Bayesian linear discriminant analysis (BLDA). In offline analysis, dynamic classification with SWLDA showed the highest ITR with short flash iteration.

Keywords— BCI, P300, SWLDA, BLDA, dynamic stopping

I. INTRODUCTION

Many machine learning techniques have been tested to increase accuracy and speed of a P300-based BCI system, such as step-wise linear discriminant analysis (SWLDA), Bayesian linear discriminant analysis (BLDA), and dynamic stopping methods [1, 2]. The outputs of SWLDA and BLDA have been examined respectively as a parameter for dynamic stopping. However, their performance in dynamic classification has never been compared.

In this paper, we compare static and dynamic P300 classifications based on SWLDA and BLDA.

II. METHODS

A. Step-wise linear discriminant analysis

SWLDA selected 30 statistically significant features from a 30Hz down-sampled EEG segment, and computed feature weights [1]. In a test session, a character with the highest score, which was the inner product of the feature weight vector and the feature vector, was regarded as a target.

B. Bayesian linear discriminant analysis

BLDA used regularization to avoid overfitting with a regularization term in a parameter distribution [2]. BLDA did not select channels automatically, we compared BCI performance with different channel sets.

C. Dynamic stopping

Given a score of a SWLDA or BLDA, the posterior probability was calculated based on Bayesian inference. Likelihood probability density function (pdf) of classifier scores was estimated for Flash/Non-flash group, where a distribution of the scores was assumed to be normal. Prior probabilities for the groups were the same as 0.5. If the posterior probability of a character exceeds threshold, corresponding character

was regarded as the one that a subject focused on. The threshold varied from 0.80 to 0.99 with an interval of 0.01.

D. Offline experiment

Ten subjects participated in offline experiment. A subject focused on a character in 6 × 6 speller in a trial, and repeated for 36 times. The stimulus-onset-asynchrony (SOA) and flash duration of stimulation was 200 ms and 80 ms, respectively.

III. RESULTS

Table 1 shows average of maximum ITRs over subjects. Dynamic classification showed higher ITR than static classification for almost subjects except Subj. 10 for BLDA ($p < .001$ for SWLDA; $p = .006$ for BLDA). In static classification, where ITR was calculated for each sequence number, the two classifier showed equivalent performance ($p = .168$). However, in dynamic classification, SWLDA outperformed BLDA by about 2 bpm ($p = .023$).

Table 1. Average of max ITRs (bpm)

Static classification		Dynamic classification	
SWLDA	BLDA	SWLDA	BLDA
17.67	16.50	21.78	19.17

IV. CONCLUSION

Dynamic classification improved ITR in agreement with previous studies [1, 2]. However, SWLDA showed higher ITR than that of BLDA in contrast with a previous study in which BLDA outperformed SWLDA in static classification. The reason of superiority of SWLDA in dynamic classification seems to be shorter flash iteration: 33.9 flashes (~2.8 sequences) for SWLDA and 44.8 flashes (~3.7 sequences) for BLDA ($p = .050$).

REFERENCES

1. C. S. Throckmorton et al., "Bayesian approach to dynamically controlling data collection in P300 spellers," *IEEE Trans. Neural Syst. Rehabil. Eng.*, vol. 21, pp. 508-517, 2013.
2. H. Verschore et al., "Dynamic stopping improves the speed and accuracy of a P300 speller," *Artificial Neural Networks and Machine Learning-ICANN 2012*, Springer Berlin Heidelberg, 2012

Classification method for detecting the Deep Sleep in human sleep based on machine learning

K. M. Joo¹, H. N. Yoon¹, D. W. Jung¹, S. H. Choi¹, H. B. Kwon¹, D. S. Lee¹ and K. S. Park²

¹Interdisciplinary Program for Bioengineering, Graduate School, Seoul National University

²Department of Biomedical Engineering, Seoul National University College of Medicine, Seoul, Korea

E-mail: jkm6510@bmsil.snu.ac.kr

Abstract—Deep sleep, called SWS (Slow Wave Sleep) is a part of sleep stages included in NREM Sleep (Non rapid eye movement). Many research find that Deep sleep is related with the physiological function like recovery of tired brain, memory consolidation. Also Deep sleep could be used to treat patients with OSA (Obstructive Sleep Apnea). Therefore detecting deep sleep could be very useful in home monitoring in healthcare area. We detect deep sleep using HRV (Heart Rate Variability) from electrocardiography signal. For classification, our classifier is one of machine learning algorithms, SVM (Support Vector Machine). To evaluate the performance of SVM 10-fold cross validation is used. As a result, it made overall accuracy of 0.88 and Cohen’s kappa of 0.77.

Keywords— SVM, Deep sleep, HRV, Classification .

I. METHODS

A. subject

9 people; healthy and normal subjects

B. HRV parameters

	HRV parameters
Time domain	SDNN
	M_HR (mean of heart rate)
Frequency domain	nHF (normalized high frequency)
	LF, HF ratio
Non linear feature	SD1
	Alpha1
	Alpha2
	SD1, SD2 ratio

Table 1. HRV parameters

C. Support Vector Machine

Support Vector Machine(SVM) is a binary classifier(two class) mapping the training set to higher dimension and separating the transformed set using hyperplane. In this study, the Radial Basic Function(RBF) as kernel was used. The SVM parameters that obtained the highest accuracy were selected.

II. RESULTS

A. Deep Sleep Estimated

Figure 1 show that upper one is sleep stage of reference data lower one is sleep stage of estimated data by SVM. This is best case which can classify the consecutive deep sleep from other sleep stages. Because most deep sleep isn’t separated, it is important to detect consecutive deep sleep. Because we used 10-fold cross validation, training data are not consecutive in each training trial.

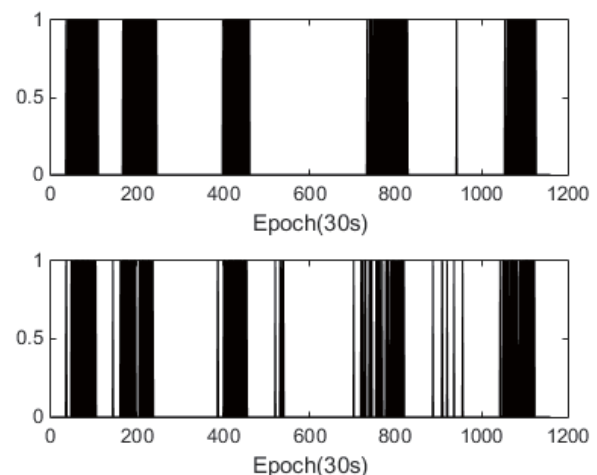


Fig. 1. Estimating deep sleep; Best case (upper one : Reference, lower one : Estimated)

	Values
Sensitivity(%)	0.6642 (0.045)
Specificity(%)	0.9118 (0.006)
Accuracy(%)	0.8857 (0.009)
Cohen’s Kappa	0.7752 (0.014)

Table 2. Statistical results

ACKNOWLEDGEMENT

This research was supported by Coway Co., Ltd..

REFERENCES

1. B. Yilmaz, M. Asyali, E. Arıkan, S. Yektin and F. Ozgen, “Sleep Stage and Obstructive Apneaic Epoch Classification Using Single-Lead ECG,”
2. A. Statnikov, C. Aliferis, D. Hardin, and I. Guyon, “A Gentle Introduction to Support Vector Macnine in Biomedicine”, 1 st. 2011, pp. 91-96.

Relative Power Distribution for Tremor Detection in Parkinson's Disease

Hyoseon Jeon¹, Hong Ji Lee¹, Hyeyoung Park², Woongwoo Lee²
Sang Kyong Kim¹, Hanbyul Kim¹, Beom Seok Jeon², Kwang Suk Park³

¹ Interdisciplinary Program of Bio Engineering, Seoul National University, Korea

² Dept. of Neurology, Seoul National University Hospital, Korea

³ Dept. of Biomedical Engineering, College of Medicine, Seoul National University, Korea

E-mail: nulpurunhs@bmsil.snu.ac.kr

Abstract— This study is about a feature for a tremor detection algorithm for a wearable device. Wearable device could be pretty suitable to give tremor information to neurologists. For this, tremor signal detection should be conducted at first. In this study, rest tremor signals from Parkinson's disease patients were collected using a wearable device including 3-axis accelerometer and then, relative power values were calculated in 3 frequency to investigate the difference between tremor group and non-tremor group. Tremor data were grouped into tremor group and non-tremor group to decide a threshold using Clinical Tremor Rating Scale (CTRS). Tremor group had averaged relative value with 73.48% in the tremor frequency and, mean of relative power was 43.8% in non-tremor group. This difference was significant by t-test.

Keywords— Tremor, Parkinson's disease, Relative power, Tremor detection, Accelerometer

I. INTRODUCTION

Tremor is one of the general and cardinal features in Parkinson's disease (PD) with bradykinesia and rigidity. This symptom is a rhythmic, oscillatory and voluntary movement and appear on extremities of body, especially hands in many cases. It is generally known that rest tremor is more common than postural tremor in PD. With tremor, plenty of patients have had difficulties in daily life. For assessments of movement disorders including tremor, neurologists have performed several tests like Unified Parkinson's Disease Rating Scale (UPDRS) or Clinical Tremor Rating Scale (CTRS). These scoring methods are conducted by watching patient's symptoms and scoring them. This way for an evaluation of tremor is not objective and quantitative. Even, since the tremor state can be vary depending on the patient's situation, clinicians may have troubles in diagnosing tremor objectively. Wearable device can be very helpful to record and store tremor signals in daily lives. Therefore, neurologists are able to know frequency, period and severity of tremor with wearable device. For this, tremor signal should be identified at first from other signals from movements in daily life. To

date, there have been several studies about a tremor detection. However, most studies attached many sensors or devices on the different parts of the patient's body to measure signals from various body part. [1] This may have advantages plenty of information from whole body but cannot give a feasibility to the PD patients in using wearable devices.

In this study, we focused on a feature for a rest tremor detection using just 2 wearable devices to raise a practicality. We compared relative power distribution between tremor group and non-tremor group in a specific frequency band associated with a tremor.

II. METHODS

A. Patients

Eighty-four rest tremor recording cases were used for developing a tremor detection algorithm. These tremor recordings were acquired from Parkinson's disease patients recruited at Parkinson Center in Seoul National University hospital. The experiments were approved by the Institutional Review Board of Seoul National University Hospital. All patients with tremor were between 41 and 81 years old (mean \pm standard deviation [SD], 65.98 ± 9.87 years).

Their rest tremors were diagnosed by 2 neurologists using Clinical Tremor Rating Scale (CTRS) and then, we averaged the 2 scores to distinguish tremor group and non-tremor group.

B. Experiments

Three-axis accelerometer (LIS3LV02DQ, STMicroelectronics N.V. Switzerland) was used to acquire tremor data. This accelerometer sensor has an ability to measure up to $\pm 6g$. All participants were asked to attach 2 accelerometers on their tip of middle fingers and sit down on an armchair placing their wrists down on the arm of chair. The accelerometer signals were transferred into a laptop and then stored digitally. The accelerometer signals were sampled at a frequency of 125Hz and band-pass-filtered with a range from 1 Hz to 16Hz after 3-seconds-windowing. In those case that some patients clearly had their dominant tremor on the other finger, we changed the location of the sensor to the

corresponded finger. During the whole experiment, we asked the patients to add up figures to provoke their tremor and recorded them for 1 minutes. For the diagnosis of the tremor, video camera (Panasonic HDC-TM700, 1920 × 1080 p HD at 60 frames per second) was also recorded at the same time. Two neurologists scored patient's tremors seeing this video and, two scores were averaged for a reference.

C. Data Analysis

Relative power values from the accelerometer signals were calculated in tremor frequency band as a feature to determine a threshold for detecting a tremor. At first, we filtered raw accelerometer signals from 3 axis with a range from 1 Hz to 16Hz. These signals were squared and then summed to remove at the first 5 seconds and the last 5 seconds of the accelerometer RMS signal. Afterwards, we computed relative power values in a tremor frequency band ranged from 3.5 Hz to 7.5 Hz [2].

To calculate a relative power, the absolute power in the tremor frequency band was divided by the total power in the range from 0 to 15 Hz as below. Each relative power value was averaged in each patient. Tremor with CTRS 0 was considered as the tremor group. Tremor more than CTRS 1 was grouped as the non-tremor group. We did not include tremor data with CTRS 0.5 to avoid ambiguity. In two groups, we averaged the relative power and conducted *t-test* to check if this feature would be appropriate to identify rest tremor in PD.

III. RESULTS

In this study, a rest tremor detection algorithm was developed using relative power values. For this, 68 tremor recordings were used. We calculated relative power values to examine their distribution in the tremor frequency bands (Fig.1). As a result, the averaged relative values were 73.48% and 43.8% in the tremor and non-tremor group respectively. These means were tested by *t-test* and, they were significant. ($p < 0.01$) Figure 1 shows averaged relative power values at respective CTRS in the tremor band. All tremor group corresponding to CTRS 1 ~ 4 had a relative power more than 50% and, non-tremor group had relative power values less than about 45%.

IV. CONCLUSIONS

We studied about a possibility for a tremor detection using a relative power in the tremor frequency band. Tremor detection is an important procedure in using a wearable device on a wrist for an analysis of the tremor and other movement because to analyze tremor data,

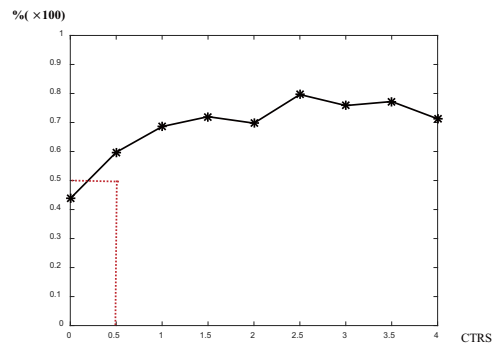


Fig. 1 Relative power values at each CTRS. CTRS means Clinical Tremor Rating Scale ranged from 0 to 4.

tremor detection should be the first step. In this study, a relative power proportion in the tremor frequency band was used to identify tremor data. As two groups had distinct relative power values significantly, this feature may have a potential for a tremor detection. In the future, we will verify this feature with more tremor data and then develop a tremor detection algorithm using this feature.

ACKNOWLEDGEMENT

This study was supported by grant no. 3420140050 from the SNUH Research Fund

REFERENCES

1. S. T. Moore, H. G. MacDougall, and W. G. Ondo, "Ambulatory monitoring of motor fluctuations and freezing of gait: Objective assessment of the efficacy of pharmacological treatments in Parkinson's disease," *Movement Disorders*, vol. 23, pp. S216-S216, 2008.
2. T. Heida, E. C. Wentink, and E. Marani, "Power spectral density analysis of physiological, rest and action tremor in Parkinson's disease patients treated with deep brain stimulation," *Journal of Neuroengineering and Rehabilitation*, vol. 10, Jul 8 2013.

The estimation of blood pressure groups using self-pressure of finger on PPG

H. J. Lee¹, J. S. Lee^{1,2}, and K. S. Park²

¹Interdisciplinary Program for Bioengineering, Seoul National University, Seoul, South Korea

²Department of Biomedical Engineering, Seoul National University, Seoul, South Korea

E-mail: hongjidan@bmsil.snu.ac.kr

Abstract—In this study, the estimation of the blood pressure groups was implemented using self-pressure of finger on a Photoplethysmography (PPG) sensor without cuff. Two slopes, from the point right after self-pressure for 5 s to 2 PPG peaks, were used for grouping of subjects' blood pressure. The slopes were larger as blood pressure was high, which indicates fast recovery and large blood amount after pressure relieved.

Keywords— Blood pressure, Cuffless, PPG, Self-pressure.

I. INTRODUCTION

Blood pressure (BP) is one of basic vital signs for monitoring hypertension, diabetes, and obesity. A sphygmomanometer with inflatable cuff is the most common method for BP measurement because it is simple and non-invasive. To reduce inconvenience caused by arm cuff, some studies developed systems with wrist cuff for BP monitoring [1-2]. However, there are several limitations because of large volume by pump system for operating inflatable cuff and difficulty in applying cuff by oneself. In this study, a PPG (Photoplethysmography) sensor was used and amplitudes of PPG signals changed by self-pressure of fingertip were used for grouping of BP.

II. METHODS

A. Experimental Protocols

A total of 8 normal male subjects participated in the examination. PPG signals (BIOPAC Systems, Inc., USA) were measured under right index finger with 500 Hz sampling rate and reference BP (NIBP) was measured simultaneously on left arm using CNAP Monitor 500 (BIOPAC Systems, Inc., USA). Subject performed self-pressure test, which included rest for 1 minute and then self-pressure of fingertip on PPG sensor for 5 seconds. This step was repeated 6 times in all.

B. Signal Analysis

The peaks of PPG signals were detected by the lab-developed peak detection algorithm. Data segments from the point right after self-pressure for 5 s (N_{peak}) to 10 PPG peaks were used (Fig. 1). Data segments on 4 or 6 trials per subject were averaged. All data were

normalized between 0 and 1. Two features, the slopes between N_{peak} and first peak (first slope) and between first and second peak (second slope), were extracted for grouping of blood pressure: (1) low BP (< 120 mmHg), (2) normal BP (120 – 130 mmHg), (3) high BP (> 130 mmHg).

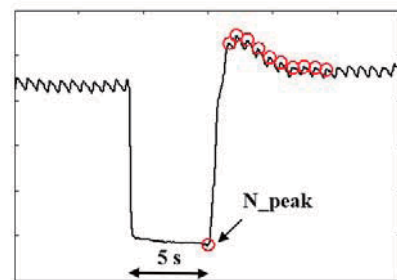


Fig. 1. PPG signals during rest, self-pressure, rest

III. RESULTS

Low BP group ($n = 2$) had small first slope than others when ignoring the time information, which indicates slow recovery of blood flow and small blood volume. High BP group ($n = 2$) had large second slope than normal BP group ($n = 4$). This indicates that subjects with high BP had consecutively fast recovery and large blood amount after pressure relieved.

IV. DISCUSSION and CONCLUSION

When relaxing the finger after self-pressure, there could be the gap between the finger and sensor momentarily which affects the DC component of PPG signals. Moreover, there is the variability in relaxing speed, gradually or instantly, in every person. Therefore, more research is needed. However, in this study, we showed the possibility of BP estimation using a PPG sensor without cuff by putting pressure by myself whenever subject wants.

REFERENCES

1. S. H. Song, H. S. Oh, J. S. Lee, Y. J. Chee, S. H. Kim, and I. Y. Kim, "Estimation of blood pressure using wrist PPG signal," *KSOMBE*, vol. 39, 2009.
2. D. B. McCombie, P. A. Shaltis, A. T. Reisner, and H. H. Asada, "Adaptive hydrostatic blood pressure calibration: Development of a wearable, autonomous pulse wave velocity blood pressure monitor," *Proc. 29th IEEE EMBS*, 2007.

EEG Based Human Identification Using Eye Blinking Signals

Jeehoon Kim¹, Changho Choi², Sunho Lee², Chungmin Han³, and Kwangsuk Park⁴

¹Interdisciplinary Program of Bioengineering, Seoul National University, Seoul, Korea

²Gyeonggi Science High School, Suwon, Korea

³Department of Biomedical Engineering, University of Texas at Austin, Texas, U.S.A.

⁴Department of Biomedical Engineering, College of Medicine, Seoul National University, Seoul, Korea

E-mail: jhkim119@bmsil.snu.ac.kr

Abstract—This In this study, we propose a method for human biometric identification using eye blink signals. We examined the capability of eye blinking signals to discriminate between individuals. 23 subjects of eyes-open data were used in resting state conditions. Various kinds of classifications is carried out to evaluate the distinctiveness feature vectors. We confirmed that time domain features of eye blinking data contain unique characteristics that represent individuals.

Keywords— biometric, identification, pattern recognition, eye blink signal, EEG.

I. INTRODUCTION

Due to the great advances in biomedical digital signal processing and biomedical instrumentation, new biometric traits have showed noticeable improvements in human identification systems. Commercial biometric authentication systems currently include finger-print, voice, face, and gait recognition. However, these traits have problems of low security [1].

Electrooculography (EOG) is the electrical recording of the potential generated due to eyeball or eyelid movements. The eye blinking signal flows through complex wiring of neurons making it different from one person to another. In this study, we tried to identify 23 individuals using various kinds of classifiers based on time domain features.

II. METHODS

A. Eye blinking database

Scalp EEG signals were gathered from the freely online database Physionet [2]. The database consists of N = 109 healthy subjects recorded in 1-minute eye open state. We extracted eye blinking signals from the EEG dataset. The EEG data were recorded with a 64-channel system (BCI2000 system) with an original sampling rate of 160Hz.

B. Data Processing

All EEG data was bandpass filtered 0.5-15Hz. We extracted time-domain features for 0.5 second after/before from the peak of each eye blinking.

C. Classification (Recognition) Algorithm

We used Euclidian distance based k-nearest neighbor (KNN) classifier (The number of neighbors was 9.) and linear discriminant analysis (LDA) and support vector machine (SVM). We used 10 trial data as training dataset and evaluated uniqueness of the individuals by conducting leave-one-out cross validation on the training set.

III. RESULTS

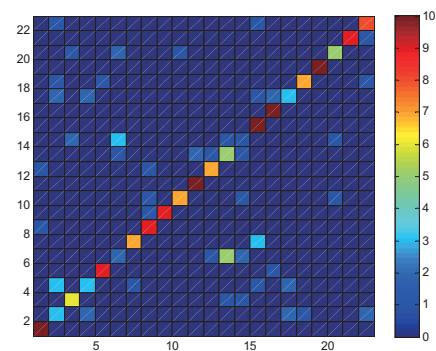


Fig. 1. Color-map of identified subject (identification mode)

Figure 1 shows that color-map of correction recognition rate for 23 subjects. Diagonal elements of image shows that the correct recognition rate. The overall classification rate from KNN, LDA, and SVM was 81.3%, 84.0%, 86.7% respectively.

IV. CONCLUSION

To recognize individuals, several metrics were conducted. We confirmed that time domain features of eye blinking data contain unique characteristics that represent individuals.

ACKNOWLEDGEMENT

This research was funded by Samsung Electronics Co. Ltd.

REFERENCES

1. T.Matsumoto, H.Matsumoto, K. Yamada, and S. Hoshino, "Impact of artificial gummy fingers on fingerprint systems," in *Proc. SPIE, Electronic Imaging*, 2002, pp. 275–289. *Biomed. Eng.*, vol. 26, pp. 111-119, 2013.
2. Database physionet bci. [Online]. Available: <http://www.physionet.org/pn4/eegmidb/>

Possibility of Thermal Comfort Estimation with Wrist Skin Temperature

M.J. Koh¹, S.Y. Shim¹, K.M. Joo¹, H.B. Kim¹, K.S. Park²

¹Interdisciplinary Program of Bioengineering, Seoul National University, Seoul, Korea

²Department of Biomedical Engineering, College of Medicine, Seoul National University, Seoul, Korea

E-mail: bioeng15@bmsil.snu.ac.kr

Abstract— Thermal comfort can be estimated from Fingertip temperature. In this study, the possibility of wrist temperature for estimating thermal comfort. Sum of peak amplitudes of wrist temperature from Fast Fourier Transform (FFT) was analyzed. Fingertip temperature and wrist temperature has been compared see the possibility if thermal comfort estimation is also possible from wrist temperature.

Keywords— Thermal Comfort, Wrist Temperature, Estimation, Wristband, Smart Watch.

I. INTRODUCTION

Smart watches have biometric sensors small enough to fit inside watch body. Biometric signals such as heartrate, temperature etc. can be easily obtained from smart watches. Indoor auto temperature control with temperature obtained from skin temperature is needed because it is bothersome for people to change temperature setting for each person's preference. In previous study, estimation of thermal sensation using fingertip temperature was possible [1]. In this study, wrist temperature will be compared to fingertip temperature.

II. METHODS

Wristband Material

Cotton sweat band material is used. Band has Velcro end for the clasp.

Temperature sensors

Wrist temperature is obtained with film type thermistors LNJT103F029-25(LATTRON, Korea). They were calibrated in water tank to show correct temperature before the experiment. They were placed on the surface of inner side of the band. Fingertip temperature is obtained with YSI Series 400 temperature probe (BIOPAC, USA). Probe was held with 3M medical porous tape.

Experiments

Experiments were done in 10 m² office. Office temperature was elevated with air heater. Volunteered healthy male subject stayed while heating the office to get used to the heated temperature. The room was cooled with air conditioner. Wrist temperature was obtained from right wrist and fingertip temperature from right index finger for 90 minutes at the sampling rate of 1 Hz. Thermistor sensors were placed on the surface of the bands to get temperatures directly from

wrist skin. Temperature from top and bottom area of the wrist were obtained. Sum of peak amplitude of fingertip and wrist temperature from FFT were compared. All temperature data was process with 15 point moving average filter and de-trending before FFT. Table 1 shows experiment protocol for temperature change.

Table 1. Experiment Protocol

	T: 32°C Humid: 37%	T: 32.5°C Humid: 38.5%	T: 29°C Humid: 39%	T: 26°C Humid: 41%
Duration	Wear sensors	30min	30min	30min

III. RESULTS

Table 2. Sum of Peaks after FFT

Thermal Comfort	Fingertip	Wrist Up	Wrist Bottom
Hot(°C ² /Hz)	343.69	18.37	50.12
Neutral(°C ² /Hz)	9393.8	1137.4	1519.7
Cold(°C ² /Hz)	426.5782	17.48	104.7712
Neutral/Hot	27.33	61.91	30.32
Neutral/Cold	22.02	65.08	14.50

IV. CONCLUSION

Table 2 shows sum of peaks from FFT of each skin temperature. Fingertip shows greater amplitude than wrist. Ratio between neutral and hot or cold is higher in wrist than fingertip. In previous study [1], neutral thermal comfort could be distinguished from hot and cold with fingertip temperature. From this experiment, there might be a possibility that neutral, hot and cold thermal comfort could be distinguished with ratio of sum of peaks of wrist temperature from FFT. However, further study should be done to distinguish hot and cold.

ACKNOWLEDGEMENT

This research was funded by Samsung Co. Ltd

REFERENCES

1. K. Nakayama, T. Suzuki, and K. Kameyama, "Estimation of Thermal Sensation Using Human Peripheral Skin Temperature," *IEEE International Conference on Systems, Man, and Cybernetics*, 2009.

Detection of Unilateral Tremor Using Directionality Analysis

S.K.Kim¹, H.J.Lee¹, H.S.Jeon¹, H.B.Kim¹, B.S.Jeon², K.S.Park³

¹Interdisciplinary Program for Bioengineering, Seoul National University, Seoul, Korea

²Department of Neurology, Seoul National University Hospital, Seoul, Korea

³Department of Biomedical Engineering, College of Medicine, Seoul National University, Seoul, Korea

E-mail: pks@bmsil.snu.ac.kr

Abstract—Tremor is typical manifestation of Parkinson's disease(PD). Acceleration and EMG were recorded from twenty patients with PD. Clear peak power appeared from acceleration signals of both dominant and non-dominant hand. However, peak power of EMGs showed only for dominant hands. Directionality index were significantly different between unilateral and bilateral tremor.

Keywords— Tremor, Directionality, Parkinson's Disease, Accelerometer, EMG

I. INTRODUCTION

Tremor is one of the main symptoms of PD. Mostly, tremor is evaluated by various kinds of clinical ratings with visual observation. These methods can be subjective and influenced by individual bias. Thus, quantitative measurement of tremor is meaningful to clinical diagnosis. Accelerometer and gyrosensor are useful to quantify symptoms of tremor. However, signals from the sensors still have ambiguous characteristics to diagnose tremors [1-2].

II. METHODS

A. Subjects

Twenty PD patients were participated in this study. All patients provided written informed consent.

B. Experimental Protocol and Signal Processing

Hand tremor was recorded by tri-axis-accelerometers attached on wrist and finger. Electromyograms(EMGs) were obtained from extensors and flexors of both forearms. EMGs were rectified after highpass filtered with cutoff frequency of 15Hz for removing motion artifact. Directionality index were calculated using acceleration of both wrists and hands.

III. RESULTS

There were not clear peaks of power spectral density of EMGs for non-dominant hands in case of unilateral tremor(Fig.1). However, clear peaks were detected for

acceleration signal. We speculated that clear peaks power of acceleration were transmitted from mechanical effect from oscillation of dominant hand. Directionality index were significantly different between unilateral and bilateral tremor of both sides.

IV. CONCLUSION

Unilateral tremor can be detected by using directionality analysis for acceleration without EMG measurement.

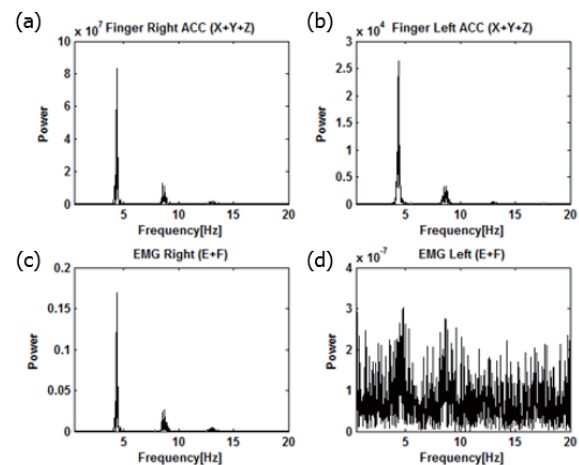


Fig. 1. Power spectral density for unilateral tremor (a) acceleration of right hand (b) acceleration of left hand (c) EMG of right forearm (d) EMG of left forearm

ACKNOWLEDGEMENT

This work was supported by Coway Co., Ltd..

REFERENCES

1. S.Morrison, N. Cortes, K.M.Newell, P.A.Silburn, G.Kerr, "Variability, regularity and coupling measures distinguish PD tremor from voluntary 5Hz tremor," *Neuroscience Letters*, vol. 534, pp. 69-74, 2013.
2. S.Morrison, G.Kerr, P.Silburn, "Bilateral tremor relations in Parkinson's disease: Effects of mechanical coupling and medication", *Parkinsonism & Related Disorders*, vol. 14, pp. 298-308, 2008.

Novel alignment algorithm of synchronized burst based on Gaussian filter convolution

Hyungsup Lee and Yoonkey Nam

Department of Bio and Brain Engineering, KAIST, Daejeon, Republic of Korea

E-mail: mrmirocu@kaist.ac.kr

Abstract—Synchronized burst is known that have causal role of firing patterns in cultured neuronal networks. However, in previous studies, it was difficult to investigate spatiotemporal patterns of synchronized bursts because of temporal alignment problems. In this research, we proposed synchronized burst alignment algorithm based on Gaussian filter convolution. Using this algorithm, we can efficiently visualize the similarity of temporal patterns.

Keywords—Synchronized burst, visualization.

I. INTRODUCTION

Characterization of synchronized burst in neural network is crucial to understand intrinsic property of neural circuits. In order to study the burst property, microelectrode array (MEA) platform has been widely used due to their spatiotemporal resolution. However, in the previous studies, useful tool for from temporal analysis of synchronized bursts is absent. For further analysis, temporal alignment of a set of synchronized bursts is needed. Here, we developed algorithm that allow us to align the bursts based on Gaussian filtering.

II. METHODS

A. Cell culture & MEA

Primary E18 hippocampal neurons were cultured on MEA chip (Multi Channel Systems, Germany). Extracellular spikes were recorded from 16DIV network using MC Rack (Multi Channel Systems).

B. Synchronized burst alignment

Let $t_{i,j}$, $i=1 \dots N$, with N the total number of bursts, $j=1 \dots M$, with M the total number of channels, be the spike train in the i th burst and j th channel. By convolution with Gaussian filter, $t_{i,j}$ can be represented as a continuous function $G_{i,j}$, which is defined as

$$G_{i,j}(t) = \sum_k \exp\left(-\frac{(t - t_{i,j}[k])^2}{2\sigma^2}\right)$$

, $k=1 \dots O$, with O the total number of spike in a channel. For each $G_{i,j}$, cross-correlation against fixed burst can be calculated, and S_i is given by

$$S_i = \sum_j \text{Cross - corr}(G_{1,j}, G_{i,j}), i = 2 \dots N$$

whose maximum, τ_i is decided as alignment parameter, and it is given by

$$\tau_i = \text{argmax}(S_i)$$

III. RESULTS

To detect the synchronized burst in neural networks, we utilized network bursts detection method used in [1].

Before alignment, it is hard to find out similarity in temporal patterns between synchronized bursts (figure 1. (a)). Using alignment algorithm, we can easily confirm similar patterns of bursts (figure 2. (b)).

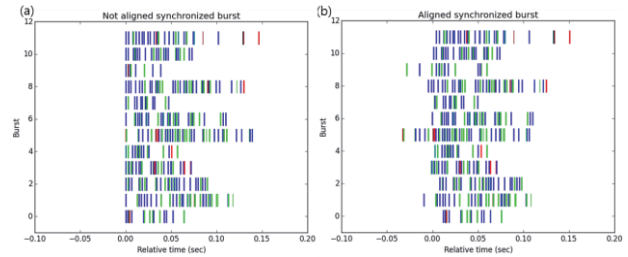


Fig. 1. Synchronized burst before (left) and after (right) alignment.

IV. CONCLUSION

In this study, we developed an alignment algorithm to use in synchronized burst analysis. We expect that this algorithm can be used for further analysis of neuronal network property.

ACKNOWLEDGEMENT

This work was supported by the National Research Foundation of Korea(NRF) grant funded by the Korea government(MSIP) (NRF-2015R1A2A1A09003605).

REFERENCES

1. van Pelt, J., et al. (2004). IEEE Trans Biomed Eng 51(11): 2051-2062.

The Measurement of Ear-EEG Signals using Dry Electrodes

H. B. Kwon¹, S. H. Hong¹, S. H. Choi¹, and K. S. Park²

¹Interdisciplinary Program for Biomedical Engineering, Seoul National University Graduate School, Seoul, Republic of Korea

²Department of Biomedical Engineering, Seoul National University College of Medicine, Seoul, Republic of Korea

E-mail: chasekwon@bmsil.snu.ac.kr

Abstract—In this study, we developed a dry electrode for measuring Ear-EEG signals. This dry electrode can help with measurement of EEG more easily and comfortable applications in brain computer interface. The dry electrode was validated by measuring alpha wave and s Steady state visually evoked potential.

Keywords— Dry electrode, Electroencephalography, Alpha wave, Steady state visually evoked potential

I. INTRODUCTION

Electroencephalography (EEG) is extensively used for the diagnosis of disorders, neurophysiology and cognitive neuro-science [1]. However, current systems are cumbersome and need the assistance of a trained person to set up the recording system [2]. Also wet electrodes which is used for measuring EEG require skin preparation and conduction gel to reduce the skin-electrode interface impedance [3].

In this study, dry electrodes for measuring Ear-EEG signals were designed and validated with comparing to reference EEG signals.

II. METHODS

A. Design of in-ear electrode

In-ear electrode was designed as Fig. 1 (a), being made of Ag.

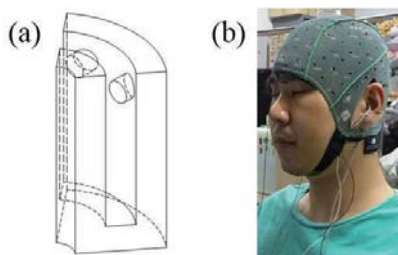


Fig. 1. (a) Design of in-ear electrode (b) Acquisition of EEG

B. Acquisition of EEG

EEG signals from electrodes were obtained from in-ear with dry electrode, P2 with conventional EEG measurement electrode using gel and FPz for GND and earlobe for reference (Fig.1. (b)). EEG signals were acquired with conventional EEG measurement system (BIOPAC MP150, BIOPAC Inc., USA) during 30sec for measuring alpha wave and 100sec for measuring steady state visually evoked potential (SSVEP).

III. RESULTS

A. Alpha wave

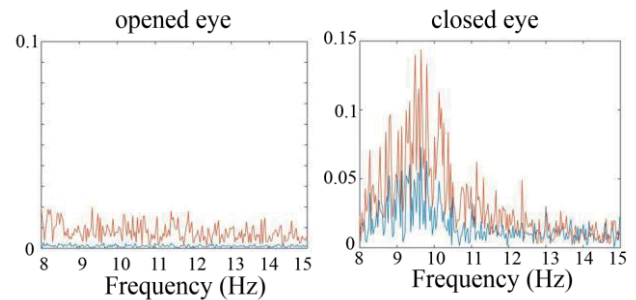


Fig. 2. Analysis in the frequency domain

B. SSVEP

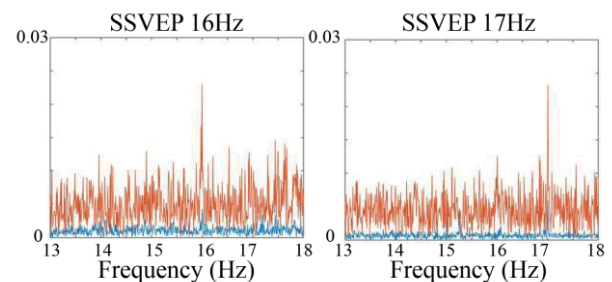


Fig. 3. SSVEP response in frequency domain. The stimulus frequency is 16Hz and 17Hz respectively

Red line indicates EEG signal from conventional EEG measurement electrode and blue line indicates EEG signal from dry electrode.

IV. CONCLUSION

Alpha wave and SSVEP were successfully measured through the in-ear dry electrode. This preliminary study suggests that a novel EEG measurement system can be used in various BCI applications.

REFERENCES

1. P. Kidmose, D. Looney, and M. Ungstrup, "A study of evoked potentials from ear-EEG," *IEEE Trans. Biomed. Eng.*, vol. 60, no. 10, pp. 2824-2830, 2013.
2. D. Looney, P. Kidmose, C. Park, M. Ungstrup, M. Rank, K. Rosenkranz, and D. Mandic, "The in-the-ear recording concept," *IEEE Pulse*, vol. 3, no. 6, pp. 32-42, Nov./Dec. 2012.
3. C. Lin, L. Liao, Y. Liu, I. Wang, B. Lin, and J. Chang, "Novel dry polymer foam electrodes for long-term EEG measurement" *IEEE Trans. Biomed. Eng.*, vol. 58, no. 5, pp. 1200-1207, 2011.

Novel noise reduction algorithm for Electrocardiography for Wearable devices

D. S. Lee¹, S. J. Kwon¹, J. H. Kim¹, and K. S. Park²

¹Interdisciplinary Program of Bioengineering, Seoul National University, Seoul, Korea

²Biomedical Engineering, Seoul National University, Seoul, Korea

E-mail: azuremoon@bmsil.snu.ac.kr

Abstract— Electrocardiography (ECG) has been used as a representative noninvasive method to investigate cardiac activity and diagnose cardiac diseases. There are various wearable devices that can measure ECG unobtrusively in daily situation. However, some artifacts appears in daily environment. In this study, we present effective noise reduction method for wearable ECG measuring devices. The sensitivity and specificity was 94.03% and 99.33%, respectively.

Keywords— Electrocardiography (ECG), noise reduction.

I. INTRODUCTION

Electrocardiography (ECG) has been used as a representative noninvasive method to investigate cardiac activity and diagnose cardiac diseases, such as arrhythmia and heart attack. Nowadays, there are various wearable devices that can measure ECG unobtrusively in daily situation. However, some artifacts appears in daily environment according to subject's motion, inconsistent position of sensor, and so on. In this study, we present effective noise reduction method for wearable ECG measuring devices.

II. METHODS

A. Experiment Setup

ECG was recorded from the brassiere-based wearable sensor using our CardioGuard sensor system [1]. One female participant were recruited for the test. The reference device was also attached to the left upper arm using a band. The participant was asked to wear the sensor and seat comfortably to get calibration data. After the acquisition of calibration data, ECG data was acquired for 12 hours during daily life.

B. ECG noise categorization

The noise was categorized into two types, 'big' noise

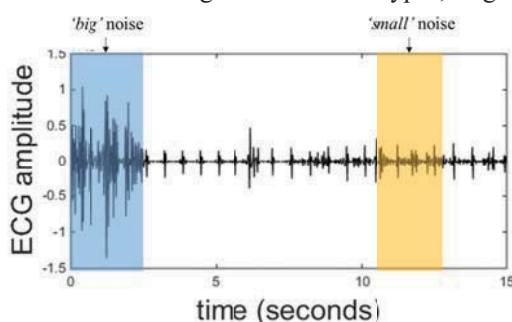


Fig. 1. Example of ECG noise.

and 'small' noise. Each example of the noise is shown in fig. 1. The big noise appears when the participant's motion appears. The amplitude of big noise is much larger than that of normal ECG signals. The small noise appears when the sensor is not attached correctly to the participant's body. The amplitude of small noise is smaller than the ECG, but it doesn't contain meaningful signals.

C. ECG noise reduction

First, we eliminated big noise using threshold. The moving window of 10 seconds was applied to the data. The threshold was determined by the equation (1).

$$th_{i+1} = \max(segment_i) + 1.96 \times std(segment_i) \quad (1)$$

After the big noise is removed, the ECG R-peak candidates were calculated. Then the real R-peak was determined using signal-to-noise ratio (SNR) threshold. SNR was determined by the equation (2).

$$SNR = \frac{p(i)}{[\sum_{t_i-0.5s \leq k \leq t_i+0.5s} p(k)] - p(i)}, \quad (2)$$

where $p(i)$ and t_i denotes i -th peak candidate power and timestamp of the i -th peak candidate, respectively.

III. RESULTS

After the real r-peak was determined, the result was compared to reference r-peak. Table 1 shows the result.

Table 1. Performance of R-peak detection of proposed method.

Sensitivity (%)	94.03
Specificity (%)	99.33
Accuracy (%)	98.93
Kappa statistics	0.92

ACKNOWLEDGEMENT

This work was supported by the Technological Innovation R&D Program (S2168146) funded by the Small and Medium Business Administration (SMBA, Korea).

REFERENCES

1. S. Kwon, J. Kim, S. Kang, Y. Lee, H. Baek, and K. Park, "CardioGuard: A Brassiere-Based Reliable ECG Monitoring Sensor System for Supporting Daily Smartphone Healthcare Applications," *Telemedicine and E-Health*, vol. 20, pp. 1093-1102, 2014.

Possibility of Thermal Comfort Estimation with Wrist Skin Temperature

M.J. Koh¹, S.Y. Shim¹, K.M. Joo¹, H.B. Kim¹, K.S. Park²

¹Interdisciplinary Program of Bioengineering, Seoul National University, Seoul, Korea

²Department of Biomedical Engineering, College of Medicine, Seoul National University, Seoul, Korea

E-mail: bioeng15@bmsil.snu.ac.kr

Abstract— Thermal comfort can be estimated from Fingertip temperature. In this study, the possibility of wrist temperature for estimating thermal comfort. Sum of peak amplitudes of wrist temperature from Fast Fourier Transform (FFT) was analyzed. Fingertip temperature and wrist temperature has been compared see the possibility if thermal comfort estimation is also possible from wrist temperature.

Keywords— Thermal Comfort, Wrist Temperature, Estimation, Wristband, Smart Watch.

I. INTRODUCTION

Smart watches have biometric sensors small enough to fit inside watch body. Biometric signals such as heartrate, temperature etc. can be easily obtained from smart watches. Indoor auto temperature control with temperature obtained from skin temperature is needed because it is bothersome for people to change temperature setting for each person’s preference. In previous study, estimation of thermal sensation using fingertip temperature was possible [1]. In this study, wrist temperature will be compared to fingertip temperature.

II. METHODS

Wristband Material

Cotton sweat band material is used. Band has Velcro end for the clasp.

Temperature sensors

Wrist temperature is obtained with film type thermistors LNJT103F029-25(LATTRON, Korea). They were calibrated in water tank to show correct temperature before the experiment. They were placed on the surface of inner side of the band. Fingertip temperature is obtained with YSI Series 400 temperature probe (BIOPAC, USA). Probe was held with 3M medical porous tape.

Experiments

Experiments were done in 10 m² office. Office temperature was elevated with air heater. Volunteered healthy male subject stayed while heating the office to get used to the heated temperature. The room was cooled with air conditioner. Wrist temperature was obtained from right wrist and fingertip temperature from right index finger for 90 minutes at the sampling rate of 1 Hz. Thermistor sensors were placed on the surface of the bands to get temperatures directly from

wrist skin. Temperature from top and bottom area of the wrist were obtained. Sum of peak amplitude of fingertip and wrist temperature from FFT were compared. All temperature data was process with 15 point moving average filter and de-trending before FFT. Table 1 shows experiment protocol for temperature change.

Table 1. Experiment Protocol

	T: 32°C Humid: 37%	T: 32.5°C Humid: 38.5%	T: 29°C Humid: 39%	T: 26°C Humid: 41%
Duration	Wear sensors	30min	30min	30min

III. RESULTS

Table 2. Sum of Peaks after FFT

Thermal Comfort	Fingertip	Wrist Up	Wrist Bottom
Hot(°C ² /Hz)	343.69	18.37	50.12
Neutral(°C ² /Hz)	9393.8	1137.4	1519.7
Cold(°C ² /Hz)	426.5782	17.48	104.7712
Neutral/Hot	27.33	61.91	30.32
Neutral/Cold	22.02	65.08	14.50

IV. CONCLUSION

Table 2 shows sum of peaks from FFT of each skin temperature. Fingertip shows greater amplitude than wrist. Ratio between neutral and hot or cold is higher in wrist than fingertip. In previous study [1], neutral thermal comfort could be distinguished from hot and cold with fingertip temperature. From this experiment, there might be a possibility that neutral, hot and cold thermal comfort could be distinguished with ratio of sum of peaks of wrist temperature from FFT. However, further study should be done to distinguish hot and cold.

ACKNOWLEDGEMENT

REFERENCES

1. K. Nakayama, T. Suzuki, and K. Kameyama, “Estimation of Thermal Sensation Using Human Peripheral Skin Temperature,” *IEEE International Conference on Systems, Man, and Cybernetics*, 2009.

Temporal Encoding of Chemical Stimulation by Nociceptive Neurons in Mouse Hairy Skin

K. W. Cho¹, J. B. Choi¹, S. P. Kim², S. J. Jung³, D. P. Jang^{1*} and I. Y. Kim¹

¹Department of Biomedical Engineering, Hanyang University, Seoul, Korea

²School of Design and Human Engineering, Ulsan National Institute of Science and Technology, Ulsan, Korea

³Department of Biomedical Sciences, Hanyang University, Seoul, Korea

E-mail: dongpjang@gmail.com

Abstract—Spike trains from primary afferent nociceptive fibers in mouse hairy skin were analyzed. Capsaicin and GABA evoked fast/regular trains and slow/irregular trains respectively. Characteristic of each responses were enhanced by inflammation mediators (bradykinin and prostaglandin E2).

Keywords— *Ex vivo* recording, ion channel, pain

I. INTRODUCTION

Under inflammatory condition, painful stimulus is felt severer. Underlying mechanism is partly revealed but it depends on the mediators interacting with ion channels on the primary afferent nociceptive fibers. Especially, bradykinin (BK) and prostaglandin E2 (PGE2) are expected to increase activation of TRP cation channel subfamily V member 1 (TRPV1)¹. Response patterns of fibers that containing TRPV1 have been investigated in recent electrophysiological studies. An agonist of such fibers is capsaicin as their function is sensing burning pain. Therefore we examine whether the capsaicin evoked response pattern is enhanced with BK and PGE2 mixed solution. We also tested gamma-aminobutyric acid (GABA) to verify an innocuous agonist evoked pattern change by BK and PGE2.

II. METHODS

A. Surgery and *ex vivo* recording

C57BL/6 mice were sacrificed before each experiment, and their hind paw skin including the saphenous nerve was extracted with surgical methods². We first applied solutions of 10 μ M capsaicin or 3mM GABA. Next the solution was switched to 10 μ M BK and 10 μ M PGE2 mixture. Finally, mixture of capsaicin or GABA with BK and PGE2 were applied. For all periods, spike data were recorded for 300 s and was further processed to spike pattern analyzer.

B. Pattern analysis

For the analysis of spike temporal pattern, a method based on the histograms of spike rate and regularity was used. Two histograms were merged to comprise a two dimensional histogram.

III. RESULTS

A. Characteristic spike pattern exist for each agonist

First, evoked responses in naïve condition were averaged for each group: capsaicin and GABA.

According to the analysis, capsaicin response had higher frequency and more regular pattern whereas GABA response was slow and irregular.

B. Characteristic pattern is enhanced under inflammation

For both agonists with BK and PGE2, patterns were maintained. But spike rate of capsaicin response and irregular feature of GABA response were increased from naïve condition.

IV. CONCLUSION

TRPV1 activated fibers have firing patterns meeting the criteria of bursts, burst and tonic, or adaptation. However, we didn't distinguish each type of responses as the mechanism of adaptation is over the scope. When applied with BK and PGE2, capsaicin response

Proportion of each characteristic components were increased.

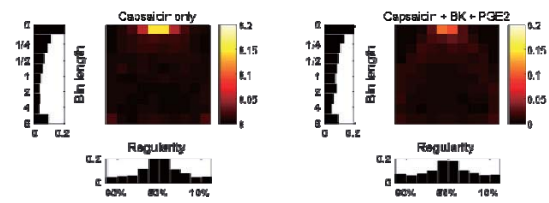


Fig. 1. Pattern of capsaicin evoked responses in naïve skin (left) and inflammatory condition (right).

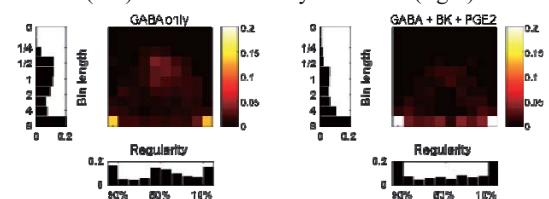


Fig. 2. Pattern of GABA evoked responses in naïve skin (left) and inflammatory condition (right).

ACKNOWLEDGEMENT

This work was supported by the NRF grant (2012M3A7B4035199).

REFERENCES

1. K. Mizumura J. Sato, and T. Kumazawa, "Effects of prostaglandins and other putative chemical intermediaries on the activity of canine testicular polymodal receptors studied *in vitro*," *Eur J Physiol*, vol. 408, pp. 565-572, 1987.
2. K. Zimmermann, A. Hein, U. Hager et al., "Phenotyping sensory nerve endings *in vitro* in the mouse," *Nat Protoc*, vol. 4, no. 2, pp. 174-96, 2009.

Decoding the Bimanual Arm Movement from the Brain Signal : Using Epidural ECoG in Non-Human Primate

K. R. Min¹, H.S. Choi¹, J. Y. Lee¹, K. H. Ahn², K. M. Lee², I. Y. Kim¹, and D. P. Jang¹

¹Department of Biomedical Engineering, Hanyang University, Seoul, Korea

²Department of Neurology, Seoul National University Hospital, Seoul, Korea

E-mail: dongpjang@gmail.com

Abstract—Recently, several studies have reported the usability of eECoG (epidural electrocorticogram) for brain computer interface. The spatial resolution of ECoG (electrocorticogram) is known to be much higher than EEG (electroencephalogram). eECoG is less invasive, less injured, and less worried about infection than traditional ECoG (subdural ECoG). However, the feasibility and performance of eECoG on BCI were not fully evaluated yet. In this study, we verified the usability of implanted eECoG in non-human primate by decoding the three dimensional arm trajectories using eECoG signals.

Keywords— brain-computer interface (BCI), electrocorticogram (ECoG), bimanual movement,

I. INTRODUCTION

On brain computer interface (BCI), decoding and predicting intention of the subject is one of the main issues.

Recently, epidural electrocorticogram (eECoG) is widely known to give a great SNR, high spatial-resolution, and broad frequency bandwidth. In this study, we verified the usability of implanted eECoG in non-human primate by predicting arm movement using eECoG signals.

II. METHODS

A. Surgical procedure

Two micro electrode patches (32 channels) were inserted over duramater on the rhesus monkey's brain, covering the premotor cortex, primary motor cortex, and primary somatosensory cortex.

B. Behavioral Task

The monkey performed three directional arm movement tasks, responding to target's location change (left, middle, right). In Figure 1, a trial began when the monkey pushed each ready button. After the ready if the task was left hand task, the red color cue appeared and if the task was right task, the blue color cue appeared. All movements were captured at a sampling rate of 20Hz by an IMU motion tracker.

C. Data Analysis

ECoG data were band-pass filtered from 0.5 to 200Hz and notch for processing. For each channel and each 1s time period (steeping by 50ms), the time-frequency representation was described by a scalogram generated by Morlet wavelet transformation at 10 different center frequencies ranging from 10 to 120Hz. Then the scalogram was resampled at 10 time lags. Using 6400

features (64 electrodes x 10 frequency bins x 10 time bins), we estimate multivariate partial least squares (PLS) regression model. [1]

III. RESULTS

To quantify the performance of decoding, we calculated correlation coefficients(r) between motion tracker and predicted trajectories. Also, we calculated time, channel, frequency contribution using PLS coefficients. (Fig. 1)

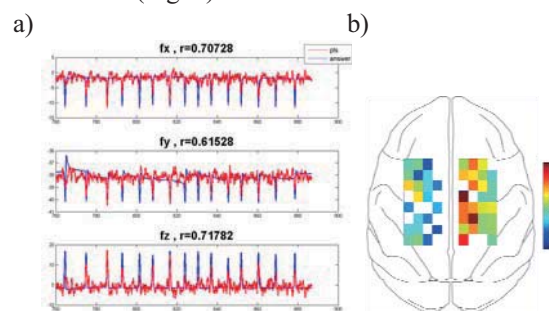


Fig. 1. (a) Left hand movement prediction result, (b) channel contribution map

IV. CONCLUSION

As a results, some frequency bands of the brain signals were significantly correlated with the arm position and arm movement preparing. So we verified the eECoG's feasibility and showed significant and stable decoding performance over several months. This could support the efficacy of BCI using eECoG and the various neuro-prosthetics fields.

ACKNOWLEDGEMENT

This study was supported by the National Research Foundation of Korea (No. 2013R1A2A2A04014987) funded by the Ministry of Education, Science and Technology (MEST), Republic of Korea.

REFERENCES

1. K. Shimoda, Y. Nagasaka, Z. C. Caho, N. Fujii, "Decoding continuous three-dimensional hand trajectories from epidural electrocorticographic signals in Japanese macaques," *Journal of Neural Engineering*, vol. 9, pp. 13-25, 2012.
2. W. Wu, M. J. Balck, Y. Gao, E. Binenstock, M. serruya, J.P.Donoghue, "Inferring Hand Motion from Multi-cell Recordings in Motor Cortex using a Kalman Filter", *Title of a Book*, City: Publisher, 2011.

System Performance Improvement in the Olfactory Event Related Potential by odorants changing

J. H. Kim^{1*}, Y. M. Park¹, J. S. Park¹, D. P. Jang¹, I. Y. Kim², S. H. Cho³

¹Department of Biomedical Engineering, Graduate School of Biomedical Science & Engineering, Hanyang University, Seoul, Korea

²Department of Biomedical Engineering, Hanyang University, Seoul, Korea

³Department of Otorhinolaryngology-Head and Neck Surgery College of Medicine, Hanyang University

*E-mail: zhongkim@bme.hanyang.ac.kr

Abstract—The Olfactory Event-Related Potential (OERP) could evaluate olfactory function objectively. Nevertheless, in clinic, OERP test has not used generally because of its infeasibility. The kind of stimuli odorants could affect whether we could get valid result or not. In this study, we designed and performed to improve acquisition rate for clinical use and comparative experiment with changing stimuli odorants. We tested two kinds of odorants; PEA (Phenethyl alcohol) and n-Butanol. The results showed that reliable potential was observed 61.5% using developed system with n-Butanol.

Keywords—smell, olfaction, ERP, OERP

I. INTRODUCTION

The Olfactory Event-Related Potential (OERP) which is one of the electrical-physiological methods, is considered as one of the alternating methods to test the human olfactory function. But, still this method has consideration. Because reliable potential was observed only 30% in OERP test with healthy subjects using existing system. In this study, we developed and evaluated enhanced OERP system for clinical feasibility.

II. METHODS

Monorhinal olfactory stimuli were delivered via an olfactometer (Fig 1). Heated air at a temperature of 36.5°C and humidified to 80% relative humidity was delivered to left nostril at a constant flow rate (8 L/min) and adjusted by a flowmeter. The flow was delivered by Teflon tubing and it placed inside the tip of the nostril during stimulation. Stimulate duration is controlled by check valve with 200ms. 98% PEA (Phenethyl alcohol) to 12 participants (9M, 3F), and 99.5% n-butanol to 13 participants (10M, 3F) aged between 23~31years was delivered each group. An ISI (Inter Stimulation Interval) of 60s was applied to allow for neuronal recovery in the olfactory system. OERPs were recorded from four electrodes (Pz, P1, P2, Cz).

III. RESULTS

Our study group get three successful OERP pattern in PEA group (25%) and eight in n-Butanol group (61.5%). As Figure 2 upper side, we could get OERP peak with n-Butanol stimuli at 1023ms successfully.

We expect OERP peak about 1000ms (400~500ms to cognize smell and 500ms stimuli to reach nasal cavity.)

IV. CONCLUSION

These findings suggest using n-Butanol in OERP test could get more successful data than using PEA and imply there are difference between stimuli odorants in OERP test result.



Fig. 1 Hanyang OERP system (Left), Olfactometer (Right)

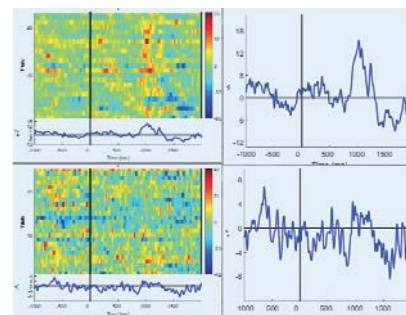


Fig. 2 OERP result at Pz with n-Butanol stimuli; Successful pattern (up), unsuccessful pattern (down)

ACKNOWLEDGEMENT

This work was supported by the NRF grant (NRF-2013R1A1A2007651).

REFERENCES

1. Morgan CD, Murphy C. Olfactory event-related potentials in Alzheimer's disease. *Journal of the International Neuropsychological Society* 2002;8:753-63.
2. Lundstrom JN, Seven S, Olsson MJ, Schaal B, Hummel T. Olfactory event-related potentials reflect individual differences in odor valence perception. *Chemical Senses* 2006;31:705-11.

Evaluation of Smartphone Feature Combination to Detect Freezing of Gait

Hanbyul Kim¹, Hong Ji Lee¹, Woongwoo Lee², Sungjun Kwon¹, Sang Kyong Kim¹, Hyo Seon Jeon¹, Hyeyoung Park³, Chae Won Shin³, Won Jin Yi⁴, Beom S. Jeon³, and Kwang S. Park⁵

¹Graduate Program of Biomedical Engineering, Seoul National University, Seoul, Korea

²Department of Neurology, Eulji General Hospital, Seoul, Korea

³Department of Neurology and Movement Disorder Center, Seoul National University, Seoul, Korea

⁴Department of Oral and Maxillofacial Radiology, School of Dentistry, Seoul National University, Seoul, Korea

⁵Department of Biomedical engineering, College of Medicine, Seoul National University, Republic of Korea

E-mail: pks@bmsil.snu.ac.kr

Abstract—Freezing of gait (FOG) is a common motor deficit of Parkinson’s disease (PD) patients. FOG interrupts daily activities and increases fall risk of patients, especially elders. We propose the combination of features and sensors to improve previous threshold based FOG detection algorithm. The combination of freezing index and energy from X-axis of gyroscope showed increased specificity to discriminate freezing and normal gait.

Keywords— Freezing of Gait, Gait Analysis, Smartphone, Accelerometer, Gyroscope

I. INTRODUCTION

Parkinson’s disease (PD) is a common motor system affecting disease caused by neuro-degenerative central nervous system. Freezing of Gait (FOG) is one of commonly experienced symptoms of PD patients, described as an inability to walk or a large reduction of steps. To overcome the limitations of subjective diagnosis of FOG, many objective methods such as force sensors, wearable accelerometers could quantify freezing events were studied in the literature. Freezing index (FI) was the most frequently used single feature in threshold based FOG detection algorithm. In this study, we suggest feature and sensor combination from smartphone to improve the accuracy of detection algorithm.

II. METHODS

Accelerometer and Gyroscope data of FOG patients were collected from smartphone, Google Nexus 5. Subjects wore their usual clothes at natural and the smartphone was fixed at the ankle using elasticized armband. Nine patients participated in this study and presented freezing symptoms during the protocols. Experiments were performed in the aisle of the hospital. Subjects were asked to go straight 3 meters and turned back to their original place. Videos were recorded to compare clinical evaluation and developed algorithm.

III. RESULTS

We first extracted relevant features to discriminate freezing episodes using fast correlation-based filter. Freezing index from each axis of accelerometer was most discriminative feature. Entropy, variance, power were also frequently chosen for feature of the model. Mean of Y-axis was most effective features computed

from gyroscope. Freezing index, energy of each index were another candidate feature for our system. We estimated general performance of the model using ten-fold cross validation. The sensitivity (Sens.) and specificity (Spec.) were used to measure classification ability of developed system. We compared the performance of combinations of promising features and tested its statistical difference using pairwise t-test. We couldn’t find meaningful difference by adding additional feature, except for combining FI and energy from X-axis of gyroscope (p-value < .1).

IV. CONCLUSION

Continuous monitoring of FOG in daily life is important to improve the quality of life of PD patients. Previous study suggested freezing index from single accelerometer to identify the symptoms. Our proposed methodology investigated the effect of combination of various features, sensors from smartphone. We could achieve higher specificity by combining freezing index and energy computed from X-axis of gyroscope.

Table 1. Performance of FOG Classification for All Patients

Moore’s		FI-x & energy-x	
Sens.	Spec.	Sens.	Spec.
0.690	0.719	0.873	0.774
0.654	0.607	0.693	0.623
0.775	0.727	0.558	0.688
0.660	0.925	0.825	0.808
0.467	0.560	0.350	0.526
0.533	0.486	0.533	0.731
0.690	0.846	0.773	0.791
0.867	0.622	0.807	0.802
0.600	0.608	0.633	0.604

ACKNOWLEDGEMENT

This work was Supported by grant no 3420140050 from the SNUH Research Fund.

REFERENCES

1. J. Jankovic, “Parkinsons disease: clinical features and diagnosis,” Journal of Neurology, Neurosurgery & Psychiatry, 2008.
2. S. T. Moore, H. G. MacDougall, and W. G. Ondo, “Ambulatory monitoring of freezing of gait in parkinson’s disease,” Journal of neuroscience methods, 2008.

Alterations in Field Potentials After Anodal Transcranial Direct Current Stimulation on the Motor Cortex of Anesthetized Rats

Ho Koo¹, Yong-Il Shin², Yu Fan³, Sang Hu Han¹ and Min Sun Kim¹

¹Department of Physiology, Wonkwang University School of Medicine, Iksan, Korea

²Department of Rehabilitation Medicine, Pusan National University School of Medicine, Research Institute for Convergence of Biomedical Science and Technology, Pusan National University Yangsan Hospital, Pusan, Korea.

³Department of Meridian & Acupoint, College of Korean Medicine, Wonkwang University, Iksan, Korea

E-mail: tiger9579@gmail.com

Abstract—Transcranial direct current stimulation (tDCS) has been used for the modulation of cortical excitability. A number of human studies have shown that tDCS applied to the motor cortex induced the long-lasting cortical excitability. However, the mechanism how tDCS elicits cortical excitability for long time is unclear. Here, we investigated alterations of field potentials, evoked by stimulating transcallosal pathway, on the motor cortex of rats before and after tDCS. Field potentials gradually increased after anodal tDCS. We suggest that long-term effects of tDCS can be demonstrated through our in-vivo animal model.

Keywords— tDCS, motor, cortex, plasticity, LTP

I. INTRODUCTION

tDCS can induce polarity-dependent changes in motor cortex excitability. The anodal stimulation generally increases neuronal excitability, while cathodal stimulation decreases it. In several animal studies, scientists demonstrated that anodal tDCS can modulate the neuronal excitability of motor cortex and especially elicit long-lasting effects after tDCS [1].

II. METHODS

All SD rats (300~450g) were anesthetized with urethane solution. A stimulation electrode to evoke field potentials in motor cortex was positioned in the left corpus callosum. Another electrode for recording evoked field potentials and tDCS was placed on the skull over the right motor cortex Fig. 1.

Anodal tDCS were applied at a current intensity of 250 μ A for 20 minutes and To evoke field potentials in the right motor cortex, biphasic, square-wave constant current stimulation pulses with the duration 0.1 ms and the intensity of 300 μ A were delivered to the left corpus callosum at 30 seconds intervals.

Evoked field potentials of the baseline were measured during 15 minutes before tDCS. After that, tDCS was continued for 20 minutes and then a recording was resumed for 60 minutes.

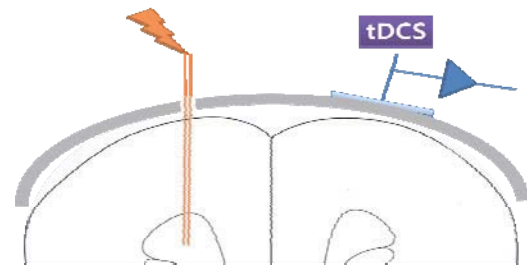


Figure 1. an electrode for evoking field potentials of the right motor cortex was positioned in the left corpus callosum. Another electrode for recording field potentials and tDCS was also located on the skull over the motor cortex.

III. RESULTS

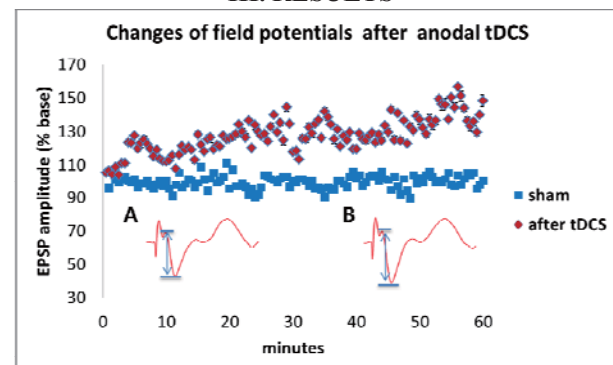


Figure 2. Changes of EPSP (Excitatory postsynaptic potential) amplitude after anodal tDCS. The distance of arrow indicates EPSP amplitude. (A: Evoked waveform before tDCS, B: Evoked wave at 1 hour after tDCS)

EPSP amplitudes in the motor cortex gradually increased after anodal tDCS.

IV. CONCLUSION

We demonstrated long-lasting effects after tDCS using minimally noninvasive animal experimental model.

REFERENCES

1. Brita Fritsch, et al., "Direct current stimulation promotes BDNF-dependent synaptic plasticity: potential implications for motor learning" *Neuron*, vol. 66, pp. 198-204, 2010.

The Effects of Clinical Test Time on the Auditory Late Response and the Spontaneous EEG in the Gap-Intense Sound Paradigm

J.Y. Kim¹, Y.S. Ku¹, J.W. Ahn¹, D.Y. Kim¹, C.H. Kwon¹,
M.W. Suh², J.H. Lee^{2,4}, S.H. Oh^{2,4}, and H.C. Kim^{3*}

¹ Interdisciplinary Program for Bioengineering, Seoul National University, Seoul, Korea

² Department of Otorhinolaryngology-Head and Neck Surgery, Seoul National University Hospital, Seoul, Korea

³ Department of Biomedical Engineering, Medical Research Center, Seoul National University College of Medicine, Seoul, Korea

⁴ Department of Otorhinolaryngology-Head and Neck Surgery, Seoul National University College of Medicine, Sensory Organ Research Institute, Seoul National University Biomedical Research Institute, Seoul, Korea
E-mail: hckim@snu.ac.kr

Abstract— Gap-intense sound paradigm has been proposed to investigate objective tinnitus diagnosis. However, some patients feel mental fatigue as the test proceeds due to its long operation time. This study aims to analyze its effect on the auditory late response (ALR) and the electroencephalograph (EEG). For the ALR analysis, peak amplitudes, signal to noise ratio (SNR) and the ability of gap prepulse inhibition (GPI) were decreased in later sessions. For the EEG analysis, the band powers of δ and θ wave were increased. The relaxation ratio indices, α /high β and $(\alpha+\theta)/\beta$ were also increased. These results indicate that the clinical test time can influence the result of gap-intense sound paradigm.

Keywords—Gap-intense sound paradigm, Auditory late response, Electroencephalograph

I. INTRODUCTION

Gap-intense sound paradigm has been investigated for objective tinnitus diagnosis [1]. In this paradigm, the intervals between intense sounds were relatively long to prevent the prediction of subjects. Due to the averaging technique for the ALR measurement, this long time interval dramatically increases the required operation time, which can induce subjects' mental fatigue. Because this mental fatigue causes the changes of the ALR and the EEG [2], we investigated the effect of long clinical test time on the ALR and the spontaneous EEG in gap-intense sound paradigm.

II. METHODS

Thirteen adults with an age range of 24 to 34 years participated in this study. All subjects have no history of tinnitus. Both ALR and EEG were recorded when performing the gap-intense sound paradigm. Among total 8 sessions for each subject, we compared first two sessions with last two sessions to observe the effect of the test time. Peak amplitudes and differences of N1P2 and P2N2, GPI ratio, and SNR were compared for the ALR analysis. In the EEG analysis, band powers of δ and θ wave and two relaxation indices (α /high β and $(\alpha+\theta)/\beta$) were selected as the analysis features.

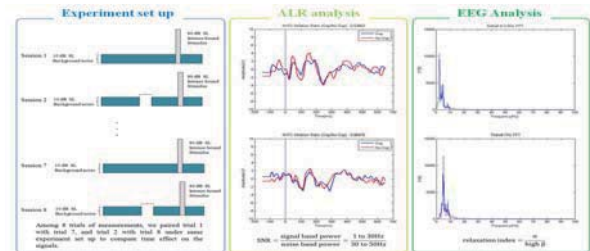


Fig. 1. Experiment set up and ALR/EEG analysis

III. RESULTS

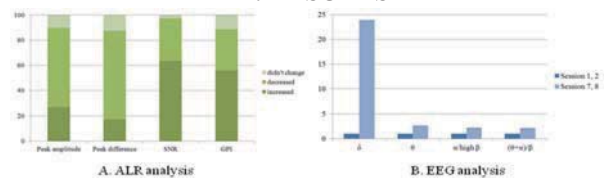


Fig. 2. The changes of features in the ALR and the EEG

In the ALR analysis, 62.5% of peak amplitudes and 70.2% of peak differences were decreased in later sessions. The SNR and the ability of GPI became lower in 63.5% and 55.8% cases, respectively. In the EEG analysis, band powers of δ and θ wave were increased 23.9 and 2.7 times, respectively. Relaxation indices were also increased 2.25 and 2.2 times, respectively.

IV. CONCLUSION

We found significant changes of some features in both the ARL and the EEG. These changes indicate that the clinical test time can influence the result of gap-intense sound paradigm.

ACKNOWLEDGEMENT

This work was supported by the National Research Foundation of Korea (NRF) grant funded by the Korea government (MSIP) (No. NRF-2015R1A2A2A04003938).

REFERENCES

1. Y.S. Ku, et al. "Gap prepulse inhibition of the auditory late response in healthy subjects", *Psychophysiology*, pp. 1511–1519, 2015.
2. T.Cao, et al. "Objective evaluation of fatigue by EEG spectral analysis in steady-state visual evoked potential-based brain-computer interfaces", *BioMedical Engineering OnLine*, 2014.

Implementation of a Low Power Consumption and Small Area Processor for Fully Implantable Middle Ear Hearing Device

D. W. Kim¹, J. H. Kim², Y. S. Park³, J. H. Lee⁴, H. G. Lim⁵, M. N. Kim² and J. H. Cho^{3,5*}

¹Kyungpook Regional Headquarters, Korea Testing Certification

²Department of Medical and Biological Engineering, Graduate School, Kyungpook National University

³Institute of Biomedical Engineering Research, Kyungpook National University, Daegu, Korea

⁴Department of Biomedical Engineering, Kyungpook National University Hospital

⁵Graduate School of Electronics Engineering, Kyungpook National University

*E-mail: jhcho@ee.knu.ac.kr

Abstract—Fully-implantable middle ear hearing device (F-IMEHD) is actively studied to compensate disadvantages of current hearing devices. The F-IMEHD has to accomplish the low power and small area consumption for easy implantation and long-term use. For the F-IMEHD, we designed a signal processor with low power consumption and small area, considering a vibrational transducer.

Keywords—Fully implantable middle ear hearing device, Signal processor, vibrational transducer, Wide dynamic range compression (WDRC).

I. INTRODUCTION

Recently, the population of hearing impaired people is increasing continuously and suffers from their hearing problems. To dealing with this problem, the various type hearing aids are being rapidly developed [1]. Especially, the F-IMEHD is actively studied for the patients with sensorineural hearing loss. The basic F-IMEHD consists of an implantable microphone, a signal processor, and a vibrational transducer. For the design of signal processor, the frequency characteristics of vibrational transducer must be considered. In addition, the signal processor had to accomplish low power and small area for long-term implantation.

II. METHODS

A. Frequency characteristics of vibrational transducer

The multi-channel WDRC was designed to 4-channel in consideration of frequency characteristics of transducer after body implant. The division of channel according to transducer characteristics is shown in Fig. 1(a).

B. Proposed WDRC algorithm

The proposed WDRC algorithm is shown in Fig. 1(b), and it based on the successive-FFT is not performs inverse FFT for signal reconstruction. The proposed successive-FFT used repetition of the twiddle factor and it calculates only data summation for signal reconstruction. This method can be improved the speed of arithmetic operation and it has advantages of low power consumption and small size design.

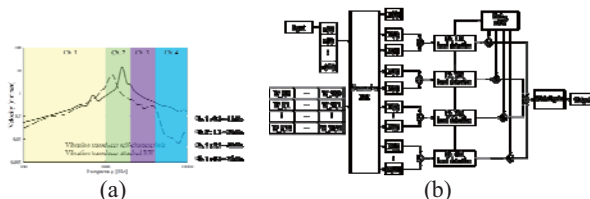


Fig. 1. (a) The division of channel based of vibrational transducer's characteristics and (b) the block diagram of proposed WDRC algorithm.

III. RESULTS

To verify the proposed WDRC based on the successive-FFT, the computer simulations and experiments have been performed, and it is shown in Fig. 2(a)(b). According to the simulation results, successive-FFT based WDRC can be divided into 4 channel, controlled channel gain and reconstructed input signal under the MATLAB (Mathworks Inc., USA) environment and FPGA development board.

The proposed processor is implemented in a SMIC 180 nm CMOS process. Fab-out results for the processor of F-IMEHD is shown in Fig. 2(c).

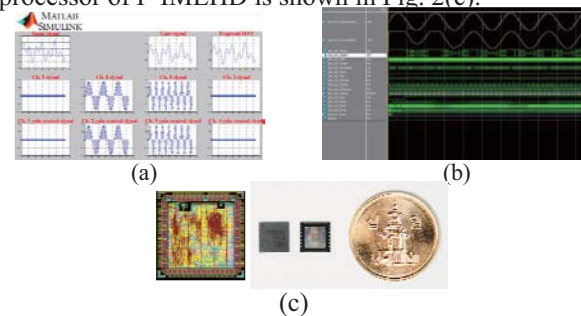


Fig. 2. (a) The output result of WDRC at channel 2(gain = 1) and channel 3(gain = 2), (b) the result of FPGA simulation using the Model-sim and (c) layout and packaging chip of the proposed processor.

IV. CONCLUSIONS

In this study, we implemented a signal processor for the F-IMEHD with the low power consumption and small area. The signal processor embedded 4-channel 64 band WDRC and 16 bit 32 kHz SAR ADC using 0.18 μ m process MPW. The experimental results show that the proposed processor was operated well and can successfully worked including channel division and reconstruction of input signal. Therefore, it is expected that the designed processor can be applied to the fully implantable hearing aids.

ACKNOWLEDGEMENT

This work was supported by the National Research Foundation of Korea (NRF) grants funded by the Korea government (No. 2013R1A2A1A09015677, 2015R1A2A2A03006113).

REFERENCES

1. D. D. Backous and W. Duke, "Implantable middle ear hearing devices: Current state of technology and market challenge," *Current Opinion in Otolaryngology & Head and Neck Surgery*, vol. 14, no. 5, pp. 314-318, October 2006.

Implementation of Analysis Tool of Electromyograph(EMG) Signals for Biosemi's ActiveTwo System

J. Park¹, C. Kwon¹, and H. Kang²

¹Department of Medical IT Engineering, Soonchunhyang University, Asan, South Korea

²Department of Sports Medicine, Soonchunhyang University, Asan, South Korea

E-mail: chunkikwon@sch.ac.kr

Abstract—ActiveTwo system of Biosemi, Inc is well known for its high accuracy in biopotential measurements. However, unlike EEGLab for use of ActiveTwo system as EEG measurement, no tool is provided to analyze digitized raw EMG signals. In this work, analysis tool as post-data processing is implemented to analyze digitized EMG signals taken from ActiveTwo system .

Keywords— EMG Signal, Analysis tool, ActiveTwo system, Biopotential measurement, post data processing

I. INTRODUCTION

ActiveTwo system of Biosemi, Inc is well known for its high accuracy in biopotential measurements. Since ActiveTwo system was originally designed for measurement of EEG signals, there were analysis tools available to analyze digitized raw EEG signals such as EEGLAB. However, analysis tool for EMG signals taken from ActiveTwo system can be hardly found. Thus, in this work, the analysis tool to analyze raw EMG signals for use of ActiveTwo system is implemented.

II. DESIGN OF ANALYSIS TOOL

Factors in wide use for EMG signal analysis are chosen in the analysis tool implemented in this work. This tool is implemented in MATLAB environment because of availability of toolboxes provided by MATLAB.

A. Butterworth Band-Pass filtering

The digitized raw EMG signals are filtered using 4th order butterworth filter from 10Hz to 450Hz, which are bandwidth of EMG signals.

B. Root-Mean-Sqaure (RMS)

RMS is one of factors which have been widely used in analysis of EMG signals in time domain. This provides intuitive information on magnitude of muscle activations.

C. Fast Fourier Transform (FFT)

FFT provides information on frequency distribution and fatigue of muscles for spectral analysis.

D. Median Frequency (MDF)

MDF is widely used factor in the analysis of muscle fatigue. MDF is mean frequency at which two areas are equal at Power Spectral Density.

III. RESULTS

The implemented analysis tool was validated using digitized raw EMG signals in biceps brachii of the right upper arm, as shown in Fig. 1.

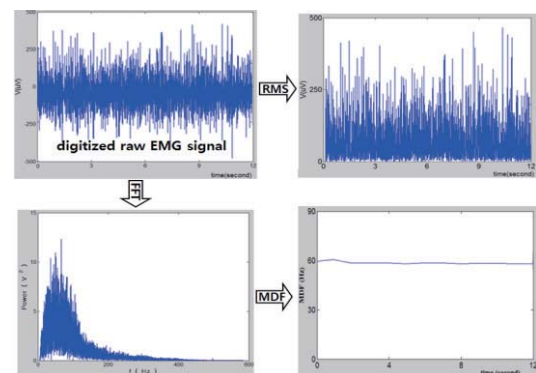


Fig. 1. Analyzed results using the implemented tool

IV. CONCLUSION

In this work, analysis tool for EMG signals taken from ActiveTwo system in Biosemi, Inc was implemented. Experiment study shows that the tool provides useful analysis in EMG signals. More work on GUI for the tool will be another work in the future.

ACKNOWLEDGEMENT

This research was supported in part by Basic Science Research Program through the National Research Foundation of Korea(NRF-2014-R1A1A1013430) and in part by the Soonchunhyang University Research Fund.

REFERENCES

1. M. B. I. Reaz, et al., "Techniques of EMG signal analysis: detection, processing, classification and applications," *Biological Procedures Online.*, pp. 11-35, 2006.
2. C. Frigoa, et al., "EMG signals detection and processing for on-line control of functional electrical stimulation," *International Society of Electrophysiology and Kinesiology*, pp. 351-360, 2000.

Obstructive Sleep Apnea Detection using a Single Channel Signal for Healthcare Applications

U. Erdenebayar, J. U. Park, P. S. Jeong and K. J. Lee

Department of Biomedical Engineering, Yonsei University, Wonju, Republic of Korea
E-mail: edenbyra@yonsei.ac.kr, lkj5809@yonsei.ac.kr

Abstract—We developed the algorithm to detect the obstructive sleep apnea (OSA) using a single channel signal. The piezoelectric sensor was used to extract the snoring, movement and heartbeats. Support vector machine was used as classifier in the region that absence snoring more than 10 seconds. To evaluate the proposed algorithm polysomnography data of 38 patients that suffered with OSA were used. The results showed that a good performance for OSA detection with sensitivity of 86.8%, specificity of 71.4% for training set and sensitivity of 93.2% and specificity of 80.1% for test set, respectively.

Keywords—obstructive sleep apnea, snoring, pulse heart, piezoelectric sensor.

I. INTRODUCTION

OSA is silently spreads out sleep-disordered breathing that and more than 80% of the suspected patients are undiagnosed [1]. The polysomnography is currently regarded as a gold standard for OSA diagnosis; however, it is a high cost, immobility and inconvenience for patients.

We developed an algorithm to detect OSA using a single-channel piezoelectric sensor for a low cost, portable and convenient OSA screening and analyzing.

II. METHODS

A. Populations and Data Acquisition

Thirty eight patients (ages: 55.6 ± 10.2 , body mass index: 25.5 ± 2.9 kg/m², apnea-hypopnea index: 35.4 ± 16.8 events/h) participated in this study. The data acquired from a piezoelectric sensor (REF 1420610, Embla Systems Inc., USA) was simultaneously recorded with the standard full-night PSG recording during sleep.

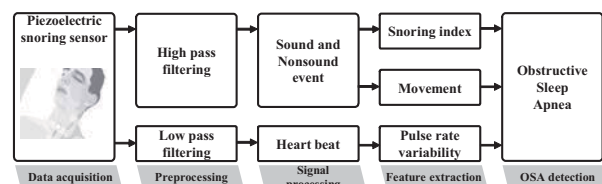


Fig. 1. Block diagram of the OSA detection algorithm using a piezoelectric sensor.

B. Signal processing

Simple signal energy method was used to detect snoring and movement, and an autocorrelation method was used to estimate the pulse rate from a piezoelectric sensor signal. Then snoring index and pulse rate variability was calculated to detect OSA.

C. OSA detection

An OSA detection criterion is performed by using snoring index, movement, and pulse rate variability. Snoring index and movements were used to figure out the apneic candidate segment and final decision is used by PRV features.

III. RESULTS

Table 1 presents the OSA detection results by the proposed algorithm. The mean sensitivity and specificity of the training set were 86.8% and 71.3%, respectively, and those of test set were 93.2% and 80.1%.

Table 1. The results of OSA detection

Features	Data set	Sensitivity (%) (mean \pm std.)	Specificity (%) (mean \pm std.)
Snoring index, PRV features	training set	86.8 \pm 16.1	71.4 \pm 8.2
	test set	93.2 \pm 9.5	80.1 \pm 13.4

These results demonstrate that the proposed method can be efficiently applied to sleep apnea screening and diagnosis. Moreover, the sensitivity of the proposed method was found to be relatively higher than existing tools.

ACKNOWLEDGEMENT

This study was funded by the 2014 Regional Innovative Manpower Training Program (NRF-2014H1C1A1063845) of the Ministry of Education and Korea Research Foundation.

REFERENCES

1. T. Young, L. Evans, L. Finn, and M. Palta, "Estimation of the clinically diagnosed proportion of sleep apnea syndrome in middle-aged men and women," *Sleep*, vol.20, no.9, pp.705-706, 1997.

Assessment of Sleep Efficiency based on Cardiopulmonary Coupling Analysis

J. U. Park, P. S. Jeong, and K. Y. Lee

Department of Biomedical Engineering, Yonsei University, Wonju, Republic of Korea
E-mail: pjwwhite01@naver.com, happy27boys@gmail.com, lkj5809@yonsei.ac.kr

Abstract— This study proposes a cardiopulmonary coupling (CPC)-based assessment of sleep efficiency (SE). CPC was induced from nasal pressure (NP) respiration and normal-to-normal interval series of photoplethysmogram (PPG). We conducted the statistical analysis between CPC parameters and sleep efficiency. CPC parameters show a significant difference between the Low SE (<85%) and the High SE ($\geq 85\%$). Therefore, this method showed the potentials to be used for assessing the sleep efficiency for CPAP device.

Keywords— Cardiopulmonary coupling (CPC) analysis, Sleep efficiency

I. INTRODUCTION

Continuous positive airway pressure (CPAP) is the most widely prescribed treatment for obstructive sleep apnea hypopnea (OSAH) [1]. The analysis software of CPAP device provides sleep-disordered breathing (SDB) indices [1]. But, it is important to provide indices able to assess the sleep efficiency (SE) as well as the SDB index.

Therefore, we investigate the feasibility for assessment of sleep efficiency based on CPC analysis in patients with sleep apnea-hypopnea syndrome for CPAP device.

II. METHODS

Figure 1 presents the schematic of the method for CPC analysis using nasal pressure (NP) and PPG. Detailed procedure of the method is described below.

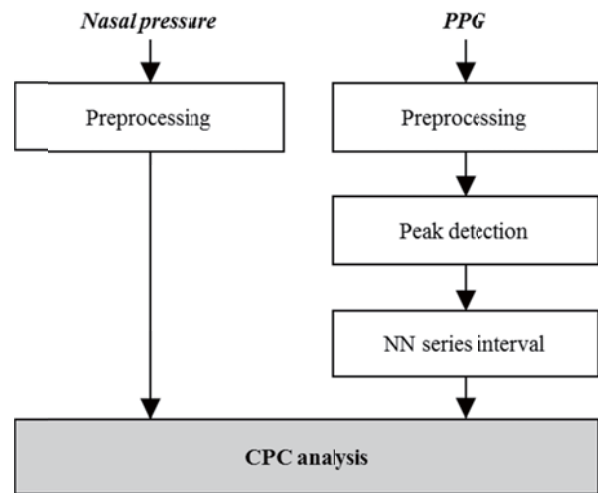


Fig. 1. Schematic of the method for CPC analysis

A. Signal processing of nasal pressure

The raw NP signal was preprocessed with the 51th order median filter to reduce unwanted background spike noise and snoring-related noise.

B. Signal processing of photoplethysmogram

To calculate pulse-to-pulse intervals of PPG, baseline wander and power noise were removed using band-pass filter of 0.1 to 5 Hz, and a maximum point of pulse was detected using an adaptive threshold algorithm.

C. Cardiopulmonary coupling (CPC) analysis

CPC is obtained as the product of the coherence and cross-power of resampled NP signal and NN interval series. And then, we extracted CPC parameters; low frequency coupling (0.01-0.1 Hz, LFC) and high frequency coupling (0.1-0.5 Hz, HFC).

III. RESULTS

A. Linear regression analysis

Compared with HFC, SE was significantly increased ($y=0.6x+3.0$, $r=0.45$, $p<0.001$). However, compared with LFC, SE was significantly decreased ($y=-0.5x+70.4$, $r=-0.36$, $p<0.001$).

B. One-way ANOVA test

One-way ANOVA test show a significant between the low SE (<85%) and high SE ($\geq 85\%$) (HFC; $p<0.001$, LFC; $p<0.001$).

IV. CONCLUSION

This method showed the potentials to be used for assessing the sleep efficiency for CPAP device.

ACKNOWLEDGEMENT

This work was supported by the Human Resource Training Program for Regional Innovation and Creativity through the Ministry of Education and National Research Foundation of Korea (NRF-2014H1C1A1063845).

REFERENCES

1. K. Ueno, et al., "Evaluation of the apnea-hypopnea index determined by the S8 auto-CPAP, a continuous positive airway pressure device, in patients with obstructive sleep apnea-hypopnea syndrome," *J. Clin. Sleep Med.*, vol. 6, no. 2, pp. 146-151, 2010.

Density-dependent changes of dielectric properties in live human breast cancer cell

Kwan Hwi Ko¹, Min Hyung Kim¹, Seungyeop Choi¹, Myeonggu Son¹ and Sang Woo Lee^{1*}

¹Department of Biomedical Engineering, Yonsei University, Wonju, Republic of Korea.
E-mail: yusuklee@yonsei.ac.kr

Abstract— We demonstrate that the microfluidic dielectrophoretic (DEP) chip enables detection of several characteristics of live MCF-7 human breast cancer cells with their confluence changing. Measurement was achieved using subtle variations in dielectrophoresis properties of the cells, which were attributed to decrease of cell vitality and their size.

Keywords— Dielectrophoresis, Cell confluence, Contact inhibition

I. INTRODUCTION

General adhesion cells grown in culture will become growth inhibited when they encounter another cell. Growth mechanisms like contact inhibition are in place to stop or continue cell growth depending on the conditions. Contact inhibition has some effects on cell's characteristics such as its size, vitality, cell cycle and so on. Microfluidic dielectrophoresis (DEP) devices are useful in cell sorting and manipulation as a result of subtle changes in dielectrophoretic properties depending on cell type, size, and surrounding conditions [1]. On the basis of quantitative analysis data, we can provide the first report of the shift of the complex permittivity of a cell induced by the confluence changing of MCF-7 human breast cancer cells.

II. METHODS

The microfluidic device was fabricated through photolithography and a lift-off process. And circular trap windows were etched resulting in exposure of circular regions on the electrode. The MCF-7 human breast cancer cell was seeded in different days and the experiment did at the same time. The experimental buffer consisted of 8.6% (w/w) sucrose, 0.3% (w/w) glucose, 1.0 mg/mL bovine serum albumin and 0.25% PBS. An ac signal was applied to the electrode of the chip at varying amplitudes and frequencies using a function generator. Cell movement was observed and recorded using a charge-coupled device camera.

III. RESULTS

The cut-off frequency of 24 hours control group in our experimental solution is about 8 kHz. And the

longer seeding time was, the higher cut-off frequency was observed, especially over 48 hours. The mean values of trapping frequency in 24, 48, 72, 96 and 120 hours seeding time, were measured 8.11, 8.22, 9.40, 10.42 and 11.25 kHz in 2 V_{p-p}, respectively. We also observed the cut-off frequency of G1 arrested cells by treatment of thymidine. And we observed that the cut-off frequency of G1 cells became lower than control group. So these results were caused by difference of DEP force and CM factor in accordance with the characteristics of cells except cell cycle factor.

IV. CONCLUSION

In this study, we investigated cellular biological properties within a microfluidic dielectrophoresis device using a novel technique for analyzing cell biological properties with the degree of their contact inhibition.

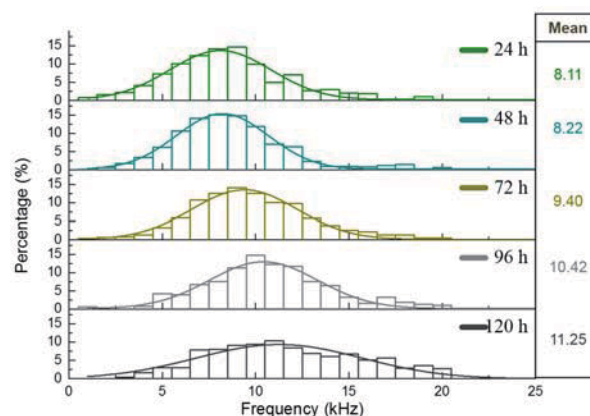


Fig. 1. The percentage graph of trapped cell in different frequency.

ACKNOWLEDGEMENT

This work was supported by the NRF grant (NRF-2013R1A2A2A03005767, NRF-2013R1A1A2053613).

REFERENCES

1. Hsiung, L. C., Chiang, C. L., Wang, C. H., Huang, Y. H., Kuo, C. T., Cheng, J. Y., Lin, C. H., Wu, V., Chou, H. Y., Jong, D. S., Lee, H., and Wo, A. M., "Dielectrophoresis-based cellular microarray chip for anticancer drug screening in perfusion microenvironments", *Lab Chip*, vol. 11, pp.2333–2342, 2011,

Pressure sensors using conductive fabric and PU/PVDF nanoweb

Y. J. Jeong¹, T.I. Oh¹, K. J. Kim², and E. J. Woo¹

¹Department of Biomedical Engineering, Kyung Hee University, Seoul, Republic of Korea

²Department of Advanced Materials Engineering for Information & Electronics, Kyung Hee University, Yongin, Republic of Korea

E-mail: tioh@khu.ac.kr

Abstract— In this study, we present the new design of pressure sensors using piezo-capacitive and piezo-electric phenomena to measure static and dynamic pressure. They have the layered structure made of pieces of nanoweb and conductive fabric to form a pressure sensor. We measured impedance changes and electric potential changes due to compressive force together. Multi-layered sensor had more sensitive to applied pressure than the simple fabric sensor.

Keywords— Pressure sensor, piezo-capacitive, piezo-electric, nanoweb, impedance.

I. INTRODUCTION

In order to provide the wearable healthcare monitoring, pressure distribution sensors using fabric materials are required. The pressure measurement method using conductive fabrics and electrical impedance imaging technique has a high potential to present pressure distribution with cost-effective way [1]. However, this method has intrinsic difficulties due to non-linearity and less sensitivity [2]. In this study, we developed pressure sensors using conductive fabrics with polyvinylidene fluoride (PVDF)/polyurethane (PU) nanoweb. It uses the piezo-electric response for dynamic pressure and the piezo-capacitive and piezo-resistive response for dynamic and static pressure sensing. We designed and evaluated the performance of multi-layered fabric pressure sensors.

II. METHODS

We made two type of pressure sensors consist of commercial conductive fabric (NW170-SLPA-20K, Enox, USA) with 1) PU and 2) PVDF nanoweb which has piezo-capacitive and piezo-electric effect, respectively. And we evaluated the basic performance of each sensor in the testing setup as shown in Fig.1.



Fig. 1 Setup for evaluating the basic performance of two types of pressure sensors (left: piezo-capacitive, right: piezo-electric)

III. RESULTS

At first, we measured impedance changes due to the compressive force of 0.5, 1, 2, 5, 10, 15 and 20 kgf. When increasing the weight on the fabric pressure

sensors, percentile impedance changes for each sensor were presented in Fig. 2(a). Fig. 2(b) and (c) show the piezo-electric outputs of multi PVDF layered sensors.

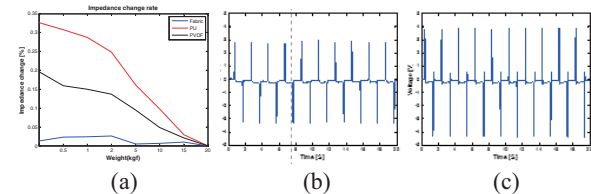


Fig. 2 (a) Percentile impedance change for 2 sensors compared with conventional fabric sensor, (b) 2 layers PVDF nanoweb measured piezo-electric (V_{p-p} : 6.33V) (c) 5 layers PVDF nanoweb measured piezo-electric (V_{p-p} : 8.51 V).

We measured the induced voltage difference at 16 adjacent pairs of electrodes at the boundary of fabric sensor when applying a constant current between a chosen pair of 16 electrodes. We reconstructed impedance images from the boundary measurement data. Fig. 3 displayed two type of pressure sensors when pressing the different positions.

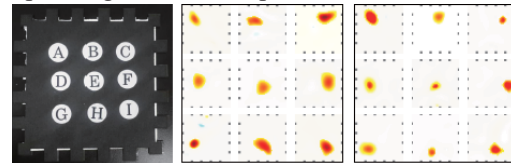


Fig 3: Reconstructed impedance images on two types of pressure sensors (mid, PU sensor / right, PVDF sensor)

IV. CONCLUSION

We proposed two kinds of fabric pressure sensors to improve the sensitivity compared to the conventional fabric sensor. Using the electrical impedance tomography (EIT) technique, we produced the pressure distribution maps on two kinds of fabric pressure sensors. We plan to optimize the measurement system to visualize pressure distribution using the multi-layered fabric pressure sensor.

ACKNOWLEDGEMENT

It was by the Industrial Strategic Technology Development Program (10047976) funded by the Ministry of Trade, Industry, and Energy of Korea.

REFERENCES

1. F. Carpi and D. De Rossi, "Electroactive polymer-based devices for e-textiles in biomedicine," *Information Technology in Biomedicine*, IEEE Transactions on, vol. 9, no. 3, pp. 295-318, 2005.
2. T. K. Bera, Y. Mohamadou, K. Lee, H. Wi, T. I. Oh, E. J. Woo, M. Soleimani, and J. K. Seo, "Electrical impedance spectroscopy for electro-mechanical characterization of conductive fabrics," *Sensors*, vol. 14, no. 6, pp. 9738-9754, 2014.

An Instant Electrical Power Generating Air Cathode Paper Battery

Y. J. Ahn¹, J. C. Lee², H. K. Park^{1,2}, and S. Choi^{1,2*}

¹ Department of Medical Engineering, Kyung Hee University, Seoul 130-701, Korea

² Department of Biomedical Engineering, College of Medicine, Kyung Hee University, Seoul 130-701, Korea

*E-mail: medchoi@khu.ac.kr

Abstract—We introduce a micro-fabricated paper-based platform to generate instant electrical power catalyzed by microbial metabolism. All layers were made by the filter paper. The anode for bacteria adhesion was fabricated through screen printing of carbon ink and the cathode for electron acceptance was fabricated through Ni-coated activated carbon (AC) printing with carbon black (CB). The proton exchange membrane (PEM) was fabricated by nafion reagent on the cathode layer. Additional series connection of *Shewanella oneidensis*-powered battery may provide the desired values of current and potential to operate single use device.

Keywords— AC+BC, instant power, paper, MFC.

I. INTRODUCTION

Microbial fuel cell (MFC) is a potential eco-friendly energy technology. It produces the electrical power by metabolism of microorganism. But, electrical power ($0.4 \mu\text{W}/\text{cm}^2$ – $1 \text{mW}/\text{cm}^2$) generated from small MFCs is somewhat low to be used in conventional electrical device [1]. This small power is suitable for single use POC device. In small MFC, a paper-based substrate has an advantage for its potential integration into simple, low-cost, portable, disposable analytic or diagnostic devices that are suitable for resource-limited [2]. Therefore, we introduce the preliminary finding regarding an instant power generating device through a paper-based air cathode electrode of activated carbon (AC) with carbon black (CB).

II. METHODS

A. Materials

Whatman #1 filter paper and nafion (Sigma Aldrich), AC Sx Plus (OS Company), CB XC 72R (Vulcan), carbon ink (GWENT), Nickel spray (MG chemical), wild-type *Shewanella oneidensis* MR-1 (ATCC).

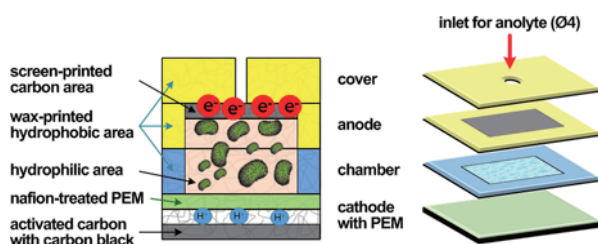


Fig. 1. Schematic diagram of paper-based instant power generating air-cathoding MFC battery device consisting of four layers. PEM indicates a proton exchange membrane.

B. Fabrication of MFC Paper Platform

Figure 1 shows a fully assembled our MFC battery device. It consists of four layers such as cover, anode, chamber, and air-cathode with proton exchange membrane (PEM). Wax printing was used for hydrophobic area or boundary of cover, anode, and chamber layers. The anode electrode was made by screen printing of carbon ink whereas the cathode electrode was made by mixture of AC and CB powers on Ni-coated layer. The cathode was retreated the nafion solution for making the PEM to pass only H^+ .

III. RESULTS

The optimal AC and CB mixture with the maximum electrical power was estimated using a 3:1 volume ratio of AC to CB. The maximum open circuit voltage (OCV) of the fabricated MFC device was about 250 mV and 50 nA. The voltage immediately after the inoculation began to generate, however the voltage continued to gradually drop throughout one hour and reached to zero.

IV. CONCLUSION

In summary, we developed a facile paper-based MFC battery with AC-based air cathode carbon electrode, generating a 250-mV OCV and a 50-nA current. Our bacteria-powered MFC device has the advantages of facile and simple fabrication, low-cost, and disposable. Although the performance of MFC battery was lower than the conventional MFC, however it is available to the power for simply single use diagnostic sensor.

ACKNOWLEDGEMENT

This work was supported by the NRF grant (2014R1A1A2054452) and the Korean Health Technology Research & Development Project grant by the Ministry of Health & Welfare (HI14C2241).

REFERENCES

1. A. Fraiwan, S. Mukherjee, S. Sundermier, H. S. Lee, and S. Choi, "A paper-based microbial fuel cell: instant battery for disposable diagnostic devices," *Biosens. Bioelectron.*, vol. 15, pp. 410-414, 2013.
2. H. Lee and S. Choi, "An origami paper-based bacteria-powered battery," *Nano energy*, vol. 15, pp. 549-557, 2015.

An Instant Electrical Power Generating Air Cathode Paper Battery

Y. J. Ahn¹, J. C. Lee², H. K. Park^{1,2}, and S. Choi^{1,2*}

¹ Department of Medical Engineering, Kyung Hee University, Seoul 130-701, Korea

² Department of Biomedical Engineering, College of Medicine, Kyung Hee University, Seoul 130-701, Korea

*E-mail: medchoi@khu.ac.kr

Abstract—We introduce a micro-fabricated paper-based platform to generate instant electrical power catalyzed by microbial metabolism. All layers were made by the filter paper. The anode for bacteria adhesion was fabricated through screen printing of carbon ink and the cathode for electron acceptance was fabricated through Ni-coated activated carbon (AC) printing with carbon black (CB). The proton exchange membrane (PEM) was fabricated by nafion reagent on the cathode layer. Additional series connection of *Shewanella oneidensis*-powered battery may provide the desired values of current and potential to operate single use device.

Keywords— AC+BC, instant power, paper, MFC.

I. INTRODUCTION

Microbial fuel cell (MFC) is a potential eco-friendly energy technology. It produces the electrical power by metabolism of microorganism. But, electrical power ($0.4 \mu\text{W}/\text{cm}^2$ – $1 \text{mW}/\text{cm}^2$) generated from small MFCs is somewhat low to be used in conventional electrical device [1]. This small power is suitable for single use POC device. In small MFC, a paper-based substrate has an advantage for its potential integration into simple, low-cost, portable, disposable analytic or diagnostic devices that are suitable for resource-limited [2]. Therefore, we introduce the preliminary finding regarding an instant power generating device through a paper-based air cathode electrode of activated carbon (AC) with carbon black (CB).

II. METHODS

A. Materials

Whatman #1 filter paper and nafion (Sigma Aldrich), AC Sx Plus (OS Company), CB XC 72R (Vulcan), carbon ink (GWENT), Nickel spray (MG chemical), wild-type *Shewanella oneidensis* MR-1 (ATCC).

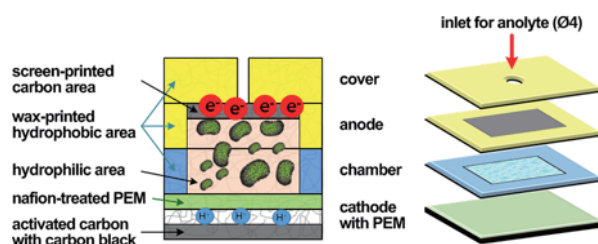


Fig. 1. Schematic diagram of paper-based instant power generating air-cathoding MFC battery device consisting of four layers. PEM indicates a proton exchange membrane.

B. Fabrication of MFC Paper Platform

Figure 1 shows a fully assembled our MFC battery device. It consists of four layers such as cover, anode, chamber, and air-cathode with proton exchange membrane (PEM). Wax printing was used for hydrophobic area or boundary of cover, anode, and chamber layers. The anode electrode was made by screen printing of carbon ink whereas the cathode electrode was made by mixture of AC and CB powers on Ni-coated layer. The cathode was retreated the nafion solution for making the PEM to pass only H^+ .

III. RESULTS

The optimal AC and CB mixture with the maximum electrical power was estimated using a 3:1 volume ratio of AC to CB. The maximum open circuit voltage (OCV) of the fabricated MFC device was about 250 mV and 50 nA. The voltage immediately after the inoculation began to generate, however the voltage continued to gradually drop throughout one hour and reached to zero.

IV. CONCLUSION

In summary, we developed a facile paper-based MFC battery with AC-based air cathode carbon electrode, generating a 250-mV OCV and a 50-nA current. Our bacteria-powered MFC device has the advantages of facile and simple fabrication, low-cost, and disposable. Although the performance of MFC battery was lower than the conventional MFC, however it is available to the power for simply single use diagnostic sensor.

ACKNOWLEDGEMENT

This work was supported by the NRF grant (2014R1A1A2054452) and the Korean Health Technology Research & Development Project grant by the Ministry of Health & Welfare (HI14C2241).

REFERENCES

1. A. Fraiwan, S. Mukherjee, S. Sundermier, H. S. Lee, and S. Choi, "A paper-based microbial fuel cell: instant battery for disposable diagnostic devices," *Biosens. Bioelectron.*, vol. 15, pp. 410-414, 2013.
2. H. Lee and S. Choi, "An origami paper-based bacteria-powered battery," *Nano energy*, vol. 15, pp. 549-557, 2015.

Enzymatic Fiber Biofuel Cell for Implantable Applications

Cheong Hoon Kwon¹, Young Bin Park¹, and Seon Jeong Kim*

Center for Self-powered Actuation and Department of Biomedical Engineering, Hanyang University, Seoul, Korea

¹These authors contributed equally to this work.

*E-mail: sjk@hanyang.ac.kr

Abstract—Biofuel cells are promising power source for implantable biomedical devices. However, there is a limitation considering toxicity of metallic mediator. Here we introduce Enzymatic Fiber biofuel cell for implantable applications with self-assembled carbon nanotube fiber to induce direct electron transfer without metallic mediator.

Keywords—enzymatic biofuel cell, carbon nanotube, self-assembly, implantable applications, fiber

I. INTRODUCTION

Enzymatic biofuel cells can be excellent bio-energy source for implantable devices. However, metallic mediators usually used in biofuel cell for effective reaction,^[1] could potentially generate toxicity issues. Here, we overcame the limitation with self-assembled yarn electrode consists of carbon nanotube (CNT) and conducting polymer poly(3,4-ethylenedioxythiophene) (PEDOT).

II. METHODS

CNT sheets were prepared on a polytetrafluoroethylene supporter and PEDOT was coated on the sheet. PEDOT-coated CNT sheet was immersed in enzyme solution, glucose oxidase and bilirubin oxidase for the anode and cathode, respectively. After 24 hours, they were taken out and dried for a few hours at room temperature. Finally, the shrunken CNT anode and cathode were fabricated as shown in Fig. 1.

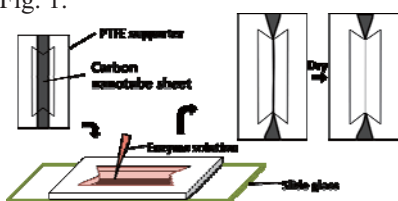


Fig. 1. Enzyme-loaded fiber electrodes fabrication

III. RESULTS

The surface images of the BFC electrode are shown in scanning electron microscopy (SEM) images in Fig. 2. Although we did not use any manual procedures, the self-assembled fiber biofuel cell electrode has a vertically aligned and compressed fiber-type structure.

Performance of biofuel cell was measured by cyclic voltammetry by two-electrode system. The maximum power density at 5 mmol L⁻¹ glucose in phosphate-

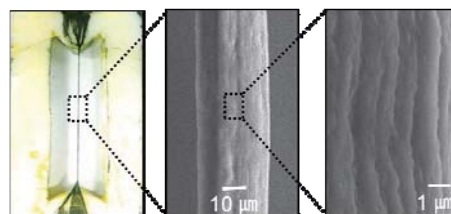


Fig. 2. SEM images showing surfaces of the fiber electrode

buffered saline (PBS) was 82 $\mu\text{W cm}^{-2}$, and 167 $\mu\text{W cm}^{-2}$ at 0.3 V in 30 mmol L⁻¹ glucose in PBS. In addition, the stability of the complete system was measured under 5 mmol L⁻¹ glucose in PBS for 10 days by cyclic voltammetry. Our system maintained 83% of its initial power after 10 days (Fig. 3).

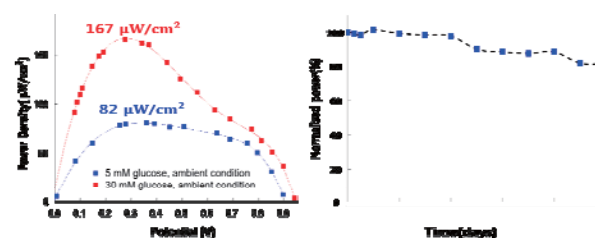


Fig. 3. Power and Stability Performance of fiber biofuel cell

IV. CONCLUSION

We fabricated fiber type biofuel cell without any chemicals such as metallic mediator and cross-linker. Our system can generate 167 $\mu\text{W cm}^{-2}$ as the maximum power density, and maintain 83% of the power density after 10 days with continuous operation. It can be used in implantable devices included in catheter, syringe needle or stent.

ACKNOWLEDGEMENT

This work was supported by the Creative Research Initiative Center for Self-powered Actuation and the Korea-US Air Force Cooperation Program Grant (No.2013K1A3A1A32035592) of the NRF of Korea

REFERENCES

1. Kwon et al., "High-power biofuel cell textiles from woven bisrolled carbon nanotube yarns" *Nat. Commun.* 5, 3928. 2014.
2. Zebda et al., "Mediatorless high-power glucose biofuel cells based on compressed carbon nanotube-enzyme electrodes", *Nat. Comm.* 2, 370. 2011.

Electrochemical Immunosensors for Pepsin Detection in Saliva utilizing 3D Network Nanostructured Polypyrrole

Doyeon Lee¹, Yong Jin Ahn¹, Young Ju Lee², Hun-Kuk Park^{1,2}, and Gi-Ja Lee^{1,2,*}

¹ Dept. of Medical Engineering, Graduate School, Kyung Hee University, Seoul 130-701, Korea

² Dept. of Biomedical Engineering & Healthcare Industry Research Institute, College of Medicine, Kyung Hee University, Seoul 130-701, Korea

*E-mail: gilee@khu.ac.kr

Abstract — We have designed an electrochemical immunosensor for the detection of pepsin in saliva utilizing conducting polypyrrole hydrogels and gold nanoparticles onto screen printed electrode.

Keywords— Pepsin, Immunosensor, Screen printed electrode, Conducting polymer, Hydrogel

I. INTRODUCTION

Pepsin is a proteolytic enzyme produced only in the stomach.¹ It is the main aggressive agent responsible for damaging oesophageal and laryngeal tissue during reflux. Therefore detection of pepsin can be utilized as a good objective clinical measurement tool for the laryngopharyngeal reflux disease (LPRD). Nanostructured conducting polypyrrole hydrogels not only retain the unique properties of conducting polymers, but also possess the characteristics of nanomaterials such as large surface area, and the 3D continuous conducting network.

II. METHODS

A. Materials

Pyrrole, ammonium persulfate, phytic acid, and gold(III) chloride trihydrate were obtained from Sigma-Aldrich (St. Louis, MO, USA). A planar screen printed electrode (SPE) (Dropsens, Spain) was used for designing of electrochemical immunosensors.

B. Fabrication of immunosensing system

The first step is electropolymerization of pyrrole to form conducting polypyrrole (PPy) hydrogels on working electrode of SPE. We utilized phytic acid as the gelatinizer and dopant to synthesize a nanometer scale conducting network. The second step is electrochemical deposition of gold nanoparticles (GNP) onto the PPy/SPE. The final step is stable immobilization of pepsin antibody onto the modified electrode. Then, the assembled immunosensor was thoroughly rinsed with PBS to remove any unbound antibody and stored at 4 °C when not in use.

III. RESULTS

The morphologies of the PPy/SPE, GNP/PPy/SPE, PPy network/SPE, and GNP/PPy network/SPE were

investigated by SEM. The surface of PPy film exhibits the typical uniform granular morphology. But 3D PPy networks were composed of small PPy spheres stuck to each other. The porous nanoscale network of PPy can provide a greater effective surface area for increasing the quantity of immobilized biomolecules and facilitated the transport of electrons and ions.

Electrochemical impedance spectroscopy and cyclic voltammetry were used to monitor the stepwise fabrication process and the performance of the immunosensor. The current response of PPy network/SPE was higher than that of a bare SPE and PPy/SPE. In contrast, the loading of anti-pepsin led to an obvious decrease of the peak current owing to the formation of an electron-blocking layer. Subsequently, it was found that the current response decreased after the immunosensor was incubated in a pepsin solution.

IV. CONCLUSION

In summary, we reported an electrochemical immunosensing system for highly sensitive and specific detection of pepsin in saliva utilizing conducting polymer networks and GNP. It may represent a useful tool to aid preliminary diagnosis of reflux (rapid, non-invasive, and low cost).

ACKNOWLEDGEMENT

This study was supported by the industrial strategic technology development program funded by the Ministry of Trade, Industry & Energy (10049035) and the National Research Foundation of Korea (NRF) funded by the Ministry of Science, ICT & Future Planning (2015M3A9E2029188).

REFERENCES

1. N Johnston, "Uptake of pepsin at pH 7 – in non-acid reflux – causes inflammatory, and perhaps even neoplastic, changes in the laryngopharynx" *Aliment. Pharmacol. Ther.*, vol. 33, pp. 13-21, 2011.
2. Q Rong, H Han, F Feng and Z Ma, "Network nanostructured polypyrrole hydrogel/Au composites as enhanced electrochemical biosensing platform" *Sci. Rep.*, vol. 5, pp. 11440, 2015.

Colorimetric Detection of Hydrogen Sulfide utilizing Silver in Gas Permeable Membrane

Yong Jin Ahn¹, Doyeon Lee¹, Young Ju Lee², Hun-Kuk Park^{1,2}, and Gi-Ja Lee^{1,2,*}

¹Dept. of Medical Engineering, Kyung Hee University, Seoul 130-701, Korea

²Dept. of Biomedical Engineering & Healthcare Industry Research Institute, College of Medicine, Kyung Hee University, Seoul 130-701, Korea

*E-mail: gilee@khu.ac.kr

Abstract—In this study, we presented a colorimetric system for selective hydrogen sulfide (H₂S) detection utilizing silver (Ag⁺) ion and Nafion resin. The sensing principle is based on the fact that H₂S react with Ag⁺ ions to form Ag₂S nanoparticle. The Ag₂S nanoparticles have a strong absorption in the UV range. As Nafion does not disturb the optical properties of the microplate cover, we utilize the conventional microplate cover for the detection of free H₂S. This H₂S assay is a simple and low cost as compared to other detection methods, as well as real-time monitoring of H₂S gas.

Keywords— Hydrogen sulfide, Colorimetric detection, Microplate, Silver

I. INTRODUCTION

Hydrogen sulfide (H₂S) is referred to as “gasotransmitter” – similar to nitric oxide (NO) and carbon monoxide (CO) and it plays an important role in mammalian physiology as a neuromodulator and transmitter, especially in the brain and heart. Direct measurement strategies are necessary for examining biological processes and diseases related to H₂S in biological conditions, in particular the action of endogenously produced H₂S. therefore we suggest a simple, low cost and real-time method for H₂S detection.

II. METHODS

A. Materials

SPL 96-well microplates were obtained from SPL LIFE SCIENCES. And nafion, glycerol and sodium sulfide nonhydrate were purchased from Sigma Aldrich (St. Louis, MO, USA). Silver nitrate was obtained from Duksan Pure Chemicals Co., Ltd. (Ansan, GyeongGi, Korea).

B. Fabrication of microplate cover

Microplate cover was coated with the mixtures (silver/Nafion+glycerol). And the cover was dried at room temperature for at least 1 h before use.

C. Sensitivity and selectivity measurement

For H₂S detection, 300 μl solutions with different concentrations of Na₂S (from 12.5 to 200 μM) were added into microplate well. Then, the plate was cov-

ered immediately with the Nafion coated cover. All measurements were done utilizing a Biotek (synergy HT) plate reader at 310nm.

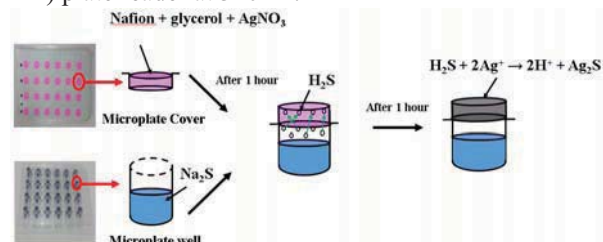


Fig. 1. Schematic diagrams of the sensing principles of our 96-well microplate based hydrogen sulfide (H₂S) detection assay

III. RESULTS

Because the hydrophilicity played an important role on the dispersion of Ag/Nafion+glycerol mixtures on microplate cover (polystyrene), we investigated the optimum mixing ratio of Nafion and glycerol. At higher ratio of glycerol, small coffee-ring effect (good dispersion) occurred.

The absorbance at 310 nm showed a good linear relationship ($R^2 = 0.99$) vs. Na₂S concentration ranging from 12.5 to 200 μM. To examine specificity, Na₂S was compared to cysteine, glutathione, and dithiothreitol. They did not interfere on the detection of H₂S, revealing excellent selectivity of the assay toward H₂S.

IV. CONCLUSION

In summary, we have introduced a simple colorimetric detection assay for hydrogen sulfide. Highly sensitive and specific H₂S detection was achieved on the basis of a silver-H₂S reaction. The high sensitivity suggests that this assay has great potential for real application like clinical sample analysis.

ACKNOWLEDGEMENT

This study was supported by the National Research Foundation of Korea (NRF) funded by the Ministry of Education (2013R1A1A2065149).

REFERENCES

1. A. P. Jarosz, T. Yep, B. Mutus, “Microplate-Based Colorimetric Detection of Free Hydrogen Sulfide”, *analytical chemistry*, vol.85, pp. 3638-3643, 2013.

Bacteria Screening System using Aptamer Probed Electrical Impedance Spectroscopy Gap Capacitance Biosensor

H. W. Lee¹, H. G. Kwon¹, J. H. Lee², D. S. Kim², S. W. Lee³, and O.C. Jeung^{1,4}

¹Shool of biomedical engineering, Inje university, Gimhea, Korea

²Shool of biological sciences, Inje university, Gimhea, Korea

³Department of chemistry, The University of Tokyo, Tokyo, JAPAN

⁴Graduate school of mechanical engineering, Inje university, Gimhea, Korea

E-mail: memsoku@inje.ac.kr

Abstract—We developed EIS gap capacitance biosensor for rapid and sensitive bacteria screening using RNA based bacteria recognized aptamer.

Keywords— Bacteria, Aptamer, Microfluidics

I. INTRODUCTION

Rapid and sensitive detection of pathogen bacteria gains great interest recently since bacterial infected diseases are one of the main threats of food safety of public health even under-developed and sometime well-developed country.

II. METHODS

Figure 1(a) shows the schematic view of the biosensor. It consists of two Au/Cr electrodes deposited on the glass substrates for impedance sensing and a fluidic PDMS channel. For the fluidic interconnection, the through-holes were fabricated using the sandblast for the upper glass substrate and the manual punching tool for PDMS fluidic layer. The surface area of electrode was 50 mm² and the height of PDMS layer was 200 μm. The fabricated upper-sensor glass plate was shown in figure 1(b).

III. RESULTS

E-coli was chosen as a model target because it is one of relevant indicator of contaminations of food and drinking water sources [1]. Thiol-modified gram-negative bacteria targeting aptamer was firstly injected and incubated into the chip. After washing of unbound aptamer, titration of bacteria solution (10⁵, 10⁷, and 10⁹ Cells/mL) was introduced into the chip. After 30 minutes incubation, washing process as followed and finally EIS measurement were performed. A Nyquist plot from impedance analysis of each bacteria solution and negative control were shown in Fig. 2. Each impedance signal is clearly different to that of negative control (No bacteria). More interestingly, a resistance of the biosensor in its high frequency (100 kHz) increases in proportional to the number of bacteria in solution.

IV. CONCLUSION

The developed biosensor currently has detection limits of bacteria around 10⁵ Cells/mL without labeling and signal amplification techniques. We are now

further developing the biosensor to improve detection sensitivity.

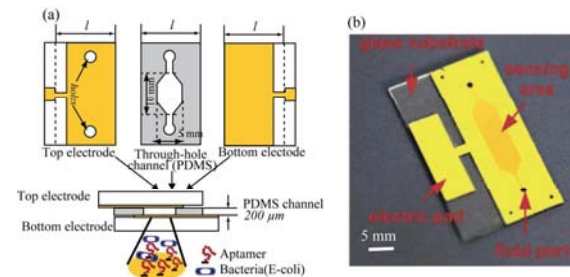


Fig. 1. Layout of the chip and fabricated sensor.

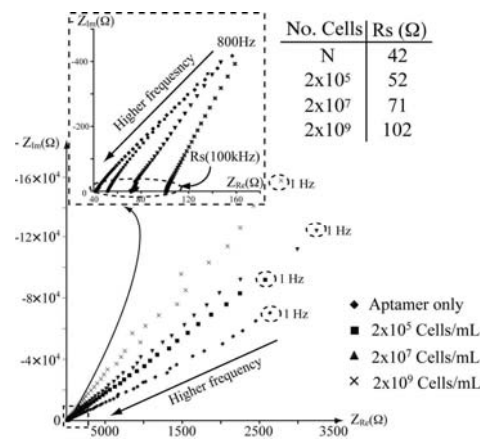


Fig. 2. Impedance analysis of bacteria solution and negative control (No bacteria).

ACKNOWLEDGEMENT

This research was supported by Basic Science Research Program through the National Research Foundation of Korea (NRF) funded by the Ministry of Education (NRF-2013R1A1A2012537).

REFERENCES

1. C. Tlili, E. Sokullu, M. Safavieh, M. Tolba, M. U. Ahmed, M. Zourob, Bacteria Screening, Viability, And Confirmation Assays Using Bacteriophage-Impedimetric / Loop-Mediated Isothermal Amplification Dual-Response Biosensors, *Anal. Chem.*, 2013, 85 (10), pp 4893–4901

Surface Potential Mapping of DNA Capped Nanoparticles for Point Mutation Detection

H. Lee¹, W. Lee¹, S. W. Lee², S. W. Lee¹ and D. S. Yoon²

¹Department of Biomedical Engineering, Yonsei University, Wonju 220-710, Republic of Korea

²School of Biomedical Engineering, Department of Bio-convergence engineering, Korea University, Seoul 136-701, Republic of Korea

E-mail: dsyoon@korea.ac.kr

Abstract— Quantitatively mapping surface potential (SP) with nanometer or single molecule resolutions is critical for advanced Kelvin probe force microscopy (KPFM) characterization. In this work, we proposed a novel gene detection approach with DNA capped nanoparticles (DCNP) to efficiently detect and predict SP mapping. SP of DCNP with various substrates such as Au, Si, SiO₂, and Fe were quantitatively characterized using KPFM, implying that a combination of DCNP and KPFM gives a chance for highly efficient detection of genetic point mutation. This novel gene detection method opens a new route toward highly efficient detections without the enhancement of instrumentation capabilities.

Keywords— Kelvin probe force microscopy, DNA, point mutation, surface potential,

I. INTRODUCTION

Genomic assay has been of great interest in diagnostic field [1]. Moreover, for the point-mutation detection of nucleic acids, researchers have employed nanotechnology. For example, nanopore systems have detected DNA sequence. Most notably, the use of hairpin-loop probe DNA in solid-state nanopore channels resulted in electrophoretic transport of DNA through nanopore, as compared with a single to three base-pair mismatch [2]. There, however, have not yet been developed to system for efficient detection with various substrates. Here we report the development of KPFM of DCNP with various substrates including Au, Si, SiO₂, and Fe, which could not only improve the detection sensitivity of the SP signal of the DCNP due to amplification, but could also provide a precise examination of DNA-DNA interactions.

II. METHODS

Double-stranded DNA (dsDNA) which is hybridized with probe DNA and target DNA is immobilized on AuNP (~100 nm, Sigma Aldrich) which is called DNA capped nanoparticle (DCNP). The SP measurements of DCNP were performed using an atomic force microscope (AFM) (Multimode V, Veeco, CA, USA). Conducting probes (SCM-PIT, Bruker, CA, USA) were mounted in a tip holder (MMEFCH, Veeco, CA, USA),

which is capable of controlling the voltage applied to the AFM tip. In SP measurement, we used the lift-mode KPFM, which is based on a dual line-scan system.

III. RESULTS

We showed that DCNP (i.e., P-C DCNP and P-M₁ DCNP) and KPFM are very useful tools to discern gene mutation with a single point level nucleotide by measuring the surface potential (SP) on various substrates.

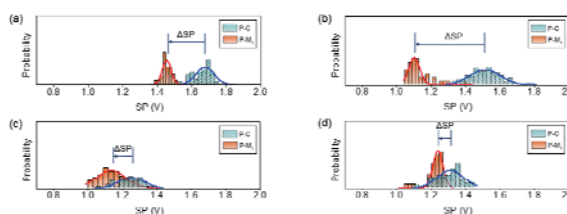


Fig. 1. Gaussian distribution of the P-C DCNP (blue bar, referred to as P-C) and the P-M₁ DCNP (red bar, referred to as P-M1) on Au substrates (a), p-type Si substrates (b), SiO₂ substrates (c), and Fe substrates.

IV. CONCLUSION

In summary, the SP Gaussian distribution of DCNP bounded on the p-type Si substrate shows large variance of SP between P-C DCNP and P-M₁ DCNP. This suggests that we can easily and more precisely discriminate the single point mismatch at the nucleotide level, which is in sequence of the target DNA, than the other substrates.

ACKNOWLEDGEMENT

This work was supported by grant of the Korea Health Industry Development Institute (KHIDI), funded by the Ministry of Health & Welfare, Republic of Korea (grant number: HI12C1837).

REFERENCES

1. E. S. Lander *et al.*, "Initial sequencing and analysis of the human genome", *Nature*, vol. 409, pp. 860-921, 2001.
2. B. M. Venkatesan, R. Bashir, "Nanopore sensors for nucleic acid analysis", *Nat. Nanotech.*, vol. 6, pp. 615-624, 2011.

Direct measurement of the interaction force between hemicytosinium duplexes using dielectrophoretic force spectroscopy

Seungyeop Choi¹, Min Hyung Kim¹, Kwan Hwi Ko¹, Gyudo Lee¹, Myeonggu Son¹
Sei-Young Lee¹, Dae Sung Yoon², Sang Woo Lee^{1*}

¹Department of Biomedical Engineering, Yonsei University, Wonju, Republic of Korea.

²School of Biomedical Engineering, Korea University, Seoul, Republic of Korea.

E-mail: yusuklee@yonsei.ac.kr

Abstract— Force spectroscopy has been applied a widespread method for studying molecular interaction and utilized to understand hydrogen bond strength in nucleic acids. Here, we measured the chemophysical interactions between hemicytosinium duplexes which was involved in the different DNA immobilized densities and chain lengths using dielectrophoretic force spectroscopy. It is found that the chain length (i.e. 24-mer) and the density (i.e. 400 nM) was rarely affected by nonspecific interaction (i.e. electrostatic repulsion) in our systems.

Keywords— Dielectrophoresis, DNA, Hydrogen bond, Microfluidic device

I. INTRODUCTION

Force spectroscopy has been applied a widespread method for studying molecular interaction and utilized to understand hydrogen bond strength in nucleic acids [1]. Various force spectroscopy techniques demanded on the fabrication of advanced biomimetically functional surface to measure inter/intra molecular interactions. In order to minimize nonspecific interaction, it is indispensable to investigate the molecular surface density and chain lengths [2]. Meanwhile, it has reported that hemicytosinium duplexes (C-H⁺-C) can be formed i-moiif structure in telomeric DNA sequence or oncogene. Many studies have shown that hemicytosinium duplexes can be utilized in many different DNA nanomachines and nanostructures [3].

Here, we report measurement of the interaction between hemicytosinium duplexes with respect to DNA surface density and chain length using DEP force spectroscopy.

II. METHODS

The method consists of a two-step process; first, The polydimethylsiloxane (PDMS) well was put into contact with the interdigitated (IDT) chip containing immobilized poly-C DNA a micro-electrode device, and then AC voltage was applied to the electrodes in the microfluidic chip to generate the DEP force.

III. RESULTS

Our approach is to measure the DNA-DNA interaction using DEP force spectroscopy that are composite materials consisting of DEP chip substrate and polystyrene microsphere which was immobilized poly-cytosine DNA. We measured Hydrogen bond as different poly-cytosine DNA surface density (200nM, 400nM, 800nM) and chain length (6-mer, 12-mer, 24-mer) using DEP force spectroscopy (Fig. 1).

IV. CONCLUSION

In this study, we confirmed that hydrogen bond between two cytosine bases (C-H⁺-C) with DEP force spectroscopy. It will shed light on the development of a disposable biosensor based on our DEP force spectroscopy technology.

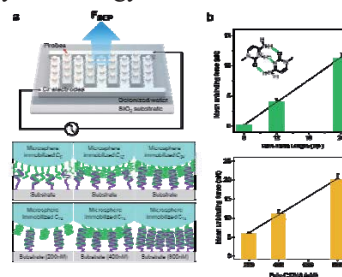


Fig. 1. Schematic view of DEP tweezers system and experimental conditions (a). Statistical analysis of mean unbinding force with respect to DNA surface density and chain lengths (b).

ACKNOWLEDGEMENT

This work was supported by the NRF grant (NRF-2013R1A2A2A03005767, NRF-2013R1A1A2053613).

REFERENCES

1. T.-H. Nguyen, L. J. Steinbock, H.-J. Butt, M. Helm & R. Berger, "Measuring Single Small Molecule Binding via Rupture Forces of a Split Aptamer," *J. Am. Chem. Soc.*, Vol 133, 2011, pp 2025-2027
2. M. M. Santore, J., Srivastava Zhang, S. & V. M. Rotello, "Beyond Molecular Recognition: Using a Repulsive Field to Tune Interfacial Valency and Binding Specificity between Adhesive Surfaces," *Langmuir*, Vol 25, 2008, pp 84-96
3. Patrizia Alberti *et al.* "DNA nanomachines and nanostructures involving quadruplexes," *Org. Biomol. Chem.*, Vol 4, 2006, pp 3383-3391

Fabrication of Paper-Based Air-Breathing Microbial Fuel Cells via Pencil

S. H. Lee¹, H. K. Park^{1,2}, and S. Choi^{1,2*}

¹ Department of Medical Engineering, Kyung Hee University, Seoul 130-701, Korea

² Department of Biomedical Engineering, College of Medicine, Kyung Hee University, Seoul 130-701, Korea

*E-mail: medchoi@khu.ac.kr

Abstract—We introduce a low cost, disposable paper-based microbial fuel cell (MFC) device. Anode electrode (bacteria adhesion) and cathode electrode (electron acceptance) were fabricated through pencil-stroked graphite on the paper. The fabricated MFC battery achieved the performance of 400 mV per one paper platform, by the metabolism of *Shewanella oneidensis* MR-1.

Keywords—pencil, graphite, paper, MFC.

I. INTRODUCTION

Microbial fuel cells (MFCs) are a promising green energy device powered by the bacteria. The MFC-based energy is generated by the oxidation and reduction reaction of the electrons produced by bacterial metabolism on an anode and the H^+ to pass proton exchange membrane (PEM) on a cathode. The selection of the anode, cathode, and PEM is critical to acquire high efficient energy [1]. However, most of MFCs have some disadvantages such as huge size, high cost for fabrication, complex peripheral devices, slow response time, etc [2]. Therefore, we introduce the preliminary finding regarding the development of a facile, low cost, disposable paper-based MFC device through a pencil-activated air-breathing electrode.

II. METHODS

A. Materials

Whatman #1 filter paper (Sigma Aldrich), 8B pencil (STAEDTLER), parchment paper (Reynolds), Nickel spray (MG chemical), wild-type *Shewanella oneidensis* MR-1 (ATCC).

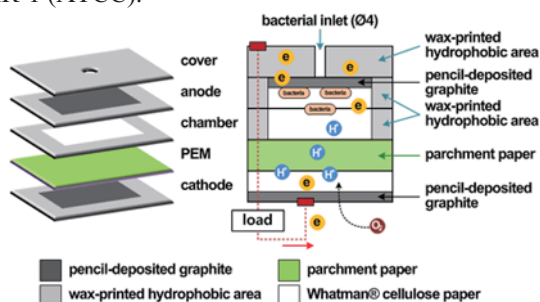


Fig. 1. Schematic diagram of paper-based bacteria-activated air-breathing battery through the pencil-deposited electrodes.

B. Fabrication of MFC Paper Platform

Figure 1 shows a fully assembled our MFC device. It consists of five layers such as cover, anode, chamber,

PEM, and cathode. Wax was used for hydrophobic area or boundary of cover, anode, and chamber layers. The anode and cathode electrodes were made by fourth pencil stroke. They were connected to Ni-coated paper strips.

III. RESULTS

Figure 2A shows the FE-SEM image of 8B pencil-stroked electrode surface (four cycles). The dense graphite deposited on cellulose fibers of the paper could be observed. The maximum open circuit voltage (OCV) of the fabricated MFC device (Fig. 2B) was about 400 mV. The voltage within 5 s after the inoculation began to generate, however the voltage continued to gradually drop throughout 1 hour and reached to zero.

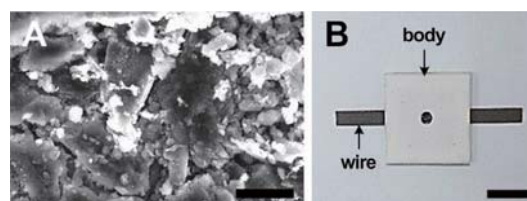


Fig. 2. (A) Representative FE-SEM image of pencil-stroked electrode surface and (B) a photo of paper-based MFC battery device. (A) Scale bar=25 μ m and (B) scale bar=15 mm.

IV. CONCLUSION

In summary, we developed a facile paper-based MFC device with pencil-activated air breathing electrode, generating a 400-mV OCV. Our MFC device has the advantages of facile and simple fabrication, low-cost, disposable. Although the performance of MFC device was lower than the conventional MFC, but, it is available to the power for simply diagnostic sensors.

ACKNOWLEDGEMENT

This work was supported by the NRF grant (2014R1A1A2054452) and the Korean Health Technology Research & Development Project grant by the Ministry of Health & Welfare (HI14C2241).

REFERENCES

1. H. Lee and S. Choi, "An origami paper-based bacteria-powered battery," *Nano energy*, vol. 15, pp. 549-557, 2015.
2. S. Choi, "Microscale microbial fuel cells: Advances and challenges," *Biosens. Bioelectron.*, vol. 69, pp. 8-25, 2015.

Cytokinetic Inter Nuclei Distance Stimulates Apoptosis of the Cancer Cell

Pawan K. Tiwari

Department of Biomedical Engineering, Catholic University of Daegu, Hayang, Republic of South Korea

E-mail: pawan.ktiwari@gmail.com ; pawankt@cu.ac.kr

Abstract—The inter nuclei distance during cytokinesis regulates the quantum of strength of electric field inducement at the cleavage furrow in response to the subjugation of the cancer cell to a moderate intensity AC electric field. A finite element analysis is presented in this paper to investigate the condition of intense electric field generation and its consequence on apoptotic death of the proliferating cancer cell.

Keywords—apoptosis, electrotherapy, extracellular matrix (ECM), finite element simulation (FEM).

I. INTRODUCTION

The treatment of cancer by means of the application of AC electric field has emerged as a modality in the clinical medical science recently. A moderate intensity electric field implemented in the cancer treatment is known as *electrotherapy* that has proved its therapeutic methodology in the treatment of solid brain tumor glioblastoma (GBM) [1]. The GBM proliferation is hindered due to the influence of distribution of electric field lines in quiescent and dividing cell. In the case of quiescent cell electric field lines delays the mitosis; while in the case of dividing cell, the intense electric field lines at the cleavage furrow stimulates electrophoresis of the cytoplasmic organelles and their disruption eventually. This kind of delay and disruption causes apoptosis of the cancer cell. The influence of electric field lines distribution is more pronounced during cytokinesis which in turn depends on the positioning of nuclei. An investigation is carried out in this paper to understand the effect of inter nuclei distance on the generation of intense electric field lines/intensity to stimulate the apoptosis.

II. METHODS

The proliferation of cancer cell results due to the weakening of the extracellular matrix (ECM) wherein the cell adhesion mechanism terminates [2]. Such termination subsequently promotes cell to divide in random direction. A dividing is simulated in a Maxwell two-dimensional (2D) finite element analyzer to explore the induced electric field intensity [3].

III. RESULTS

The strength of the induced electric field at the cleavage furrow distance depends on the center-to-

center distance (D) between the nuclei. Fig. 1-4 show the simulation results when the position of the nuclei is vertically above the cleavage furrow. When the distance D is varied between $3\mu\text{m}$ to $15\mu\text{m}$, the induced field strength at the cleavage furrow in all the four cases is of the order of 5×10^5 V/m; which is similar to the case as if the dividing cell were depleted of nuclei. Fig. 1(a)-4(a) show the corresponding electric field lines at the cleavage furrow.

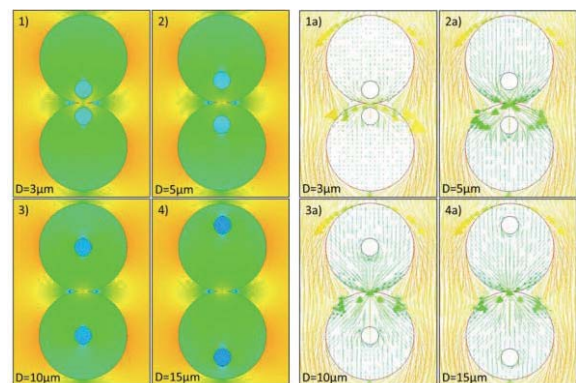


Fig. 1. Nuclei center-to-center distance (D) and its effect on electric field intensity distribution at the cleavage furrow.

IV. CONCLUSION

It is concluded that nuclei should be away from each other to a distance D greater than or equal to $3\mu\text{m}$ to create intense electric field intensity in order to affect the cytoplasmic organelles. However, if the distance D is lesser than $3\mu\text{m}$, the electric field strength at the cleavage furrow is reduced to a value of 2×10^5 V/m; which is incapable of producing any significant effect of apoptotic phenomena.

REFERENCES

1. E. D. Kirson, V. Dbaly, F. Tovarys, J. Vymazal, J. F. Soustiel, A. Itzhaki, D. Mordechovich, S. Steinberg-Shapira, Z. Gurvich, R. Schneiderman, Y. Wasserman, M. Salzberg, B. Ryffel, D. Goldsher, E. Dekel, and Y. Palti, "Alternating electric fields arrest cell proliferation in animal tumor models and human brain tumors," *Proc. Natl. Acad. Sci. U.S.A.*, vol. 104, pp. 10152-10157, 2007.
2. B. Alberts, A. Johnson, J. Lewis, M. Raff, K. Roberts, and P. Walter, *Molecular Biology of The Cell*, New York, Garland Science, 2008.
3. Pawan K. Tiwari, "Simulation and mathematical analyses of AC electric field driven apoptosis via microtubule disintegration," *Jpn. J. Appl. Phys.*, 2015, In Press.

Thermal damage control in kidney tumor model during diffuser-assisted photocoagulation

Trung-Hau Nguyen¹, Kyu Kyu Hlaing¹, Yu Gyeong Chae¹, and Hyun Wook Kang²

¹ Interdisciplinary Program of Marine-Bio, Electrical & Mechanical Engineering, Pukyong National University, Busan, Korea

² Dept. of Biomedical Engineering and Center for Marine-Integrated Biomedical Technology (BK 21 Plus), Pukyong National University, Busan, Korea

E-mail: wkang@pknu.ac.kr

Abstract— A numerical model has been developed to predict the thermal damage in a kidney tumor model. The simulation was conducted with continuous wave (CW) mode, pulsed mode, and proportional-integral-derivative (PID)-controlled mode to compare therapeutic performance. Tissue experiments were implemented under the same conditions as the simulation models (10W, 980 nm). The PID controller-based laser maintained the predetermined temperature of 60 degree (less than 5% deviation) as well as limited the coagulation depth to ~2 cm within the tissue.

Keywords—Photothermal therapy, diffuser, kidney tumor, numerical simulation, PID controller.

I. INTRODUCTION

Photo-thermal treatment has recently been employed as a minimally invasive method for various tumors such as kidney, pancreatic cancer, and prostatic cancer. To achieve safe treatment during laser irradiation, a cooling system has often been used to reduce temperature in tissue [1]. In this study, we presented a new approach to constantly maintain the peak temperature in tissue by continuously modulating the laser power with a proportional-integrative-derivative (PID) controller.

II. METHODS

Prior to experiments, a numerical model with optical diffusers was developed to predict volume of thermal damage in tissue. Due to a high penetration depth (~2.15 mm) in liver tissue, a 980-nm wavelength was selected for simulation. For *in vitro* experiments, a 600- μm fiber was used to fabricate the diffusing tip (10 mm long) and to deliver 10 W of 980-nm laser light. A K-type thermocouple in conjunction with an industrial PID controller was used to control the peak temperature in the tissue.

III. RESULTS

Figure 1 demonstrates the spatial distribution of temperature from numerical models 30 sec after laser irradiation. Due to a combination of forward and radial emissions, a diffuser tip yielded two distinctive regions of heat sources. The peak temperature at the diffuser

end was found to be 350 K, which was significantly lower than that at the tissue interface (370 K). Apparently, the temperature was developed symmetrically around the diffuser axis. According to Fig. 2, a pulsed mode gradually increased tissue temperature with irradiation time whereas the PID-based modulation rapidly increased the temperature up to 370 K (11 K/s) and constantly maintained the temperature during the laser irradiation.

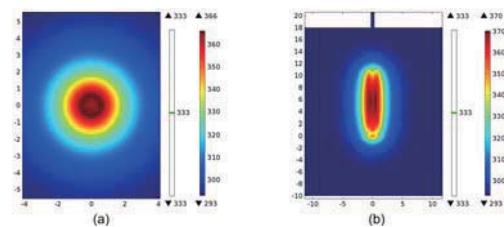


Fig. 1. Spatial temperature distribution (a) cross-sectional, and (b) longitudinal view in numerical model. Note that the gray contour represents temperature region higher than 333 K.

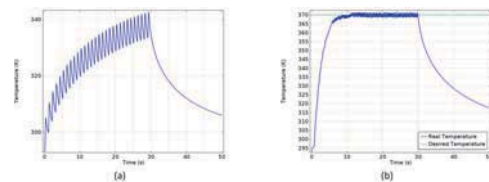


Fig. 2. Peak temperature development: (a) pulsed-mode laser (period=1 s, on time=0.5 s) and (b) PID-based modulation laser after 50 sec

IV. CONCLUSION

Application of the PID-based modulation laser can be a feasible way to control the degree of tissue coagulation and eventually to minimize unwanted thermal damage to the surrounding tissue.

ACKNOWLEDGEMENT

This work was supported by a grant from Marine Biotechnology Program (20150220) funded by Ministry of Oceans and Fisheries, Korea.

REFERENCES

1. Kamran Ahrar, Ashok Gowda, and Jason Stafford, "Preclinical Assessment of a 980-nm Diode Laser Ablation System in a Large Animal Tumor Model," *J. Vasc. Interv. Radiol.*, vol. 21(4), pp. 555-561, 2011.

Cancer Detection and Treatment with Ultrasound Technique

V.R.Singh Fellow-IEEE

Chair, IEEE IMS/EMBS Delhi Chapter
National Physical Laboratory, New Delhi -110012, India
E-mail: vrsingh@ieee.org

Abstract— A high intensity focused ultrasound hyperthermia system is developed for therapeutic treatment of deep seated tumour say in the brain, without surgery . Ultrasound characterization is made for different types of cancerous cells and tumours.

Keywords— Ultrasound, Cancer, Tumour, Hyperthermia.

I. INTRODUCTION

Cancer is a deadly disease and tumours are solid masses of cancerous cells, in different forms. There are several treatment techniques for cancer. Some of these techniques prominently used are surgery, chemotherapy RF/ Microwave/Ultrasound and nuclear radiation . However, for deep seated tumours, these techniques do not work. In order to overcome this problem, a focused ultrasound system is developed here for deep seated tmours. Cancer detection and tissue studies are reported [1,2].

II. METHODS

PZT-4 ceramic discs, with 1 MHz frequency, developed locally at NPL-India, are chosen here. The discs have curvature with focal length of 10 cm, in present case. Also, piezo-composite ultrasonic transducer is developed with focusing face. The assembly of the hyperthermia system is shown in Fig 1.

An associated electronic RF generator circuit is designed and fabricated to excite the focal transducer.

PZT-5 discs are used for high frequency transducers for the characterization of normal and cancerous cells.

III. RESULTS

A. Measurements and Performance

Use of ultrasound transducers in double probe through transmission method is made for the measurement of ultrasonic propagation parameters at 3 MHz . The results are shown in Table 1 for bone tumours.

B. Therapeutic Treatment

Te focused ultrasound system is used for therapeutic treatment of deep seated tumours. In case of yperthermia, the tumour temperature is raised from 42.5 to 45 degree C.

IV. CONCLUSION

Ultrasound technique has been used in a novel way for the detection and therapeutic treatment nof cancer and tumours. .



Fig. 1. Focused ultrasonic transducer

Table- Ultrasoc parameters of bone tumours

Tumour Specification	Ultrasonic Velocity				Attenuation			
	Maximum m/Sec	Minimum m/Sec	Average m/Sec	Standard Deviation %	Maximum dB/Cm	Minimum dB/Cm	Average dB/Cm	Standard Deviation %
Giant Cell	2600	1800	2106	1.49	28.8	22.5	26.06	0.011
Lymphoma	2700	2050	2394	1.02	29.8	22.2	19.70	0.020
Chondro Sarcoma	2852	2560	2677.5	0.44	75.9	73.2	74.4	0.002
Osteogenic Sarcoma	4000	3200	3586	0.74	74.2	71.5	73.08	0.002
Osteochondroma	*	*	*	*	*	*	*	*

* Measurements were not possible with present set-up

ACKNOWLEDGEMENT

This invite samples have been collected from local hospitals in Delhi. Thanks are due to clinicians for the support.

REFERENCES

1. V.R.Singh, "Ultrasound hyperthermia control system for deep seated tumours: in vitro study of tumours, modeling of thermal profile and future nano-engineering aspects", *ITBM* (Innovation and Technology in Biology and Medicine), France, July 9, 2008 (available on line), vol 29 (Issue 5), pp. 326-336, Nov., 2008.
2. Sanjay Yadav, Manju Singh, Om Prakash, A..K. Bandyopadhyay and V. R. Singh, "Ultrasonic Studies on High Pressure Transmitting Fluids used for Hydrostatic Pressure Measurements up to 1.0 GPa", *Int J. of Acoustics and Vibration*, vol. 13 (no. 3), pp. 123-129, 2008.

Hypoxic Gas Inhalation to Predict the Outcome of Chemotherapy

Hyeryun Jeong¹, Songhyun Lee¹, Jae Gwan Kim^{1,2*}

¹Department of Medical System Engineering, ²School of Information and Communication
Gwangju Institute of Science and Technology (GIST), Gwangju, South Korea
E-mail: jaekim@gist.ac.kr

Abstract— Currently, it takes more than 3 weeks to confirm the effectiveness of breast cancer neoadjuvant chemotherapy using X-ray mammography or MRI. In this study, we used a near-infrared spectroscopy to find its potential to predict the efficacy of chemotherapy in an animal model.

Keywords— Breast cancer, Chemotherapy, Near-Infrared Spectroscopy

I. INTRODUCTION

X-ray mammography or MRI is used to monitor the effectiveness of breast cancer neoadjuvant chemotherapy, but it takes more than 3 weeks to see the effectiveness of treatment. Therefore, a new method for predicting the early outcome of chemotherapy is necessary to provide a guide for a personalized treatment. We set our hypothesis that tumor shows its response to treatments earlier via a functional change than the structural change. We applied an inhalational gas intervention to see the breast tumor vascular reactivity during chemotherapy using a near-infrared spectroscopy (NIRS).

II. METHODS

A. NIRS System

A NIRS system consists of tungsten halogen light source, NIR spectrometer and optical fiber probe. Two NIRS systems were utilized to monitor hemodynamic changes from both normal and tumor breasts. Oxy-(OHb), deoxy-hemoglobin (RHb), and blood volume changes were monitored during tumor growth and chemotherapy.

B. Procedure

13762 MAT B-III cancer cells were inoculated to mammary fat pad of Fisher 344 female rats (n=4). Cyclophosphamide (100mg/kg) was administered i. p. for the purpose of treatment. Rats were anesthetized with ~ 2 % of isoflurane gas during experiments. NIRS data were acquired from normal and tumor breast as the inhalational gas changed from air to 16% O₂.

III. RESULTS

The change of oxyhemoglobin (OHb) concentration during hypoxia gas intervention correlated with the

change of tumor volume during its growth and chemotherapy. In a previous study, a breath holding test was performed in patients to observe the hemodynamic changes in breast tumor to see its potential as a marker to predict the chemotherapy response [1].

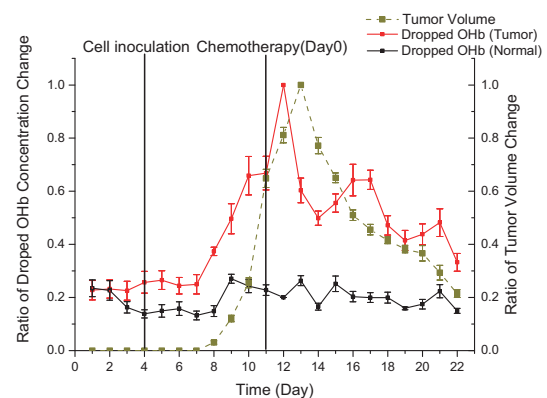


Fig. 1 The changes OHb during from air to hypoxic gas intervention in normal breast (black) and tumor breast (red)

In the same vein, we applied 16% oxygen gas to mimic a breath holding in a clinical study. In this low oxygen environment, normal tissue can make up the shortage of oxygen supply by dilating blood vessels while tumor cannot do it due to the loss of autoregulation function of blood vessels. The results show that the change of vascular reactivity occurs 1 day earlier than tumor size change after chemotherapy.

IV. CONCLUSION

We found that tumor vascular reactivity during a hypoxic gas intervention dropped earlier than the regression of tumor size after chemotherapy. These preliminary results imply that NIRS with respiratory challenges can be a prognostic tool in early prediction of tumor response during chemotherapy.

ACKNOWLEDGEMENT

This work was supported by a grant from NRF (2012K1A2B1A03000757, 2013R1A1A2013625) and institute of Medical System Engineering at GIST.

REFERENCES

1. Jacqueline E. Gunther, et al., "Dynamic Diffuse Optical Tomography for Assessing Changes of Breast Tumor

During Neoadjuvant Chemotherapy”, Proceedings of
Photonics West, 9319, 93190C, pp. 1~4, 2015

Objective Skin Pigmentation Assessment: Analysis of Skin Photo Type III

Ahmad Fadzil M. Hani¹ and Hermawan Nugroho²

¹CISIR, Universiti Teknologi PETRONAS, Tronoh, Malaysia

²Faculty of Engineering and Built Environment, SEGi University, Kota Damansara, Malaysia

E-mail: hermawan@segi.edu.my

Abstract— An objective pigmentation analysis system has developed. In this study, an observational study of skin phototype III was conducted using the system. Results indicate a promising outcome.

Keywords— eumelanin; pheomelanin; epidermal thickness, objective assessment; skin phototype III

I. INTRODUCTION

Skin-whitening creams works by inhibiting skin pigmentation. Skin pigmentation is associated with melanin production, skin colour pigment. There are two types of melanin: eumelanin and pheomelanin.

Currently, assessments of skin-whitening efficacy rely highly on the judgement of dermatologists. Consequently, development of an objective assessment tool is a necessity. This tool should be able to determine accurately melanin types and their concentrations, because during treatment, melanin production is the target of the treatment. As a result, the ratio of different melanin types is altered.

In previous report, we have developed and validated a non-invasive pigmentation analysis system [1]. In this study, the system was used to perform an analysis of skin phototype III in Malaysia .

II. METHODS

A. Study Protocol

An observational study was conducted in Universiti Teknologi PETRONAS, Malaysia. Undergraduate and postgraduate students who have skin phototype III were recruited and their skin reflectance data were obtained from the left forearm using spectrophotometer.

B. Pigmentation Analysis System

A system which provides the analysis of epidermal thickness, melanin types and its concentration using skin reflectance has been developed and validated. The system consists of a spectrophotometer and a Graphic Processing Unit (GPU) workstation.

The system analyses the skin reflectance using an inverse analysis powered by a Monte Carlo simulation as shown in Fig. 1. In this inverse procedure, the estimation of melanin types is performed by tuning the Monte Carlo simulation until achieving a match

between the simulated reflectance and the measured reflectance.

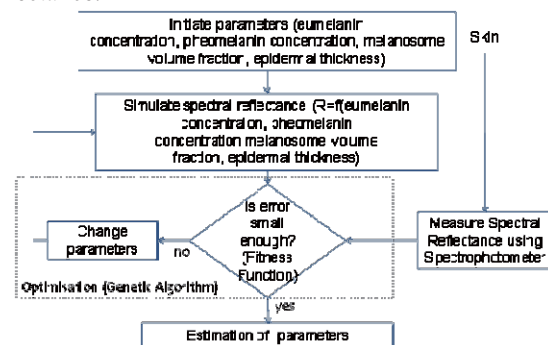


Fig. 1 Flowchart of pigmentation analysis system

III. RESULTS

There were 21 participants of SPT III recruited. From the study, it is estimated that the average relative concentrations of eumelanin of SPT III are 32.62 g/l and ratio between pheomelanin and eumelanin is 0.06. These results were in concurrent with Jacques [2]. Also the epidermal thickness is found to be 0.081 ± 0.023 mm. Lee and Hwang [3] reported that the epidermal thickness on the outer forearm were 0.083 ± 0.036 mm. The values obtained by the system are within the ranges indicating a correct estimation.

IV. CONCLUSION

In this study, objective analysis of skin pigmentation for skin phototype III is performed using a newly developed skin pigmentation system. An observational study involving 21 participants was conducted. Results from the study shows the system can accurately estimate epidermal thickness, melanin types and its corresponding concentration.

REFERENCES

- [1] A. F. M. Hani, R. Baba, N. Shamsuddin, and H. Nugroho, "Determination of melanin types and relative concentrations: an observational study using a non-invasive inverse skin reflectance analysis," *Int. J. Cosmet. Sci.*, pp. 1–8, 2014.
- [2] S. L. Jacques, "Origins of tissue optical properties in the UVA, visible and NIR region," in *Advances in Optical Imaging and Photon Migration*, Optical Society of America, 1996, pp. 364–370.
- [3] Y. Lee and K. Hwang, "Skin thickness of Korean adults," *Surg. Radiol. Anat.*, vol. 24, no. 3–4, pp. 183–189, 2002.

pH Controlled Release of Paclitaxel via Electrospun Polyurethane/Eudragit® L100-55 Composite Mat for Duodenal Stent Cover Application

L.E. Aguilar¹, J.P. Soriano¹, S.W. Ko¹, S.N. Lee¹, J.W. Kim¹, T. Batgerel¹,
A. Ghavaminejad¹, M. Samarikhalaj¹, J.I. Kim¹,
C.H. Park^{1,2*}, C.S. Kim^{1,2*}

¹Department of Bionanosystem Engineering, Graduate School, Chonbuk National University, Jeonju, South Korea

²Division of Mechanical Design Engineering, Chonbuk National University, Jeonju City, Republic of Korea

E-mail: biochan@jbnu.ac.kr, chskim@jbnu.ac.kr

Abstract— The pH controlled release of paclitaxel was successfully done with the use of PU/EL100-55 composite mats as the controlling platform. The composite mat was created using electrospinning process. The morphology and fiber diameter of different ratios of PU: EL100-55 (1:1, 2:1, 3:1) was investigated using FESEM. FTIR and DSC-TGA analysis were also performed to characterize the composite nanofibers showing that physical mixtures of PU and EL100-55 were achieved, EL100-55 retains its pH sensitivity even with the addition of PU. The release rate of paclitaxel was determined and analyzed by *In vitro* drug release method. In order to mimic the condition of a human duodenum, the fibers were submerged in PBS of different pH levels (4.0, 6.0) respectively, and then analyzed using High Performance Liquid Chromatography (HPLC). Composite mats submerged in PBS with pH 4.0 showed lesser release profile compared to mats submerged in PBS with pH of 6.0. The composite mat has adequate mechanical properties indicating that the material can be used for drug eluting stent cover application.

Keywords— Electrospinning, pH sensitive polymers, Drug Eluting Stents, Eudragit, Nanofibers

I. INTRODUCTION

One must know that controlling the dosage of drug is very crucial in achieving the goal of treatment. Especially on anti-cancer drugs because not only it affects cancer cells it can also cause harm on normal tissues surrounding it. That is why researches are being conducted in controlled release of drugs on various platforms. Medical devices nowadays like stents (vascular and non-vascular) are being developed not only for palliative purpose of treatment but also to aid for curative purposes, the development of drug eluting stents (DES) is a major leap forward on the said medical device. One major advantage on using stents is that it is being deployed on the site of obstruction where the cancer tumor is located. On the other hand such devices had their own limitations, number one is restenosis, second is migration and lastly the uncontrolled release of its drug payload. Covering the device with polymers is a strategy being used now to address these limitations. Polymers such as polyurethane, silicone, acetylated pullulan, ethylene vinyl acetate, poly (L-lactide-co-caprolactone), poly (L-lactide-co-glycolide) and other proprietary

copolymers are being studied for their drug delivery system capabilities. These polymers can be loaded with arrays of drugs e.g. NSAID's, anti-proliferative, but the ability of these polymers to react on the environment is limited.

Stimuli responsive polymers can be exploited to further enhance the capability of DES on performing its main goal and that is to give controlled dosage of its drug payload, because the human body is a dynamic environment, changes in pH, pressure, temperature; hormones etc. are needed to maintain homeostasis. These changes can be used as triggering mechanisms for smart polymers to enact their role. Smart polymers swell, harden, degrade, and undergo phase transformation under different conditions, which we can find in the human body. One example of a smart polymer is Eudragit® from Evonik Rohmm pharma Industries. The Eudragit acrylic polymers have been used for a long time dating back to the 1950's with the introduction of Eudragit® L 12.5 and Eudragit® S 12.5. The main attribute of eudragit line is that it has the ability to deliver its drug payload according to different pH conditions, based on anatomical knowledge that the GI system has a dynamic pH environment, Evonik Industries made varieties of Eudragit products to accommodate and specifically target areas of the GI.

Eudragit® L100-55 was developed by Evonik to perform drug release on the duodenum, because Eudragit® L100-55 is stable at pH lower than 5.5 it can bypass drug absorption in the stomach and release its drug payload at the duodenum which has a mean pH of 5.4 when fed and 6.5 during fasting. Reinforcing Eudragit® L100-55 with polyurethane, we increased the mechanical properties of the polymeric cover while still maintaining its pH sensitivity. We have used electrospinning as our main manufacturing method because electrospinning has been known to produce nanomaterials and nanostructures for multiple applications, the prospect of this method in biomedical application has been widely known for many years. Nanopackaging of drugs has multiple advantages compared to conventional methods of drug delivery. Controlling dosage, the site of release and rate of release is relatively easier and more effective when using nanostructures as a delivery platform. Nanofibers are already known to have high surface area, smaller

diameter and high porosity and can even enhance the effect of the drug of choice due to nano-effects. Using these premise, we developed a polymeric pH dependent drug release platform for duodenal stent device.

II. METHODS

A. Electrospinning process

The spinning solutions were loaded in 10 ml syringes. All electrospinning parameters can be found in Table 1. The finished mats were dried at a vacuum oven (200Pa) at 40°C to remove residual organic solvent and moisture.

B. Morphology of the Electrospun Nanofibers

The morphology of the composite mats was then observed using Field emission scanning electron microscope (Carl Zeiss Supra 40VP). Before the images were taken, the samples were sputter coated under argon to make them electrically conductive. The excitation voltage used to take the images was set at 2 kV. The average fiber diameter of about 50 points was surveyed using image J software (NIH, USA).

C. Physical State of the drug loaded fiber mats and Polymeric Interaction between Polyurethane and Eudragit L100-55

Differential Scanning Calorimetry (DSC) analysis data was also taken using a TMK 0017 universal analysis (TA Instruments Co., USA). The heating rate was set at 10°C/min and scanned from 10°C to 600 °C. The gas flow rate of Nitrogen was set at 40ml/min. The thermal degradation of the nanofibers was measured using TGA (Q50, TA Instruments) under same parameters as DSC. Fourier Transformed Infrared spectroscopy analysis data was obtained using a spectrum-GX FTIR spectrometer (Perkin Elmer Co., USA). The scanning range was set at 500-4000 cm⁻¹ with a resolution of 1 cm⁻¹.

D. Mechanical Strength Test

The tensile properties of the samples were obtained using an Instron bench-type tensile test machine (100 N load limit, Lloyd Instruments) using a dog-bone specimen based from ASTM [D882-10](#). The crosshead speed was 5 mm/min and the tensile property values reported here are average values from at least 5 specimens tested for each sample.

E. In Vitro Drug Release Test

The in vitro drug dissolution test for the model drug paclitaxel was done to determine the drug release capability of the PU/EL100-55 composite mats. To determine the drug release profile of the composite mats under different pH conditions, 1 L of Phosphate buffer solution (Sigma Aldrich) of different pH levels were made by titrating 0.1 N of Hydrochloric acid (HCl) (Showa Industries) directly to the PBS solution using a straight stop cock burette while being

magnetically stirred and monitored by a pH meter (HI 2215, Hanna Instruments). Two different pH levels of PBS were made pH (4 and 6); 40 ml of the different PBS solutions was then transferred to 50 ml plastic tubes. Afterwards 50 mg of the control and composite mat samples were prepared and then submersed into the PBS solutions. A shaking incubator (SI-300R, Lab. Companion) was used and set at 37 °C and 200 rpm. 1 ml aliquots of the PBS solutions were taken at predetermined time intervals and were analyzed using high performance liquid chromatography (Waters Alliance, USA). The amount of PTX present was calculated using a calibration curve constructed from a known sample. PTX dissolved at specified time intervals was plotted as percentage released versus time. All samples were conducted in triplicate and the reported data as average values.

F. Biocompatibility Test

The fibroblasts (NIH-3T3) cells were cultured at 37°C under 5% CO₂ in Dulbecco's Modified Eagle Medium (DMEM, GIBCO) supplemented with 10% fetal bovine serum (FBS, GIBCO) and 1% penicillin-streptomycin.

III. RESULTS

A. Fiber Morphology

PU/EL (3:1, 2:1, 1:1). Pure PU and pure PU with PTX have an average diameter of 850 nm and 790 nm, Pure EL100-55 has an average diameter of 250 nm. Combining the two polymers yielded nanofibers with varying fiber diameter. PU/EL 1:1 formed nanofibers with an average diameter of 590 nm, while PU/EL 2:1 and PU/EL 3:1 both have an average diameter of 637 nm and 714 nm respectively.

B. State of the drug loaded fiber mats and Polymeric Interaction between Polyurethane and Eudragit® L100-55

Paclitaxel and it exhibited one exothermic peak at 225.63 °C coinciding with its melting point indicating that the pure paclitaxel is in crystalline form. However upon loading it in the nanofibers, no more exothermic peaks can be noticed but instead endothermic peaks at 221 °C, 213 °C, 200 °C, 183 °C for PU-PTX, PU/EL (1:1)-PTX, PU/EL (2:1)-PTX, PU/EL (3:1)-PTX respectively. This implies that paclitaxel becomes amorphous upon loading in the nanofibers

C. Mechanical Strength Test

PU/EL (1:1)-PTX, PU/EL (2:1)-PTX, PU/EL (3:1)-PTX has an average tensile strength of 4.04± 4 MPa, 7.2± 0.3 MPa, and 13.15± 5 MPa and maximum strain of 95.8± 6 % 307.53± 30, 393.86± 50 % respectively.

D. In Vitro Drug Release Test

With increasing ratio of Eudragit® L100-55, the higher the percent release of drug was achieved. The release rates were ordered at PU/EL (1:1)-PTX > PU/EL (2:1)-PTX > PU/EL (3:1)-PTX. For PU/EL (1:1)-PTX

almost 100 % was released in PBS (pH 6) and in contrast with the other nanofiber composites which has a 50 % release rate and 30% release rate for PU/EL (2:1)-PTX and PU/EL (3:1)-PTX after 3 days, respectively.

E. Biocompatibility Test In Vitro

PU/EL 1:1 has the least cell viability amongst the nanofiber mats after 6 days of incubation. Nevertheless it is well known that PU and Eudragit is a biomaterial therefore no cytotoxicity was noted. With the addition of Eudragit® L 100-55 the biocompatibility was virtually the same as with pure PU.

IV. CONCLUSION

We have made a pH controlled paclitaxel releasing nanofiber composite platform for duodenal stent cover application using polyurethane and Eudragit L®100-55. We have successfully used electrospinning in fabricating nanofiber composites with uniform fiber diameter. Only physical mixture and few secondary interactions were observed using DSC-TGA and FTIR analysis. The resulting composite nanofiber maintained their pH sensitivity which is beneficial in achieving pH controlled release profile. The mechanical properties can be enhanced by adjusting the ratio of the PU component. Using PU as reinforcing polymer significantly increased the mechanical properties of the nanofiber composite compared to pure Eudragit L100-55 nanofibers. The paclitaxel release from all nanofiber composite is influenced by the pH of the PBS solution. A significantly higher release profile was noted under PBS (pH 6) compared to PBS (pH 4) which has no more than 4% of release rate. The composite nanofibers in the following order PU/EL(3:1)+PTX > PU/EL(2:1)-PTX > PU/EL(1:1)-PTX have high potential for controlled drug release application for duodenal stents with regards to mechanical strength, biocompatibility and amount of sustained drug release for the initial 6 hours.

Figures

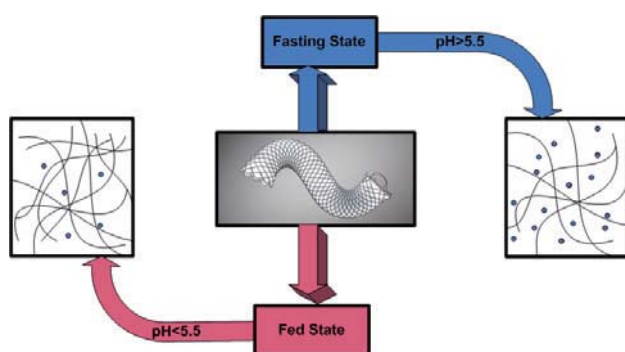


Figure 1. Graphical Abstract of the Research

Acknowledgement

This research was supported by grants from the Basic Science Research Program through the National Research Foundation of Korea (NRF) funded by the Ministry of Education, Science and Technology (Project no. 2013-012911 and 2013R1A2A2A04015484) and also partially supported by the Industrial Strategic Technology Development Program (10044021, Development of nonvascular drug eluting stent for treatment of gastrointestinal disease) funded by the Ministry of Knowledge Economy (MKE, Korea).

References:

- Blumenschein, G., A. Sandler, T. O'Rourke, M. Eschenberg, Y. Sun, G. Gladish, R. Salgia, C. Alden, R. S. Herbst and K. Reckamp (2006). "Safety and pharmacokinetics (PK) of AMG 706, panitumumab, and carboplatin/paclitaxel (CP) for the treatment of patients (pts) with advanced non-small cell lung cancer (NSCLC)." *Journal of Clinical Oncology* **24**(18): 393s-393s.
- Dressman, J. B., R. R. Berardi, L. C. Dermentzoglou, T. L. Russell, S. P. Schmaltz, J. L. Barnett and K. M. Jarvenpaa (1990). "Upper Gastrointestinal (Gi) Ph in Young, Healthy-Men and Women." *Pharmaceutical Research* **7**(7): 756-761.
- Elgindy, N. and W. Samy (2009). "Evaluation of the mechanical properties and drug release of cross-linked Eudragit films containing metronidazole." *International Journal of Pharmaceutics* **376**(1-2): 1-6.
- Greiner, A. and J. H. Wendorff (2007). "Electrospinning: A fascinating method for the preparation of ultrathin fibres." *Angewandte Chemie-International Edition* **46**(30): 5670-5703.
- Groothuis, A., P. Seifert, A. Spognardi, D. Donaghy and C. Rogers (2006). "Dissociating DES safety and efficacy: Endothelial regrowth and drug effect after abluminal or circumferential paclitaxel delivery from a bioerodible polymer in porcine coronaries." *American Journal of Cardiology* **98**(8A): 134m-135m.

Magnetic Nanovector for the down regulating CD44 and imaging of microRNA

Hwunjae Lee¹, C. Hyunkyung Park¹, Seungjoo Haam², Jin-Suck Suh¹,
Eun-Kyung Lim^{3*} and Yong-Min Huh^{1*}

¹Department of Radiology, College of Medicine, Yonsei University, Seoul, Korea

²Department of Chemical and Biomolecular Engineering, Yonsei University, Seoul, Korea

³BioNanotechnology Research Center, Korea Research Institute of Bioscience and Biotechnology, Daejeon, Korea

E-mail: ymhuh@yuhs.ac

Abstract— Synchronized gene silencing and imaging strategies using miRNA emerged with the aim to expand the clinical application in cancer treatment. Herein, we report development of smart theranostic system that can facilitate simple and efficient delivery and visualization of therapeutic miRNA by high-resolution magnetic resonance imaging. The synthesized magnetic nanovectors were facilitated in vitro CD44 down-regulation and visualization via magnetic resonance imaging in metastatic gastric cancer.

Keywords— miRNA, CD44, Magnetic nanoparticle, Surface modification, Theranostics, Magnetic resonance imaging

I. INTRODUCTION

Magnetic nanoparticles (MNPs) enable the monitoring of therapeutic agent delivery by non-invasive and real-time magnetic resonance imaging (MRI), because this technique can rapidly acquire multi-informational high resolution images. And Modifying the surface of various inorganic nanoparticles has recently become important to the development of novel biomedical technologies including therapeutics, diagnosis and clinical imaging, it is important for the treatment of the cancer in the functional aspect of nanoparticles. In addition, it is known that microRNAs (miRNA, miR), 1-2 nucleotides of non-coding small RNA, regulate various cellular functions including proliferation, differentiation and apoptosis as well as diseases. Thus, synthetic complimentary oligonucleotides against miRNAs can be potentially used as a molecular mechanism-based theragnostics biomarker in cancers by simultaneously imaging.

II. METHODS

Nitrosonium tetrafluoroborate (NOBF₄) is used to replace the original ligands attached to the magnetic nano particles, stabilizing the magnetic nanoparticles in various polar, hydrophilic media, and then surface modified magnetic nanoparticles were complexed with miRNA targeting CD44 gene via electrostatic interaction to verify the specific gene-silencing effect.

III. RESULTS

The synthesized magnetic nanovectors were facilitated in vitro CD44 down-regulation and visualization via magnetic resonance imaging in metastatic gastric cancer.

IV. CONCLUSION

In summary, we successfully formulated theranostic nanovector, for effective gene therapy and imaging. Nanovectors we designed were contributed to effective gene carrying through PEG-Tiohl. Moreover, it has potential to be a MR imaging agents as well as gene therapy. Consequently, Successful magnetic nanovector developed in this paper can be expected to expand research on carrying efficient delivery for not only cancer detecting agent but also therapeutic miRNA agents.

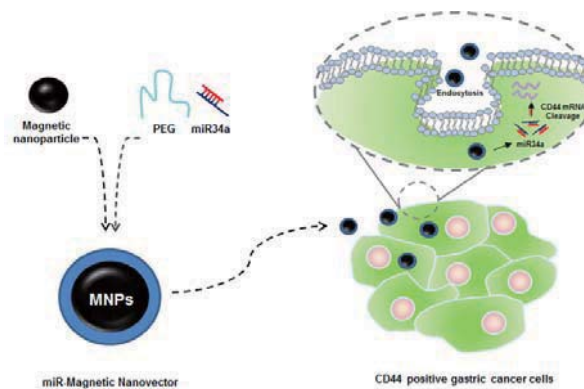


Fig. 1. Schematic illustration of the synthesis and delivery route of miRNA34a-PEG coated magnetic nanoparticles for down regulating CD44

ACKNOWLEDGEMENT

This work was supported by Ministry for Health and Welfare, Republic of Korea/the Nation Research Foundation grant (2006-2004652) funded by the Korea government (MEST).

REFERENCES

1. M. Bradbury and H. Hricak, Magnetic Resonance Imaging Clinics of North America 13, 225 (2005).
2. E. J. Delikatny and H. Poptani, Radiologic Clinics of North America, 43, 205 (2005).

Application of circumferential irradiation for low-temperature laser lipolysis

Jieun Hwang¹, Nguyen Trung Hau², Minwoo Ahn¹, Sung Yeon Park³, and Hyun Wook Kang^{1,2,4*}

¹Department of Biomedical Engineering, Pukyong National University, Busan, Korea

²Interdisciplinary Program of Marine-Bio, Electrical & Mechanical Engineering, Pukyong National University, Busan, Korea

³Molecular Environmental Biology, University of California, CA, USA

⁴Center for Marine-Integrated Biomedical Technology, Pukyong National University, Busan, Korea

E-mail: wkang@pknu.ac.kr

Abstract— The aim of the current study was to validate an optically diffusing fiber for laser lipolysis. Two different types of the fibers were tested to evaluate tissue responses during thermal interactions. The diffuser emitted an almost uniform energy along the diffuser tip with a low intensity. The diffusing optical fiber covered wider liquefied areas with uniformly lower peak temperature in comparison with the flat fiber.

Keywords— liquefaction, fat removal, lipolysis

I. INTRODUCTION

Laser lipolysis with flat fibers has frequently been associated with excessive thermal injury (burn) due to rapid temperature increase. In order to cover larger tissue area and even safer treatment with uniform temperature, a diffusing fiber was designed and developed. In this study, the proposed fiber was evaluated in terms of thermal gradient and liquefaction rate and compared with a flat fiber.

II. METHODS

To prepare 10-mm long diffusing fibers, a multimode 600- μm fiber was machined by using a CO₂ laser [1]. Figure 1 shows a set-up for laser liquefaction experiments. For *in vitro* testing, two different fibers (flat and diffusing) were tested to identify thermal responses of porcine abdomen fat tissue during laser irradiation. 980-nm laser light was irradiated on the fat tissue at various power levels (10, 20, and 30 W) for 1 min to identify the optimal treatment conditions for laser lipolysis. Each fiber was placed on top of a microscope slide and then covered with the prepared fatty tissue. With the two fibers, the rates of fat reduction during photothermal treatments were evaluated by measuring weight variations between pre- and post-laser lipolysis.

III. RESULTS

Regardless of fiber type, the temperature in tissue increased with laser power. At 20 W, a diffusing fiber took longer (5 s) than a flat fiber (2 s) to initiate fat liquefaction. Overall, the peak temperature in the fat tissue increased with irradiation time for all the tested

power levels. The results showed that the peak temperature of the flat fiber reached over 90 °C in 1 min at 20 W (1.5 °C/s) whereas the diffusing fiber generated up to 65 °C in 1 min at 20 W (1.1 °C/s). Due to generation of higher peak temperature, the flat fiber caused excessive carbonization in the fatty tissue and experienced severe fiber deterioration 2 s after the laser irradiation. However, no or minimal thermal damage occurred at the tissue and the diffusing fiber tip as the temperature became saturated 50 s after laser irradiation. At 20 W, the diffusing fiber removed 0.09 g of the fat tissue (1.5 mg/sec), which was comparable to that of the flat fiber (0.10 g, 1.6 mg/sec; $p = 0.24$). Additionally, the diffusing fiber removed a larger area of the tissue than flat fiber on account of cylindrical light emission.

IV. CONCLUSION

The proposed optical diffusing fiber can be a feasible therapeutic tool for safe and effective laser lipolysis due to low temperature development and wide coverage of tissue treatment.

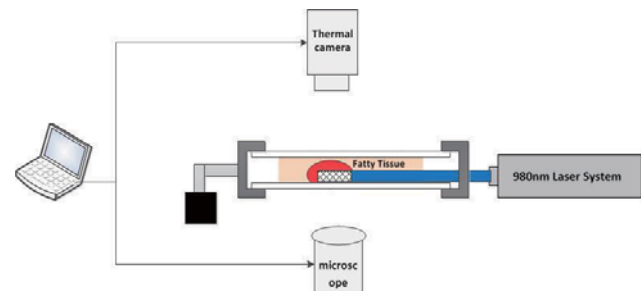


Fig. 1. Experimental set up of laser lipolysis with optical diffuser (980 nm)

ACKNOWLEDGEMENT

This work was supported by a grant from Marine Biotechnology Program (20150220) funded by Ministry of Oceans and Fisheries, Korea.

REFERENCES

1. TH Nyguyen, Y Rhee, J Ahn, HW Kang, "Circumferential irradiation for interstitial coagulation of urethral stricture", optics express, vol. 23, No. 16, 2015.

Experiment for Comparing the Performances of Heterogeneous Devices for Measuring Heart Rate and Respiratory Rate using the IR-UWB

Young-Jin Park¹, Hong-Kun Lyu¹, and Hui-Sup Cho¹

¹Division of IoT and Robotics Convergence Research, DGIST, Daegu, Korea

E-mail: yjpark@dgist.ac.kr

Abstract—The purpose of this paper is a experiment to give researchers basic performance information to developing using IR-UWB(Impulse Radio Ultra Wide Band) DVK(DeVelopment Kit) which is manufactured by NOVELDA. We compare performance between PCs and embedded platforms through an experiment in this study.

Keywords— IR-UWB, Performance Experiment

I. INTRODUCTION

In this paper, we have carried out experiments for comparing the execution times on various platforms for determining an optimal development environment. We will obtain the best environment for the experiments, such as when measurement of the heart rate or respiratory rate[1] from these results. For measuring the heart rate, it is important to determine the machine performance and processing speed of the algorithm in advance as the signaling is received after a certain time. The results in this study will give researchers with basic information to develop several applications on several platform by using IR-UWB DVK.

II. METHODS

A. Building Systems and Radar Libraries

In this study, our experiment requires building systems and radar libraries. Boot loader, the kernel and file system should be compiled and flashed for each embedded platform. In addition, the radar library should be compiled for each platform. Finally, we will refer to libraries such as *.dll or *.so in the program created for the experiment.

B. Measurement Method

The purpose of this experiment is to measure the execution time on each platform. Therefore, we only measured transmission time interval without any calculation. The total number of samplers used was 10,000, and each sampler was composed of 256 samples.

III. RESULTS

A. PC Environments

Figure 1 shows the results of the PC environment in Windows 8.1 and Ubuntu 14.04LTS.

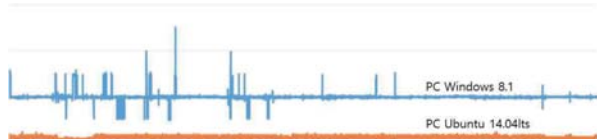


Fig. 1. PC environments

Note that the x-axis represents the received samplers(number-10,000), and the y-axis represents

the received time of each sampler. The Ubuntu PC with x-window is observed to be more reliable and faster.

B. Embedded Environments

Figure 2 shows the experiment results of embedded environments in Ubuntu14.04LTS. The x-axis and y-axis means are the same as those in the PC environments. The performing rate in an embedded environments, all the devices were similar, however, the stability is Jetson board, which is manufactured by NVIDIA in the console mode, as shown in Figure 2-(c) and Table 1, was the best. However, the results can vary considerably in stability because of execution of the x-window system or background jobs.

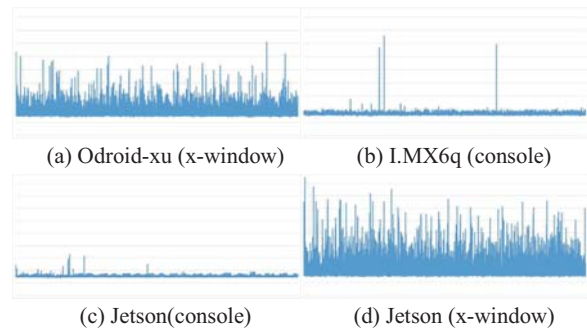


Fig. 2. Embedded environments

Table 1 lists the specifications and test results of the devices used in the experiment.

Table 1. Specifications and Results
*: windows8.1, **: ubuntu14.04LTS, *** : console mode

Platforms				
PC		Embedded Platform		
		Odroid -xu	i.MX6 q***	Jetson-T K1***
Operating Systems				
64bit*	32bit*	64bit**	32bit**	
Performance time (seconds)				
0.0039	0.0040	0.0030	0.0046	0.0043
				0.0040

IV. CONCLUSION

In this experiment, we could select the optimal hardware for an algorithm for measuring the heart rate and respiratory rate with pre-experiment.

ACKNOWLEDGEMENT

This work was supported by the DGIST R&D Program of the Ministry of Science, ICT and Technology of Korea(15-IT-01).

REFERENCES

- Novelda Public, "Heart rate and respiration monitoring", 2011 Novelda AS, Rev. No: 1.0, vol. 14 july 2014.

Application of non-compliant balloon catheters for photothermal treatment

Jinoh Park,¹ Trung Hau Nguyen,² Jieun Hwang,¹ and Hyun Wook Kang^{1,3*}

¹Department of Biomedical Engineering, Pukyong National University, Busan, Korea

²Interdisciplinary Program of Marine-Bio, Electrical & Mechanical Engineering, Pukyong National University, Busan, Korea

³Center for Marine-Integrated Biomedical Technology, Pukyong National University, Busan, Korea

*E-mail: wkang@pknu.ac.kr

Abstract— The current study demonstrated application of non-compliant balloon catheters during diffuser-integrated laser treatment on tissue stricture. Due to mechanical pressure, the inflated balloon was able to expand the narrowed tissue structure up to 6 mm in diameter with 1~2 mm tissue coagulation. The laser-induced temperature reached up to 75 °C, and minimal transmission loss was found even at 90 degree fiber bending. The proposed balloon application can be a feasible adjunctive tool to treat tubular stricture during photothermal treatment.

Keywords— Balloon catheter, tissue stricture, optical diffuser, photothermal treatment

I. INTRODUCTION

Stricture in tubular tissue is an uncommon disease in gastroenterology. Most benign strictures are iatrogenic as resulting from operative trauma. Upon occurrence, the stricture can be associated with severe pain, fever, and chills. Traditional treatments include endoscopic retrograde cholangiopancreatography (ERCP), surgical operation, and mechanical stenting. In the current research, non-compliant balloon catheters were tested to treat fibrotic tissue stricture in conjunction with diffuser-assisted laser irradiation.

II. METHODS

To prepare diffusing fibers, 400- μm core-diameter optical fibers were used and micro-machined by CO₂ laser. Multiple lozenge patterns were fabricated on the fiber surface, which could diffuse the incident laser light. A goniometer was utilized to measure spatial distributions of light emission from the diffusers. For tissue testing, bile ducts were prepared and stored at 4 °C to prevent dehydration prior to the testing. A near IR wavelength (980 nm) was implemented as a light source for the testing. Non-compliant balloon catheters (2 cm long and 6 mm in inflation diameter) were integrated with the fabricated diffusers to achieve structural deformation in tissue during laser irradiation. A thermal IR camera was implemented to monitor thermal distribution on the tissue surface during the treatment. Mechanical compliance of the fabricated diffusers was also evaluated by measuring the output power at various bending curvatures.

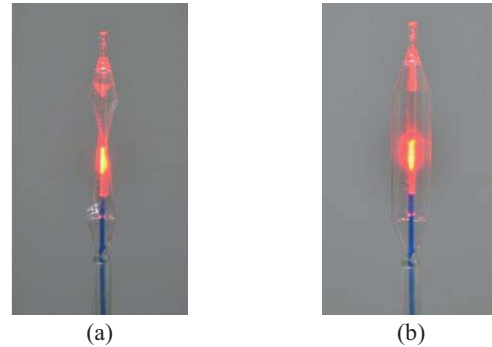


Fig. 1. Images of balloon-integrated diffuser during laser irradiation: (a) deflated balloon and (b) inflated balloon

III. RESULTS

The goniometer measurements confirmed that light was almost circumferentially irradiated from the diffuser along with uniform power distribution (i.e., 0.9 ± 0.1). Figure 1 demonstrates images of a balloon-integrated diffuser in conjunction with 633 nm irradiation. A mechanical inflator was able to control the air pressure inside the balloon and to readily inflate /deflate the balloon. *In vitro* tissue testing confirmed that compared to control, the inner area of the tested tissue was increased by up to 25% during the balloon catheter-assisted laser irradiation. IR imaging validated that the temperature during the irradiation increased up to 75 °C, which was close to the temperature for irreversible tissue denaturation. Gross examinations on the treated tissue confirmed that coagulation necrosis occurred within 1~2 mm from the inner surface of the tissue.

IV. CONCLUSION

Application of a balloon catheter integrated with an optical diffuser can expand the inner space of a tubular tissue with stricture during photothermal treatment.

ACKNOWLEDGEMENT

This work was supported by a grant from Marine Biotechnology Program (20150220) funded by Ministry of Oceans and Fisheries, Korea.

REFERENCES

1. Afdhal NH. Diseases of the gallbladder and bile ducts. In: Goldman L, Schafer AI, eds. *Goldman's Cecil Medicine*.

The study on design of metal plate for improvement of optical property

K.T. Kim¹, J.S. Kim¹, Y.H. Shin¹, M.J. Han¹, Y.J. Heo¹, J.K. Park², S.H. Nam¹
 Department of Biomedical Engineering, Inje University, Gimhae, South Korea¹
 Department of Radiological Science, International University of Korea, Jinju, South Korea²
 E-mail: radiokkt09@ril.inje.ac.kr

Abstract— This study is purposed to perform the basic research on the scattering mechanism in the diagnostic radiology area by analyzing the luminescent properties on the thickness of metal plate. According to the test result, it is evaluated that differentiated property changes occurs from 0.4 mm Al. Such outcome is considered to be possibly related with the occurrence rate of Compton scattering on the thickness.

Keywords—Phosphor, Metal plate, Compton scatter

I. INTRODUCTION

In the medical field, using a low dose, and are utilizing a phosphor-based indirect method. However, It has to problem of luminescence properties due to the low conversion efficiency of the phosphor in Indirect application. So, the study of Metal plate has been actively studied. Such a Metal plate plays the role of the reflect layer at the diagnostic energy (20-50 keV). Also, Metal plate had been reported to increment of luminescence properties through the compton scattering mechanism at the radiotherapy energy (4-15 MeV). This study is purposed to perform the basic research on the scattering mechanism in the diagnostic radiology area by analyzing the luminescent properties on the thickness of metal plate.

II. METHODS

A. Fabrication of Phosphor screen

To manufacture the phosphor screen, we used a particle-in-binder (PIB) sedimentation method, which leads to a high rate of production and facilitates easy adjustment of thickness and shape. The phosphor screens were manufactured to have a thickness of 150 μm to evaluate luminescence properties. The phosphor screens were manufactured based on these conditions after being coated and dried in an oven at 40°C for 12 h.

B. Image Acquisition and Evaluation

In order to evaluate the luminescence properties, we acquired images of a white and a dark image by using a general radiography system. Minimum exposure conditions were used; 40-kVp and 50-mAs for radiography X-ray. After the CMOS pixel values according to the amount of luminescence were analyzed using the TIFF format.

III. RESULTS

Fig.1 shows the result on the change of luminescent properties for each thickness of metal plate.

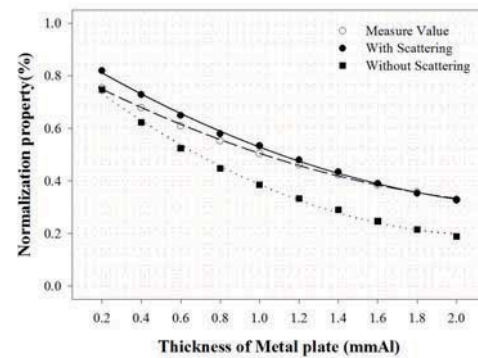


Fig. 1. Normalization property as a function of thickness

According to the test result, it is analyzed that, when the thickness of metal plate is less than 0.4 mmAl, the simulation without scattering and the similar properties within approx. 9% (0.75% at 0.2 mmAl) show while, at the thickness of 0.4 mmAl or higher, the simulation with scattering and the similar properties within approx. 8% (3.99% at 1.2 mmAl) show.

IV. CONCLUSION

In this study, the luminescent properties on the thickness are analyzed to conduct the basic research on the scattering mechanism of metal plate in the diagnostic radiology area. The result shows that the property change occurs from the metal plate of 0.4 mmAl. Such result is considered to be related to the fact that the relation between the metal plate thickness and the occurrence rate of Compton scattering is expressed as a quadratic function having the property being saturated at approx. 1.2 mmAl. And this refers that the adequate thickness of metal plate is a critical factor for the increase of fluorescence amount. Therefore, it is considered that multilateral researches on the material's electron density to increase the efficiency of metal plate should be performed in the future studies.

ACKNOWLEDGEMENT

This work was supported by the National Research Foundation of Korea(NRF) grant funded by the Korea government(MSIP) (No. 2014R1A2A1A11052504).

Inhibition Effect of Ascorbic acid against Formation of Amyloid-like Fibrils

W. Lee¹, H. Lee¹, I. Kim², S. W. Lee², S. W. Lee¹ and D. S. Yoon²

¹Department of Biomedical Engineering, Yonsei University, Wonju 220-710, Republic of Korea

²School of Biomedical Engineering, Department of Bio-convergence engineering, Korea University, Seoul 136-701, Republic of Korea.

E-mail: dsyoon@korea.ac.kr

Abstract— Ascorbic acid had been widely used and proposed as an agent of prevention and treatment of disorders. In recent, ascorbic acid is of importance not only to treat the degenerative diseases (i.e. Alzheimer's diseases) but also to hinder the formation of amyloid fibril and plaque. However, inhibition effect on formation of amyloid fibrils remains uncertain. Herein, we observe the inhibition effect of ascorbic acid against formation of amyloid-like fibrils by using a high-resolution atomic force microscopy (AFM) and fluorescent assay.

Keywords— Amyloid fibril, Ascorbic acid, Inhibition effect, Conformation change, Atomic force microscopy

I. INTRODUCTION

Many degenerative diseases, including Huntington's, Parkinson's and Alzheimer's diseases, are attributed to accumulation of amyloid fibrils and plaques [1]. It recently reported that high dose of ascorbic acid manifests amyloid degradation and ameliorates the aggregation of amyloid plaque with an animal model [2]. However, the detailed mechanism regarding its pharmaceutical efficacy is still a controversial issue today. Here, we demonstrate the inhibition effects of ascorbic acid against amyloid fibrillation in vitro by using AFM and fluorescence assay with Thioflavin T (ThT). Our result will help to develop a bio-friendly therapeutic agent for degenerative diseases related amyloidogenic proteins and fibrils.

II. METHODS

To investigate the inhibition effect of ascorbic acid, we synthesized β -lactoglobulin (β -lg) fibrils with/without ascorbic acid for 10 hours. To perform fluorescent assay with ThT molecules, we prepared a working solution of ThT by following procedure. A stock solution of 600 μ M ThT (Sigma Aldrich) in PBS buffer solution was filtered through a 0.22 μ m syringe filter (Millipore). A working solution was prepared by diluting the stock solution 10-fold in PBS buffer (pH 7). The fluorescence intensity of the β -lg samples was measured from 430 to 480 nm wavelength by a fluorescence spectrophotometer (LS 55, Perkin Elmer).

AFM images were collected using a Multimode V (Veeco) operated in tapping mode in air.

III. RESULTS

Ascorbic acid strongly affected the formation kinetics of β -lg fibrils, resulting in a decline in fibrillation. During the fibrillation, elongation phase is further delayed when the β -lg fibrils aggregate with ascorbic acid. After equilibrium state, maximum intensity of ThT decreased by 20% in the presence of 3 mM ascorbic acid.

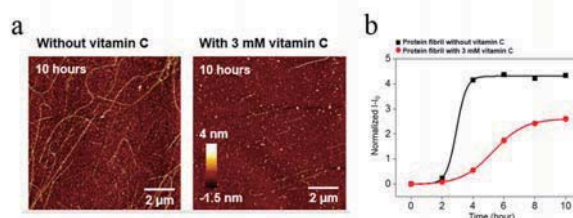


Fig. 1. β -lg fibrillation with/without ascorbic acid. AFM images of the β -lg fibrils formed with/without ascorbic acid (a). Thioflavin T fluorescent assay of the β -lg fibrils (b).

IV. CONCLUSION

In summary, ascorbic acid affected the growth and formation kinetics of the β -lg fibrils. Furthermore, ascorbic acid exhibits an effect to structurally alter the conformation of the β -lg fibrils during the fibrillation. Our results shed light on understanding the underpinning retardation and inhibition mechanism of ascorbic acid and developing the bio-friendly therapeutic agent for treatment of amyloid related diseases.

ACKNOWLEDGEMENT

This work was supported by grant of the Korea Health Industry Development Institute (KHIDI), funded by the Ministry of Health & Welfare, Republic of Korea (grant number: HI12C1837).

REFERENCES

1. G. Merlini and V. Bellotti, "Molecular Mechanisms of Amyloidosis," *N. Engl. J. Med.*, vol. 349, pp. 583-596, 2003.
2. S. Y. Kook *et.al*, "High-dose of vitamin C supplementation reduces amyloid plaque burden and ameliorates pathological changes in the brain of 5XFAD mice", *Cell Death Dis*, vol. 5, e1083, 2014.

Correlation between trabecular bone score(TBS) and age, body size, and bone mineral density(BMD) : the Korean population

Junghyun Park¹, Young-Seong Kim¹, Eunji Lee¹, and Taeyong Lee^{1,*}

¹Department of Medical Biotechnology, Dongguk University, Ilsan, Republic of Korea

E-mail: tlee@dongguk.edu

Abstract—Trabecular bone score(TBS) is a new index to measure fracture risk. We analyzed the correlation between TBS and variable factors, i.e. age, body size and bone mineral density. We found that age, BMD and women's height are highly related with TBS. This results present which factors affect bone microarchitecture related to osteoporosis.

Keywords—trabecular bone score(TBS), bone mineral density(BMD), bone microarchitecture, age, body size

I. INTRODUCTION

The factors of osteoporosis are low bone density and microarchitecture deterioration of bone tissue. As well known, bone mineral density(BMD) is not accurate to predict the fracture risk[1]. So, we used trabecular bone score(TBS) for measurement of bone microarchitecture that represents bone quality independently of bone density[2]. TBS is a new index which utilizes the same DXA image but can enhance the diagnostic precision of osteoporosis. This study provides the correlation between TBS and age, body size(weight, height, BMI: body mass index), and BMD.

II. METHODS

A. Subjects

We randomly selected 8,610 subjects(4,472 women and 4,138 men, aged 20-79 years) from several hospitals in Korea. Participants who have abnormal DXA data or lumbar spine disease were excluded. As a result, 8,344 subjects (4,374 women and 3,970 men, 96.91%) were used to analyze the correlation of fracture risk factors related to microarchitecture.

B. TBS calculations

We used TBS iN Sight software (version 2.1.1, Med-Imaps, Bordeaux, France) to calculate lumbar spine TBS. DXA images were used on this software for aBMD and TBS measurements.

C. Statistics

Pearson correlation coefficients between variables, piecewise linear regression models were used. Data were expressed as mean±SD. Results were considered significant if $p \leq 0.05$.

III. RESULTS

Baseline characteristics (mean±SD) of subjects such as age, spine BMD, weight, height, BMI and TBS were 42.0±9.0 years old, 23.2±3.4g/cm², 64.2±12.6kg, 165.9±8.7cm, and 1.5±0.1, respectively. As shown in Table 1, TBS highly correlated with the age (women: $r=0.93$, $p<0.01$; men: $r=0.78$, $p<0.01$), BMD (women: $r=0.88$, $p<0.01$; men: $r=0.85$, $p<0.01$) and women's height ($r=0.77$, $p<0.01$). TBS weakly correlated with the BMI (women: $r=-0.16$, $p<0.01$; men: $r=-0.13$, $p<0.01$), weight (women: $r=0.09$, $p=0.09$; men: $r=0.13$, $p<0.01$), men's height ($r=0.37$, $p<0.01$).

IV. CONCLUSION

TBS has a strong correlation with age, BMD in both gender. However, TBS showed a correlation with height only in women. This is because estrogens affect bone metabolism more in women than man. Our study also shows that the three factors(age, BMD, height of women) are associated with bone microarchitecture-based osteoporosis. To enhance the accuracy for predicting fracture risk, we are going to include fracture and drug history in the future study.

Table 1. Comparison of correlation coefficient between TBS and demographic variables or aBMD for women and men, respectively

	Women	Men
Age	0.93 ($p<0.01$)	0.78 ($p<0.01$)
Weight	0.09 ($p=0.09$)	0.13 ($p<0.01$)
Height	0.77 ($p<0.01$)	0.37 ($p<0.01$)
BMI	-0.16 ($p<0.01$)	-0.13 ($p<0.01$)
BMD	0.88 ($p<0.01$)	0.85 ($P<0.01$)

REFERENCES

1. S. Di Gregorio, L. Del Rio, and J. Rodriguez-Tolra, "Comparison between different bone treatments on areal bone mineral density (aBMD) and bone microarchitectural texture as assessed by the trabecular bone score (TBS)," *Bone.*, vol. 75, pp. 138-143, 2015.
2. Leslie WD, Krieg M-A, and Hans D, "Manitoba bone density program. Clinical factors associated with trabecular bone score," *J Clin Densitom.*, vol. 16, pp. 374-379, 2013.

The effect of sonic vibration massage system to prevent low back pain caused by driving postures

I. J. Jang, and J. I. Youn*

Department of Biomedical Engineering, Catholic University of Daegu, Gyeongsan, South Korea

*E-mail: jyoun@cu.ac.kr

Abstract— In this study, we proved the effect of sonic vibration massage system to prevent low back pain caused by driving postures. The electromyogram (EMG) measurement was conducted to evaluate the effectiveness of a sonic vibration. The results were shown to distinguish the optimal frequency and the control group. Therefore, the sonic vibration massage system is likely to be a good for relieving low back muscle in a car seat.

Keywords— low back pain, sonic vibration, electromyogram.

I. INTRODUCTION

Many drivers had experienced musculoskeletal disorders like low back pain from driving caused by sitting for long periods of time and unbalanced body postures [1]. But existing technologies have the technical limitations to relieve muscle pain and fatigue like discomfort and lack of feedback.

Here, we proved the effect of sonic vibration massage system using a previously found the optimal frequency (11Hz). The muscle signal was measured using EMG to prove the effectiveness of sonic vibration. This study may helpful for reducing the low back pain during driving.

II. METHODS

A. Instrumentation

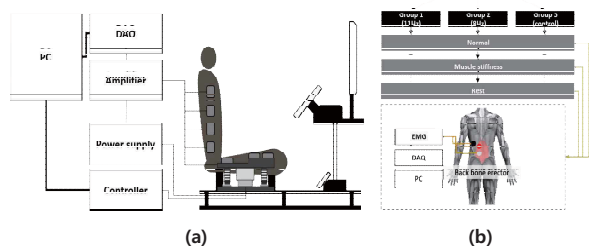


Fig. 1. Configuration of the sonic vibration massage system (a) and measurement procedures (b)

The system we developed is consisted of 14-channel load cell module connected with the amplifier, vibration actuator connected with the controller, and DAQ board connected with a PC (Fig 1). We divided into three groups (11Hz, 8Hz, and control group), and then their muscle signals were measured in back extension.

III. RESULTS

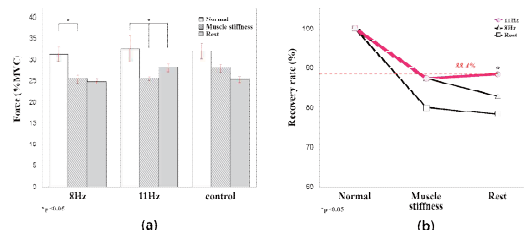


Fig. 2. Results of the time series analysis

There was a significant increase between muscle stiffness and rest at 11Hz (Fig. 2(a)). Furthermore, there was a remarkable difference for the force (%MVC) and the recovery rate of rest at 11Hz (Fig. 2(b)).

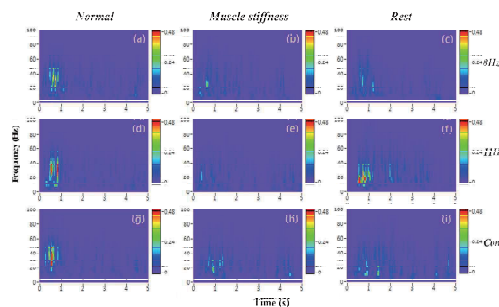


Fig. 3. Results of the wavelet transform analysis

The spectrogram of (f) in Figure 3 showed the strong low-frequency that corresponded to a strong force of muscle contraction. It means that the back bone erector are significantly recovered.

IV. CONCLUSION

The effect of the optimal vibration frequency during driving postures has proved to be reliable for reducing low back pain with high stability.

ACKNOWLEDGEMENT

This work was supported by Business for Cooperative R&D between Industry, Academy, and Research Institute funded Korea Small and Medium Business Administration in 2015 (Grant No.C0236790).

REFERENCES

1. J. L Kelsey and A. A. White III, "Epidemiology and impact of low-back pain," Spine, vol. 5. no. 2, pp. 133-142, Mar/Apr. 1980.

The Study on electrical property according to the change of bottom electrode for Bendable Sensor

G.Y. Choi¹, R.Y. Yun¹, Y.H. Shin¹, M.J. Han¹, K.T. Kim¹, Y.J. Heo¹, K.M. Oh¹, S.H. Nam¹

Department of Biomedical Engineering, Inje University, Gimhae, South Korea¹
E-mail: cgy9110@nate.com

Abstract— Recently, studies on the bendable sensor to reduce the distortion due to the patient's physical structure in X-ray shooting. This study evaluates the bendable properties and the electric properties of the bottom electrode based sensor having bendable properties.. And Cu film and ITO film are evaluated to show similar results with Ref. Sensor's for the linearity of 99% on the tube voltage. Such study result on the bottom electrode is considered to be possible to be used as a basic research of the next generation's bendable detector to improve the distortion caused by the physical structure.

Keywords— Bendable, Sensor, Photoconductor

I. INTRODUCTION

Currently, in the diagnostic radiology sector, X-ray images are acquired by using FPD(Flat Panel Detector). Since the patient's physical formation and properties are not considered for FPD, issues on image distortions exists. Therefore, this study aims to present the availability of a sensor based on the bendable bottom electrode to apply in the next generation's detector technology by producing and evaluating the sensor.

II. METHODS

In this study, for the bendable bottom electrode, the film made of Copper(Cu), Aluminum(Al) and Indium Tin Oxide(ITO) is employed. To evaluate the bendable sensor produced by such method, the analysis is conducted by using the sensor based on ITO glass bottom electrode as Ref. Sensor.

A. Fabrication of Bendable sensor

To produce the bendable sensor, the paste is made by mixing powder type Lead(II) Iodide(PbI₂) to the binder. And, through Screen Printing method to produce the sensor, the paste is applied on the bendable bottom electrode. And the top electrode is formed by plating gold in Physical Vapor Deposition(PVD) method to obtain the electric signal.

B. Measurement of Bendable property

To evaluate the bendable performance of the produced sensors, 3 Point Bending Test that applies the load on Iso-center after fixing the edge of each sensor. At this time, the load is applied repeatedly for 10 times with the angle of bending fixed to 30° and any crack occurrence on the sensor surface is examined.

C. Measurement of Electrical property

By unifying the thickness referencing the PbI₂ Sensor having the largest thickness among the bendable sensors passed the bending test, the electric property evaluation is performed. For the electric evaluation, measurements on the sensitivity and dark current are performed by increasing Tube Voltage (kVp) from 40 kVp to 120 kVp in the unit of 20 kVp. At this time, Bias Voltage driving the sensor is fixed to 1.0 V/μm while Tube Current and Exposure Time are respectively fixed to 100 mA and 100 ms.

III. RESULTS

According to the bending result, Broken Thickness on Al film shows at 120 μm or more, and, in cases of Cu film and ITO film, the bending is performed moderately up to 150 μm. Based on such result, the sensor is produced with the thickness of 100 μm, and the electric properties are evaluated.

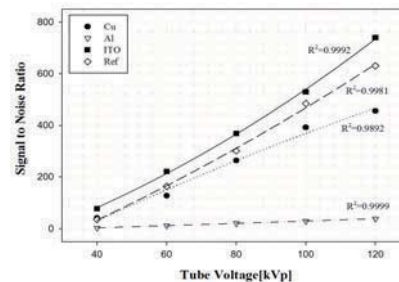


Fig. 1. SNR as a function of X-ray energy

According to SNR evaluation, Al film shows to have the lowest SNR value while Cu film and ITO film have values exceeding 200 when Ref. Sensor shows 80 kVp.

IV. CONCLUSION

ITO film is found to have the relatively insignificant sensitivity, yet have a high SNR value due to its significantly low dark current. On the other hands, Cu film is evaluated to have the electric properties of the very excellent sensitivity, yet of a little high dark current. Therefore, the application possibility in the next generation's detector is considered to be improved through multilateral researches on the dark current reduction.

ACKNOWLEDGEMENT

This work was supported by the National Research Foundation of Korea(NRF) grant funded by the Korea government(MSIP) (No. 2014R1A2A1A11052504).

The Study on electrical properties of radiation sensor according to the change of mixing ratio of metal oxide

R.Y. Yun¹, G.Y. Choi¹, M.J. Han¹, K.T. Kim¹, Y.J. Heo¹, K.M. Oh¹, S.K. Park², S.H. Nam¹

Department of Biomedical Engineering, Inje University, Gimhae, South Korea¹

Radiation Oncology, Busan paik hospital, Busan, South Korea²

E-mail: diana6268@naver.com

Abstract— Excellent reproducibility is required for the detector acquiring medical image. Studies on improvement of the reproducibility by mixing photoconductors to metal oxide to satisfy such requirement are reported. Therefore, this study aims to present an optimized mixing ratio by assessing the electric properties of a radiation sensor following the change of Metal oxide w%. According to the result of study test, excellent properties are showed in 5 - 10 w% for Ti series and in 10 - 15 w% for Si series.

Keywords—Metal oxide, Atomic weight percent, Electrical properties

I. INTRODUCTION

Various detectors are studied for the accurate diagnosis on minute lesion following the development of digital technology on acquiring medical image. For such detectors, excellent Linearity as well as super resolution and reproducibility are required. Recently, various studies are conducted to satisfy such technical requirement. While some of such study report the improvement of reproducibility by mixing metal oxides in photoconductors, the issues that the electric properties are reduced on certain mixing ratios of medal oxides. Therefore, this study aims to present an optimized mixing ratio for the radiation sensor by conducting an experiment on the change of electric properties following the mixing ratios of photoconductor and metal oxide.

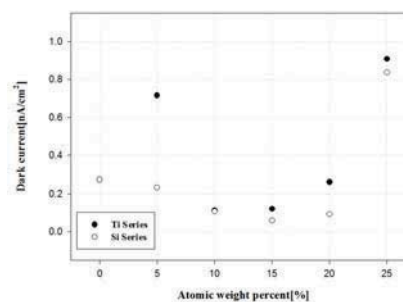
II. METHODS

For the experimentation, a radiation sensor considering the mixing ratios of photoconductor and metal oxide on the atomic weight percent (w%). For the photoconductor, PbI₂ is selected and Silicone (Si) series and Titanium (Ti) series are selected for the metal oxides. To analyze the metal oxide added sensor, comparisons on the electrical properties are conducted having a pure PbI₂ based sensor as the reference. Also, Signal to Noise Ratio (SNR) is calculated.

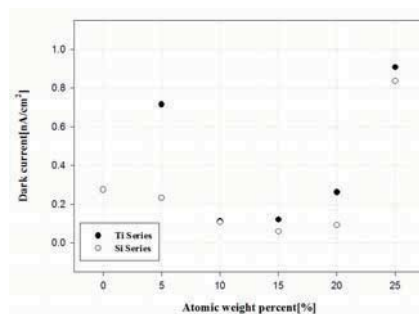
III. RESULTS

According to the analysis of the dark current on each w%, for Ti series, 10 w%, and for Si series, 15 w% are

shown to be the most excellent. Also, according to the analysis of sensitivity, the most excellent electric properties are shown at 5 w% of the mixed metal oxide.



[a] Dark Current



[b] Sensitivity

Fig. 1. Electrical properties as a function of weight percent

In the analysis of the dark current, Ti series is reduced to approx. 58% compared to Ref. Sensor while Si series is reduced to approx. 78%.

IV. CONCLUSION

In this study, the change of electric properties is assessed by mixing the metal oxide to PbI₂ in changed w%. SNR calculated by analyzing the dark current and sensitivity is shown to be 5 - 10 w% for Si series with the most excellent properties at 10 - 15 w%. Based on such result, the improvement of electric properties by studying on the optimization ratio with more detail subdivision of the maxing ration of excellent electric properties is considered to be required in the future.

ACKNOWLEDGEMENT

This work was supported by the National Research Foundation of Korea(NRF) grant funded by the Korea government(MSIP) (No. 2014R1A2A1A11052504).

The development of Radiation detector improved reproducibility study using oxide materials in radiotherapy

M.J. Han¹, G.Y. Choi¹, R.Y. Yun¹, Y.H. Shin¹, K.T. Kim¹, J.S. Kim¹, S.K. Park², S.H. Nam¹

Department of Biomedical Engineering, Inje University, Gimhae, Korea¹

Radiation Oncology, Busan paik hospital, Busan, Korea²

E-mail: gjjgyji@gmail.com

Abstract— This study is on the comparison and analysis on the signal reproducibility of Mixture HgI₂ with Pure HgO having the oxide structure and Ti based metal oxide to resolve the issue that the response property on the continuously radiated X-ray is gradually reduced due to the charge trapping. The test result shows SE value that is relatively higher than the existing Pure HgI₂. Also, Pure HgO and Mixture HgI₂ show better reproducibility with SE 1.73032%p and 0.81945%p than that of existing Pure HgI₂.

Keywords—Radiotherapy, Photoconductor, Detector

I. INTRODUCTION

In the radiotherapy using high energy, accuracy and precision are required since any insignificant error in does produces a great deal of danger for patient. Among photoconductors to calculate the does, HgI₂ (Mercury(II) Iodide) having the high stopping power has properties of the high sensitivity and the low leakage current. However, HgI₂ has the issue that the electric signal is gradually reduced by the occurrence of charge trapping on the continuously radiated high energy. Therefore, this study aims to examine the trend of electric signal change due to the charge trapping by using Pure HgO (Mercury(II) oxide) and Mixture HgI₂ with the Thallium (Ti) based metal oxide.

II. METHODS

In this study, Pure HgI₂, Pure HgO and Mixture HgI₂ of Ti based metal oxide as the photoconductor sensor converting the radiated does to the electric signal. For the bottom electrode, ITO(Indium Tin Oxide) glass is used. And the electric signal of the continuously radiated high energy is analyzed with ACQ program on the waveform acquired through the oscilloscope of Linear Accelerator (Varian Inc., LINAC 21xi). The evaluation on such electric signal is performed by analyzing of the normalized sensitivity of each sample. And, based on the evaluation, the reproducibility is evaluated by drawing SE (Standard Error; SE) having the confidence interval of 95%.

III. RESULTS

According to the test result, SE of Pure HgI₂ shows the high error rate of 1.73033%. On the other hands, Mixture HgI₂ shows the electric properties improved by 0.81945%p compared to that of Pure HgI₂. And Pure HgO shows very excellent reproducibility of approx. 0.00001% and is analyzed to have the better electric properties by approx. 1.73032%p compared to that of Pure HgI₂. Fig. 1 illustrates the response property on the continuously radiated X-ray.

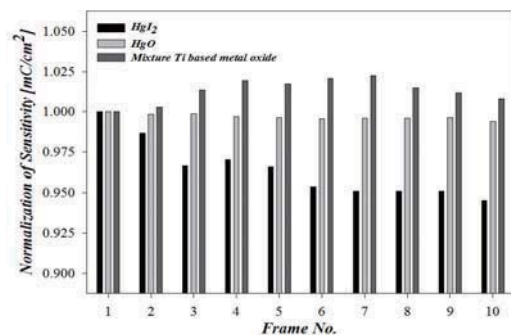


Fig. 1 Comparison of the response properties

While Pure HgI₂ shows the trend of gradual sensitivity reduction by reacting to the continuous X-ray, Mixture HgI₂ shows the trend of gradual signal increase. On the other hands, Pure HgO having the oxide structure is analyzed to have the uniformed sensitivity on X-ray.

IV. CONCLUSION

This study analyzes SE on Pure HgI₂, Pure HgO and Mixture HgI₂ and presents the result. According to the result, it is analyzed that Pure HgO and Mixture HgI₂ have excellent reproducibility of 0.00001% and 0.91087% respectively. However, in case of Mixture HgI₂, it is considered that the charge is accumulated by the charge trapping and causes the gradual signal increase. It is considered that various researches on materials having oxide structures and mixing ratios of such materials should be performed based on this result in the future.

ACKNOWLEDGEMENT

This work was supported by the National Research Foundation of Korea(NRF) grant funded by the Korea government(MSIP) (No. 2014R1A2A1A11052504).

Development of belt type falling and heart rate detection system with remote Monitoring smartphone application

Y.H. Cho¹, E.I. Cho¹, J.H. Heo¹, J.H. Cho¹, Y.R. Yoon¹

¹Department of Biomedical Engineering, Yonsei Univ., Wonju, Korea, Republic of.
E-mail: yoony@yonsei.ac.kr

Abstract—In this study, we devised efficient falling detection and heart rate detection methods making type of belt as wearable device. Then, we applied to smart phone with application to monitor status of the elder. Our falling detection algorithms reduce the number of sensors and simplify calculation. In addition, we made this module be able to transmit the heart rate information to application. So, using application, we can always monitor the heart rate and the location of user. To verify this module, we experimented sensitivity and specificity.

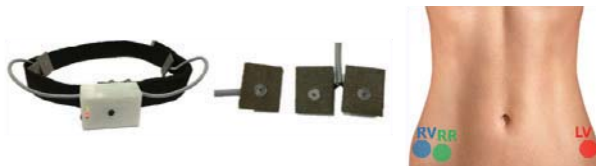
Keywords— ECG, Wearable device, Application, Falling Detection, GPS

I. INTRODUCTION

According to a survey about falling, senior has high incidence rate about fall. In this study, we made the belt type module which can detect a fall and monitor the heart rate for the senior. We simplify the sensor and the algorithm of falling detection. And we made the application which can interlock with module. This application can trace user's location and heart rate.

II. METHODS

A. Hardware



Belt type module includes the electronic circuit to detect the heart rate using conductive fabric electrodes. And 3axis acceleration sensor detects the falling. The module is made up with 3 electrodes(RV, RR, LV). Through the experiment, we decide the site of electrodes where has the lowest motion artifact.

B. Algorithm

Through the tri axis acceleration sensor, we detect the acceleration to calculate the root sum square(RSS). If the RSS is bigger than 2.2, it will detect the acceleration again after 300ms. At this moment, if the angle between ground and body is less than 30 degrees, it is decided as the falling.

C. Android Application



Through the application, protectors can monitor the user's heart rate. And when the protector requests the user's location, it will provide the address through GPS. And if user is in the emergency situation like the falling, notification will be displayed at protector's smart phone screen.

III. RESULTS

Ten healthy adults(N = 10: seven male, three female; age, 23-28yrs) wear the belt rightly. And the subjects try to fall 4 directions and act like 5 daily motions. In the case of front and back falling, sensitivity is 100% and right, left direction falling show the sensitivity of 96%. Daily Activity, sit, lie, capriole, run and pick up, shows the accuracy of 100% except the motion of lie.

ACKNOWLEDGEMENT

This research was supported by the corporate associated research development manpower training Program of the Ministry of Trade, Industry and Energy (N0001130).

IV. CONCLUSION

In this study, we simplify the functionality of the sensor and the gyro sensor's function is maintained. And we suggest the effective way to detect the heart rate at the waist with fabric electrodes. Through the application, the protector can check the user's heart rate and real-time location.

REFERENCES

1. Deaths: final data for 2005 Kung, Hoyert, Xu, Murphy, & Division of Vital Statistics, 2008
2. Evaluation of waist-mounted tri-axial accelerometer based fall-detection algorithms during scripted and continuous unscripted activities(2010) A.K.Bourke / 2010 / Journal of Biomechanics

A New Way for Cancer Surgery: Fluorescence Imaging Guided Surgery with Augmented Reality

Jungsuk Heo¹, MinJi Kim¹, Yu Hua Quan², Youngwoon Choi¹,
Hyun Koo Kim² and Beop-Min Kim¹

¹Department of Bio-Convergence Engineering, Korea University, Seoul, Korea

²Department of Thoracic and Cardiovascular Surgery, Korea University Guro Hospital, Korea University Colleague of Medicine, Seoul Korea

* J.Heo and M.Kim contributed equally to this work.

E-mail: bm515@korea.ac.kr

Abstract— This study was performed to validate a newly developed smart goggle system that implements an augmented reality based fluorescence imaging using Google Glass and a near infrared (NIR) camera. In order to achieve augmented reality, we developed a software that allows the real time NIR image processing and video streaming for the smart goggles. After obtaining the fluorescence image with the NIR camera, the image is directly transmitted for to the Google Glass platform for display. The smart goggle system utilizes a three-point matching technique in order to match the angle and size of the images between the Google Glass and NIR camera.

Keywords— augmented reality, google glass, fluorescence image, three-point matching, smart goggle

I. INTRODUCTION

Fluorescence imaging¹ is widely used to reduce unnecessary resectioning of healthy tissues that often leads to postoperative complications and morbidities in cancer patients². However, surgery using fluorescence imaging requires the surgeon to observe a monitor in order to perform the surgery. The discordance between the monitor and the surgeon's line of sight can create an uncomfortable experience. A wearable augmented reality (AR) system is a possible solution for a more comfortable and accurate fluorescence-guided surgical procedure. Therefore, we propose a smart goggle fluorescence imaging system using Google Glass and a near infrared (NIR) camera in order to aid in fluorescence-guided surgeries. This study validates the ability of our proposed smart google system to detect cancer in an animal model.

II. METHODS

A. Software

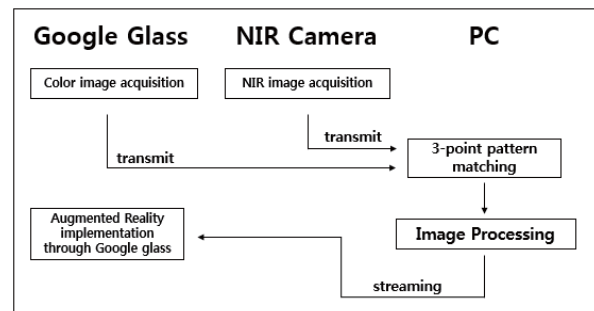


Fig. 1. Software flow chart

Figure 1 shows the general software workflow of the smart goggle system. The entire surgical procedure is captured using a NIR CMOS camera (Basler, acA2040-180kmNIR). A three-point pattern matching software is used to align the size and angle images captured by the NIR camera to the Google Glass' camera. Indocyanine green (ICG³), the NIR fluorescent agent used in the study, is detected using NIR camera, and undergoes image processing to reveal the fluorescent image. These processed images are then sent to the Google Glass platform for display via socket program⁴.

B. Animal experimental

Six-week-old female C57BL/6 mice (Orient Bio, Seoul, Korea) were used for in vivo experiments. Lewis Lung carcinoma cells were injected to the footpad and the cancer model was established 3 weeks after injection. 10 mg/kg of Zoletil (Vairbac, Carros, France) and Bayer (Seoul, Korea) was intramuscularly injected to the mouse, and approximately 2-5 mg/kg of ICG was intravenous injected directly to the footpad cancer model. The distribution of ICG in tumor was observed by our smart goggle system approximately 6 hours after cancer model establishment.

III. RESULTS

We observed cancer on the rat's left footpad (Figure 2) with the developed smart goggle system. The test was done in-vitro using a fluorescence sample and we

were able to obtain fluorescence images of the cancer. The system's user confirmed that the displayed images by the smart goggles closely matched their own line of sight. Our experiment also confirmed that the cancer can be distinguishably visualized from healthy tissue which shows the possibility of our smart goggle system to increase the accuracy and precision of the removal cancers from normal tissues.

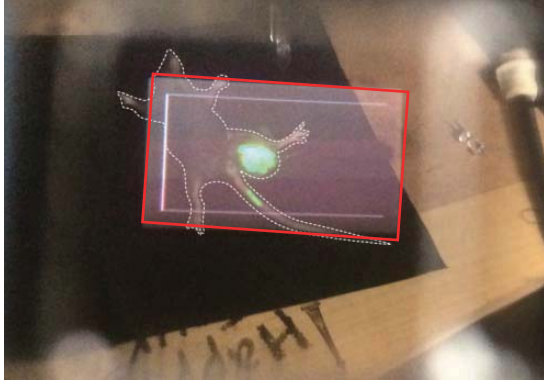


Fig. 2. A view through Google Glass

IV. CONCLUSION

We developed a smart goggle system that implements augmented reality through Google Glass' video streaming software. The smart goggle system enables real-time visualization of cancer through the guidance of fluorescence imaging, which can be very useful during surgical procedures. For future developments, we plan to broaden the field of view of the smart goggle system with further modification of the hardware.

ACKNOWLEDGEMENT

This work was supported by a Grant from the Technology Innovation Program (10049039) funded by the Ministry of Knowledge Economy. (MKE, Korea)

REFERENCES

1. Yamashita S, Tokuishi K, Anami K, et al. "Video-assisted thoracoscopic indocyanine green fluorescence imaging system shows sentinel lymph nodes in non-small-cell lung cancer." *J Thorac Cardiovasc Surg.* 2011;141:141-4
2. Nomori H, Iwatani K, Kobayashi H, Mori A, Yoshioka S. "Omission of mediastinal lymph node dissection in lung cancer: its techniques and diagnostic procedures". *Ann Thorac Cardiovasc Surg.* 2006;12:83-8
3. Choi JY, Jeong JM, Yoo BC, et al. "Development of Ga-68-labeled mannosylated human serum albumin (MSA) as a lymph node imaging agent for positron emission tomography." *Nucl Med Biol.* 2011;38:371-9
4. Moon SW, Kim YJ, Myeong HJ, Kim CS, Cha NJ, Kim DH, "Implementation of smartphone environment remote control and monitoring system

for Android operating system-based robot platform." *URAI*, 2011-pp 211-214

Development of a Control device automatically determining the angle difference between the X-ray source and detector on portable digital radiography system

D. W. Heo¹, J. H. Ryu¹, C. W. Jeong¹, T. H. Kim¹, H. Y. Jun¹, S. C. Kang¹, and K. H. Yoon^{1,2}

¹Imaging Science Research Center, Wonkwang University

²Dept. of Radiology, Wonkwang University School of Medicine

E-mail: khy1646@wonkwang.ac.kr

Abstract— We developed a control device that can obtain the angle values from X-ray source and detector, respectively. This device determines whether oblique and/or parallel plane and displays the angle difference between X-ray source and detector on the LCD monitor. The device would be useful to achieve the accurate oblique and/or parallel plane images in clinical setting.

Keywords— Digital Radiography (DR), Portable DR, Medical Devices.

I. INTRODUCTION

In present, most of commercialized portable DR system is well-equipped with tape measure to calculate X-ray source-to-detector distance (SDD). However, X-ray source-with-detector angle (SDA) is relatively little supplied on the system. Therefore, this study was to develop a control device for obtaining an SDA. This device determines whether oblique and/or parallel plane and displays the angle difference between X-ray source and detector on the LCD monitor.

II. METHODS

The developed device consisting of a main board (Arduino Uno Rev3), a 6 DOF IMU Shield (embedded the ADXL345 accelerometer and the ITG-3200 gyro), a Bluetooth Module (HC-05 master, HC-06 slave) is attached on X-ray source (device1) and detector (device2), respectively. To measure the angle difference between X-ray source and detector, processing procedures are as follows: The Arduinos of devices1, 2 receive angle data through I2C communication from 6 DOF IMU Shield. Then, the Arduinos calculate the angle values, device1 (X_S, Y_S) and device2 (X_D, Y_D) by applying an algorithm to the angle data. The Bluetooth module (HC-06) on device2 receives angle values (X_D, Y_D) via a serial communication from Arduino. Also, it transmitted angle values (X_D, Y_D) to the Bluetooth module (HC-05) of device1 in real-time. The Bluetooth module (HC-05) of device1 transmitted angle values (X_D, Y_D) to the Arduino via a serial communication. Finally, the Arduino of device1 calculates a SDA difference values (X_{SDA}, Y_{SDA}) as follows: $X_{SDA} = X_S - X_D$, $Y_{SDA} = Y_S - Y_D$.

III. RESULTS

Figure 1 demonstrates the developed device attached on X-ray source and detector, respectively. The

developed device is $80 \times 55 \times 35$ mm size (South Korea 500 Won coins - 2EA). Figure 2 shows the LCD monitor that displays angle values on X-ray source of portable DR system. With regard to the angle difference obtained from our device, the SDA value displays real-time (2 times per second) on the monitor and its accuracy is $\pm 2^\circ$ error.

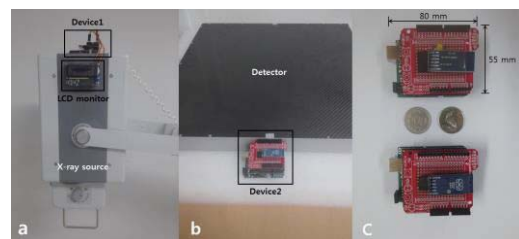


Fig. 1. The details of developed devices on X-ray source(a) and detector (b), and its actual size (c)



Fig. 2. Portable digital radiography system and display window of LCD monitor on X-ray source

IV. CONCLUSION

Our device successfully displayed the angle difference between X-ray source and detector. Our device would be useful to obtain the accurate oblique and/or orthogonal plane images using portable digital radiography system in clinical setting.

ACKNOWLEDGEMENT

This study was supported by the grants of the Korean Health Technology R&D Project (HI12C-0110-000014, Ministry of Health & Welfare, Republic of Korea), and the Technology Programs (Grants No. 10046756 and 10047759, Ministry of Trade, Industry & Energy (MOTIE)).

REFERENCES

1. B. McCarron. "Low-Cost IMU Implementation via Sensor Fusion Algorithms in the Arduino Environment," *Aerospace Eng.* 2013, URL: <http://digitalcommons.calpoly.edu/aerosp/125>.

A computational parameter study of noninvasive electrical stimulation to the epiphyseal plate

H. J. Park¹, J. H. Ku³ and S. Kim^{1,2}

¹School of Mechatronics, Gwangju Institute of Science and Technology, Gwangju, Korea

²Department of Medical System Engineering, Gwangju Institute of Science and Technology, Gwangju, Korea

³Department of Biomedical Engineering, Keimyung University, Daegu, Korea

E-mail: soheekim@gist.ac.kr

Abstract—FEM simulations were conducted for noninvasive electrical stimulation (capacitive coupling) used for treatment of short stature in Turner syndrome. The band-shaped stimulators generated relatively even electric field distribution at the growth plate than square pads. The required current intensity was reduced by increasing the distance between the stimulators.

Keywords— growth plate, electrical stimulation, FEM simulation.

I. INTRODUCTION

Turner syndrome (TS) is known as an inherited disease by X chromosomal abnormality. The patients with TS have been treated by using the recombinant human growth hormone (GH) and/or estrogen therapy and distraction osteogenesis (DO) to overcome the marked short stature. However, several studies reported accompanied side effects such as tumor formation and physical sequela. As an alternative approach rather than pharmacological or operative remedy, electromagnetic stimulation of bones are investigated in the present study, which have been used for healing of bone fracture and growth plate stimulation. In previous studies, accelerated bone healing and bone growth effects by electromagnetic field stimulation were confirmed in consequence of animal studies. Based on the preceding results, we consider non-invasive direct electrical stimulation as a substitutive method to help lengthening the bone height for the patients with turner syndrome. Using finite element method (FEM) simulation, we studied the electric field distribution and required current intensity for inducing the electric field above threshold according to the size and location of square-type and band-type stimulators.

II. METHOD

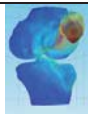
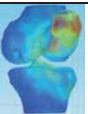
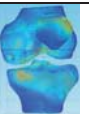
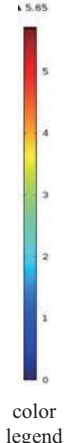
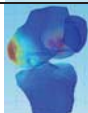

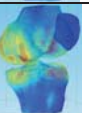
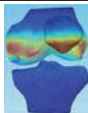
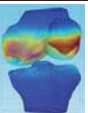
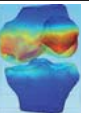
MRI data of the knee of a 35-year-old male was translated to the STL format using 3-matic (Materialise HQ Inc., Leuven, Belgium) and each component (skin, muscle and bones (femur, tibia and patella)) was united in the COMSOL 5.1 (COMSOL Inc., Los Angeles, CA, USA) for FEM modeling. To search for the threshold level for bone growth, we conducted preliminary simulations. The used parameters were adopted from a previous animal study [1]. After obtaining the threshold level, the simulations were conducted

according to the size and location of noninvasive stimulators of square- and band-type designed to be attached on the skin surface.

III. RESULT

As the pad size was larger, more current applied to the stimulator was needed to induce the electric field above the threshold for the bone growth, 5.7 V/m, and the effective area by induced electric field was also larger. When the band-shaped stimulators were located upper and lower sides of the knee, the electric field appeared to distribute relatively evenly at the growth plate than laterally arranged square pads. However, quadruple current intensity was required than the square pads due to the total area of stimulator. The required current intensity for inducing the electric field above the threshold was reduced by increasing the distances between the band-shaped stimulators. The reason is that when two stimulators were located at a short distance, the most current flowed through the skin rather than internal tissues. As the distance between two stimulators was increased, the electric field was induced more effectively in the internal tissues not only in the skin.

Table 1. Maximum electric field distribution inducing in the bone around the knee

Pad location	Pad size			color legend
	20 mm	40 mm	60 mm	
Anterior-Posterior (AP)				
Right-left (RL)				
Pad location	Gap of pads			
	10 mm	20 mm	30 mm	
Upper-lower (UL)				

REFERENCES

- [1] M. Forgon et al., "Bone Growth Accelerated by Stimulation of the Epiphyseal Plate with Electric Current," *Arch Orthop Trauma Surg*, vol. 104, pp. 121–124, 1985.

Trainable Hearing Aid Algorithm for Hearing-Impaired Persons

S. H. Yoon¹, H. P. Kim², J. Y. Kim², H. J. Ahn², K. W. Nam², and I. Y. Kim^{1,2}

¹Institute of Biomedical Engineering, Hanyang University, Seoul, Korea

²Department of Biomedical Engineering, Hanyang University, Seoul, Korea

E-mail: shyoonbme@gmail.com

Abstract— Trainable hearing aid algorithm is developed using Matlab Simulink and its performance is evaluated.

Keywords— Trainable hearing aid, Listening situation classifier, Personal preference

I. INTRODUCTION

There is a growing need for hearing aids that are trainable [1] which necessitates a trainable hearing aid algorithm. The proposed algorithm is developed using Matlab Simulink.

II. METHODS

The proposed algorithm shown in Fig. 1, contains three parts which would be listed in detail below. A training phase is required to gather user's preference to the algorithm parameters to operate optimally.

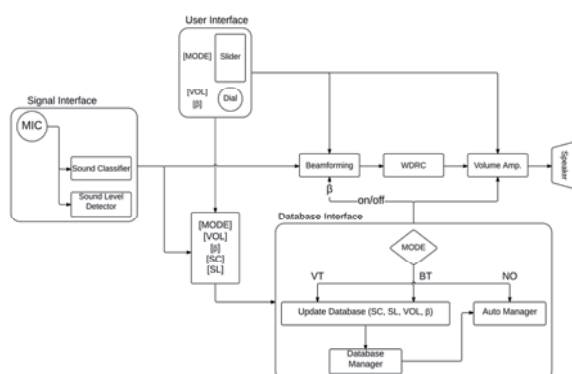


Fig. 1. Schematics of the proposed algorithm

A. Signal Interface

Signal interface gathers information of the ambient listening situation with a Sound Level Detector, which measures the ambient sound level in dB, and a Sound Classifier suggested by Yook and Nam *et al.* [2], which classifies speech-only, noise-only, and speech-in-noise situations.

B. User Interface

User interface allows the user to freely adjust the parameters of the proposed algorithm and switch between Training Mode and Normal Operation (NO) Mode.

C. Database Interface

Database interface collects data gathered during training to be used during the NO mode.

III. RESULTS

A. Algorithm Evaluation

The user preference data gathered during the training phase is compared to the output of the algorithm. Audio tracks simulating the three classified situations are used for both. As shown in Fig. 2, the output of the algorithm automatically adjusts according to the user preference.

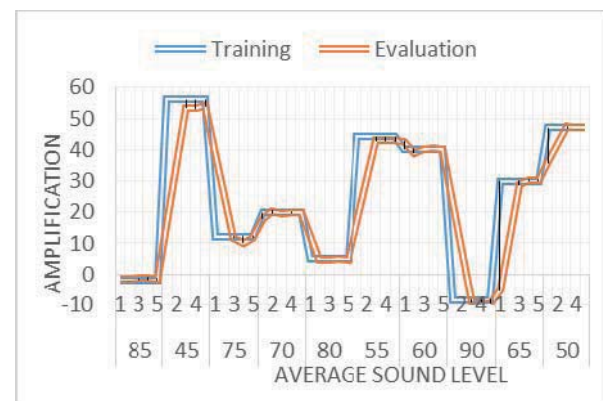


Fig. 2. Algorithm evaluation

IV. CONCLUSION

The proposed algorithm adapts accordingly to the ambient situation based on user preference and thus can conclude that it is operating as intended.

ACKNOWLEDGEMENT

This research was supported by a grant of the Korea Health Technology R&D Project through the Korea Health Industry Development Institute (KHIDI), funded by the Ministry of Health & Welfare, Republic of Korea (grant number : HI14C0771).

REFERENCES

1. World Health Organization, "WHO global estimates on prevalence of hearing loss" 2012.
2. Yook S, Nam KW, Kim H, Hong SH, Jang DP, and Kim IY, "An Environment-Adaptive Management Algorithm for Hearing-Support Devices Incorporating Listening Situation and Noise Type Classifiers" *Artif. Organs*, vol. 39, pp.361-8, 2015.

CNT/PDMS ECG electrode for long-term recording

H.C Jung¹, S.K. Yoo¹, S.A. Lee¹, Jin-Hee Moon¹ and S.H-Lee²

¹Medical Device Development Center, Osong Medical Innovation Foundation, Cheongju-si, Korea

²Department of Biomedical Engineering, College of Health Science, Korea University, Seoul, Korea

E-mail: hacher99@kbio.kr

Abstract— We fabricated a carbon nanotube (CNT)/ polydimethylsiloxane (PDMS) composite-based dry ECG electrode. To evaluate electrical characteristics, we made 36 types of electrodes which were fabricated with different concentrations of CNTs, and with a differing diameter and thickness. Skin tests were conducted over 7 days by attaching the electrodes to the forearms of 4 volunteers and the quality of ECG signal did not degrade and the skin troubles such as itching or erythema were not observed.

Keywords— CNT, PDMS, ECG, Dry electrode, flexible electrode

I. INTRODUCTION

To achieve convenient health monitoring, the development of a long-term wearable bio-electrode is critical. Electrocardiography is a key bio-signal that requires constant monitoring, and the bio-electrode most commonly used to monitor ECG is a gel-type silver/silver chloride (Ag/AgCl) electrode [1]. But they are limited in their long-term use because they can irritate the skin. The gel also dries over time, causing a dramatic decrease in the signal quality [2]. Additionally sweat is another source of signal degradation. [3]

As replacements of conventional Ag/AgCl electrodes for long-term monitoring applications, dry surface electrodes have been considered because they do not require an electrolyte layer [4-5]. In this paper, we propose a carbon nanotube (CNT)/PDMS composite-based ECG electrode that can be readily connected to the conventional ECG device, and showed its use for long-term wearable monitoring capability and robustness to environments including motion and sweat. PDMS has, recently, become a popular choice for biomedical applications for its nontoxicity, high gas, and water permeability and is amenable to a variety of fabrication methods. CNTs show excellent mechanical, electrical, and thermal properties and are inert in the context of biomedical applications. For these reasons, CNTs have been widely used in industrial and biomedical applications. Therefore, CNT/PDMS composites, which combine the characteristics of both materials, may have great potential in the biomedical field as previous research has shown [6].

The fabrication of ECG electrodes was simple and straightforward, and their biocompatibility was evaluated in vitro by continuous wearing of the electrode on a wrist for a week. Also the electrical properties of the electrode were tested. The ECG signals obtained by using CNT/PDMS electrodes were measured under static, motion, and sweating conditions. During seven days of wearing, the ECG signal was measured daily to investigate the quality of the bio-signal over time.

II. METHODS

A. Fabrication of CNT/PDMS Composite Electrodes

The fabrication of CNT/PDMS composite electrodes involved two steps. The first step was the fabrication of a PDMS master mold shown as follows. Circular acrylic plate of diverse sizes and a steel snap, which is straightforwardly connectable to conventional ECG snap clips, were prepared. These components were aligned with each other and were fixed on the bottom surfaces of the petri dish using double-sided tape [see Fig. 1(a)]. PDMS precursor (10:1 mixture of liquid prepolymer (Sylgard 184A, Dow Corning Company) and crosslinking agent (Sylgard 184B, Dow Corning, Company) were poured and thermally cured at 80 °C for 2 h [see Fig. 1(b)]. After curing, the PDMS master mold was separated carefully from the petri dish [see Fig. 1(c)]. The circular acrylic plate was removed from the PDMS mold [see Fig. 1(d)]. The second step involves the fabrication of CNT/PDMS composite electrodes via the replication process. The prepared CNT/PDMS composite was poured onto the PDMS master mold and thermally cured at 80 °C for 2 h [see Fig. 1(e)]. The completed electrode was retrieved from the master mold [see Fig. 1(f)]. To make separation easier, the PDMS master mold was immersed in methanol for 5 min. The methanol smeared into small gaps between the PDMS mold and polymerized CNT/PDMS, making separation easier.

B. Characterization of the Electrical Properties

The composition of CNT and the thickness of the electrodes may be critical in determining the electrical properties. We measured electrode-skin contact impedance as a function of the composition of CNT in PDMS and electrode thickness. The contact impedance between skin and electrode was analyzed, and two electrodes are placed in the forearm 9 cm apart for measurement. They are fixed by using a compression bandage without the skin preparation to improve

conductivity. A voltage of 50 mV is applied from 10 to 100 kHz with the impedance analyzer.

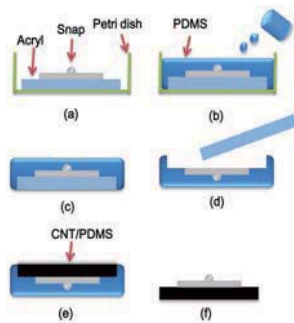


Figure 1 Schematic diagram showing the fabrication process of CNT/PDMS composite electrodes

C. Skin Compatibility Tests

The skin compatibility test was conducted for three examinees using a 2 cm × 2 cm CNT/PDMS (2.0wt%) sheet. The CNT/PDMS sheet was attached on the forearm for seven days with clinically usable air permeable tape (Himom band, JW Pharmaceutical Corporation, Seoul, Korea), and skin reactions, including itching and erythema, were investigated.

III. RESULTS

The well-dispersed CNT/PDMS composite was used to fabricate electrodes. Fig. 2 shows nine different kinds of electrodes. The electrode-skin contact impedance was measured using 2-, 3-, 4-cm diameter and 3-mm thickness CNT/PDMS electrodes from each composition rate of CNT in and plotted as log |Z| against log f in Fig. 3. The value of the contact impedance decreases strongly with increasing frequency and is affected by the diameter. The concentration of the CNT ratio at the 4.5 and 2.0wt% showed almost similar contact impedance, indicating that CNT ratio is saturated from 2.0 to 4.5wt%.

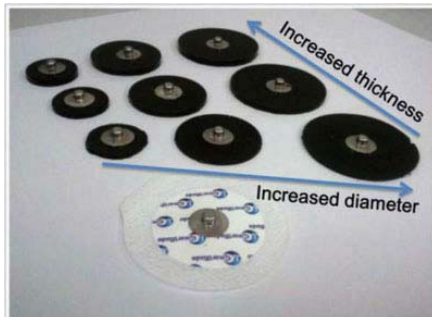


Figure 2 Image of fabricated electrode

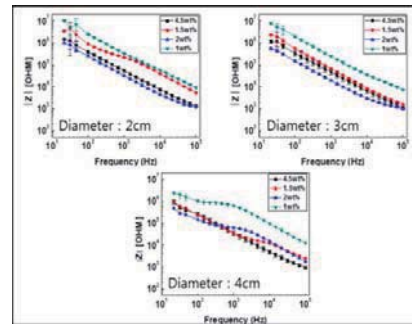


Figure 3 Electrode-skin contact impedance

To gauge the presence of motion artifacts, ECG was measured during a treadmill exercise. The treadmill speed was set to 0, 3, and 5 km/h, and the Ag/AgCl electrode and the 1.5 and 4.5wt% CNT/PDMS electrode (thickness: 3 mm) were used to gather ECG signals as illustrated in Fig. 4. The top ECG signals shown in Fig. 4(a)–(c) are the signals from the resting state, which were noiseless and almost identical. In the ECG signals during slow walking (3 km/h), low baseline noise was observed. The 1.5wt% CNT/PDMS composite electrode exhibited large noise fluctuations, and the P and T waves were not clearly observed. In contrast, the Ag/AgCl and 4.5wt% CNT/PDMS composite electrodes provided almost qualitatively comparable signals. The lowest ECG signals in Fig. 4 were measured during faster walking (5 km/h). More noise was observed under these conditions than under the normal walking state, and QRS and T waves were detected at signals from Ag/AgCl and 4.5wt% CNT/PDMS composite electrodes. These results illuminate the feasibility of robust ECG measurements using CNT/PDMS composite electrodes under normal conditions. The effects of sweat were also tested, and, as shown in Fig. 5, no critical differences among signals were observed in the presence of sweat, even though the heart rate increased after exercise. The ECG was measured for 5–7 days since wearing, and degradation of the ECG signal over time was not observed as shown in Fig. 6, indicating the superior characteristics as a long-term monitoring electrode. Skin compatibility tests were conducted over seven days of continuous wearing of the electrodes on the arms. The skin under the electrode was found to be normal and no itching or erythema was observed during and after seven days of wearing (Fig.7).

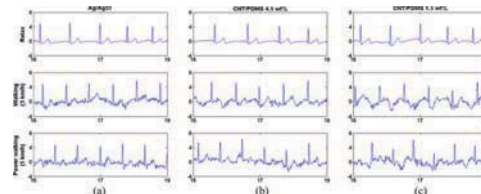


Figure 4 Motion artifact test

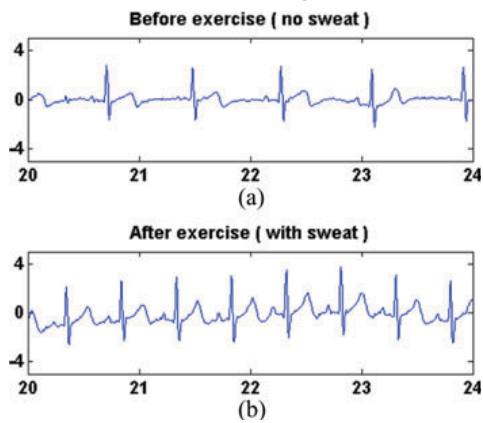


Figure 5 Sweat effect test

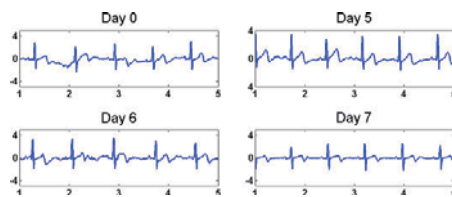


Figure 6 long-term test



Figure 7 Skin test

IV. CONCLUSION

In this paper, we successfully fabricated CNT/PDMS composite electrodes in a straightforward manner and demonstrated that it overcomes limits of conventional dry or wet electrodes. The CNT/PDMS composite electrodes were flexible, biocompatible, and suitable for long-term measurement of the ECG signals. The proposed CNT/PDMS composite electrodes measured ECG signals robustly even in the presence of motion or sweat, and was connectable to commercial ECG machine without an adaptor. The electrode did not generate any noticeable side effects, such as itching or irritation, even after one week of continuous wearing. The signal quality did not decrease over time, in contrast to Ag/AgCl electrodes. The aforementioned results indicate that the composite electrodes are suitable for long-term ECG monitoring due to biocompatibility and robust performance under conditions of motion and sweat. We expect that the proposed CNT/PDMS composite electrodes can be used in daily life to enable ubiquitous mobile health care technology. The reusability of the electrode will contribute to preserving the environment by reducing the waste of used electrodes.

REFERENCES

1. J. G. Webster, *Medical Instrumentation: Application and Design*. New York: Wiley, 1998, pp. 196–215.
2. A. Searle and L. Kirkup, “A direct comparison of wet, dry and insulating bioelectric recording electrodes,” *Physiol. Meas.*, vol. 21, pp. 271–283, 2000.
3. B. A. Taheri, R. T. Knight, and R. L. Smith, “A dry electrode for EEG recording,” *Electroencephalogr. Clin. Neurophysiol.*, vol. 90, no. 5, pp. 376–383, 1994.
4. A. Karilainen, S. Hansen, and J. Muller, “Dry and capacitive electrodes for long-term ECG monitoring,” in *Proc. 8th Annu. Workshop Semicond. Adv. Future Electron.*, Nov. 26, 2005, pp. 155–161.
5. S. Mason. (2005). Dry electrode technology: What exists and what is under development? [Online]. Available: http://www.bci-info.tugraz.at/Research_Info/research_forums/signals/0002/
6. L. Ci, J. Suhr, V. Pushparaj, X. Zhang, and P. M. Ajayan, “Continuous carbon nanotube reinforced composites,” *Nano Lett.*, vol. 8, no. 9, pp. 2762–2766, 2008.

Objective severity assessment system for the unilateral facial palsy based on 3-dimensional depth information

S. M. You¹, E. H. Lee¹, K. H. Lee¹, J.S. Cho¹, J. S. Lee¹, and I. Y. Kim^{1†}

¹Department of Biomedical Engineering, Hanyang University, Seoul, Korea

[†]E-mail: iykim@hanyang.ac.kr

Abstract—The prognosis of Bell’s palsy and Ramsay Hunt is dependent on the severity of facial paralysis. Therefore, the objective assessment is important to determine proper treatments. In this research, we use the Kinect device to extract and track the facial feature point in the purpose of simple assessment of the facial palsy.

Keywords— Kinect v2, Facial nerve palsy, Objective assessment, Facial recording system.

I. INTRODUCTION

Facial nerve palsy (FNP) is a common disorder which is mostly related to Bell’s palsy, Ramsay Hunt Syndrome, or trauma. The Bell’s palsy affects 11-40 persons per 100,000 each year in the world. A slight paralysis is usually recovered easily, but functional recovery from severe paralysis is difficult. Therefore the objective assessment of the severity of facial nerve palsy throughout treatment is important in choosing proper therapy. There have been several approaches to the facial nerve grading system in recent decades. Currently, for the assessment of facial nerve palsy, many clinicians use the House-Brackmann Facial Grading System (HB-FGB), or Sunnybrook Facial Grading System (SFGS). These methods are able to assess the severity without special equipment, but those methods are subjectively carried out by the clinicians, therefore the result was observer-dependent.[1] In this research, we use the Microsoft Kinect for Windows v2 (Kinect v2) sensor to record facial component movements in order to analyze the 3-dimensional facial motion with depth information.

II. METHODS

A. Kinect Sensor and HD Face Library

The Kinect v2 sensor provide two types of video stream. One is RGB color stream with 1920 by 1080 pixels, and the other is infrared depth stream with 514 by 424 pixels. Both video streams are able to be analyzed with the Kinect Software Development Kits (SDKs).

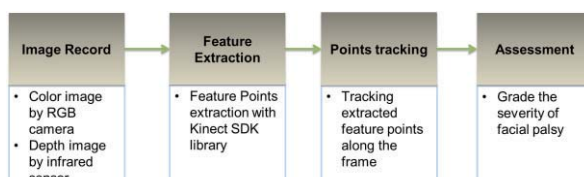


Fig. 1. System Flow

The Kinect SDKs contains HD face library which provides 3-dimensional facial models based on the Active Appearance Model (AAM) method. The systematic flow is shown in Fig. 1.

B. UI framework

The proposed UI (User Interface) program contains instructions in video, audio, and text, which follow the assessment protocol which is combined from HB-FGS and SFGS. The proposed framework is shown in Fig. 2.

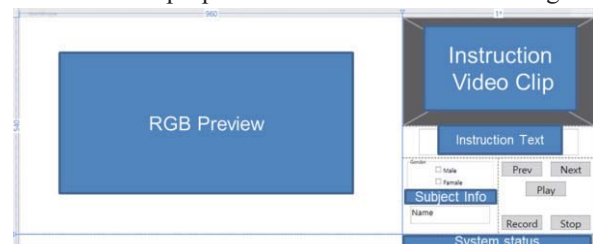


Fig. 2. Proposed System UI framework

III. RESULTS

A. UI system for the data acquisition

We developed the UI system for the data acquisition of the color video and motion of facial feature points, shown in Fig. 3.



Fig. 3. Developed System UI and recorded points data

IV. CONCLUSION

We built the UI system which is able to record both color video and motions of facial feature points following the included assessment protocol. Diagnosis with Kinect sensor, which is cheap and simple, will be helpful for the rehabilitation about the facial nerve disorder and functional recovery of facial palsy in home healthcare.

ACKNOWLEDGEMENT

This work was supported by the ICT R&D program of MSIP/IITP [10045452, Development of Multimodal Brain-Machine Interface System Based on User Intent Recognition]

REFERENCES

- Berg, T., L. Jonsson, and M. Engström, “Agreement between the Sunnybrook, House-Brackmann, and Yanagihara facial nerve grading systems in Bell’s palsy”. *Otology & Neurotology*, Vol 25(6), pp. 1020-1026. 2004

A Study on Development of Safety and Performance Test for Ultrasonic Dental Scaling System

Eun-Jeong Cho, Hong-Won Yeon, In-Hye Kim, Chang-Hyeong Lee, Hyeok Ju Kim
 Medical Device Research Division, Ministry of Food and Drug Safety, Cheongju-Si, Republic of Korea
 E-mail: khjtree@korea.kr

Abstract— This study is to develop a safety and performance test method for evaluating dental scaling system. Dental scaling system is a medical instrument used in the mouth, the scaler should have the accurate performance as well as the electrical safety. At present, no standards or guidelines applicable for the management of the quality of dental scaling system have been provided. Thus, this study is to develop a method for evaluating dental scaling system more objectively. To develop the tests, 1) technical information, including the principles and constitutions of the medical devices, were studied, 2) applicable standards, guidelines and the established test items for licenses were surveyed and analyzed, and 3) necessary test and method for evaluating the safety and performances were obtained. As the test and method for the safety and performance evaluation of dental scaling system is provided, it would make it possible to manage the quality of reasonable and scientific medical instruments, and it is expected that the healthy and safety of the people would be guaranteed.

Keywords— Ultrasonic dental scaling system, Evaluation, Safety and performance test

I. INTRODUCTION

As scaling has become covered by medical insurance, a majority of people take care of their teeth by scaling. A medical instrument used herein is a dental scaling system which removes sediment adhered to teeth so as to remove plaque and clean periodontal pocket. Since a dental scaling system is used in the mouth, it should be electrically safe. Also, the scaler is used for teeth which are not readily recoverable once damaged, so the scaler should have safety and the accurate performance.

II. METHODS

To develop tests and methods for the safety and performance evaluation of dental scaling system, first, principles, forms, structures, etc. of dental scaling system were examined to derive performance evaluation items according to the character of the scalers. Secondly, domestic and foreign standards were examined and analyzed to apply a test method suitable

for each of the performance evaluation test items of dental scaling system. Lastly the derived test items were compared with the test items pre-set when obtaining the permission and compared with the domestic technical level. The test for the test items was conducted to secure the reliability of the test items and method. In this way, necessary test and method for evaluating the safety and performances were obtained [1-2].

III. RESULTS

A dental scaling system, which removes tartar by fine vibration of high-frequency electromagnetic waves, generally consists of a main body and tips. The dental scaling system can be mounted onto a dental diagnosis and treatment device for use. The scalers are classified into two types depending on the ultrasonic generation form: A magnetostrictive method that the magnetic field is generated by the current flowing on a coil inside of the handpiece, and inserted tips vibrate along the flow of the current; and a piezoelectric method that as electronic energy is applied to a piezoelectric element such as ceramic, the change in the size of the piezoelectric element is delivered to the tips, thereby vibrating.

The standards applicable for the evaluation of dental scaling system are: the Korean industrial standard, KS P ISO 22374:2010. The Standard for Dentistry-Dental Handpieces-Electrical-powered Scalers and Scalers Tips; the International Electrical Technology Committee standard, ISO 22374:2005 Dentistry-Dental Handpieces-Electrical-powered Scalers and Scalers Tips; and the Japanese industrial standard, JIS T 5750:2009 Dentistry-Dental Handpieces-Ultrasonic Instruments and Tips for Multi-purpose Treatment [3-5].

As a result of the search and analysis of the permission status, the performance tests varied depending on the ultrasonic generation forms, but there have some similar between obtained test and pre-set test for permission. There was a product having the unique performance of a manufacturer.

For the performance evaluation of dental scaling system, the vibration and output of tips should be confirmed such that stuck matters adhered to teeth can be removed by using tips. For this reason, the number of vibrations, amplitude of vibration, the accuracy of output energy, the safety of output, supply of coolant fluid, etc. for evaluating the above should be set as test items. In addition, test items for the insertion

of scaler tips and the extraction force are required so that tips inserted for use are not taken off during the treatment. For such test items, the domestic and foreign standard test items and method can be applied. As a result of testing the developed test items for commercially-used dental scaling system, the test items are considered as test items and methods suitable for the performance evaluation. However, for the generation of the test items, a test item according to the differential performance of a manufacturer such as illuminance function was excluded.

IV. CONCLUSION

As a scientific and reasonable performance evaluation test method for dental scaling system is provided by this study, it is expected to contribute in improving the quality management, boosting the national health and enhancing the competitiveness of Korean medical instruments.

ACKNOWLEDGEMENT

This work was supported by the Ministry of Food and Drug Safety (14171Medical332).

REFERENCES

1. Hongseo Yang, Yeongjun Park, Hyeongil Kim, and Kyo-han Kim, *Practical Guide to Technology in Dentistry*, Seoul:Na Rae Publishing, 1999.
2. KS C IEC 60601-1:2011, *Medical electrical equipment - Part 1: General requirements for basic safety and essential performance*
3. Notice No. 2014-86 of the Korea Food & Drug Administration, *General requirements for basic safety - Electromagnetic waves of medical devices*
4. IEC 60601-1-2:2014, *Medical electrical equipment - Part 1-2: General requirements for basic and essential performance - Collateral Standard: Electromagnetic disturbances - Requirements and tests*
5. JIS T 5750:2009, *Dentistry - Dental handpieces - Ultrasonic instruments and tips for multi-purpose treatment*

Passive ultrasonic images constructed with acoustic emission from cavitation activities in water produced by a clinical extracorporeal shock wave source

Gwansuk Kang¹, Sung Chan Cho³, and Min Joo Choi^{1,2}

¹Intersciplinary Postgraduate Program in Biomedical Eng., Jeju Natioanl University., Jeju Korea

²Dept. of medicine, Jeju national University. Jeju, Korea.

³KORUST Ltd., Anyang, Korea

E-mail: mjchoi@jejunu.ac.kr

Abstract—The present study has demonstrated the spatial cavitation distribution colored on the top of ultrasonic B-mode image. A clinical shock wave device and diagnostic ultrasonic imaging system were employed as a cavitation generator and a multichannel passive receiver respectively. Passive beam forming method was performed with acquired 64 channel RF data to reconstruct waveform emitted from cavitation bubbles. It was shown that the focal zone of shock wave pressure field and the predicted cavitation area in reconstructed passive image coincided with each other, so that, it will be useful in monitoring cavitation activities. In addition, it can be embedded in a conventional diagnostic ultrasonic device without hardware modification.

Keywords— Cavitation, Passive mapping, Ultrasound image, shock wave.

I. INTRODUCTION

II.

Shock wave-induced cavitation plays an important role to pulverize kidney stones(Extracorporeal Shock Wave Lithotripsy) and treat chronic tendonitis(Extracorporeal Shock Wave Therapy)[1,2]. Shock wave generates cavitation cloud which results in mechanical effects toward clinical target objects. Therefore, to maintain the clinical efficiency, it is needed to monitor the spatial distribution of cavitation bubble activities produced b shock wave. When cavitation bubble collapses, it acts as a new acoustic source to emit an outward-propagating spherical

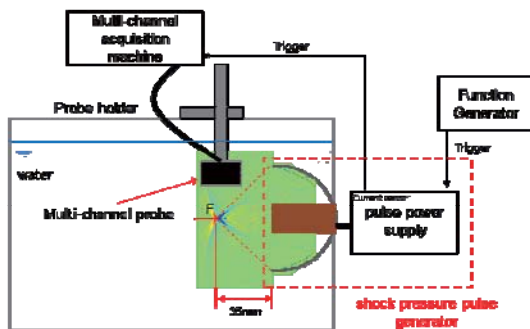


Fig 1. An experimental setup consists of shock pulse generator and multi-channel acquisition machine.

wave[3]. Typically, a hydrophone or passive cavitation detector is used to detect this acoustic signal. However, the spatial distribution of cavitation cannot be achieved by using a single acoustic receiver. The present study has demonstrated spatial cavitation mapping(SCM) on ultrasonic B-mode image.

II. METHODS

For experimental implementation, a clinical electromagnetic ESWT system(ShineWave-sonic, HnT Medical System, Korea) and ultrasonic scanner(ECUBE12R, Alpinion Medical Systems, Korea) with a convex probe(SC3-6, 128ch, Alpinion Medical Systems, Korea) were employed as a shock wave generator and multi-channel acquisition machine(MCAM), respectively(Fig 1).

MCAM can be set to record 64 channels of RF waveform data simultaneously at 40M samples per second due to hardware limitation. The elements of probe were set to span the entire aperture.

An ultrasonic B-mode image was acquired, which was taken as a background image before shock wave fired. MCAM began to record acoustic emission for 1ms when the shock wave triggered.

To reconstruct SCM, passive beam forming (delay and sum) was performed at each(pixel) location within the region for the cavitation image. When the ultrasonic

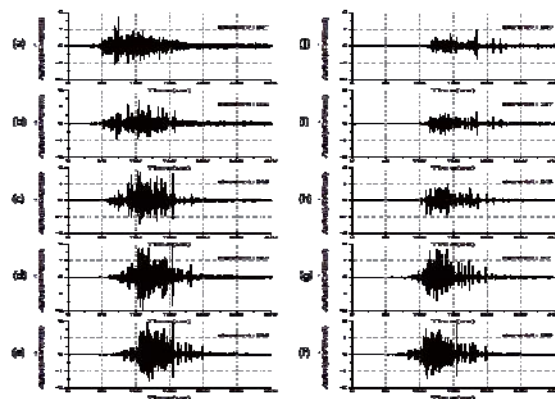


Fig 2. Typical waveforms recorded at a channel of the convex probe with 64 channels. (a) ch#1, (b) ch#8, (c) ch#16, (d) ch#24, (e) ch#32, (f) ch#33, (g) ch#41, (h) ch#49, (i) ch#57, (j) ch#64

cavitation region is similar to the focal zone of shock wave pressure field.

IV. CONCLUSION

The spatial cavitation mapping on an ultrasonic B-mode image has been demonstrated experimentally. All procedure can be done in a conventional diagnostic ultrasonic device without modification. It is expected that the SCM will be useful in monitoring clinically significant shock wave irradiation for assuring clinical outcome and patient safety.

ACKNOWLEDGEMENT

This work was supported by a grant of National Research Foundation of Korea(NRF) funded by the Korean government(MEST) (Grant No. 2012R1A2A2A03044996)..

REFERENCES

1. M.Choi, S. Cho, D. Paeng, and K. Lee, "Thickness effects of the metallic and the insulating membranes of a cylindrical electromagnetic shock wave transducer," J. Acoust. Soc. Kor., 29,pp3583-3587, 2010.
2. A. J. Coleman, J. E. Saunders and M. J. Choi, "An experimental shock wave generator for lithotripsy studies," Phys. Med. Biol. 34, pp 1733-1742,1989
3. G. Kang, S.C. Cho, A. J. Coleman, and M. J. Choi, "Characterization of the shock pulse-induced cavitation bubble activities reorded by an optical fiber hydrophone." J. Aco. Soc. Am., 135(3), pp1139-1148, 2014.

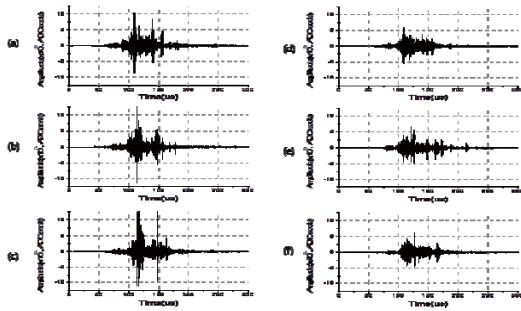


Fig 3. Reconstructed waveforms at various locations along the horizontal axis(on axis) in the image. The depth from probe surface is 43mm. (a)0mm., (b)5mm, (c)10mm, (d) 15mm, (e)20mm, (f)25mm.

pulse emitted from a single bubble collapsing is in phase, the RF signal reconstructed throughout the channels has its highest peak.

III. RESULTS AND DISCUSSION

Fig 2 shows the acquired waveforms at a channel. Acoustic emission from cavitation bubbles induced in water bu the typical clinical shock wave pulse was received at the 64 individual channels with different time delays. It has a complex structure which results from the interference and propagation of acoustic sources by multiple bubbles at different time and locations.

Fig 3 shows reconstructed waveforms at various locations along the on-axis of shock wave field with 64channel array waveforms displayed in fig 2. They have several noticeable temporal peaks(which may correspond to the 1st and 2nd collapses as reported by Kang et al.(2014)).

Fig 4 shows the reconstructed image of cavitation activity which displays SCM on the top of a background ultrasonic B-mode image. The highest peak value of the waveform reconstructed at a pixel location was assigned to the pixel value. Color pixels indicate the cavitation dominant region. Note that the colored

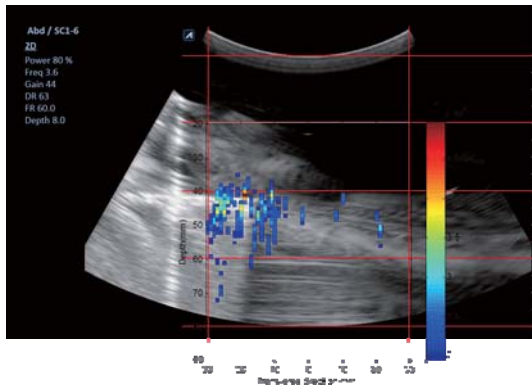


Fig 4. Reconstructed cavitation image displayed on the top of an background ultrasonic B-mode image

Development of multi-channel bio-admittance imaging probe to detect tissue property change due to the stimulation

Y. E. Kim¹, G. Y. Jang¹, H. Wi², T. I. Oh¹, and E. J. Woo¹

¹Department of Biomedical Engineering, Kyung Hee University, Seoul, Republic of Korea

²Department of Computational Science and Engineering, Yonsei University, Seoul, Republic of Korea

E-mail: tioh@khu.ac.kr

Abstract—There is the tissue property change due to the electrical or mechanical stimulation around the applied region. In order to detect this change via image, we developed the multi-channel bio-admittance imaging probe with 96 electrodes. It operates two different modes of high-speed acquisition and high-resolution imaging. In this study, we described the design of the system and evaluated the basic performances.

Keywords— Bio-admittance, imaging probe, stimulation response, high-speed, high-resolution.

I. INTRODUCTION

For medical treatments, we apply the electrical and mechanical stimulations to the treated region or related body area [1]. In order to understand the mechanism of treatments and/or to make an optimal treatment plan, non-invasive, continuous monitoring method requires. In this study, we developed the multi-channel bio-admittance imaging system with a scan probe including 96 electrode array. This system can operate in fast acquisition mode and high resolution mode around the treated region. Here, we describe the system architecture and basic performance evaluation of the new system for detecting the electrical tissue property changes due to the stimulus.

II. METHODS

Fig. 1 describes the measurement configuration and the structure of bio-admittance imaging probe system. 96 small sensing electrodes are kept at ground potential to produce uniform current density distribution when we apply the constant sinusoidal voltage from the applying electrode.

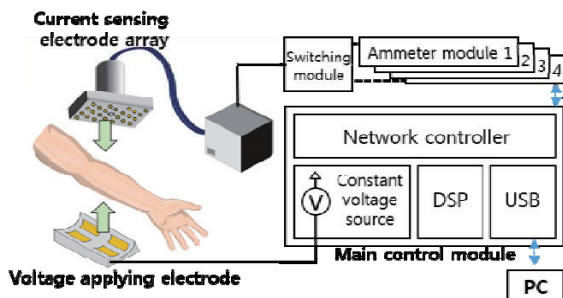


Fig. 1. Configuration of bio-admittance imaging probe

Fig. 2 shows the developed the bio-admittance imaging probe system consist of 24 ammeters, 1 voltage source, and control circuits

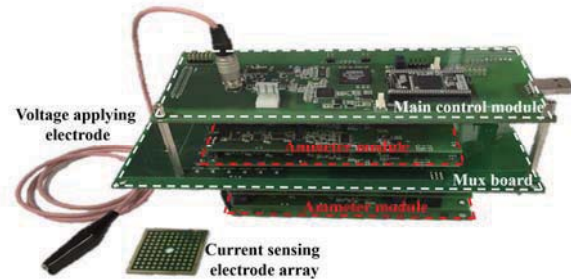


Fig. 2. Developed the bio-admittance imaging probe

III. RESULTS

In order to evaluate the system performance, we computed the simulation model developed by Comsol 3.5, and the simulated results were compared with the experimental ones. We placed a sphere shape of anomaly inside the phantom. Fig. 3 presented the admittance images at different positions and depths as shown in Fig. 3.

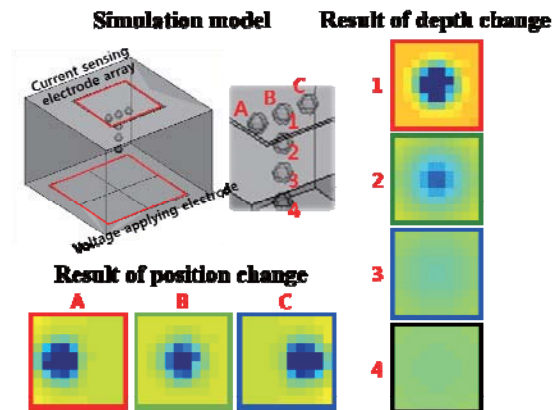


Fig. 3. Admittance images of anomaly which have different position and depth

III. CONCLUSION

We developed the bio-admittance imaging probe system to monitor the tissue property changes due to the electrical and mechanical stimulation with 96 electrodes and confirmed the basic performance in the phantom.

ACKNOWLEDGEMENT

This work was supported by the Korea Institute of Oriental Medicine grant (20150871).

REFERENCES

1. E. M. Wassermann, "Risk and safety of repetitive transcranial magnetic stimulation: report and suggested guidelines from the International Workshop on the Safety of Repetitive Transcranial Magnetic Stimulation," *Clinical Neurophysiology*, vol. 108, pp. 1-16, 1998.

Preliminary Study on the Development of Automatic Measuring Instrument for Range of Motion in Patients with Spondyloarthropathy

M. Kim^{1,*}, C. Lee², H. M. Kwon³, D. J. Go³, J. Y. Moon³, E. B. Lee³, and S. Kim^{2,4,+}

¹The Interdisciplinary Program for Bioengineering, Graduate School, Seoul National University, Seoul, Korea

²Institute of Medical and Biological Engineering, Medical Research Center, Seoul National University, Seoul, Korea

³Department of Internal Medicine, Seoul National University College of Medicine

⁴Department of Biomedical Engineering, Seoul National University College of Medicine, Seoul, Korea

E-mail: *kimmj08@snu.ac.kr and +sungwan@snu.ac.kr

Abstract—Ankylosing spondylitis is a chronic inflammatory disease that can affect the spine and the sacroiliac joint in the pelvis. In the case of severe patients, rigidity of the spine can occur. Thus, quantitative measurement for the rigidity is needed. Bath ankylosing spondylitis metrology index (BASMI) is a measuring method that has been introduced for this purpose. However, since this method can only be measured manually in current status, interobserver difference can be caused. To overcome this issue, an automatic measuring algorithm for BASMI has been developed in this study. Further studies are to be conducted for the development of automatic measuring instrument based on the developed algorithm.

Keywords— Ankylosing Spondylitis, Facial Detection, Skeleton Detection, Kinect Sensor, Automatic Measurement

I. INTRODUCTION

Ankylosing spondylitis, which is a chronic inflammatory disease of the axial skeleton, with variable involvement of peripheral joints and non-articular structures, is one of the seronegative spondyloarthropathies and has a strong genetic predisposition [1]. The main influence of the ankylosing spondylitis is the infection in the spine and the sacroiliac joint in the pelvis. In severe cases, complete fusion and rigidity of the spine can occur [2]. Thus, it is significant to quantitatively measure the rigidity occurred by ankylosing spondylitis. For this purpose, bath ankylosing spondylitis metrology index (BASMI) has been introduced [3]. However, the main issue that has to be resolved for current measurement method is that the interobserver difference due to the manual measurements. To resolve this issue, an automatic measuring instrument for range of motion in patients with spondyloarthropathy has to be developed. In this paper, as a preliminary study, an automatic measuring algorithm for the above mentioned measuring instrument has been developed.

II. METHODS

A. Measuring algorithm for BASMI concerning joints of the head and neck

To automatically measure the BASMI concerning joints of the head and neck, such as neck flexion and extension, neck rotation for right and left, and neck lateral flexion for right and left, facial detecting algorithm has been used [4]. Using the facial detecting algorithm, roll, pitch, and yaw angles of the patient's face can be detected. Then, those indexes, which are related to the joints of the head and neck, can be calculated.

B. Measuring algorithm for BASMI concerning joints of the body

For the automatic measurements of other indexes within the BASMI, such as lumbar lateral flexion for right and left, finger to floor distance, tragus to wall distance, and intermalleolar distance, the skeleton detecting algorithm has been adapted [5]. The skeleton detecting algorithm is able to track the position of head, shoulder, elbow, wrist, hand, hip, knee, ankle, and foot. Therefore, using the skeleton detecting algorithm, intermalleolar distance and lumbar lateral flexion for right and left can be calculated.

III. RESULTS

Using the facial detecting algorithm and skeleton detecting algorithm, automatic measuring algorithm for five indexes of the BASMI, neck flexion and extension, neck rotation for right and left, neck lateral flexion for right and left, intermalleolar distance, and lumbar lateral flexion for right and left, have been developed. Table 1 and Table 2 show the results of the developed measuring algorithm. Each index has been measure for ten times and compared with manual measurement results.

IV. CONCLUSION

To automatically measure the BASMI, the automatic measuring algorithm has been developed. To evaluate the proposed algorithm, its results have been compared with the manual measurements results. The results

shown that the proposed algorithm could measure the BASMI with a tiny error. For further research, automatic algorithm for two remained indexes of the BASMI, tragus to wall distance and finger to floor distance, will be developed and automatic measuring instrument will be also developed based on the proposed algorithm.

Table 1. Comparison between the results of automatic measurements and manual measurements for BASMI concerning joints of the head and neck

	Neck flexion and extension (Mean(SD))		Neck rotation (Mean(SD))		Neck lateral flexion (Mean(SD))	
	Flexion	Extension	Right	Left	Right	Left
Automatic Measurements	36.31° (0.53°)	36.11° (0.61°)	79.82° (0.25°)	75.11° (0.21°)	52.16° (0.20°)	32° (0.13°)
Manual Measurements	36.14°	37.09°	78.06°	75.28°	53.15°	32.95°

Table 2. Comparison between the results of automatic measurements and manual measurements for BASMI concerning joints of the body

	Lumbar lateral flexion		Intermalleolar distance
	Right	Left	
Automatic Measurements	45.13 cm (0.15 cm)	45.28 cm (0.21 cm)	41.54 cm (0.16 cm)
Manual Measurements	47 cm	47 cm	40 cm

ACKNOWLEDGEMENT

This research was supported by grant no. 0320150170 from the SNUH Research Fund.

REFERENCES

1. "Ankylosing Spondylitis -Professional reference for Doctors - Patient UK". Patient UK. Retrieved 26 May 2014.
2. Jiménez-Balderas FJ, Mintz G. "Ankylosing spondylitis: clinical course in women and men". J Rheumatol 20 (12): 2069-72.
3. Braun J, van den Berg R, Baraliakos X. "Update of the ASAS/EULAR recommendations for the management of ankylosing". Ann Rheum Di 2011 (70): 896-904.
4. BARTLETT, Marian Stewart, et al. "Real Time Face Detection and Facial Expression Recognition: Development and Applications to Human Computer Interaction". In: Computer Vision and Pattern Recognition Workshop, 2003. CVPRW'03. Conference on. IEEE, 2003. p. 53-53.
5. Shotton, Jamie, et al. "Real-time human pose recognition in parts from single depth images". Communications of the ACM 56.1 (2013): 116-124.

Twinkling artifact significantly enhanced by a mechanical impact

Jeonghwa Yang¹, Gwansuk Kang², and Min Joo Choi^{2,3}

¹Dept. of Radiotechn. Cheju Halla Univ, Jeju, Korea

²Interdisciplinary Postgraduate Program in Biomedical Eng., Jeju Nat'l Univ., Jeju, Korea

³Dept. of medicine, Jeju Nat'l Univ., Jeju, Korea

E-mail: mjchoi@jejunu.ac.kr

Abstract— This study shows that a mechanical impact enhances the contrast of the twinkling artifact. A series of color Doppler images were obtained for a stationary echogenic circular contrast (+15, +6, and +3dB) targets, with a clinical ultrasonic scanner. A rubber ball (diameter 60mm, 20.18g) free fell to give an mechanical impact to the base plate on which the target phantom was placed. The intensity of the impact was controlled by altering the height of the free fall. The color twinkling was observed to be sparse before the target was excited by the mechanical impact. However, the quantity of colors twinkling dramatically increased at the moment of the impact, and was gradually recovered back with time. The color disappearance was much faster in on the background than on the targets. The time and the contrast increase were found to depend on the strength of the impact. The findings are expected to serve as empirical bases for the clinical potential of TA in the diagnosis of pathological sites such as small calculi or early stages of breast cancer often not possible to detect in a conventional ultrasonography.

Keywords— Twinkling Artifact, ultrasound, color Doppler image, mechanical impact.

I. INTRODUCTION

Twinkling artifact (TA) in the color Doppler mode refers to a rapidly changing mixture of red and blue colors for objects that neither flow nor move[1,2]. It often appears behind a strong reflector with rough surface. Although the underlying mechanisms of TA are not clear yet, TA has been found to provide useful information to detect particular pathological targets, such as calculi, calcification and calcinosis[3].

It was reported that TA was enhanced by an external vibration to targets[4]. The excitation conditions such as frequency and intensity haven't been optimized yet, and the approach is not used for practical use.

A mechanical impact which contained wide frequency ranges was considered in the present study as a practical excitation condition for increasing the TA. The experimental test on the effect of a mechanical impact on TA was carried out for the hyper-echogenic contrast target phantom.

II. METHODS

GE ultrasound scanner (Voluson e, GE Healthcare, Oberosterreich, Austria) with a linear probe (12L-RS, 3-12 MHz) was used to obtain color Doppler images for circular scattering targets. The scattering targets were taken from the circular contrast targets of a commercial ultrasound standard quality assurance phantom (Model 551 small parts phantom, ATS Laboratories Inc., Bridgeport, CT, USA). The diameter of the target was 6 mm and the 3 positive contrast +15, +6 and +3dB were considered. The phantom was placed on an optical breadboard table.

The ultrasonic probe was fixed to a vibration-free supporter (RFB, NTR Systems, Seattle, WA, USA), so that the probe was isolated from external vibrations (Fig 1). Ultrasonic coupling gel was applied to the upper surface of the phantom before scanning. The focal zone of the probe was set at the center of the target [5,6]. Color Doppler images were acquired under the default settings of the control parameters except for the PRF (e.g., Doppler frequency low, Doppler gain 0, and wall motion filter high).

To give a mechanical impact to the phantom, a rubber ball (d=60mm, w=20.18g) was dropped to hit on the bread board. The drop was made on a sliding guide with an angle as illustrated in Fig 1, so that the ball was not allowed to rebound on the bread board. The height of the free fall was altered to control the magnitude of the impact. The acceleration of the ball when hitting was measured by an accelerometer (3109, B&K, Denmark) placed on the top of the phantom frame.

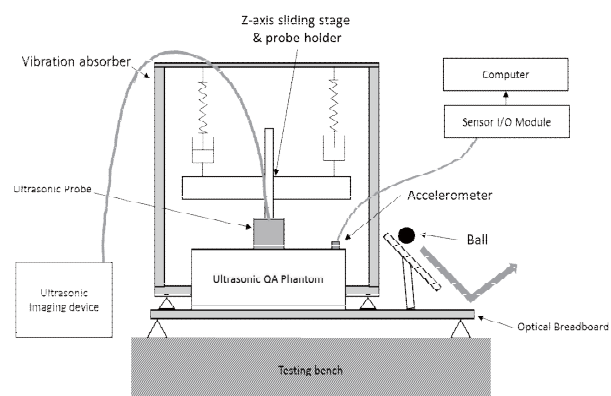


Fig 1. Experimental setup. The targets were mechanically impacted by a rubber ball(d=60mm, 20.18g) which fell free to impinge on the optical breadboard on which the target phantom was placed.

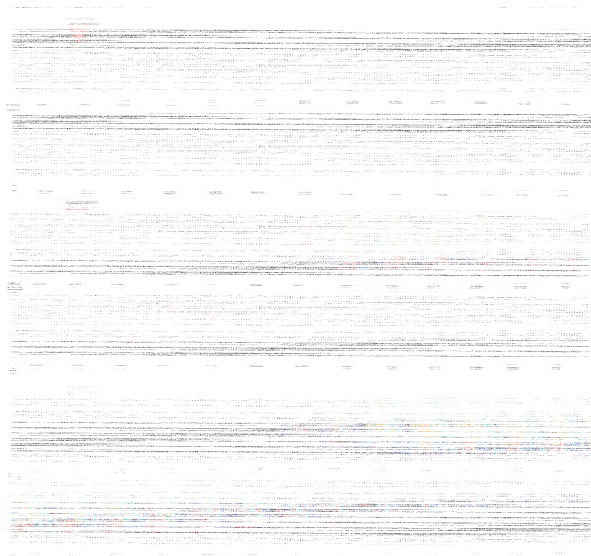


Fig 2. Temporal variations of TA images obtained for the +6dB contrast target excited by the mechanical impact with a peak acceleration of the ball to be (a) 0.37, (b) 1.27, and (c) 2.19 m/s².

Three magnitudes of the impact were considered, corresponding to the measured peak acceleration of the ball to be 0.37, 1.27 and 2.19 m/s². The color Doppler images were acquired, repeating 10 times at each condition.

III. RESULTS

Typical color Doppler images are shown in Fig 2 and 3 for the phantom on which the mechanical impacts were exerted. TA was not observed for the target before the mechanical impact was applied. However, the TA increased rapidly immediately after the impact is given, and it remained for a certain time before it recovered to

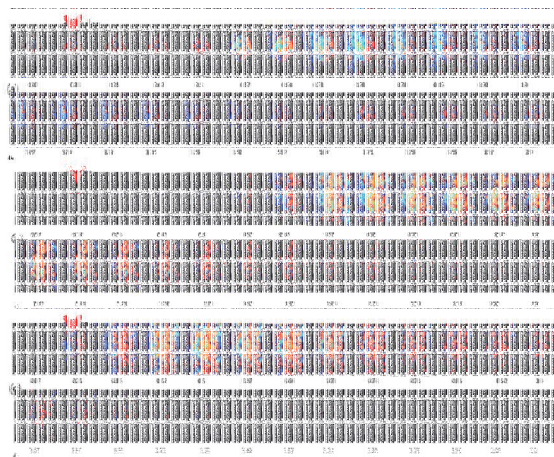


Fig 3. Temporal variations of TA images obtained for the 3 different contrast targets excited by the mechanical impact with a peak acceleration of the ball 1.27m/s² : (a) +15, (b) +6, and (c) +3dB contrast target.

the initial state. Fig 2 compares the color Doppler images of the +6dB contrast target for the three

mechanical impacts (0.37 to 1.27 and 2.19 m/s²) considered in the study. For the smallest impact (0.37 m/s²), TA appeared small on the target when the mechanical impact was applied (t=0.28s), and remained for 0.57s before gradually disappeared. When the magnitude of the impact was raised to get the peak acceleration 1.27 and 2.19 m/s², TA appeared inside as well as outside the target. The time between the onset and disappearance of the TA increased with the strength of the mechanical impact. Fig3 compares the TA images of the three different contrast targets for the same impact with the medium peak acceleration of 1.27 m/s². For the largest contrast target (+15dB), TA occurred on the target when the mechanical impact was applied (t=0.28s) and lasted for 0.35s before the TA appeared on the surrounding targets. After the TA lasted for 0.98s, the TA disappeared from the surroundings but was still observed the inside target. The persisting time of the TA was found to be shorter as the target contrast was reduced.

III. CONCLUSION

It was observed that TA appeared on a contrast target ~~was~~ significantly increased when a mechanical impact was applied to the target. The amount of TA was proportional to the strength of the mechanical impact, and the TA lasted longer for the target with higher contrasts. The observation claims that the contrast of TA on a scattering target is significantly enhanced by an appropriate mechanical impact. The results are expected to serve as an empirical basis for the clinical potential of TA in the diagnosis of pathological sites such as small calculi or early stages of breast cancer often not possible to detect in conventional ultrasonography.

ACKNOWLEDGEMENT

This work was supported by a grant of National Research Foundation of Korea (NRF) funded by the Korean government (MEST) (Grant No. 2012R1A2A2A03044996).

REFERENCES

1. B. Yanik, L. Conkbayir, E. Cakmakci and B. Hekimoglu, 'Color Doppler twinkling artifact in a calcified liver mass', J. Clin. Ultras. 33, 474-476, 2005.
2. T.F. Tsao, R.J. Kang, M.K. Gueng, Y.S. Tyan, Y.C. Lin, S.K. Lee., 'Color Doppler Twinkling Artifact and Clinical Use'. J Med Ultrasound, 17, 157-166, 2009.
3. C.H. Sohn, J.H. Lee, and K.S. Cho, J. 'Twinkling Artifact on color Doppler ultrasound: Comparison among various composition of stones and various central frequencies of transducers', Kor. Soc. Med. Ultras., 21(3), 2002
4. J. Yang, 'Twinkling Artifact in Color Doppler Ultrasonic Imaging', PhD thesis, Jeju National Univ., 1-153, 2014.
5. J.Y. Lee, S.H. Kim, J.Y. Cho, D. Han, 'Color and power Doppler twinkling artifacts from urinary stones: Clinical observations and phantom studies. AJR Am J Roentgenol, 176, 1441-1445, 2001.
6. M. Mitterberger, F. Aigner, L. Pallwein, GM. Pinggera, R. Neururer, P. Rehder, 'Sonographic Detection of renal and ureteral stone. Valued of the Twinkling sign', Int Braz J Urol., 35, 532-541 2009.

The 1st high intensity line focused ultrasonic surgical device

Sung Chan Cho¹, Gwansuk Kang², and Min Joo Choi^{2,3}

¹KORUST Ltd., Anyang, Korea

²Interdisciplinary Postgraduate Program in Biomedical Eng., Jeju National University, Jeju, Korea

³Dept. of medicine, Jeju National University, Jeju, Korea

E-mail: mjchoi@jejunu.ac.kr

Abstract—The present study considers a device which produces a high intensity line focused ultrasound (HILFU), so as to reduce the shortcomings of the existing HIFU surgery. The device employs a cylindrical piezoelectric ceramic which focuses ultrasound to the axial line of the cylinder. A FEM simulation on the 3D acoustic field of the designed HILFU transducer showed a series of multiple point foci along with the central axis of the cylindrical transducer. The line focal feature was validated by the measurement of the acoustic field produced by the prototype. The corresponding line focused thermal lesions were successfully observed, formed in an acryl-plate phantom.

Keywords— High intensity line focused ultrasound, cylindrical ceramic, surgery, acoustic field.

I. INTRODUCTION

High Intensity Focused Ultrasound (HIFU) can be used as a surgical energy in a way which a target tissue such as tumor exposed to HIFU is heated to 60~80°C in a short time (< 1s) and thus is thermally necrotized (Choi 2000, Bailey et al. 2003). The necrotized tissues are removed or absorbed through metabolic activities of the surrounding tissues.

HIFU produces a therapeutic heating in a small volume being similar to the focal volume of the corresponding acoustic field, resulting in a point like thermal lesion. In order to produce a volumetric tissue ablation, HIFU irradiation has to be repeated hundred to thousand times. This process requires a long treatment time and may not give a smooth and clean boundary of the lesion.

The present study considers a device which produces a high intensity line focused ultrasound (HILFU), so as to



Fig 1. A cylindrical piezoelectric element used to construct a HILFU transducer

reduce the shortcomings of the existing HIFU surgery. The device employs a cylindrical piezoelectric ceramic which focuses ultrasound to the axial line of the cylinder. This study presents the acoustic properties of the first prototype of HILFU surgical device.

II. METHODS

2.1 construction of prototype

Fig 1 shows the cylindrical piezoelectric ceramic which was used in the present study to construct a prototype of the HILFU transducer. The ultrasonic waves emitted from the piezoelectric ceramic are focused to the axial line of the cylinder.

The constructed HILFU transducer consists of the two piezoelectric elements which are located in parallel to get the length of the focal line be twice of the single element width. Fig 3 illustrates the geometry of the HILFU transducer. The gap (b) between the two elements was 3 mm and, as marked by 'a' in Fig 2, each element slightly (4°) tilted to the center of the focal line. The constructed transducer was electrically driven and controlled by UTIMS (A5, KORUST Co.,Ltd, KOREA).

2.2 Acoustic characterization

In order to test the performance of the HILFU prototype, the acoustic field generated by the HILFU transducer was characterized and the phantom test was carried out for illustrating the desired thermal lesions produced by the HILFU device. The 3D acoustic field of the HILFU transducer was predicted through a FEM simulation with PZFlex (Ver 2014, Weidlinger Ass. Inc., USA). The real acoustic field produced by the prototype transducer was measured to validate the predicted focal field.

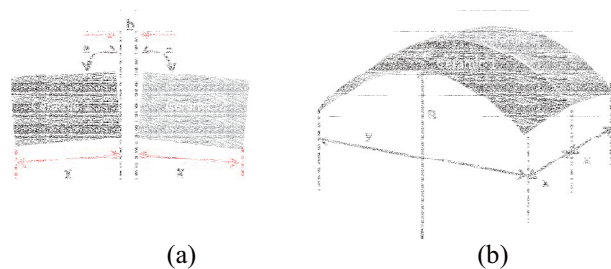


Fig 2. Geometry of HILFU transducer ($x=34\text{mm}$, $y=89.17\text{mm}$, $R=62\text{mm}$, $a=94^\circ$, $b=3\text{mm}$, frequency= 3.4MHz).

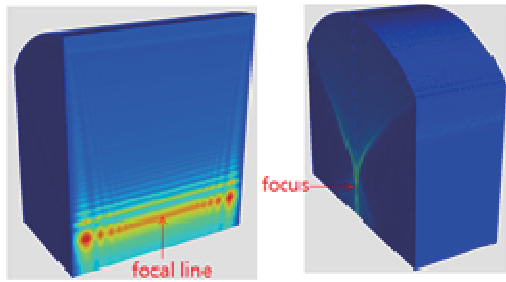


Fig 3. The acoustic field predicted using a FEM method.

III. RESULTS

Fig 3 shows the predicted 3D pressure field produced by the designed HILFU transducer. As expected, a series of multiple point foci along the axis of the cylinder is observed. Fig 4 is the 2D distribution of pressure in the near proximate to the focal line. The width of the focal line was about 60 mm, slightly less than the geometric width of the transducer. This is attributed to the tilt of each piezoelectric element of the transducer. The asymmetrical distribution in the measured field, unlike the prediction, may arise from the construction error of the transducer as well as the misalignment of the hydrophone

Fig 5 shows a series of point focal lesions formed on the acryl-plate along with the focal axis of the cylindrical transducer. The acryl-plate was immersed in a water tank and the lesion shown here was produced when one piezoelectric element of the transducer was operated. As seen in Fig 5, the thermal lesions were formed at the 7 points along the line. The point lesions varies slightly in size and shape, which may be due to the focal line which may not be on the surface of the acryl-plate or the transducer which may not produce uniform pressure. Note that as the frequency decreases and thus

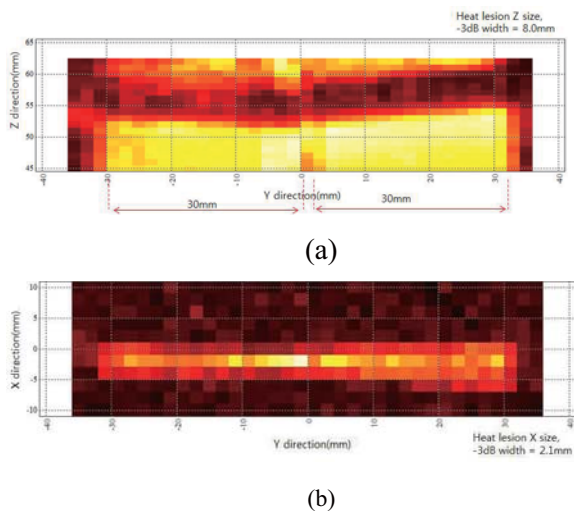


Fig 4. 2D acoustic field in the proximity if the focal line measured using AIMS. (a) x-z plan, (b) x-y plan.



Fig 5. An example of a series of point thermal lesion formed on the acrylplate produced by a single exposure of HILFU field.

the number of the point increases. Accordingly, when an appropriate high frequency is chosen, the focal line will be fairly smoothed out. In biological tissue, the heat diffusion between the heated point spots may result in more smoothly connecting the adjacent the point thermal lesions, and thus may lead to the smooth and clean boundary of the thermal lesion.

IV. CONCLUSION

The 1st prototype of a high intensity line focused ultrasound surgical device which was designed to reduce the shortcomings of existing HIFU surgery was constructed. A FEM simulation on the 3D acoustic field of the designed HILFU transducer showed a series of multiple point foci along with the central axis of the cylindrical transducer. The line focal feature was validated by the measurement of the acoustic field produced by on the prototype. The line focused thermal lesions formed on the acrylplate were observed, verifying the therapeutic performance of the prototype. In vitro and in vivo studies with the prototype are required to gain necessary information for the clinical test.

ACKNOWLEDGEMENT

This work was supported by a Technology Innovation Development Project (Grant No. S2082176) of the Small & Medium Business Administration, Republic of Korea.

REFERENCES

1. M.J. Choi, "Application of ultrasound in medicine : Therapeutic ultrasound and ultrasound contrast agent." J. Kor. Soc. Nois. & Vib. Eng., 10(4), pp743-759, 2000.
2. M.R. Bailey, V.A. Khokhlova, O.A. Sapozhnikov, S.G. Kargl, and L.A. Crum, "Physical mechanisms of the therapeutic effect of ultrasound." Aco. Phy. 49(4), pp369-388, 2003.

Passive ultrasonic images constructed with acoustic emission from cavitation activities in water produced by a clinical extracorporeal shock wave source

Gwansuk Kang¹, Sung Chan Cho³, and Min Joo Choi^{1,2}

¹Intersiciplinary Postgraduate Program in Biomedical Eng., Jeju National University., Jeju Korea

²Dept. of medicine, Jeju national University. Jeju, Korea.

³KORUST Ltd., Anyang, Korea

E-mail: mjchoi@jejunu.ac.kr

Abstract—The present study has demonstrated the spatial cavitation distribution colored on the top of ultrasonic B-mode image. A clinical shock wave device and diagnostic ultrasonic imaging system were employed as a cavitation generator and a multichannel passive receiver respectively. Passive beam forming method was performed with acquired 64 channel RF data to reconstruct waveform emitted from cavitation bubbles. It was shown that the focal zone of shock wave pressure field and the predicted cavitation area in reconstructed passive image coincided with each other, so that, it will be useful in monitoring cavitation activities. In addition, it can be embedded in a conventional diagnostic ultrasonic device without hardware modification.

Keywords— Cavitation, Passive mapping, Ultrasound image, shock wave.

I. INTRODUCTION

Shock wave-induced cavitation plays an important role in to pulverizing kidney stones (Extracorporeal Shock Wave Lithotripsy) and treat chronic tendonitis (Extracorporeal Shock Wave Therapy)[1,2]. Shock wave generates cavitation cloud which results in mechanical effects on clinical target objects. Therefore, to maintain the clinical efficiency, it is needed to monitor the spatial distribution of cavitation bubble activities produced by shock waves. When cavitation bubble collapses, it acts as a new acoustic source to emit an spherical diverging wave[3]. A hydrophone or



Fig 1. An experimental setup which consists of a shock pulse generator and a multi-channel acquisition machine.

a passive cavitation detector is used to detect the emitted this acoustic signal. However, the spatial distribution of cavitation cannot be obtained by using a single acoustic receiver. The present study was devoted to the spatial map of the strength of the cavitation activity produced by a clinical shock wave generator using a passive beam forming method.

II. METHODS

Fig 1 shows an experimental setup which consists of which consists of a shock pulse generator and a multi-channel acquisition machine. A clinical electromagnetic ESWT system (ShineWave-sonic, HnT Medical System, Korea) was taken to produce shock pulses. An commercial ultrasonic scanner (ECUBE12R, Alpinion Medical Systems, Korea) with a convex probe(SC3-6, 128ch, Alpinion Medical Systems, Korea) was employed as multi-channel acquisition machine (MCAM) to reconstruct the acoustic signals emitted from cavitation activities.

An ultrasonic B-mode image acquired before a shock wave was fired was taken as a background image. When the shock wave generator triggered, the 64 channels (either even or odd number of the 128 elements) of the array probe of the MCAM were enabled to record acoustic emission for 1 ms at 40M samples per second.

A passive beam forming (delay and sum) was



Fig 2. Typical waveforms recorded at a channel of the convex probe with 64 channels. (a) ch#1, (b) ch#8, (c) ch#16, (d) ch#24, (e) ch#32, (f) ch#33, (g) ch#41, (h) ch#49, (i) ch#57, (j) ch#64

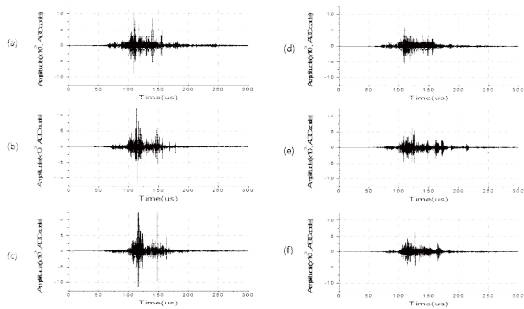


Fig 3. Reconstructed waveforms at various locations along the horizontal axis(on axis) in the image. The depth from probe surface is 43mm. (a)0mm., (b)5mm, (c)10mm, (d) 15mm, (e)20mm, (f)25mm.

performed to reconstruct the acoustic signal originated at each (pixel) location within the region for the cavitation image.

II. RESULTS AND DISCUSSION

Acoustic emission from cavitation bubbles produced in water by a typical clinical shock wave pulse was received at the 64 individual channels with different time delays. Fig 2 shows the waveforms acquired at each channel. They have complex structures which result from the interference of acoustic emissions from multiple bubbles at different time and locations.

Fig 3 shows the acoustic signals emitted at various locations along the on-axis of shock wave field, reconstructed using a passive beam forming technique with the 64 signals recorded at the 64 channels of the array probe. They have the same characteristic structures with several noticeable temporal peaks which may correspond to the 1st and 2nd collapses as reported by Kang et al.(2014).

Fig 4 shows the reconstructed image of cavitation activity (in colors) displayed on the top of a background ultrasonic B-mode image. In order to reconstruct the image, the highest peak value of the reconstructed acoustic signal emitted at a pixel location was assigned

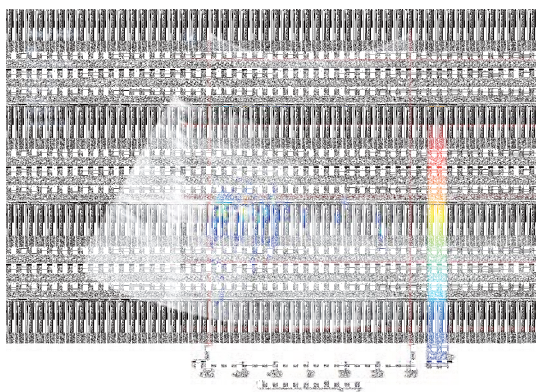


Fig 4. Reconstructed cavitation image displayed on the top of an background ultrasonic B-mode image

to the pixel value. The colored image allows on to the cavitation dominant region. Note that the colored cavitation region is similar to the focal zone of shock wave pressure field.

III. CONCLUSION

A passive beam forming technique was employed to obtain the spatial map of the cavitation activity produced by a clinical shock wave device, which is displayed on the top of the background ultrasonic B-mode image. The cavitation map is expected to be useful in monitoring clinically significant shock wave irradiation for assuring clinical outcome and patient safety.

ACKNOWLEDGEMENT

This work was supported by a grant of National Research Foundation of Korea(NRF) funded by the Korean government(MEST) (Grant No. 2012R1A2A2A03044996)..

REFERENCES

1. M.Choi, S. Cho, D. Paeng, and K. Lee, "Thickness effects of the metallic and the insulating membranes of a cylindrical electromagnetic shock wave transducer," J. Acoust. Soc. Kor., 29,pp3583-3587, 2010.
2. A. J. Coleman, J. E. Saunders and M. J. Choi, "An experimental shock wave generator for lithotripsy studies," Phys. Med. Biol. 34, pp 1733-1742,1989
3. G. Kang, S.C. Cho, A. J. Coleman, and M. J. Choi, "Characterization of the shock pulse-induced cavitation bubble activities reorded by an optical fiber hydrophone." J. Aco. Soc. Am., 135(3), pp1139-1148, 2014.

A Study for Visible Adipose Tissue Mimic Phantom to Estimate the Thermal Denaturation in Ultrasonic Lipolysis Therapy

J. Y. Kim¹, J. Y. Kim¹, S. C. Noh², and H. H. Choi¹

¹ School of Biomedical Engineering, Inje University, Gimhae, Korea

² Dept. of Radiological Science, International University of Korea, Jinju, Korea

E-mail: kjy10@bse.inje.ac.kr

Abstract—In this study, we intended to fabricate the adipose tissue mimic phantom which can visualize the thermal denaturation. In order to control the sound velocity of BSA (Bovine Serum Albumin) phantom, which is commonly used for visible ultrasonic phantom, similar to the adipose tissue, we adjusted the ratio of polymerization material (10 % APS and TEMED). And we added the corn syrup to supplement the stiffness and elasticity. As a result of adjusting, fabricated phantom was showed the similar acoustic properties of the actual adipose tissue.

Keywords— Adipose tissue, ultrasonic TM phantom, Corn syrup, Visible phantom,

I. INTRODUCTION

As increasing the interest and technical development for the ultrasonic obesity therapy, the safety and performance evaluation for ultrasonic lipolysis is essential. Because of the similar acoustic properties with human soft tissue, the BSA phantom is widely used for monitoring the ultrasonic thermal effect. But because of the difference of adipose tissue and soft tissue in acoustic properties, it has limitation to monitor the effect in adipose tissue. For these reasons, in this study, we proposed the recipe for visible adipose tissue mimic phantom to observe the thermal denaturation by adjusting composition of BSA phantom and adding corn syrup.

II. METHODS

Based on the composition of BSA phantom, amount of adding corn syrup was adjusted as 10~40 ml to increase the transparency and stiffness. In addition, as reducing the ratio of polymerization material (10% APS and TEMED) from 0.6 to 0.8 times, the sound velocity and attenuation were compared and analyzed.

In order to evaluate the acoustic properties of the fabricate phantom, the sound velocity, attenuation coefficient, density, and acoustic impedance was measured by using 3.5MHz ultrasound transducer.

III. RESULTS

As adding amount of the corn syrup increase, the sound velocity was increased and attenuation was slightly decreased. In addition, the sound velocity was decreased as the ratio of polymerization material

reduced. But there was no significant changes in attenuation with the ratio of APS and TEMED.

Consequentially fabricated phantom which adding 10 ml corn syrup and reducing the ratio of polymerization material 0.6 times showed the most similar acoustic properties. Table 1 shows the acoustic characteristics of the actual adipose tissue, BSA phantom and the fabricated phantom in this study.

Table 1. Acoustic properties of BSA, Fat mimicking phantom and Fat

Parameter	Fat	BSA	Fat phantom
Sound velocity (m/s)	1478±32	1,518.80	1454.73 ± 20.72
Attenuation coefficient (dB/cm-MHz)	0.6±0.1	0.18	0.25 ± 0.09
Density (g/cm ³)	1.4	1.041	1.007
Acoustic impedance (MRayls)	0.95	1.582	1.466

IV. CONCLUSION

In this study, we intended to fabricate the adipose tissue mimic phantom which can visualize the thermal denaturation. The ratio of APS and TEMED were adjusted to reduce the sound velocity and corn syrup was added to increase the stiffness and attenuation. As a result, fabricated phantom shows lower sound velocity and higher stiffness than BSA phantom. However, although the attenuation showed higher than BSA, but it was still slightly lower than that of adipose tissue. Subsequently through additional experiments, more similar characteristics to the actual fat tissue will be presented.

ACKNOWLEDGEMENT

The work was supported by the National Research Foundation of Korea (NRF) grant funded by the Korea government (No. 2012R1A1A2043564), and it was supported by Korea Technology and Information Promotion Agency for SMEs grant funded by the Ministry of Trade, Industry, and Energy (No. S2177131)

REFERENCES

1. M. McDonald, S. Lochhead, R. Chopra et al., "Multi-modality tissue-mimicking phantom for thermal therapy," *Physics in Medicine & Biology*, vol. 49, pp. 2767-2778, 2004.

Electrochemical Impedance Spectroscopy for Aptamer-based Biosensors

H. J. Yoo¹, W. K. Sun¹, S. J. Yang², J. H. Park¹, C. H. Ji¹, S. B. Jun^{1*}

¹Department of Electronics Engineering, Ewha Womans University, Seoul, Korea

²Institute of Convergence Medicine, Ewha Womans University Medical Center

E-mail: juns@ewha.ac.kr

Abstract— Aptamers are single-stranded DNA or RNA molecules which can bind to specific target analytes. An aptamer-based detection of analytes was analyzed using electrochemical impedance spectroscopy (EIS). After thrombin-specific aptamers were coated on the gold electrode, EIS data showed that the binding between the aptamers and thrombin increased the impedance magnitude. The EIS data was also used to model the electrode-electrolyte interface to precisely examine the effect of thrombin-aptamer binding. As a result, it was shown that resistance is the most feasible component for aptamer-based thrombin detection.

Keywords— thrombin, aptamer, modeling, electrochemical impedance spectroscopy

I. INTRODUCTION

Aptamers are known to be able to detect a variety of analytes with high stability and high sensitivity. However, there are still several challenges for the realization of aptamer-based biosensors. One of the challenges to overcome is how to transduce the chemical binding between aptamers and target analytes. In the present study, electrochemical impedance spectroscopy (EIS) is tested in order to quantitatively measure the concentration of the analyte using aptamers.

II. METHODS

A. Measurement

Impedance of gold working electrode attached with thrombin aptamer was measured by potentiostat. EIS measurement were performed in 1 M PBS containing 5 mM $K_4[Fe(CN)_6]$, 5 mM $K_3[Fe(CN)_6]$ and 100 mM KCl.[1] The electrochemical impedance were recorded with the frequency from 1MHz to 1.0 Hz.

B. Modeling

The electrochemical impedance curves were fitted to the equivalent circuit in Fig. 1 by ZView2 software. When modeling the curve, W , R , CPE(Constant Phase Element) were set as fixed value in the equivalent circuit model.[2]

CPE was defined by two values, CPE-T and CPE-P, with the expression $Z = T(j*\omega)^{-P}$. CPE was used in a

model in place of a capacitor to compensate for non-homogeneity in the system. W (Finite-Length Warburg) characterizes the electrolyte impedance due to diffusion. It was by three values, $W-R$, $W-T$ and $W-P$, with the expression $Z = R*ctnh([I*T*w]^P) / (I*T*w)^P$.

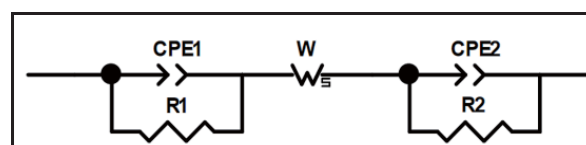


Fig. 1. Modeling circuit

III. RESULTS

The electrochemical impedance spectroscopy of gold electrode is displayed in Figure 2. The impedance was increased as thrombin concentration by 0, 20, 100 and 500 nM. Fitting data (solid line) and measurement value were similar as under 1% error rate.

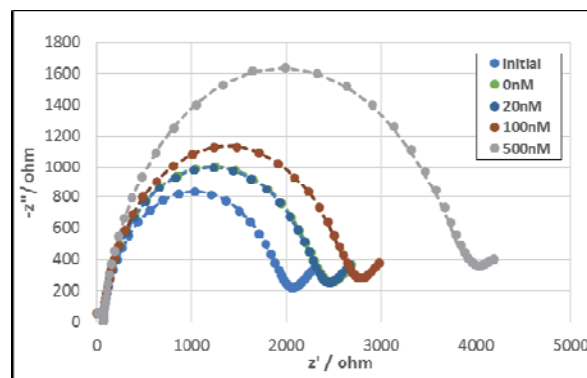


Fig. 2. The electrochemical impedance curves and fitting curves

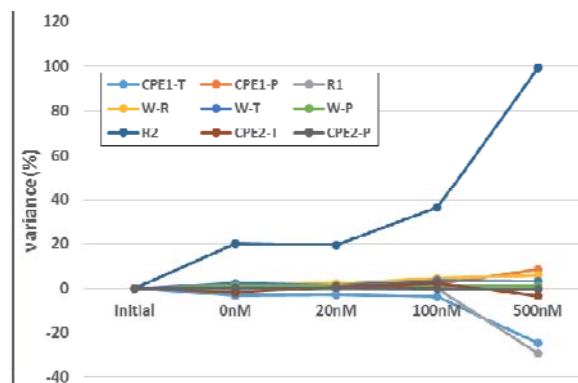


Figure 3. Variance of element values

Figure 3 is variance plot of device values to the initial value. R2 was shown as a significant factor on the impedance change. The others were not a major change.

IV. CONCLUSION

This study was confirmed that the electrochemical impedance increases as thrombin concentration in figure2 was more dependent resistance than capacitor. It shows that it is possible to estimate the concentration by simply measuring resistance without potentiostat. As the result, we aim to develop the biosensor using current source device.

ACKNOWLEDGEMENT

This study was supported by the National Research Foundation of Korea funded by the Ministry of Science, ICT & Future Planning of 2015 (No. 2014K1B1A1073720)

REFERENCES

1. Xiaoxia Li, Lihua Shen, Dongdong Zhang, Honglan Qi, Qiang Gao, Fen Maa, Chengxiao Zhang, "Electrochemical impedance spectroscopy for study of aptamer–thrombin interfacial interactions", *Biosensors and Bioelectronics*, vol. 23, pp. 1624–1630, 2008.
2. Yiming Chen, Haiyan Zhang, Yuting Chen, Jiapeng Lin, "Study on Carbon Nanocomposite Counterelectrode for Dye-Sensitized Solar Cells", *Journal of Nanomaterials*, vol. 2012, 2012.

POLYIMIDE-PDMS ELECTRODES FOR HUMAN BODY COMMUNICATION BETWEEN BINAURAL HEARING AIDS

J. H. Moon¹, H. C. Jung¹, S. A. Lee¹, S. K. Yoo¹, I. H. Song¹, D. J. Moon¹ and S. H. Lee^{2,3}

¹Integrated Medical Technology Team, Department of Research and Development, Medical Device Development Center, Osong Medical Innovation Foundation, Chungju, South Korea

²Department of Biomedical Engineering, College of Health Sciences, Korea University, Seoul, South Korea

³KU-KIST Graduate School of Converging Science and Technology, Korea University, Seoul, South Korea

E-mail: geenie@kbio.kr

Abstract—The binaural effects are induced by the differences of sound pressure and phase between both ears. Because of these effects, animals having two ears can sense the direction of sound source and hear better than single ear by summation of sound signal from both ears. These causes squelch effect that eliminates noises effectly, too. If we use two hearing aids at each side of ear, the aids serve quality-improved sound to hearing-impaired people and help to localize the direction of sound source.

But two devices on both sides need to communication for interchanging signal data and matching synchronization. Direct cable connection, wireless communication could be used, but recently Human body communication (HBC) have been escalated rapidly because of high data rates and very low consumption of power. Human body communication between binaural hearing aids could minimize size of aids and enhance device's active time without recharging. On this occasion, devices need electrodes for transmission and receive for HBC. The electrodes need to be skin compatible, flexible and non-toxic to be contacted with human skin for long times. Polyimide(PI)-PDMS electrodes suit for the purpose. So, we developed PI-PDMS electrodes for binaural hearing aids, and the transmission characteristics are evaluated. Moreover, some data are transmitted between electrodes on both sides of ear.

Keywords— Human body communication, Polyimide , PDMS, electrode

I. INTRODUCTION

The binaural effects are induced by the differences of sound pressure and phase between both ears[1]. Because of these effects, animals having two ears can sense the direction of sound source and hear better than single ear by summation of sound signal from both ears. These causes squelch effect that eliminates noises effectly, too[2]. In binaural hearing aids, each side has a microphone and a speaker. Binaural hearing aids serve quality-improved sound to hearing-impaired people using hearing aid and help them to be able to localize the direction of sound source. [3]. A system of binaural hearing aids using wire for communication was developed, but it was not preferred because it was not comfortable and consumers didn't want to spread the fact that they use hearing aids.

Recently, researches about human body communication (HBC) technology have been escalated rapidly. Because HBC have high data rates (about 10Mbps) and consumes very low power (below 1mW), these are expected to be able to solve the limits[4]. On this occasion, devices need electrodes for transmission and receive. Especially, the electrodes need to be skin

compatible, flexible and non-toxic to be contacted with human skin for long times (over quite hours per a day). Polyimide(PI)-PDMS electrodes suit for the purpose, because these are flexible, non-toxic and bio or skin compatible[5]. In this study, we developed PI-PDMS electrodes for communication between binaural hearing aids, the transmission characteristics of electrodes are experimentally evaluated and some data are transmitted through HBC between the electrodes on both sides of ear.

II. METHODS

The electrodes were fabricated by encapsulation of PI electrodes with PDMS sheets after peeling off from wafer (Figure 1(g)). PI electrodes are made on PI by MEMS fabrication process (Figure 1). First, polyimide bottom layer was spin-coated and was patterned on wafer by soft lithography process. Then, metal (Au) was evaporated on polyimide by E-beam evaporation and then patterned by the lithography process and PI top layer was fabricated through the same process of bottom layer.

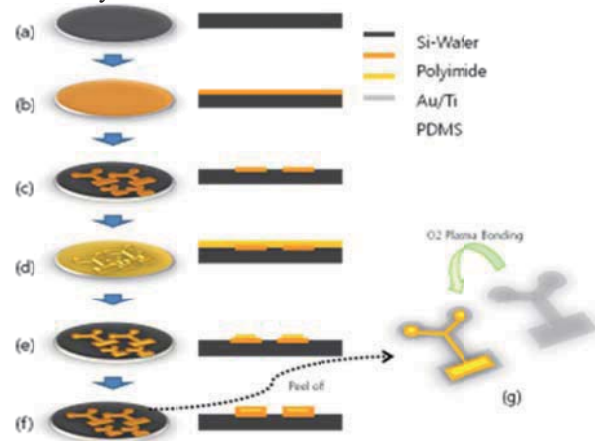


Fig. 1. Fabrication process of PI-PDMS electrodes.

The electrodes were attached on the retro auricular region of both ears after being fixed to the mock-up's inner side of Behind-the-Ear(BTE) type (Figure 2(a, b)). The transmission gains were measured by Network analyzer (NA, MS 2024A, Anritsu co.), which was calibrated from 1 kHz to 100 MHz and to 4 GHz with calibration kit (SiteMaster Precision Loads, OSLN50-1SM/PL-1, Anritsu co.) before measurements. Cables, shielded From DC to 2 GHz, are connected to NA and the cables are connected N-type connectors have two forceps at each (Figure 2(c)). Because the wire from

N-type connector to electrodes and the forceps itself could affect the gains by acting like antenna, the gains without electrodes, or just like figure 2(d), was measured. Output power from NA was set to -35dBm and the gains of five couples are normalized for each volunteer (3 volunteers). Finally, one-zero stream was transmitted at 5 kbps speed after being modulated with 10 MHz carrier (FSK), and then demodulated after receiving.



Fig. 2. Preparation for evaluation of PI-PDMS electrodes. (a) PI-PDMS electrodes for binaural hearing aids. (b) attaching electrodes on the retro auricular region after being fixed on the mock-up. (c) connection from NA to N-type connector having forceps. (d) connection of devices for modulation and demodulation with PI-PDMS electrodes for BAN between binaural hearing aids.

III. RESULTS

Figure 3 shows the transmission gains of BAN in the frequency region from 1 kHz to 4 GHz. The gains roughly have quite higher gain below about 450 MHz, but many alterations were observed. In figure 4, high gains near -20 dB were measured around 30 MHz. Even though the wire from N-type connector to electrodes affect the gains, HBC with PI-PDMS electrodes between binaural hearing aids are validated and some bit signal stream can be transmitted and received (Figure 5).

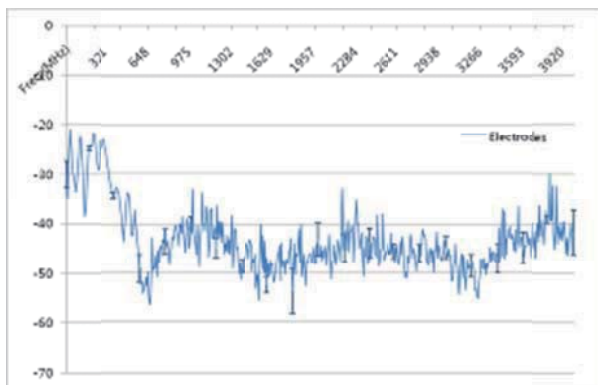


Fig. 3. Transmission gains below 4 GHz

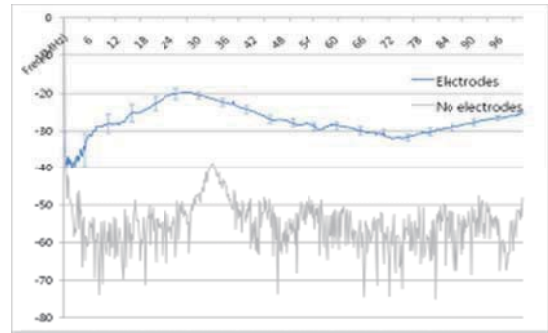


Fig. 4. Transmission gains below 100 MHz

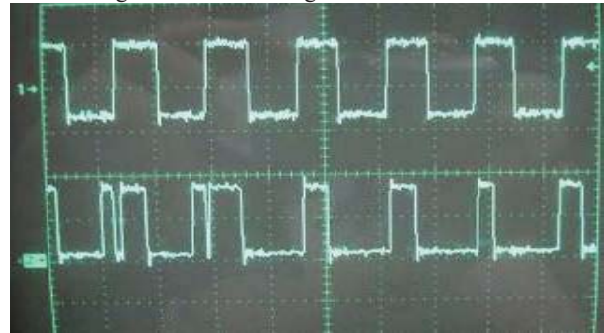


Fig. 5. Transmitted and received some bits signal. One-zero bits stream (channel 1) transmitted after being modulated with 10 MHz carrier and received, then demodulated (channel 2).

IV. CONCLUSION

In summary, PI-PDMS electrodes for BAN between binaural hearing aids are developed and the feasibility was verified by measurement of transmission characteristics and transmitting/receiving test of some signal stream. Now, we could apply PI-PDMS electrodes to communicate between binaural hearing aids and also it will be a step for application of BAN to medical instruments.

ACKNOWLEDGEMENT

This work was supported by grant no 10031779 from the strategic technology development program of Ministry of Knowledge Economy.

REFERENCES

1. Wegel, R.L., The physical examination of hearing and binaural aids for the deaf. Proceedings of the National Academy of Sciences of the United States of America, 1922. 8: p. 155-160.
2. Silman, S., S.A. Gelfand, and C.A. Silverman, Late-Onset Auditory Deprivation - Effects of Monaural Versus Binaural Hearing-Aids. Journal of the Acoustical Society of America, 1984. 76(5): p. 1357-1362.
3. Edwards, B., The future of hearing aid technology. Trends Amplif, 2007. 11(1): p. 31-45.
4. Peiravi, A. and M. Farahi, Reliability of Wireless Body Area Networks used for Ambulatory Monitoring and Health Care. Life Science Journal-Acta Zhengzhou University Overseas Edition, 2010. 7(2): p. 85-91.
5. Moon, J.H., et al., Wearable polyimide-PDMS electrodes for intrabody communication. Journal of Micromechanics and Microengineering, 2010. 20(2)

Development of biopsy gun for aspiration and drug injection

J.M.Cho¹, K.G.Kim¹, H.G.Kang²

¹Biomedical Engineering Branch, Division of Convergence Technology, National Cancer Center, Goyang-si, Rep. Korea

²Specific Organ Cancer Branch, Orthopaedic Oncology Clinic, National Cancer Center, Goyang-si, Rep. Korea

E-mail: jmo.cho@ncc.re.kr

Abstract— The present study was conducted to develop a biopsy gun that leaves a mark or injects drugs into the target area to secure various forms of tissues using one surgical tool.

To verify the performance of the developed prototype, a comparative test was done on pork. Furthermore, aspiration and injection experiments were carried out on the wide excised soft tissues. We evaluated the feasibility of the developed device using a prototype. The amount of sample that can be collected was tested. The performance of biopsy aspiration was also evaluated, including the maximum allowed viscosity of the liquid to be aspirated. Lastly, we tested the maximum amount of drug that can be injected.

We expected that the developed biopsy gun offers an alternative method for biopsy collection with procedure safety and diagnostic accuracy.

Keywords— Gun biopsy, Aspiration, Hemostasis, Track marking, Drug injectable

I. INTRODUCTION

Among many methods for obtaining tumor tissues, gun biopsy is widely used and is much simpler compare to incisional biopsy and it can collect more samples than aspiration biopsy [1]. However, conventional biopsy guns cannot perform biopsy aspiration, prevent bleeding and inject marker simultaneously [2]. In this study, we developed a biopsy gun which can perform biopsy aspiration and sampling at the same time.

II. METHODS

The developed device can simultaneously inject styptic agent and marker to prevent bleeding and contamination in the biopsy track. Considering the user's grip, the biopsy gun was modeled after existing products, whereas the firing power of the cannula needle was increased based on the resistance of the developed needle. A needle was mounted for injection and aspiration functions, and the flexible tube was connected to a syringe to facilitate the flow of fluid.

III. RESULTS

The developed aspiration injection gun presented additional functions, in addition to general features of existing biopsy for the reduction of discomfort in the user. Sampling amount was found to be higher using

the developed aspiration injection gun compared to the commercial product and this may have been caused by the fact that the tissue was not pushed away because the attractive force, which was generated by the negative pressure on the aspiration syringe and exerted through the aspiration hole before the second shot, held the tumor tissue in place at the sampling slot of the needle..

IV. CONCLUSION

We expected the developed biopsy gun can greatly improve the accuracy of the diagnosis as it can obtain both solid and liquid tissues. In addition, the ability to inject drug would help patient recovery and mark the corresponding area. With this, it is believed that the risk of infection is significantly reduced as the track can be disinfected through the injection function even when the needle is big or the surgeon is less experienced

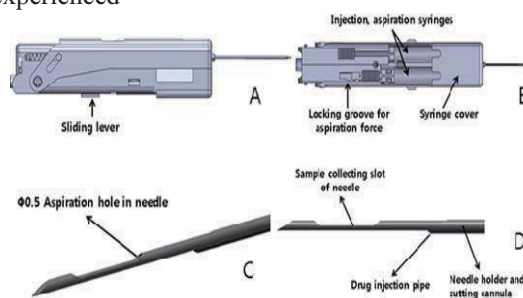


Fig. 1. Developed aspiration injection gun

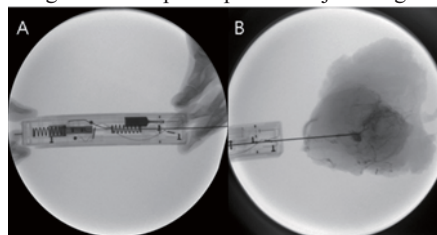


Fig. 2. Injection experiment on tissue

ACKNOWLEDGEMENT

This research was supported by grants from the National Cancer center, Rep. Korea (1510250-1).

REFERENCES

1. S. H. Parker, K.D. Hopper, W.F. Yakes, M.D. Gibson, J. L. Ownbey and T. E. Carter, "Image-directed percutaneous biopsies with a biopsy gun." *Radiology* 171(3): 663-669, 1989
2. A. Elvin, T. Andersson, L. Scheibenpflug and P.G. LindgrenA. "Biopsy of pancreas with a biopsy gun." *Radiology* 176(3):667-669, 1990.

Development of Strabismometry Software

H.-W. Moon¹, Y.-J. Kim¹, H.-K. Yang², J.-M. Hwang², and K.-G. Kim¹

¹Biomechanical Engineering Branch, Division of Convergence Technology, National Cancer Center, Goyang-si, Republic of Korea

² Department of Ophthalmology, Seoul National University Bundang Hospital, Seongnam-si, Republic of Korea
E-mail: hwmooon90@ncc.re.kr

Abstract— We developed strabismometry software program. It calculates the degree of strabismus merely taking a picture of patients. So it can make the diagnosis of strabismus more simple and accurate.

Keywords—Strabismus, Strabismometry, Image analysis, 3D eye model

I. INTRODUCTION

Clinically, the degrees of strabismus are measured by prism cover test, corneal reflex test (Hirschberg test), prism reflex test (Krimsky prism test), etc. As the measurements are depends on a clinician, we need more numerical and quantitative methods. Therefore, we developed a software program to measure the degrees of strabismus. As it uses a computer, it is expected that the diagnosis of strabismus could be more fast, accurate and easy.

II. METHODS

A. Instruments

A camera with a flash, A computer to install the software program.

B. Procedure to Take a Picture

There are some constraints. First, take picture far apart; approximately beyond 55cm. Second, make a patient look into the camera as right as possible. Now take a picture with flash.

C. Information in the Picture

If we get a picture following B, there are two corneal reflex points of flash light. The positions of two corneal reflex points carry the information about how much the eyes are rotated. To calculate them, we used 3D eye model.

D. Program Algorithm

Here is the algorithm. We first locate the corneal center of the 3D model eye at the corneal reflex point in the picture. Second, rotate the 3D model eye until the corneal boundary of 3D model eye fits that of real eye in the picture. Then we get the angle, θ' . With some careful consideration, we get key equation.

$$r \sin(-\alpha + \theta) = r \sin(-\alpha + \theta') + \beta r \sin(\theta)$$

From the equation, we can calculate strabismus angle, θ .

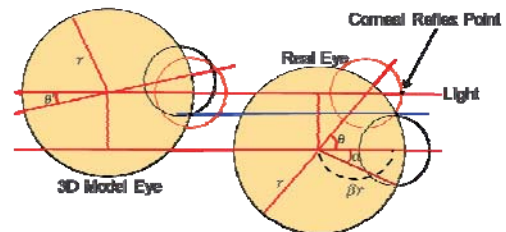


Fig. 1. Schema used in the program

III. RESULTS

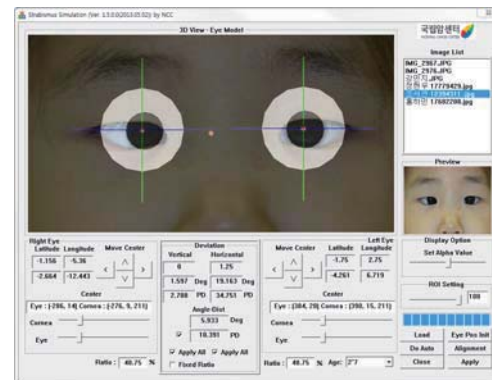


Fig. 2. The strabismometry program

Fig 2 shows our strabismometry program. The degrees of the patient are 2.8PD (vertical) and 35PD (horizontal) at the program which are comparable to the values 4.5PD (vertical) and 37PD (horizontal) at Krimsky test.

IV. CONCLUSION

This program gives strabismus angles just using a camera and a computer. Therefore, it can reduce the cost. Also as it uses a computer it gives more accurate values.

REFERENCES

1. Journal of Korea Multimedia Society Vol. 15, No 5, May 2012(pp. 595-605)
2. Michael W. Quick and Ronald G. Boothe, "A Photographic Technique for Measuring Horizontal and Vertical Eye Alignment Throughout the Field of Gaze," Investigative Ophthalmology & Visual Science, Vol. 33, No. 1, January 1992

Investigation of venous blood flow during intermittent pneumatic compression

W. Lee¹, J. H. Seo¹, H. B. Kim², S. H. Chung³, K. G. Kim¹, and H. G. Kang⁴

¹Biomedical Engineering Branch, National Cancer Center, Goyang-si, Republic of Korea

²Department of Radiology, National Cancer Center, Goyang-si, Republic of Korea

³Rehabilitation Medicine, National Cancer Center, Goyang-si, Republic of Korea

⁴Orthopaedic Oncology Clinic, National Cancer Center, Goyang-si, Republic of Korea

E-mail: wonhee88@gmail.com

Abstract Intermittent pneumatic compression (IPC) has now become a standard therapy for the prophylaxis of deep vein thrombosis. Blood flow is known to be increased by IPC treatment, but real-time change of blood flow during IPC has not been investigated because of the lack of appropriate tools. In this study, a software program which extracts instantaneous blood velocity (IV) and the vein thickness (VT) from sonography movie clips was developed. By adopting frequency analysis and 0.1 Hz low-pass filtering, a pure IV waveform by IPC could be acquired. Using IV and VT, some change of hemodynamic variables were calculated. The increase in the peak volume flow (PVF) was 49% ($\pm 24\%$), whereas total volume flow (TVF) was not significantly changed (-1.0%).

Keywords— intermittent pneumatic compression, deep vein thrombosis, real-time hemodynamics

I. INTRODUCTION

Intermittent pneumatic compression (IPC) is considered as a general therapy to reduce the risk of deep vein thrombosis after surgery [1]. However, few studies have investigated the real-time changes in blood flow in the vein during IPC. This is likely because of the non-availability of appropriate tools and methods for real time measurement of blood flow. While Doppler sonography has been used in many studies on DVT, it provides images that show blood flow for a short period. Therefore, it cannot be used to demonstrate or record the dramatic changes in blood flow that occur during IPC.

II. METHODS

A. Subjects and equipment

Thirty healthy volunteers were enrolled after approval from the clinical trial commission of the Korea National Cancer Center (NCC2014-0041). DVT-3000 (DS MAREF) and iU22 xMATRIX (Phillips) with a 12.5-MHz linear array probe was used for IPC device and sonography equipment.

B. Hemodynamic variable analysis

A software tool that extracts the blood velocity and the vein thickness was developed, and respiration and pulse effect was filtered out by 0.1 Hz low-pass filter after frequency analysis.

III. RESULTS

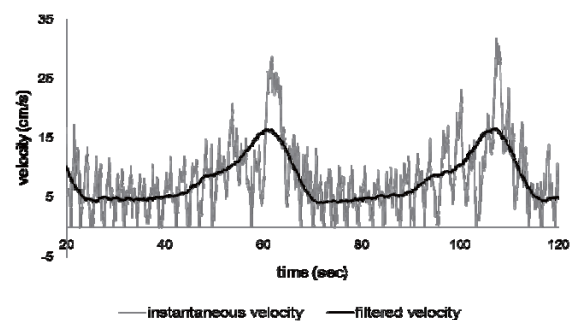


Fig. 1. Figure caption

Table 1. The change of hemodynamic variables

		Independent sample t-test				
		mean	s.d.	p	c.i.	
Baseline	PVF	11.78	6.15	0.93	-7.13	6.57
	TVF	257.13	108.87	0.81	-91.13	116.28
IPC	PVF	20.50	8.94	0.03	0.74	13.93
	TVF	250.16	106.26	0.27	-37.20	128.85

IV. CONCLUSION

Blood flow velocity was verified to be substantially affected by normal pulse and respiration as well as compression by IPC devices. From the filtered velocity waveform, it was found that a steep decrease occurred during the deflation phase and that the reason for this was the negative pressure in the vessel.

ACKNOWLEDGEMENT

This work was supported by the Technology Innovation Program (10046763) funded by the Ministry of Trade, Industry & Energy (MI, Korea)"

REFERENCES

1. Pierce TP, Cherian JJ, et. al. A Current Review of Mechanical Compression and Its Role in Venous Thromboembolic Prophylaxis in Total Knee and Total Hip Arthroplasty. The Journal of arthroplasty. 2015 May 29.

Development of an Alarm System for a Concerned High Cervical Cord Injury Patient

J. H. Ro¹, G. R. Jeon¹, S. H. Kim², J. S. Lee², Y. B. Shin²

¹Department of Biomedical Engineering, School of medicine, Pusan National University, Busan, Korea

²Department of Rehabilitation Medicine, School of Medicine, Pusan National University, Busan, Korea

E-mail: mailto:jhro@pnu.edu

Abstract— A successful way to applying noninvasive ventilation with full face mask in a concerned high cervical cord patient using novel alarm system was reported. Although there were some limitation of the prototype such as hardness of the balloon sensor or decreased durability of the pressure sensor, the alarm system has helped the psychologically anxious patient to relieve anxiety.

Keywords— Enter up to five keywords and separate them by commas.

I. INTRODUCTION

Cervical spinal cord injury often leads to an interruption of the descending bulbospinal respiratory pathways, resulting in total or partial respiratory muscle paralysis. And a fatigue of the spared muscles is surely the main cause of respiratory failure. In that case, long-term intermittent ventilator support can be one of the treatment options. Noninvasive ventilation(NIV) is more ideal way than invasive one for various reasons. But it is difficult to get cooperation from a high cervical cord injury patient. Because patients cannot take off the mask by themselves, so cannot call caregiver when needs help during a applying NIV with full face mask.

II. METHODS

A 56-year-old male with a cervical spine dislocation, tetraplegia, C3 ASIA B was admitted for pulmonary function evaluation to remove tracheostomy tube. He has been tracheostomy state for 3 years. His diaphragm movement was shallow but through the adequate pulmonary rehabilitation program peak cough flow in supine and sitting position reached 160L/min with or without assist, so we decided to remove it. At first, we used nasal mask type in applying night-time NIV but he did not adjust and sleep apnea leading to morning headache and frequent awakening from sleep continued. We reasoned that nasal mask was inappropriate because of air leakage and inadequate ventilation. We changed to full face type mask and the problems got solved. But he strongly refused full face type mask and appealed it terrorized him because he did not think he can call caregiver for help in applying NIV.

III. RESULTS

To solve that problem, we designed novel alarm system. The system uses an Arduino Uno microcontroller board which is open source electronics platform based on easy-to-use hardware. And the system had been programmed with the Arduino software. As his neck rotator function was intact, the best clear and easy intended motion for the patient was head shaking. The detection of the head movement was performed by the pressure variation of a balloon under the pillow of the patient. The sensor reacts only when the pressure over 10 cmH₂O. In that setting, the sensor ignores other reactions such as smooth variation of pressure or below threshold pressure.



Fig. 1. Alarm system which detect of the dead movement by the pressure variation of a balloon under the pillow of the patient.

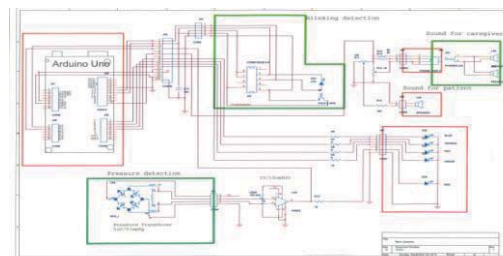


Fig. 2. A schematic diagram of alarm system

IV. CONCLUSION

In this study, we could find a psychological factor related to failure to apply NIV with full face mask in high cervical cord injury patient. Although we did not prescribe any antidepressant or antipsychotic drug for treatment of his anxiety, novel way to relieve patient's fear using new alarm system was successful. This novel alarm system will be one of the good option for anxious patients who have only neck movement. We find some limitation of this prototype such as hardness of the balloon sensor or decreased durability of the pressure sensor which is originally a component of invasive blood pressure (IBP) sensor.

Development of flexible and stretchable dry electrode using metal electroplating on a porous elastomer

Jeong hun Kim¹, Joonghoon Lee¹, Hanseop Kim¹ and Sang-Hoon Lee^{1,2}

¹KU-KIST Graduate School of Converging Science and Technology, Korea University, Seoul 136-701, Republic of Korea

²Department of Biomedical Engineering, College of Health Science, Korea University, Seoul 136-703, Republic of Korea

E-mail: dbiomed@korea.ac.kr

Abstract— Various flexible and stretchable materials have been reported for use in electronic devices or biomedical applications. Technology monitoring neural signals for a long time has developed with flexible materials. But flexible dry electrode for electrical stimulation reaches the limit because high impedance of conductive polymer or weak mechanical property of thin metal layer. Here, we propose a novel method for fabricating flexible and stretchable electronic devices using a porous elastomeric substrate.

Keywords— flexible elastomer, PDMS, stimulator, electrode, Bio-signals

I. INTRODUCTION

The development of long-term wearable or implantable bio signal-measuring devices presents an important challenge that must be overcome before realizing these goals. A key technical issue is the development of wearable or implantable to adapt to tissue and body motions while maintaining close contact with the curvature of skin or organs. To date, several flexible or stretchable electronics for biomedical or industrial applications have been developed.

In this paper, we describe a novel and simple method for fabricating flexible and stretchable electronics and for direct bonding of electronic components on the highly stretchable substrate.

II. METHODS

A. Fabrication of flexible substrate

We spin-coated polydimethylsiloxane (PDMS) on the Si-wafer at 1000 rpm for 30 sec. We inserted the wafer in the autoclave and operated the auto-clave for 30 mins.

B. Metal patterning

We deposited metal layer (Ti : 40nm, Au : 120 nm) using E-beam evaporator after attaching shadow mask designed Auto-CAD to porous PDMS substrate. And we performed nickel electroplating

C. Mechanical properties test

We performed cycling test at 10, 20, 30, and 40 % strain using X-stage and multi-meter, and bending test with edge of a plate and a sharp stick.

III. RESULTS

The electrical conductivity of the metal patterns on the porous PDMS was robust under extensions (~30%) and after a durability test over 1,000 cycles. Although the electrical conductivity was deteriorated owing to fatigue by the repeated stretching motions, electrical disconnections were not observed. These results demonstrated that the porous electrodes maintained robust electrical conductance under stretching cycles.

The electrode was also resistant to bending. Although the electrode was seriously bent along a sharp edge, electrical breakdown was not observed. The higher change in resistance based on the angle and thickness is clearly demonstrated.

IV. CONCLUSION

In summary, biocompatible metal-patterned porous PDMS with high flexibility and stretchability were successfully fabricated as electrical stimulator using simple and cost-effective techniques. Biomedical applications require stable operation under a variety of conditions, and the materials must not induce skin or tissue incompatibility. Our method satisfied most of these requirements. The robustness of the metal electroplating on porous substrate is another crucial feature of our method, and it will be widely useful for neural electrodes. Such electrodes are useful in brain-to-machine interfaces.

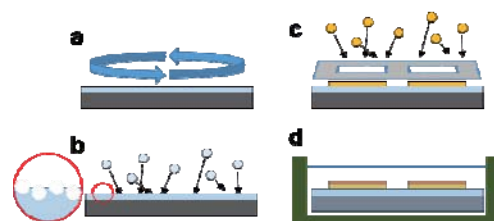


Fig. 1. Process of metal patterning on the porous PDMS layer

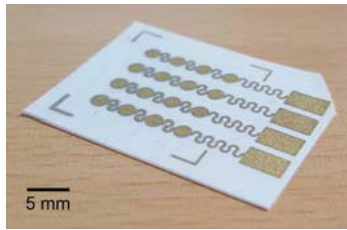


Fig. 2. Image of metal pattern on the porous PDMS

ACKNOWLEDGEMENT

This study was supported by a grant of the Korea Healthcare technology R&D Project, Ministry for Health, Welfare & Family Affairs, Republic of Korea. (HI14C0771).

REFERENCES

1. Jeong, Gi Seok, et al. "Solderable and electroplatable flexible electronic circuit on a porous stretchable elastomer." *Nature communications* (2012): 977.

A Highly Conductive and Soft CNT/AgNW/PDMS-based Electrodes for Continuous and Insensible EEG Recording

Joonghoon Lee¹, Hanseop Kim¹, Jeonghun Kim¹, Ji-Young Hwang², Sang-Hoon Lee^{1, 2, 3}

¹ KU-KIST Graduate School of Converging Science and Technology, Korea University, Seoul 136-701, Republic of Korea

² Department of Biomedical Engineering, College of Health Science, Korea University, Seoul 136-703, Republic of Korea

³ Department of Bio-convergence Engineering, College of Health Science, Korea University, Seoul 136-703, Republic of Korea

E-mail: dbiomed@korea.ac.kr

Abstract— Current Electroencephalogram (EEG) electrodes have several challenging for continuous and unconscious monitoring in daily life. This makes it difficult for wide spread using of EEG based applications. Our study here is to develop a small sized, highly conductive, flexible and biocompatible electrode for long-term EEG monitoring. We fabricated a carbon nanotube and silver-nanowire polydimethylsiloxane (CNT/AgNW/PDMS)-based electrodes for continuous and insensible EEG recording. We focused on to record EEG instable and insensible. Electrode performance was evaluated by standard EEG paradigms and toxicity tests. We observed the successful recording of EEG and biocompatibility. This electrode could be used for monitoring EEG in U-health care and BCI field.

Keywords— Highly conductive, Silver-nanowires, Carbon-nanotubes, EEG electrode, Biocompatible.

I. INTRODUCTION

Electroencephalogram (EEG) is one of the most important method to diagnose diverse neurological diseases on the scalp. With the emerging advances of information and communication technology (ICT) and biomedical engineering, numerous interests about EEG-based applications are steadily rising in the area of brain computer interface (BCI) and ubiquitous (U)-healthcare.¹ Continuous and insensible recording of EEG is highly required for applications. However, there are several problems in conventional EEG electrodes for unconscious and long-term continuous monitoring, including intrusiveness, poor biocompatibility and reducing signal quality due to conductive gel. Therefore, several research groups recently reported on dry electrodes by using diverse novel nanomaterials, such as carbon-nanotubes (CNTs), nanowires (NWs) and graphene. Nanocomposites which are combined of nanomaterials with polymers are actively studied and reported for flexible and stretchable electrodes. However, low conductivity, skin toxicity and unconscious recording for EEG are still challengeable.

In this paper, we developed highly conductive and flexible epidermal electrodes composed of CNTs, silver nanowires (AgNWs), and polydimethylsiloxane (PDMS) for continuous and insensible EEG recording to improve aforementioned problems..

II. METHODS

Previously, we developed biocompatible and conductive CNT/PDMS electrode for biomedical applications. However, EEG measurement requires extremely high conductivity to reduce contact impedance because the signal level is very small. Therefore, we added AgNWs to CNT/PDMS for improving conductivity and tested its electrical and mechanical performance by measuring the contact impedance and young's modulus. Furthermore, the cytotoxicity test was conducted with human skin cells on CNT/AgNW/PDMS sheets for a week. The feasibility of the newly developed electrode was evaluated through two standard EEG paradigms including alpha rhythm detection, steady state visually evoked potential (SSVEP).

III. RESULTS

The electrical properties of the CNT/AgNW/PDMS electrode are highly improved compare to our previous works, and the young's modulus showed that the electrode is suitable for soft epidermis. All feasibility was successfully recorded with fabricated electrodes and good biocompatibility was also proved.

IV. CONCLUSION

These results indicated that the highly conductive and soft CNT/AgNW/PDMS-base electrodes can be used for insensible and continuous EEG recording. In addition, the soft and flexible surface is perfect fitted to soft epidermis that it provides high signal to noise ratio and comfort insensible recording for patients. This new material based EEG electrode could be widely applied for clinical, U-healthcare and BCI fields.

Development of GUI Program for Objective Assessment of Facial Nerve Palsy

H. S. Kim¹, S. Y. Kim², Y. H. Kim³, and K. S. Park⁴

¹Interdisciplinary Program of Bioengineering, Seoul National University, Seoul, Republic of Korea

²Department of Otorhinolaryngology, Head and Neck Surgery, Seoul National University Hospital, Seoul, Republic of Korea

³Department of Otorhinolaryngology, Head and Neck Surgery, Seoul National University, Boramae Medical Center, Seoul, Republic of Korea

⁴Department of Biomedical engineering, College of Medicine, Seoul National University, Seoul, Republic of Korea

E-mail: khs0330kr@bmsil.snu.ac.kr

Abstract—Facial nerve palsy is a nervous system disorder. The House-Blackmann scale is a subjective assessment method which is a widely used. Objective assessment method is required for a reliable diagnosis. An objective clinical assessment GUI program is developed using Qt. The asymmetry indices of forehead and mouth regions are calculated by distance ratio between left and right side. This program could be helpful for monitoring and tracking patient's progression of disease by objective assessment.

Keywords— Facial Nerve Palsy, Objective Clinical Assessment, Asymmetry Index.

I. INTRODUCTION

Facial nerve palsy is a nervous system disorder where there is a loss of voluntary muscle movement in a patient's face caused by nerve damage. The House-Blackmann (H-B) scale is a widely used scaling system that grades from normal to total paralysis [1]. However, the H-B scale has a subjective characteristics, objective assessment method is required for a reliable diagnosis. In this study, we propose an objective facial nerve palsy assessment program to diagnosis patients.

II. METHODS

A. Asymmetry index

First, drawing a horizontal line that is passing through the left medial canthus and the right medial canthus. Then a face is divided into left and right sides by an automatic generated vertical line that is perpendicular to the horizontal line. The vertical line passes through midpoint between the left and right medial canthus. To measure asymmetry index of forehead region, draw two perpendicular lines from left and right eye brow points to the horizontal line. The asymmetry index of forehead region is distance ratio between the left and right side of forehead. To measure asymmetry index of mouth region, draw two perpendicular lines from left and right mouth points to the vertical line. The asymmetry index of mouth region is distance ratio between the left and right side of mouth.

B. Description of GUI program

We developed an objective assessment graphic-user-interface program using Qt which is a cross-platform application framework. The program make the vertical line automatically based on user-made horizontal line. A forehead- or mouth-related perpendicular line is generated by only clicking eyebrow or mouth corner point. The program can save or load parameters for measuring asymmetry indices.

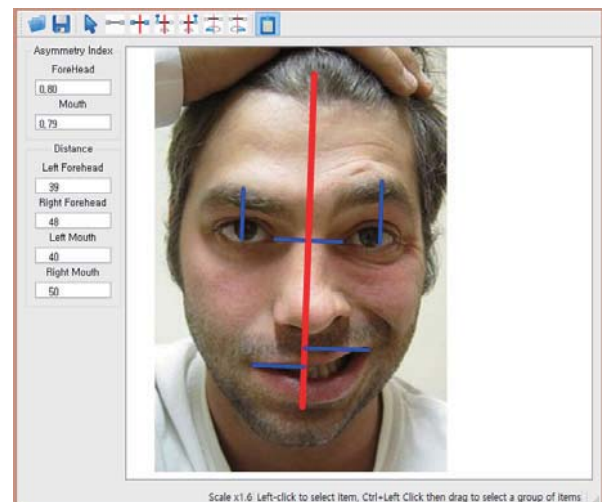


Fig. 1. Example of measuring asymmetry indices using GUI program.

IV. CONCLUSION

This program could be helpful for monitoring and tracking patient's progression of disease by objective assessment.

ACKNOWLEDGEMENT

This work was supported by the Seoul National University Hospital and Coway Co., Ltd..

REFERENCES

1. J.W. House and D. E. Brackmann, "Facial nerve grading system," *Otolaryngology--head and neck surgery : official journal of American Academy of Otolaryngology-Head and Neck Surgery.*, vol. 93, pp. 146-119, 2013.

Anthropometric study on Mongolians with metabolic syndrome

Dashdulam.Ts¹, Otgonbat.J², Tuul.B³, Enebish.S⁴, Amgalanbaatar.D⁵,

¹ School of Pharmacy and Bio-Medicine, MNUMS, Mongolia.

² School of Pharmacy and Bio-Medicine, MNUMS, Mongolia.

E-mail; dashdulam@mnums.edu.mn

Abstract

Background; Development of up-to-date technologies has changed the lifestyle of humanity and accordingly non infectious diseases, especially metabolic syndromes, which involve 20-25% of adults in the world, have been increasing. The metabolic syndromes which cause morphological changes alter the human body figure or human anthropometric measures. Recently we have found the studies on metabolic syndrome risk factors, but not the papers related to the anthropometric measurements. Thus there is a real need to determine the anthropometric measurements of Mongolians.

Purpose; Determine the human body figure types or the anthropometric measurement changes caused by the metabolic syndromes.

Materials and Methods; 387 Mongolians aged 18-68 were involved in the study. Basic methods of anthropometric measurements, metabolic syndrome diagnosis and statistics were used in it.

Results; According to the defining of height differences, value of Student distribution, and statistical significant threshold between participants, healthy and with metabolic syndromes, of both sex, there were no

evident variation. The statistical significance of the participants' humerus diameter because of obesity, caused by metabolic syndrome, was observed ($P < 0.05$ and $P < 0.01$). Also the body mass index (BMI) of the both type's participants has statistical great differences, and it is shown by modified waist indexes ($P < 0.01$). Metabolic syndromes cause the statistical differences between diastole and systole of participants, both sexes ($P < 0.01$). In accordance with sex differentiation their BMI has statistically marked difference ($P < 0.01$). All in all the metabolic syndromes affect on human anthropometric measurements, especially it modifies the BMI more than the height.

Conclusion; For healthy men and women the anthropometric indexes are in normal distribution. And according to the sex the men anthropometric indexes are different from the women. An average BMI for men is 27.29 ± 0.43 , for women – 24.95 ± 0.28 . In proportion to healthy and metabolic syndrome suffered participants the anthropometric indexes are in normal distribution. And according to the sex the men anthropometric indexes are different from the women. An average BMI for men is 31.81 ± 0.75 , for women – 30.53 ± 1.32 . The waist index, the most modified anthropometric criteria, of all participants explained by the metabolic syndromes caused overweight. There were no distribution differences.

Key words: Anthropometry, metabolic syndrome, age, sex

Meshed silver nanowires with flexible substrate for mechanical-stable and transparent electrodes.

Hyejin Jang, Tae Hyung Kim, Jooseung Lee, Tae-il Kim*

Center for Neuroscience Imaging Research (CNIR), Institute for Basic Science (IBS), Suwon 440-746, South Korea

School of Chemical Engineering, Sungkyunkwan University (SKKU), Suwon 440-746, South Korea

(taeilkim@skku.edu*)

Silver nanowires (AgNWs) have been used for durable and flexible electrodes with transparency. Arrayed AgNWs are attached on a flexible substrate using ultrathin adhesive. In spite of an extreme bending on 0.15mm radius of curvature, disregardable hysteresis proved its mechanical stability. We arranged a meshed NWs structure by multiple transfer printing instead of randomly spreading. The meshed structure has advantages in that it has low areal fraction and it leads to high transmittance i.e. enhanced optoelectrical performance contrasting with the random structure. Besides, we described a concise lithography of NWs array. Definitely, this flexible and transparent electrode can be applied in numerous fields including optoelectronic devices and flexible/wearable electronics.

Ultrasensitive Mechanosensor based Geometrically Modulated Nanoscale Cracks

Byeonghak Park, Jisun Kim, Chanho Jeong, Tae-il Kim[†]

Center for Neuroscience Imaging Research (CNIR), Institute for Basic Science (IBS), Suwon 440-746, South Korea
School of Chemical Engineering, Sungkyunkwan University (SKKU), Suwon 440-746, South Korea
(taeilkim@skku.edu[†])

In previous research, ultrasensitive nanoscale crack based mechanosensor inspired by spider's sensory organ is presented.[1] The sensors are sensitive to pressure and vibration with the ability to detect amplitude of approximately 10nm scale attributed to the phenomenon of disconnection-reconnection process by zip-like nanoscale crack interfaces under tiny extremal stimulations. To enhance the sensitivity, we considered the geometry of cracks. However, among many geometrical parameters of the cracks, crack depth is considered as a key factor to improve sensor's performance. In this presentation, we present ultrahighly improved performance of the nanoscale crack-based sensors by modulation of nanoscale crack geometry. By understanding of the main issue of crack sensors, we develop the sensor which shows superior sensing capability with a gauge factor over 15,000 in the 0-2% in strain range. We also demonstrate the sensors are applicable to wearable electronics like electronic skins.

[1] D. Kang et al., "Ultrasensitive mechanical crack based sensor inspired by the spider sensory system" Nature 516.7530 (2014); 222-226

Characteristics of Muscle Fatigue during Pedaling

J. W. Seo¹, D. W. Kang¹, D. H. Kim¹, S. T. Yang¹, J. S. Choi^{2,3} and G. R. Tack^{2,3}

¹Department of Biomedical Engineering, Graduate school of Konkuk University, Chungju, Korea

²Department of Biomedical Engineering, College of Biomedical & Health Science, Konkuk University, Chungju, Korea

³BK21 Plus Research Institute of Biomedical Engineering, Konkuk University, Chungju, Korea

E-mail: grtack@kku.ac.kr

Abstract— The aim of this study is to investigate effects of pedaling time on muscle frequency characteristics. Eight subjects performed 20 min pedaling with 70 rpm. Results showed that the median frequency at Vastus lateralis was significantly different by time. The thigh muscle was easily tired than lower leg muscles.

Keywords— Cycle pedaling, Muscle fatigue, Median frequency

I. INTRODUCTION

Accumulation of muscle fatigue is important while pedaling. For the same distance, low fatigue is efficient for pedaling. The median frequency, which is related to muscle motor unit recruitments [1], of the power spectrum of electromyography (EMG) was used for checking the muscle fatigue. The aim of this study is to investigate effects of time on muscle frequency characteristics.

II. METHODS

A. Subject

Eight healthy young adult male who can normally pedal without musculoskeletal diseases participated in the experiment (age: 24.3±4.1, height: 167.5±9.8cm).

B. Experiment

A 3D motion analysis system with six infra-red cameras (Motion Analysis Corp., USA) and wireless surface EMG (Trigno, Delsys Corp., USA) were used to acquire motion and EMG with 120 Hz and 1,200 Hz sampling frequency. The pedaling event and frequency analysis of EMG were calculated by MATLAB R2013a (Mathworks Inc., USA). EMG was analyzed by 5 min interval with four periods. Vastus lateralis (VL), Tibialis Anterior (TA), Biceps Femoris (BF) and Gastrocnemius Medialis (GM) muscles were used. Subjects performed a test of 20 min pedaling with 70 rpm (revolution per minute) at 45° of knee angle saddle height. The fast Fourier transform (FFT) was conducted for the calculation of median frequency by using acquired EMG data.

III. RESULTS & CONCLUSION

The median frequency of the last period was lower than the first period. The main effect (time variable) was observed at only VL. The median frequencies were significantly different between at 0~5min and 15~20min, 5~10min and 10~15min, 10~15 and

15~20min at VL muscle. Therefore, the VL is easily tired than the other muscles. It means that the thigh muscle is easily tired than lower leg muscle. The results of this study might help to determine the effective pedaling exercise for muscle fatigue.

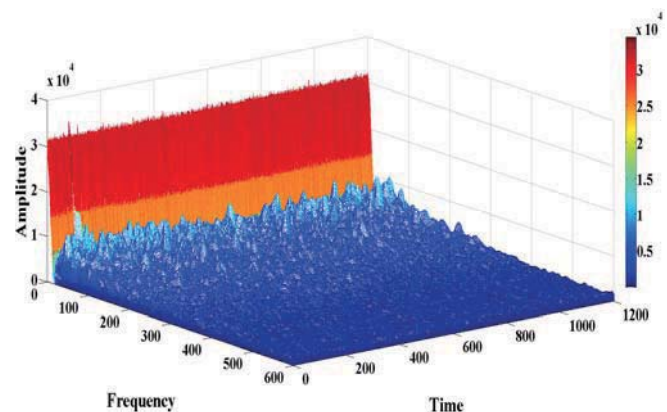


Fig. 1. An example of the power spectrum of EMG

Table 1. Results of EMG median frequency

	VL	TA	BF	GM
main effect	.02*	.07	.20	.27
0~5 min	5.61±0.24*	6.00±0.68	5.65±0.56	6.05±0.76
5~10 min	5.56±0.21#	5.86±0.36	6.03±0.60	6.28±0.73
10~15 min	5.66±0.27#!	6.02±0.61	5.77±0.66	6.17±0.72
15~20 min	5.48±0.26*!	5.99±0.77	5.60±0.55	6.02±0.70
P	.02* .03# .02!	NS	NS	NS

Repeated measure ANOVA, paired T-test, M ± SD, NS: No significant
*,#,! p<.05

ACKNOWLEDGEMENT

This research was supported by National Research Foundation of Korea funded by the Ministry of Education, Science and Technology (No. 2012R1A1A4A01008158).

REFERENCES

1. Vøllestad, N.K., "Measurement of human muscle fatigue", *J Neurosci Methods*, 74(2), 219-227, 1997.

Quantification of plantar soft tissues stiffness according to the change of the BMI

Yuri Kim¹, Haein Lee², Young-Seong Kim², Junghyun Park², Eunji Lee², Yisuk Kim³, Taeyong Lee^{2,*}

¹Department of Medical Device Industry, Dongguk University, Goyang-Si, Republic of Korea

²Department of Medical Biotechnology, Dongguk University, Goyang-Si, Republic of Korea

³Department of Mechanical Engineering, Korea Advanced Institute of Science and Technology, Daejeon, Republic of Korea

E-mail: tlee@dongguk.edu

Abstract—This article is the relationship between the stiffness of plantar soft tissue and BMI for young subjects. We measured stiffness of plantar soft tissue on sub-MTH and heel pad of males and females in their twenties. As a result, we found that women's MTH stiffness is highly related with BMI. So BMI can be considered as the factor of foot's rupture.

Keywords— Body mass index, plantar tissue, indentation test, ultrasound instrumentation, stiffness

I. INTRODUCTION

The increase of the plantar soft tissues stiffness increases the possibility of the tissues rupture, commonly occurs at the sub-MTH (Metatarsal Head) and heel pad where the load is concentrated[1,2]. However, the quantitative analysis of the correlation of the tissue stiffness and the contributing factors is not clearly conducted[3].

This experiment aim to quantify the correlation between the tissue stiffness and BMI on sub-MTH and heel pad of young males and females.

II. METHODS

A. Subjects

Twenty seven young healthy subjects (8 males and 19 females) in their twenties were recruited from Dongguk University. Consent was obtained from the subjects prior to testing.

BMI was classified according to the criteria presented by the Korean society for the study of obesity.

B. Experiment equipment

The thickness of plantar soft tissue on sub-MTH and heel pad was measured with 40mm linear transducer incorporated with ultrasound platform (MyLab one, Esaote, Italy). The thickness and indentation depth of the soft tissue layer were determined from the flight time of the US echo signal that reflected from soft tissue-bone interface.

The indenter used in this experiment measures the soft tissue's stiffness in the environment similar to

actual gait condition. Indentation tests only conducted at selected at 2nd sub-MTH and heel.

III. RESULTS

In the sub-MTH area of male subjects, BMI did not show any significance with stiffness nor thickness. However, BMI showed a linear relationship with stiffness ($r=0.774$) and thickness ($r=0.6433$) as shown in the Figure 1.

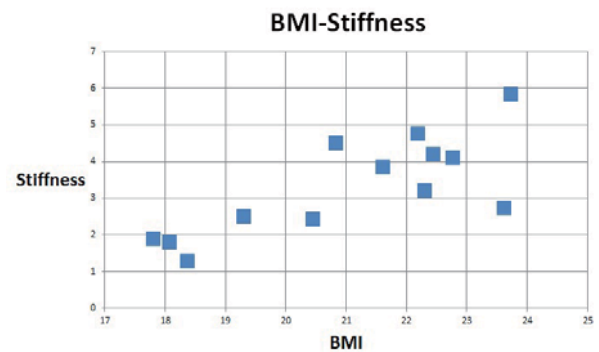


Fig 1. Distribution of BMI-stiffness

IV. CONCLUSION

Based on the linear relationship between BMI and two factors (stiffness and tissue thickness), we believe BMI can be considered as a factor of foot rupture. Result from the experiment may be helpful to study the risk factors of foot ulceration. To understand the ulceration mechanism related to BMI, we are going to recruit subjects with different BMI.

REFERENCES

1. Bojsen-Moller, F. Flagstad, K.E, "Plantar aponeurosis and internal architecture of the ball of the foot", *Journal of Anatomy.*, vol. 21, pp. 599-611, 1976.
2. Cavanagh, P.R, "Plantar soft tissue thickness during ground contact in walking", *Journal of Biomechanics.*, vol. 32, pp. 623-628, 1999.
3. Jahss MH, Michelson JD, Dasai P, et al. 1992. Investigations into the fat pads of the sole of the foot: *Anatomy and histology. Foot Ankle* 13:233-242.

Characterizing the Dynamical Structure of Postural Sway in the Faller Using Entropy

D. W. Kang¹, J. W. Seo¹, D. H. Kim¹, S. T. Yang¹, J. S. Choi^{2,3}, and G. R. Tack^{2,3}

¹Department of Biomedical Engineering, Graduate school of Konkuk University, Chungju, Korea

²Department of Biomedical Engineering, College of Biomedical & Health Science, Konkuk University, Chungju, Korea

³BK21 Plus Research Institute of Biomedical Engineering, Konkuk University, Chungju, Korea

E-mail: grtack@kku.ac.kr

Abstract— This paper studied the characteristics of the structural change in the postural sway of the faller using the Sample Entropy (SamEn). Postural sway was measured by using a waist-worn inertial sensor. All subjects with normal balance ability (Berg balance scale, BBS ≥ 50) who divided into two groups as non-fallers and fallers performed six different standing tests. During more challenging tasks, a discriminative difference in SamEn was observed and the faller had small values in SamEn. This means even fallers with normal balance ability showed the loss of complexity in postural control system by the degree of standing tasks.

Keywords— Postural sway, Inertial sensor, Sample Entropy (SamEn)

I. INTRODUCTION

Characteristics of the postural control system with/without fall history was investigated for the elderly with equal balance ability. Although preceding studies presented the changes in postural sway with various linear measures, these studies included the factor for physical states such as injury. Therefore, it is necessary to investigate the characteristics of the postural control system of the fallers with normal balance ability. This study investigated structural changes of the fallers using SamEn [1] which is related to the complexity of the system.

II. METHODS

A. Subjects

83 community-dwelling elderly (62 non-fallers, 21 fallers with at least 65 years old) participated in this study. The inclusion criteria for the study were with normal balance ability (BBS ≥ 50) with or without fall history.

B. Experiment

The postural sway of standing tests was measured by using a wireless inertial sensor module (APDM Inc., Portland, OR, USA) attached to the lower back (L3). A series of standing test was conducted with six conditions such as standing on the firm surface (firm), on foam pad (1foam, size : 50×50×7.5cm), and on two foam pad (2foam) with eye-open (EO) or eye-closed

(EC). Each test was conducted for one minute, and SamEn was calculated using anterior-posterior (AP) and medio-lateral (ML) directional acceleration. The derived SamEn was examined to the difference between two groups using Wilcoxon rank sum test of Meann-Whitney version ($p < .05$).

III. RESULTS

Fig 1 shows SamEn by six conditions. ML SamEn shows a decreasing tendency by conditions (firm, one foam, two foam) in both groups, and AP SamEn shows more steady value than ML. There were significant differences in EC-1foam and EC-2foam in ML and AP. The fallers showed lower complexity than the non-fallers in all the conditions.

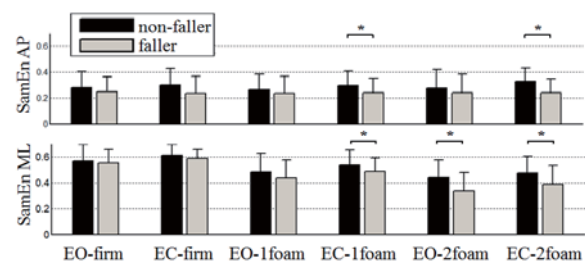


Fig. 1. Results of SamEn measure due to six standing conditions (* $p < .05$)

IV. CONCLUSION

Faller with normal balance ability showed the discriminative characteristics by the direction of sway and test conditions compare to the non-faller. During more challenging tasks (EC-1foam, EO-2foam, EC-2foam), a discriminative difference in SamEn was observed and the faller had small values in SamEn. Thus, SamEn during standing test could provide an important and unique information for the loss of complexity in the faller's postural control system.

ACKNOWLEDGEMENT

This research was supported by the National Research Foundation of Korea (NRF) grant funded by the Korea government (MSIP) (No. 2013R1A2A2A03014511).

REFERENCES

1. F. G. Borg, and G. Laxåback, "Entropy of balance-some recent results", *J. Neuroeng. Rehabil.*, vol. 7, pp. 38-49, 2010.

Effects of Functional Treatment on Gastrocnemius Spasticity Using the Ultrasound in Patients with Stroke

Y. H. Jeon¹, H. J. Lee¹, and K. S. Tae²

¹Department of Physical Therapy, Konyang University, Daejeon, South Korea

²Department of Biomedical Engineering, Konyang University, Daejeon, South Korea

E-mail: tae@konyang.ac.kr

Abstract— The purpose of this study is to present the technique of functional massage treatment and to evaluate the changes in the ROM, MAS (Modified Ashworth Scale), pennation angle and balance ability in response to stretching and functional massage of the hypertonic GCM of patients with stroke using the typical clinical techniques. Between and within the groups, significant differences in ROM, MAS score, and pennation angle were observed ($p < 0.05$) by the ultrasound, but none in the categories of balance ability ($p > 0.05$). Static stretching and functional massage as passive soft tissue mobilization techniques are considered effective methods for the relaxation of muscle spasticity. In particular, functional massage in combination with strength training is recommended for rehabilitation of patients with stroke.

Keywords— Balance ability, Functional massage, Gastrocnemius, Stroke, Ultrasound.

I. INTRODUCTION

Most patients with stroke have problems with balance because of stiffness of the affected gastrocnemius (GCM) [1]. Soft tissue mobilization is a medical treatment for mechanical structural alterations [2]. Although stretching and massaging is widely used in patients with stroke, there is limited clinical evidence. The purpose of this study is to present the massage technique of functional massage and to evaluate the changes in the ROM, MAS (Modified Ashworth Scale), pennation angle using the ultrasound and balance ability in response to stretching and functional massage of the hypertonic GCM of patients with stroke using the typical clinical techniques.

II. METHODS

A total of 21 patients were randomly allocated among a traditional NDT group ($n=7$), a traditional NDT with static stretching group ($n=7$), and a traditional NDT with functional massage group ($n=7$). The experimental patient groups underwent the assigned intervention (stretching on an inclined board or functional massage of the GCM for 20 min, once a day, on five days per week for a period of 6 weeks. ROM, MAS, pennation angle and balance ability of

ankle were outcome measures. The data was analyzed using SPSS(ver.18.0 for Windows). One-way analysis of variance were used with time as the within- subjects variable and group as the between- subjects variable in order to examine the effects of the interventions.

III. RESULTS

Between and within the groups, significant differences in ROM, MAS score, and pennation angle were observed ($p < 0.05$), but none in the categories of balance ability ($p > 0.05$).



Fig 1. Measurement of medial GCM pennation angle using the ultrasound

IV. CONCLUSION

Static stretching and functional massage as passive soft tissue mobilization techniques are considered effective methods for the relaxation of muscle spasticity. In particular, functional massage in combination with strength training is recommended for rehabilitation of patients with stroke. Also pennation angle of GCM using ultrasound is useful as an objective measurement tool.

REFERENCES

1. F. Gao, Y. Ren, E. J. Roth, R. Harvey, and L. Q. Zhang, "Effects of repeated ankle stretching on calf muscle-tendon and ankle biomechanical properties in stroke survivors", *Clin Biomech.*, vol. 26, pp.516-522, 2011.
2. C. I. Morse, H. Degens, O. R. Seynnes, C. N. Maganaris, and D. A. Jones, "The acute effect of stretching on the passive stiffness of human gastrocnemius muscle tendon unit", *J Physiol.*, vol. 586, pp. 97-106, 2008.

Development of Humanoid Dummy for Optimizing Driving Posture

D.H Kim, Y.E Song, S.G Kim and H.S Kim

Department of Biomedical Engineering, Yonsei University, Won-ju, Korea

E-mail: hanskim@yonsei.ac.kr

Abstract— Seat comfort is important factor for selecting a car, but quantitative value about seat comfort didn't exist. Humanoid dummy was developed to evaluate car seat comfort by lumbar moment value. Depending on the seat back $F_y(N)$ by force plate, the seat Cushion moment and dummy lumbar moment was shown as U shape. It suggested that the humanoid dummy can be evaluate seat comfort and optimize driving posture.

Keywords— humanoid dummy, seat comfort, driving posture, lumbar moment, evaluation seat

I. INTRODUCTION

Recently trend of auto industry, the vehicle seat comfort was one of the most important factors for selecting a car[1]. Previous studies have shown that physical fatigue is mainly caused by driving posture. In order to reduce the fatigue, there are some items developed[2]. But, these are for refreshing or decelerating the fatigue, not for reducing causes. In this study, driving posture was optimized using a dummy.

II. METHODS

A. Humanoid dummy for lumbar moment analysis

The dummy(Fig. 1) was made for analyzing lumbar moment using information of 50%tile of Korean male stature and weight(stature:172cm, weight 72kg). The Force Torque sensor(ATI Industrial Automation, USA) set up the lumbar collected lumbar moment(Tx).



Fig. 1 The picture of dummy experiment system

B. Force plate system

Two force plates(Advanced Mechanical Technologies, Inc., USA) were placed under each of seat pan and back. Dummy's reaction forces were measured with two force plates and these data were captured at 1000 Hz. Seat pan and back were taken apart to support each weight of dummy's lower body and upper body, separately. Cushion Moment (Mx) can be collected by the seat reaction forces.

C. Setting of driving posture

The change of moment was measured maintaining 0 degrees of clavicle and thoracic vertebrae, regulating degrees of hip, pelvis and lumbar joint from anterior to posterior.

III. RESULTS

A. Cushion moment and lumbar moment

Using the force torque sensor and force plate, depend on the seat back $F_y(N)$, cushion moment and lumbar moment was shown as U shape(Fig. 2).

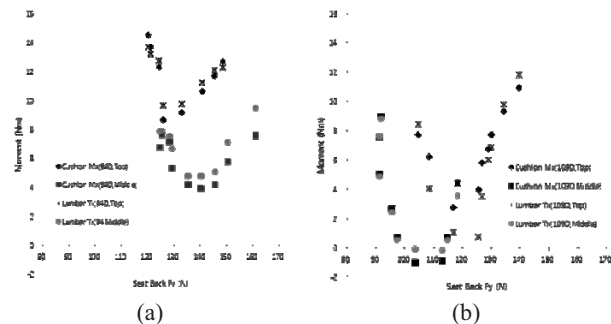


Fig. 2 (a) 94 degree of seat back, Cushion Moment(Mx) and Lumbar moment(Tx) to force of seat back F_y by anterior/posterior posture, (b) 109 degree of seat back, Cushion Moment(Mx) and Lumbar moment(Tx) to force of seat back F_y by anterior/posterior posture

The cushion moment and lumbar moment at 94 degree of seatback both were higher than 109 degree of seatback. The range of moments of 94 degree of seatback were bigger than 109 degree of seatback. Difference of seat pan height non-influence moments.

IV. CONCLUSION

In this study, development a humanoid dummy for evaluation of seat comfort. As a result, humanoid dummy's force torque sensor which was located at lumbar joint value similar cushion moment, calculated by force plate. Therefore Humanoid dummy can optimized driving posture and evaluation car seat.

REFERENCES

- Zenk, R., Franz, M., Bubb, H. and Vink, P., "Technical note: Spine loading in automotive seating" *Applied Ergonomics*, vol. 43(2), pp. 290-295, 2012.
- Kolich, M., Taboun S. M. and Mohamed, A. I., "Low back Muscle Activity in an Automobile Seat with a Lumbar Massage System" *International J. Occupational Safety and Ergonomics*, vol. 6(1), pp. 113-128, 2000.

Comparison in the On-Off Timing of Lower Limbs Muscle between the Young and the Elderly during Pedaling

Y. H. Shin¹, J. H. Hong¹, J. S. Kong¹, E. S. Jung¹, J. H. Roh¹,
J.W. Seo², J.S. Choi^{3,4} and G. R. Tack^{3,4}

¹Medical Device Development Center, Daegu Gyeongbuk Medical Innovation Foundation, Daegu, Korea

²Department of Biomedical Engineering, Graduate school of Konkuk University, Chungju, Korea

³Department of Biomedical Engineering, College of Biomedical & Health Science, Konkuk University, Chungju, Korea

⁴BK21 Plus Research Institute of Biomedical Engineering, Konkuk University, Chungju, Korea

E-mail: grtack@kku.ac.kr

Abstract—

This paper aims to compare the difference in the on-off set timing of lower limbs muscle activities between the twenties and the seventies. Each subject performed 40 rpm (revolution per minute) pedaling for 180 seconds. EMG was measured primarily on the muscles at Tibialis Anterior (TA) and Gastrocnemius Medialis (GM). Results showed that the active period of TA of the elderly was reduced compared with the young and that of GM was increased by the reduction of TA.

Keywords— Pedaling, EMG, Lower Limbs Muscle

I. INTRODUCTION

Cycling is a sport recommended for the aged, osteoporotic patients. It helps to strengthen the muscular power of the lower body and the cardiopulmonary function, and maintains & improves physical strength. As the age increases, the strength and elasticity of the muscles decrease, which is related with the injury. However, the published studies regarding the pedaling of the elderly were insufficient. In this study, the measured muscle activities while pedaling are compared between the young and the elderly.

II. METHODS

A. Subject

The experiment was performed with eight 20's and eight 70's who do not have injuries in lower extremities. Before the experiment, all experimental procedures were explained to the subjects, and written consents were received.

B. Experimental

The subjects performed warm-up exercises before the experiment. The subjects pedaled for 180 seconds with a constant cadence of 40 RPM. For a constant cadence in pedaling, Metronome and SRM (Schoberer Rad Messtechnik, Germany) power meter were used.

For the determination of the pedaling phase, a three-dimensional motion analysis system (Motion Analysis System Corp., USA) with six infra-red cameras was used. Muscle activities at TA & GM which are mostly activated while pedaling were measured by a wireless EMG system (Trigno, Delsys Corp., USA).

C. Data Analysis

The on-set timing was defined where the amount of muscle activation exceeded 20% of maximum voluntary contraction (MVC) and the off-set timing was defined where the amount of muscle activation declined 20% of MVC.

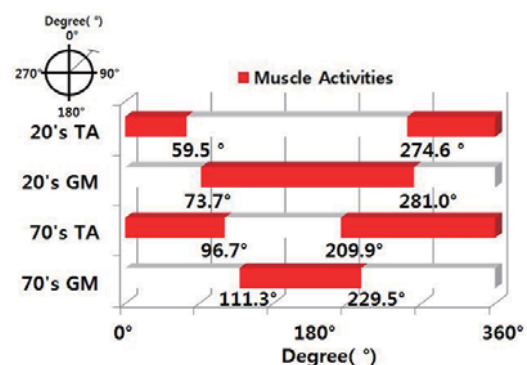


Fig. 1 Muscle Activities : the On-Off set Timing

III. RESULTS & CONCLUSION

Muscle activation period of the elderly differed from that of the young. Results showed that the active period of TA of the elderly was reduced compared with the young and that of GM was increased by the reduction of TA (as shown Fig. 1). During propulsive phase, the activation of GM was reduced for the elderly compared with the young. Thus the compensatory mechanism was activated where the duration of TA activation was increased during the recovery phase compared with the young.

ACKNOWLEDGEMENT

This research was supported by National Research Foundation of Korea funded by the Ministry of Education, Science and Technology (No. 2012R1A1A4A01008158) & This work was supported by the Innovation Medical Device Development Program (No. 10049769) funded by the Korea government Ministry of Trade, Industry and Energy.

REFERENCES

1. J. H. Lee, D. W. Kang, J. H. Bae, Y. H. Shin, J. S. Choi and G. R. Tack, "Development of three-dimensional force plate adapted for measuring force effectiveness in the cycle," *The Korean Institute of Electrical Engineer*, vol. 2, pp. 87-89, 2014

Emotional response to thermal stimuli applied to the back for the elderly

C.Y. Ko¹, S.Y. Jung¹, G.S. Kim¹, J. Ryu¹, M. Mun¹

¹Korea Orthopedics Rehabilitation Engineering Center, Incheon, Republic of Korea
E-mail: cyko@kcomwel.or.kr / monamicyko@gmail.com

Abstract—The aim of this study was to verify the emotional response to temperature stimuli on the back of the elderly. Ten healthy elderly individuals over 65 years old enrolled (male: 5, female: 5). They laid on a mat those temperature could controlled and were asked to express feeling, comfort or discomfort. Before and after thermal stimuli, core temperature and the back's skin temperature were measured. The subject expressed comfort ranging from 37.8 ± 1.0 to 32.8 ± 1.9 °C, and discomfort at 21.9 ± 2.8 °C. No changes in core temperature ($p > 0.05$) but significant decreases in skin temperature were observed (all $p < 0.05$). Taken together, range of thermal comfort in the elderly was 32.8~37.8 °C.

Keywords— thermal comfort, pressure ulcer, core temperature, skin temperature, mat

I. INTRODUCTION

The elderly population has increased. The prevalence of pressure ulcer (PU) has been increased over time[1, 2]. Skin microclimate as well as mechanical force (e.g. pressure, shear force, and friction) is one of the pathological factors to cause PU. To manage skin microclimate, many methods have been practically applied, such as repositioning, and skin care. However, these methods required high efforts of family and/or caregiver. On the other hand, skin microclimate management systems has been developed and can regulate skin temperature to remove the moisture on the skin surface and to suppress increase in skin temperature, leading to prevention of perspiration. Controlling skin temperature can induce discomfort for the elderly. Thus the aim of this study was to verify the emotional response to temperature stimuli on the back of the elderly.

II. METHODS

Ten healthy elderly individuals over 65 years old enrolled (male:5, female: 5). They laid on a mat those temperature ranging from 40°C to 10°C could controlled and are asked to express feeling, comfort or discomfort. If the subjects expressed extreme chill, the experiment was quit. Before and after thermal stimuli, core temperature and the back's skin temperature at 9 sites (shoulder, below scapula, and waist at row and left, middle, and right at column) were measured by using thermometer and using the infrared temperature measuring system (Medicore. co, Korea). The results of 2 subjects were excluded because their temperature

at extreme chill was markedly higher as compared to the others.

III. RESULTS

The subject expressed comfort ranging from 37.8 ± 1.0 to 32.8 ± 1.9 °C, and discomfort at 21.9 ± 2.8 °C. No change in core temperature was shown ($p > 0.05$). Significant decreases in skin temperature at all 9 sites were observed (all $p < 0.05$).

IV. CONCLUSION

Range of thermal comfort was 32.8~37.8 °C in this study. Low limit of thermal comfort was similar with known value (32.3 °C), while high limit was higher as compared with known value (35.3 °C)[3]. These differences might be due to difference of age. Thermal stimuli affected only skin temperature, not core temperature. Taken together, range of thermal comfort was 32.8~37.8 °C in the elderly and should consider to develop skin microclimate management system for preventing and/or treating PU of the elderly.

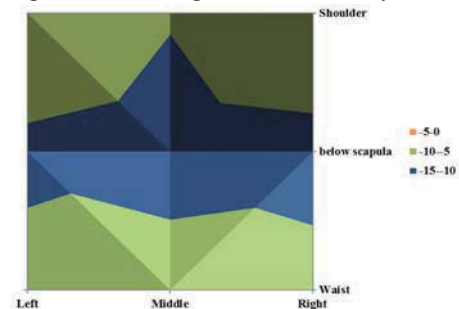


Fig. 1. Changes in skin temperature before and after thermal stimuli

ACKNOWLEDGEMENT

This work was supported by the Industrial Strategic Technology Development Program(10031270) funded by the Ministry of Trade, Industry and Energy(MOTIE, Korea)

REFERENCES

1. E. Jauland J. Menzel. "Pressure Ulcers in the Elderly, as a Public Health Problem." *J Gen Practice*, Vol. 2, pp. 1000174, 2014.
2. E. Jaul. "Assessment and management of pressure ulcers in the elderly." *Drugs & aging*, Vol. 27, pp. 311-325, 2010.
3. M.W. Strykerand S. Balakrishnan, "Microclimate management system", 2010

A study of EMG signal processing for gait intention detection

Taekyeong Lee¹, Heesuk Roh¹, Hunhee Kim¹ and Junghwa Hong^{1#}

¹Department of Control and instrumentation Engineering, Korea University, Se-Jong 339-700, Republic of Korea

[#]Corresponding author: Ph.D., Department of Control and Instrumentation Engineering, Korea University, 2511 Sejong-ro, Sejong 30019, Republic of Korea.

E-mail: hongjh32@korea.ac.kr

Abstract— Detecting intention of gait initiation using EMG under dynamic condition is essential to understand mechanisms of movement control in areas of clinical research, such as rehabilitation medicine, orthopedic and sports. In this study, a joint angle was predicted using adaptive filter and TDNN to aware of the various walking environment. Estimated EMG signal was used to artificial neural network (ANN) input data for training to prediction of joint angle, then it was used for knee joint angle prediction.

Keywords— sEMG, gait intention, signal processing

I. INTRODUCTION

Many researchers have been performed a study to understand the biomechanical relationship using biosignal. These kinds of study using biosignal have advantage for researching medical therapy and rehabilitation which is possible to predict human motion. Human biosignal such as electrocardiogram (ECG), electroencephalogram (EEG), electromyogram (EMG) represents human motion and statement. Among them, EMG signal is particularly interesting part for human rehabilitation system in order to detect the gait intention and widely studied in the field of rehabilitation system. Intention detection of gait initiation using EMG for human under dynamic condition is essential to understand mechanisms of movement control, and joint mechanism in areas of clinical research, such as rehabilitation medicine, orthopedic and sports. Particularly, accurate prediction of joint angle becomes a key point for developments of advanced mechatronic rehabilitation prostheses and orthoses to control human rehabilitation system or robotics for the disables and the elderly. The purpose of this study is a study of a joint angle prediction algorithm using adaptive filter and ANN for aware of the various walking environment.

II. METHODS

A. Experimental setup

When human being walk, most of all the body part muscle affect to human motion but, among them, EMG signal was acquired on Rectus femoris and Biceps femoris of 10 healthy male adults which appears to large motion of human body. Walking process was

occupied in 4 statement for level walk to stair ascent and descent, level walk to slope ascent and descent. Motion data was measured using wireless EMG (Noraxon), 3D motion analysis camera. A rate of inclination of slope is 1/12, stair height is 11cm. (Fig. 1)

B. EMG signal processing

EMG signal processing was digital filtered and features were extracted before the classification process begins. The classification is divided two distinct phased by training phase and angle prediction phase. EMG amplitude was estimated using adaptive filter through acquiring MA (Moving average) model to estimate coefficient of AR (Autoregressive) model because reject noise effect such as motion artifacts and additive noise. Estimated EMG signal was used to artificial neural network (ANN) input data for training to prediction of joint angle. Training objective data was acquired from Motion analysis data. Each statement data (level walk, stair ascent and descent, slope ascent and descent) adapt to TDNN (time delayed artificial neural network) algorithm for comparing.



Fig. 1. Experimental setup

III. RESULTS

Knee joint angle was predicted using sEMG signal that adjusted adaptive filter and TDNN. Estimating EMG signal using adaptive filter traced well real EMG signal without amplitude loss, and better effect than other filter like moving average filter only or differential filter. (Fig. 2) After training, time delay under a few milliseconds was exist, trained EMG data predicted well joint angle comparing with Motion analysis data. The trained EMG signal is sufficient to distinguish gait statement. (Fig. 3)

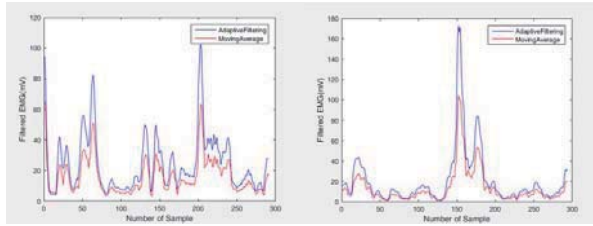
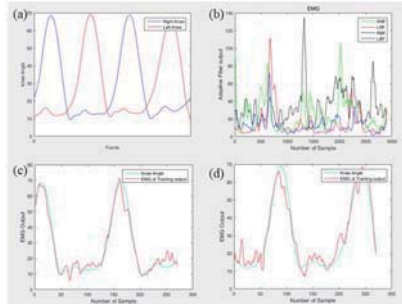
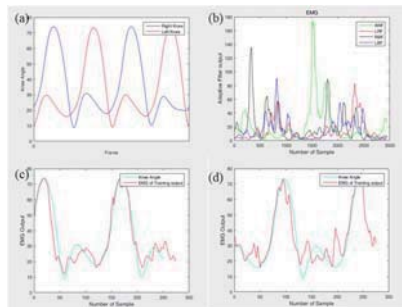


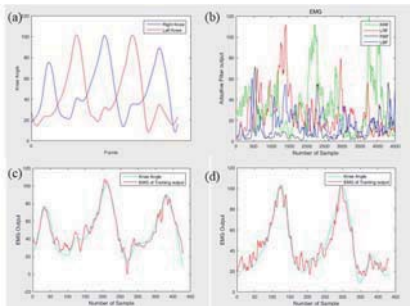
Fig. 2 sEMG amplitude result of moving average filter and adaptive filter output



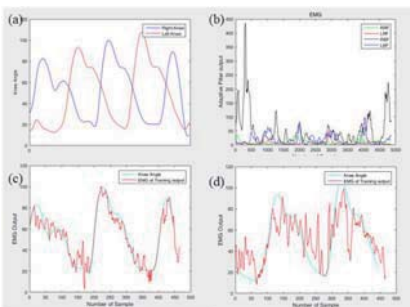
(A) Level walk to slope descent



(B) Level walk to slope ascent



(C) Level walk to stair descent



(D) Level walk to stair ascent

Fig. 3 Result of experiment and estimated knee angle using filtered sEMG (a) Motion data output (b) sEMG output (RRF : Right rectus femoris, RBF : Right biceps femoris,

LRF : Left rectus femoris, LBF : Left biceps femoris) (c) Estimated right knee joint angle (d) Estimated Left knee joint angle

IV. CONCLUSION

In this study, a method using adaptive filter and ANN algorithm was applied to predict in knee joint angle from the measured EMG. The prediction was successful, particularly the knee joint angle. But, also different part of lower limb muscle and reduction of noise problem of sEMG signal are needed to study for more exact prediction without latency and amplitude loss.

ACKNOWLEDGEMENT

This work was supported by industrial core technology development program (10048732) funded by the Ministry of Trade, industry & Energy (MI, Korea).

REFERENCES

1. Delis, A. L., Carvalho, J. L., Seisdodos, C. V., Borges, G. A., & da Rocha, A. F. Myoelectric control algorithms for leg prostheses based on data fusion with proprioceptive sensors. In Proceedings ISSNIP Biosignals and Biorobotics Conference 2010, pp. 137-142, 2010
2. Poliakov, Oleksandr M., Victor B. Lazarev, and Olena O. Chepenyuk. "Transfemoral Prosthesis with Polycentric Knee Mechanism: Design, Kinematics, Dynamics and Control Strategy." Journal of Rehabilitation Robotics 1.2 , pp. 109-123, 2013
3. Sennels, S., Biering-Sorensen, F., Hansen, S. D., & Andersen, O. T. Adaptive filters for muscle response suppression. In Engineering in Medicine and Biology Society, 1996. Bridging Disciplines for Biomedicine. Proceedings of the 18th Annual International Conference of the IEEE. Vol. 2, pp. 518-520. 1996.
4. Clancy, E. A., Bouchard, S., & Rancourt, D. Estimation and application of EMG amplitude during dynamic contractions. IEEE engineering in medicine and biology, 20(6), 47-54, 2001
5. Clancy, E. A., Morin, E. L., & Merletti, R. Sampling, noise-reduction and amplitude estimation issues in surface electromyography. Journal of Electromyography and Kinesiology, 12(1), 1-16, 2002.
6. Roetenberg, D., Buurke, J. H., Veltink, P. H., Cordero, A. F., & Hermens, H. J. Surface electromyography analysis for variable gait. Gait & posture, 18(2), 109-117, 2003

The study of active muscle property by contraction experiment of animals gastro-intestine

Youngho Lee¹, Soonmoon Jung¹, Jaemin Kim¹, Dongwook Yang¹ and #Junghwa Hong¹

¹Department of Control and instrumentation Engineering, Korea University, Se-Jong 339-700, Republic of Korea

#Corresponding author : Ph.D., Department of Control and Instrumentation Engineering, Korea University, 2511 Sejong-ro, Sejong 30019, Republic of Korea.
E-mail: hongjh32@korea.ac.kr

Abstract— In this study, a three-month-old pig with the weight of 30kg and 12-weeks-old rats with the weight of 375g was selected as an experimental animal, and the isometric and isotonic experiments were conducted in order to obtain an active characteristic parameter. As a result of experiments, the myotility (muscular contractile force) of maximum 12.35mN in the porcine and of maximum 1.558mN in the rats is obtained by isometric experiments and the maximum velocity of muscular contraction of 8.253 μ m/sec in porcine and of 3.921 μ m/sec in rat is obtained by isotonic experiments.

Keywords— Intestine, porcine, contraction, isometric, isotonic

I. INTRODUCTION

The smooth muscle tissue exists in the stomach, intestines, bladder, and blood vessel, and because it can no do the conscious control as an involuntary muscle on the contrary to the skeletal muscle which is a voluntary muscle, they do the muscle contraction exercise themselves. This study propose the biomechanical parameter of smooth muscle in gastro-intestine which is important role in digestion and peristalsis. Experiments progress using porcine and rat.

II. METHODS

In this study, acetylcholine is used to cause muscle contraction for isometric and isotonic experiments. Tissue specimen is prepared to optimal size by extracting from porcine and rats intestine, and is mounted into organ bath with Krebs-Henseleit buffer solution. And experiments progress in same boundary conditions that animals is alive.



Fig. 1. Tissue in organ bath filled Krebs-Henseleit buffer

III. RESULTS

Biomechanical active characteristic parameter of smooth muscle is obtained by isometric and isotonic experiments. For porcine large intestine, average of maximum muscle contractile force is 12.35 \pm 0.5mN by isometric and average of maximum muscle contractile velocity is 8.253 \pm 0.083 μ m/sec by isotonic. For rat small intestine, average of maximum muscle contractile force is 1.558 \pm 1.25mN by isometric and average of maximum muscle contractile velocity is 3.921 \pm 0.11 μ m/sec by isotonic.

Table 1. Average of maximum force and velocity of tissue

Animal	Avg. Max. force (mN)	Avg. Max. velocity (μ m/sec)
Porcine	12.35 \pm 0.5	8.253 \pm 0.083
Rats	1.558 \pm 1.25	3.921 \pm 0.11

IV. CONCLUSION

Through this research, a study for measuring the biomechanical active properties parameter is conducted by contraction experiments of smooth muscle. The study of biomechanical comprehensive models of smooth muscle should be involved with a study of passive characteristics parameter.

ACKNOWLEDGEMENT

This work was supported by Basic Science Research Program through the National Research Foundation of Korea (NRF) funded by the Ministry of Science (No. R0710149).

REFERENCES

1. ALI, F, PAR, P. D & SEOW, C. Y. (2005) Models of contractile units and their assembly in smooth muscle. *Can. J. physiol. Pharmacol.*, 83, 825-831.
2. HILL, A. V (1938) The heat of shortening and the dynamic constants of muscle. *Proc. R. Soc. Lond. B*, 126, 136-195
3. FUNG, Y. C. (1970) Mathematical representation of the mechanical properties of the heart muscle. *J. Biomech.*, 3, 381-404.

Characteristics of stent expansion according to plaque composition and structural design

D. H. Hwang¹, S. H. Kim¹, B. S. Namgung², S. H. Kim², H. S. Kim^{1,3}
and S. K. Cho^{3*}

¹Department of Biomedical Engineering, Yonsei University, Korea

²Department of Bioengineering & Surgery, National University of Singapore, Singapore

³Yonsei-Fraunhofer IZFP Medical Device Lab, Korea

E-mail: biecsk@naver.com

Abstract— Stent is an effective device to alleviate plaque-induced blockage in arteries. The mechanical behaviors of stenting are dependent on the stent design and circumferential property such as plaque composition. Since failure of stenting may induce the restenosis, it is necessary to establish how to reduce in-stent restenosis. This study compared the stent expansion and the stress distribution in a stenosed vessel wall by using finite element method. Based on the results, we can conclude that the extent of stress and non-uniformity of stent expansion may be affected by stent structure and stiffness of plaque material.

Keywords— Stent, Plaque, Structural design, FEM

I. INTRODUCTION

Stent is a device used to alleviate plaque-induced blockage in arteries by stimulating vessel expansion. The stent has been widely used for various vascular disease treatments with its high therapeutic efficacy. Despite the clinical effectiveness of the stent, restenosis has emerged and is considered as a critical potential failure of stenting for long-term prognosis. Many clinical and computational studies have reported that restenosis could be significantly relevant to the mechanical stent behaviors and the pathological condition of the arterial stenotic lesion. Therefore, designed criteria for a new stent are required to minimize the in-stent restenosis. To achieve a better understanding of the relation between structure-dependent mechanical behavior of stent and potential risk of restenosis, the present study simulated the luminal stress of vessel with two commercially available stents based on a finite element model.

II. METHODS

3-dimensional computational models were developed to predict mechanical behaviors and stress distributions in a vessel wall during the stent expansion. The models were built and meshed by using Hypermesh 10.0. After that, the meshed models were solved by ABAQUS 6.10. The plaque was designed as a semi-ellipsoidal shape; the diameter of maximum blockage area reached a level of 50% at the mid-section. This value was chosen by considering correlation between fractional flow reserve

(FFR) and stenosis level. Realistic transient non-uniform balloon-stent expansion simulations were performed with three different plaque compositions (cellular, hypocellular and calcified).

III. RESULTS

A. Results of expansion behavior of stents

Both stents showed that non-uniform expansion increased as the stiffness of plaque composition increased (cellular → calcified). The Stent A structure showed a significantly higher dogboning index compared to it of Stent B structure. Unlike free expansion, a high dogboning effect was emerged even at the stabilized stage. This indicated that plaque can impede the full stent expansion.

B. Results of stress distributions

Both stents showed that non-uniformity of stress distribution in the stenting area increased as the stiffness of plaque composition increased (cellular → calcified). Implanting stent in stiffer plaque would arise lower extent of stress, while it would increase non-uniformity in stress distribution at the same time. In addition to that, varying a certain structural parameter of stent could significantly enhance or reduce the stress distribution in the wall.

IV. CONCLUSION

The distribution and magnitude of stress levels on vessel wall after stent deployment, as well as non-uniform stent expansion behavior are significantly dependent on stent structure and stiffness of plaque material.

Optimal selection of stent in treatment should be a patient-specific solution with consideration based on a certain patient's plaque composition as well as stent's structure itself.

REFERENCES

1. D. H. Lim, S. K. Cho, W. P. Park, A. Kristensson J. Y. Ko, S. T. S. AL-HASSANI and H. S. Kim, "Suggestion of Potential Stent Design Parameters to Reduce Restenosis Risk driven by Foreshortening or Dogboning due to Non-uniform Balloon-Stent Expansion," *Annals of Biomedical engineering*, vol. 36, pp. 1118-1129, 2008.

Evaluation of preferred driving posture on car seat

S. G. Kim¹, D. H. Kim¹, Y. E. Song¹, Y. K. Cho¹, H. S. Kim¹

¹Department of Biomedical Engineering and Research Institute for Medical Instruments & Rehabilitation Engineering, Yonsei University, Wonju, Gangwon 220-842, Republic of Korea
E-mail: hanskim@yonsei.ac.kr

Abstract—This study was experimented to evaluate the body posture and pressure ratio on car seat at preferred driving posture. We measured point of length, angle and body pressure. Pressure of lower body had minimum value in slumped posture.

Keywords— Posture, pressure ratio, distance, angle

I. INTRODUCTION

Body posture is a determinant of comfort and discomfort on car seat [1]. Also, body pressure is related to inconvenience during driving for a long time [2]. Many studies evaluated inconvenience between posture and pressure. However, few studies to evaluate postures according to preference. The aim of this study was to set three types of posture and evaluate posture and pressure ratio.

II. METHODS

A. Participants

This experiment involved 5 male participants (age, 28.2 ± 5.4 years; height, 174.2 ± 2.9 cm; mass, 72.8 ± 6.3 kg).

B. Postures and Measurement

Posture type is three. First posture is preferred posture (basic). Second posture is closed to the steering wheel as much as possible (erected). Third posture pulled back from the steering wheel as much as possible (slumped). But, Driving should be possible at all postures.

Fig. 1 showed the measurement point of length and angle. Also, we measured body pressure and evaluated ratio of body pressure between upper body and lower body by pressure mat (LX200 XSENSOR, Canada).

III. RESULTS

Table 1 showed the results of the measurement. Angle of upper arm and lower leg had minimum value in slumped posture, while angle of backrest had maximum value in slumped posture. Erected posture was moved -5.6 cm from basic posture. And, Slumped posture was move + 2.5 cm from basic posture. Height between frame of a car and front of seat had minimum value in slumped posture. Height between frame of a car and end of seat had maximum value in slumped posture. Pressure of lower body had minimum value in slumped posture

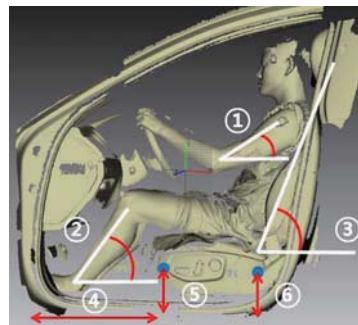


Fig. 1. Measurement points: ① angle of upper arm, ② angle of lower leg, ③ angle of backrest, ④ distance between frame of a car and seat, ⑤ height between frame of a car and front of seat, ⑥ height between frame of a car and end of seat

Table 1. Results of the measurement

Measurement points	Erected	Basic	Slumped
①	35.1	28.2	24.8
②	53.2	49.2	47.5
③	82.4	83	86.2
④	60.2	65.8	68.3
⑤	20.4	18.7	17.7
⑥	14.3	14.3	15.5
Pressure ratio (Seat : Backrest)	1 : 0.3	1 : 0.26	1 : 0.23

IV. CONCLUSION

Angle of upper arm and lower leg had minimum value in slumped posture because it's need to manipulate steering handle, brake and accelerator. Angle of backrest had maximum value in slumped posture because it's need to secure a clear view. Pressure of lower body (seat : backrest) had minimum value in slumped posture. This result showed that slumped posture will provide more comfortable than erected posture on lower body.

REFERENCES

1. M. Vergara, A. Page, "Relationship between comfort and back posture and mobility in sitting-posture," *Appl Ergon*, vol. 33, pp. 1-8, 2002
2. S. Park, C. Kim, " The evaluation of seating comfort by the objective measures", *SAE Technical Paper*, 970595, 1997

Differences in Kinematic Characteristics by Pedal Types

I. G. Han¹, D. W. Kang², J. W. Seo², D. H. Kim², J. S. Choi^{1,3} and G. R. Tack^{1,2,3}

¹Department of Biomedical Engineering, College of Biomedical & Health Science, Konkuk University, Chungju, Korea

²Department of Biomedical Engineering, Graduate school of Konkuk University, Chungju, Korea

³BK21 Plus Research Institute of Biomedical Engineering, Konkuk University, Chungju, Korea

E-mail: grtack@kku.ac.kr

Abstract— The purpose of this study was to identify the differences in kinematic characteristics among different pedal types (Flat, Clip, Cleat). Results showed that there were significant differences between flat and the others in both knee and ankle. For improvement of performance and prevention of injury, it is recommended to choose a proper pedal by considering the kinematic as well as the kinetic variables.

Keywords—Cycle pedal types, Kinematics, Knee, Ankle, Joint angle.

I. INTRODUCTION

Most cyclists want to know an effective cycling method. There are various ways to improve the pedaling performance. Changing the pedal is one of the easy methods [1]. There are in general three types of the pedal, a well-used flat pedal, a clip pedal fixed under the metatarsal, and a cleat pedal with fixed shoe at a lower foot. The aim of this paper was to investigate the differences in kinematic characteristics among pedal types and perform a basic study to prevent injuries and improve performances.

II. METHODS

Fifteen healthy young males without a history of musculoskeletal diseases participated in the experiment (age: 24.0±2.0, height: 175.0±4.3). Subjects performed 10 min warm-up and 2 min pedaling with 60 rpm (revolution per minute) and 25° of knee angle. A 3D motion analysis system with six infra-red cameras (Motion Analysis Corp., USA) was used to acquire motion with 120 Hz sampling frequency. The middle one minute data was used and the variables such as minimum & maximum angle and the range of motion (ROM) of knee and ankle were calculated by MATLAB R2013a (Mathworks Inc., USA). SPSS v19 (SPSS Inc., USA) was used for statistical analysis, and the significant level was set to 0.05.

III. RESULT & DISCUSSION

Results showed that the max and min knee angle for the flat pedal was the smallest among three pedals. Knee ROM for the flat pedal was the largest and that for the cleat was the smallest. On the other hand, the max and min ankle angle for the flat pedal was the smallest among three pedals. Min ankle angle for the cleat pedal was the largest, and max ankle angle for the clip pedal was the largest. Ankle ROM for the flat pedal was the largest and that for the cleat was the

smallest. There was a significant difference in all variables between the flat and two other pedals. However there was no significant difference between the clip pedal and the cleat pedal.

Knee ROM differences among flat & two other pedals occurred due to the difference in knee extension. In general, excessive knee extension causes excessive use of Vastus Lateralis muscle, which in turn increases the possibility of an injury of knee joint. There were no differences in all variables between the cleat pedal and the clip pedal. Since the clip pedal is easy to separate and it has similar kinematic properties of the cleat pedal, it is good to select the clip pedal compared with the cleat pedal that is difficult to separate during emergency situation.

This study focused only kinematic characteristics. For further study, it is necessary to conduct the pedal force analysis based on the index of effectiveness and EMG analysis for the identification of efficient pedal types.

Table 1. Results of kinematic variables

	Knee			Ankle		
	Min	Max	ROM	Min	Max	ROM
Flat	31.57 ±5.88 ^{##}	104.50 ±4.27 [#]	72.93 ±4.54 ^{##}	1.35 ±6.93 ^{##}	23.79 ±7.23	22.44 ±6.68 [#]
Clip	37.57 ±5.70 [*]	107.50 ±3.76	69.52 ±4.83 [*]	9.03 ±11.66 [*]	28.41 ±10.65	19.38 ±7.12
Cleat	40.34 ±4.41 [#]	107.77 ±3.25 [#]	67.43 ±5.03 [#]	9.37 ±12.80 [#]	26.07 ±11.97	16.71 ±6.47 [#]
<i>p</i>	0.001 [*] 0.000 [#]	0.009 [#]	0.014 [*] 0.001 [#]	0.014 [*] 0.019 [#]	NS	0.015 [#]

Repeated measure ANOVA & Bonferroni, M ± SD, NS: No significant
*:# $p < .05$

ACKNOWLEDGEMENT

This research was supported by National Research Foundation of Korea funded by the Ministry of Education, Science and Technology (No. 2012R1A1A4A01008158).

REFERENCES

1. G.Mornieux, B. Stapelfeldt, A. Gollhofer and A.Belli, "Effects of Pedal Type and Pull-up Action during Cycling" *Int J Sports Med.*, vol. 29, pp. 817-822, 2008.

Comparison of Pedicle Screw Designs upon Pull-out Test Using FEM

Gihyun Lee¹, Dong-Ah Shin³, and Sohee Kim^{1,2*}

¹Department of Medical System Engineering, Gwangju Institute of Science and Technology, Gwangju, Korea

²School of Mechatronics, Gwangju Institute of Science and Technology, Gwangju, Korea

³Department of Neurosurgery, Yonsei University College of Medicine, Seoul, Korea

E-mail: soheekim@gist.ac.kr

Abstract— The pullout property of 4 pedicle screws inserted in bone block cylinder was compared using finite element method (FEM). The magnitude and spatial distribution of stress in the screws were compared. It was concluded that conical screw was better to bone than cylindrical screw and stress distribution can be controlled by using dual thread or cortical screw design.

Keywords— Pedicle screw, Pullout test, FEM

I. INTRODUCTION

Spinal fixation using pedicle screws is one of the common methods to treat degenerative spine diseases. Although the technology has been advanced in the last decades, complications such as screw or bone failures can occur. The biomechanical evaluation of screws is required to prevent such problems. In this study, the pullout test was simulated using FEM for 4 differently designed pedicle screws. And the stress distribution for them was compared.

II. METHODS

A. Pedicle screw designs

The pedicle screws of 4 different types made of titanium alloy were used: conical screw (CS), conical dual thread screw (CDTS), conical cortical screw (CCS), and cylindrical screw (CyS).

B. Finite element method

The quarter symmetric model to simplify the screws was constructed using ABAQUS software (SIMULIA Inc., USA). A bone block in cylindrical shape was used, for which the material properties of bone was assigned, and assembled with screws. Young's modulus of screws and bone block were 110 GPa and 2.5 GPa, respectively, and Poisson's ratio was 0.3 for both. The contact between the screw and bone block was set to be frictionless [1].

The bottom surface of bone block was fixed and a force of 250 N was applied to the top surface of screws.

Global and local seed sizes for mesh generation were 1 mm and 0.25 mm, respectively. And tetrahedral elements were used for mesh. The numbers of elements and nodes were 30,000 ~ 90,000 and 50,000 ~ 140,000, respectively.

III. RESULTS

The stress was generated in the screws by the applied force as shown in Fig. 1. From the simulated results, the highest stress values in screws of CS, CDTS, CCS, and CyS were 268 MPa, 245 MPa, 448 MPa, and 190 MPa, respectively. In the bone block, the highest stress were 289 MPa, 177 MPa, 395 MPa, and 502 MPa, respectively. The stress was distributed mostly in the threads.

The CyS was under lower stress than CS. But it causes higher stress in bone block by sharper thread. In the CDTS, the stress was lower than the screw that has one type of thread because stress in dual threads was distributed more widely. For CCS, higher stress was observed in the outer thread of screw than in inner thread.

IV. CONCLUSION

It is concluded that the CyS may cause more stress to the bone than CS. It is estimated that CDTS would be good as the stress is widely distributed in inner region as well as outer region. CCS will be more useful for fixation in cortical bone.

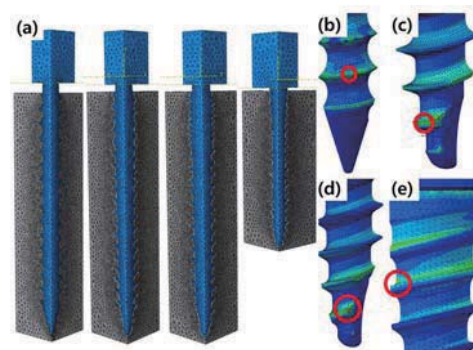


Fig. 1. FEM models of assembled screw and bone block and stress distribution upon pullout

ACKNOWLEDGEMENT

This work was supported by the NRF grant (No. NRF-2014R1A1A3050285) and the Institute of Medical System Engineering (IMSE) at GIST, Korea.

REFERENCES

1. C-K. Chao, C-C. Hsu, J-L. Wang, and J.L. Lin, "Increasing Bending Strength and Pullout Strength in conical Pedicle Screws: Biomechanical Tests and Finite Element Analysis", *J. Spine. Disord. Tech.*, vol. 21, pp.130-138, 2008.

A study on the effect of vibratory stimulation with perception threshold on muscle functions

H. G. Kim¹, K. Y. Kwak¹, and D. W. Kim^{2,3}

¹Department of Healthcare Engineering, Chonbuk National University

²Division of Biomedical Engineering, Chonbuk National University

³Research Center of Healthcare & Welfare Instrument for the Aged, Chonbuk National University

E-mail: hekun1249@naver.com

Abstract— Improved function of muscles and gait stability are required to prevent any injuries that may be caused by decreased physical function with ageing. Thus this study is the effect of vibratory stimulation on the function of muscles that are known to improve posture stability and function of muscles. The results of this study showed that vibratory stimulation activates the function of muscles and the characteristic of vibration, vibration frequency-vibration intensity also affected on the function of muscles.

Keywords— perception threshold, proprioceptive sense, vibration stimulus, frequency, MVC

I. INTRODUCTION

Decreased physical function such as visual, vestibular and proprioceptive senses by ageing leads to unstable gait and decreased ability to balance [1]. Also it increases risk of fall and results in abnormal gait. Improved function of muscles and gait stability are required to prevent any injuries that may be resulted in decreased physical function by ageing. Many studies have conducted on somatosensory stimulation using vibration and reported that it improves function of muscles, posture stability and postural sway[2]. However, previous studies did not take into consideration the facts that the frequency range of vibration to which proprioceptive senses are known to sensitively respond and vibration perception threshold that may affect differently to the bodies. Thus this study investigated the vibration perception threshold in the range of 100-300Hz[3-5] to which proprioceptive senses the most sensitively respond according to the frequency and intensity of vibration to see the effect of mechanical vibratory stimulation depending on vibration characteristics.

II. METHODS

A. Subject

Seven healthy adult males without diseases in nerve and musculoskeletal system participated in this study (Age:25.3±1.1, Height:171.1cm±2.3, Weight:65.3kg±

6.2). This study was approved by Chonbuk National University Institutional Review Board (IRB File No. JBNU 2015-06-012).

B. Equipment

A cable stimulation vibrator was established by combining a Mini-Linear actuator to apply vibration stimulation and Function generator to control vibration frequency, intensity and wave type.

An electromyograph and analysis program (Bagnoli TM Desktop EMG System, DELSYS, Inc. USA) was used to collect and analyze the electromyograms of targeted muscle groups. To evaluate the function of muscles according to vibration characteristics, DELSYS, Inc. Signal Acquisition and Analysis Software, EMGworks®3.5 was used to analyze the electromyogram.

C. Protocol

The perception threshold was measured according to the vibration characteristics in the frequency range of 100Hz-300Hz, to which the proprioceptive senses the most sensitively respond. The results were used to investigate the effect of vibratory stimulation of perception threshold on the function of muscles. The electrodes(DELAYS, Inc. Surface EMG Sensor) were attached to Triceps Surae muscle and Tibialis Anterior muscle of the subjects. The Maximum Voluntary Contraction(MVC) were performed three times and electromyogram was obtained each time. The vibration of perception threshold was locally applied on the Achilles tendon and Tibialis Anterior tendon.

D. Analysis

The mean EMGrms of MVC was analyzed to evaluate the function of muscles according to the characteristics of vibration. As there were differences between the muscles and subjects, the results of mean EMGrms of MVC without stimulation were used as baseline for standardization and the increase or decrease of activity of each muscle was compared. A SPSS 18 was used for statistical analysis.

III. RESULTS

A. Perception threshold according to the frequency and intensity of vibration

The results of perception threshold according to vibration intensity in the frequency range of 100Hz-300Hz are as follows.

Table 1. Vibration perception threshold

	Achilles Tendon	Tibialis Tendon
180Hz	1.018	1.027
190Hz	1.015	1.025
200Hz	1.019	1.040
210Hz	1.031	1.069
220Hz	1.043	1.074
250Hz	1.061	1.089

The vibration perception threshold was the lowest at 190Hz and the highest at 250Hz in the Achilles tendon. The vibration perception threshold was the lowest at 190Hz and highest at 250Hz in the Tibialis Anterior tendon. The results showed that the perception threshold could be different from the vibration application site and frequency and the function of muscles may also be shown differently.

B. Effect on the function of muscles according to the frequency and intensity of vibration

In the most sensitive frequency bands in the Achilles tendon and Tibialis Anterior tendon applied on the vibration perception threshold intensity. The following graph shows the increase or decrease of muscle activities upon the vibratory stimulation compared to muscle activity of 0 without stimulation.

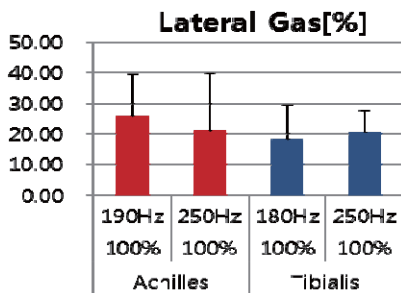


Fig. 1. Lateral Gas EMGrms Avg

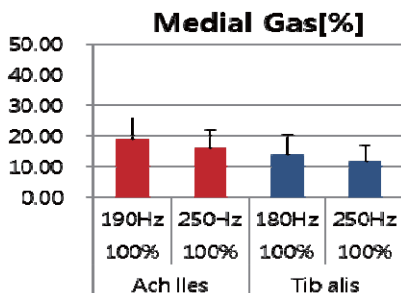


Fig. 2. Medial Gas EMGrms Avg

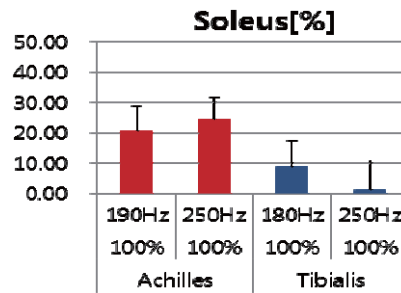


Fig. 3. Soleus EMGrms Avg

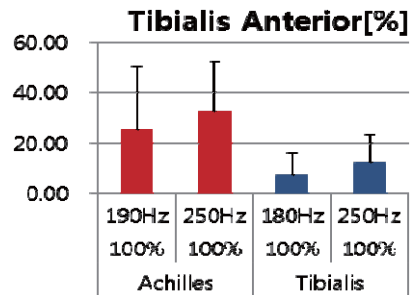


Fig. 4. Tibialis Anterior EMGrms Avg

The mean EMGrms increased upon the vibratory stimulation of perception threshold in the Triceps Surae muscle and Tibialis Anterior muscle compared to that without stimulation as shown in Figure 1 – 4. The increased degree of mean EMGrms was greater when the vibratory stimulation was applied in the Achilles tendon than in the Tibialis Anterior tendon.

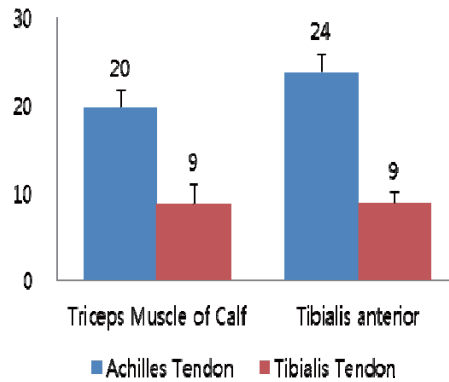


Fig. 5. Change of vibration stimulus on the EMGrms Avg increase [%]

The mean EMGrms increased by 20% when the stimulation was applied from the Triceps Surae muscle to the Achilles tendon while by 9% when the stimulation was applied on the Tibialis Anterior tendon. The difference was statistically significant ($p < 0.001$). The mean EMGrms increased by 24% when the stimulation was applied from the Tibialis Anterior muscle to the Achilles tendon while by 9% when the stimulation was applied on the Tibialis Anterior tendon. The difference was statistically significant ($p < 0.001$).

The results confirmed that the stimulation of the Achilles tendon activated the muscles greater.

IV. CONCLUSION

From this study, the profile of vibration frequency and intensity was obtained by measuring the vibration perception threshold in the frequency range of 100Hz-300Hz, to which proprioceptive senses the most sensitively respond. Also, we investigated the effect of vibration on the function of muscles according to its frequency and intensity using the profile. The results of this study confirmed that the effect of vibration on the muscle activity was different from the presence of vibratory stimulation, vibration frequency-vibration intensity and application site. The result will be used to establish database on this topic with further studies and to obtain meaningful information that can be applied in the clinical practices in the future.

ACKNOWLEDGEMENT

This work was supported by the National Research Foundation of Korea(NRF) grant funded by the Korea government (MSIP) (NRF-2014R1A2A1A11053073).

REFERENCES

1. Tideiksaar.R. Falling in elder persons. New York : Springer,1997.
2. Issever, H., Aksoy, C., Sabuncu, H. and Karan, A., "Vibration and its effects on the body", Medical Principles and Practice, 12, 34-38, 2003.
3. Handy Oey, Volker Mellert, "Vibration thresholds and equal vibration levels at the human fingertip and palm", ICA 2004 4-9 Aprill, Kyoto, Japan, Th.P2 Noise and Vibration(NSP01).
4. Ana Picu, "Study about evaluation of human exposure to hand-transmitted vibration", Journal of Science and Arts, 2, 355-360, 2010
5. Tatsuma Sakurai, Masashi Konyo, Shogo Okamoto, Satoshi Tadokoro, "Research of Conditions of stimulus for Inducing Grasping Force Control Reflex", System Integration, 2010 IEEE/SICE International Symposium, 408-413, 2010.

Cognitive Ability Evaluation and Analysis

According to LED Illumination for Light-care Contents

S. J. Lee¹, W. B. Park³, H. C. Kim⁴ and D. W. Kim^{2,5}

¹Department of Healthcare Engineering, Chonbuk National Univ, Jeonju, Korea

²Division of Biomedical Engineering, Chonbuk National Univ, Jeonju, Korea

⁵Research Center of Healthcare & Welfare Instrument For the Aged, Chonbuk

³USys co.,Ltd

⁴AinA co.,Ltd

E-mail: biomed@jbnu.ac.kr

Abstract—The existing past researches related to color have limitations of psychological, subjective, that is, qualitative researches. This research is conducted through digitized data by measuring cognitive reaction quantitatively. Among the computerized neurocognitive function test whose validity as cognitive measurement tests was proved, the visual span test that can measure the level of concentration and memory and the card sorting test that can measure thinking flexibility or cognitive flexibility were conducted. Through a survey, the colors both preferred and not preferred by the subjects were selected. Through LED, the color stimulation system was composed, and the neurocognitive function test was conducted by approving color stimulation randomly to the subjects. As a result, it was found that there were differences in the subjects' cognitive ability in the color stimulation of the preferred colors or non-preferred colors. This research presented the quantitative results with regard to color research and, by extension, can propose diverse ways of utilizing color stimulation that can influence cognitive ability.

Keywords— color environment, color stimulation, neurocognitive function test, color therapy

I. INTRODUCTION

Currently, the color always exists in goods and space that people use, such as clothes, products, automobiles, residential space, and business space. Utilization of color influences diverse fields ranging from psychological to therapeutic fields, such as color design, color marketing, color interior, and color therapy. Thus, color is utilized so diversely that researches on color are expanding and its importance becomes higher. As a result of investigating past researches, psychological researches that utilize emotional adjectives or image maps were many but in the case of physiological researches, either the experiment environmental system was inadequate or the results of the researches were too subjective [1-2]. So in this research, quantitative research based on numerical data is conducted.

II. METHODS

A. Subjects

Since the experiments were related to color, the subjects were a total of 15 adult men and women without color deficiency, cognitive disorders, and autonomic nervous system diseases (age:22.8 ±1.7 years). And to reduce the influence of the subjects' personal noise, the intake of smoking, caffeine, alcohol 12 hours before the beginning of the experiments was prohibited so that the nervous system should not be affected.

B. Experiment Environment

Since cognitive ability can be affected by various extrinsic factors, the experiment environment that can minimize the influence caused by extrinsic noise should be built. Accordingly, the sound-proof chamber that obstructs outside noise in order to minimize extrinsic noise and prevent the reduction of concentration was installed. Also, the experiments were conducted in the darkroom so as not to be affected by other light except LED.

C. Color Stimulation System

The color stimulation system that presents 7 colors: red, orange, yellow, green, blue, indigo, and violet using LED as realized.



Fig. 1. Color Stimulation System.

D. Neurocognitive Function Test Instrument

To evaluate cognitive ability, the experiments were conducted using CNT40 (MAXMEDICA INC. Korea). CNT40, which is diverse neurocognitive function test using Hangul stimulation, is composed of a total of 17 test items. Particularly, it can distinguish between diverse neurocognitive function disorders such as linguistic skills, memory, attentiveness, planned thinking ability, motor ability, so it is used for the diagnosis of clinical diseases and research purposes [3-4].

E. Test Sort

In this research, of the 17 tests, the visual span test that measures the level of concentration and memory and the card sorting test that measures thinking flexibility or cognitive flexibility were conducted. The visual span test is a test that evaluates attention skills and attention breadth to stimulations in time and space [4]. The place number completed by arranging the circles in the order determined in the LED environment of preferred color and non-preferred color or by arranging the circles in the reverse direction of the predetermined order is considered “economic strength” that reflects the awakened state in the color stimulation [5]. The card sorting test is the test of selecting the card that accords with the criteria among the three criteria of color, shape, and number. The judgment of the test results is done by the percent total errors that are the total number of errors divided by the total number of trials multiplied by 100.

F. Protocol

The subjects chose their most preferred and non-preferred color among the 7 colors through investigation and then within the chosen colors, the above-mentioned two experiments were conducted. The color stimulation was approved without predetermined order and every time the stimulation changed, 10 minute break was given to prevent the influence of the previous stimulation, and then the next experiment was conducted.

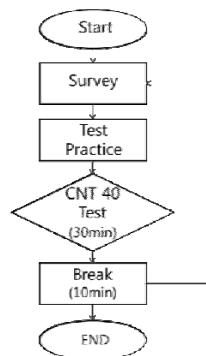


Fig. 2. Protocol



Fig. 3. Example of Color Experiment

III. RESULTS

A. Visual Span Test

As a result of dividing the 15 subjects by gender into the two groups, the male subjects completed with 7.5 places in the normal direction, 6.5 places in the reverse direction in the preferred color. In the non-preferred color, they completed with 7.9 places in the normal direction, 6.8 places in the reverse direction. The female subjects completed with 7.1 places in the normal direction, 6.2 places in the reverse direction in the preferred color. In the non-preferred color, they completed with 7.7 places in the normal direction, 6.4 places in the reverse direction. This shows that in the color environment of preferred color, the number breath and the time and space breadth that both male and female subjects can remember were reduced. The results of the subjects are shown in Fig. 4 and Fig. 5.

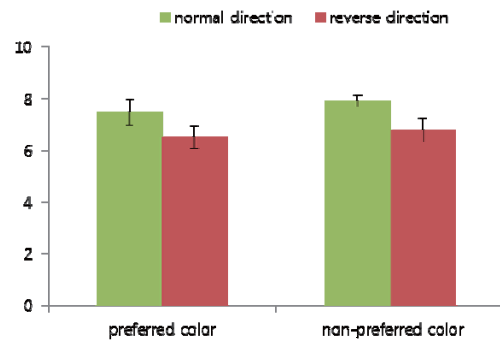


Fig. 4. Male Subject's Completed Number

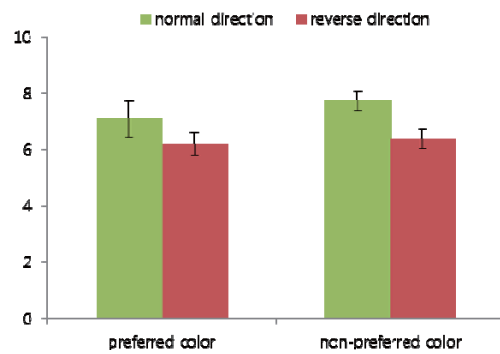


Fig. 5. Female's Completed Number

B. Carding Sorting Test

As a result of dividing the 15 subjects by gender into the two groups, in the male subjects, the percent total errors were 13.3% in the preferred color, 12.1% in the non-preferred color. In the female subjects, the percent total errors were 13.0% in the preferred color, 12.2% in the non-preferred color. This means that, in the color environment of preferred color, the ability to restrain the tendency to follow the reaction principles that were already chosen, the ability to discern visually detailed characteristics, and the ability to establish hypotheses and solve problems and to infer of both male and female subjects were reduced. The results are shown in Fig. 6 and Fig. 7.

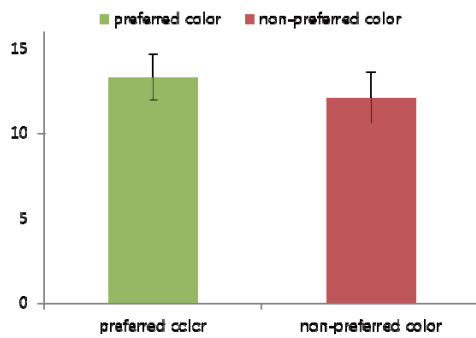


Fig. 6. Male's percent total errors(%)

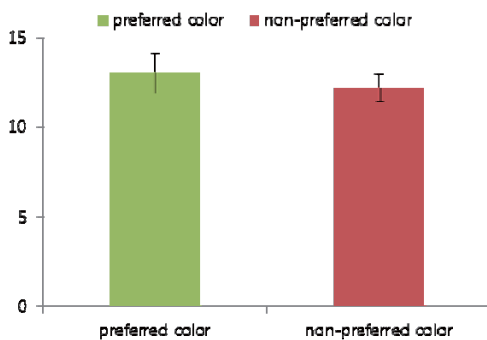


Fig. 7. Female's percent total errors(%)

IV. CONCLUSION

This research examined changes in cognitive ability that occurred in the LED environment of preferred color and non-preferred color. Through this research, it was shown that there were differences in concentration and cognitive flexibility according to LED of preferred or non-preferred color. Through diverse tests and additional experiments, researches on changes in cognitive ability will continue to be conducted,

REFERENCES

1. Amber, R. B, "Color Therapy," Aurora Press, p. 120-135, 1983.
2. H. W. Kim, "Review of Color Psychology and Color Therapy", Journal of Architectural Institute of Korea, Vol. 45, No. 6, p. 40-48, 2001.

3. K. S. Lee, "The Effects of Color and Luminous Transmittance of Tinted Lenses on Attention to Word-Color Test in Computerized Neurocognitive Function Test", Department of Optical Science, Graduate School Konyang University, 2013.
4. J. S. Kwon, I.K. Lyoo, K. S. Hong, B. K. Yeon, and K. S. Ha, "Development and Standardization of the Computerized Memory Assessment for Korean Adults," J Korean Neuropsychiatr Assoc., Vol. 41, No. 2, p. 335-346, 2002
5. K. S. Ha, J. S. Kwon, I. K. Lyoo, S. W. Kong, D. W. Lee, T. Youn, "Development and Standardization Process, and Factor Analysis of the Computerized Cognitive Function Test System for Korea Adults," J Korean Neuropsychiatr Assoc., Vol 41, No. 3, p. 551-562, 2002.

Biomechanical change of ankle according to perception threshold of applied vibration during gait

K.Y.Kwak¹, H.G. Kim¹, and *D. W. Kim^{2,3}

¹Department of Healthcare Engineering, Chonbuk National University, Jeonju, Korea

²Division of Biomedical Engineering, Chonbuk National University, Jeonju, Korea

³Research Center of Healthcare and Welfare Instrument for Aged, Chonbuk National University, Jeonju, Korea

*E-mail: biomed@jbnu.ac.kr

Abstract— The purpose of this study is to investigate biomechanical change depending on the perception thresholds of applied vibration during gait. The vibration perception threshold was investigated according to the frequency of vibration and the frequency to which the body the most sensitively respond was applied during gait. A 3D motion analysis system and biomechanical analysis software were used to analyze biomechanical change of ankle during gait. The angle, moment and power of ankle were analyzed. The results showed that the biomechanical changes of the vibration of perception threshold are same changes of sub-threshold vibration. Also there was biomechanical difference depending on applied site.

Keywords— Somatosensory, Biomechanics, Gait, Vibration, Aging.

I. INTRODUCTION

The muscles in lower limbs perform complex tasks during gait such as shock absorption, body support, shift of center of mass and control of postural balance. Ageing, however, weakens the muscles and makes them difficult to function properly, which may result in risks of performing daily activities. As such, many studies have been conducted on strengthening the functions of muscles and among them, vibratory stimulation has been actively investigated to activate proprioceptive senses.

There are many studies that reported improved posture stability, decreased postural sway [1-2] and enhanced function of muscles [3-4]. However, previous studies used one type of vibratory stimulation and individual difference was not taken into consideration even if the frequency range that proprioceptive sense shows the most sensitive response was proven to be 100Hz~300Hz. In other words, they did not consider the effect of different vibration perception thresholds.

Some following studies investigated the effect of different intensity of vibration perception in active status such as gait [5] but biomechanical analysis was not performed. As such, this study analyzed biomechanical effect of vibratory stimulation during gait considering individual vibration perception threshold.

II. METHODS

A. Subjects

Five adult males (Age: 25.4±1.1 years, Height: 171.6±2.3cm, Weight: 65.7±4.9Kg) voluntarily participated in this study. This study was approved by Chonbuk National University Institutional Review Board (IRB File No. JBNU 2015-06-012).

B. Equipment

A self-developed wired vibration stimulator that generates mechanical vibration was used to apply vibration stimulation. A total of 21 active infrared emitting markers were attached to major joints to measure the motion of gait. Three position sensors (Optotrak Certus, Northern Digital Inc, Canada) were used to collect signals from the markers. Four force platforms (Bertec Co., Ltd, U.S.A) were used to measure ground reaction force during gait. A musculoskeletal modelling and analysis software (SIMM, MusculoGraphics Inc., USA) was used for biomechanical analysis of lower limbs during gait.

C. Protocol

To investigate the biomechanical changes according to vibration perception threshold, we measured vibration perception threshold at each frequency. The vibration frequency to which the subjects responded the most sensitively was selected for an application. The Achilles tendon and tibialis anterior tendon were targeted for vibration to stimulate muscles in the lower limbs. The vibration conditions were established by combining different vibration application sites and degree of vibration perception thresholds. The subjects walked three times on the flat ground for each condition.

D. Analysis

The results of angle, moment and power of ankle during stance phase were selected as analysis parameters. The biomechanical change was analyzed at each application site by comparing different vibration stimulation conditions and one without stimulation.

III. RESULTS

A. Measurement of vibration perception threshold

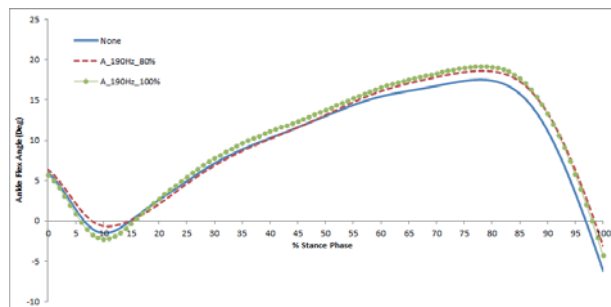
The vibration threshold in the Achilles tendon(ACT) was the lowest at 190Hz and the highest at 250Hz when the results were obtained between 180 and 250Hz. In the tibialis anterior tendon(TAT), the vibration threshold was the lowest at 180Hz and highest at 250Hz.

Table 1. Perception threshold according to vibration frequency (unit : G)

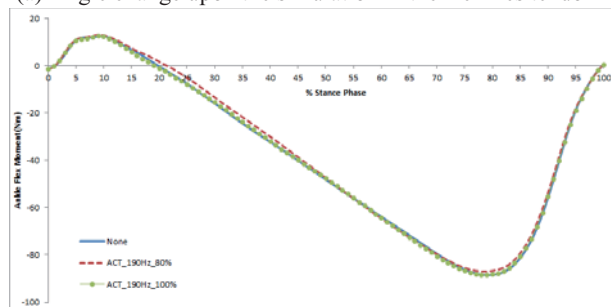
	180 Hz	190 Hz	200 Hz	210 Hz	220 Hz	250 Hz
ACT	1.018	1.014	1.021	1.03	1.04	1.061
TAT	1.048	1.052	1.078	1.081	1.14	1.167

B. Change upon the application of vibratory stimulus in the Achilles tendon

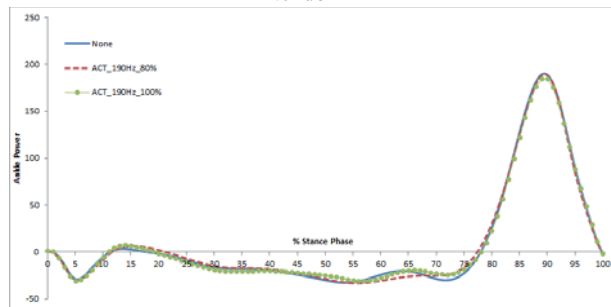
The biomechanical change in the Achilles tendon upon vibratory stimulation according to perception threshold compared to condition without stimulation was shown in the Fig. 1.



(a) Angle change upon the simulation in the Achilles tendon



(b) Moment change upon the simulation in the Achilles tendon



(c) Power change upon the simulation in the Achilles tendon

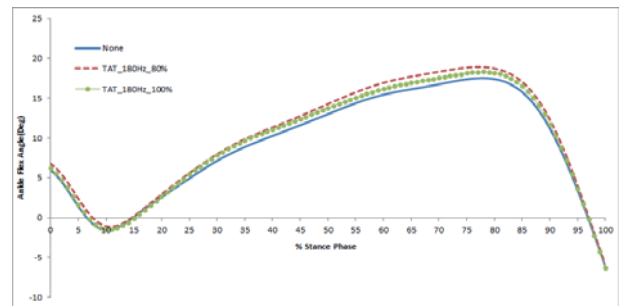
Fig. 1. Change in angle, moment and power upon the simulation in the Achilles tendon

When the stimulus of perception threshold was applied in the ankle, the angle of flexion increased between mid-stance to pre-swing phase compared to that under without stimulation. The same results were observed when sub-perception threshold stimulation was applied. The moment showed similar results in two conditions with stimulation and one without stimulation. The power also showed similar results as those of the moment.

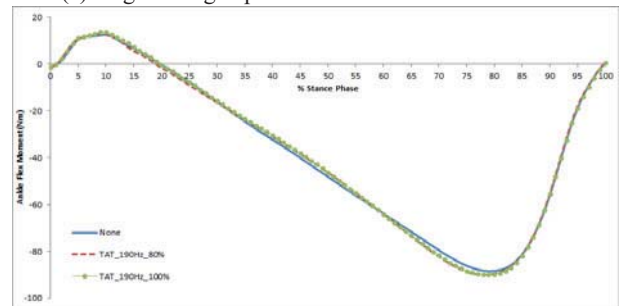
These similar results in biomechanical change with different perception thresholds explained that the stimulus of perception threshold affect to the same as sub-perception threshold do.

C. Change upon the application of vibratory stimulus in the tibialis anterior tendon

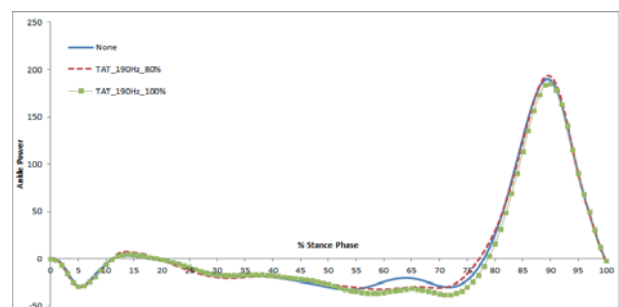
The biomechanical change in the tibialis anterior(TA) tendon upon vibratory stimulation according to perception threshold was shown in the Fig. 2.



(a) Angle change upon the simulation in TA tendon



(b) Moment change upon the simulation in TA tendon



(c) Power change upon the simulation in TA tendon

Fig. 2. Change in angle, moment and power upon the simulation in the tibialis anterior tendon

The angle of ankle upon flexion increased when a 180Hz-perception threshold was applied. The plantar flexor moment slightly increased upon stimulation compared to that without stimulation. The power showed increased negative and positive results between terminal-stance to pre-swing phase.

These similar results in biomechanical change with different perception thresholds in the tibialis anterior tendon also explained that the stimulus of perception threshold affect to the same as sub-perception threshold do.

Moreover, the results of moment and power slightly increased and angle, increased upon vibratory stimulation compared to those without stimulation. These results were different from those when the stimulation was applied in the Achilles tendon. It may be interpreted that the stimulation of the tibialis anterior tendon could have directly affected the activity of muscles. Further studies need to conduct to investigate the results further.

IV. CONCLUSION

This study analyzed biomechanical change of ankle according to vibration perception threshold on each application site.

Similar biomechanical change was shown both in the Achilles tendon and tibialis anterior tendon at perception threshold and sub-perception threshold. Due to the difference in the application site, the increase of the plantar flexor moment and negative power was slightly greater upon the stimulation of the tibialis anterior tendon than that of the Achilles tendon. This result may imply the vibratory stimulation of the tibialis anterior tendon directly affected the activity of muscles.

ACKNOWLEDGEMENT

This work was supported by the National Research Foundation of Korea(NRF) grant funded by the Korea government (MSIP) (NRF-2014R1A2A1A11053073)

REFERENCES

1. M. Yu, H. I. Eun, D. W. Kim, T. K. Kwon and N. G. Kim, "Effects of Vibratory Stimulus on Postural Balance Control during Standing on a Stable and an Unstable Support", *J. Biomed. Eng. Res.*, Vol. 28, pp.647-656, Oct 2007.
2. H. I. Eun, M. Yu, D. W. Kim, T. K. Kwon, and N. G. Kim, "The effects of human lower limb vibration on postural stability during unstable posture", *J. Biomed Eng. Res.*, Vol. 28, pp.628-635, Oct 2007.
3. T. Lapole and P. Chantal, "Effect of repeated Achilles tendon vibration on triceps surae force production", *Journal of Electromyography and Kinesiology*, Vol. 20, Issue. 4, pp.648-654, Aug 2010.
4. J. Luo, B. McNamara and K. Moran, "The use of vibration training to enhance muscle strength and power", *Sports Med*, Vol. 35, Issue. 1, pp.23-41, Sep 2005.
5. H. J. So, S. H. Kim and D. W. Kim, "The effects of application site and time of vibration stimulation : Changes in gait pattern and muscle activity", *Applied Mechanics and Materials*, Vols. 479-480, pp.475-479, Dec 2013.

Which Threshold Define Best for Muscle Onset Time in MMG and EMG?

S. J. Kim¹, H. S. Lee¹, M. Jo¹, I. S. Shin¹ and Y. H. Kim¹

¹Department of Biomedical Engineering and Institute for Medical Engineering, Yonsei University, Wonju, Republic of Korea
E-mail: youngbokim@yonsei.ac.kr

Abstract—In this study, we suggest a method to detect the muscle activation using 3-axis mechanomyogram. Twenty healthy males performed six different exercises. Obtained EMG and MMG signals were applied with the standard deviation (SD) method. Results showed that the best muscle activity detection was accomplished by the 5SD method based on the standard deviation of the baseline signals.

Keywords— muscle, activation, mechanomyogram (MMG), electromyogram (EMG), isotonic, isometric.

I. INTRODUCTION

Mechanomyography (MMG) measures muscle vibrations, which are generated by the muscle contraction mechanism, by using accelerometers. It is a non-invasive method to determine the mechanical events of a muscle activation. In this study, we analyzed accelerometer-based MMG signals to apply the standard deviation (SD) method, and determined the best threshold to define muscle onset time.

II. METHODS

Twenty healthy males with no history of upper and lower limb disorders participated in this study. Subjects performed joint flexion/extension exercises on an isokinetic dynamometer (Biodex System 3, Biodex Medical Systems, USA). Six kinds of exercises were chosen to detect the muscle onset time (Table 1). A MMG sensor, LIS3111 (STMicroelectronics, USA) was used to measure the 3-axis acceleration (x: anterior-posterior; y: medial-lateral; z: superior-inferior). An EMG sensor (DELSYS, Trigno wireless system, USA) was placed along the longitudinal axis of muscles. EMG sensor was placed adjacent to the upper border of the proximal MMG sensor. MMG, EMG, and torque acquired from the isokinetic dynamometer were recorded simultaneously at a sampling rate of 1 kHz.

MMG and EMG signals were band-pass filtered (MMG and EMG bandwidth: 8-100 Hz and 10-450 Hz, respectively) prior to the signal analysis. MMG signals were calculated as SVM (Signal Vector Magnitude) for linear envelope processing using the following equations:

$$SVM = \sqrt{MMG_x^2 + MMG_y^2 + MMG_z^2} \quad (1)$$

MMG and EMG signals were low-pass filtered with a 4 Hz cut-off (second-order Butterworth) to linear envelope a data. After data processing, muscle activation event was identified as the time point when exceeded the standard deviation of the baseline signal.

Table 1. Characteristics of seven different exercises

Isotonic	Elbow (biceps brachii) flexion	ROM: from 100° to 40° Ten repeated (40% MVC)
	Knee (rectus femoris) extension	ROM: from 90° to 0° Ten repeated (40% MVC)
	Ankle (tibialis anterior) dorsiflexion	ROM: from -25° to 5° Ten repeated (40% MVC)
Isometric	Elbow flexion	MVC measurement at 90°
	Knee extension	MVC measurement at 90°
	Ankle dorsiflexion	MVC measurement at -10°

III. RESULTS

Experimental results are summarized in Table 2. With the 5SD, the best threshold for onset detection was accomplished by showing 95.14 % and 100 % for isotonic and isometric exercises respectively.

Table 2. Detection of muscle onset time with different SD thresholds

Thresholds	MMG		EMG	
	Isotonic (%)	Isometric (%)	Isotonic (%)	Isometric (%)
2SD	80.90	100	97.92	100
3SD	89.93	100	95.83	100
4SD	90.63	100	96.53	100
5SD	95.14	100	99.31	100
6SD	93.06	100	98.61	100
7SD	91.32	100	98.96	100
8SD	89.93	100	98.96	100

IV. CONCLUSION

In this paper, we have proposed a method to detect MMG onset events. When compared with the EMG, the proposed threshold can be adopted as a reliable method to detect muscle activation using MMG

ACKNOWLEDGEMENT

The followings are the results of a study on the “Leaders Industry-University Cooperation” Project,

supported by the Ministry of Education, Science & Technology (MEST).

Coupling of Upper Body Parts in Patients with Parkinson's disease during Level Walking

J. W. Kim¹, Y. R. Kwon¹, and G. M. Eom^{1,2}

¹School of Biomedical Engineering, Konkuk University, Choonju, Korea

²Research Institute of Biomedical Engineering, Konkuk University, Choonju, Korea

E-mail: gmeom@kku.ac.kr

Abstract—The aim of this study was to investigate phase difference among pelvis, shoulder and head accelerations during gait in patients with Parkinson's disease (PD). Twenty-three PD patients and age-matched twenty-nine elderly subjects participated in this study. Antero-posterior (AP) accelerations were measured during level walking using accelerometers located at pelvis, shoulder, and head. The phase lag of head acceleration against shoulder and pelvis accelerations was significantly smaller in PD compared to normal ($p < 0.05$). This result suggests that upper body segments of PD patients may be more rigid.

Keywords— level walking, upper body, Parkinson's disease, acceleration, time lag

I. INTRODUCTION

Movements of upper body, as well as lower body, may be relevant and informative for the investigation of pathological effect in the gait strategy. The aim of this study was to investigate phase lags in the accelerations of parts in upper body during level walking in patients with Parkinson's disease (PD).

II. METHODS

A. Experiments and Outcome Measures

Twenty nine elderly subjects (70 ± 6 years) and 22 PD patients (age of 69 ± 9 years) participated in this study. All subjects were instructed to walk straight along a 12 m on a linear walkway at self-selected comfortable speed. Accelerometers (Trigno wireless system, Delsys, MA) were used to collect acceleration data at 1,000Hz sampling frequency at pelvis, shoulder, and head.

B. Analysis

From cross-correlation analysis, phase differences were calculated as a measure of the degree of coupling among accelerations of the body parts [1]. Independent t-test was performed in order to compare phase differences in PD patients to those of age-matched controls. The statistical analyses were performed using SPSS ver.16 for Windows (SPSS Inc., Chicago, IL, USA).

III. RESULTS

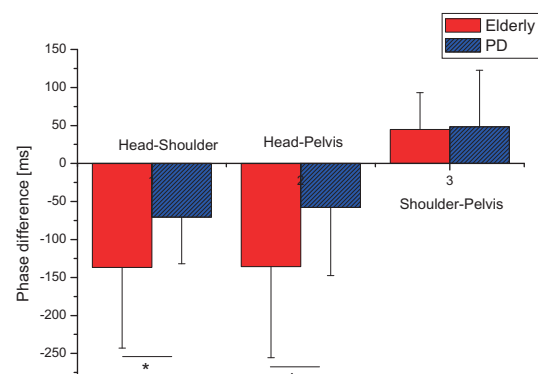


Fig. 1 comparison between PD patient and control group in phase difference

The magnitude of phase differences of head-shoulder and head-pelvis accelerations were significantly smaller for the PD patient compared to those of the controls ($p < 0.05$). This indicates that PD patients have a stronger coupling between head and trunk (pelvis and shoulder) and also suggests that upper body segments may be more rigid in PD patients compared to controls.

IV. CONCLUSION

PD patients had stronger coupling of head to trunk than in normals. This information would be useful to understand the mechanisms underlying the gait strategy in PD patients.

ACKNOWLEDGEMENT

This study was supported by Basic Science Research Program through the National Research Foundation of Korea and Business for Cooperative R&D between Industry, Academy and Research Institute funded the Ministry of Education and Korea Small and Medium Business Administration (2014R1A1A2057508, C0297714).

REFERENCES

1. J. J. Kavanagh, R.S. Barrett, and S. Morrison, "Upper body accelerations during walking in healthy young and elderly men," *Gait and posture.*, vol. 20, pp. 291-298, 2004.

Effect of sensory stimulation for suppression of action tremor

J.H. Heo¹, J.W. Kim¹, Y.R. Kwon¹, G.M. Eom^{1,2}, D.Y. Kwon³, and C.N. Lee⁴. K.W. Park⁴

¹School of Biomedical engineering, Konkuk University, Choongju 380-701, Korea

²Research institute of Biomedical engineering, Konkuk University, Choongju 380-701, Korea

³Department of Neurology, College of Medicine, Korea University, Ansan, Korea

⁴Department of Neurology, College of Medicine, Korea University, Anam, Korea

E-mail: gmeom@kku.ac.kr

Abstract—Essential tremor interrupt daily life. This study investigates the effect of sensory stimulation on multiple segments and joints. Eighteen patients participated in this study. The task, ‘Archimedes circle drawing’, was performed and sensory stimulation was applied on four muscles during task. RMS angular velocity was compared among before, during, and after stimulation. At post-stimulation, RMS velocity was reduced by sensory stimulation in all segments and joints than pre-stimulation. The results suggest that the sensory stimulation may be an effective clinical method to suppress the essential tremor.

Keywords—essential tremor, sensory stimulation, archimedes circle drawing, action tremor, RMS velocity

I. INTRODUCTION

Essential tremor is an involuntary trembling of body limbs in people without tremor-related disease [1]. Action tremor occurs when body parts are under movement. Traditional treatments of essential tremor include medication and surgery. Javidan suggested FES as an effective method for tremor suppression [2]. However, this method has a limitation, that is, continuous muscle contraction by FES induces muscle fatigue. Therefore, we suggest sensory electrical stimulation for suppression of action tremor.

The purpose of this study was to investigate the effect of the sensory stimulation of the upper limb during drawing action.

II. METHODS

Eighteen patients with essential tremor (68.8 ± 7.7 yrs) participated in this study. Gyro sensor was attached on index finger, hand, and forearm. Electrical stimulators were used for stimulation of flexor carpi radialis, extensor carpi radialis, and biceps brachii, triceps brachii. ‘Archimedes circle drawing’ task was performed for three time phase i.e., before-stimulation (Pre), during stimulation (On), 5 min after stimulation (Post). For each phase, 3 trials were repeated, resulting in a total of 9 trials. Five min of rest time was inserted between sessions. Vector sum of 3-D angular velocities was calculated for each of finger, hand, and forearm segment and each of metacarpoihalangeal (MP) joint, and wrist joint. Root-mean-squared (RMS) angular velocity was derived from the vector sum. Reduction of

the tremor was calculated for the Pre-On phases and Pre-Post phases.

III. RESULTS

RMS velocity at Post phase was reduced from Pre phase in all segments and joints ($p < 0.01$).

Table 1. Reduction ratio of angular velocity

RR (%)	Finger	Hand	Forearm	MP	Wrist
Pre-Post	14.92	12.15	15.08	13.29	13.61

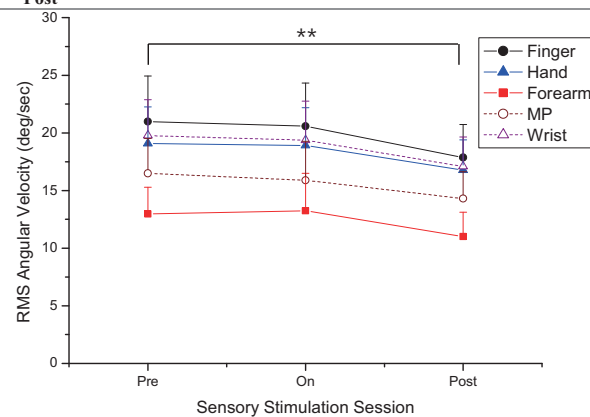


Fig. 1. RMS angular velocity for different phases of sensory electrical stimulation (**: $p < 0.01$)

IV. CONCLUSION

Action tremor after sensory stimulation is reduced from that of before stimulation.

ACKNOWLEDGEMENT

This study was supported by Basic Science Research Program through the National Research Foundation of Korea and Business for Cooperative R&D between Industry, Academy and Research Institute funded the Ministry of Education and Korea Small and Medium Business Administration (2014R1A1A2057508, C0297714).

REFERENCES

1. G. Deuschl, P. Bain and M. Brin, "Consensus statement of the Movement Disorder Society on Tremor. Ad Hoc Scientific Committee", Movement disorders : official journal of the Movement Disorder Society, vol. 13 no. 3, pp. 2-23, 1998.
2. M. Javidan, J. Elek and A. Prochazka, Attenuation of pathological tremors by functional electrical stimulation, II: Clinical evaluation, Annals of Biomedical Engineering 20, pp. 225-236. 1992

Study on the Effect of Spine Deformities on the Intervertebral Disc

Bokku Kang¹, Han Sung Kim¹

¹Department of Biomedical Engineering, College of Health Science, Yonsei University, Wonju, South Korea
E-mail: bokku01@gmail.com

Abstract— Bad postures taken repeatedly in everyday life have a serious impact on not only the spine but the intervertebral disc. In this paper, we compared a stress of a disc according to the spine angle by the finite element method.

Keywords— Intervertebral Disc, Spine, Finite Element Analysis.

I. INTRODUCTION

In recent years, the rapid development of electronic device has been subjected to many changes in human life. Especially the use of computers and smart phones has been adversely affected in many human lives. However, physical side effects have been reported due to long-term use of electronic devices. In particular, the people who complained of fatigue and disc disease caused by incorrect posture are becoming increasingly more. Therefore, we analyzed the effects of the disc by the wrong posture with numerical methods.

II. METHODS

A. Disc Finite element analysis general

The spine used for finite element analysis was thoracolumbar full model. The spine model consisted of cortical bone, cancellous bone and intervertebral disc. The element type of spine model was applied c3d4 tetrahedral element. The element number of spine model was 146,151 and the number of nodes was 34,943. To assess the stress of the intervertebral disc, we used Cobb's angle between L1 to T2. The Cobb's angle was increased by 5° up to 30°. Analysis commercial package was Abaqus 6.4 (2004, Abaqus, Inc.) and HyperMesh (2004, Altair Engineering, Inc.) was used in FE mesh generation.

B. Material properties

The material properties of cortical bone, cancellous bone and intervertebral disc were adopted as the data of M.A. Tyndyk et al. (2007) [1].

C. Boundary conditions

The thoracolumbar spine model was used for stress analysis of intervertebral disc. For stress analysis, we applied Cobb's angle between L1 to T2. By 5° up to 30° we compared each stress value.

III. RESULTS

FEA result of spine model showed consistency in their parameter. According to their results, the greater the Cobb's angle value was, the higher the stress value of intervertebral disc was. In addition, it was confirmed that more stress in the thoracic bone (T5) than lumber bone.

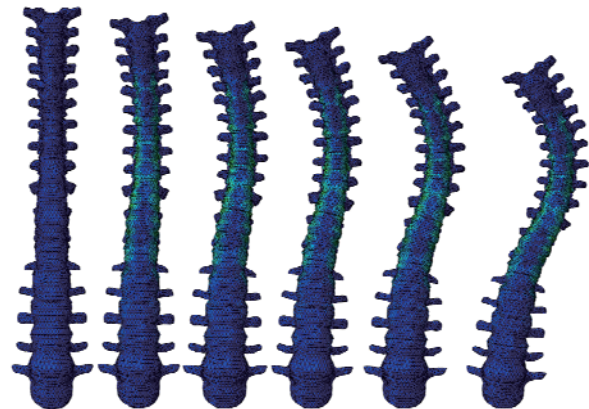


Fig. 1. The FEA results of spine model. We conformed that the spine was deformed in accordance with the angle increased.

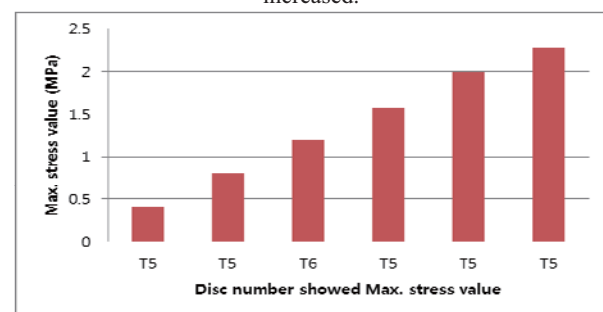


Fig. 2. The graph showed the results of spine finite element analysis. Mainly disc on the Thoracic received more stress than on the lumber.

IV. CONCLUSION

We compared a stress of a disc according to the Cobb's angle between L1 and T2 by the finite element method. The big of Cobb's angle between L1 and T2 means the posture of pelvis is unstable. According to the results of analysis, unstable pelvis posture might effect on the thoracolumbar spine.

REFERENCES

1. M.A. Tyndyk, V. Barron, P.E. Mchugh, D. O'Mahoney, "Generation of a finite element model of the thoracolumbar." *Acta of Bioengineering and Biomechanics*, vol. 9, No. 1, 207, 2007.

Use of Microsoft Kinect for detecting gait event while three kinds of walking speeds on a treadmill

S. T. Yang¹, J. S. Choi^{1,2}, D. W. Kang¹, J. W. Seo¹, D. H. Kim¹, and G. R. Tack^{1,2,#}

¹Department of Biomedical Engineering, Konkuk University, Chungju, Korea

²BK21 Plus Research Institute of Biomedical Engineering, Konkuk University, Chungju, Korea

E-mail: grtack@kku.ac.kr

Abstract—The purpose of this study is to detect gait events based on upper body movement during treadmill walking using a Kinect sensor. Even though the walking speed was varied, the error of events remained below 0.040sec for all walking speeds. This study can give simple gait analysis with the low-cost Kinect sensor.

Keywords— Kinect, Gait event, Treadmill walking, Speeds, Upper body

I. INTRODUCTION

Kinect sensor has been widely used for motion and balance assessment. In recent, it has been tried to detect gait event during treadmill walking. However, since Kinect has difficulty in discriminating between the treadmill belt and the foot, it is difficult to find gait events using foot movement [1]. Thus, the purpose of this study is to find gait events based on upper body movement using a Kinect sensor.

II. METHODS

A. Subjects & experiments

Ten male adults (age: 25.3±0.9years, height: 177.8±4.9cm) participated in 5 min treadmill walking experiment with three kinds of walking speeds (3.5, 4.5, 5.5km/h).

B. Measurement & analysis

Kinect was placed on the front of the subject and synchronized with the 3D motion capture system (3DMA) for the comparison. Foot velocity algorithm (FVA) was used to find heel-strike (HS) and toe-off (TO) events from 3DMA data [2]. HS and TO events with Kinect sensor were derived from the medial-lateral velocity at mid-shoulder (MSV).

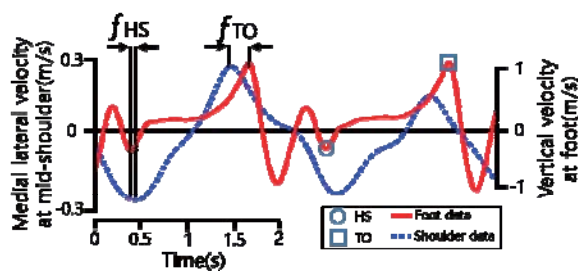


Fig. 1. HS & TO events from Kinect and 3DMA

C. Algorithm

Fig. 1 shows the HS and TO events by MSV with Kinect sensor and those by FVA with 3DMA data. It was believed that the error was due to different subject information and treadmill speeds.

$$HS = \max MSV_{time} + f_{HS}(S_{info}) \quad (1)$$

$$TO = \min MSV_{time} + f_{TO}(S_{info}) \quad (2)$$

As shown in equations (1) and (2), error correction function $f(S_{info})$ was a regression equation based on subject's physical information (S_{info}) such as height, length of lower body, upper body & shoulder and treadmill speed. HS and TO events by MSV with Kinect sensor were given by the equation (1) and (2).

III. RESULTS

Table 1 shows the average error (HS: 0.029sec and TO: 0.027sec) between Kinect and 3DMA data during three different speeds walking on a treadmill.

Table 1. The average error in HS & TO between Kinect and 3DMA during treadmill walking with 3kinds of speeds

Speed(km/h)	HS(sec)	TO(sec)
3.5	0.027±0.022	0.028±0.020
4.5	0.027±0.023	0.027±0.028
5.5	0.031±0.024	0.038±0.027
mean	0.029±0.023	0.027±0.024

IV. CONCLUSION

Results showed that the average error between Kinect and 3DMA data was below 0.030sec both HS and TO. Even though the walking speed was varied, the error remained below 0.040sec for all walking speeds. This study can give simple gait analysis with the low-cost Kinect sensor. An additional comparative study with more subjects and various walking speeds and gradients is in progress.

ACKNOWLEDGEMENT

This research was supported by the National Research Foundation of Korea (NRF) Grant funded by the Korea government (MSIP) (Nos. 2013R1A1A1009571 and 2013R1A2A2A030145 11).

REFERENCES

1. E. Auvinet, F. Multon, C. E. Aubin, J. Meunier and M. Raison, "Detection of gait cycles in treadmill walking using a Kinect," *Gait & Posture*. Vol. 41, pp. 722-725, 2015.
2. C. M. O'Connor, S. K. Thorpe, M. J. O'Malley and C. L. Vaughan, "Automatic detection of gait events using kinematic data," *Gait & Posture*. Vol. 25, pp. 469-474, 2007.

The Effect of Brake Force on Human Response during Low Speed Rear-End Collision

JiHye Han¹, LeeYong Song¹, JaeYeong Lee¹, HyungJoo Kim², Inju Lee², Dohyung Lim¹

¹ Department of Mechanical Engineering, Sejong University, Korea

² Human Factors & Devices Research Team, Hyundai Motor Group, Korea

E-mail: dli349@sejong.ac.kr

Abstract—The aim of this study is to determine human response (e.g. neck joint angle and muscle activation) to the brake force during the low speed rear-end collision. 3D motion capture infrared cameras and surface wireless electromyogram (EMG) system have been used to evaluate neck joint angle and muscle activation during the experiment. Results indicate that the brake force can be one of the main factors of whiplash injury in car collision.

Keywords— Whiplash injury, Rear-end collision, Low speed

I. INTRODUCTION

Incidence of whiplash injury in low speed rear-end collision still very high in Asia, United States and Europe resulting in socio-economic burden over approximate one billion annually. Due to these reason, many researches have been conducted to reduce a risk of whiplash injury during the low speed rear-end collision. Most previous studies, however, did not consider brake force which might be frequently operated by occupant during the actual rear-end collision. The aim of this study is, therefore, to identify how much human response (e.g. neck joint angle and muscle activation) are affected by the brake force during the low speed rear-end collision.

II. METHODS

Following Institutional Review Board approval, ten healthy participants (25.6±4.2 years, 173±2.6 cm, 70.5±3.9 kg) with no sign of musculoskeletal pathology were tested. Experimental platform was designed for the low speed rear-end collision and experimental tests were performed according to the procedure of Korea New Car Assessment Program. The neck joint angles and muscle activations of the participants responded to the low speed rear-end collision were then measured using 3D motion analysis system with eight infrared cameras and surface wireless electromyogram (EMG) system, respectively. The EMG sensors were attached to 3 muscles (Sternocleidomastoid, Trapezius, Splenius capitis) on both side of the neck.

III. RESULTS

A degree of the neck joint angle alteration and an onset time for the retraction phase were significantly influenced by the brake force ($p < 0.05$), while a range of the neck joint angle alteration was not ($p > 0.05$). A muscle activation was significantly increased by the brake force ($p < 0.05$). Particularly the muscle activation of the splenius capitis was increased about 2.1 times compared to the low speed rear-end collision with no consideration of the brake force (113.5±103.7% relative to maximum voluntary contraction) ($p < 0.05$).

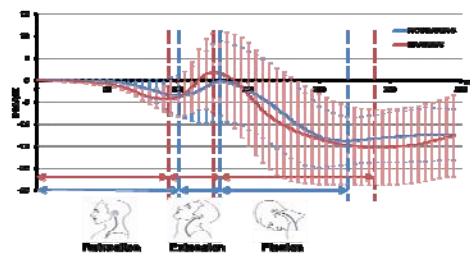
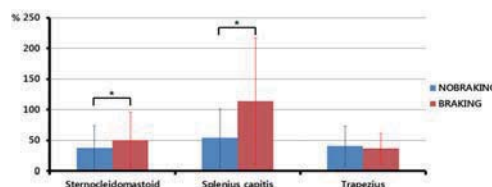


Fig. 1. Neck joint angle during low speed rear-end collision



	Sternocleidomastoid		Splenius capitis		Trapezius	
	No braking	Braking*	No braking	Braking*	No braking	Braking
AVG±STD[%]	37.8±35.7	50.2±45.6	53.7±47.7	113.5±103.7	40.5±32.4	36.7±24.7
DOMINANT	81.82%	18.18%	72.73%	27.27%	54.55%	45.45%
T-TEST (P<0.05)		0.020566		0.049847		0.459175

Fig. 2. Muscle activations of the neck during low speed rear-end collision

IV. CONCLUSION

These findings may indicate that the brake force can be one of main factors of whiplash injury pathogenesis and should be considered in the researches for the reduction of whiplash injury.

REFERENCES

1. M. M. Panjabi, S. Ito, P. C. Ivancic and W. Rubin, "Evaluation of the Intervertebral Neck Injury Criterion Using Simulated Rear Impacts," Journal of Biomechanics, Vol.38, pp.1694-1701, 2005.

Identification of Potential Injury Risk via Analysis of Human Responses during Low Speed Front-head Collision

JaeYeong Lee¹, LeeYong Song¹, JiHye Han¹, HyungJoo Kim², InJu Lee², Dohyung Lim^{1*}

¹ Department of Mechanical Engineering, Sejong University, Seoul 143-747, Korea

² Human Factors & Devices Research Team, Automotive Research & Development Division, Hyundai Motor Group, Uiwang 437-815, Korea

* dli349@sejong.ac.kr

Abstract—The aim of this study is, therefore, to identify a potential injury risk induced by it via understanding the human responses (e.g. joint angle and muscle activation) during the low speed front-head collision simulated in the current study.

Keywords— Whiplash injury, Front-head collision, Potential Injury

I. INTRODUCTION

Most previous studies have investigated the human responses during a low speed rear-end collision for understanding whiplash injury mechanism. Little information is, however, available for the human responses related to a low speed front-head collision. The aim of this study is, therefore, to identify a potential injury risk induced by it via understanding the human responses (e.g. joint angle and muscle activation) during the low speed front-head collision simulated in the current study.

II. METHODS

Following Institutional Review Board approval, thirteen healthy participants (25.6±4.2 years, 173±2.6 cm, 70.5±3.9 kg) with no sign of musculoskeletal pathology were tested. Experimental platform was designed for the low speed front-head collision and experimental tests were performed according to the procedure of Korea New Car Assessment Program.

The joint angles and muscle activations of the participants responded to the low speed front-head collision were then measured using motion analysis and surface wireless electromyogram systems, respectively.

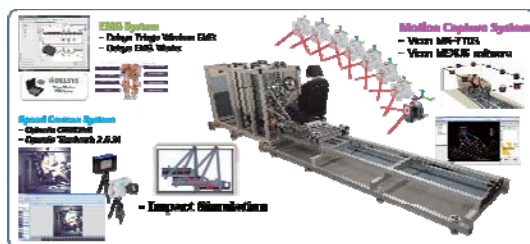
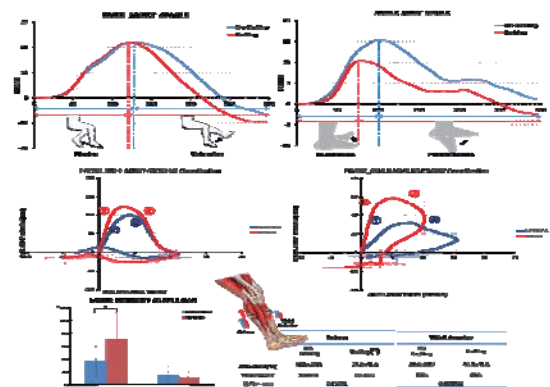


Fig. 1 System design and Measurements and data Acquisition

III. RESULTS

The results showed that the joint angles in the lower extremity were altered meaningfully by the low speed front-head collision in a potential injury risk point of view, compared to those by the low speed rear-end



collision ($p < 0.05$).

Fig. 2 Joint angles, Muscle activations and Joint stiffness of lower extremity during low speed front-head collision with/without force .

IV. CONCLUSION

These might influence the muscle activation, resulting in an injury of the lower extremity in a serious auto accident, particularly in the Soleus and Tibial Anterior related to the ankle joint motions.

These findings indicate that the low speed front-head collision may induce dominantly a high potential injury risk on the anatomic regions of the lower extremity of the occupant, otherwise the low speed rear-end collision.

These may indicate that a methodology for the reduction of the potential injury risk on the lower extremity should be considered additionally in the auto collision safety system for the reduction of the potential injury risk on the neck joint frequently induced by the low speed rear-end collision.

REFERENCES

1. A. Kim et. al., "A Comparison of the Hybrid III and BioRID II Dummies in Low-severity, Rear-impact Sled Tests," Stapp Car Crash Journal, Vol.45, 2001- 22-0012, 2001.

Biomechanical assessment of the proximal interphalangeal implants following collateral ligament release using a finite element analysis

W. H. Kim¹, J. H. Park², J. W. Park², J. W. Jang³, J. W. Lee¹, W. M. Chen¹, S. J. Lee¹

¹Department of Biomedical Engineering, Inje University, Gimhae, Korea

²Orthopaedic Department, Korea University College of Medicine, Seoul, Korea

³R&D center, Medyssey Co., Ltd, Uijeongbu, South Korea

E-mail: sjl@bme.inje.ac.kr

Abstract— Proximal interphalangeal (PIP) joint arthroplasty may cause abnormal motion due to the out-of-plane forces during pinch or grasp tasks. This is considered to be a leading cause of abnormal functions of the treated finger. This study was done to quantitatively investigate the influences of insertion of finger joint devices following collateral ligament release. Two different configurations of the post-op FE model of PIP joint arthroplasty were considered: one-piece and two-piece designs. The PIP joint model was reconstructed from CT and MRI images. With ligaments intact, the one-piece Silicone and two-piece (SRTM PIP) designs showed the lateral stiffness of 0.41 N/mm and 50 N/mm, respectively. As for the two-piece design, an initial reduction in the lateral stiffness by 8% was noted with the first 20% ligament release and then the decrease remained more or less constant at 21% thereafter. The results shed new lights on the complex interplay between implant designs and joint's ligaments to better understand an acceptable level of stability needed for the PIP joint arthroplasty.

Keywords— Finger joint, PIP implant, lateral stability.

I. INTRODUCTION

Proximal interphalangeal (PIP) arthroplasty has gained popularity in the treatment of patients with hand rheumatoid and osteoarthritis. One of the major goals is to restore the normal joint motion of the affected finger. Currently, there are two major types of PIP implants: one-piece as a flexible spacer and two-piece with more capability to provide functional range of motion (ROM). However, abnormal motion may still occur due to the out-of-plane forces during pinch or grasp tasks [1-2]. This is considered to be a leading cause of abnormal functions of the treated finger. In addition, the lateral stability of PIP implants is often compromised due to collateral ligament release during implant insertion. Despite that PIP implants are designed to ensure some degree of lateral stability, biomechanical investigations into the post-operative lateral stability are very limited. In the present study, biomechanical characteristics of the two types of PIP implants were investigated by using anatomical-accurate PIP joint finite element (FE) model. In

particular, the lateral stability was compared by varying the order of serial release of the collateral ligament.

II. METHODS

In the present study, a PIP joint FE model, consisting of index finger bones, collateral ligaments, and tendons, were constructed based on CT and MRI images of a normal right hand (25 years old, male) (Fig. 1). Referring to a lateral surgical approach, post-op FE models were constructed by removing the articular surface of the PIP joint of the index finger and inserting implants. The post-op FE models was implanted with two types of PIP implants (Figure 1B & C), namely the one-piece Silicone PIP (Small bone innovations Inc., USA) and a two-piece SRTM PIP (Small bone innovations Inc., USA). The material properties for the anatomical joint and implant components were obtained from the literature (Table 1). Collateral ligament release was simulated by introducing sequential reduction of its elastic modulus by 20%, 40%, 60% and 80% respectively, from the stiffness value of the intact ligament [6]. A lateral displacement of 1 mm was imparted to the distal region of the middle phalangeal bone in the radial and ulnar directions, respectively. The proximal region of the PIP joint was fully constrained. Pre-tensions were applied to tendons of extensor digitorum communis (EDC, 2N), flexor digitorum profundus (FDP, 1.25N), and flexor digitorum superficialis (FDS, 1.25N) to simulate muscle stabilization effects [1]. Bone to implant interface were hypothesized as fused after surgery. The lateral stability of the PIP implanted models under all simulated conditions were assessed as the load (reaction forces) per displacement (N/mm).

III. RESULTS

With ligaments intact, the one-piece Silicone and two-piece designs showed the lateral stiffness of 0.41 N/mm and 50 N/mm, respectively. The lateral stability of the one-piece design appeared to be dependent on the material stiffness of the silicone, and it was susceptible to lateral load regardless of extent of ligament release (<2%). (Fig. 2). As for the two-piece design (SRTM PIP),

an initial reduction in the lateral stiffness by 8% was noted with the first 20% ligament release and then the decrease remained more or less constant at 21% thereafter (Fig. 2). It appears that the initial lateral stability was provided by both the collateral ligaments and the conformity of the joint surfaces of the two-piece implant design. For ligament release beyond 20%, the lateral stability seems to be solely provided by the presence of the collateral ligaments alone.

IV. CONCLUSION

Many factors contribute to the stability of the PIP joint following finger arthroplasty. These may include materials and designs of the implants, as well as the constraints provided by collateral ligaments and tendons. In this study, we showed that compared to the two-piece design, lateral stability provided by the one-piece design provides an overall lower stability. However, the use of more compliant silicon materials and one-piece “spacer” design made it less susceptible (stability reduction within 2%) to the release of collateral ligaments. In contrast, the two-piece design which features congruent joint geometry and use of stiffer materials such as Titanium generally results in higher lateral stability. Interestingly, the stability provided the two-piece design had a non-linear relationship with the state of the collateral ligaments. With an initial ligament lease by 20%, stability only decreased by 8%; further ligament lease to the same extent, however, results in 21% drop in stability.

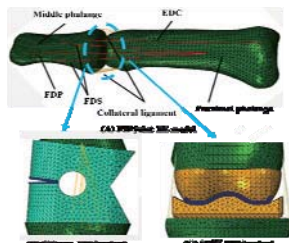


Fig. 1. FE models of PIP joint & implant

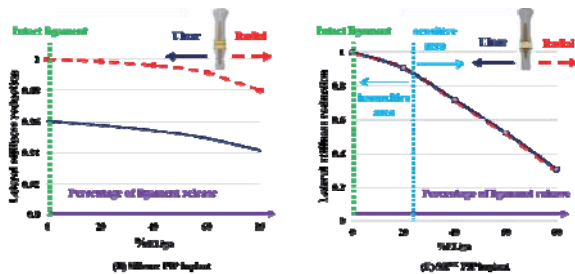


Fig. 2. Lateral stiffness reduction of the silicone- and SR™-implanted PIP joint following ligament release

Table 1. Material properties of finite element model of PIP joint and implants

Materials	Young’s modulus (MPa)	Poisson’s ratio (ν)
Bone[3]	15,000	0.3
Collateral ligament[3]	515	-
Silicone[4]	2.41	0.45
Ti-alloy[5]	110,000	0.35
CoCr-alloy[5]	218,000	0.33
UHMWPE[6]	763	0.317

ACKNOWLEDGEMENT

This project was funded with a grant from the Small and Medium Business Administration (SMBA), South Korea (S2177713).

REFERENCES

1. S. Uchiyama et al., “Kinematics of the Proximal Interphalangeal Joint of the Finger after Surface Replacement,” *Journal of Hand Surgery*, vol. 25, pp. 305-312, 2000.
2. Health Quality Ontario, “Pyrocarbon Finger Joint Implant: An Evidence-Based Analysis,” *Ont Health Technol Assess Ser.*, vol. 4, pp. 1-31, 2004.
3. S. Y. Huang et al., “Rubber Band Selection for a Dynamic Splint for Flexor Tendon Repair – A Finite Element Study,” *Journal of Medical and Biological Engineering*, vol 27, pp. 156-160, 2007.
4. N. W. Williams et al., “Computer Model Analysis of the Swanson and Sutter Metacarpophalangeal Joint Implants,” *Journal of Hand Surgery*, vol. 25, pp. 212-220, 2000.
5. Farzad Ebrahimi, *Finite Element Analysis - New Trends and Developments*, Croatia: INTECH, 2012.
6. Brian Croop et al., “Mechanical and Visco-Elastic Properties of UHMWPE for In-vivo Product Development,” *SPE European Conference on Medical Polymers*, 2010.

Effects of Dual-Task Difficulty and Priority Option during Gait

J.M. Kim, E.K. Choi, I.S. Shin, S.J. Ahn, S.J. Kim, J.S. Ryu and Y.H. Kim*

Biomedical Engineering, Yonsei University, Wonju, Republic of Korea

E-mail: younghokim@yonsei.ac.kr

Abstract—We investigated the effects of dual-task difficulty (three difficult levels) and priority option (gait priority option and calculation priority option) during gait. Results showed that significantly different gait characteristics were found according to three difficulty levels, and priority option.

Keywords— Dual-task, Difficulty level, Priority option, Kinematics

I. INTRODUCTION

Dual-task is common in daily living such as listening to music or texting during walking. Dual-task increases safety risks by increasing attentional and cognitive demands. The aims of this study were determining the effects of dual-task difficulty and priority option in gait kinematics during gait.

II. METHODS

Fifteen healthy male subjects participated in this study. They were free of muscular-skeletal injuries, disease or limitations. After providing written informed consent, the subjects walked in laboratory at self-selected walking speed. Dual-task was suggested calculation in subtraction, and five different dual-task conditions were performed : no dual-task gait(NG), calculation to subtract 1(C1), 3(C3) and 7(C7) from the number in calculation priority option, and calculation to subtract 7 from the number in gait priority option(GP). Experiments were conducted in a random order to prevent the training effect, and the random numbers were given among 100s.

3D motion capture system(VICON MX system, UK) and Helen Hayes marker set were used to measure 3D gait kinematics. In this study, K1 and K2 represent knee flexion angle in stance and swing phase, respectively. A1 represents ankle plantarflexion angle in loading response and A3 represents the maximum plantarflexion angle in pre swing. All data were analyzed using Mann-Whitney and ANOVA in SPSS statistics 19(SPSS 19, IBM, USA).

III. RESULTS

A. The effects of dual-task difficulty

Walking speed, cadence, stride length, Hip RoM(range of motion), K1, K2, A1, and A3 were significantly decreased in high difficulty level. Stride time and DST ratio(double-limb support time/stride time) were significantly increased in high difficulty level.

B. The effects of dual-task priority option

Walking speed, cadence, stride length, Hip RoM, K1, K2 and A3 were significantly decreased in calculation priority option. Stride time and DST ratio were significantly increased in calculation priority option. There were no significant difference in A1.

Table 1. The effects of dual-task difficulty

	Walking Speed [m/s]	Cadence [steps/min]	Stride Length [m]	Stride Time [sec]	DST Ratio [%]
NG	1.27 ± 0.15	112.10 ± 7.05	1.51 ± 0.09	1.07 ± 0.07	19.03 ± 3.60
C1	1.11 ± 0.16*	105.52 ± 7.80*	1.40 ± 0.12*	1.14 ± 0.09*	20.51 ± 3.62*
C3	1.07 ± 0.17*	102.87 ± 8.93*	1.38 ± 0.12*	1.18 ± 0.11*	21.16 ± 3.79*
C7	0.97 ± 0.18*	96.21 ± 12.82*	1.33 ± 0.13*	1.28 ± 0.24*	22.15 ± 4.08*
	Hip RoM	K1 [degree]	K2 [degree]	A1 [degree]	A3 [degree]
NG	43.63 ± 2.99	12.35 ± 3.84	60.58 ± 5.18	-8.07 ± 1.80	-21.76 ± 5.09
C1	40.92 ± 3.12*	8.48 ± 5.10*	58.79 ± 5.59*	-9.11 ± 2.28*	-18.77 ± 5.23*
C3	40.46 ± 3.63*	7.82 ± 4.43*	58.49 ± 5.22*	-9.42 ± 2.25*	-18.28 ± 5.43*
C7	39.57 ± 3.58*	6.82 ± 4.28*	57.41 ± 4.51*	-9.62 ± 2.71*	-16.83 ± 4.86*

(* : $p < 0.05$)

Table 2. The effects of dual-task priority option

	Walking Speed [m/s]	Cadence [steps/min]	Stride Length [m]	Stride Time [sec]	DST Ratio [%]
GP	1.20 ± 0.17	108.58 ± 7.58	1.46 ± 0.12	1.11 ± 0.08	19.78 ± 3.62
C7	0.97 ± 0.18*	96.21 ± 12.82*	1.33 ± 0.13*	1.28 ± 0.24*	22.15 ± 4.08*
	Hip RoM	K1 [degree]	K2 [degree]	A1 [degree]	A3 [degree]
GP	42.12 ± 3.12	9.64 ± 5.25	59.67 ± 5.29	-9.17 ± 2.37	-20.33 ± 5.56
C7	39.57 ± 3.58*	6.82 ± 4.28*	57.41 ± 4.51*	-9.62 ± 2.71	-16.83 ± 4.86*

(* : $p < 0.05$)

IV. CONCLUSION

In this study, almost all of gait kinematic parameters showed significant differences according to different in dual-task and priority option. This results represent that gait is influenced by dual-task priority option as well as dual-task difficulty.

ACKNOWLEDGEMENT

This study was supported by the National Research Foundation of Korea(NRF) funded by the Ministry of Education(2013H1B8A2032194).

REFERENCES

1. S. Schaefer, D. Jagenow, J. Verrel and U. Lindenberger, "The influence of cognitive load and walking speed on gait regularity in children and young adult," *Gait&Posture*, vol. 41, pp. 258-262, 2015.

Biomechanical efficacies of a new surgical procedure using metatarsal sliding osteotomy for the treatment of the metatarsalgia

J. D. Eom¹, W. M. Chen¹, H. C. Gwak², J. H. Lee³ and S.J. Lee¹

¹Department of Biomedical Engineering, Inje University, Kimhae, Korea

²Department of Orthopaedic surgery, Inje University Baik Hospital, Busan, Korea

³Section of Foot and Ankle, Korea Orthopaedic Hospital, Busan, Korea

E-mail: sjl@bme.inje.ac.kr

Abstract— In this study, we performed a biomechanical analysis of a new metatarsal sliding osteotomy (MSO) procedure for surgical treatment of metatarsalgia. This MSO procedure is expected to have improved structural stability by using a bone plating system and securing the wide osteotomy plane. We constructed metatarsal and soft-tissue finite element (FE) models and analyzed biomechanical efficacies of the MSO. We applied push-off loading conditions to the model, and evaluated plantar pressure, stresses of the bone and implant and interfacial motion. The plantar pressure was decreased as the elevation distance of the procedure increased. The new metatarsal osteotomy was effective in stress relief of the plantar soft-tissue. It was also noted that the structural stability was decreased as the elevation distance increased. In particular, maintaining structural stability is required when the distal fragment is elevated by 4mm or more during the procedure.

Keywords— Metatarsalgia, Metatarsal sliding osteotomy, Biomechanical stability, Pressure relief

I. INTRODUCTION

The decompression surgery called metatarsal osteotomy has been widely used to surgically treat metatarsalgia, which causes compressed nerve pain on plantar soft-tissue. The metatarsal osteotomy is known to be effective in pain relief by elevating or translating the position of the metatarsal head to reduce localized plantar pressure. However, some complications, like the transfer metatarsalgia as well as non-union, delayed-union, angulation, and fixation failure, have been reported after surgery [1]. This study is aimed at proposing a new surgical procedure called metatarsal sliding osteotomy (MSO) to compensate for the complications and evaluating its biomechanical efficacies by using the finite element method (FEM). The plantar pressure, stresses and interfacial motion were predicted to quantitatively analyze the biomechanical efficacies and stability of the MSO.

II. METHODS

The MSO may possess an advantage in decompression capability by cutting metatarsal bone obliquely and sliding the distal fragment to the dorsal direction. And structural stability can be also secured by using an orthopaedic plating system to fix the metatarsal fragments.

A finite element model composed of 3rd metatarsal bone and soft-tissue was constructed based on CT images of the foot (male, 65kg, 27 years old) [3]. To validate the model, peak plantar pressure during push-off stance was compared with the results from the previous study and was found to be within 5% error ranges [4]. The MSO surgical models were constructed by cutting the 3rd metatarsal bone 45° obliquely to the long axis 1.5cm apart from the proximal end, followed by elevating the distal fragment to the dorsal direction. The elevation was varied with incremental increase of 1mm (Model types 1 ~ 5). Following MSO, a Leibinger plating system (pure titanium, 4-holes, 1.0×24mm, Stryker, USA) including four screws (Pure titanium, Ø2) were implanted for bone fixation using the bi-cortical fixation method (Fig. 1).

The loading and boundary conditions were applied to the models assuming that the models were undergoing toe-off phase in the gait cycle. The models were subject to the 125N loading which is equivalent to about 20% of the total body weight while the metatarsal angle was kept constant at 30° to the ground [3-4]. Frictional contact interaction between the plantar surface and the ground was defined using a coefficient of friction of 0.5 which means a sock was worn as suggested in previous studies [3]. The surgical model represented here was an immediate post-op with the coefficient of friction of 0.3 and 0.4 at the bone to bone contact and the implant to bone contact, respectively [2]. The plate and screws were completely tied to illustrate the locking mechanism of the plating system (Fig. 2).

To analyze decompression effect of the procedure, changes in plantar pressure distribution and peak plantar pressure were predicted. And peak von Mises stress (PVMS) of the cortical bone and implant was used to produce the likelihood of yield to each material's yield strength to quantitatively analyze the

structural stability after the procedure. Interfacial motion was also predicted to verify the union of the bone contact.

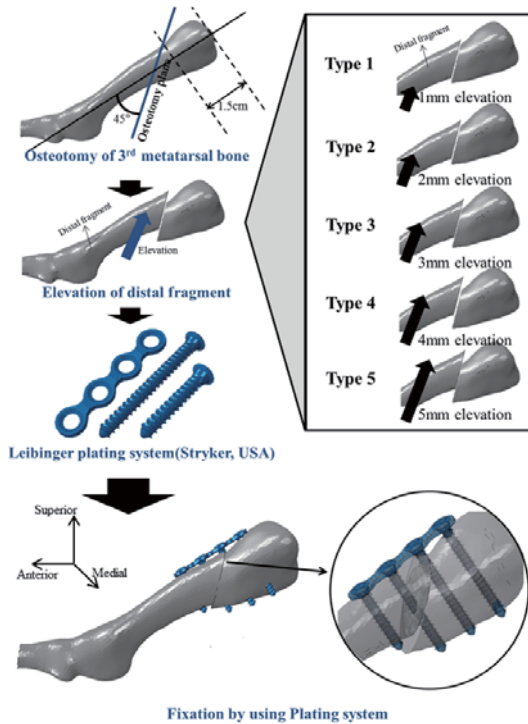


Fig. 1. The construction of MSO surgical FE model

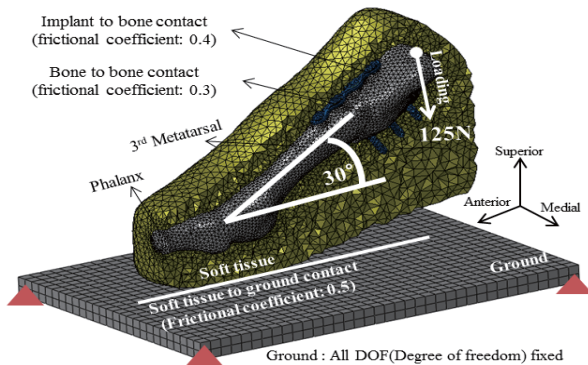


Fig. 2. Imposed loading and boundary conditions to simulate push-off phase in gait

III. RESULTS

As the distal fragment elevates, plantar pressure was gradually distributed to the rear (Fig. 3). The maximum plantar pressure reduced to at least 23.9% in Type 1 and up to 39.4% in Type 5 from the intact value. Therefore, it was predicted that with the MSO procedure gradual decompression was noted as the elevation distance increases (Fig. 4). However, the structural stability was shown to continue to decrease with the distal fragment elevating. In particular, in Type 4, the stability sharply decreased with the distal fragment elevating by 1mm. Here, the likelihood of yield, in the area of the cortical bone where a screw was inserted, was 38.6%. The likelihood of yield at the

interface between plate and screw was 19.4%. And the interfacial motion was 9.2µm (Fig. 4).

IV. CONCLUSION

In this study, we proposed a new metatarsal osteotomy where a wider bone contact can be secured and the structural stability improve by using the plating fixation system. Its biomechanical efficacy was demonstrated by inducing gradually decompressing the plantar structure with the distal fragment elevating, which in turn is likely to reduce foot pain. However the structural stability was slightly decreased with the distal fragment elevating. Especially, a relatively large decrease was predicted when the distal fragment elevated by around 4mm. Thus, when the distal fragment is elevated by 4mm or higher to significant decompression, it is needed to focus on maintaining stability more after the procedure.

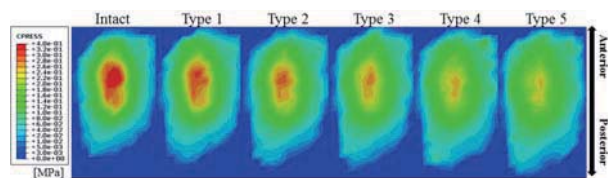


Fig. 3. Model predicted changes in plantar pressure distribution as a function of dorsal elevation distance.

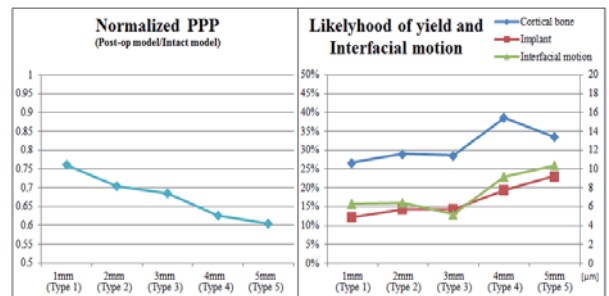


Fig. 4. Normalized peak plantar pressure (PPP)(left) and the likelihood of implant yielding and interfacial motion(right)

REFERENCES

- Espinosa, N., Maceira, E., & Myerson, M. S., "Current concept review: metatarsalgia". *Foot & ankle international*, 29(8), 871-879, 2008
- Ramlee, M. H., Kadir, M. R. A., Murali, M. R., & Kamarul, T., "Finite element analysis of three commonly used external fixation devices for treating Type III pilon fractures". *Medical engineering & physics*, 36(10), 1322-1330, 2014
- Chen, W. M., Lee, S. J., & Lee, P. V. S., "The in vivo plantar soft tissue mechanical property under the metatarsal head: implications of tissues' joint-angle dependent response in foot finite element modeling. *Journal of the mechanical behavior of biomedical materials*", 40, 264-274. 2014
- Hayafune, N., Hayafune, Y., & Jacob, H. A. C., "Pressure and force distribution characteristics under the normal foot during the push-off phase in gait". *The Foot*, 9(2), 88-92. 1999

Comparative biomechanical analysis of postoperative lumbar spine implanted with 3D printed porous cage in terms of various porosity levels

S. H. KIM¹, S. J. Yoo¹, J. W. Lee¹, S. H. Woo², J. W. Jang², K. M. Lim², D. S. Huh³, S. S. Chung⁴, H. Yong⁵, W. M. Chen¹ and S. J. Lee¹

¹Department of Biomedical Engineering, Inje University, Gimhae, South Korea

²R&D center, Medyssey Co., Ltd, Uijeongbu, South Korea

³CM Chungmu General Hospital, Department of Orthopedic Surgery, Seoul, Korea

⁴Samsung Hospital, Department of Orthopedic Surgery, Seoul, Korea

⁵Chaoyang Hospital, Capital Medical University, Department of Orthopedic Surgery, Beijing, China

E-mail: sjl@bme.inje.ac.kr

Abstract— Recently, 3D printing techniques have gained popularity in constructing personalized implants that could enhance bone ingrowth with porous structure. This study aimed to quantitatively investigate the influences in spinal biomechanical response after insertion of porous cage with different porosity levels using finite element (FE) analysis. The post-op FE model considered different porosity cages (0%, 64%, 80%, 92%, 100%) which were implanted into a functional spinal unit of lumbar spine (L4-L5). Values of maximum principal strain at the cage increased as porosity increased and rapidly increased between the porosity levels of 80% and 92%. However, changes in cage mechanical properties by varying porosity levels do not significantly affect the spinal load-sharing characteristics.

Keywords— Finger joint, PIP implant, lateral stability.

I. INTRODUCTION

Interbody fusion implants (cages) is widely used to maintain the height of the disc and to prevent spinal instability. Recently, 3D printing techniques have been used to make patient-specific implant that could enhance bone ingrowth using porous structure [1,2]. However, studies on biomechanical changes in stress distribution around the bone and implant interface after fusion surgery with cages at different porosity levels are still insufficient. Therefore, the present study was intended to derive mechanical properties of porous cages at controlled porosity levels using mechanical tests, and to analyze the cage yielding risks and changes in load-sharing between the anterior and posterior elements of the vertebral body following implantation of a porous cage using the finite element method.

II. METHODS

Porous cubes (12mm×12mm×12mm) at porosity levels of 0%, 64%, 80%, and 92% made of Ti-6Al-4V-ELI were prepared using an EBM 3D printer (Arcam, Sweden). All cubes were subjected to compression

tests under a load rate of 0.6mm/min with a MTS (MTS system corp., USA) (Figure1.(a)). The Young's modulus of porous Ti was derived from the mechanical testing results. A 3D finite element model of functional spinal unit of lumbar spine (L4-L5) was used[3]. A cage surgical model was constructed by inserting a porous cage (Medussa TM PL, Medyssey, Korea) in place of the excised annulus fibrosus and nucleus pulposus. In this case, the Young's modulus derived earlier was used as the material property for the porous cage and the Poisson's ratio was set at 0.33. All the nodal points of the inferior end plate of L5 were fully constrained and a compressive load of 1600N was applied (Figure2.(a)) [4]. The contact surfaces between the end plates of L4-L5 and the cage were defined with "Tied" contacts assuming complete bone fusion conditions. To analyze the risk of yielding of the porous cage, the maximum principal strain (MPS) according to changes in the material properties of the porous cage and the changes in anterior/posterior load-sharing through facet joint loads were compared.

III. RESULTS

As porosity increased, the elastic modulus of porous titanium gradually decreased (Figure1.(b)). From the results of FEA, the value of maximum principal strain at the cage increased as porosity increased and rapidly increased between the porosity levels of 80% and 92% (Figure2.(b)). In addition, under a compressive load of 1600N, the MPS of all porous cages with porosity levels between 0% and 92% was shown to be lower than 1%.

Under the same loading conditions, load-sharing changes as porosity increased were shown to be lower than 0.05% (anterior : around 82%, posterior: around18%).

IV. CONCLUSION

All the MPS levels of porous cages derived through the present study are not higher than 1%. Since these values are much lower than the elongation to failure values of the Ti-6Al-4V-ELI, the risk of cage yielding

is considered to be very low [5]. Also, the change in mechanical properties by porosity do not significantly affect the load-sharing characteristics

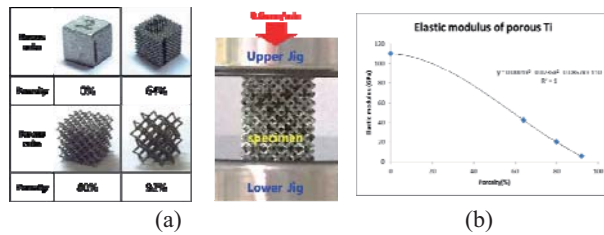


Fig 1. Mechanical test of porous cube (a) Porous cube specimens by porosity, (b) derived elastic modulus of porous titanium.

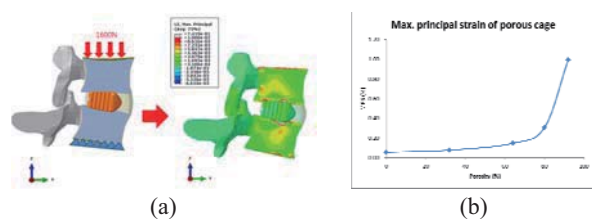


Fig 2. Results from FEA in implanted model (a) Surgical model of FEA, (b) Maximum principal strain of porous cage

ACKNOWLEDGEMENT

This project has been funded with support from the Ministry of Food and Drug Safety (MFDS), South Korea (15172MFDS421).

REFERENCES

1. Brett Russell Levine et al., "Experimental and clinical performance of porous tantalum in orthopedic surgery," *Biomaterials*, vol. 27, pp. 4671-4681, 2006.
2. Jia Ping Li et al., "Bone ingrowth in porous titanium implants produced by 3D fiber deposition," *Biomaterials*, vol. 28, pp. 2810-2820, 2007.
3. Ahn YH et al., "Comparison of the load-sharing characteristics between pedicle-based dynamic and rigid rod devices," *Biomedical Materials*, vol 3, pp. 044101, 2008.
4. Schmidt Hendrik et al. "Response analysis of the lumbar spine during regular daily activities—a finite element analysis." *Journal of biomechanics*, vol. 43, pp. 1849-1856, 2010
5. H. J. Rack et al. "Titanium alloys for biomedical applications." *Materials Science and Engineering: C*, vol. 26, pp. 1269-1277, 2006.

Alterations in cervical spine kinematics and implant stresses following uni- and bi- lateral laminoplasty procedures for the surgical treatment of cervical spondylosis myelopathy

S. J. Yoo¹, J. W. Lee¹, S. H. Woo², J. W. Jang², K. M. Lim², K. D. Riew³, G. R. Tark⁴,
W. M. Chen¹ and S. J. Lee¹

¹Department of Biomedical Engineering, Inje University, Gimhae, South Korea

²R&D center, Medyssey Co., Ltd, Uijeongbu, South Korea

³Department of Orthopedic surgery, Columbia University Medical Center, New York, U.S.A

⁴Department of Biomedical Engineering, Konkuk University, Chungju, Korea

E-mail: sjl@bme.inje.ac.kr

Abstract— Recently, laminoplasty has become the choice for the surgical treatment of cervical spondylosis myelopathy. This study aims to quantitatively investigate the influences in cervical spine kinematics and implant stress following uni- and bi- lateral laminoplasty. Four different types of the post-op Finite Element (FE) model were constructed. Classification was made based on changes in surgical technique and device. Our study showed that at the surgical and adjacent segment (C3-C4, C4-C5), all the post-op cases predicted increase in flexion ROM (range from 13~82%). Open-door Laminoplasty showed asymmetric motion in axial rotation (difference by 5%), and the fracture risk of implants was around 14 ~ 17% during flexion and left axial rotation. It is concluded that total laminoplasty is expected to provide improved biomechanical stability at surgical and adjacent segments than existing laminoplasty procedures.

Keywords— Laminoplasty, Biomechanics, Range of motion, Finite element analysis.

I. INTRODUCTION

Open-door Laminoplasty (ODL) is widely used in surgical treatment of cervical spondylosis myelopathy [1]. However, due to asymmetric implant insertion, traditional ODL commonly results in complications, including hinge area fracture, ligament misalignment, and imbalanced spinal motions [1-2]. Recently, a new implant for total laminoplasty (TTL) has been introduced. Because of the absence of any asymmetric hinge, a more physiological spinal motions following TTL is expected, though biomechanical studies on TTL implants are insufficient. Therefore, in this study, the biomechanical behavior and stability of a newly-introduced TTL implants will be evaluated in terms of ROM at postoperative spinal segments and stress

distributions in implants and bone-implant interface using the finite element (FE) method.

II. METHODS

A validated 3D multi-level cervical spine FE model (C3-C7) (Type 1: Intact) was used [3]. A laminectomy model was created (Type 2), where the spinous process, the ISL, the ligamentum flavum (LF), and the lamina were removed using a posterior decompressive method. An ODL model was created (Type 3), where, with one side of lamina and LF excised, a Centerpiece™ (Medtronic Inc., USA) was inserted. A TTL surgical model (Type 4) was created, where a TTL implant (Medyssey Corp., Korea) was inserted into the laminectomy model (Type 2). The constructed four types of FE models was shown in Fig. 1. C7 inferior endplate fully constrained, pure moments of 2Nm were applied at the C3 superior endplate to simulate Flexion (FLX), extension (EXT), left and right lateral bending (LLB&RLB), and left and right axial rotation (LAR&RAR) respectively. A follower load of 73.6N was applied to simulate muscle stabilization. A “Tied” contact condition was applied between implant interface to assume complete fusion. Changes in 3D ROM of surgical and adjacent segments before and after surgery were evaluated. To analyze the failure risks of the implant and hinge, Peak von Mises Stress and yield strength were compared.

III. RESULTS

Compared to Type 1, FLX ROM in surgical segments for Types 2~4 increased by 38%~59%, 33%~45%, and 13%~35% respectively. At adjacent segments, FLX ROM for Types 2~4 increased by 56~82%, 38~60%, and 23%~42% respectively. In Types 3~4, ROM increase rates decreased as loads increased (Fig. 2). Type 3 showed asymmetric axial rotation motion, RAR ROM was 5% larger than LAR

ROM. During EXT, RLB and LLB motions, no difference was identified. The fracture risk of Type 3(hinge and plate) was 14~17% during FLX and LAR motions.

IV. CONCLUSION

TTL is generally more effective in restricting FLX ROM at both the surgical and adjacent segments compared to laminectomy or ODL. Also, since the ligament imbalance associated with ODL was avoided, RAR and LAR ROM was more close to the intact models. Therefore, TTL is expected to provide improved biomechanical stability at surgical and adjacent segments than existing laminoplasty procedures.

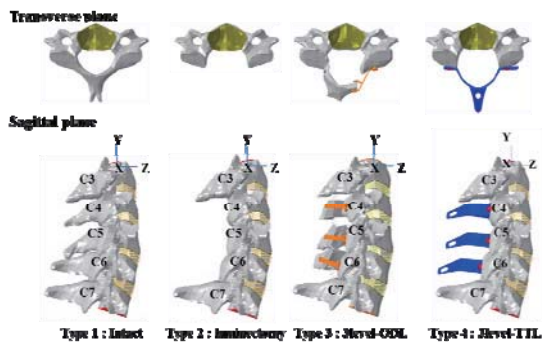


Fig. 1. Transverse and sagittal views of the Intact, laminectomy, Open-door Laminoplasty (ODL), and total laminoplasty (TTL) finite element models.

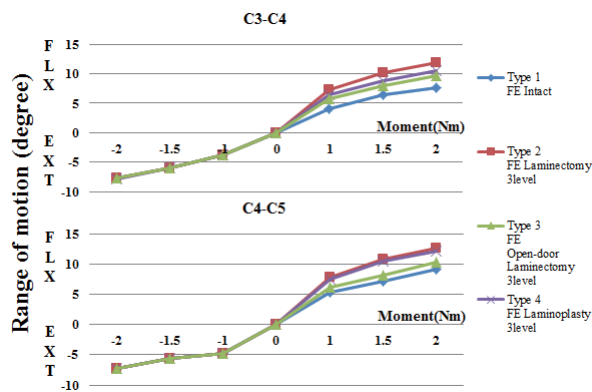


Fig. 2. Changes in sagittal-plane range of motion (ROM) at the surgical and adjacent segments as predicted by the intact, laminectomy, Open-door Laminoplasty (ODL), and total laminoplasty (TTL) FE models.

ACKNOWLEDGEMENT

This project has been funded with support from the Small and Medium Business Administration, Korea (S2086379)

REFERENCES

1. J. M. Rhee, "Posterior Surgery for Cervical Myelopathy: Laminectomy, Laminectomy with Fusion, and Laminoplasty," *Seminars in Spine Surgery*, 19(1), 35-43, 2007
2. M. Okada, M. Yoshida, H. Yamada, H. Hashizume, and A. Minamide, "Adjacent Segment Diseases Following Expansive Cervical Laminoplasty: A Report of Five Cases," *J Spine Neurosurg*, 3(2), 2014
3. T. G. Jung, S. H. Woo, K. M. Park, J. W. Jang, D. W. Han, and S. J. Lee, "Biomechanical behavior of two different cervical total disc replacement designs in relation of concavity of articular surfaces ProDisc-C® vs. Prestige-LP®," *IJPEM*, 14(5) 819-824, 2013

POSSIBILITY OF POTENTIAL BONE RESORPTION OCCURRENCE IN REVISION TOTAL KNEE ARTHROPLASTY USED WITH METAL BLOCK AUGMENTATION: MECHANICAL EXPERIMENT

Kwan-Soo Kang¹, Trinh Ngoc Tien¹, Young-Woong Jang², Owi Sik Yoo², Myung Chul Lee³, #Dohyung Lim¹

¹Department of Mechanical Engineering, Sejong University, Seoul, Korea

²Central R&D Center, Corentec Co. Ltd., Seoul, Korea

³Department of Orthopedic Surgery, College of Medicine, Seoul National University, Seoul, Korea
E-mail: dli349@sejong.ac.kr

Abstract—This study is to identify a possibility of the potential occurrence of bone resorption beneath metal block augmentation. The posterior region were increased and the medial region were decreased. The strains on the medial region were generally lower than 50-100 μ strain. In conclusion, this study demonstrates that a possibility of the potential bone resorption occurrence in revision TKA used with a metal block augmentation may be dependent on loading patterns applied on the knee joint related to personal lifestyle history.

Keywords—TKA, Revision TKA, Bone Resorption, Metal Augmentation, Mechanical Experiment.

I. INTRODUCTION

Revision total knee arthroplasty (TKA) has been often used with a metal block augmentation for patients with poor bone quality. However, bone resorption beneath metal block augmentation has been still reported. The aim of the current study is to identify a possibility of the potential occurrence of bone resorption beneath metal block augmentation, through evaluation of strain distribution beneath metal block augmentation in revision TKA with metal block augmentation, during high deep flexion.

II. METHODS

LOSPA, revision TKA with a metal block augmentation was considered in this study. For the test, the tibia component of LOSPA was implanted to the tibia sawbone. The femoral component of LOSPA was mounted to a customized jig attached to the Instron 8872, which was designed specially to represent the angles ranged from 0° to 140°. Here, a compressive load of 1,600N (10N/s) was applied for each angle. Strain distribution was then measured from rosette strain gauge together (Fig 1).

III. RESULTS & DISCUSSIONS

The strain distribution on the cortical bone of the tibia was shown in Fig 2. The results showed that the

strains on the posterior region were gradually increased from extension to high deep of the knee joint. The strains on the medial region were gradually decreased after 60° or 90° flexion position.

Particularly, the strains on the medial region were generally lower than 50-100 μ strain, which is known as critical value range able to inducing bone resorption, during high deep flexion. This fact indicate that the medial region is possible a bone resorption.

IV. CONCLUSION

A possibility of the potential bone resorption occurrence in revision TKA used with a metal block augmentation may be dependent on loading patterns applied on the knee joint related to personal lifestyle history. Particularly, it may be relatively increased in patients who are frequently exposed to a personal lifestyle history with the loading conditions of the high flexion.

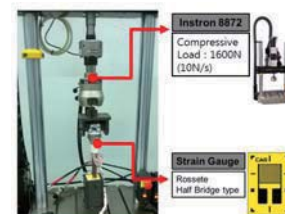


Fig. 1. Experimental Configuration

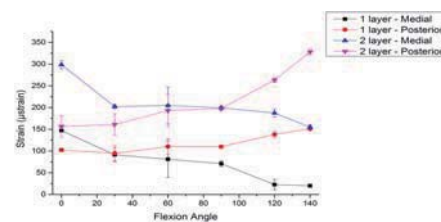


Fig. 2. Strain Distribution

ACKNOWLEDGEMENTS

This research was supported by a grant (15172 신기평 393) from Ministry of Food and Drug Safety in 2015.

Study on the Features of 3-axis Accelerometer Signal for Activity Monitoring and Step-count Detection

H. S. Park^{1,2}, I. W. Jung¹, Y. J. Lee¹, and I. Youn¹

¹Department of Bionics, Korea Institute of Science and Technology, Seoul, Republic of Korea

²Department of Biomedical Engineering, Korea University of Science and Technology, Daejeon, Republic of Korea

E-mail: iyoun@kist.re.kr

Abstract—This study describes detecting step-count methods and the classification of physical activities among level walking, ascending stairs and descending stairs activities using several feature extraction methods with a wrist-worn accelerometer. Physical activities using time-domain features and wavelet features were accurately classified and compared to the reference system, the accuracy of counting the number of steps was 97.21%. The finding showed reliable methods to measure gait patterns and step-counts during physical activity.

Keywords— 3-axis accelerometer, physical activity recognition, step-count, gait pattern, discrete wavelet transform

I. INTRODUCTION

The ability to monitor different movements and postures involved in daily life has received increasing attention due to a wide range of potential applications, including physical fitness tracking, rehabilitation, and sleep quality monitoring. There has been considerable research effort toward the monitoring and classification of physical activity patterns from body-fixed sensor [1,2]. In this research, we present methods to extract classification features from accelerometer signals to classify physical activities and count the number of steps.

II. METHODS

A. Sensing platform and dataset

Accelerometer data were collected using 9-axis MEMS sensor developed by Inversense, U.S. The sensor was attached to dominant wrist and set to 100Hz. Subjects completed routines of four different activities (level walking, running, ascending stairs, descending stairs).

B. Activity classification

For improving the accuracy of classification, we used time-domain features and wavelet features. The features obtained from time-domain signal were used to classify two activities (walking and running). The three walking activities (level walking, ascending stairs,

descending stairs) were classified by the features using DWT (Discrete Wavelet Transform).

C. Step count detection

Frequency-domain features were used to detect subjects' step count.

$$\text{Step Counts} = \sum_{i=1}^N (F * W)$$

F = frequency with maximum power

W=window size

N=Number of Windows

III. RESULTS

The time-domain based features showed accurate performance to classify two activities (walking and running). The features extracted by DWT classified correctly three activities of level walking and ascending/descending stairs (Figure 1). The step-count detecting accuracy rates were 97.21% by this algorithm.

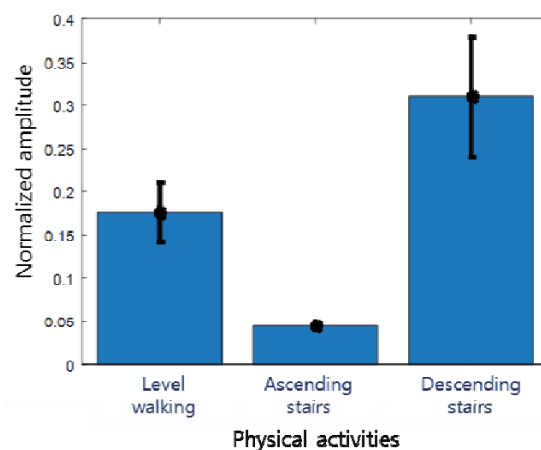


Fig. 1. Wavelet features of three activities

IV. CONCLUSION

Our results proved a reliable technique of measuring gait patterns and step-count during physical activity.

ACKNOWLEDGEMENT

This research was supported by the Bio & Medical Technology Development Program of the NRF funded

by the Korean government, MSIP
(2014M3A9D7070128).

REFERENCES

1. T. P. Kao, C. W. Lin, and J. S. Wang, "Development of a portable activity detector for daily activity recognition," *IEEE International Symposium on Industrial Electronics*, pp. 115-120, 2009.
2. A. Author and B. Author, "Machine Learning Methods for Classifying Human Physical Activity from On-Body Accelerometers," *Sensors*, vol. 10, pp. 1154-1175, 2010.

A Predictable development infant head-cervical spine model for measurable cranial deformation

Youngho Lee¹, Hoechan Kim¹ and Junghwa Hong^{1#}

¹Department of Control and instrumentation Engineering, Korea University, Se-Jong 339-700, Republic of Korea

[#]Corresponding author : Ph.D., Department of Control and Instrumentation Engineering, Korea University, 2511 Sejong-ro, Sejong 30019, Republic of Korea.
E-mail: hongjh32@korea.ac.kr

Abstract— The purpose of this study is to develop the detailed finite element model applying the biological trait of infant and babies based on the literature and video data. A detailed finite element model of the infant is formed the head part, cervical vertebra part and the upper body. Developed a detailed finite element model of the infant was fulfilled the intercomparison with hybrid III dummy model that have been used for validation is the most advanced human model among the currently developed human model. The verification is head part impact simulation using the impact hammer. The developed infant finite element model was confirmed that the behavior was similar to hybrid III dummy model. In addition to, comparison of deformation simulation result indicated that interface pressure was big differences between developed detailed infant finite element model and hybrid III dummy model. In this study, detailed infant finite element model which is measurable for occipital region deformation was developed and validated through simulation.

Keywords— Infant cranial, FEM, human model, cranial deformation

I. INTRODUCTION

Positional Plagiocephaly which is a kind of Plagiocephaly is caused cranial deformation occurred by external force. [1] Before-4-month-old infant usually lie in a row in uniform sites of the cranium because muscle strength is not enough to move the head. Especially, as the skeleton of Infant who get sleep 14 to 18 hours per day is composed of cartilage approximately 80% or more, so a correct posture of sleep is necessary in order to prevent Positional Plagiocephaly. Moreover, the cranium have the alcification low level of bone, therefore, the structure is flexible and soft, so likely to be change. Thus, due to the supine position of sleeping for a long time, the number of infant patient whose occipital is repeatedly pressed get the transformation of occipital bone.[2-4] Since the previously developed models (CRABI, Q3, Hybrid III, etc) were designed to evaluate the injury by

car accidents. And there is no model that can predict the deformation of the skeleton because they are consisted with multi body.

II. METHODS

In this study, use adult finite element model and remove unnecessary elements and remodel the cranium and the cervical spine and scaling and rework mesh and simulate a developed infant finite element model by Madymo program. A model is consisted of shell elements to express similar form to cranium and divided to frontal bone, parietal bone, temporal bone and occipital bone, and connect between bone and bone to supplement elements in order to express sutures. To express a detailed model, compose additionally meninges and brain. Scalp and brain is composed to solid element and meninges is composed to shell element. An infant finite element cervical spine model consist of cortical bone, annulus fibrosus and nucleus pulposus, and consist of solid element. Ligament is modeled by truss element which can cause resistance if it is a shortening structure on a single load. This model is compared with Hybrid III dummy model by impact hammer test and head freefall by acceleration of gravity to a mat. A mat is divided to each layer, upper layer is transmutable material. And two case that stiffness is rigid and soft.

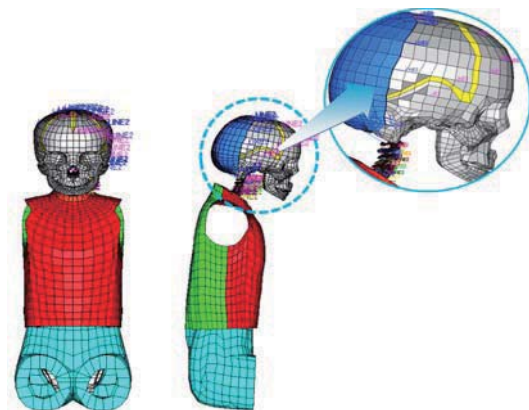


Fig. 1. An infant finite element model of the head-cervical spine restricted at center of upper body

III. RESULTS

Comparing simulation between a developed infant model and hybrid III dummy model using impact hammer test, at front impact, development child model is 2113.0m/sec² and hybrid III dummy model is 1786.1m/sec² as linear acceleration and development child model is 8617.4rad/sec² and hybrid III dummy model is 8817.7rad/sec² as angular acceleration. At rear impact, development child model is 2385.1m/sec² and hybrid III dummy model is 2049.6m/sec² as linear acceleration and development child model is 6155.0rad/sec² and hybrid III dummy model is 6877.9rad/sec² as angular acceleration. The result of simulation of freefall by acceleration of gravity, contact area and interface pressure of a developed infant model and hybrid III model are following when a stiffness of a mat is rigid of soft.

Table 1. Result of Impact hammer simulation test

acceleration	Front impact		Rear impact	
	Linear [m/sec ²]	Angular [rad/sec ²]	Linear [m/sec ²]	Angular [rad/sec ²]
Development Child model	2113.0	8617.4	2385.1	6155.0
Hybrid III dummy model	1786.1	8817.7	2049.6	6877.9

Table 2. Compare simulation results of different mat

	Contact area [mm ²]		Interface pressure [KPa]	
	Rigid	Soft	Rigid	Soft
Development Child model	3100 (7.03%)	11369 (25.78%)	5.27	0.07
Hybrid III dummy model	1550 (3.51%)	12745 (28.90%)	8.82	0.10

IV. CONCLUSION

In this study, a predictable development infant head-cervical spine model by reconstitution and scaling of the model based on the reference and image data in adult head-cervical spine model. The head is composed of scalp, cranium, meninges and brain, and the cervical spine is composed of cortical bone, annulus fibrosus, nucleus pulposus, and ligament. Ligament is expressed by using truss element, and each element is linked by using spring-damper. As verification of model is impact test by using impact hammer, we confirm similar tendency between the development infant model and hybrid III dummy model by comparing linear acceleration and angular acceleration. In simulation of stiffness of a mat if material of a mat is soft we confirm that pressure distribution of scalp occur evenly and interface pressure is low. Through a infant finite element model, we develop a predictable model for deformation of cranium depending on a load

form. If developing the structure of head to detail and supplement the shape of infant cranium by three-dimensional CT and MRI, the model is considered to be a more accurate model to predict deformation of cranium.

ACKNOWLEDGEMENT

This work was supported by the Industrial Strategic technology development program (No.10045347, Development of the pelvic airbag cushion system for absorbing falling impact energy at falling of the elderly and disables) funded by the Ministry of Trade, industry & Energy(MI, Korea)..

REFERENCES

1. M. B Habal "Avoiding the sequel associated with deformational plagiocephaly" Journal of Craniofacial Surgery 14(4), 430-437(2003)
2. Timothy R. Littlefield, Jeanne K. Pomatto, and Kevin M. Kelly. "Dynamic orthotic cranioplasty: treatment of the older infant. Report of four cases" Neurosurgical Focus. 9(3), 1-4. (2000)
3. John M. Graham, Jeannie Kreutzman, Andy Halberg, Carlos Samayoa, and Xiuqing Guo, "Deformational Brachycephaly In Supine-Sleeping Infants." The Journal of Pediatrics February: 253-257 (2005)
4. Walker ML, Conllins JJ. "Nonsyndromic craniosynostosis and abnormalities of head shape." Youmans neurological surgery, 5th edition, Elsevier : 3300-3314. (2004)

Gait Phase Detection using FSRs during Level-Ground Walking

J. Y. Cha¹, J. U. Chu¹, Y. H. Choi¹ and J. U. Jung¹

¹Daegu Research Center for Medical Devices and Rehab. Engineering, Korea Institute of Machinery & Materials, Daegu, Korea
E-mail: jjoung@kimm.re.kr

Abstract—In developing ankle-foot prostheses for amputees, accurate gait phase detection is an important factor. Inaccurate detection can easily lead to falls while walking. To address this, we performed gait phase detection studies using FSR sensors to obtain stable results.

Keywords— Gait Phase Detection. Force Sensitive Resistor (FSR). Robotic Ankle-Foot Prosthesis.

I. INTRODUCTION

The active prosthetic foot/arm was recently developed, and some are commercially available to patients who have lost an arm or foot due to diabetes complications or peripheral arterial diseases. In developing prosthetic feet, precise gait recognition is an important component along with hardware development. In this study, we investigate gait phase detection using FSR sensors during level-ground walking.

II. METHODS

A typical level-ground walking gait cycle is divided into five phases: heel strike, foot flat, heel rise, push-off, and toe-off (Fig. 1).



Fig. 1 A typical level-ground walking gait cycle

Since each phase in a level-ground walking gait cycle has a difference contact point between the foot and the ground. FSR sensors (Interlink Electronics, FSR 402) were located at four points on the insoles of shoes to measure voltage changes during level-ground walking (Fig. 2 (a)). The sensor signals were sampled at a frequency of 1000 Hz at 16-bit resolution.

III. RESULTS

Raw data with no sensor calibration and the resultant waveform from the gait phase detection algorithm are shown in Fig. 2 (b).

Fig. 2 (c) shows the real-time processing results for the normal patient during level-ground walking.

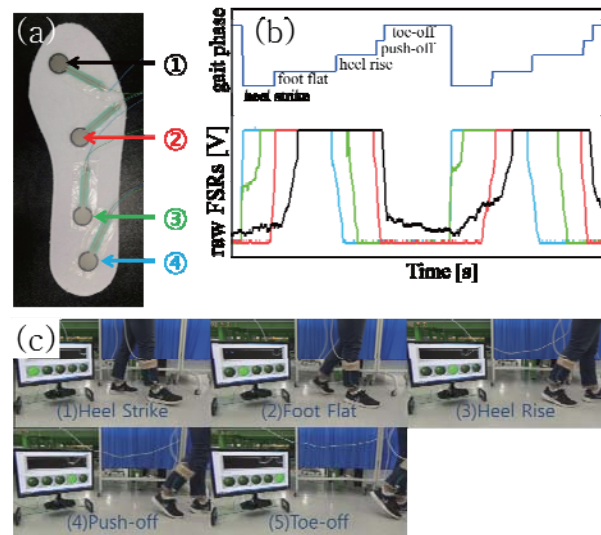


Fig.2 (a) FSRs adhesion position, (b) raw data by FSRs (bottom) and resultant waveform from gait phase detection (upper), and (c) real-time processing results

IV. CONCLUSION

We obtained a stable result in this study by developing a gait phase detection algorithm using FSR sensors. While the results from an encoder and a potentiometer were not presented in this study, we are trying to improve the detection ability with ankle angle and torque detection adding this FSRs results. This capability will be applied to the development of robotic ankle-foot prostheses.

ACKNOWLEDGEMENT

This work was supported by KIMM (NK186G).

REFERENCES

1. I. P. I. Pappas, M. R. Popovic, T. Keller, V. Dietz, and M. Morari, "A Reliable Gait Phase Detection System," *IEEE Trans Neural Syst Rehabil Eng*, vol. 9, no. 2, pp. 113-125, 2001.
2. S. R. Lee, G. S. Heo, O. H. Kang and C. Y. Lee, "Recognition of Stance Phase for Walking Assistive Devices by Foot Pressure Patterns," *J of Institute of Control Robotics and System*, vol. 17, no. 8, pp. 223-228, 2011.

A study of artificial disc nucleus replacement for human lumbar spine discs restoration

Taekyeong Lee¹, Junghwa Hong^{1#}

¹Department of Control and instrumentation Engineering, Korea University, Se-Jong 339-700, Republic of Korea

[#]Corresponding author: Ph.D., Department of Control and Instrumentation Engineering, Korea University, 2511 Sejong-ro, Sejong 30019, Republic of Korea.

E-mail: hongjh32@korea.ac.kr

Abstract—Discogenic back pain is associated with degenerative changes of the lumbar intervertebral disc, but the cause of discogenic pain varies and is often uncertain. Although poorly understood, the concept of discogenic pain has paved the road for a myriad of conservative and surgical therapeutic procedures. Recent innovative motion - sparing surgical techniques include artificial disc replacement technologies, posterior dynamic stabilization, and disc nucleus replacement etc. Disc nucleus replacement is one of the viable options for degenerative disc disease treatment without fusion. The objective of this was a study of artificial disc nucleus replacement for human lumbar spine discs restoration.

Keywords— Lumbar spine, Artificial discs, FEM.

I. INTRODUCTION

Lately, the incidence of the back pain is one of the disease that is difficult to treat and most highly occurred. It takes to greater economic burden directly or indirectly for treatment. Kwok et al reported that age-related disc changes could be affected by change in vertebral body shape because of the decreasing BMD by aging. [1] Likewise, discogenic back pain is occasioned by the disc degeneration or injury such as abnormal change by aging or accident. There are treatments which are for the spinal surgery such as spinal fusion, artificial disc implantation, discectomy, nucleotomy etc. The most of treatments, however, lead to side effects.[2-3] One of the treatment that minimally invasive procedure takes advantage of reduction of unnecessary exposure and tissue trauma. This procedure has advantage but no absolute standard of treatment for spine disorder because of technical limitation and other factors like fiberized nucleus pulposus. The aim of this study is to provide a methodology of artificial disc implantation by minimally invasive surgery using fluid type artificial nucleus pulposus.

II. METHODS

The parameter of artificial disc was figured out when 2types of artificial intervertebral discs were replaced by minimally invasive surgery using FEM.

The balloon typed fluidic artificial nucleus system is designed to replace the nucleus pulposus for low back pain caused by degenerative intervertebral disc disease through comparing 2-difference type model.

The three-dimensional finite element model (FEM) of the lumbar spine were reconstructed based on computed tomography (CT) images. Two types of FE lumbar spine model were acquired from reference model, compared with each model through finite element analysis was performed. The reference model is produced intact L4-L5 lumbar model to represent the actual behavior of the lumbar spine. This is to determine the effect of a single disc, the L1-L3 was removed from the entire L1-L5 lumbar spine model to L4-L5 lumbar spine model based on partial model was designated. (Fig. 1) Other models are produced fluid cavity model and fluid cavity contact model. Fluid cavity model is replaced nucleus pulposus as a fluid cavity, fluid cavity contact model is that the balloon part is replaced fluid cavity then, nucleus pulposus is removed. Part of the fluid entering nucleus pulposus is construct that fluid flux is possible through reference node of center of fluid cavity. This is possible to measure fluid pressure by fluid flux that the model is produced for setting up the required pressure after making artificial disc for the surgery. (Fig. 2, Fig. 3)



Fig. 1. Reference model

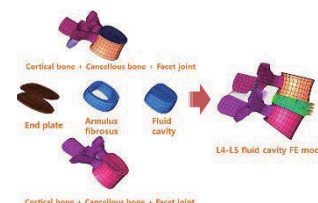


Fig. 2. Fluid cavity model. Nucleus pulposus was replaced by fluid cavity that could be measured nucleus inner pressure

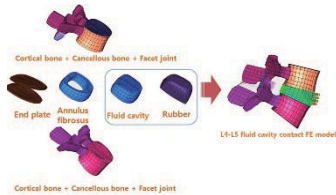


Fig. 3. Fluid cavity contact model. Balloon was replaced by fluid cavity that could be measured nucleus inner pressure

III. RESULTS

The design variables of fluid cavity and fluid cavity contact model were single variable which is pressure by fluid flux so that the relationship of fluid flux-displacement was acquired from 2types results of fluid flux because optimal design was not necessary. The design variables of fluid cavity and fluid cavity contact model were single variable so that fluid pressure results were deducted which was similar to reference model behavior. From fluid cavity model, relation between displacement and fluid pressure was obtained that deduction of intradiscal pressure from relation of fluid flux-deflection. (Table 1)(Fig. 4) Using this result, proper fluid pressure was obtained 0.30536MPa. Under axial compression of 400N, deflection of reference model is -1.125mm, fluid cavity contact model is -1.129mm. Under axial compression of 400N and pure moment of 6Nm, deflection of reference model is -1.812mm, fluid cavity contact model is -1.872mm. Under same condition, rotation angle was that reference model is 1.348°, fluid cavity contact model is 1.519° (400N). Reference model is 5.305°, fluid cavity contact model is 5.844° (400N and 6Nm). (Fig. 5)

Table 1. Inference of FMF (Fluid Mass Flux) by Reference Model deflection under axial load

Loading Condition (N)	Displacement of Reference Model (mm)	Fitting FMF Values of each Displacement (kg/sec)
400	-1.1288	1.54E-04
600	-1.63568	1.32 E-04
800	-2.11757	1.01 E-04
1000	-2.58814	7.36 E-05
1200	-3.05819	7.03 E-05

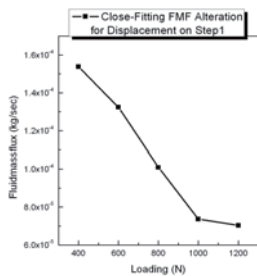


Fig. 4. Close-Fitting FMF alteration for displacement on axial force

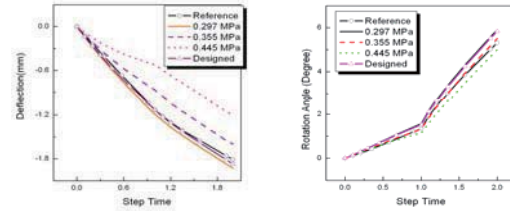


Fig. 5. Comparing reference model with fluid cavity model

IV. CONCLUSION

This study started to minimize that disadvantage and acquired a good result even some deficiency like clinical study and reduction of repetition on experiment. In this study two kinds of model were compared, and figured out which one the better effect for artificial disc. Artificial nucleus pulposus of fluid cavity FE model is easy to control and accessibility. Using the result, it's possible to make fluid type artificial nucleus pulposus.

ACKNOWLEDGEMENT

This research was supported by a grant of the Korea Health Technology R&D Project through the Korea Health Industry Development Institute (KHIDI), funded by the Ministry of Health & Welfare, Republic of Korea (grant number : HI15C1025).

REFERENCES

1. Kwok AW, Wang YX, Griffith JF, Deng M, Leung JC, Ahuja AT, et al. Morphological changes of lumbar vertebral bodies and intervertebral discs associated with decrease in bone mineral density of the spine: a cross-sectional study in elderly subjects. Spine. 15;26(6):652-7, 2012.
2. Yorimitsu E, Chiba K, Toyama Y, Hirabayashi K. Long-term outcomes of standard discectomy for lumbar disc herniation: a follow-up study of more than 10 years. Spine, 2001.
3. Kumar MN, Jacquot F, Hall H. Long-term follow-up of functional outcomes and radiographic changes at adjacent levels following lumbar spine fusion for degenerative disc disease. European spine journal : official publication of the European Spine Society, the European Spinal Deformity Society, and the European Section of the Cervical Spine Research Society. 10(4):309-13, 2001.

Characteristics of Cycle Pedaling Cadence by Index of Effectiveness

J. W. Seo¹, D. W. Kang¹, D. H. Kim¹, S. T. Yang¹, J. S. Choi^{2,3} and G. R. Tack^{2,3}

¹Department of Biomedical Engineering, Graduate school of Konkuk University, Chungju, Korea

²Department of Biomedical Engineering, College of Biomedical & Health Science, Konkuk University, Chungju, Korea

³BK21 Plus Research Institute of Biomedical Engineering, Konkuk University, Chungju, Korea

E-mail: grtack@kku.ac.kr

Abstract— Aim of this study is to investigate effects of cycle pedaling cadence by index of effectiveness (IE). Eight subjects performed 2 min pedaling with 40, 60 and 80 rpm. Results showed that the significant differences in IE at total & each phase among the 40, 60, 80 RPM except for the phase 3. The optimal cycle exercise cadence can identify by IE.

Keywords— Cycle pedaling, Index of Effectiveness, Optimal cadence.

I. INTRODUCTION

A proper load and cadence lead to the effective exercise. The preceding study has shown that optimal pedaling was performed between 60 to 80 RPM by examining average power against cadence [1]. However, it is necessary to study actual pedal force based on the index of effectiveness (IE), not power itself. Thus, this study tried to examine the cadence on the effectiveness of cycle pedaling using IE. IE is defined as the ratio of the force perpendicular to the crank (effective force) and the total force applied to the pedal (resultant force) [2].

II. METHODS

Eight male subjects (age: 24.0±2.4 years, height: 174.6±5.3 cm, weight: 70.5±11.2 kg, inseam: 77.8±4.5 cm) participated in two minutes 40, 60 & 80 RPM cycle pedaling tests with the same load. Subject's saddle height was determined by 25° knee flexion angle when the pedal crank was at the 6 o'clock position. A 3D motion analysis system with six infrared cameras (Motion Analysis Corp., USA) and 3-axis pedal force plate (Dacell Corp, Korea) were used to acquire kinematic and pedal reaction force data with 120 Hz and 1,200 Hz frequency, respectively. IE was compared by measuring 3D motion and 3-axis pedal reaction force data during 4 pedaling phases (Total phase:0°-360°, phase1: 330°-30°, phase2: 30°-150°, phase3: 150°-210°, phase4: 210°-330°). All calculation was carried out with MATLAB R2013a (Mathworks Inc., USA) software. Statistical analysis was carried out using SPSS v 22 (IBM Co., USA). Repeated measure ANOVA was used to investigate the

difference and Bonferroni correction was used to locate the differences ($\alpha=.05$).

III. RESULTS & DISCUSSION

Results showed that the significant differences in IE at total & each phase among the 40, 60, 80 RPM except for the phase 3. The 80 RPM pedaling performed more efficiently than 40 and 60 RPM pedaling (Fig.2). It means that the cadence affects the pedaling effectiveness. It is believed that change in cadence caused a change in muscle coordination pattern since there might be inappropriate muscle coordination and recruitment in the outside of appropriate cadence region.

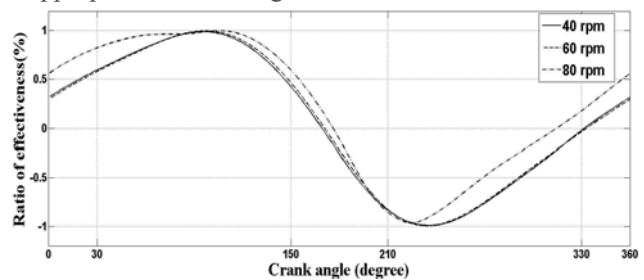


Fig. 1. Average ratio of effectiveness by RPM

Table 1. IE at each phase due to RPM

	Total phase	Phase 1	Phase 2	Phase 3	Phase 4
40	0.35 ±0.04 [#]	0.34 ±0.09 [#]	0.82 ±0.02 [*]	-0.13 ±0.07	-0.66 ±0.03 [*]
60	0.43 ±0.03 ^{*s}	0.33 ±0.13 ^{*s}	0.83 ±0.03 [#]	-0.09 ±0.13	-0.62 ±0.08 [#]
80	0.56 ±0.03 ^{#s}	0.55 ±0.18 ^{#s}	0.92 ±0.03 [#]	0.04 ±0.17	-0.37 ±0.11 [#]
Main effect	.00 [*]	.00 [*]	.00 [*]	NS	.00 [*]
P	.01 [*] .00 [#] .00 ^s	.01 [*] .00 [#] .00 ^s	.00 [*] .00 [#]	NS	.00 [*] .00 [#]

Repeated measure ANOVA & Bonferroni, M ± SD, NS: No significant
*, #, s $p < .05$

REFERENCES

1. M. Sacchetti, M. Lenti, A Di palumbo and G. De vito, "Different effect of cadence on cycling efficiency between young and older cyclists," *Med Sci Sports Exerc*, vol. 42, pp. 2128-2133, 2010.
2. R. R. Bini, P. Hume, J. Croft and A. Kilding, "Pedal force effectiveness in cycling: a review of constraints and training effects," *J Sci Cycling*, vol. 2, pp. 11-24, 2013.

Regularity of the Upper Body Accelerations during Walking in Patients with Parkinson's Disease

J. W. Kim¹, Y. R. Kwon¹, and G. M. Eom^{1,2}

¹School of Biomedical Engineering, Konkuk University, Choonju, Korea

²Research Institute of Biomedical Engineering, Konkuk University, Choonju, Korea

E-mail: kjw802@kku.ac.kr

Abstract— The aim of this study was to investigate regularity of upper body accelerations during level walking in patients with Parkinson's disease (PD) in comparison with normal (young and elderly) subjects. Twenty-six young subjects, twenty-nine elderly subjects and twenty-three PD patients participated in this study. Upper body accelerations were measured during level walking using 3-axis accelerometers located at pelvis, shoulder, and head. Effect of disease was observed only in vertical direction in all body parts. The result suggests that PD patients' walking is less rhythmical compared to those of normal (young and elderly) subjects.

Keywords— Gait regularity, level walking, upper body, Parkinson's disease, acceleration

I. INTRODUCTION

Movements of upper body, as well as lower body, may be relevant and informative for the investigation of pathological effect in the gait strategy [1]. The aim of this study was to compare regularity in the accelerations of upper body parts during level walking in normal subjects (young and elderly) and patients with Parkinson's disease (PD).

II. METHODS

A. Experiments and Outcome Measures

Twenty-six young subjects (21±1 years), 29 elderly subjects (70±6 years) and 22 PD patients (69±9 years) participated in this study. All subjects were instructed to walk straight along a 12 m on a straight walkway at self-selected comfortable speeds. Accelerometers (Trigno wireless system, Delsys, MA) were used to measure the acceleration at pelvis, shoulder, and head with sampling frequency of 1kHz.

B. Analysis

Coefficient of variation (CV) of acceleration data was used to represent gait regularity of the subjects. Analysis of variance (ANOVA) and post hoc (Tukey) test were performed to investigate any subject group difference. The statistical analyses were performed using SPSS ver.16 for Windows (SPSS Inc., Chicago, IL, USA).

III. RESULTS

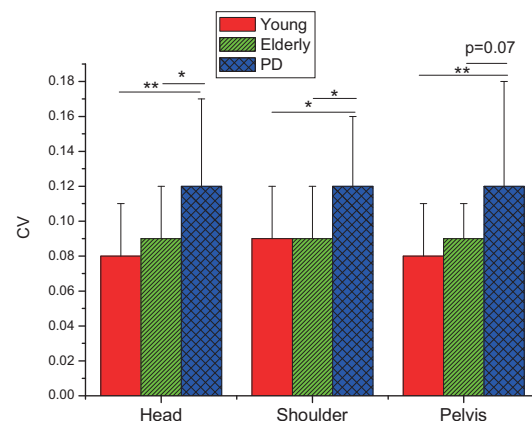


Fig. 1 Comparison among the groups in gait regularity of vertical direction

Regularity of patients at all body parts were significantly greater than those of normal (young and elderly) subjects only in vertical direction ($p < 0.05$). There was no significant difference between young and elderly subjects. This indicates that PD patients walked with less regularity compared to normal (young and elderly) subjects.

IV. CONCLUSION

PD patients had less stable gait rhythmicity in upper body than young and elderly subjects. This information may be useful to understand the gait strategy in PD patients.

ACKNOWLEDGEMENT

This study was supported by Basic Science Research Program through the National Research Foundation of Korea and Business for Cooperative R&D between Industry, Academy and Research Institute funded the Ministry of Education and Korea Small and Medium Business Administration (2014R1A1A2057508, C0297714).

REFERENCES

1. J. J. Kavanagh, R.S. Barrett, and S. Morrison, "Upper body accelerations during walking in healthy young and elderly men," *Gait and posture*, vol. 20, pp. 291-298, 2004.

Basic Gait Analysis of Knee Brace for Leisure Sports Gear

S.J. Kang, Y.H. Chang C.Y. Ko, J.C. Ryu, M.S.Mun

Korea Orthopedics & Rehabilitation Engineering Center
Research Team, Incheon, Korea
E-mail: vvibe637@nate.com

Abstract— For the operation to run or jump landing to the hip impact force and absorb the kinetic energy is applied knees and ankles, Role of the knee is more great. Therefore, the knee is frequently injured area well, for those athletes that a lot of the action that the running or jumping. The greater the injury of the knee joint is often generated large physique. Foot problems are often about 10% of the population, such as metatarsal and hallux rigidus barrel and foot fasciitis problem. In particular, a common symptom in 24% of more than 65 years and it is inconvenient for everyday life

Keywords—Knee brace, Sports Gear, Sports ,Biomechanics, Sports medicine,

I. INTRODUCTION

For the operation to run or jump landing to the hip strength and shock absorbing kinetic energy applied weight, knee, ankle receive greater the role of the double lap. Therefore, the run or injuries that occur frequently to athletes without repeating the behavior that you can jump in the sport are knee. The higher the physique of a knee injury frequently occurs in large. Days to provide the optimum gear for sports injury prevention and rehabilitation and training of the knee joint is one of the most important problems in the field of sports medicine. And supporting the weight Biomechanical with Knee brace is wrapped around the knee, the unit distribute the power to the minimum to be applied per area, the muscles for movement of the knee has to be designed / it produced the optimum shape so as not to degrade the function currently being used The brace is your representative in Defiance Custom Knee Brace with Hitech Knee brace, which is being used for injury prevention in various sporting activities. However, sporting activities and basic research for the design of your knee brace for injury prevention and rehabilitation of joint and executive, it is necessary data accumulation through kinematic and kinetic data acquisition. Knee guards, but to demonstrate the motor skills, abnormal movements, it was conceived with the aim of prevention. In particular, the tibia with respect to the femur (femur) (tibia) is a function that prevents an excessive movement in the

forward direction to the [1]. Improvement of exercise performance by these features (Rebel & Paessler, 2001), reduction in the activity four bridge branches muscle (quadriceps) [2], there is an effect, such as excessive load reduction [3] as applied to the anterior cruciate ligament. Studies of high load or an unexpected load, while it does not protect the knee when subjected also been reported[4]. As such the efficacy and benefits of knee situation is still controversial. In this study, not the 3D motion analyzer through the EMG analysis of the muscle, then you brace attached to the activities of the Relief and neopda Rhine-pronged muscle of the knee joint during exercise verify that reduction..

II. METHODS

The subjects participated in this study, 25 ~ 30 (27.9 \pm 3.8) normal males between the ages of five adults. Person who has experienced injury in the past or currently injured were excluded from this study. Obtaining consent to participate in the experiment was carried out in this study. The knee pads used in the experiments (CTi, OSSUR, USA) is the same as in Figure 1, the knee's ACL, MCL, was designed to protect the PCL ligaments. By attaching the reflective markers 29 on the anatomical location of the subjects performed a static test, and, after removing the four inner markers was performed dynamic scan. The subjects were repeated a total of 3 times jump in the two conditions then you Bridget S. worn before eight while walking infrared cameras (Eagle4, Motion Analysis, USA) of the kinematic data and thigh muscle with a sampling rate of 120Hz using EMG was obtained.

IV. RESULTS

Than if the patient is not wearing a jump time, and jump knee brace be worn inside the knee rotation was smaller (Table 1). If you did not wear your brace with medial rotation of the knee increases, as well as the flexor of the knee affects the contraction of the adductor and abductor muscle, muscle activity is increased

Table 1 Knee

Biomechanical Assessment of Novel Bone Lengthening Plate by Changing Material Properties of Supporting Axis

T. G. Jung¹, S. W. Suh², J. H. Yang², and D. W. Han³

¹Department of Medical Device Development Center, Osong Medical Innovation Foundation, Cheongju-si, Chungbuk, Korea

²Scoliosis Research Institute, Department of Orthopedics, Korea University Guro Hospital, Seoul, Korea

³Department of Nanomedical Engineering, Pusan National University, Busan, Korea

E-mail: nanoohan@pusan.ac.kr

Abstract—The purpose of this study is to describe a novel bone lengthening plate (BLP) and evaluate the biomechanical performance of the plate before clinical use with the finite element analysis. The structural stiffness was measured by changing the material properties of the supporting axis, including the lengthening shaft and column. Peak von Mises Stress, risk of screw breakage between the bone and screw were also evaluated. Results showed a 158% decrease in the structural stiffness when the distraction length was increased from 10mm to 30mm. The first locking screw which was inserted at the osteotomy site of the proximal femur in the proximal to distal direction showed the highest risk of breakage (75%).

Keywords— Femur, Finite Element Analysis, Bone Lengthening Plate, Distraction, Von Mises Stress.

I. INTRODUCTION

External fixators, such as mono fixators and circular fixators, are commonly used in distraction osteogenesis. However, external fixators can cause a variety of complications leading to discomfort while walking[1].

The purpose of this study is to describe a novel bone lengthening plate and evaluate the biomechanical performance of the plate before clinical use with the finite element (FE) analysis.

II. METHODS

In this study, we introduce a novel bone lengthening plate (BLP) that uses an internal form of a plate for distraction osteogenesis. The novel bone lengthening plate functions as a lengthening agent by using the one threaded axis and two columns between separated proximal and distal plates. In addition, although BLP is form of plate, it functions as an external fixator due to its use of the locking plate and screw system. The FE analysis is used to evaluate the performance of the BLP. The biomechanical stability of the BLP was analyzed after verifying the following: the FE model of the femur using in-vitro test of cadaveric femurs during a compression test and the FE model of the osteotomized femur with the BLP undergoing distraction with in-vitro cadaveric test under compression load. The Structural stiffness was measured by changing the material properties of the supporting axis, including the lengthening shaft and column(Table 1)[2]. Peak von Mises Stress and risk of screw breakage between the bone and screw were also

evaluated.

Table 1. Material variations of components in BLP

	Lengthening Shaft	Columns
Type I	Titanium alloys	Titanium alloys
Type II	Co-Cr alloys	Titanium alloys
Type III	Titanium alloys	Co-Cr alloys
Type IV	Co-Cr-alloys	Co-Cr-alloys

III. RESULTS

The structural stiffness of the femoral FE model and the bending stiffness of the BLP FE model were similar to those of test on the cadaveric femurs and the BLP respectively. Furthermore, the structural stiffness of the FE model of the osteotomized femur with the BLP undergoing distraction manifest similar to the cadaveric test results. The FE analysis of the BLP attached femur was carried out while varying both the BLP's distraction conditions and its supporting axis's material property. Results showed a 158% decrease in the structural stiffness when the distraction length was increased from 10mm to 30mm; moreover, a 128% increase in the structural stiffness was manifest as different BLP materials were substituted from Type I to Type. The first locking screw which was inserted at the osteotomy site of the proximal femur in the proximal to distal direction showed the highest risk of breakage (75%).

IV. CONCLUSION

This study investigated the biomechanical stability of the new bone lengthening plate's supporting structures by taking into account its material properties. The bone lengthening plate appeared to be most biomechanically stable when the column and lengthening shaft were composed of Cobalt-Chrome-alloys.

REFERENCES

1. O. Baran, H. Havitcioglu, H. Tatari, and B. Cecen, "The stiffness characteristics of hybrid Ilizarov fixators" *J. Biomech.*, vol. 41, pp. 2960-2963, 2008.
2. J. Stolk, N. Verdonshot, L. Cristofolini, A. Toni, and R. HuiskesO, "Finite element and experimental models of cemented hip joint reconstructions can produce similar bone and cement strains in pre-clinical tests" *J. Biomech.*, vol. 35, pp. 499-510, 2002.

A Novel Jig System of Expulsion Test for Intervertebral Fusion Device

J. W. Yang, J. H. Park, D. G. Kim, J. Y. Jeong, Y. H. Jeong, and T. G. Jung

Department of Medical Device Development Center, Osong Medical Innovation Foundation, Cheongju-si, Chungbuk, Korea

E-mail: bygon@kbio.kr

Abstract— This work shows the novel designed jig system of expulsion test for spinal cage which can lead to be more accuracy. A novel jig could be better to apply more constant pressure than that of previous system.

Keywords— Expulsion test, Intervertebral fusion device, Cage migration, Universal Test Machine.

I. INTRODUCTION

The intervertebral fusion device (Spinal cage) has been contributed to improve the stability and fusion rate of lumbar that can be applied with surgical treatment for the degenerative spinal disease. But, some of patient reports show the side effect of cage migration that can cause back pain and waist-down paralysis after surgery [1]. Recently, the expulsion test system has been developed to analyze the risk of cage migration which could be utilized as an evaluation indicator to have the stability of spinal cage. From previous system of loading device for expulsion test, it has not enough test usability and equality of pre-loading to hold the cage with the reason of the problem from multi-axis guide which can cause the oblique phenomenon from the pre-load plate to the specimen [2].

The object of this work was to investigate *the pressure distribution on the novel jig system for expulsion test of spinal cage migration* by comparing with that of previous system.

II. METHODS

Novel jig system of expulsion test was consisted of horizontal plate to combine with universal test machine (UTM, MTS 858 Bionix, MTS System Corp., USA), load cell (MNC-100L, CAS, Korea) to apply pre-load for clamping of a specimen with lateral direction, and rod to apply compressive load on a specimen with downward, respectively (Fig. 1).

A horizontal plate was designed to adjust the center of cage specimen can apply constant load from the actuator, jig system was consisted of pre-load plate and load cell to hold a specimen. Pressure distribution of jig system was measured on a pressure sensor (*k*-scan EH-2, Tekscan, USA) to verify the oblique phenomenon between pre-load plate and specimen (N=5). Specimen pre-load was 500 N with uni-axis guide.

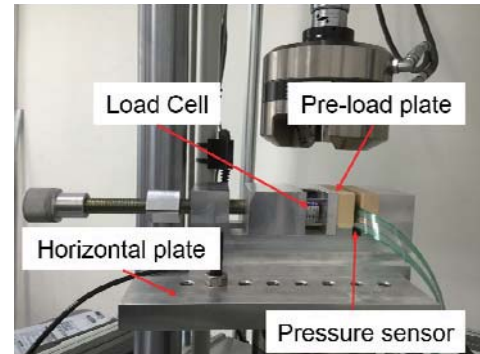


Fig. 1. Expulsion test system set up.

III. RESULTS

A novel jig system of expulsion test could be applied constant and stable pressure ($500 \pm 1.66\text{N}$) on the cage specimen [Fig. 2 (a)] while the pre-load was constantly distributed as shown in the sensor image [Fig. 2 (b)] without oblique phenomenon and tilt of the pre-load plate.

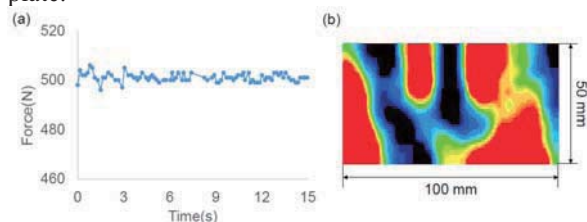


Fig. 2. (a) Force-time data acquisition and (b) sensor image of pressure distribution with novel designed jig system.

IV. CONCLUSION

This study suggests that novel jig system of expulsion test designed to apply constant pressure without any of oblique phenomenon which also has an advantage of versatile application can easily utilize for several kind of UTM and use for the unskilled operator.

REFERENCES

1. J. Chrastil and A. A. Patel, "Complications Associated With Posterior and Transforaminal Lumbar Interbody Fusion," *J Am Acad Orthop Surg.*, vol. 20, pp. 283-291, 2012.
2. V. K. Goel, D. David, M. Jackson, H. Kuroki, and N. Ebraheim, "Expulsion Testing of an Intervertebral Fusion Cage: Effect of Tooth Design on Pull out Resistance," *Summer Bioengineering Conference abstract*, 2003.

Evaluation of Contact Pressure at Articular Surface of Knee in Neutral, Varus and Valgus Alignment

Jeongwoo Seo¹, Oui Sik Yoo¹, Yong In², Byoung Min Kang²,
Doo Hoon Sun^{1,3}, Yong-Sik Kim²

¹R&D Center, Corentec Co., Ltd., Cheonan, Korea

²Department of Orthopedic Surgery, Seoul ST. Mary's Hospital, Seoul, Korea

³Department of Orthopedic Surgery, Sun General Hospital, Daejeon, Korea

E-mail: iy1000@catholic.ac.kr

Abstract—The knee alignment affects surface contact condition. Contact analysis was performed in varus, neutral, and valgus. The contact pressed area is greatest in neutral stance. The maximum value of contact stress is no visible difference among stances. When contact pressed area is greatest, the contact stress can be induce lowest. But the alignment does not make critical maximum stress among them.

Keywords—contact analysis, total knee replacement, varus, valgus

I. INTRODUCTION

Although a surgeon try to correct the alignment of a knee joint in TKR(Total Knee Replacement), sometimes varus/valgus alignment has been tried in order to reconstruct function of knee joint. As a result, the varus or valgus alignment affects to ligaments and soft tissue, and the contact condition is changed between femoral component and tibial insert. One of important factor, wear characteristics of an implant can be changed due to the contact condition. In this study, we performed static contact tests from extension to flexion in varus and valgus to define the effect to contact condition when the alignment is varus or valgus.

II. METHODS

LOSPA TKR femoral component #6 and Tibial insert #5 manufactured by Corentec Co., Ltd. were used as test specimens. The tests have performed with adapting ASTM F2777-10[1]. The test set like as Fig. 1. The load is applied at 7:3 ratio of lateral-medial by adapting gait analysis. The 5° of jig is used to compare the result in neutral, varus and valgus. The fuji films were used in tests were scanned, and the results were analyzed the compressed area and contact stress as angles of flexion in neutral stance and varus/valgus from scanning. The tests were performed 5 times per each for reliability.

III. RESULTS

The results of compressed area became decreasing as the angle of flexion was increased. The compressed areas in varus alignment was little smaller than the

results in varus. The compressed areas in neutral stance were the greatest in all results(Fig. 2). There were little differences between the results in varus and valgus in view point of peak contact stress(Fig. 2).

IV. CONCLUSION

Because the neutral stance makes the compressed area become more increasing than varus/valgus alignment, so that the lowest contact stress is induced between femoral component and Tibial insert. There is little difference between varus and valgus in viewpoint of peak contact stress if the varus/valgus alignment is not excess. It is considered that the alignment is tried to correct because low contact stress makes wear improve[2].



Fig. 1. Test sets-up of contact analysis in varus(left), neutral(middle), and valgus stance(right)

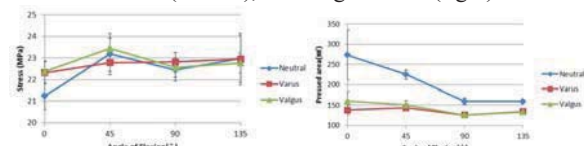


Fig. 2. Results of contact pressed area(left) and maximum contact stress(right) in varus, neutral, and valgus stance.

ACKNOWLEDGEMENT

This study was supported by ‘Advanced Technology Center(Project number:10048394)’.

REFERENCES

1. ASTM F2777-10 ‘Standard Test Method for Evaluating Knee Bearing (Tibial Insert) Endurance and Deformation under High Flexion’ 2010,
2. McEwen, H.M.J, Barnett, P.I., Bell, C.J., Farrar, R., Auger, D.D., Stone, M.H., Fisher, J., “The influence of design, materials and in vitro wear of total knee replacements”, Journal of Biomechanics, 38(2), pp.357-365.

The quantitative assessment of the tibia bony surface for proper screw insertion angle by re-aligning CT coordinate in high tibial osteotomy

Yong Seuk Lee¹, Myung Chul Lee², Deok Gill Choi³, Doo Hoon Sun³ and Oui Sik Yoo³

¹Department of Orthopaedic Surgery, Seoul National University College of Medicine, Bundang Hospital, Sungnam, South Korea

²Department of Orthopaedic Surgery, Seoul National University College of Medicine, Seoul National University Hospital, Seoul, South Korea

³Central R&D Center, Corentec Co. Ltd., Seoul, South Korea

E-mail: osyoo@corentec.com

Abstract— Evaluate the screw insertion angle that is inserted to the direction of the lateral hinge with a surface geometry of the proximal tibia after the OWHTO. Results were Compared according to the correction degree and surgical technique.

Keywords— Open wedge high tibial osteotomy, 3D reconstruction, Screw angle, Screw insertion

I. INTRODUCTION

Open wedge high tibial osteotomy (OWHTO) is an operation by the proper load re-distribution in the treatment for medial uni-compartmental arthritis of the knee joint. For the stable fixation screws should be inserted from the central area of the medial side to the hinge area of the lateral side in the proximal fragment because most failures occur at the relatively lesser supported lateral hinge area. Therefore, the purpose of this study was to evaluate the screw insertion angle that is inserted to the direction of the lateral hinge with a surface geometry of the proximal tibia after the OWHTO. The hypothesis of this study was that the position and orientation would be different according to the correction degree and surgical technique.

II. METHODS

Thirty-one uni-planar and thirty-eight bi-planar osteotomies were evaluated. Postoperative CT data obtained after OWHTO were used for the 3D reconstruction of the proximal tibia. Axis realignment was needed during reconstruction of the 3D model because the coordinates of the postoperative CT data were respectively different according to the posture of the patient and their progress after surgery. And then, Anterior AP dimension (L1) and posterior AP dimension (L2) of the proximal tibia were measured based on axis of the lateral hinge to tibial spine in sagittal plane. Screw insertion points using four holes were even distributed using L1, L2value, medial tibial plateau and proximal fragment of osteotomy. Screw insertion angle was set from four holes to lateral hinge of the ‘Safe Zone’. Those four angles were measured in the axial (A_01, A_02, A_03, and A_04) and coronal

plane (C_01, C_02, C_03, and C_04). These were compared according to the correction degree and surgical technique.

III. RESULTS

Anterior AP dimension ‘L1’and posterior AP dimension ‘L2’were measured 24.0 ± 3.6 mm, 22.6 ± 3.1 mm. Angulations of screw from respectively screw hole to lateral hinge were measured $11.2 \pm 1.7^\circ$, $9.5 \pm 1.1^\circ$, $3.5 \pm 3.2^\circ$, and $3.2 \pm 1.5^\circ$ (A_01, A_02, A_03, and A_04) in the axial plane and $81.5 \pm 6.0^\circ$, $99.2 \pm 2.8^\circ$, $101.5 \pm 2.6^\circ$, and $90.8 \pm 3.7^\circ$ (C_01, C_02, C_03, and C_04) in coronal plane, respectively. None of the comparisons were statistically different, regardless of the correction degree and operative technique (Table1).

IV. CONCLUSION

Range of screw angulation showed regular pattern according to the site of the screw hole and it was not different, regardless of the correction degree and operative technique. This study provided range of the screw angulation by the anatomical surface modeling. Future study would give additional benefit for the optimal screw angle and stability such as finite element analysis or other methods.

Table 1. Table caption

		Group1 (Cap < 10mm, n=17)		Group2 (Cap > 10mm, n=12)		Group3 (Uni Planar, n=11)		Group4 (Bi Planar, n=18)		Total (n=60)	P-value (Group1-2)	P-value (Group1-3)	
		Mean	Standard Deviation	Mean	Standard Deviation	Mean	Standard Deviation	Mean	Standard Deviation				
AP Dimension (mm)	L1(Anterior)	24.0	3.6	22.6	3.1	25.0	2.8	22.4	3.3	22.6	3.1	0.718	0.171
	L2(Posterior)	23.2	3.0	22.0	3.0	25.0	2.8	22.4	3.3	22.6	3.1	0.093	0.482
Axial Plane Angle	A_01 (°)	11.1	1.9	11.6	1.4	11.1	1.7	11.1	1.7	11.1	1.7	0.77	0.708
	A_02 (°)	3.3	1.4	3.5	1.7	3.3	1.3	3.6	1.4	3.5	1.3	0.131	0.348
	A_03 (°)	3.3	1.3	3.0	1.7	3.2	1.2	3.1	1.7	3.2	1.5	0.544	0.862
	A_04 (°)	9.7	1.1	9.3	1.1	9.7	1.03	9.1	1.1	9.5	1.1	0.103	0.213
Coronal Plane Angle	C_01 (°)	81.2	5.7	82.2	5.9	81.7	4.9	81.7	6.1	81.7	5.7	0.513	0.988
	C_02 (°)	101.6	1.9	101.3	1.6	101.9	1.7	101.9	1.9	101.3	1.7	0.588	0.177
	C_03 (°)	90.8	3.6	90.8	3.3	90.5	2.7	90.0	4.0	90.8	3.5	0.958	0.56
	C_04 (°)	99.2	2.9	99.5	2.5	99.2	2.2	99.4	3.1	99.3	2.7	0.622	0.679

REFERENCES

- Amis AA (2012) Biomechanics of high tibial osteotomy. Knee Surg Sports Traumatol Arthrosc 21:197-205.
- Agneskirchner JD, Freiling D, Hurschler C, Lobenhoffer P (2006) Primary stability of four different implants for opening wedge high tibial osteotomy. Knee Surg Sports Traumatol Arthrosc 14:291-300.

Mechanical Evaluation of the Novel Laser-Aided Direct Metal Tooling for Porous Coating on Arthroplasty

Tae-Jin Shin¹, Kwan-Soo Kang², Sung-Jae Park¹, Soon-Yong Kwon³, Young-Wook Lim³, and Dohyung Lim²

¹Central R&D Center, Corentec Co. Ltd., Seoul, Korea

²Department of Mechanical Engineering, Sejong University, Seoul, Korea

³Department of Orthopaedic Surgery, St. Mary's hospital, Catholic University, Seoul, Korea

E-mail: dli349@sejong.ac.kr

Abstract—We were developed a novel porous coating technology on the arthroplasty for bone ingrowth based on additive manufacturing (AM) and conducted evaluation of efficacy of the coating, compared to the commercial coating technology.

Keywords— Porous coating, Arthroplasty, Mechanical Evaluation, additive manufacturing

I. INTRODUCTION

Cementless arthroplasty has been commonly used for younger patients with joint pathology, and is required to porous surface which is similar to the trabecular bone for bone ingrowth on the arthroplasty^[1]. Titanium Plasma Spray (TPS) is one of the most widely used porous coating method on arthroplasty^[2]. However, TPS coating is limited that would not to establish optimal porosity for bone ingrowth due to arbitrary position of melted powder on substrate. In addition, detached debris from coating were induced implant loosening. Thus, a novel Laser-aided Direct Metal Tooling (DMT) based on AM was developed to overcome these limitations. In this study, we were done to assess stereological evaluation, mechanical test, and physical analysis for evaluation of the efficacy of DMT coating technology. Then, mechanical characteristics of DMT coating were compared to that of TPS coating

II. METHODS

First, porosity of the DMT coating was evaluated using Scanning Electron Microscopy (SEM). Second, static tensile and shear test for assessment of mechanical characteristics in relation to the DMT and TPS coating specimens were conducted on the basis of ASTM F1147 and F1044 using universal testing machine (Endolab[®], DE). Maximum tensile strength and maximum shear strength were evaluated for each specimen (n=5). Abrasion test was performed based on ASTM F1978 using Taber[®] Rotary Platform Abraser (TABER[®] Industries, USA). Abrasion losses for each specimen (n=6) were measured at 2, 5, 10, and 100 cycles, respectively. Finally, roughness of each coating were measured according to ISO 4288.

III. RESULTS

Porosity of the DMT coating was found to be 64 ± 11%. Maximum tensile strength (mean ± SD) of the DMT coating (48.6 ± 4.3 MPa) was lower than TPS's (51.5 ± 11.6 MPa) about 5.6%, but detached position of one of the TPS specimens was observed at coating layer, not in adhesive layer. Maximum shear strength of the DMT coating (46.3 ± 1.9 MPa) was 10.2% higher, compared to TPS's (42.0 ± 0.6 MPa). Abrasion losses of the DMT (2 cycles, 1.0 ± 0.5 mg; 5 cycles, 2.5 ± 0.9 mg; 10 cycles, 4.2 ± 0.7 mg; 100 cycles, 20 ± 1.4 mg) were significantly higher (71.9% - 77.8% higher) than that of TPS's (2 cycles, 4.5 ± 1.4 mg; 5 cycles, 9.8 ± 2.8 mg; 10 cycles, 17.0 ± 3.4 mg; 100 cycles, 71.1 ± 4.2 mg). Roughness of the DMT coating was Ra 62.5 ± 2 μm, Rz 316.1 ± 8.1 μm which were 33.5%, 40.6% (Ra, Rz sequence) higher than that of TPS coating (Ra, 46.8 ± 8.9 μm; Rz, 224.9 ± 28.8 μm).

IV. CONCLUSION

Our results suggested that a novel DMT coating technology was feasible to apply coating method on the arthroplasty in terms of outstanding mechanical characteristics.

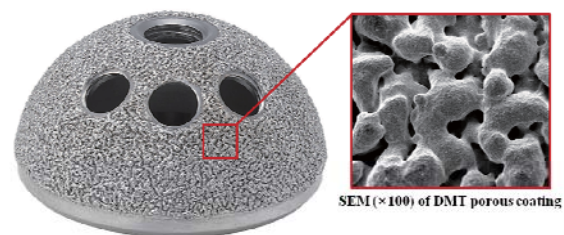


Fig. 1. DMT porous coating on the hip arthroplasty, SEM images of DMT coating used magnification of 100x for evaluation of porosity is shown in the box.

REFERENCES

1. K. Chiu, W. Shen, C. Ko, and K. Chan, "Osteonecrosis of the femoral head treated with cementless total hip arthroplasty" *J. Arthroplasty*, vol. 12, pp.683-688.
2. G. Ryan, A. Pandit, and D. Apatsidis, "Fabrication methods of porous metals for use in orthopaedic applications, *Biomaterials*, vol. 27, pp.2651-2670, 2006

Comparative analysis between asymmetric and symmetric tibial stem position using the virtual surgical planning of TKA

Y. K. Lee¹, J. W. Kim², O. S. Yoo², D. S. Sun^{2,3}, Y. S. Kim⁴, and J. S. Kim^{1*}

¹Department of Biomedical Materials, Konyang University, Korea

²R&D Center, Corentec Co., Ltd., Cheonan, Korea

³Department of Orthopedic Surgery, Sun General Hospital, Daejeon, Korea

⁴Department of Orthopedic Surgery, Seoul St. Mary's Hospital, Seoul, Korea

E-mail: jskimky@konyang.ac.kr

Abstract— The objective of this study was to validate clinical efficacy of TB-ASP using aligning outlier rate. We constructed 3D bone models of 20 OA patients. All virtual surgery has done by one surgeon with consistent surgical procedure for the analysis criteria. The ratio using offset adaptor was compared to those of TB-SSP. Our results indicate that TB-ASP using aligning outlier rate was decreased by 35% comparing to that of TB-SSP. These results suggest that asymmetric tibial stem be going to improve the alignment without offset adaptor in TKR.

Keywords—Stem extension; Virtual surgery;

I. INTRODUCTION

A stem extension improves fixation stability of a tibial component.[1] A symmetric tibial stem design often requires the component's re-positioning with negative effects.[2] Therefore, the objective of this study was to validate clinical efficacy of a tibial baseplate with asymmetric stemmed position (TB-ASP) using aligning outlier rate. We hypothesized that TB-ASP design will be better aligned without unessential offset adaptor than a tibial baseplate with symmetric stemmed position (TB-SSP).

II. METHODS

TB-ASP was designed based on the anthropometric standard model (58 female cadavers, 54.7±11.4 years). [3] To validate the stem position, 3D bone models of 20 OA patients (71.8±7.2 years) was reconstructed. All virtual surgery has done by one surgeon with consistent surgical procedure for the analysis criteria.

An analysis of TB-ASP's aligning outlier was proceeded by following steps; 1) aligning tibial base plate to the line from medial 1/3 tuberosity to the center of PCL, 2) selecting tibial baseplate's size for maximal bone coverage without problematic overhang, 3) trying to displace tibial baseplate and stem extension(120mm long) not to contact tibial cortex. A case invading tibial cortex was considered to be an outlier. The ratio using offset adaptor was compared to those of TB-SSP. Statistical analysis was performed using paired t-test.

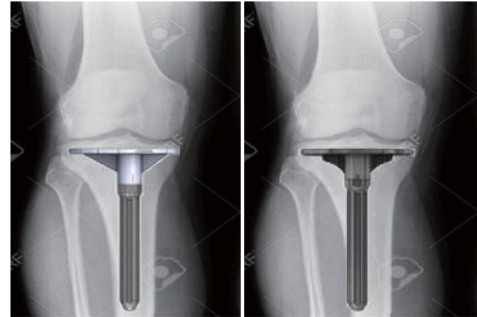


Fig. 1. TB-ASP, TB-SSP

III. RESULTS

TB-ASP's stem was optimized 31% AP position from the anterior and 45% ML position from the lateral. Its aligning outlier rate was decreased by 35% comparing to that of TB-SSP. For the offset from tibial medullary center to the stem extension center, there was no significant difference ($p=0.66<0.05$) between TB-ASP (3.60 ± 3.05) & TB-SSP(3.8 ± 2.30).

IV. CONCLUSION

TB-ASP design based on the standard model was better aligned with a proposed position of tibial stem. The findings from this study suggest that asymmetric tibial stem will improve the alignment without offset adaptor in total knee replacement

ACKNOWLEDGEMENT

This research was supported by a grant of Korea Health Technology R&D Project through the Korea Evaluation Institute Of Industrial Technology(KEIT), funded by the Ministry of Trade, Industry & Energy, Republic of Korea (grant number: 10048394)

REFERENCES

1. I. Yoshii, L.A. Whiteside, M.T. Milliano, and S.E. White, "The effect of central stem and stem length on micromovement of the tibial tray", *J Arthroplasty*, vol. 7, pp. 433-438, 1992.
2. P.A. Lethke, M.L. Ecker, "Influence of positioning of prosthesis in total knee replacement", *J Bone Joint Surg [Am]*, vol. 59, pp. 77-79, 1977
3. Kwak D.S. et al., *The Knee*, vol. 14, pp. 295-300, 2007

Measuring shooting-postural stability using an accelerometer

Tanmoy Chowdhury¹, Hyo Sung Joo¹, Minjung Woo², Hyejin Yang¹,
Jihwan Woo¹

¹Department of Biomedical Engineering, University of Ulsan, Ulsan, Korea

²School of Exercise and Sport Science, University of Ulsan, Ulsan, Korea

E-mail: jhwoo@ulsan.ac.kr

Abstract— This study aims to develop a ubiquitous shooting training system (u-shot) using accelerometer and smartphone. An algorithm for detecting gunshot trigger-time was developed using the audio-signal and acceleration data recorded by a smartphone microphone and the motion sensor, respectively so that movement prior to shooting can be measured. The validation of the performance was investigated by comparing with the data obtained from the commercialized optoelectronic device. The result shows that this system can be a good alternative solution for the shooting training system.

Keywords—motion sensor, shooting training, smartphone, gunshot detection.

I. INTRODUCTION

Among all the physical-physiological parameters postural stability is a great fact for the shooters and knowledge of performance plays a vital role in performance. (Mononen et al., 2003). Though many measuring device as like camera, infrared laser, strain-gauge transducers, optoelectronic training system have already been used for shooting training purpose, but all of these system have limitations regarding training place, cost and complexity. In this study we developed a system by using accelerometer and smartphone which is cost effective, easily portable, easy-to-use solution for the target shooting training system.

II. METHODS

The smartphone (Galaxy Note III, Samsung, Korea) was connected to the triaxial accelerometer (BMA250, BOSCH, Germany; $\pm 2g$) and SoC(nRF51822, Nordic Semiconductor, Norway) via Bluetooth. We attached the u-shot and the optoelectronic system on the gun barrel as seen in Fig. 1. The trigger time was detected by the sound data recorded by the smartphone microphone and the acceleration signal. We used standard deviation of the acceleration both of the accelerometer and a commercial optoelectronics trajectory as a stability score to compare with each other.

III. RESULTS

Figure 2 shows an example of acceleration extracted from u-shot (a) and SCATT (b). The result shows that

our trigger detection system has an averaged accuracy of 97.75% and the correlation between u-shot and optoelectronic system is 0.70.

IV. CONCLUSION

In this study we presented an alternate, cost effective, easily portable solution to the market available shooting training system. We will do further study to see the effect of this training system on the shooters.

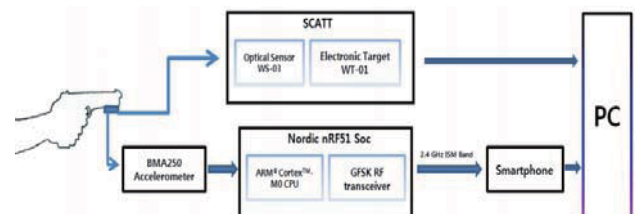


Fig. 1. Schematic of the ubiquitous shooting training system

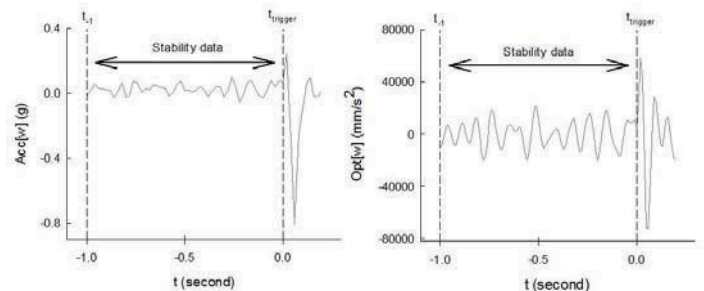


Fig.2. (a) Acceleration in u-shot; (b) Acceleration in SCATT

ACKNOWLEDGEMENT

This work was supported by the 2014 Korea Sports Promotion Foundation Grant.

REFERENCES

1. Mononen, K.; Viitasalo, J.T.; Kontinen, N.; Era, P. The effects of augmented kinematic feedback on motor skill learning in rifle shooting. *J. Sports Sci.* 2003, 21, 867-76.

Stiffness sensing ability of bovine aortic endothelial cells (BAECs) on collagen type I coated surface

Yujin Shin¹, Jinwon Kim², Hongki Yoo¹, and Bomi Gweon¹

¹Department of biomedical engineering, Hanyang University, Seoul, Korea

²Cardiovascular Center, Korea University Guro Hospital, Seoul, Republic of Korea

E-mail: yuzuholic@hanyang.ac.kr

Abstract— From previous reports, it has been known that cells can sense substrate compliance through adhesion proteins, such as focal adhesion complexes. To study the stiffness sensing ability of aortic endothelial cells on collagen dominant environment, we cultured bovine aortic endothelial cells (BAECs) on various stiffness (0.3 kPa ~ 153.6 kPa). Cells were culture for 24 h before experiment and observed for another 24 h under microscope. From the time laps images, cellular proliferation rate and morphological change were analyzed. Proliferation rate of cells on different stiffness did not show any difference. Interestingly, we found that cells cultured on soft (0.3 kPa) substrate had the highest aspect ratio compared to the cells on stiffer substrates. Conversely, cells on stiffer substrate (19.2 and 153.6 kPa) spread more than the ones on softer substrate. However, overall cellular function did not seem to be significantly different across the cells on difference stiffness. To further investigate the stiffness sensing mechanism of endothelial cells, more experiments considering *in vivo* conditions (ex. shear stress) seems to be essential.

Keywords— Endothelial cell, Substrate stiffness, Cell migration, Cell proliferation, Cellular morphology

I. INTRODUCTION

Cells can sense substrate stiffness through adhesion proteins, such as focal adhesion complexes. Interestingly, integrins composing focal adhesions change depending on the extracellular matrix (ECM) proteins because each ECM protein has different integrin ligand [1]. This implies that ECM may affect the stiffness sensing ability of cells grown on it. As endothelial cells in normal aorta has collagen as its major ECM, we cultured bovine aortic endothelial cells (BAECs) on collagen dominant environment to study the stiffness sensing ability of aortic endothelial cells. BAECs were seeded on collagen coated polyacrylamide gels of various stiffness; 0.3, 2.4, 19.2, and 150 kPa of Young's moduli. We chose these conditions to cover both the physiological and pathological stiffness condition. In general, 2.5 ~ 70

kPa is considered as the healthy biophysical range of vascular basement membrane [2].

II. METHODS

A. Cell culture

Bovine aortic endothelial cells (BAECs) were cultured on collagen type I coated polyacrylamide (PA) gels with different stiffness; 0.3 kPa, 2.4 kPa, 19.2 kPa and 153.6 kPa. Cells were seeded on gel and incubated for 24 hours before experiment.

B. Cellular behavior analysis

Cell samples were loaded on microscope equipped with incubator (5% CO₂ and 37 °C) and their phase contrast images were obtained every 5 min for 24 h. From selected images (every 6 h), we counted cell numbers to quantify proliferation rate using ImageJ software [3]. Cellular aspect ratio and spreading area were also analyzed by ImageJ. Additional cell dynamics (migration speed and directionality) were measured from the time lapse images.

III. RESULTS

A. Proliferation

As shown in figure 1, proliferation rate did not show any difference across different culture conditions.

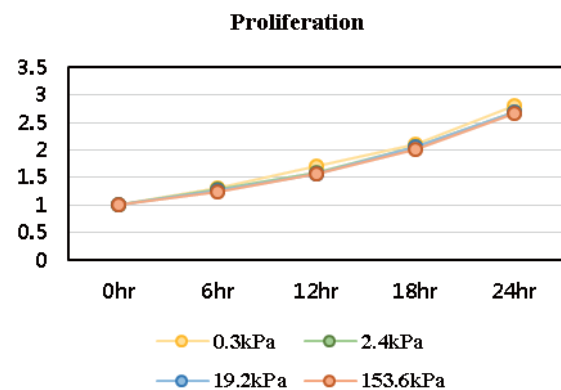


Fig. 1. Proliferation rate of the each stiffness cells compared with every 6 hour.

B. Aspect ratio and spreading area

Aspect ratio of cells on 0.3 kPa had the highest value compared to the ones of cells on stiffer substrate. Cells on 19.2kPa, cells spread more than other conditions. These results were shown to be statistically significant, however, the amount of difference was very small (< 10%) and, thus, did not seem to be physiologically meaningful.

IV. CONCLUSION

Based on our results, it has been shown that BAECs on collagen coated substrate is minimally affected by the substrate stiffness.

ACKNOWLEDGEMENT

This work was supported by the NRF Grant funded by the Korean Government (NRF-2014R1A6A3A04059713).

REFERENCES

1. Humphries JD, Byron A, Humphries MJ 2006. *Journal of Cell Science* 119: 3901-3903.
2. Wooda JA, Shaha NM, McKee CT, Hughbanks ML, Liliensiekb SJ, P Russella, and Murphya CJ 2011. *Biomaterials*. 32(22): 5056–5064.
3. Rasband, W.S., ImageJ, U. S. National Institutes of Health, Bethesda, Maryland, USA, <http://imagej.nih.gov/ij/>, 1997-2015

Kinematics of the Lower Extremities during V-shaped Slope Walking

Jiyoung Jeong¹, and Choongsoo S. Shin¹

¹Department of Mechanical Engineering, Sogang University, 35 Baekbeom-ro, Mapo-gu, Seoul 04107, Republic of Korea
E-mail: cshin@sogang.ac.kr

Abstract—Transitioning to different surface could change the walking strategy. The purpose of this study was to determine the hip, knee and ankle joint kinematics during V-shaped slope walking (VSW) tilted at 15°. Fifteen healthy males participated in this study. Three-dimensional motion capture system equipped with eight infrared cameras sampled at 200Hz was used. Different walking pattern and peak value indicated that adjustments needed to control the lowered body and to lift the body up immediately after lowering during VSW.

Keywords— V-shaped slope walking, Lower extremity, Kinematics

I. INTRODUCTION

Military training is often performed in challenging outdoor environments where the ground surface is uphill, downhill, or a combination of both. Although movement on either uphill or downhill roads has been studied [1,2], the biomechanics of movements on a tilted surface, where uphill and downhill road conditions are combined, has not been reported. Actual outdoor ground surfaces often consist of different shapes of slope such as a valley, which is a combination of declination and inclination. Therefore, the purpose of this study is to determine the three-dimensional hip, knee, and ankle joint kinematics and kinetics during V-shaped slope walking (VSW).

II. METHODS

Fifteen males without any current pain or history of lower extremity musculoskeletal injuries requiring surgery participated in this study (age: 23.8 ± 2.5 years, height: 173.3 ± 3.7 cm, mass: 67.4 ± 4.4 kg).

A three dimensional motion capture system equipped with eight infrared cameras (Motion Analysis Corp., Santa Rosa, CA, USA) was used to record the motion of hip, knee, and ankle joints at a sampling rate of 200 Hz during VSW. Reflective markers were placed on the following anatomical bony landmarks. Each subject was asked to wear a pair of military boots.

The valley-shaped walkway was constructed to mimic the ground surface where uphill and downhill conditions are combined. It began with the declination angle of 15° and was followed by an inclination angle of 15°. The experiment was performed in two sets: in

condition i), the force plate was embedded in the declined walkway, indicating a downhill walkway of a valley-shaped slope; in condition ii), the force plate was moved to the inclined walkway, which indicated an uphill walkway of a V-shaped slope

III. RESULTS

The hip, knee, and ankle peak joint angles at initial contact (IC), stance, and swing phase during VSW are reported in Table 1.

Table 1 Mean \pm confidence intervals of the peak hip, knee and ankle joint angles in the sagittal plane during VSW. Positive angles represent hip flexion, knee flexion, and ankle plantarflexion, respectively.

	Phase	Condition i)	Condition ii)
Hip (deg)	IC	24.3 ± 1.9	31.2 ± 2.9
	Stance	-7.7 ± 3.1	-5.6 ± 3.1
	Swing	52.7 ± 2.6	47.8 ± 3.2
Knee (deg)	IC	15.5 ± 2.0	15.8 ± 2.5
	Stance	41.7 ± 3.9	35.1 ± 3.2
	Swing	78.3 ± 2.2	81.7 ± 3.7
Ankle (deg)	IC	-5.2 ± 1.5	-14.4 ± 2.6
	Stance	-15.4 ± 2.9	-25.0 ± 2.1
	Swing	9.8 ± 3.5	0.3 ± 2.9

IV. CONCLUSION

The adjustments needed to control the lowered body and to lift the body up immediately after lowering during VSW were found. These findings demonstrate that the joint kinematics changed depending on the shape of the ground surface during downhill/uphill VSW compared with that during LW. These changes in the pattern and magnitude of the joint kinematics indicate that different movement strategies are required to provide stability and mobility during VSW.

ACKNOWLEDGEMENT

This work was supported by the Sogang University Research Grant (201519031.01)

REFERENCES

1. Redfern, M. S., and DiPasquale, J., "Biomechanics of descending ramps," *Gait & Posture*, Vol. 6, No. 2, pp. 119-125, 1997.
2. Lay, A. N., Hass, C. J., and Gregor, R. J., "The effects of sloped surfaces on locomotion: A kinematic and kinetic analysis," *Journal of Biomechanics*, Vol. 39, No. 9, pp. 1621-1628, 2006.

The Relationship between Crush Extent and Injury Severity in Occupant Motor Vehicle Accident

J. H. Lee¹, H. Y. Lee¹, J. I. Lee¹, I. H. Kang¹, K. K. Wijenayake^{1,2},
B. V. A. Mendis^{1,3} and K. H. Lee¹

¹ Department of Emergency Medicine, Wonju College of Medicine, Yonsei University, Republic of Korea

² Base Hospital Avissawella, Sri Lanka

³ Base Hospital Tangalle, Sri Lanka

E-mail: ed119@yonsei.ac.kr

Abstract—The purpose of this study was to evaluate the relationship between crush extent (CE) of collision deformation classification code including scale of the collision and the severity of injury of the patient. Among patients who visited the emergency department of four domestic hospitals due to crash accidents. CE 3 showed more than moderate severity. The average Injury severity score (ISS) of truck group and left-side collision group was the highest. The safety-belt reduced severity patients when crush extent 3.

Keywords— Traffic accident, Crush extent (CE), Injury severity score (ISS)

I. INTRODUCTION

Development of safety system such as ABS, airbag, and mandatory to wear seat belt lead to decreasing the mortality. Otherwise, injured patients have increased. In the domestic, collection of data including the amount of deformation in traffic accident and injury severity has not been continuously performed. Understanding of traffic accidents is possible to reduce the mortality of patients by the immediate treatment and adequate management. In this study, we evaluate the relationship between Crush extent (CE) and injury severity score (ISS).

II. METHODS

A. Subjects

We collected 866 patients from August 2012 to February 2014. The patients were transported to emergency room due to crash accident. We collected data related to traffic accident through direct or indirect investigation.

B. Crush extent and injury severity score

Crush extent (CE) was classified by using a nine-zone extent system. Extent zones are applied to front, rear, side, top, or undercarriage deformation. Injury severity score (ISS) was classified from mild to severe (mild: 1-8, moderate: 9-15, and severe: >16).

II. RESULTS

A. The relationship between CE and ISS

The ISS was higher in CE 3, 4 than in CE1, 2, and in CE 5 higher than in CE 3, 4 (11.0±13.5 vs. 6.1±7.9, $p < 0.001$, 14.9±16.0 vs. 11.0±13.5, $p < 0.002$). The average ISS of truck in the car types was the highest (sedan: 10.0±13.2, SUV: 8.1±10.9, truck: 14.0±16.4, and van: 8.3±7.5), and front collision in the crash direction was the highest (front collision: 9.7±12.0, left-side collision: 14.3±17.1, right-side collision: 9.3±9.4, rear collision: 5.3±8.1, and roll-over: 11.0±14.2). The safety-belt reduced severity patients (odds ratio 0.44; 95% CI, 0.24 to 0.82, $p < 0.05$) when crush extent 3.

A. Safety-belt

The safety-belt reduced severity patients (odds ratio 0.44; 95% CI, 0.24 to 0.82, $p < 0.05$) when crush extent 3. Severe patients (ISS>16) who wore a seat belt showed a trend 0.44 times lower severity than patients who did not

IV. CONCLUSION

The study was to analyze the relationship between CE and ISS. CE 3 showed more than moderate severity. The average ISS of truck group and left-side collision group was the highest. The safety-belt reduced severity patients when crush extent 3.

ACKNOWLEDGEMENT

This research is supported by a grant from Dr. LEE Jong-wook Fellowship program funded by Korea Foundation for International Healthcare.

REFERENCES

1. Kim S, and Choi HY, "Estimation of Injury Severity of Occupant based on the Vehicle Deformation at Frontal Crash Accident," *Transactions of KSAE*, vol. 21, pp. 63-71, 2013.

Ankle Kinematics during Triangle-shaped Slope Walking

Yoon No G. Hong¹, Pankwon Kim¹, and Choongsoo S. Shin¹

¹Department of Mechanical Engineering, Sogang University, 35 Baekbeom-ro, Mapo-gu, Seoul 04107, Republic of Korea
E-mail: cshin@sogang.ac.kr

Abstract—Transitioning to different surface could change the walking strategy. The purpose of this study was to determine the ankle joint kinematics during triangle-shaped slope walking tilted at 15°. Fifteen healthy males participated in this study. Three-dimensional motion capture system equipped with eight infrared cameras sampled at 200Hz was used. Greater peak ankle dorsiflexion angle was observed both during uphill and downhill walking at triangle-shape slope than level walking. Different walking pattern and peak values from level walking suggest that a modified strategy may be used during transition between uphill and downhill walking at triangle-shape slope.

Keywords— triangle-shaped slope walking, ankle joint, Kinematics

I. INTRODUCTION

Transitioning to different surface could change the walking strategy [1,2]. However, no study has examined the kinematics of ankle joint during transition between uphill and downhill surfaces. Therefore, the purpose of this study is to determine how the ankle joint kinematics are altered during the transition from uphill to downhill walking at triangle-shaped slope compare to level walking.

II. METHODS

Fifteen males without any current pain or history of lower extremity musculoskeletal injuries requiring surgery participated in this study (age: 23.8 ± 2.5 years, height: 173.3 ± 3.7 cm, mass: 67.4 ± 4.4 kg).

A three dimensional motion capture system equipped with eight infrared cameras (Motion Analysis Corp., Santa Rosa, CA, USA) was used to record the motion of ankle joint at a sampling rate of 200 Hz. Reflective markers were placed on the anatomical bony landmarks. Each subject was asked to wear a pair of military boots.

The triangle-shaped walkway was constructed to mimic the ground surface where uphill and downhill conditions are combined. It began with the inclination angle of 15° and was followed by the declination angle of 15°. The 95% confidence interval (CI) for the peak values of ankle joint angle was calculated to determine the significant differences between the level walking and triangle-shaped slope walking.

III. RESULTS

All the three peak ankle joint angles at each local maximum and minimum are significantly different compare to level walking (Fig. 1, Table 1)

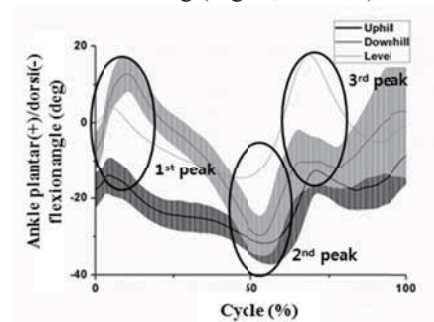


Fig. 1 Ensemble curves for ankle joint angle were obtained by averaging across all 15 subjects during level walking, uphill and downhill walking at triangle-shaped slope. The shaded areas with grey and dark grey represent the mean \pm one standard deviation.

Table 1 Mean \pm confidence intervals of the peak ankle joint angles in the sagittal plane during triangle-shape slope walking. Positive angles represent ankle plantarflexion.

ankle joint angle(deg)	Level walking	Uphill	Downhill
1st peak	4.1 ± 1.3	$-14.1 \pm 2.3^*$	$12.7 \pm 2.1^*$
2nd peak	-14.8 ± 1.4	$-31.8 \pm 2.4^*$	$-29.8 \pm 2.4^*$
3rd peak	17.6 ± 3.6	$-12.9 \pm 2.7^*$	$-7.2 \pm 4.0^*$

The asterisk (*) represents a significant difference from level walking at 95% confidence level.

IV. CONCLUSION

Greater peak ankle dorsiflexion was observed both during uphill and downhill walking at triangle-shape slope. Different walking patterns and peak values from level walking suggest that a modified walking strategy was used during transition between uphill and downhill walking at triangle-shape slope.

ACKNOWLEDGEMENT

This work was supported by the Agency for Defense Development (UD1300731D)

REFERENCES

1. Sheehan, R. C., and Gottschall, J. S., "Stair walking transitions are an anticipation of the next stride," *J Electromyogr Kinesiol*, Vol. 213, pp.533-541, 2011.
2. Gottschall, J. S., Okorokov, D. Y., Okita, N., and Stern, K. A., "Walking strategies during the transition between level and hill surfaces," *J Appl Biomech*, Vol. 274, pp. 355-361, 2011.

Development of the EDAMS using Algometer and Bio-potential Measurement

S. S. Kim¹, J. H. Ro², J. H. Kim³ and G. R. Jeon²

¹Department of Biomedical Engineering, Pusan National University, Pusan, Korea

²Department of Biomedical Engineering, School of medicine, Pusan National University, Pusan, Korea

³Department of Computer Simulation, Inje University, Gimhae, Korea

E-mail: grjeon@pusan.ac.kr

Abstract—A system based on an algometer for measuring the electrodermal activity (EDA) signal occurring at the region of the sweat glands in human body was implemented.

Keywords— Myofascial Pain Syndrome(MPS), Electrodermal Activity(EDA), Algometer

I. INTRODUCTION

The electrodermal activity measurement system (EDAMS) was implemented in this study for measuring the EDA signal occurring at the finger and the palm while applying the pressure stimulus to the scapula region using an algometer.

II. METHODS

A. Experimental Protocols

The block diagram of the EDAMS consisting of an algometer and the BPMS is shown in Fig.1.

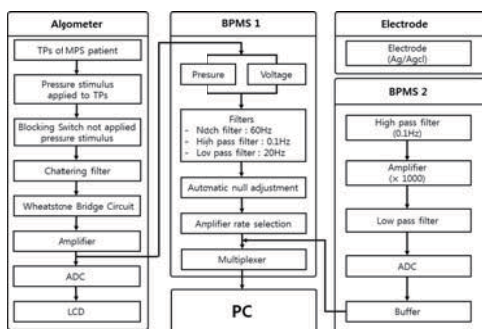


Fig. 1. Block diagram of the electrodermal activity measurement system.

A. Experimental Protocols

To measure the EDA signal, Ag/AgCl electrodes were attached to the fingers and the palm of a subject (Fig. 2.).

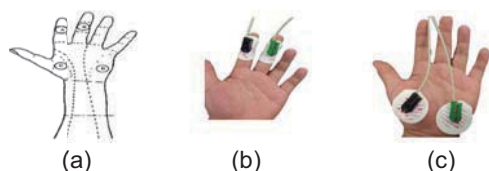


Fig. 2. The position of electrode attached for measuring the EDA signal: (a) method of Venables and Christie, (b) finger (A-B), and (c) palm (C-D).

III. RESULTS

A. Measurement of the EDA Signal using an Algometer and the BPMS

For measuring the EDA signal, electrodes were attached to the fingers and the palms of 10 experimental subjects as shown in Fig. 3. Then, an algometer was put on the scapular region for applying the pressure stimulus. While applying the output voltage of an algometer from 0.1 to 0.8 V, the EDA signal was measured using the BPMS.

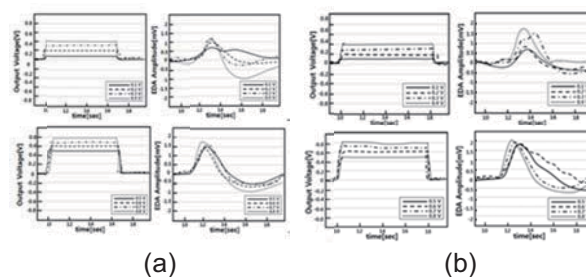


Fig. 3. (a) EDA signal measured at the fingers (A and B) when the output voltage of an algometer from 0.1 to 0.8V (b) EDA signal measured at the palm (C and D) when the output voltage of an algometer from 0.1 to 0.8V.

IV. CONCLUSION

The difference of EDA signals measured according to the electrode attached to the finger and palm were analyzed, while raising the intensity of pressure stimulus from 0.1 to 0.8 kgf/cm². When the pressure stimulus of algometer applied to the scapula increased, the amplitude of EDA signal being measured increased. The amplitude of EDA signal measured at the palm was observed to be higher than that measured at the fingers. These phenomena are determined by the path difference of sensory nervous system between region being applied to pressure stimulus and regions measuring EDA signal.

ACKNOWLEDGEMENT

This work was supported from the basic research project (NO. 2013R1A2A2A04015325) Korea in 2013.

REFERENCES

1. A. Jarrett, "The physiology and pathophysiology of the skin," *The Lancet*, vol. 302, no. 7826, pp. 445, 1973.
2. M. E. Dawson, "Psychophysiology at the Interface of Clinical Science, Cognitive Science and

Neuroscience,” *Psychophysiology*, vol. 27, no. 3,
pp. 243-255, 1990.

Implementation of Bellows Type Electromagnetic Transducer for Round Window Drive-Type Middle-Ear Implants

D. H. Shin¹, H. G. Lim¹, Y. J. Jo², E. S. Jung³, K. W. Seong⁴,
M. N. Kim⁴ and J. H. Cho^{1,5*}

¹ Graduate School of Electronics Engineering, Kyungpook National University, Daegu, Korea

² Graduate School of Medical & Biological Engineering, Kyungpook National University, Daegu, Korea

³ Medical Device Development Center, Daegu-Gyeongbuk Medical Innovation Foundation, Daegu, Korea

⁴ Department of Biomedical Engineering, Kyungpook National University Hospital, Daegu, Korea

⁵ School of Electronics Engineering, College of IT Engineering, Kyungpook National University, Daegu, Korea

E-mail: jhcho@ee.knu.ac.kr

Abstract— Up to recently, various types of hearing aids have developed to deliver sound signal to the cochlear. Especially, the round window drive-type middle-ear implants (MEIs) have been paying attention. In this study, the bellows type electromagnetic transducer is proposed and implemented for round window drive-type MEIs. The proposed transducer is easy to implant on round window niche and have high performance.

Keywords— Round window, Middle-ear implants, Bellows type electromagnetic transducer.

I. INTRODUCTION

Various kinds of hearing aids have been utilized to overcome hearing impairment in humans. Recently, for the treatment of patients with severe conductive hearing loss or sensory-neural hearing loss, MEIs that mechanically drive the cochlea with tiny middle-ear transducers have been widely used. But MEIs can cause necrosis by coupling spot along incus long process. To improve these issues, a new method in which the transducer is installed at the round window (RW) has been widely investigated. Because, this method can maintain merits of MEIs and it can be applied to patients without ossicles.

In this paper, we propose and implement the bellows-type electromagnetic transducer that can be installed at RW niche.

II. METHODS

The structure of the proposed bellows-type electromagnetic transducer is shown Fig. 1(a). The proposed bellows-type electromagnetic transducer has a diameter of 1.75 mm and a length of 2.3 mm. The coils consists of the three coils, one of the coils has forward direction, and the others coils has reversal direction against one. The two magnets are glued in same poles directions. When current flows in the coil, the Lorentz force is produced in axial direction by interaction with the magnetic fields.

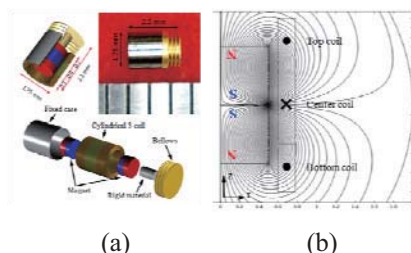


Fig. 1. (a) Structure of the proposed transducer, (b) flux line due to magnet.

To produce maximum Lorentz force, the allocation of length ratio among three coils is very important. Therefore, we performed a finite element analysis to determine the optimal length of the coil, and found that the best length ratio that would provide highest efficiency was 0.5 mm : 0.8 mm : 0.5 mm when the magnet length is 1.2 mm. Fig. 1(b) is shown flux line due to magnet.

III. RESULTS

The input source for the driving proposed transducer was operated at 1 mA_{rms} between 0.1 and 10 kHz. And then, bellows membrane of transducer was measured using LDV. To verify the performance of proposed transducer, vibrational characteristics of transducer and previous EM transducer (D:1.75 mm, L:2.4 mm) were compared [1]. The comparison result is shown in Fig. 2. The magnitude of proposed transducer was about 12 dB higher than that of previous EM transducer in 0.1 ~ 3 kHz range and both transducer have similar magnitude in high-frequency range.

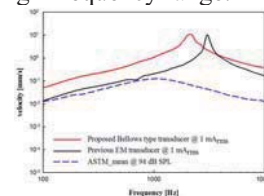


Fig. 2. Comparison of vibrational characteristics of the proposed transducer and previous EM transducer.

IV. CONCLUSION

In this study, we proposed a bellows-type electromagnetic transducer that can be installed at RW niche. The output of the proposed transducer with a driving force of 1 mA_{rms} were 96 dB and 129 dB equivalent SPL for respective frequency range below 1 kHz and above 3 kHz. In particular, the output of the high frequency band was excellent, so it is expected that the proposed transducer is usable for RW transducer of MEIs.

ACKNOWLEDGEMENT

This work was supported by the National Research Foundation of Korea (NRF) through a grant funded by the Korean Government (MSIP) (No. 2013R1A2A1A09015677, No. 2015R1A2A2A03006113, No 2013R1A1A2004991).

REFERENCES

1. D. H. Shin, H. G. Lim, J. H. Lee, K. W. Seong and J. H. Cho, "Design of 3-poles electromagnetic transducer for human round window mount," *The 7th Asia-Pacific Conference on Transducers and Micro/Nano Technologies.*, pp. 41, 2014.

Development of wireless charging low-frequency stimulator for wearable

Hojong Chang^{1*}, Hyeon Dock Kim¹

¹Bio Medical Team, Institute for Information Technology Convergence, KAIST

E-mail: hojounge@itc.kaist.ac.kr

Abstract— These days, the trend of the development of individual medical devices is a wireless charging and nonrestraint. Based on these technologies, we can use the medical equipment in daily life. So we develop the small low-frequency stimulator which can be charging by wireless. As an effect of low frequency stimulator, pain reduced and activating physiological functions have been reported. Developed product has the effect of stimulation of the human body in normal.

Keywords— **Low-frequency stimulator, Wireless charging, Wearable, Nonrestraint**

I. INTRODUCTION

Currently a lot of individual medical device is developed. One of the trend is combine the various fields like a convergence of traditional medicine and information technology. These techniques are for the user's convenience. So we designed a low-frequency stimulator which can insert into the shoes and clothes. So we designed a low-frequency stimulator inserted into the shoes and cloths easily, that has a wireless charging function for a user's convenience[1, 2].

II. METHODS

A. Waveform analysis of Low-frequency stimulator

We analyzed output signals about 4 products that are sales on the market. The frequency of waveform is around 2 Hz and maximum output voltage is 3V P-to-P and single-phase. This is because of the side effects. If the current flow as a one direction into the body it can damage the skin. To prevent this problem we also using a single phase direct current.

B. Implement of stimulate module and wireless charging module

In this study, to control voltage circuit, frequency-divider and a PLL (Phase Locked Loop) structure were

applied. Stimulation module was made up of an oscillator, a frequency modulator, the modulator waveform, and a buffer. We use an oscillating generator to get a stable low frequency output and low power. To make a wireless power transmission device, magnetic resonance method was used, and it was measured as the major parameter Q and k. Its circuit is shown in Fig. 1

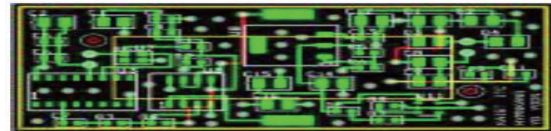


Fig 1. Circuit module of stimulation

III. RESULTS

In this paper we developed output of the stimulator module is 2 Hz, 1mA by using a high-frequency-band filter to produce an output waveform.

IV. CONCLUSION

In order to increase the power efficiency of the system the low-power low-frequency structure was designed using the Current Source with Capacitor. High Efficiency Rectifier, described in the RLC resonant circuit, impedance matching technology will have to be followed.

ACKNOWLEDGEMENT

This work was supported by KAIST Institute for Information Technology Convergence (Project No. N10150027, A0702001002)

REFERENCES

1. Yeon Hee Ryu et al., "Original Article : EEG Changes due to Low-Frequency Electrical Stimulation to the BL62 and KI6 of Elderly Women," *Korean Journal of Acupuncture.*, vol. 30, pp. 135-142, 2013.
2. K. S. Tae et al., "The Effects of Low-Frequency Electrical Stimulation on Muscle Force and Thickness," *Rehabilitation Engineering and Assistive Technology Society of Korea.*, vol. 2013, pp. 122-124, 2013.

IBEC2015, Road to Better Life through Biomedical Engineering

Thickness,” *Rehabilitation Engineering and Assistive Technology Society of Korea*, vol. 2013, pp. 122-124, 2013.

Closed-Loop Control of Functional Neuromuscular Stimulation using Cuff Electrode for Sit-to-Stand Maneuver in Spinal Cord Injury Animal Model

Kang-Il Song^{1,2}, Joongkee Min⁴, Sunghee E. Park^{1,3}, Kuiwon Choi¹,
Dosik Hwang², and Inchan Youn^{1,*}

¹Biomedical Research Institute, Korea Institute of Science and Technology, Seoul, Republic of Korea

²Department of Electrical and Electronics Engineering, Yonsei University, Seoul, Republic of Korea

³Department of Mechanical Engineering, Korea University, Seoul, Republic of Korea

⁴Department of Neurological Surgery, ASAN MedicalCenter, University of Ulsan College of Medicine, Seoul, Republic of Korea

E-mail: iyoun@kist.re.kr

Abstract—Spinal cord injury beagle model was controlled following the sit-to-stand (STS) movement using closed-loop functional neural stimulation (FNS) system. For eliciting the STS movement, electrical pulse was stimulated on the nerves through the cuff electrode implanted on the femoral and distal branch of sciatic nerve. The controller was designed to the proportional–integral–derivative controller with position feedback for adjusted the stimulation intensity. The STS motion was successfully controlled from the beagle SCI model.

Keywords— Spinal cord injury, Functional neuro stimulation system, Nerve cuff electrode, Sit-to-stand maneuver.

I. INTRODUCTION

The spinal cord injury (SCI) patient is characterized as having difficulty with transitional movement such as the sit-to-stand (STS) movement. Closed-loop controlled functional neural stimulation (FNS) system has proposed to be a valuable technique to restore motor function in SCI patients [1]. Several studies were suggested to control the motor function using the surface electrodes. However, such FNS scheme has limitation requirements due to environmental interference. Otherwise, direct nerve stimulation enables control of motor unit from distal and requires less energy consumption [2]. The goal of the present work was to produce a physiological, graceful sit-to-stand maneuver in the anesthetized beagle SCI model using the closed-loop controlled FNS system.

II. METHODS

The SCI model was developed to induce the pressure on the spinal cord thoracic 7 using balloon catheter. The nerve cuff electrode was implanted on the femoral nerve and the sciatic nerve to elicit the STS movement. The animal model was positioned on the seesaw to support the body and elicit the STS movement. The controller was designed to control the STS movement using the proportional–integral–derivative controller. For closed-loop control strategies, the knee angle position was measured for using the feedback signal.

III. RESULTS

The STS motion was controlled successfully using the reference STS trajectory motion. As shown in Fig. 1, the beagle SCI model was generated STS movement. The statistic values were shown that the settling time was approximately within the 150 ms under optimal PID gain, the steady state error was 1 degree, and percent overshoot was 3%.

IV. CONCLUSION

In this study, the beagle SCI model was generated by T7 injury approaches. Also, the beagle SCI model was controlled through the closed-loop FNS system for following the STS motion.

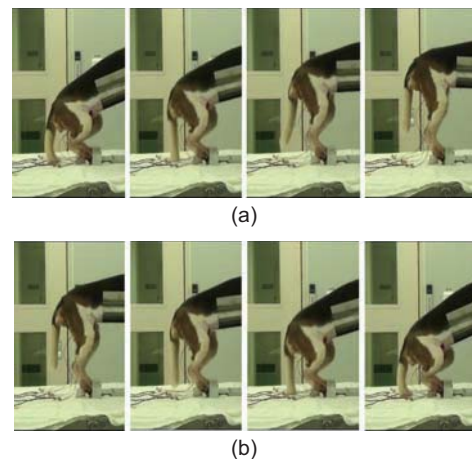


Fig. 1. Generating a sit-to-stand movement in a beagle SCI model: (a) standing motion, (b) sit motion.

ACKNOWLEDGEMENT

This research was supported by National Agenda Project funded by the Korea Research Council of Fundamental Science & Technology, and KIST Institutional Program (NAP-09-04).

REFERENCES

1. T. Sinkjaer, et al., "Biopotentials as command and feedback signals in functional electrical stimulation systems," *Med. Eng. Phys.*, vol. 25, pp. 29–40, 2003.
2. Polasek KH, et al., "Human nerve stimulation thresholds and selectivity using a multi contact nerve cuff electrode." *IEEE Trans. Neural Syst. Rehabil. Eng.*, vol. 15, pp 76–82, 2007.

Study on Verifying Detection of the Gait Intention by IMU Sensors using Rollator during Walking

H. J. Lee¹, S. R. Kang², G. T. Yang², Y. S. Kim³, H. S. Shim³, C.U. Hong² and T. K. Kwon²

¹Department of Healthcare Engineering, College of Engineering, Chonbuk National University

²Division of Biomedical Engineering, College of Engineering, Chonbuk National University

³EasyMove Co., Ltd.

E-mail: kwon10@jbnu.ac.kr

Abstract This study investigated detecting the gait intention of walkers by IMU sensors using a rollator. The beginning part of walking from the stop condition was measured according to the use of a rollator with IMU sensors. Seven IMU sensors were attached to the neck, chest, waist, left and right thighs, and calf. The 3D body model was created using analyzed the pitch values of the waist. As a result, the pitch values of the waist changed greatly in the first motion during walking in every experiment.

Keywords— Rollator, IMU sensor, Gait

I. INTRODUCTION

Human gait walking plays a critical role in the quality of life for the elderly. Our muscles are atrophied and we feel discomfort in walking [1]. We use walker to aid in walking for the elderly. Many studies on walking aids are being conducted, but there are few studies on the detection for gait intention of walkers using a rollator [2]. This paper is a basic study to detection of gait intention according to the use of rollator. The beginning part of walking from stop condition was measured using IMU sensors.

II. METHODS

For this experiment, an IMU sensor system was used. The IMU sensor is a 9-axis sensor consisting of 3-axis gyro sensors, 3-axis acceleration sensors, and 3-axis magnetic sensors. The 3D human body model was created using seven IMU sensors, and the pitch angle values of the pelvis which has the smallest variations among the parts that are moved during walking were examined. The experiments were conducted with 10 males in their 20s who walked 10 m on a flat ground using Standard Active Walker (SAW), Prototype Active Walker (PAW), and no Active Walker (noAW).

III. RESULTS

The beginning part of walking from stop condition was measured using IMU sensors. The experiment results are shown in Fig. 1. In the case of SAW, the pitch value was 15.72 degrees at the start of walking

and in the case of PAW, it was 13.35 degrees. The pitch value was small at 6.98 degrees in the case of noAW. After the large pitch value of the first step, the pitch values in the later steps were almost constant. Furthermore, they showed more stable motions when walking with the walking aids than walking with no aids.

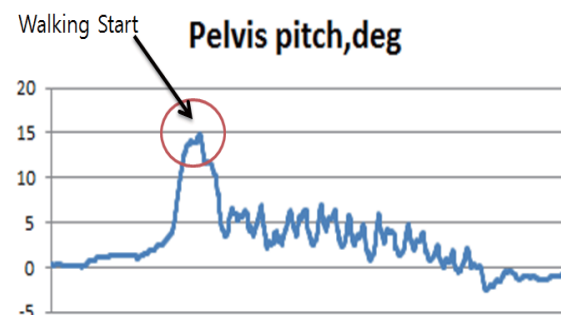


Fig. 1 Flat walking a result of 10m using a rollator

IV. CONCLUSION

In every walking, the pitch value of the pelvis was large at the beginning part. This appears to be due to the forward leaning of the body to receive momentum for moving forward. This study was meaningful as a basic study for detection of gait intention. In next study will be conducting this experiment with elderly subjects aged 65 or older.

ACKNOWLEDGEMENT

This work was supported by Ministry of Trade, Industry & Energy (MOTIE) (QoLT Technology Development, No. 10048001)

REFERENCES

1. R. L. Cromwell, R. A. Newton, and G. Forrest, "Influence of vision on head stabilization strategies in older adults during walking", *J Gerontol A Biol Sci Med Sci.*, vol. 57, pp. 442-448, 2002.
2. B. C. Muir, S. Rietdyk, and J. M. Haddad, "Gait initiation: The first four steps in adults aged 20-25 years, 65-75 years, and 80-91 years", *Gait Posture*, vol. 39, pp. 490-494, 2014.

Development of a mobile game and wearable device for upper limb rehabilitation.

H. J. Lim¹, J. H. Ku¹

¹Department of Biomedical Engineering, College of Medicine, Keimyung University
E-mail: kujh@kmu.ac.kr

Abstract— In this paper, we have developed a wearable interface and mobile game based on the EMG(electromyogram) signal and motion sensors for upper limb rehabilitation. Patients wearing the device including EMG and motion sensor can play the game. It could provide a suitable game contents for patients in order that they can do actively rehabilitation training. If the developed system is applied to upper limb rehabilitation, positive effectiveness could be expected.

Keywords— EMG, Interface, Rehabilitation, Mobile Game, Wearable

I. INTRODUCTION

Rehabilitation game motivates patients to attend the training actively. This training approach solves the problem of the previous training whose repetitive pattern possibly causes the boredom to patients[1]. However, problem that is inconvenient for patient to use was brought up because interface and game which was used in preceding search not suitable for them. Thus, this study aimed to offer a suitable system for patients who need rehabilitation training through developing interface and game based on the EMG signal and motion sensor.

II. METHODS

A. Wearable Device Design

Wearable device developed in this study is consisted of EMG acquisition module, motion sensor, active dry electrode and bluetooth. EMG acquisition module was designed to amplify about 3000 times an EMG signal and the frequency range was set up from 10 to 450Hz using a second order low pass filter and second order high pass filter. In addition, active dry electrode was used to get the signal. We combined motion sensor in order to recognize the patient's movement. The integrated data was transferred to a mobile device by using Bluetooth.

B. Game Content

The game is designed for patients to obtain an ingredients for cooking to achieve the mission. In addition, game was designed to enable the rehabilitation through the game by inducing grasp force, flexion, extension, abduction and adduction for patients. Motion sensor recognizes a patient's movements and translocate a character. EMG signals

are used to obtain the food ingredients. When the character is located on the food ingredients and the EMG signals reach a desired intensity by grasping motion, the food ingredients can be obtained. After the game, data like a patient's name, age, and real-time EMG signal data are saved. Later on, they make it possible to analyze.

III. RESULTS

Fig. 1 shows hardware composition and the wearable device wear image. Also it shows game progress designed by this study.

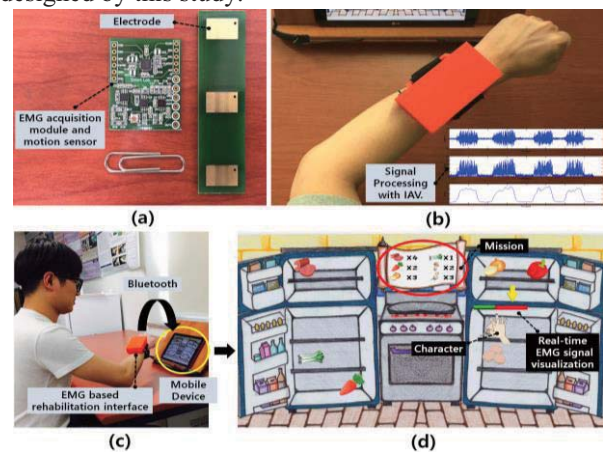


Fig.1. a) Hardware composition, b) Wearable device wear image and EMG signal processing course, c) Rehabilitation proceeding image, d) Game content

IV. CONCLUSION

In this study, we proposed a development of system for an upper limb rehabilitation of patients. We could offer convenience for patients through a wearable interface, and try to increase a training efficiency by providing suitable game contents for upper limb rehabilitation training. Also, if there are interface and mobile device, rehabilitation training is possible without restrictions in place, and it is possible for patients to adjust game difficulty depending on their exercise performance ability. Although it wasn't applied patients yet, a positive effect will be expected if it is applied to the patients in the future.

ACKNOWLEDGEMENT

This research was supported by Basic Science Research Program through the National Research Foundation of Korea (NRF) (2013R1A1A2060973).

REFERENCES

1. Rego. P, Moreira. P.M, Reus. L.P, "Serious games for rehabilitation", *Information system and technologies(CISTI) 5th conference*, pp.1-6,2010

Neurofeedback guided Upper Extremity Rehabilitation Using smartphone

Hyunmi Lim, Jeonghun Ku

Department of Biomedical Engineering, College of Medicine, Keimyung University, Daegu, Korea
E-mail: kujh@kmu.ac.kr

Abstract— In this paper, we developed a smartphone-based upper extremity rehabilitation program with neurofeedback and investigated the beneficial effect of the program. An experiment was conducted with 13 healthy volunteers and it showed positive results in the motor associated area.

Keywords— neurofeedback, upper extremity rehabilitation, smartphone, motor associated area

I. INTRODUCTION

EEG neurofeedback may be a promising tool for more organic investigations into the mechanism and functional intersection of neuronal oscillations, neuromodulators, synaptic plasticity and homeostasis. A study showed that as little as 30 minutes of neurofeedback training is able to induce mean changes in corticospinal excitability and decreases in intracortical inhibition of up to 200% [1]. We aim to develop a mobile-rehabilitation program with neurofeedback and to investigate effects of developed program on the brain.

II. METHODS

We made a module that could track a part of body motions and transfer the movements to smartphone through Bluetooth connection. For acquisition of a concentration level from brain, we used a medical instrumentation device (BRAINNO).



Fig. 1. System of the smartphone-based exercise rehabilitation with neurofeedback

The game app was designed to lead high-level concentration during exercise.

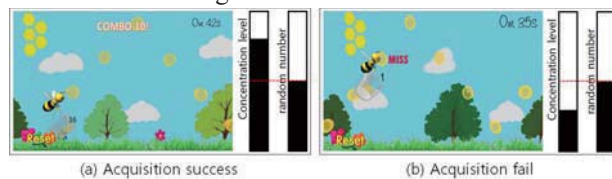


Fig. 2. Item acquisition by concentration level

A character in the game can be moved by body movement for taking target objects. Concentration level

of given tasks controls success rate of acquisition of target objects.

III. EXPERIMENT

13 healthy volunteers (age: 23 ± 1.87 years) were recruited for investigating the beneficial effects of the application of smartphone-based exercise rehabilitation with neurofeedback. ‘Neurofeedback guided mobile-rehab’ and ‘mobile-rehab alone’ were provided in random order in same day. We compared gamma power under two conditions. Data were analyzed for paired t-test using SPSS 21.

IV. RESULTS

The results of the experiment is below.

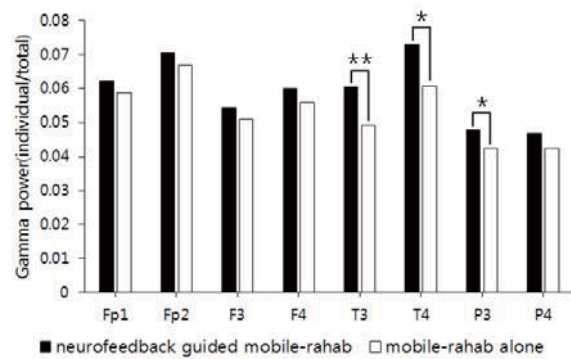


Fig. 3. The comparison of the Gamma power

The gamma power at T3, T4 and P3 was significant higher in neurofeedback guided mobile-rehab compared than mobile-rehab alone (T3: $**p < 0.01$; T4 and P3: $*p < 0.05$).

V. CONCLUSION

We developed a neurofeedback guided upper limb rehabilitation system. The results of the experiment showed a significant effectiveness on motor associated area and suggested that the developed mobile rehabilitation program with neurofeedback could be an effective rehabilitation intervention.

ACKNOWLEDGEMENT

This research was supported by Basic Science Research Program through the National Research Foundation of Korea (NRF) (2013R1A1A2060973)

REFERENCES

1. Tomas Ros, MSc, “Optimising perceptuo-motor performance and learning with eeg neurofeedback”, a dissertation presented for the philosophy doctor degree in psychology, goldsmiths university of london united kingdom, 2010

Gait characteristics of flexed knee type of RGO for paraplegia: A preliminary study

Y. H. Chang¹, H. J. Choi¹, B. R. Jeong¹, J. C. Ryu¹, and M. S. Mun¹

¹Korea Orthopedic & Rehabilitation Engineering Center, Incheon, Korea
E-mail: yhchang@korec.re.kr

Abstract— We developed the new type of RGO that had function with knee flexion. This Orthosis has been made for the improvement of gait efficiency and decrease of energy consumption in patients with paraplegia. Our study was aimed to compare fixed and flexed type of knee joint. Patient with T12 complete SCI participated in this study and used by 3D motion analysis, surface electrography and respiratory gas analyzer. In results, Decrease in COM displacement of Y and Z direction and muscle activity in upper limb and VO₂ uptake in flexed knee type of RGO. Conclusively, we thought that the new type of RGO is more effective for the decrease energy consumption and further studies will be conducted.

Keywords— Reciprocal Gait Orthoses (RGO), flexed knee type, paraplegia, gait efficiency

I. INTRODUCTION

Reciprocal gait orthoses(RGO) were developed to assist gait of patients with paraplegia [1], and consisted of two KAFO's and pelvic band. Also, knee joint of orthosis is fixed. The patient wearing the RGO pushes the pelvic band to backward with his/her trunk and one of leg braces moves forward. These induce excessive trunk movement and rigid gait pattern. Therefore, during the gait with RGO, the energy is excessively consumption and the use of RGO is not widely accepted [2]. We developed the knee flexed type of RGO which permit natural movement of trunk and pelvis including hip and knee joint. Our study was aimed to compare gait characteristics of knee fixed type and knee flexed type of RGO.

II. METHODS

T12 complete SCI patient was participated(61 years, 166 cm, 55kg). An injury period was 11 years and RGO use had more than 2 years. Experiment used by 3D motion analyzer(Motion Analysis Ltd), surface electromyography(TeleMyo 2400T/R, Noraxon) and respiratory gas analyzer(K4, KOSMED). We conducted 7 muscles within upper limb including pectoralis major and upper trapezius. Before an experiment, a patient had adaptation period for each type of RGO and then accepted 5 trials. We analyzed value of mean and SD of each trial.

III. RESULTS

In the flexed knee type of RGO, walking velocity and stride length were decreased, whereas increased step width and stance time. Also, Displacement (mm) of COM direction to Y and Z were decreased (table 1). Muscle activities (%MVC) of 4 muscles were decreased except for anterior deltoid, biceps brachii and flexor carpi ulnaris. Oxygen uptake (VO₂/kg) was reduced by 10%.

IV. CONCLUSION

We concluded that gait with the flexed knee type of RGO more effective than that of the fixed type of RGO in terms of decrease displacement of COM, muscle activity and energy consumption. We expected to be able to induce a natural gait with the flexed knee type of RGO. Furthermore, additional research is required.

Table 1. Comparison of fixed and flexed knee type of RGO

	Type of knee joint	
	Fixed	Flexed
Walking speed(cm/s)	25.4±0.3*	21.7±0.7
Cadence(steps/min)	28.8±0.4	29.5±0.5
Stride length(cm)	104.8±0.8	89.4±2.2
Step width(cm)	11.6±0.4	14.7±0.8
Stance time(%GC)	74.8±0.7	75.9±1.0
Z axis_COM(mm)	30.5±6.9	26.9±3.8
Y axis_COM(mm)	71.9±0.7	63.4±3.8

*mean±sd

ACKNOWLEDGEMENT

This study was supported by Ministry of Culture, Sports and Tourism, Republic of Korea.

REFERENCES

1. Douglas R, Larson PF, Dambrosia R, McCall RE. ,“The LSU reciprocation gait orthosis”, Orthopedics.,Vol. 6, pp 834-839, 1983
2. M. Safizadeh, M. Hussein, M. Yaacob, M. M. Zain, M. Abdullah, M. C. Kob, et al., "Kinematic Analysis of Powered Lower Limb Orthoses for Gait Rehabilitation of Hemiplegic and Hemiparetic Patients," order, vol. 7, p. 17, 2011

Rollover detection of indoor mobile devices using an inertia sensor unit

S.J. Ahn¹, E.K. Choi¹, M. Jo¹, J.M. Kim¹ and Y.H. Kim¹

¹Department of Biomedical Engineering, Yonsei University, Wonju, Republic of Korea
E-mail: Younghokim@yonsei.ac.kr

Abstract— In this study, rollover detection algorithm of the indoor mobile device was developed for the safety of the occupant. The algorithm successfully detected a rollover and rollover risk using acceleration, angular velocity, and inclination angle. To detect rollover risks, the thresholds of angular velocity and inclination were set to 20°/s and 15° respectively. To detect rollover, the threshold of inclination angle was set by 45°. Results showed 100% sensitivity and 100% specificity.

Keywords— Indoor mobile devices, Rollover risk, Inertial sensor

I. INTRODUCTION

The number of the elderly and the disabled has increased every year [1]. Indoor mobile devices (IMD) can ensure the indoor activities of the elderly and the disabled [2]. However, the rollover of IMD is very dangerous. In this study, we implemented a rollover risk of IMD detection algorithm using an inertial sensor. To verify our algorithm, two different types of rollover and three types of driving test (driving, barrier, and slalom) were examined in terms of the angular movements of the sensor.

II. METHODS

A. Experiment equipments

The indoor mobile device (KOREC, Korea) was used for the experiment. An inertia sensor unit (Invensens®, USA), placed at 30cm height of the IMD, was used to measure acceleration, angular velocity and inclination angle.

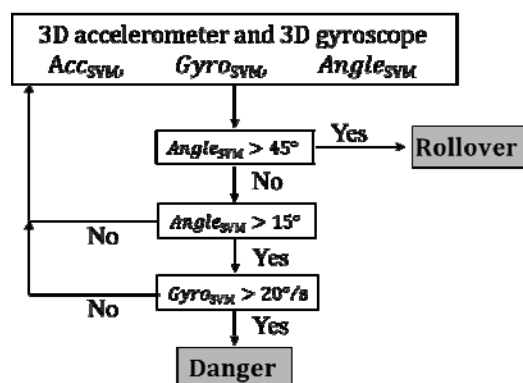


Fig. 1. Rollover risk detection algorithm

B. Experiment and Rollover risk detection algorithm

For the detection of rollover risk, the thresholds of angular velocity and inclination angle were set by 20°/s and 15° respectively, based on the data from two different types of rollover(forward and side) and three types of test (driving, barrier, and slalom). For the detection of rollover, the threshold of inclination angle was set by 45° based on the data from two different types of rollover (forward and side). The thresholds were determined from the optimization based on the maximum sensitivity and specificity.

III. RESULTS and CONCLUSION

In rollover tests and driving tests, the false detection rate was zero (100% sensitivity) for the two different types of rollover test and there was no incorrect detection (100% specificity) for the three different types of driving test. Furthermore, rollover can be prevented by detecting a rollover risk. Our algorithm can inform rollover risks to the occupant by the alarm. Our algorithm can be implemented in an emergency call system. In this study, only a small number of test types were evaluated. Thus, further studies are needed.

ACKNOWLEDGEMENT

This study was supported by the National Research Foundation of Korea (NRF) funded by the Ministry of Education (2013H1B8A2032194) and the National Convenience Enhancement Technology Development Program (10047894) funded by the Ministry of Trade, Industry and Energy (MOTIE, Korea)

REFERENCES

1. R. Ankeny and D. O'Shea, "Falls and syncope in elderly patients," *Clinics in Geriatric Medicine*, vol. 18, pp.xiii–xiv, 2002.
2. H. G. Nguyen, J. Morrell, K. Mullens, A. Burmeister, S. Miles, N. Farrington, K. Thomas, and D. W. Gage, "Segway robotic mobility platform", *Mobile Robots XVII, Proceedings of the SPIE*, vol. 5609, 2004.

Development of Emotion & Gesture recognition system using eMotion Glove

K. H. Lee¹, J. S. Cho¹, S. I. Kang¹, S. J. Lee¹, J. S. Lee¹, and I. Y. Kim^{1*}

¹Department of Biomedical Engineering, Hanyang University, Seoul, Korea

E-mail: khlee0114@bme.hanyang.ac.kr

Abstract— In this paper, we present the development of portable emotion/gesture recognition system using multi-sensor embedded glove (eMotion Glove).

Keywords— Glove, Emotion, Gesture, IMU, PPG

I. INTRODUCTION

In this paper, we present the development of portable emotion/gesture recognition system using multi-sensor embedded glove (eMotion Glove). We measure hand movement using inertial measurement units (IMU), finger movement using flex sensor, blood pressure using photoplethysmography (PPG), and skin impedance using Galvanic skin response sensor (GSR) [1]. From measured value, we can calculate Euler angle (Phi, Theta, Psi), Flexion/Extension (Degree), Heart rate (Beat/min), and Impedance (Ohm). Sensors are embedded in custom designed glove. For the result, we make signal viewer program using data acquisition program.

II. METHODS

A. Glove design

Fig. 1. shows the design of eMotion Glove. We focused on mobility, performance, and comfortability.

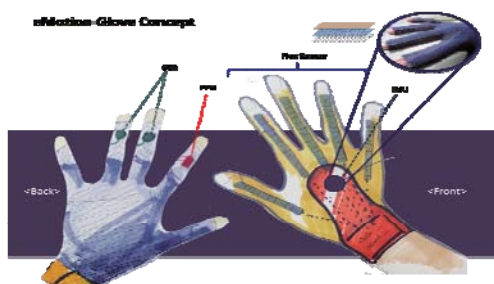


Fig. 1. Glove design

B. Sensors

We developed eMotion Glove sensor module that is composed of MCU (MSP430F5338), blue-tooth (PAN-1321i), inertial sensor (MPU9150), flex sensor, PPG sensor, and GSR sensor. Each sensor (inertial, flex, PPG, GSR) measure the various hand signal (hand/finger movement, blood pressure, skin impedance). Fig. 2. shows the exterior of sensor module.

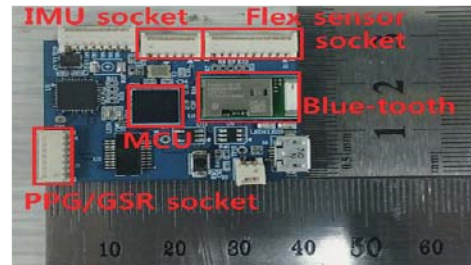


Fig. 2. Sensor module exterior

III. RESULTS

A. Implemented system

Fig. 3. shows the implemented eMotion Glove and its data acquisition program. Data acquisition program consists of PPG/GSR plots, hand model, and emotion evoking video.



Fig. 3. Implemented system (left) and data acquisition program (right)

IV. CONCLUSION

We could successfully make emotion/gesture recognition system from multi-sensor embedded glove (eMotion glove). Our future works are evaluating of emotion evoking video system and stabilizing sensor module.

ACKNOWLEDGEMENT

This work was supported by the ICT R&D program of MSIP/IITP [10045452, Development of Multimodal Brain-Machine Interface System Based on User Intent Recognition].

REFERENCES

1. S. I. Kang, J. S. Lee, I. Y. Kim, "Implementation of Motion Analysis System based on Inertial Measurement Units for Rehabilitation Purposes," *J. RESKO.*, vol. 7, pp. 47-54, 2013.

Stimulation Frequency Compensation of a Vibration System Based on the Open-loop Circuit for the Body Stimulation

H. W. Jin, S. H. Jeon, L. Y. Hwang, W. H. Choi, and T. M. Shin

Department of Biomedical Engineering, Yonsei University, Wonju, Korea

E-mail: jinyungwon@gmail.com

Abstract—In this paper, the stimulation frequency compensation of a vibration system based on the open-loop circuit for the body stimulation was studied. For this purpose, PWM duty cycle determining random vibration frequency was calculated after measuring the vibration frequency of the system versus PWM duty cycle and constructing the characteristic curve. As a result, RMS error for the linearity of the characteristic curve of the calibrated system was 2.748.

Keywords— Stimulation frequency compensation, Vibration system, Open-loop, Body stimulation, Linearity

I. INTRODUCTION

There are positive effects on the function of muscle, balance ability, and metabolism of bone and musculoskeletal unit if proper vibration is applied to human body[1]. The vibration system developed in the prior study[2] was designed to apply the vibration with PWM waveform input to eccentric motors on the open-loop circuit for applying desired vibration to human body regardless of the characteristics of human body.

However, it is impossible to apply the desired frequency to human body with controlling PWM duty cycle linearly because vibration frequency of the eccentric motors is non-linear. In this paper, therefore, the stimulation frequency compensation of the vibration system based on the open-loop circuit for body stimulation was studied.

II. METHODS

A. Curve fitting

For calibrating the stimulation frequency of the vibration system, the vibration frequency was measured from 27.3% to 100% of PWM duty cycle and first order exponential curve fitting was performed.

B. Calibration

The values of PWM duty cycle versus each frequency were calculated using the curve fitted characteristic curve and the linearity of the calibrated stimulation frequency with input values.

III. RESULTS

Fig. 1 shows the curve fitted characteristic curve and the result of the linearity evaluation. Also, Fig. 2 shows the results of measuring the actual vibration frequency with PWM duty cycle versus desired frequency using curve fitted characteristic curve and the linearity evaluation.

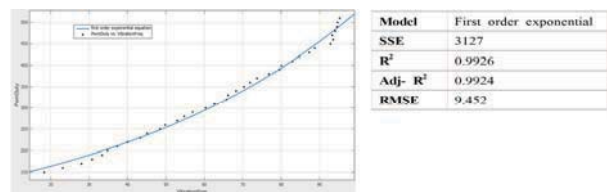


Fig. 1. Actual frequency vs PWM duty cycle

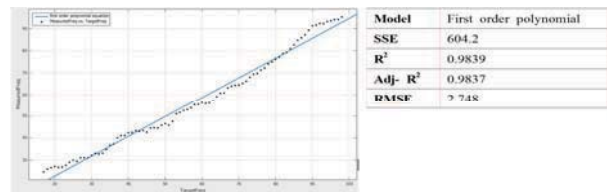


Fig. 2. Actual frequency vs Desired frequency

IV. CONCLUSION

In this paper, the stimulation frequency compensation of a vibration system based on the open-loop circuit for the body stimulation was studied. For this purpose, PWM duty cycle determining random vibration frequency was calculated after measuring the vibration frequency of the system versus PWM duty cycle and constructing the characteristic curve.

As a result, RMS error for the linearity of the characteristic curve of the calibrated system was 2.748 and the Adjusted R-square was 0.9837.

It could be possible to be more precise vibration system for the human body stimulation if combining the linearity of the eccentric motors calibrated in this paper and the vibration stimulation system based on the closed-loop circuit.

REFERENCES

1. K. Kawanabe, A. Kawashima, I. Sashimoto, T. Takeda, Y. Sato, J. Iwamoto, "Effect of whole-body vibration exercise and muscle strengthening, balance, and walking exercises on walking ability in the elderly", *The Keio journal of medicine*, vol.56, no.1, pp28-33, 2006.
2. H. W. Jin, W. H. Choi, D. H. Kim, H. S. Kim, T. M. Shin, "The Development of Vibration Stimulus System for Scoliosis Correction", 50th The Korean Society of Medical & Biological Engineering, pp.637-639, May, 2015.

Personalized Toe Spreaders with Three-Dimensional Scanning and Printing for Hallux Valgus

Sung Jae Kim, BS¹, Yong Ho Cha, MS², Geun ho Lee, MS², Jae Lim Kim, MD²,
Dong Kyu Kim, BS², Sang Jun Kim, MD, PhD²

¹Department of Medical Device Management & Research, SAHIST, Sungkyunkwan University

²Department of Physical and Rehabilitation Medicine, Samsung Medical Center, Sungkyunkwan University School of Medicine

E-mail: cathedral.sjk@gmail.com

Abstract—We made 14 Personalized toe spreaders for hallux Valgus with the 3D scanning and printing technique. Hallux valgus angle (HVA) and inter-metatarsal angle (IMA) were compared before and after wearing. Changes of HVA and IMA after wearing the toe spreader were significantly different. Total amount of time for making a personalized toe spreader was 7 hours and total price was 50 dollars.

Keywords— Hallux valgus, 3D printing, 3D scanning, Toe spreader

I. INTRODUCTION

The 3D printer is revolutionary tool that has a merit in producing individualized medical products. Toe spreader for hallux valgus must be highly individualized. We made personalized toe spreaders for hallux valgus with the 3D scanning and printing.

II. METHODS

A. Patients

We selected 8 patients (14 feet) who were diagnosed with hallux valgus. Hallux valgus was diagnosed when the hallux valgus angle(HVA) was less than 160° according to the previous article.

B. Design of toe spreader.

Two kinds of 3D scanners were used in this study; Eva (Artec™ EVA, Artec group, Luxembourg) and Spider (Artec™ Spider, Artec group, Luxembourg) for scanning of feet.

We inserted therapy putty into the interdigital space between the first and second toes and scanned the patients' feet in the inserted state with Eva. The size of the putty was modified till the first toe was in line with the first metatarsal. After extracting the putty from the foot, we scanned the molded putty again with Spider. Using these scanned files, we designed toe spreaders with the modeling program (Geomagic Freeform, 3D SYSTEMS, SC, USA). (Figure 1)

The designed toe spreaders were printed using Polyjet type 3D printer (Object500 Connex 1, Stratasys,

USA). For the materials of toe spreaders, VeroClear-RGD810 (Stratasys Ltd, Minnesota, USA) and TangoGray FLX950 (Stratasys Ltd, Minnesota, USA) were used.

C. Evaluation

We used personalized toe spreaders in the patients for one week and conducted the evaluation after one week. For the evaluation, we used the Foot and Ankle Outcome Score (FAOS) and User Satisfaction Survey (USS). In addition, simple radiographic anterior-posterior (AP) images of the foot in standing position were checked after wearing the toe spreaders for the measurement of HVA and IMA. We used Image J software (NIH, USA) for the measurement of HVA and IMA.

III. RESULTS

Initial HVA was $154.0 \pm 8.8^\circ$ and this was changed to $160.5 \pm 7.8^\circ$ after wearing on toe spreaders, which was statistically significant (Paired-t=-5.263, P<0.001). IMA also changed from $16.5 \pm 1.9^\circ$ to $17.7 \pm 0.8^\circ$ after wearing on the toe spreader, which was statistically significant (Paired-t=-2.376, P=0.034). Average USS was 7.4 ± 5.4 and all the sub-items of FAOS except quality of life were over 50.

IV. CONCLUSION

Personalized toe spreaders for hallux valgus were made by 3D scanning and 3D printing techniques and improved HVA and IMA. This suggests the possibility of the commercial use of 3D printed customized toe spreaders for hallux valgus.

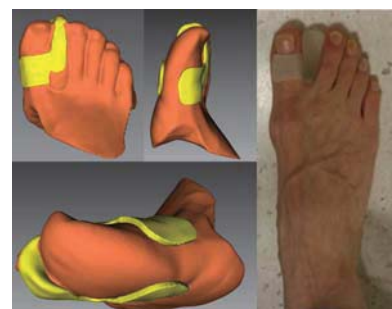


Fig. 1. Figure caption

A Study on Human Gait Analysis in Accordance With Change of Body-Weight Support Percentage

S. M. Song¹, C. H. Yu², K. Kim³, J. J. Kim³, W. K. Song⁴, C. U. Hong² and T. K. Kwon²

¹Department of Healthcare Engineering, College of Engineering, Chonbuk National University, Korea

²Division of Biomedical Engineering, College of Engineering, Chonbuk National University, Korea

³Chonbuk National University Automobile-parts & mold Technology Innovation Center, Jeonju, Korea

⁴ Translational Research Center for Rehabilitation Robot, National Rehabilitation Center, Seoul, Korea

E-mail: kwon10@jbnu.ac.kr

Abstract—The purpose of this paper is to analyze lower extremities pattern of walking on the treadmill with passive body support system. The experimental procedure has been validated on 5 healthy male subjects and measured EMG signal and foot pressure. EMG Patterns were lower with passive body weight support. Foot pressure results were decreased according to increase of body weight support percentage.

Keywords— Body Weight-Support, Pattern of Treadmill Walking, Gait Rehabilitation, EMG, Foot Pressure

I. INTRODUCTION

The rehabilitation training systems based on robot have been developed these days [1-3]. Especially on the gait rehabilitation systems were highlighted in order to satisfy patients' needs. There are a lot of rehabilitation robots to help gait training by supporting their weight [3-8]. However these systems are too bulky to train active daily lives such as sitting, standing, and etc. Therefore we are trying to develop active harness system to support patients' activities. In order to provide proper body support, in this paper we measure the lower extremities patterns through the body support percentages.

II. METHODS

Five healthy subjects participated to the study. (age 23 ± 2 years; body mass 76 ± 6 kg; height 173 ± 5 cm) The support weight percentages were 0%, 10%, 20%, and 30% of body weight (%bw). The percentages of body weight were calculated individually with load cell in passive harness system (Biodex Harness, USA). Gait speed was 3km/h that is normal walking speed for healthy adults. EMG was registered with an 8-channel wireless electromyography signals, TeleMyo Desktop DTS System (Noraxon, USA). The muscle selected were: Rectus Femoris(RF), Vastus Lateralis(VL), Tibialis Anterior(TA), Lateral Gastrocnemius(Lat.Ga). The foot pressures were measured during walking with Pedar-X system (USA).

III. RESULTS

A. EMG Signal

Fig.1. is EMG signal results. It shows that upper leg EMG signals are more decrease than lower leg. It implies that the upper leg muscles are used for body weight support. Also the vastus laterus muscle is remarkably decreased. It means that hip joint motion range is declined through the body weight support. However the variation of lateral gastrocnemius muscle is weaker than any other muscles.

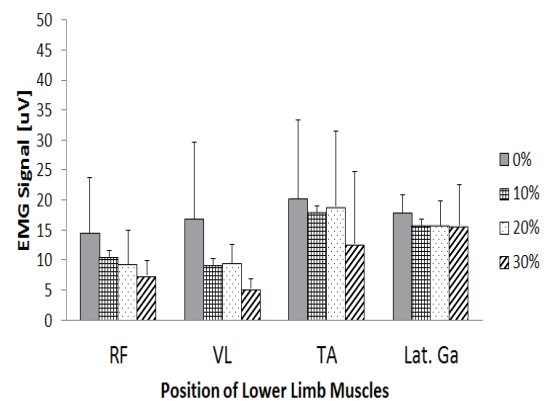


Fig. 1. EMG Pattern by body weight percentages

B. Foot Pressure

Fig 2. is foot pressure results by 3sections of foot (fore, mid, and rear foot) according to the body weight support percentages. The total foot pressures are decreased according to the body weight support percentages. The fore and rear foot which is more used during walking are more decline than mid foot. The decrease pattern imply that the passive harness system support the body weight against the gravity.

IV. CONCLUSION

The EMG signals were decreased when the passive harness system support body weight especially on the vastus lateralis muscle. These results imply that the body weight support gait rehabilitation systems can use for PFPS patients who have trouble with kneecap due to imbalance between vastus lateralis and vastus medialis muscle. The declines of foot pressure show

that body support system can widely use for rehabilitation program for patients who have irregular foot pressure in daily lives because of illness like diabetes.

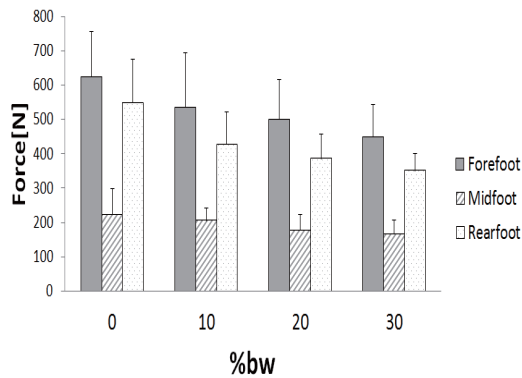


Fig. 2. Foot Pressre by body weight support percentages

ACKNOWLEDGEMENT

This work was supported by the Translational Research Center for Rehabilitation Robot of National Rehabilitation Center Grant (NRCTR-EX002).

REFERENCES

1. P. S. Lum, C. G. Burgar, P. C. Shor, M. Majmundar, and M. V. Loos, "Robot-Assisted Movement Training Compared With Conventional Therapy Techniques for the Rehabilitation of Upper-Limb Motor Function After Stroke", *J. Arch Phys Med Rehabil*, Vol. 83, pp. 952-959, 2002.
2. L. Lunenburger, G. Colombo and R. Riener, "Biofeedback for robotic gait rehabilitation", *J. NeuroEngineering and Rehabilitation*, Vol. 4, No. 1, 1743-0003(ISSN), 2007.
3. S. K. Banala, S. H. Kim, S. K. Agrawal and J.P. Scholz, "Robot Assisted Gait Training With Active Leg Exoskeleton", *Transactions on Neural System and rehabilitation Engineering*, Vol. 17, No. 1, pp 2-8, 2009.
4. J.K. Burgess, G.C. Weibel and D.A. Brown, " Overground walking speed changes when subjected to body weight support conditions for non impaired and post stroke individuals", *J. NeuroEngineering and Rehabilitation*, Vol. 7, No. 6, 1743-0003(ISSN), 2010.
5. J. Patton, D.A. Brown, M. Peshkin, J.J. Santos-Munne, A. Makhlin, E. Lewis, J.E. Colgate, and D.Schwandt, "KineAssist:Design and Development of a Robotic Overground Gait and Balance Therapy Device", *J. Topics in Stroke Rehabilitation*, Vol.15, no. 2 , pp. 131-139, 2008
6. M. Bouri, Y. Stauffer, C. Schmitt, Y. Aallemand, S. Gncmmi, and R. Clavel, "The WalkTrainer : A Robotic System for Walking Rehabilitation", *International Conference on Robotics and Biomimetics*, pp. 1616-1621, 2006

7. Y. Stauffer, Y. Allemand, M. Bouri, J. Fournier, R. Clavel, P. Metrailler, R. Brodard, and F. Reynard, "The WalkerTrainer-A New Generation of Walking Reeducation Device Combining Orthoses and Muscle Stimulation", *IEEE Transactions on Neural System and Rehabilitation Engineering*, Vol. 17, No. 1, pp. 38-45, 2009.
8. M. Patrick, B. Roland, S. Yves, C. Reymond, and F. Rolf, "Cyberthosis; Rehabilitation robotics with controlled electrical muscle stimulation", *J. Rehabilitation Robotics*, No. LSRO-CHAPTER, pp. 303-317, 2007

Real-Time, Simultaneous and Propositional Myoelectric Control for Robotic Rehabilitation Therapy of Stoke Survivors

Hae Yean Park¹, JunYong Hong², Harold Martin³, Leonard Elbaum⁴, Hye-Min EJ Kang⁵, Mangai Prabakar³, Nagarajan Prabakar³, Kyuwon Park⁶, Jong-Hoon Kim³, YoungJin Jung^{2,5}

¹Occupational Therapy, Yonsei University, Wonju, 26493, Korea

²Radiological Science, Dongseo, Busan, 47011, South Korea

³School of Computing and Information Sciences, Florida International University, Miami, FL, USA

⁴Physical Therapy, Florida International University, Miami, FL, USA

⁵CARE center, Florida International University, Miami, FL, USA

⁶School of Nursing & Health Studies, University of Miami, Miami, FL, USA

E-mail: microbme@dongseo.ac.kr / youngjin.jung@fiu.edu

Abstract—Conventional therapy approaches for stroke survivors have require considerable demands on therapist’s effort and patient’s expense. Thus, new robotics rehabilitation therapy technologies have been proposed but they have suffered from lack of optimal control algorithms. This article presents a novel technical healthcare solution for the real-time, simultaneous and propositional myoelectric control for stroke survivors upper limb robotic rehabilitation therapy.

Keywords—Proportional control, robot rehabilitation, regression model, surface EMG

I. INTRODUCTION

Over the last few decades, control based on externally captured electromyographic signals (sEMG) has been suggested. However, control algorithms presented to date have many limitations. These include limited ability to simulate the smooth, multiple degree of freedom movements of non-disabled individuals, and an inability to employ more than one sEMG signal at a time. These limitations may be overcome by using regression techniques. [1]

II. METHODS

In this study, the cost-effective sEMG measuring system and wearable sEMG electrode. In addition, the game software developed using MATLAB in order to increase patient concentration for enhancing rehabilitation therapy.

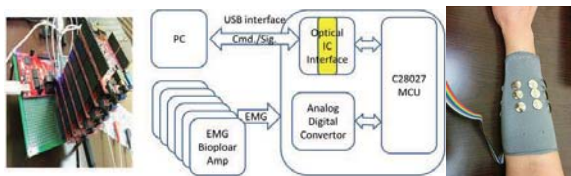


Fig. 1 The EMG sensing module & structure diagram, & sEMG electrode



Fig. 2 Procedure of Preprocessing diagram

III. RESULTS

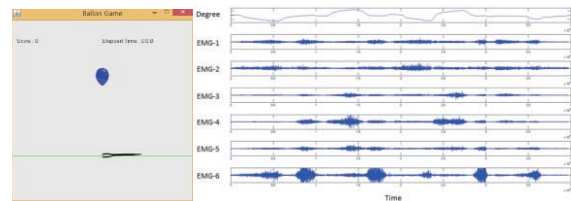


Figure 3 Left Scene is balloon game software for rehabilitation. Right is measured 6-CH sEMG signals during game software.

The full degree of wrist movement was used 0 to maximum degree of wrist for the training. On the other hand, the half degree of wrist movement was used only 0 to 40 degree for the training. Table 1 shows the experiment results.

Table 1 The score of rehabilitation game

Trial	Subject 1			Subject 2			Subject3		
	1	2	3	1	2	3	1	2	3
Full	16	15	17	15	14	16	17	15	16
Half	14	12	11	12	13	15	12	12	15

According to the table 1, ‘half’ task shows significantly lower scores than ‘full’ task based on a t-test (p-value = 0.002).

IV. CONCLUSION

In this study, the real-time, simultaneous and proportional myoelectric control was demonstrated to explore its potential for robotic rehabilitation therapy for stroke survivors. Although this was a modest pilot study, it demonstrated feasibility of simultaneous, proportional control based on sEMG for therapy. Thereby, this approach may have a potential to enhance the quality of life for stroke survivors.

REFERENCES

- [1] N. Jiang and S. Dosen, “Myoelectric control of artificial limbs—Is there a need to change focus,” *IEEE Signal Process. Mag.*, vol. 29, no. 5, pp. 148–152, 2012.

Proportional Myoelectric Control based on Frequency Features for Robotic Rehabilitation Therapy

Hae Yean Park¹, Hye-Min EJ Kang², JunYong Hong³,
Jong-Hoon Kim⁴, YoungJin Jung^{3,5}

¹Occupational Therapy, Yonsei University, Wonju, 26493, South Korea

²Linguistics, University of Minnesota, TwinCities, MN 55414, USA

³Radiological Science, Dongseo, Busan, 47011, South Korea

⁴School of Computing and Information Sciences, Florida International University, Miami, 33172, USA

⁵CARE center, Florida International University, Miami, 33172, USA

E-mail: microbme@dongseo.ac.kr / youngjin.jung@fiu.edu

Abstract—In this study, A modified linear regression model for robotic rehabilitation therapy was demonstrated and compared to conventional methods. According to the results, we assure of the possibility that the suggested model will be used for stroke robot rehabilitation.

Keywords—Proportional control, robot rehabilitation, regression model, surface EMG

I. INTRODUCTION

Recently, a few studies have shown that the regression technique can be applied for proportional and simultaneous myoelectric control for upper-limb prostheses [1], [2]. Actually, the regression technique for control of ERS has advantages for practical use: 1) the linear regression technique can control multi DOFs at one time using sEMG signals measured from electrode array. 2) it is not simple calculating structure to implement but also requires low computational load [1].

In this study, we hypothesized that various frequency feature (filter banks) can enhance the accuracy of linear regression model for myoelectric control or rehabilitation robot. The suggested approach was demonstrated and compared to conventional linear regression approaches.

II. METHODS

In this study, the different frequency feature was employed and demonstrated to estimate the accuracy of myoelectric control for robotic rehabilitation therapy.

A. Proposed Procedure for estimation of frequency feature.

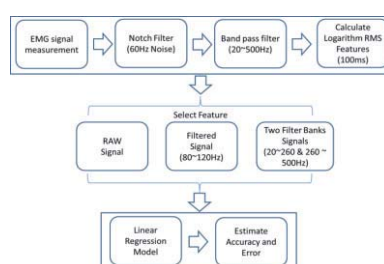
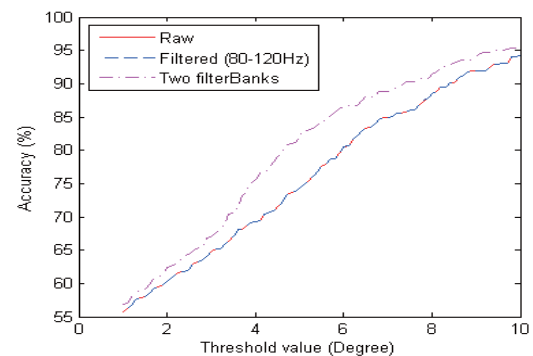


Fig. 1 Procedure of proposed algorithm for rehabilitation robot control

III. RESULTS

A. Accuracy results from two different models.

Fig. 2 shows that the combination of collected sEMG signal data by using 6 electrodes, which are enough to tell instinctively different directions of wrist



movement that have been performed.

Fig. 2 Accuracy of the different regression models corresponding to various threshold values

IV. CONCLUSION

In this study, the different frequency feature was employed and demonstrated to estimate the accuracy of myoelectric control for robotic rehabilitation therapy. The results use two filter banks signals as an input source show significantly higher accuracy than other features.

REFERENCES

- 1 J. M. Hahne, F. Biessmann, N. Jiang, H. Rehbaum, D. Farina, F. C. Meinecke, K.-R. Müller, and L. C. Parra, "Linear and nonlinear regression techniques for simultaneous and proportional myoelectric control.," *IEEE Trans. Biomed. Eng.*, vol. 22, no. 2, pp. 269–79, Mar. 2014.
- 2 J. M. Hahne, B. Graimann, and K.-R. Müller, "Spatial filtering for robust myoelectric control.," *IEEE Trans. Biomed. Eng.*, vol. 59, no. 5, pp. 1436–43, May 2012.

Real-Time, Simultaneous and Propositional Myoelectric Control for Robotic Rehabilitation Therapy of Stoke Survivors

Hae Yean Park¹, JunYong Hong², Harold Martin³, Leonard Elbaum⁴, Hye-Min EJ Kang⁵, Mangai Prabakar³, Nagarajan Prabakar³, Kyuwon Park⁶, Jong-Hoon Kim³, YoungJin Jung^{2,5}

¹Occupational Therapy, Yonsei University, Wonju, 26493, Korea

²Radiological Science, Dongseo, Busan, 47011, South Korea

³School of Computing and Information Sciences, Florida International University, Miami, FL, USA

⁴Physical Therapy, Florida International University, Miami, FL, USA

⁵Nicole Wertheim College of Nursing & Health Sciences, Florida International University, Miami, FL, USA

⁶School of Nursing & Health Studies, University of Miami, Miami, FL, USA

E-mail: microbme@dongseo.ac.kr / youngjin.jung@fiu.edu

Abstract—Conventional therapy approaches for stroke survivors have require considerable demands on therapist’s effort and patient’s expense. Thus, new robotics rehabilitation therapy technologies have been proposed but they have suffered from lack of optimal control algorithms. This article presents a novel technical healthcare solution for the real-time, simultaneous and propositional myoelectric control for stroke survivors upper limb robotic rehabilitation therapy.

Keywords—Proportional control, robot rehabilitation, regression model, surface EMG

I. INTRODUCTION

Over the last few decades, control based on externally captured electromyographic signals (sEMG) has been suggested. However, control algorithms presented to date have many limitations. These include limited ability to simulate the smooth, multiple degree of freedom movements of non-disabled individuals, and an inability to employ more than one sEMG signal at a time. These limitations may be overcome by using regression techniques. [1]

II. METHODS

In this study, the cost-effective sEMG measuring system and wearable sEMG electrode. In addition, the game software developed using MATLAB in order to increase patient concentration for enhancing rehabilitation therapy.

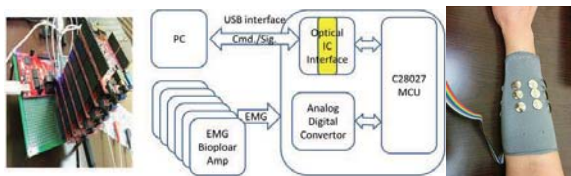


Fig. 1 The EMG sensing module & structure diagram, & sEMG electrode



Fig. 2 Procedure of Preprocessing diagram

III. RESULTS

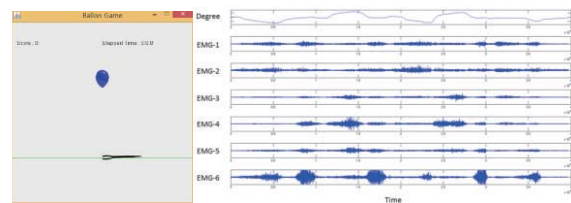


Figure 3 Left Scene is balloon game software for rehabilitation. Right is measured 6-CH sEMG signals during game software.

The full degree of wrist movement was used 0 to maximum degree of wrist for the training. On the other hand, the half degree of wrist movement was used only 0 to 40 degree for the training. Table 1 shows the experiment results.

Table 1 The score of rehabilitation game

Trial	Subject 1			Subject 2			Subject3		
	1	2	3	1	2	3	1	2	3
Full	16	15	17	15	14	16	17	15	16
Half	14	12	11	12	13	15	12	12	15

According to the table 1, ‘half’ task shows significantly lower scores than ‘full’ task based on a t-test (p-value = 0.002).

IV. CONCLUSION

In this study, the real-time, simultaneous and proportional myoelectric control was demonstrated to explore its potential for robotic rehabilitation therapy for stroke survivors. Although this was a modest pilot study, it demonstrated feasibility of simultaneous, proportional control based on sEMG for therapy. Thereby, this approach may have a potential to enhance the quality of life for stroke survivors.

REFERENCES

[1] N. Jiang and S. Dosen, “Myoelectric control of artificial limbs—Is there a need to change focus,” *IEEE Signal Process. Mag.*, vol. 29, no. 5, pp. 148–152, 2012.

Real-Time, Simultaneous and Propositional Myoelectric Control for Robotic Rehabilitation Therapy of Stoke Survivors

Hae Yean Park¹, JunYong Hong², Harold Martin³, Leonard Elbaum⁴, Hye-Min EJ Kang⁵, Mangai Prabakar³, Nagarajan Prabakar³, Kyuwon Park⁶, Jong-Hoon Kim³, YoungJin Jung^{2,5}

¹Occupational Therapy, Yonsei University, Wonju, 26493, Korea

²Radiological Science, Dongseo, Busan, 47011, South Korea

³School of Computing and Information Sciences, Florida International University, Miami, FL, USA

⁴Physical Therapy, Florida International University, Miami, FL, USA

⁵Nicole Wertheim College of Nursing & Health Sciences, Florida International University, Miami, FL, USA

⁶School of Nursing & Health Studies, University of Miami, Miami, FL, USA

E-mail: microbme@dongseo.ac.kr / youngjin.jung@fiu.edu

Abstract—Conventional therapy approaches for stroke survivors have require considerable demands on therapist's effort and patient's expense. Thus, new robotics rehabilitation therapy technologies have been proposed but they have suffered from lack of optimal control algorithms. This article presents a novel technical healthcare solution for the real-time, simultaneous and propositional myoelectric control for stroke survivors upper limb robotic rehabilitation therapy.

Keywords—Proportional control, robot rehabilitation, regression model, surface EMG

I. INTRODUCTION

Over the last few decades, control based on externally captured electromyographic signals (sEMG) has been suggested. However, control algorithms presented to date have many limitations. These include limited ability to simulate the smooth, multiple degree of freedom movements of non-disabled individuals, and an inability to employ more than one sEMG signal at a time. These limitations may be overcome by using regression techniques. [1]

II. METHODS

In this study, the cost-effective sEMG measuring system and wearable sEMG electrode. In addition, the game software developed using MATLAB in order to increase patient concentration for enhancing rehabilitation therapy.

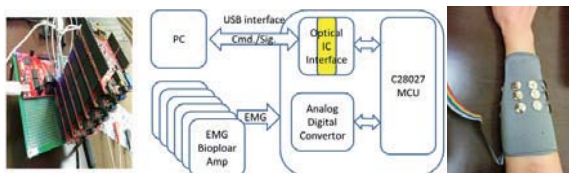


Fig. 1 The EMG sensing module & structure diagram, & sEMG electrode



Fig. 2 Procedure of Preprocessing diagram

III. RESULTS

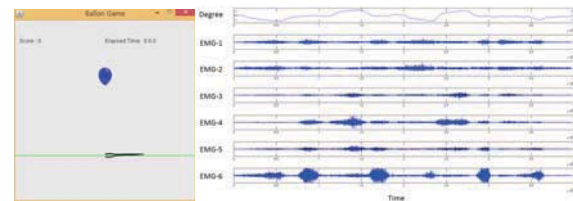


Figure 3 Left Scene is balloon game software for rehabilitation. Right is measured 6-CH sEMG signals during game software.

The full degree of wrist movement was used 0 to maximum degree of wrist for the training. On the other hand, the half degree of wrist movement was used only 0 to 40 degree for the training. Table 1 shows the experiment results.

Table 1 The score of rehabilitation game

Trial	Subject 1			Subject 2			Subject3		
	1	2	3	1	2	3	1	2	3
Full	16	15	17	15	14	16	17	15	16
Half	14	12	11	12	13	15	12	12	15

According to the table 1, 'half' task shows significantly lower scores than 'full' task based on a t-test (p-value = 0.002).

IV. CONCLUSION

In this study, the real-time, simultaneous and proportional myoelectric control was demonstrated to explore its potential for robotic rehabilitation therapy for stroke survivors. Although this was a modest pilot study, it demonstrated feasibility of simultaneous, proportional control based on sEMG for therapy. Thereby, this approach may have a potential to enhance the quality of life for stroke survivors.

REFERENCES

- [1] N. Jiang and S. Dosen, "Myoelectric control of artificial limbs—Is there a need to change focus," *IEEE Signal Process. Mag.*, vol. 29, no. 5, pp. 148–152, 2012.

A New Similarity Metric and Its Application for 2D Image Registration

Duc-Manh Ta¹, Seungbum Koo^{1*}

¹Department of Mechanical Engineering, Chung-Ang University, Seoul, Republic of Korea

*E-mail: skoo@cau.ac.kr

Abstract—Measuring the similarity between two finite sets of points in a metric space is an important step in feature-based three-dimensional (3D) to two-dimensional (2D) image registration. The purpose of this study is to propose a new distance measure for 2D image registration. The performance of the proposed method was evaluated by using a data set including 100 sample images and compare to that of previous studies. The proposed method showed accurate results and was better than other methods.

Keywords—Image Registration, Similarity Measure, Chamfer Matching, Distance Transform.

I. INTRODUCTION

Alignment of a projected three-dimensional (3D) model and an X-ray fluoroscopy is a key step in feature-based three-dimensional to two-dimensional (3D-2D) image registration [1]. Chamfer matching was first introduced by Barrow et al. [2] and has widely used in computer vision for comparing two sets of contour points. Chamfer matching, however, is not always reliable in complex scenes [3]. The aim of this study is to propose a new similarity metric based on Chamfer matching for image registration. Its accuracy and robustness were compared to those of the truncated Chamfer matching [4] and the conventional Chamfer Matching (CCM) [2].

II. METHODS

A data set including one hundred silhouettes of femoral Total Knee Replacement (TKR) was generated. Sample X-ray image of TKR were obtained with the approval of IRB of Chung-Ang University Hospital. The images was then added random noise by two noise models: Salt and Pepper, and Uniform noise model.

X-ray image was segmented by using the popular Canny edge detector and the obtained binary image was transformed to distance transform image. Assuming that the 2D Euclidean transformation W denotes by $s = (\theta, t_x, t_y)$. DT is the distance transform of the target X-ray image. The template edge pixel x_i are transformed onto the distance map of target image as the following equation:

$$W(x, s) = \begin{bmatrix} \cos(\theta) & -\sin(\theta) \\ \sin(\theta) & \cos(\theta) \end{bmatrix} x + \begin{bmatrix} t_x \\ t_y \end{bmatrix}$$

An image pyramid structure and optimization method were implemented in searching for the optimal position of template in the target image. The matching measure

between the template image and the target image is defined as below similarity measure:

$$\tau = \sqrt{\frac{1}{N} \sum_{i=1}^N f_i^2 + \frac{1}{N} \sum_{i=1}^N \|cross(r_i, f_i)\|^2}$$

Where τ is the new similarity measure

$$f_i = DT(W(x_i, s))$$

N is the number of pixels in the template image

r_i is the displacement vector corresponding to f_i

The accuracy of the proposed method was determined as root mean square position error while its robustness was evaluated as its behavior with different noise levels.

III. RESULTS

The average accuracy for all noise levels of the proposed method was 0.64 ± 0.31 , while those of the truncated CM and CCM were 2.83 ± 1.90 and 1.06 ± 0.60 respectively. Fig. 1 showed the robustness of the proposed method with regard to noise differences

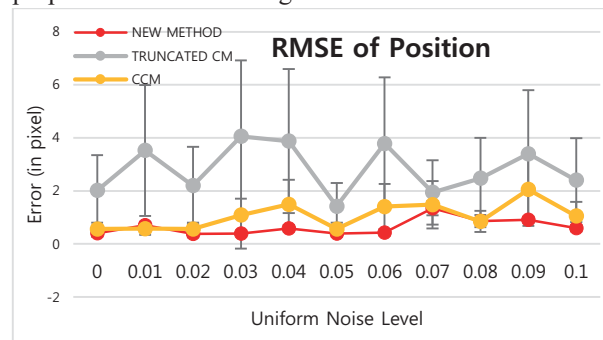


Fig. 1. A comparison of the proposed method with the truncated CM and conventional CM.

IV. CONCLUSION

A new similarity metric was proposed for edge-based 2D image registration. This method is accurate and robust even when images are in presence of noise, thus it may promise to be an good distance measure for 3D-2D image registration.

ACKNOWLEDGEMENT

This research was supported by the National Research Foundation of Korea (2012R1A1A2043793 and 2013R1A2A2A03015668).

REFERENCES

1. Markelj, P., et al., *Medical image analysis*, 2012. **16**(3): p. 642-661.
2. Barrow, H.G., et al., 1977, *DTIC Document*.
3. Liu, W., et al., *MVA2013*
4. Leibe, B., E. Seemann, and B. Schiele, *CVPR 2005. IEEE Computer Society Conference on*. 2005. IEEE.

Full-Bridge Ultrasound Pulser Circuit for Muscle Rehabilitation System Using Low Intensity Focused Ultrasound Stimulation

S. Oh¹, K. Song^{1,2}, H. Kim¹, and I. Youn^{1,*}

¹Center for Bionics, Biomedical Research Institute, Korea Institute of Science and Technology (KIST), Seoul, Korea

²School of Electrical and Electronic Engineering, Yonsei University, Seoul, Korea

E-mail: iyoun@kist.re.kr

Abstract— Ultrasound can evoke muscle activities by stimulating motor neurons. Thus, it is possible to rehabilitate muscles using the ultrasound stimulation. In this paper, a new ultrasound pulser circuit for a muscle rehabilitation system using low intensity focused ultrasound (LIFU) is presented. Attributed to a full-bridge structure, the developed circuit generates automatically balanced bipolar voltage pulses without a negative supply voltage. In the experiment, the ultrasound pulses with large enough energy to stimulate the motor cortex are generated using the developed circuit.

Keywords— Ultrasound stimulation, Ultrasound pulser circuit, Muscle rehabilitation

I. INTRODUCTION

Ultrasound can evoke muscle activities by stimulating motor neurons [1]. Based on this phenomenon, a muscle rehabilitation system using low intensity focused ultrasound (LIFU) is being developed. In this paper, a new ultrasound pulser circuit for the muscle rehabilitation system is presented. Due to a full-bridge structure used in the developed circuit, automatically balanced bipolar voltage pulses can be generated without a negative supply voltage that is necessary in the general ultrasound pulser circuits.

II. METHODS

A. Design

A schematic of the presented circuit is shown in Fig. 1. From a field-programmable gate array (FPGA), switching signals for power metal-oxide-semiconductor field effect transistors (MOSFET) are generated. Two gate driver integrated circuits (IC) (IR2011, International Rectifier, El Segundo, CA) are used for driving a single transducer. The automatically balanced bipolar voltage pulses up to 400 V_{PP} can be generated with fundamental frequency up to 4.17 MHz.

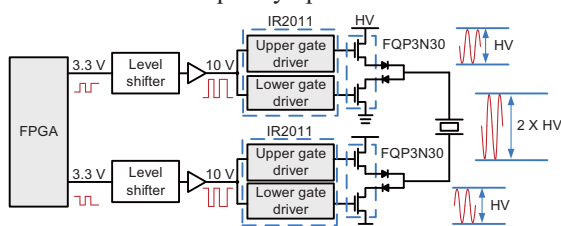


Fig. 1. Schematic of the full-bridge ultrasound pulser circuit

B. Experiment

An ultrasound transducer with a center frequency of 1.5 MHz (Digital ECHO, Hwaseong, Korea) is used to evaluate operation and performance of the developed circuit. A hydrophone (HNR-0500, ONDA Co., Sunnyvale, CA) is used to measure the ultrasound intensity. The developed circuit generates 100 V_{PP} bipolar pulses (1.5 MHz fundamental frequency, 50% duty cycle, and 1.5 kHz pulse repetition frequency).

III. RESULT

Measured ultrasound pulses are shown in Fig. 2. At the hydrophone, 1.5 MHz sinusoidal waveform with the amplitude of 23.6 mV is measured. The spatial peak-pulse average intensity (I_{SPPA}) is calculated as 0.199 W/cm², which is large enough to evoke the muscle activity by stimulating the motor cortex [1].

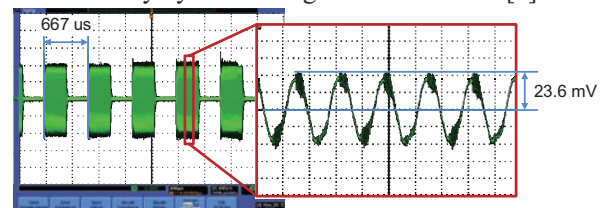


Fig. 2. Ultrasound pulses generated from the transducer

IV. CONCLUSION

In this paper, the full-bridge ultrasound pulser circuit for the muscle rehabilitation system is presented. In the developed circuit, the automatically balanced bipolar voltage pulses can be generated without the negative supply voltage, in contrast with the general ultrasound pulser circuits. The experimental result shows that the developed circuit can be utilized for the muscle rehabilitation system using the ultrasound stimulation.

ACKNOWLEDGEMENT

This Research was supported by a grant of the Korea Health Technology R&D Project through the Korea Health Industry Development Institute (KHIDI) funded by the Ministry of Health & Welfare (HI14C3477), and by the KIST Institutional Program (2E25505).

REFERENCES

1. Y. Tufail et al., "Transcranial Pulsed Ultrasound Stimulates Intact Brain Circuits," *Neurons*, vol. 66, pp. 681-694, 2010.

Quantification of mechanical properties of multi-layer elastic specimen using an indentation method

Yoon Kwak¹, Seungbum Koo¹

¹Chung-Ang University, Seoul, Korea
*E-mail: skoo@cau.ac.kr

Abstract— Ulceration of the plantar foot soft tissue is the most common symptom of diabetic foot. Understanding the characteristics of soft tissue is important to quantify disease state of ulceration. In this study, indentation test and fitting experimental data to a result from finite element method (FEM) were performed with two-layer elastic specimens with three different thickness combinations, replicating multiple soft tissue layers. Estimated mechanical properties had agreement with known mechanical properties.

Keywords—Finite Element Method, Indentation Test, Diabetic Foot, Hyperelastic, Plantar Tissue

I. INTRODUCTION

Measuring mechanical properties of plantar tissue is important to quantify diseases state and to predict ulceration of diabetic foot [1]. Ulceration of the plantar soft tissue is the most common symptom of diabetes with foot and ankle problems [2]. Measuring the mechanical properties by ex vivo is impossible to measure in clinical purpose. In this study, we proposed a method for estimating the mechanical properties of multi-layer elastic materials using an indentation test.

II. METHODS

Two-layer elastic materials were designed referring to the geometry of foot plantar soft tissue [3]. Two-layer elastic materials were made from Polydimethylsiloxane and silicone rubber for each layer. Three different thickness combinations were used to make A1, A2 and A3 materials. Using different curing conditions another set of two-layer elastic materials were made – B1, B2 and B3. Indentation test on each two-layer material was performed using our custom device (Fig. 1) and force-displacement data were recorded. Mechanical properties were estimated using the FEM optimization tool in Abaqus as elastic model (Young's modulus) for A1, A2 and A3 and hyperelastic model (Mooney-Rivlin 2 Parameter) for B1, B2 and B3. Estimated results were compared with the known values.

III. RESULTS

Estimated mechanical properties and the errors between the estimation and the values from an agency are shown in Table.1 and 2.

Material	Estimation (MPa)	Known(MPa)	Error(%)
A1	1.345	1.393	3.45
A2	1.856	1.889	1.75
A3	1.602	1.613	0.68

Table 1. Estimation using an elastic material (1st set)

Material	Estimation(Pa)	Known(Pa)	Error(%)
B1	C10: 40338	38385	5.09
	C01: 1622	2418	32.9
B2	C10: 73373	79011	7.14
	C01: 3016	4333	30.4
B3	C10: 58521	60453	3.20
	C01: 302	9122	96.7

Table 2. Estimation using a hyperelastic material (2nd set)

IV. CONCLUSION

Results show that estimated Young's modulus and C10 constant of Mooney-Rivlin hyperelastic model had good agreement with known values. However, C01 constant of hyperelastic model were not estimated properly. Small constant of hyperelastic model had small effect on hyperelastic characteristics. The errors between estimated C01 constants and known values were higher than the errors of Young's modulus and C10 constant.



Fig. 1. Indentation test (left) and FEM simulation (right)

ACKNOWLEDGEMENT

This work was supported by the NRF grant (2012R1A1A2043793 and 2013R1A2A2A03015668)

REFERENCES

- Gefen, A., et al., Clin Biomech. 16(10): 921-25, 2001.
- Cheung, Jason Tak-Man, et al., J Biomech. 38(5): 1045-1054, 2005.
- Gooding, G. A., et al., J Ultrasound Med. 4(4): 173-4, 1985.

A preliminary study on robot-guided orthognathic surgery system

Sang-Yoon Woo¹, Sang-Jeong Lee¹, and Won-Jin Yi²

¹Department of Biomedical Radiation Sciences, Graduate School of Convergence Science and Technology, Seoul National University, Seoul, Korea

²Department of Oral and Maxillofacial Radiology, BK21, and Dental Research Institute, School of Dentistry, Seoul National University, Seoul, Korea

E-mail: woodli14@snu.ac.kr

Abstract— This article is a preliminary study on robot-guided system for orthognathic surgery. A robot tip was calibrated with optical tracking tool. Then, registration procedure was performed in coordinates among a robot, optical tracking system (OTS) and CT image. Average fiducial registration error was 0.25 mm and average target registration error was 1.20 mm. This system can be integrated with surgery navigation system.

Keywords— robot assisted surgery, surgical robot, orthognathic surgery, robot registration, hand-eye calibration

I. INTRODUCTION

Recently, robotic systems have been applied in surgery to improve accuracy and to minimize invasiveness. However, these approaches have not been used in dentistry area yet. Based on our previous research regarding to navigation system [1], we studied a robotic guide system for orthognathic surgery.

II. METHODS

A. System overview

The proposed system consisted of four degree of freedom robot (CRCH4-S100-Z300, Cybog-Lab, Suwon, Korea), robot motion controller (Precise Automation, Fremont, CA, USA), optical tracking system (Polaris, Northern Digital Inc., Waterloo, Ontario, Canada). CT image of registration body was obtained with a MDCT (Siemens SOMATOM Sensation 10, Munich, Germany). An overview of our robotic guide system was described in Figure 1.

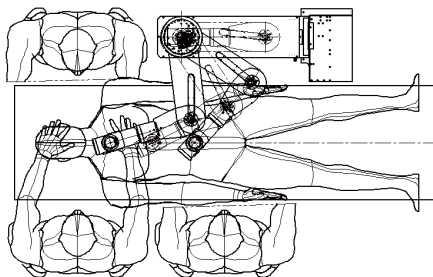


Fig. 1. System overview

B. Robot tooltip-optical tracking tool calibration

Robot tooltip was calibrated with optical tracking tool in equation (Eq. 1) [2].

$$P_{offset} = M_{probe}^{-1} M_{ref} P_{ref_offset} \text{ ----- (1)}$$

where P_{offset} is robot tooltip offset, M_{probe}^{-1} is inverse transform of optical tracking tool attached on robot arm, M_{ref} is known matrix of reference optical tracking tool, and P_{ref_offset} is known offset of reference.

C. Robot-OTS-CT image registration

Registration body contained six fiducial markers and the locations of markers were acquired in each coordinates of robot, OTS and CT. ITK registration algorithm (ITK, Kitware Inc., Kitware Inc., New York, USA) was used for point-to-point registration.

D. Validation of registration

Target registration error was measured using three landmarks located 70 mm distant from fiducials

III. RESULTS

Fiducial registration error was 0.16mm (between Robot and OTS), 0.25mm (between Robot and CT image) and 0.34mm (between OTS and CT image). Average target registration error was 1.20 mm.

IV. CONCLUSION

Accuracy of our system was acceptable for clinical tolerance (2mm). We expect that our system improve drawbacks of current system such as tremor and inaccuracy. Further research will be study regarding accuracy and phantom study.

ACKNOWLEDGEMENT

This study was supported by a grant of the Korean Health Technology R&D Project, Ministry of Health & Welfare, Republic of Korea (HI13C1491).

REFERENCES

1. Dae-Seung Kim, Sang-Yoon Woo, Won-Jin Yi and et al., "An integrated orthognathic surgery system for virtual planning and image-guided transfer without intermediate splint," *Journal of Cranio-Maxillofacial Surgery*, vol. 42, pp.2010-2017, 2014.
2. Tsai RY, Lenz R, "A new technique for fully autonomous and efficient 3D robotics hand/eye calibration," *IEEE Trans. Robot Autom.*, vol. 5(3), pp.345-358,1989.

Quantitative Analysis on Gait-training Effect of Stroke Rats

J. K. Ko, C.B. Yeo, and C. Song*

Department of Robotics Engineering, Daegu Gyeongbuk Institute of Science and Technology (DGIST), Daegu, Korea
E-mail: * csong@dgist.ac.kr

Abstract—Gait-training rehabilitation could be useful method to help stroke recovery. In this study, we analyze the correlations between recovery level and neurological evaluation with oxygenation monitoring in ischemic stroke rat model. It shows that regular gait-training could affect blood oxygenation level so that it helps to recover ischemic stroke.

Keywords—Ischemic stroke, Gait training, Rehabilitation, Neurological evaluation, Laser blood oxygenation monitor

I. INTRODUCTION

Ischemic stroke can result in the change both rat's behavior and brain function. Invasive stroke inspection such as TTC staining [1] and Immunohistochemistry [2] has been proposed. Non-invasive neurological evaluation such as Garcia test [3] is also able to monitor it without any sacrifice. By introducing neurological evaluation and brain oxygenation monitoring, we could quantitatively evaluate the importance of treadmill exercise for the recovery of ischemic stroke rat model.

II. METHODS

A. Preparation of ischemic stroke rats

Middle cerebral artery occlusion at the left side brain of SD rats was induced. Reperfusion was performed after the occlusion of 90 minutes.

B. Rehabilitation with treadmill training

30-minute treadmill training per day was applied to stroke rats after 24 hours of reperfusion. Break of 10-minute are followed by treadmill training of 10-minute. Treadmill training velocity is 15 m/min.

C. Neurological Evaluation

Neurological test follows Garcia score chart [3]. Garcia test is non-invasive method for evaluation of stroke recovery state without any device.

D. Laser Blood Oxygenation Monitor (LBOM)

Laser for measurement is semiconductor type laser, which is available to occur 635nm, 655nm and 690nm wavelengths. LBOM measures blood oxygenation (%) and total hemoglobin (A.U) on left brain. Measurement is performed directly on the skin without anesthesia.

III. RESULTS

Neurological evaluation shows that exercise group recovered gradually while non-exercise group got worse. LBOM measurement shows that gait-training could affect the level of blood oxygenation and total hemoglobin.

IV. CONCLUSION

In this study, we demonstrate that neurological evaluation of stroke rats has something to do with brain oxygenation. Both methods show that exercise group is better than non-exercise group in terms of its recovery level. We hope that this study would be useful for the quantitative evaluation of stroke rats' recovery.

ACKNOWLEDGEMENT

This work was supported by the DGIST R&D Program of Ministry of Science, ICT and Future Planning (15-BD-0401) and the MIREBrain project of DGIST (2015010026)

REFERENCES

1. T.R. Han, S.U. Lee, D.Y. Kim, S.H. Park, D.H. Choi, H.W. Park, J.E. Lee, "Influence of Exercise Intensity in Early Rehabilitation on Neurological after Focal Ischemia in Rats," *Korean Stroke Society* vol. 8, no.1, pp. 107-118, 2006.
2. G.A. Rosenberg, L.A. Cunningham, J. Wallace, S. Alexander et al, "Immunohistochemistry of matrix metalloproteinase in reperfusion injury to rat brain: activation of MMP-9 linked to stromelysin-1 and microglia in cell cultures", *Brain Research* vol. 893, no. 1, pp.104-112, 2001
3. JH. Garcia, S. Wagner, KF. Liu, XJ. Hu, "Neurological deficit and extent of neuronal necrosis attributable to middle cerebral artery occlusion in rats. Statistical validation." *Stroke* vol. 26, pp. 627-634, 1995.

Optimization of TMS Coil Position Using Magnetic Vector Potential

Donghyeon Kim, Sung Chan Jun*

School of Information and Communications, Gwangju Institute of Science and Technology, Gwangju, South Korea
E-mail: {danielkim, scjun}@gist.ac.kr

Abstract—The effect of Transcranial magnetic stimulation (TMS) has been well investigated. However, optimized coil position is not well understood. Here, an optimization strategy maximizing target intensity of electric field from distribution of magnetic vector potential was proposed. This optimization protocol to healthy subject's head MRI was implemented and obtained optimized coil position was determined in an automatic manner. Our strategy is parallelizable, cost effective, and clinically well applicable.

Keywords— Transcranial magnetic stimulation, Optimization

I. INTRODUCTION

The computational study of transcranial magnetic stimulation (TMS) informs the distribution of electric field in the brain and neural responses. To better apply to clinical field, however, the optimization strategy guiding coil positions depending on stimulation target is quite compelling. In this study, a simple and fast TMS optimization method (called RABO (R-rAdius Ball based TMS Optimization)) based on the distribution of magnetic vector potential (MVP) was proposed.

II. METHODS

A. Optimization procedure of RABO

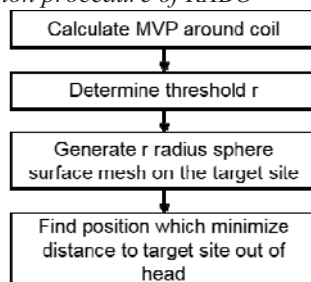


Fig. 1. General procedure of RABO

The general procedure of RABO was illustrated in Figure 1. The main idea of RABO is using MVP to estimate electric field due to TMS. Thus, MVP was estimated around coil and maximum coil distance (r) based on the magnitude of MVP was determined. Within r distance, stimulation of TMS was assumed to be valid. In RABO, the type of coil design is only available for figure-8 and butterfly shape coil due to the cone shape of MVP field. Then, r radius sphere

surface mesh on the target site was generated. Each node of surface mesh would be a possible coil position but not optimized yet. Starting from a possible coil position, RABO minimizes the distance to target position iteratively. If the coil on the possible coil position and head model were overlapped, an iteration would be terminated and previous coil position was determined as a candidate coil position. After finishing whole iteration procedure for all nodes, the minimum distance to the target site among candidate coil positions is an optimized position which maximizes target intensity of electric field.

III. RESULTS

For the test, a healthy subject's brain MRI [1] and double 70mm alpha coil (magstim, UK) were used. The target site is deep region around precentral gyrus (Fig. 2A). The optimization procedure was done in 245sec (i7 quad core @ 3.6Ghz and 32GB RAM) and electric field of optimized coil position was obtained by finite element method (Fig. 2B&C).

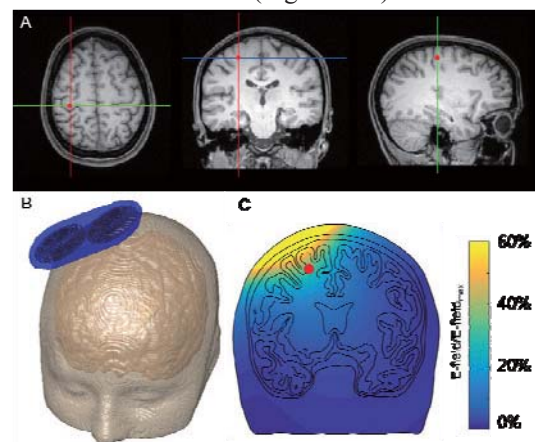


Fig. 2. (A) Stimulation target, (B) Optimized coil position using RABO, (C) electric field distribution around target site.

IV. CONCLUSION

RABO is quite cost-effective and parallelizable. Using this method, clinicians may determine target-optimized TMS coil position easily and quickly.

ACKNOWLEDGEMENT

This work was supported by a grant from the Integrative Aging Research Center of GIST.

REFERENCES

1. Kim D *et al.*, PLoS One, 2014.

Analyze human skin injury types caused by collision

Moony Young Park¹, Ki Hong Kim², Min Kyung Shin³, Sung Soo Rhim², Kyung Sook Kim^{1*}

¹Department of Biomedical Engineering, College of Medicine, Kyung Hee University, Seoul, Korea

²Department of Mechanical Engineering, Kyung Hee University, Gyeonggi-do, Korea

³Department of Dermatology, College of Medicine, Kyung Hee University, Seoul, Korea
E-mail: moosou94@khu.ac.kr

Abstract— Human skin injury analyzing system was designed by animal model and impactors for safety assessment of the collaborative robots.

Keywords— Skin injury, White Yucatan minipig, collaborative robot

I. INTRODUCTION

Over the last years, the robotics research has been developed rapidly in mechanical design and control. The development made it possible to have direct cooperation between humans and robots in same place. As this collaborative robot system is increasingly used in various fields including industry and medical service, the safety assessment of the collaborative robot become very important issues. The direct physical interaction between human and robot can be happen in various situations. Therefore, it is rather difficult to quantify the safe behavior of robot and asses the human injury. In this work, we focused on the human injury, especially skin injury, caused by collision with robot. Using animal model, Yucatan minipig which has skin close to human, the effect of impactor on skin was evaluated. The pattern of skin injury was analyzed by changing the impulse with four different impactors.

II. METHODS

A. White Yucatan minipig.

SPF (specific pathogen free) white Yucatan minipig was used in this work, which is female, 32 weeks, and 25kg weights. This study was approved by the Institutional Review Board (IRB) of Kyung Hee Medical Center (No. KHMC-IACUC 15-027).

B. Impactors

Four different shaped impactors (semi-cylindrical, pyramid edge, rectangle, and sphere) were used (Figs. 1(a) and (b)). Collision speed of the impactor was increased by increasing the angle (20°, 40°, 60°, and 90°) (Fig. 1(c)).

C. H&E Staining.

Injured skin tissues were fixed in 10% formalin, embedded in paraffin, sectioned with 5 μm thicknesses and then stained with hematoxylin and eosin (H&E).

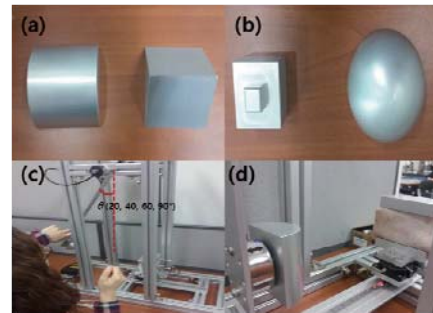


Fig. 1 Four different shaped impactors and collision test system.

III. RESULTS

Human skin can be roughly divided into epidermis, dermis, and subcutaneous tissue. In medical, the skin injury is usually considered as a secondary injury that accompanies e.g. fractures. There is no definition or criteria only for the skin injury. In this work, we first focused on defining skin injury type which depends on the impactor shape and impluse. Figure 2 shows two typical types of the skin injury, cutting (Fig. 2a) and disorder of the organization (Fig. 2b).

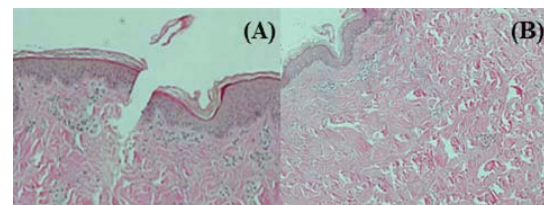


Fig. 2 Typical types of skin injury caused by collision, cutting (A) and disorder of the organization (B).

IV. CONCLUSION

In this work, we designed and conducted collision experiments between animal model and impactor to generate skin injury analysis data that is still missing even in biomechanics and dermatology.

ACKNOWLEDGEMENT

This research was supported by the Ministry of Trade, Industry & Energy, Republic of Korea through the Industry Convergence Program (Project No:10051117).

Enhanced apoptotic cell death by magnetic hyperthermia with chitosan-coated MnFe_2O_4 nanoparticles

Yunok Oh¹, and Junghwan Oh^{1,2,3}

¹Center for Marine-integrated Biotechnology (BK21 Plus), Pukyong National University, Busan, Korea

²Department of Biomedical Engineering; ³Interdisciplinary Program of Marine-Bio, Electrical & Mechanical Engineering, Pukyong National University, Busan, Korea

E-mail: jungoh@pknu.ac.kr

Abstract—Magnetic nanoparticles (MNPs) have widely been investigated as a hyperthermic agent for cancer treatment. In this study, thermally responsive Chitosan-coated MnFe_2O_4 (Chitosan- MnFe_2O_4) nanoparticles were developed to conduct the localized magnetic hyperthermia for cancer treatment. Chitosan- MnFe_2O_4 nanoparticles exhibited high magnetization and excellent biocompatibility along with low cell cytotoxicity. *In vitro* Chitosan- MnFe_2O_4 -assisted MHT at 42 °C led to drastic and irreversible changes in cell morphology and eventual cellular death in association with induction of apoptosis through heat dissipation from the excited magnetic nanoparticles. Therefore, the Chitosan- MnFe_2O_4 nanoparticles can be an effective nano-mediated agent for MHT on cancer.

Keywords— MnFe_2O_4 nanoparticles, magnetic hyperthermia, apoptosis.

I. INTRODUCTION

As a therapeutic agent, MNPs have received significant attention due to have been used as a magnetic agent in various biomedical applications including magnetic resonance imaging (MRI), diagnostic sensing, cancer hyperthermia, and drug delivery due to their unique physical and chemical features. Particularly, Magnetic hyperthermia treatment (MHT) using MNPs is one of the promising non-invasive approaches for thermal activation therapy on cancerous tumors [1]. Therapeutic efficacy of MHT greatly depends on physical properties of MNPs [2]. Although a number of researches have demonstrated the feasibility of cancer hyperthermia with application of biocompatible MNPs, few studies reported the optimal dosage and treatment conditions pertaining to the delayed cellular death induced by MHT. Besides, it is still difficult to deliver the optimal thermal energy to cancerous tumors due to dependence of heat capacity on tumor characteristics such as type, stage, size, and hardness. Typically, cancer cells are more sensitive to mild heat (40~45 °C) than normal cells, in that compactly disorganized vasculature and reduced blood flow in tumor hardly dissipates heat to the surrounding area. Thus, the cancer cells treated by the localized heat during hyperthermia undergo apoptosis, leading to cellular death. In this study, *in vitro* study on the effective cancer hyperthermia using Chitosan-

MnFe_2O_4 nanoparticles was demonstrated in terms of apoptotic cell death with minimal damage to surrounding normal cells.

II. METHODS

Preparation of chitosan coated MnFe_2O_4 MNPs

Figure 1 illustrates a synthesis process for MnFe_2O_4 coated with chitosan. MnFe_2O_4 magnetic nanoparticles were synthesized by thermal decomposition procedure reported by sun et al. MnFe_2O_4 nanoparticles were transferred to be hydrophilic by a ligand exchange reaction using DMSA. The chitosan-coated MnFe_2O_4 nanoparticles were prepared by the cross-linking technique [3].



Figure 1 Schematic diagram of synthesis of Chitosan- MnFe_2O_4 nanoparticles.

In vitro MHT

MDA-MB-231 breast cancer cells were used for *in vitro* MHT of the Chitosan- MnFe_2O_4 nanoparticles. MDA-MB-231 cells were seeded at a density of 2×10^5 cells/mL in a 35 mm culture dish of 2 mL medium. To investigate MHT effects of Chitosan- MnFe_2O_4 nanoparticles on breast cancer cells *in vitro*, MDA-MB-231 cancer cells were further incubated with 1.5 mg (magnetic atoms)/mL of Chitosan- MnFe_2O_4 nanoparticles for 24 hr. The cell dish was subjected to A/C magnetic field of 0.6 Tesla, of which the field generator contained 3-turn and 65 mm of inner radius of copper coil equipped with an optical thermocouple for 30 min.

Apoptosis assay

Changes in cell morphology and populations by optical microscopy were observed to evaluate

apoptosis-inducing effects of Chitosan-MnFe₂O₄ nanoparticles on cancer cells after *in vitro* MHT. For qualitative and quantitative determination of *in vitro* apoptosis, the fluorescence microscopy and flow cytometric analysis were performed by using an Annexin V-FITC Apoptosis Detection Kit.

III. RESULTS

Highly ordered ~18 nm cube-like chitosan-coated MnFe₂O₄ nanoparticles were successfully synthesized by thermal decomposition and cross-linking method.

Figure 2 shows flow cytometric analysis on apoptosis and necrosis of MDA-MB-231 cells at various testing conditions with or without Chitosan-MnFe₂O₄ nanoparticles and A/C magnetic field after 24 h incubation. Both control and CM (Figure (a), (b)) demonstrated that most cells were viable (i.e., 93.2% for control and 92.5% for CM). For MHT-42 in Figure 1 (c), a substantial increase in the cell populations was found in LR (42.2%) and UR (32.9%) regions, evidencing the incidence of significant apoptosis in the cells. For MHT-52 in Figure 1(d), the cell populations increased exclusively in UL (77.0%) region, representing that necrosis became dominant, compared to MHT-42.

Chitosan-DMSA-MnFe₂O₄ nanoparticles led to an increase in 42 °C of hyperthermia therapeutic hyperthermia level. This temperature increase could disrupt the cytoskeleton and nucleus of MDA-MB-231 cancer cell and eventually, cell death occurred *via* induction of apoptosis after exposure A/C magnetic field.

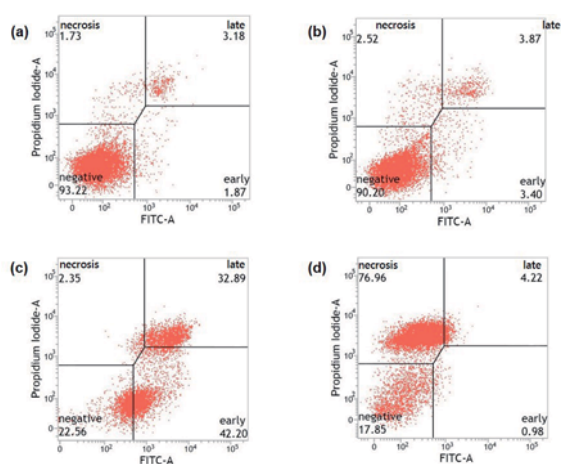


Figure 2 Flow cytometry analysis on apoptosis and necrosis of MDA-MB-231 cells using Annexin V-FITC Apoptosis Detection Kit assay at different conditions: (a) control (untreated cells without MNPs and MHT), (b) CM (cells treated with MNPs and without MHT), (c) MHT-42 (cells treated with MNPs and MHT at 42 °C), (d) MHT-52 (cells treated with MNPs and MHT at 52 °C).

IV. CONCLUSION

Chitosan-coated MnFe₂O₄ nanoparticles were fabricated as an effective magnetic adjuvant for hyperthermic cancer therapy. 1.5 mg/mL of Chitosan-MnFe₂O₄ nanoparticles during magnetic field strength-controlled MHT delivered the appropriate therapeutic heating temperature (~42 °C) to the target cells and induced cellular death through apoptosis in association with thermal diffusion. Due to biocompatibility and high magnetic heating capability, Chitosan-MnFe₂O₄-combined MHT can be a safe and effective therapeutic method for various types of cancers.

ACKNOWLEDGEMENT

This research was supported by a grant from Marine Biotechnology Program (20150220) funded by the Ministry of Oceans and Fisheries, Republic of Korea.

REFERENCES

1. Laurent S, Dutz S, Hafeli U O and Mahmoudi M, "Magnetic fluid hyperthermia: focus on superparamagnetic iron oxide nanoparticles," *Adv Colloid Interface Sci*, vol. 166, pp. 8-23, 2011.
2. Kolhatkar A G, Jamison A C, Litvinov D, Willson R C and Lee T R, "Tuning the magnetic properties of nanoparticles," *Int J Mol Sci*, vol. 14, pp. 15977-6009, 2013.
3. Kim D-H, Nikles D E and Brazel C S, "Synthesis and Characterization of Multifunctional Chitosan-MnFe₂O₄ Nanoparticles for Magnetic Hyperthermia and Drug Delivery," *Materials*, vol. 3, pp. 4051-65, 2010.

Chitosan-polypyrrole nanocomposites for anticancer drug delivery

Bian Jang¹, Panchanathan Manivasagan¹, Seungjae Lee², Junghwan Oh^{1,3*}

¹Marine-Integrated Bionics Research Center, Pukyong National University, Busan 608-737, Republic of Korea.

²Hankuk Academy of Foreign Studies, Gyeonggi-do, 449-854, Republic of Korea

³Department of Biomedical Engineering and Center for Marine-Integrated Biotechnology (BK21 Plus), Pukyong National University, Busan 608-737, Republic of Korea

E-mail: jungoh@pknu.ac.kr

Abstract— Chitosan-polypyrrole nanocomposites have attracted increasing interest owing to the current exploration of novel diagnostic and therapeutic agents. The chitosan-polypyrrole nanocomposites were characterized by UV-vis spectroscopy, XRD, FTIR, SEM, EDXA and TEM. Chitosan-polypyrrole nanocomposites. The polypyrrole nanoparticles are spherical in shape with an average size of 65 nm. Chitosan-polypyrrole nanocomposites exhibited enhanced cytotoxicity on human breast cancer cell line (MDA-MB 231). Chitosan-polypyrrole nanocomposites will have essential meaning and practical application in future.

Keywords— Chitosan, Polypyrrole, Nanocomposites, Anticancer, Biocompatibility.

I. INTRODUCTION

Polypyrrole have been widely used a matrices of biomolecules because the controlled growth of such molecules could satisfy different requirements such as polymer layer thickness, electrical properties and bio-regent loading, etc. As functional materials, Chitosan offers a unique set of characteristics: biocompatibility, biodegradability to harmless products, nontoxicity, physiological inertness, antibacterial properties, gel forming properties and hydrophilicity, and remarkable affinity to proteins.

II. METHODS

A. Synthesis of polypyrrole

The polypyrrole was prepared account to the previous reports (1).

B. Preparation of Chitosan-polypyrrole Nanocomposites

The chitosan-polypyrrole nanocomposites were prepared account to the literature (1).

C. Characterization of Chitosan-polypyrrole nanocomposites

The morphology of the chitosan-polypyrrole nanocomposites were studies using a XRD, FTIR, EDXA SEM and TEM

D. In vitro cytotoxicity

MDA-MB 231 were treated with a series 1-10 µg/ml concentration of chitosan-polypyrrole nanocomposites along with cell control. After 24 h, cells were washed

with PBS and then these plates were subjected for MTT assay.

III. RESULTS

A. Synthesis of polypyrrole

Fig. 1. Show the UV-Vis absorption spectrum of the polypyrrole nanoparticles.

B. Preparation of chitosan-polypyrrole nanocomposites

The present study develops a simple and a convenient one-step process for the synthesis of chitosan-polypyrrole nanocomposites.

C. In vitro cytotoxicity

In order to demonstrate the cytotoxic effect of the chitosan-polypyrrole nanocomposites, we have performed cytotoxicity of chitosan-polypyrrole nanocomposites on MDA-MB 231 cell line using *in vitro* MTT assay method.

IV. CONCLUSION

Chitosan has been widely used a biomedical material due to its good biocompatibility, while polypyrrole is a representative of conducting polymers which have attracted much interest in recent years. Chitosan-polypyrrole nanocomposites can be potentially advantageous in both biocompatibility and conductivity. This established the potential of these chitosan-polypyrrole nanocomposites as a novel carrier for anticancer drug delivery.

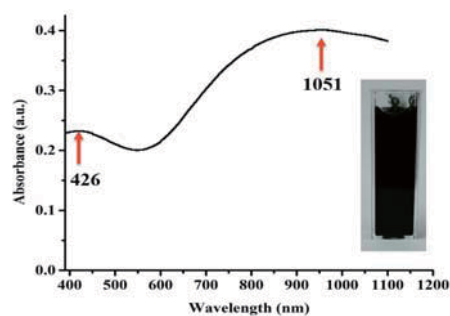


Fig. 1. UV-absorbance spectra of polypyrrole NPs

ACKNOWLEDGEMENT

This research was supported by a grant from Marine Biotechnology Program (20150220) funded by the Ministry of Oceans and Fisheries, Republic of Korea.

REFERENCES

1. M. Ayad, N. Salahuddin, A. Fayed, B.P. Bastakoti, N. Suzukic, Y. Yamauchi, "Chemical design of a

smart chitosan–polypyrrole–magnetite
nanocomposite toward efficient water treatment,”
Phys. Chem. Chem. Phys., 16: 21812-21819, 2014.

Development of three-dimensional fibrous cellulose scaffold via post electrospinning treatment for tissue engineering applications

Mahesh Kumar Joshi¹, Arjun Prasad Tiwari¹, Bikendra Maharjan¹, Han Joo kim¹, Chan Hee Park^{1*}, Cheol Sang Kim^{2*}

Department of Bionano System Engineering, Graduate School, Chonbuk National University, Jeonju 561-756, Republic of Korea

*Corresponding authors: Tel.: +82-63-270-4284; fax: +82-63-270-2460. E-mail: chskim@jbnu.ac.kr (C. S. Kim), biochan@jbnu.ac.kr (C. H. Park)

Abstract— The physical and spatial geometries of the electrospun scaffold are important to their applications in tissue engineering. In this study, a cellulose based scaffolds were produced by electrospinning of cellulose acetate (CA) followed by its saponification with NaOH/ethanol system for 24 h. The resulting nonwoven cellulose mat was treated with sodium borohydride (SB) solution. In-situ hydrolysis of SB solution into the pores of the membrane produces hydrogen gas resulting three-dimensional (3D) cellulose scaffold. 3D cellulose sponge showed the better cell infiltration, spreading and proliferation compared to 2D cellulose mat. Therefore, a facile expansion of 2D electrospun membrane into 3D cellulose nanofibrous scaffold with improved cellular activity represents the innovative strategy for the tissue engineering applications.

Keywords— Cellulose; 3-D scaffold; Biocompatibility; Saponification; Cell infiltration.

I. INTRODUCTION

In the past decade, considerable efforts have been made to fabricate the biomimetic scaffolds from electrospun nanofibers for tissue engineering applications. However, one of the major concerns with electrospun nanofibrous scaffolds is the densely packed fibers in two-dimensional (2-D) array which impedes their applicability in tissue regeneration. However, existing strategies required special manufacturing protocols, still do not offer a three-dimensional fibrous structure effective for cell proliferation and growth. Nevertheless, gas foaming techniques exhibit a strong advantage, especially in the processing of cellular polymers for various biomedical and industrial applications. The gas foaming process utilizes the nucleation and growth of gas bubbles that are generated *in-situ* either via chemical reaction or by adding inert gases to the polymer phase at different physical environments, still this versatile technique is not reported for the processing of electrospun nanofibrous mat. Electrospun membranes have densely packed nanofibers with interconnected micro/nano pores. Generation of gas bubbles *in-situ* into the pores of the nonwoven electrospun mat via chemical reaction is a potential strategy to reorganize the nanofibers in a loosely packed, 3-D architecture.

II. METHODS

Cellulose acetate nanofibrous membrane was prepared by electrospinning techniques. Electrospun

CA mat was immersed into 0.05 M NaOH in H₂O/ethanol (1:4 v/v) solution for 24 h at room temperature in order to remove acetyl group via alkali catalyzed saponification. 3D scaffold was obtained by treating cellulose mat (5×5 cm) with sodium borohydride solution (0.05M, 50ml) for 2h. Resulting 3-D scaffold was thoroughly rinsed with distilled water followed by vacuum drying at 35° C for 24h.

III. RESULTS

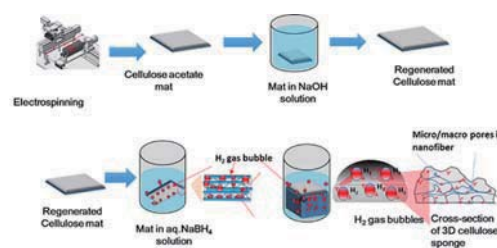


Fig. 1. Schematic illustration for the fabrication of 3D cellulose sponge.

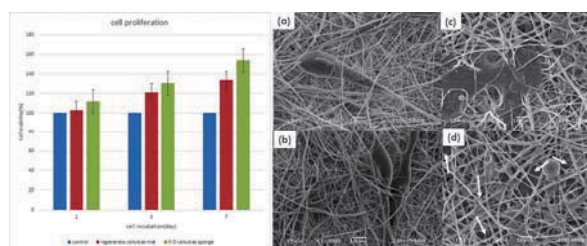


Fig. 2. Cell viability (left) and SEM image (right) showing cell infiltration and proliferation in different scaffold. (a and b) cellulose mat and (c and d) 3D cellulose scaffold

IV. CONCLUSION

The 3D cellulose scaffold showed better cell infiltration, growth and proliferations compared to cellulose mat. Therefore, a 3D cellulose sponge prepared by electrospinning and subsequent post treatment has great potentiality in tissue engineering applications.

REFERENCES

- Joshi, M. K.; Pant, H. R.; Tiwari, A. P.; kim, H. J.; Park, C. H.; Kim, C. S. Chemical Engineering Journal 2015, 275, 79-88.
- Joshi, M. K.; Pant, H. R.; Tiwari, A. P.; Maharjan, B.; Liao, N.; kim, H. J.; Park, C. H.; Kim, C. S. Carbohydrate Polymers 2016, 136, 154-162.

Heterogeneous Tissue Engineered Constructs (hetTECs) Recapitulate the Micromechanical and Mechanobiologic Complexity of Native Dense Connective Tissues

Su-Jin Heo¹, Woojin M. Han¹, Claire M. McLeod¹, Dawn M. Elliott² and Robert L. Mauck¹

¹Dept. Bioengineering, University of Pennsylvania, Philadelphia, PA, USA

²Dept. Biomedical Engineering, University of Delaware, Newark, DE, USA

E-mail: lemauck@mail.med.upenn.edu

Abstract — Fibrocartilaginous tissues contain highly inhomogeneous microstructures that influence mechanotransduction in tissues. In this study, we developed a novel method to generate heterogeneous tissue engineered constructs ('hetTECs') with micro-scale non-fibrous proteoglycan-rich micro-domains (PGmD) 'engineered-into' the fibrous collagen-rich micro-domains (FmD). These hetTECs match the microstructural, micromechanical, and mechanobiological benchmarks of the native tissue.

Keywords — Engineered fibrocartilage, Tissue heterogeneity, Micromechanics, Mechanobiology

I. INTRODUCTION

Native fiber-reinforced dense connective tissues play important roles in load transmission. These tissues have highly ordered FmDs that provide for the tensile mechanics. With increasing age or with degeneration, this ordered structure is often lost, however, and PGmDs emerge within the tissue and become more prevalent [1]. We recently reported that PGmDs attenuate local strain and cell deformation in native tissue, altering the local mechano-response [2]. To enable a more systematic study of this context-dependent mechanotransduction, this study developed μ -engineered heterogeneous tissue engineered constructs (hetTECs) containing PGmDs 'engineered-into' an otherwise ordered FmD, and evaluated their mechanics and mechanobiology relative to native tissue.

II. METHODS

To fabricate hetTECs, bovine MSC micro-pellets were formed and underwent chondrogenesis for 1 week. These micropellets, along with meniscal fibrochondrocytes, were then seeded onto aligned nanofibrous PCL scaffolds. An additional sheet of a scaffold was layered on top of the construct followed by culture in the media containing TGF- β 3 for up to 8 weeks. Alcian Blue and Picrosirius Red staining were performed. RNA fluorescent in situ hybridization (FISH) was carried out at the single cell-level. Local ECM strain was evaluated using a custom device on a fluorescent microscope [2] and calculated using either a custom MATLAB script or VIC-2DTM. To monitor changes in $[Ca^{2+}]_i$, cells were labeled with Cal-520TM, and constructs stretched on a confocal microscope [2].

III. RESULTS

By 8 weeks, PGmD size significantly increased, and these inclusions became enmeshed within the surrounding FmD (not shown). FISH analysis showed that the AGG/GAPDH mRNA ratio was significantly higher in cells in PGmDs than in FmDs (not shown). With stretch, hetTECs containing PGmDs showed highly heterogeneous strain fields, where the strain magnitude within the PGmD was lower than that of the surrounding FmD (Fig. 1a). Strain transfer in the FmD regions of the hetTEC was direct, while in the PGmDs strain transfer was significantly attenuated at week 8 (Fig. 1b). Similar trends were observed in hetTECs containing only PGmD or FmD regions (PGmD only or FmD only in Fig. 1b). Moreover, application of 6% strain increased the number of $[Ca^{2+}]_i$ oscillations in FmD cells, while cells within PGmDs were largely unresponsive to this perturbation (not shown). These results demonstrate that hetTECs with 'engineered-in' PGmDs recapitulate the heterogeneous strain transfer to the micro-scale level that is seen in native tissue [2].

IV. CONCLUSION

In this study, we developed a novel technique to generate hetTECs, and showed that PGmDs contribute to emergence of local strain heterogeneity and alteration of local mechano-response, consistent with findings in native tissue.

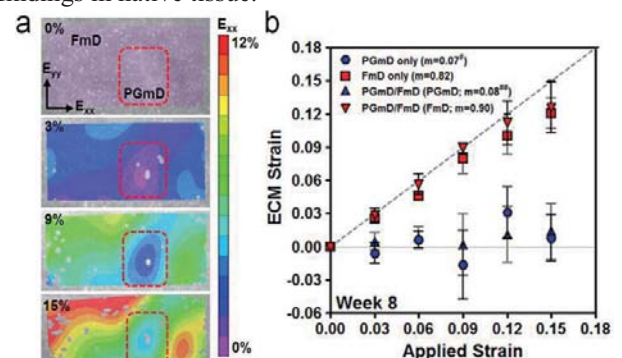


Fig. 1: (a) Color maps of ECM strain (E_{xx} ; loading direction) for hetTEC at week 8, (b) Quantification of local ECM strain of hetTEC at week 8 ($n \sim 45$).

ACKNOWLEDGEMENT

This work was supported by the NIH (R01 EB02425).

REFERENCES

1. W.H. Han et al., "Macro- to microscale strain transfer in fibrous tissues is heterogeneous and tissue-specific," *Biophys J*, 105 (3), 807-817, 2013.
2. W.H. Han et al., "Emergence of proteoglycan-rich micro-domains during development affects tissue-to cell strain transfer in the knee meniscus," BMES-CMBE 2015.

The study on MG-63 cells proliferation with various mechanical stimulation on auxetic hybrid scaffold

HongJin Choi¹, JinHo Kang², JunJae Lee², JeongKoo Kim^{1,2*}

¹Department of Interdisciplinary Medical Sciences, Inje University, Gimhae, Korea

²Department of Biomedical Engineering, Inje University, Gimhae, Korea

E-mail: jkkim@inje.ac.kr

Abstract—In this study, we were checked about the mechanical properties and NPR(negative Poisson's ratio) of the composite scaffold consisting of PLGA (poly(lactide-co-glycolide)) and HA (hydroxyapatite) composite. It can make auxetic HA/PLGA scaffold with mechanical properties, that were increased by increment of HA content, and good hydrophilicity. The 10wt% HA/PLGA scaffold's recovery rate was about 10% higher than only PLGA.

Keywords— Negative Poisson's ratio, PLGA, Hydroxyapatite, Dynamic compression, Osteoblast

I. INTRODUCTION

HA and PLGA have good biocompatibility and mechanical property. The scaffold with negative Poisson's ratio has advantage for cell proliferation by isotropic permanent volumetric compression [1].

II. METHODS

A. Fabrication of the scaffold with (-) Poisson's ratio

Only PLGA 5050 were used to make control group. The scaffold with 10wt% HA powder incorporated PLGA 5050 is experimental group. In order to make NPR scaffold, we were made the scaffold with salt-solvent casting method and then subjected to permanent volumetric compression method for to create the NPR porous structure.

B. Mechanical properties of the scaffold

The compressive strength of scaffold was measured using MTS at 5 and 10% strain. Compression condition was applied 1.3mm/min (ASTM D-695). In order to analyze the mechanical properties of the scaffold in cell culture conditions, we were carried out MTS measurement in the wet state. The wet-state scaffolds were immersed into EtOH/PBS/DMEM/37°C. The Measurement of recovery rate of the scaffold was conducted after compressing 10% strain for 5 minutes to the scaffold and then measured the recovery position after 5 minutes.

C. Analysis of contact angle

Scaffold's hydrophilicity were measured by Video contact angle system.

III. RESULTS

A. Negative Poisson's ratio of the scaffold

The 10wt% HA/PLGA 5050 by using 3-dimensional permanent volumetric compression scaffold was shown negative Poisson' ratio.

B. Mechanical properties of the scaffold

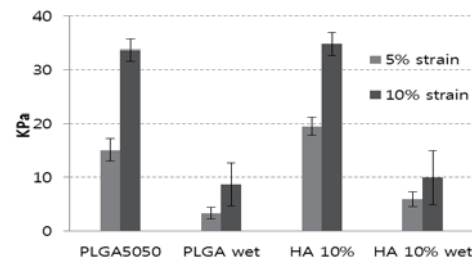


Fig 1. Compressive strength of scaffold as HA content

PLGA scaffold's mechanical properties was increased by increment of HA content at dry and wet state. PLGA scaffold's mechanical properties were decreased sharply at wet state about 70% of dry state (Fig 1). PLGA scaffold's recovery rate was increased by HA content at dry and wet state. PLGA scaffold's recovery rate was decreased at wet state about 30% of dry state.

C. Contact angle

With increasing of HA content, the hydrophilicity of films was increased generally. The 10% HA in PLGA was good effect for the hydrophilic property.

IV. CONCLUSION

As a result, PLGA 5050 with HA had good mechanical properties and recovery rate than only PLGA 5050. So this scaffold will be effect for supplying the isotropic compression stimulus to bone cell proliferation.

ACKNOWLEDGEMENT

This work was supported by the Human Resource Training Program for Regional Innovation and Creativity through the Ministry of Education and National Research Foundation of Korea (NRF-20104H1C1A1066694)

REFERENCES

1. Park, Y. J.. & Kim, J. K., "The effect of negative Poisson's ratio polyurethane scaffolds for articular cartilage tissue engineering application." *Advances in Materials Science and Engineering*, 2013.

A comprehensive electric field analysis of cylinder-type multi-nozzle electrospinning system for mass production of nanofibers

In Gi Kim ^{a,1}, Jung-Ho Lee ^{a,1}, Afeesh Rajan Unnithan ^a, Do Hee Lee ^a, Sung Won Ko ^a, Chan-Hee Park ^{a,b,*},
Cheol Sang Kim ^{a,b,*}

^a Department of Bionanosystem Engineering, Chonbuk National University, Jeonju, Jeonbuk 561-756, South Korea

^b Division of Mechanical Design Engineering, Chonbuk National University, Jeonju, Jeonbuk 561-756, South Korea

E-mail: biochan@jbnu.ac.kr (C.-H. Park), chskim@jbnu.ac.kr (C.S. Kim)

Abstract— Electrospinning is the commonly used method for fabrication of micro/nano fibers due to simple setup and intuitive understanding of mechanism. In laboratory scale, single or dual nozzle systems are mainly used to conduct specific experiments and use simple electric power connections and it has uncomplicated electric field distributions. An industrial scale mass production of micro/nano fiber is an essential prerequisite for price competitiveness. For the first time in South Korea, we developed a novel upward cylindrical-type electrospinning system and the study demonstrates the comprehensive electric field simulations of multi-nozzle system and practical test results of the electrospinning system.

Keywords— Multi-nozzle electrospinning, Electric field analysis, Nanofibers, Scaffolds

I. INTRODUCTION

Several methods have been developed to enhance the electro-spinning production rate. Cylinder-type nozzleless electrospinning system was introduced by EIMARCO and multi-nozzle electro-spinning set-ups were developed to increase the mass production of nonwoven matrix [1–8]. The multi-nozzle system still needs study as it can be designed to both increase productivity and to produce composite fibers of two or more than two polymers where they have no common solvents. To improve the mass production and morphology of nanofibers, several types of multi-nozzle electrospinning systems have been studied. However, several multi-nozzle electrospinning studies have shown that electric field distribution in less than two nozzle system influenced the electrospinning process and the morphology of obtained nanofibers [9,10].

This study aims to study the electric field analysis of 1 m length upward cylinder-type multi-nozzle configurations with the help of computer simulation followed by experimental observations. The effect of 1 m length cylinder-type multi-nozzle configurations on electric field distribution and its impact on fiber diameter was first simulated using COMSOL1 multiphysics software. This study shows a possibility that further development of multi-nozzle electrospinning system for commercial application.

II. METHODS

A. Materials

High molecular weight thermoplastic polyurethane (PU) was purchased from Lubrizol advanced Materials and dried in an oven at 80 °C for at least 3 h prior to dissolution in solvents. N,N dimethylformamide (DMF) and methyl ethyl ketone (MEK) were purchased from Showa Chemicals and Junsei Japan, respectively. All reagents were commercial grade and were used without any further purification. 10 wt% PU in DMF/MEK (50/50, wt%) was prepared and kept overnight with magnetic stirring.

B. Electrospinning setup

Electrospinning was carried out using the setup shown in Fig. 1, which is designed by our group. It was composed of a cylindrical collector with Teflon sheet, two 10-ml plastic syringe, two metal capillary (nozzle) with $d_i = 0.51$ mm (21 G), two syringe pump, and a 1-D robot system that moves laterally controlled by LabVIEW 9.0 program (National Instrument). The whole setup was placed in a sealed chamber, with automatic, dehumidifier and heating system.

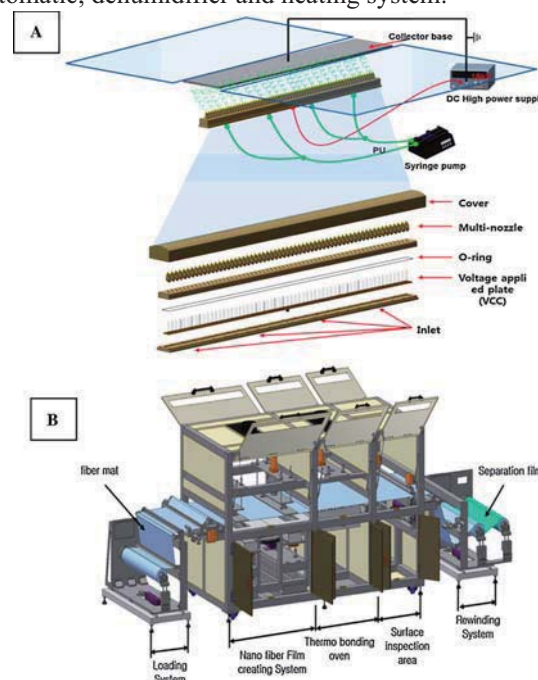


Fig. 1. (a) Schematic diagram of the components of multi-nozzle electrospinning system (upper part), (b) The nanofiber mass production system.

C. Electric field analysis use COMSOL

The simulation on electric field measurement of our newly introduced multi-nozzle electrospinning system with different nozzle configurations was carried out using COMSOL1 Ver.4.3 add on AC/DC module under Windows Vista operational system. Simulation was performed using the actual configuration of electrospinning setup as shown in Fig. 1. The morphological properties of all samples were observed using scanning electron microscopy (SEM, Hitachi X-650, Japan). The fiber diameter distribution was determined using Image J (NIH, USA) software.

III. RESULTS

A. Practical performance test

The performance test of our cylindrical-type multi-nozzle system is carried out using PU 10 wt% solution and nano fibers were collected (Fig. 2). As seen in Fig. 2, the SEM images showed smooth nanofiber morphology without any beads. An optimum concentration results in more extensive polymer chain entanglements within the solution which is necessary for maintaining the continuity of the jet during electrospinning to form fine nanofibers with an average diameter of 230 nm as seen in Fig. 2.

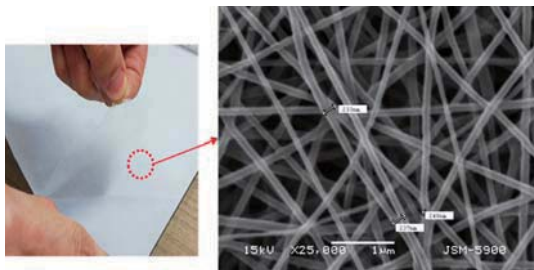


Fig. 2. SEM image of electrospun PU nano fibers obtained from multi-nozzle electrospinning system.

B. Electric field analysis

The Fig. 3a represents the distribution of the electric field on surface and direction is denoted by arrow. The Fig. 3b denotes the surface and contour distribution of the electric field and Fig. 3c represents surface, contour and arrow and finally Fig. 3d shows contour and arrow.

Fig. 4 shows the effect of the nozzle-to-substrate distance variation in electric field intensity and it is analyzed by separating horizontal and vertical line in order to quantitatively analyze the result.

Fig. 5 shows the side view of the electric field distribution simulation on the charged nozzles. Therefore, arrow streams flow from the nozzle to the

collector base and is shown in surface and arrow (Fig. 5a).

The electric field intensity is extreme at the nozzle tip and as the distance from nozzle tip to collector increases, the electric field intensity diminishes. The obtained result is again confirmed with the side view analysis of electric field intensity with distance as shown in Fig. 6.

IV. CONCLUSION

High-quality low-cost mass production of nanofiber mats is essential to support the fast growing researches in the nanotechnology field. For enhancement in the applicability of nanofibers, various new revolutions in electrospinning were used. The lab-scale electrospinning machine that researchers currently used has a few numbers of nozzles. It takes quite long time to fabricate nanofiber mats. Moreover, the thickness of the mat depends on the spinning time. So, it is necessary to have a fast and convenient system for the production of nanofibers. This study proved that the mass production of electrospun nanofibers by modified upward cylindrical-type multi-nozzle system method. The results obtained here suggest that our upward cylindrical-type multi-nozzle electrospinning system can be applied for the mass production of nanofiber at laboratory as well as industrial site.

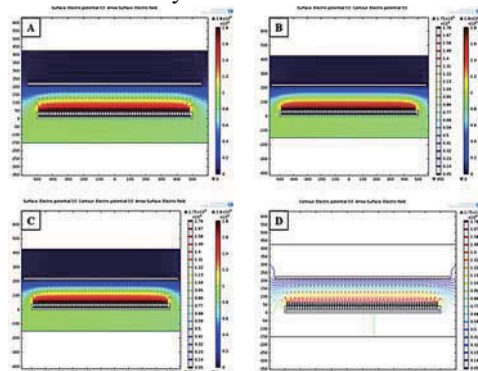


Fig. 4. Results of electric field distribution simulation (front view)

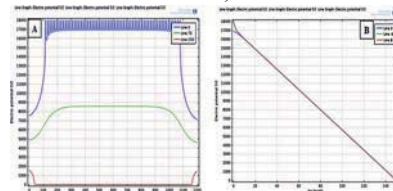


Fig. 5. Variation of electric field intensity with variation in distance (front view)

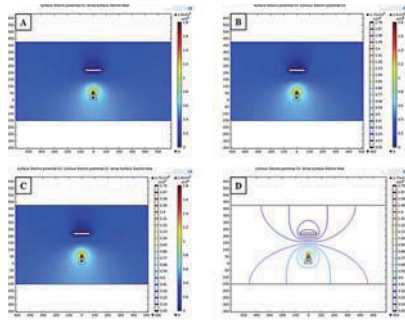


Fig. 6. Results of electric field distribution simulation (side view)

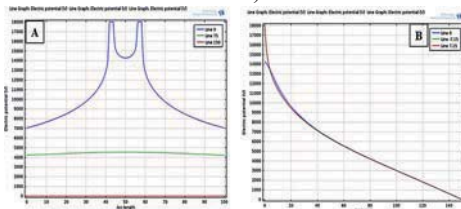


Fig. 7. Variation of electric field intensity with variation in distance (side view)

ACKNOWLEDGEMENT

This work was supported by the grant from the Basic Science Research Program through National Research Foundation of Korea (NRF) by Ministry of Education, Science and Technology (Project no. 2013R1A2A2A04015484 and 2013-012911) and partially supported by the research funds from Korean Small and Medium Business Administration (Project no. C0208053)..

REFERENCES

1. C. Burger, B.S. Hsiao, B. Chu, *Annu. Rev. Mater. Res.* 36 (2006) 333..
2. H.R. Pant, D.R. Pandeya, K.T. Nam, W.I. Baek, S.T. Hong, H.Y. Kim, *J. Hazard. Mater.* 189 (2011) 465.
3. Y.Z. Zhang, C.T. Lim, S. Ramakrishna, Z.M. Huang, *J. Mater. Sci. -Mater. Med.* 16 (2005) 933.
4. H.R. Pant, P. Risal, C.H. Park, L.D. Tijing, Y.J. Jeong, C.S. Kim, *Colloid Surf. B* 102 (2013) 152.
5. X.F. Wang, J.L. Wang, Y. Si, B. Ding, J.Y. Yu, G. Sun, W.J. Luo, G. Zheng, *Nanoscale* 4 (2012) 7585.
6. R. Neppalli, S. Wanjale, M. Birajdar, V. Causin, *Eur. Polym. J.* 49 (2013) 90.
7. R. Neppalli, C. Marega, A. Marigo, M.P. Bajgai, H.Y. Kim, V. Causin, *Eur. Polym. J.* 46 (2010) 968.
8. A.R. Unnithan, N.A.M. Barakat, P.B.T. Pichiah, G. Gnanasekaran, R. Nirmala, Y.S. Cha, C.H. Jung, M. El-Newehy, H.Y. Kim, *Carbohydr. Polym.* 90 (2012) 1786.
9. P.P. Tsai, H. Schreuder-Gibson, P. Gibson, *J. Electrostat.* 54 (2002) 333.
10. G. Kim, Y.S. Cho, W.D. Kim, *Eur. Polym. J.* 42 (2006) 2031.

High sensitive detection of apple scar skin viroid (ASSVd) by using loop-mediated isothermal amplification (LAMP)

Se Hee Lee, Ga-Young Park, Gna Ahn, Eunji Lee, and Ji-Young Ahn*

Department of Microbiology, Chungbuk National University, Cheongju, Korea

E-mail: jyahn@chungbuk.ac.kr

Abstract— Viroids are about 250-400 base pair of short single strand RNA fragments and have been associated with economically important plant diseases. We here designed specific primer-sets for detection of viroid by grafting loop mediated isothermal amplification (LAMP) which can amplify target in isothermal without the need to change temperature. We extracted total RNA of apple leaves infected with apple scar skin viroid (ASSVd). Extracted RNAs were converted to cDNA by using a cDNA synthesis kit and specific primer sets. Viroid identification process was performed by T-vector cloning and sequencing. LAMP primers were then specifically designed from the sequence information. LAMP experimental condition for amplifying ASSVd was critically optimized and amplification efficiency was compared with.

Keywords— Apple scar skin viroid (ASSVd), Loop mediated isothermal amplification (LAMP), Viroid

I. INTRODUCTION

For detecting viroid, molecular techniques such as polyacrylamide gel electrophoresis (PAGE), DNA-hybridization and conventional RT-PCR are reliable for ASSVd detection in apple, but were not conclusive for the ASSVd variants in the apple leaves because of their low concentrations [1-3]. Ribonuclease protection assay (RPA) has been shown to be a robust method for detecting ASSVd in field surveys, but it required radioactive probes [4]. The methods described above do not have the combination of specificity, sensitivity and reliability required for routine detection of oil palm ASSVd variants from field samples. LAMP has been reported to be rapid and sensitive in detecting viroids and has been used for detection of Potato spindle tuber viroid and Peach latent mosaic viroid [5].

II. METHODS

A. Viroid sample

Apple leaf samples were obtained from three trees (positive Sample 1 (pS1), positive Sample 2 (pS2) and negative Sample 3 (nS3)) grown in National Institute of Horticultural & Herbal Science (NIHHS) plantation in Korea, which had been reported to contain ASSVd variants (pS1 and pS2), together with one known ASSVd-negative palm (nS3).

B. LAMP-Primer

ASSVd LAMP primers were designed based on a 331-nt ASSVd variant sequence using the PrimerExplorer V4 software. The primer set comprised an inner pair (FIP and BIP), and an outer pair (F3 and B3) and listed in Table 1.

III. RESULTS

A. Amplification of ASSVd from Apple leaves

A conventional PCR amplification was attempted with the forward/reverse primers to validate the ASSVd infection (Figure 1). In this experiment, pS1 and pS2 were used as positive samples. First, cDNA strand was synthesized with reverse primer. This was amplified by PCR using a PCR master mix. Annealing temperature was set at 63 °C. Amplified product was then analyzed on 1.5 % agarose gel and the expected region of 300–400 bp was excised and eluted using MinElute kit (QIAGEN, Hilden, Germany) and sent for sequencing.

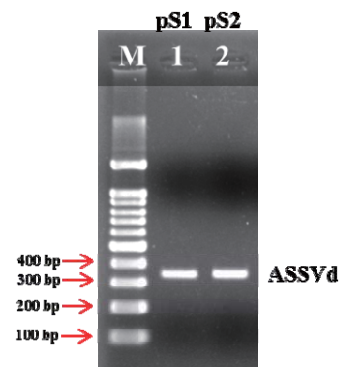


Figure 1. Conventional PCR amplification result of ASSVd

B. Specific amplification of ASSVd by LAMP

A reliable LAMP assay is highly dependent on a primer set of high specificity, which uses four primers recognizing six distinct regions on the target template (Table 1). The ASSVd-LAMP primers tested in this study amplified specifically and sensitively ASSVd from total nucleic acids extracted from leaf samples of apple.

IV. CONCLUSION

ASSVds were successfully detected in the two known ASSVd positive leaf samples and one negative sample (pS, pS2 and nS3) used in this study. ASSVd was detected as early as 1 hour at temperatures ranging

from 60 to 65 °C. Positive reactions of the LAMP were distinguished by colour change from orange to green after addition of the fluorescent reagent, and when the tubes were viewed under UV light, the positive reaction showed fluorescence. The low concentration of ASSVd variants in apple and the increasing incidence of apple scar skin disease warranted a rapid, sensitive and reliable diagnostic method.

Table 1. LAMP-PCR primer sets for ASSVd

ID	sequence
forward	TCGTCGACGACGACAGGTGAGTTCC
reverse	GTCGTCGACGAAGGCCGGTGAGAAAG
F3	CGCCCTCGCACCAGTT
B3	CCACAGGAACCGCACG
FIP	CCCGGTAAACACCGTGCGGT
BIP	ACCGGAAACACCTATTGTG

ACKNOWLEDGEMENT

This work was carried out with the support of "Cooperative Research Program for Agriculture Science & Technology Development (Development of fast sensing platform for viroids in subtropical plants, PJ011642)" Rural Development Administration, Republic of Korea

REFERENCES

1. R. Flores, C. Hernandez, A.E. Martinez de Alba, J.A. Daros, F. Di Serio, "Viroids and viroid-host interactions", *Annu. Rev. Phytopathol.*, vol. 43, pp. 117–139, 2005.
2. A. Gora-Sochaka, Viroids: unusual small pathogenic RNAs, *Acta Biochim. Pol.*, vol. 51, pp. 587–607, 2004.
3. K. Mi Jo, H. Seung Lark, L. Sung Joon, L. Dong Hyuk, Lee Jai Youl, "Occurrence of Apple scar viroid-Korean strain (ASSVd-K) in Apples Cultivated in Korea", *Plant Pathol. J.* vol. 17, pp.300-304, 2001.
4. P. Jun, F. Zaifeng, H. Junsheng, "Rapid detection of banana streak virus by loop-mediated isothermal amplification assay in South China", *J. Phytopathol.*, vol. 160, pp. 248–250, 2012.
5. Nagamine, Y. Kuzihara, T. Notomi, Isolation of single-stranded DNA from loop-mediated isothermal amplification products, *Biochem. Biophys. Res. Commun.*, vol. 290, pp. 1195–1198, 2002.

Improvement of Multifunctional Loading rate System on Dielectrophoretic Tweezers

M. H. Kim, K. H. Ko, S. Choi and S. W. Lee

Department of Biomedical Engineering, Yonsei University, Wonju, Republic of Korea
E-mail: yusuklee@yonsei.ac.kr

Abstract— We have additionally developed linear force loading rate system that we have already developed linear voltage applying systems before. It could be applied for subdivision of force loading rate. Then we examined critical step how the system can measure stabilized binding force. We identified that as a number of force steps decrease below 10, mean unbinding forces were destabilized because of resolution reduction. This could be utilized as index for measuring binding force on dielectrophoretic force spectroscopy system.

Keywords— Dielectrophoresis, Force Spectroscopy, Loading rate, DEP tweezers, Non-covalent bond.

I. INTRODUCTION

Precise measurement of intermolecular binding force is one of the important issues for understanding of living system. Recently, Lee *et. al.* have introduced the dielectrophoretic (DEP) tweezers that can measure the biomolecular interactions with wide force loading rate in microfluidic chip [1].

In this study, we have developed the automatically operating multifunctional loading rate system based on DEP tweezers technique by LabVIEW program. In addition, we investigated the stabilization force step to apply as an index for measuring binding force.

II. METHODS

A. Microfluidic chips

A chromium interdigitated electrode array pattern (thick 0.1 μm) was created on an oxidized silicon wafer by using the thermal evaporator. The insulator layer (thick 0.8 μm) is deposited on metal electrode by silicon dioxide through PECVD process. We functionalized surface such as carboxyl-terminated oxide surface by 3-(triethoxysilylpropyl) succinic acid anhydride (TESPSA, 0.1M). Also we used carboxyl functionalized beads (Kisker Biotech GmbH & Co.KG, 15 μm).

B. Multifunctional loading rate system

The system include three modes; linear force applying mode, linear voltage applying mode and linear frequency applying mode, respectively. The program can be simultaneously applied force, voltage and

frequency. It can be captured images by arbitrary function generator (NI PCI-5421, National Instrument) and high-speed CCD camera (Motion Scope M3, Integrated Design Tools, Inc.), respectively. The system was coded by LabVIEW program.

III. RESULTS

We additionally developed linear force applying system. The DEP force to voltage conversion was coded by the program that simulated DEP force values were calculated to voltage values reversely. The converted voltages are applied into microfluidic device then we can observe linear force increment.

To verification of stability and reliability, we investigated critical step that which force step we can allow for precise and accurate measurement. We found that when a number of step decrease below 10 step, measured unbinding forces were inaccurate (Fig. 1 (b)).

IV. CONCLUSION

In conclusion, we improved our system for DEP tweezers and we identified the appropriate force step for measuring the intermolecular binding force by linear force step loading conditions. This system would be accurately and quantitatively tools in understanding between the external force rate and intermolecular interactions in the future.

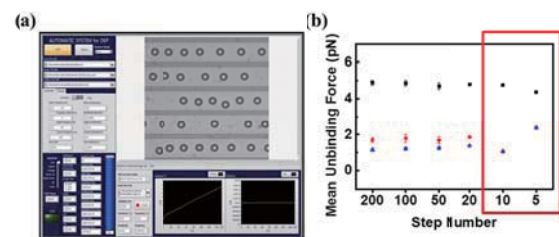


Fig. 1 (a). Control panel of the multifunctional loading rate system. (b). Measurement of mean unbinding force as decreasing the force step number (electrostatic repulsion).

ACKNOWLEDGEMENT

This work was supported by the NRF grant (2013R1A2A203005767, 2013R1A1A2053613).

REFERENCES

1. Lee *et. al.*, "Dielectrophoretic tweezers for examining particle-surface interactions within microfluidic devices," *Appl. Phys. Lett.*, 90, 223902, 2007.

Fabrication, Maturation, and Implantation of a Tissue-Engineered Composite Intervertebral Disc

D.H. Kim^{1,2}, J.T. Martin^{1,2}, S.E. Gullbrand^{1,2}, and R.L. Mauck^{1,2*}

¹ Department of Orthopaedic Surgery, University of Pennsylvania, Philadelphia, USA

² Translational Musculoskeletal Research Center, Philadelphia VA Medical Center, Philadelphia, USA

E-mail: lemauck@mail.med.upenn.edu

Abstract— Low back pain (LBP) arising from disc degeneration is one of the most common health problems in adults. Tissue engineering approaches are showing promise for disc regeneration. In this work, we demonstrate the fabrication, maturation, and in vivo function of a composite engineered disc based on both native disc cells and mesenchymal stem cells. Engineered discs maintained their structure after 5 weeks in vivo, though some loss of proteoglycan was evident in the NP. These findings provide evidence for the potential of an engineered disc.

Keywords— Disc cells, Mesenchymal stem cells, Tissue engineering, Total disc replacement

I. INTRODUCTION

Low back pain (LBP) arising from disc degeneration is one of the most common causes of limited function in adults [1]. Current treatment options are limited, and do not restore native tissue structure and function. As such, a number of tissue engineering strategies have emerged that are focused on the creation of a composite tissue engineered total disc replacement [2]. To further this line of inquiry, we fabricated a composite engineered disc based on the combination of a porous polymer foam annulus fibrosus (AF) and a hyaluronic acid (HA) gel nucleus pulposus (NP). These constructs were seeded with either native AF/NP cells or with mesenchymal stem cells (MSCs) and matured for 9 weeks in vitro, and were evaluated in vivo in a rat tail model of disc replacement.

II. METHODS

Porous polycaprolactone (PCL) foams were fabricated by salt-leaching to form the AF regions. To form the NP regions, HA hydrogels were produced. AF cells or MSCs were seeded onto the PCL foam, whereas NP cells or MSCs were encapsulated in HA. AF and NP regions were cultured separately in a chemically defined media and combined at 2 weeks. At regular intervals over 9 weeks, mechanical, and histologic properties were evaluated. Additionally, AF/NP cell and MSC/MSC cell-seeded constructs were implanted into the rat caudal disc space, after 5 weeks of pre-culture. After 5 weeks, disc height, hydration, and structure were assessed by μ CT, T2 MRI, and histological analyses.

III. RESULTS

During in vitro culture, the NP region of all the groups stained intensely for proteoglycans, while collagen staining in the NP increased. In the AF region, staining gradually increased, though to a lesser extent than in the NP (not shown). After 5 weeks of pre-culture and 5 weeks of implantation, disc height index (DHI) for implanted constructs was significantly greater than pre-operative levels, with only small differences between groups (Fig. 1A). Alcian blue/picrosirius red staining showed abundant collagen in the disc, but little proteoglycan in the NP region in either *in vivo* group. However, collagen type II staining was intense and localized to the NP at this time point (Fig. 1B). MRI showed that implanted discs had a similar structure to native discs, however T2 mapping showed reduced signal in the NP for both groups (not shown).

IV. CONCLUSION

This study demonstrated that a tissue engineered disc composed of a PCL foam AF region and a hydrogel NP region could be fabricated, matured in vitro, and implanted and maintained in the rat caudal spine.

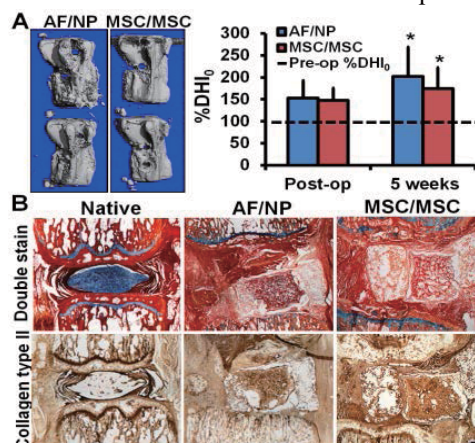


Fig. 1: (A) μ CT and (B) histology at 5 weeks after implantation. (*: $p < 0.05$ vs. pre-op) (bar = 500 μ m)

ACKNOWLEDGEMENT

This study was supported by the Department of Veterans Affairs and the PCMD.

REFERENCES

1. B. R. Whatley, X Wen, "Intervertebral disc (IVD): Structure, degeneration, repair and regeneration," Mater. Sci. Eng., vol. 32, pp.61-77, 2012
2. J. T. Martin, A. H. Milby, et al., "Translation of an engineered nanofibrous disc-like angle-ply structure for intervertebral disc replacement in a small animal model," Acta Biomater., vol. 10, pp.2473-2481, 2014

Dielectrophoresis Force Spectroscopy for defining the directional effect of intermolecular bonds

I. S. Park¹, K. H. Ko¹, M. H. Kim¹, S. W. Lee¹

¹Department of Biomedical Engineering, Yonsei University, Won-Ju, 220-710, Korea
E-mail: yusuklee@yonsei.ac.kr

Abstract—We firstly demonstrate a biaxial dielectrophoresis force spectroscopy (BDFS), which is a novel combination of vertical DEP force spectroscopy (VDFS) and lateral DEP force spectroscopy (LDFS). By using BDFS, we quantitatively assess the intermolecular binding interactions with regard to hydrogen bond and ionic interactions, which are compared simultaneously with respect to pulling direction and speed with all-in-one microfluidic device.

Keywords—Dielectrophoresis, Force Spectroscopy, Intermolecular interaction

I. INTRODUCTION

In this paper, we verified the reliability of the developed LDFS system by comparing it with VDFS. In addition, through the system being capable to observe rupture events by associating LDFS with VDFS, we firstly demonstrated the massive measurements of non-covalent intermolecular forces between single functional groups as a model system consisting of different force pulling directions under the same environment.

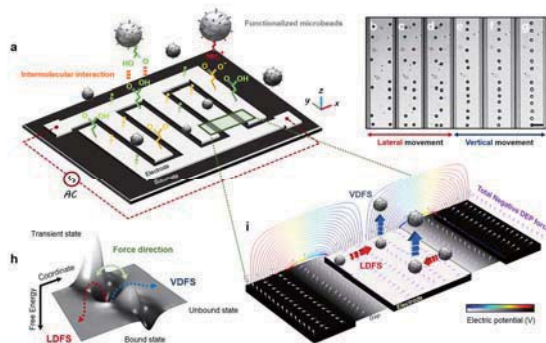


Fig 1. Concept of BDFS system. (a) Schematic illustration of BDFS. (b-g) Time-lapse optical images exhibit how BDFS with a combination of LDFS and VDFS works. (h) The simulation result that depicts electric field intensity at the part of IDT electrode in a microfluidic chip. (i) Schematic illustration of energy pathway depending on force directions.

II. METHODS

Fig. 1a shows the schematic diagram of the measurement system, when AC signal was applied into the electrode. By the carefully control of the magnitude of the applied signal, the beads on the functionalized

silicon dioxide were laterally moved toward the center of electrodes (Fig. 1b-d), and sequentially the aligned beads on the center of electrodes were moved upward from the silicon dioxide surface (Fig. 1e-g), where using the grayscale measurement method.

III. RESULTS

We measured the single binding forces of hydrogen bond and ionic interaction along the external force loading rates. Energy barrier height (ΔG), energy barrier width (Δx) were significantly affected by the force direction (Fig. 2). This implies that those different energy landscape values by the force pulling direction lead to the difference energy path way in a free energy landscape surface (Fig. 1h) along the same experiment conditions.

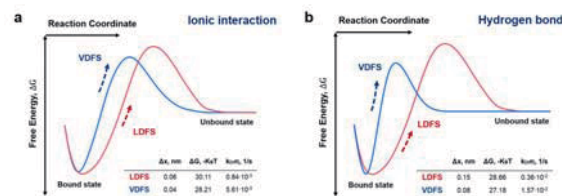


Fig 2. Free energy reaction coordinate along the force direction. (a) Hydrogen bond. (b) Ionic bond.

IV. CONCLUSION

The results of the future studies based on the confirmed results of the studies so far, the lateral and vertical dielectrophoresis are expected to help greatly in studying the relationship of surface and biomolecules or in the research field of investigating and measuring the relationship between the surface and electrostatic bonds of biomolecules and cells.

ACKNOWLEDGEMENT

This research was supported by grants from the National Research Foundation (NRF) funded by the Ministry of Education, Science, and Technology (NRF-2013R1A2A2A03005767, NRF-2013R1A1A2053613), Republic of Korea.

REFERENCES

1. Park I. S. et al. Microfluidic Multifunctional Probe Array Dielectrophoretic Force Spectroscopy with Wide Loading Rates. ACS Nano 6, 8665-8673 (2012)

Mucoadhesive polymer loaded nanostructured microparticles for their enhanced retention in gastrointestinal tract

C. G. Park¹, B. K. Huh¹, S. N. Kim¹, S. H. Lee¹, M. Park¹, H. R. Hong¹, K. R. Kim¹, H. Won¹, and Y. B. Choy^{1,*}

¹Interdisciplinary program for Bioengineering, Seoul National University, Seoul, Republic of Korea
E-mail: ybchoy@snu.ac.kr

Abstract— We fabricate drug and mucoadhesive polymer loaded nanostructured microparticles (NMs) for prolonged transit time in the GI tract so that the bioavailability of drug is increased. In the final product of microparticles, the NMs have 7 times higher specific surface area than spherical microparticles (MS) which brings the large interaction area with mucous layer in GI tract by in vivo imaging system.
Keywords— nanostructured microparticles, bioavailability, specific surface area, mucous layer, in vivo imaging system.

I. INTRODUCTION

Oral drug often needs multiple daily administrations to maintain a therapeutic level of systemic drug concentration mostly due to first pass metabolism and short elimination half-life. In this sense, the carrier that can reside in the gastrointestinal (GI) tract for a prolonged period of time while releasing drug in a sustained manner can be advantageous for oral drug delivery. Therefore, in this work, we propose the nanostructured microparticles (NM) which possessed a high specific surface area, hence improved interaction with the mucous layer in a GI tract and thereby prolonged residence time in GI tract [1]. We examined the residence time of the NM herein after their oral administration into living rats in this study.

II. METHODS

Four different types of the microparticles were prepared to examine the effect of particle morphology (i.e., spherical or nanostructured) and mucoadhesiveness on their residence time in GI tract: spherical microparticles (MS) of PLGA only (PLGA MS), MS of PLGA and PEG (PLGA/PEG MS), nanostructured microparticles (NM) of PLGA only (PLGA NM) and NM of PLGA and PEG (PLGA/PEG NM). The MS was prepared by the conventional emulsion method. The NM was prepared by freeze-milling the nanofibrous sheets prepared via electrospinning. All microparticles were labeled with near-infrared fluorescent dye, 3,3'-Diethylthiatriacarbocyanine iodide (DTTCI) and orally administered to living rat to monitor their retention property in the GI tract (IVIS (Lumina II); excitation and emission wavelengths of 745 and 840 nm, respectively). The suspensions containing the dye only was also evaluated for comparison.

III. RESULTS & CONCLUSION

The MS prepared by the emulsion method exhibited a spherical shape with a smooth surface (Fig. 1(a-b)). The NM showed the morphology with randomly entangled nanofibers to give a rough surface (Fig. 1(c-d)). The presence of PEG in microparticles did not seem to influence their own surface morphology (Fig. 1) Figure 1(e) shows the in vivo fluorescence images of the whole rats at scheduled times after oral administration of the formulations. When the dye suspension was administered, fluorescence signal was observed for up to 12 h. The PLGA/PEG MS and PLGA NM were also not detectable after 12 h. On the other hand, the PLGA/PEG NM showed the best retention in GI tract, which could be visible until 36 h. This suggested that with the PLGA/PEG NM herein, mucoadhesiveness was synergistically improved by the enlarged specific surface area originated from the nanostructure.

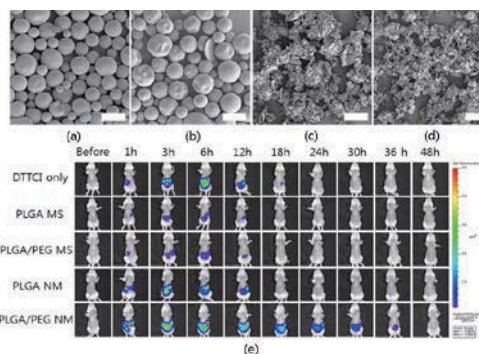


Figure 1. Representative scanning electron micrographs of (a) PLGA MS, (b) PLGA/PEG NM, (c) PLGA NM and (d) PLGA/PEG NM. (e) Representative *in vivo* fluorescence images over time after oral administration of each of the different formulations. The scale bars (a-b) = 100 μ m.

ACKNOWLEDGEMENT

This research was supported by BK21 Plus Program (grant numbers 22A20130011025) and Basic Science Research Program (NRF-22013R1A1A2A10011055) through the National Research Foundation of Korea (NRF) funded by the Ministry of Education.

REFERENCES

1. C. G. Park, et al, "Nanostructured mucoadhesive microparticles for enhanced preocular retention," *Acta Biomaterialia.*, vol. 10, pp. 77-86, 2014.

Absorbable Fibrin Glue Formulated with PLGA Microparticles for Sustained Delivery of Bupivacaine

S. N. Kim¹, B. H. Choi², B. K. Huh¹, S. H. Lee¹, H. K. Kim*² and Y. B. Choy*¹

¹Interdisciplinary program for Bioengineering, Seoul National University, Seoul, Republic of Korea

²Department of Thoracic and Cardiovascular Surgery, Korea University Guro Hospital, Korea University College of Medicine, Seoul, Republic of Korea

E-mail: ybchoy@snu.ac.kr

Abstract— To control a post-operative pain, a local anesthetic drug is often injected at the site of interest. However, this bolus drug injection is limited in its short residence time, thereby low bioavailability of drug. To resolve this, we fabricated biodegradable microparticles loaded with bupivacaine and formulated them in fibrin glue. we evaluated their in vitro drug release profile in pH 7.4 PBS. After a burst release of 38% on day, the drug was slowly released for more than 30 days. In vivo experiments were conducted using living rats. Our formulation revealed that the pain-relief efficacy could be prolonged for up to 14 days.

Keywords— Bupivacaine, PLGA, Fibrin glue, Microparticles, Drug Delivery System

I. INTRODUCTION

Bupivacaine is one of the most widely used local anesthetic drugs belonging to the amino amide group. It is widely used in the treatment of pre/post-operative pain because of its rapid acting and relatively long-lasting anesthetic effect for up to several hours. However, for the patients experiencing chronic pain, a much longer period of drug exposure is needed at the site of interest. For this purpose, we prepared biodegradable microparticles loaded with bupivacaine and formulated them in fibrin glue. In this way, drug release could be more sustained via both microparticles and fibrin glue. Fibrin glue herein could also localize the microparticles at the specific site of pain for a prolonged period, hence better local drug efficacy.

II. METHODS

A. Preparation of Bupivacaine Loaded Microparticles

Bupivacaine hydrochloride-loaded microparticles were prepared by the O/W emulsion method. The drug loaded microparticles were then suspended in fibrin glue to give a formulation for actual application.

B. In Vitro and In Vivo Test

In vitro drug release experiments were performed in pH 7.4 PBS at 37 °C for 35 days. In vivo experiments were conducted for 27 days using living rats, where the pain was induced with L5-spinal nerve ligation. At a local site of pain, we administered the formulations and the paw withdrawal latency was evaluated in response to thermal stimulation.

III. RESULTS

The bupivacaine loaded microparticles (BMP) were successfully prepared with the O/W emulsion method, where the drug loading amount was 73.8 µg per mg microparticles. Figure 1(a) shows the in vitro drug release profiles of the microparticles formulated in fibrin glue. After a burst release of 38% on the first day, the drug was slowly released for more than a month. We also performed the in vivo experiments to evaluate the pain-relief efficacy of our formulation. As shown in Figure 1(b), the withdrawal latency decreased to less than 5 s with the pain-induced animal groups (control). The group treated with a bupivacaine solution (BS) exhibited the increase in withdrawal latency for 1 day, indicating the pain reduction, which, however, decreased again afterwards. Notably, the BMP in fibrin glue exhibited that the withdrawal latency was higher than those of sham and control and this could be retained for 14 days. This result suggested that a local effect of bupivacaine could be prolonged and improved due to sustained drug release and microparticle localization with fibrin glue.

IV. CONCLUSION

In this work, we suggest anesthetic drug loaded microparticles formulated in fibrin glue as potential formulation for sustained drug delivery to the local site of pain. Our formulation revealed that the pain-relief efficacy could be prolonged for up to 14 days, where the enhancement was evident as compared with the conventional treatment with an aqueous drug formulation.

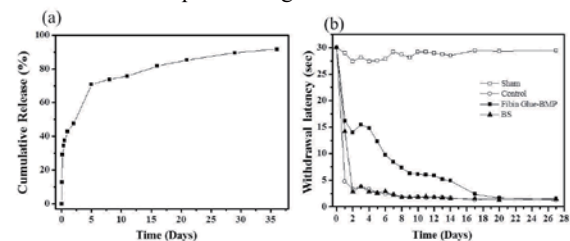


Fig. 1. (a) In vitro drug release profiles of the bupivacaine loaded microparticles in fibrin glue. The experiments were performed in pH=7.4 PBS at 37 °C. (b) In vivo evaluation on paw withdrawal latency in response to thermal stimulation. (□; Sham group, ○; Control group, ■; Fibrin glue + bupivacaine loaded microparticles (BMP), ▲; bupivacaine solution (BS) group)

ACKNOWLEDGEMENT

BK21 Plus Program through the National Research Foundation of Korea (NRF) funded by the Ministry of Education (grant numbers 22A20130011025)

REFERENCES

- [1] R. J. Landreanu, J Thorac, Cardiovasc Surg, 1994.
- [2] A. J. Rajeev, Biomaterials, vol. 21, pp. 2275-2490, 2000.

***In vitro* evaluation of doxorubicin loaded fucoidan reduced gold nanoparticles for anticancer drug delivery**

Panchanathan Manivasagan¹, Seo Jaehoon², Junghwan Oh^{1, 3*}

¹Marine-Integrated Bionics Research Center, Pukyong National University, Busan 608-737, Republic of Korea.

²Baejung High School, Busan Busan 608-828, Republic of Korea.

³Department of Biomedical Engineering and Center for Marine-Integrated Biotechnology (BK21 Plus), Pukyong National University, Busan 608-737, Republic of Korea

E-mail: jungoh@pknu.ac.kr

Abstract—Gold nanoparticles are widely used in many applications such as medical, pharmaceutical, diagnostics, drug delivery and sensors. Fucoidan is a type of complex sulfated polysaccharide, mainly found in the extracellular matrix of various marine brown seaweed species. The gold nanoparticles were formed readily within 15-30 min. TEM micrograph also confirmed the size of the gold nanoparticles, which were in the range of 40-90 nm with an average particle size of 76 nm. The biosynthesized gold nanoparticles were characterized by UV-vis spectroscopy, FTIR, XRD, FE-SEM, EDXA, and TEM and the present synthetic method is truly a greener approach. Cytotoxicity of biosynthesized gold nanoparticles against *in vitro* human breast cancer cell line (MDA-MB 231). IC₅₀ value was found to be 250 µg/ml of gold nanoparticles against human breast cancer cell line.

Keywords—Fucoidan, Doxorubicin, Gold nanoparticles, Anticancer, Drug delivery.

I. INTRODUCTION

Polymer nanoparticle are considered as nanomedicine presenting high potential for diagnosis and therapeutical proposes with possibility to achieve site-specific drug delivery. Until now, dextran, chitosan and heparin were used as coating materials of nanoparticles. Among them, Fucoidan appears to be an excellent candidate for anticancer drug delivery (1).

II. METHODS

A. Synthesis of gold nanoparticles (AuNPs)

The 0.005 g of fucoidan was added to 10 ml of aqueous solution of 1×10^{-4} M HAuCl₄ and pH of solution was adjusted at 11 to yield dark ruby red AuNps on heating for 15 min at 70 °C on water bath.

B. Preparation of doxorubicin (DOX) loaded fucoidan reduced AuNPs

A calculated amount of DOX was added to AuNPs dispersion, obtained as described above, resulting in a final DOX concentration of 10^{-4} M in solution.

C. Characterization of AuNPs and DOX loaded AuNPs

The AuNPs and DOX loaded AuNPs were characterized by XRD, FTIR, EDXA SEM and TEM

D. In vitro cytotoxicity study

Cytotoxicity of DOX loaded AuNPs were evaluated on MDA-MB 231 using the MTT assay.

III. RESULTS

A. Synthesis of AuNPs

The pale yellowish reaction mixture changed to pinkish color indication the formation of AuNPs. Fig. 1. Show the UV-Vis absorption spectrum of the AuNPs nanoparticles.

B. Evaluation of DOX loaded AuNPs

After the successful synthesis of stable AuNPs, we have envisaged this system for drug delivery application through subsequent loading of a bioactive molecule.

C. In vitro cytotoxicity

In the cancer cells without increased drug efflux characteristics (MDA-MB 231), the cytotoxicity of the DOX loaded AuNPs was similar to that of the free drug: the IC₅₀ values were 250 µg/ml.

IV. CONCLUSION

The present study involves the development of a simple, ecological and eco-friendly method in synthesizing gold nanoparticles by fucoidan as reducing and stabilizing agents. Doxorubicin (DOX) was used as a model chemotherapeutic agent and the drug was loaded in the fucoidan nanoparticles. These preliminary results indicate the potential of DOX-fucoidan nanoparticles for anticancer drug delivery.

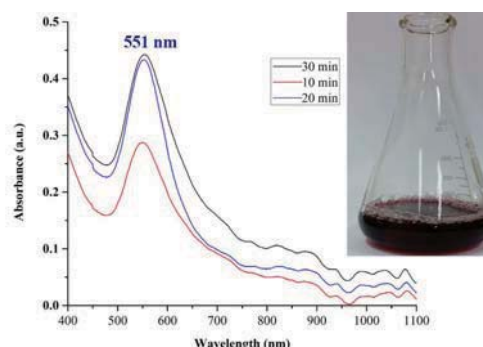


Fig. 1. UV-absorbance spectra of AuNPs

ACKNOWLEDGEMENT

This research was supported by a grant from Marine Biotechnology Program (20150220) funded by the Ministry of Oceans and Fisheries, Republic of Korea.

REFERENCES

1. K.W. Lee, D. Jeong, K. Nab, "Doxorubicin loading fucoidan acetate nanoparticles for immune and chemotherapy in cancer treatment," *Carbohydr. Poly.* 94: 850-856, 2013.

Biomimetic of bone like apatite nanostructure via anodization / hydrothermal processes on magnesium alloy for bone implant

Hamouda M. Mousa¹, Jinwoo kim¹, Madhav Prasad Neupane¹, Woo Jin Lee¹,
Chan Hee Park^{1,2*}, Cheol Sang Kim^{1, 2*}

¹ *Department of Bionanosystem Engineering, Chonbuk National University, Jeonju, Jeonbuk 561-756, Republic of Korea,*

² *Division of Mechanical Design Engineering, Chonbuk National University, Jeonju, Jeonbuk 561-756, Republic of Korea,*

The use of biodegradable material to support bone cell and tissue growth is a longstanding area of interest. Current challenges include the engineering of materials that can match both the mechanical and biological conditions of real bone tissue matrix. Magnesium (Mg) is promising materials for medical applications as it has many appealing advantage such as density and modulus of elasticity similar to that of bone however, Mg highly degradable in physiological media and tend to loss its properties.

In this study a nanostructure bone like apatite was formed on the surface of AZ31B magnesium alloy using SBF solution via anodization followed by hydrothermal process using NaOH and SBF at 60 °C for 2hr and 72 hr, respectively to control Mg biodegradation. The apatite layer was characterized using FE-SEM, EDS, XRD, and FT-IR, moreover the degradability of magnesium was evaluated by means of corrosion resistance using electrochemical corrosion test. Surface hydrophobicity was measured using contact angle test for both the naked sample and treated one. The in vitro biocompatibility and cell attachment was performed by using cultured MC3T3-E1 cells seeding for different days of intervals. The results show that the bone like apatite layer deposited on the Mg alloy not only enhanced biodegradation control and bioactivity but also find highly cells attachment and osteoconductivity for bone formation.

Keywords: Bone implant, nanostructure, magnesium, biodegradation, biomimetic

***Corresponding authors:**

(Chan Hee Park) biochan@jbnu.ac.kr , (Cheol Sang Kim) chskim@jbnu.ac.kr

An Osteogenic Composite Scaffold for Bone Tissue Engineering: A Unique Combination of Growth Factor and Nanotopography Induced Osteogenesis

Afeesh Rajan Unnithan^{1*}, Sunny Lee¹, Jin Woo Kim¹, Sung Won Ko¹, Joshua Lee¹, Min Hyuk Kim¹, Francis.O.Obiweluzor¹, Chan Hee Park¹, Cheol Sang Kim¹

¹ Department of Bionanosystem Engineering Graduate School, Chonbuk National University, Jeonju, Republic of Korea

E-mail: afeesh@jbnu.ac.kr

I. INTRODUCTION

Recently there is an increased interest in developing new bioactive scaffolds for tissue engineering or enhancing the capabilities of existing bioactive scaffolds for various tissue engineering applications [1]. In view of bone tissue engineering, mainly the clinical treatments of bone defects caused by trauma, cancer, pathological infection, or congenital deformity have been generally repaired by the application of auto- and allografts. But these methods possess serious limitations due to poor donor availability, risk of disease transmission, immune rejection etc [2]. In order to challenge such limits, tissue engineering methods has been trying to develop more bioactive viable bone implants. Considering this approach, the novel tissue engineering strategies aim at developing biocompatible scaffolds using a combination of specific cells, growth factors and 3D porous scaffolds that maintains cell attachment, proliferation and migration [3].

II. RESULTS

The present study explores the Graphene oxide (GO)-Chitosan (CS)-Hyaluronic acid (HA) biomimetic composite scaffold containing an osteogenesis-inducing drug simvastatin (SV). Porosity, density, swelling, degradation and biomineralization studies favored the SV loaded GO-CS-HA scaffold in comparison to the conventional CS and HA scaffolds. The results showed that the composite scaffolds can function as a template material for the biomineralization of hydroxyapatite, which is crucial for bone regeneration. The in vitro results showed that the SV possess a significant influence on osteogenesis and biomineralization. Cytotoxicity and cell viability studies suggested that SV loaded composite scaffold have proper biocompatibility to be used as a scaffold which can induce osteogenesis and mineralization. The obtained remarkable results indicate the prepared nanocomposite scaffold as a potential candidate for bone tissue engineering applications.

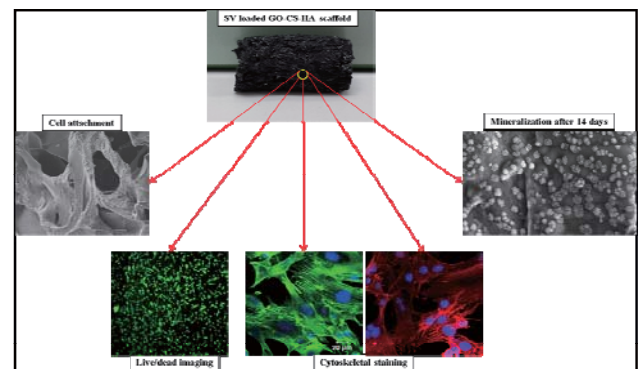


Fig. 1. Graphical illustration of present work

ACKNOWLEDGEMENT

This work was supported by the NRF grant 2013-012911.

REFERENCES

- [1] Mohandas A, Anisha BS, Chennazhi KP, Jayakumar R. Chitosan-hyaluronic acid/VEGF loaded fibrin nanoparticles composite sponges for enhancing angiogenesis in wounds. *Colloid Surface B*. 2015;127:105-13.
- [2] Burg KJL, Porter S, Kellam JF. Biomaterial developments for bone tissue engineering. *Biomaterials*. 2000;21(23):2347-59.
- [3] Kavya KC, Jayakumar R, Nair S, Chennazhi KP. Fabrication and characterization of chitosan/gelatin/nSiO(2) composite scaffold for bone tissue engineering. *Int J Biol Macromol*. 2013;59:255-63.

1.

g-C₃N₄ sheet decorated ZnO flowers with improved photocatalytic activity

Surya Prasad Adhikari^{1,2}, Jun Hee Kim¹, Min Hyeok Kim¹, Jeong In Kim¹, Bishnu Kumar Shrestha¹, Arjun Tiwari¹, Ganesh Awasthi¹, Bikendra Maharjan¹, Chan Hee Park^{1,2}, Cheol Sang Kim^{1,2}

¹Department of Bionanosystem Engineering, Graduate School, Chonbuk National University, Jeonju 561-756, Republic of Korea

²Division of Mechanical Design Engineering, Chonbuk National University, Jeonju 561-756, Republic of Korea

Abstract

Zinc oxide (ZnO) flowers were grown on the surface of graphitic carbon nitride (g-C₃N₄) by using a one pot hydrothermal process. ZnO flowers on g-C₃N₄ sheet were grown by heat treating a solution of ZnO precursors with g-C₃N₄ particles at 130 °C for 3h. Scanning electron microscopy (SEM), transmission electron microscopy (TEM), X-ray diffraction (XRD), Fourier transform infrared spectroscopy (FT-IR), and photoluminescence (PL) spectroscopy were used to characterize the as-prepared samples. The resulting composites exhibited with flower-like ZnO microparticles attached on the surface of sheet like g-C₃N₄. The composite photocatalyst demonstrated better performance over the photocatalytic degradation of methylene blue than those of g-C₃N₄ or ZnO alone. The reusability experiment of photocatalyst revealed that the as-synthesized composite was stable and could be reused.

Keywords: Hydrothermal; g-C₃N₄; ZnO; Composite; Photocatalyst

1. Introduction

One of the most promising semiconductor photocatalysts, ZnO has received considerable interest because of its high biocompatibility, low cost, physical and chemical stability, high photosensitivity, high electronic carrier mobility, and availability [1-4]. However, it has a low quantum efficiency due to its large energy band gap, which results in rapid recombination of photo generated electron-hole (e⁻-h⁺) pairs. Therefore, various attempts have been made to improve the photocatalytic activity of ZnO-based photocatalysts such as incorporating novel

metal into the photocatalyst lattice [5, 6], coupling ZnO with dyes or semiconductors that absorb light [7, 8].

Recently, polymeric graphite-like carbon nitride (g-C₃N₄), which has a medium band gap of 2.70 eV has been explored as a promising metal free photocatalyst. However, there are still some inherent drawbacks of that limit the use of g-C₃N₄ in photocatalysts including the high recombination rate of photogenerated e⁻-h⁺ pairs. Therefore, the synthesis of ZnO and g-C₃N₄ composites is of interest and there have been a few studies related to the synthesis and application of ZnO/g-C₃N₄

In this work, graphitic carbon nitride sheets with ZnO flowers attached to the surfaces were synthesized via a simple facile one-pot hydrothermal method. Characterization showed that the ZnO flowers were well attached to the surface of the g-C₃N₄ sheet. The photo degradation activity of the composite photocatalyst and its reusability were evaluated by degradation of a methylene blue (MB) solution under UV light irradiation. The photocatalytic properties of the synthesized photocatalyst were better than those of ZnO or g-C₃N₄ alone. ZnO flowers on the g-C₃N₄ sheets assisted the e⁻-h⁺ separation during the photocatalytic process.

2. Experimental

2.1. Materials

Commercially available g-C₃N₄ particles (Nicanite[®], Carbedon, Finland), zinc nitrate hexahydrate (Sigma Aldrich, Croatia), hexamethylene tetramine (Samchun Chemicals, Korea), ethanol, and methylene blue were used without further purification.

2.2. Material synthesis

Desired amounts of g-C₃N₄ (10, 20, 30, 40, and 50 mg) were dispersed in 10 mL of distilled water and were ultrasonically pulverized in a bath sonicator for 30 min. Solutions containing 0.5 g of hexamethylene tetramine in 50 ml water and 0.75 g of zinc nitrate hexahydrate in 40 ml water were prepared in a separate bottle. After stirring for 30 min, these two solutions were mixed and were stirred for 1 hour. Then, a g-C₃N₄ solution was added to this slurry. The pH of the mixed solution was adjusted to 11 using a 1 M NaOH solution. After stirring for one hour, the solution was poured into a Teflon crucible

and kept inside an autoclave at 130°C for 3 h. In addition, pristine ZnO flowers were prepared without g-C₃N₄. After cooling at room temperature, the obtained product was filtered and washed repeatedly with distilled water and ethanol. The product was dried in a vacuum oven at 60°C for 24 h. This composite was further dried at 160°C for 12 h to increase the crystallinity and remove moisture from the photocatalyst.

2.3. Characterization

The composite were characterized by using field-emission scanning electron microscopy (FE-SEM, Hitachi S-7400, Hitachi, Japan), transmission electron microscopy (JEM-2200, JEOL, Japan), and X-ray diffractometer (XRD, Rigaku, Japan) with Cu K α ($\lambda=1.540 \text{ \AA}$) radiation over Bragg angles ranging from 20 to 80°.

2.4. Photocatalytic activity test

The photocatalytic activities of ZnO, g-C₃N₄ and ZnO/g-C₃N₄ photocatalysts were studied by using them in the degradation of an aqueous MB solution (10 ppm) under mild UV irradiation at room temperature. After completing the experiment, MB concentration in the suspension was observed using a UV–visible spectrophotometer (HP 8453 UV–visible spectroscopy system, Germany) at the corresponding wavelength.

3. Results and discussion

The morphologies of the different samples were examined by FE-SEM. Synthesized ZnO particles have flower-like micro structures (Fig. 1c and 1d). The flower-like ZnO is well attached to the surface of g-C₃N₄ in the composites after hydrothermal treatment of g-C₃N₄ and ZnO precursors (Fig. 1e and 1f). Interestingly, the ZnO particle size in the composite is significantly smaller than that of neat ZnO which can be seen clearly from the magnified images of ZnO and ZnO/g-C₃N₄ (Fig. 1d and 1f).

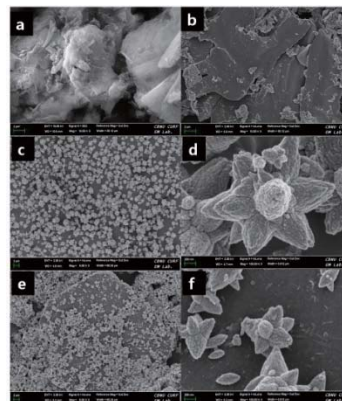


Figure 1. FE-SEM images of g-C₃N₄ before and after hydrothermal treatment (a and b), flower like pristine ZnO (c and d) and ZnO/g-C₃N₄ (e and f) in low and high magnification.

The crystallographic structures of pure and composite photocatalysts can be inferred from the XRD patterns shown in Fig. 2. An additional diffraction peak observed at $2\theta=27.4^\circ$ in the composite suggests effective attachment of ZnO particles on the surface of g-C₃N₄.

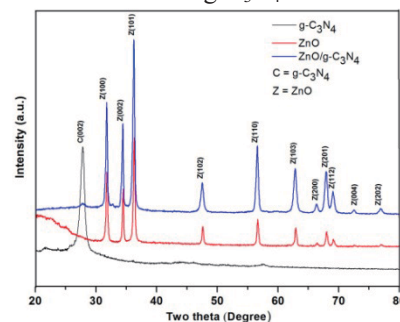


Figure 2. XRD patterns of pure g-C₃N₄, Pure ZnO and ZnO/g-C₃N₄

The photocatalytic performance of each product was tested under UV light by degradation of the organic dye MB, a typical pollutant in the textile industry. Figure 3 shows photocatalytic degradation of MB as a function of time with different loading amounts of g-C₃N₄ before and after UV light irradiation. Figure 3 shows that the photocatalytic performance of ZnO was enhanced with the addition of g-C₃N₄. Moreover, the photocatalytic activity decreased at higher g-C₃N₄ levels, suggesting that the optimal g-C₃N₄ amount for composite formation is 20 mg. The significant improvement in the photocatalytic activity of ZnO is due to effective separation of the photogenerated electron–hole pairs induced by energy level match between C₃N₄ and ZnO.

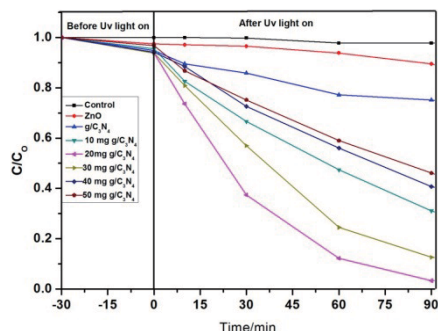


Figure 6. Comparison of the photodegradation using different photocatalysts under UV light.

4. Conclusions

A ZnO/g-C₃N₄ composite photocatalyst was synthesized from a solution containing commercial g-C₃N₄ particles and precursors of ZnO via a facile one pot hydrothermal process. Characterization of morphologies illustrate that the composite photocatalyst consists of flower-like ZnO particles attached to the surface of g-C₃N₄. Photocatalytic efficiency of the as prepared ZnO/g-C₃N₄ composite was significantly enhanced compared to ZnO or g-C₃N₄ particles alone. Moreover, there was no obvious loss of photocatalytic efficiency after multiple runs using the same catalyst. Therefore, this ZnO/g-C₃N₄ composite photocatalyst is a potential candidate for practical applications in the field of photocatalyst.

Acknowledgements

This research was supported by research funds of Chonbuk National University in 2014 and by grants from the Korean Ministry of Education, Science, and Technology (MEST) through the National Research Foundation (NRF) (Project Nos. 2014-R1A1A1009068 and 2013-R1A2A2A04015484). We would also like to thank the staff of the Center for University Research Facility (CURF), Chonbuk National University for access to the FE-SEM.

References

- [1] J. Yu, L. Zhang, B. Cheng, Y. Su, Hydrothermal Preparation and Photocatalytic Activity of Hierarchically Sponge-like Macro-/Mesoporous Titania, *The Journal of Physical Chemistry C*, 111 (2007) 10582-10589.
- [2] J. Liqiang, W. Dejun, W. Baiqi, L. Shudan, X. Baifu, F. Honggang, S. Jiazhong, Effects of noble metal modification on surface oxygen composition,

charge separation and photocatalytic activity of ZnO nanoparticles, *Journal of Molecular Catalysis A: Chemical*, 244 (2006) 193-200.

[3] J. Yu, S. Liu, H. Yu, Microstructures and photoactivity of mesoporous anatase hollow microspheres fabricated by fluoride-mediated self-transformation, *Journal of Catalysis*, 249 (2007) 59-66.

[4] H.R. Pant, C.H. Park, B. Pant, L.D. Tijing, H.Y. Kim, C.S. Kim, Synthesis, characterization, and photocatalytic properties of ZnO nano-flower containing TiO₂ NPs, *Ceramics International*, 38 (2012) 2943-2950.

[5] H.M. Coleman, K. Chiang, R. Amal, Effects of Ag and Pt on photocatalytic degradation of endocrine disrupting chemicals in water, *Chemical Engineering Journal*, 113 (2005) 65-72.

[6] V. Vamathevan, R. Amal, D. Beydoun, G. Low, S. McEvoy, Photocatalytic oxidation of organics in water using pure and silver-modified titanium dioxide particles, *Journal of Photochemistry and Photobiology A: Chemistry*, 148 (2002) 233-245.

[7] C.-H. Wu, Comparison of azo dye degradation efficiency using UV/single semiconductor and UV/coupled semiconductor systems, *Chemosphere*, 57 (2004) 601-608.

[8] D.L. Liao, C.A. Badour, B.Q. Liao, Preparation of nanosized TiO₂/ZnO composite catalyst and its photocatalytic activity for degradation of methyl orange, *Journal of Photochemistry and Photobiology A: Chemistry*, 194 (2008) 11-19.

Micro-tube Cell Organization for Artificial Micro-Blood Vessel

J. Choi¹, S. Lee¹, S. Lee¹, K. Koo¹

¹Department of Biomedical Engineering, University of Ulsan, Ulsan, Republic of Korea
E-mail: uoubmemdl@gmail.com

Abstract— We propose a simple method for forming fibroblast (NIH/3T3)-laden alginate lumen gels using a coaxial laminar flow for artificial micro-blood vessel. We mixed NIH/3T3 into alginate gel and cultured the cells during 5 days of cell culture, and this showed fibroblast cells to be well organized and cultured maintaining the blood-vessel shape.

Keywords— Artificial vascularization, microfluidic device, micro-tube, fibroblast

I. INTRODUCTION

Every year, over millions of patients suffer tissue loss or end-stage organ failure in the developed countries [1]. One of the primary issues in the engineered tissue is vascularization [2]. In this paper, we designed the device to fabricate micro hydrogel tube and cultured a fibroblast, NIH/3T3 (Fig. 1). This method composed micro hydrogel tubes guiding vessel-shaped growth of the NIH/3T3.

II. METHODS

A. Device Design and Fabrication

Figure 1 shows the microfluidic device consisting of two glass capillaries, two inlets for a 1.5 wt% sodium alginate solution (Ducksan, Korea) and 100mM CaCl_2 solution (Kanto chemical, Japan), and one outlet [4].

B. NIH/3T3 Culture

NIH/3T3 fibroblasts (CRL-1658, ATCC, Korea) were cultured in well-known 3T3 culture medium. Cells were incubated at 5 % of CO_2 and 37 °C.

C. Encapsulation of NIH/3T3 and Experimental Setup

Sodium alginate solution was mixed NIH/3T3 cell number density of the mixed solution was 560,000 cells/mL.



Fig. 1. Photograph of the Microfluidic device for micro-tube composition [3].

III. RESULTS

A. Functional Analysis of Encapsulated Fibroblasts

To investigate NIH/3T3 growth in this alginate tubes, we cultured the cell-laden tubular gels for 5 days (Fig. 2). The results indicate that NIH/3T3 had no significant decrease for 5 days and stayed aligned along with the tube structures. It means that cell organization and proliferation could be enhanced in the alginate micro-tubes.

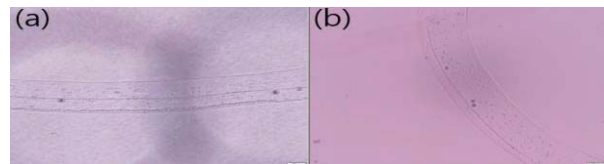


Fig. 2. A microscopic image of NIH/3T3 in an alginate tube (a) for 1 day and (b) 5 days.

IV. CONCLUSION

In this work, we developed the microfluidic device to compose tubular alginate-NIH/3T3 gel. NIH/3T3 within alginate micro-tubes lived for 5 days.

ACKNOWLEDGEMENT

This work was supported by Basic Science Research Program through the National Research Foundation of Korea (NRF) funded by the Ministry of Science, ICT & Future Planning (NRF-2014R1A1A1 038335).

REFERENCES

1. Langer R, Vacanti JP, "Tissue engineering," *Science*. vol. 260, pp. 920-926, 1993.
2. Rouwkema J, Rivron NC, van Blitterswijk CA. "Vascularization in tissue engineering," *Trends* vol. 26, pp. 434-441, 2008.
3. Oh D, Lee S, Koo K, Seo J, "Microscopic Tubular Cell Organization for Artificial Vascularization," *6th European Conference of the International Federation for Medical and Biological Engineering*, pp. 322-325, 2015.
4. Lee S, Oh D, Seo J, Koo K., "Micro-tube generating microfluidic device design and simulation for artificial micro-blood vessel network vascularization," *The Korean society of medical & biological Engineering*, pp. 526-528, 2014.

Effect of tourmanium on muscle atrophy following sciatic nerve injury

D. H. Hwang¹, S. H. Kim¹, D. H. Seo¹, S. K. Cho² and H. S. Kim^{1,2}

¹Department of Biomedical Engineering, Yonsei University, Korea

²Yonsei-Fraunhofer IZFP Medical Device Lab, Korea

E-mail: hanskim@yonsei.ac.kr

Abstract— In this study the authors evaluate the effect of tourmanium on musculoskeletal disorders caused by sciatic nerve injury. Mice(12-week-old C57BL/6 mice) underwent sciatic neurectomy and were stimulated by tourmanium thermotherapy for 4 weeks. As a result, the total volume of lower limb muscles were significantly increased.

Keywords— Tourmanium, sciatic nerve injury, denervation, ceramic therapy.

I. INTRODUCTION

Tourmanium is a therapeutic ceramic created by sintering the ultra-micro particulated mixture of tourmaline, germanium, volcanic rock and elvan at 1300C. When this ceramic is heated, far-infrared radiation, which has an effect of improving muscle pain, is emitted. In this study the authors evaluate the effect of tourmanium, which is effective on muscle pain relief through emitting far-infrared, on musculoskeletal disorders caused by sciatic nerve injury.

II. METHODS

A. Animals and sciatic neurectomy

The protocols for all the procedures were approved by the Yonsei University Animal Care Committee. 14 male 12-week-old C57BL/6 mice were randomly assigned to 2 groups(7 mice each) including tourmanium treatment(T group) and none treatment(CON group). Sciatic neurectomy(SNx) was performed on the right side of leg. The leg paralysis induced by SNx was lasted for 4 weeks. All mice were freely accessed to food and water. The mice were kept under a 12:12-hour light-dark cycle (25±1°C, 50±5% humidity).

B. Tourmanium stimulation

T group were stimulated by thermotherapy with tourmanium pad for 4 weeks. (5 days per week, temperature 37°C, 20 min.).

C. Micro-CT

Muscles of lower right limb in each mouse were scanned by using in-vivo micro-CT (Skyscan 1076, Bruker, Germany) at 0week (before stimulations) and 4weeks (after stimulations).

III. RESULTS

A. Total volume of lower limb muscle

The changes in the total volume of the lower limb muscles are shown in fig. 1. During the study period, there were significant changes in total muscle volume.(p<0.05)

The 2D images of right lower limb muscles are shown in fig 2.

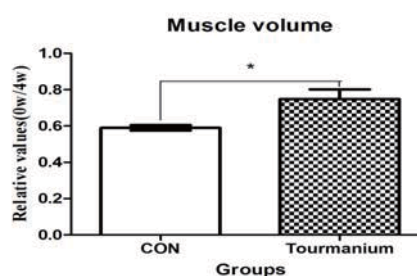


Fig. 1. 2D image of right lower limb muscle

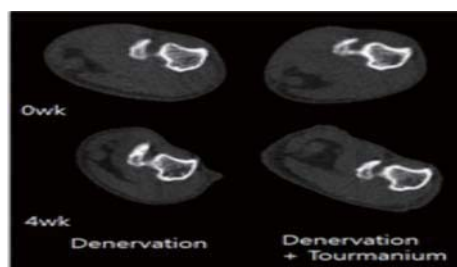


Fig. 1. 2D image of right lower limb muscle

IV. CONCLUSION

Sciatic nerve injury is known to cause significant muscle loss in the lower extremities. We evaluated the effects of tourmanium. The results showed that tourmanium could suppress muscular atrophy. Therefore, tourmanium can be effective treatment or inhibition of sciatic nerve injury.

REFERENCES

1. H. S. Park, E. H. Rho, Y. Hwan and G. Wung, "A Study on the Improvement Characteristics of Bio Active Energy Radiated Fabric in Muscle Fatigue," *The Korean Society of Dyers and Finishers.*, vol. 26, pp. 181-186, 2014.
2. J. Iwamoto, T. Takeda, T. Katsumata, T. Tanaka, S. Ichimura, and Y. Toyama, "Effect of Etidronate on Bone in Orchidectomized and Sciatic Neurectomized Adult Rats," *Bone*, Vol. 30, pp. 360-367, 2002.

Protective Effect of Nitric Oxide Releasing Nanofiber in Hypoxia/Reoxygenation-induced Cardiomyocytes Injury

Young Ju Lee¹, Ki Bum Kim², Jae Ho Shin², Hun-Kuk Park¹ and Gi-Ja Lee¹

¹Department of Biomedical Engineering and Healthcare Industry Research Institute, Kyung Hee University, Seoul, Korea

²Department of Chemistry, College of Natural Science, Kwangwoon University, Seoul, Korea

E-mail: younglee@khu.ac.kr

Abstract—Nanofiber-based Nitric Oxide (NO) Delivery System was produced using the electrospinning technique, and the cytoprotection effect of NO was confirmed in hypoxia/reoxygenation (HR)-induced cardiomyocytes injury. NO releasing nanofibers protected H9c2 cells from DNA damage by inhibiting the generation of oxidative stress.

Keywords—Nitric oxide, Nanofiber, Hypoxia-Reoxygenation cardiomyocytes model, Cytoprotection.

I. INTRODUCTION

Nitric oxide (NO) is involved in several physiological processes including vasodilation, angiogenesis, immune response and wound healing, as well as preventing ischemia/reperfusion injury [1].

II. METHODS

A. Production of NO release nanofiber

The NO-releasing fiber ($1.49 \mu\text{mol}\cdot\text{mg}^{-1}$) was prepared by mixing the NO donor material and biodegradable polymer using electrospinning devices.

B. HR cardiomyocytes model

After seeding the cells overnight, the culture medium was replaced by glucose deprivation DMEM medium and incubated in a multi-gas incubator under a stream of hypoxic gas (1% O₂ and 5% CO₂) for 24 h. For reperfusion, the glucose deprivation DMEM medium was replaced with normal medium (DMEM-high glucose) under normoxia (20% O₂ and 5% CO₂) for 4 h.

C. Cell viability measurement with NO-releasing fiber pretreatment

H9c2 cells (2×10^5 cells/12well) were treated control and NO-releasing fiber (0.2 mg) for 48 h in normal condition. Cells were performed with HR injury. Cell viability was measured using WST assay.

D. Extracellular H₂O₂ assay

Measurement of extracellular H₂O₂ following HR damage was performed according to the Amplex® red hydrogen peroxide/peroxidase assay manufacturer's manual.

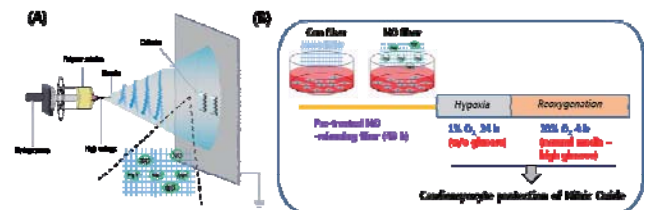


Fig. 1. (A) A schematic diagram of the electrospinning system (B) Evaluation of NO delivery system in HR cardiomyocytes injury model

III. RESULTS

A. Cardiomyocytes protection effect of NO

NO-releasing fiber pretreatment group did not cause cell death in HR injury.

B. Oxidative stress inhibitory effect of NO

Reactive oxygen species (ROS) generation was inhibited by NO-releasing fiber treatment in HR cardiomyocytes injury model. In addition, 8-Hydroxyl-2-deoxyguanosine (8-OHdG) level was obviously decreased at NO-releasing fiber pretreatment.

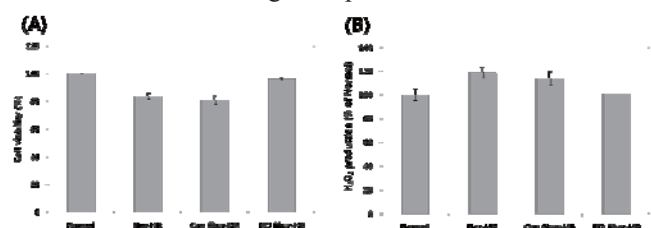


Fig. 1. (A) Cytoprotective effects and (B) ROS generation inhibitory effect of NO-releasing fiber pretreatment system in HR injury.

IV. CONCLUSION

We confirmed that nanofiber-based NO delivery system protects H9c2 cells from DNA damage by inhibiting the generation of oxidative stress in HR cardiomyocytes injury model.

ACKNOWLEDGEMENT

This study was supported by the National Research Foundation of Korea (NRF) funded by the Ministry of Science, ICT & Future Planning (2015M3A9E2029188) and the Ministry of Education (2013R1A1A2065149).

REFERENCES

1. L. Phillips et al., Nitric oxide mechanism of protection in ischemia and reperfusion injury, *J Invest Surg.* 22(1), 46-55, 2009

Developing the uniaxial 3D scaffold for highly matured skeletal muscle

Suk-Hee Park¹, Ung Hyun Ko², Jinseung Choung², and Jennifer H. Shin²

¹ Micro/Nano Scale Manufacturing R&BD Group, Korea Institute of Industrial, Republic of Korea

² School of Mechanical Engineering & Aerospace System, KAIST, Republic of Korea

E-mail: insect@kaist.ac.kr

Abstract— In skeletal muscle tissue engineering, the customized-scaffold was required to mimic the hierarchical structure of muscle fibrils and also required to promote myogenic differentiation. In this study, we develop a uniaxial 3D scaffold with the electrospinning technique and verified the suitability for skeletal tissue application.

Keywords— Tissue Engineering, Electrospinning, Skeletal Muscle, Hydrogel, Biomechanics

I. INTRODUCTION

At the beginning of tissue engineering, scaffold provided only a supporting role of cells and maintains the outer shape of target tissue. However, with the growth of biomechanical understanding, the physical and geometrical properties of the scaffold become a very important issue to induce the tissue maturation.

The skeletal muscle tissue, which has a unique uniaxial structure *in vivo*, exhibits the topological dependence in myogenic differentiation. Therefore, find the suitable customized scaffold should be given priority in skeletal muscle development. In this study, we developed the 3D uniaxial scaffold to promote myogenic differentiation in the biomechanics manner. In addition, our scaffold can mimic the hierarchical structure of muscle fiber *in vivo*, and this feature is expected to give an advantage on future clinical application.

II. METHODS

A. Scaffold Fabrication

The basic structure of the customized-scaffold was fabricated by electrospinning technique. Polycaprolactone (PCL, Sigma Aldrich, 80000 Da), which are known as a biocompatible material, was dissolved at 3:1 mixed solvent of Dichloromethane (DM, Junsei) and N, N - Dimethylformamide (NDF, Junsei) for 20% w/v. electrospun fiber was collected with tilted gap collector who generated the uniaxial topology. 3D environment was provided using collagen hydrogel (ECM675, Millipore).

B. Cell Culture

The myoblasts (C2C12, mouse cell line) were used to verify the customized scaffold. Cells were expanded in DMEM supplemented with 10% FBS and 1% penicillin streptomycin for 6 days, and differentiated in DMEM supplemented with 5% equine serum and 1% penicillin streptomycin for 7 days.

III. RESULTS

A. Scaffolds Characteristic

To verify the hierarchical structure of our customized scaffolds, scanning electron microscope (SEM, Magellan400) was used. From the SEM images, we observed that the single bundle of the scaffold consists of micro-fibers and collagen hydrogel was embedded between fibers. (Fig 1, a)

B. Cell Elongation in 3D Environment

The collagen gel was added at two different stages of myogenic differentiation to understanding the effect of 3D environment during maturation. The level of differentiation was judged by myosin heavy chain (MHC) expression and myotube formation using the immunofluorescence images. From the results, the myoblasts were more elongated in 3D environments, and this effect caused the positive effect on myogenic differentiation. (Fig 2, b) Additionally, we found that this elongation phenomenon gave more advantages in early stage of differentiation.

IV. CONCLUSION

In this paper, we verified that our customized scaffold not only mimics the hierarchical structure *in vivo*, but also promotes the myogenic differentiation.

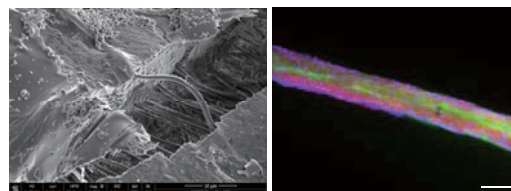


Fig 1. (a) SEM image of customized scaffold. Image was taken with 2500x magnitude with Pt sputter coating. (Scale bar: 10 μ m) (b) Immunofluorescence image of myoblasts in customized scaffold. (MHC: green, actin: red, nuclei: blue)

ACKNOWLEDGEMENT

This work was supported by the National Research Foundation of Korea (NRF) grant funded by the Korea government (MEST) (2013R1A2A2A01017014).

REFERENCES

1. Suk-Hee Park, Ung Hyun Ko, Mina Kim, Dong-Yol Yang, Kaph-Yang Suh, and Jennifer H. Shin, "Hierarchical multilayer assembly of ordered nanofiberous scaffold via thermal fusion bonding" *Biofabrication*, vol. 6, 024107, 2014.

Characterization of cellular transition within the expanding cell monolayer

Youngbin Cho¹, Bomi Gweon², Jacob Notbohm³, Ung Hyun Ko¹, Hwanseok Jang⁴,
Yongdoo Park⁴, and Jennifer H. Shin¹

¹Department of mechanical engineering, KAIST, Daejeon, Korea

²Department of biomedical engineering, Hanyang University, Seoul, Korea

³Department of environment health, Harvard University, MA, USA

⁴Department of biomedical engineering, Korea University, Seoul, Korea

E-mail: cyb6026@kaist.ac.kr

Abstract— As a cellular monolayer expands, cells within the cluster undergo phenotypic change from a stable to a migratory state, so called, epithelial-mesenchymal-transition (EMT). EMT affects the physical forces in cellular monolayer, especially cell-cell and cell-substrate adhesion force. So far, extensive biochemical studies on EMT have been reported, but its physical characteristics are still remained largely unknown. In a circularly patterned cellular monolayer ($\varphi \sim 300 \mu\text{m}$), we observed a group of cells within the peripheral band of the monolayer, where cells showed mesenchymal phenotype. Interestingly, cells migrate faster within this EMT-band, whereas cells within the interior of island migrate much slower. To correlate this cellular kinematics to forces, we quantified the forces that cells generate at the cell-substrate using traction force microscopy (TFM).

Keywords— Mammary breast epithelial cell, Micro-patterning, Collective migration, EMT, Traction force microscopy

I. INTRODUCTION

To migrate from the stable epithelial monolayer, cells change their phenotypes from a stable state to a migratory state, which is defines as the epithelial-mesenchymal transition (EMT) [1]. Recent finding in biology and biochemistry have shown that EMT is closely related to cancer invasion [2,3], but not much of the physical characteristics of EMT have been understood. Here, we aimed to understand the correlation between cellular motion and forces. We patterned an expanding circular cell monolayer and analyzed the kinematics using particle image velocimetry (PIV) analysis. Also, we quantified forces that cells exerted on the substrate by using traction force microscopy (TFM).

II. METHODS

A. Micro-patterning monolayer island

To measure the deformation of soft hydrogel, we used 3 kPa polyacrylamide hydrogel. Circular epithelial islands were, then, patterned on PA hydrogel.

B. Traction Force Microscopy (TFM)

Traction field can be calculated from measured displacement field of hydrogel by TFM based on the PIV analysis [4].

III. RESULTS

A. Phenotype and motion analysis

As the cells monolayer expands, cells at the edge of the monolayer transforms to a migratory phenotype and show fast migration speed, whereas the cells at the center maintain the epithelial phenotype and show slower movement.

B. Cell-substrate stress analysis

The distribution of traction made certain pattern as shown in color maps (Fig 1). At the edge of the monolayer, majority of the cells pulled the substrate inward, thus, a thick blue band-radially negative traction region-emerged. Interestingly, this blue band correlated well to the region of fast migrating cells at the edge. This strong blue band attenuated overtime when cells started to scatter (15 hr).

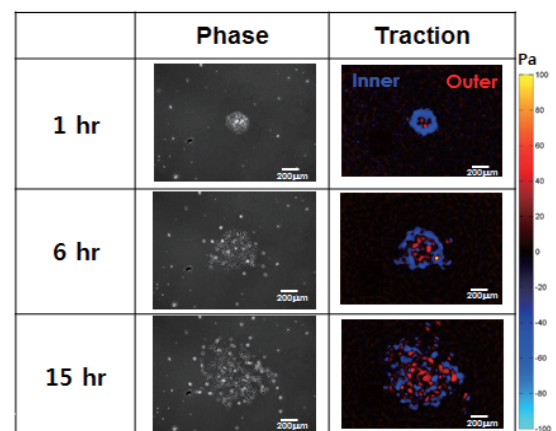


Figure 1 Traction force in radial direction of the cell monolayer

IV. CONCLUSION

In this study, we quantified cellular motion and physical forces within a circularly patterned cell monolayer. We revealed that the EMT-band, where cells migrate fast, exhibited high inward traction, however how this traction contributes to EMT still remained as an open question.

ACKNOWLEDGEMENT

This work was supported by the National Research Foundation of Korea Grant funded by the Korean Government (NRF-2013S1A2A2035518, NRF-2014R1A6A3A04059713)

REFERENCES

1. I. Y. Wong, S. Javaid, E. A. Wong, S. Perk, D. A. Haber, M. Toner, D. Irimia, 2014, "Collective and individual migration following the epithelial - mesenchymal transition," *Nature materials*, vol. 13, pp. 1063~1071
2. J. D. Rooij, A. Kerstens, G. Danuser, M. A. Schwartz, and C. M. Waterman-Storer, 2005, "Integrin dependent actomyosin contraction regulates epithelial cell scattering", *The Journal of cell biology*, vol. 171, no. 1, pp. 154~164
3. E. M. Howard, S. K. Lau, R. H. Lyles, G. G. Birdsong, J. N. Umbreit, and R. Kochhar, 2005, "Expression of E-cadherin in high-risk breast cancer", *Journal of cancer research and clinical oncology*, vol. 131, no. 1, pp. 14~18
4. D. T. Tambe, C. C. Hardin, T. E. Angelini, K. Rajendran, C. Y. Park, X. S. Picamal, E. H. Zhou, M. H. Zaman, J. P. Butler, D. A. Weitz, J. J. Fredberg, X. Trepat, 2011, "Collective cell guidance by cooperative intercellular forces", *Nature Materials*, vol. 10, no. 6, pp. 469~475

Mesenchymal Stem Cells Labeled with Indocyanine Green for Noninvasive Tracking using Ultrasonic and Photoacoustic Imaging, *In Vitro* Study

Kyu Kyu Hlaing¹, Nhat Quang Bui¹, Jin Myoung Yoo¹, Yun-Ok Oh¹, Seung Yun Nam² and Junghwan Oh^{2,3*}

¹Interdisciplinary Program of Biomedical Mechanical & Electrical Engineering, Pukyong National University, Busan, South Korea

²Department of Biomedical Engineering, Pukyong National University, Busan, South Korea

³Center of Marine-Integrated Biomedical Technology (BK21 Plus), Pukyong National University, Busan, South Korea

E-mail: jungoh@pknu.ac.kr

Abstract—In the present study, we investigated photoacoustic (PA) signal changes of labeled mesenchymal stem cells (MSCs) labeled with indocyanine green (ICG) at three different time points (day 1, 3, and 5). PAI system that could visualize transplanted MSCs and enhance stem cell delivery techniques. Therefore, we focused on understand tracking stem cells with FDA- approved contrast agents ICG using US/PA imaging techniques. For *in vitro* study, we utilized polyvinyl alcohol (PVA) tissue mimicking phantom which excluded four compartments to inject MSCs (1×10^6) labeled with ICG (1 mg/ml) with different loading times. According to our experiment, there were significantly higher PA signals from labeled on day 1 compared to others because of fluorescence gradually decreased that could be influenced PA signal changes. These results revealed the feasibility of using US/PA imaging techniques for longitudinal cells tracking and monitoring as well as detecting PA signals at different time points.

Keywords— Photoacoustic imaging (PAI), Indocyanine green (ICG), Polyvinyl alcohol (PVA), Ultrasonic and photoacoustic (US/PA) and Mesenchymal stem cells (MSCs).

I. INTRODUCTION

Recently, stem cell monitoring has been widely demonstrated with various noninvasive imaging modalities to enhance efficacy and safety of stem cell therapy. Photoacoustic (PA) imaging is an emerging noninvasive imaging technique which can visualize both endogenous and exogenous contrast agents with optical absorption properties. Our previous studies demonstrated that PA imaging is feasible to monitor stem cells labeled with gold nanoparticle with excellent detection sensitivity and selectivity [1]. However, biocompatibility of gold nanoparticles are still controversial so that clinical application of them is limited and not guaranteed yet. In this study, we proposed to use FDA-approved near infrared dyes, indocyanine green (ICG) for noninvasive tracking of stem cells using with combined ultrasound and photoacoustic (US/PA) imaging technique. US/PA imaging of ICG labeled stem cells can enhance safety

and biocompatibility of stem cell tracking technique, which has a great potential for clinical trials.

II. METHODS

We prepared bone marrow derived mesenchymal stem cells labeled with ICG for three different time points and control which were injected into each compartment of PVA phantom that was held in degassed water. For US/PA imaging, a tunable OPO laser ($\lambda=650\sim 1064$ nm, Surelite OPO Plus, Continuum) was pumped by a pump source Q-switched Nd: YAG (Surelite III, Continuum, San Jose, CA, USA). The laser light from OPO was coupled into a fiber optic (600- μm core) before irradiating onto each sample, they induced photoacoustic signals, which were detected by high-frequency intravascular ultrasonic transducer. Laser pulses at the wavelengths of 700, 800 and 900 nm with fluencies around $9 \text{ mJ}/\text{cm}^2$ (45, 28.4, and 17.9 % of the safety limit: $20 \times 10^{0.002[\lambda-700]} \approx 20, 31.7$, and $50.2 \text{ mJ}/\text{cm}^2$, respectively) were performed in this experiment.

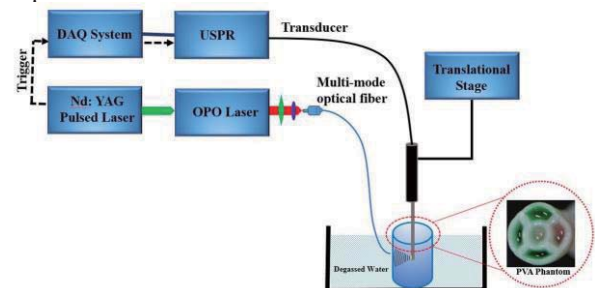


Fig. 1. Schematic diagram for PA imaging *in vitro*. DAQ: data acquisition; OPO: optical parametric oscillator; USPR: ultrasound pulse receiver.

III. RESULTS

According to the Figure. 2 (b) PA images, the control which cells without ICG shows that PA signals were undetected because cell itself difficult to absorb the light within the wavelength range of 700-900 nm, on the other hand, the compartments injected with ICG were clearly visible, and the PA image contrast was strong because ICG has an absorption and fluorescence maxima in the near infrared (NIR) region, at around 780 nm and 820 nm, respectively [2]. Especially the day 1 samples obtainable the highest contrast to the image, and the contrast gradually decreased from Day 3 and 5, respectively.

Fig. 3 shows the amplitudes of the photoacoustic signals changes from stem cell labeled with ICG at each successive time point. The spectra were the averages of tenth independent measurements. The results also approved that high-amplitude PA signals were obviously detected from compartment 4 (Day 1) compared to other parts (Day 3 and 5).

A. US/PA imaging of tissue mimicking phantom

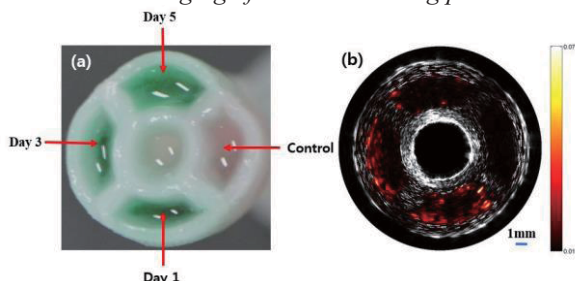


Fig. 2. (a) Top view of the cylindrical PVA phantom containing four compartments with ICG loaded stem cells (1×10^6 cells at different time points per compartment) suspended in 150 μ l medium in the tissue mimicking PVA phantom and a control (cells only). (b) US/PA image at 800-nm wavelength. Color-map: standard hot. Measurement unit: mm.

B. Photoacoustic spectra

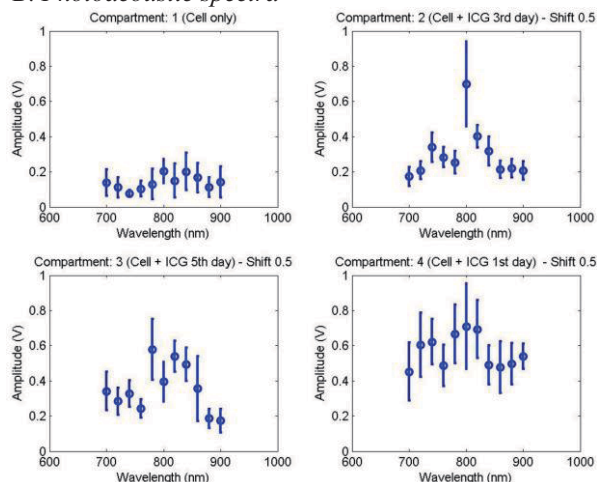


Fig. 3. PA signal amplitudes spectrum of four compartments (Control, Day 1, 3 and 5) shows the photoacoustic amplitude spectra (circles) measured in 4 compartments and their corresponding specific extinction spectra PA signal intensity, at 700, 800 and 900 nm.

IV. CONCLUSION

The cells were subsequently incubated in culture media at each successive time point, fluorescence gradually decreased and influenced the changes of PA signals for imaging methods. In addition, *in vivo* studies and clinical applications are needed to develop new commercial products.

ACKNOWLEDGEMENT

This research was supported by a grant from Marine Biotechnology Program (20150220) funded by Ministry of Oceans and Fisheries, Republic of Korea.

REFERENCES

1. Seung Yun Nam, Laura M. Ricles¹, Laura J. Suggs, Stanislav Y. Emelianov¹, S.Y. Nam, L.M. Ricles, L.J. Suggs, S.Y. Emelianov, "In Vivo Ultrasound and Photoacoustic Monitoring of Mesenchymal Stem Cells Labeled with Gold Nanotracers, PLoS One, 7 (2012) e37267.
2. Jung B, Anvari B, "Synthesis and characterization of bovine serum albumin-coated nanocapsules loaded with indocyanine green as potential multifunctional nanoconstructs", Biotechnol Prog. 2012 Mar-Apr; 28(2):533-9. doi: 10.1002/btpr.732. Epub 2011 Oct 14.

The effect of three-dimension(3D) scaffolds using Poly-L-Lactic Acid(PLLA) and Tricalcium Phosphate(TCP) on bone regeneration in rat calvarial defect model.

JiYun Nam¹, SeungHoon Kang¹, Hong-Hee Jung², JoonHo Wang*

¹Department of Medical Device Management and Research, SAIHST, Sungkyunkwan University, Seoul, Republic of Korea

¹Department of Orthopaedic Surgery, Samsung Medical Center, Seoul, Republic of Korea

The Institute of Biomaterial and Medical Engineering, Cellumed Co., Ltd, Seoul, Republic of Korea

*Samsung Advanced Institute for Health Sciences and Technology, Sungkyunkwan University, Seoul, Republic of Korea

E-mail: njy3239@gmail.com

Abstract—This study evaluated the capability of three dimensional printing Poly-L-Lactic Acid(PLLA) with tricalcium phosphate(TCP) scaffolds as bone defect replacement matrix when grafted in a calvarial bone defect of rats. A total 48 male Sprague-Dawley rats were used in this study. 2, 8 weeks after surgery, each 24 rats were sacrificed and collected defect regions. And bone formation was evaluated with micro computed tomography(micro CT) and histologically.

Keywords— Bone regeneration, 3D printing, Bioceramics, Bone grafts, Tricalcium Phosphate.

I. INTRODUCTION

Regeneration of bone gap defects due to trauma, injury, or tumor resection can be accomplished by transplantation of either autografts or allografts or alloplastic[1, 2]. 3D printing is becoming popular in bone tissue engineering due to the ability to directly print porous scaffolds with designed shape, controlled chemistry and interconnected porosity[3].

The purpose of this study is to evaluated the capability of 3D composite scaffolds(Poly-L-Lactic Acid with tricalcium phosphate) as a bone grafting in a calvarial bone defect of rat *in vivo*.

II. METHODS

A. Printing of 3D porous synthetic scaffolds

Porous synthetic scaffolds were prepared using an 3D BIO plotting System, using a blend of PLLA(poly-L-lactic acid)(R207S, EVONIK industries, Germany) and b-tricalcium phosphate (B-TCP, 49963, Sigma Aldrich, MO, USA).

B. Surgical Procedure

A total 48 eight-week-old male Sprague-Dawley rats weighing 190-220g were used. The rats were anesthetized by intramuscular injection of a 4:1 solution of ketamine hydrochloride (Ketalar, Yuhan, Seoul, Korea) and xylazine (Rompun, Bayer, Korea, Seoul, Korea). Calvarial defect formation was surgically created using Trepine bur 8mm. The defects were transplated with (1)Poly-L-Lactic Acid(n=16) and (2) Poly-L-Lactic Acid and

Tricalcium phosphate(70%) composite scaffolds(n=16) (3)no graft material(n=16).

III. RESULTS

A. Micro CT findings

Eight weeks after surgery, PLLA scaffolds and 70% TCP scaffolds were maintained 3D dimensional shape. After 8 weeks of healing, radiodensity was increased near to defect sites compared with at 2weeks.

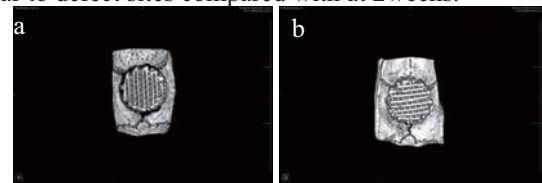


Figure 1. a micro CT images from rat calvarial defect grafting 70% TCP scaffolds after 2 weeks surgery. b. after 8weeks surgery.

B. Histological findings

There is no significant differences between 2 weeks PLLA group and 70% TCP group. However, at 8 weeks specimens, we confirmed that more bone formations were formed in 70% TCP scaffolds compared with Poly-L-Lactic Acid scaffolds at 8weeks after surgery.

IV. CONCLUSION

The results indicate that the combination of Poly-L-Lactic Acid with 70% tricalcium phosphate three dimension scaffolds may be an effective means of enhancing bone formation in calvarial bone defect of rats.

REFERENCES

1. Khan Y, Yaszemski MJ, Mikos AG, Laurencin CT, J Bone Joint Surg Am. 2008 Feb;90 Suppl 1:36-42
2. Yaszemski MJ¹, Payne RG, Hayes WC, Langer R, Mikos AG. Biomaterials. 1996 Jan;17(2):175-85.
3. H. Seitz, et al. J. Biomed. Mater. Res. B 74B (2005) 782–788.

Silicon-Doped Hydroxyapatite Coating on Low Elastic Titanium Alloy for Dental Implant Application

Y. H. Jeong¹, T. G. Jung¹, J. W. Yang¹, J. Y. Jeong¹, H. C. Choe²

¹Department of Medical Device Development Center, Osong Medical Innovation Foundation, Cheongju-si, Chungbuk, Korea

²Department of Dental Materials, Research Center of Nano-Interface Activation for Biomaterials, & Research Center for Oral Disease Regulation of the Aged School of Dentistry, Chosun University, Gwangju, Korea

E-mail: hcchoe@chosun.ac.kr

Abstract— This work shows the effect of silicon doping on the hydroxyapatite coating on the titanium alloy for dental implant application. The coating was performed by magnetron sputtering and electrochemical deposition method, silicon doping could effect on the degradation rate that verified with corrosion test.

Keywords— Hydroxyapatite, Silicon, Titanium, Electrochemical, Deposition

I. INTRODUCTION

Titanium and its alloys basically have good physical and biological properties that can use for dental and orthopedic field. By the way, the earliest biomedical implants were not enough to lead a biocompatible function at the interface that were not optimized for bone regeneration. The goal of the bio-implant is to improve the osteointegration which could have been develop for the surface modification such as blasting, anodizing, Ca/P coating, F⁻, and laser treatment, etc [1].

The hydroxyapatite (HA) coating is very known to be bioactive can develop bone formation. But, the HA has limited with their slow rate of interaction, and there needs to improve release rate from HA coated implants. Recently, the silicon-doped HA (Si-HA) has been reported that showed better dissolution, suggesting a decrement of grain size can lead to increase solubility and hence achieve better biocompatibility [2].

The aim of this study was to investigate *the Si-HA deposition on Ti-Nb-Zr alloy* by electro-chemical and magnetron sputtering method.

II. METHODS

A. Sample preparation

The β phase stabilized Ti-Nb-Zr alloys were fabricated with 35 wt.% of Nb and 10 wt.% of Zr element by arc melting furnace as a substrate. HA deposition was performed by pulsed potential with a method of cyclic voltammetry (30 cycles) in the electrolyte of 5 mM-Ca(NO₃)₂·4H₂O + 6.0 mM-NH₄H₂PO₄ at 85 °C. The Si doping was performed with a pure Si target by a magnetron

sputtering with variable deposition time (30-120 min with 60 W).

B. Surface analysis

The surface characteristics were analyzed by field emission scanning electron microscopy (FE-SEM), energy dispersive X-ray spectroscopy (EDS), and X-ray diffraction (XRD). Corrosion properties were performed by potentiodynamic test for the ion release on the coating surface.

III. RESULTS

The portion of Ca, P, and Si were little increased while the Ca/P ratio was decreased by sputtering time. The peaks of X-ray diffraction for HA coating were increased and, there was not phase shifting or other peaks by annealing treatment. The Si-HA coating surface had not different peaks by Si sputtering time. Increment of Si sputtering time could show higher corrosion potential and lower corrosion current density (Shifting to left-up). Also, the corrosion resistance of passivation region was increased by Si sputtering time, but, the corrosion rate was not different.

IV. CONCLUSION

These findings showed that the Si-HA deposition could be successfully deposited by chemical (electro-deposition) and physical (sputtering) method, Si-HA layer had higher degradable than that of HA single layer with proving the electrochemical corrosion test.

ACKNOWLEDGEMENT

Supported by the NRF grant (2008-0062283).

REFERENCES

1. Y. Shibata, and Y. Tanimoto, "A review of improved fixation methods for dental implants. Part 1: surface optimization for rapid osseointegration" *J Prosthodont. Res.*, vol. 59, pp. 20-33, 2015.
2. Y. H. Jeong, H. C. Choe, and W. A. Brantley, "Silicon-substituted hydroxyapatite coating with Si content on the nanotube-formed Ti-Nb-Zr alloy using electron beam-physical vapor deposition" *Thin Solid Films*, vol. 546, pp. 189-195, 2013.

Cell-based Scaffolds for Bioartificial Muscle by PEDOT/MWCNT

Tae Hyeob Kim^{*1}, Cheong Hoon Kwon^{*1}, and Seon Jeong Kim¹

¹Center for Self-powered Actuation and Department of Biomedical Engineering, Hanyang University

*These authors contributed equally to this work.

E-mail: sjk@hanyang.ac.kr

Abstract—Cell-based scaffolds has been developed for biomedical engineering system. However, they have several limitations of low cell-adhesiveness, and inflexibility that causes small actuation. Here, we introduce novel bioartificial muscle powered by C2C12 muscle cells with functionalized multiwalled carbonnanotube.

Keywords—bioartificial muscle, C2C12 cells, biomimetic actuation, multi-walled carbon nanotubes, scaffold

I. INTRODUCTION

In cell engineering, bioartificial muscles are generally produced by containing living cells and cell scaffolds.^[1] Furthermore, actuation of bioartificial muscles is relies on the adhesiveness of the cells to the scaffolds. However, previous scaffolds have low cell-adhesive and inflexible property. Here, we overcome the limitation with stable muscle scaffold consists of multiwalled carbon nanotube (MWCNT) and hydrophilic polymer poly(3,4-ethylenedioxythiophene) (PEDOT).^[2]

II. METHODS

C2C12 muscle myoblasts were cultured on a PEDOT-coated on MWCNT sheet supporter. and PEDOT was coated on the sheet. Furthermore, polytetrafluoroethylene cell isolator was mounted on the PEDOT/MWCNT sheet. After 7 days, C2C12 myoblasts was growth to the myotubes, and cell isolator removed PEDOT/MWCNT sheet. Finally, the whole systems of our scaffolds and cell culture protocol were prepared as shown in Fig. 1.

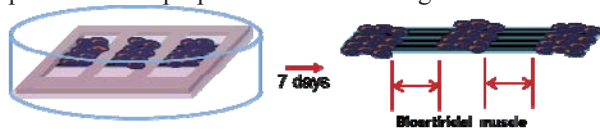


Fig. 1 An illustration of bioartificial muscle.

III. RESULTS

A surface microscope image of the myotubes on PEDOT/MWCNT is shown in Fig. 2. Compared to bare MWCNT, that is popular materials in cell culture system, the myotubes have good state in PEDOT/MWCNT. Although we did just only polymerization on the MWCNT, it has a good biocompatibility about cell growth.

Moreover, we confirm that PEDOT/MWCNT is more stable during cell culture in cell culture medium, because of hydrophilicity of PEDOT/MWCNT.

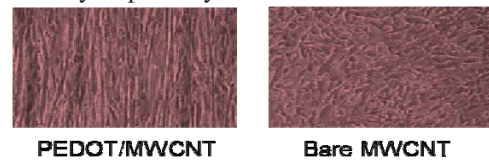


Fig. 2 Comparison microscope images of myotube growth states between PEDOT/MWCNT and bare MWCNT.

Moreover, actuation of whole system is similar to a single myotube. It means that C2C12 muscle myotubes, which is power source of bioartificial muscle, have similar kinetics of a single myotube.

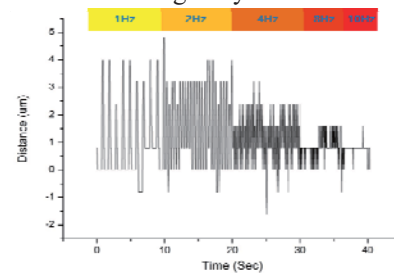


Fig. 3 Comparison of actuation performance between a single cell and the bioartificial muscle.

IV. CONCLUSION

We developed a new cell-based scaffold for bioartificial muscle based on PEDOT-coated MWCNT sheet. This muscle not needs complicate protocol for cell adhesive. Furthermore, it has a good potential for multifunctional cell or tissue engineering scaffolds.

ACKNOWLEDGEMENT

This work was supported by the Creative Research Initiative Center for Self-powered Actuation and the Korea-US Air Force Cooperation Program Grant No.2013K1A3A1A32035592 in Korea.

REFERENCES

1. Ricotti et al., "Bio-hybrid Muscle Cell-based Actuators" *Biomed Microdevices*. 14, 987-998. 2012.
2. Lee et al., "Hybrid Nanomembranes for High Power and High Density Supercapacitors and Their Yarn Application", *ACS Nano*. 6, 327-334. 2012.

Decellularization with pulsatile perfusion

S. M. Park¹, S. R. Yang¹, S.W. Choi², J. R. Park¹, J. W. Yang¹, H. Lee¹, E. C. Kim¹

¹Dept of Thoracic and Cardiovascular Surgery, School of Medicine, Kangwon National University, Chuncheon, South Korea

²Dept of Mechanical and Biomedical Engineering, Kangwon National University, Chuncheon, South Korea

E-mail: heartlung@gmail.com

Abstract—Perfusion with detergent is the most commonly used decellularization method to make a bioscaffold from an organ. Two different perfusion methods, one with pulsatile flow and the other with continuous, were compared using isolated rat hearts. The results revealed that decellularization is more efficient in pulsatile perfusion than non-pulsatile perfusion.

Keywords— Decellularization, pulsatile flow, bioscaffold, energy equivalent pressure.

I. INTRODUCTION

Decellularized animal organs are used as bioscaffolds for tissue engineering. Continuous flow perfusion with detergent is the most common method for decellularization. Pulsatile flow is known to be beneficial for tissue perfusion and strengthening vascular structure. Using Energy Equivalent Pressure (EEP) as a pulsatility parameter, the efficiency of pulsatile flow in decellularization process is studied.

II. METHODS

A. Decellularization and measurement

Rat hearts were isolated and connected to the modified rat heart isolation system. The hearts were perfused with 1% SDS (Sodium dodecyl sulfate) solution for two hours. They were divided into two groups, one pulsatile perfusion group and the other continuous perfusion group. The pressure and flow were measured and record for 2 min in every 30 min. The EEP values were Calculated applying Following equation (1).

$$EEP = \frac{(\int f p dt)}{(\int f dt)} \quad (1)$$

f = flow and p = pressure

B. Analysis of decellularization level

Gross findings and histologic findings were examined. Genomic DNA were analyzed to find out the level of decellularization. To detect damages of the ECM, assays for collagen, elastine and glycoaminoglycan were performed

III. RESULTS

A. The mean pressure and flow

The initial mean perfusion pressure and flow were same in both groups. The perfusion flow increased more rapidly in the pulsatile group while the mean perfusion pressure was maintained at the same level throughout the decellularization period and between the groups.

B. Decellularization level

Decellularization is more profound in the pulsatile group after two hours of SDS perfusion (Fig 1). The pulsatile group had lower residual DNA content than the non-pulsatile group. However, the ECM components showed no difference after the decellularization procedure.

IV. CONCLUSION

Decellularization is more efficient in pulsatile perfusion than non-pulsatile perfusion.

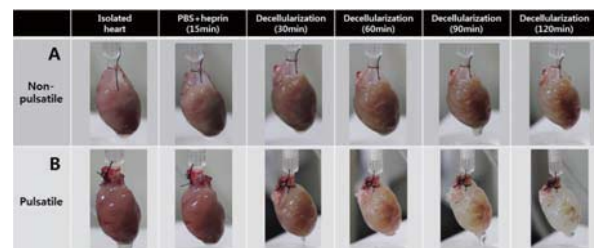


Fig. 1. Serial photographs of decellularizing rat hearts

ACKNOWLEDGEMENT

This research was supported by the iPET (Korea Institute of Planning and Evaluation for Technology in Food, Agriculture, Forestry and Fisheries) (112008-5-2-SB030).

REFERENCES

1. H. C. Ott, T. S. Matthiesen, S.K. Goh, et al, "Perfusion-decellularized matrix: using nature's platform to engineer a bioartificial heart" *Nature Medicine*, vol. 14, pp. 213-221, 2008.
2. S. Kato, A.C. Chokshi, P. Singh et al, "Effects of Continuous-Flow Versus Pulsatile-Flow Left Ventricular Assist Devices on Myocardial Unloading and Remodeling" *Circ Heart Fail*, vol. 4, pp. 546-553, 2011.

Applying biomechanical stresses to cells on a stretchable substrate using bioreactor

GeonHui Lee¹, Sung Ho Ko², Soo Hyun Kim³, Sang-Hoon Lee*^{1,2}

¹ KIST Graduate School of Converging Science and Technology, Korea University, Seoul 136-701, Republic of Korea;

² Department of Biomedical Engineering, College of Health Science, Korea University, Seoul, 136-703, Republic of Korea;

³ Division of Life & Health Sciences, Biomaterials Research Center, Korea Institute of Science and Technology, Seoul, Republic of Korea;

E-mail: sharafm@gmail.com

Abstract—We present development of a novel reciprocating bioreactor as well as a miniaturized cell culture system that fluid and solid mechanical stress can be generated. To apply mechanical strain on cells, poly(L-lactide-co-ε-caprolactone) (PLCL) copolymers membrane was used because of its elasticity. A PLCL matrix was prepared by crystallization the PLCL microspheres and densely packed as a membrane by effect of nonsolvent. . Three forces, cyclic stretch, hydraulic pressure and laminar shear stress, were applied to mimic physiologic conditions. The effect of these forces on cells was examined by bioreactor. The effect of these forces on cells was examined by bioreactor. MSCs were aligned and differentiated to smooth muscle cells (SMCs).

Keywords— Bioreactor, biomechanics, stretchable membrane, shear stress, tissue engineering

I. INTRODUCTION

Tissue engineering is an attractive strategy to address the increasing clinical need for tissue replacement. Tissue engineering aims to provide functional biological substitutes of native tissues for potential clinical application in the repair of damaged or diseased tissues and organ. Bioreactors, such as spinner flasks, rotator wall vessel, perfusion cultures, and mechanical strain cultures have been developed for cell and tissue engineering applications. Here, we demonstrated the effect of mechanical force on SMCs

II. METHODS

A. bioreactor set up

The bioreactor consisted of four parts: a peristaltic pump containing two pump heads, a custom-designed metering valve, a culture chamber, and tubing. The pulsatile pump head was also custom designed. The pressure was gauged by a custom-designed digital manometer using software in real time and was

measured at two points, in and out of the scaffold chamber

B. microchip fabrication

Microfluidic chips were fabricated using an SU-8 photoresist-patterned silicon wafer as a mold. The PDMS pre-polymer and cross-linker (Sylgard 184, Dow Corning) were mixed in a 10:1 ratio, poured onto the mold, and cured at 80°C for 2 hours. The PDMS substrates were then bonded together using oxygen plasma treatment. The prepared devices were heated in an oven at 80°C for 1 day to recover the hydrophobic surface properties..

C. cell culture & immunostaining

The cells were grown in Dulbecco's modified Eagle's medium supplemented with 10% fetal calf serum, penicillin. Cells were retrieved from each type of microwell and fixed by immersing in 4% paraformaldehyde for 30 minutes at 4 ° and then incubating in 0.1% Triton X-100 in phosphate-buffered saline. These cells were washed and incubated with Alexa Fluor 488-conjugated anti-rabbit IgG or Alexa Fluor 568-phalloidin for F-actin staining, as appropriate. All spheroids were then incubated with DAPI

III. RESULTS

Use Bioreactor was successfully worked with microchip. Cells were cultured on PLCL membrane between PDMS chamber. Bioreactor was connected with PDMS chip and media tank were connected for dynamic cell culture. It generated diverse range and frequency of pressure. The shear stress and strain group of cells were aligned in a microchip. Control group was randomly aligned. Shear stress with strain group shows the most alignment of cells and high differentiation to smooth muscle cells.

IV. CONCLUSION

We developed dynamic cell culture system using reciprocating bioreactor for cell alignment and differentiation on a PLCL membrane. Various range of cyclic pressure can be generated and PLCL membrane can be stretched up to 40% by bioreactor. With this bioreactor, MSCs were cyclically applied in strain, hydraulic pressure and shear stress. MSCs were aligned and differentiated to SMCs under shear stress and strain

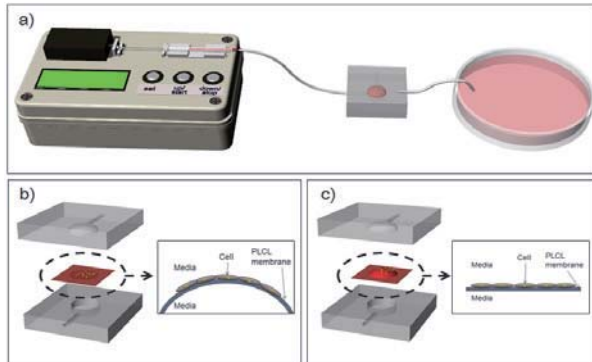


Figure 1. Schematic of bioreactor and microfluidic chip. Cells were cultured on PLCL membrane between PDMS chamber. (a) Bioreactor, PDMS chip and media tank were connected for dynamic cell culture. (b) Normal state of membrane. (c) Cells were stretched with membrane by hydraulic force.

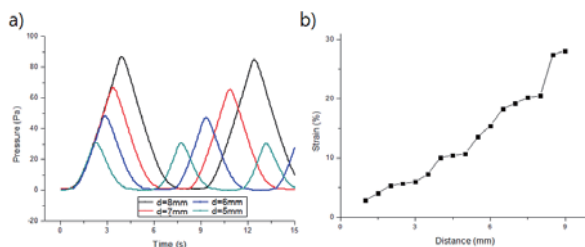


Fig.2 Graphs of mechanical stress generated by bioreactor. (a) range of hydraulic pressure, (b) stretched percentage of PLCL substrate membrane.

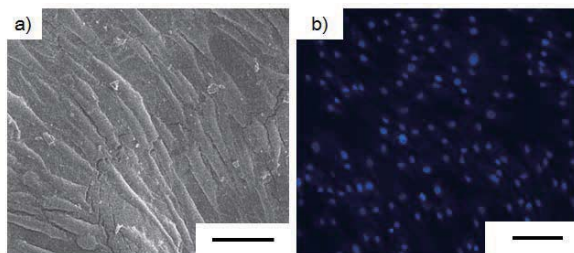


Fig.3 morphology of cells. (a) SEM image of cells, (b) optical image of DAPI stained cell. Scale bar : 100 μm.

ACKNOWLEDGEMENT

This work was supported by the KU-KIST Graduate School of Converging Science and Technology Program.

REFERENCES

1. T. M. Maul, D. W. Chew, A. Nieponice, D. A. Vorp, Biomechanics and modeling in mechanobiology, 10(2011),pp. 939.
2. J. P. Winer, P. A. Janmey, M. E. McCormick, M. Funaki, Tissue Engineering Part A , 15(2008), pp. 147.
3. C. H. Mun, Y. Jung, S. H. Kim, H. C. Kim, S. H. Kim, Artificial organs, 37(2013), pp. E168.
4. T. P. Kunzler, T. Drobek, M. Schuler, N. D. Spencer, Biomaterials, 28(2007), pp. 2175.
5. A. J. Engler, S. Sen, H. L. Sweeney, D. E. Discher, Cell, 126(2006), pp.677.

Cytolethal distending toxin of *Escherichia coli*'s and their virulence

Tuyatsatsral .L¹ and Sarantuya. J²

¹Midwifery, MNUMS, Mongolia

²School of Pharmacy and Bio-Medicine, MNUMS, Mongolia

Abstract

Background The infection caused pathogen *Escherichia coli* (*E.coli*) penetrate through mucous layer unlimited which it spreads out human body then causes many diseases. The pathogen *E.coli* categorized into three classifications which based on the disease clinic symptoms: 1) Uropathogenic disease, 2) Sepsis and meningitides, and 3) Diarrhea. Diarrheagenic *E.coli* also classified into several categories: enterohemorrhagic *E.coli* (EHEC), enterotoxigenic *E.coli* (ETEC), enteropathogenic *E.coli* (EPEC), enteroinvasive *E.coli* (EIEC), enteroaggregative *E.coli* (EAEC). Each class has own specific disease causing mechanism and virulent factors. These pathogens cause severe food poisoning and diarrheal diseases, even can reach to death. Recently, in 2011, a new and more virulent strain of *E.coli* bacterium caused the outbreak that killed 17 people and left more than 1500 ill across Europe. Bioinformatics analysis revealed that this *E.coli* is a new strain of bacteria that is

highly infectious and toxic. Therefore *E.coli* infection is spreading over the world, it is necessary to study and investigate this bacterium. Recent years has defined *E.coli* producing cytolethal distending toxin (CDT).

Many pathogens produce CDT. This toxin causes sensitive eucariotic cells to become blocked in G2 phase and leading eventually to cell death. CDT producing *E.coli* has been studied in India, Bangladesh, Nigeria, Brazil and Japan, that cause pediatric diarrhea, but epidemiological significance has not been determined. In some area CDT-I subtype occurs more frequently. Therefore our aim of study is *E.coli* CDT from Mongolian diarrheagenic pediatric patients, their virulent factors and genomic structures.

Methods All 249 *E.coli* strains had been collected from diarrheagenic patients aged until 16 years old. Have been used methods purification of DNA, amplification of *cdtB* and other gens of

virulent factors by polymerase chain reaction (PCR), cell toxic activity experiment, genome subtyping and DNA sequencing, serotyping.

Results *cdtB* gen from 249 strains have been amplified by PCR and the *cdtB* positive strains evaluated as a cell detaching *E.coli*. Although *cnf1* and *cnf2* genes have been amplified and the positive strains evaluated as a Necrotising *E.coli* (NTEC). In our study CTEC detected 1.6% (4 of 249), but necrotizing factors have not detected. Comparing with previous study and CTEC from this study has listed after all categories. One CTEC has *virF* and *ipaH* genes of EIEC, which explained that virulence of this strain is very high. When identified inner structure of *cdtB* gen by DNA sequencing method, it has 98-100% homology with Genbank CDT sequencing, so it has been confirmed that our study CDT samples via this method.

Conclusion CTEC is one of the pathogen causing diarrhea in Mongolian diarrheal patients as same with other categories of *E.coli*, by genomic methods they have various gensubtypings and highly virulent. This toxin is detected first time by our study. Further, it is necessary in vitro investigation of this toxin.

Key word: *E.coli*, Cytolethal distending toxin, bacterium

Different therapeutic potential of non-responder and responder MSCs in SOD1 mice

H. Kim^{1,2}, H.Y. Kim², H. Jang¹, W. Jo¹, K.S. KIM³, C.Y. KIM¹ and S.H. KIM²

¹Laboratory animal center, Daegu-Gyeongbuk Medical Innovation Foundation, Daegu, South Korea

²Department of Neurology, College of Medicine, Hanyang University, Seoul, South Korea

³Bioengineering Institute, Corestem Inc., Seoul, South Korea

E-mail: hkim@dgmif.re.kr

Abstract— MSCs isolated from one patient in responder/non-responder cells therapy groups were transplanted into the cisterna magna of mutant SOD1-G93A transgenic mice to measure their lifespans, locomotor activity, and motor neuron numbers. The levels of VEGF, ANG, and TGF- β were significantly higher in responders than in non-responders. In the mouse model, the recipients of responder MSCs had a significantly slower onset of symptoms and a significantly longer lifespan than the recipients of non-responders or controls.

Keywords—Amyotrophic lateral sclerosis, SOD1, Responder, Non-responder, MSCs therapy

I. INTRODUCTION

Amyotrophic lateral sclerosis (ALS) is caused by motor neuron (MN) death and is one of the most fatal neurodegenerative diseases.

In this study, we investigated the MSCs therapeutic potential using different MSCs which were isolated from the non-responder and responder patients to MSCs cells therapy.

II. METHODS

A. In Vivo MSC Transplantation and Functional Observation

SOD1 mice were randomly assigned to three groups: a control group treated with PBS, and two ALS groups (ALS-N and ALS-R) that received MSCs isolated, respectively, from the non-responder and responder patients.

B. In Vivo Tissue Analysis

Six mice (three female and three male) from each group were killed by isoflurane inhalation at 109 days. For ICH staining, every 10th lumbar section was incubated GFAP and Iba-1 antibodies. To count MNs, every 10th section was stained with 1% cresyl violet and counted bilaterally in 10 sections.

III. RESULTS

A. In Vivo Functional Observation

Symptom onset was significantly delayed in the MSC-treated groups than in the PBS group. The

survival time was significantly longer in the ALS-R group than in the PBS group. In the rotarod test, only the ALS-R group showed a significantly slower decline in motor performance than the PBS group.

B. Tissue Analysis

Both groups treated with MSCs (ALS-N and ALS-R) had lost significantly fewer MNs than the PBS group. The two MSC treated groups showed significantly lower immunoreactivity for Iba1 and GFAP than the PBS group.

IV. CONCLUSION

We propose that it may be possible to identify the best candidates for autologous MSC therapy in ALS if we screen patients according to the amounts of trophic factors their MSC's secrete

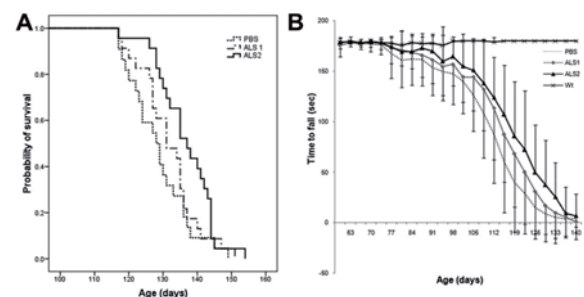


Fig. 1. Effects of transplantation on survival time and rotarod performance.

ACKNOWLEDGEMENT

This work was supported by the Korean Health Technology R&D Project, Ministry for Health, Welfare and Family Affairs, Republic of Korea (grants A101712 and A120182).

REFERENCES

1. Kim H et al "Dose-dependent efficacy of ALS-human mesenchymal stem cells transplantation into cisterna magna in SOD1-G93A ALS mice." *Neurosci Lett*, 468, 190–194, 2010.
2. Koh SH et al. "The functional deficiency of bone marrow mesenchymal stromal cells in ALS patients is proportional to disease progression rate." *Exp Neurol* 233, 472–480, 2012

To explain results of hepatocellular modeling in Mongolians by non linear theory

B.Odmaa¹, B.Tserennadmid², M.Tuul³,

¹School of Pharmacy and Bio-Medicine MNUMS

²School of Pharmacy and Bio-Medicine MNUMS

E-mail: odmaa@mnumns.edu.mn

Abstract

Background: Liver cancer is the 5th most common cancer worldwide with 500,000 cases diagnosed per year. It is a disease with a high death rate (14000-15000 per year). By the last news of national center of health development, liver cancer is first most common cancer in our country.

Goal: To study and to compare volumetric modeling of hepatocyte's cytoplasm, nucleus and stereometric indices in condition of comparatively healthy, acute intoxication, chronic inflammation, cancerous condition and clear cell tumor, and to explain by non linear theory.

Materials and Methods:

It was prepared sections for histometric materials. Linear measurements of hepatocytes and nucleus were carried out by computer microscope 'Leica' with program Diskus 3.2 version from GermanOn linear measurement in condition of comparatively healthy, acute intoxication, chronic inflammation, cancerous condition and clear cell tumor were processed by mathematic modeling.

Results:

In comparatively healthy condition the volume of the hepatocyte's cytoplasm was determined $2140.73 \pm 19.97 \text{ mkm}^3$, the volume of the hepatocyte's nucleus was $295.19 \pm 2.60 \text{ mkm}^3$, ration between hepatocyte's cytoplasm and nucleus was 7:1 ($P < 0.001$). In condition of acute intoxication the volume of the hepatocyte's cytoplasm was determined $4281.36 \pm 77.83 \text{ mkm}^3$, the volume of the hepatocyte's nucleus was $895.00 \pm 13.42 \text{ mkm}^3$, ratio between hepatocyte's cytoplasm and nucleus was 5:1 ($P < 0.001$). In condition of chronic

inflammation the volume of the hepatocyte's cytoplasm was determined $4887.84 \pm 75.72 \text{ mkm}^3$, the volume of the hepatocyte's nucleus was $888.65 \pm 12.46 \text{ mkm}^3$, ration between hepatocyte's cytoplasm and nucleus was 5:1 ($P < 0.001$). In cancerous condition the volume of the hepatocyte's cytoplasm was determined $3852.63 \pm 116.06 \text{ mkm}^3$, the volume of the hepatocyte's nucleus was $463.09 \pm 12.95 \text{ mkm}^3$, ratio between hepatocyte's cytoplasm and nucleus was 8:1 ($P < 0.001$). In clear cell tumor the volume of the hepatocyte's cytoplasm was determined $15062.69 \pm 348.41 \text{ mkm}^3$, the volume of the hepatocyte's nucleus was $801.05 \pm 22.56 \text{ mkm}^3$, ratio between hepatocyte's cytoplasm and nucleus was 19:1 ($P < 0.001$).

Conclusions:

1. We have determined volume of hepatocyte's volume and nucleus, ratio between cytoplasm and nucleus in condition of comparatively healthy, acute intoxication, chronic inflammation, cancerous and clear cell tumor.

2. Volume of hepatocyte's cytoplasm was increased 2.28 times, volume of hepatocyte's nucleus was increased 3.01 times in condition of chronic inflammation and volume of hepatocyte's cytoplasm was increased 1.99 times, volume of hepatocyte's nucleus was increased 3.03 times in condition of acute intoxication. Also volume of hepatocyte's cytoplasm was increased 1.79 times, volume of hepatocyte's nucleus was increased 1.5 times in cancerous condition and volume of hepatocyte's cytoplasm was increased 7.03 times, volume of hepatocyte's nucleus was increased 2.7 times in condition of clear cell tumor.

3. By the comparison between volumes of hepatocyte's cytoplasm and nucleus in condition of comparatively healthy, acute intoxication, chronic inflammation, cancerous was determined medium direct correlation rather by the comparison between volumes of hepatocyte's cytoplasm and nucleus in condition of clear cell tumor wasn't determined correlation.

Key words: cytoplasm, hepatocyte, nucleus, volume, condition

The study of location and structure of blue spots in Mongolian children aged from 0 to 3 in Ulaanbaatar city

Baigalmaa.B¹, Avirmed.A², Amgalanbaatar.D³

¹School of Pharmacy and Bio-Medicine, MNUMS.Mongolia

²School of Pharmacy and Bio-Medicine, MNUMS.Mongolia

E-mail: baigalmaa.bs@mnums.edu.mn

ABSTRACT

BACKGROUND

Mongolian children have the blue spots on any part of their body from the birth.¹ The incidence of the blue spots is occurring in other country, however its very rare. It were detected in central Asian Mongolian felt tent dwellers, such as the Buryatia, Tuva, Khalimag, Mongolia, Inner Mongolia as well as the Shinjian; also it was occurred in Korea, Afghanistan and Hungary. It's known as the Mongolian blue spots in medical science thorough the world. The blue spots could be the specific genetic pattern of the Mongolian felt tent dwellers.

The blue spot is classified by its location as persistent, deep penetrated and extensive. Some researchers noted that it is a normal condition however it is still not determined yet whether as normal or abnormal.

There are a number of studies which focused on the prevalence of the blue spots. However there are lack of studies which emphasized the size and structure of the blue spots. Therefore, the incidence of the blue spot is decreasing nowadays according to the data of obstetricians and gynecologists, pediatricians. It may influence to the national security.

PURPOSE

Determine the features of form, shape and size, location as well as the microstructure of the Mongolian blue spots in children aged from newborn until three years old

MATERIALS AND METHODS

There were enrolled totally 60 children of both sexes, including 20 newborns, 20 infants and 20 early childhoods from the maternity hospitals and kindergartens in Ulaanbaatar. The cross-sectional research method was used in the study.

We used the morphometric analysis to determine the form and size of the blue spots. The papyrine was used to determine the form and size of the blue spots by putting it on the area of blue spots. After that it was evaluated by the common used methods by Avtandilov. The participants were classified into the newborn, infants and the early childhoods.

The location and sex differentiation of the blue spots were determined by the statistical methods and developed using the program "SPSS-17".

The microstructure of the blue spots were evaluated in 45 cadavers and 350 units of the study.

RESULTS OF THE STUDY

According to the study results of the blue spot location, the 23.3% of all cases had the blue spot along the buttock and sacral region, the 21.67% were detected on the sacral region and vertebra, the 13.33% on buttock-sacral-vertebra, the 10.0% the sacral, the 1.67% - on the other parts of the body, for instance, on the limbs.

Due to the sex differentiation study, the both sexes have equal tendency to have a blue spots on the sacrum. The 44.5% of male and the 55.5% of females were born with the blue spots. So there is no significant difference regarding to the sex.

There were not any cases, which have the blue spot on vertebra, backbone, buttock- vertebra, sacral - vertebra, buttock - backbone, buttock – shoulder, buttock – shoulder – lumbar, buttock-sacral – vertebra - lumbar, buttock-sacral – vertebra – hip among the total male. But the 1.67% of female cases had the spot on these areas. Adversely all-female infants and babies have no blue spot on thigh, buttock- lumbar, buttock-sacral – lumbar, backbone – sacral – vertebra , but the 1.67 % of male from each group has the spot there.

The 57.3% and 42.7% of all male and female children; and the 23.3% all of those cases has the blue spot along the buttock and sacrum.

Any female cases not found with the blue spot on the hip and hip-sacrum, but the 33.3% of male has the blue spots in there. The 100% of all male cases had the blue spots, but female have no blue spot on buttock-sacral-vertebra. The sacral – lumbar type had dominant (75% and 25%) in females due to the sex differentiation study.

1. The location of the blue spot is not same and there were not any tendency regarding to age
2. Outer position of the blue spot along the buttock and sacrum on the body is dominant (23.3%) in males at the age of 0-3.
3. The melanocytes were determined predominantly in the stratum papillare in derma of the skin.

Keywords: melanocytes, derma, epidermis

CONCLUSION.

STEMYNA: A Smartphone Application for Cardiorespiratory Endurance Evaluation in Daily Environment

S. J. Kwon¹ and K. S. Park²

¹Interdisciplinary Program of Bioengineering, Seoul National University, Seoul, Korea

²Department of Biomedical Engineering, College of Medicine, Seoul National University, Seoul, Korea

E-mail: sjkwon@bmsil.snu.ac.kr

Abstract— Cardiorespiratory endurance is highly related with physical strength and health. The quantitative measurement of cardiorespiratory endurance encourages daily exercises and helps to decide personalized exercise intensity. Although there is a relatively convenient method called as step test for quantitative measurement of cardiorespiratory endurance, it has limitations to be conducted in daily environment. In this study, we proposed STEMYNA, a smartphone application for cardiorespiratory endurance evaluation in daily environment. The proposed application helps the user easily measures cardiorespiratory endurance in daily environment by guiding to execute the step test protocol accurately

Keywords— Step Test, Cardiorespiratory Endurance, Mobile Application, Smartphone

I. INTRODUCTION

Cardiorespiratory endurance is highly related with physical strength and health. Cardiorespiratory endurance is a quantitative index for aerobic ability of a body and it shows the endurance of cardiac and respiratory function. Cardiorespiratory endurance enhancement reduces fatigue and prevents chronic diseases including cardiovascular disease, hypertension, and glycosuria by increasing immunity.

The quantitative measurement of cardiorespiratory endurance encourages daily exercises and helps to decide personalized exercise intensity. The observation of health enhancement motivates people to exercise consistently. The quantitative measurement of cardiorespiratory endurance helps to decide most effective and efficient exercise intensity reflecting the personal physical ability.

Although there is a relatively convenient method called as *step test* for quantitative measurement of cardiorespiratory endurance, it has limitations to be conducted in daily environment. The step test requires the exact height of the stepper, a heart rate monitor, a metronome and the expert's guidance. However, the required stuffs are not easily obtained from daily environment.

In this study, we proposed STEMYNA, a smartphone application for cardiorespiratory endurance evaluation in daily environment. The proposed application helps the user easily measures cardiorespiratory endurance in daily environment by guiding to execute the step test protocol accurately.

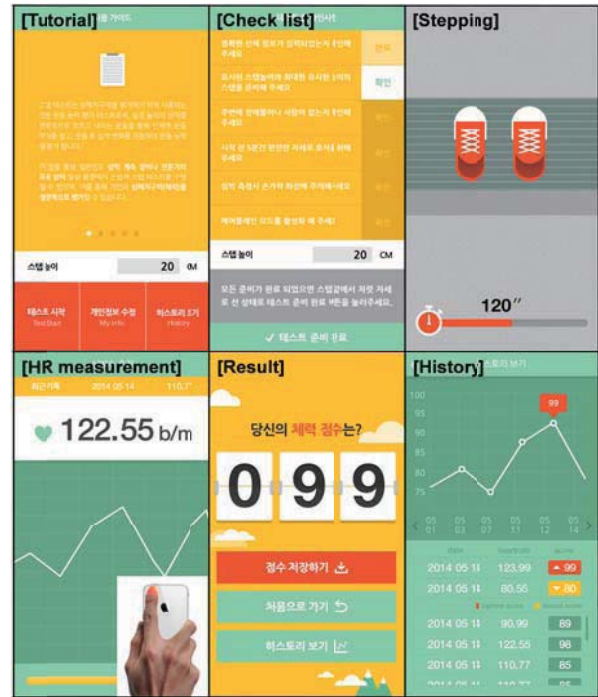


Figure 1. The application UIs.

II. METHODS

The proposed application guides users to accurately execute the personalized step test using the embedded sensors and application user interfaces (UI). The application allow to use the stuffs such as a table, stairs, and bench as a stepper, which the users can get easily from around. In addition, the application increases the accuracy of the test result by measuring user's exact heart rate using the embedded camera. Furthermore, the guidance including intuitive UIs leads users to follow the test protocol easily. The test results are automatically updated on STEMYNA server and the users can track cardiorespiratory endurance changes using historical result view.

III. CONCLUSION AND FUTURE WORK

In this study, we proposed STEMYNA, a smartphone application which enables the users to conduct a step test using only their smartphone and daily stuffs. In future study, we will evaluate the accuracy of the results produced by our application and its usability.

IV. ACKNOWLEDGEMENT

This research was supported by Coway Co., Ltd..

Hazardless Environment Monitoring System by Multichannel VLC using CMOS camera

ZhenYang Ong¹ and Wan-Young Chung¹

Department of Electronic Engineering, Pukyong National University, Busan 608-737, South Korea.

E-mail: wychung@pknu.ac.kr

Abstract—This paper presents environment monitoring system for temperature, humidity and carbon dioxide concentration in hazardless optical multichannel visible light communication (VLC) technology. Each transmission channel is differentiated by different color wavelength light beam and three sensor data are transmitted simultaneously in same medium. 0.1W LED is used for transmission and CMOS camera of mobile device is used as receiver. Transmission range are up to 5m.

Keywords— CMOS, mobile device, visible light communications, multichannel transmission

I. INTRODUCTION

VLC is an alternative wireless technology that is eco-friendly and harmless to human body. Radio Frequency (RF) is replaced by light beam which is within visible light spectrum from 380 to 780 nm. In [1], a single channel mobile health-monitoring system is developed which uses white led in transmitter module and photodiode in receiver module. Transmission rate is further extended by using wavelength division multiplexing technique in [2]. Multichannel transmission is achieved by using color sensor and three light emitting diode (LED) which have different visible light spectrum. However, the transmission distance is limited. In this study, an environment monitoring system which utilizes multichannel VLC technology using CMOS camera of mobile device and LEDs.

II. METHODS

Fig.1 shows the experiment setup of the multichannel environment monitoring system. The sensor module consists of three different sensor which are temperature sensor, humidity sensor and carbon dioxide sensor. Three different channel transmission with three LED with different visible light spectrum which are red, green and blue. Data packet consists of header, three sensor data and footer is constructed as shown in Fig.2 .Data packet is modulated by using On-Off Keying (OOK) modulation and transmits simultaneously in same medium with 3 different channel at data rate of 2 bit/s. A tablet with CMOS camera is used as receiver module. An android application which utilize the CMOS camera for data receiving. Camera captures image stream and signal detection algorithm is used to process the image stream.

Data packet is reconstructed and sensor data is extracted from data packet. Current data is shown on User Interface (UI) and three graph will be drawn based on 20 latest data from each sensor.



Fig.1 Experiment Setup of Multichannel VLC environment monitoring system

Header	Temperature Data	Footer
	Humidity Data	
	CO ₂ Concentration Data	

Fig.2 Data Packet

III. RESULTS

Data rate are three times faster compared to single channel transmission. Experiment is carry out in indoor environment during daytime and nighttime. Transmission distance, d is sets at 5m. Error rate of the system is 4.33% during daytime and 4.6% during nighttime. The results show that transmission is not affected by ambient light. Error rate mainly cause by the time drift of the android system.

IV. CONCLUSION

This system provides safer environment especially for elderly person or patient with clinical diseases. Environment quality can be monitored by the system with high reliable, long range and hazardless wireless data transmission.

ACKNOWLEDGEMENT

This work was supported by the BK21 Plus Program (Creative Human Resource Development Team for ICT-based smart devices, 214-C000066) funded by the Ministry of Education(MOE, Korea) and National Research Foundation of Korea(NRF).

REFERENCES

1. Y.Y. Tan, W.-Y. Chung, "Mobile health-monitoring system through visible light communication", *Bio-Medical Materials and Engineering*, Vol. 24, No. 6, pp. 3529–3538, September 2014.
2. K.H. Lim, Y.Y. Tan, and W.-Y. Chung, "VLC Multiplexing For Medical Data Transmission," 7th

IBEC2015, Road to Better Life through Biomedical Engineering

Asia-Pacific-Conf. on Transducer and Micro/Nano
Technologies (APCOT), June 29 – July 2, 2014.

Two Steps Association Rule Mining for Medical Clinical Data

Sang Hun Han¹, Ho Sun Shon¹, Kyung Ah Kim², Eun Jong Cha²,
and Keun Ho Ryu¹

¹Database and Bioinformatics Laboratory, School of Electrical & Computer Engineering, Chungbuk National University, South Korea

²Department of Biomedical Engineering, School of Electrical & Computer Engineering, Chungbuk National University, South Korea

E-mail: likelamb@gmail.com

Abstract— this paper proposes a method to run into association rule mining in two steps for medical clinical data that contains quantitative and numerical data. For two steps association rule mining proposed in this paper it was used Korea Acute Myocardial Infarction Registry (KAMIR) data.

Keywords— Association rule mining, KAMIR

I. INTRODUCTION

Association rule mining is the most simple and effective method of data mining techniques [1]. Mining association rule is to find the hidden information of data by analyzing the relationships between items. Association rule mining procedure is as follows. First, using the item included in the transaction, the length k is obtained for the candidate itemset. Second, the candidate itemset is compared with transaction data to find k -frequent itemset. Finally, using these k -frequent itemset to find the $(k+1)$ -candidate itemset. Repeat this procedure until to get the k -frequent itemset in the maximum length. If the number of entries in the k - frequent itemset n , the number of candidates is 2^n-1 itemset is generated. So many candidate itemset can be a major problem in performance because all of the transaction data to be compared. There have been various studies in order to solve these performance problems [3, 5]. In particular, FP-growth algorithm generates FP-tree with a frequent itemset in the transaction data. Using the FP-tree solves performance issues by finding all frequent itemset [4]. In addition, different algorithms should be applied in accordance with the data attribute of a mining association rules is to find an association item. Various algorithms according to the properties of the data to apply the association rule mining has been also studied [2]. However, if the transaction data has quantitative attributes and continuous attributes items both, continuous property is divided into a specific section to match the attribute and others, it is common to run the association rule mining. In this paper, we implemented an association rule mining algorithms to

analyze the medical clinical data on the MapReduce-based big data analytics platform Hadoop. This association rule mining algorithm can be applied to a medical clinical data consisting of various properties. Most medical clinical data has the characteristics as much as possible with the relevant information to meet the clinical objective of the experimental group. That is, the medical clinical data must have large items in transaction database. KAMIR data used in this paper is a comprehensive clinical data of patients with acute myocardial infarction 24 hospitals in the country from November 1, 2005 to January 31, 2008. One of items in the transaction data is a data with continuous attributes such as age, waist circumference, and are also mixed data with quantitative data attributes, such as smoke and emergency measures carried out or not.

II. METHODS

KAMIR data used in this paper has a 14,885 transactions consisting of 134 items. Association rule mining technique used in this study is largely divided into two phases. First, the association rule mining is performed by using only the data item of the quantitative attribute. To this end, FP-growth algorithm was applied to only the 80 items of quantitative data in the KAMIR. Second, by using the association rules generated in the previous step are combined to a new prospective itemset including the item with the rest of the continuous property. This candidate itemset find association rules are included in all of the data item properties. When extending the association rules found in the quantitative data for the data that have different properties as the candidate itemset, it follows the following rules:

1. For all associated rules for the itemset with quantitative data of more than one attribute by adding a new item to create a candidate itemset.
2. To scan the transaction data, when the additional item is numerical data, and has a value of the first transaction data as the initial value, as compared to the second transaction data, that is, the period in the process of comparing the association of two or more transaction and changes to the data. For example, the value of the first item is old and if the transaction data 29, associated rules, will have a value of 29 as the initial value, if the value

of the second transaction data 32, association rule is the interval value 29-32.

3. As the association rules, including the interval value compared to all transaction data that period if the value includes both the minimum or maximum value of the items that candidate association rule is discarded.

It follows the association rules mining algorithm proposed in this paper.

Algorithm 1. Proposed algorithm in this paper

Step 1 FP-Growth Algorithm for quantitative items

- 1 Build a compact data structure called the FP-tree
 - 2 Extracts frequent itemsets from the FP-tree
 - 3 Save all the $(k-1)$ -length frequent itemsets in L_{k-1}
-

Step 2 Extended Algorithm for continuous items

- 1 Generate all the candidate itemsets in C_k from the frequent itemsets in L_{k-1} by add each all continuous items
 - 2 Scan the transaction database to determine the support for each candidate itemset in C_k
 - 3 Save the frequent itemsets in L_k when it is not discarded
-

III. RESULTS

In this paper, the minimum support value of 30%, and run only when the item of data mining association rules with quantitative data attributes, 16,734,311 could find association rules. If you expand the rules related to the item it does not have quantitative data attributes and extract meaningful association rules, such as survival analysis could find an association of more than 6,000 rules.

Table 1. Experimental results

Minimum Support	Total num. of rules	Rules of survival related
5,000	16,734,311	14,342,900
6,000	2,613,319	2,180,066
7,000	444,256	357,202
8,000	75,438	57,187
9,000	12,509	8,627
10,000	1,944	938

IV. CONCLUSION

In this paper, Applied an association rule mining for the KAMIR that is large medical clinical data with the properties of the various items. For this purpose we propose the association rules algorithm step, divided in two to find the correspondence between the items having various data attributes. In addition, the rules of the association have found more than 6000 were

extracted item that relate to survival analysis. This produced the data for finding the prediction of death and prevention of symptoms for patients with acute myocardial infarction. It will proceed to clinical validation using the data in the future.

ACKNOWLEDGEMENT

This research was supported by Basic Science Research Program through the National Research Foundation of Korea (NRF) funded by the Ministry of Science, ICT & Future Planning (No-2013R1A1A206518).

REFERENCES

1. J. Hipp, U. Güntzer, and G. Nakhaeizadeh, "Algorithms for association rule mining—a general survey and comparison", *ACM sigkdd explorations newsletter*, Vol. 2(1), pp. 58-64, 2000.
2. J. Arora, N. Bhalla, S. Rao, "A Review on Association Rule Mining Algorithms", *IJIRCCCE International Journal of Innovative Research in Computer and Communication Engineering*, Vol. 1(5), 2013.
3. L. Li, M. Zhang, "The strategy of mining association rule based on cloud computing. In Business Computing and Global Informatization (BCGIN)", *2011 International Conference on IEEE*, pp. 475-478, 2011.
4. M. Suman, T. Anuradha, K. Gowtham, A. Ramakrishna, "A Frequent Pattern Mining Algorithm Based On Fp-Tree Structure Andapriori Algorithm", *International Journal of Engineering Research and Applications*, Vol. 2(1), pp. 114-116, 2012.
5. Y. Zeng, S. Yin, J. Liu, M. Zhang, "Research of Improved FP-Growth Algorithm in Association Rules Mining", *Scientific Programming 2015*, 2015.

A preliminary study on simulation of electrocardiogram using neural oscillators and networks

Min Hyuk Lim¹, and Sungwan Kim^{1*}

¹Department of Biomedical Engineering, Seoul National University College of Medicine
E-mail: dizzyday@gmail.com, *: corresponding authors

Abstract— Electrocardiogram (ECG) is important to determine normality of cardiac function. We construct the signal transduction network in the heart by using of neural oscillators. Normal ECG and abnormal ECG from a reentrant circuit were simulated. This study has possibilities to establish control tactics for arrhythmia and an advanced model based on integrated physiology.

Keywords—Electrocardiogram, Neural oscillators, Neural networks, Arrhythmia, Cardiac simulation

I. INTRODUCTION

Electrocardiogram (ECG) is an useful diagnostic tool for observing conditions of the heart. For deeper understanding of cardiac function, structural modelling is essential. So we construct the network of neural cells via dynamical systems.

II. METHODS

A. Construction of the network on electric conduction of the heart

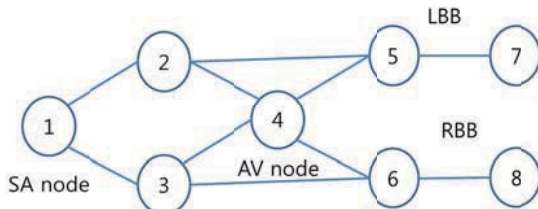


Fig. 1. The network of electrical conduction of the heart (SA node: sinoatrial node, AV node: Atrioventricular node, LBB: left bundle branch, RBB: right bundle branch)

Connections between nodes which represent important regions for signal transduction in the heart is established.

B. Neural oscillators for each neural node

Wilson-Cowan model have been adopted for describing a rhythmic stimulus of SA node and excitatory/inhibitory actions of other nodes.

$$\tau_e \frac{dx_e}{dt} = -x_e + (1 - r_e x_e) S_e(w_{e_e} x_e - w_{e_i} x_i + I_e)$$

$$\tau_i \frac{dx_i}{dt} = -x_i + (1 - r_i x_i) S_i(-w_{i_e} x_e + w_{i_i} x_i - I_i)$$

C. Simulation

Each node is affected by neighbor nodes. The directions of transduction can be modified by adjusting parameters.

$$I^i = \sum_{j=neighbors\ of\ i} W^j x^j \text{ for excitatory and inhibitory}$$

Signals of all nodes are integrated for construction of ECG with weighting factors related with distribution of electrical vector fields.

III. RESULTS

A signal similar to normal ECG was firstly derived. After that a reentrant circuit (1-2-3-4) from modified the parameters of 2nd node is constructed to obtain an abnormal ECG pattern.

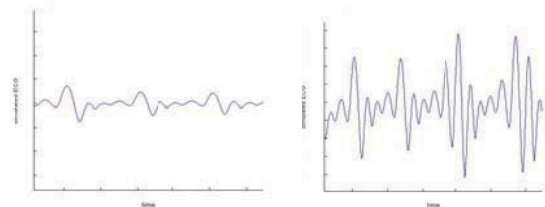


Fig. 2. Simulated ECG signals (Left: normal case, Right: a circuit occurred among 1st, 2nd, 3rd and 4th nodes.)

IV. CONCLUSION

A simulation study can describe cardiac transduction system via ECG signal and neural cells connections. To establish more accurate model, data-driven parameters and more complex relationship between nodes are needed. Nonetheless, this study has several possibilities to be applied to several conditions. To cure and to care of arrhythmia, control tactics via electrical stimulus can be developed. To survive in harsh condition such as space, electrical signals and blood flows in the heart can be integrated via an advanced model.

ACKNOWLEDGEMENT

This work was supported by National Research Foundation of Korea (NRF) grants funded by the Korean Government (2015M1A3A3A02012636).

REFERENCES

1. H.R. Wilson, J.D. Cowan. "Excitatory and inhibitory interactions in localized populations of model neurons.", *Biophys. J.*, 12:1-24, 1972
2. Strumiłło P, Strzelecki M, "Application of coupled neural oscillators for image texture segmentation and modeling of biological rhythms." *Int J Appl Math Comput Sci* 16:513-523, 2006

Method of Ballistocardiogram Measurement for Infants

W. K. Lee¹, H. Yoon¹, and K. S. Park^{1,2}

¹Interdisciplinary Program in Bioengineering, Graduate School, Seoul National University, Seoul, Republic of Korea

²Department of Biomedical Engineering, College of Medicine, Seoul National University, Seoul, Republic of Korea

E-mail: pks@bmsil.snu.ac.kr

Abstract—Ballistocardiogram (BCG), which measures heart activity based on the mechanical recoil movement of body, has been an interesting subject for several years, and it has the advantage of unobtrusive physiological signal sensing. BCG-derived biological information, such as heartbeat, respiration, and body movements of subjects, could be used for various health related study. However, cases of applying BCG on infants are very rare. For this reason, we developed a physiological signal monitoring bed utilizing BCG technology for infants by using a load cell. Heartbeat and respiration information was assessed by comparing the results obtained with a commercial device.

Keywords— Ballistocardiogram, Breathing rate, Heart rate, Load cell sensor, Physiological signal monitoring

I. INTRODUCTION

Ballistocardiogram (BCG) has been a subject of interest for several years owing to its ability to acquire unobtrusive physiological measurements. Investigators have actively studied and clinically applied various sleep-related conditions through biological information, such as heartbeat, respiration, and body movements. Many studies have attempted to utilize BCG signals both separately and in combination with other biological signals pertaining to sleep structure analysis and its clinical applications. However, most of these studies involved only adults. Techniques to monitor unobtrusive biological signals may be even more important for infants than adults. For example, the sleep of infants is closely related to their health, growth, and development. This is a preliminary study conducted to assess the possibility of monitoring the physiological information of infants by using BCG signals [1].

II. METHODS

A. Hardware

To differentiate smaller vibrations related to physiological information more clearly, the hardware system consisted of load cell sensors with alternating current (AC)-coupled circuit. Four load cell sensors were installed at the bottom of the bed. The output signal of the load cells is filtered by a 20 Hz low-pass filter and amplified 2000 times by analog circuits to increase the resolution and to decrease the amount of frequency interference.

B. Software

Noise removal and peak detection methods for BCG signals were developed. The information was obtained from the software by following procedures mentioned in previous literature [2]. Heartbeat and respiration information estimated from the load cell sensors were compared with those of commercial devices.

III. RESULTS

Heart rate (HR) and breathing rate (BR) estimated from heartbeat and respiration signals extracted from load cell data were compared with those obtained from electrocardiogram and chest belt sensor, respectively. The estimated HR and BR obtained from the experiments conducted for two infants showed average errors of 1.25% and 2.50%, respectively, upon comparing the results with those of commercial devices.

IV. CONCLUSION

We devised a physiological signal monitoring bed, which uses a load cell, for infants. We, then tested if heartbeat and breathing information could be measured well. We were able to detect HR and BR per minute with average errors of 1.25% and 2.50%, compared to commercial devices. In accordance with these results, it is expected that practical application of BCG technology for sleep structure analysis of infants is possible.

ACKNOWLEDGEMENT

This work was supported by the Technological Innovation R&D Program (S2168146) funded by the Small and Medium Business Administration (SMBA, Korea).

REFERENCES

1. O. T. Inan, P.-F. Migeotte, K.-S. Park, M. Etemadi, K. Tavakolian, R. Casanella, J. Zanetti, J. Tank, I. Funtova, G. K. Prisk, and M. D. Rienzo, "Ballistocardiography and Seismocardiography: A Review of Recent Advances," *IEEE J. Biomed. Health Inform.*, vol. 19, pp. 1414-1427, 2015.
2. W. K. Lee, H. Yoon, D. W. Jung, S. H. Hwang, and K. S. Park, "Ballistocardiogram of Baby during Sleep," In: *37th Annual International Conference of the IEEE Engineering in Medicine and Biology Society (EMBS 2015)*, Milano, Italy, 2015.

The Effect of Electrical Conduction Velocity on Cardiac Electromechanical Delay and Pumping Efficacy: Computational Study

A. R. Yuniarti, A. K. Heikhmakhtiar, and K. M. Lim*

Department of Medical IT Convergence Engineering, Kumoh National Institute of Technology, Gumi, Republic of Korea
E-mail: kmlim@kumoh.ac.kr

Abstract— The purpose of this study is to predict the effect of electrical conduction velocity on cardiac electro-mechanical delay and pumping efficacy using computational model. We used 3D electro-mechanical model of normal canine ventricles with three different conduction velocities. We compared the PV loop, stroke work, stroke volume, ATP consumption, and electro-mechanical delay (EMD) as the mechanical responses for each cases. The results showed that cardiac pumping efficacy is better on the higher conduction velocity.

Keywords— Conduction velocity, Computational model, ATP consumption, Electro-mechanical delay.

I. INTRODUCTION

One of the subset of the heart failure (HF) is dyssynchrony of the heart depolarization and the myofiber shortening phase which lead to severe HF condition. There are four major aspects that contribute to prolong the electro-mechanical delay (EMD) in dyssynchronous HF condition. The four factors are geometry of the structure (both shape and fiber structure), electrical conduction, disarranged Ca²⁺ handling, and stiffness of the tissue. In this study, we will analyze cardiac electro-mechanical delay and pumping function under various electrical conduction velocity conditions.

II. METHODS

A. Electro-Mechanical Model

We combined the 3D image-based electromechanical model of failing canine ventricles with a lumped model of the circulatory system [1].

B. Simulation Protocol

We applied three different conduction velocities on canine ventricle model which is 53cm/s, 64cm/s, and 75cm/s. First, we conduct the electrical simulation for each case. Then, the results of the electrical simulation were used as the input to the mechanical simulation. To analyze the effect of conduction velocity on mechanical responses, we simulated cardiac mechanics model.

III. RESULTS

A. Pressure-Volume (PV) Loop

Fig.1 (a) shows that higher conduction velocity has higher stroke volume. It means that the blood is ejected more by the ventricle in single contraction.

B. Energy Efficiency

Fig.1 (b) and (c) show the energy efficiency in term of stroke work to ATP ratio and stroke volume to ATP ratio. On the higher conduction velocity, ventricle consumes lesser energy (ATP) and do more work in each contraction.

C. Mechanical activation time (MAT) & EMD

Fig.1 (d) represents the synchronization between the electrical activation and mechanical activation of the ventricle. On the higher conduction velocity, the synchronization was increased.

IV. CONCLUSION

Our result shows that the higher conduction velocity decreases cardiac electro-mechanical delay but increases pumping efficacy.

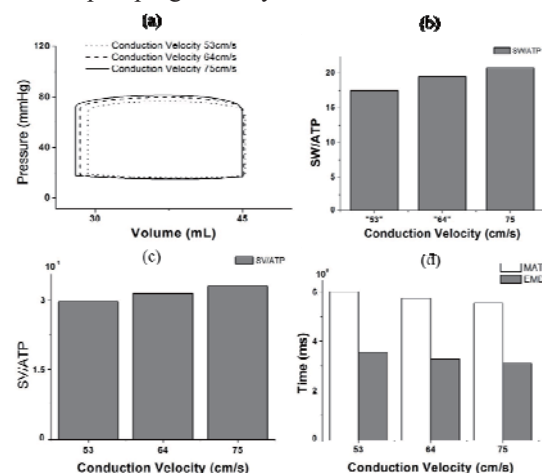


Fig.1. Comparison of the cardiac mechanical responses under various electrical conduction velocities.

ACKNOWLEDGEMENT

This work was supported by the MSIP, Korea, under the CITRC support program (IITP-2015-H8601-1511011) supervised by the IITP, NRF (NRF-2011-0009335) and Quality of Working Life (QWL) (N0000842) Program funded by MTIE.

REFERENCES

1. K. M. Lim et al., "Comparison of the effects of continuous and pulsatile left ventricular-assist device on ventricular unloading using a cardiac electromechanics model," *The Journal of Physiological Science*, Vol. 62, pp. 11-19, 2012.

Increased Variation in Blood Pressure during REM Sleep Detected from Ballistocardiogram

H. Yoon¹, S. H. Hwang¹, J. W. Choi², Y. J. Lee², D. U. Jeong², and K. S. Park³

¹Interdisciplinary Program of Bioengineering in Seoul National University, Seoul, Korea

²Center for Sleep and Chronobiology, Seoul National University Hospital

³ Department of Biomedical Engineering, College of Medicine, Seoul National University, Seoul, Korea

E-mail: hnyoon@bmsil.snu.ac.kr

Abstract—In this study, we monitored interval between R peak of electrocardiogram (ECG) and J peak of ballistocardiogram during sleep. We found that variations of RJ intervals during REM sleep were significantly higher than NREM sleep. It is related to fluctuations between sympathetic and parasympathetic activity in REM sleep.

Keywords— ballistocardiogram, RJ interval, REM, autonomic nervous system

I. INTRODUCTION

Ballistocardiogram (BCG) is an unobtrusive measure of the recoil forces of the body in reaction to cardiac activity [1]. Previous researches have shown that interval between R peak of ECG and J peak of BCG is highly correlated with blood pressure [1]. Blood pressure which is one of important vital signs is fluctuated during REM sleep influenced by autonomic nervous system [2]. Based on the facts, we hypothesized that RJ intervals would be highly fluctuated during REM sleep.

II. METHODS

A. PSG and Data recording

BCG was measured from 7 subjects when they conducted nighttime polysomnogram (PSG). For the BCG recoding, load-cells were placed underneath the bed legs. The following morning, PSG data were manually scored by polysomnography technician.

B. Data analysis

Based on the sleep scoring result, ECG and BCG data from 20 minutes of NREM periods before REM sleep to those after REM sleep were gathered. From the data, we manually detected ECG R-peaks and BCG J-peaks and calculated RJ intervals. The Coefficient of variance (CV) for the RJ intervals in every 30 seconds was calculated. CVs were presented as percentages based on the mean CV during the beginning of 5 minutes of the NREM preceding each REM period.

Table 1. Percentages of variation in RJ intervals

REM-20min	REM	REM+20min
20.9%	412.4%	242.3%

III. RESULTS

Table 1 presents the result of this study. The variation in RJ intervals was significantly increased during REM sleep ($p < 0.05$). REM sleep is highlighted by remarkable fluctuations between sympathetic and parasympathetic activity and it leads to sudden changes in blood pressure [2]. Previous research showed that changes in RJ intervals are related to blood pressure changes [1]. Thus, the increases in variation of RJ intervals were influenced by increases in blood pressure variability during REM sleep represented by fluctuations between sympathetic and parasympathetic activity. This suggested method has potential to monitor blood pressure variability which is important index to predict cardiovascular mortality with relatively less constrained environment during sleep [3].

IV. CONCLUSION

RJ intervals during REM sleep were more fluctuated than RJ intervals during NREM sleep. It was influenced by REM property of autonomic nervous system.

ACKNOWLEDGEMENT

This research was supported by Coway Co., Ltd..

REFERENCES

1. O. T. Inan, P. F. Migeotte, K. S. Park, M. Etemadi, K. Tavakolian, R. Casanella, et al., "Ballistocardiography and Seismocardiography: A Review of Recent Advances," *Ieee Journal of Biomedical and Health Informatics*, vol. 19, pp. 1414-1427, Jul 2015.
2. Lanfranchi, P. A., and V. K. Somers. "Cardiovascular physiology: autonomic control in health and in sleep disorders." *Principles and practice of sleep medicine*. Saunders, Philadelphia (2011): 226-236.
3. E. Dolan, A. Stanton, L. Thijs, K. Hinedi, N. Atkins, S. McClory, et al., "Superiority of ambulatory over clinic blood pressure measurement in predicting mortality - The Dublin Outcome Study," *Hypertension*, vol. 46, pp. 156-161, Jul 2005.

Simulation study of bio-impedance measurements to estimate the cardiovascular disease

H. Wi¹, G. Y. Jang², T. I. Oh², and E. J. Woo²

¹Department of Computational Science and Engineering, Yonsei University, Seoul, Republic of Korea

²Department of Biomedical Engineering, Kyung Hee University, Seoul, Republic of Korea

E-mail: tioh@khu.ac.kr

Abstract—We need a continuous monitoring method to estimate the status of cardiovascular system using a simple, inexpensive, and non-invasive way. Bio-impedance is varied with each heart beat due to the arterial volume changes. We evaluated the capability of bio-impedance measurements to estimate the cardiovascular disease from the numerical simulation.

Keywords— Cardiovascular system, bio-impedance, continuous monitoring, optimal electrode position, FEM simulation.

I. INTRODUCTION

Cardiovascular disease is one of the major causes of death and disabilities around the world. There are some treatment methods using drugs and implanting surgeries. However, current monitoring methods such as ECG based photoplethysmography and ultrasound systems are too bulky and expensive relatively. Also, it requires the continuous monitoring of cardiovascular system. In the previous studies, bio-impedance is the one of candidate for estimating physiological status and cardiovascular parameters [ref]. It is varied by arterial volume change at each heart beat and peripheral resistance to the arterial blood flow provides arterial distensibility. In this study, we numerically simulated the bio-impedance measurements to obtain the best sensitivity with the specific pairs of measuring electrodes.

II. METHODS & RESULTS

We made a realistic cross-sectional forearm model using Comsol 3.5a. After meshing, 32 electrodes was attached at equal angle for find the best electrode position to get higher sensitivity.

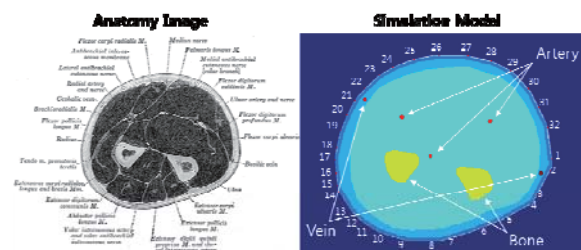


Fig. 1. Cross-sectional forearm model with 32 electrodes

We assumed to adopt the balanced current source and chose the 8 difference positions for current source

electrodes (Fig. 2. red position). In each case, computation were repeated when moving the position of current sink electrode from 90 degree to 270 degree. Total computation number was 160 cases (source 8 x sink 20) to find the optimum positions of electrodes.

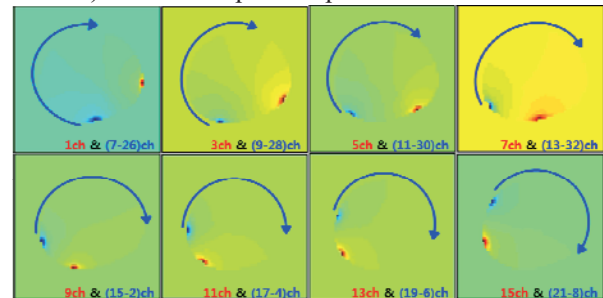


Fig. 2. Electrode pairs of current injection.

(red : source electrode, blue : sink electrode)

Each cases, we computed the boundary voltage variation due to the conductivity changes due to arterial volume changes. From them, we calculated sensitivity and found the 3 higher sensitive cases in Fig.3.

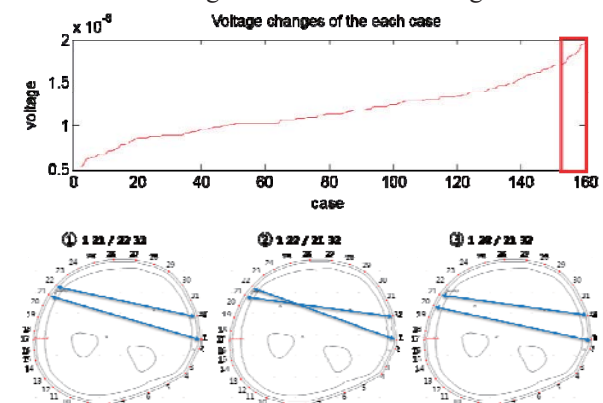


Fig. 3. Voltage variation plot (upper) and 3 higher sensitive electrode configuration (lower).

III. CONCLUSION

From the simulation using realistic cross-sectional forearm model, we found the optimal position of electrodes to have the best sensitivity to detect the large impedance variation due to the arterial blood flow changes

ACKNOWLEDGEMENT

This work was supported by Mid-career Research Program (NRF-2015R1A2A2A04006172) through NRF grant funded by the MEST.

REFERENCES

1. R. González-Landaeta, O. Casas, and R. Pallàs-Areny, "Heart Rate Detection From Plantar Bioimpedance Measurements," *IEEE Trans. Biomed. Eng.*, vol. 55, pp. 1163-1167, 2008.

NT-ProBNP as a Predictor of Cardiovascular Events in Patients with Non ST-segment Elevation Myocardial Infarction

Ho Sun Shon¹, Keun Ho Ryu¹, Eun Jong Cha², Kyung Ah Kim²

¹Database / Bioinformatics Lab, College of Electrical and Computer Engineering, Chungbuk National University, Korea

²Department of Biomedical Engineering, School of Medicine, Chungbuk National University, Korea

E-mail: shon0621@gmail.com

Abstract— NT-proBNP (N-terminal pro-brain natriuretic peptide) is well-known biomarker of the diagnosis and prognosis for heart failure, and is directly associated with myocardial necrosis. We evaluated the prognostic role of NT-proBNP for MACE (major adverse cardiac event) in NSTEMI (Non ST-segment elevation myocardial infarction) patients during mid-term follow up period from the KAMIR (Korea Acute Myocardial Infarction Registry). In this paper, we plan to estimate the prognosis through NT-proBNP as a risk evaluation marker, when the patients who are as risky as STEMI patients visit a hospital despite early NSTEMI patients. We find out the prognosis estimation results after conducting PCI with the patients in the severely risk group within 24 hours among NSTEMI patients. NT-proBNP is found to be an important risk factor to predict MACEs for 12 month follow-up after underwent early coronary intervention within 12 hours after the admission in NSTEMI patients.

Keywords—NSTEMI, Risk factor, NT-proBNP, MACE, Multivariate logistic Regression

I. INTRODUCTION

Cardiovascular diseases were the one of top ranked major causes of death in the world by the announcement of WHO in 2011 [1]. The most common cause of world population death was the ischemic heart disease (12.9%), and followed by strokes and cerebrovascular disease (10.5%) in 2008 population statistics [1]. The proportion of cardiovascular death is continuously increasing in Korea, and major part of it is AMI (acute myocardial infarction). With this background, the KAMIR (Korean Myocardial Infarction Registry) project was initiated nationwide from 2003 with the grant of Korean Society of Cardiology to define characteristics of AMI, and find the exit to reduce incidence and mortality of AMI in Korea [2]. There are many data to support the benefit of the timely fashioned primary revascularization for STEMI (ST segment elevation myocardial infarction), and several kinds of prognostic factors were already enlightened including rapid revascularization, Killip classification etc. But, the useful single prognostic factor which can be translated to make decision of necessity of urgent revascularization in NSTEMI (non-ST segment elevation myocardial infarction) is still under investigated. There are some multifactorial laboratories or clinical decision criteria to support the efficacy of urgent revascularization, but useful single prognostic factor is still ambiguous in NSTEMI. [3, 4, 5, 7, 8, 9, 10, 11, 12]. NT-proBNP is very useful biomarker to

diagnosis for HF (heart failure), predicts short and long-term prognosis, and determines treatment strategy for HF patients [6].

II. METHODS

A. Study Population

Data for this research was obtained from NSTEMI patients among the patients registered in KAMIR under the diagnosis of acute myocardial infarction from November of 2005 to January of 2008. NSTEMI patients were 1,074 in total, composed of 682 (63.5%) males and 392 (36.5%) females. Males were more than females, and the average age was 69.4±11.8 year-old. Among the data, this research analyzed the characteristics of clinical data and laboratory blood tests during initial and hospital visits of the patients who had MACE and were followed up for 12 months. We retrospectively analyzed the clinical data such as gender, age, systolic blood pressure(SBP) during initial and follow-up hospital visit, Killip classification, TIMI grade before PCI, culprit coronary lesion (target lesion) and vessel (target vessel) associated with infarction, the disease extent (number of significant stenotic coronary vessel) by coronary angiogram, left ventricular ejection fraction, and so on. Also, we conducted significance test for blood test such as glucose, creatinine, CK, CK-MB, hs-CRP (High-Sensitivity C-Reactive Prote), troponin-I, total cholesterol, triglyceride, NT-proBNP, and so on.

B. Statistical Analysis

We represented continuous variable as average ± standard deviation and used SPSS for windows 18.0 program for analysis. We retrospectively analyzed the factors that influenced MACE using multivariate logistic regression for statistical analysis. The test result was found to be statistically significant in case p-value was less than 0.05. Also, while analyzing multivariate logistic regression, it is possible to occur multicollinearity. Therefore, to solve this problem, we categorized the existing data and deleted the independent variables with strong linear relations. Among NSTEMI patients, we found the risk factors and analyzed the variables that could influence MACE of the patients who arrived at the hospital after chest pain within 12 hours, received early coronary PCI within 12 hours, and were monitored up to 12 months.

MACE is monitored for 12 months including 3 and 6 months.

III. RESULTS

The clinical characteristics about whether the patients monitored up to more than 12 months have MACE are as follows. Table 1 shows the result of T-test to calculate the average of continuous variables depending on whether the patients have MACE, has a significant difference. Assuming equal variance, age (p=0.005), glucose (p=0.002), maximum value (max) of Troponin-I (p=0.010), and NT-ProBNP (p=0.000) are statistically significant. However, the rest of variables such as heart rate, creatinine, max-CK, max-CK-MB, total cholesterol, triglyceride, HDL-C, LDL-C, hsCRP, and so on proved to be non-significant statistically.

Table 1. Baseline characteristics of study patients

Characteristics	MACE		P-value
	No	Yes	
Age (year-old)	68.7±12.4	72.4±10.8	0.005
Heart rate (beast/min)	76.8±17.5	79.8±17.0	0.124
SBP (mmHg)	129.9±24.2	132.3±22.8	0.363
Glucose (mg/dl)	158.8±80.3	187.9±112.7	0.002
Creatinine (mg/dl)	1.2±1.5	1.5±1.4	0.085
Max-CK (IU/L)	667.4±982.9	687.3±1468.5	0.875
Max-CK-MB (ng/ml)	64.9±109.0	59.2±100.0	0.622
Max-Troponin I (ng/ml)	17.2±23.2	27.9±75.8	0.010
Total-cholesterol (C) (mg/dl)	182.4±44.0	178.9±53.6	0.491
Triglyceride (mg/dl)	135.8±100.3	117.5±59.0	0.095
HDL-C (mg/dl)	44.2±16.6	44.8±12.9	0.760
LDL-C (mg/dl)	114.9±44.7	111.4±51.9	0.467
hs-CRP (mg/dl)	21.8±92.8	7.9±19.8	0.207
NT-proBNP (pg/ml)	2198.4±4909.0	7735.3±10736.2	0.000

Table 2 shows the result of significance test in the estimation of parameter and MACE through multivariate logistic regression analysis. Table 2 represents estimates of the multivariate logistic significant value, odds ratio (Exp(B)), and 95% Confidence Interval for Exp(B) of OR estimation. According to the result, among the data monitored for 12 months, in case MACE was Cardiac death, the estimation of odds ratio of NT-proBNP was 1.00008 and 95% Confidence Interval was (1.00002, 1.00015). This means that among MACE patients monitored for 12 months, in case of Cardiac death, the Odds ratio was 1.00008 times more compared with No MACE.

That is, as NT-proBNP increases, it influenced slightly on Cardiac death compared with No MACE.

As a result, it is estimated that NT-proBNP is the significant variable among cardiac deaths (p-value=0.016), MI (p-value=0.000), CABG (p-value=0.000), and so on to MACE patients followed up for 12 months compared without MACE. Also, the two-vessel (p-value=0.037) between Max-CK (p-value=0.031) and CAG vessel produces significant results in Re-PCI.

Table 2. Risk factor estimates using multivariate logistic regression

12 Months MACE ^a	Exp(B)	95% CI		P-value
		Lower Bound	Upper Bound	
Cardiac Death	Intercept			.000
	NT-proBNP	1.00008	1.00002 1.00015	.016
	Max_CK	0.99991	.99913 1.00070	.832
MI	Intercept			.000
	NT-proBNP	1.00016	1.00007 1.00024	.000
	Max_CK	.998	.993 1.003	.351
Re-PCI	Intercept			.000
	NT-proBNP	1.00004	0.99994 1.00013	.424
	Max_CK	1.00041	1.00004 1.00078	.031
CABG	Intercept			.000
	NT-proBNP	1.00012	1.00006 1.00018	.000
	Max_CK	.999	.997 1.000	.121

As a result, setting no MACE as a reference category, the most significant variable as compared with other variables was NT-proBNP, which was shown to be significant statistically in Cardiac death, MI, and CABG. To analyze in detail, NT-proBNP was predicted as the fittest cutoff value by ROC (Receiver Operating Characteristic) curve about each MACE. Table 3 shows the ROC analysis result based on each category of MACE.

Table 3. ROC analysis of each MACE

MACE	AUC	P-value	95% CI	Cut-off value
Cardiac Death	0.816	0.0001	(0.782, 0.848)	1180
MI	0.651	0.2623	(0.610, 0.690)	930
Re-PCI	0.539	0.5624	(0.497, 0.581)	516
CABG	0.716	0.0019	(0.676, 0.753)	3903

In case MACE was cardiac death and CABG, AUC (area under the curve) was statistically significant. In the case of cardiac deaths, the cut-off value was 1180, sensitivity was 90% (95%CI: (68.3, 98.5)), and specificity was 66.2% (95% CI: (62.1, 70.2)). In the case of CABG, cut-off value was 3903, sensitivity was 61.1% (95%CI: (35.8, 82.6)), and specificity was 83.5% (95% CI: (80.1, 86.5)). In the case MACE was MI and Re-PCI, AUC was statistically insignificant.

IV. CONCLUSION

This study retrospectively analyzed the 12 month-MACE of NSTEMI patients who arrived at the hospital after chest pain within 12 hours and were underwent early coronary intervention within 12 hours base on KAMIR data. Significant risk factors of 12 month-MACE were NT-proBNP, max-CK and CAG vessel. None of other clinical and laboratory data including hs-CRP, troponin-I, CK, CK-MB, and BNP did influence. Especially, through cutoff value by ROC curve of NT-proBNP, the fittest value was predicted to diagnose MACE. Taken together, NT-proBNP is useful predictor for 12-month MACE of NSTEMI as well as heart failure. And, new index using NT-proBNP, max-CK, and CAG vessel will be useful for prognostic indicator of MACE.

ACKNOWLEDGEMENT

This research was supported by Basic Science Research Program through the National Research Foundation of Korea (NRF) funded by the Ministry of Science, ICT & Future Planning (No-2013R1A1A206518).

REFERENCES

1. <http://www.kostat.go.kr/>
2. <http://www.kormi.org/>
3. Kim SS, Choi HS, Jeong MH, Cho JG, Ahn YK, Kim JH, Chae SC, Kim YJ, Hur SH, Seong IW, Hong TJ, Choi D, Cho MC, Kim CJ, Seung KB, Chung WS, Jang YS, Rha SW, Bae JH, Park SJ; Korea Acute Myocardial Infarction Registry Investigators. Clinical outcomes of acute myocardial infarction with occluded left circumflex artery, *J Cardio*. 2011, 57(3), pp. 290-296.
4. SONG Y, Analyses of Studies on Cardiac Rehabilitation for Patients with Cardiovascular Disease in Korea, *J Korean Acad Nurs*. 2009, 39(3), pp. 311-320.
5. Deedwania PC, Ahmed MI, Feller MA, Aban IB, Love TE, Pitt B, Ahmed A, Impact of diabetes mellitus on outcomes in patients with acute myocardial infarction and systolic heart failure, *Eur J Heart Fail*. 2011, 13(5), pp. 551-559.
6. Yoo BS, Kim WJ, Jung HS, Kim JY, Lee SW, Hwang SO, Yoon J, Choe KH, The Clinical experience of B-type natriuretic peptide blood concentrations for diagnosis in congestive heart failure the single hospital experience based on the large clinical database, *Korean Circ J*. 2004, 34(7), pp. 684-692.
7. Cho JY, Jeong MH, Choi OJ, Lee S, Jeong SY, Kim IS, Cho JS, Hwang SH, Hwang SH, Yoon NS, Moon JY, Hong YJ, Kim JH, Kim W, Ahn YK, Cho JG, Park JC, Kang JC, Predictive factors after percutaneous coronary intervention in young patients with acute myocardial infarction, *Korean Circ J*. 2007, 37(8), pp. 373-379.
8. Lim SY, Jeong MH, Yang BR, Kim KH, Sohn IS, Hong YJ, Park HW, Kim JH, Kim W, Ahn YK, Cho JG, Park JC, Kang JC, Long-term clinical outcomes after primary percutaneous coronary intervention in patients with acute myocardial infarction older than 75 years, *Korean Circ J*. 2005, 35, pp. 613-619.
9. Tong W, Lai H, Yang C, Ren S, Dai S, Lai S, Age, gender and metabolic syndrome-related coronary heart disease in U.S. adults, *Int J Cardiol*. 2005, 104(3), pp. 288-291.
10. Park JS, Lee HC, Lee HW, Ahn SG, Cha KS, Hong TJ, Kim SP, Kim YD, Lee SK, Kim HK, Jeong MH, Prognosis according to the timing of percutaneous coronary intervention in non-ST segment elevation myocardial infarction, based on the Korean Acute Myocardial Infarction Registry (KAMIR), *Cardiol J*. 2011, 18(4), pp. 421-429.
11. Bashir ME, Lee DG, Li M, Bae JW, Shon HS, Cho MC, Ryu KH, Trigger Learning and ECG Parameter Customization for Remote Cardiac Clinical Care Information System, *IEEE Trans Inf Technol in Biomed* 2012, 16(4), pp. 561-71.
12. Nam Yoon Kim, In Hyae Park, Myung Ho Jeong, Sook Ja Lee, Dong Han Kim, Gi Hong Lee, Min Goo Lee, Doo Sun Sim, Keun-Ho Park, Nam Sik Yoon, Hyun Ju Yoon, Kye Hun Kim, Young Joon Hong, Ju Han Kim, Youngkeun Ahn, Jeong Gwan Cho, Jong Chun Park, and Jung Chae Kang, " Comparison of Clinical Outcomes between ST-Segment Elevation Myocardial Infarction and Non-ST-Segment Elevation Myocardial Infarction in Patients Younger Than 40 Years Who Underwent Percutaneous Coronary Artery Intervention", *The Korean Journal of Medicine: vol. 82, No. 2, 2012, 175-184.*

Application of pig model in development of a simple mechanical anastomosis device

J. S. Kim, S. H. An, K. S. Jeon, S. D. Kim, D. B. Kim, C. Y. Kim*

Laboratory Animal Center (LAC), Daegu-Gyeongbuk Medical Innovation Foundation (DGMIF), Daegu, Korea

E-mail: jskim@dgmif.re.kr

Abstract— This project was funded by grants from the technological innovation project, the Small and Medium Business Administration (SMBA) of Korea. Dentis Co., Ltd and Keimyung University Dongsan Medical Center have designed a pilot type of an anastomotic ring device. In vivo biocompatibility was assessed with following evaluations: epithelization, foreign body reaction, suitable thickness and width of the ring device. For evaluation, we applied prototype devices manufactured in several different design in micro-pig model that contain similar size of jugular vein compared to humans at Daegu-Gyeongbuk Medical Innovation Foundation-Laboratory Animal Center (DGMIF-LAC).

Keywords— Anastomosis, Titanium, Inflammation

I. INTRODUCTION

Hand-sewn anastomotic technique used for suture anastomosis is one of surgery processes required for long operating time. The objective of this project, therefore, is to develop a new simple anastomotic ring device capable of uniting vessels diameters to reduce the operating time.

II. METHODS

A. Using experimental devices

The scope of this venture is to create a commercially available vascular coupling device that would allow surgeons to quickly attach vessels together. The ring device is designed to increase reliability and reduce the amount of time spent on connecting two vessels.

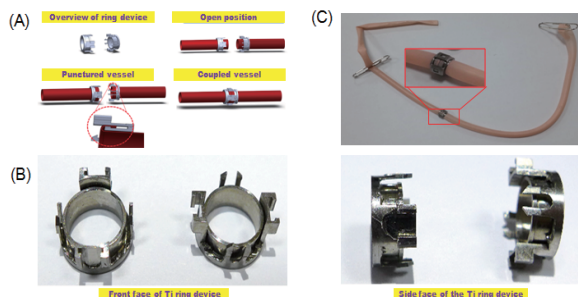


Fig. 1. (A) The design of the device, (B) The fabricated titanium ring device, (C) Bench testing of the ring device.

B. Animal experimental process

First step, *in vivo* biocompatibility and suitable size of the rings was tested through that the ring devices were placed on external jugular vein. The experiment was carried out on 2 pigs of 10 month-old, with body weights of 25~30 kg. Implants made of titanium, measuring 4~8 mm width and 0.1~0.125 mm thickness, were used.

III. RESULTS

The ring device with 6 mm width and 0.125 mm thickness was the most suitable one without vessels strain. Histologic and hematopathological evaluations revealed no sign of inflammation and fibrosis at the anastomosis site. The pigs were kept under observation for 8 weeks, and body weight of pigs was normally observed after implantation.

Cytotoxicity and systemic toxicity represents the easily method for the analysis of detrimental effects of substances and allows a rapid and sensitive diagnosis of the biological reactivity of diffusible components of test materials. Therefore, the rings were tested for cytotoxicity and systemic toxicity according to the ISO 10993 standard. Biological safety test revealed no sign of toxicity.

IV. CONCLUSION

The biocompatibility was tested through that the ring devices were placed on external jugular vein during 4 weeks. Histological and hematopathological evaluations showed complete epithelization with no sign of foreign body reaction. Furthermore, 6 mm width and 0.125 mm thickness of the ring device was the most suitable one without vessels strain. Next step, we will perform end-to-end anastomosis using a sutureless anastomotic device that is suitable for repairing damaged blood vessels and inserting vein grafts in animal model having injured vessel.

REFERENCES

1. Vilhjalmsón DÍ, Olofsson P, Syk I, Thorlacius H, and Grönberg A, The compression anastomotic ring-locking procedure: a novel technique for creating a sutureless colonic anastomosis. *Eur Surg Res.* 2015;54(3-4):139-47

Establishment of evaluation method for wearable cardiac defibrillators in a pig model with induction of cardiac arrhythmia

K. S. JEON¹, S. D. KIM¹, D. B. KIM¹, S. H. AN¹, J. S. KIM¹,
S. T. SEO², J. H. HONG², C. Y. KIM^{1*}

¹Laboratory Animal Center (LAC), Daegu-Gyeongbuk Medical Innovation Foundation (DGMIF), Daegu, Korea,

²Medical Device Development Center, Daegu-Gyeongbuk Medical Innovation Foundation (DGMIF), Daegu, Korea

E-mail: eksq16342@naver.com

Abstract—We have developed an wearable (non-implantable type) defibrillator that is able to detect cardiac arrhythmia followed by defibrillation. We established a pig model that cardiac arrhythmia were induced by ventricular fibrillation (VF) termination generated with an implantable cardiac defibrillator (ICD) shock, and tested the performance of a prototype of wearable cardiac defibrillator (WCD). In order to induce a cardiac arrhythmia, the micro-pigs were given inappropriate shocks by ICD lead accessed through an external jugular vein under C-arm guidance.

Keywords—Cardiac arrhythmia, Ventricular fibrillation, ICD, WCD, Arrhythmia pig model,



Fig. 1. Experimental devices

I. INTRODUCTION

Sudden cardiac death (SCD) is one of the leading causes of death. Performance of defibrillation in the early stage of cardiac arrhythmia dramatically increases survival rate and prognosis of the cardiac arrest patients. An automated defibrillator placed in the body is helpful to make the patient better, however, implantation of the device is also a burden requiring surgical operation and maintenance of the device such as battery charging.

II. METHODS

A. Devices

Implantable cardiac defibrillator (ICD) is existing device used cardiac arrest. In this experiment, we used ICD to induce cardiac arrhythmia with program that controls the ICD (Fig. 1a). And the new developed wearable cardiac defibrillator is operated automatically by Electrocardiogram (ECG) signal detection when cardiac arrhythmia (Fig. 1b).

B. Animal experiment

To induce a cardiac arrhythmia, the micro-pigs were generated ventricular fibrillation (VF) termination by giving inappropriate electrical shocks by ICD. We checked immediate working of wearable cardiac defibrillator (WCD) by immediate Electrocardiogram (ECG) detection when VF is induced.

III. RESULTS

A. Evaluation of performance

The ECG shows operating state of wearable cardiac defibrillator (WCD). Implantable cardiac defibrillator (ICD) was occurred ventricular tachycardia (VT) and then ventricular fibrillation (VF) induction by inappropriate electrical shocks. When cardiac arrest is occurred in the pig, WCD gave shocks automatically by Electrocardiogram (ECG) signal detection.

IV. CONCLUSION

As the result of our study, an arrhythmia pig model and the evaluation method are successfully established, and we tested immediate operation of WCD worked by immediate Electrocardiogram (ECG) signal detection when a cardiac arrest is occurred. DGMIF-LAC is trying to make additional value creation by collaborative project and we have successfully carried out customized performance evaluation for a new developed medical device, which is the one of goals of the DGMIF-LAC.

REFERENCES

1. Nascimento FO1, Krishna RK, Hrachian H, and Santana O, Wearable cardioverter defibrillator in stress cardiomyopathy and cardiac arrest, *BMJ Case Re.*, 2013 Sep 13.

Motion noise reduction from wrist-type Photoplethysmography(PPG) Based on Empirical mode decomposition

S.J. Hong¹, S.H. Song¹, D.H. Kim¹, S.I. Kang¹, J.S. Lee¹ and I.Y. Kim¹
BIOMEDICAL ENGINEERING, HANYANG UNIVERSITY, SEOUL, KOREA¹
E-mail: sungjun@bme.hanyang.ac.kr

Abstract— In this study, we developed a new photoplethysmography (PPG) signal sensing method using a wrist type device. PPG signal is a noninvasive method for detecting the blood volume pulse wave generated by the elastic nature of the peripheral vascular arteries using an electro-optical technique. However, the inherent weakness behind PPG is that in addition to the volumetric changes caused by the blood pulse, there are many other factors such as motion artifact. To reduce motion artifact, we proposed an Empirical Mode Decomposition (EMD) based motion noise cancellation method

Keywords— PPG, Motion artifact, Empirical Mode Decomposition.

I. INTRODUCTION

PPG is vulnerable to motion artifact, and uncomfortable to wear for a long periods of time. Therefore, we developed a wrist type PPG monitoring system and proposed a new method for motion artifact reduction based on EMD.

II. METHODS

A. EMD Basic

The starting point of the EMD is to consider oscillations in signals at a very local level. In fact, if we look at the evolution of a signal $x(t)$ between two consecutive extrema(maxima and minima), we can heuristically define a high-frequency part, or local detail, which corresponds to the oscillation terminating at the two minima and passing through the maximum which necessarily exists in between them [1].

Given a signal $x(t)$, the effective algorithm of EMD can be summarized as follows .

1. Identify all extrema of $x(t)$
2. Interpolate between minima (maxima), resulting with some envelope $e_{\min}(t)$ ($e_{\max}(t)$)
3. Compute the mean $m(t) = (e_{\min}(t) + e_{\max}(t)) / 2$
4. Extract the detail $d(t) = x(t) - m(t)$
5. Iterate on the residual $m(t)$

B. Motion noise reduction process by EMD

1. Detect human motion state with motion sensor.
2. Detect the extreme PPG signal value.
3. Connect all the local maxima extreme value by spline interpolation method as the upper envelope.

4. Connect all the local minima extreme value by spline interpolation method as the lower envelope.

5. Take their average of upper envelop and lower envelop to yield a lower frequency component than the original PPG signal.

6. By subtracting envelop mean from the original signal, the high frequency component pattern is eliminated.

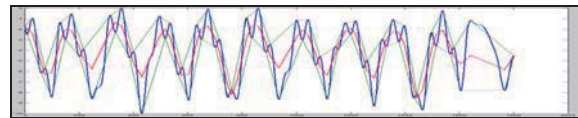


Fig.3 Motion noise reduction process
(Blue: Before processing, Green: interpolation signal, Red: After processing)

III. RESULTS

The results show that the proposed wrist type PPG and motion noise reduction method. Reduces motion noise artifact and assesses the R-R interval results.

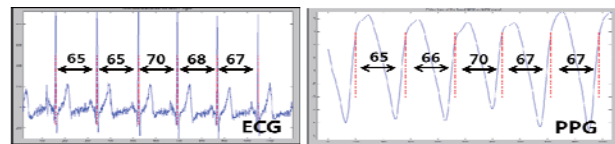


Fig.7 After application of the algorithm

IV. CONCLUSION

Experiments proved the efficiency of the proposed method. In the future, we plan to compare the proposed device against other commercialized devices such as Holter type ECG device for the other motion noise reduction results.

ACKNOWLEDGEMENT

This work was partly supported by the ICT R&D program of MSIP/IITP [10045452, Development of Multimodal Brain-Machine Interface System Based on User Intent Recognition] and the NRL program of MOST/KOSEF[10045452,Development of Multimodal Brain-Machine Interface System Based on User Intent Recognition]

REFERENCES

1. N.E. Huang, Z. Shen, and H.H Liu, The empirical mode decomposition and Hilbert spectrum for nonlinear and nonstationary time series analysis, Proc. Roy. Soc. London A, Vol. 454. pp. 903-995, 1988.

The Development of Convergence Diagnostic Mobile Device and Platform

J. Y. Lee¹, W. S. Kim², J. E. Lee¹, H. Kim^{1,2}

¹Department of Medical Device Management and Research, SAIHST, Sungkyunkwan University, Suwon, Korea

²Division of Pulmonary and Critical Care Medicine, Samsung Medical Center, Seoul, Korea

E-mail: hj3425.kim@samsung.com

Abstract— Due to IT convergence technology, mobile healthcare has emerged as an industry with great prospects. Hardware technologies have been spread to all medical fields including diagnostic medicine. So, in this study, we planned to develop a brand new mobile healthcare device which integral various sensors that measure multiple bio-signals and plus, a new healthcare platform that embedded variable diagnostic algorithms and clinical data. We expect that the new convergence device and platform will bring several economical and clinical benefits.

Keywords— Convergence, Mobile Healthcare Device, Diagnostic Device, Platform

I. INTRODUCTION

As BT and IT technology has been developed, convergence mobile healthcare device has attracted great attention. [1] Many mobile healthcare devices are being released with wireless technology and diverse sensors.

The *QARDIOCORE* from Qardio, Fig 1, is a wearable device which records and analyzes over 20 million data points a daily via sensors. It records ECG, body temperature, respiratory rate and stress level.



Fig 1. QARDIOCORE

Fig 2-A is *AliveCor Mobile ECG* from AliveCor company. It can be used as a smart phone case and electrodes are at the back of the case. Placing fingers on the electrodes then ECG is checked within 30 seconds. It is wirelessly communicate with the Alive ECG application. This is a medical device which already cleared FDA approval. [2, 3]



Fig 2-A. AliveCor ECG



Fig 2-B. Scout

The *Scout* from Scanadu, Fig 2-B, looks like hockey puck. It measures ECG, body temperature, blood pressure, oximetry and more in about 10 seconds after placing the device on the forehead. Using acquired data, 15 diseases could be diagnosed.

But still, platforms which combine various algorithms for diagnosis are insufficient in mobile healthcare device.

II. METHODS

Thus, we planned to develop a new concept medical device and platform system which communicates each other and includes variable diagnostic algorithms.

A. Convergence Device Development

The aimed device will include multiple sensors to measure PPG, ECG, PSG and more in mobile size. Placing the device itself at different location of the body or using accessories, acquires valuable bio-signals. This medical data could be shared with doctors and others through wireless communication.

B. Healthcare Platform Development

Various diagnostic algorithms and clinical diagnosis data will be included in the new healthcare platform as shown in Fig 3.

Diagnostic Algorithms – Several algorithms for convergence diagnosis are being developed such as cardiopulmonary diagnostic algorithm, fetal and maternal diagnostic algorithm.

Clinical Diagnostic Data – The diagnostic results will be digitalized based on clinicians' interview and auscultation. Also, clinicians' advice on related diseases will be digitalized for convergence diagnosis.

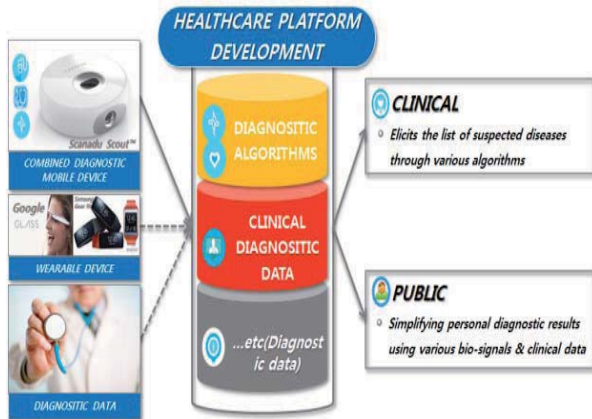


Fig 3. Healthcare Platform

III. RESULTS

The new convergence device is expected to bring several economical and clinical benefits. In the economical aspect, there will be no need to develop a device separately for use of experts and non-medical professionals. Both clinical experts and public markets are targeted with one device at the same time. In addition, it will be an opportunity that creates a new healthcare platform market. In clinically, it is expected to increase the reliability and objectivity of treatment via various bio-signals. Also, it will be able to guide primary clinical organizations which have little experience. Lastly, it will allow the telemedicine through real-time data that monitoring patients.

IV. CONCLUSION

Through the study, it revealed that mobile technology, use of multiple sensors and convergence healthcare platform are key features for future healthcare systems. We believe that developing a mobile healthcare device which uses multiple sensors and obtains bio-signals together with new diagnostic platform will be a chance to improve the quality of life.

ACKNOWLEDGEMENT

This research was supported by the Ministry of Science, ICT and Future Planning and National Research Foundation of Korea (NRF) through ‘Development of Mobile Cardiopulmonary Diagnosis Device’ project. (NRF-2014M3A9E2062267).

REFERENCES

1. Jeong-Heon Kim, Seung-Chul Lee, Boon-Giin Lee, and Wan-Young Chung, “Mobile Healthcare System Based on Buletooth Medical Device,” Journal of Sensor Science and Technology., vol. 21, No.4 (2012) pp. 241-248
2. 임팩트 편집부, *IoT 로 주목받는 스마트 헬스케어 시장전망 및 개발동향*. 임팩트, 2015.

3. 이보경, *스마트 헬스케어 시장을 여는 열쇠, 모바일 의료기기*, kt 경제경영연구소, 2014
4. Ee-May Fong and Wan-Young Chung, “Mobile Cloud-Computing-Based Healthcare Service by Noncontact ECG Monitoring,” Sensors 2013, 13, 16451-16473
5. Sandeep Kumar Vashist, E. Marion Schneider and John H.T. Luong, “Commercial Smartphone-Based Devices and Smart Applications for Personalized Healthcare Monitoring and Management,” Diagnostic 2014, 4, 104-128
6. Caroline Free, Gemma Phillips, Louise Watson, Leandro Galli, Lambert Felix, Phil Edwards, Vikram Patel and Andy Haines, “The Effectiveness of Mobile-Health Technologies to Improve Health Care Service Delivery Processes: A Systematic Review and Meta-Analysis,” PLOS Medicine 2013
7. Tae-Soo and Joo-Hyun Hong, “Current Developments of Biomedical Mobile Devices for Ubiquitous Healthcare,” J.Biomed. 185-190, 2009.

Prediction of the Effect of IABP pumping phase on Ventricular Mechanics by using 3D Cardiac Electromechanical Model

K. M. Lim¹, and E. B. Shim²

¹Department of Medical IT Convergence Engineering, Gumi, Republic of Korea

²Department of Mechanical & Biomedical Engineering, Chuncheon, Republic of Korea

E-mail: kmlim@kumoh.ac.kr

Abstract— An intra-aortic balloon pump (IABP) is realized via counter-pulsation of the IABP. The purpose of this study is to predict the effect of IABP pumping phase on ventricular mechanics by using 3D cardiac electromechanical model.

Keywords— Intra aortic balloon pump (IABP), cardiac electromechanical model, Ventricular mechanics

I. INTRODUCTION

An intra-aortic balloon pump (IABP) is realized via counter-pulsation of the IABP. Appropriate inflation timing is important in order to produce a rapid rise in aortic diastolic pressure (optimize augmentation), thereby increasing O₂ supply to coronary circulation. Deflation timing is also important because of reducing aortic end diastolic pressure (afterload), thereby decreasing MVO₂ while improving the CO (cardiac output). However, there are common timing errors of balloon inflation and deflation. The purpose of this study is to predict the effect of IABP pumping phase on ventricular mechanics by using 3D cardiac electromechanical model.

II. METHODS

A. Model description

The ventricular mechanics component was based on the continuum mechanics equations, with the myocardium assumed to be an orthotropic, hyperelastic, nearly incompressible material defined by an exponential strain energy function. The mechanics model of the ventricles comprised 356 nodes and 172 elements in terms of Hermite polynomial interpolation. Myofilament model by Rice et al. [1] was incorporated to the mechanical model.

B. Model of IABP function

Briefly, the IABP component was modeled as the time-varying compliance of the systemic arteries. To generalize the patterns of inflation and deflation of an IABP, a harmonic waveform was used for the time-varying compliance of the systemic arteries. The harmonic waveforms for the compliance of the aorta were expressed as follows:

$$C_{SA,IABP}(t) = C_{SA} \times SF_{IABP}(t) \quad (1)$$

$$SF_{IABP}(t) = (1 - sf) + sf \times \cos\left(\frac{2\pi t}{CL} - \phi\right) \quad (2)$$

Here, $C_{SA,IABP}$ is the time-varying compliance of the systemic arteries with the IABP, C_{SA} is the compliance of the systemic arteries without the IABP, SF_{IABP} is a scale factor for the IABP, sf is the level of the scale factor, BCL indicates the cycle length of the ventricle, and indicates the time shift between the ventricular contraction cycle and IABP inflation cycle. The sf is major parameter which is proportional to the stroke volume of IABP and related to the pumping compliance of IABP. In this study, sf was given values of 0.05, 0.1, 0.15, 0.2, and 0.25, and was set to 3.66 radians (350ms shift), instead of end-systole.

III. RESULTS

Under counter-pulsation phase provided minimum tension distribution and contractile ATP consumption rate. However co-pulsation phase provided maximum tension distribution and contractile ATP consumption rate (Fig. 1).

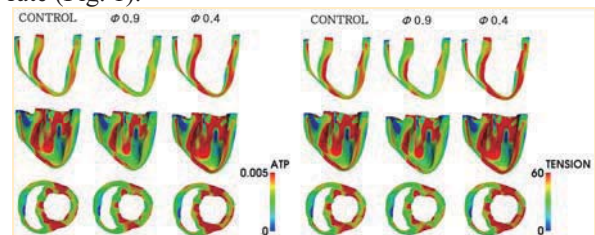


Fig. 1 Transmural distribution of myocardial contractile ATP consumption rate and tension under control (no IABP), 0.9 phase (counter-pulsation), and 0.4 phase (co-pulsation).

IV. CONCLUSION

According to the results (Fig. 1), appropriate IABP timing is very important for ventricular unloading and energy efficacy. Optimal counter-pulsation lead to reduce largest amount of afterload and ATP consumption.

ACKNOWLEDGEMENT

"This research was partially supported by IITP (IITP-2015-H8601-15-1011), NRF (NRF-2011-0009335), and QWL (N0000842) Program"

REFERENCES

1. Rice, John Jeremy, et al. "Approximate model of cooperative activation and crossbridge cycling in cardiac muscle using ordinary differential equations." *Biophysical journal* 95.5 (2008): 2368-2390.

Combined Effect of LVAD and CRT on Cardiac Electromechanical Delay: a Simulation Study

A. K. Heikhmakhtiar¹, A. J. Ryu², Y. S. Kim¹, E. B. Shim², and K. M. Lim^{1*}

¹Department of Medical IT Convergence Engineering, Kumoh National Institute of Technology, Gumi, Republic of Korea

²Department of Mechanical and Biomedical Engineering, Kangwon National University, Chuncheon, Republic of Korea

E-mail: kmlim@kumoh.ac.kr

Abstract—Electromechanical delay (EMD) is very important to the performance of the hemodynamic of the heart. Using computer simulation, we studied the effect of LVAD and CRT combined to the EMD in canine ventricle models which designed to have long conduction velocity. The result shows that, regardless of the CRT pacing spot, LVAD contribute the most to shorten EMD in heart.

Keywords— ventricular model, electromechanical delay, LVAD, CRT, and computational study.

I. INTRODUCTION

Heart Failure is the major cause of death around the world. In this era there are many artificial organ to support heart failure such as cardiac resynchronization therapy (CRT) and left ventricular assist device (LVAD). The goal of this study is to computationally examine the effect of combination of CRT and LVAD as the heart failure treatment to the electromechanical delay (EMD). EMD is the time interval between cardiac electrical activation time (EAT) and cardiac mechanical activation time (MAT) [1]. We try to analyze the effect of both devices (CRT and LVAD) in order to find the best way to recover patient whom suffer from long EMD in order to prevent or treat heart failure.

II. METHODS

A. Electromechanical Model

To construct an integrated model of LVAD & CRT implanted cardiovascular system, we combined 3D MR imaged based electromechanical model of canine ventricle with a lumped model of the circulatory system, LVAD function, and CRT model [2].

B. Simulation Protocol

We simulate 8 different simulation distinguished by LVAD usage and CRT pacing site. 4 models were integrated with LVAD function (LVAD group) and the other 4 were not combined (control group). Each simulation will have unique CRT pacing site which are sinus rhythm, lvpacing, rvpacing, and bipacing pacing.

C. Data Analysis.

We analyze the ATP consumption rate & EMD for each simulation. EMD was defined by interval time of

the local EAT and local MAT. The EAT defined when the local transmembrane voltage exceeded 0 mV. The MAT defined as the 10% of the strain lowest value [1].

III. RESULTS

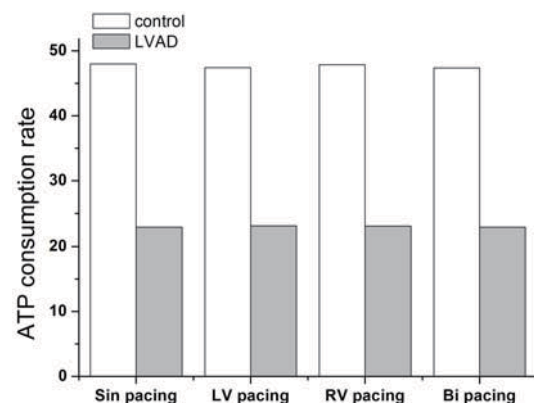


Fig. 1. ATP

A. ATP Consumption Rate

Fig. 1 shows the energy consumption in terms of ATP consumption rate for control and LVAD groups and in all CRT pacing sites (sinus rhythm, LV, RV and bipacing). Overall the ATP consumption were higher in control group compared to the LVAD group. This is showing that under LVAD treatment, the heart works better with low energy consumption regardless the CRT initiation pacing site. The ATP consumption rates were similar for each group. For the control group, the ATP consumption rates were approximately 47, and for the LVAD group, the ATP consumption rates were approximately 23.

IV. CONCLUSION

CRT initiation pacing spot has not significant impact to the EMD while LVAD performs significantly not only to reduce EMD but also energy consumption.

REFERENCES

1. V. Gurev et al., "Distribution of electromechanical delay in the heart: insights from a three-dimensional electromechanical model," *Biophysical Journal*, vol. 99, pp. 745-754, 2010.
2. K. M. Lim et al., "Comparison of the effects of continuous and pulsatile left ventricular-assist device on ventricular unloading using a cardiac electromechanics model," *The Journal of Physiological Science*, Vol. 62, pp. 11-19, 2012.

Effects of the Mechanical Properties of the Atherosclerotic Coronary Wall on Fibrous Cap Stress

J.H. Park, M. Kang, and K. Rhee

Department of Mechanical Engineering, Myongji University, Yongin, Republic of Korea
E-mail: khanrhee@mju.ac.kr

Abstract— An ideal three dimensional coronary artery with an eccentric stenosis was modeled. Transient fluid-structure interaction (FSI) analysis was performed using the commercial software, and stenotic wall stress was analyzed. The maximum stresses are found in the fibrous cap region, and the peak stress is about 50% higher for the soft lipid core model comparing to the stiff lipid core model.

Keywords— Vulnerable plaque, stress, fluid structure interaction, coronary artery

I. INTRODUCTION

Acute coronary syndrome is one of the leading causes of death, which is related to the rupture of atherosclerotic plaque. Rupture of a fibrous cap is related to the mechanical stress. It has been shown that cap and lipid core thickness has a significant influence on cap stress [1]. The aim of this study is to investigate the variation of mechanical properties of atherosclerotic plaque on wall stress distribution in the idealized coronary artery model

II. METHODS

An ideal three dimensional coronary artery with an eccentric stenosis was modeled. The lumen diameter was 3mm and the length of a stenosis was 8 mm. The area reduction was about 36% at the throat. The vessel wall thickness was 1mm, and the stenotic wall was composed of thin fibrous cap (40 μm) and lipid core (2 mm) at its thickest region. The mechanical property of vessel wall, lipid core, and fibrous cap were assumed to be hyperelastic, and they were modeled using the Mooney-Rivlin model. The various material properties were based on the literature [2] transient fluid-structure interaction (FSI) analysis was performed using the commercial software ADINA (ADINA R&D Inc., MA). Local change of the material property of fibrous cap was considered. The computational domain was divided into meshes for a finite element analysis

III. RESULTS

In order to clarify the effects of material properties of the lipid pool, the parameter of strain energy function of the Mooney-Rivlin model, which is proportional to the elastic modulus, was reduced from

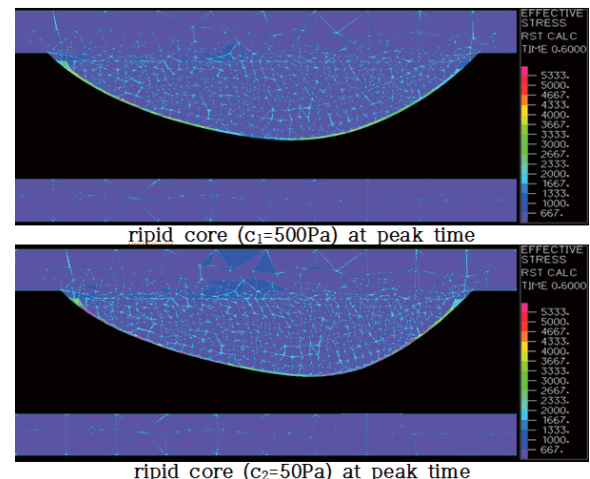


Fig. 1. Distribution of stress at peak flow

500Pa to 50Pa while other parameters were kept constant. Distribution of effective stress within the wall at peak flow (0.6 s) in the central axial cross section is shown in Fig. 1. The peak stresses are found in the fibrous cap region, and they are 8.54kPa and 5.60kPa for soft and stiff lipid core model, respectively. Because the material properties of the wall and plaque components affect peak wall stress, they should be carefully considered to predict rupture of the vulnerable plaque.

IV. CONCLUSION

Mechanical property of lipid core affected the cap stress, and soft core increased the cap stress about 50%. Because the mechanical properties of atherosclerotic wall affect the wall stress, they should be carefully considered for prediction of atherosclerotic plaque rupture.

ACKNOWLEDGEMENT

This work was supported by the Research Fund (NRF-2014R1A2A1A11051357).

REFERENCES

1. A. C. Akyildiz et al, "Effects of intima stiffness and plaque morphology on peak cap stress," *Biomedical Eng Online*, vol. 19, pp. 25, 2011.
2. C. A. Holzapfel et al, "Computational approaches for analyzing the mechanics of atherosclerotic plaque: A review," *J Biomech*, vol. 47, pp. 859-869, 2014.



PUBLISHED BY

The Korean Society of Medical & Biological Engineering

1407, Seocho World Office Build., 19, Seoun-ro, Seocho-gu,
Seoul 06732, Korea

Tel: 02-921-8551, 8552, Fax: 02-921-8502

Email: kosombe@kosombe.or.kr

PRINTED BY

MEDrang Inc.

8-17 Worldcupbuk-ro 5ga-gil, Mapo-gu, Seoul 04001, Korea

Tel: 02-325-2093, Fax: 02-325-2095

E-mail: info@medrang.co.kr

Homepage: www.medrang.co.kr